frontiers | Research Topics

Drug discovery in cancer research: success stories and open challenges

Edited by
Tashinga E. Bapiro, Wagdy Mohamed Eldehna and Viviana di Giacomo

Published in
Frontiers in Pharmacology
Frontiers in Oncology

FRONTIERS EBOOK COPYRIGHT STATEMENT

The copyright in the text of individual articles in this ebook is the property of their respective authors or their respective institutions or funders. The copyright in graphics and images within each article may be subject to copyright of other parties. In both cases this is subject to a license granted to Frontiers.

The compilation of articles constituting this ebook is the property of Frontiers.

Each article within this ebook, and the ebook itself, are published under the most recent version of the Creative Commons CC-BY licence. The version current at the date of publication of this ebook is CC-BY 4.0. If the CC-BY licence is updated, the licence granted by Frontiers is automatically updated to the new version.

When exercising any right under the CC-BY licence, Frontiers must be attributed as the original publisher of the article or ebook, as applicable.

Authors have the responsibility of ensuring that any graphics or other materials which are the property of others may be included in the CC-BY licence, but this should be checked before relying on the CC-BY licence to reproduce those materials. Any copyright notices relating to those materials must be complied with.

Copyright and source acknowledgement notices may not be removed and must be displayed in any copy, derivative work or partial copy which includes the elements in question.

All copyright, and all rights therein, are protected by national and international copyright laws. The above represents a summary only. For further information please read Frontiers' Conditions for Website Use and Copyright Statement, and the applicable CC-BY licence.

ISSN 1664-8714
ISBN 978-2-8325-6343-4
DOI 10.3389/978-2-8325-6343-4

About Frontiers

Frontiers is more than just an open access publisher of scholarly articles: it is a pioneering approach to the world of academia, radically improving the way scholarly research is managed. The grand vision of Frontiers is a world where all people have an equal opportunity to seek, share and generate knowledge. Frontiers provides immediate and permanent online open access to all its publications, but this alone is not enough to realize our grand goals.

Frontiers journal series

The Frontiers journal series is a multi-tier and interdisciplinary set of open-access, online journals, promising a paradigm shift from the current review, selection and dissemination processes in academic publishing. All Frontiers journals are driven by researchers for researchers; therefore, they constitute a service to the scholarly community. At the same time, the *Frontiers journal series* operates on a revolutionary invention, the tiered publishing system, initially addressing specific communities of scholars, and gradually climbing up to broader public understanding, thus serving the interests of the lay society, too.

Dedication to quality

Each Frontiers article is a landmark of the highest quality, thanks to genuinely collaborative interactions between authors and review editors, who include some of the world's best academicians. Research must be certified by peers before entering a stream of knowledge that may eventually reach the public - and shape society; therefore, Frontiers only applies the most rigorous and unbiased reviews. Frontiers revolutionizes research publishing by freely delivering the most outstanding research, evaluated with no bias from both the academic and social point of view. By applying the most advanced information technologies, Frontiers is catapulting scholarly publishing into a new generation.

What are Frontiers Research Topics?

Frontiers Research Topics are very popular trademarks of the *Frontiers journals series*: they are collections of at least ten articles, all centered on a particular subject. With their unique mix of varied contributions from Original Research to Review Articles, Frontiers Research Topics unify the most influential researchers, the latest key findings and historical advances in a hot research area.

Find out more on how to host your own Frontiers Research Topic or contribute to one as an author by contacting the Frontiers editorial office: frontiersin.org/about/contact

Drug discovery in cancer research: success stories and open challenges

Topic editors

Tashinga E. Bapiro — AstraZeneca, United Kingdom

Wagdy Mohamed Eldehna — Kafrelsheikh University, Egypt

Viviana di Giacomo — University of Studies G. d'Annunzio Chieti and Pescara, Italy

Citation

Bapiro, T. E., Eldehna, W. M., di Giacomo, V., eds. (2025). *Drug discovery in cancer research: success stories and open challenges*. Lausanne: Frontiers Media SA.

doi: 10.3389/978-2-8325-6343-4

Table of contents

06 Impact of oseltamivir on the risk of cancer
Pei-Hua Chuang, Bor-Show Tzang, Chih-Chen Tzang, Chun-Ching Chiu, Chun-Yu Lin and Tsai-Ching Hsu

14 Targeted intracellular delivery of dimeric STINGa by two pHLIP peptides for treatment of solid tumors
Anna Moshnikova, Michael DuPont, Marissa Iraca, Craig Klumpp, Hannah Visca, Dana Allababidi, Phoebe Pelzer, Donald M. Engelman, Oleg A. Andreev and Yana K. Reshetnyak

26 Case report: Cutaneous metastases as a first manifestation from breast cancer with concurrent gastric metastases
Lulu Xu, Congcong Wang, Xiaoling Yang and Liangliang Dong

37 Article review: Brazilin as potential anticancer agent
Callista Najla Raptania, Syifa Zakia, Alistia Ilmiah Fahira and Riezki Amalia

46 Discovery of a novel natural compound, vitekwangin B, with ANO1 protein reduction properties and anticancer potential
Yohan Seo, Sion Lee, Minuk Kim, Dongguk Kim, Sung Baek Jeong, Raju Das, Armin Sultana, SeonJu Park, Nguyen Xuan Nhiem, Phan Thi Thanh Huong, Oh-Bin Kwon, Wan Namkung and Joohan Woo

57 Activation of p53 signaling and regression of breast and prostate carcinoma cells by spirooxindole-benzimidazole small molecules
Assem Barakat, Saeed Alshahrani, Abdullah Mohammed Al-Majid, Abdullah Saleh Alamary, Matti Haukka, Marwa M. Abu-Serie, Alexander Dömling, Luis R. Domingo and Yaseen A. M. M. Elshaier

79 Marine-derived EGFR inhibitors: novel compounds targeting breast cancer growth and drug resistance
Qi Li, Bo Li, Qian Wang, Chengen Wang, Miao Yu and Tianfu Xu

91 Benserazide, a cystathionine beta-synthase (CBS) inhibitor, potentially enhances the anticancer effects of paclitaxel via inhibiting the S-sulfhydration of SIRT1 and the HIF1-α/VEGF pathway
Wei Zhao, Shasha Feng, Jian Wang, Zhenshuai Zhang, Lu Chen, Li Jiang, Ming Li and Tianxiao Wang

106 QL1604 combined with bevacizumab as an innovative first-line treatment for HCC patient with extensive metastasis who showed remarkable effect: a case report
Yanzhi Wan, Keqin Tan and Hong Zhu

111 Niraparib for the treatment of metastatic ccRCC in a patient with *CDK12* and *RAD51C* mutations: a case report
Xiaolong Yue, Chenkang Yang, Dandan Cao and Yue Li

116 Repurposing therapy of ibrexafungerp vulvovaginal candidiasis drugs as cancer therapeutics
Tedi Rustandi, Abdul Mahmud Yumassik, Fitrah Shafran Ilahi, Riza Alfian, Erna Prihandiwati, Yugo Susanto, Yudi Hardi Susilo, Maria Ulfah and Faizatun Faizatun

121 Sugemalimab combined with chemotherapy for the treatment of advanced esophageal squamous cell carcinoma: a cost-effectiveness analysis
Hongfu Cai, Ling Fang and Zhiwei Zheng

131 Structure-based screening of FDA-approved drugs identifies potential histone deacetylase 3 repurposed inhibitor: molecular docking and molecular dynamic simulation approaches
Anas Shamsi, Mohd Shahnawaz Khan, Dharmendra Kumar Yadav and Moyad Shahwan

142 Nutrient vitamins enabled metabolic regulation of ferroptosis via reactive oxygen species biology
Junjie Wu, Yanting Shi, Man Zhou, Min Chen, Shuying Ji, Xingxing Liu, Mengjiao Zhou, Rui Xia, Xiaohua Zheng and Weiqi Wang

154 Case report: Pyrotinib and tegafur combined with radiotherapy achieved notable response in HER2-amplified rectal cancer with multiple metastases after multiline treatments
Peng Huang, Feng Wen and Xin Wang

161 CAR-T therapy pulmonary adverse event profile: a pharmacovigilance study based on FAERS database (2017–2023)
Jing Shi, Xinya Liu, Yun Jiang, Mengjiao Gao, Jian Yu, Yuanming Zhang and Li Wu

172 Dual roles of inflammatory programmed cell death in cancer: insights into pyroptosis and necroptosis
Shuai Wang, Huanhuan He, Lailiang Qu, Qianhe Shen and Yihang Dai

183 A case report: deep and durable response to low-dose lenvatinib and tislelizumab in an elderly patient with advanced intrahepatic cholangiocarcinoma
Pei Zhang, Xin Wang, Ruizhen Li, Xiaoying Li, Ke Cheng and Dan Cao

189 Case report: Treatment with ensartinib shows good response to SQSTM1-ALK fusion in lung adenocarcinoma
Pandeng Wang, Zhuo Jiang, Jianji Guo, Tao Liu, Zhen Liu, Dongdong Wang and Honglin Li

195 PU-H71 (NSC 750424): a molecular masterpiece that targets HSP90 in cancer and beyond
Sameh Saber, Rasha Abdelhady, Mai A. Elhemely, Elsayed A. Elmorsy, Rabab S. Hamad, Mustafa Ahmed Abdel-Reheim, Attalla F. El-kott, Mohammed A. AlShehri, Kareem Morsy, Ali S. AlSheri and Mahmoud E. Youssef

222 Efficacy and safety of regorafenib for the treatment of metastatic colorectal cancer in routine clinical practice: results from a Spanish hospital
Pilar Sotoca Rubio, Ana María Barrill Corpa, Víctor Alia Navarro, Patricia Pérez de Aguado Rodríguez, Jaime Moreno Doval, Juan Carlos Calvo Pérez, Patricia Guerrero Serrano, Carlos García Merino, Coral García de Quevedo Suero, Jorge Fernández-Fradejas, Juan José Serrano Domingo, Íñigo Martínez Delfrade, Blanca Isabel Morón García, María Reyes Ferreiro Monteagudo and Belén de Frutos González

230 Synthesis, characterization, and computational evaluation of some synthesized xanthone derivatives: focus on kinase target network and biomedical properties
Wisam Taher Muslim, Layth Jasim Mohammad, Munaf M. Naji, Isaac Karimi, Matheel D. Al-Sabti, Majid Jabir, Mazin A. A. Najm and Helgi B. Schiöth

246 Peritoneal chemotherapy delivery systems for ovarian cancer treatment: systematic review of animal models
Marcelo Simonsen, Rossana Verónica Mendoza López, Simone Maistro, Lucas Takeshi Ikeoka, Glaucia Fernanda de Lima Pereira, Ademar Benévolo Lugão, José Carlos Sadalla, Maria Lúcia Hirata Katayama and Maria Aparecida Azevedo Koike Folgueira

261 Long term survival of advanced hepatoid adenocarcinoma of lung secondary to idiopathic pulmonary fibrosis: a case report
Xiaoli Wang, Nan Wei, Huizhen Yang, Xiaoyan Wang, Xiaoju Zhang and Qianqian Zhang

266 Adverse drug reactions to atezolizumab in combination with bevacizumab in hepatocellular carcinoma patients: an analysis of the food and drug administration adverse event reporting system database
Wanming He, Lihua Tong, Yanling Yuan, Xia Yang, Wen Yang and Xingxi Pan

275 Discovery of highly potent and novel LSD1 inhibitors for the treatment of acute myeloid leukemia: structure-based virtual screening, molecular dynamics simulation, and biological evaluation
Ye Hong, Yuting Wang, Ziyi Hao, Xingxia Zhang, Yejun Si, Guoqiang Lin, Shurong Zhang, Miao-Miao Niu, Xiaotian Yang and Yanming Zhang

frontiers | Frontiers in Oncology

TYPE Original Research
PUBLISHED 26 February 2024
DOI 10.3389/fonc.2024.1329986

Check for updates

OPEN ACCESS

EDITED BY
Antonis Valachis,
Örebro University, Sweden

REVIEWED BY
Hong-Yue Lai,
China Medical University, Taiwan
Aglaia Schiza,
Uppsala University, Sweden

*CORRESPONDENCE
Chun-Yu Lin
linchunyumed@gmail.com
Tsai-Ching Hsu
htc@csmu.edu.tw

RECEIVED 01 November 2023
ACCEPTED 26 January 2024
PUBLISHED 26 February 2024

CITATION
Chuang P-H, Tzang B-S, Tzang C-C, Chiu C-C, Lin C-Y and Hsu T-C (2024) Impact of oseltamivir on the risk of cancer. *Front. Oncol.* 14:1329986. doi: 10.3389/fonc.2024.1329986

COPYRIGHT
© 2024 Chuang, Tzang, Tzang, Chiu, Lin and Hsu. This is an open-access article distributed under the terms of the Creative Commons Attribution License (CC BY). The use, distribution or reproduction in other forums is permitted, provided the original author(s) and the copyright owner(s) are credited and that the original publication in this journal is cited, in accordance with accepted academic practice. No use, distribution or reproduction is permitted which does not comply with these terms.

Impact of oseltamivir on the risk of cancer

Pei-Hua Chuang[1], Bor-Show Tzang[1,2,3,4], Chih-Chen Tzang[5], Chun-Ching Chiu[1,6], Chun-Yu Lin[7,8]* and Tsai-Ching Hsu[1,3,4]*

[1]Institute of Medicine, Chung Shan Medical University, Taichung, Taiwan, [2]Department of Biochemistry, School of Medicine, Chung Shan Medical University, Taichung, Taiwan, [3]Department of Clinical Laboratory, Chung Shan Medical University Hospital, Taichung, Taiwan, [4]Immunology Research Center, Chung Shan Medical University, Taichung, Taiwan, [5]School of Medicine, College of Medicine, National Taiwan University, Taipei, Taiwan, [6]Department of Neurology and Department of Medical Intensive Care Unit, Changhua Christian Hospital, Changhua, Taiwan, [7]Division of Allergy, Immunology, and Rheumatology, Department of Internal Medicine, Kaohsiung Veterans General Hospital, Kaohsiung, Taiwan, [8]School of Medicine, National Yang Ming Chiao Tung University, Taipei, Taiwan

Purpose: Mounting evidence has revealed the anti-cancer activity of various anti-viral drugs. Oseltamivir phosphate (OP), namely Tamiflu®, is routinely used to combat influenza infections. Although evidence has indicated the anti-cancer effects of OP *in vitro* and *in vivo*, little information is known about the effect of OP use on cancers in humans.

Methods: A nationwide population-based cohort study involving 13,977,101 cases with 284,733 receiving OP was performed to examine the association between OP use and cancers using the National Health Insurance Research Database in Taiwan between 2009 and 2018.

Results: The cohort study found that OP users showed a significantly lower incidence of lung cancer, colon cancer, liver, and intrahepatic bile duct cancer, oral cancer, pancreas cancer, esophagus cancer, stomach cancer, and prostate cancer. Additionally, OP users exhibited a lower risk of cancer-related mortality (adjusted HR=0.779; 95% confidence interval [CI] 0.743-0.817; p<0.001) and a reduced risk of developing liver cancer (adjusted HR=0.895; 95% CI 0.824-0.972; p=0.008), esophagus cancer (adjusted HR=0.646; 95% CI 0.522-0.799; p<0.001) and oral cancer (adjusted HR=0.587; 95% CI 0.346-0.995; p=0.048). Notably, OP users had a significant reduction in liver cancer occurrence over a 10-year period follow-up and a lower cancer stage at liver cancer diagnosis.

Conclusion: These findings first suggest the beneficial effects and therapeutic potential of OP use for certain cancers, especially liver cancer.

KEYWORDS

anti-viral drugs, oseltamivir phosphate (OP), cohort study, cancer, liver cancer

Introduction

Mounting studies on anti-viral drugs have been focused on their anti-cancer properties (1). Acyclovir, as a synthetic nucleoside analog for attenuating the proliferation and spread of the herpes virus, has been reported to reveal benefit potentials when used as an adjuvant for the treatment of breast cancer (2). Acyclovir disrupts and hinders the proliferation and colony formation of breast cancer cells and inhibits their invasion, without affecting the expressions of metastasis-related genes (2). Azido thymidine (AZT), the first licensed drug for HIV therapy, has also been reported to exhibit inhibitory effects against a variety of cancer types, including leukemia, lymphoma, Kaposi sarcoma, and pancreatic cancer, by leading apoptosis (3). Brivudine, an antiviral medicine against herpes simplex virus (HSV), also exhibited anti-cancer properties by suppressing chemoresistance in both animal experiments and pancreatic cancer patients (4, 5). Nelfinavir, a protease inhibitor against HIV infection, also showed anti-cancer activity by inhibiting Akt-signaling and inducing endoplasmic reticulum (ER) stress in NSCLCs, ovarian cancers, liposarcomas, and breast cancers (6, 7). These findings strongly indicated the anti-cancer properties of anti-viral drugs (AVD) and attracted intensive attention to investigating the potential of AVD in cancer therapy.

Increasing experience regarding the perilous consequence of emerging respiratory viruses caused by influenza has received intensive attention in recent decades (8). Although influenza vaccines provide a crucial tool for influenza virus prevention, the efficacy for preventing annual influence epidemics is still limited (8, 9). To address and overcome this issue, inhibitors have been synthesized to target influenza viral components such as neuraminidase enzymes, hemagglutinin proteins, Matrix-2 (M2) protein ion channels, nucleoproteins, and RNA-dependent RNA polymerases (10, 11). To date, the currently available anti-influenza drugs such as peramivir, zanamivir, oseltamivir (OP), and rimantadine are obtained through chemical modifications of clinically used drugs, which exhibit inhibitory activity to their target viral component (12, 13).

Oseltamivir, namely Tamiflu®, approved in late 1999 is a further sialidase-targeted anti-influenza drug based on zanamivir (14, 15). As a well-tolerated neuraminidase inhibitor, oseltamivir significantly ameliorates the symptomatic illness and accelerates the return to normal activity levels in patients with natural influenza infection (16–18). Notably, evidence has indicated that OP reveals anti-proliferative and anti-metastatic effects on various cancer cell types like hepatic, pancreatic, and breast cancer cells (19–21), suggesting the anti-cancer potentials of OP. Additionally, our recent study demonstrated the cytotoxic effects of OP on liver cancer cells both *in vitro* and *in vivo* by inducing apoptosis and autophagy (21). However, the clinical information for OP use and human cancers remains lacking. Therefore, the current study further investigated the association between OP users and the risk of different cancers, especially HCC, by conducting a large-scale nationwide cohort in the Taiwan National Health Insurance Research Database (NHIRD) retrospectively.

Materials and Methods

Data source

This study employed an observational retrospective cohort design. All the data utilized in this study were sourced from the National Health Insurance Research Database, Ministry of Health and Welfare (NHIRD_MOHW) at the Health and Welfare Data Science Center in Taiwan (grant no. H110290). The NHIRD was established in conjunction with an insurance program launched in Taiwan in 1995. At present, nearly 99% of Taiwan's residents are enrolled in this program, which covers the cost of ambulatory care, inpatient services, dental treatments, medications, invasive procedures, and surgeries through Taiwan's national health insurance program. Consequently, the NHIRD houses an extensive repository of healthcare information and ranks among the most comprehensive administrative health databases worldwide. Numerous epidemiological and comparative effectiveness studies have been previously published using the NHIRD in various prestigious journals. To protect individuals' privacy and maintain data security, personal information and identification were anonymized. As a result, our study was exempted from requiring informed consent, and the study protocol received approval from the Institutional Review Board of the Chung Shan Medical University Hospital (CS2-21180). Data in this study were retrieved and analyzed from the Health and Welfare Data Science Center in Taiwan.

Patients with oseltamivir use

Patients who had received treatment with OP were identified by corresponding drug codes in NHIRD between January 1, 2009, and December 31, 2018. The date when the patients received the prescription of OP for the first time was defined as the index date and the age of each individual was determined based on the index date. To ensure the integrity of the study, several exclusion criteria were applied. We excluded Individuals who had died before the index date, cases registered more than once in the database, were under the age of 20, had unknown gender, had used other neuraminidase inhibitors before and during the follow-up period, and had been diagnosed with any type of malignancy before the index date.

Control group

Patients without a prescription for OP were identified between 2009 and 2018 to be included in the control group. The index dates of patients in the control group were randomly assigned. The control group's exclusion criteria align with those of the patients with OP use.

Outcome ascertainment

Identification of the outcome was based on the International Classification of Diseases for Oncology, Third Edition (ICD-O-3) codes. The study aimed to investigate the occurrence of common types of cancer in Taiwan, including "trachea, bronchus, and lung cancer"(C34), "colon, rectum, and anus cancer"(C18), "breast cancer"(C50), "liver and intrahepatic bile duct cancer"(C22), "oral cancer"(C04), "pancreatic cancer"(C25), "esophageal cancer"(C15), "gastric cancer"(C16), "prostate cancer"(C61), and "ovarian cancer"(C56). To ensure the accuracy of cancer diagnoses, patients who were counted as having canners were also required to possess a valid certificate of major illness specifically for cancer, in addition to having the aforementioned diagnostic codes. Patients with serious diseases, such as cancer, autoimmune diseases, or type-1 diabetes, are eligible to apply for a certificate of major illness under the Taiwan National Health Insurance system, thereby enhancing the reliability of the study's findings.

Follow-up

Individuals were followed from the index date, until the date of their cancer diagnosis, death, or end of the study period (December 31, 2018), whichever came first. Patients who died before cancer diagnosis would be treated as censoring.

Statistical analysis

Continuous variables were presented as mean and standard deviation (SD), while categorical variables were presented as counts and percentages. Independent sample t-tests or Pearson chi-squared tests were used to compare the demographic differences between patients with and without the use of OP. The Kaplan-Meier method was used to estimate the cumulative incidence rate of liver cancer between OP users and non-users. The Cox regression was used to derive hazard ratio for developing malignancy. Multivariate analysis was performed with adjustment for age, gender. A two-tailed P-value less than 0.05 was considered significant. All data processing and statistical analysis were conducted using Stata 15 software (StataCorp, College Station, TX, USA).

Results

Participants' characteristics

Figure 1 shows the flowchart of participant selection in this population-based study. Characteristics of participants are shown in Table 1. This cohort study encompassed 13,977,101 individuals. Among these cases, 284,733 individuals (2.04%) had a history of receiving at least one OP administration and the other 13,692,368 (97.96%) individuals received no OP administration. Significant disparities were observed in terms of gender and age distribution between these two cohorts (Table 1). Upon closer examination of the age variable, the OP use group exhibited a noteworthy concentration of individuals aged 20 to 39 years ($p<0.001$). Conversely, the group without OP use showed a significantly prominent cluster of individuals aged 40 to 59 years ($p<0.001$), aged 60 years and those above ($p<0.001$). Remarkably, within OP use group, a total of 7,113 patients (2.5%) were diagnosed with malignant tumors. Within the non-OP use group, a total of 509,267 patients (3.7%) were diagnosed with malignant tumors (Table 1).

Correlation between OP use and cancers

To investigate the correlation between OP use and the top 10 common cancers in Taiwan, chi-squared tests were performed. As shown in Table 2, a significant difference was observed between OP use group and non-OP use groups in lung cancer (64,179 patients,

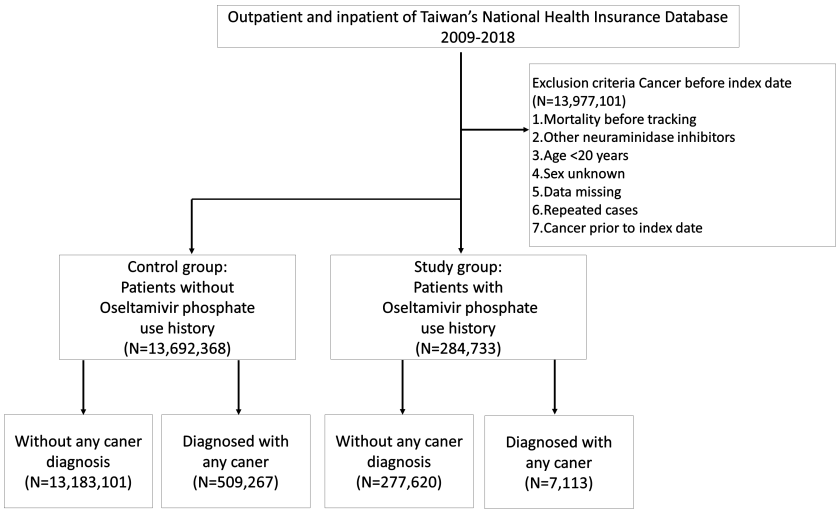

FIGURE 1
Flowchart of participant selection in a population-based study from Taiwan National Health Insurance Database.

TABLE 1 Demographic characteristics of participants.

Variable	Total		OP use group		Non-OP use group		P value
	N	%	N	v%	N	%	
Total	13,977,101	100%	284,733	100%	13,692,368	100%	
Gender							<0.001
Male	6,491,215	46%	127,780	45%	6,363,435	46%	
Female	7,485,886	54%	156,953	55%	7,328,933	54%	
Age, years	46.5±16.2		40.34±15.5		46.7±16.2		<0.001
20-39	5,349,323	38%	159,254	56%	5,190,069	38%	<0.001
40-59	5,444,928	39%	87,807	31%	5,357,121	39%	<0.001
> 60	3,182,850	23%	37,672	13%	3,145,178	23%	<0.001
Overall cancers	516,380	100%	7,113	2.5%	509,267	3.7%	

OP, Oseltamivir phosphate; N, Number.

12.43%, p<0.001), colon cancer (47,223 patients, 9.15%, p<0.001), liver and intrahepatic bile ducts cancer (58,259 patients, 11.28%, p<0.001), oral cancer (1,522 patients, 0.29%, p=0.002), pancreas cancer (11,932 patients, 2.31%, p<0.001), esophagus cancer (9,450 patients, 1.83%, p<0.001), stomach cancer (11,101 patients, 2.15%, p<0.001) and prostate cancer (25,749 patients, 4.99%, p<0.001).

Risk of different cancers in individuals with OP use

The overall mortality rate (death due to cancer) of the top ten cancers in Taiwan was analyzed after adjusting for age and gender. As shown in Table 3, the negative association between OP use and mortality in all cancer incidence was observed after controlling for other covariates (adjusted HR=0.779; 95% CI 0.743-0.817; p<0.001). The correlation between OP use and the incidence rates of different cancer was further investigated. Notably, OP use revealed a negative association with the risk of developing liver cancer (adjusted HR=0.895; 95% CI 0.824-0.972; p=0.008), oral cancer (adjusted HR=0.587; 95% CI 0.346-0.995; p=0.048) and esophageal cancer (adjusted HR=0.646; 95% CI 0.522-0.799; p<0.001) as compared to the control group. Notably, Figure 2 demonstrated the Kaplan-Meier failure curves for the individuals with OP use and those without OP use on the risk of developing liver cancer over a 10-year

TABLE 2 Association between OP use and non-OP use in top 10 cancers in Taiwan.

	Total		OP use group		Non-OP use group		P value
	N	%	N	%	N	%	
Overall cancers	516,380	100%	7,113	100%	509,267	100%	
Lung cancer	64,179	12.43%	739	10%	63,440	12.46%	<0.001
Colon cancer	47,223	9.15%	544	8%	46,679	9.17%	<0.001
Breast cancer	58,956	11.42%	1,160	16%	57,796	11.35%	0.231
Liver and intrahepatic bile ducts cancer	58,259	11.28%	626	9%	57,633	11.32%	<0.001
Oral cancer	1,522	0.29%	14	0.2%	1,508	0.30%	0.002
Pancreas cancer	11,932	2.31%	119	1.7%	11,813	2.32%	<0.001
Esophagus cancer	9,450	1.83%	86	1.2%	9,364	1.84%	<0.001
Stomach cancer	11,101	2.15%	116	1.6%	10,985	2.16%	<0.001
Prostate cancer	25,749	4.99%	267	3.8%	25,482	5.00%	<0.001
Ovary cancer	5,506	1.07%	93	1.3%	5,413	1.06%	0.067

OP, oseltamivir phosphate; N, Number.

TABLE 3 Crude and adjusted hazard ratios for incidence of cancers in patients with OP use.

Variables	Crude HR	95% CI	P value	Adjusted HR	95% CI	P value
Mortality [a]	0.363	0.346-0.381	<0.001	0.779	0.743-0.817	<0.001
Lung cancer	0.511	0.475-0.550	<0.001	0.982	0.913-1.055	0.619
Breast cancer	0.852	0.804-0.903	<0.001	1.049	0.989-1.112	0.110
Colon cancer	0.505	0.465-0.550	<0.001	0.942	0.866-1.025	0.166
Liver cancer	0.489	0.451-0.531	<0.001	0.895	0.824-0.972	0.008
Stomach cancer	0.467	0.389-0.561	<0.001	0.908	0.756-1.091	0.304
Prostate cancer	0.451	0.400-0.509	<0.001	1.018	0.902-1.149	0.767
Pancreas cancer	0.446	0.372-0.534	<0.001	0.852	0.711-1.021	0.083
Ovary cancer	0.741	0.604-0.910	0.004	0.877	0.714-1.078	0.213
Oral cancer	0.408	0.241-0.691	0.001	0.587	0.346-0.995	0.048
Esophagus cancer	0.409	0.331-0.507	<0.001	0.646	0.522-0.799	<0.001
Bile duct cancer	0.413	0.316-0.540	<0.001	0.772	0.591-1.010	0.059

OP, oseltamivir phosphate; [a], death due to cancer.

period and showed that OP users has a lower risk of liver cancer compared to non-OP users.

Correlation between OP use and malignancy grade and cancer stage of liver cancer

To investigate the correlation between the use of OP and cancer status, further determination of liver cancer grade and stage was conducted. Table 4 represents the distribution of OP use and non-OP use group across different tumor differentiation grades and cancer stages. Patients who received OP exhibited a significantly lower cancer stage at the time of liver cancer diagnosis (p<0.0001), whereas no significant correlation was observed with tumor differentiation grade (Table 4).

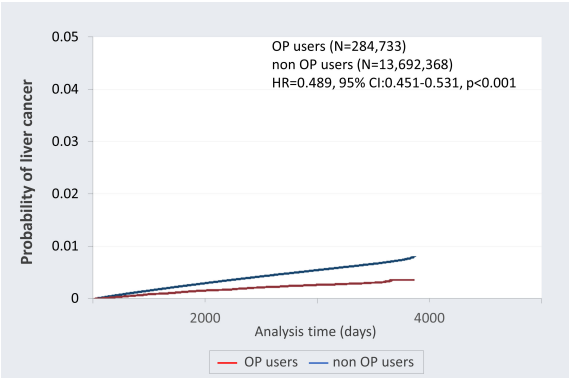

FIGURE 2
Kaplan-Meier failure curves with development of liver cancer stratified by oseltamivir phosphate (OP) use. This follow-up study was up to 10 years and the probability of developing liver cancer was greater among non-OP users (blue) compared with the OP users (red).

Discussion

Despite common practices including prevention through vaccination, improved control of hepatitis, and advances in anti-viral medication, the incidence of HCC continues to exhibit as the seventh most frequently diagnosed cancer and the third leading cause of cancer-related mortality worldwide (22, 23). This study retrospective cohort reported a reduced risk of mortality observed in all cancer patients with prior OP use. Additionally, significantly lower incidence of the liver (adjusted HR=0.895; 95% CI 0.824-0.972; p=0.008), oral (adjusted HR=0.587; 95% CI 0.346-0.995; p=0.048) and esophageal cancers (adjusted HR=0.646; 95% CI 0.522-0.799; p<0.001) were found in the group that had OP use. Notably, a markedly lower cumulative occurrence rate of liver cancer over the 10 years was detected in OP users as compared to non-OP users. The HCC patients who had used OP revealed a lower cancer stage at diagnosis. For the first time, this study represents the initial investigation in the human population elucidating the relationship between OP use and the occurrence of cancer within a real-world context.

The growing interest in studying the therapeutic potentials of OP for diverse diseases extends beyond its well-established anti-influenza activity, especially in cancer therapy. A previous report indicated that intraperitoneal OP injection as a monotherapy significantly reduced tumor vascularization and growth rate in a mouse model of human breast adenocarcinoma (24). In a study of pancreatic cancer, administration of OP in conjunction with aspirin has been proposed as a potential strategy to enhance the efficacy of gemcitabine, the standard chemotherapeutic agent for human pancreatic cancer, by reducing proliferation, metabolic activity, migration, and clonogenic formation on pancreatic cancer cells via targeting Neu-1 (25). Another investigation of human triple-negative breast cancer indicated that the concurrent administration of metformin, acetylsalicylic acid, and OP demonstrated a notable reduction in MDA-MB-231 triple-negative-breast cancer cells and

TABLE 4 Tumor grade and stage in liver cancer patients with or without OP use.

Variables	Liver cancer with OP use	Liver cancer without OP use	Total	P value
	N	N		
Grade	465	44,199	44,664	0.6
Grade 1	17	1,442	1,459	
Grade 2	76	7,623	7,699	
Grade 3	47	3,371	3,418	
Grade 4	4	277	281	
Unknown	321	31,486	31,807	
Stage	554	48,721	49,275	<0.0001
Stage 1	249	17,892	18,141	
Stage 2	97	8,479	8,576	
Stage 3	98	12,059	12,157	
Stage 4	46	6,030	6,076	
Unknown	64	4,261	4,325	

OP, oseltamivir phosphate; N, Number.

its tamoxifen-resistant variant by inducing apoptosis (26). Based on the fact that combination therapy is currently one of the most popular strategies for cancer treatment (27, 28), this result pointed out the potential of the combinatorial approaches of OP with other medicines on treatments of certain cancer types.

Previous clinical trials have shown that OP is well-tolerated with the only clinically significant adverse event being mild gastrointestinal discomfort (29). A similar report was also revealed in recent clinical trials that asymptomatic and transient elevation of aminotransferase (ALT) are observed in 2% of patients receiving OP with no instance of acute liver failure manifestations (30). Additionally, resistance to OP is rarely seen in influenza A virus-infected children with the highest incidence of 5%. Less virulent and replication-efficient were detected in the OP-resistant influenza viruses than in their parent strains (29). These studies may provide credible references for the medication of OP on drug safety and efficacy in treating liver cancer.

Oseltamivir is known to disable human pancreatic cancer (PANC1) cell survival by inhibiting NEU-1 (sialidase) activity and its intrinsic signaling (20). Evidence has indicated that OP overcomes the chemoresistance to cisplatin and gemcitabine in PANC1 cells by reversing changes in E-cadherin and N-cadherin expressions (20). Notably, highly expressed NEU 1 in HBV-related HCC tissues is due to the binding of HBV core protein to NF-κB on NEU-1 promoter that leads to oncogenic signaling and epithelial-mesenchymal transition (EMT) in HCC cells (31). Hence, these findings may suggest a possible rationale that OP attenuates the development of HCC by disabling the NEU-1 activity and its downstream signaling.

In addition to liver cancer, our results also revealed a significantly lower incidence of oral and esophagus cancers in OP users. However, the reason for this finding remains unclear. As known, the major etiological factors of oral and esophagus cancers are tobacco chewing, betel nut, and alcohol consumption, which lead to the development of squamous cell carcinoma, the most prevalent histopathological subtype in oral and esophagus cancers (32). Notably, a previous case report indicated that the elevation of squamous cell carcinoma antigen is due to influenza B infection (33). Another study also reported that Unc-93 homolog B1 (UNC93B1), a transmembrane protein correlated with influenza infection, plays essential roles in oral squamous cell carcinomas by regulating GM-CSF levels (34). These findings suggest a possible link between influenza infection and squamous cell carcinoma and provide a rational explanation for the lower incidence of oral and esophagus cancers in OP users. Anyway, further investigations are required to verify the underlying mechanism of OP in attenuating oral and esophagus cancers.

Understanding the stage of cancer and the grade of tumor differentiation is critical for the treatment and outcome prediction of cancer patients [32, 35, 36; American Joint Committee on Cancer (37); 38, 39]. The differentiation grade and cancer staging were assessed using the AJCC 8th Edition Staging System, where lower numerical values indicate milder tumor differentiation and earlier stages of cancer progression, while higher values reflect increased malignancy and advanced disease stages [36; American Joint Committee on Cancer (37); 38, 39]. Leveraging data from the cancer registry database, we analyzed the tumor differentiation grade and cancer staging among liver cancer patients. In this nationwide retrospective cohort study, we found that HCC patients with prior OP use had a significantly lower HCC stage at diagnosis but no difference in tumor cell differentiation grade. Although the exact causation of this finding is unclear, one possible explanation is that the migration and invasion abilities of OP-treated HCC cells are significantly attenuated as we proposed previously (21).

Regarding this study, there is a particularly noteworthy issue worth mentioning. We did not examine whether the use of other

anti-influenza drugs such as inhibitors against hemagglutinin protein, the Matrix-2 (M2) protein ion channel, nuclear proteins, or RNA-dependent RNA polymerase (RdRP) may serve as a confounding factor. Although Amantadine, an M2 inhibitor, has been approved for influenza by the Food and Drug Administration (FDA) in Taiwan, it has been obsoleted for treating influence use due to its prevalent strains such as H1N1 has gained drug resistance and the serious neurological adverse effects (40–42). Baloxavir marboxil, a class of polymerase inhibitors, has also been approved by Taiwan FDA since 24/06/2019. However, the included timeline of this study is from 2009 to 2018. Additionally, other anti-influenza drugs such as Rimantadine (M2 inhibitor) and Favipiravir (RNA polymerase inhibitor) have not yet been approved by the FDA in Taiwan. Therefore, this drug will not be a confounding factor. However, further research design and evaluation are required to verify the precise influence of these anti-influenza inhibitors in liver cancers. Some potential limitations in this study also need to be mentioned. Firstly, it is difficult to describe whether OP use reduces the onset or progression of liver cancer in this study. Conducting such a study within the National Health Insurance Research Database (NHIRD) is challenging due to confounding effects resulting from various cancer therapies that patients typically receive after diagnosis, making it toilful to isolate the specific impact of OP on cancer progression. Another limitation of our study is that it combined patients who were prescribed multiple OP courses, but did not differentiate those receiving OP treatment more than once. Future studies may look into the dose-dependent relationship between OP and efficacy towards liver cancer. Additionally, our study is the potential presence of unaccounted residual confounders. The NHIRD does not provide information on the patient's socioeconomic status, family history, personal health behaviors such as smoking, alcohol consumption, and serum parameters. These unmeasured confounding factors may have an impact on the outcome of HCC.

Conclusions

This study utilized longitudinal population-based data with a follow-up period of up to 10 years, allowing for a comprehensive understanding of the topic and ensuring that the findings were representative of the general population in Taiwan. The large sample size further enhanced the robustness and generalizability of the results. Overall, OP use exhibits promising effects in lowering the risk of various cancer types, particularly hepatocellular carcinoma, and reducing mortality in liver cancer patients. These novel findings highlight the advantage of prior OP use in reducing liver cancer risk and suggest the potential of OP as an alternative approach for cancer treatment.

Data availability statement

The original contributions presented in the study are included in the article/supplementary material. Further inquiries can be directed to the corresponding authors.

Ethics statement

The studies involving humans were approved by Institutional Review Board (IRB) of Chung Shan Medical University Hospital. The studies were conducted in accordance with the local legislation and institutional requirements. The ethics committee/institutional review board waived the requirement of written informed consent for participation from the participants or the participants' legal guardians/next of kin because The ethics committee/institutional review board waived the requirement of written informed consent for participation from the participants or the participants' legal guardians/next of kin because there is no identified personal information.

Author contributions

P-HC: Conceptualization, Data curation, Formal analysis, Writing – original draft, Writing – review & editing. B-ST: Conceptualization, Writing – original draft, Writing – review & editing. C-CT: Conceptualization, Writing – original draft, Writing – review & editing. C-CC: Conceptualization, Writing – original draft. C-YL: Conceptualization, Data curation, Formal analysis, Methodology, Writing – original draft, Writing – review & editing. T-CH: Conceptualization, Data curation, Formal analysis, Funding acquisition, Methodology, Project administration, Supervision, Writing – original draft, Writing – review & editing.

Funding

The author(s) declare financial support was received for the research, authorship, and/or publication of this article. This research was supported in part by Chung Shan Medical University, Taiwan (grant no. M108N0044). The funder had no role in study design, data collection and analysis, decision to publish, or preparation of the manuscript.

Conflict of interest

The authors declare that the research was conducted in the absence of any commercial or financial relationships that could be construed as a potential conflict of interest.

Publisher's note

All claims expressed in this article are solely those of the authors and do not necessarily represent those of their affiliated organizations, or those of the publisher, the editors and the reviewers. Any product that may be evaluated in this article, or claim that may be made by its manufacturer, is not guaranteed or endorsed by the publisher.

References

1. Siddiqui S, Deshmukh AJ, Mudaliar P, Nalawade AJ, Iyer D, Aich J. Drug repurposing: re-inventing therapies for cancer without re-entering the development pipeline-a review. *J Egypt Natl Canc Inst* (2022) 34(1):33. doi: 10.1186/s43046-022-00137-0

2. Shaimerdenova M, Karapina O, Mektepbayeva D, Alibek K, Akilbekova D. The efects of antiviral treatment on breast cancer cell line. *Infect Agent Cancer* (2017) 12 (1):1–10. doi: 10.1186/s13027-017-0128-7

3. Chow WA, Jiang C, Guan M. Anti-HIV drugs for cancer therapeutics: back to the future? *Lancet Oncol* (2009) 10(1):61–71. doi: 10.1016/S1470-2045(08)70334-6

4. Heinrich JC, Tuukkanen A, Schroeder M, Fahrig T, Fahrig R. RP101 (brivudine) binds to heat shock protein HSP27 (HSPB1) and enhances survival in animals and pancreatic cancer patients. *J Cancer Res Clin Oncol* (2011) 137(9):1349–61. doi: 10.1007/s00432-011-1005-1

5. Mercorelli B, Palù G, Loregian A. Drug repurposing for viral infectious diseases: how far are we? *Trends Microbiol* (2018) 26(10):865–76. doi: 10.1016/j.tim.2018.04.004

6. Gills JJ, Lopiccolo J, Tsurutani J, Shoemaker RH, Best CJ, Abu-Asab MS, et al. Cancer therapy: preclinical nelfnavir, a lead HIV protease inhibitor, is a broad-spectrum, anticancer agent that induces endoplasmic reticulum stress, autophagy, and apoptosis in *vitro* and in *vivo*. *Clin Cancer Res* (2007) 13(17):5183–95. doi: 10.1158/1078-0432.CCR-07-0161

7. Koltai T. Nelfnavir and other protease inhibitors in cancer: mechanisms involved in anticancer activity. *F1000Res* (2015) 4:9. doi: 10.12688/f1000research.5827.2

8. Romeo R, Legnani L, Chiacchio MA, Giofrè SV, Iannazzo D. Antiviral compounds to address influenza pandemics: an update from 2016-2022. *Curr Med Chem* (2023). doi: 10.2174/0929867331666230907093501

9. Saito T, Tashiro M. Vaccines and therapeutics against influenza virus infections. *Pediatr Int* (2000) 42(2):219–25. doi: 10.1046/j.1442-200x.2000.01201.x

10. Bouvier NM, Palese P. The biology of influenza viruses. *Vaccine* (2008) 26(Suppl 4):D49–53. doi: 10.1016/j.vaccine.2008.07.039

11. Wille M, Holmes EC. The ecology and evolution of influenza viruses. *Cold Spring Harb Perspect Med* (2020) 10(7):a038489. doi: 10.1101/cshperspect.a038489

12. Boltz DA, Aldridge JRJr., Webster RG, Govorkova EA. Drugs in development for influenza. *Drugs* (2010) 70(11):1349–62. doi: 10.2165/11537960-000000000-00000

13. Zhao Y, Huang G, He W, Sun Q, Zhao X, Li D, et al. Efficacy and safety of single-dose antiviral drugs for influenza treatment: A systematic review and network meta-analysis. *J Med Virol* (2022) 94(7):3270–302. doi: 10.1002/jmv.27729

14. Hayden FG, Atmar RL, Schilling M, Johnson C, Poretz D, Paar D, et al. Use of the selective oral neuraminidase inhibitor oseltamivir to prevent influenza. *N Engl J Med* (1999) 341(18):1336–43. doi: 10.1056/NEJM199910283411802

15. Dreitlein WB, Maratos J, Brocavich J. Zanamivir and oseltamivir: two new options for the treatment and prevention of influenza. *Clin Ther* (2001) 23(3):327–55. doi: 10.1016/s0149-2918(01)80042-4

16. Kim CU, Chen X, Mendel DB. Neuraminidase inhibitors as anti-influenza virus agents. *Antivir Chem Chemother* (1999) 10(4):141–54. doi: 10.1177/095632029901000401

17. Lew W, Chen X, Kim CU. Discovery and development of GS 4104 (oseltamivir): an orally active influenza neuraminidase inhibitor. *Curr Med Chem* (2000) 7(6):663–72. doi: 10.2174/0929867003374886

18. McClellan K, Perry CM. Oseltamivir: a review of its use in influenza. *Drugs* (2001) 61(2):263–83. doi: 10.2165/00003495-200161020-00011

19. Haxho F, Allison S, Alghamdi F, Brodhagen L, Kuta VE, Abdulkhalek S, et al. Oseltamivir phosphate monotherapy ablates tumor neovascularization, growth, and metastasis in mouse model of human triple-negative breast adenocarcinoma. *Breast Cancer (Dove Med Press)* (2014) 6:191–203. doi: 10.2147/BCTT.S74663

20. O'Shea LK, Abdulkhalek S, Allison S, Neufeld RJ, Szewczuk MR. Therapeutic targeting of Neu1 sialidase with oseltamivir phosphate (Tamiflu®) disables cancer cell survival in human pancreatic cancer with acquired chemoresistance. *Onco Targets Ther* (2014) 7:117–34. doi: 10.2147/OTT.S55344

21. Huang PJ, Chiu CC, Hsiao MH, Yow JL, Tzang BS, Hsu TC. Potential of antiviral drug oseltamivir for the treatment of liver cancer. *Int J Oncol* (2021) 59(6):109. doi: 10.3892/ijo.2021.5289

22. Shao YY, Wang SY, Lin SM. Management consensus guideline for hepatocellular carcinoma: 2020 update on surveillance, diagnosis, and systemic treatment by the Taiwan Liver Cancer Association and the Gastroenterological Society of Taiwan. *J Formos Med Assoc* (2021) 120:1051–60. doi: 10.1016/j.jfma.2020.10.031

23. Wen N, Cai Y, Li F, Ye H, Tang W, Song P, et al. The clinical management of hepatocellular carcinoma worldwide: A concise review and comparison of current guidelines: 2022 update. *BioScience Trends* (2022) 16(1):20–30. doi: 10.5582/bst.2022.01061

24. Fattovich G, Stroffolini T, Zagni I, Donato F. Hepatocellular carcinoma in cirrhosis: Incidence and risk factors. *Gastroenterology* (2004) 127(5 Suppl 1):S35–50. doi: 10.1053/j.gastro.2004.09.014

25. Qorri B, Mokhtari RB, Harless WW, Szewczuk MR. Next generation of cancer drug repurposing: therapeutic combination of aspirin and oseltamivir phosphate potentiates gemcitabine to disable key survival pathways critical for pancreatic cancer progression. *Cancers (Basel)* (2022) 14(6):1374. doi: 10.3390/cancers14061374

26. Sambi M, Samuel V, Qorri B, Haq S, Burov SV, Markvicheva E, et al. A triple combination of metformin, acetylsalicylic acid, and oseltamivir phosphate impacts tumour spheroid viability and upends chemoresistance in triple-negative breast cancer. *Drug Des Devel Ther* (2020) 14:1995–2019. doi: 10.2147/DDDT.S242514

27. Di Maio M, De Maio E, Perrone F, Pignata S, Daniele B. Hepatocellular carcinoma: systemic treatments. *J Clin Gastroenterol* (2002) 35(5 Suppl 2):S109–14. doi: 10.1097/00004836-200211002-00007

28. Cavalli F, Kaye SB, Hansen HH, Armitage JO, Piccart-Gebhart M. *Textbook of medical oncology*. Boca Raton, FL, USA: CRC Press (2009).

29. Doucette KE, Aoki FY. Oseltamivir: a clinical and pharmacological perspective. *Expert Opin Pharmacother* (2001) 2(10):1671–83. doi: 10.1517/14656566.2.10.1671

30. Bethesda. LiverTox: clinical and research information on drug-induced liver injury. *Natl Institute Diabetes Digestive Kidney Dis* (2012).

31. Kong F, Li N, Tu T, Tao Y, Bi Y, Yuan D, et al. Hepatitis B virus core protein promotes the expression of neuraminidase 1 to facilitate hepatocarcinogenesis. *Lab Invest.* (2020) 100(12):1602–17. doi: 10.1038/s41374-020-0465-9

32. Edge SB, Compton CC eds. *The American Joint Committee on Cancer: The 7th edition of the AJCC cancer staging manual and the future of TNM*. New York, NY: Springer (2010).

33. Sano A. Transient elevation of squamous cell carcinoma antigen levels with influenza virus infection. *Respirol Case Rep* (2018) 6(8):e00362. doi: 10.1002/rcr2.362

34. Wagai S, Kasamatsu A, Iyoda M, Hayashi F, Hiroshima K, Yoshimura S, et al. UNC93B1 promotes tumoral growth by controlling the secretion level of granulocyte macrophage colony-stimulating factor in human oral cancer. *Biochem Biophys Res Commun* (2019) 513(1):81–7. doi: 10.1016/j.bbrc.2019.03.172

35. Elston CW, Ellis IO. Pathological prognostic factors in breast cancer. I. The value of histological grade in breast cancer: experience from a large study with long-term follow-up. *Histopathology* (1991) 19(5):403–10. doi: 10.1111/j.1365-2559.1991.tb00229.x

36. Abdel-Rahman O. Assessment of the discriminating value of the 8th AJCC stage grouping for hepatocellular carcinoma. *HPB (Oxford)* (2018) 20(1):41–8. doi: 10.1016/j.hpb.2017.08.017

37. American Joint Committee on Cancer. *AJCC cancer staging manual. 8th ed*. New York, NY: Springer (2017).

38. Martins-Filho SN, Paiva C, Azevedo RS, Alves VAF. Histological grading of hepatocellular carcinoma-A systematic review of literature. *Front Med (Lausanne)* (2017) 4:193. doi: 10.3389/fmed.2017.00193

39. Nagtegaal ID, Odze RD, Klimstra D, Paradis V, Rugge M, Schirmacher P, et al. WHO Classification of Tumours Editorial Board. WHO Classification of Tumours Editorial Board. The 2019 WHO classification of tumours of the digestive system. *Histopathology* (2020) 76(2):182–8. doi: 10.1111/his.13975

40. Shih SR, Lee CN, Tsai HR, Chen GW, Tsao KC. Amantadine-resistant influenza A virus in Taiwan. *J Formos Med Assoc* (2001) 100(9):608–12.

41. Crosby N, Deane KH, Clarke CE. Amantadine in parkinson's disease. *Cochrane Database Syst Rev* (2003) 2003(1):CD003468. doi: 10.1002/14651858.CD003468

42. Deyde VM, Xu X, Bright RA, Shaw M, Smith CB, Zhang Y, et al. Surveillance of resistance to adamantanes among influenza A (H3N2) and A (H1N1) viruses isolated worldwide. *J Infect Dis* (2007) 196(2):249–57. doi: 10.1086/518936

frontiers | Frontiers in Pharmacology

TYPE Original Research
PUBLISHED 01 March 2024
DOI 10.3389/fphar.2024.1346756

Check for updates

OPEN ACCESS

EDITED BY
Parmanand Malvi,
University of Alabama at Birmingham, United States

REVIEWED BY
Vivek Anand,
University of Texas MD Anderson Cancer Center, United States
Ashish Toshniwal,
The University of Utah, United States

*CORRESPONDENCE
Yana K. Reshetnyak,
reshetnyak@uri.edu

RECEIVED 04 December 2023
ACCEPTED 13 February 2024
PUBLISHED 01 March 2024

CITATION
Moshnikova A, DuPont M, Iraca M, Klumpp C, Visca H, Allababidi D, Pelzer P, Engelman DM, Andreev OA and Reshetnyak YK (2024), Targeted intracellular delivery of dimeric STINGa by two pHLIP peptides for treatment of solid tumors.
Front. Pharmacol. 15:1346756.
doi: 10.3389/fphar.2024.1346756

COPYRIGHT
© 2024 Moshnikova, DuPont, Iraca, Klumpp, Visca, Allababidi, Pelzer, Engelman, Andreev and Reshetnyak. This is an open-access article distributed under the terms of the Creative Commons Attribution License (CC BY). The use, distribution or reproduction in other forums is permitted, provided the original author(s) and the copyright owner(s) are credited and that the original publication in this journal is cited, in accordance with accepted academic practice. No use, distribution or reproduction is permitted which does not comply with these terms.

Targeted intracellular delivery of dimeric STINGa by two pHLIP peptides for treatment of solid tumors

Anna Moshnikova[1], Michael DuPont[1], Marissa Iraca[1], Craig Klumpp[1], Hannah Visca[1], Dana Allababidi[2], Phoebe Pelzer[1], Donald M. Engelman[3], Oleg A. Andreev[1] and Yana K. Reshetnyak[1]*

[1]Physics Department, University of Rhode Island, Kingston, RI, United States, [2]Department of Chemical Engineering, University of Rhode Island, Kingston, RI, United States, [3]Molecular Biophysics and Biochemistry Department, New Haven, CT, United States

Introduction: We have developed a delivery approach that uses two pHLIP peptides that collaborate in the targeted intracellular delivery of a single payload, dimeric STINGa (dMSA).

Methods: dMSA was conjugated with two pHLIP peptides via S-S cleavable self-immolating linkers to form 2pHLIP-dMSA.

Results: Biophysical studies were carried out to confirm pH-triggered interactions of the 2pHLIP-dMSA with membrane lipid bilayers. The kinetics of linker self-immolation and dMSA release, the pharmacokinetics, the binding to plasma proteins, the stability of the agent in plasma, the targeting and resulting cytokine activation in tumors, and the biodistribution of the construct was investigated. This is the first study demonstrating that combining the energy of the membrane-associated folding of two pHLIPs can be utilized to enhance the targeted intracellular delivery of large therapeutic cargo payloads.

Discussion: Linking two pHLIPs to the cargo extends blood half-life, and targeted delivery of dimeric STINGa induces tumor eradication and the development of robust anti-cancer immunity.

KEYWORDS

tumor acidity, cold tumors, biophysics, imaging, immuno-suppressive tumors

1 Introduction

Immune evasion is a hallmark of cancer. Overcoming that evasion to harness the power of the immune system to attack tumors has become a widely employed strategy (Lesterhuis et al., 2011; Hainaut and Plymoth, 2013). Activation of the stimulator of interferon genes (STING) pathway causes the release of factors that trigger the immune response in the tumor microenvironment (TME) (Woo et al., 2014). As a consequence, a variety of STING agonist (STINGa) therapeutic molecules have been developed and tested in anti-tumor strategies (Klarquist et al., 2014). However, the poor pharmacokinetics of STINGa and nonspecific systemic immuno-activation required intra-tumoral dosing in most cases, significantly limiting applications. In general, the first clinical trials have resulted in

disappointingly modest efficacy (Motedayen Aval et al., 2020). Also, recent findings indicate that, under certain conditions, the STING pathway can also be implicated in promoting tumor burdens, which worsens disease outcomes (Decout et al., 2021). These findings led to a realization that kinetics and strength of activation are significant factors for efficacy: transient strong activation leads to immune activation and tumor suppression, while prolonged weak activation leads to further immuno-suppression promoting tumor development. Further, it is now clear that activation of the STING pathway in different types of cells within the TME has different benefits (Decout et al., 2021; Chamma et al., 2022). Reprogramming of M2-type tumor-associated macrophages (M2-TAMs) toward an M1 phenotype, suppression of cancer-associated fibroblasts (CAFs) and myeloid-derived suppressor cells (mMDSCs), as well as activation of dendritic cells (DCs) to train T-cells are advantageous. The activation of T-cells is also associated with the development of pro-apoptotic signals. Thus, a successful STING approach should rely on the targeted delivery of potent STINGa to induce the transient activation of the STING pathway in myeloid and cancer cells. pH Low Insertion Peptides (pHLIP® peptides) triggered by local acidity to fold and directionally insert across the membranes of acidic cells (Reshetnyak et al., 2020) were used for intracellular delivery of therapeutic cargoes (Cheng et al., 2015; Wyatt et al., 2018a; Svoronos et al., 2020; Gayle et al., 2021; Moshnikova et al., 2022a), including targeting of STINGa to cancer cells, M2-TAMs, CAFs, DCs and mMDSCs within TME (Moshnikova et al., 2022b). In this study we used two pHLIP peptides for a targeted delivery of dimeric STINGa for tumor eradication and development of anti-cancer immunity.

2 Materials and methods

2.1 Synthesis of pHLIP-STINGa compounds

Modified monomeric and dimeric STING agonists mMSA-PAB-SS-Py and Py-SS-Et-dMSA-Et-SS-Py, respectively, were synthesized and purified by Iris Biotech GmbH. pHLIP peptides consisting of all D amino acids were synthesized and purified at CSBio and Biosynth. To prepare pHLIP-mMSA and 2pHLIP-dMSA, Var3 pHLIP peptide was synthesized with single Cys residues at the membrane-inserting end: ADQDNPWRAYLDLLFPTDTLLLDLLWCG. pHLIP peptide was mixed with mMSA-PAB-SS-Py or Py-SS-Et-dMSA-Et-SS-Py in dimethyl sulfoxide (DMSO) at molar ratios of 1:1 or 2:1, respectively. Sodium phosphate buffer (100 mM) containing 150 mM NaCl at pH 7.4 saturated with argon was added to the reaction mix (1/10 of the total volume) and the reaction mixture was kept for 2 h at room temperature (RT). pHLIP-mMSA and 2pHLIP-dMSA constructs were purified by reverse phase high-performance liquid chromatography (HPLC) using Zorbax SB-C18 or Zorbax SB-C8, 9.4 × 250 mm, 5 µm columns (Agilent Technology) with a gradient from 20% to 80% acetonitrile in water containing 0.05% trifluoroacetic acid (TFA). For the preparation of a fluorescent version of 2pHLIP-dMSA (2(ICG-pHLIP)-dMSA), an N-terminal acetylated version of the pHLIP peptide with a lysine introduced near the N-terminus (AKDQDNPWRAYLDLLFPTDTLLLDLLWCG) was used. First, pHLIP was conjugated with Py-SS-Et-dMSA-Et-SS-Py, followed by purification. Then, ICG-NHS ester (Iris Biotech GmbH) was conjugated with the lysine residue at the N-terminal end of pHLIP in DMSO at molar ratio of 2.5:1. Sodium bicarbonate buffer (100 mM) at pH 8.3 was added to the reaction mix (1/10 of the total volume) and the reaction mixture was kept at RT until the conjugation was completed. The final purification was performed as described above. The products were lyophilized and characterized by matrix-assisted laser desorption/ionization-time of flight (MALDI-TOF) mass-spectrometry and analytical HPLC. The molecular weight of pHLIP-mMSA and 2pHLIP-dMSA are 3,781 Da and 7,574 Da, respectively. The concentration of pHLIP-STINGa conjugates was determined by absorbance using the following molar extinction coefficients: for pHLIP-mMSA ε_{325} = 15,000 $M^{-1}cm^{-1}$; ε_{325} = 30,000 $M^{-1}cm^{-1}$ for 2pHLIP-dMSA and ε_{800} = 137,000 $M^{-1}cm^{-1}$ for 2(ICG-pHLIP)-dMSA.

2.2 Biophysical studies

The interactions of pHLIP-mMSA and 2pHLIP-dMSA with liposomes were investigated by recording the construct's fluorescence and circular dichroism (CD) using a PC1 spectrofluorometer (ISS) and a MOS-450 spectrometer (Bio-Logic Science Instruments), respectively, with temperature control set to 25°C. Liposomes, constituting of large unilamellar vesicles were prepared by extrusion. 1-palmitoyl-2-oleoyl-*sn*-glycero-3-phosphocholine (POPC) lipids (Avanti Polar Lipids) in chloroform were desolvated on a rotary evaporator and dried under vacuum for a minimum of 2 h. The phospholipid film was rehydrated in 2 mM citrate phosphate buffer, pH 7.4, vortexed, and passed through the extruder (using a 50 nm membrane pore size) 21 times.

Fluorescence spectra were recorded from 310 nm to 390 nm at an excitation wavelength of 295 nm and 1.0 mm sized slits. The excitation polarizer was set to 54.7° ("magic angle") while the emission polarizer was set to 0° in order to reduce Wood's anomalies. CD spectra were recorded from 190 to 260 nm with a step size of 1 nm. The concentrations of pHLIP-mMSA/2pHLIP-dMSA and POPC were 7 µM and 1.4 mM, respectively.

The pH-dependent insertion of pHLIP-mMSA or 2pHLIP-dMSA into the lipid bilayer of POPC liposomes was studied by monitoring changes in the molar ellipticity as a function of pH. After the addition of aliquots of citric acid, the pHs of solutions containing pHLIP-mMSA/2pHLIP-dMSA and POPC liposomes were measured using an Orion PerHecT ROSS Combination pH Micro Electrode and an Orion Dual Star pH and ISE Benchtop Meter. The millidegree ellipticity values were plotted as a function of pH. The pH-dependence was fit with the Henderson-Hasselbach equation to determine the cooperativity (n) and the mid-point (pK) of transition. The fitting equation used was the following:

$$pH\ dependence = S2 + \frac{S3 - S2}{1 + 10^{n\,(pH - \mathrm{pK})}} \text{ for a single transition}$$

where $S2$ represents CD signal of pHLIP-mMSA or 2pHLIP-dMSA in presence of POPC at pH 7.4, when pHLIP peptides are adsorbed, but not inserted across lipid bilayer, and $S3$ represents CD signal of pHLIP-mMSA or 2pHLIP-dMSA in presence of POPC at pH 4.5, when pHLIP peptides are inserted across lipid bilayer of membrane.

Fluorescence kinetics was measured using a SFM-300 mixing system (Bio-Logic Science Instruments) in combination with the MOS-450 spectrometer with the temperature control set to 25°C. All samples were degassed before measurement to minimize air bubbles in the samples. pHLIP-mMSA/2pHLIP-dMSA and POPC samples were incubated overnight to reach equilibrium, when most of the agent was associated with liposome lipid bilayers. To follow insertion into a membrane, a solution containing 14 μM pHLIP-mMSA/2pHLIP-dMSA and 2.8 mM POPC was mixed with citric acid to lower the pH from pH 7.4 to 4. To follow exit of pHLIP-mMSA/2pHLIP-dMSA from the membrane, a low pH solution containing 14 μM pHLIP-mMSA/2pHLIP-dMSA and 2.8 mM POPC was mixed with dibasic phosphate buffer to raise the pH from 4 to 7.4. To monitor the fluorescence intensity changes during pHLIP-mMSA/2pHLIP-dMSA insertion induced by the pH change, the emission signal was observed through a cut-off 320 nm filter at an excitation of 295 nm.

All data were fit to the appropriate equations by nonlinear least squares curve fitting procedures employing the Levenberg Marquardt algorithm using Origin 8.5.

2.3 Binding of mMSA and dMSA to STING protein

Binding of mMSA and dMSA to STING protein was measured with human STING WT binding kit (Cisbio). Briefly: mMSA (MSA2, from MCE), dMSA (Iris Biotech GmbH) or 2′3′-cGAMP (Cisbio) control were added in increasing concentrations to the 96-well microplate (PerkinElmer), followed by addition of 6His-tagged human STING WT protein. STING WT ligand d2 reagent was premixed with 6His Tb antibodies, and it was added to each well and the plate was incubated for 3 h at RT. Fluorescence intensities at 616 nm and 665 nm excited at 450 nm were recorded on the SpectraMax ID5 plate reader (Molecular Devices). The homogeneous time resolved fluorescence (HTRF) ratio was calculated to establish the binding of each agent to the STING protein and to calculate EC50.

2.4 Binding to human serum albumin

Binding affinities of pHLIP-mMSA and 2pHLIP-dMSA to human serum albumin (HSA) (MilliporeSigma) were investigated using a series of competitive fluorescence binding assays measured on a SpectraMax ID5 plate reader with SoftMax 7.1.2 software. HSA was initially dissolved to 500 μM in deionized water and further diluted using pH 7.6 phosphate buffer. Dansylamide (DNSA) or dansylglycine (DNSG) (both from Tokyo Chemical Industry) were used as fluorescent markers, which are known to bind to specific sites on HSA. Each well contained 100 μL of sample consisting of the fluorescent marker DNSA or DNSG (1 μM), with different concentrations of pHLIP agents (0, 5, or 10 μM) and concentrations of HSA ranging from 0 μM to 100 μM. Samples were incubated for 2 h at 37°C. As controls, warfarin and ibuprofen, drugs known to bind different sites on HSA, were used instead of pHLIP agents. Fluorescence measurements from each well were performed at 485 nm with excitation at 365 nm at 37°C. As a control, binding of DNSA and DNSG were probed with each agent in absence of HSA. Before the measurements a plate reader optimization test was run. Data were fitted individually and globally using the Michaelis-Menten equation. In the global fits, a common Vmax value was used, established for 0 μM of pHLIP agents for both DNSA and DNSG. Data was fitted by nonlinear least squares curve fitting procedures employing the Levenberg Marquardt algorithm using Origin 8.5.

2.5 Self-immolation kinetics

To trigger S-S cleavage and self-immolation of the linker connecting pHLIP peptide and mMSA or dMSA payloads, solutions of pHLIP-mMSA or 2pHLIP-dMSA were treated with dithiothreitol (DTT). At different time points (from 30 min to 48 h of treatment) the samples were analyzed by HPLC using a Zorbax SB-C18 (for pHLIP-mMSA) or a Zorbax SB-C8 (for 2pHLIP-dMSA) 4.6 × 250 mm, 5 μm columns with a gradient from 20% to 80% acetonitrile in water containing 0.05% TFA. The chromatograms were recorded at 220 nm, 280 nm and 325 nm. mMSA, dMSA and pHLIP were used as controls at the same HPLC conditions.

2.6 Stability in mouse and human plasma

To establish the stability of agents (2pHLIP-dMSA, pHLIP-mMSA, dMSA, mMSA, and pHLIP) in plasma, each agent was mixed with single donor human or BALB/c mouse plasma (Innovative Research) at a concentration of 200 μM, and kept in plasma for 0, 1, 2, 4 or 24 h at 37°C. Plasma proteins were precipitated by methanol (1:5 volume ratio of plasma to methanol) and centrifuged for 10 min at 13.4 rpm. The supernatant was collected and analyzed by HPLC using a Zorbax SB-C18 4.6 × 250 mm, 5 μm column with a gradient from 20% to 80% acetonitrile in water containing 0.05% TFA. Chromatograms were recorded at 220 nm, 280 nm and 325 nm.

2.7 Activation of IFN in M2 macrophages

THP-1-Blue™-ISG cells (Invivogen) expressing an interferon (IFN) regulatory factor (IRF)-inducible secreted embryonic alkaline phosphatase (SEAP) reporter construct were used. Cells were maintained in RPMI growth medium supplemented with L-glutamine, sodium pyruvate, 10% fetal bovine serum (FBS), normocin and ciprofloxacin hydrochloride in a humidified atmosphere of 5% CO_2 and 95% air at 37°C. Cells were seeded in 96-well plates at a density of 75,000 cells/well. To generate M2 polarized macrophages, cells were treated first with 185 ng/mL phorbol 12-myristate 13-acetate (PMA) for 6 h and then 20 ng/mL of interleukin 4 (IL-4) and 20 ng/mL of interleukin 13 (IL-13) (both from PeproTech) were added for another 16 h of treatment. At the completion of polarization, the growth medium was replaced with Dulbecco's Modified Eagle Medium (DMEM) medium without FBS, pH 6.9, containing increasing amounts of 2pHLIP-dMSA or dMSA (up to 10.0 μM). After a 2-h incubation, an equal volume of

RPMI supplemented with 20% heat-inactivated FBS was added, and cells were incubated for another 48 h. SEAP activity was accessed using the QUANTI-Blue™ Solution (Invivogen) to evaluate type I interferon protein levels: 150 µL of the colorimetric reagent was added to 50 µL of cell supernatant for 30 min, 37°C, followed by absorption measurement at 655 nm.

2.8 Treatment of mice

All animal studies were conducted at the University of Rhode Island (URI) according to the approved by URI Institution Animal Care and Use Committee (IACUC) animal protocols AN04-12-011 and AN 1920-003. The studies complied with the principles and procedures outlined by the National Institutes of Health for the care and use of animals.

For the treatment of CT26 tumors, 5×10^4 CT26 murine colorectal cancer cells (ATCC, CRL-2638) were injected subcutaneously (SQ) in 100 µL of growth medium into the right flank of female Balb/c mice ranging in age from 7 to 9 weeks (Envigo RMS, Inc.). On day 1, when tumors reached a volume of 100–130 mm^3, mice were randomized into groups, body weight was measured and agents, including 2pHLIP-dMSA, pHLIP-mMSA, dMSA, mMSA or vehicle, were given as the first intraperitoneal (IP) injection. The second IP injection was given after 48 h mMSA, dMSA and pHLIP-mMSA were given as two IP injections of 300 µM 500 µL. 2pHLIP-dMSA was given as two IP injections of 300 µM 500 µL or 100 µM 500 µL (low dose). The compounds were dissolved in DMSO as a stock solution and transferred to PBS (vehicle). The residual DMSO in the final solution injected into animals was less than 2%. Tumor volume and body weight were measured 3 times per week throughout the study. Measurements of tumors were performed using calipers, and the tumor volume (V) was calculated with the formula:

$$V = 0.52 \cdot L \cdot W^2$$

where L is the length and W is the width of the measured tumor. Mice were removed from the study and euthanized when the tumor volume was greater than 2,000 mm^3.

In the 2pHLIP-dMSA treated groups the mice that stayed tumor-free were re-challenged with tumor cells injected into the tumor-free flank on day 65 after the first injection of 2pHLIP-dMSA. Tumor-free mice were kept for an additional 40 days (total of 105 days after the treatment with 2pHLIP-dMSA) and then were euthanized.

2.9 Biodistribution and PK

For biodistribution studies 5×10^4 of CT26 cancer cells were injected SQ in 100 µL of growth medium into the right flank of female Balb/c mice and tumors were grown until they reached 150–250 mm^3 in volume. Then a single retro-orbital (RO) injection of 50 µM 100 µL of 2(ICG-pHLIP)-dMSA was performed. Animals were euthanized at 5 min, 1, 4, 24, 48, 72, and 120 h post-injection, blood was collected in K_2 EDTA vacutainer blood collection tubes (BD), and necropsy was performed immediately after animals were euthanized. Blood, tumors and major organs (kidney, liver, spleen, pancreas, lung, heart, large and small intestines, bone, muscle, brain) were collected, and imaged *ex vivo* immediately after necropsy. Blood (200 µL) was imaged in 96-well plates with black bottom and walls. The zero-time point (0 min) was obtained by imaging of 2(ICG-pHLIP)-dMSA diluted in blood collected from a control mouse that did not receive any injection (the dilution was made based on the assumption that a mouse contains 80 mL/kg of blood).

The *in vivo* and *ex vivo* bright field and near-infrared fluorescent imaging employed a Stryker 1588 AIM endoscopic system with L10 AIM Light Source (808 nm excitation and collection of light in the range of approximately of 815–850 nm), and a 1588 AIM Camera using a 10 mm scope. The lens was kept at a fixed distance from the surface of the organs, within an enclosed (light-protected) area. Calibration curves converting laser and gain settings were established by imaging of pHLIP-ICG solution at different concentrations. The *ex vivo* fluorescence imaging of tissue specimens was performed using three different laser settings and six different gain settings. The digital fluorescence images were split into RGB channels, with the green channel being analyzed using ImageJ program to calculate the average fluorescence intensity. All average intensities were adjusted based on their capture settings and using calibration curves to present fluorescence intensities corresponding to the unified (the same) settings.

2.10 ELISA on blood and tumor samples

To establish levels of cytokines in blood and tumor samples, 5×10^4 CT26 cancer cells were injected SQ in 100 µL of growth medium into the right flank of female Balb/c mice. When tumors reached 250–500 mm^3 in volume, the mice received a single IP injection of 300 µM 500 µL 2pHLIP-dMSA or no injections. Animals were euthanized at 6- and 24-h post-injection, blood and tumors were collected. Blood samples were kept for 40 min at RT, centrifuged at 5,000 *g* for 20 min at +4°C and supernatant (serum) was collected. Tumors were frozen in liquid nitrogen. Both the serum and the tumor tissue samples were kept at −80°C until further processing and analysis. The tumor samples were processed while on ice, using a bullet blender (Next Advance) with 1 mm diameter zirconium silicate beads (Next Advance). The supernatant of the processed tumors was used for enzyme-linked immunoassay (ELISA) assays. Matched antibody pair kits for mouse TNF alpha (Sino Biological), mouse IL-6 (Abcam), mouse IFN gamma (Invitrogen), mouse IFN beta (Bio-Techne), and a precoated mouse IFN alpha kit (Invitrogen) were used. For TNF alpha and IFN beta the capture antibodies were diluted in PBS (Cytiva), while the IL-6 and IFN gamma capture antibodies were diluted in their respective coating buffers. The diluted capture antibodies were incubated in the plates overnight at +4°C and washed the next day with PBS/Tween washing buffer (Sigma-Aldrich). The TNF alpha plate was blocked using 2% BSA (Thermo-Scientific) diluted in washing buffer, the IFN beta plate was blocked using 1% BSA diluted in PBS, while the IFN alpha, IFN gamma, and IL-6 plates were blocked using their respective dilution buffers. Blocking was done for 2 h at RT on an orbital shaker at 200 rpm. After blocking, the plates were washed and then incubated with the diluted tumor

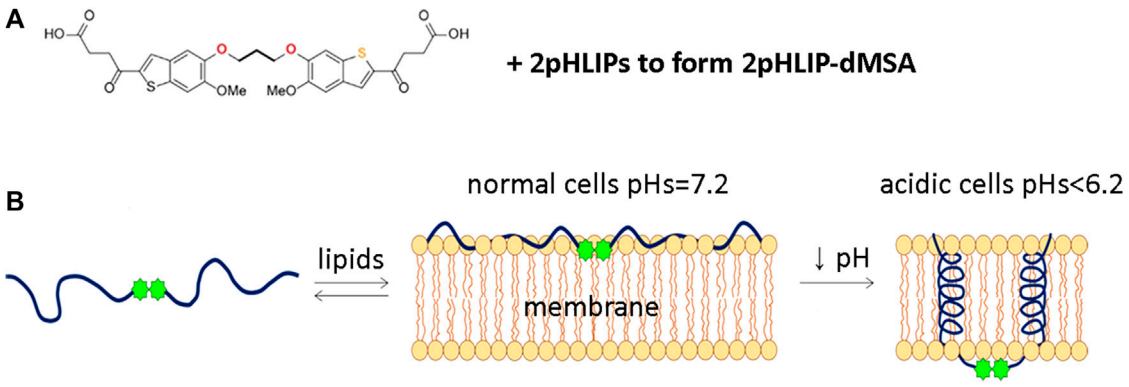

FIGURE 1
Schematic representation of 2pHLIP-dMSA interaction with a membrane lipid bilayer. The chemical structure of dMSA and proposed interaction with 2 pHLIP peptides are shown **(A)**. In **(B)**, schematics are shown of 2pHLIP-dMSA reversible interactions with the membranes of cells with normal surface pH (pH = 7.2) in healthy tissue and membranes of acidic cells with surface pH < 6.2 found in diseased tissues.

and serum samples along with the corresponding standard solutions for each ELISA kit. The samples were incubated for 2 h at RT on an orbital shaker at 200 rpm. The TNF alpha plate was incubated for 1 h at RT with a diluted detection antibody conjugated with horseradish peroxidase (HRP). The IL-6, IFN alpha, IFN beta, and IFN gamma plates were incubated for 1 h at RT with a diluted detection antibody conjugated with biotin followed by incubation for 1 h at RT with their respective diluted HRP-streptavidin conjugates. All plates were washed and incubated with 3,3′,5,5′-tetramethylbenzidine (TMB) (Invitrogen) and peroxide solution mixed at a ratio of 1:1 (Thermo Scientific) for up to 20 min, then a stop solution (10% H_2SO_4) was added to the plates. The signal from the wells was quantified by absorbance measured at 450 nm using a Bio-Rad iMark microplate reader. Antibody standards were used to plot calibration curves.

2.11 Statistical analysis

The Kolmogorov-Smirnov two-tailed nonparametric test was used to establish *p-levels*.

3 Results

3.1 Binding affinity of monomeric and dimeric STINGa

The majority of synthetic STINGa, used for systemic administration, are monomers like MSA-2 (mMSA), which occupy two adjacent binding sites in the STING protein dimer. Perceiving that linking two STINGa molecules might enhance affinity via entropic effects, several dimers were designed based on the MSA-2 monomer (dMSA) (Pan et al., 2020). Indeed, dimers bound more strongly to the STING protein (Pan et al., 2020). We confirmed this finding by testing the binding of both mMSA and dMSA to the STING protein and establishing that binding affinities were 7.5 μM for mMSA and 24 nM for dMSA, so the dimer is much more potent than the monomer (Supplementary Figure S1). Despite their high protein potency, dimers exhibit limited membrane permeability and significantly reduced cellular activity. Their potential bioavailability is low compared with MSA-2, which was developed as an oral drug. In any case, untargeted delivery of STINGa leads to systemic activation of the immune system and is associated with systemic toxicity.

3.2 Chemical conjugation with pHLIP

We have developed a delivery approach that uses multiple pHLIP peptides that collaborate in the targeted intracellular delivery of a single payload. Both mMSA and dMSA payloads were modified with the attachment of S-S cleavable self-immolating linkers to their carboxyl groups. A disulfide bond was exchanged with the SH group of a unique Cys residue placed at the C-terminal end of a version of a pHLIP peptide to obtain two compounds. In 2pHLIP-dMSA two pHLIP peptides were linked to a single dMSA dimeric STINGa (Figure 1A). We would like to note that it is challenging to conjugate and purify a single pHLIP linked to dMSA, since dMSA carries two identical linkers and it is impossible to stop conjugation reaction, since it continues during the purification. In pHLIP-mMSA a single pHLIP peptide was linked with a single mMSA monomeric STINGa (Supplementary Figure S2A). We used a Var3 version of pHLIP peptide made from D amino acids. In the case of 2pHLIP-dMSA, the energy of folding of two pHLIP peptides is expected to be used in a cooperative manner for the intracellular delivery of the dMSA payload across the membranes of acidic cells (Figure 1B), while in the case of pHLIP-mMSA, a single pHLIP peptide can translocate a single mMSA payload across the membrane of acidic cells (Supplementary Figure S2B).

3.3 Kinetics of self-immolation

To confirm that the dMSA payload can be released after the cleavage of the S-S bond, we monitored the kinetics of self-immolation by HPLC analysis as a function of time after the addition of DTT into

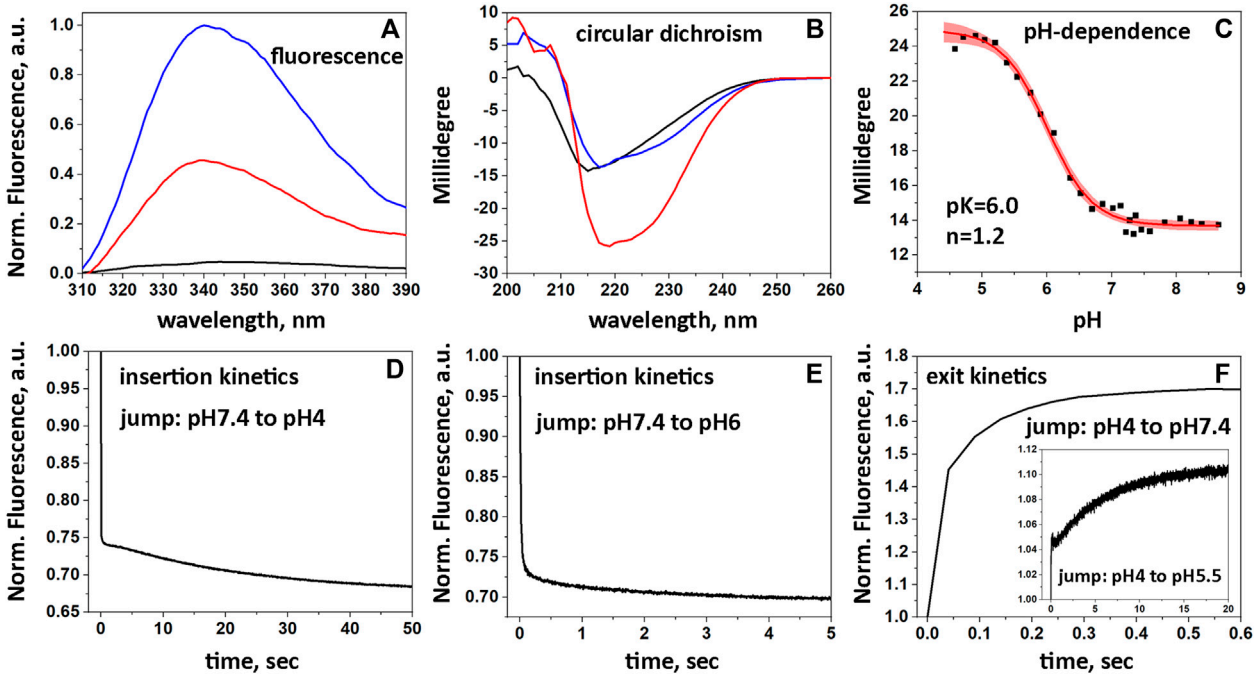

FIGURE 2
Interactions of 2pHLIP-dMSA with liposome lipid bilayers. Fluorescence **(A)** and CD **(B)** spectra of 2pHLIP-dMSA in solution at pH 7.4 (black lines), in the presence of POPC liposomes at pH 7.4 (blue lines) and in the presence of POPC liposomes at pH 3.5 (red lines) are shown. CD spectral signals were normalized per peptide and multiplied by (−1), since the D-amino acid pHLIP peptides used in the study invert the usual CD spectrum. pH-dependent transitions monitored by changes of CD spectral signal in presence of POPC liposomes (experimental points and fitting curves, red, with 95% confidence interval, pink) are presented **(C)**. Kinetics of fluorescence changes triggered by pH drops **(D, E)** and pH increases **(F)** in presence of POPC liposomes are shown.

solutions containing 2pHLIP-dMSA. The cleavage of S-S bonds is followed by the formation of multiple intermediates during the self-immolation process, which is mostly completed within 48 h with the release of dMSA in its original form (Supplementary Figure S3). A similar process, but with a smaller number of intermediates, was observed for self-immolation and release of mMSA, which was completed within 24 h (Supplementary Figure S4).

3.4 Biophysical characterization

Biophysical studies using POPC liposomes confirmed the pH-dependent interactions of 2pHLIP-dMSA with the membrane lipid bilayer. Fluorescence (Figure 2A) and circular dichroism (Figure 2B) measurements reflect the partitioning of pHLIP into the lipid bilayer accompanied by the formation of helical structure in the membrane at low pH. 2pHLIP-dMSA is observed to insert into the POPC bilayer with a pK of 6.0 and a cooperativity of 1.2 (Figure 2C). Interactions of 2pHLIP-dMSA with bilayers were similar to those of pHLIP-mMSA (Supplementary Figures S5A–C). Insertion of 2pHLIP-dMSA into the lipid bilayer triggered by a pH drop from pH 7.4 to 4 was fast (completed within 100 msec) and small conformational adjustments were observed for another 50 s (Figure 2D). The kinetics of membrane insertion of 2pHLIP-dMSA resulting from a pH drop from pH 7.4 to 6 (Figure 2E), which is more similar to biological conditions, was more efficient and faster than the insertion of pHLIP-mMSA (Supplementary Figure S5E). We also followed the exit of the agents from the lipid bilayer induced by a pH rise from pH 4 to 7.4 and from pH 4 to 5.5 (Figure 2F; Supplementary Figure S5F). The exit of 2pHLIP-dMSA is slightly slower, which is better illustrated during the intermediate pH jump (insert in Figure 2F), compared to the exit of pHLIP-mMSA (Supplementary Figure S5F). The data indicates that two pHLIP peptides trigger efficient partitioning of dMSA into a lipid bilayer as the result of a pH drop, with a less efficient exit compared to a single pHLIP-cargo conjugate.

3.5 Cellular activation of STING pathway

To complete the characterization of 2pHLIP-dMSA, the activation of the interferon signaling pathway was confirmed in polarized M2 macrophages. Activation was studied in THP1-Blue cells derived from a human THP-1 monocyte cell line by stable integration of an interferon regulatory factor (IRF)-inducible secreted embryonic alkaline phosphatase (SEAP) reporter construct. We found that THP1-Blue cells exhibited a concentration-dependent activation of IRF signaling when polarized by phorbol 12-myristate 13-acetate (PMA), interleukin 4 (IL-4) and interleukin 13 (IL-13) into M2-type macrophages and treated with 2pHLIP-dMSA (Figure 3A). EC50 for 2pHLIP-dMSA was calculated to be 200 nM, while EC50 for mMSA was established to be 2,200 nM (data not shown). Thus, we confirmed successful intracellular delivery and cytoplasmic release of dMSA by pHLIP

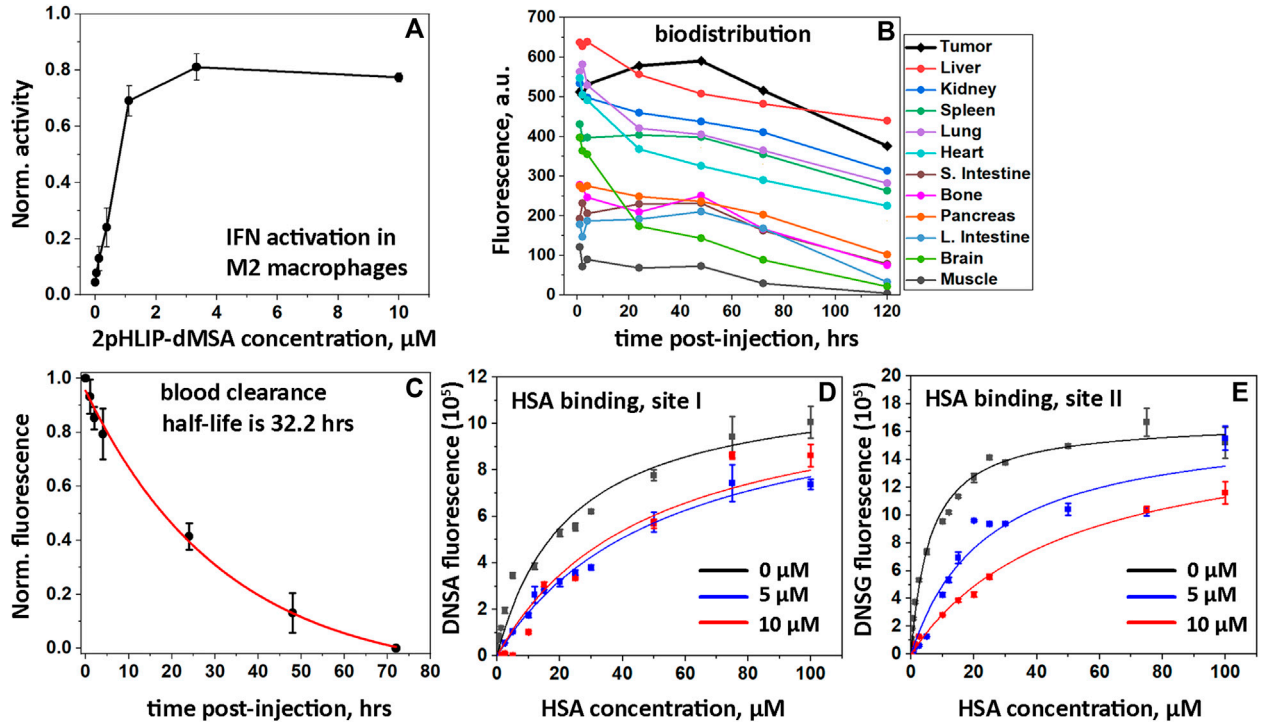

FIGURE 3
In vitro IFN activations, biodistribution, PK and HSA binding. Activation of the IFN signaling pathway induced by 2pHLIP-dMSA in THP1-Blue-ISG cells polarized by PMA, IL-4/IL-13 into M2-type macrophages is shown **(A)**. The results were normalized to the activity of dMSA alone at the maximum concentration tested, which was taken as 1. Kinetics of 2(ICG-pHLIP)-dMSA targeting CT26 tumor and clearance of the agent from major organs are shown **(B)**. The mean fluorescence per area was calculated for each organ and tissue collected at different timepoints after single RO injection of 2(ICG-pHLIP)-dMSA (50 μM 100 μL). Normalized fluorescence recorded in blood, which was collected at different time points after single RO injection of 2(ICG-pHLIP)-dMSA is shown (mean and Sd.) **(C)**. The data were fitted with an exponential function (red line). Changes of DNSA **(D)** and DNSG **(E)** fluorescence with increasing HSA concentration in absence (black symbols) or presence of 5 μM (blue symbols) or 10 μM (red symbols) of 2pHLIP-dMSA. The global fitting was performed with each set of data **(D and E)** and the fitting curves are shown as black, blue and red lines.

peptides and showed that the dimeric construct is significantly more active.

3.6 Biodistribution and PK

Biodistribution, tumor uptake and pharmacokinetics (PK) studies were conducted by conjugating a near infrared indocyanine green (ICG) fluorescent dye to the non-inserting end of pHLIP peptides to make a 2(ICG-pHLIP)-dMSA fluorescent construct. When CT26 tumors, established in the right flanks of female Balb/c mice, reached volumes of about 150–250 mm^3, 2(ICG-pHLIP)-dMSA (50 μM 100 μL) was given as a single retro-orbital (RO) injection. For biodistribution and PK studies, the animals were euthanized, followed by harvesting of blood, tumors and major organs. Fluorescence of the samples was quantitatively measured at 1-, 4-, 24-, 48-, 72-, and 120-h time points after a single RO injection of 2(ICG-pHLIP)-dMSA (Supplementary Figures S6, S7). The kinetics of the fluorescence signal of 2(ICG-pHLIP)-dMSA indicate a significant accumulation of the agent in the tumor from 1 h and up to 48 h followed by a slight decrease of the signal at later time points (Figure 3B). The organ and tissue clearances were slow (Figure 3B). It is important to note that 1) CT26 tumors increase in size over 5 days (120 h time point), so normalized fluorescence may be lower in tumors at later time points; 2) the presence of the agent in an organ does not mean cellular delivery of dMSA, which only occurs in a low pH environment where pHLIP inserts into cell membranes, followed by dMSA cleavage from pHLIP, linker self-immolation, and release of dMSA; and 3) the agent has two ICG dyes, which potentially can affect the clearance profile by significant binding to plasma proteins. Slow tissue clearance is associated with slow blood clearance. Whole blood imaging was performed to establish clearance of the agent (Figure 3C). The observed half-life of 2(ICG-pHLIP)-dMSA is 32.2 h, which is significantly longer compared to any previously investigated pHLIP-cargo conjugate (Gayle et al., 2021; Moshnikova et al., 2022b). We studied binding of 2pHLIP-dMSA with human serum albumin (HSA) in a competitive binding assay using DNSA and DNSG fluorescent dyes, which are known to bind site I and site II on HSA, respectively (Sudlow et al., 1975). Interactions of DNSA or DNSG with increasing concentration of HSA were investigated in the absence and presence of 2pHLIP-dMSA, pHLIP-mMSA, pHLIP, warfarin (binds site I) and ibuprofen (binds site II) (Figures 3D,E; Supplementary Figure S8). The binding of DNSA to HSA was reduced about 2-fold in the presence of 2pHLIP-dMSA, while warfarin at concentration of 10 μM reduced DNSA binding to HSA by 5.3-fold (Supplementary Table S1). The binding of DNSG to HSA was reduced 7.8-fold in the presence of 10 μM of

2pHLIP-dMSA, while ibuprofen reduced DNSG binding to HSA by 5.3-fold (Supplementary Table S1). The obtained results indicate strong binding of 2pHLIP-dMSA to HSA, especially to its site II, which is known to interact with cyclic compounds including ibuprofen, tryptophan, and compounds with free carboxyl groups (Sudlow et al., 1976). We also cannot exclude binding of 2pHLIP-dMSA to other plasma proteins.

3.7 Selective activation of cytokines in tumor

Activation of interferon types I and II, and induction of proinflammatory cytokines in tumors and serum were measured following a single IP injection of 2pHLIP-dMSA (300 μM 500 μL) (Figure 4). In tumors, the level of TNF-α increased 23-fold 6-h post-injection and then fell to a normal level at 24 h (Figure 4A). In serum, the level of TNF-α was insignificant both in treated and in untreated mice (Figure 4B). The blood level of IL-6 rose about 2.4-fold at 6-h post-treatment (Figure 4C) with a slight increase of its level in blood (Figure 4D), which returned to its normal level at 24 h. The level of IL-6 in serum was an order of magnitude lower compared to its level in tumors. The tumor levels of type I interferon, IFN-β, increased 8-fold in treated animals (Figure 4E), accompanied by a slight increase in serum (two orders of magnitude lower than the level in tumors) (Figure 4F). The levels of IFN-α and IFN-γ did not change much (Figures 4G–J). Thus, 2pHLIP-dMSA induced transient tumor-targeted increases of type I interferon, IFN-β, and the pro-inflammatory cytokines TNF-α and IL-6, indicating activation of the NF-kB and IRF3 signaling pathways, without systemic activation. Activation of type II interferons was not noted. The relatively fast (6 h after 2pHLIP-dMSA administration) activation of cytokines followed by their decay does not match the observed slow blood clearance. Therefore, we assessed the stability of 2pHLIP-dMSA and dMSA alone in mouse and human plasma (pHLIP peptides, especially consisting of D amino acids, exhibit high stability in plasma). The stability of 2pHLIP-dMSA (and pHLIP-mMSA) in human plasma was very high, however the stability of the agents in mouse plasma was low. The cargoes, dMSA or mMSA, were released from the pHLIP and underwent degradation within 24 h in mouse plasma. It is likely that only a fraction of injected 2pHLIP-dMSA reaches the tumor in its native form in mice.

3.8 Therapeutic efficacy

Due to the rapid degradation of the agent in mouse blood, we tested the therapeutic efficacy of 2pHLIP-dMSA by performing 2 injections of two different dose levels in Balb/c female mice bearing right flank CT26 tumors. When a tumor reached about 100–150 mm^3 in volume, designated as day 1, two IP injections of 2pHLIP-dMSA, either 300 μM in 500 μL or 100 μM in 500 μL (called lower dose or l.d.) per injection, were performed on days 1 and 3 (Figures 5B,C). Tumor growth was monitored for 65 days or until the tumor volume endpoint was achieved (2,000 mm^3, when animals were euthanized). All animals in the control groups that received either dMSA alone at a dose level of 300 μM 500 μL per injection (Figure 5D) or vehicle (Figure 5E) developed endpoint size tumors within 14–20 days p.i. In the treated groups, the tumors disappeared in 7 mice out of 10 for the higher dose and for mice treated with the lower dose of 2pHLIP-dMSA 4 out of 10 survived. 11 survivors were re-injected with cancer cells on day 65, and none of them developed tumors, indicating the development of robust immune memory. Treatment of mice led to temporary weight loss followed by complete recovery and regain of weight (Figures 5F,G). The Kaplan-Meier survival plots demonstrate dramatic differences between the controls and 2pHLIP-dMSA treated groups (Figure 5H). Thus, while dimeric STINGa, dMSA, does not exhibit any therapeutic activity by itself, when it is conjugated with two pHLIP peptides that target dMSA to the TME, the tumor is eradicated, and immune memory is developed. We also checked activity of pHLIP-mMSA at the same dose level. While mMSA did not demonstrate any activity on animals, tumor was eradicated in 2 mice out of 10 treated with pHLIP-mMSA (Supplementary Figure S9).

4 Discussion

We have previously tested the idea of using several pHLIPs in bundles for the targeted intracellular delivery of several cargoes. Two and four individual pHLIP peptides were bundled together by using 2-armed and 4-armed PEG polymers attached to the membrane non-inserting ends of the pHLIP peptides, while cargoes were conjugated to the membrane inserting ends of each pHLIP peptide (Wyatt et al., 2018b). This strategy gave agents containing *n* pHLIP peptides with *n* payloads, where *n* was 2 or 4. Bundling of the pHLIP peptides resulted in more efficient intracellular delivery of the cargoes. This led to the idea that multiple pHLIPs might combine their insertion energies to facilitate delivery of a single, otherwise challenging cargo.

In this study we have developed a delivery approach that uses multiple pHLIP peptides that collaborate in the targeted intracellular delivery of a single payload. Specifically, we employed two pHLIP peptides symmetrically linked to the opposite ends of a dimeric STINGa to construct the 2pHLIP-dMSA agent. We demonstrated that two pHLIPs have a kinetic advantage in translating cargo across membrane at mildly acidic pH found at the surface of metabolically active acidic cells. It was shown previously that pHLIP can extend blood circulation of small molecules by an order of magnitude (Crawford et al., 2020; Gayle et al., 2021; Moshnikova et al., 2022b). Notably, 2pHLIP-dMSA exhibits the longest circulation in blood (half-life >30 h) among other investigated pHLIP-cargo conjugates. As a result, blood and tissue clearance was slow, while tumor targeting was significant. Importantly, activation of type I interferon and pro-inflammatory cytokines were high and transient in tumors without systemic activation, which is crucial for the development of safe and effective STINGa treatments. Tumors were eradicated in seven out of ten mice treated with 2pHLIP-dMSA. In the other three animals, the tumor initially disappeared, however later they redeveloped the tumors, which quickly progressed to large sizes. In the group treated with the lower dose of 2pHLIP-dMSA, just 4 animals out of 10 survived. Others either developed tumors quickly or with some delay. All survived animals, irrespective of dose of treatment, did not develop

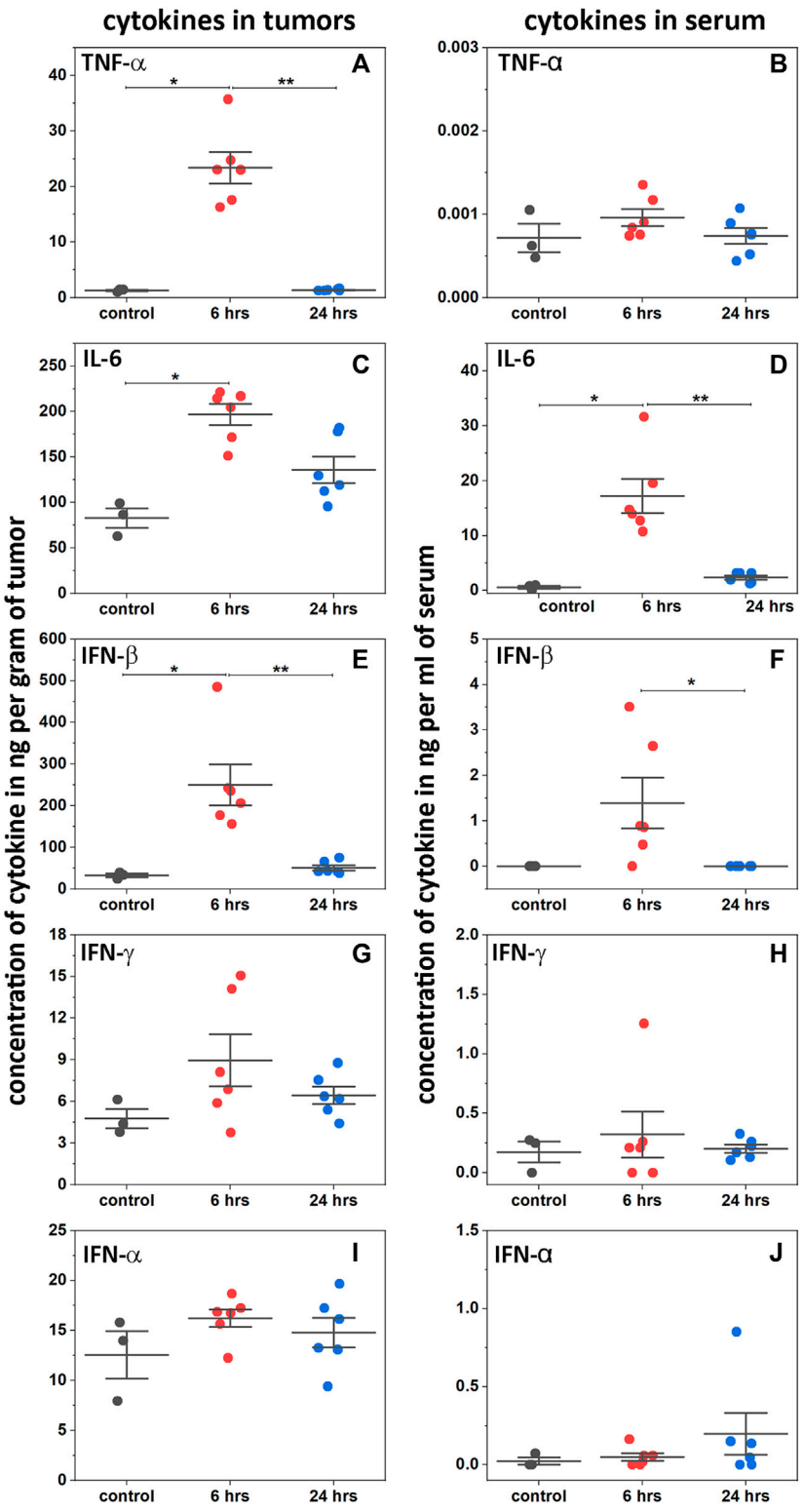

FIGURE 4
Activation of cytokines. Levels of TNF-α **(A and B)**, IL-6 **(C and D)**, INF-β **(E and F)**, IFN-γ **(G and H)** and INF-α **(I and J)** cytokines are shown in tumors and serum as established by ELISA at 6 and 24 h after a single RO injection of 2pHLIP-dMSA (300 μM 500 μL) in comparison to control mice (all points, mean, and SE are shown, * indicates that the *p*-level is < 0.02 and ** indicates that the *p*-level is < 0.002, otherwise differences are statistically insignificant, *p*-levels were calculated using the Kolmogorov-Smirnov two-tailed nonparametric test).

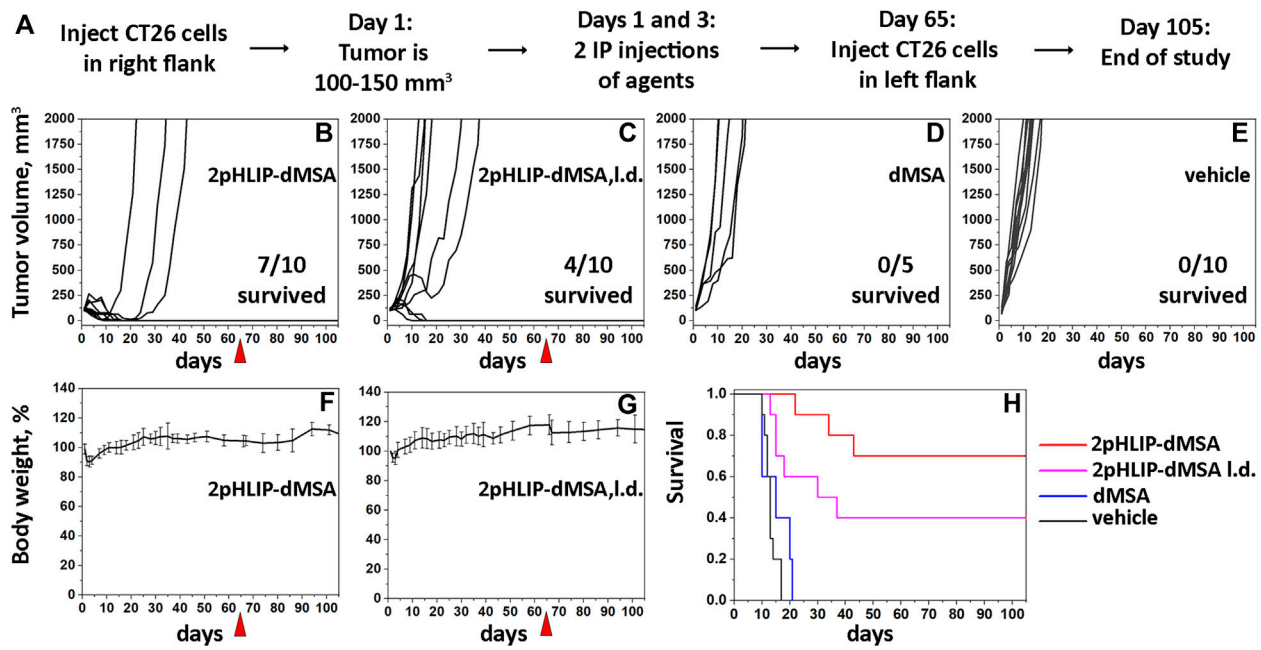

FIGURE 5
Eradication of CT26 tumors and development of immune memory. The experimental design is presented **(A)**. Right flank CT26 tumor growth curves in Balb/c mice are shown after two IP injections of 2pHLIP-dMSA **(B)**, dMSA **(D)** at dose 300 μM 500 μL per injection, 2pHLIP-dMSA at lower dose (L.d.) 100 μM 500 μL per injection **(C)**, and vehicle **(E)** performed on days 1 and 3, when tumors had reached about 100–150 mm^3 in volume. The surviving mice were re-injected with CT26 cancer cells in the contralateral left flank on day 65, indicated by red triangle. The average changes of mouse body weights after two IP injections of 2pHLIP-dMSA **(F)** and 2pHLIP-dMSA at lower dose **(G)** are shown. Kaplan-Meier survival plots are shown **(H)**.

tumors after re-challenge with another injection of cancer cells. At the same time non-targeted dMSA at dose equivalent to the highest dose used in the experiment, was non-effective in treatment of tumors. It is interesting to note that therapeutic effect of targeted STINGa is threshold-based. Either the immune system is actively reacting to the treatment, which leads to the tumor eradication and development of a very robust protective response, or there is an escape and tumor will develop quickly. At the higher dose of treatment, the probability of escape is lower, while at the lower dose of treatment the probability of escape is increasing. At the same time, the responded animals have similar effects in groups of higher or lower doses. More studies would be required to understand which parameters drive an escape. Potential successful treatment should be associated with strong, but transient effect without systemic activation, which could be achieved by targeted delivery of STINGa to immune, tumor stroma and cancer cells.

Our results demonstrate that the energy of pH-triggered membrane-associated folding of two pHLIP peptides could be utilized in targeted intracellular delivery of a payload. It could be especially advantageous for intracellular delivery of large, potentially polar, and challenging therapeutic payloads like dimers of STINGa, peptide nucleic acids or other therapeutic cargo molecules.

The STING pathway plays a central role in regulating the anti-tumor immune response. However, untargeted use of STINGa is associated with serious side effects and the clinical utility is poor. Thus, there is a significant effort underway to introduce and develop targeted approaches for more effective delivery of STINGa. Immune-stimulating antibody-conjugates (ISACs) are under development and have entered clinical trials. An antibody against, the epidermal growth factor receptor (EGFR) conjugated with STINGa via cleavable linker, demonstrated enhanced preclinical efficacy (Wu et al., 2022). STINGa conjugated with human epidermal growth factor receptor 2 (HER2), Mersana's XMT-2056 conjugate, has demonstrated very good preclinical results as well. However, a grade 5 (fatal) serious adverse event was observed during clinical trials. Takeda undertook a different approach by developing TAK-500, an IgG1 anti-cysteine-cysteine chemokine receptor 2 (CCR2) antibody conjugated with their TAK-676 STINGa via a self-immolating maleimide-containing protease-cleavable peptide linker, targeting TAMs. Currently TAK-500 is in clinical trials and is showing good activity (Diamond et al., 2022). Another approach is to use nanomaterials for the encapsulation and protection of STINGa. Lipid nanodiscs (LNDs), formed from the self-assembly of PEGylated lipids encapsulated with cyclic dinucleotide (CDN) were successfully tested in preclinical tumor models (Dane et al., 2022). Nanoparticles comprising a pH-sensitive polymer with a cyclic seven-membered ring (PC7A) and multiple STINGa molecules were also tested preclinically and showed improved performance compared with use of STINGa alone (Li et al., 2021).

pHLIP has several potential advantages compared with other delivery mechanisms: 1) pHLIP senses and targets pH at the surface of all acidic cells within the TME including cancer cells, TAMs, CAFs, mMDSCs, and DCs in a manner that is not dependent upon molecular tumor biomarkers, which change and can be evaded as a result of ongoing selection pressure, 2) pHLIP efficiently translocates large polar molecules directly into the cytoplasms of acidic cells; and 3) pHLIP exhibits improved tumor penetration compared with

antibodies and nanoparticles. Our previous and current studies demonstrate significant promise in use of pHLIP for targeted intracellular delivery of dimeric STINGa. Specifically, employing the combined energy of the membrane-associated folding of two pHLIP peptides for the delivery of a single dimeric STINGa offers a number of advantages including a kinetic advantage in the translocation of cargo across the membrane, long blood circulation, excellent tumor targeting and selective activation of cytokines in the TME without systemic activation. The prolonged, 1–2 days, circulation of the 2pHLIP-dMSA in the blood leads to the improvement of tumor targeting and delivery of sufficient amounts of STINGa to tumors, which is required to induce strong transient activation of the STING pathway in cancer, stromal and immune cells simultaneously. At the same time, prolonged circulation increases the requirement for stability of the agent in the plasma. While the agent exhibits better stability in human plasma compared to mouse plasma, searching for more stable agents, with better linkers connecting the pHLIP peptides to dimeric STINGa, will be desirable. Moreover, the kinetics of self-immolation were slow and complex, which would require improvement prior to clinical translation.

Besides the challenge of the targeted delivery of STINGa, there is also a biological limitation associated with the silencing of the STING pathway in variety of tumors (Konno et al., 2018). In a TCGA based analysis it was reported that STING expression is lost or downregulated mainly through promoter hypermethylation-driven silencing, and silencing can be restored by employing DNA methylation inhibitors (Konno et al., 2018; Falahat et al., 2019; Falahat et al., 2021; Low et al., 2022; Falahat et al., 2023).

Combining approaches for targeting of STINGa and restoring STING expression by DNA methylation inhibitors, when needed, may lead to a breakthrough in clinically effective STING-therapies.

Data availability statement

The original contributions presented in the study are included in the article/Supplementary Material, further inquiries can be directed to the corresponding author.

Ethics statement

Ethical approval was not required for the studies on humans in accordance with the local legislation and institutional requirements because only commercially available established cell lines were used. The animal study was approved by URI Institution Animal Care and Use Committee (IACUC) animal protocols AN04-12-011 and AN 1920-003. The study was conducted in accordance with the local legislation and institutional requirements.

Author contributions

AM: Conceptualization, Data curation, Formal Analysis, Investigation, Methodology, Supervision, Writing–review and editing, Project administration, Validation. MD: Data curation, Formal Analysis, Investigation, Methodology, Software, Supervision, Writing–review and editing. MI: Formal Analysis, Investigation, Writing–review and editing. CK: Data curation, Formal Analysis, Investigation, Supervision, Validation, Writing–review and editing, Methodology. HV: Data curation, Formal Analysis, Investigation, Methodology, Supervision, Validation, Writing–review and editing. DA: Formal Analysis, Investigation, Writing–review and editing. PP: Investigation, Writing–review and editing. DE: Conceptualization, Funding acquisition, Resources, Writing–review and editing. OA: Conceptualization, Funding acquisition, Investigation, Methodology, Resources, Supervision, Validation, Writing–review and editing. YR: Conceptualization, Data curation, Funding acquisition, Investigation, Project administration, Supervision, Validation, Writing–original draft, Writing–review and editing, Formal Analysis, Methodology, Resources.

Funding

The author(s) declare financial support was received for the research, authorship, and/or publication of this article. This work was supported by the National Institute of General Medical Sciences of the National Institutes of Health under grant number R01GM073857 (DE, OA, and YR.) and under grant number T34GM131948 (DA).

Acknowledgments

The authors are grateful for the support of members of the URI Institutional Development Award (IDeA) Network for Biomedical Research Excellence supported by NIH P20 GM103430, and Stryker Endoscopy (San Jose, CA) for providing their imaging system.

Conflict of interest

DE, OA, and YR are founders of pHLIP, Inc., and they have shares in the company. pHLIP, Inc. sponsored synthesis and purification of dMSA and modified dMSA prepared by the Iris Biotech GmbH.

The remaining authors declare that the research was conducted in the absence of any commercial or financial relationships that could be construed as a potential conflict of interest.

Publisher's note

All claims expressed in this article are solely those of the authors and do not necessarily represent those of their affiliated organizations, or those of the publisher, the editors and the reviewers. Any product that may be evaluated in this article, or claim that may be made by its manufacturer, is not guaranteed or endorsed by the publisher.

Supplementary material

The Supplementary Material for this article can be found online at: https://www.frontiersin.org/articles/10.3389/fphar.2024.1346756/full#supplementary-material

References

Chamma, H., Vila, I. K., Taffoni, C., Turtoi, A., and Laguette, N. (2022). Activation of STING in the pancreatic tumor microenvironment: a novel therapeutic opportunity. *Cancer Lett.* 538, 215694. doi:10.1016/j.canlet.2022.215694

Cheng, C. J., Bahal, R., Babar, I. A., Pincus, Z., Barrera, F., Liu, C., et al. (2015). MicroRNA silencing for cancer therapy targeted to the tumour microenvironment. *Nature* 518, 107–110. doi:10.1038/nature13905

Crawford, T., Moshnikova, A., Roles, S., Weerakkody, D., DuPont, M., Carter, L. M., et al. (2020). pHLIP ICG for delineation of tumors and blood flow during fluorescence-guided surgery. *Sci. Rep.* 10, 18356. doi:10.1038/s41598-020-75443-5

Dane, E. L., Belessiotis-Richards, A., Backlund, C., Wang, J., Hidaka, K., Milling, L. E., et al. (2022). STING agonist delivery by tumour-penetrating PEG-lipid nanodiscs primes robust anticancer immunity. *Nat. Mater* 21, 710–720. doi:10.1038/s41563-022-01251-z

Decout, A., Katz, J. D., Venkatraman, S., and Ablasser, A. (2021). The cGAS-STING pathway as a therapeutic target in inflammatory diseases. *Nat. Rev. Immunol.* 21, 548–569. doi:10.1038/s41577-021-00524-z

Diamond, J. R., Henry, J. T., Falchook, G. S., Olszanski, A. J., Singh, H., Gregory, R. C., et al. (2022). Phase 1a/1b study design of the novel STING agonist, immune-stimulating antibody-conjugate (ISAC) TAK-500, with or without pembrolizumab in patients with advanced solid tumors. *J. Clin. Oncol.* 40, TPS2690. doi:10.1200/jco.2022.40.16_suppl.tps2690

Falahat, R., Berglund, A., Perez-Villarroel, P., Putney, R. M., Hamaidi, I., Kim, S., et al. (2023). Epigenetic state determines the *in vivo* efficacy of STING agonist therapy. *Nat. Commun.* 14, 1573. doi:10.1038/s41467-023-37217-1

Falahat, R., Berglund, A., Putney, R. M., Perez-Villarroel, P., Aoyama, S., Pilon-Thomas, S., et al. (2021). Epigenetic reprogramming of tumor cell-intrinsic STING function sculpts antigenicity and T cell recognition of melanoma. *Proc. Natl. Acad. Sci. U. S. A.* 118. doi:10.1073/pnas.2013598118

Falahat, R., Perez-Villarroel, P., Mailloux, A. W., Zhu, G., Pilon-Thomas, S., Barber, G. N., et al. (2019). STING signaling in melanoma cells shapes antigenicity and can promote antitumor T-cell activity. *Cancer Immunol. Res.* 7, 1837–1848. doi:10.1158/2326-6066.CIR-19-0229

Gayle, S., Aiello, R., Leelatian, N., Beckta, J. M., Bechtold, J., Bourassa, P., et al. (2021). Correction to "Tumor-selective, antigen-independent delivery of a pH sensitive peptide-topoisomerase inhibitor conjugate suppresses tumor growth without systemic toxicity. *Nar. Cancer* 3, zcab047. doi:10.1093/narcan/zcab047

Hainaut, P., and Plymoth, A. (2013). Targeting the hallmarks of cancer: towards a rational approach to next-generation cancer therapy. *Curr. Opin. Oncol.* 25, 50–51. doi:10.1097/CCO.0b013e32835b651e

Klarquist, J., Hennies, C. M., Lehn, M. A., Reboulet, R. A., Feau, S., and Janssen, E. M. (2014). STING-mediated DNA sensing promotes antitumor and autoimmune responses to dying cells. *J. Immunol.* 193, 6124–6134. doi:10.4049/jimmunol.1401869

Konno, H., Yamauchi, S., Berglund, A., Putney, R. M., Mule, J. J., and Barber, G. N. (2018). Suppression of STING signaling through epigenetic silencing and missense mutation impedes DNA damage mediated cytokine production. *Oncogene* 37, 2037–2051. doi:10.1038/s41388-017-0120-0

Lesterhuis, W. J., Haanen, J. B., and Punt, C. J. (2011). Cancer immunotherapy--revisited. *Nat. Rev. Drug Discov.* 10, 591–600. doi:10.1038/nrd3500

Li, S., Luo, M., Wang, Z., Feng, Q., Wilhelm, J., Wang, X., et al. (2021). Prolonged activation of innate immune pathways by a polyvalent STING agonist. *Nat. Biomed. Eng.* 5, 455–466. doi:10.1038/s41551-020-00675-9

Low, J. T., Chandramohan, V., Bowie, M. L., Brown, M. C., Waitkus, M. S., Briley, A., et al. (2022). Epigenetic STING silencing is developmentally conserved in gliomas and can be rescued by methyltransferase inhibition. *Cancer Cell* 40, 439–440. doi:10.1016/j.ccell.2022.04.009

Moshnikova, A., DuPont, M., Visca, H., Engelman, D. M., Andreev, O. A., and Reshetnyak, Y. K. (2022b). Eradication of tumors and development of anti-cancer immunity using STINGa targeted by pHLIP. *Front. Oncol.* 12, 1023959. doi:10.3389/fonc.2022.1023959

Moshnikova, A., Golijanin, B., Amin, A., Doyle, J., Kott, O., Gershman, B., et al. (2022a). Targeting bladder urothelial carcinoma with pHlip-ICG and inhibition of urothelial cancer cell proliferation by pHLIP-amanitin. *Front. Urol.* 2, 868919. doi:10.3389/fruro.2022.868919

Motedayen Aval, L., Pease, J. E., Sharma, R., and Pinato, D. J. (2020). Challenges and opportunities in the clinical development of STING agonists for cancer immunotherapy. *J. Clin. Med.* 9, 3323. doi:10.3390/jcm9103323

Pan, B. S., Perera, S. A., Piesvaux, J. A., Presland, J. P., Schroeder, G. K., Cumming, J. N., et al. (2020). An orally available non-nucleotide STING agonist with antitumor activity. *Science* 369, eaba6098. doi:10.1126/science.aba6098

Reshetnyak, Y. K., Moshnikova, A., Andreev, O. A., and Engelman, D. M. (2020). Targeting acidic diseased tissues by pH-triggered membrane-associated peptide folding. *Front. Bioeng. Biotechnol.* 8, 335. doi:10.3389/fbioe.2020.00335

Sudlow, G., Birkett, D. J., and Wade, D. N. (1975). The characterization of two specific drug binding sites on human serum albumin. *Mol. Pharmacol.* 11, 824–832.

Sudlow, G., Birkett, D. J., and Wade, D. N. (1976). Further characterization of specific drug binding sites on human serum albumin. *Mol. Pharmacol.* 12, 1052–1061.

Svoronos, A. A., Bahal, R., Pereira, M. C., Barrera, F. N., Deacon, J. C., Bosenberg, M., et al. (2020). Tumor-targeted, cytoplasmic delivery of large, polar molecules using a pH-low insertion peptide. *Mol. Pharm.* 17, 461–471. doi:10.1021/acs.molpharmaceut.9b00883

Woo, S. R., Fuertes, M. B., Corrales, L., Spranger, S., Furdyna, M. J., Leung, M. Y., et al. (2014). STING-dependent cytosolic DNA sensing mediates innate immune recognition of immunogenic tumors. *Immunity* 41, 830–842. doi:10.1016/j.immuni.2014.10.017

Wu, Y. T., Fang, Y., Wei, Q., Shi, H., Tan, H., Deng, Y., et al. (2022). Tumor-targeted delivery of a STING agonist improvescancer immunotherapy. *Proc. Natl. Acad. Sci. U. S. A.* 119, e2214278119. doi:10.1073/pnas.2214278119

Wyatt, L. C., Moshnikova, A., Crawford, T., Engelman, D. M., Andreev, O. A., and Reshetnyak, Y. K. (2018a). Peptides of pHLIP family for targeted intracellular and extracellular delivery of cargo molecules to tumors. *Proc. Natl. Acad. Sci. U. S. A.* 115, E2811–E2818. doi:10.1073/pnas.1715350115

Wyatt, L. C., Moshnikova, A., Crawford, T., Engelman, D. M., Andreev, O. A., and Reshetnyak, Y. K. (2018b). Peptides of pHLIP family for targeted intracellular and extracellular delivery of cargo molecules to tumors. *Proc. Natl. Acad. Sci. U. S. A.* 115, E2811–E2818. doi:10.1073/pnas.1715350115

frontiers | Frontiers in Pharmacology

TYPE Case Report
PUBLISHED 04 March 2024
DOI 10.3389/fphar.2024.1356167

Check for updates

OPEN ACCESS

EDITED BY
Viviana di Giacomo,
University of Studies G d'Annunzio Chieti and Pescara, Italy

REVIEWED BY
Ruo Wang,
Shanghai Jiao Tong University, China
Nektarios Koufopoulos,
University General Hospital Attikon, Greece

*CORRESPONDENCE
Liangliang Dong,
18562206013@163.com
Xiaoling Yang,
123258453@qq.com

†These authors have contributed equally to this work

RECEIVED 15 December 2023
ACCEPTED 12 February 2024
PUBLISHED 04 March 2024

CITATION
Xu L, Wang C, Yang X and Dong L (2024), Case report: Cutaneous metastases as a first manifestation from breast cancer with concurrent gastric metastases.
Front. Pharmacol. 15:1356167.
doi: 10.3389/fphar.2024.1356167

COPYRIGHT
© 2024 Xu, Wang, Yang and Dong. This is an open-access article distributed under the terms of the Creative Commons Attribution License (CC BY). The use, distribution or reproduction in other forums is permitted, provided the original author(s) and the copyright owner(s) are credited and that the original publication in this journal is cited, in accordance with accepted academic practice. No use, distribution or reproduction is permitted which does not comply with these terms.

Case report: Cutaneous metastases as a first manifestation from breast cancer with concurrent gastric metastases

Lulu Xu[1†], Congcong Wang[1†], Xiaoling Yang[2*] and Liangliang Dong[1*]

[1]Departments of Oncology, The Affiliated Yantai Yuhuangding Hospital of Qingdao University, Yantai, Shandong, China, [2]Department of Obstetrics, Feicheng People's Hospital, Feicheng, China

Background: Breast cancer represents a leading cause of malignancy among Chinese women, posing a significant health burden. The diagnosis of metastatic breast cancer, particularly to uncommon sites like the skin and stomach, presents distinct challenges.

Case introduction: This case report describes a 71-year-old Chinese women with a persistent back rash lasting more than 6 months. Physical examination revealed red papules on her back. Immunohistochemistry confirmed positive for cytokeratin 7(CK7), GATA-3 and GCDFP15, as well as negative staining of cytokeratin 20 (CK20), suggesting breast cancer metastasis. Further evaluation revealed a breast nodule and axillary lymph node enlargement, with biopsies confirming invasive lobular carcinoma (ILC). Abdominal computed tomography (CT) revealed thickening of the gastric and ascending colon walls. Gastroscopy revealed chronic superficial atrophic gastritis. However, gastric metastasis was further confirmed by pathology. The patient initiated endocrine therapy with fulvestrant and exemestane, resulting in rash resolution and stable breast and stomach lesions after 3 months. Overall, the patient is experiencing an improvement in her condition and remains stable while continuing treatment.

Conclusion: This case highlights the importance of considering atypical metastatic patterns in breast cancer and the potential efficacy of endocrine therapies in managing such cases. Moreover, it emphasizes the need for vigilance in breast cancer patients, especially those with ILC, as gastrointestinal symptoms may indicate gastric metastasis (GMs). Ultimately, early detection and appropriate treatment strategies, such as endocrine therapy, can contribute to improved outcomes in these challenging cases.

KEYWORDS

cutaneous metastases, breast cancer, gastric metastases, invasive lobular carcinoma, endocrine therapy

Abbreviations: BI-RADS, breast imaging reporting and data system; CA153, carbohydrate antigen 153; CDX2, caudal-related homeobox 2; CK20, cytokeratin 20; CK5/6, cytokeratin 5/6; CK7, cytokeratin 7; CMs, Cutaneous metastases; CT, computed tomography; ER, estrogen receptors; EVE, everolimus; EXE, exemestane; GMs, gastric metastases; HER2, epidermal growth factor receptor 2; IDC, invasive ductal carcinoma; ILC, invasive lobular carcinoma; OS, overall survival; PR, progestogen receptors; TTF-1, thyroid transcription factor-1.

Introduction

In recent years, the incidence of breast cancer has ranked first among female malignant tumors in China, accounting for approximately 57.27% of case and posing a serious health threat to Chinese women (Zheng et al., 2023). The integration of surgical intervention, chemotherapy, radiotherapy, endocrine, and targeted therapies has markedly enhanced patient survival rates. Nevertheless, breast cancer continues to be a predominant health issue. The predominant histological variants of invasive breast cancer are invasive ductal carcinoma (IDC) and invasive lobular carcinoma (ILC), with IDC constituting about 80% of breast cancers and ILC comprising roughly 5%–15% (Carcoforo et al., 2012). ILC is distinguished by its origin in the lobular units of the terminal duct (Waldman et al., 2019) and demonstrates distinct metastatic behaviors compared to IDC, complicating early detection efforts.

Despite advancements, the scarcity of efficacious targeted treatments for metastatic breast cancer persists due to diagnostic limitations (Liang et al., 2020). Early-stage diagnosis is crucial, as it significantly influences prognosis: the 5-year survival rate for localized breast cancer is 99%, but only 27% for metastatic breast cancer (Wang et al., 2019). Cutaneous metastases (CMs), manifesting in about 24%–50% of breast cancer instances as the primary tumor spreads to skin and soft tissues, presenting as a "fungal breast mass (Huang et al., 2022)" The lymph nodes, bones, lungs, liver, and brain are the most frequent metastatic destinations (Liang et al., 2020). Unfortunately, due to the early appearance of erythema and rashes on the breast's skin, these patients are often diagnosed at an advanced stage. Metastasis to less common areas such as the back, upper arms, lower abdomen, and notably rare, the buttocks and perianal region, further complicates the disease management. Data on treating CMs are sparse and show little impact on survival rates.

A notably low incidence of gastric metastasis (GMs) from breast cancer was reported by Borst and Ingold, at just 0.26% (Borst and Ingold, 1993). McLemore et al. also demonstrated a relatively low incidence rate of gastrointestinal (GI) metastases originating from breast cancer, about 0.34% (McLemore et al., 2005). A case reported by Güler et al. highlighted a patient with breast cancer-related GI metastasis presenting with acute abdominal pain due to gastric perforation (Güler et al., 2019).

This report uniquely discusses a case of invasive ILC initially manifesting with CMs and accompanied by GMs. The purpose of this article is to provide comprehensive insights into the characteristics, clinical diagnosis, and treatment of such rare cases, thus contributing to the medical knowledge regarding this atypical metastatic pattern in breast cancer.

Case presentation

Chief complaints

A Chinese female, who is 71-year-old, came to our hospital, (The Affiliated Yantai Yuhuangding Hospital of Qingdao University) for treatment due to "More than half a year after the discovery of the back rash" in 14 November 2021.

History of past illness

The patient described no other discomfort prior to this visit and no history of multiple chest wall nodules.

Physical examination

Physical examination revealed multiple scattered red papules on the back, protruding from the surface of the skin with clear boundaries and no itching (Figures 1A–D). No abnormalities were found in the bilateral mammary glands, and no mass was palpated. There is no palpable mass in the abdomen, and there is no tenderness on palpation. There are no positive signs in other parts.

Preliminary laboratory diagnosis

A needle biopsy was performed in the dermatology outpatient department of our hospital. Histopathological studies showed mild keratinization in the epidermis of the skin tissue, chronic inflammatory cell infiltration around small vessels in the superficial dermis and subcutaneous adipose septum, moderate and mild heterotypic cells scattered among collagen fibers in the dermis, arranged in a nest-like pattern. Immunohistochemistry showed strong positive for estrogen receptors (ER) and progestogen receptors (PR), both ER and PR percentages are 80%, positive for CK7, GATA-3, GCDFP15 and KI67, as well as negative staining of CK20 and E-cadherin (Figure 2, The image shows only part of the results). Combined with the above results, breast cancer metastasis was considered.

Comprehensive diagnosis

On 19 November 2021, the patient then underwent a thorough examination. Tumor markers indicate that carbohydrate antigen 153 (CA153) is 126 U/mL (normal range 0–25 U/mL), and no abnormalities are found in the rest. Breast ultrasonography revealed a hypoechoic nodule in the left breast tomography, located 6 cm away from the nipple in the direction of 1–2o'clock, 0.7 × 0.6 cm in size, irregular in shape, aspect ratio<1, unclear boundaries, uneven internal echo, and attenuation of rear echo. There is no obvious blood flow signal within the nodule. Breast imaging reporting and data system (BI-RADS) category 6 (Figure 3A). Enlarged lymph nodes can be seen in the left axilla, the largest being 0.8 cm × 0.4 cm, with full shape, clear boundaries, thickened cortex, clear lymph nodes, and no obvious blood flow signal in lymph nodes (Figure 3B). The pathological findings of the left breast hypoechoic area and left axillary lymph node after biopsy showed that the immunohistochemistry of the left breast hypoechoic area was strong positive for ER (90%) and PR (80%), and negative for human epidermal growth factor receptor 2 (HER2) and E-cadherin, P120 was positive in the cytoplasm, and the positive rate of Ki67 was about 30% (Figure 4). Combined with the morphological and immunohistochemical results, it was consistent with invasive lobular carcinoma (ILC) of the breast.

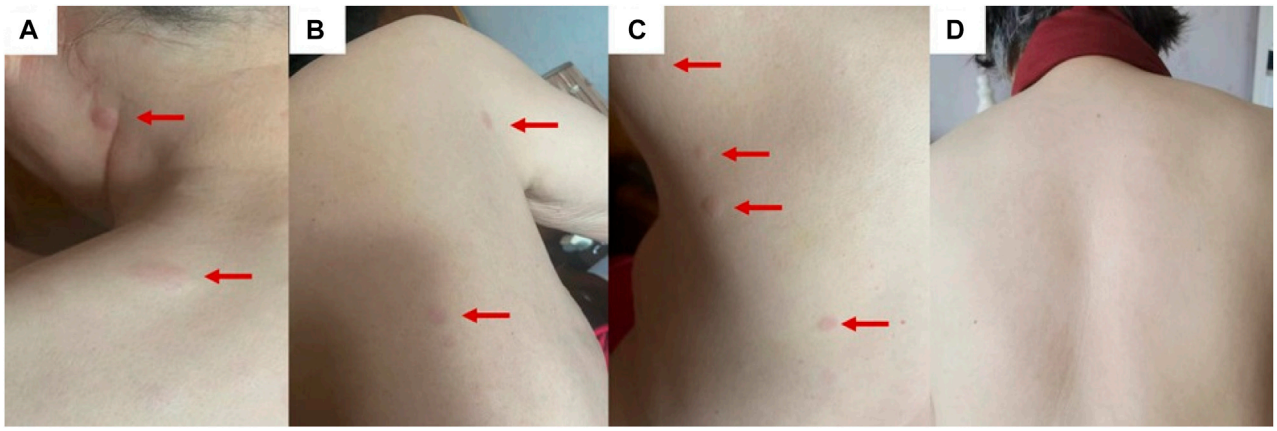

FIGURE 1
The clinical presentation is multiple red papules scattered on the back **(A–C)**. After 3 months of endocrine therapy, the back rash disappeared **(D)**.

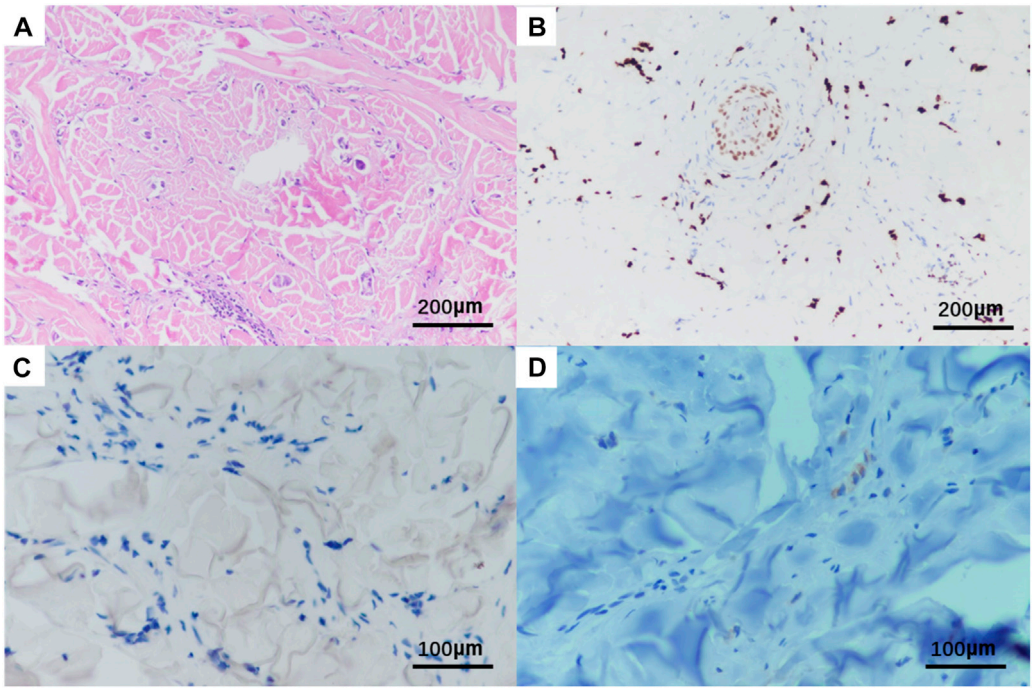

FIGURE 2
Histopathological HE and immunohistochemistry of patient's skin biopsy. Original magnification × 20: **(A)** HE; **(B)** positivity for GATA3; Original magnification × 400: **(C)** negative for E-cadherin; **(D)** positivity for GCDFP15.

Imaging examination

Subsequent staging tests, including abdominal and chest CT, brain magnetic resonance imaging and, bone scan, revealed synchronous metastases to stomach. The pathological results of left axillary lymph nodes were consistent with the pathological findings of the breast. Abdominal enhanced computed tomography (CT) (Figure 5A) showed poor gastric filling, thickening of gastric wall, and mild to moderate enhancement on enhanced scans. The local intestinal wall of the ascending colon is rough and slightly thick. Gastroscopy and colonoscopy were recommended. Chest CT, brain magnetic resonance imaging and bone scan showed no obvious abnormality. On 21 November 2021, The patient underwent gastroscopy, and under the microscope, congestion and roughness of the gastric antrum mucosa were observed, accompanied by scattered erosive lesions. Two gastric antrum biopsies were performed, with soft texture. Chronic superficial atrophic gastritis is considered (Figure 5B). Pathological examination showed that a small number of heterotypic cells were infiltrated in the lamina propria on the mucosal surface of the antrum.

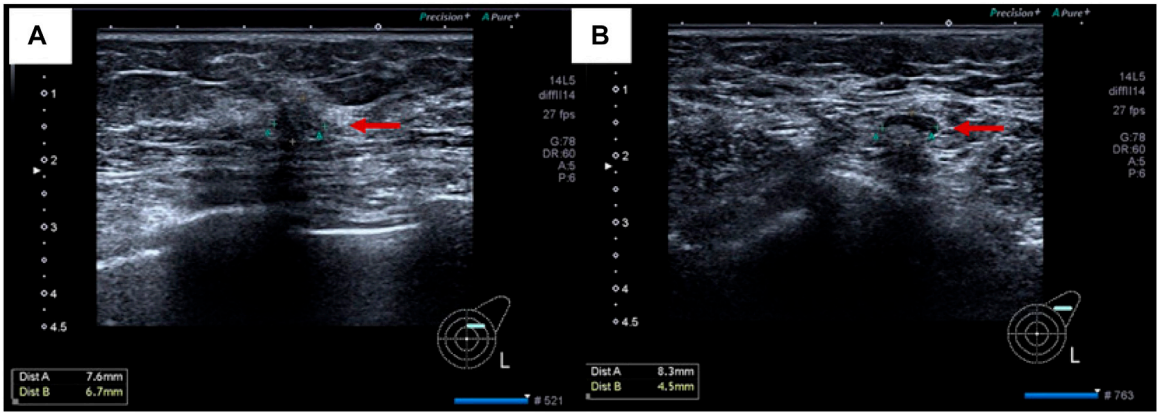

FIGURE 3
Imaging pictures of the patient at admission. **(A)** breast ultrasound; **(B)** lymph node ultrasound.

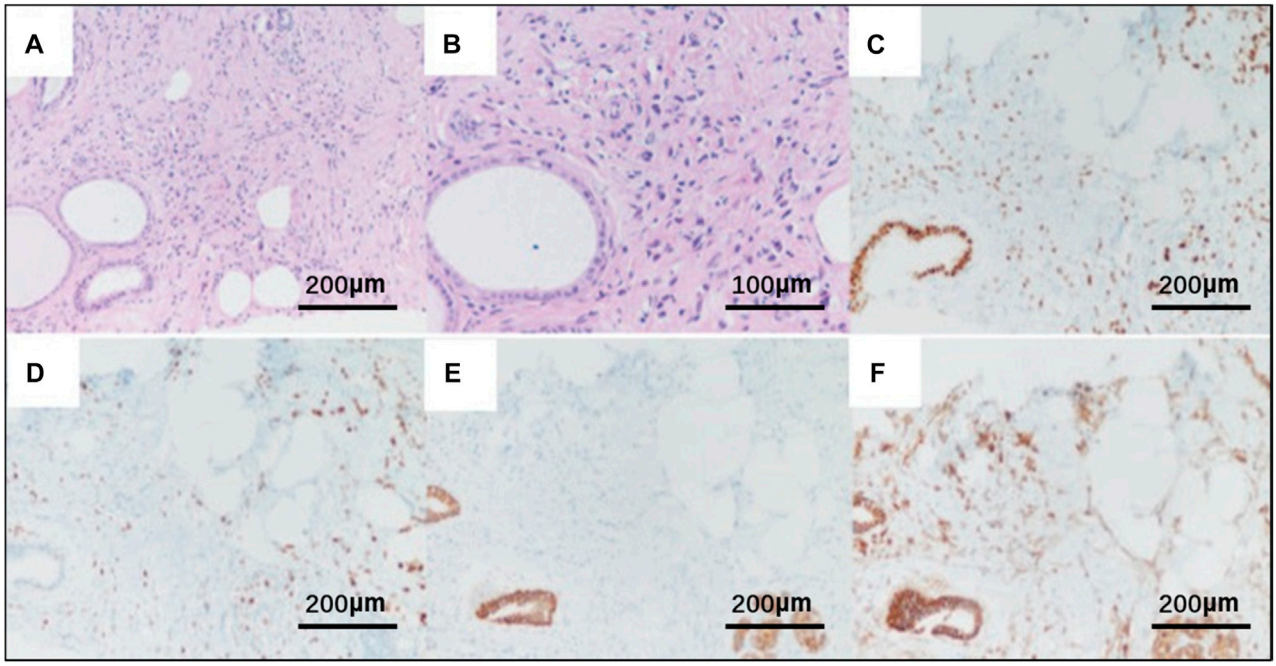

FIGURE 4
Pathological HE and immunohistochemistry of breast tissue biopsy of the patient. **(A)** HE × 20; **(B)** HEx40; Original magnification × 20: **(C)** strong positivity for the estrogen receptor (ER); **(D)** strong positivity for the progesterone receptor (PR); **(E)** negative for E-cadherin; **(F)** P120 was positive in the cytoplasm.

Immunohistochemistry showed strong positive for ER (90%) and PR (80%), positive for CK7, KI67, GCDFP15 and GATA3, and negative for CK20 and E-cadherin, which was consistent with invasive lobular breast carcinoma metastasis (Figure 6, The image shows only part of the results).

Treatment

Subsequently, endocrine therapy with fulvestrant (Turner et al., 2020) (500 mg, the first two times are 2 weeks apart, and every 4 weeks after that) combined with exemestane [EXE (Turner et al., 2020)] (25 mg, once a day) was started on 14 December 2021. After 3 months of treatment, the patient's rash disappeared (Figure 1D), and the breast and stomach lesions were stable, and the patient is still receiving treatment.

Outcome and follow-up

On 21 October 2022, a follow-up gastroscopy revealed alternating red and white mucosa in the gastric antrum, mainly

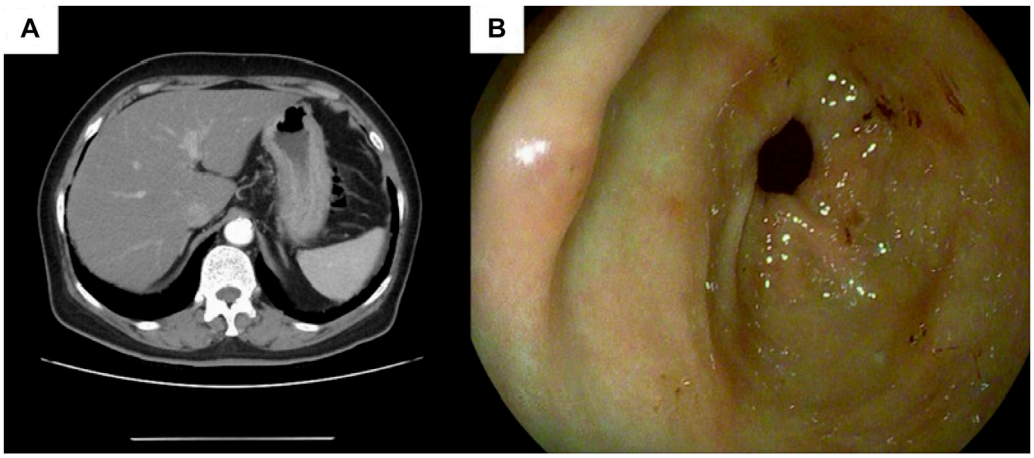

FIGURE 5
Gastric endoscopy and CT images of the patient. **(A)** Abdominal CT shows gastric wall thickening,the thickest part of which was about 2.3 cm in diameter, involving the whole circumference of the lumen, with a length of about 5 cm; **(B)** Endoscopy prompts chronic superficial atrophic gastritis.

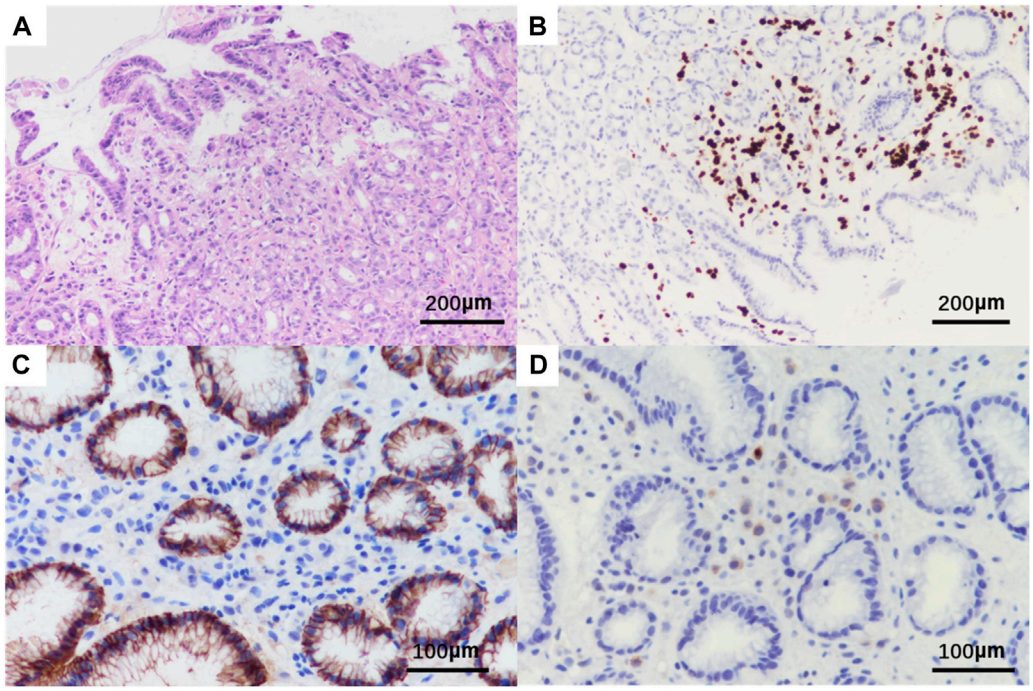

FIGURE 6
Pathological HE and immunohistochemistry of gastric tissue biopsy of the patient. Original magnification × 20: **(A)** HE; **(B)** positivity for GATA3; Original magnification × 400: **(C)** negative for E-cadherin; **(D)** positivity for GCDFP15.

in red. Scattered congested and rough mucosa can be seen on the anterior and posterior walls of the gastric antrum. Three biopsies were taken at the lesion site of the gastric antrum, with soft texture (Figure 7A). Pathological findings suggest chronic inflammation of mucosal tissue with mild intestinal metaplasia of glandular epithelium (Figure 7B). On 19 August 2023, tumor markers indicated a decrease in CA153 to 46.6 U/mL. Breast ultrasound shows no obvious nodules or liquid dark areas in the left breast layer; Lymph nodes can be seen in the left armpit, with a size of approximately 2 cm × 0.6 cm. The last application of fluvastatin was from 16 September 2023, and EXE continued to be orally administered daily. Our last follow-up was on 16 September 2023. The entire diagnosis and treatment process of the patient is shown in Figure 8.

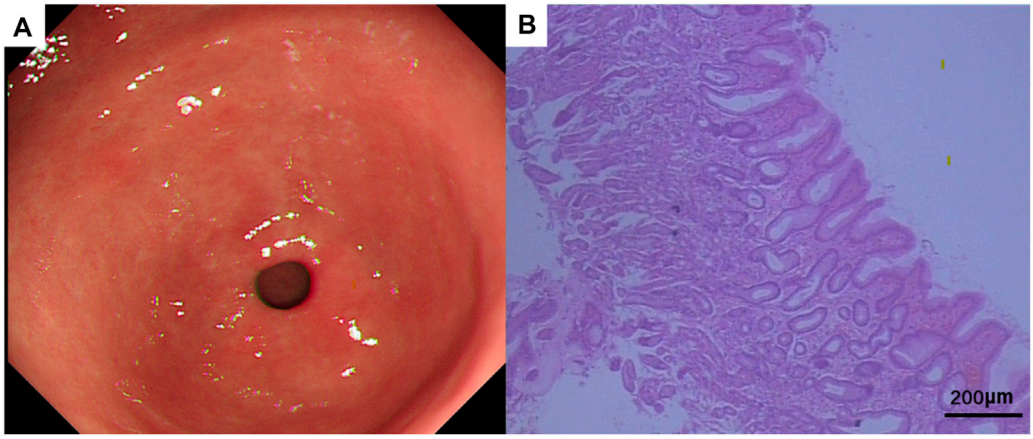

FIGURE 7
(A) Gastroscopic manifestations after treatment. **(B)** Pathological HE of gastric tissue biopsy after treatment. HE × 20.

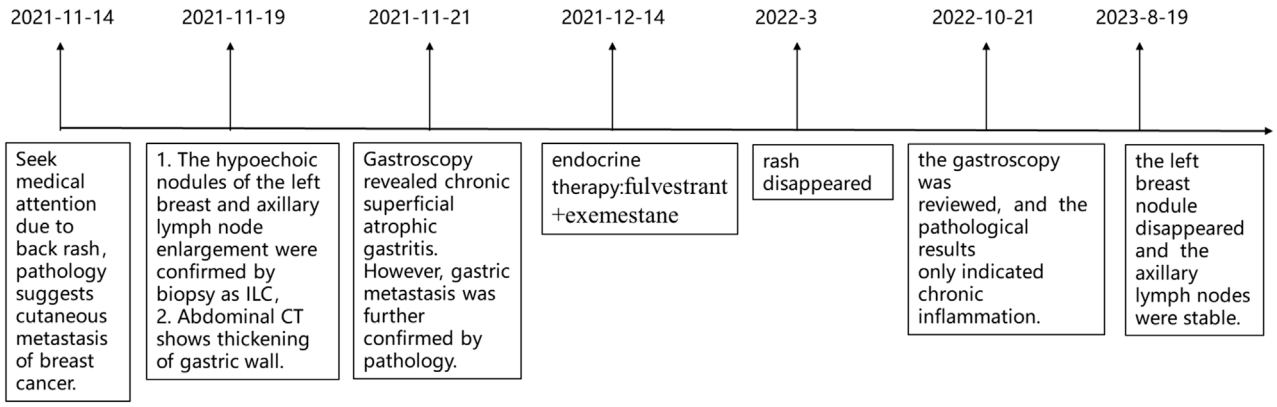

FIGURE 8
The timeline diagram of patient diagnosis and treatment process.

Discussion

Research has elucidated that ILC and IDC manifest distinct patterns of distant metastasis (Teo et al., 2018). IDC predominantly metastasizes to bone, lung and liver, while ILC is more prone to gastrointestinal, female reproductive organ, peritoneal, retroperitoneal, adrenal, bone marrow and pleural metastasi (Borst and Ingold, 1993). The unique immunological milieu and specific genomic modifications in ILC are pivotal in its metastatic tendencies. Studies have identified a higher non-synonymous tumor mutation burden in metastatic ILC compared to its primary form, with notable variations in the mutation frequencies of pivotal genes such as CDH1, PIK3CA, TP53, and ERBB2 (Du et al., 2018), and differences in CDH1, PIK3CA, ERBB2, TBX3, NCOR1, and RFWD2 compared to metastatic IDC of no special type (IDC-NST) (Pareja et al., 2020). This indicates that ILC's metastasis involves distinct genetic alterations compared to IDC. Further research highlights that LumA ILC has a higher proportion of high-immune phenotypes and expresses critical immune checkpoint genes more highly than LumA IDC, indicating possible molecular mechanisms for the different metastasis tendencies between ILC and IDC (Pareja et al., 2020).

ILC is considered a major risk factor for CMs (González-Martínez et al., 2022). Silvia et al. discovered that Luminal HER2-type was more common in patients with CMs, of whom 43.7% were ILC. According to Table 1, we summarized some key factors of ILC triggering CMs, and carried out targeted analysis. About 65.4%–97% of gastric metastases were derived from ILC (Almubarak et al., 2011; Mantiero et al., 2018). At present, the molecular mechanism of metastasis is still unclear. E-cadherin is thought to be associated with increased tumor invasion and metastasis in terms of maintenance of intercellular adhesion as well as loss with EMT or gene deletion (Jeanes et al., 2008; Petrova et al., 2016). Removing E-cadherin in IDC cells led to weaker cell-to-cell connections and a shift towards more dispersed cellular aggregates in suspension (Elangovan et al., 2022). Additionally, the absence of E-cadherin correlated with increased independent growth without attachment and greater resistance to cell death when detached, characteristics that are also present in ILC tumors. Since E-cadherin loss and

TABLE 1 ILC triggers some risk factors of CMs.

Biology of the cancer	Advanced Stage of ILC
	Lymphatic Spread
	Hormone Receptor Status
	Treatment History
	Tumor Characteristics
	Rare Skin Involvement at Diagnosis
Patient's individual characteristics	Genetic Factors
	Patient's Overall Health
	Immune System Function

cytoplasmic localization of p120 catenin are unique to ILC, this may be a useful diagnostic tool for differentiating ILC from IDC (Dabbs et al., 2007; Comprehensive molecular portraits of human, 2012; Pramod et al., 2021). It has been proposed that the hallmark genetic loss of CDH1 plays an important role in the metastatic spread of ILC to abnormal anatomical sites, and that mutations in CDH1 lead to inactivation of E-cadherin and loss of adhesion between tumor cells and other epithelial cells, thereby promoting Invasion and metastasis of tumor cells (Zarrilli et al., 2020). Analysis of invasive breast cancer cases in the Cancer Genome Atlas (TCGA) dataset (http://www.cbioportal.org) showed that 66% (107/162) of ILCs carried CDH1 mutations compared to only 3% (22/741) of IDCs (Cerami et al., 2012; Gao et al., 2013; Pramod et al., 2021).

ILC was prone to luminal A subtype, CDH1 mutations and deletion of E-cadherin mRNA expression (Han et al., 2022). The E-cadherin gene function prevents tumor invasion, and in ILC the deletion of E-cadherin results in an increased capacity for tissue invasion (Vleminckx et al., 1991). Eradicating E-cadherin led to a heightened vulnerability to inhibitors targeting the IGF1R/PI3K/Akt and MEK pathways following the removal of the CDH1 gene (Elangovan et al., 2022). FOXA1 and ER are co-expressed at high levels in endocrine-resistant metastatic breast cancer (Ross-Innes et al., 2012). A higher rate of FOXA1 mutations (7% vs. 2%) and a lower rate of GATA3 mutations (5% vs. 20%) were observed in ILC compared to IDC (Ciriello et al., 2015). Suggesting that ILC and IDC may rely on different mechanisms to regulate ER-mediated transcription (Pramod et al., 2021). A comprehensive study shows that profiles 817 breast tumors, including 127 ILC and 490 IDC cases, providing insights into the molecular differences between ILC and IDC (Ciriello et al., 2015). The study identifies E-cadherin loss, mutations in PTEN, TBX3, and FOXA1 as features enriched in ILC (Ciriello et al., 2015; Teo et al., 2018). It highlights PTEN loss associated with increased AKT phosphorylation, which is highest in ILC, suggesting a unique pathway of tumor progression and potential therapeutic targets.

This patient is part of a unique cohort where CMs were identified before the detection of the primary tumor, initially manifesting as papular nodular lesions on the upper back. Firstly, CMs can serve as the inaugural indication of clinically silent tumors (Virmani et al., 2011), albeit rarely presenting as the initial symptom. Their emergence is potentially linked to the individual's autoimmune or genetic predispositions (Table 1). Secondly, CMs are postulated to arise through lymphatic or vascular dissemination (Table 1), often manifesting as a recurrence of the primary malignancy (Moore, 2002). Histological types encompass glandular, Indian file, lymphoid embolism of malignant cells between collagen fibers, as well as fibrotic and epidermoid phenotypes (Panasiti et al., 2009; Waldman et al., 2019). The incidence of cutaneous metastasis in breast cancer is about 23.9% (Lookingbill et al., 1993). But compared with other solid malignancies, breast cancer has the highest incidence of skin metastases, accounting for about 70% (Khodair et al., 2021). They typically occur months or years after breast cancer diagnosis and often coincide with visceral metastases (Hu et al., 2008) It has been reported that the occurrence of CMs is associated with poor prognosis (González-Martínez et al., 2022). Usually, the prognosis depends on the type (Table 1) and behavior of the primary tumor, and the expected survival at diagnosis is less than 1 year (Cox and Cruz, 1994). CMs present with nonspecific clinical manifestations, complicating the differentiation from other benign conditions.

CMs of breast cancer are most common in the chest, followed by the head and neck, back, and abdomen. The most prevalent clinical manifestation is solitary erythematous invasive papules and nodules (80%) (Prabhu et al., 2009), usually ranging from 1–3 cm in diameter (Busbait et al., 2022). With disease progression, these nodules may ulcerate or undergo infection. Commonly, patients with CMs at mastectomy scars are erroneously diagnosed with surgical site infections (Waldman et al., 2019). Reports have indicated that skin metastases can spread during core needle biopsies, underlining that the notable incidence of intra-scar metastases also mirrors tumor dissemination during surgical interventions. Consequently, securing a biopsy sample is imperative for affirming the diagnosis in individuals suspected of having breast cancer skin metastases, as histological evaluation of the biopsy may reveal cellular proliferation akin to the primary neoplasm. Breast cancer metastasis diagnosis can be validated by detecting markers like cathepsin D among other antigens (Waldman et al., 2019). The sensitivity of certain diagnostic imaging modalities is low, with mammography and ultrasound showing sensitivity rates of 57%–81% and 68%–98%, respectively. Therefore, combining these with highly sensitive MRI (93%) may lead to a successful diagnosis (Busbait et al., 2022). Moreover, individuals with a history of breast cancer ought to undergo comprehensive skin examinations, even years subsequent to breast cancer surgery and chemotherapy. Conversely, the persistence of an extended rash should warrant further evaluation for early detection of breast cancer.

We present an exceedingly rare instance where breast cancer and GMs were identified subsequent to the initial detection of CMs, despite the primary tumor being diminutive. The stomach is an uncommon site of tumor metastasis, with a reported incidence of 0.2%–0.7% according to clinical and autopsy results (De Palma et al., 2006; Namikawa and Hanazaki, 2014). Primary malignancies most frequently metastasized to the stomach included breast cancer (27.9%), lung cancer (23.8%), esophageal cancer (19.1%), renal cell carcinoma (7.6%), malignant melanoma (7.0%) (Namikawa and Hanazaki, 2014). Although GMs from breast malignancies are the most common, the incidence is only 0.3% in clinical reports and 2%–18% in autopsy case reports (Taal et al., 1992; Taal et al., 2000). The average time from breast cancer diagnosis to

detection of GMs is estimated to be 5–8 years (De Palma et al., 2006; Almubarak et al., 2011; Xu et al., 2017). At the time of diagnosis of GMs, 90%–94% of patients had concurrent metastases (Cormier et al., 1980; Borst and Ingold, 1993), there are only a few case reports of GMs diagnosed before or at the same time as breast cancer.

GMs of breast cancer and primary gastric adenocarcinoma are very similar in clinical symptoms, imaging, gastroscopic findings and pathological morphology, and are often difficult to distinguish. Predominantly, patients with GMs experience non-specific gastrointestinal symptoms like anorexia, epigastric pain, indigestion, nausea, fever, and weight loss (Tang et al., 2020), with acute abdominal pain due to gastric perforation being a rarity (Koike et al., 2014). The condition usually entails diffuse involvement of the gastric wall, characterized by linitis plastica and predominantly affecting the submucosal and seromuscular layers (Tang et al., 2020). Some authors have suggested that linitis plastica is the most common type of gastric metastasis in breast cancer (73%–83%) (Taal et al., 1992; Eo, 2008). It resembles Borrmann type 4 advanced gastric cancer with diffuse hypertrophy and sclerosis of the gastric mucosal folds and deep invasion of the submucosa and muscularis propria (Geada et al., 2020). Given that GMs predominantly reside in the submucosa and muscularis propria, sparing the superficial mucosal layer, there is a high likelihood of endoscopy yielding false-negative results. Therefore, if the index of suspicion is high, unconventional techniques such as macroscopic biopsy or endoscopic ultrasound-guided fine-needle aspiration cytology should be used whenever possible (Geada et al., 2020). This patient had no symptoms of gastric discomfort, and abdominal CT revealed thickening of the stomach wall, so a gastroscopy was performed. Nonetheless, the endoscopic examination only revealed chronic superficial atrophic gastritis, with no malignancy detected, underscoring the critical role of endoscopic biopsy in such cases.

In cases lacking pertinent clinical history, pinpointing the origin of metastatic cancer can prove challenging. However, metastases often exhibit similar histopathological features as the primary tumor. Diagnosis is relatively easy due to the convenient sampling of skin lesions. However, cancer cells metastasized to the stomach predominantly present as poorly differentiated adenocarcinoma and signet-ring cell carcinoma, complicating their differentiation from primary gastric adenocarcinoma on conventional HE stained sections. The distinction between primary and metastatic must rely on immunohistochemical examination. In this case, the primary tumor, skin and GMs were all strongly positive for ER and PR. Nevertheless, the ER positivity rate in female gastric cancer patients is between 26.6% and 31%, and for PR, it is between 11.9% and 20.6% (Karat et al., 1999). Moreover, even if the primary breast tumor is ER and PR positive, GMs might still test negative for these receptors (Kim et al., 2018), indicating that ER and PR status alone cannot conclusively determine tumor origin. Since HER2 has a comparable positive rate (less than 5%) in ILC and low-adhesion gastric cancers, it is also not an appropriate diagnostic marker (Mantiero et al., 2018). The combination of three antibodies, GCDFP15, mammaglobin and GATA-3, is often used to identify breast cancer metastasis. The sensitivity and specificity of the three expressions in breast cancer were 5%–74% and 9%–100%, 7%–84% and 85%–100%, 32%–100% and 7%–93%, respectively (Gown et al., 2016). In addition, breast tissues were mostly CK7(+)/CK20(−) and gastrointestinal tissues were mostly CK7(−)/CK20(+) (Xu et al., 2017). The immunohistochemistry of CMs and GMs in this patient showed CK7(+), CK20(−) and (+). It is suggested that the tumor may originate from the breast. Furthermore, immunohistochemical staining of this patient showed E-cadherin (−) and P120 (cytosolic +), suggesting that the pathological type was lobular breast carcinoma. Combined with the patient's medical history, cutaneous and gastric metastasis from ILC of the breast could be clearly diagnosed. In summary, by detecting the expression of specific protein markers by immunohistochemistry, doctors can identify whether metastatic lesions are associated with primary breast cancer, or whether they are associated with other types of cancer. In particular, for patients with no history of breast cancer as in this case, it is helpful to formulate accurate diagnosis and treatment plan, and improve the accuracy of patient treatment effect and prognosis assessment.

CMs in conjunction with visceral metastasis signify advanced disease and a grim prognosis, with mortality typically occurring within a year of diagnosis (González-Martínez et al., 2022). Xu et al. found that pre-gastric involvement metastasis to multiple organs was an independent predictor for overall survival reduction. At present, there is no standard guideline for the treatment of CMs and GMs (Rech et al., 2023), and the treatment principles for advanced breast cancer are mostly followed. Systemic therapy, encompassing chemotherapy [including anti-HER2 therapy (Huang et al., 2022)] and endocrine therapy, is the mainstay of treatment. GMs from breast cancer are generally not treated surgically unless acute complications occur (Kim et al., 2018). Anti-HER2 drugs, including chemotherapy drugs specifically used for HER2-positive breast cancer (Huang et al., 2022) such as trastuzumab, ado-trastuzumab emtansine, and lapatinib, have been employed. In one case, patients with HER2+ skin lesions experienced complete regression after initiating ado-trastuzumab emtansine treatment, with the response lasting up to 135 weeks (Giarratano et al., 2018; Huang et al., 2022). But XU et al. suggested that surgical intervention and chemotherapy did not significantly prolong OS, while endocrine therapy proved to be an effective strategy (Xu et al., 2017). This may be because most patients with GMs are from ILC, and their hormone receptors are usually positive, mainly luminal-type, which is relatively sensitive to endocrine therapy. Endocrine therapy has been reported to play an important role in improving patient survival (Busbait et al., 2022). Over an 8-year follow-up period, tamoxifen showed a disease-free survival (DFS) and OS of 66% and 74%, respectively, compared to 82% and 89% for letrozole (Metzger Filho et al., 2015; Busbait et al., 2022). There is a case report that CMs from ILC is rapidly and completely relieved with aromatase inhibitor (Parietti et al., 2022), especially in ER+ (Huang et al., 2022). Aromatase inhibitors are sometimes used as maintenance therapy after controlling CMs with conventional means, such as chemotherapy, radiation, and surgery. In particular, the skin lesions partially or completely resolved, and they survived within 2–5 years of follow-up. In addition, EXE and everolimus (EVE) have been reported to better control metastatic lesions in the skin (Li et al., 2022). For patients with hormone receptor positive advanced breast cancer, NCCN guidelines recommend aromatase inhibitor + CDK (Cyclin-dependent Kinase) 4/6 inhibitor or fulvestrant + CDK4/6 inhibitor. CDK4/6 inhibitor is more expensive, and the patient's economic conditions are poor, so he did not choose the drug. One clinical study demonstrated that Ribociclib combined with Fulvestrant

had a 67.0% OS for 36 months, which was higher than Fulvestrant alone (Slamon et al., 2020). Ultimately, endocrine therapy with fulvestrant combined with EXE was administered, leading to satisfactory disease control, with ongoing treatment.

This highlights the uniqueness of each case, emphasizing the need for personalized prognosis discussions based on all relevant clinical and pathological factors. In this rare case, a 71-year-old Chinese female initially presented with CMs as her primary symptom, which led to the subsequent diagnosis of ILC of the breast. Further evaluation revealed synchronous GMs from breast cancer, an exceptionally uncommon occurrence. The diagnosis relied heavily on immunohistochemistry, as the clinical presentation and histopathological features resembled primary gastric adenocarcinoma. It underscores the importance of thorough evaluations in patients with atypical metastatic patterns and the pivotal role of immunohistochemistry in confirming tumor origins.

Conclusion

In conclusion, CMs and GMs of breast cancer represent uncommon clinical phenomena, particularly when CMs precede the identification of the primary tumor. CMs and GMs often signify advanced disease and poor prognosis, emphasizing the urgency of precise diagnosis and timely intervention. In the absence of relevant clinical history, it is difficult to determine the primary site of metastatic cancer. Without a detailed clinical history, pinpointing the origin of metastatic cancer can be challenging. Furthermore, the symptoms associated with these metastatic sites are often non-specific, leading to potential diagnostic oversight and misdiagnosis. In this context, the interaction between the clinician and the pathologist is critical. The appearance of persistent papular nodular skin lesions necessitates immediate pathological biopsy. The discovery of CMs usually coincides with multiple metastases from other organs, warranting a thorough patient evaluation. Particularly for patients with ILC of the breast, gastrointestinal symptoms should prompt urgent endoscopic biopsy, with immunohistochemical staining aiding in lesion characterization. Early diagnosis and optimal treatment can delay disease progression and reduce mortality. Treatment strategies, including endocrine therapy and targeted agents, must be customized based on the tumor's molecular profile.

Data availability statement

The raw data supporting the conclusion of this article will be made available by the authors, without undue reservation.

Ethics statement

Written informed consent was obtained from the individual(s) for the publication of any potentially identifiable images or data included in this article.

Author contributions

LX: Writing–original draft, Writing–review and editing. CW: Writing–review and editing. XY: Writing–review and editing. LD: Writing–review and editing.

Funding

The author(s) declare financial support was received for the research, authorship, and/or publication of this article. Yantai Science and Technology Innovation Development Plan, 2022YD042.

Conflict of interest

The authors declare that the research was conducted in the absence of any commercial or financial relationships that could be construed as a potential conflict of interest.

Publisher's note

All claims expressed in this article are solely those of the authors and do not necessarily represent those of their affiliated organizations, or those of the publisher, the editors and the reviewers. Any product that may be evaluated in this article, or claim that may be made by its manufacturer, is not guaranteed or endorsed by the publisher.

References

2012). Comprehensive molecular portraits of human breast tumours. *Nature* 490, 61–70. doi:10.1038/nature11412

Almubarak, M. M., Laé, M., Cacheux, W., de Cremoux, P., Pierga, J. Y., Reyal, F., et al. (2011). Gastric metastasis of breast cancer: a single centre retrospective study. *Dig. Liver Dis.* 43, 823–827. doi:10.1016/j.dld.2011.04.009

Borst, M. J., and Ingold, J. A. (1993). Metastatic patterns of invasive lobular versus invasive ductal carcinoma of the breast. *Surgery* 114, 637–642. ; discussion 641-632.

Busbait, S., Alkhalifa, A. M., Aljohani, S., and Alhaddad, H. (2022). Occult invasive lobular carcinoma presenting as an axillary skin metastatic lesion underwent neoadjuvant endocrine therapy and surgical resection: a case report and review of literature. *Breast Cancer* 14, 145–152. doi:10.2147/BCTT.S366785

Carcoforo, P., Raiji, M. T., Langan, R. C., Lanzara, S., Portinari, M., Maestroni, U., et al. (2012). Infiltrating lobular carcinoma of the breast presenting as gastrointestinal obstruction: a mini review. *J. Cancer* 3, 328–332. doi:10.7150/jca.4735

Cerami, E., Gao, J., Dogrusoz, U., Gross, B. E., Sumer, S. O., Aksoy, B. A., et al. (2012). The cBio cancer genomics portal: an open platform for exploring multidimensional cancer genomics data. *Cancer Discov.* 2, 401–404. doi:10.1158/2159-8290.CD-12-0095

Ciriello, G., Gatza, M. L., Beck, A. H., Wilkerson, M. D., Rhie, S. K., Pastore, A., et al. (2015). Comprehensive molecular portraits of invasive lobular breast cancer. *Cell.* 163, 506–519. doi:10.1016/j.cell.2015.09.033

Cormier, W. J., Gaffey, T. A., Welch, J. M., Welch, J. S., and Edmonson, J. H. (1980). Linitis plastica caused by metastatic lobular carcinoma of the breast. *Mayo Clin. Proc.* 55, 747–753.

Cox, S. E., and Cruz, P. D., Jr. (1994). A spectrum of inflammatory metastasis to skin via lymphatics: three cases of carcinoma erysipeloides. *J. Am. Acad. Dermatol* 30, 304–307. doi:10.1016/s0190-9622(94)70028-1

Dabbs, D. J., Bhargava, R., and Chivukula, M. (2007). Lobular versus ductal breast neoplasms: the diagnostic utility of p120 catenin. *Am. J. Surg. Pathol.* 31, 427–437. doi:10.1097/01.pas.0000213386.63160.3f

De Palma, G. D., Masone, S., Rega, M., Simeoli, I., Donisi, M., Addeo, P., et al. (2006). Metastatic tumors to the stomach: clinical and endoscopic features. *World J. Gastroenterol.* 12, 7326–7328. doi:10.3748/wjg.v12.i45.7326

Du, T., Zhu, L., Levine, K. M., Tasdemir, N., Lee, A. V., Vignali, D. A. A., et al. (2018). Invasive lobular and ductal breast carcinoma differ in immune response, protein translation efficiency and metabolism. *Sci. Rep.* 8, 7205. doi:10.1038/s41598-018-25357-0

Elangovan, A., Hooda, J., Savariau, L., Puthanmadhomnarayanan, S., Yates, M. E., Chen, J., et al. (2022). Loss of E-cadherin induces IGF1R activation and reveals a targetable pathway in invasive lobular breast carcinoma. *Mol. Cancer Res.* 20, 1405–1419. doi:10.1158/1541-7786.MCR-22-0090

Eo, W. K. (2008). Breast cancer metastasis to the stomach resembling early gastric cancer. *Cancer Res. Treat.* 40, 207–210. doi:10.4143/crt.2008.40.4.207

Gao, J., Aksoy, B. A., Dogrusoz, U., Dresdner, G., Gross, B., Sumer, S. O., et al. (2013). Integrative analysis of complex cancer genomics and clinical profiles using the cBioPortal. *Sci. Signal* 6, pl1. doi:10.1126/scisignal.2004088

Geada, L., Kantor, M., Mohan, K., Weingrad, D., and Nasiff, L. S. (2020). An uncommon presentation of a common disease: a review of gastric metastasis from breast carcinoma. *Cureus* 12, e11920. doi:10.7759/cureus.11920

Giarratano, T., Miglietta, F., Giorgi, C. A., Tsvetkova, V., Michieletto, S., Evangelista, L., et al. (2018). Exceptional and durable responses to TDM-1 after trastuzumab failure for breast cancer skin metastases: potential implications of an immunological sanctuary. *Front. Oncol.* 8, 581. doi:10.3389/fonc.2018.00581

González-Martínez, S., Pizarro, D., Pérez-Mies, B., Caniego-Casas, T., Rodríguez-Peralto, J. L., Curigliano, G., et al. (2022). Differences in the molecular profile between primary breast carcinomas and their cutaneous metastases. *Cancers (Basel)* 14, 1151. doi:10.3390/cancers14051151

Gown, A. M., Fulton, R. S., and Kandalaft, P. L. (2016). Markers of metastatic carcinoma of breast origin. *Histopathology* 68, 86–95. doi:10.1111/his.12877

Güler, S. A., Şimşek, T., Pösteki, G., Güreşin, A., Çınar, S., Onbaşılar, U., et al. (2019). A very rare reason for gastric perforation, caused by gastric metastasis of breast cancer: case presentation. *Eur. J. Breast Health* 15, 59–62. doi:10.5152/ejbh.2018.4285

Han, B., Gu, Z., Liu, Z., and Ling, H. (2022). Clinical characteristics and survival outcomes of infiltrating lobular carcinoma: a retrospective study of 365 cases in China. *Cancer Manag. Res.* 14, 647–658. doi:10.2147/CMAR.S346319

Hu, S. C., Chen, G. S., Lu, Y. W., and Wu, C. S. (2008). Cutaneous metastases from different internal malignancies: a clinical and prognostic appraisal. *J. Eur. Acad. Dermatol Venereol.* 22, 735–740. doi:10.1111/j.1468-3083.2008.02590.x

Huang, S., Parekh, V., Waisman, J., Jones, V., Yuan, Y., Vora, N., et al. (2022). Cutaneous metastasectomy: is there a role in breast cancer? A systematic review and overview of current treatment modalities. *J. Surg. Oncol.* 126, 217–238. doi:10.1002/jso.26870

Jeanes, A., Gottardi, C. J., and Yap, A. S. (2008). Cadherins and cancer: how does cadherin dysfunction promote tumor progression? *Oncogene* 27, 6920–6929. doi:10.1038/onc.2008.343

Karat, D., Brotherick, I., Shenton, B. K., Scott, D., Raimes, S. A., and Griffin, S. M. (1999). Expression of oestrogen and progesterone receptors in gastric cancer: a flow cytometric study. *Br. J. Cancer* 80, 1271–1274. doi:10.1038/sj.bjc.6990497

Khodair, S., Ewais, I., Abolmagd, H., El Sheikh, R., Raza, S., Portnow, L. H., et al. (2021). Skin nodules as a first presentation of synchronous bilateral invasive lobular breast carcinoma: a case report. *J. Glob. Radiology* 7. doi:10.7191/jgr.2021.1147

Kim, D. H., Son, S. M., and Choi, Y. J. (2018). Gastric metastasis from invasive lobular breast cancer, mimicking primary gastric cancer: a case report. *Med. Baltim.* 97, e0258. doi:10.1097/MD.0000000000010258

Koike, K., Kitahara, K., Higaki, M., Urata, M., Yamazaki, F., and Noshiro, H. (2014). Clinicopathological features of gastric metastasis from breast cancer in three cases. *Breast Cancer* 21, 629–634. doi:10.1007/s12282-011-0284-3

Li, Z. H., Wang, F., Zhang, P., Xue, P., and Zhu, S. J. (2022). Diagnosis and guidance of treatment of breast cancer cutaneous metastases by multiple needle biopsy: a case report. *World J. Clin. Cases* 10, 345–352. doi:10.12998/wjcc.v10.i1.345

Liang, Y., Zhang, H., Song, X., and Yang, Q. (2020). Metastatic heterogeneity of breast cancer: molecular mechanism and potential therapeutic targets. *Semin. Cancer Biol.* 60, 14–27. doi:10.1016/j.semcancer.2019.08.012

Lookingbill, D. P., Spangler, N., and Helm, K. F. (1993). Cutaneous metastases in patients with metastatic carcinoma: a retrospective study of 4020 patients. *J. Am. Acad. Dermatol* 29, 228–236. doi:10.1016/0190-9622(93)70173-q

Mantiero, M., Faggioni, G., Menichetti, A., Fassan, M., Guarneri, V., and Conte, P. (2018). Gastric linitis plastica and peritoneal carcinomatosis as first manifestations of occult breast carcinoma: a case report and literature review. *Case Rep. Oncol. Med.* 2018, 4714708. doi:10.1155/2018/4714708

McLemore, E. C., Pockaj, B. A., Reynolds, C., Gray, R. J., Hernandez, J. L., Grant, C. S., et al. (2005). Breast cancer: presentation and intervention in women with gastrointestinal metastasis and carcinomatosis. *Ann. Surg. Oncol.* 12, 886–894. doi:10.1245/ASO.2005.03.030

Metzger Filho, O., Giobbie-Hurder, A., Mallon, E., Gusterson, B., Viale, G., Winer, E. P., et al. (2015). Relative effectiveness of letrozole compared with tamoxifen for patients with lobular carcinoma in the BIG 1-98 trial. *J. Clin. Oncol.* 33, 2772–2779. doi:10.1200/JCO.2015.60.8133

Moore, S. (2002). Cutaneous metastatic breast cancer. *Clin. J. Oncol. Nurs.* 6, 255–260. doi:10.1188/02.CJON.255-260

Namikawa, T., and Hanazaki, K. (2014). Clinicopathological features and treatment outcomes of metastatic tumors in the stomach. *Surg. Today* 44, 1392–1399. doi:10.1007/s00595-013-0671-9

Panasiti, V., Devirgiliis, V., Curzio, M., Rossi, M., Roberti, V., Bottoni, U., et al. (2009). Erythema annulare centrifugum as the presenting sign of breast carcinoma. *J. Eur. Acad. Dermatol Venereol.* 23, 318–320. doi:10.1111/j.1468-3083.2008.02848.x

Pareja, F., Ferrando, L., Lee, S. S. K., Beca, F., Selenica, P., Brown, D. N., et al. (2020). The genomic landscape of metastatic histologic special types of invasive breast cancer. *npj Breast Cancer* 6, 53. doi:10.1038/s41523-020-00195-4

Parietti, M., Carugno, A., Gianatti, A., Sena, P., Quaglino, P., and Vezzoli, P. (2022). Rapid remission of atypical cutaneous lobular breast cancer metastases after aromatase inhibitor therapy: a case report and literature review. *J. Eur. Acad. Dermatol Venereol.* 36, e824–e826. doi:10.1111/jdv.18308

Petrova, Y. I., Schecterson, L., and Gumbiner, B. M. (2016). Roles for E-cadherin cell surface regulation in cancer. *Mol. Biol. Cell.* 27, 3233–3244. doi:10.1091/mbc.E16-01-0058

Prabhu, S., Pai, S. B., Handattu, S., Kudur, M. H., and Vasanth, V. (2009). Cutaneous metastases from carcinoma breast: the common and the rare. *Indian J. Dermatol Venereol. Leprol.* 75, 499–502. doi:10.4103/0378-6323.55395

Pramod, N., Nigam, A., Basree, M., Mawalkar, R., Mehra, S., Shinde, N., et al. (2021). Comprehensive review of molecular mechanisms and clinical features of invasive lobular cancer. *Oncologist* 26, e943–e953. doi:10.1002/onco.13734

Rech, M. B., da-Cruz, E. R., Salgado, K., Balbinot, R. A., Balbinot, S. S., and Soldera, J. (2023). Metastatic gastric cancer from breast carcinoma presenting with paraneoplastic rheumatic syndrome: a case report. *World J. Clin. Cases* 11, 3282–3287. doi:10.12998/wjcc.v11.i14.3282

Ross-Innes, C. S., Stark, R., Teschendorff, A. E., Holmes, K. A., Ali, H. R., Dunning, M. J., et al. (2012). Differential oestrogen receptor binding is associated with clinical outcome in breast cancer. *Nature* 481, 389–393. doi:10.1038/nature10730

Slamon, D. J., Neven, P., Chia, S., Fasching, P. A., De Laurentiis, M., Im, S. A., et al. (2020). Overall survival with Ribociclib plus fulvestrant in advanced breast cancer. *N. Engl. J. Med.* 382, 514–524. doi:10.1056/NEJMoa1911149

Taal, B. G., den Hartog Jager, F. C., Steinmetz, R., and Peterse, H. (1992). The spectrum of gastrointestinal metastases of breast carcinoma: I. Stomach. *Gastrointest. Endosc.* 38, 130–135. doi:10.1016/s0016-5107(92)70377-0

Taal, B. G., Peterse, H., and Boot, H. (2000). Clinical presentation, endoscopic features, and treatment of gastric metastases from breast carcinoma. *Cancer* 89, 2214–2221. doi:10.1002/1097-0142(20001201)89:11<2214::aid-cncr9>3.3.co;2-4

Tang, T., Zhang, L., Li, C., and Zhou, T. (2020). Gastric and adrenal metastasis from breast cancer: case report and review of literature. *Med. Baltim.* 99, e18812. doi:10.1097/MD.0000000000018812

Teo, K., Gómez-Cuadrado, L., Tenhagen, M., Byron, A., Rätze, M., van Amersfoort, M., et al. (2018). E-cadherin loss induces targetable autocrine activation of growth factor signalling in lobular breast cancer. *Sci. Rep.* 8, 15454. doi:10.1038/s41598-018-33525-5

Turner, N. C., Swift, C., Kilburn, L., Fribbens, C., Beaney, M., Garcia-Murillas, I., et al. (2020). ESR1 mutations and overall survival on fulvestrant versus exemestane in advanced hormone receptor-positive breast cancer: a combined analysis of the phase III SoFEA and efect trials. *Clin. Cancer Res.* 26, 5172–5177. doi:10.1158/1078-0432.CCR-20-0224

Virmani, N. C., Sharma, Y. K., Panicker, N. K., Dash, K. N., Patvekar, M. A., and Deo, K. S. (2011). Zosteriform skin metastases: clue to an undiagnosed breast cancer. *Indian J. Dermatol* 56, 726–727. doi:10.4103/0019-5154.91838

Vleminckx, K., Vakaet, L., Mareel, M., Fiers, W., and van Roy, F. (1991). Genetic manipulation of E-cadherin expression by epithelial tumor cells reveals an invasion suppressor role. *Cell.* 66, 107–119. doi:10.1016/0092-8674(91)90143-m

Waldman, R. A., Finch, J., Grant-Kels, J. M., Stevenson, C., and Whitaker-Worth, D. (2019). Skin diseases of the breast and nipple: benign and malignant tumors. *J. Am. Acad. Dermatol* 80, 1467–1481. doi:10.1016/j.jaad.2018.08.066

Wang, R., Zhu, Y., Liu, X., Liao, X., He, J., and Niu, L. (2019). The Clinicopathological features and survival outcomes of patients with different metastatic sites in stage IV breast cancer. *BMC Cancer* 19, 1091. doi:10.1186/s12885-019-6311-z

Xu, L., Liang, S., Yan, N., Zhang, L., Gu, H., Fei, X., et al. (2017). Metastatic gastric cancer from breast carcinoma: a report of 78 cases. *Oncol. Lett.* 14, 4069–4077. doi:10.3892/ol.2017.6703

Zarrilli, G., Businello, G., Dieci, M. V., Paccagnella, S., Carraro, V., Cappellesso, R., et al. (2020). The tumor microenvironment of primitive and metastatic breast cancer: implications for novel therapeutic strategies. *Int. J. Mol. Sci.* 21, 8102. doi:10.3390/ijms21218102

Zheng, R. S., Zhang, S. W., Sun, K. X., Chen, R., Wang, S. M., Li, L., et al. (2023). Cancer statistics in China, 2016. *Zhonghua Zhong Liu Za Zhi* 45, 212–220. doi:10.3760/cma.j.cn112152-20220922-00647

frontiers | Frontiers in Pharmacology

TYPE Mini Review
PUBLISHED 07 March 2024
DOI 10.3389/fphar.2024.1355533

Check for updates

OPEN ACCESS

EDITED BY
Wagdy Mohamed Eldehna,
Kafrelsheikh University, Egypt

REVIEWED BY
Haytham O. Tawfik,
Tanta University, Egypt
Moataz Ahmed Shaldam,
Kafrelsheikh University, Egypt

*CORRESPONDENCE
Riezki Amalia,
riezki.amalia@unpad.ac.id

†These authors have contributed equally to this work

RECEIVED 14 December 2023
ACCEPTED 14 February 2024
PUBLISHED 07 March 2024

CITATION
Raptania CN, Zakia S, Fahira AI and Amalia R (2024), Article review: Brazilin as potential anticancer agent.
Front. Pharmacol. 15:1355533.
doi: 10.3389/fphar.2024.1355533

COPYRIGHT
© 2024 Raptania, Zakia, Fahira and Amalia. This is an open-access article distributed under the terms of the Creative Commons Attribution License (CC BY). The use, distribution or reproduction in other forums is permitted, provided the original author(s) and the copyright owner(s) are credited and that the original publication in this journal is cited, in accordance with accepted academic practice. No use, distribution or reproduction is permitted which does not comply with these terms.

Article review: Brazilin as potential anticancer agent

Callista Najla Raptania[1†], Syifa Zakia[1†], Alistia Ilmiah Fahira[1,2] and Riezki Amalia[1,2,3*]

[1]Department of Pharmacology and Clinical Pharmacy, Faculty of Pharmacy, Universitas Padjadjaran, Bandung, Indonesia, [2]Laboratory of Cell and Molecular Biology, Faculty of Pharmacy, Universitas Padjadjaran, Bandung, Indonesia, [3]Center of Excellence in Pharmaceutical Care Innovation, Universitas Padjadjaran, Bandung, Indonesia

Brazilin is the main compound in *Caesalpinia sappan* and *Haematoxylum braziletto*, which is identified as a homoisoflavonoid based on its molecular structure. These plants are traditionally used as an anti-inflammatory to treat fever, hemorrhage, rheumatism, skin problems, diabetes, and cardiovascular diseases. Recently, brazilin has increased its interest in cancer studies. Several findings have shown that brazilin has cytotoxic effects on colorectal cancer, breast cancer, lung cancer, multiple myeloma, osteosarcoma, cervical cancer, bladder carcinoma, also other cancers, along with numerous facts about its possible mechanisms that will be discussed. Besides its flavonoid content, brazilin is able to chelate metal ions. A study has proved that brazilin could be used as an antituberculosis agent based on its ability to chelate iron. This possible iron-chelating of brazilin and all the studies discussed in this review will lead us to the statement that, in the future, brazilin has the potency to be a chemo-preventive and anticancer agent. The article review aimed to determine the brazilin mechanism and pathogenesis of cancer.

KEYWORDS

brazilin, anticancer agent, cytotoxic effect, iron chelation, molecular mechanism

1 Introduction

Cancer is the second-leading cause of death among noncommunicable diseases (NCDs), after cardiovascular disease (Cadoná et al., 2022). As of 2022, there were 19.9 million incidents of cancer overall, with 9.7 million of those cases resulting in death (IARC, 2024). According to the Global Burden of Cancer Study (GLOBOCAN), the global incidence of cancer will rapidly reach 30.2 million cases by 2040, with a mortality rate of 16.3 million cases (Sung et al., 2021). Cancer is the largest cause of death in Asia, which accounts for 49.3% of all deaths (Arnold et al., 2022).

Cancer research has always been complex due to its complexity. Despite the fact that numerous treatment options are available, their effectiveness is dependent on the stage and form of the disease. Considering the different therapeutic methods, meticulous surgical excision of aggressive tissues or tumors, chemotherapy, radiation therapy, and immunotherapy are commonly used. Surgery and radiotherapy have local effects, whereas chemotherapy and targeted therapy have systemic effects. Whether these medicines are employed individually or in combination with other treatments depends on the type and stage of cancer (Muhammad et al., 2022). They could trigger processes that promote medication resistance (Naeem et al., 2022). Combinations with additional treatments (for example, radiation therapy and conventional chemotherapy) will

probably kill both normal and malignant cells, resulting in substantial hematological toxicities and tissue damage (Sharifi-Rad et al., 2021).

Historically, natural products (NPs) have played an essential role in drug discovery. Compared to conventional synthetic compounds, NPs have unique properties that provide advantages and difficulties in drug discovery. NPs are the most abundant source of high chemical diversity and structural complexity. Attempts to identify interesting therapeutic chemicals from natural sources may be one explanation for this (Feher and Schmidt, 2003; Mangal et al., 2013; Atanasov et al., 2015). Approximately 80% of NPs have previously been developed for cancer treatment (Newman and Cragg, 2016). Phenolic compounds, one of the NPS, which are molecular functional compounds that target multiple signaling pathways involved in activation or transformation of cells (Bakrim et al., 2022). Flavonoids exhibit a variety of anticancer properties, including the modification of ROS-scavenging enzyme activities, cell cycle arrest, the induction of apoptosis and autophagy, and the inhibition of cancer cell growth and invasion (Kopustinskiene et al., 2020).

Caesalpinia sappan is a medicinal plant with many flavonoids (Nguyen et al., 2020). *Caesalpinia sappanwood*'s high flavonoid concentration supports anti-cancer research. The primary flavonoid ingredient isolated from *C. sappanwood* is brazilin (Mottaghipisheh and Stuppner, 2021). Brazilin can also be found in heartwood trees, including brazilwood (*Caesalpinia echinata*) and bralette (*Caesalpinia Violaceae*) (Dapson and Bain, 2015). In several studies, we found that brazilin has the ability to treat several types of cancer, such as breast cancer (Jenie et al., 2018; Hermawan and Putri, 2020; Jang et al., 2020; Chatterjee et al., 2022; Haryanti et al., 2022; Yang et al., 2023), colorectal cancer (Handayani et al., 2017), multiple myeloma (Kim et al., 2012), osteosarcoma (Kang et al., 2018), lung cancer (Suyatmi et al., 2022), cervical cancer (Kitdamrongtham et al., 2013; Jeon et al., 2014), bladder carcinoma (Zhang et al., 2015; Zhang et al., 2018), and others (Lee et al., 2013; Mitani et al., 2013; Zhang et al., 2014; Bello-Martínez et al., 2017; He et al., 2017; Correia Soeiro et al., 2022; Yan et al., 2022).

A study stated that Brazilin substances can be used to chelate iron because of their structure, which reacts with metal ions such as iron (Fe) to form a stable complex (Safitri et al., 2022). Iron chelators have long been considered potential anticancer agents (Kulp et al., 1996; Kovář et al., 2001). Iron is a major substance essential in cell growth, metabolism, and replication. Metabolism of iron is regulated in cells with cancer to cope with greater replicative demands (Theil and Goss, 2009). Iron chelating substance were initially created to treat iron overload disorders, but their potential for anticancer use is becoming increasingly apparent (Ibrahim and OSullivan, 2020).

Based on the mentioned evidence, this article review aims to determine the future potential of brazilin as an anticancer agent and its mechanism to conclude whether there is a relationship between the activity of iron chelation from the brazilin compound and cancer pathogenesis.

2 Methods

Relevant articles were obtained from the PubMed database with the terms "brazilin" and "cancer." In total, 32 articles were identified. We exclude 11 articles that are not in English, not review articles, not Brazilin, and not cancer studies. Therefore, the rest 21 articles were included. The relevant research articles published without any time limit were included according to the criteria.

3 Brazilin: Source and structure

Brazilin, one of the main compounds originating from fractionation of the heartwood extract of *C. sappan* and *Haematoxylum brasiletto*, is most widely distributed in Southeast Asia and America (Toegel et al., 2012). Traditionally, brazilin has been taken as a red dye for cosmetics, beverages, fabrics, and food in Malaysia, China, Thailand, Mexico and Vietnam because it produces a red color (Nava-Tapia et al., 2022).

Brazilin is an organic compound of the homoisoflavonoid type, named by IUPAC as (6aS,11bR)-7,11b-dihydro-6*H*-indeno [2,1-*c*] chromene-3,6a,9,10-tetrol, with molecular formula $C_{16}H_{14}O_5$ and the molecular weight 286.28 g/mol (National Center for Biotechnology Information, 2023). It may also be named as natural red, braziletto, or brasilin (Edwards et al., 2003). Brazilin is a colorless phenolic compound consisting of one pyrone, one five-membered ring, and two aromatic rings (Rondão et al., 2013). However, the hydroxyl group of the brazilin structure is readily oxidized. It can be converted into carbonyl groups, leading to transformation of the structure and forming a colored substance called Brazilein (Harborne et al., 2013).

Brazilin is the main component of the crude dye, and brazilein is a polyphenolic compound that may be separated in large amounts by exposing the organic extract to air and light, which oxidizes the hydroxyl of brazilin to a carbonyl group. Brazilin and brazilein are tetracyclic. The aromatic ring attached to the pyrone ring should originate in the acetate pathway, while the aromatic ring bonded to the five-membered ring in the shikimic acid pathway (de Oliveira et al., 2002).

4 Brazilin pharmacological activities

Traditionally, extracts of *C. sappan* and *H. brasiletto* have been applied to fever, hemorrhage, diabetes, skin problems, cardiovascular diseases, and diabetes as an anti-inflammatory because of their potential for medicinal use (Pawar et al., 2008; Nirmal and Panichayupakaranant, 2015; Mueller et al., 2016; Hwang and Shim, 2018). Specifically, as a major compound of both plants, brazilin possesses various pharmacological activities. Brazilin is a significant inhibitor of nitrite oxide (NO) production. It is a valuable therapy for antioxidants, anti-inflammation, and vascular relaxation (Hu et al., 2003; Sasaki et al., 2007). Brazilin significantly inhibited J444.1 cell line nitrite oxide (NO) generation produced by lipopolysaccharide (LPS). It has been discovered that brazilin significantly lowers iNOS gene expression at 100 μM, while its derivative, brazilein, does so even at 10 μM[54]. As an essential relaxing factor in the circulatory system, brazilin increases NO production, NOS activity, and extracellular Ca^{2+} influx in human umbilical vein endothelial cells (Hu et al., 2003). Compared to its derivate, Brazilein, which has activity to reducing liver damage that

TABLE 1 Summary of Brazilin activity in several types of cancer.

No.	Methods			Mechanism	References
	In Silico	*In Vitro*	*In Vivo*		
1	—	Breast cancer MDA-MB-231 and 4T1 cells	Subcutaneous xenotransplantation in BALB/C mice	-	Yang et al. (2023)
2	*MMP14*, *PTGS2*, *ADAM17*, *PTEN*, *CCL2*, *PIK3CB*, *MAP3K8*, and *CXCL3*	-	-	TNFα signaling	Hermawan and Putri (2020)
3	-	Breast cancer MCF-7/HER-2 cells	-	Cytotoxicity and cell migration	Jenie et al. (2018)
4	MMP-9, MMP-2, and PTGS2 enzymes	Triple Negative Breast Cancer (TNBC) 4T1 cell line	-	Cell migration	Haryanti et al. (2022)
5	-	Human breast cancer MCF-7 cell line		Hemin-induced HO-1 protein expression	Jang et al. (2020)
6	S-adenosyl-L-homocysteine (SAH) and DNMT1 protein	Human breast cancer cell line MCF7 and the gene expression of DNMT1, p38 MAPK, p53, and p21		Cell proliferation and DNMT1 expression	Chatterjee et al. (2022)
7	-	Colorectal cancer WiDr cell line		Apoptosis and Cell cycle	Handayani et al. (2017)
8	-	Multiple Myeloma U266 cell line	-	Histone deacetylases (HDACs)	Kim et al. (2012)
9	-	Osteosarcoma MG-63 cell line	-	Apoptosis	Kang et al. (2018)
10	-	Non-Small Lung Carcinoma A549 cell line	-	Intrinsic apoptosis	Suyatmi et al. (2022)
11	-	Human cervical cancer HeLa cell line	-	NF-κB luciferase	Jeon et al. (2014)
12	-	SRB assay in human cervical cancer HeLa cell line	HeLa xenograft and sub chronic toxicity in nude mice and rats	Antitumor and antiproliferative	Kitdamrongtham et al. (2013)
13	-	Bladder carcinoma T24 cell line	-	Cell proliferation	T. Zhang et al. (2015)
14	-	Bladder carcinoma T24 cell line	-	Apoptosis	T. Zhang et al. (2018)
15	BAF1 (barrier-to-autointegration factor 1) protein	-	-	-	Correia Soeiro et al. (2022)
16	-	Glioblastoma multiforme U87 cell line	-	Cell growth and apoptosis	Lee et al. (2013)
17	-	Head and neck squamous cell carcinoma	-	Apoptosis	He et al. (2017)
18	-	SiHa, MDA-MB-231, A549, and NCI-H1299 cell lines	-	Cell proliferation	Bello-Martínez et al. (2017)
19	-	HEK293T cell line and cancer cell lines, including HTC75, HeLa, DLD1, MDA-MB-231, Hs578t and A549	6–8-week-old nude mice *in situ*	Telomerase *in vitro* and *in vivo*	Yan et al. (2022)
20	-	Human melanoma HMV-II cell line	-	Tyrosinase and *TYRP2* mRNAs	Mitani et al. (2013)
21	-	RAW 264.7 macrophage cells	S180 mouse sarcoma cells	DNA binding activity of NF-κB and AP-1	Zhang et al. (2014)

caused by excess iron, increasing cytotoxicity and apoptosis in T47D cells, and inhibiting NFκB1/p50 in human osteoarthritic (Safitri et al., 2016; Utomo et al., 2018; Weinmann et al., 2018). Brazilein also can be invented as potential antibacterial agent against *Escherichia coli* MDR, a sensitive antibiotic using *in silico* method (Krihariyani et al., 2020).

Brazilin has antimicrobial effects through decreasing DNA and protein production. Brazilin inhibited the growth of bacteria that

cause methicillin-resistant *Staphylococcus aureus* (MRSA), dental caries (*Streptococcus mutans*), periodontal disease (*Prevotella intermedia*), acne (*Propionibacterium acnes*), and strep throat (Group A strep) (Xu and Lee, 2004). Brazilin has an increased pyruvate kinase activity mechanism. In addition, it may play a role in the anti-gluconeogenic action of brazilin. Brazilin enhanced the levels of 6-phosphofructo-2-kinase (PFK-2), fructose-6-phosphate (F-6-P), and hexose-6-phosphate (H-6-P) extensively (You et al., 2005).

5 Brazilin mechanisms in cancer

Brazilin has been studied in several types of cancer, such as cervical cancer, cervical squamous cell carcinoma, breast cancer, colorectal adenocarcinoma, colorectal cancer, colon cancer, hepatocellular carcinoma, lung adenocarcinoma, and sarcoma. A compound's ability to impede biological or biochemical function may be measured through its half-maximal inhibitory concentration (IC_{50}) (Hendriks, 2010). Drug potency, or the quantity of a drug required to have a therapeutic effect, is correlated with the IC_{50} value. Like a drug, the IC_{50} value of a natural compound must be determined to know the cytotoxicity. The lower the IC_{50} value, the more cytotoxic the substance is (Meyer et al., 2019). Based on its IC_{50} value from different types of cancer cell lines (Bello-Martínez et al., 2017; Handayani et al., 2017; Haryanti et al., 2022; Jenie et al., 2018; Suyatmi et al., 2022; Yang et al., 2023; Zhang et al., 2014), brazilin has a strong ability to treat breast cancer on 4T1 cell lines with the measured IC_{50} value of 3.7 μM. The methods used in several studies to know the mechanism of brazilin to treat several types of cancer are shown in Table 1.

In treating cancer, brazilin has different types of mechanisms, but the general mechanism is to induce apoptosis and inhibit cell proliferation. Most of the studies were carried out using breast cancer cell lines. Brazilin inhibits cell proliferation, migration, and invasion as the primary therapy and co-therapy with doxorubicin (Jenie et al., 2018; Haryanti et al., 2022). Hemin-induced heme oxygenase-1 (HO-1) in breast cancer cells is slightly inhibited by brazilin (Jang et al., 2020). Besides, HO-1 has cytoprotective properties to promote cancer progression in cancer cells, yet HO-1 overactivation also promotes unconventional ferroptosis due to an accumulation of prooxidant-free iron (Nitti et al., 2021). Other findings were obtained to help arrange possible molecular mechanisms of brazilin as a novel anticancer agent. Brazilin suppressed the activity of transcription factors called histone deacetylases (HDACs), which are involved in controlling cell cycle arrest and apoptosis in multiple myeloma (Kim et al., 2012).

An *in silico* study predicted several targets that brazilin inhibited. In triple breast cancer, brazilin was found to attach more firmly and effectively to MMP-2, MMP-9, and PTGS2 compared to its native ligand (Haryanti et al., 2022). These enzymes are involved in cell migration and metastasis (Webb et al., 2017; Ercolano et al., 2019). According to these findings, brazilin could potentially disrupt the activities of the enzymes by binding to their active sites (Haryanti et al., 2022).

Brazilin has also shown its activity in several other types of cancer, but its mechanism has not yet been studied further. Brazilin mechanisms are limited to *in silico*, *in vitro*, and *in vivo*. No clinical research has ever been done. Apoptotic-related pathways are still the most interesting to explore for a new potential anticancer agent. Every discovery is valuable to guide us for new pathways regarding anticancer therapy mechanisms by brazilin. Of all the findings about brazilin mechanisms towards cancer, the iron chelation mechanism has not been mentioned yet. In the meantime, using iron chelators as an adjuvant cancer treatment is becoming more popular, even though they have been developed initially to treat iron overload disorders (Wang et al., 2019; Safitri et al., 2022).

6 Brazilin as iron chelators

Brazilin belongs to the class of flavonoids that are likely to interact with metals, mainly Fe (Kejík et al., 2021). A study has found that brazilin could be used as an antituberculosis because of its mechanism of inhibiting *Mycobacterium tuberculosis* (Mtb) extracellularly by iron chelation (Safitri et al., 2022). Iron overload removal and prevention are the main goals of chelation therapy. By chelating extra iron, iron levels can be maintained at normal levels. Iron chelation therapy was first developed for transfusion-dependent anemias, including myelodysplasia, sickle cell disease, and thalassemia. However, this is only a small portion of the potential spectrum of activity for iron chelators (Porter, 2001). Transferrin (Tf), a protein with a strong affinity for iron, carries iron in plasma. After the iron transferrin complex attaches to the cell surface's transferrin receptor 1 (TfR1), the complex is internalized through receptor-mediated endocytosis, and endosomal acidification releases the iron from Tf (Hentze et al., 2004). On the other hand, cancer cells have a few different mechanisms to keep the balance of iron within their cells. In neoplastic cells, iron metabolism is altered in order to fulfill higher replicative needs. Numerous processes contribute to the increased iron uptake in neoplastic cells, but the most prominent one is the increased protein expression of the TfR1 receptor, which has been found in several cases, including renal, colorectal, liver, breast, and lung cancer (Kindrat et al., 2016; Greene et al., 2017; Horniblow et al., 2017; Rychtarcikova et al., 2017). In these neoplasms, its level has been connected to the growth of the tumor (Brookes et al., 2006). Numerous neoplasms have also been reported to have elevated levels of the homologous TfR2 (Calzolari et al., 2007). It has been shown in melanoma and hepatoma cell lines that intake occurs via non-receptor-mediated pinocytosis once TfR1 is saturated (Richardson and Baker, 1994; Trinder et al., 1996).

Iron chelators that are clinically approved are as follows: Deferoxamine (DFO) (Kontoghiorghes et al., 1987; Hernlem et al., 1996), Deferiprone (L1) (Rombos et al., 2000; Cohen et al., 2003; Hoffbrand et al., 2003), and Deferasirox (DFX) (Gaboriau et al., 2010). Iron chelators were initially developed to treat iron overload disorders like thalassemia, but there is increasing interest in their potential as adjunctive therapy for cancer. The combination of iron-chelating agents like DFO or DFX with cisplatin, doxorubicin, and carboplatin has been shown to increase the cytotoxic effects of these chemotherapeutics in some studies (Wang et al., 2019; Safitri et al., 2022). Another natural compound that has iron chelator activity is curcumin. Curcumin shows great potential as a therapeutic substance and is being studied in humans for a

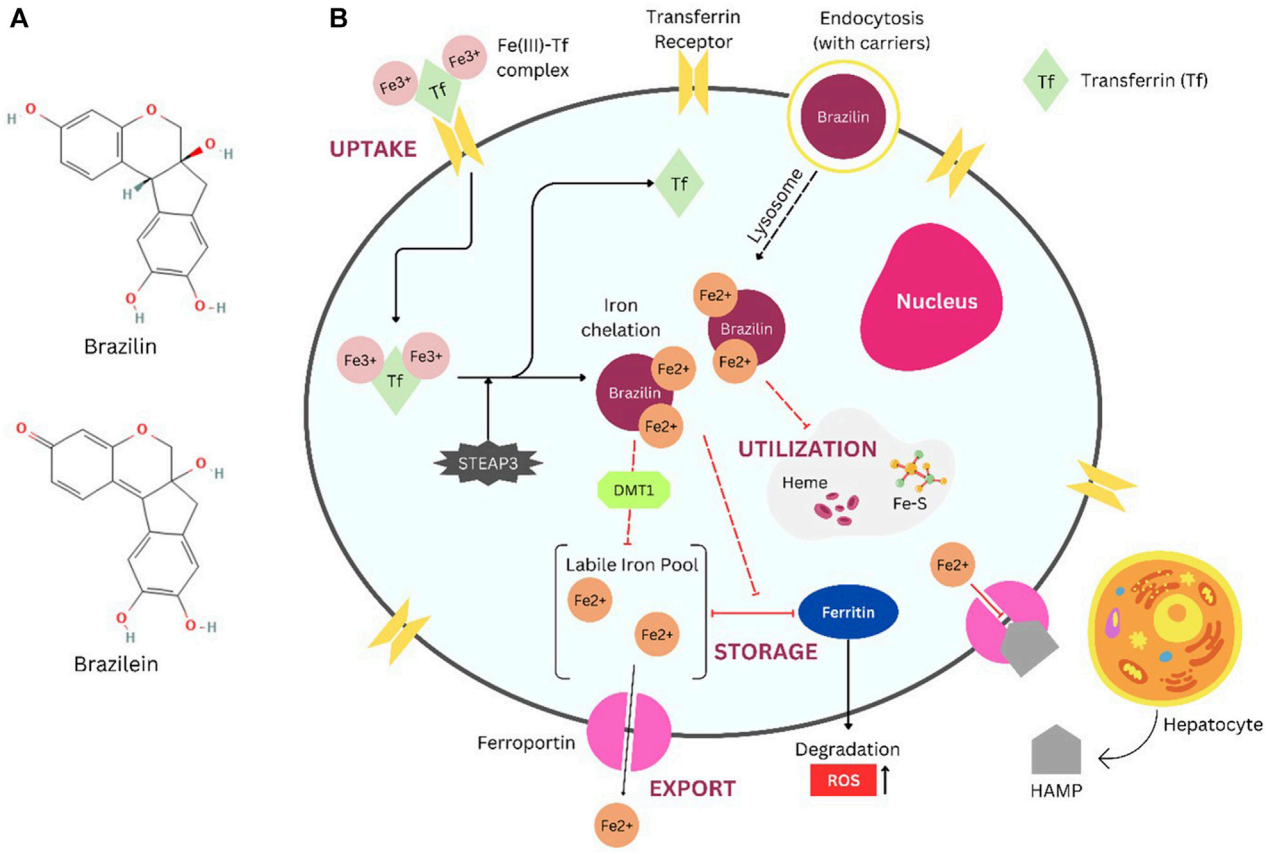

FIGURE 1
Brazilin (National Center for Biotechnology Information, 2024b) and Brazilein ((National Center for Biotechnology Information, 2024a) structure **(A)**, Brazilin predicted mechanism as iron chelators in cancer cells **(B)**. Illustration refers to the common mechanism of clinically approved iron chelators (i.e., Deferoxamine (DFO)). DFO and other compounds with similar structures have poor pharmacokinetics profiles. Conjugation with drug carriers, such as polymers, could help increase therapeutical efficacy (Komoto et al., 2021). Brazilin with carriers (polymer, plasmid, etc.) entering cell cytoplasm via endocytosis. Iron uptake involves Transferrin that binds two irons and enters cells by interaction with the Transferrin Receptor (TfR1). Iron is typically transported by DMT1 toward the labile iron pool (LIP) and then scavenged and stored by Ferritin (Pfeifhofer-Obermair et al., 2018). In cancer cells, the requirements of iron are relatively high, and there is also an accumulation of free iron inside cells caused by Hepcidin (HAMP) binding to Ferroportin (FPN), which is beneficial for iron export to maintain iron homeostasis (Bystrom et al., 2014). Iron chelation occurs inside cells toward free labile iron (Fe^{2+}). Thereby, storage and utilization of iron are inhibited by this chelation mechanism. Further research is recommended to clarify whether brazilin promotes pro-oxidant and iron depletion effects. **Abbreviations:** DMT1, divalent metal transporter 1; Fe-S, iron sulfide; HAMP, hepcidin antimicrobial peptide; ROS, reactive oxygen species; STEAP3, six-transmembrane epithelial antigen of prostate 3; Tf, transferrin.

number of diseases, such as psoriasis, pancreatic cancer, multiple myeloma, colon cancer, and myelodysplastic syndromes. Curcumin inhibits the development and progression of cancer by targeting different stages in the malignant process (Hatcher et al., 2009).

Due to the bidentate ligand, a strong metal cation scavenger that can tightly bind iron (III) at pH 7, brazilin also happens to have a catechol group that may chelate iron, according to various research (Hruby et al., 2021). Brazilin's structure shares a few similarities to that of DFO, a hexadentate compound that can bind iron in a 1: 1 ratio to form a stable complex that prevents the free radicals that iron produces (Zhou et al., 2012). An iron chelator's potency is determined by how well it can bind transferrin-bound iron that is not circulating in the plasma. Among other iron chelators, L1 is considered very effective in iron chelating (Maskoen et al., 2016). The substance has the benefit of quickly penetrating membranes to remove potentially harmful iron from tissues since the Fe(III) chelate of L1 has no net charge (Kattamis et al., 2006). To chelate one iron atom, L1 molecules are required (Kontoghiorghes et al., 1987; Merson and Olivier, 2002). Structurally, brazilin has properties similar to L1 due to its bidentate structure, indicating that brazilin can bind iron with the same ratio as L1. Mechanism prediction of brazilin as iron chelators is shown in Figure 1.

7 Iron chelating activity in cancer pathogenesis

The development of iron chelators as therapeutic agents can also be useful anticancer agents (Buss et al., 2005) either by depleting iron in the tumor or by causing selective oxidative stress in the tumor due to redox perturbations in its environment (Hatcher et al., 2009; Fibach and Rachmilewitz, 2017). One of the metabolic characteristics of malignant cancer cells is dysregulated iron homeostasis, where iron is crucial for the growth, survival, proliferation, and metastasis of tumors at every stage of the process (Ludwig et al., 2015). Tumor cells are

more susceptible to iron deficiency than normal cells because they rely heavily on iron for development and proliferation (Bystrom and Rivella, 2015). Iron reductase, primarily found in some members of the metal reductases six-transmembrane epithelial antigen of the prostate (STEAP1-4) family, reduces Fe^{3+} to Fe^{2+} in the endosome. Many human cancer types, including breast, colon, prostate, cervix, bladder, pancreatic, testis, ovary and Ewing sarcoma, have high expression levels of STEAP1 and STEAP2. In malignant gliomas, STEAP3 is overexpressed, and STEAP3 knockdown suppresses glioma cell metastasis, proliferation, and clonality, *in vitro* and tumor growth *in vivo*. Under hypoxic conditions, STEAP4 is activated, which increases the incidence of colitis-associated colon cancer in mice models, enhances the formation of reactive oxygen species (ROS), and causes an iron imbalance in the mitochondria (Wang et al., 2019).

Deferoxamine (DFO) and Deferasirox (DFX) are widely used for iron overload disease in cancer therapy (Ibrahim and OSullivan, 2020). Among all iron chelators available on market, DFX is the first-choice iron chelator used globally to treat non-transfusion-dependent thalassemia syndromes in patients from age of 10 and above, along with chronic iron overload on by blood transfusions in patients from age of 2 (Piga et al., 2006). DFO chelates non-transferrin bound iron (free iron), hemosiderin, and iron in transit between transferrin and ferritin (labile chelating iron pool). DFO is able to directly attach to iron and remove it away from heart cells, but it is unable to bind iron that has already been integrated into other molecules, such as hemoglobin, transferrin, or cytochromes (Hershko et al., 2001; Komoto et al., 2021). However, DFX preferentially binds to iron in its oxidized ferric (Fe^{3+}) state than to the reduced or ferrous (Fe^{2+}) state. Every DFX molecule binds two ferric irons (Valentovic and Enna, 2008). Additionally, it was discovered that DFX caused apoptosis by reducing ER stress responses (Kim et al., 2016). Based on previous discussion, we conclude that brazilin has the potential ability to chelate iron. Concerning its activity, it has previously been developed as a targeted anticancer therapy. As a result, brazilin can potentially be an anticancer agent through the iron chelation mechanism.

8 Discussion

Brazilin has different mechanisms in treating cancer, but mainly induces apoptosis and inhibits cell proliferation. Most of the studies were carried out using breast cancer cell lines. Brazilin inhibits cell proliferation, migration, and invasion as the primary therapy and co-therapy with doxorubicin (Jenie et al., 2018; Haryanti et al., 2022). Brazilian mechanism studies are limited to *in silico* and *in vivo*. Every discovery is valuable to guide us for new pathways regarding anticancer therapy mechanisms by brazilin. The iron chelation mechanism in brazilin to treat cancer is not mentioned yet. Iron chelators were originally created to treat iron overload problems, however there has been rising interest in using them as adjuvant therapy for cancer (Wang et al., 2019; Safitri et al., 2022).

Other pathways are present in cancer cells for keeping the equilibrium of iron within the cell. In neoplastic cells, iron metabolism is altered to satisfy higher replicative needs. Numerous processes contribute to the increased iron uptake in neoplastic cells, but the most prominent one is the increased protein expression of the TfR1 receptor, which has been found in several cases, including renal, colorectal, liver, breast, and lung cancer (Kindrat et al., 2016; Greene et al., 2017; Horniblow et al., 2017; Rychtarcikova et al., 2017). Brazilin's bidentate ligand, a strong metal cation scavenger that can tightly bind iron (III) at pH 7, is responsible for the catechol group's ability to chelate iron (Hruby et al., 2021). Brazilin's structure shares a few similarities to that of deferoxamine (DFO), a hexadentate compound that can bind iron in a 1:1 ratio to form a stable complex that prevents the free radicals that iron produces (Zhou et al., 2012).

In conclusion, we have found that brazilin has activities toward cancer pathogenesis via apoptosis mechanism and cell cycle arrest. There is a study stating that brazilin has the ability to chelate iron as an antituberculosis agent. The development of iron chelators also can be useful as anticancer agents. Throughout the whole process of tumor growth, survival, proliferation, and metastasis, iron is essential. Therefore, brazilin has the potential as an anticancer agent through the iron chelation mechanism. However, further research and investigations must be conducted on brazilin to confirm this finding.

Author contributions

CR: Data curation, Methodology, Writing–original draft. SZ: Data curation, Methodology, Writing–original draft. AF: Data curation, Formal Analysis, Methodology, Visualization, Writing–original draft, Writing–review and editing. RA: Conceptualization, Formal Analysis, Funding acquisition, Methodology, Project administration, Supervision, Visualization, Writing–original draft, Writing–review and editing.

Funding

The author(s) declare that financial support was received for the research, authorship, and/or publication of this article. Universitas Padjadjaran funded this research study under the Universitas Padjadjaran Research Grant Scheme.

Acknowledgments

Universitas Padjadjaran funded this research study under the Universitas Padjadjaran Research Grant Scheme.

Conflict of interest

The authors declare that the research was conducted in the absence of any commercial or financial relationships that could be construed as a potential conflict of interest.

Publisher's note

All claims expressed in this article are solely those of the authors and do not necessarily represent those of their affiliated

organizations, or those of the publisher, the editors and the reviewers. Any product that may be evaluated in this article, or claim that may be made by its manufacturer, is not guaranteed or endorsed by the publisher.

References

Arnold, M., Morgan, E., Rumgay, H., Mafra, A., Singh, D., Laversanne, M., et al. (2022). Current and future burden of breast cancer: global statistics for 2020 and 2040. *Breast* 66, 15–23. doi:10.1016/j.breast.2022.08.010

Atanasov, A. G., Waltenberger, B., Pferschy-Wenzig, E. M., Linder, T., Wawrosch, C., Uhrin, P., et al. (2015). Discovery and resupply of pharmacologically active plant-derived natural products: a review. *Biotechnol. Adv.* 33 (8), 1582–1614. doi:10.1016/j.biotechadv.2015.08.001

Bakrim, S., El Omari, N., El Hachlafi, N., Bakri, Y., Lee, L. H., and Bouyahya, A. (2022). Dietary phenolic compounds as anticancer natural drugs: recent update on molecular mechanisms and clinical trials. *Foods* 11 (21), 3323. doi:10.3390/foods11213323

Bello-Martínez, J., Jiménez-Estrada, M., Rosas-Acevedo, J. L., Avila-Caballero, L. P., Vidal-Gutierrez, M., Patiño-Morales, C., et al. (2017). Antiproliferative activity of Haematoxylum brasiletto H. Karst. *Pharmacogn. Mag.* 13 (50), S289-S293–S293. doi:10.4103/pm.pm_466_16

Brookes, M. J., Hughes, S., Turner, F. E., Reynolds, G., Sharma, N., Ismail, T., et al. (2006). Modulation of iron transport proteins in human colorectal carcinogenesis. *Gut* 55 (10), 1449–1460. doi:10.1136/gut.2006.094060

Buss, J., Torti, F., and Torti, S. (2005). The role of iron chelation in cancer therapy. *Curr. Med. Chem.* 10 (12), 1021–1034. doi:10.2174/0929867033457638

Bystrom, L. M., Guzman, M. L., and Rivella, S. (2014). Iron and reactive oxygen species: friends or foes of cancer cells? *Antioxidants Redox Signal* 20 (12), 1917–1924. doi:10.1089/ars.2012.5014

Bystrom, L. M., and Rivella, S. (2015). Cancer cells with irons in the fire. *Free Radic. Biol. Med.* 79, 337–342. doi:10.1016/j.freeradbiomed.2014.04.035

Cadoná, F. C., Dantas, R. F., de Mello, G. H., and Silva-, F. P., Jr (2022). Natural products targeting into cancer hallmarks: an update on caffeine, theobromine, and (+)-catechin. *Crit. Rev. Food Sci. Nutr.* 62 (26), 7222–7241. doi:10.1080/10408398.2021.1913091

Calzolari, A., Oliviero, I., Deaglio, S., Mariani, G., Biffoni, M., Sposi, N. M., et al. (2007). Transferrin receptor 2 is frequently expressed in human cancer cell lines. *Blood Cells, Mol. Dis.* 39 (1), 82–91. doi:10.1016/j.bcmd.2007.02.003

Chatterjee, B., Ghosh, K., Swain, A., Nalla, K. K., Ravula, H., Pan, A., et al. (2022). The phytochemical brazilin suppress DNMT1 expression by recruiting p53 to its promoter resulting in the epigenetic restoration of p21 in MCF7cells. *Phytomedicine* 95, 153885. doi:10.1016/j.phymed.2021.153885

Cohen, A. R., Galanello, R., Piga, A., De Sanctis, V., and Tricta, F. (2003). Safety and effectiveness of long-term therapy with the oral iron chelator deferiprone. *Blood* 102 (5), 1583–1587. doi:10.1182/blood-2002-10-3280

Correia Soeiro, M. de N., Vergoten, G., and Bailly, C. (2022). Molecular docking of brazilin and its analogs to barrier-to-autointegration factor 1 (BAF1). *Ann. N. Y. Acad. Sci.* 1511 (1), 154–163. doi:10.1111/nyas.14742

Dapson, R. W., and Bain, C. L. (2015). Brazilwood, sappanwood, brazilin and the red dye brazilein: from textile dyeing and folk medicine to biological staining and musical instruments. *Biotech. Histochem* 90 (6), 401–423. doi:10.3109/10520295.2015.1021381

de Oliveira, L. F. C., Edwards, H. G. M., Velozo, E. S., and Nesbitt, M. (2002). Vibrational spectroscopic study of brazilin and brazilein, the main constituents of brazilwood from Brazil. *Vib. Spectrosc.* 28 (2), 243–249. doi:10.1016/S0924-2031(01)00138-2

Edwards, H. G. M., De Oliveira, L. F. C., and Nesbitt, M. (2003). Fourier-transform Raman characterization of brazilwood trees and substitutes. *Analyst* 128 (1), 82–87. doi:10.1039/b209052j

Ercolano, G., De Cicco, P., Rubino, V., Terrazzano, G., Ruggiero, G., Carriero, R., et al. (2019). Knockdown of PTGS2 by CRISPR/CAS9 system designates a new potential gene target for melanoma treatment. *Front. Pharmacol.* 10, 1456. doi:10.3389/fphar.2019.01456

Feher, M., and Schmidt, J. M. (2003). Property distributions: differences between drugs, natural products, and molecules from combinatorial chemistry. *J. Chem. Inf. Comput. Sci.* 43 (1), 218–227. doi:10.1021/ci0200467

Fibach, E., and Rachmilewitz, E. A. (2017). Iron overload in hematological disorders. *Press Medicale* 46 (12P2), e296–e305. doi:10.1016/j.lpm.2017.10.007

Gaboriau, F., Leray, A. M., Ropert, M., Gouffier, L., Cannie, I., Troadec, M. B., et al. (2010). Effects of deferasirox and deferiprone on cellular iron load in the human hepatoma cell line HepaRG. *BioMetals* 23 (2), 231–245. doi:10.1007/s10534-009-9281-9

Greene, C. J., Attwood, K., Sharma, N. J., Gross, K. W., Smith, G. J., Xu, B., et al. (2017). Transferrin receptor 1 upregulation in primary tumor and downregulation in benign kidney is associated with progression and mortality in renal cell carcinoma patients. *Oncotarget* 8 (63), 107052–107075. doi:10.18632/oncotarget.22323

Handayani, S., Susidarti, R. A., Jenie, R. I., and Meiyanto, E. (2017). Two active compounds from Caesalpinia sappan L. in combination with cisplatin synergistically induce apoptosis and cell cycle arrest on WiDr cells. *Adv. Pharm. Bull.* 7 (3), 375–380. doi:10.15171/apb.2017.045

Harborne, J. B., Marby, H., and Marby, T. J. (2013). *The flavonoids*. London, New York: Chapman and Hall Ltd.

Haryanti, S., Zulfin, U. M., Salsabila, I. A., Wulandari, F., and Meiyanto, E. (2022). The cytotoxic and anti-migratory properties of Caesalpinia sappan and Ficus septica, in combination with doxorubicin on 4T1 TNBC cells with nephroprotective potential. *Asian Pac. J. Cancer Prev.* 23 (2), 743–752. doi:10.31557/APJCP.2022.23.2.743

Hatcher, H. C., Singh, R. N., Torti, F. M., and Torti, S. V. (2009). Synthetic and natural iron chelators: therapeutic potential and clinical use. *Future Med. Chem.* 1 (9), 1643–1670. doi:10.4155/fmc.09.121

He, Z. J., Zhu, F. Y., Li, S. S., Zhong, L., Tan, H. Y., and Wang, K. (2017). Inhibiting ROS-NF-κB-dependent autophagy enhanced brazilin-induced apoptosis in head and neck squamous cell carcinoma. *Food Chem. Toxicol.* 101, 55–66. doi:10.1016/j.fct.2017.01.002

Hendriks, B. S. (2010). Functional pathway pharmacology: chemical tools, pathway knowledge and mechanistic model-based interpretation of experimental data. *Curr. Opin. Chem. Biol.* 14 (4), 489–497. doi:10.1016/j.cbpa.2010.06.167

Hentze, M. W., Muckenthaler, M. U., and Andrews, N. C. (2004). Balancing acts: molecular control of mammalian iron metabolism. *Cell* 117 (3), 285–297. doi:10.1016/S0092-8674(04)00343-5

Hermawan, A., and Putri, H. (2020). Integrative bioinformatics analysis reveals potential target genes and TNFα signaling inhibition by brazilin in metastatic breast cancer cells. *Asian Pac. J. Cancer Prev.* 21 (9), 2751–2762. doi:10.31557/APJCP.2020.21.9.2751

Hernlem, B. J., Vane, L. M., and Sayles, G. D. (1996). Stability constants for complexes of the siderophore desferrioxamine b with selected heavy metal cations. *Inorganica Chim. Acta* 244 (2), 179–184. doi:10.1016/0020-1693(95)04780-8

Hershko, C., Konijn, A. M., Nick, H. P., Breuer, W., Cabantchik, Z. I., and Link, G. (2001). ICL670A: a new synthetic oral chelator: evaluation in hypertransfused rats with selective radioiron probes of hepatocellular and reticuloendothelial iron stores and in iron-loaded rat heart cells in culture. *Blood* 97 (4), 1115–1122. doi:10.1182/blood.V97.4.1115

Hoffbrand, A. V., Cohen, A., and Hershko, C. (2003). Role of deferiprone in chelation therapy for transfusional iron overload. *Blood* 102 (1), 17–24. doi:10.1182/blood-2002-06-1867

Horniblow, R. D., Bedford, M., Hollingworth, R., Evans, S., Sutton, E., Lal, N., et al. (2017). BRAF mutations are associated with increased iron regulatory protein-2 expression in colorectal tumorigenesis. *Cancer Sci.* 108 (6), 1135–1143. doi:10.1111/cas.13234

Hruby, M., Martínez, I. I. S., Stephan, H., Pouckova, P., Benes, J., and Stepanek, P. (2021). Chelators for treatment of iron and copper overload: shift from low-molecular-weight compounds to polymers. *Polym. (Basel)* 13 (22), 3969. doi:10.3390/polym13223969

Hu, C. M., Kang, J. J., Lee, C. C., Li, C. H., Liao, J. W., and Cheng, Y. W. (2003). Induction of vasorelaxation through activation of nitric oxide synthase in endothelial cells by brazilin. *Eur. J. Pharmacol.* 468 (1), 37–45. doi:10.1016/S0014-2999(03)01639-X

Hwang, H. S., and Shim, J. H. (2018). Brazilin and Caesalpinia sappan L. extract protect epidermal keratinocytes from oxidative stress by inducing the expression of GPX7. *Chin. J. Nat. Med.* 16 (3), 203–209. doi:10.1016/S1875-5364(18)30048-7

IARC (2024). *Cancer today*. Available at: https://gco.iarc.who.int/(Accessed February 2, 2024).

Ibrahim, O., and OSullivan, J. (2020). Iron chelators in cancer therapy. *BioMetals* 33 (4-5), 201–215. doi:10.1007/s10534-020-00243-3

Jang, H. Y., Hong, O. Y., Chung, E. Y., Park, K. H., and Kim, J. S. (2020). Roles of JNK/NRF2 pathway on hemin-induced heme oxygenase-1 activation in MCF-7 human breast cancer cells. *Med. Lith.* 56 (6), 268. doi:10.3390/medicina56060268

Jenie, R. I., Handayani, S., Susidarti, R. A., Udin, L. Z., and Meiyanto, E. (2018). The cytotoxic and antimigratory activity of Brazilin-doxorubicin on MCF-7/HER2 cells. *Adv. Pharm. Bull.* 8 (3), 507–516. doi:10.15171/apb.2018.059

Jeon, J., Lee, J. H., Park, K. A., Byun, H. S., Lee, H., Lee, Y., et al. (2014). Brazilin selectively disrupts proximal IL-1 receptor signaling complex formation by targeting an

IKK-upstream signaling components. *Biochem. Pharmacol.* 89 (4), 515–525. doi:10.1016/j.bcp.2014.04.004

Kang, Y., He, P., Wang, H., Ye, Y., Li, X., Xie, P., et al. (2018). Brazilin induces FOXO3A-dependent autophagic cell death by disturbing calcium homeostasis in osteosarcoma cells. *Cancer Chemother. Pharmacol.* 82 (3), 479–491. doi:10.1007/s00280-018-3633-5

Kattamis, A., Ladis, V., Berdousi, H., Kelekis, N. L., Alexopoulou, E., Papasotiriou, I., et al. (2006). Iron chelation treatment with combined therapy with deferiprone and deferioxamine: a 12-month trial. *Blood Cells, Mol. Dis.* 36 (1), 21–25. doi:10.1016/j.bcmd.2005.11.002

Kejík, Z., Kaplánek, R., Masařík, M., Babula, P., Matkowski, A., Filipenský, P., et al. (2021). Iron complexes of flavonoids-antioxidant capacity and beyond. *Int. J. Mol. Sci.* 22 (2), 646. doi:10.3390/ijms22020646

Kim, J. L., Lee, D. H., Na, Y. J., Kim, B. R., Jeong, Y. A., Lee, S. I., et al. (2016). Iron chelator-induced apoptosis via the ER stress pathway in gastric cancer cells. *Tumor Biol.* 37 (7), 9709–9719. doi:10.1007/s13277-016-4878-4

Kim, S. H., Kim, B., Kim, S. H., Jeong, S. J., Sohn, E. J., Jung, J. H., et al. (2012). Brazilin induces apoptosis and G2/M arrest via inactivation of histone deacetylase in multiple myeloma U266 cells. *J. Agric. Food Chem.* 60 (39), 9882–9889. doi:10.1021/jf302527p

Kindrat, I., Tryndyak, V., Conti, A. de, Shpyleva, S., Mudalige, T. K., Kobets, T., et al. (2016). MicroRNA-152-mediated dysregulation of hepatic transferrin receptor 1 in liver carcinogenesis. *Oncotarget* 7 (2), 1276–1287. doi:10.18632/oncotarget.6004

Kitdamrongtham, W., Manosroi, A., Akazawa, H., Gidado, A., Stienrut, P., Manosroi, W., et al. (2013). Potent anti-cervical cancer activity: synergistic effects of Thai medicinal plants in recipe N040 selected from the MANOSROI III database. *J. Ethnopharmacol.* 149 (1), 288–296. doi:10.1016/j.jep.2013.06.037

Komoto, K., Nomoto, T., El Muttaqien, S., Takemoto, H., Matsui, M., Miura, Y., et al. (2021). Iron chelation cancer therapy using hydrophilic block copolymers conjugated with deferoxamine. *Cancer Sci.* 112 (1), 410–421. doi:10.1111/cas.14607

Kontoghiorghes, G. J., Aldouri, M. A., Hoffbrand, A. V., Barr, J., Wonke, B., Kourouclaris, T., et al. (1987). Effective chelation of iron in beta thalassaemia with the oral chelator 1,2-dimethyl-3-hydroxypyrid-4-one. *Br. Med. J. Clin. Res. Ed.* 295 (6612), 1509–1512. doi:10.1136/bmj.295.6612.1509

Kopustinskiene, D. M., Jakstas, V., Savickas, A., and Bernatoniene, J. (2020). Flavonoids as anticancer agents. *Nutrients* 12 (2), 457. doi:10.3390/nu12020457

Kovář, J., Valenta, T., and Štýbrová, H. (2001). Differing sensitivity of tumor cells to apoptosis induced by iron deprivation *in vitro*. *Vitr. Cell Dev. Biol. - Anim.* 37 (7), 450–458. doi:10.1290/1071-2690(2001)037<0450:DSOTCT>2.0.CO;2

Krihariyani, D., Wasito, E. B., Isnaeni, I., Siswodihardjo, S., Yuniarti, W. M., and Kurniawan, E. (2020). *In silico* study on antibacterial activity and brazilein ADME of sappan wood (Caesalpinia sappan L.) against *Escherichia coli* (strain K12). *Syst. Rev. Pharm.* 11 (10), 290–296. doi:10.31838/srp.2020.10.49

Kulp, K. S., Green, S. L., and Vulliet, P. R. (1996). Iron deprivation inhibits cyclin-dependent kinase activity and decreases cyclin D/CDK4 protein levels in asynchronous MDA-MB-453 human breast cancer cells. *Exp. Cell Res.* 229 (1), 60–68. doi:10.1006/excr.1996.0343

Lee, D. Y., Lee, M. K., Kim, G. S., Noh, H. J., and Lee, M. H. (2013). Brazilin inhibits growth and induces apoptosis in human glioblastoma cells. *Molecules* 18 (2), 2449–2457. doi:10.3390/molecules18022449

Ludwig, H., Evstatiev, R., Kornek, G., Aapro, M., Bauernhofer, T., Buxhofer-Ausch, V., et al. (2015). Iron metabolism and iron supplementation in cancer patients. *Wien Klin. Wochenschr* 127 (23-24), 907–919. doi:10.1007/s00508-015-0842-3

Mangal, M., Sagar, P., Singh, H., Raghava, G. P. S., and Agarwal, S. M. (2013). NPACT: naturally occurring plant-based anti-cancer compound-activity-target database. *Nucleic Acids Res.* 41 (D1), D1124–D1129. doi:10.1093/nar/gks1047

Maskoen, A. M., Safitri, R., Milanda, T., Reniarti, L., and Fauziah, P. N. (2016). Iron chelation ability of granule sappan wood (Caesalpinia sappan, L.) extract on Iron-overloaded. *Int. J. PharmTech Res.* 9 (5), 299–305.

Merson, L., and Olivier, N. (2002). Orally active iron chelators. *Blood Rev.* 16 (2), 127–134. doi:10.1054/blre.2002.0009

Meyer, C. T., Wooten, D. J., Paudel, B. B., Bauer, J., Hardeman, K. N., Westover, D., et al. (2019). Quantifying drug combination synergy along potency and efficacy axes. *Cell Syst.* 8 (2), 97–108. doi:10.1016/j.cels.2019.01.003

Mitani, K., Takano, F., Kawabata, T., Allam, A. E., Ota, M., Takahashi, T., et al. (2013). Suppression of melanin synthesis by the phenolic constituents of sappanwood (Caesalpinia sappan). *Planta Medica* 79 (1), 37–44. doi:10.1055/s-0032-1327897

Mottaghipisheh, J., and Stuppner, H. (2021). A comprehensive review on chemotaxonomic and phytochemical aspects of homoisoflavonoids, as rare flavonoid derivatives. *Int. J. Mol. Sci.* 22 (5), 2735. doi:10.3390/ijms22052735

Mueller, M., Weinmann, D., Toegel, S., Holzer, W., Unger, F. M., and Viernstein, H. (2016). Compounds from Caesalpinia sappan with anti-inflammatory properties in macrophages and chondrocytes. *Food Funct.* 7 (3), 1671–1679. doi:10.1039/c5fo01256b

Muhammad, N., Usmani, D., Tarique, M., Naz, H., Ashraf, M., Raliya, R., et al. (2022). The role of natural products and their multitargeted approach to treat solid cancer. *Cells* 11 (14), 2209. doi:10.3390/cells11142209

Naeem, A., Hu, P., Yang, M., Zhang, J., Liu, Y., Zhu, W., et al. (2022). Natural products as anticancer agents: current status and future perspectives. *Molecules* 27 (23), 8367. doi:10.3390/molecules27238367

National Center for Biotechnology Information (2023). PubChem compound summary for CID 73384, brazilin. Available at: https://pubchem.ncbi.nlm.nih.gov/compound/Brazilin (Accessed June 7, 2023).

National Center for Biotechnology Information (2024a). *PubChem compound summary for CID 6453902, brazilein*. Available at: https://pubchem.ncbi.nlm.nih.gov/compound/Brazilein.

National Center for Biotechnology Information (2024b). *PubChem compound summary for CID 73384, brazilin*. Available at: https://pubchem.ncbi.nlm.nih.gov/compound/Brazilin.

Nava-Tapia, D. A., Cayetano-Salazar, L., Herrera-Zúñiga, L. D., Bello-Martínez, J., Mendoza-Catalán, M. A., and Brazilin, N.-T. N. (2022). Brazilin: biological activities and therapeutic potential in chronic degenerative diseases and cancer. *Pharmacol. Res.* 175, 106023. doi:10.1016/j.phrs.2021.106023

Newman, D. J., and Cragg, G. M. (2016). Natural products as sources of new drugs from 1981 to 2014. *J. Nat. Prod.* 79 (3), 629–661. doi:10.1021/acs.jnatprod.5b01055

Nguyen, V. B., Vu, B. D., Pham, G. K., Quang Le, B., Men, C. V., et al. (2020). Phenolic compounds from Caesalpinia sappan. *Pharmacogn. J.* 12 (2), 410–414. doi:10.5530/pj.2020.12.63

Nirmal, N. P., and Panichayupakaranant, P. (2015). Antioxidant, antibacterial, and anti-inflammatory activities of standardized brazilin-rich Caesalpinia sappan extract. *Pharm. Biol.* 53 (9), 1339–1343. doi:10.3109/13880209.2014.982295

Nitti, M., Ivaldo, C., Traverso, N., and Furfaro, A. L. (2021). Clinical significance of heme oxygenase 1 in tumor progression. *Antioxidants* 10 (5), 789. doi:10.3390/antiox10050789

Pawar, C. R., Landge, A. D., and Surana, S. J. (2008). Phytochemical and pharmacological aspects of Caesalpinia sappan. *Journal of Pharmacy Research* 1(2), 131–138.

Pfeifhofer-Obermair, C., Tymoszuk, P., Petzer, V., Weiss, G., and Nairz, M. (2018). Iron in the tumor microenvironment-connecting the dots. *Front. Oncol.* 8 (NOV), 549. doi:10.3389/fonc.2018.00549

Piga, A., Galanello, R., Forni, G. L., Cappellini, M. D., Origa, R., Zappu, A., et al. (2006). Randomized phase II trial of deferasirox (Exjade●, ICL670), a once-daily, orally-administered iron chelator, in comparison to deferoxamine in thalassemia patients with transfusional iron overload. *Haematologica* 91 (7), 873–880.

Porter, J. B. (2001). Practical management of iron overload. *Br. J. Haematol.* 115 (2), 239–252. doi:10.1046/j.1365-2141.2001.03195.x

Richardson, D. R., and Baker, E. (1994). Two saturable mechanisms of iron uptake from transferrin in human melanoma cells: the effect of transferrin concentration, chelators, and metabolic probes on transferrin and iron uptake. *J. Cell Physiol.* 161 (1), 160–168. doi:10.1002/jcp.1041610119

Rombos, Y., Tzanetea, R., Konstantopoulos, K., Simitzis, S., Zervas, C., Kyriaki, P., et al. (2000). Chelation therapy in patients with thalassemia using the orally active iron chelator deferiprone (L1). *Haematologica* 85 (2), 115–117.

Rondão, R., Seixas De Melo, J. S., Pina, J., Melo, M. J., Vitorino, T., and Parola, A. J. (2013). Brazilwood reds: the (photo)chemistry of brazilin and brazilein. *J. Phys. Chem. A* 117 (41), 10650–10660. doi:10.1021/jp404789f

Rychtarcikova, Z., Lettlova, S., Tomkova, V., Korenkova, V., Langerova, L., Simonova, E., et al. (2017). Tumor-initiating cells of breast and prostate origin show alterations in the expression of genes related to iron metabolism. *Oncotarget* 8 (4), 6376–6398. doi:10.18632/oncotarget.14093

Safitri, R., Chaidir, L., Kuntana, Y. P., Syamsunarno, M. R. A. A., Yuliana, T., Utama, G. L., et al. (2022). Antituberculosis activity and iron chelation ability of brazilin isolated from Caesalpinia sappan L. *Int. J. Adv. Sci. Eng. Inf. Technol.* 12 (4), 1707–1713. doi:10.18517/IJASEIT.12.4.16210

Safitri, R., Ratningsih, N., Maskoen, A. M., Fauziah, P. N., and Panigoro, R. (2016). The effects of Caesalpinia sappan L. Extract granule to antioxidant activity in blood serum of wistar rat (rattus norvegicus) with excessive iron condition. *Int. J. PharmTech Res.* 9 (11), 497–512. doi:10.18502/kls.v3i6.1159

Sasaki, Y., Hosokawa, T., Nagai, M., and Nagumo, S. (2007). *In vitro* study for inhibition of NO production about constituents of Sappan lignum. *Biol. Pharm. Bull.* 30 (1), 193–196. doi:10.1248/bpb.30.193

Sharifi-Rad, J., Quispe, C., Patra, J. K., Singh, Y. D., Panda, M. K., Das, G., et al. (2021). Paclitaxel: application in modern oncology and nanomedicine-based cancer therapy. *Oxid. Med. Cell Longev.* 2021, 3687700. doi:10.1155/2021/3687700

Sung, H., Ferlay, J., Siegel, R. L., Laversanne, M., Soerjomataram, I., Jemal, A., et al. (2021). Global cancer statistics 2020: GLOBOCAN estimates of incidence and mortality worldwide for 36 cancers in 185 countries. *CA Cancer J. Clin.* 71 (3), 209–249. doi:10.3322/caac.21660

Suyatmi, S., Mudigdo, A., Purwanto, B., Indarto, D., Hakim, F. A., and Krisnawati, D. I. (2022). Brazilin isolated from caesalpina sappan wood induces intrinsic apoptosis on A549 cancer cell line by increasing p53, caspase-9, and caspase-3. *Asian Pac. J. Cancer Prev.* 23 (4), 1337–1343. doi:10.31557/APJCP.2022.23.4.1337

Theil, E. C., and Goss, D. J. (2009). Living with iron (and oxygen): questions and answers about iron homeostasis. *Chem. Rev.* 109 (10), 4568–4579. doi:10.1021/cr900052g

Toegel, S., Wu, S. Q., Otero, M., Goldring, M. B., Leelapornpisid, P., Chiari, C., et al. (2012). Caesalpinia sappan extract inhibits IL1β-mediated overexpression of matrix metalloproteinases in human chondrocytes. *Genes Nutr.* 7 (2), 307–318. doi:10.1007/s12263-011-0244-8

Trinder, D., Zak, O., and Aisen, P. (1996). Transferrin receptor-independent uptake of differic transferrin by human hepatoma cells with antisense inhibition of receptor expression. *Hepatology* 23 (6), 1512–1520. doi:10.1053/jhep.1996.v23.pm0008675172

Utomo, R. Y., Novarina, A., Tirtanirmala, P., Kastian, R. F., and Jenie, R. I. (2018). Enhancement of cytotoxicity and apoptosis induction of doxorubicin by brazilein containing fraction of secang (Caesalpinia sappan L.) on T47D cells. *Indones. J. Cancer Chemoprevention* 9 (1), 32–383. doi:10.14499/indonesianjcanchemoprev9iss1pp32-40

Valentovic, M. (2008). "Deferasirox," in *Bylund DBBT xPharm: TCPR*. Editor S. J. Enna (Amsterdam, Netherlands: Elsevier), 1–4. doi:10.1016/B978-008055232-3.64057-7

Wang, L., Li, X., Mu, Y., Lu, C., Tang, S., Lu, K., et al. (2019a). The iron chelator desferrioxamine synergizes with chemotherapy for cancer treatment. *J. Trace Elem. Med. Biol.* 56, 131–138. doi:10.1016/j.jtemb.2019.07.008

Wang, Y., Yu, L., Ding, J., and Chen, Y. (2019b). Iron metabolism in cancer. *Int. J. Mol. Sci.* 20 (1), 95. doi:10.3390/ijms20010095

Webb, A. H., Gao, B. T., Goldsmith, Z. K., Irvine, A. S., Saleh, N., Lee, R. P., et al. (2017). Inhibition of MMP-2 and MMP-9 decreases cellular migration, and angiogenesis in *in vitro* models of retinoblastoma. *BMC Cancer* 17 (1), 434. doi:10.1186/s12885-017-3418-y

Weinmann, D., Mueller, M., Walzer, S. M., Hobusch, G. M., Lass, R., Gahleitner, C., et al. (2018). Brazilin blocks catabolic processes in human osteoarthritic chondrocytes via inhibition of NFKB1/p50. *J. Orthop. Res.* 36 (9), 2431–2438. doi:10.1002/jor.24013

Xu, H. X., and Lee, S. F. (2004). The antibacterial principle of Caesalpina sappan. *Phyther Res.* 18 (8), 647–651. doi:10.1002/ptr.1524

Yan, S., Lin, S., Chen, K., Yin, S., Peng, H., Cai, N., et al. (2022). Natural product library screens identify sanguinarine chloride as a potent inhibitor of telomerase expression and activity. *Cells* 11 (9), 1485. doi:10.3390/cells11091485

Yang, X., Liang, Y., Zhao, L., Chen, L., Yang, Y., Wang, J., et al. (2023). Brazilin inhibits the invasion and metastasis of breast cancer. *Biol. Pharm. Bull.* 46 (6), 773–780. doi:10.1248/bpb.b22-00637

You, E. J., Khil, L. Y., Kwak, W. J., Won, H. S., Chae, S. H., Lee, B. H., et al. (2005). Effects of brazilin on the production of fructose-2,6-bisphosphate in rat hepatocytes. *J. Ethnopharmacol.* 102 (1), 53–57. doi:10.1016/j.jep.2005.05.020

Zhang, Q., Liu, J. L., Qi, X. M., Qi, C. T., and Yu, Q. (2014). Inhibitory activities of Lignum Sappan extractives on growth and growth-related signaling of tumor cells. *Chin. J. Nat. Med.* 12 (8), 607–612. doi:10.1016/S1875-5364(14)60092-3

Zhang, T., Fan, X., Song, L., Ren, L., Ma, E., Zhang, S., et al. (2015). c-Fos is involved in inhibition of human bladder carcinoma T24 cells by brazilin. *IUBMB Life* 67 (3), 175–181. doi:10.1002/iub.1357

Zhang, T., He, J., Zhang, S., Wang, G., Ma, E., Wang, J., et al. (2018). Brazilin induces T24 cell death through c-Fos and GADD45β independently regulated genes and pathways. *IUBMB Life* 70 (11), 1101–1110. doi:10.1002/iub.1921

Zhou, T., Ma, Y., Kong, X., and Hider, R. C. (2012). Design of iron chelators with therapeutic application. *Dalt Trans.* 41 (21), 6371–6389. doi:10.1039/c2dt12159j

frontiers | Frontiers in Pharmacology

TYPE Original Research
PUBLISHED 03 April 2024
DOI 10.3389/fphar.2024.1382787

Check for updates

OPEN ACCESS

EDITED BY
Wagdy Mohamed Eldehna,
Kafrelsheikh University, Egypt

REVIEWED BY
Shaza Hussiny Aly,
Badr University in Cairo, Egypt
Zhixing Wu,
University of Florida, United States

*CORRESPONDENCE
Yohan Seo,
ddukdae12@gmail.com
Joohan Woo,
gabriel929@dongguk.ac.kr

RECEIVED 06 February 2024
ACCEPTED 20 March 2024
PUBLISHED 03 April 2024

CITATION
Seo Y, Lee S, Kim M, Kim D, Jeong SB, Das R, Sultana A, Park S, Nhiem NX, Huong PTT, Kwon O-B, Namkung W and Woo J (2024), Discovery of a novel natural compound, vitekwangin B, with ANO1 protein reduction properties and anticancer potential. *Front. Pharmacol.* 15:1382787. doi: 10.3389/fphar.2024.1382787

COPYRIGHT
© 2024 Seo, Lee, Kim, Kim, Jeong, Das, Sultana, Park, Nhiem, Huong, Kwon, Namkung and Woo. This is an open-access article distributed under the terms of the Creative Commons Attribution License (CC BY). The use, distribution or reproduction in other forums is permitted, provided the original author(s) and the copyright owner(s) are credited and that the original publication in this journal is cited, in accordance with accepted academic practice. No use, distribution or reproduction is permitted which does not comply with these terms.

Discovery of a novel natural compound, vitekwangin B, with ANO1 protein reduction properties and anticancer potential

Yohan Seo[1]*, Sion Lee[1], Minuk Kim[2], Dongguk Kim[2], Sung Baek Jeong[1], Raju Das[3], Armin Sultana[3], SeonJu Park[4], Nguyen Xuan Nhiem[5], Phan Thi Thanh Huong[5], Oh-Bin Kwon[1], Wan Namkung[6] and Joohan Woo[3,7]*

[1]New Drug Development Center, Daegu Gyeongbuk Medical Innovation Foundation (KMEDIhub), Daegu, Republic of Korea, [2]Department of Medical Device Development Center, Daegu-Gyeongbuk Medical Innovation Foundation (KMEDI Hub), Daegu, Republic of Korea, [3]Department of Physiology, Dongguk University College of Medicine, Gyeongju, Republic of Korea, [4]Metropolitan Seoul Center, Korea Basic Science Institute (KBSI), Seoul, Republic of Korea, [5]Institute of Marine and Biochemistry, Vietnam Academy of Science and Technology (VAST), Hanoi, Vietnam, [6]College of Pharmacy, Yonsei Institute of Pharmaceutical Science, Yonsei University, Incheon, Republic of Korea, [7]Channelopathy Research Center (CRC), Dongguk University College of Medicine, Goyang, Gyeonggi-do, Republic of Korea

Background: Prostate cancer and non-small cell lung cancer (NSCLC) present significant challenges in the development of effective therapeutic strategies. Hormone therapies for prostate cancer target androgen receptors and prostate-specific antigen markers. However, treatment options for prostatic small-cell neuroendocrine carcinoma are limited. NSCLC, on the other hand, is primarily treated with epidermal growth factor receptor (EGFR) tyrosine kinase inhibitors but exhibits resistance. This study explored a novel therapeutic approach by investigating the potential anticancer properties of vitekwangin B, a natural compound derived from *Vitex trifolia*.

Methods: Vitekwangin B was chromatographically isolated from the fruits of *V. trifolia*. ANO1 protein levels in prostate cancer and NSCLC cells were verified and evaluated again after vitekwangin B treatment.

Results: Vitekwangin B did not inhibit anoctamin1 (ANO1) channel function but significantly reduced ANO1 protein levels. These results demonstrate that vitekwangin B effectively inhibited cancer cell viability and induced apoptosis in prostate cancer and NSCLC cells. Moreover, it exhibited minimal toxicity to liver cells and did not affect hERG channel activity, making it a promising candidate for further development as an anticancer drug.

Conclusion: Vitekwangin B may offer a new direction for cancer therapy by targeting ANO1 protein, potentially improving treatment outcomes in patients with prostate cancer and NSCLC. Further research is needed to explore its full potential and overcome existing drug resistance challenges.

KEYWORDS

anoctamin 1, vitekwangin B, prostate cancer, lung cancer, protein reduction, apoptosis

1 Introduction

Prostate cancer is characterized by the overexpression of androgen receptors and prostate-specific antigen markers (Tan et al., 2015), which significantly influences its pathogenesis. Hence, hormone therapies for prostate cancer primarily target these markers (Tan et al., 2015; Dai et al., 2017). However, patients with prostatic small cell neuroendocrine carcinoma encounter treatment limitations, particularly with hormone therapy, because this type of cancer does not express androgen receptors or prostate-specific antigen markers (Shafi et al., 2013; Tan et al., 2015; Dai et al., 2017).

Non-small cell lung cancer (NSCLC) is a major subtype of lung cancer, constituting approximately 85% of all lung cancer cases (Imyanitov et al., 2021). Despite considerable progress in NSCLC diagnosis and therapy, the five-year survival rate remains low (Hirsch et al., 2017). The growth and survival of NSCLC cells rely on epidermal growth factor receptor (EGFR) signaling (Wu and Shih, 2018). EGFR tyrosine kinase inhibitors, including gefitinib, have been adopted as the first-line treatment for NSCLC (Westover et al., 2018). Unfortunately, nearly one-third of patients exhibit resistance initially, and those who are responsive may eventually develop resistance (Westover et al., 2018; Wu and Shih, 2018; Kohsaka et al., 2019). Therefore, there is an urgent need to identify novel therapeutic targets and develop innovative agents for treating prostate cancer and NSCLC.

Anoctamin 1 (ANO1), also known as transmembrane protein 16A, is a calcium-activated chloride channel that is upregulated in various cancer cells and contributes to cancer progression (Bill and Gaither, 2017). Numerous *in vitro* and *in vivo* studies have shown that pharmacological downregulation of ANO1 significantly inhibits cancer cell proliferation, growth, and migration (Zhong et al., 2021). Notably, our previous studies revealed high ANO1 expression in PC3 and PC9 NSCLC cells (Seo et al., 2017; 2021). Moreover, the pharmacological inhibition of ANO1 using diethylstilbestrol, luteolin, and other inhibitors affects both its channel function and protein levels and thus suppresses cancer cell proliferation and migration (Seo et al., 2017; 2021). Notably, some ANO1 functional inhibitors impede ANO1-mediated chloride secretion, thereby inducing side effects such as hypotension, constipation, and dry mouth syndrome (Namkung et al., 2011; Jang and Oh, 2014; Wang et al., 2021). These findings imply that reducing ANO1 protein levels without rapidly impairing ANO1 channel function could be advantageous for cancer treatment. To address this, we used high-throughput screening to identify vitekwangin B, a natural product that gradually decreases ANO1 protein levels.

Vitex trifolia, a small wild shrub that is extensively distributed in the northern mountains of Vietnam, has traditionally been employed in the treatment of various ailments, including liver disorders, tumors, rheumatic pain, inflammation, and sprains (Li et al., 2005; Shukri and Hasan, 2021). This plant is renowned for its multifaceted medicinal properties, including larvicidal, wound-healing, anti-HIV, anticancer, trypanocidal, antimicrobial, and antipyretic effects (Kiuchi et al., 2004; Li et al., 2005; Shukri and Hasan, 2021). Among the phytochemicals present in this plant, flavonoids, such as casticin (vitexicarpin), persicogenin, and penduletin, induce apoptosis in cancer cell lines by inhibiting the G2/M phase of the cell cycle (Li et al., 2005).

Vitekwangin B, a lignan previously isolated from *V. kwangsiensia* and *V. negundo* (Shen et al., 2019; Kamal et al., 2022), has been reported to have minimal inhibitory effects on nitric oxide production (Shen et al., 2019; Kamal et al., 2022). However, its potential anticancer effects via the regulation of other molecular targets, including ion channels, remain unknown. Therefore, we isolated vitekwangin B from *V. trifolia* fruit for the first time and investigated the potential pharmacological effects of vitekwangin B extracted from *V. trifolia*, with a primary focus on the inhibition of ANO1 and its physiological impact on prostate and NSCLC cancer cells. Through a comprehensive investigation, we aimed to determine the anticancer properties of vitekwangin B.

2 Materials and methods

2.1 Plant material

The fruits of *V. trifolia* L. were collected from the Xuan Thuy National Garden, Namdinh, Vietnam, in October 2021. Taxonomic identification was conducted by Dr. Nguyen The Cuong from the Institute of Ecology and Biological Resources, Vietnam Academy of Science and Technology (VAST). A voucher specimen (No. NCCT-P133) was submitted to the Institute of Chemistry at VAST.

2.2 Extraction and isolation

Dried *V. trifolia* L. fruit powder (5 kg) was subjected to methanol-based sonication (three times, each with 15 L MeOH). After solvent evaporation, the resulting methanol extract (150 g) was reconstituted in water and subsequently partitioned with *n*-hexane (H), CH_2Cl_2 (D), and EtOAc (E) to yield the H (30 g), D (7 g), and E (5 g) fractions, and an aqueous layer.

Fraction D was initially subjected to silica gel column chromatography using a stepwise hexane/acetone gradient, yielding seven sub-fractions (D1–D7). Subsequently, Fraction D2 was chromatographed on a YMC RP-18 column using a 1:1 v/v mixture of MeOH and water, leading to the isolation of D2I (0.8 g). D2I was further subjected to silica gel column chromatography using a hexane and acetone (10:1 v/v) mixture to yield D2I1 (0.1 g). Finally, prep-HPLC employing a J'sphere ODS H-80 column (250 mm × 20 mm) was performed with a mobile phase of 25% aqueous acetonitrile at a flow rate of 3 mL/min to isolate vitekwangin B (15 mg).

2.3 Cell culture

PC9 cells stably expressing ANO1 and yellow fluorescent protein (YFP) were established as previously described (Jeong et al., 2022). Additionally, PC9 (an NSCLC cell line), PC3 (a human prostate cancer cell line), and HT29 (a human colon cancer cell line) cells were cultured in RPMI 1640. CHO cells were maintained in Dulbecco's modified Eagle's medium. All

culture media were supplemented with 10% fetal bovine serum, 2 mM L-glutamine, 100 U/mL penicillin, and 100 μg/mL streptomycin.

2.4 Construction of ANO1-knockout (KO) cells

PLentiCRISPRv2 vector containing Cas9 and CRISPR guide RNA targeting ANO1 (CCTGATGCCGAGTGCAAGTA; clone ID: X35909) was procured from GenScript (Piscataway, NJ, United States). A co-transfection of 1,500 ng CRISPR plasmid, 1,200 ng packaging plasmid (psPAX2), and 400 ng envelope plasmid (pMD2.G) was performed in HEK293T cells cultured in 6-well plates. After 48 h, the supernatant, which contained lentiviral particles, was filtered using a 0.45-μm syringe filter. Subsequently, the cells were treated with lentiviral particles mixed with fresh medium in a 1:1 ratio in 24-well plates. ANO1-KO cells were selected using puromycin (Sigma-Aldrich, St. Louis, MO, United States) 72 h after viral transduction.

2.5 Yellow fluorescent protein fluorescence quenching analysis

PC9 cells stably expressing the YFP variant (YFP-H148Q/I152L/F46L) and endogenous ANO1 were seeded into 96-well plates at a density of 5×10^3 cells/well. After 48 h of incubation, the cells were washed twice with phosphate-buffered saline and incubated for 10 min with the test compounds dissolved in phosphate-buffered saline. YFP fluorescence was measured every 0.4 s for 5 s using the FLUOstar® Omega microplate reader (BMG Labtech, Ortenberg, Germany). ANO1-mediated iodide influx was measured 1 s after injecting 100 μL of 70 mM iodide solution with 100 μM adenosine triphosphate (ATP) into each well. The inhibitory effects of the test compounds on ANO1 activity were assessed based on the initial iodide influx rate, which was calculated from the initial slope of the decrease in fluorescence following ATP injection.

2.6 Measurement of intracellular calcium levels

PC9 cells were cultured in black-walled 96-well microplates and loaded with Fluo-4 NW (Invitrogen, Carlsbad, CA, United States) according to the manufacturer's protocol. After 1 h of incubation, the plates were transferred to a FLUOstar® Omega microplate reader with custom Fluo-4 excitation/emission filters (485/538 nm) and Fluo-4 fluorescence was assessed.

2.7 Western blot analysis

Protein samples (20–60 μg) were separated using 4%–12% Tris-Glycine-PAG Pre-Cast Gel (Koma Biotech, South Korea) and transferred onto polyvinylidene fluoride membranes. Blocking was performed for 1 h using 5% bovine serum albumin in Tris-buffered saline containing 0.1% Tween 20. The membranes were incubated with primary antibodies, including anti-ANO1 (Abcam, United Kingdom) and anti-β-actin (Santa Cruz Biotechnology, Dallas, TX, United States), followed by horseradish peroxidase-conjugated anti-secondary IgG antibodies (Enzo Life Sciences, Inc., Farmingdale, NY, United States) for 1 h. Visualization was performed using the ECL Plus Western Blotting System (GE Healthcare, Chicago, IL, United States).

2.8 Cell viability assay

Cell viability assay was performed using the Cell Counting Kit CCK -8 (Dojindo, Rockville, MD, United States) and MTS cell viability assay was performed using CellTiter 96® Aqueous One Solution Cell Proliferation Assay Kit (Promega, Madison, WI, United States). PC3, PC9, and HT29 cells were cultured in 96-well plates for 24 h. Once the cells reached approximately 20% confluence, vitekwangin B (0.03–300 μM) or vehicle (dimethyl sulfoxide) were added to the medium. After 48 h of treatment, the medium was completely removed, and CCK-8 or MTS assay was performed according to the manufacturer's instructions. The absorbance of formazan was measured at a wavelength of 490 or 450 nm using a microplate reader (Synergy™ Neo, BioTek, Winooski, VT, United States).

2.9 Molecular docking analysis

Molecular docking predicts the preferred orientation of one molecule relative to another when bound to form a stable complex (Meng et al., 2011). The Glide XP docking module was employed in this study to provide structural details of the protein–ligand complex. Ligand preparation, protein preparation, active site determination, and grid generation were sequentially performed using Schrödinger Suite 2017-1 software (Adebesin et al., 2022). The ligands selected for analysis were obtained in an SDF file format from the PubChem database (Adebesin et al., 2022) and processed with the LigPrep module to ensure accurate 3D conformation at a low state and proper chiral position, maintaining pH 7.0 ± 2.0. The protein of interest was retrieved from the Protein Data Bank and subjected to a protein preparation wizard that optimized the bond angles, bond orders, and topology to generate the best possible structure. Irrelevant water was removed from the active site at 5 Å, and the root-mean-square deviation for heavy atoms was fixed at 0.30 Å. A cubic box was built around the reference ligand during grid generation to define the active sites. The van der Waals scaling factor and charge cutoff were set to 1.00 and 0.25, respectively. The entire process was followed by the all-atom OPLS3 force field (Das et al., 2023).

Glide offers three tiers of scoring functions: Glide-HTVS, Glide-SP (Standard Precision), and Glide-XP (Extra Precision). These scoring functions employ the Emodel scoring function, which primarily consists of the Glide-score and the protein–ligand coulomb–vdW energy. We chose Glide-XP docking for maximum accuracy, in which ligand sampling was performed in a flexible manner. The scaling factor and partial charge for nonpolar parts of the ligand were set at 0.80 and 0.15,

respectively. After final docking, the complex with the best binding position was selected for further analysis.

2.10 Prime molecular mechanics with generalised born and surface area solvation (MM-GBSA)

MM-GBSA analysis of the prime module was performed on the complexes formed by the docking simulation. Using the OPLS3 molecular mechanics force field, MM-GBSA (Rastelli et al., 2010) calculates the relative binding energy by combining the molecular mechanics energies (EMM), an SGB solvation model for polar solvation (GSGB), and a nonpolar solvation term (GNP) composed of a non-polar solvent-accessible surface area and van der Waals interactions.

The total free energy of binding:

$$\Delta Gbind = Gcomplex - (Gprotein + Gligand)$$

where G = EMM + GSGB + GNP

2.11 Caspase-3/CPP32 colorimetric assay

Caspase-3/CPP32 colorimetric assay was performed according to the manufacturer's instructions (#K106; Biovison, Milpitas, CA, United States). PC3 and PC9 cells were cultured in 6-well plates until they reached 70% confluence, and the test compound or Ani9 (an ANO1 inhibitor) was then added in the wells. After incubation for 24 h, 5×10^6 cells were lysed in cell lysis buffer for 10 min at 4°C. The cells were centrifuged for 10 min, and the supernatants were collected. Thereafter, 100 µg protein or 50 µL buffer was added to each well with 2× reaction buffer containing 10 mM DTT. To measure caspase-3 activity, 5 µL DEVD-pNA substrate was added and incubated for 1 h at 37°C. The optical density was measured at the wavelength of 400 nm using a microplate reader (Synergy™ Neo).

2.12 Human cleaved PARP-1 activity assay

The human cleaved PARP-1 activity assay was performed according to the manufacturer's instructions (#ab174441; Abcam). PC3 and PC9 cells were cultured in 6-well plates until they reached 80% confluence. The test compounds were then added and incubated with the cells for 24 h. Subsequently, 5×10^7 cells were lysed in cell extraction buffer for 20 min. Supernatants were collected after the cells were centrifuged (13,000 RPM) for 20 min at 4°C. Next, 100 µg protein or 50 µL buffer was added to an antibody cocktail containing capture and detector antibodies in each well and incubated for 1 h. The wells were washed twice with 1× wash buffer. TMB development solution was added and the contents of the wells were incubated for 10 min. Finally, the stop solution was added and the optical density was measured at the wavelength of 450 nm using a microplate reader (Synergy™ Neo).

2.13 Cell cycle analysis

PC9 cells were seeded at 2×10^5 cells/well in 100-phi culture plates and treated with the test compound for 24 h. Cells were fixed with cold 70% ethanol and incubated for 2 h at −20°C. The ethanol was removed, and the cells were re-suspended in propidium iodide, Triton X-100, or DNAse-free RNAse A staining solution for 30 min. The cell cycle distribution was analyzed using Gallios (Beckman Coulter, Brea, CA, United States). Approximately 2×10^3 cells per group were analyzed.

2.14 hERG inhibition assay by patch-clamping electrophysiology

To assess the cardiotoxic effects of the tested hERG channel-dependent chemical compounds, we measured the rate of hERG channel inhibition in an hERG-overexpressing HEK cell line (Eurofins Scientific, Luxembourg) using the PatchLiner automated patch-clamping system (Nanion, Germany).

The cells were incubated at 37°C under 5% CO_2. Subsequently, the cells were detached from the cell culture plates using trypsin (SH30042.02; HyClone, Logan, UT, United States) and centrifuged at 200 × g. After washing with external standard buffer solution (08 3001; Nanion), the cells were resuspended in 5 mL of fresh external standard buffer solution. The resulting cell suspension was loaded into a PatchLiner system. The cells were then automatically dispensed into the wells of an NPC-16 chip (071102; Nanion) and one cell per well was sealed in a microhole at the bottom. Once a GΩ seal was formed, light and short suction pulses were applied to break through the membrane and establish whole-cell mode to electrically connect the cell with the Internal KF110 buffer solution (08 3007; Nanion).

To generate voltage stimulation specific to the hERG channel, the membrane potential of the cells was initially maintained at −80 mV, sequentially followed by −40 mV (0.5 s), +40 mV (0.5 s), −40 mV (0.5 s), and −80 mV (0.2 s) to generate hERG tail currents. The peak hERG tail current recorded from each well represented the baseline level of hERG channel activity. To investigate the changes in the hERG activity caused by the tested chemical compounds, the relevant chemical stock solutions were diluted with an external standard buffer solution to achieve the desired concentrations, which were automatically added to the wells of the NPC-16 chip. The hERG channel activity was then measured under the same voltage conditions. Finally, the relative changes in hERG activity induced by the tested chemical compounds were calculated and expressed as percentages using the following formula:

$$\%hERG\,activity = (peak\,hERG\,tail\,current\,after\,compound\,treatment / peak\,hERG\,tail\,current\,before\,compound\,treatment) \times 100$$

2.15 Resazurin reduction assay for evaluating hepatocellular viability

Hepatocellular viability was assessed using a resazurin reduction assay. HepG2 hepatocellular carcinoma cells (10,000 cells) were

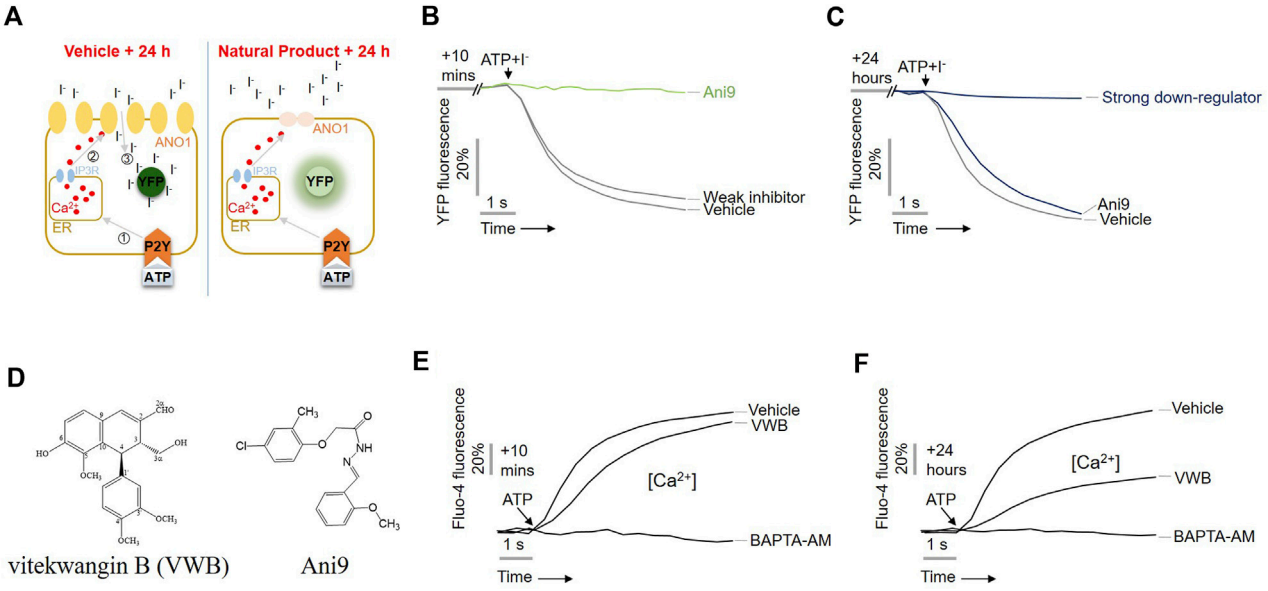

FIGURE 1
Identification of vitekwangin B using yellow fluorescent protein (YFP)-based high-throughput screening. **(A)** Schematic representation of the cell-based YFP-reduction assay. Activation of ATP-induced P2Y receptor increases calcium release from the endoplasmic reticulum, thereby activating ANO1 channel, resulting in an influx of iodide that quenches YFP. **(B,C)** YFP fluorescence levels corresponding to the inhibitory effect of the compounds Ani9 and vitekwangin B in cells treated for 10 min or 24 h. **(D)** Chemical structure of vitekwangin B and Ani9. **(E,F)** Intracellular Ca^{2+} levels were measured using Fluo-4 NW in CHO-K1 cells treated with 1 μM vitekwangin B for 20 min or 24 h and then with 100 μM ATP (mean ± SD, n = 5). ER, endoplasmic reticulum; VWB, vitekwangin B. ***$p < 0.001$, Student's unpaired t-test.

seeded in each well of a black and clear-bottom 96-well plate, with Dulbecco's modified Eagle's medium High glucose media supplemented with 10% (v/v) fetal bovine serum and 100 μg/mL penicillin–streptomycin. The cells were then incubated in a 5% CO_2-supplied 37°C incubator for 15–20 h.

The following day, cells were treated with the tested compounds at four different concentrations (0, 0.05, 0.5, 5, and 50 μM) using Dulbecco's modified Eagle's medium High glucose media supplemented with 1% (v/v) fetal bovine serum and 100 μg/mL penicillin–streptomycin. For the maximum and minimum cell viability control experiments, 0.5% (v/v) dimethyl sulfoxide solvent and 0.01% (v/v) Triton X-100 were used, respectively.

After incubation for 20 h, each well was treated with 20% (v/v) resazurin reagent (#G8080; Promega) and further incubated for 2 h. Colorimetric analysis of resorufin levels in each well was performed by detecting the fluorescence intensity at the wavelength of 590 nm. Each data point was normalized using the maximum/minimum cell viability data and presented as "%Relative viability" using the following formula:

$$\%Relative\ viability = (experimental\ datum - minimal\ viability\ datum) / (maximal\ viability\ datum - minimal\ viability\ datum) \times 100$$

2.16 Statistical analysis

All experiments were conducted independently at least three times. The results for the multiple trials are presented as mean ± standard error. Statistical analyses were performed using the Student's t-test or analysis of variance, as appropriate. Statistical significance was set at $p < 0.05$. Prism software (GraphPad) was used to plot dose–response curves and calculate IC_{50} values.

3 Results

3.1 Identification of vitekwangin B from *Vitex trifolia* fruits

In previous studies, we conducted phytochemical investigations of the *Vitex* genus, including *V. limonifolia* and *V. trifolia*. These investigations led to the isolation of various compounds, including diterpenoids, flavonoids, triterpenes, and ecdysteroids (Thoa et al., 2017; Ban et al., 2018). In this study, we isolated a lignan named vitekwangin B: 4-(3,4-dimethoxyphenyl)-6-hydroxy-3-(hydroxymethyl)-5-methoxy-3,4-dihydronaphthalene-2-carbaldehyde. We also extensively determined its chemical structure using HR-ESI-MS and NMR spectra and compared the NMR data with those reported in the literature (Supplementary Table S1A; Supplementary Figures S1–S4, Shen et al., 2019).

3.2 Cell-based high-throughput screening for the identification of a novel natural compound that downregulates ANO1 channel

The downregulation of ANO1 by the substances extracted from *V. negundo* was previously evaluated using a modified cell-based

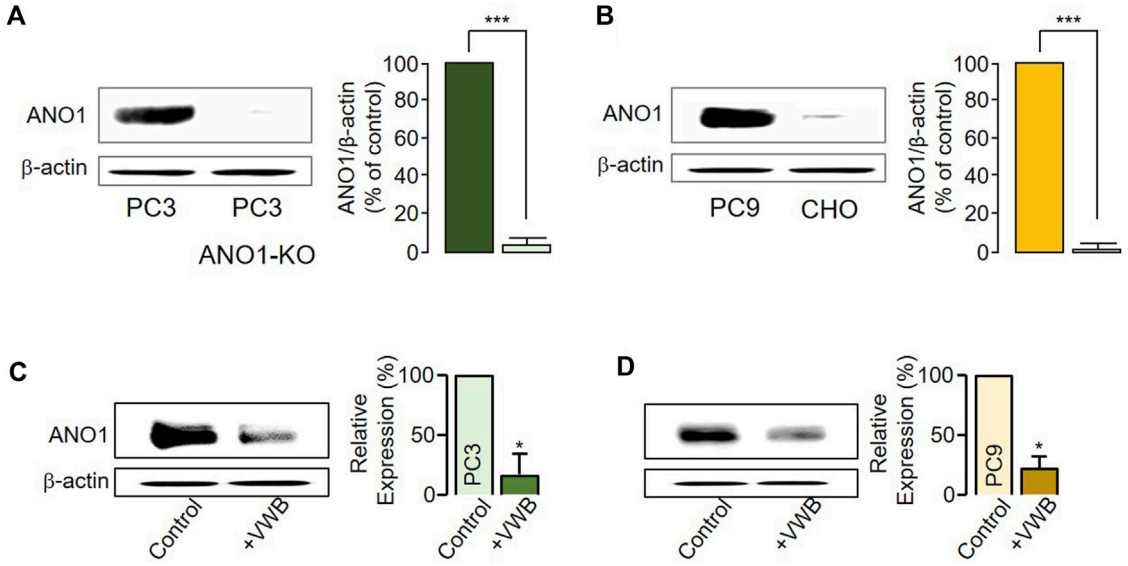

FIGURE 2
Changes in ANO1 protein expression induced by vitekwangin B. **(A)** ANO1 expression levels in PC3 and PC3 ANO1-KO cells. ANO1 protein intensities were normalized by β-actin (mean ± S.D., $n = 5$). **(B)** ANO1 expression levels in PC9 and CHO cells. ANO1 protein intensities were normalized by β-actin (mean ± S.D., $n = 5$). **(C,D)** ANO1 protein expression levels in PC3 and PC9 cells treated with 1 μM vitekwangin B. ANO1 protein intensities were normalized by β-actin (mean ± SD, $n = 5$). VWB, vitekwangin B. *$p < 0.05$, ***$p < 0.001$, Student's unpaired t-test.

high-throughput screening system (Jeong et al., 2022). As shown in Figure 1, upon treatment of cells with ATP, intracellular calcium levels increased, leading to the flow of iodine into the cell through the ANO1 channel, which also acts as an iodide channel (Twyffels et al., 2014). Intracellular iodine binds to mutant YFP and strongly reduces its fluorescence. However, when an ANO1 inhibitor inhibited the ANO1 channel and blocked the iodine influx, no decrease in YFP fluorescence was observed (Figure 1A). To screen the substances isolated from *V. negundo*, that exhibit ANO1-downregulating effects, PC9-YFP cells were treated with *V. negundo* compounds for 10 min or 24 h.

Treatment with Ani9 for 10 min inhibited YFP reduction via ANO activation (Figure 1B), whereas treatment for 24 h does not; however, treatment with vitekwangin B for 24 h strongly inhibited YFP reduction via ANO1 activation (Figure 1C). The chemical structure of vitekwangin B is shown in Figure 1D. Since ANO1 is also activated by low calcium levels (Yang et al., 2008), we checked whether vitekwangin B inhibited intracellular calcium levels. PC9 cells were treated with 1 μM vitekwangin B for 10 min or 24 h to determine the effect of vitekwangin B on ATP-mediated increase in intracellular calcium signaling. Vitekwangin B treatment for 10 min did not inhibit the ATP-mediated increase in cytosolic calcium, but vitekwangin B treatment for 24 h inhibited ATP-induced increase in cytosolic calcium significantly (Figures 1E, F).

3.3 Effect of vitekwangin B on ANO1 protein levels and prediction of binding sites

Previous studies have reported that a decrease in ANO1 protein levels can lead to decreased cancer cell viability (Seo et al., 2017; 2021; Park et al., 2023). To establish whether vitekwangin B decreased ANO1 protein levels, PC3 ANO1-KO cells were generated using the CRISPR-Cas9 system, and ANO1 protein levels in PC9 and CHO cells were verified (Figures 2A, B). After cancer cells were treated with 1 μM vitekwangin B, ANO1 protein levels were significantly decreased in PC3 and PC9 cells (Figures 2C, D).

To verify whether vitekwangin B and Ani9 interact with the calcium-binding sites on ANO1, a cryogenic structure (5OYB) was used to perform molecular docking (Figures 3A, B). Ligand binding to ANO1 is not fully understood, but this study considered potential calcium-binding residues as ligand-binding sites based on previous mutagenesis studies. Vitekwangin B achieved a highly negative docking score of −5.091 kcal/mol, surpassing the score of Ani9 (−4.083 kcal/mol). The docking analysis and MM-GBSA scores are provided in Supplementary Table S1B. The stability of a protein–ligand complex is primarily attributed to intermolecular interactions, including hydrogen bonds, van der Waals forces, and carbon–hydrogen bonds. In this context, non-bonded interactions of protein–ligand complex were assessed, focusing on the XP docking position. Figure 3C illustrates the involvement of vitekwangin B in hydrogen and hydrophobic interactions. Specifically, vitekwangin B formed hydrogen bonds with residues Lys 661 and Gly 698 and hydrophobic interactions with residues Lys 741, Ile 657, and Leu 746. Furthermore, a pi-cation interaction was observed between vitekwangin B and the amino acid residue Lys 741. Figure 3D shows the interaction between Ani9 and ANO1, indicating hydrophobic interactions with Leu 699 and pi-cation interactions with Lys 327 and Lys 574. Notably, Ani9 did not exhibit any hydrogen bonding interactions with ANO1 residues.

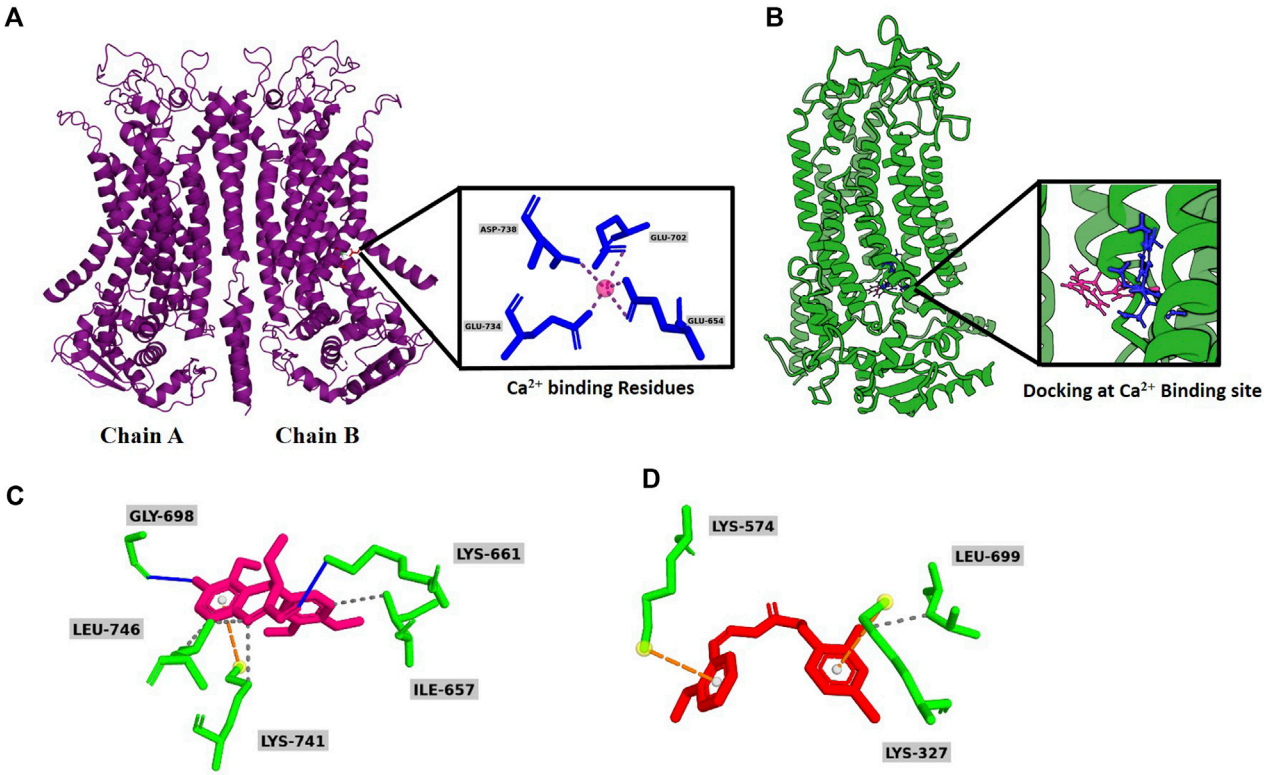

FIGURE 3
Overall graphical representation. **(A)** Secondary homodimeric structure of ANO1 (PDB ID: 5OYB) with Ca^{2+} binding site. **(B)** Molecular docking of vitekwangin B and Ani9 at Ca^{2+} binding site. **(C)** Predicted binding mode of Ani9 and **(D)** vitekwangin B with ANO1.

3.4 Effect of vitekwangin B on cell viability and migration

Pharmacological inhibition of ANO1 inhibits the growth of various types of cancer cells (Seo et al., 2017; Seo et al., 2021; Park et al., 2023). Vitekwangin B was tested to determine whether it inhibited the growth of prostate cancer and NSCLC cells by decreasing ANO1 protein levels (Figure 4). Vitekwangin B decreased the cell viability of PC3 cells in a dose-dependent manner when incubated for 72 h, with an IC_{50} of 2.64 μM, whereas XTANDI® (enzalutamide; a positive control for prostate cancer treatment) decreased cell viability with an IC_{50} of 81.42 μM. Vitekwangin B exhibited a stronger effect on PC3 cell viability, approximately 31-fold greater than that of enzalutamide (Figure 4A). Furthermore, vitekwangin B inhibited the growth of PC9 cells in a dose-dependent manner over 72 h and had an IC_{50} of 5.37 μM, whereas cisplatin (a chemotherapy drug) decreased PC9 cell viability with an IC_{50} greater than 30 μM (Figure 4B). To assess whether vitekwangin B inhibited PC3 cell migration, cells were cultured with different doses of vitekwangin B, which revealed dose-dependent inhibition of PC3 cell migration (Figure 4C). Notably, vitekwangin B showed differences in cell viability depending on ANO1 protein levels. Up to 1 μM vitekwangin B significantly inhibited the viability of ANO1-expressing cells more strongly compared to cells not expressing ANO1 and MRC-5 cells (Figures 4D, E; Supplementary Figure S5). These results indicated that vitekwangin B effectively inhibited cell viability in ANO1-expressing cells by reducing ANO1 protein levels.

3.5 Measurement of apoptotic effect, effect on hERG activity, and liver toxicity of vitekwangin B

As the pharmacological inhibition of ANO1 in various cancer cell types has been reported to cause apoptosis (Song et al., 2018; Park et al., 2023), we evaluated the apoptotic effects of vitekwangin B in PC3 and PC9 cells. Vitekwangin B significantly increased caspase-3 activity and PARP-1 cleavage, which represent two hallmarks of apoptosis (Figures 5A–D) and increased the sub-G1 population (Supplementary Figure S2). In contrast, Ani9 does not affect caspase-3 activity or PARP-1 cleavage because it does not decrease ANO1 protein levels (Seo et al., 2018). These results showed that vitekwangin B exerts anticancer effects by inducing apoptosis and reducing ANO1 protein levels.

To verify whether vitekwangin B is toxic to liver cells, HepG2 cells were treated with vitekwangin B, and their viability was measured. Vitekwangin B did not inhibit liver cell viability up to 50 μM, as compared with paracetamol (Figures 5E, F). In addition, the effects of vitekwangin B on hERG channel activity were tested in hERG channel-expressing HEK293 cells to confirm its potential applications in cancer treatment. Vitekwangin B did not inhibit hERG channel activity at concentrations up to 100 μM, and 10 μM

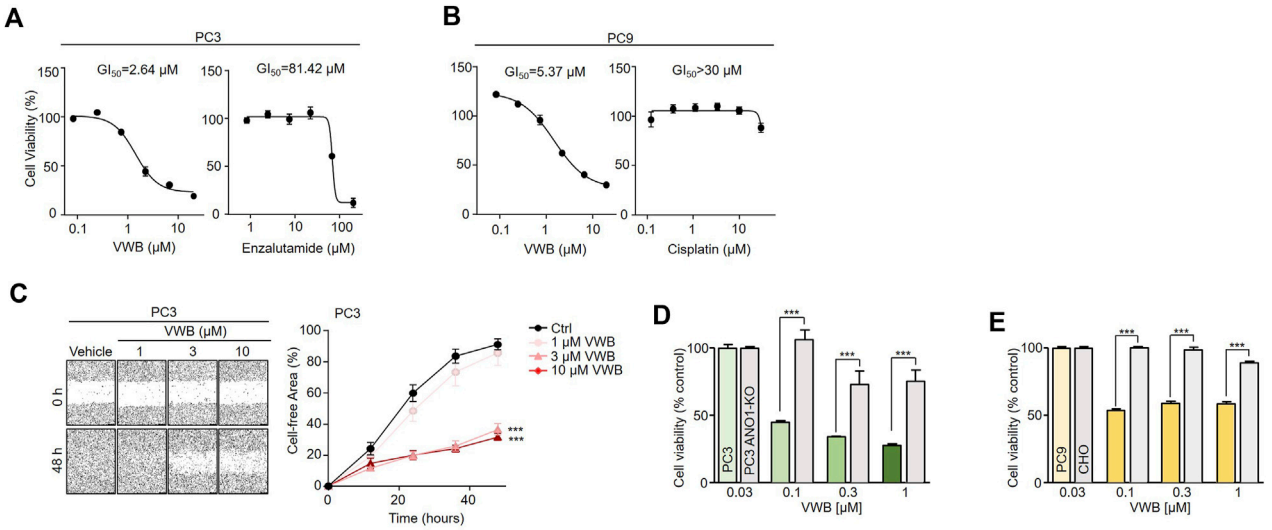

FIGURE 4
Effects of vitekwangin B on cell viability. **(A)** PC3 cells were cultured with 0.1–30 μM vitekwangin B and enzalutamide for 72 h, and cell viability was determined using CCK-8 assay. **(B)** PC9 cells were cultured with 0.1–30 μM vitekwangin B and cisplatin for 72 h, and cell viability was determined using CCK-8 assay. **(C)** Wound-healing assay was performed on ANO1-expressing PC3 cells. The cells were treated with 1, 3, and 10 μM of vitekwangin B, and representative images were acquired 0 and 64 h post-wound induction. The wound closure was quantified at 64 h. **(D,E)** Effects of the indicated concentrations of vitekwangin B on cell viability of PC3 or PC3 ANO1-KO cells and PC9 or CHO cells (mean ± SD, n = 5). VWB, vitekwangin B. ***p < 0.001., Student's unpaired t-test.

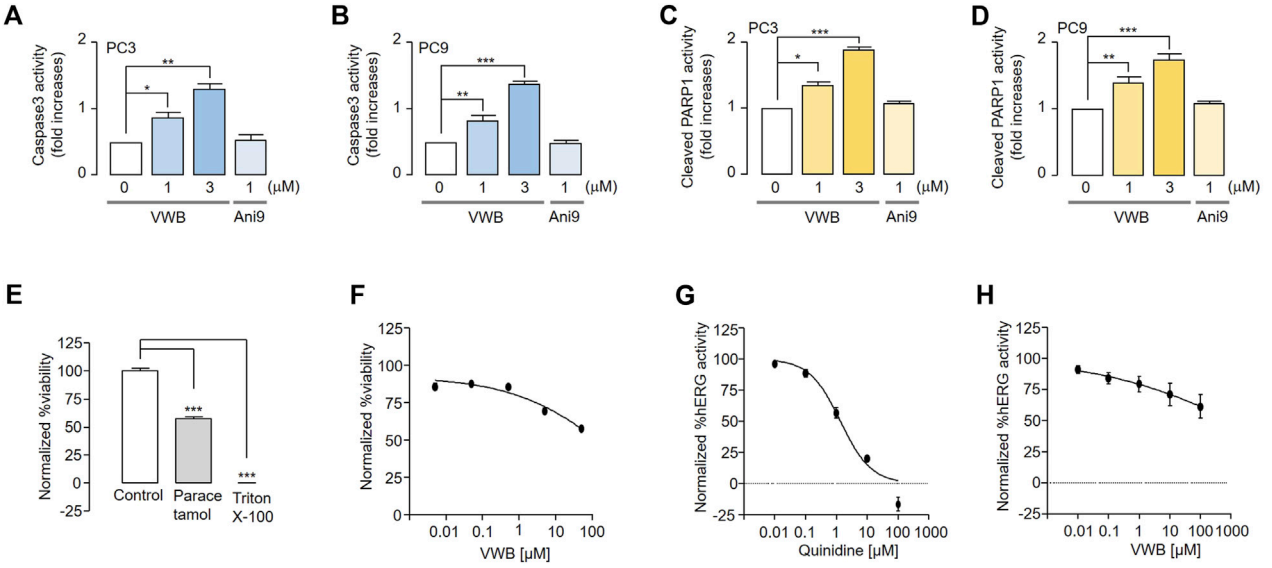

FIGURE 5
Evaluation of apoptosis and inhibition of hERG channel activity and liver cell viability induced by vitekwangin B and Ani9. **(A,B)** Caspase-3 activity in PC3 and PC9 cells cultured with vitekwangin B and Ani9 at the indicated concentrations for 24 h. **(C,D)** Cleaved PARP1 levels in PC9 cells incubated with the indicated concentrations of vitekwangin B and Ani9 for 24 h. **(E,F)** Relative viability of HepG2 cells treated with the tested compounds at five different concentrations (0.005, 0.05, 0.5, 5, and 50 μM) was determined. The viability data points were normalized while considering the maximum viability obtained with 0.5% (v/v) dimethyl sulfoxide solvent treatment as 100% viability and the minimum viability obtained with 0.01% (v/v) Triton X-100 treatment as 0% viability. **(G,H)** hERG channel activity of HEK cells treated with the tested compounds at five different concentrations (0, 0.01, 0.1, 1, 10 and 100 μM). Each data point was normalized using the baseline level of hERG channel current (mean ± SD, n = 3–5). VWB, vitekwangin B. *p < 0.05, **p < 0.01, ***p < 0.001, Student's unpaired t-test.

quinidine (positive control) completely inhibited the hERG channel (Figures 5G,H).

4 Discussion

While ANO1 plays multifaceted roles in various physiological processes, such as chloride ion secretion and cancer development, its chemotherapeutic potential is realized through the inhibition of its function and reduction of its protein expression (Britschgi et al., 2013; Liu et al., 2021). Therefore, several ANO1 inhibitors have been developed (Zhong et al., 2021). Several research groups have attempted to develop specific ANO1 inhibitors, starting from hit to lead chemical compounds via lead optimization (Seo et al., 2018; Zhong et al., 2021) but reported that ANO1 inhibitors may have side effects such as dry mouth syndrome, lowered blood pressure, and inhibited intestinal motility because they inhibit ANO1 channel function (Britschgi et al., 2013; Bill and Gaither, 2017; Liu et al., 2021; Wang et al., 2021; Zhong et al., 2021; Jeong et al., 2022). Therefore, it is necessary to develop novel small-molecule drugs that can gradually reduce ANO1 protein levels without causing side effects in humans.

In this study, we found that vitekwangin B did not inhibit ANO1 channel function but reduced ANO1 protein levels strongly. Remarkably, treatment with vitekwangin B for 10 min did not inhibit ATP-induced calcium influx but treatment for 24 h inhibited ATP-induced increase in cytosolic calcium significantly (Figure 1).

Because vitekwangin B reduced ANO1 protein levels notably, thereby reducing cell survival, it appeared to affect intracellular calcium changes (Figure 2). In addition, this phenomenon may have occurred because vitekwangin B interacts with a known calcium-binding site in ANO1 (Figure 3). Ani9, a known ANO1 inhibitor, also interacted with the calcium binding site on ANO1; however, vitekwangin B appeared to have better hydrogen bond binding than Ani9, and other compounds appeared to interact with the ANO1 protein (Figure 3). ANO1 is a homodimer channel harboring two pores that function independently, with one pore in each monomer. Each pore is activated by voltage-dependent binding of two intracellular calcium ions to a high-affinity binding site. In addition, the binding of phosphatidylinositol 4,5-bisphosphate to sites scattered throughout the cytosolic side of the protein aids in calcium activation process (Arreola et al., 2022). Moreover, Shi et al. (2021) demonstrated that theaflavin plays an important role in the pore blockade of ANO1 through mutagenesis experiments and inhibits viability in lung adenocarcinoma cells. However, because of the structural diversity of compounds and binding pockets on ANO1, it will be necessary to measure the binding affinity of vitekwangin B and ANO1 accurately through mutation experiments in the future. However, it is important to note that vitekwangin B reduced protein levels without inhibiting the function of the ANO1 channel, thereby contributing to reduced cell survival (Figure 4).

According to our experimental findings, the reduction in the cell viability of cells treated with drugs for prostate cancer and general anticancer drugs were less than that observed upon treatment with vitekwangin B (Figure 4). Thus far, no synthetic ANO1 inhibitors have entered clinical trials, and no substances have been developed with *in vitro* safety and excellent *in vivo* effectiveness using animal models (Namkung et al., 2011; Britschgi et al., 2013; Bill and Gaither, 2017; Seo et al., 2017; 2018; 2021; Liu et al., 2021; Wang et al., 2021; Zhong et al., 2021; Jeong et al., 2022). Therefore, natural products that reduce the ANO1 protein levels notably are novel and could be a breakthrough in the development of ANO1 inhibitors.

We discovered that vitekwangin B suppresses cell survival by notably reducing ANO1 protein levels and that its effect on cell viability in ANO1-KO cells was relatively weak (Figures 2, 4). In addition, vitekwangin B induced apoptosis, a characteristic feature of anticancer drugs (Supplementary Figure S6). It was confirmed that Ani9, which only inhibits the function of ANO1 channel, does not cause apoptosis (Figure 5). Therefore, it can be inferred that vitekwangin B reduced cell survival via apoptosis. Considering that it has little effect on hepatocellular toxicity and hERG channel function, which is important for the heartbeat, vitekwangin B can be developed as an anticancer drug. During the initial stages of drug development, it is crucial to assess cardiotoxicity and hepatotoxicity. However, it is equally important to evaluate additional pharmacokinetic factors such as absorption, distribution, metabolism, excretion, and toxicity to determine the properties and toxicity of a substance in animal models prior to its application in the human body.

In summary, our cell-based high throughput screening led us to discover the anticancer potential of vitekwangin B, which significantly reduced ANO1 protein levels, diminished cell viability, and triggered apoptosis. Vitekwangin B, a natural product with no hepatocellular toxicity or adverse effects on cardiac channels, holds promise as a valuable pharmacological tool for ANO1 inhibitor research. Furthermore, its potential application in the treatment of prostate and lung cancers is noteworthy, particularly considering the common resistance of these cancers to existing anticancer drugs. Further investigations are warranted to determine whether vitekwangin B, a relatively nontoxic natural product, can help overcome resistance to current anticancer medications in these specific cancer types.

Data availability statement

The datasets presented in this study can be found in online repositories. The names of the repository/repositories and accession number(s) can be found in the article/Supplementary Material.

Author contributions

YS: Conceptualization, Data curation, Formal Analysis, Funding acquisition, Supervision, Writing–original draft, Writing–review and editing. SL: Project administration, Writing–original draft. MK: Formal Analysis, Writing–original draft. DK: Methodology, Writing–original draft. SJ: Data curation, Writing–original draft. RD: Methodology,

Writing–original draft. AS: Methodology, Writing–original draft. SP: Methodology, Writing–original draft. NN: Formal Analysis, Writing–original draft. PH: Methodology, Writing–original draft. O-BK: Data curation, Writing–original draft. WN: Writing–original draft. JW: Conceptualization, Supervision, Writing–original draft, Writing–review and editing.

Funding

The author(s) declare financial support was received for the research, authorship, and/or publication of this article. This work was supported by a National Research Foundation of Korea (NRF) grant funded by the Korean government (NRF-2021R1F1A1060694, NRF-2022M3A9J3073020, NRF-2022R1F1A1063364, NRF-2022K2A9A1A06088842, and RS-2023-00247033); the Vietnam Academy of Science and Technology (VAST) under grant number QTKR01.01/22-23; and the Korea Basic Science Institute (Grant no. C313000). This research was also supported by a grant from the Dongguk University Research Program of 2021 (grant number K-2021-G0002-00516).

Conflict of interest

The authors declare that the research was conducted in the absence of any commercial or financial relationships that could be construed as a potential conflict of interest.

Publisher's note

All claims expressed in this article are solely those of the authors and do not necessarily represent those of their affiliated organizations, or those of the publisher, the editors and the reviewers. Any product that may be evaluated in this article, or claim that may be made by its manufacturer, is not guaranteed or endorsed by the publisher.

Supplementary material

The Supplementary Material for this article can be found online at: https://www.frontiersin.org/articles/10.3389/fphar.2024.1382787/full#supplementary-material

References

Adebesin, A. O., Ayodele, A. O., Omotoso, O., Akinnusi, P. A., and Olubode, S. O. (2022). Computational evaluation of bioactive compounds from Vitis vinifera as a novel β-catenin inhibitor for cancer treatment. *Bull. Natl. Res. Cent.* 46, 183–189. doi:10.1186/s42269-022-00872-3

Arreola, J., Pérez-Cornejo, P., Segura-Covarrubias, G., Corral-Fernández, N., León-Aparicio, D., and Guzmán-Hernández, M. L. (2022). Function and regulation of the calcium-activated chloride channel anoctamin 1 (TMEM16A). *Handb. Exp. Pharmacol.* 283, 101–151. doi:10.1007/164_2022_592

Ban, N. K., Thoa, N. T. K., Linh, T. M., Trang, D. T., Van Kiem, P., Nhiem, N. X., et al. (2018). Labdane-type diterpenoids from *Vitex limonifolia* and their antivirus activities. *J. Nat. Med.* 72 (1), 290–297. doi:10.1007/s11418-017-1125-2

Bill, A., and Gaither, L. A. (2017). The mechanistic role of the calcium-activated chloride channel ANO1 in tumor growth and signaling. *Adv. Exp. Med. Biol.* 966, 1–14. doi:10.1007/5584_2016_201

Britschgi, A., Bill, A., Brinkhaus, H., Rothwell, C., Clay, I., Duss, S., et al. (2013). Calcium-activated chloride channel ANO1 promotes breast cancer progression by activating EGFR and CAMK signaling. *Proc. Natl. Acad. Sci. U. S. A.* 110, E1026–E1034. doi:10.1073/pnas.1217072110

Dai, C., Heemers, H., and Sharifi, N. (2017). Androgen signaling in prostate cancer. *Cold Spring Harb. Perspect. Med.* 7, a030452. doi:10.1101/cshperspect.a030452

Das, R., Habiba, S. U., Dash, R., Seo, Y., and Woo, J. (2023). Unveiling the potentiality of shikonin derivatives inhibiting SARS-CoV-2 main protease by molecular dynamic simulation studies. *Int. J. Mol. Sci.* 24, 3100. doi:10.3390/ijms24043100

Hirsch, F. R., Scagliotti, G. V., Mulshine, J. L., Kwon, R., Curran, W. J., Jr., Wu, Y. L., et al. (2017). Lung cancer: current therapies and new targeted treatments. *Lancet* 389, 299–311. doi:10.1016/S0140-6736(16)30958-8

Imyanitov, E. N., Iyevleva, A. G., and Levchenko, E. V. (2021). Molecular testing and targeted therapy for non-small cell lung cancer: current status and perspectives. *Crit. Rev. Oncol. Hematol.* 157, 103194. doi:10.1016/j.critrevonc.2020.103194

Jang, Y., and Oh, U. (2014). Anoctamin 1 in secretory epithelia. *Cell Calcium* 55, 355–361. doi:10.1016/j.ceca.2014.02.006

Jeong, S. B., Das, R., Kim, D. H., Lee, S., Oh, H. I., Jo, S., et al. (2022). Anticancer effect of verteporfin on non-small cell lung cancer via downregulation of ANO1. *Biomed. Pharmacother.* 153, 113373. doi:10.1016/j.biopha.2022.113373

Kamal, N., Asni, N. S. M., Rozlan, I. N. A., Azmi, M. A. H. M., Mazlan, N. W., Mediani, A., et al. (2022). Traditional medicinal uses, phytochemistry, biological properties, and health applications of Vitex sp. *Plants (Basel)* 11, 1944. doi:10.3390/plants11151944

Kiuchi, F., Matsuo, K., Ito, M., Qui, T. K., and Honda, G. (2004). New norditerpenoids with trypanocidal activity from *Vitex trifolia*. *Chem. Pharm. Bull. (Tokyo)* 52, 1492–1494. doi:10.1248/cpb.52.1492

Kohsaka, S., Petronczki, M., Solca, F., and Maemondo, M. (2019). Tumor clonality and resistance mechanisms in EGFR mutation-positive non-small-cell lung cancer: implications for therapeutic sequencing. *Future Oncol.* 15, 637–652. doi:10.2217/fon-2018-0736

Li, W.-X., Cui, C.-B., Cai, B., Wang, H.-Y., and Yao, X.-S. (2005). Flavonoids from *Vitex trifolia* L. inhibit cell cycle progression at G2/M phase and induce apoptosis in mammalian cancer cells. *J. Asian Nat. Prod. Res.* 7, 615–626. doi:10.1080/10286020310001625085

Liu, Y., Liu, Z., and Wang, K. (2021). The Ca(2+)-activated chloride channel ANO1/TMEM16A: an emerging therapeutic target for epithelium-originated diseases? *Acta Pharm. Sin. B* 11, 1412–1433. doi:10.1016/j.apsb.2020.12.003

Meng, X. Y., Zhang, H. X., Mezei, M., and Cui, M. (2011). Molecular docking: a powerful approach for structure-based drug discovery. *Curr. Comput. Aided Drug Des.* 7, 146–157. doi:10.2174/157340911795677602

Namkung, W., Yao, Z., Finkbeiner, W. E., and Verkman, A. S. (2011). Small-molecule activators of TMEM16A, a calcium-activated chloride channel, stimulate epithelial chloride secretion and intestinal contraction. *Faseb. J.* 25, 4048–4062. doi:10.1096/fj.11-191627

Park, S., Das, R., Nhiem, N. X., Jeong, S. B., Kim, M., Kim, D., et al. (2023). ANO1-downregulation induced by schisandrathera D: a novel therapeutic target for the treatment of prostate and oral cancers. *Front. Pharmacol.* 14, 1163970. doi:10.3389/fphar.2023.1163970

Rastelli, G., Del Rio, A. D., Degliesposti, G., and Sgobba, M. (2010). Fast and accurate predictions of binding free energies using MM-PBSA and MM-GBSA. *J. Comput. Chem.* 31, 797–810. doi:10.1002/jcc.21372

Seo, Y., Jeong, S. B., Woo, J. H., Kwon, O.-B., Lee, S., Oh, H. I., et al. (2021). Diethylstilbestrol, a novel ANO1 inhibitor, exerts an anticancer effect on non-small cell lung cancer via inhibition of ANO1. *Int. J. Mol. Sci.* 22, 7100. doi:10.3390/ijms22137100

Seo, Y., Kim, J., Chang, J., Kim, S. S., Namkung, W., and Kim, I. (2018). Synthesis and biological evaluation of novel Ani9 derivatives as potent and selective ANO1 inhibitors. *Eur. J. Med. Chem.* 160, 245–255. doi:10.1016/j.ejmech.2018.10.002

Seo, Y., Ryu, K., Park, J., Jeon, D.-K., Jo, S., Lee, H. K., et al. (2017). Inhibition of ANO1 by luteolin and its cytotoxicity in human prostate cancer PC-3 cells. *PLoS One* 12, e0174935. doi:10.1371/journal.pone.0174935

Shafi, A. A., Yen, A. E., and Weigel, N. L. (2013). Androgen receptors in hormone-dependent and castration-resistant prostate cancer. *Pharmacol. Ther.* 140, 223–238. doi:10.1016/j.pharmthera.2013.07.003

Shen, T., Wang, Y., Zhu, Z., Wang, X., and Tian, T. (2019). Lignans and terpenoids from the fruits of *Vitex kwangsiensis* and their inhibitory activity on nitric oxide production in macrophages. *Nat. Prod. Commun.* 14, 1934578X1984817. doi:10.1177/1934578X19848178

Shi, S., Ma, B., Sun, F., Qu, C., and An, H. (2021). Theaflavin binds to a druggable pocket of TMEM16A channel and inhibits lung adenocarcinoma cell viability. *J. Biol. Chem.* 297, 101016. doi:10.1016/j.jbc.2021.101016

Shukri, N. A. B. M., and Hasan, M. H. (2021). Pharmacological review of *Vitex trifolia*. *Int. J. Pharm. Nutraceut. Cosmet. Sci.* 3, 49–65. doi:10.24191/IJPNaCS.v3.05

Song, Y., Gao, J., Guan, L., Chen, X., Gao, J., and Wang, K. (2018). Inhibition of ANO1/TMEM16A induces apoptosis in human prostate carcinoma cells by activating TNF-α signaling. *Cell Death Dis.* 9, 703. doi:10.1038/s41419-018-0735-2

Tan, M. H. E., Li, J., Xu, H. E., Melcher, K., and Yong, E. (2015). Androgen receptor: structure, role in prostate cancer and drug discovery. *Acta Pharmacol. Sin.* 36, 3–23. doi:10.1038/aps.2014.18

Thoa, N. T. K., Ban, N. K., Linh, T. M., Giang, V. H., Nhiem, N. X., and Van Kiem, P. (2017). Triterpenes from *Vitex limonifolia*. *Viet. J. Chem.* 55, 715. doi:10.15625/2525-2321.2017-00531

Twyffels, L., Strickaert, A., Virreira, M., Massart, C., Van Sande, J., Wauquier, C., et al. (2014). Anoctamin-1/TMEM16A is the major apical iodide channel of the thyrocyte. *Am. J. Physiol. Cell Physiol.* 307, C1102–C1112. doi:10.1152/ajpcell.00126.2014

Wang, H., Ma, D., Zhu, X., Liu, P., Li, S., Yu, B., et al. (2021). Nimodipine inhibits intestinal and aortic smooth muscle contraction by regulating Ca(2+)-activated Cl(−) channels. *Toxicol. Appl. Pharmacol.* 421, 115543. doi:10.1016/j.taap.2021.115543

Westover, D., Zugazagoitia, J., Cho, B. C., Lovly, C. M., and Paz-Ares, L. (2018). Mechanisms of acquired resistance to first- and second-generation EGFR tyrosine kinase inhibitors. *Ann. Oncol.* 29, i10–i19. doi:10.1093/annonc/mdx703

Wu, S. G., and Shih, J. Y. (2018). Management of acquired resistance to EGFR TKI-targeted therapy in advanced non-small cell lung cancer. *Mol. Cancer.* 17, 38. doi:10.1186/s12943-018-0777-1

Yang, Y. D., Cho, H., Koo, J. Y., Tak, M. H., Cho, Y., Shim, W. S., et al. (2008). TMEM16A confers receptor-activated calcium-dependent chloride conductance. *Nature* 455, 1210–1215. doi:10.1038/nature07313

Zhong, J., Xuan, W., Tang, M., Cui, S., Zhou, Y., Qu, X., et al. (2021). Advances in anoctamin 1: a potential new drug target in medicinal chemistry. *Curr. Top. Med. Chem.* 21, 1139–1155. doi:10.2174/1568026621666210607125614

frontiers | Frontiers in Pharmacology

TYPE Original Research
PUBLISHED 08 April 2024
DOI 10.3389/fphar.2024.1358089

Check for updates

OPEN ACCESS

EDITED BY
Wagdy Mohamed Eldehna,
Kafrelsheikh University, Egypt

REVIEWED BY
Ahmed Sabt,
National Research Centre, Egypt
Moataz Ahmed Shaldam,
Kafrelsheikh University, Egypt
Mahmoud Rashed,
University of Bonn, Germany

*CORRESPONDENCE
Assem Barakat,
ambarakat@ksu.edu.sa

RECEIVED 19 December 2023
ACCEPTED 14 February 2024
PUBLISHED 08 April 2024

CITATION
Barakat A, Alshahrani S, Al-Majid AM, Alamary AS, Haukka M, Abu-Serie MM, Dömling A, Domingo LR and Elshaier YAMM (2024), Activation of p53 signaling and regression of breast and prostate carcinoma cells by spirooxindole-benzimidazole small molecules.
Front. Pharmacol. 15:1358089.
doi: 10.3389/fphar.2024.1358089

COPYRIGHT
© 2024 Barakat, Alshahrani, Al-Majid, Alamary, Haukka, Abu-Serie, Dömling, Domingo and Elshaier. This is an open-access article distributed under the terms of the Creative Commons Attribution License (CC BY). The use, distribution or reproduction in other forums is permitted, provided the original author(s) and the copyright owner(s) are credited and that the original publication in this journal is cited, in accordance with accepted academic practice. No use, distribution or reproduction is permitted which does not comply with these terms.

Activation of p53 signaling and regression of breast and prostate carcinoma cells by spirooxindole-benzimidazole small molecules

Assem Barakat[1]*, Saeed Alshahrani[1], Abdullah Mohammed Al-Majid[1], Abdullah Saleh Alamary[1], Matti Haukka[2], Marwa M. Abu-Serie[3], Alexander Dömling[4], Luis R. Domingo[5] and Yaseen A. M. M. Elshaier[6]

[1]Department of Chemistry, College of Science, King Saud University, Riyadh, Saudi Arabia, [2]Department of Chemistry, University of Jyväskylä, Jyväskylä, Finland, [3]Medical Biotechnology Department, Genetic Engineering and Biotechnology Research Institute, City of Scientific Research and Technological Applications (SRTA City), Alexandria, Egypt, [4]Institute of Molecular and Translational Medicine, Faculty of Medicine and Dentistry, and Czech Advanced Technology and Research Institute, Palack University, Olomouc, Czechia, [5]Department of Organic Chemistry, University of Valencia, Valencia, Spain, [6]Department of Organic and Medicinal Chemistry, Faculty of Pharmacy, University of Sadat City, Menoufiya, Egypt

This study discusses the synthesis and use of a new library of spirooxindole-benzimidazole compounds as inhibitors of the signal transducer and activator of p53, a protein involved in regulating cell growth and cancer prevention. The text includes the scientific details of the [3 + 2] cycloaddition (32CA) reaction between azomethine ylide **7a** and ethylene **3a** within the framework of Molecular Electron Density Theory. The mechanism of the 32CA reaction proceeds through a *two-stage one-step* process, with emphasis on the highly asynchronous transition state structure. The anti-cancer properties of the synthesized compounds, particularly **6a** and **6d**, were evaluated. The inhibitory effects of these compounds on the growth of tumor cells (MDA-MB 231 and PC-3) were quantified using IC_{50} values. This study highlights activation of the p53 pathway by compounds **6a** and **6d**, leading to upregulation of p53 expression and downregulation of cyclin D and NF-κB in treated cells. Additionally, we explored the binding affinity of spirooxindole analogs, particularly compound **6d**, to MDM2, a protein involved in regulation of p53. The binding mode and position of compound **6d** were compared with those of a co-crystallized standard ligand, suggesting its potential as a lead compound for further preclinical research.

KEYWORDS

spirooxindole, benzimidazole, MEDT, p53, MDM2 inhibitors, NF-κB, CDK (cyclin-dependent kinase)

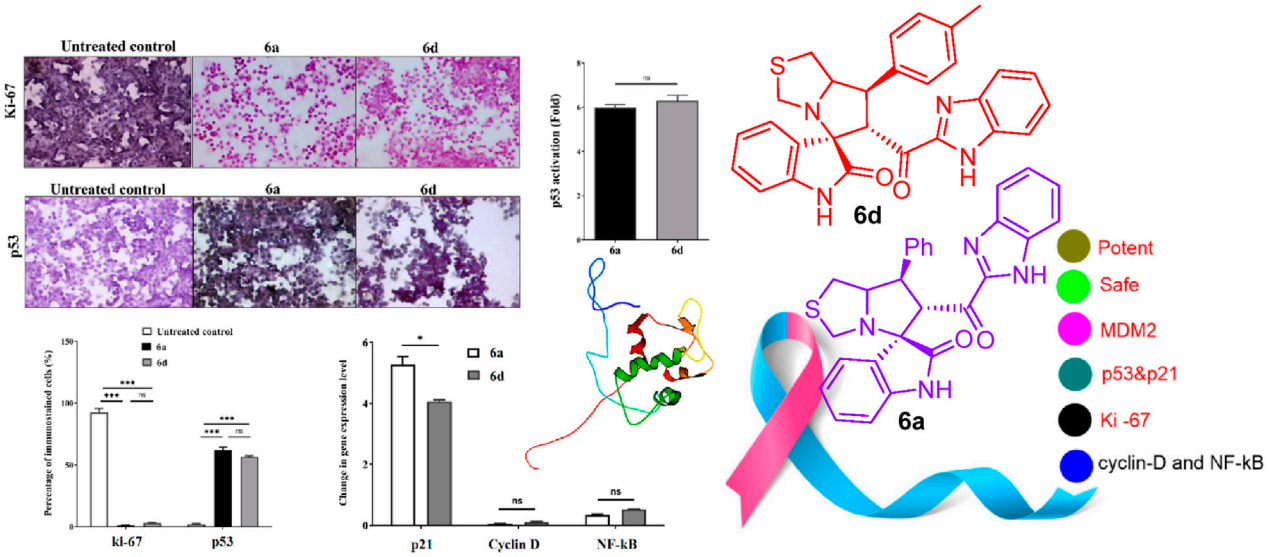

GRAPHICAL ABSTRACT

1 Introduction

Many diseases have become more common as a result of natural, industrial, and economic issues. Cancer is the second-leading cause of death worldwide, affecting health in all societies. Unfortunately, it is a tissue-level disease, which presents a major challenge in specific diagnosis and treatment efficacy. Prostate, lung, and colorectal cancers are the most common cancers in men worldwide, accounting for 46% of all newly diagnosed cancers in 2021. Breast cancer is the most common cancer in women worldwide, representing 30% of new cases diagnosed in 2021 (Siegel et al., 2021). Cancer is caused by successive mutations in genes that alter cellular functions proliferation and apoptosis (Chaudhry et al., 2022).

p53 is one of the most-studied tumor-suppressor proteins (Kandoth et al., 2013). Mutations in this protein are found in 60% of human cancers. Changing the DNA binding domain inhibits p53 activity as a transcription factor (Janjua, 2004; Estrada-Ortiz et al., 2016); there is evidence to suggest that restoration or reactivation of p53 function has significant therapeutic benefits (Di Agostino et al., 2006; Demma et al., 2010). The p53 pathway is inactivated in the remaining tumors either by downregulation of p53 cooperators such as ARF or upregulation of p53 inhibitors such as mouse double-minute proteins (MDM2 and MDMX) or downregulation of p53 cooperators such as ARF (Hsu and Ip, 2011). Mutations in p53 and upregulation of MDM2 do not typically occur in the same tumor, indicating that MDM2 overexpression is an effective pathway for inactivating p53 function in tumorigenesis. MDM2 inhibits the N-terminal transactivation domain (TAD) of p53 and promotes p53 degradation via the ubiquitin–proteasome system (E3 ligase activity). Substantial data have confirmed that MDM2 is the central node of the p53 pathway. Genetic and biochemical researchers have mapped MDM2-p53 interaction sites to the 106–amino acid-long N terminal domain of MDM2 and the N-terminus of the transactivation domain of p53. Interaction between p53 and MDM2 involves four key hydrophobic residues (Phe 19, Leu 22, Trp 23, Leu 26) in a short amphipathic helix formed by p53 and a small but deep hydrophobic pocket in MDM2. Atomic-level understanding of the MDM2–p53 interaction through x-ray crystallography provides a solid foundation for structure-based design of nonpeptidic, small-molecule antagonists of this interaction (Chen et al., 1993; Kussie et al., 1996). Herein, we set our design rationale to tailor new MDM2 inhibitors endowed with nuclear factor (NF)-κB inhibitory potential to maximize p53 induction capacity (such as enhancing the expression of p21-arrested cell cycle). Previous studies have illustrated that p53 acts as a unique regulator for suppressing NF-κB and aids in preventing its binding to promotor DNA binding sites (Murphy et al., 2011) NF-κB may become overactive in cancer cells because p53 activity is lost (Murphy et al., 2011). NF-κB is an essential transcription factor for expressing several key genes for tumor progression, angiogenesis, and metastasis (Xia et al., 2014; Pires et al., 2017) Thus, it is critical to evaluate the impact of these spirooxindoles on both key transcription factors (p53 and NF-κB).

Several examples based on spirooxindoles (Islam et al., 2023) and benzimidazole core structures have been identified for binding with the MDM2 receptor and activating p53 (Figure 1) (Vassilev, 2007; Li et al., 2008; Riedinger and Mcdonnell, 2009; Millard et al., 2011; Tovar et al., 2013; Zhao et al., 2013; Zhang et al., 2014; Gollner et al., 2016b; Barakat et al., 2019; Islam et al., 2019; Beloglazkina et al., 2020; Aziz et al., 2021; Lotfy et al., 2021; Barakat et al., 2022). Barakat *et al.* designed a new lead compound based on the core structure of spirooxindole clubbed with a benzimidazole moiety that has been shown to be highly effective against cancer cells targeted as inhibitors of protein–protein interaction between MDM2-p53 genes. This compound also exhibited a potential anti-metastatic effect (Islam et al., 2019; Aziz et al., 2021; Lotfy et al., 2021; Barakat et al., 2022). With this finding and the high potentiality of the benzimidazole nucleus toward cancer treatment-targeted NF-κB (Okolotowicz et al., 2010; Poltz and Naumann, 2012; Boggu et al., 2016; Jonak et al., 2016; Boggu et al., 2017; Dunphy et al.,

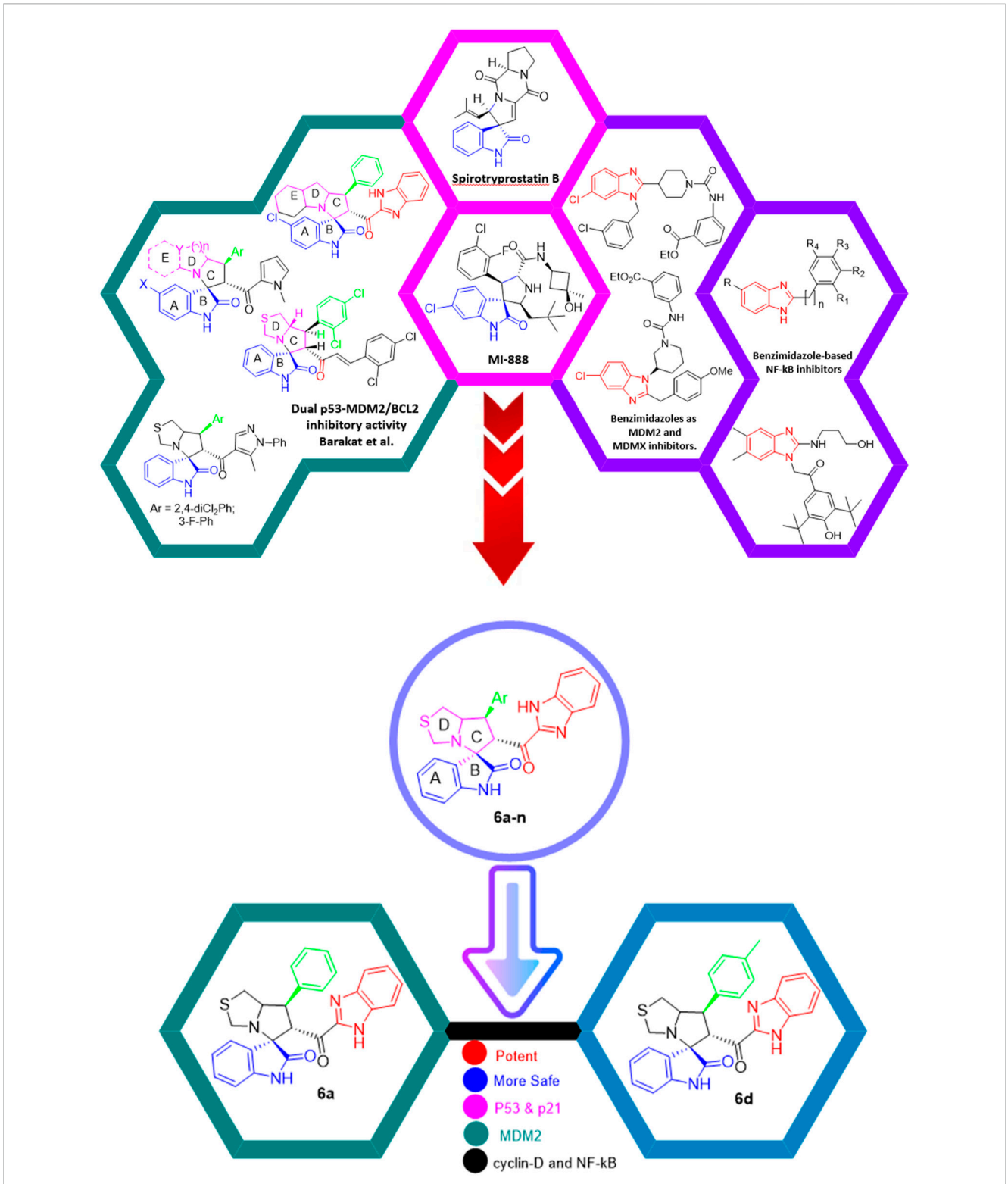

FIGURE 1
Rationale design of scaffold **6a-n** from naturally occurring or synthetic spirooxindole, benzimidazoles and our previous works.

2018; Błaszczak-Świątkiewicz, 2019), we were encouraged to increase the libraries of these analogs and assess them against different cancer cells. Based on the abovementioned data, the rational design of this work was conceptualized by merging some key features from naturally occurring spirooxoindoles with anticancer activities; reported Benzimidazole-based NF-κB inhibitors; our previous works with dual p53-MDM2/BCL2 (A, B,C,D,E system); and previous spiroxoxindoles–imidazole hybrid with A, B,C,D,E system. The designed compounds contain spirooxoindoles-imidazole with A, B,C,D system.

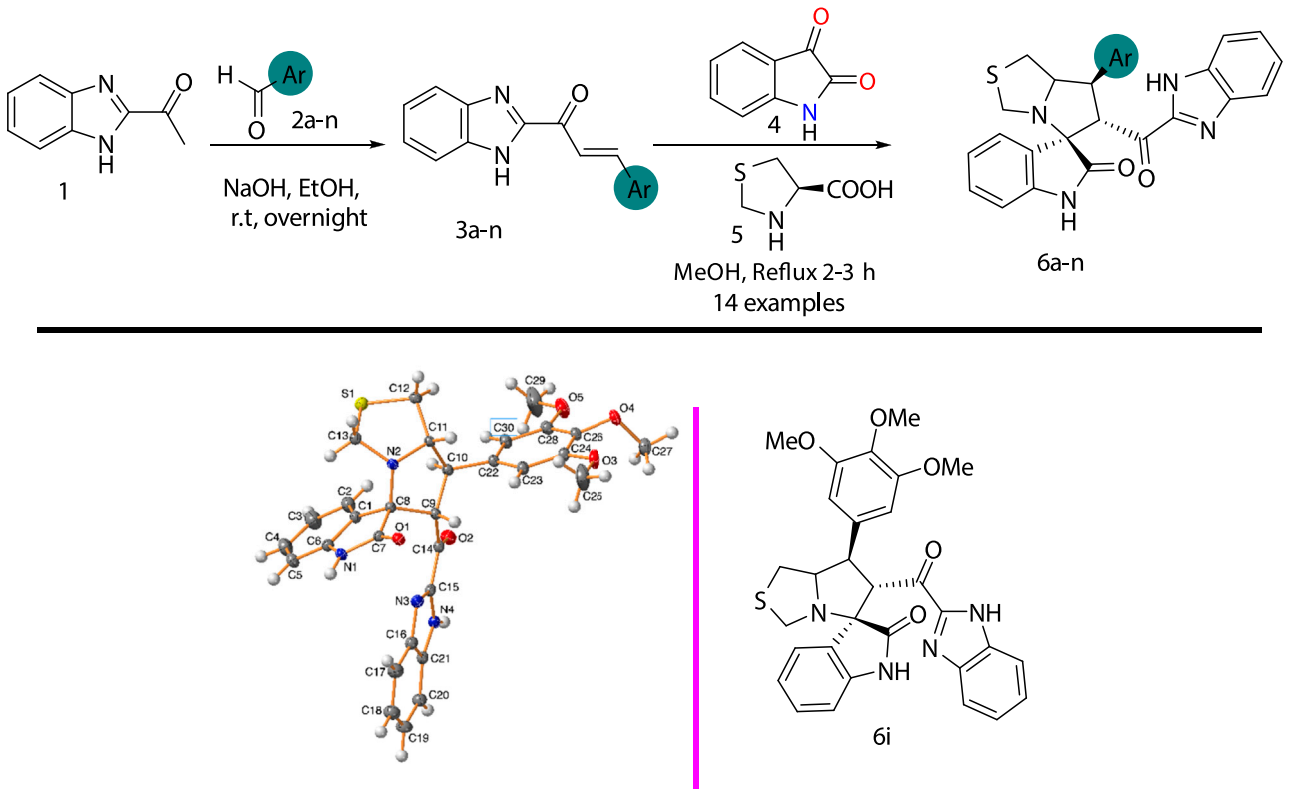

SCHEME 1
Synthesis of the desired spirooxindole derivative **6a-n;** ORTEP for spirooxindole analog **6i**.

2 Results and discussion

2.1 Chemistry

To increase the library of spirooxindole scaffolds as lead compounds for development of new drugs for cancer treatment targeting MDM2 inhibitors (Alshahrani et al., 2023), new spirooxindole derivatives (**6a–n**) were synthesized by the reaction of chalcones **3a–n** (Supplementary Table S1) with isatin **4** and thiazolidine-4-carboxylic acid **5** in methanol under reflux for 2–3 h, as shown in Scheme 1. The new spiro-derivatives **6a–n** was fully characterized by FT-IR, ^{1}H- and ^{13}C- NMR, and elemental analysis; spirooxindole analog **6i** was characterized by single-crystal x-ray diffraction analysis (data provided in SI, Supplementary Tables S1–S4). The stereochemistry and absolute configuration were assigned using experimental or theoretical approaches, and confirmed that the [3 + 2] cycloaddition (32CA) reaction proceeded *via* the *ortho/endo* pathway reaction mechanism (Scheme 2).

2.2 MEDT study of 32CA reaction between AY 7a and ethylene 3a

The 32CA reaction of AY **7a** with ethylene **3a** yielding *ortho/endo* spirooxindole **6a** was theoretically studied within the Molecular Electron Density Theory (MEDT) (Domingo, 2016) to understand its behaviors (Scheme 2).

2.2.1 Study of 32CA reaction of AY **7a** with ethylene **3a**

Owing to the non-symmetry of both reagents, two pairs of *endo* and *exo* stereoisomeric and two pairs of *ortho* and *meta* regioisomeric reaction paths were studied (Scheme 2). Analysis of the stationary points found along the four reaction paths indicated that the 32CA reaction occurs through a one-step mechanism. ωB97X-D/6-311G(d,p) relative enthalpies and Gibbs free energies are presented in Table 1. The thermodynamic data are presented in Supplementary Table S7.

A series of molecular complexes (MCs) were also found, in which the two reagents were joined by weak intermolecular interactions. Only the most stable **MC-on** was selected as an energy reference. The distance between the two frameworks at this MC was *ca.* 3.2 Å; **MC-on** was 18.6 kcal·mol^{-1} below the separated reagents (Table 1). Some conclusions can be drawn from the relative enthalpies in methanol given in Table 1: i) the most favorable **TS-on** was 11.7 kcal·mol^{-1} below the separated reagents; if formation of **MC-on** is considered, the activation enthalpy becomes positive by 6.9 kcal·mol^{-1}; ii) this 32CA reaction is completely *endo* stereoselective as **TS-ox** was 5.7 kcal·mol^{-1} above **TS-on**; iii) this 32CA reaction is completely *ortho* regioselective as **TS-mn** was 4.5 kcal·mol^{-1} above **TS-on**. *Endo* stereoselectivity and *ortho* regioselectivity are in complete agreement

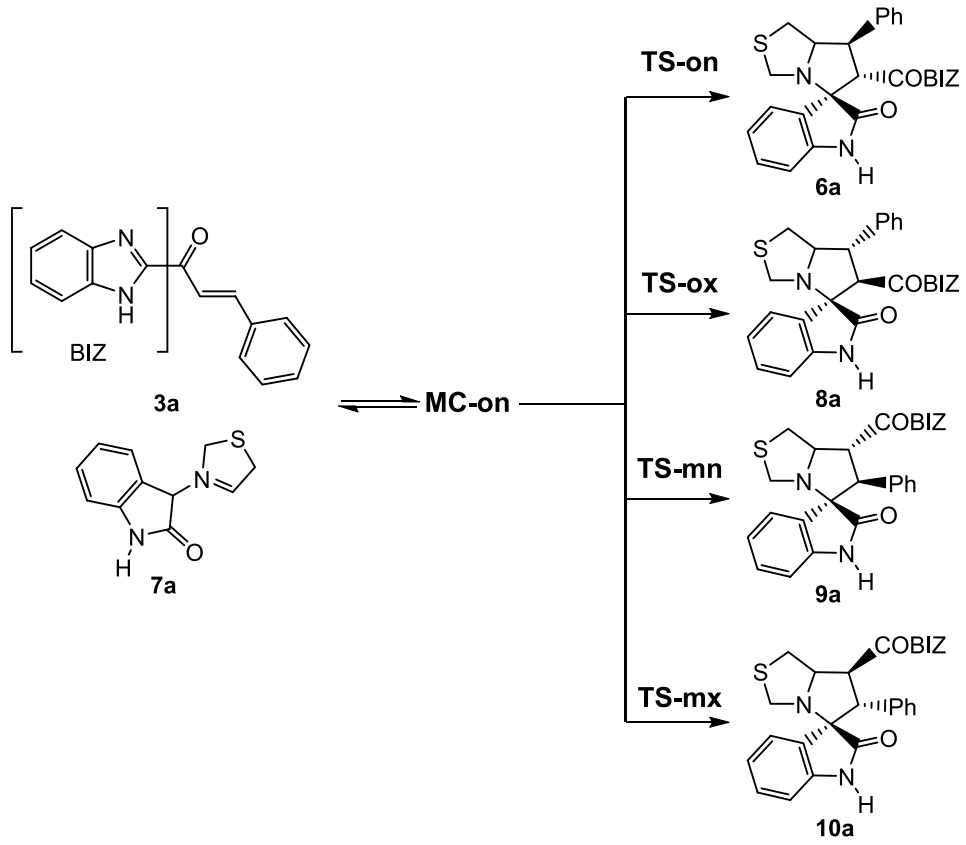

SCHEME 2
32CA reaction of AY **7a** with the ethylene **3a**.

with the experimental outcomes; iv) this 32CA reaction was strongly exothermic as spirooxindole **6a** was 47.9 kcal·mol^{-1} below the separated reagents. Consequently, spirooxindole **6a** was formed via kinetic control.

The enthalpy and Gibbs free energy profiles associated with the four competitive reaction paths are shown in Figure 2. Inclusion of the thermal corrections and entropies to enthalpies increases the relative Gibbs free energies by 14.2–17.9 kcal·mol^{-1} as a consequence of the unfavorable relative entropies associated with this bimolecular process, which were between −42.0 cal·mol^{-1}·K^{-1} and −52.9 cal·mol^{-1}·K^{-1}. Formation of **MC-on** was exergonic by 4.4 kcal·mol^{-1}. The activation Gibbs free energy associated with the 32CA reaction of AY **7a** with ethylene **3a** *via* **TS-on** increased to 10.5 kcal·mol^{-1}; formation of spirooxindole **6a** was exergonic by 31.5 kcal·mol^{-1}. Considering the activation Gibbs free energies, this 32CA reaction is completely *endo* stereoselective and *ortho* regioselective as **TS-ox** and **TS-mn** are 4.7 kcal·mol^{-1} and 3.1 kcal·mol^{-1}, respectively, above **TS-on** (Figure 2).

The geometries of the four TSs optimized in methanol are shown in Figure 3. The C–C distances between the four interacting carbons in the four TSs indicate that aside from the most unfavorable **TS-mx**, the other three TSs correspond to asynchronous C–C single-bond formation processes in which the shorter C–C distance corresponds to participation of the most electrophilic β-conjugated C4 carbon of ethylene **3a**. At the most favorable **TS-on**, the C–C distances between the two pairs of interacting carbons, 2.137 Å (C3–C4) and 2.757 Å (C1–C5), indicate that this TS is associated with a high asynchronous C–C single-bond formation process. Analysis of the intrinsic reaction coordinates (IRC) (Fukui, 1970) associated with the highly asynchronous **TS-on** indicates that this 32CA reaction occurs through a non-concerted *two-stage one-step* mechanism (Domingo et al., 2008), in which the formation of the second C–C single bond begins after the first C–C single bond is completely formed.

Detailed analysis of the geometry of **TS-on** shows that one of the hydrogens of the benzene framework of ethylene **3a** is located at 2.484 Å of the carbonyl oxygen of AY **7a**, and one hydrogen of the dihydrothiopyrrole ring of AY **7a** is located at 2.391 Å of the carbonyl O7 oxygen of ethylene **3a** (Figure 3). These distances suggest the presence of two hydrogen bonds (HBs) between the hydrogen and oxygen centers. However, analysis of the geometry of the regioisomeric **TS-mn** shows the presence of only one HB between carbonyl O7 oxygen of ethylene **3a** and dihydrothiopyrrole hydrogen of AY **7a**, with H–O distances of 2.374 Å (Figure 3).

Global electron density transfer (GEDT) analysis (Domingo, 2014) at the most favorable **TS-on** was used to assess the polar character of this 32CA reaction. GEDT values less than 0.05 e correspond to non-polar processes; values greater than 0.20 e correspond to polar processes. The high GEDT value found at

TABLE 1 ωB97X-D/6–311G(d,p) relative enthalpies (ΔH in kcal·mol^{-1}), entropies (ΔS in cal·mol^{-1}K^{-1}), and Gibbs free energies (ΔG in kcal·mol^{-1}), with respect to the separated reagents, computed at 337.85 K and 1 atm in methanol, for the stationary points involved in the 32CA reaction of AY 7a with ethylene 3a.

	ΔH	ΔS	ΔG
MC-on	−18.6	−42.0	−4.4
MC-mn	−15.2	−37.9	−2.3
TS-on	−11.7	−52.9	6.1
TS-ox	−6.1	−50.1	10.9
TS-mn	−7.2	−48.6	9.2
TS-mx	−4.4	−46.5	11.4
6a	−47.9	−48.6	−31.5
8a	−44.2	−47.3	−28.3
9a	−45.1	−48.1	−28.8
10a	−48.3	−48.5	−31.9

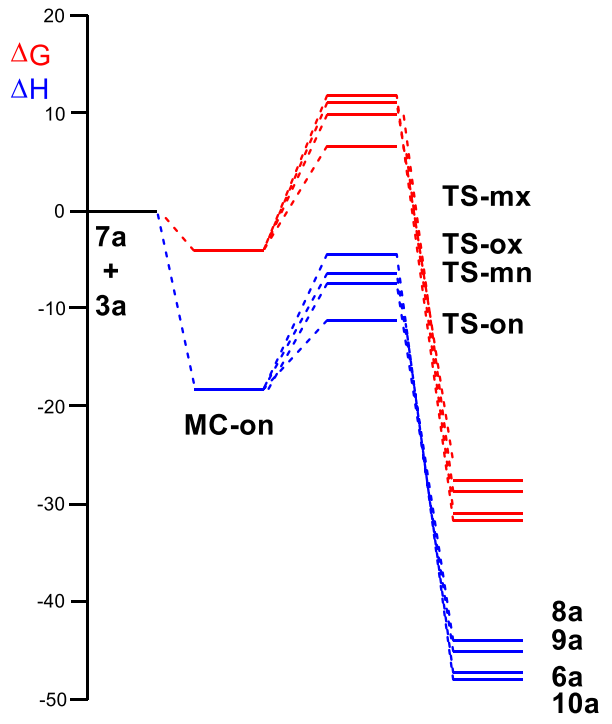

FIGURE 2
ωB97X-D/6–311G(d,p) enthalpy, in blue, ΔH in kcal mol^{-1}, and Gibbs free energy, in red, ΔG in kcal mol^{-1}, profiles, in methanol at 65°C, for the 32CA reaction of AY **7a** with the ethylene **3a**.

TS-on (0.23 e), a consequence of the supernucleophilic character of AY **7a** (N = 4.39 eV) and the strong nucleophilic character of ethylene **3a** (ω = 2.39 eV) (see Conceptual DFT (CDFT) analysis (Parr, 1983; Domingo et al., 2016) of the reagents in the Supplementary Material), indicates that this 32CA reaction is highly polar. The flux of the electron density, from AY **7a** to ethylene **3a**, classifies this 32CA reaction as a forward electron density flux (FEDF) (Domingo et al., 2020), in agreement with the analysis of the CDFT indices.

2.2.2 What is the origin of the *ortho* regioselectivity?

Topological analysis of the electron localization function (ELF) (Becke and Edgecombe, 1990) of AY **7a** showed the presence of two monosynaptic basins, V(C1) and V' (C1), integrating a total of 0.76 e at the C1 carbon, characterizing this three-atom-component as a *pseudo*(*mono*)*radical* species (Ríos-Gutiérrez et al., 2022) (Figure 4). Analysis of the nucleophilic P_k^- Parr functions (Domingo et al., 2013) of AY **7a** indicates that the C1 carbon is more nucleophilic than the C3 carbon (see CDFT analysis of the reagents in the Supplementary Material). Consequently, the 32CA reaction of AY **7a** with ethylene **3a** is expected to be *meta* regioselective (Ríos-Gutiérrez et al., 2022).

A recent MEDT study on the unexpected *ortho* regioselectivity in the 32CA reactions of AYs derived from L-proline showed that the presence of two HBs at the **MC-on**, which are enhanced at the corresponding **TS-on**, can be responsible for the *ortho* regioselectivity of these 32CA reactions (Domingo et al., 2022).

MC-on was 3.4 kcal mol^{-1} more stable than **MC-mn** (Table 1). Analysis of the geometries of the two MCs shows the presence of an HB between one hydrogen of the CH_2 methylene continuous with the sulfur of AY **3a** and the carbonyl O7 oxygen of ethylene **7a**, with an O–H distance of 2.37 Å (Figure 5). **MC-on** shows an additional HB between a hydrogen of the aromatic ring of ethylene **3a** and the oxygen atom of AY **7a,** with an O–H distance of 2.69 Å (Figure 5). Formation of this HB required twisting of the benzene ring by 15.9°.

These two HBs, which are also present in the most stable **TS-on** (Figure 3), may account for the *ortho* and *endo* selectivity found in this 32CA reaction. The enthalpy difference between **MC-on** and **MC-mn** (3.4 kcal mol^{-1}) was increased to 4.5 kcal·mol^{-1} at the TSs as a consequence of stronger HB interactions.

An atom-in-molecules (AIM) (Richard et al., 1982) topological analysis of the electronic structure of the most favorable **TS-on** characterizes the two HBs responsive to the *ortho* reactions (see AIM topological analysis of the electronic structure of the most favorable **TS-on** in the Supplementary Material Table S6).

2.3 Biological evaluation and MTT assay

Initially, the target compounds of the spirooxindole analogs **6a–n** were submitted to NCI for screening against 60 panels of cancer cells. Preliminary results showed promising feedback for the synthesized compounds of spirooxindole analogs (SI, Supplementary Table S8). For example, compounds **6a–n** perfectly inhibited the growth of leukemia cells (CCRF-CEM; HL-60 (TB); K-562; MOLT-4; RPMI-8226, SR), with a GI% exceeding 80% except for compounds **6b**, **6g**, and **6l**, which showed a smaller GI% (75%) for MOLT-4, RPMI-8226, and SR cancer cells. In non-small-cell lung cancer cells (A549/ATCC, EKVX, HOP-92, HOP62, NCI-H226, NCI-H23, NCI-H322M, NCI-H460, NCI-H460), the synthesized compounds showed complete growth inhibition, with the exception of **6g** and **6l**, which were the most reactive. We also observed that compounds **6g** and **6l** exhibited growth inhibition of less than 80% in CNS cancer cells (SF-268, SF-

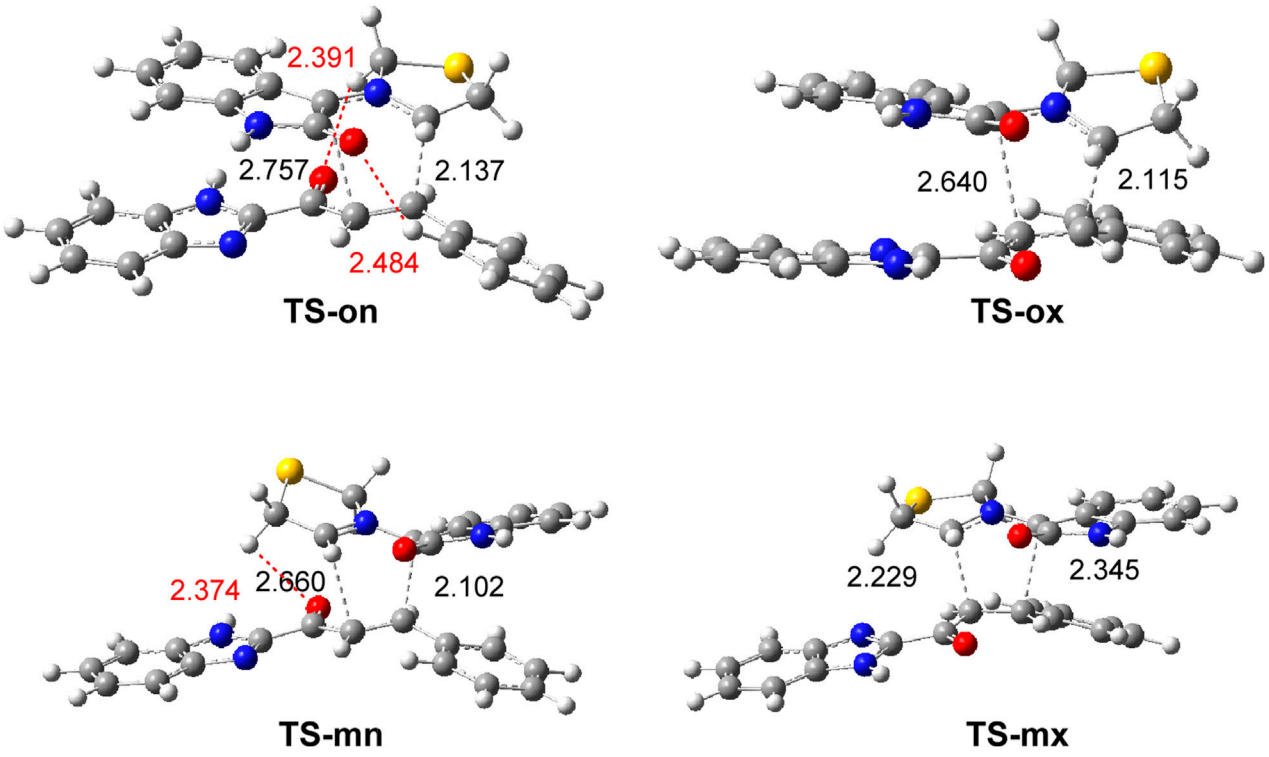

FIGURE 3
ωB97X-D/6−311G(d,p) geometry of the TSs involved in the 32CA reaction of AY **7a** with ethylene **3a**, optimized in methanol. The distances are given in Angstrom. HB distances are given in red.

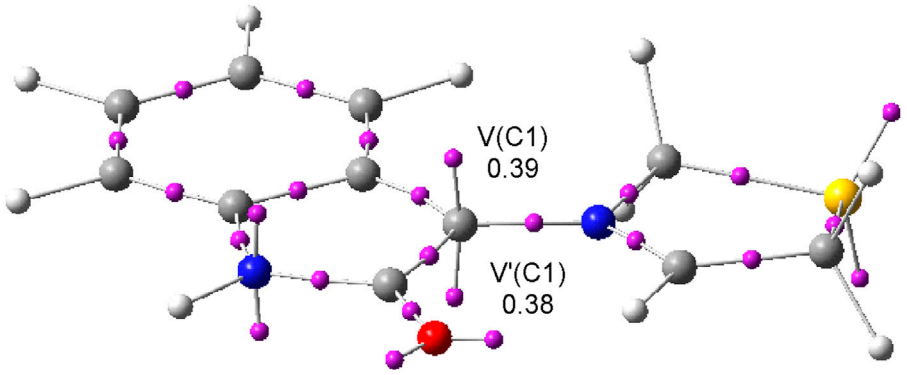

FIGURE 4
ωB97X-D/6−311G(d,p) ELF basin attractor positions of AY **3a**. The populations of the V(C1) and V′ (C1) monosynaptic basins are given in average number of electrons, e.

295, SF-539, SNB-19, SNB-75, U251). The GI% of melanoma cells was completely inhibited by these compounds. For ovarian cancer cells (IGROVI), compounds **6b, 6c, 6d, 6g**, and **6l** showed less reactivity, with a GI% from 55% to 75%. The other compounds showed excellent growth inhibition. For renal cancer cells (UO-31), the compounds exhibited less reactivity than with other renal cancer cells (786–0, A49, ACHN, CAKI-1, RXF393, SN12C, TK-10, DU-145). For breast cancer cells, complete growth inhibition was observed; however, compounds **6b–d, 6g, 6h**, and **6m** were less reactive against T-47D cancer cells, with a GI% between 54% and 80%.

The percentage of wi-38 viability and the growth inhibition percentages of MDA-MB231 and PC-3 cells after incubation with 5 μM of different tested compounds were assessed using the MTT assay (Supplementary Table S9). From Supplementary Table S9, the viability of normal human lung cells (wi-38) exceeded 81% after incubation with 5 μM of **6a** and **6d** compared to all other tested compounds, producing wi-38 cell death over 50%. The safest compound was **6a,** which did not affect the cell viability of wi-38 (~ 96%). Compounds **6a** and **6d** produced maximum viability on wi-38 and triggered death (>50%) in human cancer cells

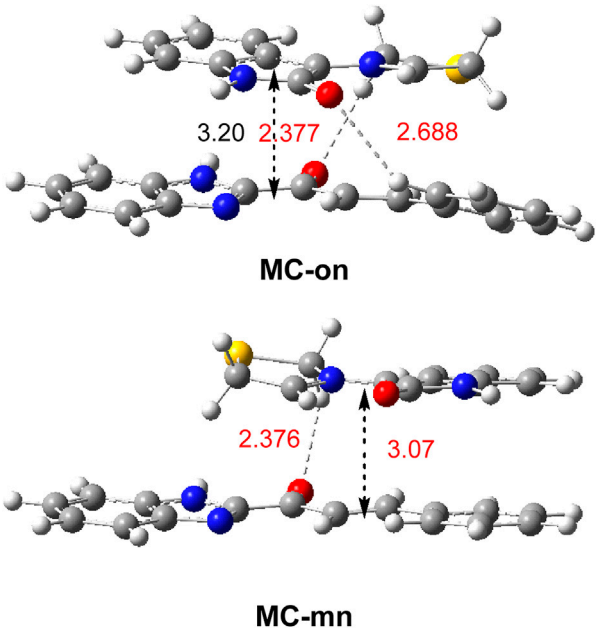

FIGURE 5
ωB97X-D/6–311G (d,p) optimized geometries of **MC-on** and **MC-mn**. Distances in methanol are given in angstroms, Å. HB distances are given in red.

(MDA-MB 231 and PC-3) (Supplementary Table S9). The values of the IC_{50} (μM) of **6a-n** on Wi-38 viability and the growth of MDA-MB 231, and PC-3 cells are summarized in Table 2. This powerful anti-cancer effect was supported by severe morphological alterations (cell shrinkage and loss of normal spindle shape) in treated cancer cells compared with untreated cancer cells (Figure 6).

Figures 7A, B shows that **6a**- and **6d**-treated cancer cells demonstrated a higher percentage of annexin-stained cells than untreated cells. Furthermore, **6a** and **7d** induced apoptosis-dependent death (53.89%–55.34%) in treated breast- and prostate-cancer cell lines. This effect may be attributed to the potency of **6a** and **6d** for upregulating p21 expression by greater than three times and downregulating the expression level of cyclin D and NF-κB in treated MDA-MB 231 cells compared to untreated cells (Figure 8). **6a** had the most significant effect on induction of p21 expression (5.3 times) and suppression of cyclin D and NF-$_{k}$B gene expression compared with **6d** ($p < 0.05$).

Figure 9A shows the immunohistochemistry results for the proliferation marker (Ki-67) and apoptosis marker (p53) in the MDA-MB 231 cell line after treatment for 72 h with **6a** and **6d**. These compounds reduced Ki-67 levels (from 82.425% to 1.18% and 3.03%, respectively), as indicated by the increase in purple-stained cells in comparison with brown-stained untreated control cells (Figures 9AI, III). Figures 9AII, III show that **6a** and **6d** increased the protein levels of p53 by 60.2% and 54.7%, respectively, compared to the untreated MDA-MB 231 cells, which mostly lacked brown p53-nuclear staining. Moreover, the active p53 transcription factor was assessed in the treated MDA-MB 231 cells compared to untreated cells by quantifying the p53 bound to a target oligonucleotide-coated plate. Both compounds exhibited high efficiency for p53 activation, 5.983 ± 0.142 and 6.287 ± 0.254, respectively (Figure 9B). This may be due to their inhibitory potency against MDM2, which limits its degradation.

Some of the synthesized spirooxindoles based on benzimidazole were selected for further MDM2 binding affinity using the MST assay. The results are summarized in Table 3; the binding curve is presented in the Supplementary Information. Compounds **6a, 6b, 6d, 6e, 6h, 6i**, and **6l** exhibited moderate to excellent binding affinity with the MDM2 receptor, with a range of K_D = 6.68–113 μM (SI; Supplementary Figures S3–S9). The most active compound was **6h** (K_D = 6.68 μM); the spirooxindole-based benzimidazole had a benzene ring with a hydroxyl group in the *meta*-position for further binding interaction with the key amino acid. Having electron-donating groups such as methyl or trimethoxy groups on the benzene ring (**6d** and **6i**) showed good binding, with K_D = 17.4 μM and 21 μM, respectively. However, the presence of halogens such as chlorine or bromine atoms decreased the binding affinity with MDM2 to 38.2 μM and 49.9 μM for compounds **6b** and **6l,** respectively. Without any substitution on the benzene ring (compound **6a**) or change to a heterocycle such as thiophene (compound **6e**), the least reactivity toward binding with the protein receptor was observed.

2.4 Molecular docking study

The designed compounds (**6a–l**) and standard co-crystallized spirooxindole compounds were docked with the MDM2 protein, which was retrieved from the Protein Data Bank (PDB code: 5law) (Gollner et al., 2016a). The docking protocol was performed using OpenEye scientific software (Docking, 2016). To validate the docking protocol, the standard ligand **6SJ** was re-docked with the receptor. The standard ligand **6SJ** exhibited the same binding mode and pose as its co-crystallized complex (Gollner et al., 2016a), completely overlaying each other, as shown in Figure 10A. It formed HBs with Leu:54AA through the NH of the indole and with Lys:94AA through the protonated nitrogen of the pyrrolidine amino acid. Compound **6h** exhibited high similarity in binding pose and mode with the co-crystallized ligand (Figure 10B). It interacts with the receptor through formation of HBs with Leu:54AA through the NH of the indole, and with Lys:94AA through phenolic functionality. Figure 10C shows the deposition of compound **6d** inside the active receptor domains. The compound interacted with its receptor via hydrophobic interactions. Figure 10D shows the docking pose and mode of compound **6d** compared with those of the standard ligand **6SJ**. The benzimidazole ring of compound **6d was** overlaid with the indole moiety of the standard ligand **6SJ**. However, the remaining features of both compounds were oriented in different directions.

2.5 Shape alignment and ROCS analysis

The rapid overlay chemical similarity (ROCS) approach was used to determine compound similarity based on 3D structures and automated crafted descriptors using OpenEye software. Shape similarity was determined using Tanimoto scores. The Tanimoto Combo (maximum value = 2) is the sum of the shape (maximum

10.3389/fphar.2024.1358089

TABLE 2 The estimated IC_{50} (μM) of 6a-n on Wi-38 viability and the growth of MDA-MB 231, and PC-3 cells.

Chemical structure	Wi-38	MDA-MB 231	PC-3
	IC_{50} (μM)		
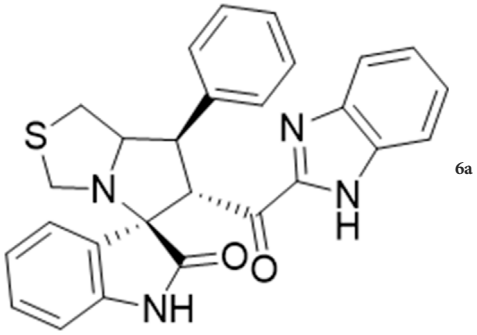 6a	22.163 ± 1.586	2.968 ± 0.047	4.107 ± 0.167
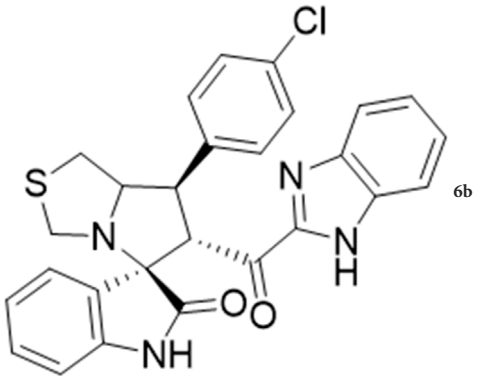 6b	4.962 ± 0.117	4.757 ± 0.265	4.819 ± 0.000
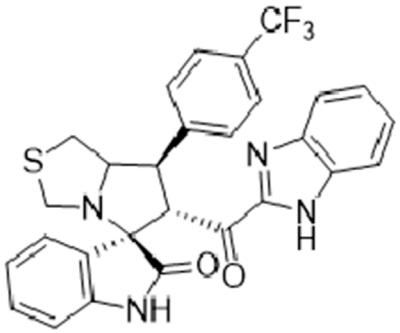 6c	12.887 ± 1.512	3.341 ± 0.210	4.151 ± 0.232
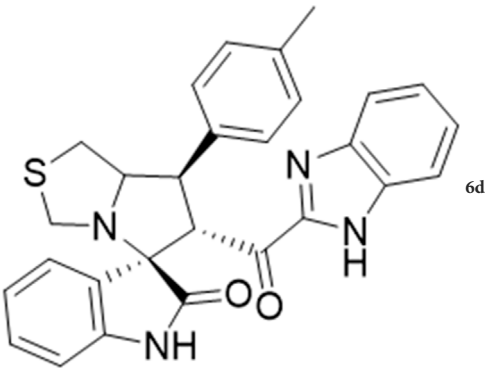 6d	5.180 ± 0.138	4.303 ± 0.137	4.294 ± 0.054

(Continued on following page)

10.3389/fphar.2024.1358089

TABLE 2 (*Continued*) The estimated IC_{50} (μM) of 6a-n on Wi-38 viability and the growth of MDA-MB 231, and PC-3 cells.

Chemical structure	Wi-38	MDA-MB 231	PC-3
	IC_{50} (μM)		
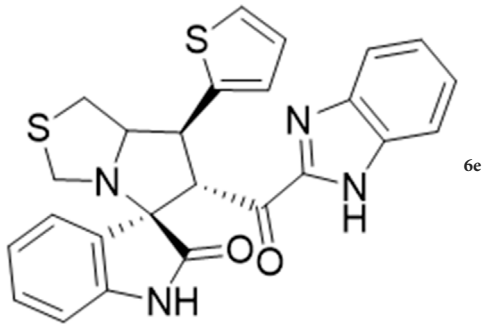 6e	4.752 ± 0.008	5.605±	5.432 ± 0.098
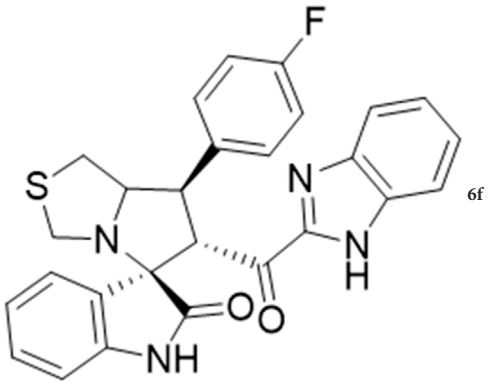 6f	4.166 ± 0.076	4.407 ± 0.448	4.593 ± 0.132
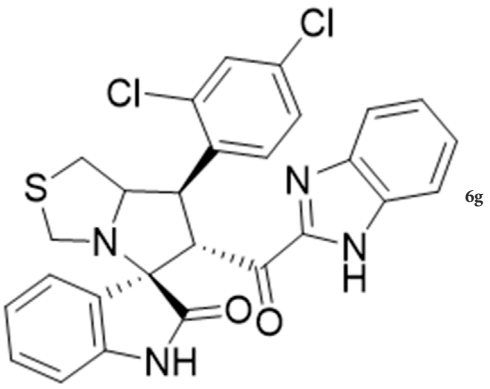 6g	5.106 ± 0.191	6.216 ± 0.000	6.191 ± 0.191
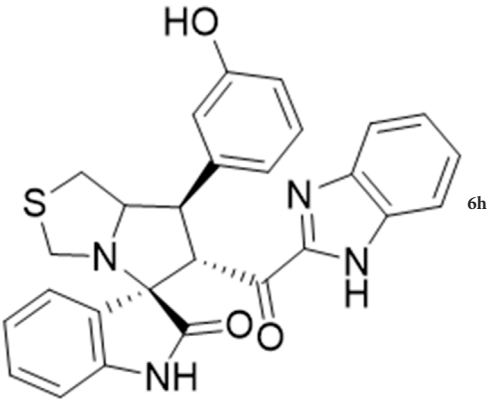 6h	4.408 ± 0.07	5.442 ± 0.167	5.041 ± 0.316
	4.081 ± 0.201	6.680 ± 0.463	6.017 ± 0.106

(Continued on following page)

TABLE 2 (*Continued*) The estimated IC_{50} (μM) of 6a-n on Wi-38 viability and the growth of MDA-MB 231, and PC-3 cells.

Chemical structure	Wi-38	MDA-MB 231	PC-3
	IC_{50} (μM)		
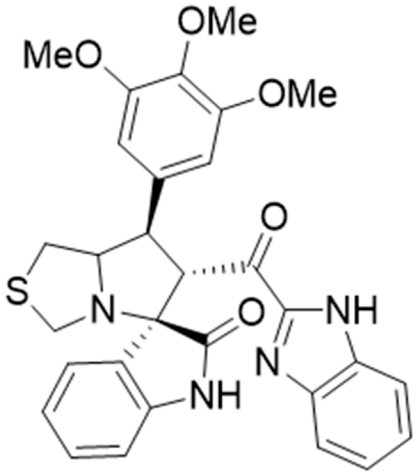 6i			
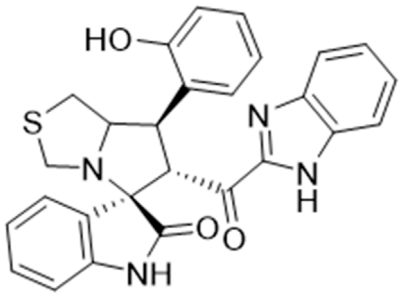 6j	3.998 ± 0.129	4.665 ± 0.009	4.543 ± 0.163
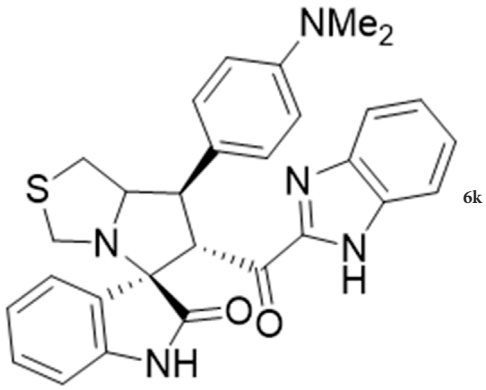 6k	3.950 ± 0.319	3.995 ± 0.249	4.160 ± 0.036
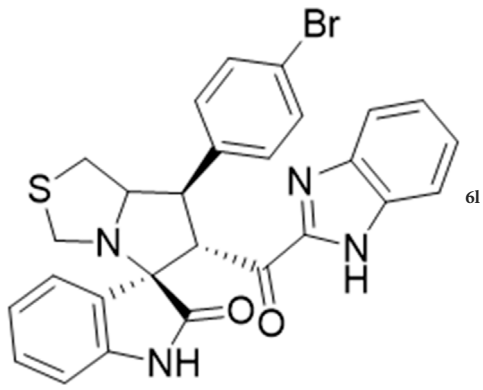 6l	6.259 ± 0.443	4.510 ± 0.203	4.627 ± 0.116
	4.650 ± 0.127	4.733 ± 0.224	4.766 ± 0.132

(Continued on following page)

10.3389/fphar.2024.1358089

TABLE 2 (*Continued*) The estimated IC_{50} (μM) of 6a-n on Wi-38 viability and the growth of MDA-MB 231, and PC-3 cells.

Chemical structure	Wi-38	MDA-MB 231	PC-3
	IC_{50} (μM)		
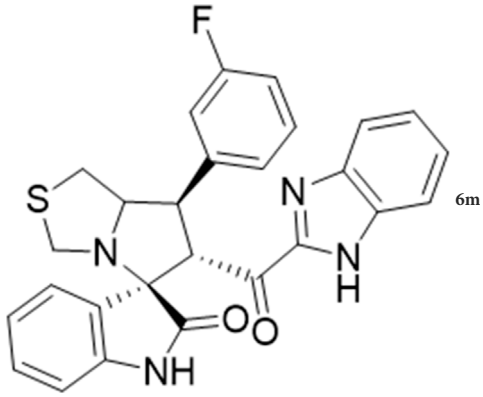 6m			
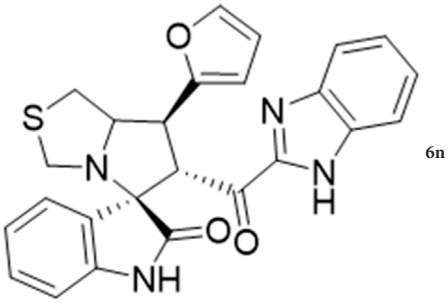 6n	4.171 ± 0.166	6.143 ± 0.246	6.247 ± 0.533

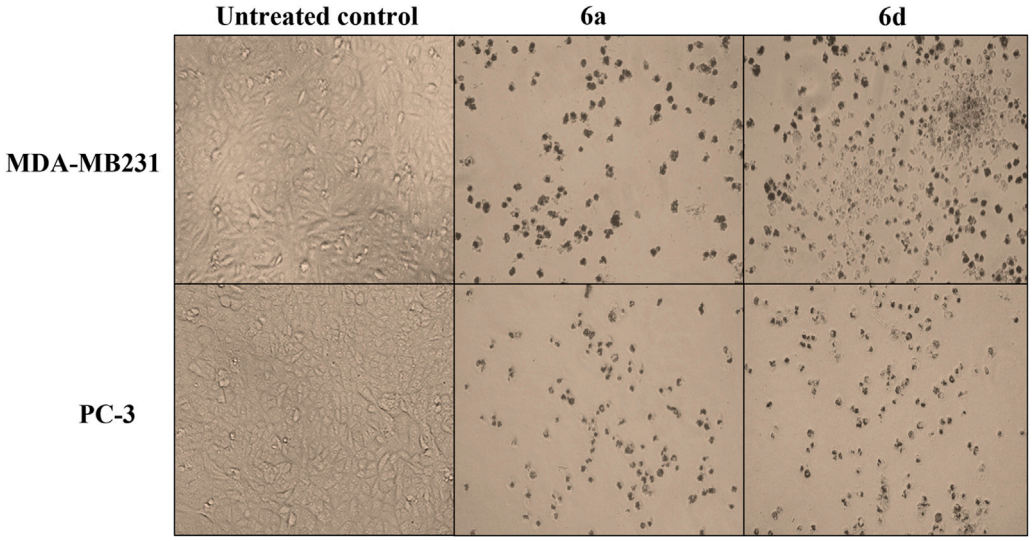

FIGURE 6
Morphological alteration of the most active anticancer compounds-treated MDA-MB 231 and PC-3 cells in comparison with the untreated control cells.

value = 1) and color (maximum value = 1) Tanimoto scores. Considering **6SJ**, compound score was not correlated to activity. Compounds **6d** and **6h** had TC scores of 0.83 and 0.81, respectively, as shown in Table 4. The results indicated that our scaffolds could resemble another target or have unique chemometric characteristics.

For compounds **6d** and **6h**, the color and shape atoms (generated by the ROCS application, OpenEye software) are shown in Figures 11A–C compared with the standard ligand (**6SJ**).

The most important descriptors for compounds **6d** and **6h** are presented in Table 5, compared with the **6SJ** standard. Both

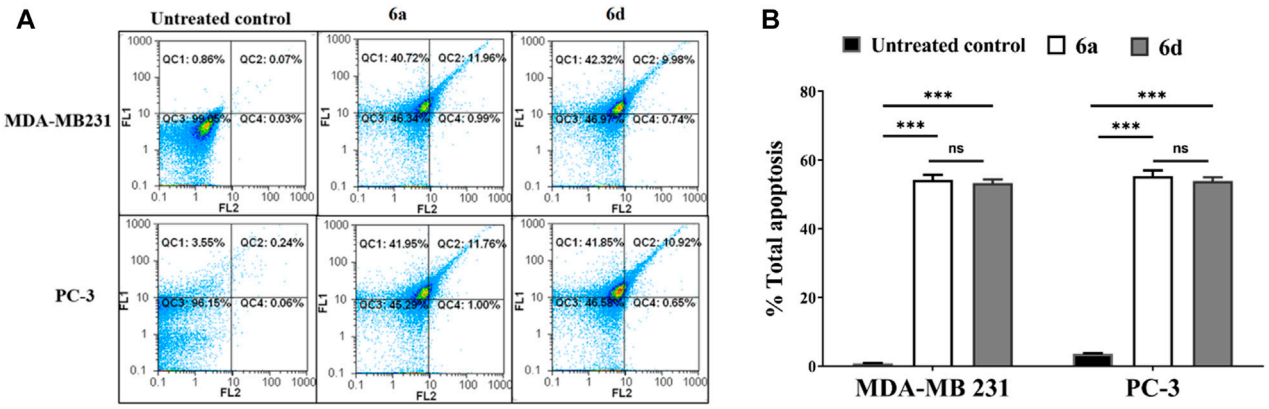

FIGURE 7
Flow analysis of the most active compounds-treated MDA-MB 231 and PC3 cell lines after dual staining with annexin and propidium iodide. **(A)** Flow charts and **(B)** the total percentage of the apoptotic cell population in the treated cancer cells. Data considered statistically significant at $p \leq 0.05$*, ≤0.005**, and ≤0.001***. ns: Not statistically significant.

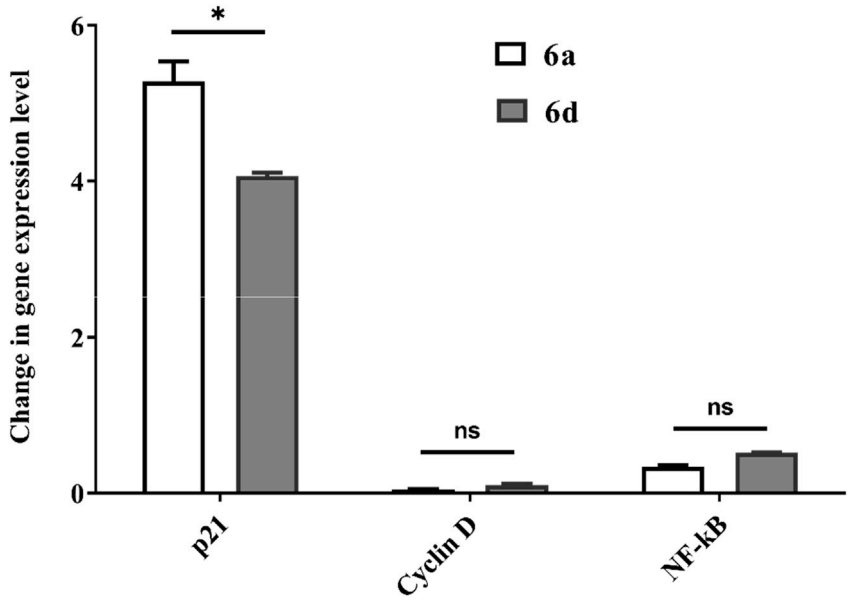

FIGURE 8
Relative change in gene expression of p21, cyclin-D, and NF-κB in the **6a** and **6d**-treated MDA-MB 231 cells. Data considered statistically significant at $p \leq 0.05$*, ≤0.005**, and ≤0.001***. ns: Not statistically significant.

compounds showed values similar to the standard; however, the number of rotatable bonds was three in compounds **6d** and **6h** and five in **6SJ**. These results highlight the importance of the number of rotatable bonds, as previously reported (Abdelhady et al., 2022).

3 Structure activity relationship

For MDM2 binding, compound **6h** showed stronger binding activity than **6d, 6i, 6b, 6l, 6a,** and **6e**. The electronic positions of the substituents on the phenyl rings of the benzaldehyde derivatives contributed in both the electronic and geometric properties of the final scaffolds. Compound **6h** contained a phenolic OH group at the meta position and formed a HB with Lys:94AA in the receptor. Furthermore, compound **6h** showed a unique orientation inside the receptor; none of the compounds overlapped with it. Compound **6d,** with a mildly activating group (Me) at the para position, showed low Logp and PSA values (Table 5). The PSA level was similar to that of **6SJ**. Compounds with electron-withdrawing groups, namely, *p*-Cl and *p*-Br, and thiophene moieties, exhibited lower activity, probably due to the electronic effect of the compound topology. The meta-position with formation of an extra HB was preferable for inhibitory activity (SI, Supplementary Figure S10).

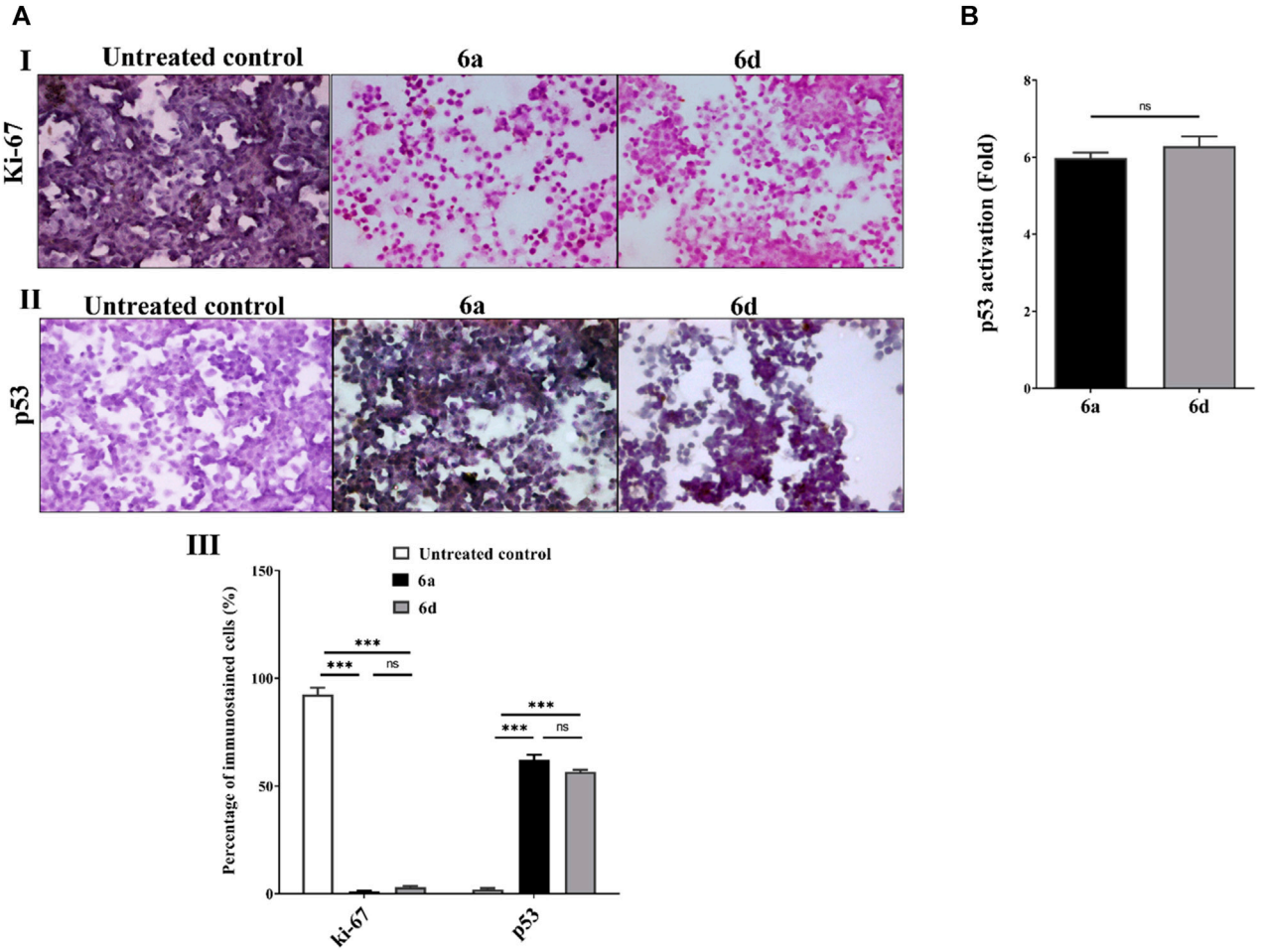

FIGURE 9
Immunohistochemical staining Ki-67 and p53 as well as fold increment in p53 activation in MDA-MB 231 cells. **(A)** Immunostaining pattern of **(I)** Ki-67 and (**II**) p53 in the untreated and **6a** and **6d**-treated MDA-MB 231 cells (magnificationx100) with (**III**) representative percentages of positive immunostaining MDA-MB 231 cells **(B)** Fold activation of p53 transcription factor in **6a** and **6d**-treated MDA-MB 231 cells relative to the untreated cells. Data considered statistically significant at $p \leq 0.05$*, ≤0.005**, and ≤0.001***. ns: Not statistically significant.

3.1 Experimental

3.1.1 General

"All chemicals were purchased from Aldrich, Sigma-Aldrich, and Fluka, and were used without further purification unless otherwise indicated. All melting points were measured using a Gallenkamp melting point apparatus in open glass capillaries and were uncorrected. The crude products were purified using silica gel through column chromatography (100–200 mesh). IR spectra were recorded as KBr pellets using a Nicolet 6700 FT-IR spectrophotometer. NMR spectra were recorded using a Varian Mercury Jeol-400 NMR spectrometer. ^{1}H NMR (400 MHz) and ^{13}C NMR (100 MHz) spectroscopy were performed in either deuterated dimethyl sulfoxide (DMSO-d_6) or deuterated chloroform ($CDCl_3$) (SI; Supplementary Figures S11–23). Chemical shifts (δ) are reported in ppm; coupling constant J *is* given in Hz. Elemental analysis was performed using an Elmer 2400 Elemental Analyzer in CHN mode. Chalcones **3a–n** was prepared as reported previously by (Alshahrani et al., 2023)".

3.1.2 General procedure for synthesis of spiro compounds (6a–n)

A mixture of chalcone derivative **3a–n** (0.5 mmol), thiazolidine-4-carboxylic acid (66.59 mg, 0.5 mmol), and isatin (73.57 mg, 0.5 mmol) in methanol (20 ml) was stirred at 60–65°C in an oil bath for 2–3 h. The final spirooxindole-based benzimidazole was separated using either by filtration if the final product precipitated or by column chromatography ((Silica Gel 60, granulometry 0.015–0.040 mm, Merck); eluent: EtOAc/nHexane gradient polarity according to the specified compound starting from 30: 70 until 50:50).

3.1.3 (3*S*,6′*R*)-6′-(1*H*-benzo [*d*]imidazole-2-carbonyl)-7′-phenyl-3′,6′,7′,7a′-tetrahydro-1′H-spiro [indoline-3.5′-pyrrolo [1,2-*c*]thiazol]-2-one (6a)

White solid; yield (89%); m.p: 240°C–242°C; IR (KBr, cm^{-1}): 3432 (NH), 3276 (NH), 3094 (CH), 2934 (CH), 1732 (CO), 1684 (CO); ^{1}H-NMR (400 MHz, DMSO-d_6): δ 12.95 (1H, s, NH), 10.39 (1H, s,

TABLE 3 MST binding assay results of MDM2.

#	Code	Chemical structures	K_D (μM)
1	**6a**	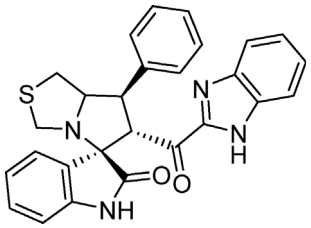	87.7
2	**6b**	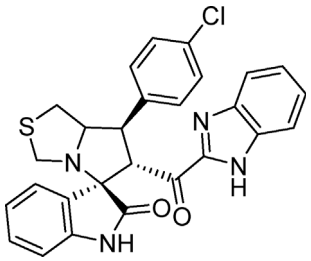	38.2
3	**6d**	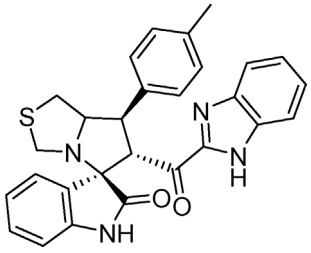	17.4
4	**6e**	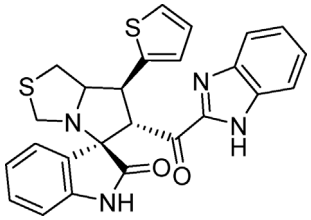	113
5	**6h**	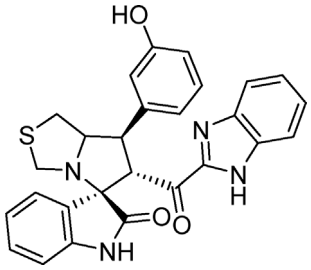	6.68
6	**6i**	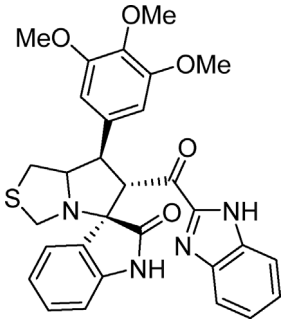	21

(Continued in next column)

TABLE 3 (*Continued*) MST binding assay results of MDM2.

#	Code	Chemical structures	K_D (μM)
7	**6l**	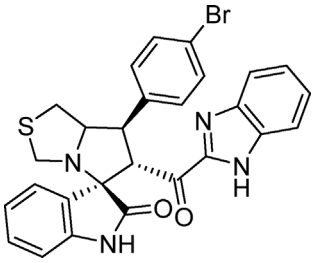	49.9

NH), 7.69 (1H, d, *J* = 8 Hz, ArH), 7.50 (2H, d, *J* = 8 Hz, ArH), 7.38–7.18 (7H, m, ArH), 6.99 (1H, t, *J* = 8 Hz, ArH), 6.84 (1H, t, *J* = 8 Hz, ArH), 6.44 (1H, d, *J* = 8 Hz, ArH), 5.17 (1H, d, *J* = 11.2 Hz, CHCO), 4.26 (1H, q, *J* = 8 Hz, CHN), 3.94 (1H, t, *J* = 10.2 Hz, CHPh), 3.68 (1H, d, *J* = 8.8 Hz), 3.40 (1H, d, *J* = 8.4 Hz), 3.18 (2H, d, *J* = 5.2 Hz), 2.98 (2 H, dd, *J* = 19.2, 5.3Hz); ^{13}C-NMR (101 MHz, DMSO-d_6): δ 190.05, 178.85, 147.94, 143.19, 142.94, 140.21, 135.11, 129.41, 128.55, 127.64, 124.31, 122.07, 113.19, 109.89, 74.51, 72.44, 63.53, 51.82, 50.08, 35.28; Anal. for $C_{27}H_{22}N_4O_2S$; calcd: C, 69.51; H, 4.75; N, 12.01; O, 6.86; S, 6.87; Found: C, 69.49; H, 4.77; N, 12.04; O, 6.82; S, 6.88.

3.1.4 (3*S*,6′*R*)-6′-(1*H*-Benzo [*d*]imidazole-2-carbonyl)-7′-(4-chlorophenyl)-3′,6′,7′,7a′-tetrahydro-1′*H*-spiro [indoline-3.5′-pyrrolo [1,2-*c*] thiazol]-2-one (6b)

Pale yellow solid; yield (57%); m.p.: 210–212°C; IR (KBr, cm^{-1}): 3434 (NH), 3277 (NH), 3093 (CH), 2929 (CH), 1729 (CO), 1682 (CO); ^{1}H-NMR (400 MHz, DMSO-d_6): δ 12.96 (1H, s, NH), 10.41 (1H, s, NH), 7.54 (3H, d, *J* = 8 Hz, ArH), 7.41 (3H, d, *J* = 8 Hz, ArH), 7.23 (3H, d, *J* = 7.3 Hz, ArH), 6.98 (1H, t, *J* = 7.6 Hz, ArH), 6.82 (1H, t, *J* = 7.6 Hz, ArH), 6.44 (1H, d, *J* = 7.8 Hz, ArH), 5.12 (1H, d, *J* = 11 Hz, CHCO), 4.23 (1H, q, *J* = 8 Hz, CHN), 3.95 (1H, t, *J* = 10 Hz, CHPh), 3.67 (1H, d, *J* = 8.8 Hz), 3.39 (2H, d, *J* = 8.8 Hz), 2.98 (2H, m); ^{13}C-NMR (101 MHz, DMSO-d_6): δ 189.91, 178.79, 147.91, 143.23, 139.26, 132.41, 130.42, 129.30, 124.23, 121.36, 109.96, 74.32, 72.35, 63.16, 49.17, 35.10, 27.77; Anal. for $C_{27}H_{21}ClN_4O_2S$; calcd: C, 64.73; H, 4.22; Cl, 7.08; N, 11.18; O, 6.39; S, 6.40; Found: C, 64.69; H, 4.27; Cl, 7.06; N, 11.20; O, 6.35; S, 6.43.

3.1.5 (3*S*,6′*R*)-6′-(1*H*-Benzo [*d*]imidazole-2-carbonyl)-7′-(4-(trifluoromethyl) phenyl)-3′,6′,7′,7a′-tetrahydro-1′*H*-spiro [indoline-3.5′-pyrrolo [1,2-*c*]thiazol]-2-one (6c)

Yellow solid; yield (13.5%); m.p.:185–187°C; IR (KBr, cm^{-1}): 3429 (NH), 3282 (NH), 3099 (CH), 2927 (CH), 1724 (CO), 1686 (CO); ^{1}H-NMR ($CDCl_3$, 400 MHz): δ 12.90 (1H, s, NH), 10.42 (1H, s, NH), 7.45 (2H, d, *J* = 8 Hz, ArH), 7.23 (4H, d, *J* = 8 Hz, ArH), 7.08 (1H, d, *J* = 8, ArH), 6.98 (1H, t, *J* = 7.7 Hz, ArH), 6.90 (1H, t, *J* = 7.7 Hz, ArH), 6.84 (1H, d, *J* = 7.3 Hz, ArH), 6.45 (2H, t, *J* = Hz, ArH), 5.16 (1H, d, *J* = Hz, CHCO), 4.24 (1H, q, *J* = Hz, CHN), 4.06 (1H, t, *J* = Hz, CHPh), 3.68 (2H, d, *J* = 8.8 Hz), 3.25 (1H, d, *J* = 12 Hz), 3.00 (2H, m); Anal. for $C_{28}H_{21}F_3N_4O_2S$; calcd: C, 62.91; H, 3.96; F, 10.66; N, 10.48; O, 5.99; S, 6.00; Found: C, 62.96; H, 3.92; F, 10.67; N, 10.42; O, 6.01; S, 6.02.

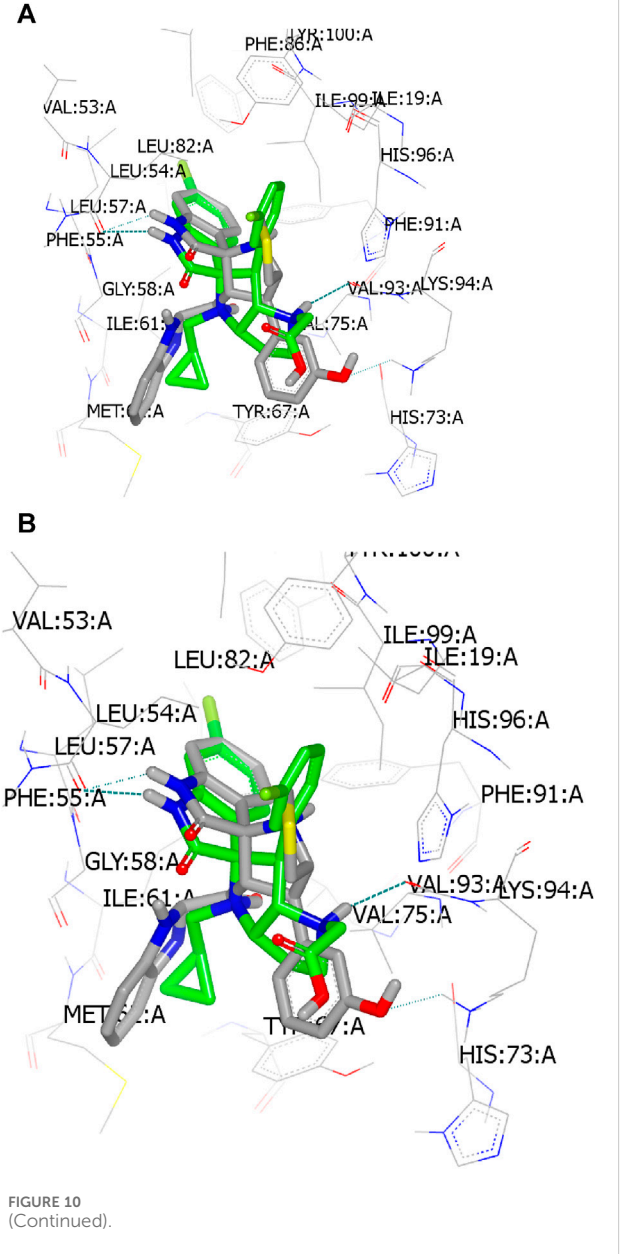

FIGURE 10
(Continued).

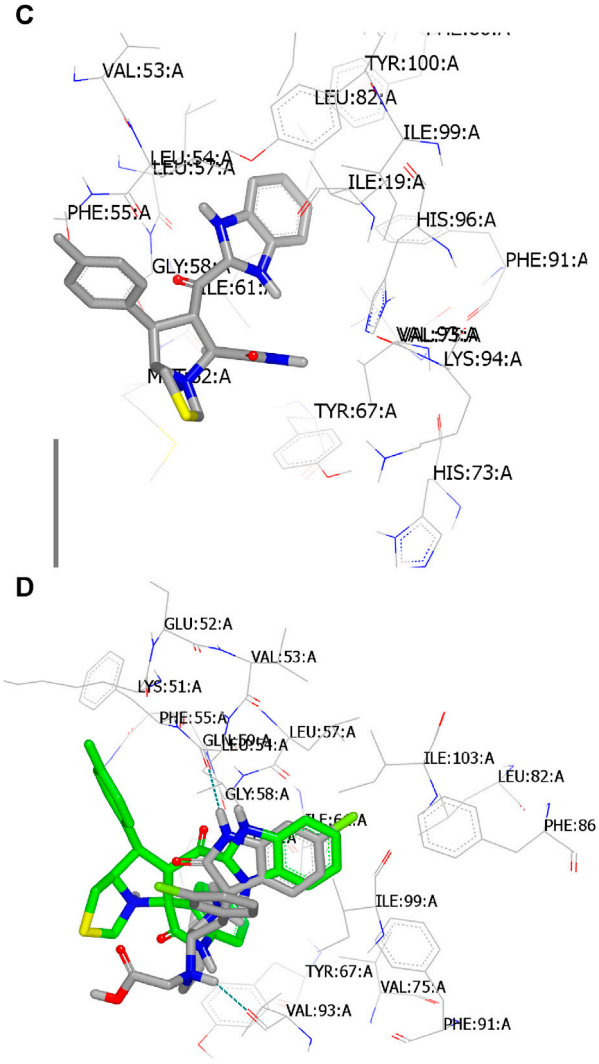

FIGURE 10
(Continued). Snap shot visualization of compounds docked with PDB: ID 5law as represented by Vida: **(A)** standard ligand re docked with its co-crystalized coordinate; **(B)** compound **6h** showed HB interaction with Leu:54AA, and with Lys:94AA (green dotted line); **(C)** compound **6d** docked with the receptor through formation of hydrophobic-hydrophobic interactions; **(D)** compound **6d** (green) in comparison with standard ligand **6SJ** (grey).

3.1.6 (3*S*,6′*R*)-6′-(1*H*-Benzo [*d*]imidazole-2-carbonyl)-7′-(p-tolyl)-3′,6′,7′,7a′-tetrahydro-1′*H*-spiro [indoline-3.5′-pyrrolo [1,2-*c*]thiazol]-2-one (6d)

White solid; yield (66%); m.p.:228–230°C; IR (KBr, cm^{-1}): 3649 (NH), 3277 (NH), 3087(CH), 2926 (CH), 1727 (CO), 1690 (CO); ^{1}H-NMR (400 MHz, DMSO-d_6): δ 12.94 (1H, s, NH), 10.37 (1H, s, NH), 7.69 (1H, d, J = Hz, ArH), 7.38–7.20 (6H, m, ArH), 7.15 (2H, d, J = Hz ArH), 6.99 (1H, t, J = 7.6 Hz, ArH), 6.84 (1H, t, J = 7.6 Hz, ArH), 6.44 (1H, d, J = 7.8 Hz, ArH), 5.15 (1H, d, J = 11.3 Hz, CHCO), 4.20 (1H, q, J = 8 Hz, CHN), 3.88 (1H, t, J = 10.6 Hz, CHPh), 3.67 (1H, d, J = 8.8 Hz), 3.39 (2H, d, J = 8.8 Hz), 3.18 (1H, d, J = 5.1 Hz), 2.96 (2H, m), 2.23 (3H, s, CH_3); ^{13}C-NMR (101 MHz, DMSO-d_6): δ 190.08, 178.84, 147.98, 143.16, 142.96, 137.03, 136.93, 135.10, 130.01, 128.37, 127.49, 126.34, 124.35, 123.43, 122.00, 121.94, 121.37, 113.28, 109.93, 74.49, 72.44, 63.24, 51.84, 49.89, 35.25, 21.23; Anal. for $C_{28}H_{24}N_4O_2S$; calcd: C, 69.98; H, 5.03; N, 11.66; O, 6.66; S, 6.67; Found: C, 69.95; H, 5.06; N, 11.68; O, 6.63; S, 6.68.

3.1.7 (3*S*,6′*R*)-6′-(1*H*-Benzo [*d*]imidazole-2-carbonyl)-7′-(thiophen-2-yl)-3′,6′,7′,7a′-tetrahydro-1′*H*-spiro [indoline-3.5′-pyrrolo [1,2-*c*] thiazol]-2-one (6e)

White solid; yield (76%); m.p.:240–242°C; IR (KBr, cm^{-1}): 3624 (NH), 3258 (NH), 3091(CH), 2927 (CH), 1728 (CO), 1689 (CO); ^{1}H-NMR (400 MHz, DMSO-d_6): δ 13.02 (1H, s, NH), 10.35 (1H, s, NH), 7.71 (1H, d, J = 8 Hz, ArH), 7.40 (1H, d, J = 5.1 Hz, CHS), 7.37–7.21 (4H, m, ArH), 7.12 (1H, d, J = 3.5 Hz, ArH), 7.04–6.94 (2H, m, ArH), 6.84 (1H, t, J = 7.5 Hz, ArH), 6.44 (1H, d, J = 7.5 Hz, ArH), 5.07 (1H, d, J = 10.3 Hz, CHCO), 4.25–4.18 (2H, m), 3.68 (1H, d, J = 9.3 Hz), 3.39 (1H, d, J = 9.1 Hz), 3.21–3.01 (4H, m); ^{13}C-NMR (101 MHz,

TABLE 4 Tanimto combo scores of designed compounds using 6SJ standard as ShapeQuery.

Vida name	Tanimoto combo	Shape tanimoto	Color tanimoto
6sj law standard	2	1	1
6n	0.902	0.658	0.244
6j	0.882	0.663	0.219
6e	0.843	0.634	0.209
6m	0.835	0.626	0.209
6d	0.834	0.625	0.209
6h	0.819	0.627	0.192
6a	0.816	0.598	0.218
6k	0.806	0.598	0.209
6b	0.805	0.587	0.218
6g	0.799	0.580	0.218
6l	0.797	0.588	0.209
6c	0.789	0.580	0.209
6i	0.710	0.535	0.175

DMSO-d_6): δ 189.66, 178.54, 147.84, 143.13, 143.00, 142.76, 135.15, 130.26, 127.66, 126.00, 124.01, 113.42, 109.93, 74.31, 72.66, 63.78, 52.25, 45.39, 35.45; Anal. for $C_{25}H_{20}N_4O_2S_2$; calcd: C, 63.54; H, 4.27; N, 11.86; O, 6.77; S, 13.57; Found: C, 63.49; H, 4.24; N, 11.84; O, 6.80; S, 13.63.

3.1.8 (3*S*,6′*R*)-6′-(1*H*-Benzo [*d*]imidazole-2-carbonyl)-7′-(4-fluorophenyl)-3′,6′,7′,7a′-tetrahydro-1′*H*-spiro [indoline-3.5′-pyrrolo [1,2-*c*] thiazol]-2-one (6f)

White solid; yield (31%); m.p.:233–235°C; IR (KBr, cm^{-1}): 3431 (NH), 3268 (NH), 3096 (CH), 2960 (CH), 1732 (CO), 1684 (CO); ^{1}H-NMR (400 MHz, DMSO-d_6): δ 12.95 (1H, s, NH), 10.39 (1H, s, NH), 7.68 (1H, d, *J* = 8 Hz, ArH), 7.54 (2H, t, *J* = 6.8 Hz, ArH), 7.36–7.14 (6H, m, ArH), 6.98 (1H, t, *J* = 7.7 Hz, ArH), 6.83 (1H, t, *J* = 7.7 Hz, ArH), 6.43 (1H, d, *J* = 7.4 Hz, ArH), 5.11 (1H, d, *J* = 11 Hz, CHCO), 4.20 (1H, q, J = 9.6 Hz, CHN), 3.95 (1H, t, *J* = 10.3 Hz, CHPh), 3.67 (1H, d, *J* = 8.8 Hz), 3.40 (1H, d, *J* = 12 Hz), 2.98 (2H, m); ^{13}C-NMR (101 MHz, DMSO-d_6): δ 189.97, 178.79, 169.71, 147.90, 143.21, 135.10, 130.23, 124.24, 72.33; Anal. for $C_{27}H_{21}FN_4O_2S$; calcd C, 66.93; H, 4.37; F, 3.92; N, 11.56; O, 6.60; S, 6.62; Found: C, 66.97; H, 4.34; F, 3.94; N, 11.53; O, 6.63; S, 6.59.

3.1.9 (3*S*,6′*R*)-6′-(1*H*-Benzo [*d*]imidazole-2-carbonyl)-7′-(2,4-dichlorophenyl)-3′,6′,7′,7a′-tetrahydro-1′*H*-spiro [indoline-3.5′-pyrrolo [1,2-*c*] thiazol]-2-one (6g)

White solid; yield (38%); m.p.:235–237°C; IR (KBr, cm^{-1}): 3436 (NH), 3281 (NH), 3090 (CH), 2925 (CH), 1730 (CO), 1685 (CO); ^{1}H-NMR (400 MHz, DMSO-d_6): δ 12.96 (1H, s, NH), 10.44 (1H, s, NH), 7.85 (1H, d, *J* = 8.5 Hz, ArH), 7.69 (1H, d, *J* = 8 Hz, ArH), 7.63 (1H, s, ArH), 7.51 (1H, d, *J* = 8 Hz, ArH), 7.34–7.14 (4H, m, ArH), 6.97 (1H, t, *J* = 7.6 Hz, ArH), 6.82 (1H, t, *J* = 7.6 Hz, ArH), 6.43 (1H, t, *J* = 7.6 Hz, ArH), 5.11 (1H, d, *J* = 10 Hz, CHCO), 4.57 (1H, t, *J* = 9.1 Hz, CHPh), 4.14 (1H, q, *J* = 8 Hz, CHN), 3.72 (1H, d, *J* = 8.8 Hz), 3.42 (1H, d, *J* = 8.8 Hz), 3.09 (1H, dd, *J* = 11, 5.9 Hz), 2.92 (1H, dd, *J* = 11, 4.4 Hz); ^{13}C-NMR (101 MHz, DMSO-d_6): δ 189.72, 178.88, 147.75, 143.42, 142.88, 137.30, 134.99, 132.88, 130.31, 129.50, 128.68, 127.37, 126.42, 123.69, 121.85, 121.39, 113.26, 109.96, 75.13, 72.88, 62.72, 52.52, 44.70, 35.44; Anal. for $C_{27}H_{20}Cl_2N_4O_2S$; calcd C, 60.56; H, 3.76; Cl, 13.24; N, 10.46; O, 5.98; S, 5.99; Found: C, 60.50; H, 3.71; Cl, 13.34; N, 10.41; O, 6.03; S, 6.01.

3.1.10 (3*S*,6′*R*)-6′-(1*H*-Benzo [*d*]imidazole-2-carbonyl)-7′-(3-hydroxyphenyl)-3′,6′,7′,7a′-tetrahydro-1′*H*-spiro [indoline-3.5′-pyrrolo [1,2-*c*] thiazol]-2-one (6h)

White solid; yield (82%); m.p.:205–207°C; IR (KBr, cm^{-1}): 3626 (NH), 3257 (OH), 2931 (CH), 1726 (CO), 1688 (CO); ^{1}H-NMR (400 MHz, DMSO-d_6): δ 12.94 (1H, s, NH), 10.36 (1H, s, NH), 9.46 (1H, s, OH), 7.69 (1H, d, *J* = 8 Hz, ArH), 7.33 (1H, d, *J* = 8 Hz, ArH), 7.28 (1H, t, *J* = 8 Hz, ArH), 7.21 (2H, d, *J* = 6.7 Hz, ArH), 7.13 (1H, t, *J* = 8 Hz, ArH), 6.98 (1H, t, *J* = 7.7 Hz, ArH), 6.89 (2H, d, *J* = 7.3 Hz, ArH), 6.83 (1H, t, *J* = 7.3 Hz, ArH), 6.62 (1H, d, *J* = 8 Hz, ArH), 6.43 (1H, d, *J* = 8 Hz, ArH), 5.14 (1H, d, *J* = 11.7 Hz, CHCO), 4.18 (1H, q, *J* = 8 Hz, CHN), 3.83 (1H, t, *J* = 10.3 Hz, CHPh), 3.66 (1H, d, *J* = 8.8 Hz), 3.02 (1H, dd, *J* = 11.0, 5.9 Hz), 2.92 (1H, dd, *J* = 10.6, 4.8 Hz); ^{13}C-NMR (101 MHz, DMSO-d_6): δ 190.06, 178.84, 158.20, 147.97, 143.14, 142.94, 141.56, 135.11, 130.12, 127.50, 124.36, 123.55, 121.88, 119.21, 114.98, 109.83, 72.32, 63.26, 51.59, 49.90, 35.27; Anal. for $C_{27}H_{22}N_4O_3S$; calcd C, 67.20; H, 4.60; N, 11.61; O, 9.95; S, 6.64; Found: C, 67.15; H, 4.64; N, 11.65; O, 9.91; S, 6.65.

3.1.11 (3*S*,6′*R*)-6′-(1*H*-Benzo [d]imidazole-2-carbonyl)-7′-(3,4,5-trimethoxyphenyl)-3′,6′,7′,7a′-tetrahydro-1′*H*-spiro [indoline-3.5′-pyrrolo [1,2-*c*] thiazol]-2-one (6i)

White solid; yield (70%); m.p.:245–247°C; IR (KBr, cm^{-1}): 3430 (NH), 3269 (NH), 3093 (CH), 2996 (CH), 1722 (CO), 1683 (CO);

10.3389/fphar.2024.1358089

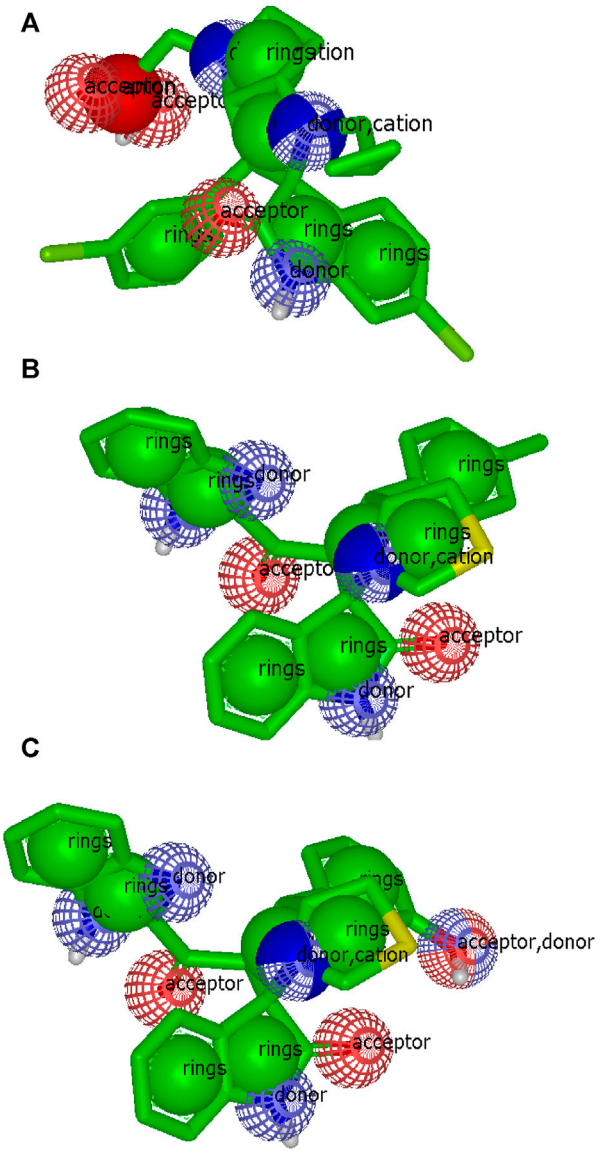

FIGURE 11
Topology display of color atoms and shape atoms. **(A)** standard **6SJ** (5 rings, 3 acceptors, 3 donors, 2 cations, 1 anion); **(B)** compound **6d** (7 rings, 2 acceptors, 4 donors, 1 cation; **(C)** compound **6h** (7 rings, 3 acceptors, 5 donors, 1 cation).

^{1}H-NMR (400 MHz, DMSO-d_6): δ 12.95 (1H, s, NH), 10.35 (1H, s, NH), 7.70 (1H, d, J = 8 Hz, ArH), 7.35–7.21 (5H, m, ArH), 7.00 (1H, t, J = 7.6 Hz, ArH), 6.85 (2H, d, J = 7.7 Hz, ArH), 6.46 (1H, d, J = 7.8 Hz, ArH), 5.13 (1H, d, J = 11 Hz, CHCO), 4.20 (1H, m, CHN), 3.88 (1H, t, J = 9.9 Hz, CHPh), 3.79 (6H, s, OCH_3), 3.69 (1H, d, J = 8.8 Hz), 3.60 (3H, s, OCH_3), 3.32 (2H, d, J = 3 Hz), 3.03 (2H, m); ^{13}C-NMR (101 MHz, DMSO-d_6): δ 190.06, 178.90, 153.56, 148.00, 143.13, 142.97, 137.12, 135.94, 135.08, 130.17, 127.79, 126.43, 124.10, 123.64, 121.88, 121.25, 109.89, 105.71, 74.66, 73.00, 62.56, 60.48, 56.47, 52.43, 50.62, 35.70; Anal. for $C_{30}H_{28}N_4O_5S$; calcd C, 64.73; H, 5.07; N, 10.07; O, 14.37; S, 5.76; Found: C, 64.69; H, 5.10; N, 10.11; O, 14.33; S, 5.77.

3.1.12 (3*S*,6′*R*)-6′-(1*H*-Benzo [d]imidazole-2-carbonyl)-7′-(2-hydroxyphenyl)-3′,6′,7′,7a′-tetrahydro-1′*H*-spiro [indoline-3.5′-pyrrolo [1,2-*c*] thiazol]-2-one (6j)

Pale yellow solid; yield (25%); m.p.:186–188°C; IR (KBr, cm^{-1}): 3311 (OH), 3063 (CH), 2925 (CH), 1716 (CO), 1667 (CO); ^{1}H-NMR (400 MHz, DMSO-d_6): δ 12.87 (1H, s, NH), 10.28 (1H, s, NH), 9.63 (1H, s, OH), 7.70 (1H, d, J = 8 Hz, ArH), 7.41 (1H, d, J = 8 Hz, ArH), 7.34–7.22 (4H, m, ArH), 7.05–6.98 (2H, m, ArH), 6.86–6.76 (3H, m, ArH), 6.44 (1H, d, J = 3 Hz, ArH), 5.40 (1H, d, J = 11.0 Hz, CHCO), 4.27–4.22 (1H, m, CHN), 3.68 (1H, t, J = 9.5 Hz, CHPh), 3.55–3.48 (2H, m), 3.33 (2H, d, J = 7.3 Hz); ^{13}C-NMR (101 MHz, DMSO-d_6): δ 190.40, 178.94, 156.17, 148.15, 143.14, 129.74, 129.31, 129.09, 128.33, 125.87, 124.22, 121.45, 119.85, 115.99, 109.78, 73.56, 73.05, 60.40, 52.69, 44.80, 35.87, 28.42; Anal. for $C_{27}H_{22}N_4O_3S$; calcd C, 67.20; H, 4.60; N, 11.61; O, 9.95; S, 6.64; Found: C, 67.26; H, 4.66; N, 11.54; O, 9.89; S, 6.65.

3.1.13 (3*S*,6′*R*)-6′-(1*H*-Benzo [d]imidazole-2-carbonyl)-7′-(4-(dimethylamino)phenyl)-3′,6′,7′,7a′-tetrahydro-1′*H*-spiro [indoline-3.5′-pyrrolo [1,2-*c*]thiazol]-2-one (6k)

Yellow solid; yield (45%); m.p.:178–180°C; IR (KBr, cm^{-1}): 3434 (NH), 3275 (NH), 3094 (CH), 2929 (CH), 1729 (CO), 1682 (CO); ^{1}H-NMR (400 MHz, DMSO-d_6): δ 12.91 (1H, s, NH), 10.33 (1H, s, NH), 7.69 (1H, d, J = 8 Hz, ArH), 7.35–7.21 (6H, m, ArH), 6.99 (1H, t, J = 7.7 Hz, ArH), 6.84 (1H, t, J = 7.3 Hz, ArH), 6.69 (2H, d, J = 8 Hz, ArH), 6.45 (1H, d, J = 8 Hz, ArH), 5.10 (1H, d, J = 11.7 Hz, CHCO), 4.20–4.10 (1H, m, CHN), 3.78 (2H, t, J = 10.6 Hz, CHPh), 3.67 (2H, d, J = 9.5 Hz), 3.54 (3H, d, J = 3.7 Hz), 2.95 (2H, m), 2.82 (6H, s, NCH_3); ^{13}C-NMR (101 MHz, DMSO-d_6): δ 190.23, 178.95, 150.25, 148.05, 143.04, 142.96, 135.07, 130.10, 128.96, 127.69, 127.02, 126.39, 124.37, 123.58, 121.93, 121.34, 113.35, 109.86, 74.50, 72.63, 63.05, 55.45, 52.21, 49.73, 40.70, 35.44; Anal. for $C_{29}H_{27}N_5O_2S$; calcd C, 68.35; H, 5.34; N, 13.74; O, 6.28; S, 6.29; Found: C, 68.45; H, 5.39; N, 13.54; O, 6.27; S, 6.26.

TABLE 5 Selected physiochemical properties of compounds 6d,h and standard 6SJ as generated by OpenEye software.

Compound	Molecular weight	LogP	PSA	No. of rotatable bond	No. of heavy atom	No. of donor	No. of acceptor
6SJ	488	3.19	75	5	33	4	6
6d	483	2.20	74	3	35	4	6
6h	485	3.19	94	3	35	5	7

3.1.14 (3*S*,6′*R*)-6′-(1*H*-Benzo [d]imidazole-2-carbonyl)-7′-(4-bromophenyl)-3′,6′,7′,7a′-tetrahydro-1′*H*-spiro [indoline-3.5′-pyrrolo [1,2-*c*] thiazol]-2-one (6l)

White solid; yield (80%); m.p.:172–174°C; IR (KBr, cm^{-1}): 3625 (NH), 3422 (NH), 3088 (CH), 2913 (CH), 1725 (CO), 1682 (CO); ^{1}H-NMR (400 MHz, DMSO-d_6): δ 12.95 (1H, s, NH), 10.40 (1H, s, NH), 7.68 (1H, d, J = 8 Hz, ArH), 7.55 (2H, d, J = 8 Hz, ArH), 7.47 (2H, d, J = 8.4 Hz, ArH), 7.36–7.19 (4H, m, ArH), 6.98 (1H, t, J = 7.6 Hz, ArH), 6.82 (1H, t, J = 7.6 Hz, ArH), 6.43 (1H, d, J = 7.6 Hz, ArH), 5.10 (1H, d, J = 10.9 Hz, CHCO), 4.24–4.14 (1H, m, CHN), 3.93 (1H, t, J = 8 Hz, CHPh), 3.67 (1H, d, J = 8.8 Hz), 3.38 (2H, d, J = 8.8 Hz), 3.04–2.92 (2H, m); ^{13}C- NMR (101 MHz, DMSO-d_6): δ 189.88, 178.76, 147.85, 143.23, 142.92, 139.67, 135.10, 132.27, 130.51, 130.10, 127.41, 124.21, 123.99, 121.47, 120.91, 113.25, 109.86, 74.15, 72.34, 62.95, 51.65, 49.41, 33.89; Anal. for $C_{27}H_{21}BrN_4O_2S$; calcd C, 59.45; H, 3.88; Br, 14.65; N, 10.27; O, 5.87; S, 5.88; Found: C, 59.51; H, 3.81; Br, 14.55; N, 10.31; O, 5.97; S, 5.85.

3.1.15 (3*S*,6′*R*)-6′-(1*H*-Benzo [d]imidazole-2-carbonyl)-7′-(3-fluorophenyl)-3′,6′,7′,7a′-tetrahydro-1′*H*-spiro [indoline-3.5′-pyrrolo [1,2-*c*] thiazol]-2-one (6m)

White solid; yield (30%); m.p.:224–226°C; IR (KBr, cm^{-1}): 3625 (NH), 3422 (NH), 3088 (CH), 2913 (CH), 1725 (CO), 1682 (CO); ^{1}H-NMR (400 MHz, DMSO-d_6) δ 12.97 (s, 1H, NH), 10.41 (s, 1H, NH), 7.68 (d, J = 8.1 Hz, 1H, ArH), 7.46–7.19 (m, 7H, ArH), 7.09 (t, J = 8.4 Hz, 1H, ArH), 6.98 (t, J = 7.7 Hz, 1H, ArH), 6.82 (t, J = 7.7 Hz, 1H, ArH), 6.43 (d, J = 7.3 Hz, 1H, ArH), 5.11 (d, J = 11.0 Hz, 1H, COCH), 4.22 (dt, J = 11.0, 5.5 Hz, 1H, CHN), 3.98 (t, J = 10.3 Hz, 1H, CHPh), 3.67 (d, J = 8.8 Hz, 1H), 3.38 (d, J = 5.1 Hz, 1H), 3.04 (dd, J = 11.0, 5.9 Hz, 1H), 2.96 (dd, J = 11.0, 5.9 Hz, 1H); ^{13}C-NMR (101 MHz, DMSO-d_6) δ 189.88, 178.79, 147.86, 143.36, 143.23, 142.91, 135.10, 131.42, 131.33, 130.20, 127.44, 126.44, 124.57, 124.17, 123.60, 121.90, 121.38, 115.37, 114.54, 113.27, 109.90, 74.36, 72.39, 63.35, 51.67, 49.41, 35.17; Anal. for $C_{27}H_{21}FN_4O_2S$; calcd C, 66.93; H, 4.37; F, 3.92; N, 11.56; O, 6.60; S, 6.62; Found: C, 66.84; H, 4.44; F, 3.95; N, 11.49; O, 6.60; S, 6.68.

3.1.16 (3*S*,6′*R*)-6′-(1*H*-Benzo [d]imidazole-2-carbonyl)-7′-(furan-2-yl)-3′,6′,7′,7a′-tetrahydro-1′*H*-spiro [indoline-3.5′-pyrrolo [1,2-*c*]thiazol]-2-one (6n)

White solid; yield (29%); m.p.:240–242°C; IR (KBr, cm^{-1}): 3435 (NH), 3256 (NH), 3090 (CH), 2928 (CH), 1729 (CO), 1687 (CO); ^{1}H-NMR (DMSO-d_6, 400 MHz): δ 13.01 (1H, s, NH), 10.33 (1H, s, NH), 7.71 (1H, d, J = 8 Hz, ArH), 7.58 (1H, d, J = 4 Hz, ArH), 7.38–7.18 (4H, m, ArH), 6.99 (1H, t, J = 7.7 Hz, ArH), 6.83 (1H, t, J = 7.7 Hz, ArH), 6.42 (1H, d, J = 8 Hz, ArH), 6.40–6.31 (2H, m), 5.14 (1H, d, J = 11 Hz, CHCO), 4.20 (1H, m, CHN), 4.02 (1H, t, J = 8 Hz, CHPh), 3.66 (1H, d, J = 9.5 Hz), 3.37 (2H, d, J = 8.8 Hz), 3.12 (2H, m); ^{13}C-NMR (DMSO-d_6, 100 MHz): δ 189.60, 178.55, 153.16, 147.78, 143.17, 142.99, 135.16, 126.57, 124.00, 110.01, 72.40; Anal. for $C_{25}H_{20}N_4O_3S$; calcd C, 65.77; H, 4.42; N, 12.27; O, 10.51; S, 7.02; Found: C, 65.73; H, 4.38; N, 12.31; O, 10.47; S, 7.11.

3.1.3 Computational details

"The ωB97X-D (Chai and Head-Gordon, 2008) functional, together with the standard 6–311G (d,p) basis set (Warren et al., 1986) were used in this MEDT study. The TSs were characterized by the presence of only one imaginary frequency. IRC (Fukui, 1970) calculations were performed to establish a unique connection between the TSs and corresponding minima (Gonzalez and Schlegel, 1990; Gonzalez and Schlegel, 1991). Solvent effects of methanol were considered through full optimization of gas phase structures at the same computational level using the polarizable continuum model (PCM) (Tomasi and Persico, 1994; Simkin and Sheikhet, 1995) in the framework of the self-consistent reaction field (SCRF) (Cossi et al., 1996; Cancès et al., 1997; Barone et al., 1998). Values of ωB97X-D/6–311G (d,p) enthalpies, entropies, and Gibbs free energies in methanol were calculated using standard statistical thermodynamics (Warren et al., 1986) at 337.8 K and 1 atm, with PCM frequency calculations at the solvent optimized structures.

The GEDT (Domingo, 2014) values were computed using the equation GEDT(f) = Σq_f, where q represents the natural charges (Reed et al., 1985; Reed et al., 1988) of the atoms belonging to one of the two frameworks (f) in the TS geometries. Global and local CDFT indices were calculated using the equations given in Domingo et al. (2016).

The Gaussian 16 program suite was used to perform the calculations. (Frisch et al. 2016) and ELF (Becke and Edgecombe, 1990) analyses of the ωB97X-D/6–311G (d,p) monodeterminantal wavefunctions were conducted using the TopMod (Noury et al., 1999) package with a cubical grid with a step size of 0.1 Bohr. AIM (Richard et al., 1982) calculations were performed using Multiwfn (Version 3.8) software (Lu and Chen, 2012). Molecular geometries and ELF basin attractors were visualized using GaussView (Serİn and Doğan Ulu, 2023)".

3.1.4 Molecular docking

The x-ray crystal structure coordinates of the angiotensin receptors were retrieved from PDB (PDB ID: 5law) (Gollner et al., 2016a) with their co-crystallized bound ligand and MDM2. The docking study was performed using OpenEye scientific software, version 2.2.5 (Santa Fe, NM, United States of America) (Gollner et al., 2016a). A virtual library of the synthesized compounds was used; their energies were minimized using the MMFF94 force field, followed by generation of multi-conformers using the OMEGA application. The library was compiled into one file using Omega software. The target proteins were retrieved from PDB, and the created receptor was operated using the OeDocking application. Both ligand and receptor input files were subjected to FRED in the molecular docking study. Multiple scoring functions were used to predict the energy profiles of the ligand–receptor complex. The Vida application was used for visualization. The dimensions for the created box of receptors were as follows. Box volume: 5544 A, dimensions: 21.00 A°×18.00 A° ×14.67 A°.

3.1.5 Shape similarity and ROCS analysis

ROCS analysis was performed using OpenEye scientific software. The compound library was used as a database file. Both the query and database files were energy-minimized using Omega applications. The

vROCS was used to run, analyze, and visualize the results. The ROCS application searches the database with a query to identify molecules with similar shapes and colors. The results were visualized using the Vida application. Compound conformers were scored based on the Gaussian overlap with the query. The best scoring parameters were the Tanimoto Combo scores (shape + color); the highest score indicated the best match with the query compound.

4 Conclusion

A new set of spirooxindole hybrids with a benzimidazole unit was designed, synthesized, and further assessed for anti-cancer reactivity. An MEDT study of the 32CA reaction of azomethine ylide (AY) **7a** with ethylene **3a** indicated that the reaction proceeded *via* a non-concerted *two-stage one-step* mechanism involving a highly asynchronous **TS-on** resulting from the nucleophilic attack of AY **7a** on the β-conjugated position of ethylene **3a**. Formation of two HBs at an earlier stage of the reaction accounted for the *ortho/endo* selectivities experimentally observed in these 32CA reactions. The anti-cancer reactivity results are promising; two compounds (**6a** and **6d**) were identified as most potent, safe, and as p53 activators in triple negative breast (MDA-MB 231) cancer cells to suppress expression, upregulating p21 expression by greater than three times and downregulating the expression of cyclin D and NF-kB. Moreover, the synthesized compounds showed high binding affinity for MDM2. Compound **6d** showed high similarity in binding mode to the co-crystallized standard ligand. Both compounds showed good physicochemical properties, which motivated us to investigate them further in preclinical studies.

Data availability statement

The original contributions presented in the study are included in the article/Supplementary Material, further inquiries can be directed to the corresponding author.

Author contributions

AB: Conceptualization, Funding acquisition, Supervision, Writing–original draft, Writing–review and editing. SA: Formal Analysis, Investigation, Methodology, Writing–review and editing. AA-M: Supervision, Visualization, Writing–review and editing. AA: Formal Analysis, Investigation, Methodology, Validation, Writing–review and editing. MH: Data curation, Formal Analysis, Software, Writing–review and editing. MA-S: Data curation, Formal Analysis, Software, Writing–original draft. AD: Formal Analysis, Supervision, Validation, Writing–review and editing. LD: Data curation, Investigation, Software, Validation, Writing–review and editing. YE: Data curation, Software, Validation, Writing–review and editing.

Funding

The author(s) declare financial support was received for the research, authorship, and/or publication of this article. The authors would like to extend their sincere appreciation to the Researchers Supporting Project (RSP2023R64), King Saud University, Riyadh, Saudi Arabia.

Acknowledgments

The authors would like to extend their sincere appreciation to the Researchers Supporting Project (RSP2024R64), King Saud University, Riyadh, Saudi Arabia, project number PID 2019-110776GB-I00 (AEI/FEDER, UE), and Ministerio de Ciencias, Innovación y Universidades of the Spanish Government.

Conflict of interest

The authors declare that the research was conducted in the absence of any commercial or financial relationships that could be construed as a potential conflict of interest.

Publisher's note

All claims expressed in this article are solely those of the authors and do not necessarily represent those of their affiliated organizations, or those of the publisher, the editors and the reviewers. Any product that may be evaluated in this article, or claim that may be made by its manufacturer, is not guaranteed or endorsed by the publisher.

Supplementary material

The Supplementary Material for this article can be found online at: https://www.frontiersin.org/articles/10.3389/fphar.2024.1358089/full#supplementary-material

References

Alshahrani, S., Al-Majid, A. M., Ali, M., Alamary, A. S., Abu-Serie, M. M., Dömling, A., et al. (2023). Rational design, synthesis, separation, and characterization of new spiroxindoles combined with benzimidazole scaffold as an MDM2 inhibitor. *Separations* 10 (4), 225. doi:10.3390/separations10040225

Amariucai-Mantu, D., Mangalagiu, V., and Mangalagiu, , II (2021). [3 + n] cycloaddition reactions: a milestone approach for elaborating pyridazine of potential interest in medicinal chemistry and optoelectronics. *Molecules* 26, 3359. doi:10.3390/molecules26113359

Aziz, Y. M. A., Lotfy, G., Said, M. M., El Ashry, E. S. H., El Tamany, E. S. H., Soliman, S. M., et al. (2021). Design, synthesis, chemical and biochemical insights into novel hybrid spirooxindole-based p53-MDM2 inhibitors with potential Bcl2 signaling attenuation. *Front. Chem.* 9, 735236. doi:10.3389/fchem.2021.735236

Barakat, A., Alshahrani, S., Al-Majid, A. M., Alamary, A. S., Haukka, M., Abu-Serie, M. M., et al. (2022). Novel spirooxindole based benzimidazole scaffold: *in vitro*, nanoformulation and *in vivo* studies on anticancer and antimetastatic activity of

breast adenocarcinoma. *Bioorg. Chem.* 129, 106124. doi:10.1016/j.bioorg.2022.106124

Barakat, A., Islam, M. S., Ghawas, H. M., Al-Majid, A. M., El-Senduny, F. F., Badria, F. A., et al. (2019). Design and synthesis of new substituted spirooxindoles as potential inhibitors of the MDM2–p53 interaction. *Bioorg. Chem.* 86, 598–608. doi:10.1016/j.bioorg.2019.01.053

Barone, V., Cossi, M., and Tomasi, J. (1998). Geometry optimization of molecular structures in solution by the polarizable continuum model. *J. Comput. Chem.* 19, 404–417. doi:10.1002/(sici)1096-987x(199803)19:4<404::aid-jcc3>3.3.co;2-l

Becke, A. D., and Edgecombe, K. E. (1990). A simple measure of electron localization in atomic and molecular systems. *Chem. Phys.* 92, 5397–5403. doi:10.1063/1.458517

Beloglazkina, A., Zyk, N., Majouga, A., and Beloglazkina, E. J. M. (2020). Recent small-molecule inhibitors of the p53–MDM2 protein–protein interaction. *Molecules* 25, 1211. doi:10.3390/molecules25051211

Błaszczak-Świątkiewicz, K. J. M. (2019). Antiproliferative aspect of benzimidazole derivatives' activity and their impact on NF-κB expression. *Molecules* 24, 3902. doi:10.3390/molecules24213902

Boggu, P., Venkateswararao, E., Manickam, M., Kim, Y., and Jung, S.-H. J. A. o. p. r. (2017). Exploration of SAR for novel 2-benzylbenzimidazole analogs as inhibitor of transcription factor NF-κB. *Arch. Pharm. Res.* 40, 469–479. doi:10.1007/s12272-017-0886-1

Boggu, P., Venkateswararao, E., Manickam, M., Kwak, D., Kim, Y., Jung, S.-H. J. B., et al. (2016). Exploration of 2-benzylbenzimidazole scaffold as novel inhibitor of NF-κB. *Biorg. Med. Chem.* 24, 1872–1878. doi:10.1016/j.bmc.2016.03.012

Cancès, E., Mennucci, B., and Tomasi, J. (1997). A new integral equation formalism for the polarizable continuum model: theoretical background and applications to isotropic and anisotropic dielectrics. *J. Chem. Phys.* 107, 3032–3041. doi:10.1063/1.474659

Chai, J.-D., and Head-Gordon, M. (2008). Long-range corrected hybrid density functionals with damped atom–atom dispersion corrections. *Phys. Chem. Chem. Phys.* 10, 6615–6620. doi:10.1039/b810189b

Chaudhry, G. E., Md Akim, A., Sung, Y. Y., and Sifzizul, T. M. T. (2022). Cancer and apoptosis: the apoptotic activity of plant and marine natural products and their potential as targeted cancer therapeutics. *Front. Pharmacol.* 13, 842376. doi:10.3389/fphar.2022.842376

Chen, J., Marechal, V., Levine, A. J. J. M., and Biology, c. (1993). Mapping of the p53 and mdm-2 interaction domains. *Mol. Cell. Biol.* 13, 4107–4114. doi:10.1128/mcb.13.7.4107

Cossi, M., Barone, V., Cammi, R., and Tomasi, J. (1996). *Ab initio* study of solvated molecules: a new implementation of the polarizable continuum model. *Chem. Phys. Lett.* 255, 327–335. doi:10.1016/0009-2614(96)00349-1

Demma, M., Maxwell, E., Ramos, R., Liang, L., Li, C., Hesk, D., et al. (2010). SCH529074, a small molecule activator of mutant p53, which binds p53 DNA binding domain (DBD), restores growth-suppressive function to mutant p53 and interrupts HDM2-mediated ubiquitination of wild type p53. *J. Biol. Chem.* 285, 10198–10212. doi:10.1074/jbc.M109.083469

Di Agostino, S., Strano, S., Emiliozzi, V., Zerbini, V., Mottolese, M., Sacchi, A., et al. (2006). Gain of function of mutant p53: the mutant p53/NF-Y protein complex reveals an aberrant transcriptional mechanism of cell cycle regulation. *Cancer Cell* 10, 191–202. doi:10.1016/j.ccr.2006.08.013

Docking, F. (2016). OpenEye scientific software. Receptor; Version 2.2. 5 Available at: http://www.eyesopen.com.

Domingo, L. R. (2014). A new C–C bond formation model based on the quantum chemical topology of electron density. *RSC Adv.* 4, 32415–32428. doi:10.1039/c4ra04280h

Domingo, L. R. (2016). Molecular electron density theory: a modern view of reactivity in organic chemistry. *Molecules* 21, 1319. doi:10.3390/molecules21101319

Domingo, L. R., Pérez, P., and Sáez, J. A. (2013). Understanding the local reactivity in polar organic reactions through electrophilic and nucleophilic Parr functions. *RSC Adv.* 3, 1486–1494. doi:10.1039/c2ra22886f

Domingo, L. R., Rios-Gutierrez, M., and Barakat, A. (2022). A molecular electron density theory study of the [3+2] cycloaddition reaction of an azomethine ylide with an electrophilic ethylene linked to triazole and ferrocene units. *Molecules* 27, 6532. doi:10.3390/molecules27196532

Domingo, L. R., Ríos-Gutiérrez, M., and Pérez, P. (2016). Applications of the conceptual density functional theory indices to organic chemistry reactivity. *Molecules* 21, 748. doi:10.3390/molecules21060748

Domingo, L. R., Rios-Gutierrez, M., and Perez, P. (2020). A molecular electron density theory study of the participation of tetrazines in aza-Diels-Alder reactions. *RSC Adv.* 10, 15394–15405. doi:10.1039/d0ra01548b

Domingo, L. R., Saéz, J. A., Zaragozá, R. J., and Arnó, M. (2008). Understanding the participation of quadricyclane as nucleophile in polar [2sigma + 2sigma + 2pi] cycloadditions toward electrophilic pi molecules. *J. Org. Chem.* 73, 8791–8799. doi:10.1021/jo801575g

Dunphy, G., Flannery, S. M., Almine, J. F., Connolly, D. J., Paulus, C., Jønsson, K. L., et al. (2018). Non-canonical activation of the DNA sensing adaptor STING by ATM and IFI16 mediates NF-κB signaling after nuclear DNA damage. *Mol. Cell* 71, 745–760. doi:10.1016/j.molcel.2018.07.034

Estrada-Ortiz, N., Neochoritis, C. G., and Dömling, A. J. C. (2016). How to design a successful p53–MDM2/X interaction inhibitor: a thorough overview based on crystal structures. *Chem. Med. Chem.* 11, 757–772. doi:10.1002/cmdc.201500487

Frisch, M. J., Trucks, G. W., Schlegel, H. B., Scuseria, G. E., Robb, M. A., Cheeseman, J. R., et al. (2016). *Gaussian 16*. Wallingford, CT: Rev. C.01.

Fukui, K. (1970). Formulation of the reaction coordinate. *J. Phys. Chem.* 74, 4161–4163. doi:10.1021/j100717a029

Gollner, A., Rudolph, D., Arnhof, H., Bauer, M., Blake, S. M., Boehmelt, G., et al. (2016b). Discovery of novel spiro [3 H-indole-3, 2′-pyrrolidin]-2 (1 H)-one compounds as chemically stable and orally active inhibitors of the MDM2–p53 interaction. *J. Med. Chem.* 59, 10147–10162. doi:10.1021/acs.jmedchem.6b00900

Gollner, A., Rudolph, D., Arnhof, H., Bauer, M., Blake, S. M., Boehmelt, G., et al. (2016a). Discovery of novel spiro[3H-indole-3,2′-pyrrolidin]-2(1H)-one compounds as chemically stable and orally active inhibitors of the MDM2–p53 interaction. *J. Med. Chem.* 59, 10147–10162. doi:10.1021/acs.jmedchem.6b00900

Gonzalez, C., and Schlegel, H. (1990). Reaction path following in mass-weighted internal coordinates. *J. Phys. Chem.* 94, 5523–5527. doi:10.1021/j100377a021

Gonzalez, C., and Schlegel, H. B. (1991). Improved algorithms for reaction path following: higher-order implicit algorithms. *Chem. Phys.* 95, 5853–5860. doi:10.1063/1.461606

Hsu, Y.-C., and Ip, M. (2011). Conjugated linoleic acid-induced apoptosis in mouse mammary tumor cells is mediated by both G protein coupled receptor-dependent activation of the AMP-activated protein kinase pathway and by oxidative stress. *Cell. Signal.* 23, 2013–2020. doi:10.1016/j.cellsig.2011.07.015

Islam, M. S., Al-Majid, A. M., Sholkamy, E. N., Barakat, A., Viale, M., Menichini, P., et al. (2023). Optimized spirooxindole-pyrazole hybrids targeting the p53-MDM2 interplay induce apoptosis and synergize with doxorubicin in A549 cells. *Sci. Rep.* 13, 7441. doi:10.1038/s41598-023-31209-3

Islam, M. S., Ghawas, H. M., El-Senduny, F. F., Al-Majid, A. M., Elshaier, Y. A., Badria, F. A., et al. (2019). Synthesis of new thiazolo-pyrrolidine–(spirooxindole) tethered to 3-acylindole as anticancer agents. *Bioorg. Chem.* 82, 423–430. doi:10.1016/j.bioorg.2018.10.036

Janjua, S. (2004). The guardian of genome: p53. *J. Pak. Assoc. Dermatol.* 14, 107–109.

Jonak, K., Kurpas, M., Szoltysek, K., Janus, P., Abramowicz, A., and Puszynski, K. (2016). A novel mathematical model of ATM/p53/NF- κB pathways points to the importance of the DDR switch-off mechanisms. *BMC Syst. Biol.* 10, 75. doi:10.1186/s12918-016-0293-0

Kandoth, C., Mclellan, M. D., Vandin, F., Ye, K., Niu, B., Lu, C., et al. (2013). Mutational landscape and significance across 12 major cancer types. *Nature* 502, 333–339. doi:10.1038/nature12634

Kussie, P. H., Gorina, S., Marechal, V., Elenbaas, B., Moreau, J., Levine, A. J., et al. (1996). Structure of the MDM2 oncoprotein bound to the p53 tumor suppressor transactivation domain. *Science* 274, 948–953. doi:10.1126/science.274.5289.948

Li, J., Viallet, J., and Haura, E. (2008). A small molecule pan-Bcl-2 family inhibitor, GX15-070, induces apoptosis and enhances cisplatin-induced apoptosis in non-small cell lung cancer cells. *Cancer Chemother. Pharmacol.* 61, 525–534. doi:10.1007/s00280-007-0499-3

Lotfy, G., Aziz, Y. M. A., Said, M. M., El Sayed, H., El Sayed, H., Abu-Serie, M. M., et al. (2021). Molecular hybridization design and synthesis of novel spirooxindole-based MDM2 inhibitors endowed with BCL2 signaling attenuation; a step towards the next generation p53 activators. *Bioorg. Chem.* 117, 105427. doi:10.1016/j.bioorg.2021.105427

Lu, T., and Chen, F. (2012). Multiwfn: a multifunctional wavefunction analyzer. *J. Comput. Chem.* 33, 580–592. doi:10.1002/jcc.22885

Millard, M., Pathania, D., Grande, F., Xu, S., and Neamati, N. J. C. p. d. (2011). Small-molecule inhibitors of p53-MDM2 interaction: the 2006-2010 update. *Curr. Pharm. Des.* 17, 536–559. doi:10.2174/138161211795222649

Murphy, S. H., Suzuki, K., Downes, M., Welch, G. L., De Jesus, P., Miraglia, L. J., et al. (2011). Tumor suppressor protein (p)53, is a regulator of NF-kappaB repression by the glucocorticoid receptor. *PNAS* 108, 17117–17122. doi:10.1073/pnas.1114420108

Noury, S., Krokidis, X., Fuster, F., and Silvi, B. J. C. C. (1999). Computational tools for the electron localization function topological analysis. *Comput. Chem.* 23, 597–604. doi:10.1016/s0097-8485(99)00039-x

Okolotowicz, K. J., Shi, R., Zheng, X., Macdonald, M., Reed, J. C., and Cashman, J. R. (2010). Selective benzimidazole inhibitors of the antigen receptor-mediated NF-kappaB activation pathway. *Bioorg. Med. Chem.* 18, 1918–1924. doi:10.1016/j.bmc.2010.01.039

Parr, R. (1983). Density functional theory. *Annu. Rev. Phys. Chem.* 34, 631–656. doi:10.1146/annurev.pc.34.100183.003215

Pires, B. R., Mencalha, A. L., Ferreira, G. M., De Souza, W. F., Morgado-Díaz, J. A., Maia, A. M., et al. (2017). NF-kappaB is involved in the regulation of EMT genes in breast cancer cells. *PLoS One* 12, e0169622. doi:10.1371/journal.pone.0169622

Poltz, R., and Naumann, M. (2012). Dynamics of p53 and NF-κB regulation in response to DNA damage and identification of target proteins suitable for therapeutic intervention. *BMC Syst. Biol.* 6, 125. doi:10.1186/1752-0509-6-125

Reed, A. E., Curtiss, L. A., and Weinhold, F. (1988). Intermolecular interactions from a natural bond orbital, donor-acceptor viewpoint. *Chem. Rev.* 88, 899–926. doi:10.1021/cr00088a005

Reed, A. E., Weinstock, R. B., and Weinhold, F. (1985). Natural population analysis. *Chem. Phys.* 83, 735–746. doi:10.1063/1.449486

Richard, F. W., Bader, T.-H. T., Yoram, T., and Friedrich, W. (1982). Properties of atoms and bonds in hydrocarbon molecules. *J. Am. Chem. Soc.* 104, 946–952. doi:10.1021/ja00368a004

Riedinger, C., and Mcdonnell, J. (2009). Inhibitors of MDM2 and MDMX: a structural perspective. *Future Med. Chem.* 1, 1075–1094. doi:10.4155/fmc.09.75

Ríos-Gutiérrez, M., Barakat, A., and Domingo, L. R. (2022). A molecular electron density theory study of the [3+2] cycloaddition reaction of pseudo(mono)radical azomethine ylides with phenyl vinyl sulphone. *Organics* 3, 122–136. doi:10.3390/org3020010

SerÎn, S., and Doğan Ulu, Ö. (2023). Theoretical insights into the effects of positional isomerism: DFT/TD-DFT approach. *Avrupa Bilim ve Teknol. Derg.*, 122–135. doi:10.5281/zenodo.10259308

Siegel, R. L., Miller, K. D., Fuchs, H. E., and Jemal, A. (2021). Cancer statistics, 2021. *CA Cancer J. Clin.* 71, 7–33. doi:10.3322/caac.21654

Simkin, B. I. A., and Sheikhet, I. I. (1995). *Quantum chemical and statistical theory of solutions: a computational approach*. London: Ellis Horwood London.

Tomasi, J., and Persico, M. (1994). Molecular interactions in solution: an overview of methods based on continuous distributions of the solvent. *Chem. Rev.* 94, 2027–2094. doi:10.1021/cr00031a013

Tovar, C., Graves, B., Packman, K., Filipovic, Z., Xia, B. H. M., Tardell, C., et al. (2013). MDM2 small-molecule antagonist RG7112 activates p53 signaling and regresses human tumors in preclinical cancer models. *Cancer Res.* 73, 2587–2597. doi:10.1158/0008-5472.CAN-12-2807

Vassilev, L. (2007). MDM2 inhibitors for cancer therapy. *Trends Mol. Med.* 13, 23–31. doi:10.1016/j.molmed.2006.11.002

Warren, J., Hehre, L. R., Paul von, R., and Schleyer, J. P. (1986). *AB INITIO molecular orbital theory*, 576. 978-0-471-81241-8.

Xia, Y., Shen, S., and Verma, I. (2014). NF-κB, an active player in human cancers. *Cancer Immunol. Res.* 2, 823–830. doi:10.1158/2326-6066.CIR-14-0112

Zhang, Z., Chu, X.-J., Liu, J.-J., Ding, Q., Zhang, J., Bartkovitz, D., et al. (2014). Discovery of potent and orally active p53-MDM2 inhibitors RO5353 and RO2468 for potential clinical development. *ACS Med. Chem. Lett.* 5, 124–127. doi:10.1021/ml400359z

Zhao, Y., Liu, L., Sun, W., Lu, J., Mceachern, D., Li, X., et al. (2013). Diastereomeric spirooxindoles as highly potent and efficacious MDM2 inhibitors. *J. Am. Chem. Soc.* 135, 7223–7234. doi:10.1021/ja3125417

frontiers | Frontiers in Pharmacology

TYPE Original Research
PUBLISHED 01 May 2024
DOI 10.3389/fphar.2024.1396605

Check for updates

OPEN ACCESS

EDITED BY
Wagdy Mohamed Eldehna,
Kafrelsheikh University, Egypt

REVIEWED BY
Mohammed Abu El-Magd,
Kafrelsheikh University, Egypt
Hazem Elkady,
Al-Azhar University, Egypt

*CORRESPONDENCE
Qian Wang,
qian.wang@bjmu.edu.cn

†These authors have contributed equally to this work

RECEIVED 06 March 2024
ACCEPTED 15 April 2024
PUBLISHED 01 May 2024

CITATION
Li Q, Li B, Wang Q, Wang C, Yu M and Xu T (2024), Marine-derived EGFR inhibitors: novel compounds targeting breast cancer growth and drug resistance.
Front. Pharmacol. 15:1396605.
doi: 10.3389/fphar.2024.1396605

COPYRIGHT
© 2024 Li, Li, Wang, Wang, Yu and Xu. This is an open-access article distributed under the terms of the Creative Commons Attribution License (CC BY). The use, distribution or reproduction in other forums is permitted, provided the original author(s) and the copyright owner(s) are credited and that the original publication in this journal is cited, in accordance with accepted academic practice. No use, distribution or reproduction is permitted which does not comply with these terms.

Marine-derived EGFR inhibitors: novel compounds targeting breast cancer growth and drug resistance

Qi Li[1†], Bo Li[1†], Qian Wang[1*†], Chengen Wang[2], Miao Yu[3] and Tianfu Xu[1]

[1]State Key Laboratory of Natural and Biomimetic Drugs, School of Pharmaceutical Sciences, Peking University, Beijing, China, [2]Department of Minimally Invasive Tumor Therapies Center, Beijing Hospital, National Center of Gerontology, Institute of Geriatric Medicine, Chinese Academy of Medical Sciences, Beijing, China, [3]Engineering Research Center for Medicine, Ministry of Education, Harbin University of Commerce, Harbin, China

Breast cancer (BC) continues to be a major health challenge globally, ranking as the fifth leading cause of cancer mortality among women, despite advancements in cancer detection and treatment. In this study, we identified four novel compounds from marine organisms that effectively target and inhibit the Epidermal Growth Factor Receptor (EGFR), crucial for BC cell growth and proliferation. These compounds not only induced early apoptosis through Caspase-3 activation but also showed significant inhibitory effects on EGFR mutations associated with drug resistance (T790M, L858R, and L858R/T790M), demonstrating high EGFR kinase selectivity. Cell Thermal Shift Assay (CETSA) experiments indicated that Tandyukisin stabilizes EGFR in a concentration-dependent manner. Furthermore, binding competition assays using surface plasmon resonance technology revealed that Tandyukisin and Trichoharzin bound to distinct sites on EGFR and that their combined use enhanced apoptosis in BC cells. This discovery may pave the way for developing new marine-derived EGFR inhibitors, offering a promising avenue for innovative cancer treatment strategies and addressing EGFR-mediated drug resistance.

KEYWORDS

breast cancer (BC), EGFR inhibitors, marine-derived compounds, apoptosis induction, EGFR kinase selectivity

1 Introduction

Breast cancer, a prevalent malignancy among women, poses a significant threat to their health and well-being (Torre et al., 2015). Characterized by its high heterogeneity, breast cancer presents a challenge in drug selection and sensitivity due to the vast molecular diversity observed even among patients with similar pathological features (Shigematsu et al., 2018). This variability often results in markedly different prognoses (Sun et al., 2021). The current clinical approach to treating breast cancer involves a comprehensive strategy primarily centered on surgery, with adjunctive treatments including radiotherapy, chemotherapy, endocrine therapy, and targeted therapy. The advent of molecular targeted therapy has revolutionized breast cancer treatment by focusing on the signaling pathways pivotal to the cancer's genesis and progression. This method offers treatment at the cellular and molecular levels, enabling the specific elimination of cancer

cells while sparing healthy surrounding tissue (Walker et al., 2015). Such advancements have significantly enhanced the prognosis for breast cancer patients, marking a new era in the biological treatment of this disease.

Targeted therapies for breast cancer specifically focus on molecules crucial for the growth and survival of cancer cells. Among these, HER2-targeting agents such as trastuzumab (Herceptin), pertuzumab (Perjeta), ado-trastuzumab emtansine (Kadcyla), and lapatinib (Tykerb) have shown significant efficacy (Swain et al., 2023). Additionally, CDK4/6 inhibitors, including palbociclib (Ibrance), ribociclib (Kisqali), and abemaciclib (Verzenio) (Pandey et al., 2019), offer a strategic advantage when combined with hormone therapy for certain breast cancer subtypes.

The Epidermal Growth Factor Receptor (EGFR), also known as ErbB1 or HER1, serves as the foundational member of the ErbB/HER family of receptor tyrosine kinases (RTKs). This receptor plays a critical role in regulating developmental processes via several signaling pathways, including the phosphatidylinositol 3-kinase (PI3K)/Akt, Ras/Raf/MEK/ERK, and STAT3 pathways (Burgess, 2008). EGFR, upon ligand binding, is capable of forming either homodimers with itself or heterodimers with its family counterparts-ErbB2/HER2, ErbB3/HER3, and ErbB4/HER4. This dimerization triggers conformational changes that activate the kinase domain of the receptor (Zhang et al., 2006; Ferguson, 2008; Jura et al., 2009). Overactivation of EGFR signaling, whether through point mutations, intragenic deletions, or overexpression, has been conclusively linked to the pathogenesis of various diseases, underscoring its significance in cellular regulation and disease development (Normanno et al., 2006; Roskoski, 2014).

Research indicates that the EGFR plays a crucial role in the initiation, progression, and metastasis of primary breast cancer (Lakis et al., 2016). Notably, EGFR is overexpressed in a wide range of breast cancer cells, including in approximately 50% of triple-negative breast cancers (TNBC). TNBC is characterized by the absence of estrogen receptors, progesterone receptors, and HER2, which contributes to poor clinical outcomes and a scarcity of effective therapeutic options (Nielsen et al., 2004; Alvarez et al., 2010; Harbeck and Gnant, 2017). In TNBC, the overexpression of EGFR leads to the constant activation of the PI3K/AKT/mTOR signaling pathway (El Guerrab et al., 2020). The synergistic application of EGFR and mTOR inhibitors has been shown to significantly enhance the anti-tumor efficacy of these drugs. Furthermore, combinations such as the EGFR-targeting drug erlotinib with bevacizumab, and cetuximab with cisplatin, have demonstrated substantial benefits in extending the survival time of breast cancer patients (Symonds et al., 2019) and alleviating symptoms (Baselga et al., 2013), respectively. Additionally, a clinical study (NCT00066378) has revealed that EGFR tyrosine kinase inhibitors (TKIs) can postpone the development of endocrine resistance in breast cancer. Consequently, EGFR presents a promising target for the development of effective breast cancer treatments.

Currently, third-generation drugs targeting the EGFR are predominantly employed in the treatment of non-small cell lung cancer (NSCLC). At the initial stages of NSCLC treatment, EGFR TKIs demonstrate significant efficacy. First- and second-generation EGFR-TKIs, such as gefitinib and afatinib, have shown considerable success in managing advanced NSCLC in patients with activating EGFR mutations. However, resistance often develops due to EGFR T790M mutations (Recondo et al., 2018), which do not hinder the binding of TKIs to EGFR but rather enhance the affinity of EGFR for ATP (Yun et al., 2008). To address the challenge of resistance mediated by EGFR T790M mutations, third-generation EGFR-TKIs, exemplified by osimertinib, achieve irreversible inhibition of EGFR kinase activity. This is accomplished through the formation of a covalent bond with the C797 residue of the EGFR kinase domain (Zeng et al., 2022). Despite this advancement, patients undergoing treatment with third-generation EGFR-TKIs may eventually exhibit resistance mechanisms independent of EGFR, often several months post-treatment. Presently, fourth-generation EGFR-TKIs are under development and have not yet received clinical approval, indicating that significant research and development efforts remain necessary to overcome these emerging resistance pathways.

The combination of breast cancer-targeting drugs with EGFR-TKIs holds promising potential in significantly enhancing drug efficacy, underscoring the importance of discovering a newer generation of EGFR-TKIs for breast cancer treatment. However, first-generation EGFR-TKIs exhibit severe hepatotoxicity and skin toxicity, while second-generation EGFR-TKIs present even more pronounced adverse reactions. Although third-generation EGFR-TKIs boast reduced incidence of adverse effects compared to their predecessors, they still pose risks such as diarrhea, rash, dry skin, paronychia, QTc interval prolongation on electrocardiograms, and interstitial pneumonia. Consequently, there exists an urgent imperative to explore novel EGFR inhibitors characterized by structural diversity, enhanced safety profiles, and heightened efficacy.

In our study, we identified a novel EGFR inhibitor, characterized by a unique chemical structure derived from marine organisms. This inhibitor demonstrated the capacity to concurrently suppress the enzymatic activities of both the wild-type EGFR and its pathogenic mutants at nanomolar concentrations, exhibiting notable selectivity for tyrosine kinase inhibition. Cellular Thermal Shift Assay (CETSA) results affirmed the inhibitor's effective intracellular engagement with EGFR. Tandyukisin demonstrated significant inhibitory activity against cancer cells expressing high levels of EGFR, while exhibiting negligible inhibitory effects on both low EGFR-expressing cancer cells and normal human breast cells. These findings suggested that Tandyukisin possessed enhanced selectivity for cancer cells and exhibited reduced cytotoxicity towards normal cells. Moreover, our findings from flow cytometry and Western Blot (WB) analyses indicated that this inhibitor induced Caspase-3 activation via the mitochondrial pathway, thereby facilitating early apoptosis in cancer cells. Importantly, synergistic effects were observed when this inhibitor was used in combination with other inhibitors targeting distinct regions of EGFR, namely, the extracellular ligand-binding domain and the intracellular kinase domain, leading to a significant enhancement in the suppression of breast cancer cell proliferation.

2 Materials and methods

2.1 Materials

The extracellular ligand-binding domain of EGFR, tagged with His, and the intracellular tyrosine kinase (TK) domain of EGFR, tagged with GST, were acquired from Sinobiological, China. Kinase assay systems for both wild-type EGFR and its mutants—T790M,

L858R, and the dual L858R/T790M—were procured from Promega Corporation, USA. Cell lines including MCF-7, A549, A431, H1299, HL-60, and MCF-10A were obtained from the China Infrastructure Cell Line Resources.

2.2 Cell culture

The cell lines MCF-7 and A431 were cultured in Dulbecco's Modified Eagle's Medium (DMEM, Gibco, USA), while HL-60, H1299, and A549 cells were maintained in RPMI-1640 medium (Gibco, USA). Both mediums were enriched with 10% fetal bovine serum and 1% penicillin/streptomycin. The MCF-10A cell line was cultured in a 1:1 mixture of DMEM and F12 medium (Gibco), supplemented with 5% horse serum, 10 μg/mL insulin, 0.1 μg/mL cholera toxin, 0.5 μg/mL hydrocortisone, and 0.02 μg/mL epidermal growth factor (EGF). All cell cultures were incubated at 37°C in an atmosphere containing 5% CO2.

2.3 MTT assay

Cells in the exponential growth phase were seeded into 96-well plates and allowed to adhere overnight. Subsequently, they were treated in triplicate with various concentrations of the compounds (0, 1.56, 3.13, 6.25, 12.5, 25, 50, 100 μM), either with or without. After 24 h, 20 μL of Methyl-thiazolyldiphenyl-tetrazolium bromide (MTT, 5 mg/mL, Thermo Fisher Scientific) was added to each well and incubated for a minimum of 4 h. Following the incubation, the medium containing the compounds and MTT was removed from each well, and 200 μL of dimethyl sulfoxide (DMSO) was added. The plates were then shaken for 10 min at 37°C to dissolve the formazan crystals. The absorbance was measured using a microplate reader (BioTek Synergy 4) at a wavelength of 490 nm.

2.4 Cell cycle and early stage apoptosis analysis

After 24 h of treatment with various concentrations of compounds, MCF-7 cells were harvested and washed twice with phosphate-buffered saline (PBS). For cell cycle analysis, the cells were initially fixed with 70% ethanol at 4°C overnight and subsequently washed with PBS. The fixed cells were then resuspended in 1× PBS containing 0.5% Triton X-100, 50 μg/mL propidium iodide (PI), and 50 μg/mL DNase-free RNase A, and incubated at 37°C for 30 min in darkness. Following incubation, cell cycle distribution was assessed using a BD FACSCanto™ flow cytometer.

Apoptosis was evaluated using the Annexin V-FITC/PI Apoptosis Detection Kit (Vazyme). The harvested MCF-7 cells were first resuspended in 1× binding buffer from the kit to achieve a final concentration of 1×10^6 cells/ml. Next, 100 μL of the cell suspension, 5 μL of Annexin V, and 10 μL of PI were mixed and incubated in the dark for 15 min. Subsequently, 400 μL of 1× binding buffer was added to the mixture in preparation for apoptosis analysis.

2.5 Western blotting

MCF-7 cell lysates were prepared by rinsing the cells twice with PBS and then solubilizing them in lysis buffer (NP40 supplemented with protease and phosphatase inhibitor cocktails) on ice. The solubilization process involved rotating the lysis buffer/cell mixture end over end for 10 min at 4°C. After centrifugation for 10 min at 4°C to remove insoluble material, the protein concentration of the solubilized protein was determined using a BCA assay. Subsequently, samples were diluted in SDS sample buffer. Equivalent amounts of protein were separated by SDS-PAGE, transferred to PVDF membranes, and probed with the indicated antibody. Prior to incubation with primary antibodies overnight at 4°C, the membranes were blocked with 5% skim milk-TBST. The antibodies and their sources were as follows: PARP1 (1:500, Santa Cruz Biotechnology), Cleaved Caspase-3 (1:1000, Cell Signaling Technology), BAX (1:500, Santa Cruz Biotechnology), BCL-2 (1:500, Santa Cruz Biotechnology), and GAPDH (1:500, Santa Cruz Biotechnology). Following incubation with horseradish peroxidase-conjugated goat anti-mouse or goat anti-rabbit secondary antibody (Santa Cruz Biotechnology), the detected proteins were visualized using the Pierce Enhanced Chemiluminescence (ECL) reagent and a UV Products imaging system. Band intensities were quantified using the National Institutes of Health ImageJ software.

2.6 Kinase inhibition assays

The experiments were conducted in accordance with the manufacturer's guidelines (Promega). The procedure began with a kinase reaction, where 5 μL of 1× kinase buffer was utilized, and the mixture was incubated at room temperature for 60 min. This step was followed by the addition of 5 μL of ADP-Glo™ reagent to terminate the kinase reaction and to deplete any remaining ATP, with a subsequent incubation period of 40 min at room temperature. Next, 10 μL of kinase detection reagent was added to convert ADP back into ATP, and luciferase along with luciferin was introduced to facilitate ATP detection. This mixture was then incubated at room temperature for an additional 30 min. Detection was carried out using a BioTek Synergy4 instrument, and data analysis, including curve fitting and presentation, was performed using GraphPad Prism version 5.0. Staurosporine, a potent indolecarbazole alkaloid, was employed as a specific inhibitor of protein kinases to validate the specificity of the assay (Omura et al., 1977; Song et al., 2017; Abou-Zied et al., 2019).

2.7 EGFR thermal stability analysis

In the CETSA, MCF-7 cells were treated with varying concentrations of Tandyukisin (5, 10, 20 μM) or a control solution of 0.2% DMSO for 24 h. Following treatment, cells were harvested and washed with PBS to eliminate any residual drug, then an equal number of cells were allocated into 0.2 mL PCR tubes. These cells were resuspended in 100 μL PBS supplemented with a complete protease inhibitor cocktail and subjected to a heating step at 50°C for 3 min. Post-heating, the cells underwent lysis through three cycles of

freeze-thaw using liquid nitrogen, followed by centrifugation at 12,000g for 20 min at 4°C to separate the lysate. The clarified supernatant from each tube was then carefully transferred to fresh tubes for Western blotting.

In the Differential Scanning Fluorimetry (DSF) study, concentrations of Tandyukisin-1.3, 2.5, 5, and 10 μM-were incubated with 0.05 mg/mL of the EGFR kinase domain. A control sample, containing only 5% DMSO, was used alongside the EGFR kinase domain. The thermal stability of the EGFR kinase domain was assessed using PR NT.48 (NanoTemper). The assay conditions were set to a temperature range of 25°C–95°C with a ramp rate of 1 °C/min.

2.8 Surface plasmon resonance (SPR) experiments

The binding affinities of compounds towards EGFR extracellular ligand binding domain and EGFR intracellular kinase domain were assayed using the SPR-based Biacore 8K instrument (Cytiva). Considering the purchased EGFR was fused with GST tag, GST alone was also immobilized on the chip to do the binding measurement. All the proteins were respectively immobilized on a CM5 sensor chip by using standard amine-coupling at 25°C with running buffer HEPES-P (20 mM HEPES buffer, 2.7 mM NaCl, 137 mM KCl, 0.05% surfactant P20, pH 7.4). A reference channel was only activated and blocked to eliminate compound unspecific binding to the surface of the chip. The immobilization level of EGFR extracellular ligand binding domain, EGFR intracellular kinase domain and GST were all about 10,000 RU. Different concentrations of compounds containing 5% DMSO were serially injected into the channel to evaluate the binding affinity. Extra wash with 50% DMSO was added to remove the last remaining sample in the pipeline. The association constants (k_a), the dissociation constants (k_d) and the equilibrium dissociation constants (K_D) of the compounds were obtained by fitting the data sets to 1:1 Langmuir binding model using Biacore 8K Evaluation Software.

2.9 SPR based competition experiments

To elucidate the binding sites of the compounds exhibiting the highest affinity towards the extracellular ligand-binding domain and intracellular kinase domain of EGFR, Trichoharzin and Tandyukisin were selected based on their optimal binding affinities for competition experiments with EGF and ATP, respectively.

In the EGF competition experiments, a buffer scouting strategy using the A-B-A mode from the Biacore 8K method wizard was employed to assess the impact of EGF on the binding affinity of Trichoharzin and *vice versa*, towards the EGFR extracellular ligand-binding domain. The protocol fixed the pre-flank contact time, analyte contact time, and post-flank contact time at 60 s, 60 s, and 120 s, respectively. To evaluate the influence of EGF on Trichoharzin, A represented a single concentration of EGF, whereas B denoted a combination of varying concentrations of Trichoharzin with the identical EGF concentration as in A. Conversely, to examine the effect of Trichoharzin on EGF, A indicated a single concentration of Trichoharzin, and B comprised various EGF concentrations mixed with the same concentration of Trichoharzin as in A.

For ATP competition experiments, the LWM kinetic/affinity analysis protocol from the Biacore 8K method wizard was utilized to determine the effect of ATP on the binding affinity of compounds to the EGFR intracellular kinase domain. The investigation involved running buffers both with and without 1 mM ATP to ascertain whether ATP and the compounds compete for the same binding site.

2.10 Molecular docking and molecular dynamics simulation

The program Glide Standard Precise (SP) mode and Extra Precise (XP) mode with default parameters were proposed to do the molecular docking studies. The crystal structure of EGFR intracellular kinase domain (PDB code: 5CAV), CDK4 (PDB code: 2W96), CDK6 (PDB code: 3NUP), mTOR (PDB code: 3OAW), and HER2 (PDB code: 5O4G) was used as the target receptor for the docking of the compound. Tandyukisin with best cancer cell inhibition activities was successively docked into the above functional binding sites. Binding mode from XP was used to analyze key interactions between molecules and the corresponding binding site.

The docking results from Glide XP was also used for the binding mode prediction of Trichoharzin in EGFR extracellular ligand binding domain (PDB code: 1IVO).

Molecular dynamics (MD) simulations of ligand-protein complexes were conducted using Desmond in Schrodinger. Initially, a water model was established utilizing the System Builder tool, followed by the addition of sodium and chloride ions to achieve neutralization. The minimization processes employed the OPLS3 force field. Subsequently, the complexes underwent simulations for 1 ns and an extended 100 ns under NPT conditions at a temperature of 300 K. Trajectory analysis facilitated the extraction of key parameters, including the root mean square deviation (RMSD), root mean square fluctuation (RMSF), ligand contact maps, and binding profiles from the simulation data.

2.11 Synergistic experiments between Tandyukisin and Trichoharzin in enzymatic and cell-based assays

MCF-7 cells were seeded at a density of 5,000 cells per well in 96-well plates and allowed to adhere overnight. Subsequently, the cells were treated with various concentrations of Trichoharzin (0, 1.56, 3.125, 6.25, 12.5, 25, 50 μM) and Tandyukisin (0, 1.56, 3.125, 6.25, 12.5, 25, 50 μM) for 24 h. The efficacy of these treatments was assessed using the MTT assay to determine the inhibitory effects of the compound combinations.

In the enzymatic assay examining the combination of Tandyukisin and Trichoharzin, Tandyukisin was used at various concentrations (0, 0.31, 0.63, 1.25, 2.5, 5, 10, 20 nM). Each concentration of Tandyukisin was then combined with differing concentrations of Trichoharzin (0, 0.31, 0.63, 1.25, 2.5, 5, 10, 20 nM). The resultant mixtures were pre-incubated with enzyme samples to evaluate their inhibitory effects on EGFR activity.

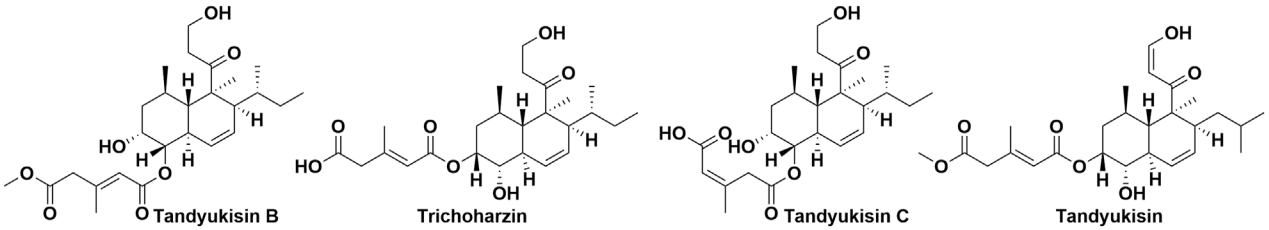

FIGURE 1
The chemical structures of Tandyukisin B, Trichoharzin, Tandyukisin C and Tandyukisin.

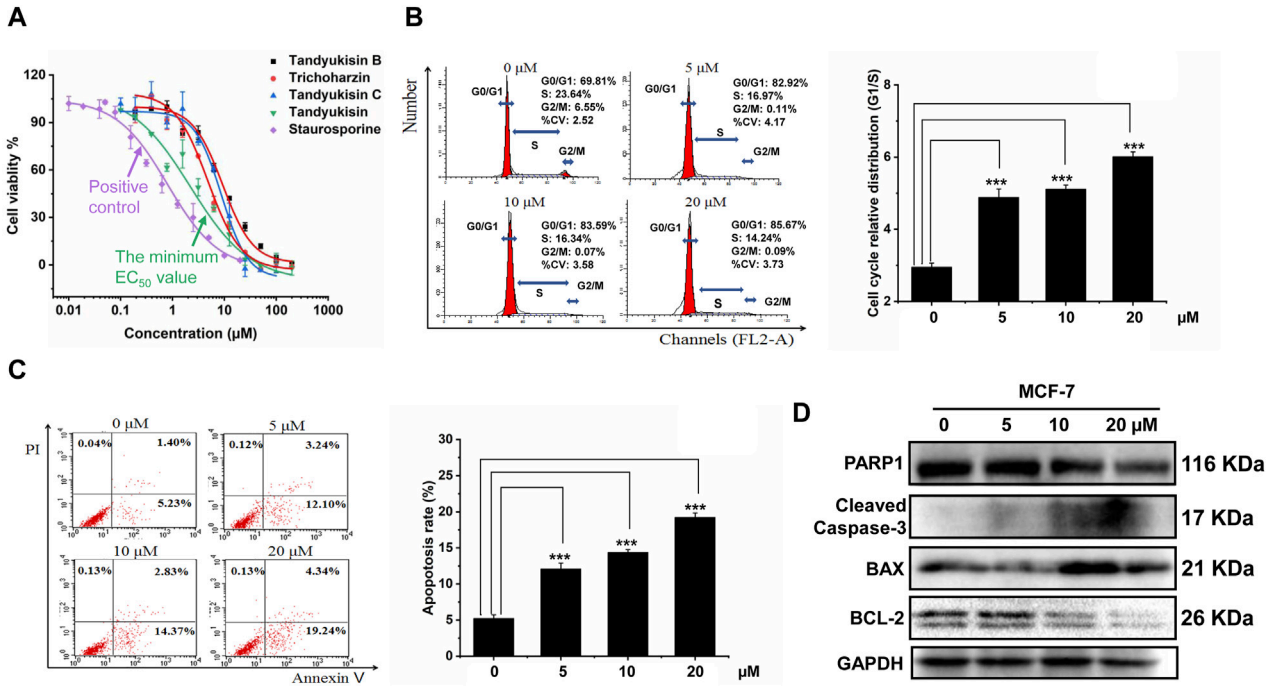

FIGURE 2
Identification of compounds that can significantly inhibit MCF-7 cell growth and induce cell apoptosis. **(A)** Growth inhibition activity of compounds in MCF-7 cells. The effect of treating MCF-7 cells with these increasing concentrations of compounds for 24 h was evaluated using MTT assay. **(B)** Percentage of MCF-7 cells in different phases of the cell cycle after respectively treatment with 5, 10, and 20 μM Tandyukisin for 24 h using flow cytometric analysis. **(C)** The effect of Tandyukisin in cell apoptosis of MCF-7 cells. The apoptosis of cells was confirmed by Annexin-V/PI double-staining after Tandyukisin treatment for 24 h. **(D)** The expression levels of PARP1 and cleaved caspase-3 in MCF-7 cells after Tandyukisin treatment. All values were repeated three times and represented as the mean ± SD. *p* values were obtained from a two-tailed Student's t-test, **p* < 0.05, ***p* < 0.01, ****p* < 0.001.

2.12 Statistical analysis

All experiments were repeated at least three times, and the data are presented as mean ± standard deviation (SD). The statistical analyses were performed using Origin. EC_{50} or IC_{50} values were obtained by fitting the data to a four-parameter Hill model of the graph of log dose against percentage cell viability or inhibition from at least three sets of experiments. Difference between two groups were analyzed by Student's t test (two-sided) and significance was set at $p < 0.05$. The specific details about statistical methods are introduced in respective figure legends.

3 Results

3.1 Tandyukisin inhibits MCF-7 growth by promoting early-stage cell apoptosis

According to data from the International Agency for Research on Cancer (IARC) released in December 2020, breast cancer has surpassed lung cancer as the most frequently diagnosed cancer worldwide. In light of this, our laboratory chose the MCF-7 breast cancer cell line for evaluating the bioactivity of 675 natural products. Initial screenings identified four compounds that significantly inhibited the proliferation of MCF-7 cells at a concentration of 10 μM, with their structures depicted

in Figure 1. Subsequent dose-response analyses revealed that these compounds exerted dose-dependent inhibitory effects on cell viability at micromolar concentrations, as illustrated in Figure 2A. The half-maximal effective concentration (EC_{50}) values for Tandyukisin B, Trichoharzin, Tandyukisin C, and Tandyukisin were determined to be 9.2 ± 1.2, 4.8 ± 0.4, 8.7 ± 1.0, and 3.0 ± 1.0 μM, respectively. The EC_{50} value for the positive control Staurosporine was 0.5 ± 0.2 μM.

To further assess the anti-proliferative properties of Tandyukisin, with the best cell growth inhibition activity, we analyzed its impact on the cell cycle of MCF-7 cells. Following 24 h of treatment at varying concentrations, the cells were collected for cell cycle analysis using flow cytometry. The results indicated a marked increase in the proportion of cells in the G0/G1 phase and a decrease in the S and G2/M phases at a concentration of 20 μM, elevating the G0/G1-phase cells to 85.67%, as shown in Figure 2B.

Additionally, the potential of Tandyukisin to induce apoptosis in MCF-7 cells was investigated employing the Annexin V-FITC/PI Apoptosis Detection Kit and immunoblotting techniques. Cells in early apoptosis were identified as PI negative and annexin V-FITC positive, whereas late apoptotic cells were positive for both markers. The data, presented in Figure 2C, revealed a significant increase in the percentage of apoptotic cells following Tandyukisin treatment, in a concentration-dependent manner. Specifically, apoptosis ratios in untreated MCF-7 cells were at 5.23%, while treatment with Tandyukisin at concentrations of 5, 10, and 20 μM resulted in apoptosis ratios of 12.10%, 14.37%, and 19.24%, respectively. Meanwhile, upon Tandyukisin treatment, the expression level of PARP1 was decreased, while the expression level of cleaved caspase-3 protein increased (Figure 2D; Supplementary Table S1).

These findings suggest that the antitumor activity of Tandyukisin may be attributed to its ability to modulate the cell cycle and induce early apoptosis through the activation of caspase-3.

3.2 Compound functions by targeting to EGFR

To further investigate which target compounds bound in, based on MCF-7 is the breast cancer cell line, we selected five widely recognized breast cancer treatment targets and docked Tandyukisin with best cancer cell growth inhibition activities to their respectively functional binding site. The five targets are mammalian target of rapamycin (mTOR) (Yu et al., 2001), human epidermal growth factor receptor 2 (HER2, ERBB2/neu) (Jerusalem et al., 2019), cyclin-dependent kinase 4/6 (CDK4/6) (Pandey et al., 2019), breast cancer susceptibility gene (BRCA) (Engel and Fischer, 2015), and EGFR (HER1/ERBB1) (Kjaer et al., 2018). The docking results, summarized in Supplementary Table S2, revealed that Tandyukisin displayed the highest binding affinity to the EGFR intracellular kinase active site, with an optimal docking score of −7.2 kcal/mol. Notably, the docking scores for Tandyukisin with CDK4 and CDK6 were −6.0 and −5.9 kcal/mol, respectively. No binding information of the other three proteins were obtained.

To further evaluate the selectivity and cytotoxicity of Tandyukisin across a range of cancer cell lines, we expanded our analysis beyond the EGFR-amplified breast cancer cell line MCF-7 to include high EGFR-expressing cancer cells (A549, A431, H1299) and low EGFR-expressing cancer cells (HL-60), as well as the non-tumorigenic epithelial cell line MCF-10A. The cytotoxic effects of Tandyukisin, at a concentration of 10 μM, were quantitatively assessed. The results, depicted in Figure 3A, indicated cell lethality percentages of 75.7% ± 2.3% for MCF-7, 72.1% ± 1.8% for A549, 67.3% ± 2.7% for A431, 60.3% ± 3.9% for H1299, 11.1% ± 1.2% for HL-60, and 8.9% ± 1.5% for MCF-10A, respectively.

The results demonstrate that the anti-tumor activity of Tandyukisin is largely achieved by targeting EGFR.

3.3 Tandyukisin targets both wild-type EGFR and its pathogenic mutants

In light of the significant challenge posed by drug-resistant mutations in EGFR-associated diseases, where over 50% of patients develop resistance, our research extended to evaluate the efficacy of compounds against both wild-type (WT) EGFR and prevalent drug-resistant mutants. Considering that the T790M point mutation in exon 20 confers resistance to EGFR-targeted therapeutics, and approximately two-thirds of patients treated with such drugs develop this mutation, its significance is underscored (Pao et al., 2005). Concurrently, the exon 19 deletion mutation (Ex19Del) and the exon 21 L858R point mutation represent the predominant pathogenic EGFR mutations, affecting the principal cohort treated with oral EGFR inhibitors, and constitute over 80% of all EGFR mutations (Rosell et al., 2009). Therefore, in our study on the enzyme activity of EGFR pathogenic mutants, we prioritized the inclusion of the T790M, L858R, and potentially the combined L858R/T790M mutations to align with their clinical prevalence and therapeutic relevance (Figure 3B, C; Supplementary Figure S1). The *in vitro* kinase assays demonstrated that the four studied compounds exhibited potent inhibition across these variants at nanomolar concentrations. Specifically, Tandyukisin showcased notable inhibitory concentrations (IC_{50}) against WT EGFR, T790M, L858R, and L858R/T790M mutants, with values of 10.6 ± 0.6, 32.6 ± 0.6, 3.1 ± 0.1, and 237 ± 28 nM, respectively (Figure 3B). The IC_{50} values of positive control Staurosporine to WT, T790M, L858R, and L858R/T790M EGFR were 119.1 ± 0.1, 0.4 ± 0.1, 19.3 ± 0.1, and 3.4 ± 0.1 nM, respectively (Figure 3C). Remarkably, the IC_{50} for Tandyukisin against WT EGFR was determined to be 10 nM, revealing a potency 20-fold greater than that of the positive control Staurosporine against the same target.

To further ascertain the specificity of Tandyukisin's action, we subjected it to tests against a panel of eight distinct tyrosine kinases. The results from these experiments elucidated that Tandyukisin exhibited selective inhibitory activity predominantly towards tyrosine kinases within the EGFR family (Figures 3D, E). Certainly, a more comprehensive evaluation of the selectivity and safety of Tandyukisin necessitates the validation across a broader spectrum of kinase types.

3.4 Tandyukisin efficiently promotes concentration-induced EGFR stability in MCF-7 cells

To confirm Tandyukisin directly bound EGFR in cells, CETSA was conducted. Currently, CETSA is widely used in drug target

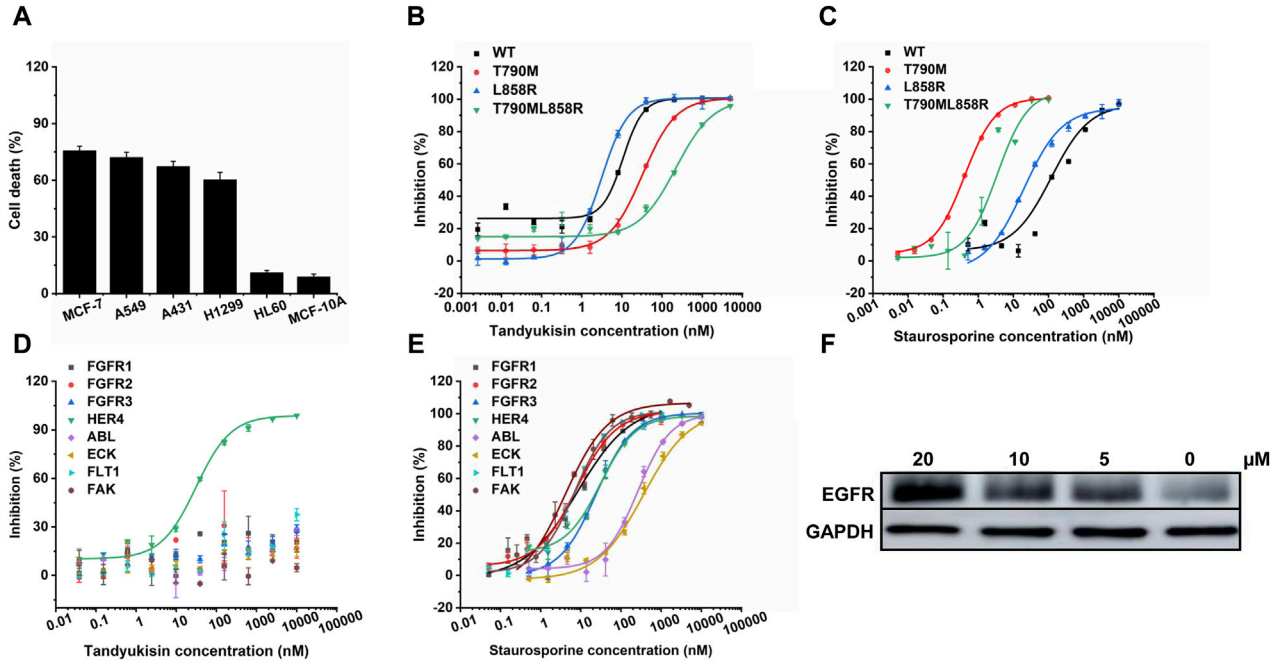

FIGURE 3
Compounds selectively target EGFR. **(A)** MTT assays of compound Tandyukisin for MCF-7, A549, A431, H1299, HL-60 and MCF-10A cells. **(B)** Inhibition of Tandyukisin on EGFR kinases determined by ELISA assay. **(C)** Inhibition of Staurosporine on EGFR kinases determined by ELISA assay. **(D)** Kinase profiling of Tandyukisin against eight human tyrosine kinases. The IC_{50} value of Tandyukisin for HER4 was 31.1 ± 0.1 nM, while the IC_{50} value of Tandyukisin for other seven tyrosine kinases were larger than 100 μM. **(E)** Kinase profiling of Staurosporine against eight human tyrosine kinases. The IC_{50} value of Staurosporine for FGFR1, FGFR2, FGFR3, HER4, ABL, ECK, FLT1 and FAK were 8.3 ± 2.0, 7.7 ± 0.9, 23.9 ± 1.0, 30.5 ± 0.1 nM, 262 ± 19, 361 ± 90, 7.0 ± 0.6 and 4.0 ± 2.0 nM, respectively. **(F)** CETSA was performed to evaluate the binding effects of Tandyukisin on the thermal stability of EGFR. IC_{50} values are shown as the mean ± SD from at least three independent experiments. Staurosporine was the positive control. FGFR1/2/3: fibroblast growth factor receptor 1/2/3, HER4: epidermal growth factor receptor 4, ABL: Abelson tyrosine-protein kinase, ECK: Epithelial cell kinase, FLT1: Vascular endothelial growth factor receptor 1, FAK: Focal Adhesion Kinase.

discovery assay and is based on the thermal stability changes after drugs bind to their targets (Martinez Molina et al., 2013; Jafari et al., 2014). After treatment with Tandyukisin at 5, 10, 20 μM for 24 h, the multiple aliquots of the cell suspension were heated at 55°C. The heated cells were subsequently lysed and centrifuged to separate soluble fractions from precipitated denatured EGFR. After thermal denaturation, EGFR in the soluble fraction was examined by Western blotting. As shown in Figure 3F; Supplementary Table S3, compared with DMSO control, cells treated with Tandyukisin showed a markable increase in the accumulation of EGFR in the soluble fraction at the examined temperatures, indicating the binding of Tandyukisin stabilized EGFR. At the protein level, Tandyukisin could also enhance the thermal stability of EGFR in a concentration-dependent manner, as demonstrated at concentrations of 1.3, 2.5, 5, 10, and 20 μM (Supplementary Figure S2).

3.5 Compounds specifically bind to EGFR by disrupting EGF or ATP binding

To elucidate the direct interaction between EGFR and various compounds, SPR was employed. Given the membranous nature of EGFR, both its extracellular ligand-binding domain and intracellular kinase domain were procured for SPR analysis. An initial screening on a GST-immobilized chip was conducted to identify any nonspecific binding to the GST tag, which, fortunately, yielded no such interactions, as shown in Supplementary Figure S3. The sensorgrams suggested that the observed response changes were more attributable to bulk effects rather than specific interactions. All compounds showed concentration dependent binding responses for the two domains. The K_D values of compounds Tandyukisin B, Trichoharzin, Tandyukisin C and Tandyukisin for EGFR intracellular kinase domain were 7.02, 6.34, 6.56 and 5.57 μM, respectively (Figure 4A, B; Supplementary Figure S4A, B); while the K_D values of Tandyukisin B, Trichoharzin, Tandyukisin C and Tandyukisin for EGFR extracellular ligand binding domain were 30.0, 7.98, 55.1, and 101 μM, respectively Figure 4C, D; Supplementary Figure S4C, D).

The interaction between EGF and EGFR's extracellular domain, known to trigger EGFR dimerization, autophosphorylation, and subsequent cellular proliferation and metastasis, was further explored (Citri and Yarden, 2006). A binding competition assay with Trichoharzin, which demonstrated the best affinity for the EGFR extracellular domain, was conducted to assess its potential to inhibit EGF-EGFR binding. SPR analysis confirmed a high-affinity interaction between EGF and EGFR (26.1 nM, Supplementary Figure S5), with Trichoharzin significantly inhibiting this interaction in a concentration-dependent manner, reducing the binding affinity of EGF to EGFR to 191, 372, and 1740 nM at concentrations of 125,

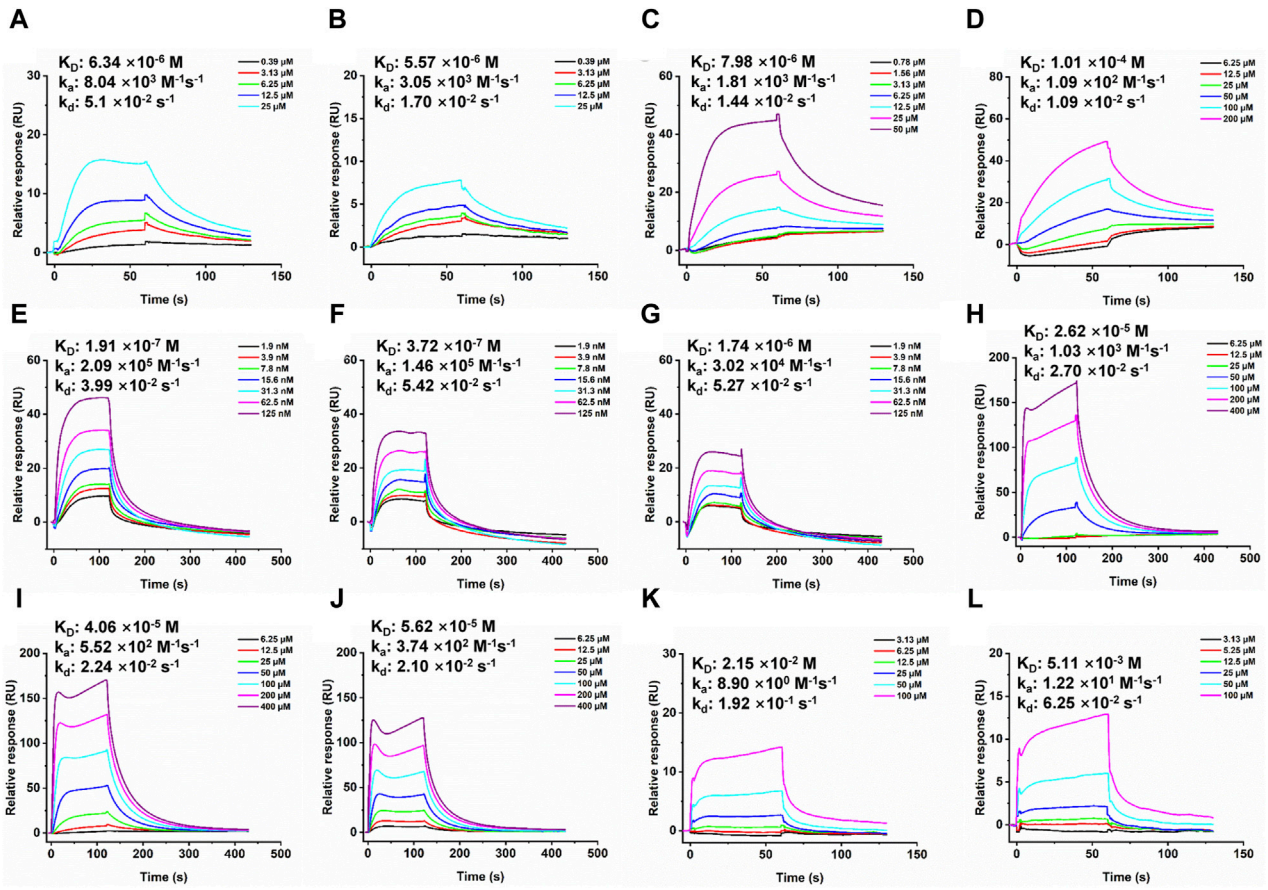

FIGURE 4
SPR dose response curves of Trichoharzin and Tandyukisin for EGFR. A-B. Trichoharzin **(A)** and Tandyukisin **(B)** bound to EGFR kinase domain without ATP. C-D. Trichoharzin **(C)** and Tandyukisin **(D)** bound to EGFR ligand binding domain. E-J. SPR competition experiment performed between Trichoharzin and EGF. In the presence of Trichoharzin at 125 **(E)**, 250 **(F)**, and 500 **(G)** μM, the K_D values of EGF decreased to 191, 372, and 1740 nM, respectively. **(H–J)**. In the presence of EGF at 2.5 **(H)**, 10 **(I)**, and 20 **(J)** nM, the K_D values of Trichoharzin reduced to 26.2, 40.6, and 56.2 μM, respectively. K-L. Trichoharzin **(K)** and Tandyukisin **(L)** bound to EGFR kinase domain in the presence of ATP.

250, and 500 μM, respectively (Figures 4E–G). This represented a 7.3, 14.3, and 66.7-fold decrease in EGF binding affinity, respectively. A dose dependent decrease in the binding affinity for Trichoharzin upon addition of EGF at 0, 5, 10, and 20 nM was also observed. The K_D values of Trichoharzin against EGF at 2.5, 10, 20 nM incubated EGFR extracellular ligand binding domain were 26.2, 40.6, and 56.2 μM, respectively, which were also 3.3, 5.1, and 7.0 folds weaker than Trichoharzin binding alone (Figures 4H–J).

Considering EGFR belongs to receptor tyrosine family, we also examined the effect of ATP on compound binding by using EGFR intracellular kinase domain immobilized sensor chip. After adding 1 mM ATP to HEPES-P running buffer, nearly all compounds complete lost their binding ability to EGFR intracellular kinase domain and exhibited K_D values larger than 200 μM (Figure 4K, L; Supplementary Figure S6). This observation suggests that the presence of ATP significantly disrupts compound binding to the intracellular kinase domain of EGFR.

SPR results indicated that compounds can disrupt EGFR function by binding to EGF binding site, or ATP binding site, or both sites. SPR results also support that compounds did not aggregate under the experimental conditions.

3.6 Binding mode prediction

To elucidate the molecular interactions between the compounds and specific domains of EGFR, computational docking studies were performed using Glide (Friesner et al., 2004; Halgren et al., 2004), focusing on the binding of Trichoharzin to the EGF binding site and Tandyukisin to the ATP binding site.

The EGF/EGFR interaction interface is comprised of three primary sites: site I located in domain I, and sites II and III situated in domain III (Ogiso et al., 2002). At site I, the hydrophobic interactions involve the side chains of Leu14, Tyr45, Leu69, and Leu98 of EGFR with EGF, complemented by hydrogen bonding between residues 15–18 of EGFR and EGF. Site II is characterized by hydrophobic interactions involving Val350 and Phe357 of EGFR, a salt bridge formation by the Asp355 side chain with EGF, and van der Waals contacts between Phe357 and EGF. Site III features hydrophobic interactions with Leu382, Phe412, Val417, and Ile438 of EGFR, alongside a hydrogen bond formed by the Gln384 side chain with EGF.

Based on the docking results, Trichoharzin mainly occupied site I yielding a docking score of −6.2 kcal/mol (Figure 5A). Trichoharzin was anchored into site I by five hydrogen bonds,

10.3389/fphar.2024.1396605

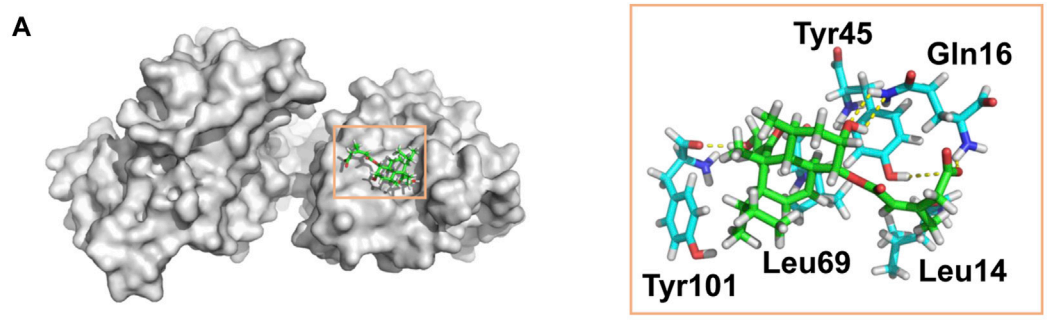

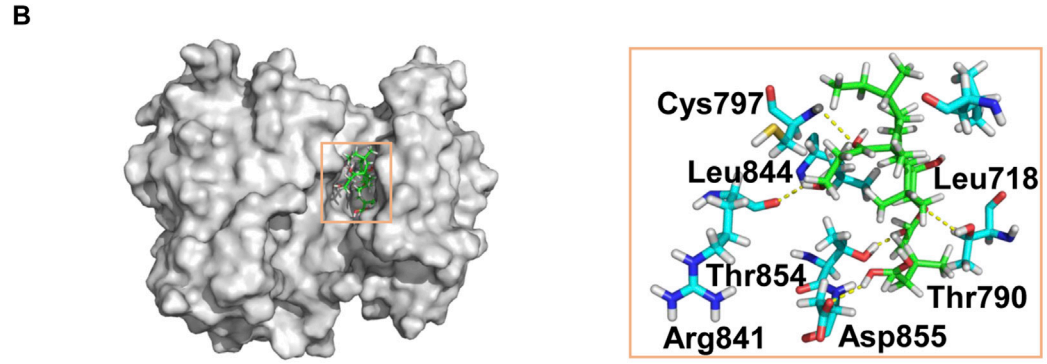

C

Description	Range of CI
Synergism	0.3-0.7
Moderate synergism	0.7-0.85
Slight synergism	0.85-0.9
Nearly additive	0.9-1.1
Slight antagonism	1.1-1.2
Antagonism	>1.2

Tandyukisin (μM)

Trichoharzin (μM)	1.56	3.13	6.25	12.5	25	50
1.56	1.05	0.97	0.87	0.82	1.1	1.32
3.13	0.94	0.7	0.66	0.67	0.88	1.17
6.25	0.83	0.63	0.6	0.56	0.71	0.92
12.5	0.82	0.62	0.53	0.44	0.59	0.83
25	0.77	0.6	0.51	0.49	0.59	0.68
50	0.86	0.71	0.63	0.52	0.56	0.68

FIGURE 5
Trichoharzin and Tandyukisin synergize to induce rapid cell death in MCF-7 cell line. **(A)** The binding mode of Trichoharzin to EGFR ligand binding domain. **(B)** The binding mode of Tandyukisin to EGFR kinase domain. **(C)** CI values for each Trichoharzin and Tandyukisin combination were quantified by CompuSyn Software. CI values are heat mapped with lowest values in green and highest values in red.

including a donor and two acceptor interaction with Gln16, an acceptor interaction with the polar side chain of Tyr45, and a donor interaction with the Tyr101 backbone. Hydrophobic interaction also exited between Trichoharzin and Leu 14 and Leu 69. Notably, the shallow nature of site I results in substantial exposure of Trichoharzin to the solvent.

The ATP binding site, a target for two generations of FDA-approved ATP-competitive inhibitors for cancer treatment, involves key residues such as Thr790, Met793, and Cys797 for drug-EGFR interactions (Hossam et al., 2016). The docking model of Tandyukisin highlighted seven EGFR residues in proximity (Figure 5B), with five crucial hydrogen-bond interactions involving donor and acceptor interactions with Cys797 and Arg841, an acceptor interaction with the Asp855 backbone, and donor interactions with the Thr854 and Thr790 backbones. Hydrophobic interactions are also observed between Tandyukisin and the alkyl side chains of Leu718 and Leu844. As illustrated in Supplementary Figure S7, MD simulation revealed that Tandyukisin could stably bind to the predicted sites within the kinetic simulation timeframe of 100 ns.

These docking results corroborate the experimental findings regarding the binding sites of the compounds, demonstrating a consistent alignment with the observed competition results. Considering that the pivotal residues facilitating the binding of Trichoharzin to EGFR are situated within the ligand-binding domain, and notwithstanding that the critical residues for the

interaction of Tandyukisin with EGFR encompass Thr790, the hydrogen bond length formed by Tandyukisin and Thr790 measures 2.6 Angstroms. Consequently, the impact of this hydrogen bond on the interaction between Tandyukisin and EGFR appears non-decisive. This observation suggests a potential rationale for Trichoharzin and Tandyukisin exhibiting inhibitory activity against EGFR pathogenic mutants T790M and L858R.

3.7 Trichoharzin and Tandyukisin synergize to induce rapid cell death in MCF-7

Given the enhanced therapeutic efficacy, reduced side effects, and capability to circumvent multidrug resistance (MDR) associated with combination therapy, this approach has become a cornerstone in the treatment of cancer patients (Botham et al., 2014; Yang et al., 2015). In light of this, and following the identification of a suite of compounds exhibiting preferential binding to distinct sites on EGFR, we opted to investigate the combined effects of Trichoharzin, targeting the EGF binding site, and Tandyukisin, aimed at the ATP binding site, through MTT assays designed to assess their synergistic potential.

The synergy between Trichoharzin and Tandyukisin was quantitatively evaluated using the Chou and Talalay method (Chou, 2006), which calculates the Combination Index (CI). A CI value less than one signifies a synergistic interaction, a CI greater than one denotes antagonism, and a CI equal to one indicates an additive effect. Among these, the lowest CI value is indicative of the most potent synergistic interaction. The results of synergistic experiments for Trichoharzin and Tandyukisin in cell assays were shown in Figure 5C; Supplementary Figure S8. As can be seen, the combination of Trichoharzin and Tandyukisin creates a synergistic anti-tumor effect as CI values are lower than 1. The relative strong synergistic interactions (CI values between 0.4 and 0.6) were observed with Trichoharzin concentration ranging from 6.25 to 50 μM, while Tandyukisin concentration ranging from 6.25 to 25 μM. When the concentration of Trichoharzin is 1.56 μM or the concentration of Tandyukisin is 50 μM in the matrix, antagonistic interaction was more likely observed. Moreover, the synergistic effect of Trichoharzin and Tandyukisin on WT EGFR enzyme activity was investigated. The experimental results demonstrated a consistent synergistic effect almost across all concentrations of Trichoharzin within the concentration range of 1.25–10 nM of Tandyukisin, as depicted in Supplementary Figure S9. Synergistic results further confirm our competition and docking results about the binding sites of the compounds.

4 Discussion

From our in-house natural products library, we successfully identified a novel EGFR inhibitor, Tandyukisin, characterized by a unique chemical scaffold. Tandyukisin has demonstrated the ability to inhibit cancer cell growth in the micromolar range, selectively target EGFR-amplified breast cancer cell proliferation, and induce apoptosis through Caspase-3 activation. It effectively inhibited both wild-type and mutant forms of EGFR (T790M, L858R, and L858R/T790M) with a concentration range from 3 to 240 nM, showcasing pronounced selectivity for EGFR tyrosine kinase. The use of CETSA demonstrated that Tandyukisin targeted EGFR in cells and promoted concentration-induced EGFR stability. SPR assay provided the exact binding affinity of Tandyukisin to EGFR. Moreover, competition experiments between Tandyukisin or Trichoharzin and ATP or EGF further confirmed the truth that compound bound in the orthogonal site. Molecular docking studies specified Cys797, Arg 841, Asp855, Thr854 and Thr790 were the key residues to stabilize Tandyukisin in the site. In addition, Tandyukisin and Trichoharzin used in combination can accelerate the death of breast cancer cells.

This marks the inaugural report of Tandyukisin as an EGFR inhibitor, although its anti-tumor properties were previously identified in a study by Takeshi Yamada's group in 2015, which isolated a new decalin derivative from the marine sponge Halichondria okadai (Yamada et al., 2015). They characterized the structure of the compound using 1D and 2D NMR techniques, and the compounds were then tested for their liver cancer cell inhibitory activity. Marine organisms, thriving under extreme environmental conditions, are prolific producers of bioactive compounds with potential anti-tumor, antibacterial, and antiviral properties (Bull et al., 2005). According to incomplete statistics, more than 25,000 marine natural product compounds have been studied so far, and they are expected to be further developed into marine drugs and other marine biological products. There are currently about 14 marine drugs approved for marketing, and more than 50 marine drugs are in the clinical trial stage (Ruiz-Torres et al., 2017), underscoring the marine ecosystem's vast potential for novel drug discovery, particularly in oncology. However, due to the relatively low distribution density of marine biological resources, and the anti-tumor active substances in marine organisms are at the microgram or milligram level, the large-scale preparation of active substances has become one of the keys limiting factors in the development of marine anti-tumor drugs.

Theoretically, the binding affinity of inhibitor (K_D value) in the orthogonal site should be coordinate with its enzymatic inhibition ability (IC_{50} value). For Tandyukisin, its K_D value is 5.57 μM, while its EGFR inhibition activity IC_{50} value is about 10 nM. The difference between K_D and IC_{50} value is mainly caused by that the compound may inhibit enzyme activity by inducing conformational changes in the kinase domain. Immobilizing the kinase domain on the chip will hinder the conformational changes of the protein, so it showed weaker binding activity. Another reason may be related to the inconsistent activity status of the protein under different experimental conditions. The mechanism of Tandyukisin inhibiting EGFR activity involves two main actions: firstly, by directly occupying the ATP binding site, and secondly, potentially by restricting the mobility of the kinase domain's rigid regions. This restriction could prevent the active site from adopting a closed conformation, thereby stabilizing EGFR in an inactive state. However, elucidating the precise mechanism of inhibition necessitates further experimental and computational investigations to fully understand how Tandyukisin influences EGFR activity and conformation.

Although a small number of cancer patients can benefit from EGFR inhibitors as monotherapy in patients with malignancies such as breast cancer and non-small cell lung cancer, cancer cells may

activate different mechanisms to evade the antitumor activity of EGFR-targeted anti-tumor drugs. Consequently, combination therapy involving EGFR inhibitors is increasingly favored due to its potential to surmount acquired resistance, thereby enhancing the responsiveness of drug-resistant cells and extending patient progression-free survival (PFS). As per predictions from ADMET lab3.0 (https://admetlab3.scbdd.com/), Tandyukisin demonstrates low toxicity across three commonly utilized cell lines (RPMI-8226, A549, HEK293) and exhibits minimal adverse effects on neurological, genetic, and cardiac functions, among others, indicating overall favorable performance. However, the conjugated structure of Tandyukisin's active double-bonded carbonyl group may impact its distribution and metabolism, potentially leading to renal and respiratory toxicity. Nonetheless, Tandyukisin shows no inhibitory effects on most P450 isoenzymes in the human body and exhibits excellent stability in human liver microsomes (HLM), thereby not interfering with the pharmacokinetic properties of other therapeutic drugs. Hence, Tandyukisin presents itself as highly suitable for combination therapy. We anticipate that our discovery of an EGFR inhibitor with a novel scaffold will address the issue of low yield post-completion of full chemical synthesis steps. However, before Tandyukisin can progress to clinical trials, it necessitates pharmacophore optimization, scaffold transition, and other medicinal chemistry approaches to enhance its pharmacokinetic properties and optimize drug efficacy. The strategic co-administration of EGFR inhibitors has the potential to amplify therapeutic outcomes and mitigate the risk of resistance development. Of course, the safety and efficacy of such combination therapies necessitate further comprehensive investigation.

5 Conclusion

In this study, we have identified Tandyukisin as a novel EGFR inhibitor capable of significantly suppressing the enzymatic activity of both EGFR and its drug-resistant mutants at nanomolar concentrations. Derived from compounds isolated from marine organisms, Tandyukisin offers valuable insights for the development of marine-derived antitumor drugs. The EGFR receptor can activate three signaling pathways, namely, the JAK/STAT signaling pathway involved in immune regulation, the RAS-RAF-MEK pathway (MAPK/ERK pathway) involved in cell proliferation, and the PI3K-AKT-mTOR pathway involved in cell survival. Our research has demonstrated that EGFR inhibitors can activate Caspase-3, increase BAX, and reduce BCL-2 to promote early apoptosis of cells. However, further investigation into molecular and protein-level mechanisms, such as the impact of BCL-2 like protein 11 mRNA and protein expression, and the phosphorylation levels of EGFR, AKT, and ERK, should be pursued diligently. Despite the current limitations in the yield of Tandyukisin impeding further *in vitro* or *in vivo* experimental validation, the identification of Tandyukisin could facilitate the development of next-generation EGFR inhibitors and enable the investigation of their potential synergistic effects with inhibitors that target related pathways.

Data availability statement

The original contributions presented in the study are included in the article/Supplementary Material, further inquiries can be directed to the corresponding author.

Author contributions

QL: Data curation, Methodology, Writing–original draft, Validation. BL: Data curation, Methodology, Validation, Writing–original draft. QW: Conceptualization, Funding acquisition, Methodology, Project administration, Supervision, Writing–review and editing. CW: Funding acquisition, Methodology, Validation, Writing–original draft. MY: Data curation, Methodology, Writing–original draft. TX: Data curation, Validation, Writing–original draft.

Funding

The author(s) declare that financial support was received for the research, authorship, and/or publication of this article. This work was supported by the National Natural Science Foundation of China (22107004), Beijing Hospital New-star Plan of Science and Technology (BJ-2020-084), Startup Foundation for Doctors of Beijing Hospital (BJ-2019-132) and Key Research and Development Program of Heilongjiang Province (2022ZX02C07).

Conflict of interest

The authors declare that the research was conducted in the absence of any commercial or financial relationships that could be construed as a potential conflict of interest.

Publisher's note

All claims expressed in this article are solely those of the authors and do not necessarily represent those of their affiliated organizations, or those of the publisher, the editors and the reviewers. Any product that may be evaluated in this article, or claim that may be made by its manufacturer, is not guaranteed or endorsed by the publisher.

Supplementary material

The Supplementary Material for this article can be found online at: https://www.frontiersin.org/articles/10.3389/fphar.2024.1396605/full#supplementary-material

References

Abou-Zied, H. A., Youssif, B. G. M., Mohamed, M. F. A., Hayallah, A. M., and Abdel-Aziz, M. (2019). EGFR inhibitors and apoptotic inducers: design, synthesis, anticancer activity and docking studies of novel xanthine derivatives carrying chalcone moiety as hybrid molecules. *Bioorg. Chem.* 89, 102997. doi:10.1016/j.bioorg.2019.102997

Alvarez, R. H., Valero, V., and Hortobagyi, G. N. (2010). Emerging targeted therapies for breast cancer. *J. Clin. Oncol.* 28, 3366–3379. doi:10.1200/jco.2009.25.4011

Baselga, J., Gómez, P., Greil, R., Braga, S., Climent, M. A., Wardley, A. M., et al. (2013). Randomized phase II study of the anti-epidermal growth factor receptor monoclonal antibody cetuximab with cisplatin versus cisplatin alone in patients with metastatic triple-negative breast cancer. *J. Clin. Oncol.* 31, 2586–2592. doi:10.1200/jco.2012.46.2408

Botham, R. C., Fan, T. M., Im, I., Borst, L. B., Dirikolu, L., and Hergenrother, P. J. (2014). Dual small-molecule targeting of procaspase-3 dramatically enhances zymogen activation and anticancer activity. *J. Am. Chem. Soc.* 136, 1312–1319. doi:10.1021/ja4124303

Bull, A. T., Stach, J. E., Ward, A. C., and Goodfellow, M. (2005). Marine actinobacteria: perspectives, challenges, future directions. *Ant. Van Leeuwenhoek* 87, 65–79. doi:10.1007/s10482-004-6562-8

Burgess, A. W. (2008). EGFR family: structure physiology signalling and therapeutic targets. *Growth Factors* 26, 263–274. doi:10.1080/08977190802312844

Chou, T. C. (2006). Theoretical basis, experimental design, and computerized simulation of synergism and antagonism in drug combination studies. *Pharmacol. Rev.* 58, 621–681. doi:10.1124/pr.58.3.10

Citri, A., and Yarden, Y. (2006). EGF-ERBB signalling: towards the systems level. *Nat. Rev. Mol. Cell Biol.* 7, 505–516. doi:10.1038/nrm1962

El Guerrab, A., Bamdad, M., Bignon, Y. J., Penault-Llorca, F., and Aubel, C. (2020). Co-targeting EGFR and mTOR with gefitinib and everolimus in triple-negative breast cancer cells. *Sci. Rep.* 10, 6367. doi:10.1038/s41598-020-63310-2

Engel, C., and Fischer, C. (2015). Breast cancer risks and risk prediction models. *Breast Care (Basel)* 10, 7–12. doi:10.1159/000376600

Ferguson, K. M. (2008). Structure-based view of epidermal growth factor receptor regulation. *Annu. Rev. Biophys.* 37, 353–373. doi:10.1146/annurev.biophys.37.032807.125829

Friesner, R. A., Banks, J. L., Murphy, R. B., Halgren, T. A., Klicic, J. J., Mainz, D. T., et al. (2004). Glide: a new approach for rapid, accurate docking and scoring. 1. Method and assessment of docking accuracy. *J. Med. Chem.* 47, 1739–1749. doi:10.1021/jm0306430

Halgren, T. A., Murphy, R. B., Friesner, R. A., Beard, H. S., Frye, L. L., Pollard, W. T., et al. (2004). Glide: a new approach for rapid, accurate docking and scoring. 2. Enrichment factors in database screening. *J. Med. Chem.* 47, 1750–1759. doi:10.1021/jm030644s

Harbeck, N., and Gnant, M. (2017). Breast cancer. *Lancet* 389, 1134–1150. doi:10.1016/s0140-6736(16)31891-8

Hossam, M., Lasheen, D. S., and Abouzid, K. A. (2016). Covalent EGFR inhibitors: binding mechanisms, synthetic approaches, and clinical profiles. *Arch. Pharm.* 349, 573–593. doi:10.1002/ardp.201600063

Jafari, R., Almqvist, H., Axelsson, H., Ignatushchenko, M., Lundbäck, T., Nordlund, P., et al. (2014). The cellular thermal shift assay for evaluating drug target interactions in cells. *Nat. Protoc.* 9, 2100–2122. doi:10.1038/nprot.2014.138

Jerusalem, G., Lancellotti, P., and Kim, S. B. (2019). HER2+ breast cancer treatment and cardiotoxicity: monitoring and management. *Breast Cancer Res. Treat.* 177, 237–250. doi:10.1007/s10549-019-05303-y

Jura, N., Endres, N. F., Engel, K., Deindl, S., Das, R., Lamers, M. H., et al. (2009). Mechanism for activation of the EGF receptor catalytic domain by the juxtamembrane segment. *Cell* 137, 1293–1307. doi:10.1016/j.cell.2009.04.025

Kjaer, I. M., Bechmann, T., Brandslund, I., and Madsen, J. S. (2018). Prognostic and predictive value of EGFR and EGFR-ligands in blood of breast cancer patients: a systematic review. *Clin. Chem. Lab. Med.* 56, 688–701. doi:10.1515/cclm-2017-0592

Lakis, S., Dimoudis, S., Kotoula, V., Alexopoulou, Z., Kostopoulos, I., Koletsa, T., et al. (2016). Interaction between beta-catenin and EGFR expression by immunohistochemistry identifies prognostic subgroups in early high-risk triple-negative breast cancer. *Anticancer Res.* 36, 2365–2378.

Martinez Molina, D., Jafari, R., Ignatushchenko, M., Seki, T., Larsson, E. A., Dan, C., et al. (2013). Monitoring drug target engagement in cells and tissues using the cellular thermal shift assay. *Science* 341, 84–87. doi:10.1126/science.1233606

Nielsen, T. O., Hsu, F. D., Jensen, K., Cheang, M., Karaca, G., Hu, Z., et al. (2004). Immunohistochemical and clinical characterization of the basal-like subtype of invasive breast carcinoma. *Clin. Cancer Res.* 10, 5367–5374. doi:10.1158/1078-0432.ccr-04-0220

Normanno, N., De Luca, A., Bianco, C., Strizzi, L., Mancino, M., Maiello, M. R., et al. (2006). Epidermal growth factor receptor (EGFR) signaling in cancer. *Gene* 366, 2–16. doi:10.1016/j.gene.2005.10.018

Ogiso, H., Ishitani, R., Nureki, O., Fukai, S., Yamanaka, M., Kim, J.-H., et al. (2002). Crystal structure of the complex of human epidermal growth factor and receptor extracellular domains. *Cell* 110, 775–787. doi:10.1016/s0092-8674(02)00963-7

Omura, S., Iwai, Y., Hirano, A., Nakagawa, A., Awaya, J., Tsuchya, H., et al. (1977). A new alkaloid AM-2282 OF Streptomyces origin. Taxonomy, fermentation, isolation and preliminary characterization. *J. Antibiot.* 30, 275–282. doi:10.7164/antibiotics.30.275

Pandey, K., An, H. J., Kim, S. K., Lee, S. A., Kim, S., Lim, S. M., et al. (2019). Molecular mechanisms of resistance to CDK4/6 inhibitors in breast cancer: a review. *Int. J. Cancer.* 145, 1179–1188. doi:10.1002/ijc.32020

Pao, W., Miller, V. A., Politi, K. A., Riely, G. J., Somwar, R., Zakowski, M. F., et al. (2005). Acquired resistance of lung adenocarcinomas to gefitinib or erlotinib is associated with a second mutation in the EGFR kinase domain. *PLoS Med.* 2, e73. doi:10.1371/journal.pmed.0020073

Recondo, G., Facchinetti, F., Olaussen, K. A., Besse, B., and Friboulet, L. (2018). Making the first move in EGFR-driven or ALK-driven NSCLC: first-generation or next-generation TKI? *Nat. Rev. Clin. Oncol.* 15, 694–708. doi:10.1038/s41571-018-0081-4

Rosell, R., Moran, T., Queralt, C., Porta, R., Cardenal, F., Camps, C., et al. (2009). Screening for epidermal growth factor receptor mutations in lung cancer. *N. Engl. J. Med.* 361, 958–967. doi:10.1056/NEJMoa0904554

Roskoski, R., Jr. (2014). The ErbB/HER family of protein-tyrosine kinases and cancer. *Pharmacol. Res.* 79, 34–74. doi:10.1016/j.phrs.2013.11.002

Ruiz-Torres, V., Encinar, J. A., Herranz-López, M., Pérez-Sánchez, A., Galiano, V., Barrajón-Catalán, E., et al. (2017). An updated review on marine anticancer compounds: the use of virtual screening for the discovery of small-molecule cancer drugs. *Molecules* 22, 1037. doi:10.3390/molecules22071037

Shigematsu, H., Ozaki, S., Yasui, D., Yamamoto, H., Zaitsu, J., Taniyama, D., et al. (2018). Overexpression of topoisomerase II alpha protein is a factor for poor prognosis in patients with luminal B breast cancer. *Oncotarget* 9, 26701–26710. doi:10.18632/oncotarget.25468

Song, X., Liu, X., and Ding, X. (2017). Staurosporine scaffold-based rational discovery of the wild-type sparing reversible inhibitors of EGFR T790M gatekeeper mutant in lung cancer with analog-sensitive kinase technology. *J. Mol. Recognit.* 30, e2590. doi:10.1002/jmr.2590

Sun, N., Gao, P., Li, Y., Yan, Z., Peng, Z., Zhang, Y., et al. (2021). Screening and identification of key common and specific genes and their prognostic roles in different molecular subtypes of breast cancer. *Front. Mol. Biosci.* 8, 619110. doi:10.3389/fmolb.2021.619110

Swain, S. M., Shastry, M., and Hamilton, E. (2023). Targeting HER2-positive breast cancer: advances and future directions. *Nat. Rev. Drug Discov.* 22, 101–126. doi:10.1038/s41573-022-00579-0

Symonds, L., Linden, H., Gadi, V., Korde, L., Rodler, E., Gralow, J., et al. (2019). Combined targeted therapies for first-line treatment of metastatic triple negative breast cancer-A phase II trial of weekly nab-paclitaxel and bevacizumab followed by maintenance targeted therapy with bevacizumab and erlotinib. *Clin. Breast Cancer.* 19, e283–e296. doi:10.1016/j.clbc.2018.12.008

Torre, L. A., Bray, F., Siegel, R. L., Ferlay, J., Lortet-Tieulent, J., and Jemal, A. (2015). Global cancer statistics, 2012. *CA Cancer J. Clin.* 65, 87–108. doi:10.3322/caac.21262

Walker, S. R., Liu, S., Xiang, M., Nicolais, M., Hatzi, K., Giannopoulou, E., et al. (2015). The transcriptional modulator BCL6 as a molecular target for breast cancer therapy. *Oncogene* 34, 1073–1082. doi:10.1038/onc.2014.61

Yamada, T., Umebayashi, Y., Kawashima, M., Sugiura, Y., Kikuchi, T., and Tanaka, R. (2015). Determination of the chemical structures of tandyukisins B-D, isolated from a marine sponge-derived fungus. *Mar. Drugs.* 13, 3231–3240. doi:10.3390/md13053231

Yang, Q., Yang, Y., Li, L., Sun, W., Zhu, X., and Huang, Y. (2015). Polymeric nanomedicine for tumor-targeted combination therapy to elicit synergistic genotoxicity against prostate cancer. *ACS Appl. Mater. Interfaces.* 7, 6661–6673. doi:10.1021/am509204u

Yu, K., Toral-Barza, L., Discafani, C., Zhang, W. G., Skotnicki, J., Frost, P., et al. (2001). mTOR, a novel target in breast cancer: the effect of CCI-779, an mTOR inhibitor, in preclinical models of breast cancer. *Endocr. Relat. Cancer* 8, 249–258. doi:10.1677/erc.0.0080249

Yun, C. H., Mengwasser, K. E., Toms, A. V., Woo, M. S., Greulich, H., Wong, K. K., et al. (2008). The T790M mutation in EGFR kinase causes drug resistance by increasing the affinity for ATP. *Proc. Natl. Acad. Sci.* 105, 2070–2075. doi:10.1073/pnas.0709662105

Zeng, Y., Yu, D., Tian, W., and Wu, F. (2022). Resistance mechanisms to osimertinib and emerging therapeutic strategies in nonsmall cell lung cancer. *Curr. Opin. Oncol.* 34, 54–65. doi:10.1097/cco.0000000000000805

Zhang, X., Gureasko, J., Shen, K., Cole, P. A., and Kuriyan, J. (2006). An allosteric mechanism for activation of the kinase domain of epidermal growth factor receptor. *Cell* 125, 1137–1149. doi:10.1016/j.cell.2006.05.013

frontiers | Frontiers in Pharmacology

TYPE Original Research
PUBLISHED 17 May 2024
DOI 10.3389/fphar.2024.1404532

Check for updates

OPEN ACCESS

EDITED BY
Wagdy Mohamed Eldehna,
Kafrelsheikh University, Egypt

REVIEWED BY
Sawsan A. Zaitone,
Suez Canal University, Egypt
Eugenia Piragine,
University of Pisa, Italy

*CORRESPONDENCE
Ming Li,
liming96001@126.com
Tianxiao Wang,
wtx1975@126.com

RECEIVED 21 March 2024
ACCEPTED 06 May 2024
PUBLISHED 17 May 2024

CITATION
Zhao W, Feng S, Wang J, Zhang Z, Chen L, Jiang L, Li M and Wang T (2024), Benserazide, a cystathionine beta-synthase (CBS) inhibitor, potentially enhances the anticancer effects of paclitaxel via inhibiting the S-sulfhydration of SIRT1 and the HIF1-α/VEGF pathway. *Front. Pharmacol.* 15:1404532. doi: 10.3389/fphar.2024.1404532

COPYRIGHT
© 2024 Zhao, Feng, Wang, Zhang, Chen, Jiang, Li and Wang. This is an open-access article distributed under the terms of the Creative Commons Attribution License (CC BY). The use, distribution or reproduction in other forums is permitted, provided the original author(s) and the copyright owner(s) are credited and that the original publication in this journal is cited, in accordance with accepted academic practice. No use, distribution or reproduction is permitted which does not comply with these terms.

Benserazide, a cystathionine beta-synthase (CBS) inhibitor, potentially enhances the anticancer effects of paclitaxel via inhibiting the S-sulfhydration of SIRT1 and the HIF1-α/VEGF pathway

Wei Zhao, Shasha Feng, Jian Wang, Zhenshuai Zhang, Lu Chen, Li Jiang, Ming Li* and Tianxiao Wang*

School of Pharmacy, Henan University, Kaifeng, Henan, China

Cancer targeted therapy is essential to minimize damage to normal cells and improve treatment outcomes. The elevated activity of Cystathionine beta-synthase (CBS), an enzyme responsible for producing endogenous hydrogen sulfide (H_2S), plays a significant role in promoting tumor growth, invasiveness, and metastatic potential. Consequently, the selective inhibition of CBS could represent a promising therapeutic strategy for cancer. Currently, there is much interest in combining paclitaxel with other drugs for cancer treatment. This study aimed to investigate the efficacy of combining benserazide, a CBS inhibitor, with paclitaxel in treating tumors. Firstly, we demonstrated CBS is indeed involved in the progression of multiple cancers. Then it was observed that the total binding free energy between the protein and the small molecule is −98.241 kJ/mol. The release of H_2S in the group treated with 100 μM benserazide was reduced by approximately 90% compared to the negative control, and the thermal denaturation curve of the complex protein shifted to the right, suggesting that benserazide binds to and blocks the CBS protein. Next, it was found that compared to paclitaxel monotherapy, the combination of benserazide with paclitaxel demonstrated stronger antitumor activity in KYSE450, A549, and HCT8 cells, accompanied by reduced cell viability, cell migration and invasion, as well as diminished angiogenic and lymphangiogenic capabilities. *In vivo* studies showed that the combined administration of benserazide and paclitaxel significantly reduced the volume and weight of axillary lymph nodes in comparison to the control group and single administration group. Further mechanistic studies revealed that the combination of benserazide and paclitaxel significantly suppressed the S-sulfhydration of SIRT1 protein, thereby inhibiting the expression of SIRT1 protein and activating SIRT1 downstream Notch1/Hes1 signaling pathway in KYSE450, A549, and HCT8 cells. Meanwhile, we observed that benserazide combined with paclitaxel induced a more significant downregulation of HIF-1α, VEGF-A, VEGF-C, and VEGF-D proteins expression levels in KYSE450, A549, and HCT8 cells compared to paclitaxel alone. These findings indicated that benserazide enhances the anticancer effects of paclitaxel via inhibiting the

S-sulfhydration of SIRT1 and down-regulating HIF-1α/VEGF signaling pathway. This study suggests that benserazide may have potential as a chemosensitizer in cancer treatment.

KEYWORDS

benserazide, paclitaxel, SIRT1, HIF1-α, VEGF, cancer

1 Introduction

Cancer incidence and mortality are increasing in China, making it a global cancer burden hotspot. Challenges like low early diagnosis rates and drug resistance hinder effective treatment. The need to enhance the effectiveness of chemotherapy is prompting researchers to explore innovative approaches like targeted therapy, thus providing new hope for cancer patients.

|Cystathionine beta-synthase (CBS) is an enzyme that catalyzes the synthesis of H_2S from homocysteine and cysteine (Conter et al., 2020). H_2S is a gasotransmitter that plays important roles in various physiological processes, including regulation of blood pressure, cardiovascular function, and inflammation (Han et al., 2019). In recent years, there has been growing interest in the role of CBS and H_2S in cancer development and progression. Studies have shown that the elevated activity of CBS plays a significant role in promoting tumor growth, invasiveness, and metastatic potential (Youness et al., 2020; Padmanabhan et al., 2021; Santos et al., 2023). Consequently, the targeted inhibition of CBS could emerge as a promising therapeutic approach for cancer intervention.

Benserazide is a drug that inhibits the peripheral dopamine decarboxylase enzyme, which is used in combination with levodopa to treat Parkinson's disease and Parkinson's syndrome (Baba et al., 2022; Yang et al., 2023). Recently, it has been discovered that benserazide can also inhibit the activity of CBS protease by binding to pyridoxal phosphate (PLP), a coenzyme of the CBS protein (Druzhyna et al., 2016). Studies have shown that

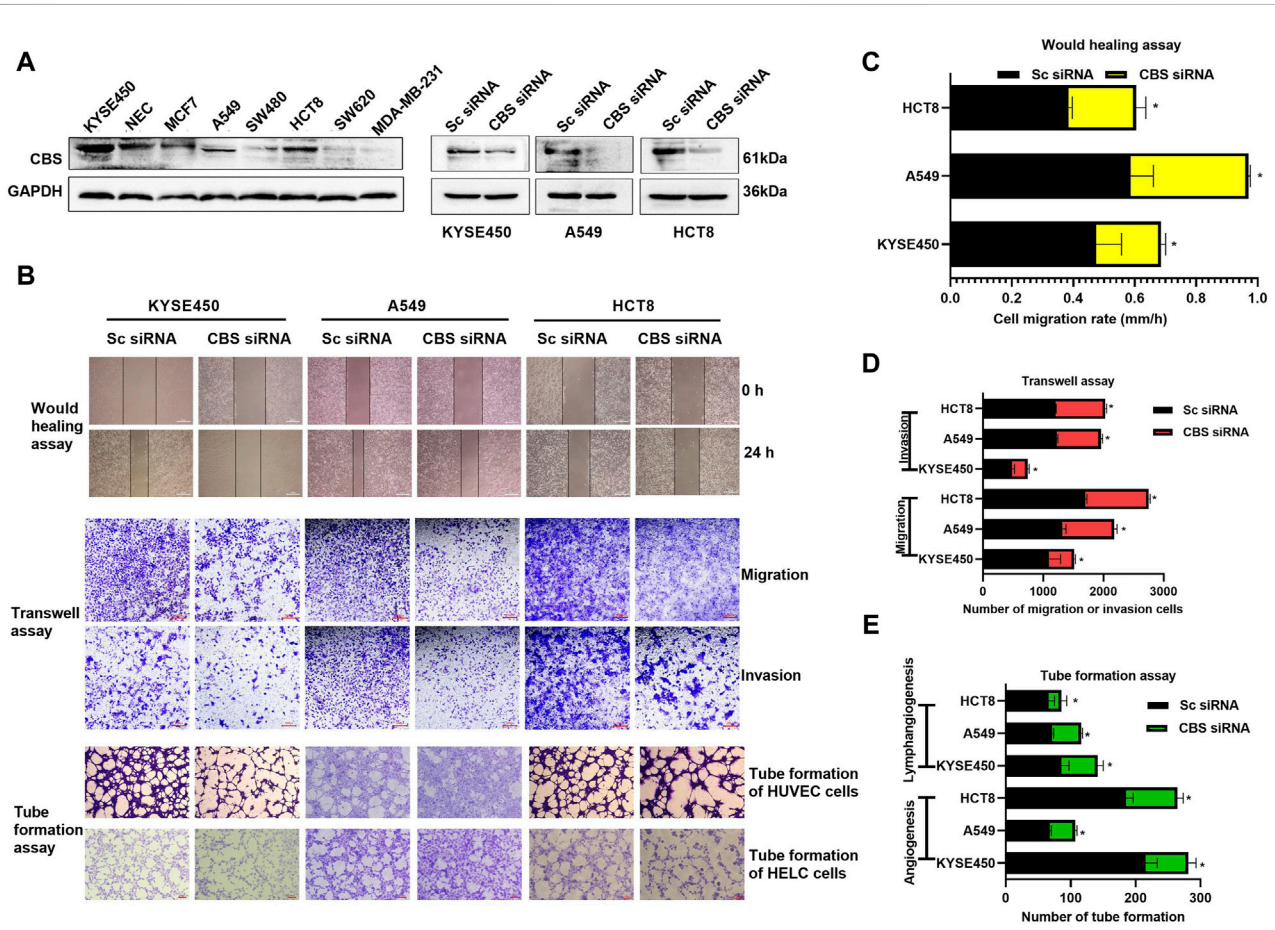

FIGURE 1
The impact of CBS expression on tumor cell growth and metastasis. **(A)** Expression levels of CBS protein in various cancer cells and validation of activity following CBS siRNA-mediated downregulation of CBS expression. **(B–E)** The effects of CBS downregulation on cancer cell migration, invasion, angiogenesis, and lymphangiogenesis. The scale of the images in the wound healing assay is 500 μm. The scale of the images in the transwell and tube formation assays is 200 μm. All data are expressed as mean ± standard deviation. *P < 0.05. CBS, cystathionine beta-synthase.

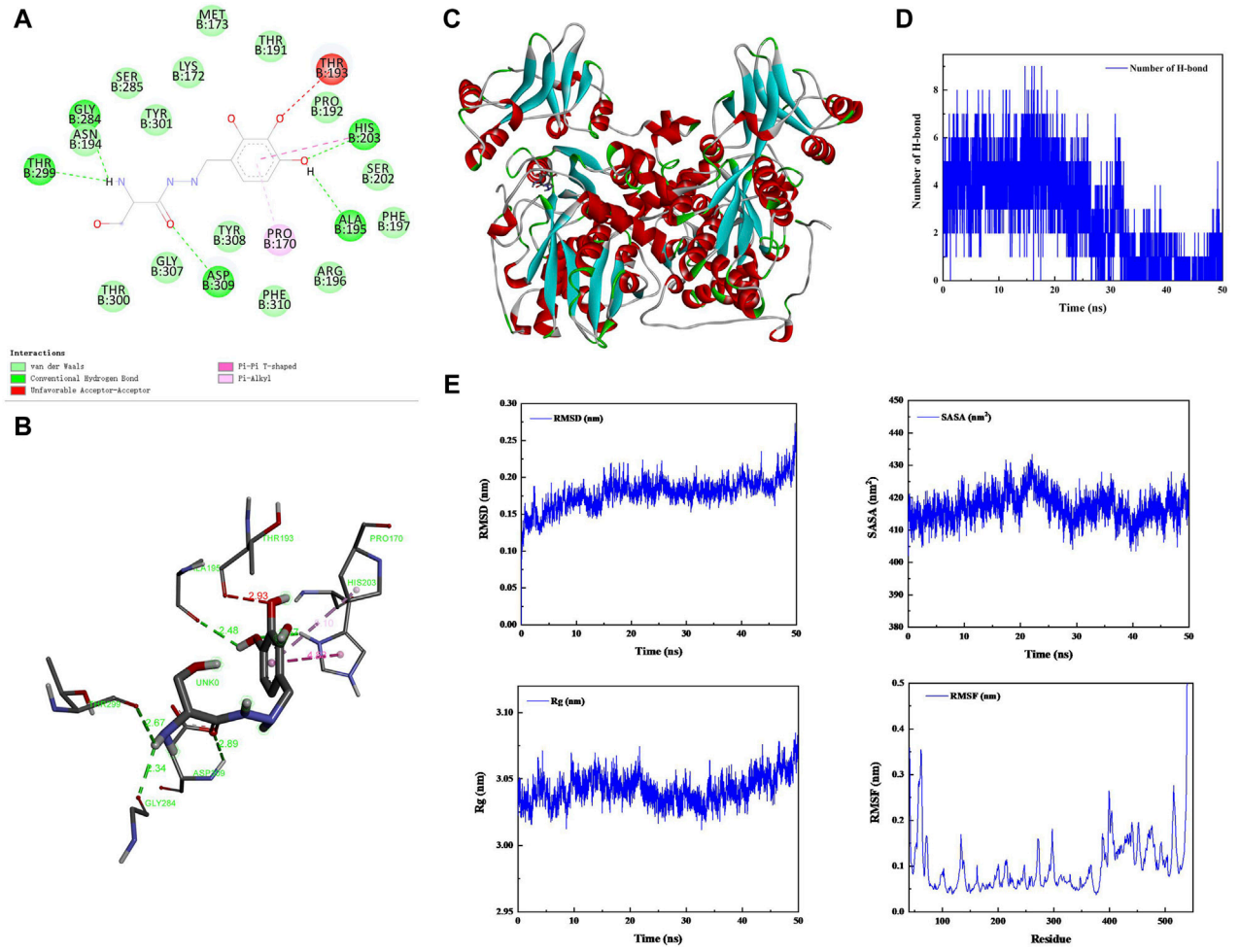

FIGURE 2
Analysis of the bingding mode of Benserazide with CBS protein. **(A–C)** 2D and 3D images of the molecular docking between Benserazide and CBS protein. **(D)** The curve showing the change in the number of hydrogen bonds over time during the simulation process of the protein-ligand complex. **(E)** The curves illustrating the changes in the protein's RMSD, SASA, Rg, and RMSF over time during the simulation process of the protein-ligand complex. RMSD, Root Mean Square Deviation; SASA, Solvent-accessible Surface Areas; Rg, rotation radius; RMSF, Root Mean Square Fluctuation.

TABLE 1 Analysis of protein ligand MMPBSA.

Energy	Complex
Van der Waals Energy (KJ/mol)	−121.873
Electrostatic energy (kJ/mol)	−8.680
Polar solvation energy (KJ/mol)	49.798
Nonpolar solvation Energy (KJ/mol)	−17.486
Total Binding Energy (KJ/mol)	−98.241

benserazide has inhibitory activity on both HCT116 cells and drug-resistant cells with high expression of CBS (Li et al., 2017; Untereiner et al., 2018).

Paclitaxel is a natural anticancer drug that has been shown to be effective against various types of cancer. However, the development of resistance to paclitaxel and its toxic side effects have limited its effectiveness when used alone (Abu et al., 2019; Smith et al., 2022; Hashemi et al., 2023). Currently, there is a lot of interest in combining paclitaxel with other drugs for cancer treatment (Yu et al., 2020; Xu et al., 2021; Škubník et al., 2023). This combination therapy approach not only helps to reduce the toxic side effects of chemotherapy but also allows for the reduction of the dosage of traditional chemotherapy drugs. Additionally, this approach can improve the overall curative effect of cancer treatment.

The purpose of this study was to investigate the potential benefits of using a combination of benserazide and paclitaxel in tumor treatment. The methodologies included the assessment of benserazide as a CBS inhibitor using advanced techniques like molecular docking (MD) and CETSA. Additionally, an exhaustive examination of the synergistic effects of the benserazide and paclitaxel combination was conducted through *in vitro* studies on antitumor activity and *in vivo* research on the inhibition of tumor lymph node metastasis, with the goal of gathering relevant data to guide future therapeutic strategies that may improve patient prognosis.

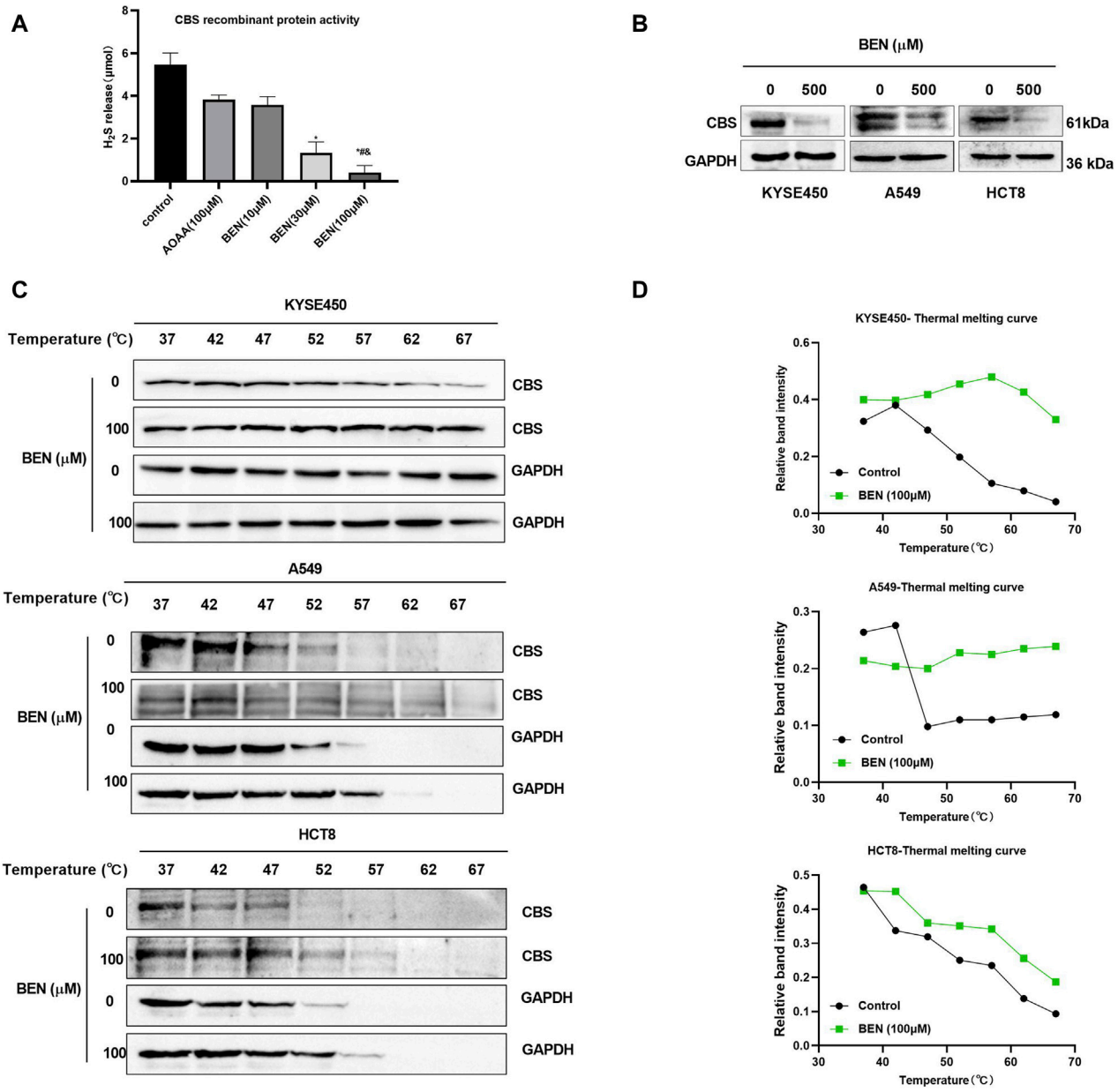

FIGURE 3
Benserazide binds to and blocks the activity of CBS in cancer cells. **(A)** Detection of H_2S release from CBS recombinant protein after drug treatment using the methylene blue method. All data are expressed as mean ± standard deviation. $^{*}p < 0.05$ vs. control group. $^{\#}p < 0.05$ vs. AOAA group. $^{\&}p < 0.05$ vs. BEN (10 μM) group. **(B)** The effect of benserazide on CBS expression in cancer cells. **(C, D)** CETSA to assess the binding capacity of Benserazide with CBS in tumor cells. BEN, Benserazide; CBS, cystathionine beta-synthase; CETSA, Cellular Thermal Shift Assay.

2 Materials

2.1 Cell lines

Human esophageal squamous cell line KYSE450 was donated by Xinxiang Medical College (Henan Province, China). Human lung cancer cell line A549 was a gift from Professor Li Hong at Henan University. Human colon cancer cell line HCT8 was donated by The Third Military Medical University (Chongqing, China). Human vascular endothelial cell (HUVEC) was generously donated by Shanghai University (Shanghai, China). Human lymphatic endothelial cells (HLEC) were purchased from Shanghai Binsui Biotechnology Co., Ltd. (Shanghai, China). The cells were cultured in RPMI-1640 medium (Gibco, Grand Island, New York, United States) supplemented with 10% fetal bovine serum (FBS; Zeta Life, Inc., San Francisco, CA, United States) at 37°C 5% CO_2. All of cells were authenticated by STR.

2.2 Drugs

Benserazide (CAS: 14919-77-8) was procured from Selleck Chemicals LLC (Houston, Texas, United States), while Paclitaxel

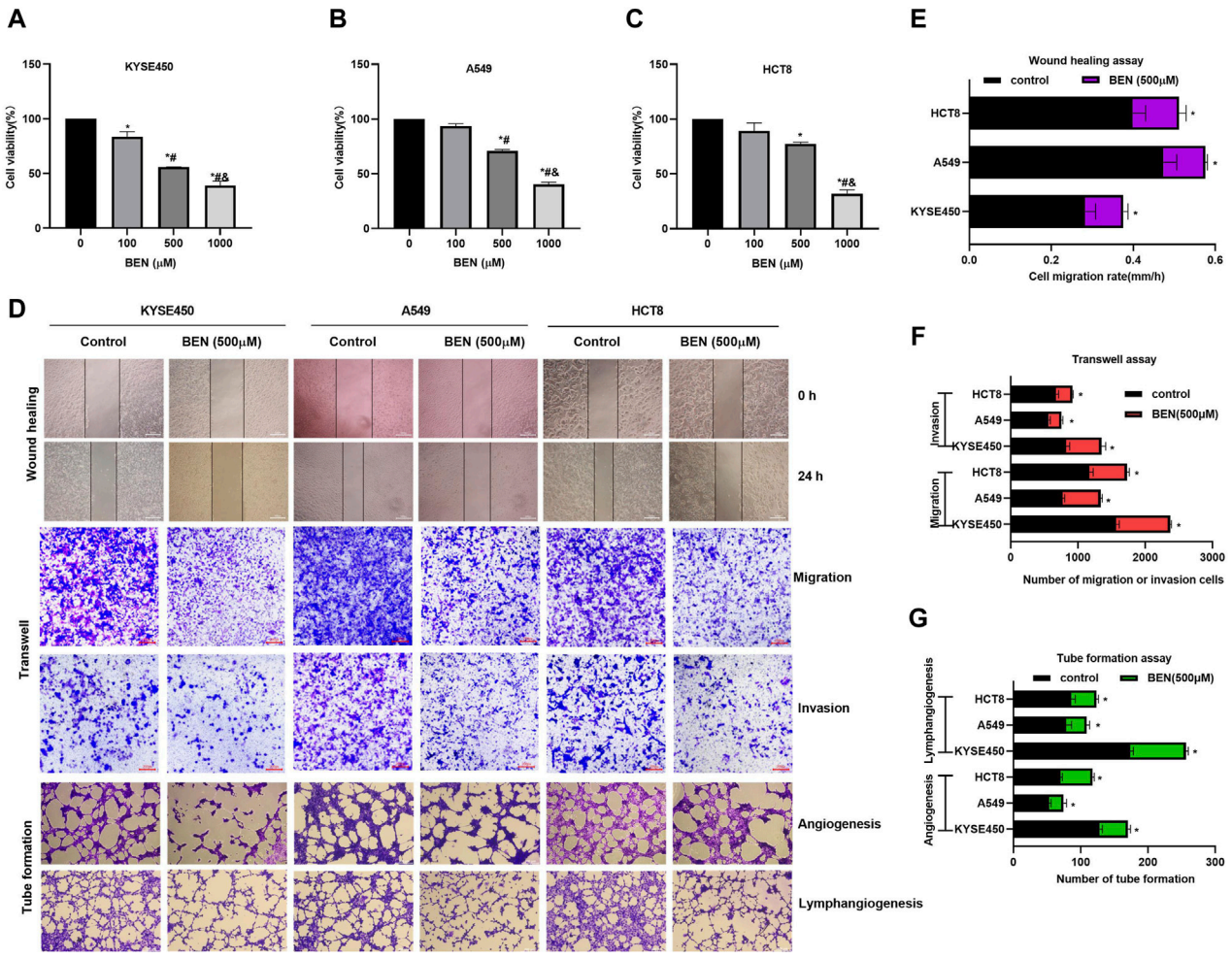

FIGURE 4
Benserazide inhibits the growth and metastasis of tumor cells. **(A–C)** The impact of Benserazide on the viability of KYSE450, A549 and HCT8 cells. All data are expressed as mean ± standard deviation. $*p < 0.05$ vs. BEN (0 μM) group. $\#p < 0.05$ vs. BEN (100 μM) group. & $p < 0.05$ vs. BEN (50 μM) group. **(D–G)** The effect of benserazide on the migration, invasion, angiogenesis, and lymphangiogenesis of KYSE450, A549 and HCT8 cells. The scale of the images in the wound healing assay is 500 μm. The scale of the images in the transwell and tube formation assays is 200 μm. All data are expressed as mean ± standard deviation. $*p < 0.05$ vs. control group. BEN, Benserazide.

(CAS: MB1178-1) was sourced from Dalian Meilun Biotechnology Co., Ltd. (Dalian, Liaoning, China). For cell experiments, paclitaxel is dissolved in DMSO (Dimethyl sulfoxide), while benserazide is dissolved in PBS (Phosphate Buffer Saline). In animal experiments, paclitaxel is administered in saline with 1% Tween 80, and benserazide is administered in saline. The dosages and preparations of the drugs were based on references (Hu et al., 2020; Zhou et al., 2020).

3 Methods

3.1 Investigation into the binding affinity of benserazide with CBS protein

3.1.1 Molecular docking (MD)

Molecular docking uses the 3D structure of CBS protein in the RCSB database, obtains the sdf structure of Benserazide through the Pubchem database, and converts it into a PDB file using OpenBabel. AutoDock Tools 1.5.6 software was used to dehydrate and hydrogenate protein targets, and the active ingredient and target protein formats were converted to pdbqt format. Finally, it is docked through AutoDock Vina. The molecular dynamics (MD) simulations were carried out by GROMACS 2020.3 software. The amber99sb-ildn force field and the general Amber force field (GAFF) were used to generate the parameter and topology of proteins and ligands, respectively. The simulation box size was optimized with the distance between each atom of the protein and the box greater than 1.0 nm. Then, fill the box with water molecules based on a density of 1. To make the simulation system electrically neutral, the water molecules were replaced with Cl- and Na + ions. Following the steepest descent method, energy optimization of 5.0 × 104 steps was performed to minimize the energy consumption of the entire system, and finally to reduce the unreasonable contact or atom overlap in the entire system. After energy minimization, first-phase equilibration was performed with the NVT ensemble at 300 K for 100 ps to stabilize the temperature of the system. Second-phase equilibration was simulated with the NPT

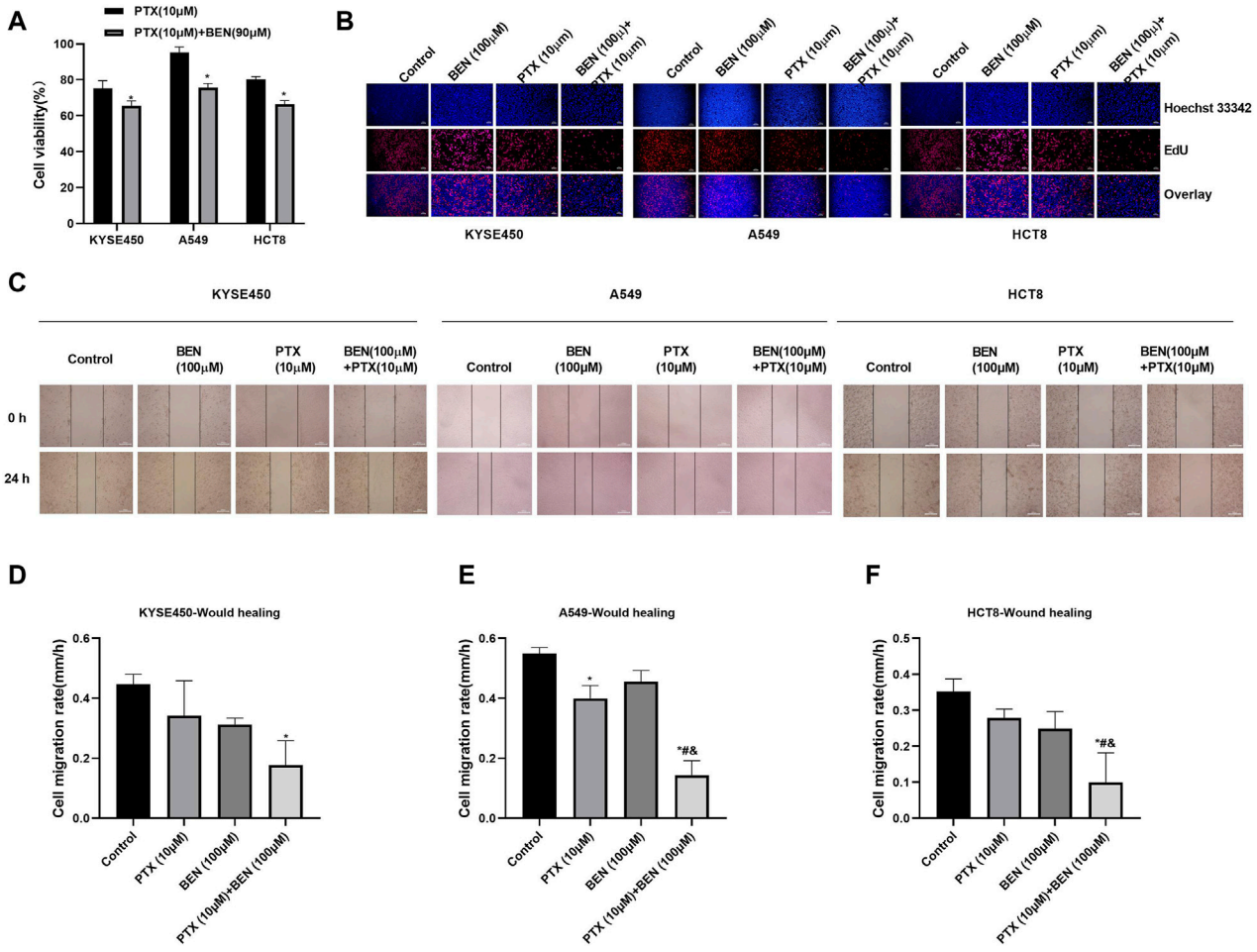

FIGURE 5
Benserazide in combination with Paclitaxel suppresses the proliferation of tumor cells. **(A)** The effect of Benserazide in combination with Paclitaxel on cell viability of KYSE450, A549 and HCT8 cells. All data are expressed as mean ± standard deviation. $^{*}p < 0.05$ vs. control group. **(B)** The effect of Benserazide in combination with Paclitaxel on cell proliferation of KYSE450, A549 and HCT8 cells. The scale of the images in the EdU assay is 200 μm. **(C–F)** The effect of Benserazide in combination with Paclitaxel on the migration of KYSE450, A549 and HCT8 cells. The scale of the images in the wound healing assay is 500 μm. All data are expressed as mean ± standard deviation. $^{*}p < 0.05$ vs. control group. $^{\#}p < 0.05$ vs. PTX group. $^{\$}p < 0.05$ vs. BEN group. BEN, Benserazide; PTX, Paclitaxel; EdU, 5-Ethynyl-2′-deoxyuridine.

ensemble at 1 bar and 100 ps. The primary objective of the simulation is to optimize the interaction between the target protein and the solvent and ions so that the simulation system is fully pre-equilibrated. All MD simulations were performed for 50 ns under an isothermal and isostatic ensemble with a temperature of 300 K and a pressure of 1 atm.

3.1.2 CBS recombinant protein activity assay

CBS recombinant protein activity assay was designed to detect the inhibitory activity of benserazide on CBS protein. The following is a brief description of the method for detecting the activity of CBS recombinant protein. First, different concentrations of benserazide (14919-77-8, Selleck Chemicals LLC, Houston, Texas, United States) and the positive control aminooxyacetic acid (AOAA) (C13408-1G, sigma-aldrich, St. Louis, Missouri, United States) were added to a 96-well plate. Then, 50 μL of active buffer containing human recombinant CBS protein (5μg/well, Abt-P-1006, Beijing Ambition Biotechnology Co., Ltd., Beijing, China), 50 mM Tris HCl (pH8.0), L-cysteine (2 mM final concentration) (C0012, Solarbio Science & Technology Co.,Ltd., Beijing, China) and 5′-phospho pyridoxal 5′-phosphate (PLP) (5 mM final concentration) (LP8221, Bomei Biotechnology Co.,Ltd., Hefei, Anhui, China) was added to each well, followed by incubation at 37°C for 2 h. After incubation, 1% ZnAc (60 μL) (5970-45-6, Yinfeng Chemical Co. , Ltd. Weifang, Shandong, China), 10% TCA (60 μL), 0.2% (w/v) N,N-dimethyl-p-phenylenediamine (10 μL) (6606, Tianjin Chemical Reagent Institute Co. , Ltd., Tianjin, China) and 10% (w/v) ammonium ferric sulfate (10 μL) were added. The plate was incubated at room temperature in the dark for 15 min, followed by measuring the absorbance at 650 nm using the EnSpire Multimode Reader (PerkinElmer, United States). The H_2S release amount was calculated based on the absorbance to evaluate the activity of CBS protein.

3.1.3 Cellular thermal shift assay (CETSA)

CETSA was used to detect the binding efficiency of benserazide to CBS protein in tumor cells. Tumor cells treated with benserazide or vehicle (control group) were lysed using RIPA buffer and divided into seven groups. The protein extracts were heated at 37°C, 42°C,

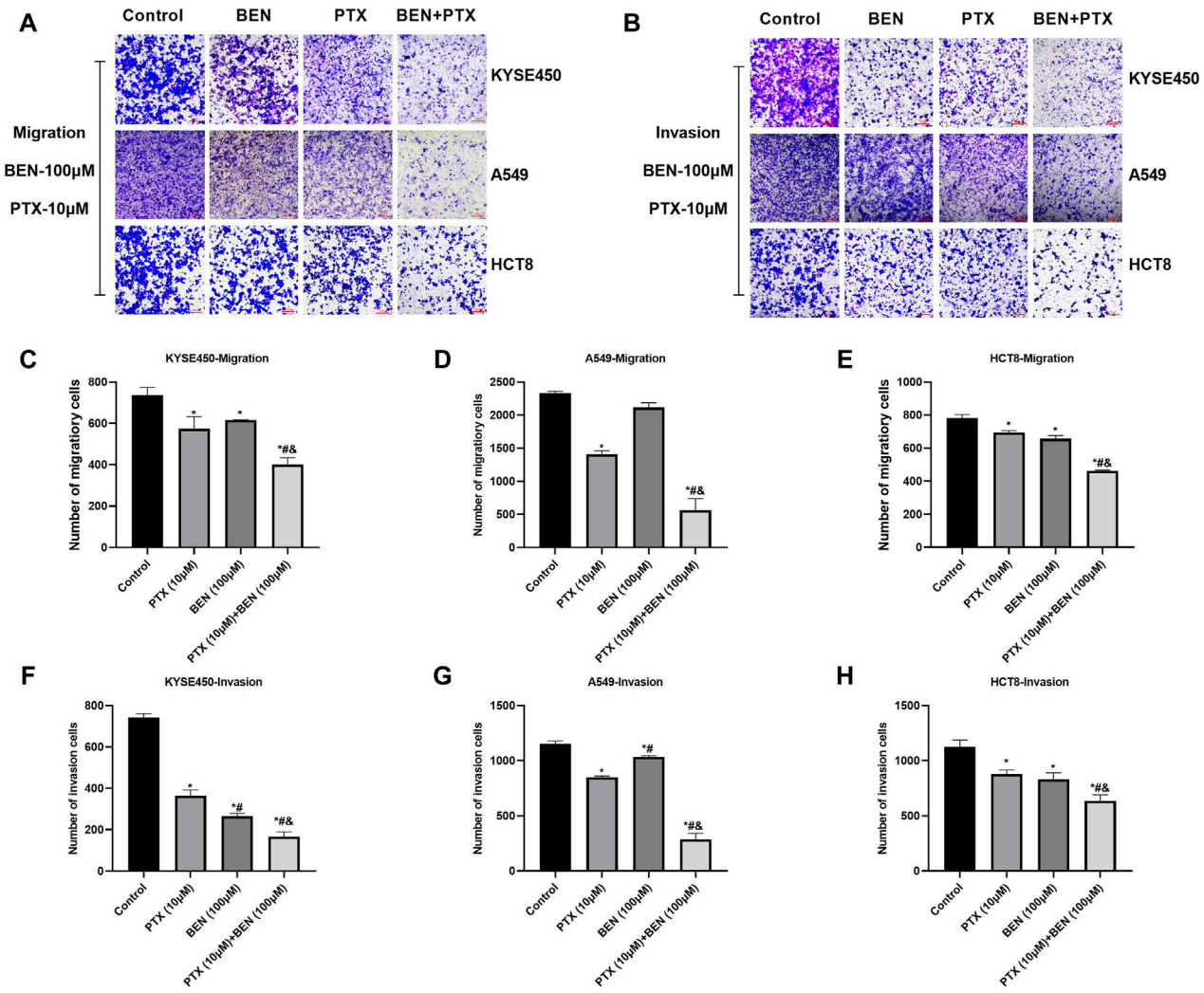

FIGURE 6
Benserazide in combination with Paclitaxel inhibits the migration and invasion of tumor cells. **(A, B)** The effect of Benserazide in combination with Paclitaxel on the migration and invasion of KYSE450, A549 and HCT8 cells. The scale of the images in the transwell assay is 200 μm. **(C–H)** The statistical analysis of migratory or invasion cells. All data are expressed as mean ± standard deviation. $^{*}p < 0.05$ vs. control group. $^{\#}p < 0.05$ vs. PTX group. $^{\&}p < 0.05$ vs. BEN group. BEN, Benserazide; PTX, Paclitaxel.

47°C, 52°C, 57°C, 62°C, and 67°C for 20 min each before undergoing repeated freeze-thaw cycles to extract proteins. Western blot analysis was then performed to detect the expression of CBS protein and internal control protein at each heating temperature. The resulting thermal melting curves for the benserazide-treated and control groups were obtained by plotting the "CBS/Loading Control" *versus* temperature.

3.2 *In vitro* study

3.2.1 MTS assay

The MTS assay was used to measure the cell viability *in vitro*. In this study, the KYSE450, A549, and HCT8 cells were cultured with test compounds in 96-well plates containing a final volume of 100 μL/well for 48 h. The MTS reagent (M8180, Solarbio Science &Technology Co.,Ltd., Beijing, China) was then added to each well and incubated with the cells for 4 h under standard culture conditions. The absorbance at 490 nm was measured using the EnSpire Multimode Reader (PerkinElmer, United States). These results were expressed as a percentage of control values, which represent the amount of formazan product produced by viable cells.

3.2.2 EdU assay

The EdU assay was performed to determine the cell proliferation *in vitro*. In this study, the KYSE450, A549, and HCT8 cells were cultured with test compounds in 96-well plates for 24 h. The EdU assay kit (C10310-1, Guangzhou Ribbio Co., Ltd., Guangzhou, China) was then used to evaluate cell proliferation by measuring the number of EdU^{+} cells.

3.2.3 Wound healing assay

The wound healing assay is a commonly used method to assess cell migration. In this study, the cells were seeded into six-

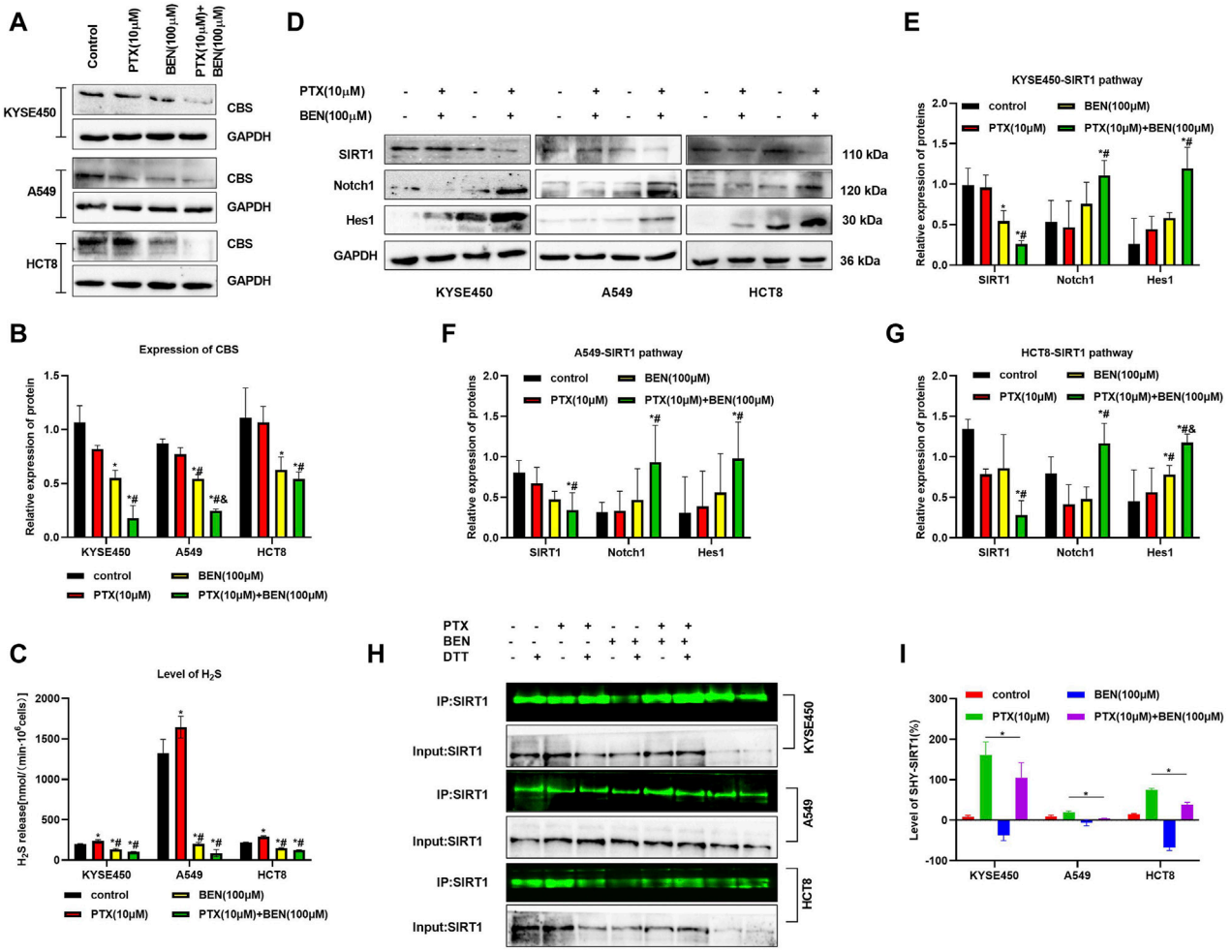

FIGURE 7
Benserazide in combination with Paclitaxel prevents the S-sulfhydration of SIRT1 protein. **(A, B)** Benserazide in combination with Paclitaxel reduces the level of CBS protein in KYSE450, A549 and HCT8 cells. **(C)** Benserazide in combination with Paclitaxel inhibits the production of H2S in KYSE450, A549 and HCT8 cells. **(D–G)** Benserazide in combination with Paclitaxel downregulates the SIRT1 signal pathway in KYSE450, A549 and HCT8 cells. **(H–I)** Benserazide in combination with Paclitaxel decreases the S-sulfhydration level of SIRT1 protein in KYSE450, A549 and HCT8 cells. All data are expressed as mean ± standard deviation. The data pertaining to panel B (KYSE450 cells), panel C (A549 cells), and panel E (Hes1 protein) do not adhere to a normal distribution. $^{*}p < 0.05$ vs. control group. $^{\#}p < 0.05$ vs. PTX group. $^{\&}p < 0.05$ vs. BEN group. BEN, Benserazide; PTX, Paclitaxel; SIRT1, Sirtuin 1; Notch1, Notch homolog 1; Hes1, Hairy and Enhancer of Split 1.

well plates at a density of 4×10^5 cells per well and a linear wound was created by pipetting with a 10 μL nozzle. The cells were then treated with test compounds and migration photos were taken at 0h and 24 h post-treatment. The gap closure rate was calculated by comparing the distance between the edges of the wound at 0h and 24 h.

3.2.4 Transwell assay

The transwell assay is a method for assessing cell migration and invasion. In this study, the cells were seeded into the upper compartment of the transwell chamber at a density of 2×10^4 cells per well in 200 μL of serum-free medium for the migration assay or with the matrix gel for the invasion assay. The lower chamber was filled with 500 μL of medium containing 10% serum. After 24 h of incubation, the cells on the upper surface of the membrane were fixed with 4% paraformaldehyde for 10 min and then stained with crystal violet for 30 min. The number of cells that had migrated or invaded through the membrane to the lower surface was counted under an inverted microscope.

3.2.5 Tube formation assay

This experiment aims to investigate angiogenesis. Initially, 100 μL of matrix glue was added to each well of a 24-well plate and allowed to solidify for 30 min. Subsequently, 500 μL of conditioned medium and either HUVECs (2×10^5) or HLECs (2×10^5) were added to each well containing the matrix glue. The plate was then incubated at 37°C and 5% CO_2 for 6–8 h. Finally, the capillaries formed were photographed under a 100× bright field microscope, and the number of capillaries in each well was counted.

3.2.6 Western blot assay

The cells were lysed in a cell lysate containing 1% benzoyl fluoride (PMSF), and the protein concentration was determined using a BCA protein detection kit. Western blot analysis was then

performed using a standard protocol. The protein samples were separated by electrophoresis on a gel plate and transferred to a PVDF membrane. After being closed at room temperature for 2 h, the membrane was incubated with primary antibodies overnight, washed three times with TBST buffer, and then incubated with secondary antibodies at room temperature for 2 h. Finally, the Enhanced Chemiluminescence (ECL) Assay Kit (PE0010, Solarbio Science &Technology Co.,Ltd., Beijing, China) was used to visualize the protein bands. The primary antibodies: CBS (14782, Cell Signaling Technology, Boston, United States), VEGF-C (2445, Cell Signaling Technology, Boston, United States), HIF-1α (20960-1-AP,Proteintech, Wuhan, Hubei, China), VEGF-A (19003-1-AP, Proteintech, Wuhan, Hubei, China), Notch1 (20687-1AP, Proteintech, Wuhan, Hubei, China), GAPDH (AG019, Bieyotime, Zhengzhou, Henan, China), SIRT1(CY5023, Abways, Shanghai, China), Hes1(CY5649, Abways, Shanghai, China), VEGF-D (CY10042,Abways, Shanghai, China).

3.2.7 Methylene blue assay

Methylene blue assay was performed to determine the levels of H_2S in tumor cells. L-cysteine (2 mM final concentration) and 5′-phospho pyridoxal 5′-phosphate (PLP) (5 mM final concentration) were added to the tumor cells cultured in a 6-well plate to promote H2S production. At the same time, 1% ZnAc (500 μL) was dropped onto filter paper attached to the lid of the 6-well plate to absorb the H2S released by the cells. After 24 h, the filter paper was placed into an eppendorf tube containing 0.2% (w/v) N, N-dimethyl-p-phenylenediamine (500 μL), 10% (w/v) ammonium ferric sulfate (50 μL), and 3 mL ddH2O. The tube was incubated at room temperature for 20 min before measuring the absorbance at 670 nm.

3.2.8 The maleimide assay

Maleimide is a commonly used thiol-modifying reagent, and Cys residues are its reaction sites. Therefore, maleimide is used to detect the sulfhydryl modifications of proteins. Firstly, proteins are immunoprecipitated, and then maleimide (E1271-1G, Henan Puyingmei Biotechnology Co., Ltd., Zhengzhou, Henan, China) selectively labels unmodified and sulfonated cysteines. DTT (D1070-1, Solarbio Science &Technology Co.,Ltd., Beijing, China) is then used to reduce disulfides (-S-S-Mal). Finally, the samples are placed on polyacrylamide gels for scanning to detect fluorescently labeled proteins, and image analysis software is used for fluorescence quantification.

3.2.9 ELISA

ELISA (Enzyme-Linked Immunosorbent Assay) was used to measure the concentration of proteins in a sample. In this case, VEGF-A, VEGF-C, and VEGF-D levels in the cell culture supernatant were detected using ELISA kits (ELK1129, ELK1194, ELK1195, ELK Biotechnology CO., LTD., Wuhan, China). The optical density (OD) was measured the EnSpire Multimode Reader (PerkinElmer, United States) at a wavelength of 450 nm. By comparing the OD values obtained for different samples or controls, we obtained the relative levels of VEGF-A, VEGF-C, and VEGF-D in the cell culture supernatant.

3.3 *In vivo* study

C57BL/6J mice (Four-week-old, weighing 16–18 g) were housed in sterile breeding cages, with six animals per cage, under constant temperature (approximately 22°C), humidity (45%–65%), a 12-h light/12-h dark cycle, minimal noise conditions, and provided with ample access to food, water, and sterile bedding. After a 1-week acclimation period in this environment, each mouse received a subcutaneous injection of 1.5×10^6 AKR mouse esophageal cancer cells into the right hind paw pad to establish a lymph node metastasis model. The mice were then randomly divided into four groups (control group, benserazide treatment group, paclitaxel treatment group, benserazide plus paclitaxel treatment group), six mice per group. The treatment groups received daily intraperitoneal injections (benserazide 20 mg/kg, paclitaxel 5 mg/kg), while the control group received an equivalent volume of saline. During the treatment, pain and distress were minimized and alleviated through close monitoring of the mice's behavior and weight changes, environmental enrichment, and humane endpoints. After 14 days, the mice were humanely sacrificed using cervical dislocation. Immediately after sacrifice, Lymph nodes and visceral organs such as the heart, liver, spleen, lungs, and kidneys were harvested from mice and fixed in 10% paraformaldehyde for HE staining. The experiment was conducted according to the methods described in reference (Liu et al., 2015). This experiment was approved by the Ethics Committee of Medical School of Henan University (HUSOM 2020-095, 25 March 2020).

3.4 Statistical analysis

The experiments were conducted with at least three repetitions. The data was presented as mean ± standard deviation (SD), and analyzed using GraphPad Prism eight software. For comparing paired data, the *t*-test is used to determine if there is a significant difference between the means of two groups. When comparing multiple groups of data, we first employ the Shapiro-Wilk test to check for normality. For data that are normally distributed, one-way Analysis of Variance (ANOVA) followed by Tukey's multiple comparisons test is used, whereas for data that do not follow a normal distribution, such as those presented in Figure 7B (KYSE450 cells), Figure 7C (A549 cells), Figure 7E (Hes1 protein), Figure 8G (VEGF-A protein), Figure 8J (VEGF-A/D proteins), and Figure 9C, the Kruskal–Wallis H test is utilized to assess the significance of differences. Every possible comparison between the study groups was considered. $p < 0.05$ was considered statistically significant.

4 Results

4.1 CBS is involved in the progress of multiple cancers

Previous research has indicated that Cystathionine β-synthase (CBS) is highly expressed and contributes to the progression of various types of cancer. Here, we further demonstrated that CBS is highly expressed in KYSE450, NEC, MCF7, A549 and HCT8 cells

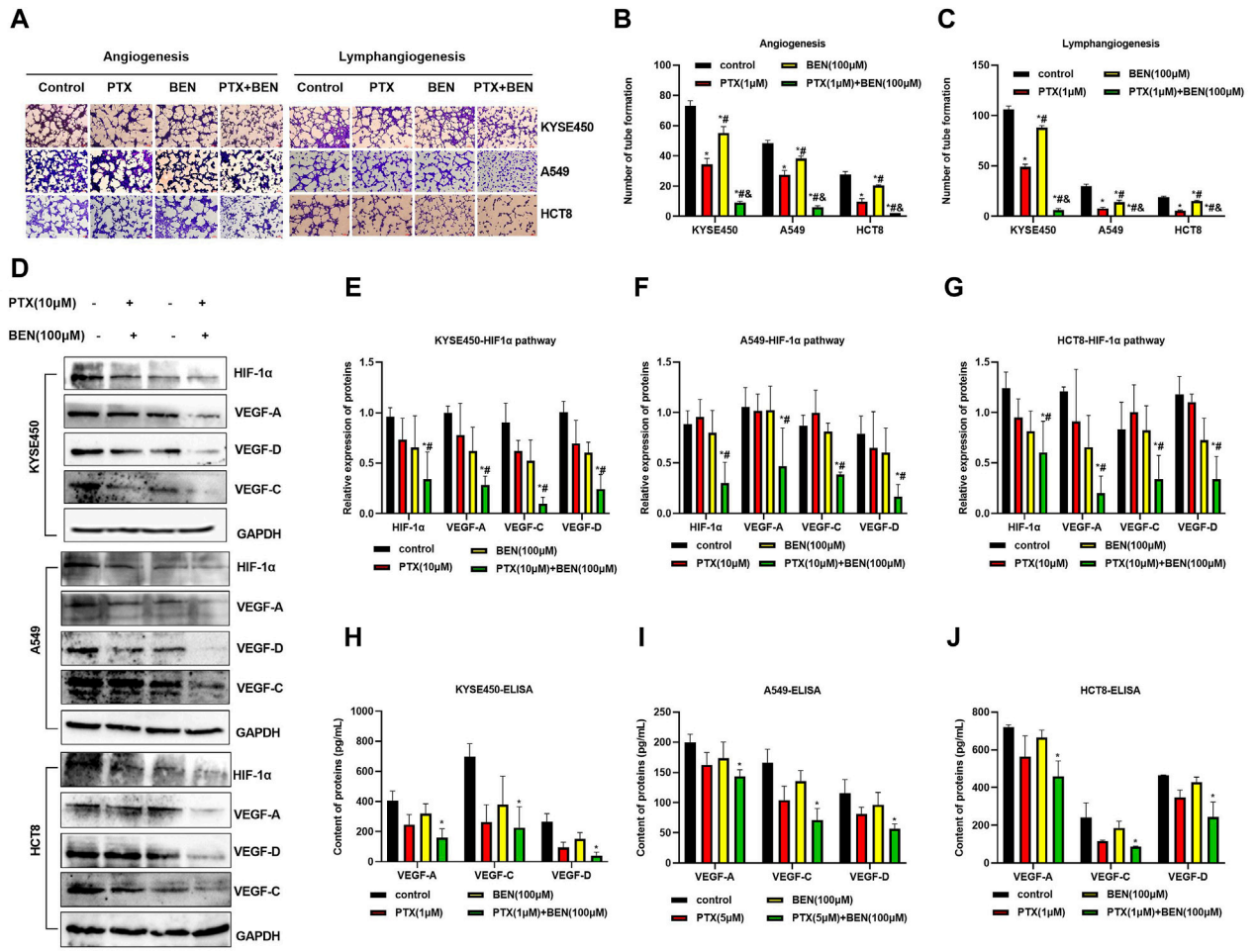

FIGURE 8
Benserazide combined with paclitaxel inhibits angiogenesis and lymphangiogenesis through suppressing the HIF1-1α/VEGF pathway. **(A–C)** The impact of Benserazide combined with Paclitaxel on angiogenesis and lymphangiogenesis induced by KYSE450, A549 and HCT8 cells. The scale of the images in the tube formation assays is 200 μm. **(D–G)** The effect of Benserazide combined with Paclitaxel on the HIF1-1α/VEGF pathway in KYSE450, A549 and HCT8 cells. **(H–J)** ELISA assay to detect intracellular VEGF-A, VEGF-C and VEGF-D levels. All data are expressed as mean ± standard deviation. The data pertaining to panel G (VEGF-A protein) & panel J (VEGF-A/D proteins) do not adhere to a normal distribution. $^{*}p < 0.05$ vs. control group. $^{\#}p < 0.05$ vs. PTX group. $^{\&}p < 0.05$ vs. BEN group. BEN, Benserazide; PTX, Paclitaxel; HIF-1α, Hypoxia-inducible factor 1α; VEGF, Vascular Endothelial Growth Factor.

(Figure 1A) and downregulation of CBS (Figure 1A) has been shown to inhibit tumor cell migration and invasion, as well as suppress angiogenesis and lymphangiogenesis (Figures 1B–E) in KYSE450, A549 and HCT8 cells. This suggests that CBS plays an important role in the progression of various types of cancer.

4.2 Benserazide inhibits CBS by forming a stable complex with CBS protein

Benserazide is a peripheral dopamine decarboxylase inhibitor that has been shown to have CBS protease inhibitory activity. To verify the function of benserazide, we first analyzed its binding mode with CBS protein using molecular docking. It is found that the binding free energy of benserazide and CBS protein is −6.9 kcal/mol and CBS protein contains several amino acid residues that are capable of forming hydrogen bonds with benserazide, namely, ALA195, THR299, ASN194, HIS203, and ASP309. Furthermore, HIS203 is also able to engage in π-π interactions with benserazide. Additionally, PRO170 of the protein can form Pi-Alkyl interactions with benserazide. The binding mode of benserazide to CBS protein is shown in Figures 2A–C. Subsequently, molecular dynamics analysis was employed to assess the stability of the conformation. The analysis of Hydrogen bond, root mean square deviation (RMSD), solvent-accessible surface areas (SASA), rotation radius (Rg) and Root Mean Square Fluctuation (RMSF) showed that benserazide and CBS protein are able to bind stably (Figures 2D, E). To better explain the interaction energy between protein and ligand, we used the gmx_mmpbsa (https://jerkwin.github.io/gmxtool/) script to determine all binding energies of protein-ligand complexes during the equilibrium stage. The results showed that in the protein-ligand complex system, the total binding free energy between protein and small molecule is −98.241 kJ/mol (Table 1), indicating a stable binding between protein and small molecule.

In addition, the inhibitory effect of benzserazide on CBS protein was further investigated. It was discovered that the release of H_2S in

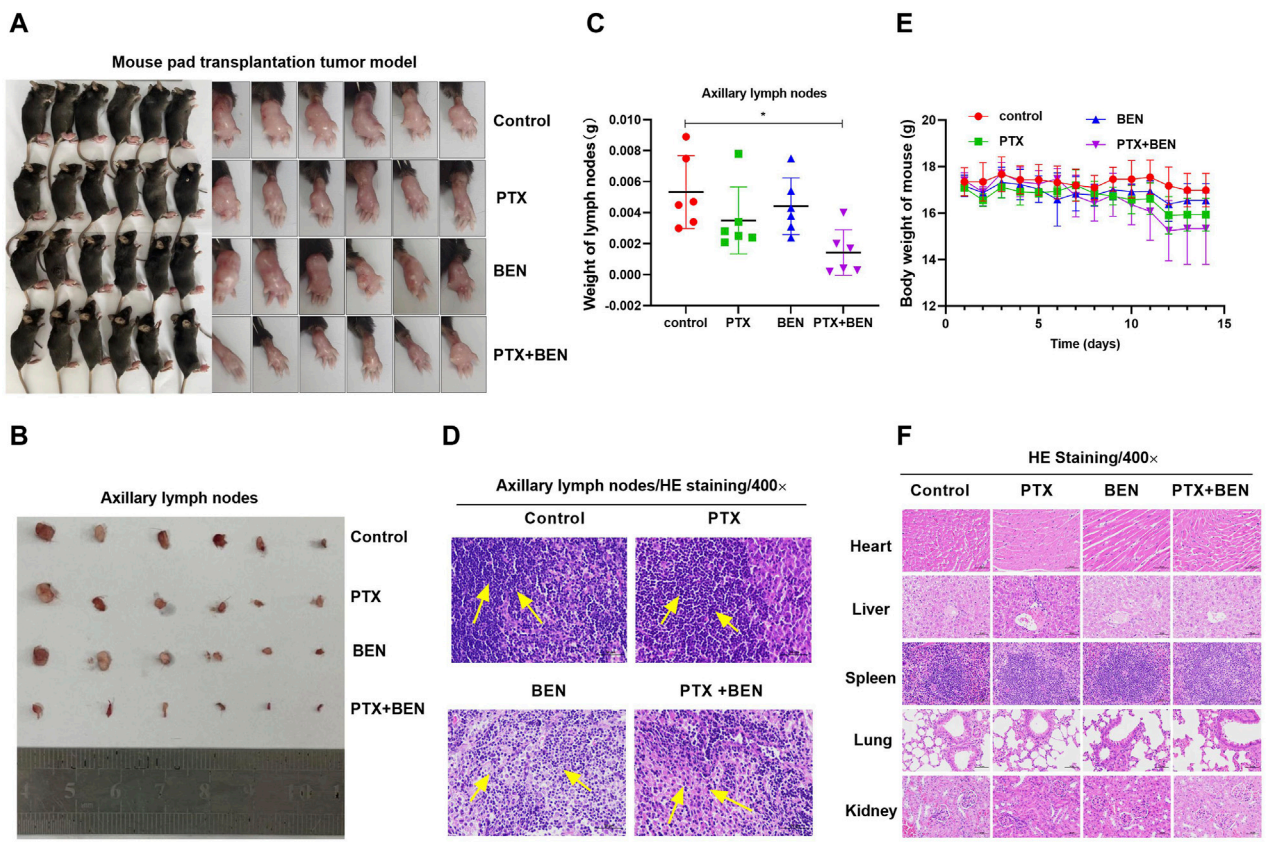

FIGURE 9
Benserazide combined with paclitaxel inhibits lymph node metastasis of mouse transplanted tumors. (A) Mouse pad transplantation tumor model. **(B, C)** The effect of Benserazide combined with Paclitaxel on volume and weight of axillary lymph nodes. **(D)** H&E staining to detect the tumor cell infiltration in the lymph nodes. The arrows indicate the infiltration of inflammatory or tumor cells. **(E)** The effect of Benserazide combined with Paclitaxel on the body weight of mice. **(F)** H&E staining to detect the morphology changes of heart, liver, spleen, lung, and kidney of mice. All data are expressed as mean ± standard deviation. The data pertaining to panel C do not adhere to a normal distribution. $^{*}p < 0.05$ vs. control group. BEN, Benserazide; PTX, Paclitaxel.

the 100 μM benserazide-treated group was merely 7.5% of that in the negative control, and significantly lower than that in the positive control AOAA-treated group (Figure 3A). Furthermore, our observations revealed that benserazide had an inhibitory effect on the expression of CBS protein in cancer cells, as shown in Figure 3B. Additionally, CETSA assay was performed to detect whether benserazide can bind to CBS in cancer cells and it was found that the amount of undegraded CBS protein increased in the presence of benserazide, and the thermal melting curve of the complex protein shifted to the right at the denaturation temperature of 52°C–67°C (Figures 3C, D), indicating that benzserazide can bind to CBS protein in cancer cells. The findings suggest that Benserazide can inhibit the activity of CBS protein by forming a stable complex with it.

4.3 Benserazide inhibits the growth and metastasis of tumor cells

In order to investigate the role of benserazide in cancer cells, we conducted a series of experiments. Our results from the MTT assay showed that benserazide inhibited tumor cell growth in a concentration-dependent manner (Figures 4A–C). Furthermore, we examined the effect of benserazide on tumor cell metastasis *in vitro* using a wound healing assay and a transwell assay. The findings suggested that benserazide could impede the migratory and invasive abilities of cancer cells (Figures 4D–F). In addition, our tube formation experiment revealed that benserazide significantly inhibited tumor cell angiogenesis and lymphangiogenesis when compared to the control group (Figures 4D, G). These findings suggest that benserazide possesses potential antitumor activity.

4.4 Benserazide enhances the antitumor activity of paclitaxel by modulating the SIRT1 pathway

In order to find a new therapeutic strategy that can increase the sensitivity of tumor therapy while reducing the dose of traditional chemotherapy drugs, we investigated the sensitization effect of benserazide on paclitaxel. By administering a nontoxic dose of benserazide (100 μM), we found that the combined administration of benserazide and paclitaxel could significantly reduce the viability of tumor cells (Figure 5A) and inhibit tumor cell proliferation (Figure 5B), migration and invasion (Figures 5C–F, 6) more effectively than paclitaxel alone. These results suggest that

10.3389/fphar.2024.1404532

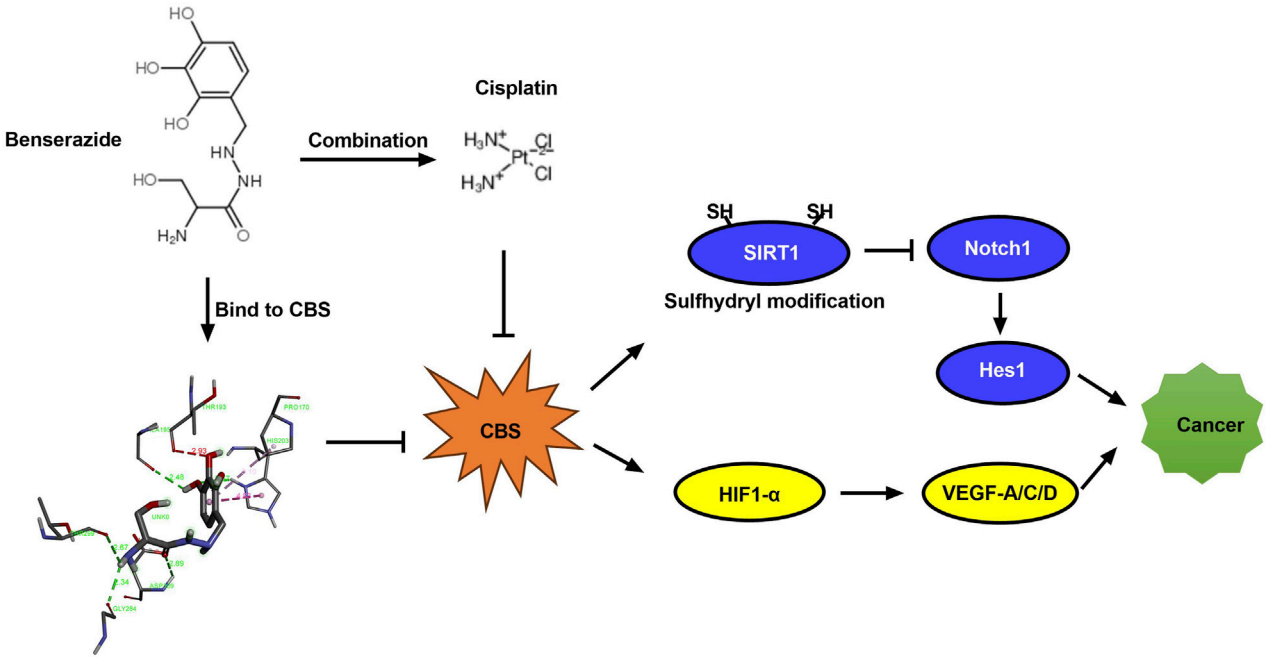

FIGURE 10
Diagram illustrating how benserazide augments the tumoricidal effect of paclitaxel. CBS, cystathionine beta-synthase; SIRT1, Sirtuin 1; Notch1, Notch homolog 1; Hes1, Hairy and Enhancer of Split 1; HIF-1α, Hypoxia-induced factor 1α; VEGF, Vascular Endothelial Growth Factor.

the addition of benserazide can enhance the sensitivity of chemotherapy drug, thereby increasing the efficiency of tumor therapy.

SIRT1 upregulation has already been demonstrated in various cancer cells, such as esophageal squamous cell carcinoma (ESCC), lung cancer, and colon cancer. In addition, some studies have found that the activation of Notch1/Hes1 signaling pathway, as a downstream pathway of SIRT1, can induce apoptosis in esophageal squamous cell carcinoma and colon cancer cells, as well as inhibit their lymph node metastasis. Furthermore, research has demonstrated that H_2S can enhance the expression of SIRT1 by facilitating its S-sulfhydration. In this study, we examined the impact of benserazide on the SIRT1 pathway to elucidate the mechanism by which CBS inhibitor benserazide enhances paclitaxel's antitumor activity. Our investigation found that benserazide alone and in combination with paclitaxel significantly decreased the level of CBS/H_2S system in KYSE450, A549, and HCT8 cells (Figures 7A–C). Western blot results showed that the combination of benserazide and paclitaxel significantly inhibited the expression of SIRT1 and caused an increase in the levels of SIRT1 downstream proteins Notch1 and Hes1 in KYSE450, A549, and HCT8 cells compared to paclitaxel alone (Figures 7D–G). Furthermore, maleimide assay results showed that the combination of benserazide and paclitaxel significantly reduced the levels of S-sulfhydration of SIRT1 in KYSE450, A549, and HCT8 cells compared to paclitaxel alone (Figures 7H, I). These findings suggest that benserazide inhibits SIRT1 signaling pathway by preventing the S-sulfhydration of SIRT1, which in turn potentiates the antitumor effects of paclitaxel.

4.5 Benserazide combined with paclitaxel inhibits angiogenesis and lymphangiogenesis through suppressing the HIF1-1α/VEGF pathway

Angiogenesis and lyrmphangiogenesis are essential processes for the metastasis of tumor cells. In this study, we investigated the effect of benserazide combined with paclitaxel on angiogenesis and lymphangiogenesis of tumor cells *in vitro*. Our results from the tube formation experiment showed that the combined administration significantly inhibited the ability of tumor cells to induce neovascularization through HUVECs and HLECs (Figures 8A–C).

The hypoxia-induced factor HIF-1α and VEGF play a crucial role in tumor angiogenesis and lymphangiogenesis. Specifically, HIF-1α can increase the expression of VEGF, which in turn promotes both angiogenesis and lymphangiogenesis. In this study, we observed that benserazide combined with paclitaxel induced a more significant downregulation of HIF-1α expression levels in KYSE450, A549, and HCT8 cells compared to paclitaxel alone (Figures 8D–G). Additionally, we found that the expression of VEGF-A, VEGF-C, and VEGF-D proteins was significantly reduced in the combination treatment group (Figures 8D–G). We further used ELISA to detect the levels of VEGF-A, VEGF-C, and VEGF-D and observed that the combination treatment group had lower levels of all three proteins (Figures 8H–J). These findings indicate that benserazide enhances the inhibitory effect of paclitaxel on tumor cell angiogenesis and lymphangiogenesis via the HIF-1α/VEGF pathway.

4.6 Benserazide combined with paclitaxel inhibits lymph node metastasis of mouse transplanted tumors

Based on the aforementioned results that benserazide in combination with paclitaxel has an inhibitory effect on angiogenesis and lymphangiogenesis, we aimed to further investigate their *in vivo* activity when used together. To achieve this, we established a mouse pad transplantation tumor model to study their impact on lymph node metastasis (Figure 9A). Our observations revealed that the combined administration of benserazide and paclitaxel significantly reduced the volume and weight of axillary lymph nodes in comparison to the control group and single administration group (Figures 9B, C). Furthermore, H&E staining results demonstrated that tumor cell infiltration in the lymph nodes was also significantly lower in the combined administration group compared to the single administration group (Figure 9D). Additionally, the body weight of mouse and the morphology of heart, liver, spleen, lung, and kidney of mice had no significant differences in the combined administration group when compared to the control group and single administration group (Figures 9E, F). These findings suggest that benserazide in combination with paclitaxel has a potent inhibitory effect on tumor lymph node metastasis *in vivo*.

5 Discussion

As an advanced or metastatic tumor treatment, chemotherapy is the primary option. Paclitaxel-based regimens are the most commonly used chemotherapy treatments. Recent clinical trials have focused on adding targeted therapies to chemotherapy. In this study, we evaluated the therapeutic potential of benserazide, a targeting CBS inhibitor, in combination with paclitaxel to inhibit tumor growth and understand the mechanism of action of these drugs.

Firstly, we verified whether benserazide targets and inhibits the CBS protein. Molecular docking results showed that the binding free energy of benserazide and CBS protein is −6.9 kcal/mol, and CBS protein contains amino acid residues capable of forming hydrogen bonds, π-π interactions, and Pi-Alkyl interactions with benserazide. Additionally, it was discovered that benserazide significantly inhibits the activity of recombinant CBS protein with a stronger inhibition than AOAA. Furthermore, CETSA assay found that the presence of benserazide increased the amount of undegraded CBS protein and caused the thermal melting curve of the complex protein to shift to the right at the denaturation temperature of 52°C–67°C, indicating that benserazide can bind to CBS protein in cancer cells. Our observations also revealed that benserazide had an inhibitory effect on the expression of CBS protein in cancer cells. The findings suggest that Benserazide Inhibits CBS by Forming a Stable Complex with CBS Protein.

Next, we investigated the sensitization effect of benserazide on paclitaxel *in vitro* and *in vivo* to find a new therapeutic strategy that can increase the sensitivity of tumor therapy. We found that the combined administration of a nontoxic dose of benserazide (inhibitory rate of cells <10%) and paclitaxel could significantly reduce the viability of tumor cells and inhibit tumor cell proliferation, migration, invasion, angiogenesis, and lymphangiogenesis more effectively than paclitaxel alone *in vitro*. In addition, Benserazide combined with paclitaxel inhibits lymph node metastasis of mouse transplanted tumors. These results suggest that the addition of benserazide can enhance the sensitivity of chemotherapy drugs, thereby increasing the efficiency of tumor therapy.

To further explore the mechanism of benserazide enhancing paclitaxel anticancer activity, we investigated the effect of the combination of benserazide and paclitaxel on SIRT1 and HIF-1a signaling pathways.

Sirtuin-1 (SIRT1) is a class-III histone deacetylase (HDAC), an NAD + -dependent enzyme deeply involved in gene regulation, genome stability maintenance, apoptosis, autophagy, senescence, proliferation, aging, and tumorigenesis (Alves-Fernandes and Jasiulionis, 2019). SIRT1 upregulation has already been demonstrated in some cancer cells, such as esophageal squamous cell carcinoma (ESCC), lung cancer, and colon cancer (Hong and Pyo, 2018; Ma et al., 2018; Guo et al., 2021; Otsuka et al., 2022). Furthermore, increased expression of SIRT1 has been found to confer resistance to cisplatin in cancer cells (Cao et al., 2015; Wang et al., 2022; Sun et al., 2023). Moreover, research has demonstrated that H_2S can enhance the expression of SIRT1 by facilitating its S-sulfhydration (Wu et al., 2023), which involves altering the Cys residues on the target protein to convert the sulfhydryl group (R-SH) into a persulfide group (R-SSH). In this study, we found that the combination of benserazide and paclitaxel significantly inhibited the S-sulfhydration of SIRT1 protein and the expression of SIRT1 protein, consequently activating downstream Notch1/Hes1 signaling pathway in KYSE450, A549, and HCT8 cells.

The hypoxia-induced factor HIF-1α and VEGF play a crucial role in tumor angiogenesis and lymphangiogenesis (Alam et al., 2023; Song et al., 2023). Specifically, HIF-1α can increase the expression of VEGF, which in turn promotes both angiogenesis and lymphangiogenesis. In this study, we observed that benserazide combined with paclitaxel induced a more significant downregulation of HIF-1α, VEGF-A, VEGF-C, and VEGF-D proteins expression levels in KYSE450, A549, and HCT8 cells compared to paclitaxel alone. The results indicated that Benserazide enhances the anticancer effects of paclitaxel via inhibiting the S-sulfhydration of SIRT1 and enhancing the anti-angiogenic effect of paclitaxel through downregulation of HIF-1α/VEGF signaling pathway proteins expression.

This study suggests that benserazide may have potential as a chemosensitizer in cancer treatment by enhancing the anti-cancer effect of paclitaxel through the inhibition of S-sulfhydration of SIRT1 and enhancing the anti-angiogenic effect of paclitaxel through downregulation of HIF-1α/VEGF signaling pathway proteins expression, as shown in Figure 10. This finding provides a new insight into the development of combination therapy for cancer treatment. In subsequent research, we will employ animal xenograft models by transplanting human cancer cells into immunodeficient mice to observe the impact of the drugs on the growth of the transplanted tumors. Additionally, we will assess the *in vivo* anticancer activity by measuring pharmacodynamic parameters, such as drug concentration, bioavailability, and half-life. It is hoped that benserazide may find application in the field of oncology in the future.

Data availability statement

The original contributions presented in the study are included in the article/Supplementary material, further inquiries can be directed to the corresponding authors.

Ethics statement

The animal study was approved by The Ethics Committee of Medical School of Henan University (HUSOM2020-095). The study was conducted in accordance with the local legislation and institutional requirements.

Author contributions

WZ: Investigation, Writing–original draft. SF: Investigation, Methodology, Writing–original draft. JW: Methodology, Software, Writing–original draft. ZZ: Data curation, Methodology, Writing–original draft. LC: Validation, Writing–original draft. LJ: Validation, Writing–original draft. ML: Supervision, Writing–review and editing. TW: Conceptualization, Funding acquisition, Resources, Supervision, Writing–review and editing.

Funding

The author(s) declare that financial support was received for the research, authorship, and/or publication of this article. This work was supported by the grants from National Natural Science Foundation of China (82072726).

Conflict of interest

The authors declare that the research was conducted in the absence of any commercial or financial relationships that could be construed as a potential conflict of interest.

Publisher's note

All claims expressed in this article are solely those of the authors and do not necessarily represent those of their affiliated organizations, or those of the publisher, the editors and the reviewers. Any product that may be evaluated in this article, or claim that may be made by its manufacturer, is not guaranteed or endorsed by the publisher.

References

Abu, S. T. M., Samec, M., Liskova, A., Kubatka, P., and Büsselberg, D. (2019). Paclitaxel's mechanistic and clinical effects on breast cancer. *Biomolecules* 9 (12), 789. doi:10.3390/biom9120789

Alam, M. M., Fermin, J. M., Knackstedt, M., Noonan, M. J., Powell, T., Goodreau, L., et al. (2023). Everolimus downregulates STAT3/HIF-1α/VEGF pathway to inhibit angiogenesis and lymphangiogenesis in TP53 mutant head and neck squamous cell carcinoma (HNSCC). *Oncotarget* 14, 85–95. doi:10.18632/oncotarget.28355

Alves-Fernandes, D. K., and Jasiulionis, M. G. (2019). The role of SIRT1 on DNA damage response and epigenetic alterations in cancer. *Int. J. Mol. Sci.* 20 (13), 3153. doi:10.3390/ijms20133153

Baba, Y., Futamura, A., Kinno, R., Nomoto, S., Takahashi, S., Yasumoto, T., et al. (2022). The relationship between the distinct ratios of benserazide and carbidopa to levodopa and motor complications in Parkinson's disease: a retrospective cohort study. *J. Neurol. Sci.* 437, 120263. doi:10.1016/j.jns.2022.120263

Cao, B., Shi, Q., and Wang, W. (2015). Higher expression of SIRT1 induced resistance of esophageal squamous cell carcinoma cells to cisplatin. *J. Thorac. Dis.* 7 (4), 711–719. doi:10.3978/j.issn.2072-1439.2015.04.01

Conter, C., Fruncillo, S., Fernández-Rodríguez, C., Martínez-Cruz, L. A., Dominici, P., and Astegno, A. (2020). Cystathionine β-synthase is involved in cysteine biosynthesis and H2S generation in Toxoplasma gondii. *Sci. Rep.* 10 (1), 14657. doi:10.1038/s41598-020-71469-x

Druzhyna, N., Szczesny, B., Olah, G., Módis, K., Asimakopoulou, A., Pavlidou, A., et al. (2016). Screening of a composite library of clinically used drugs and well-characterized pharmacological compounds for cystathionine β-synthase inhibition identifies benserazide as a drug potentially suitable for repurposing for the experimental therapy of colon cancer. *Pharmacol. Res.* 113 (Pt A), 18–37. doi:10.1016/j.phrs.2016.08.016

Guo, H., Ding, H., Tang, X., Liang, M., Li, S., Zhang, J., et al. (2021). Quercetin induces pro-apoptotic autophagy via SIRT1/AMPK signaling pathway in human lung cancer cell lines A549 and H1299 *in vitro*. *Thorac. Cancer* 12 (9), 1415–1422. doi:10.1111/1759-7714.13925

Han, Y., Shang, Q., Yao, J., and Ji, Y. (2019). Hydrogen sulfide: a gaseous signaling molecule modulates tissue homeostasis: implications in ophthalmic diseases. *Cell. Death Dis.* 10 (4), 293. doi:10.1038/s41419-019-1525-1

Hashemi, M., Zandieh, M. A., Talebi, Y., Rahmanian, P., Shafiee, S. S., Nejad, M. M., et al. (2023). Paclitaxel and docetaxel resistance in prostate cancer: molecular mechanisms and possible therapeutic strategies. *Biomed. Pharmacother.* 160, 114392. doi:10.1016/j.biopha.2023.114392

Hong, W. G., and Pyo, J. S. (2018). The clinicopathological significance of SIRT1 expression in colon cancer: an immunohistochemical study and meta-analysis. *Pathol. Res. Pract.* 214 (10), 1550–1555. doi:10.1016/j.prp.2018.07.022

Hu, Q., Shang, L., Wang, M., Tu, K., Hu, M., Yu, Y., et al. (2020). Co-delivery of paclitaxel and interleukin-12 regulating tumor microenvironment for cancer immunochemotherapy. *Adv. Healthc. Mater* 9 (10), e1901858. doi:10.1002/adhm.201901858

Li, W., Zheng, M., Wu, S., Gao, S., Yang, M., Li, Z., et al. (2017). Benserazide, a dopadecarboxylase inhibitor, suppresses tumor growth by targeting hexokinase 2. *J. Exp. Clin. Cancer Res.* 36 (1), 58. doi:10.1186/s13046-017-0530-4

Liu, Z., Zhou, J., Wang, Z., and Bai, L. (2015). MTA1-specific shRNA inhibits the growth and metastasis of mouse xenograft of laryngeal squamous cell carcinoma. *Xi Bao Yu Fen Zi Mian Yi Xue Za Zhi* 31 (9), 1194–1199.

Ma, M. C., Chiu, T. J., Lu, H. I., Huang, W. T., Lo, C. M., Tien, W. Y., et al. (2018). SIRT1 overexpression is an independent prognosticator for patients with esophageal squamous cell carcinoma. *J. Cardiothorac. Surg.* 13 (1), 25. doi:10.1186/s13019-018-0718-5

Otsuka, R., Sakata, H., Murakami, K., Kano, M., Endo, S., Toyozumi, T., et al. (2022). SIRT1 expression is a promising prognostic biomarker in esophageal squamous cell carcinoma: a systematic review and meta-analysis. *Cancer Diagn Progn.* 2 (2), 126–133. doi:10.21873/cdp.10086

Padmanabhan, N., Kyon, H. K., Boot, A., Lim, K., Srivastava, S., Chen, S., et al. (2021). Highly recurrent CBS epimutations in gastric cancer CpG island methylator phenotypes and inflammation. *Genome Biol.* 22 (1), 167. doi:10.1186/s13059-021-02375-2

Santos, S. S., Rodrigues, LOCP, Martins, V., Petrosino, M., Zuhra, K., Ascenção, K., et al. (2023). Role of cystathionine β-synthase and 3-mercaptopyruvate sulfurtransferase in the regulation of proliferation, migration, and bioenergetics of murine breast cancer cells. *Antioxidants (Basel)* 12 (3), 647. doi:10.3390/antiox12030647

Škubník, J., Svobodová Pavlíčková, V., Ruml, T., and Rimpelová, S. (2023). Autophagy in cancer resistance to paclitaxel: development of combination strategies. *Biomed. Pharmacother.* 161, 114458. doi:10.1016/j.biopha.2023.114458

Smith, E. R., Wang, J. Q., Yang, D. H., and Xu, X. X. (2022). Paclitaxel resistance related to nuclear envelope structural sturdiness. *Drug Resist Updat* 65, 100881. doi:10.1016/j.drup.2022.100881

Song, S., Zhang, G., Chen, X., Zheng, J., Liu, X., Wang, Y., et al. (2023). HIF-1α increases the osteogenic capacity of ADSCs by coupling angiogenesis and osteogenesis via the HIF-1α/VEGF/AKT/mTOR signaling pathway. *J. Nanobiotechnology* 21 (1), 257. doi:10.1186/s12951-023-02020-z

Sun, Y., Liu, X., Tong, H., Yin, H., Li, T., Zhu, J., et al. (2023). SIRT1 promotes cisplatin resistance in bladder cancer via Beclin1 deacetylation-mediated autophagy. *Cancers (Basel)* 16 (1), 125. doi:10.3390/cancers16010125

Untereiner, A. A., Pavlidou, A., Druzhyna, N., Papapetropoulos, A., Hellmich, M. R., and Szabo, C. (2018). Drug resistance induces the upregulation of H2S-producing enzymes in HCT116 colon cancer cells. *Biochem. Pharmacol.* 149, 174–185. doi:10.1016/j.bcp.2017.10.007

Wang, X. W., Guo, Q. Q., Yu, Y., Zhou, T. T., Zhang, S. Y., Wang, Z., et al. (2022). The deacetylation of Foxk2 by Sirt1 reduces chemosensitivity to cisplatin. *J. Cell. Mol. Med.* 26 (2), 491–506. doi:10.1111/jcmm.17107

Wu, D., Sun, Y., Gu, Y., and Zhu, D. (2023). Cystathionine γ-lyase S-sulfhydrates SIRT1 to attenuate myocardial death in isoprenaline-induced heart failure. *Redox Rep.* 28 (1), 2174649. doi:10.1080/13510002.2023.2174649

Xu, R. H., Zhang, Y., Pan, H., Feng, J., Zhang, T., Liu, T., et al. (2021). Efficacy and safety of weekly paclitaxel with or without ramucirumab as second-line therapy for the treatment of advanced gastric or gastroesophageal junction adenocarcinoma (RAINBOW-Asia): a randomised, multicentre, double-blind, phase 3 trial. *Lancet Gastroenterol. Hepatol.* 6 (12), 1015–1024. doi:10.1016/S2468-1253(21)00313-7

Yang, Y., Gao, F., Gao, L., and Miao, J. (2023). Effects of rasagiline combined with levodopa and benserazide hydrochloride on motor function and homocysteine and IGF-1 levels in elderly patients with Parkinson's disease. *BMC Neurol.* 23 (1), 360. doi:10.1186/s12883-023-03411-3

Youness, R. A., Gad, A. Z., Sanber, K., Ahn, Y. J., Lee, G. J., Khallaf, E., et al. (2020). Targeting hydrogen sulphide signaling in breast cancer. *J. Adv. Res.* 27, 177–190. doi:10.1016/j.jare.2020.07.006

Yu, K. D., Ye, F. G., He, M., Fan, L., Ma, D., Mo, M., et al. (2020). Effect of adjuvant paclitaxel and carboplatin on survival in women with triple-negative breast cancer: a phase 3 randomized clinical trial. *JAMA Oncol.* 6 (9), 1390–1396. doi:10.1001/jamaoncol.2020.2965

Zhou, Y., Huang, Z., Su, J., Li, J., Zhao, S., Wu, L., et al. (2020). Benserazide is a novel inhibitor targeting PKM2 for melanoma treatment. *Int. J. Cancer* 147 (1), 139–151. doi:10.1002/ijc.32756

frontiers | Frontiers in Pharmacology

TYPE Case Report
PUBLISHED 20 May 2024
DOI 10.3389/fphar.2024.1364871

Check for updates

OPEN ACCESS

EDITED BY
Viviana di Giacomo,
University of Studies G. d'Annunzio Chieti and Pescara, Italy

REVIEWED BY
Marwa Balaha,
Kafrelsheikh University, Egypt
Hongji Zhang,
University of Virginia, United States

*CORRESPONDENCE
Hong Zhu,
zhuhong938@wchscu.cn

RECEIVED 03 January 2024
ACCEPTED 08 May 2024
PUBLISHED 20 May 2024

CITATION
Wan Y, Tan K and Zhu H (2024), QL1604 combined with bevacizumab as an innovative first-line treatment for HCC patient with extensive metastasis who showed remarkable effect: a case report. *Front. Pharmacol.* 15:1364871. doi: 10.3389/fphar.2024.1364871

COPYRIGHT
© 2024 Wan, Tan and Zhu. This is an open-access article distributed under the terms of the Creative Commons Attribution License (CC BY). The use, distribution or reproduction in other forums is permitted, provided the original author(s) and the copyright owner(s) are credited and that the original publication in this journal is cited, in accordance with accepted academic practice. No use, distribution or reproduction is permitted which does not comply with these terms.

QL1604 combined with bevacizumab as an innovative first-line treatment for HCC patient with extensive metastasis who showed remarkable effect: a case report

Yanzhi Wan, Keqin Tan and Hong Zhu*

Department of Medical Oncology, Cancer Center, West China Hospital, Sichuan University, Chengdu, China

Hepatocellular carcinoma (HCC) is a common and highly malignant tumor with poor outcomes, especially when it metastasizes. In this report, we present the case of a 64-year-old male patient diagnosed with recurrence and multiple metastases of HCC 7 years after surgery. As the tumor invaded the spinal canal and pressed on the spinal cord, the patient experienced paralysis in the lower limbs. After undergoing surgical resection for spinal decompression, the patient chose an innovative regimen: QL1604 200 mg every 3 weeks plus bevacizumab 675 mg every 3 weeks as first-line treatment. From July 2022 to February 2024, the patient has regularly received the treatment. During the treatment, the paralysis symptoms of the patient gradually improved, and the motor function of the lower limbs completely returned to normal. When re-evaluated his spinal cord injury, the Frankel grade of the patient was downgraded from C to E. The tumor shrank to reach a state of PR and lasted for one and a half years. QL1604 combined with bevacizumab demonstrated excellent efficacy and minimal side effects in this patient. This new combined therapy holds potential as a first-line treatment strategy.

KEYWORDS

hepatocellular carcinoma, QL1604, bevacizumab, intraspinal metastasis, paralysis

Introduction

Hepatocellular carcinoma (HCC) is the most common primary tumor of the liver and has a very poor prognosis (Nagaraju et al., 2022). In China, HCC incidence is higher due to the prevalence of hepatitis B infection among the majority of patients, resulting in a greater malignant potential of HCC (Tanaka et al., 2011). HCC is known for its tendency to develop portal tumor thrombosis, intrahepatic metastasis, and lung metastasis. However, bone metastasis is rare in HCC (Bhatia et al., 2017).

For patients with advanced HCC, comprehensive treatment is crucial. Available options include systemic treatments, such as immunotherapy and targeted therapy, and local treatments, such as transarterial chemoembolization, hepatic artery infusion chemotherapy, radiotherapy, and so on (Llovet et al., 2021). Sorafenib and lenvatinib are the standard first-line single-agent targeted therapies for advanced HCC. In recent

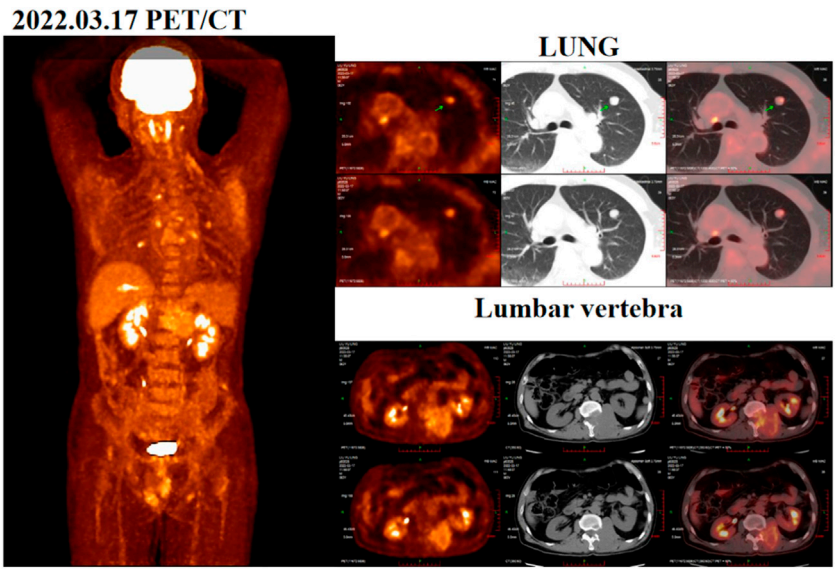

FIGURE 1
Positron emission tomography/computed tomography (PET/CT) images acquired before surgery on 17 March 2022.

years, there have been breakthroughs in HCC treatment, particularly in systemic therapies evolving from single-agent targeted therapy to the combination of immunotherapy and targeted therapy (Yang et al., 2023). Nevertheless, immunotherapy combined with bevacizumab as the standard first-line treatment for HCC has shown better efficacy and fewer side effects (Ren et al., 2021).

In the case presented here, a patient with HCC developed intraspinal metastasis, leading to compression of the spinal cord and subsequent lower limb paralysis. Following emergency surgical resection for metastasis and spinal decompression, the patient chose QL1604 plus bevacizumab as the first-line treatment. QL1604 is a highly selective, humanized anti-PD-1 monoclonal antibody (mAb). It remains an experimental drug that has been studied in at least three clinical trials for solid tumors (Huang et al., 2023). Surprisingly, after using this treatment strategy, the patient achieved a state of partial response (PR) and has maintained this response for one and a half years. Throughout the treatment, adverse reactions were minimal, and the paralysis was completely cured, enabling the patient to move and resume normal daily life activities. QL1604 combined with bevacizumab exhibited significant efficacy in this patient. This case provides a new treatment plan for advanced liver cancer patients, hoping that more patients can benefit from it.

Case presentation

Pre-treatment

A 64-year-old male patient diagnosed with chronic hepatitis B infection for over 30 years ago underwent a radical complex liver cancer resection in 2015. Following the surgery, the patient opted for intermittent use of oral traditional Chinese medicine instead of any antitumor therapy or regular follow-up. Unfortunately, in January 2022 (7 years after the surgery), the patient began experiencing lumbosacral pain, which progressively worsened. Symptoms included numbness in the lumbosacral and left hip area, difficulty in walking, and paralysis. In March 2022, the patient visited our hospital for a thorough diagnosis and subsequent treatment.

During the physical examination, the patient was found to have decreased skin sensation below the left groin area, reduced tendon reflexes in both knees, and decreased muscle strength in both lower limbs. He was classified with "incomplete" injuries (grades C) using the Frankel system. A positron emission tomography/computed tomography (PET/CT) scan conducted in March 2022 revealed an increase in residual liver margin glucose metabolism following the liver cancer surgery. Additionally, abnormal glucose metabolism was observed in a nodule in their left upper lung, first lumbar vertebrae, and left adnexa (Figure 1). A chest-enhanced computed tomography (CT) scan showed a 1.3 × 1.5 cm lesion in the left upper lung, suggesting possible recurrence and metastasis of HCC. Besides, his liver function was Child-Pugh grade A and ECOG performance status score was 2. As part of the diagnostic process and to alleviate symptoms, the patient underwent surgery (lumbar-tumor excision plus spinal decompression) on 1 April 2022. Intraoperatively, extensive osteolytic destruction involving the lumbar and vertebral bodies was observed. Preoperative and postoperative digital radiographs of the thoracolumbar vertebrae were obtained, and the postoperative pathological examination indicated metastatic carcinoma in the first lumbar vertebrae. The results of immunohistochemistry staining of lumbar biopsy tissue were: CK8/18 (+), Hepar (+), GATA-3 (–), EMA (–), CK7 (–), CDX-2 (–), PAX-8 (–), GPC-3 (+), AFP (–), confirming the metastasis of HCC. Starting from postoperative, patients regularly use bisphosphonates and wear lumbar spine stents for a long time to reduce the risk of bone adverse events.

In treatment

Two months post-surgery, following thorough discussions with the patient, it was mutually agreed upon to enroll the patient in a

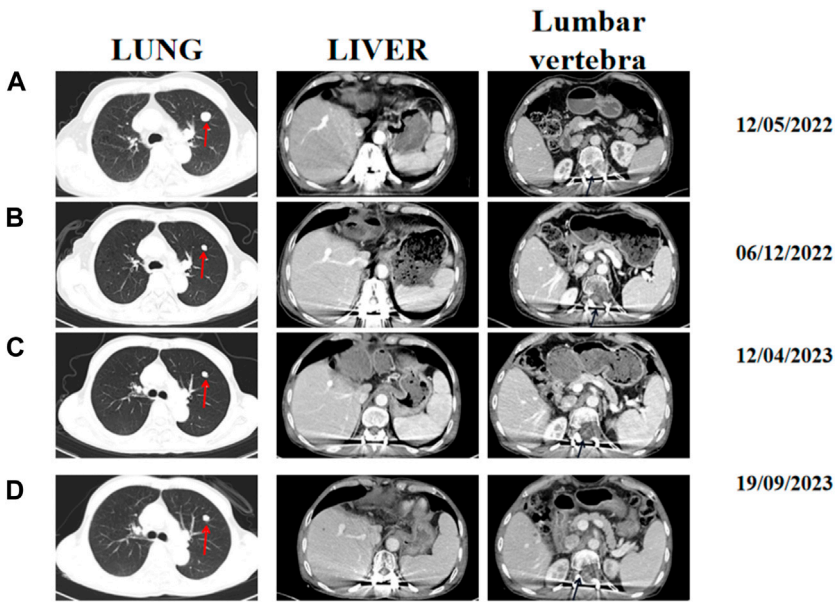

FIGURE 2
Representative abdominal and chest-enhanced CT images acquired at different times during treatment. **(A)** Baseline CT images acquired on 12 May 2022. **(B)** CT image assessment performed on 6 December 2022. **(C)** CT image assessment performed on 12 April 2023. **(D)** CT images acquired on 19 September 2023. The red arrows indicate lung lesions, and black arrows indicate lumbar soft tissue.

phase Ib/II clinical study to evaluates the safety, pharmacokinetics, and initial efficacy of QL1706/QL1604 in combination with bevacizumab for advanced HCC. Prior to enrollment, the patient underwent comprehensive assessment of their condition. The patient was diagnosed with stage C HCC of the Barcelona Clinic Liver Cancer with Child-Pugh A and an ECOG performance status score of 1. A baseline contrast-enhanced CT conducted in May 2022 confirmed a 1.7 × 1.5 cm reinforced nodule with lobed margins in the upper lobe of the left lung, along with scattered multiple lesions measuring 0.2–0.3 cm in both the lungs. Partial absence of the liver with a lamellar residual margin, slightly low density, and a slightly enhanced shadow were also observed. Furthermore, bone disruption was noted in the 12th thoracic spine, first lumbar vertebra, and left adnexa (Figure 2A). From July 2022 onward, the patient has received regular treatment with QL1604 (200 mg) every 3 weeks combined with bevacizumab (675 mg) every 3 weeks. During the treatment, the patient underwent chest and abdominal enhanced CT multiple times to reexamine their condition. Each time, the efficacy of the treatment was assessed consistently as a PR (Figures 2B, C).

Post-treatment

The most gratifying thing is that the patient's quality of life has significantly improved. Until now, the paralysis symptoms have been completely resolved, and the patient had experienced minimal side effects. After treatment, the lung metastasis decreased in size and the bone destruction of the affected vertebrae had also diminished (Figure 2D). There was a significant decrease in tumor markers such as serum alpha fetoprotein (AFP) and protein induced by vitamin K deficiency/antagonist II (PIVKA-II) of the patient. Additionally, the patient's clinical symptoms improved significantly, and his Frankel grade was downgraded from C to E, indicating that sensory and motor functions below the injury plane have almost completely recovered. Furthermore, the patient's ECOG performance status score decreased from 1 to 0, reflecting a substantial improvement in his overall health and functionality. Remarkably, the patient has survived for over 2 year despite multiple systemic metastases and have achieved a positive therapeutic outcome without experiencing any serious treatment-related adverse reactions. Until February 2024, the lung metastasis increased in size, however, the patient is still maintain a good sensory and motor function until now.

Discussion

HCC is the most common primary malignancy of the liver, with a poor prognosis and a high rate of recurrence and metastasis (Nagaraju et al., 2022). Even with curative-intent options, the probability of recurrence and metastasis in patients with HCC within 5 years remains as high as 70% (Akateh et al., 2019). Moreover, epidemiological statistics show that in most of Asia and Africa, 60% of HCC cases are associated with a long history of HBV infection (Iavarone and Colombo, 2013). In the present case, our patient developed HCC due to a long history of chronic hepatitis without antiviral therapy. Unfortunately, it is worth noting that patients with liver cancer and hepatitis B virus infection often have a worse prognosis.

The patient initially experienced lumbosacral pain, followed by paralysis and was diagnosed with HCC recurrence and metastasis 7 years after surgery. While extra-hepatic metastasis in HCC often affects the lungs, bone metastases are relatively rare (Bhatia et al.,

2017). In particular, metastatic epidural spinal cord compression (MESCC) is a devastating complication of cancer, usually caused by the metastasis of soft tissue to the epidural space. It is considered a medical emergency, and if the patient is nonambulatory or paraplegic, the chances of functional recovery are significantly reduced. Treatment options for MESCC include corticosteroids, radiotherapy, and surgery (Grant et al., 1994; Cole and Patchell, 2008). In the present case, due to the pressure of the tumor, the patient's symptoms progressed rapidly. Upon visiting the hospital, the spinal cord compression symptoms were so severe that the patient had lost the ability to move and was bedridden. Therefore, the patient had to undergo an emergency surgery (lumbar tumor excision plus spinal decompression) in April 2022. The postoperative pathological result confirmed the metastasis of HCC. Studies have shown that if MESCC progresses slowly, decompression, even when performed 7 days after the initial onset, can reverse neurological deficits (Rades and Abrahm, 2010). However, despite undergoing surgery, the patient experienced compression symptoms for over a month and only achieved partial relief of pain and neurological recovery.

Despite the breakthrough in the treatment of HCC in recent years, the median survival time of HCC combined with bone metastasis (BM) is less than half a year (Guo et al., 2019). Unfortunately, The patient was found to have both bone and lung metastases, which worsened his prognosis. Radiotherapy and surgical treatment aim to alleviate pain symptoms in patients, but cannot improve bone destruction caused by bone metastasis (Kodama et al., 2007). The patient requires systemic anti-tumor treatment.

In recent years, we entered the immune era of liver cancer treatment. Immunotherapy combined with targeted therapy has become a new research focus (Yang et al., 2023). Combination treatment regimens for the first-line treatment of HCC, including the use of atezolizumab + bevacizumab and durvalumab + tremelimumab have been approved by FDA (Kudo, 2022; Yang et al., 2023). In our country, a phase 2-3 study (ORIENT-32) showed that in the first-line setting for Chinese patients with unresectable HCC, there was a significant effect of sintilimab (a PD-1 inhibitor) combined with bevacizumab compared with sorafenib (Ren et al., 2021). Immunotherapy combined with bevacizumab has become a standard first line treatment for HCC which has shown better efficacy and fewer side effects than a single target drug (Ren et al., 2021). Previous studies have shown that the etiology of HCC impacts the immune response and leads to unique microenvironmental features. However, the microenvironment of HBV-related HCC is more immunosuppressive and depleted than that of non-viral-related HCC. Therefore, HCC caused by chronic viral hepatitis B may be more suitable for immunotherapy (Lim et al., 2019; Llovet et al., 2022; Liu et al., 2023). Furthermore, incorporating antiangiogenic drugs into immune checkpoint inhibitors (PD-L1/PD-1) can enhance the antitumor immune response by synergistically regulating the tumor vasculature and immune microenvironment (Xing et al., 2021).

After extensive communication with the patient, the decision was made to opt for QL-1604 (a PD-1 inhibitor) combined with bevacizumab as the first-line treatment. The patient chose this treatment plan primarily because anti-PD-1 immune checkpoint inhibitor combined with bevacizumab is considered as a standard treatment option in China (Ren et al., 2021), and also due to the poor economic conditions of the patient's family. The patient hoped to treat the disease by participating in a free clinical trial. Bevacizumab, a monoclonal antibody, targets vascular endothelial growth factor and inhibits angiogenesis and tumor growth. Notably, this medication stands as one of the first targeted therapies and the first approved angiogenesis inhibitor.

In contrast, QL1604, an anti-PD-1 immune checkpoint inhibitor, is a novel and unmarketed inhibitor. The clinical trial protocol involved the regular use of the immunotherapy QL1604 (anti-PD-1) in combination with bevacizumab, along with scheduled assessments. This new clinical trial aimed to further explore the efficacy of immunotherapy in patients with advanced HCC. It is important to note that this strategy is not a standard first-line therapy, and no previous research has shown that QL1604 combined with bevacizumab alone is an effective treatment for a patient with advanced HCC.

A clinical study IMbrave150 has shown that the median progression free survival (PFS) was 6.8 months in advanced HCC patients treated with atezolizumab plus bevacizumab (Finn et al., 2020). According to ORIENT-32, a clinical study in China, the median PFS of patients treated with combination therapy of sintilimab and bevacizumab was 4.6 months (Ren et al., 2021). A Phase 3 HIMALAYA trial showed a median PFS of 3.8 months in advanced HCC patients treated with Durvalumab combined with Tremelimumab (Kudo, 2022). Surprisingly, the PFS of the patient who treated with QL1604 + bevacizumab reached one and a half years. Even better, the patient is now completely cured of his paralysis. The patient is able to move freely, exceeding all expectations. The synergistic effect of the combined drug regimen surpasses that of individual treatments alone, highlighting the potential of such combination therapies in HCC. This case inspires us to conduct further investigations into the combination treatment regimen for liver cancer and reaffirms the significant role of immunotherapy alongside antivascular drugs in managing HCC.

In this particular case, two challenging events occurred during treatment. Specifically, before treatment, the patient developed intraspinal metastasis, a series of symptoms of spinal cord compression, and paralysis. Notably, few reports have focused on the successful first-line treatment of such an advanced case of HCC with QL1604 (a new PD-1 inhibitor) plus bevacizumab. There is still relatively little information on the efficacy of immunotherapy for bone metastases (Lasagna et al., 2021). The patient had demonstrated a state of PR for one and a half years, resulting in a notable improvement in the quality of life. Furthermore, the side effects of the treatment were observed to be mild and tolerable.

Conclusion

With the continuous advancement of biological knowledge, more and more new drugs have begun to be applied. Additionally, the strategy of immunotherapy combined with targeted therapy has been increasingly recognized in HCC treatment. In this case, a patient with HCC in both lung and

intraspinal metastasis experienced progression-free survival for one and a half years after systemic therapy with QL1604 and bevacizumab. Its efficacy was evaluated based on the patient's sustained PR and complete recovery from paralysis. Accordingly, the combination of QL1604 and bevacizumab may be a better first-line treatment than the individual drugs alone for HCC. However, further prospective studies are required to confirm this hypothesis.

Data availability statement

The original contributions presented in the study are included in the article/supplementary material, further inquiries can be directed to the corresponding author.

Ethics statement

The studies involving humans were approved by Medical Ethics Committee of West China Hospital, Sichuan University. The studies were conducted in accordance with the local legislation and institutional requirements. The participants provided their written informed consent to participate in this study. Written informed consent was obtained from the individual(s) for the publication of any potentially identifiable images or data included in this article.

Author contributions

YW: Writing–original draft. KT: Writing–review and editing. HZ: Writing–review and editing.

Funding

The author(s) declare that no financial support was received for the research, authorship, and/or publication of this article.

Conflict of interest

The authors declare that the research was conducted in the absence of any commercial or financial relationships that could be construed as a potential conflict of interest.

Publisher's note

All claims expressed in this article are solely those of the authors and do not necessarily represent those of their affiliated organizations, or those of the publisher, the editors and the reviewers. Any product that may be evaluated in this article, or claim that may be made by its manufacturer, is not guaranteed or endorsed by the publisher.

References

Akateh, C., Black, S. M., Conteh, L., Miller, E. D., Noonan, A., Elliott, E., et al. (2019). Neoadjuvant and adjuvant treatment strategies for hepatocellular carcinoma. *World J. Gastroenterol.* 25, 3704–3721. doi:10.3748/wjg.v25.i28.3704

Bhatia, R., Ravulapati, S., Befeler, A., Dombrowski, J., Gadani, S., and Poddar, N. (2017). Hepatocellular carcinoma with bone metastases: incidence, prognostic significance, and management-single-center experience. *J. Gastrointest. Cancer* 48, 321–325. doi:10.1007/s12029-017-9998-6

Cole, J. S., and Patchell, R. A. (2008). Metastatic epidural spinal cord compression. *Lancet Neurol.* 7, 459–466. doi:10.1016/S1474-4422(08)70089-9

Finn, R. S., Qin, S., Ikeda, M., Galle, P. R., Ducreux, M., Kim, T. Y., et al. (2020). Atezolizumab plus bevacizumab in unresectable hepatocellular carcinoma. *N. Engl. J. Med.* 382, 1894–1905. doi:10.1056/NEJMoa1915745

Grant, R., Papadopoulos, S. M., Sandler, H. M., and Greenberg, H. S. (1994). Metastatic epidural spinal cord compression: current concepts and treatment. *J. Neurooncol* 19, 79–92. doi:10.1007/BF01051052

Guo, X., Xu, Y., Wang, X., Lin, F., Wu, H., Duan, J., et al. (2019). Advanced hepatocellular carcinoma with bone metastases: prevalence, associated factors, and survival estimation. *Med. Sci. Monit.* 25, 1105–1112. doi:10.12659/MSM.913470

Huang, Z., Xu, Y., Hong, W., Gong, L., Chen, K., Qin, J., et al. (2023). A first-in-human, open-label, dose-escalation and dose-expansion phase I study to evaluate the safety, tolerability, pharmacokinetics/pharmacodynamics, and antitumor activity of QL1604, a humanized anti-PD-1 mAb, in patients with advanced or metastatic solid tumors. *Front. Immunol.* 14, 1258573. doi:10.3389/fimmu.2023.1258573

Iavarone, M., and Colombo, M. (2013). HBV infection and hepatocellular carcinoma. *Clin. Liver Dis.* 17, 375–397. doi:10.1016/j.cld.2013.05.002

Kodama, H., Aikata, H., Uka, K., Takaki, S., Mori, N., Waki, K., et al. (2007). Efficacy of percutaneous cementoplasty for bone metastasis from hepatocellular carcinoma. *Oncology* 72, 285–292. doi:10.1159/000113040

Kudo, M. (2022). Durvalumab plus tremelimumab in unresectable hepatocellular carcinoma. *Hepatobiliary Surg. Nutr.* 11, 592–596. doi:10.21037/hbsn-22-143

Lasagna, A., Cuzzocrea, F., Maccario, G., Mahagna, A., Sacchi, P., and U Mondelli, M. (2021). Bone metastases and hepatocellular carcinoma: some food for thought. *Future Oncol.* 17, 3777–3780. doi:10.2217/fon-2021-0689

Lim, C. J., Lee, Y. H., Pan, L., Lai, L., Chua, C., Wasser, M., et al. (2019). Multidimensional analyses reveal distinct immune microenvironment in hepatitis B virus-related hepatocellular carcinoma. *Gut* 68, 916–927. doi:10.1136/gutjnl-2018-316510

Liu, Y., Xun, Z., Ma, K., Liang, S., Li, X., Zhou, S., et al. (2023). Identification of a tumour immune barrier in the HCC microenvironment that determines the efficacy of immunotherapy. *J. Hepatol.* 78, 770–782. doi:10.1016/j.jhep.2023.01.011

Llovet, J. M., Castet, F., Heikenwalder, M., Maini, M. K., Mazzaferro, V., Pinato, D. J., et al. (2022). Immunotherapies for hepatocellular carcinoma. *Nat. Rev. Clin. Oncol.* 19, 151–172. doi:10.1038/s41571-021-00573-2

Llovet, J. M., De Baere, T., Kulik, L., Haber, P. K., Greten, T. F., Meyer, T., et al. (2021). Locoregional therapies in the era of molecular and immune treatments for hepatocellular carcinoma. *Nat. Rev. Gastroenterol. Hepatol.* 18, 293–313. doi:10.1038/s41575-020-00395-0

Nagaraju, G. P., Dariya, B., Kasa, P., Peela, S., and El-Rayes, B. F. (2022). Epigenetics in hepatocellular carcinoma. *Semin. Cancer Biol.* 86, 622–632. doi:10.1016/j.semcancer.2021.07.017

Rades, D., and Abrahm, J. L. (2010). The role of radiotherapy for metastatic epidural spinal cord compression. *Nat. Rev. Clin. Oncol.* 7, 590–598. doi:10.1038/nrclinonc.2010.137

Ren, Z., Xu, J., Bai, Y., Xu, A., Cang, S., Du, C., et al. (2021). Sintilimab plus a bevacizumab biosimilar (IBI305) versus sorafenib in unresectable hepatocellular carcinoma (ORIENT-32): a randomised, open-label, phase 2-3 study. *Lancet Oncol.* 22, 977–990. doi:10.1016/s1470-2045(21)00252-7

Tanaka, M., Katayama, F., Kato, H., Tanaka, H., Wang, J., Qiao, Y. L., et al. (2011). Hepatitis B and C virus infection and hepatocellular carcinoma in China: a review of epidemiology and control measures. *J. Epidemiol.* 21, 401–416. doi:10.2188/jea.je20100190

Xing, R., Gao, J., Cui, Q., and Wang, Q. (2021). Strategies to improve the antitumor effect of immunotherapy for hepatocellular carcinoma. *Front. Immunol.* 12, 783236. doi:10.3389/fimmu.2021.783236

Yang, C., Zhang, H., Zhang, L., Zhu, A. X., Bernards, R., Qin, W., et al. (2023). Evolving therapeutic landscape of advanced hepatocellular carcinoma. *Nat. Rev. Gastroenterol. Hepatol.* 20, 203–222. doi:10.1038/s41575-022-00704-9

frontiers | Frontiers in Pharmacology

TYPE Case Report
PUBLISHED 17 June 2024
DOI 10.3389/fphar.2024.1396606

Check for updates

OPEN ACCESS

EDITED BY
Wagdy Mohamed Eldehna,
Kafrelsheikh University, Egypt

REVIEWED BY
Mina Noshy,
King Salman International University, Egypt
Mahmoud Abdallah,
University of Sadat City, Egypt
Keith Schmidt,
National Institutes of Health (NIH), United States

*CORRESPONDENCE
Yue Li,
liyue_0617@163.com
Dandan Cao,
dandan.cao@genetronhealth.com

†These authors have contributed equally to this work

RECEIVED 06 March 2024
ACCEPTED 30 May 2024
PUBLISHED 17 June 2024

CITATION
Yue X, Yang C, Cao D and Li Y (2024), Niraparib for the treatment of metastatic ccRCC in a patient with *CDK12* and *RAD51C* mutations: a case report.
Front. Pharmacol. 15:1396606.
doi: 10.3389/fphar.2024.1396606

COPYRIGHT
© 2024 Yue, Yang, Cao and Li. This is an open-access article distributed under the terms of the Creative Commons Attribution License (CC BY). The use, distribution or reproduction in other forums is permitted, provided the original author(s) and the copyright owner(s) are credited and that the original publication in this journal is cited, in accordance with accepted academic practice. No use, distribution or reproduction is permitted which does not comply with these terms.

Niraparib for the treatment of metastatic ccRCC in a patient with *CDK12* and *RAD51C* mutations: a case report

Xiaolong Yue[1†], Chenkang Yang[2†], Dandan Cao[2*] and Yue Li[1*]

[1]Medical Oncology Department, Affiliated Tumor Hospital, Harbin Medical University, Harbin, China, [2]Genetron Health (Beijing) Co., Ltd., Beijing, China

Background: Niraparib, a poly ADP-ribose polymerase inhibitors (PARPi), has been widely applied in the intervention of epithelial ovarian, fallopian tube, or primary peritoneal cancer. Nevertheless, as of the present moment, there are limited instances demonstrating favorable outcomes stemming from niraparib therapy in patients with clear cell renal cell carcinoma (ccRCC).

Case presentation: Here, we report a case of a 50-year-old patient with ccRCC who subsequently developed distant metastasis. The patient received monotherapy with pazopanib and combination therapy with axitinib and tislelizumab, demonstrating limited efficacy. Liquid biopsy revealed missense mutations in the *CDK12* and *RAD51C* of the homologous recombination repair (HRR) pathway, suggesting potential sensitivity to PARPi. Following niraparib treatment, the patient's condition improved, with no significant side effects.

Conclusion: In summary, patients with ccRCC harboring HRR pathway gene mutation may potentially benefit from niraparib. This will present more options for ccRCC patients with limited response to conventional treatments.

KEYWORDS

ccRCC, PARPi, CDK12, RAD51C, niraparib

Introduction

Renal cell carcinoma (RCC) constitutes 90%–95% of kidney cancers in adults (Siegel et al., 2018), encompassing clear cell RCC (ccRCC), papillary RCC (pRCC), chromophobe RCC (chRCC), and other rare subtypes (Hsieh et al., 2017). Among these, ccRCC is the most common subtype, accounting for about 75% of cases (Li et al., 2019). It originates from renal tubule epithelial cells and is primarily managed through surgical intervention. However, even after successful surgery, approximately 30% of patients may experience postoperative metastasis (Hsieh et al., 2017). The standard of care for metastatic ccRCC comprise anti-angiogenic agents, mammalian target of rapamycin (mTOR) inhibitors, et al. (Yang et al., 2023). While a significant number of individuals derive relief from standard treatment, there are cases where some individuals fail to derive apparent benefits or eventually develop resistance to the standard interventions (Posadas et al., 2013).

The U.S. Food and Drug Administration (FDA) has approved four poly ADP-ribose polymerase inhibitors (PARPi): olaparib, niraparib, talazoparib, and rucaparib (Lai et al., 2022). In alignment with other PARPi, niraparib is an innovative cancer treatment based on

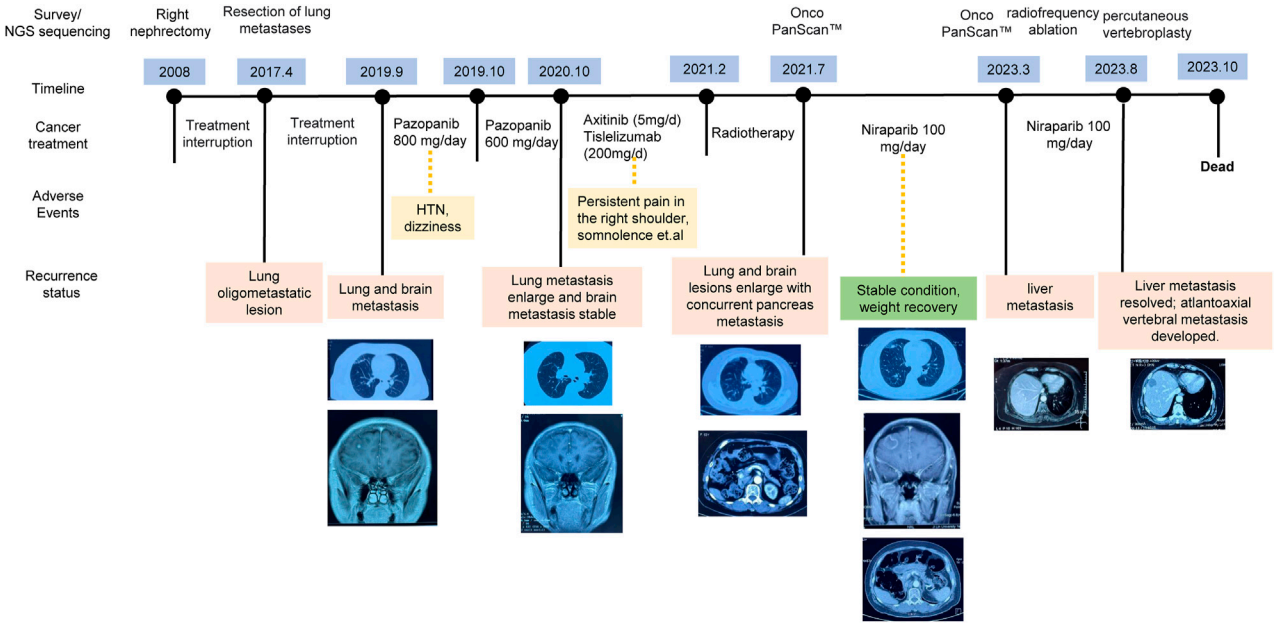

FIGURE 1
Overview of Treatment Interventions in a 50-Year-Old Patient Diagnosed with ccRCC.

the synthetic lethality effect (Lai et al., 2022). Niraparib has been widely applied in the intervention of epithelial ovarian, fallopian tube, or primary peritoneal cancer. Recent literature suggests that the applicability of PARPi, including niraparib, may extend to a broader range (Eiriz et al., 2023). Niraparib elevated the objective response rate (ORR) among ovarian cancer patients with HRD-positive tumors, regardless of the presence of BRCA mutations (Eiriz et al., 2023). On 11 August 2023, the FDA approved the combined use of niraparib and abiraterone acetate for the treatment of castration-resistant prostate cancer (mCRPC) in adult patients with deleterious or suspected deleterious BRCA mutations. Simultaneously, for other PARPi, on 30 June 2023, the FDA expanded approval for talazoparib to include the care of prostate cancer with mutations in multiple HRR pathway genes, such as *BRCA1*, *BRCA2*, *PALB2*, *ATM*, *ATR*, *CHEK2*, *FANCA*, *RAD51C*, *NBN*, *MLH1*, *MRE11A*, and *CDK12* (Akbıyık and Ürün, 2023).

Olaparib, an earlier-generation PARPi compared to niraparib, is presently under assessment as a monotherapy in a Phase II clinical trial for patients with DDR-altered RCC, with an anticipated completion date in 2025 (NCT03786796). Currently, there is insufficient clinical evidence to support the efficacy of PARPi for ccRCC patients with HRD. Here, we report for the first time a case of a ccRCC patient with *RAD51C* and *CDK12* mutations benefiting from niraparib treatment.

Case description

In this case study, we outline the treatment course of a 50-year-old patient diagnosed with ccRCC and a history of diabetes mellitus, as depicted in Figure 1. In 2008, the patient was diagnosed with stage II ccRCC in the right kidney and subsequently underwent a nephrectomy. After the initial surgery, the patient abstained from further medical interventions until the identification of lung metastases in 2017. Subsequent surgery addressed recurrent lung metastatic lesions, without other interventions. Postoperative immunohistochemistry revealed expression of CD10, PAX-8, and Vimentin, aligning with the patient's medical history, indicating metastatic ccRCC.

In September 2019, lung and brain metastases were identified, prompting adherence to the treatment guidelines outlined by the National Comprehensive Cancer Network (NCCN) (Jonasch, 2019). The patient initiated first-line pazopanib therapy at an initial oral dose of 800 mg daily. However, after 1 month, the patient presented elevated blood pressure and dizziness, resulting in a reduction of the pazopanib dosage to a reduced oral intake of 600 mg per day. A year later, the patient presented with increased somnolence, confusion, persistent headaches, and the CT image revealed larger lesions in the lung and brain. Brain edema and two nodular shadows in the right frontal lobe were also identified through imaging. Following NCCN guidelines, the patient initiated to a treatment consisting of axitnib (5 mg/day) combined with tislelizumab (200 mg/day). During the treatment, the patient developed persistent right shoulder pain.

In February 2021, the patient presented with severe headaches, profound somnolence, substantial weight loss, and impaired consciousness. While radiotherapy provided partial relief from symptoms, by July 2021, there occurred worsening lung and brain metastases, as well as concurrent pancreatic metastasis. Comprehensive genomic profiling (Onco PanScan™) was conducted, revealing two import gene mutations: the missense mutation in *CDK12* and *RAD51C*. Considering the limited effectiveness with conventional treatments for the patient and the identification of the gene mutations in the HRR pathway, we recommend PARPi therapy. After discussing with her family, the patient provided informed consent to participate in an

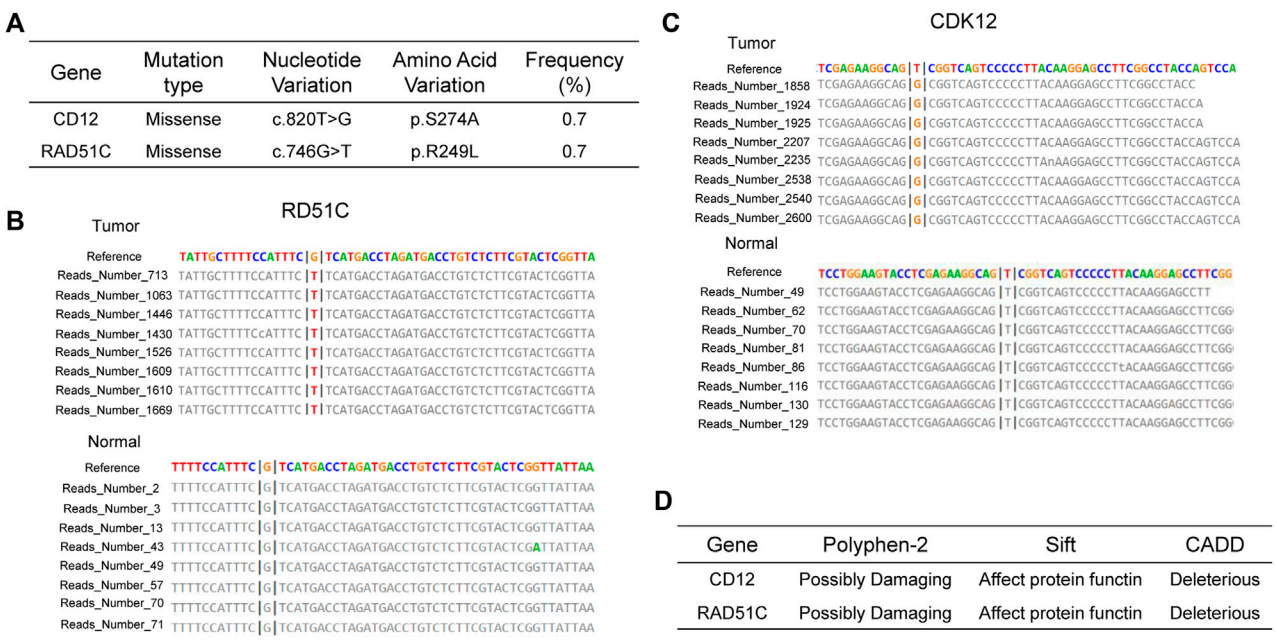

FIGURE 2
Mutational Characteristics **(A–C)** and Predicted Pathogenicity **(D)** of HRR Genes in the Patient. **(A)** Mutation sites and mutation types of *CDK12* and *RAD51C*. Mutation reads for *RAD51C* **(B)** and *CDK12* **(C)** in the tumor sample and the wild-type reads from the paired normal sample. **(D)** Prediction of functional effects of *RAD51C* and *CDK12* mutation sites by three algorithms.

TABLE 1 Patient information with deleterious co-mutations in *CDK12* and *RAD51C*.

Sample ID	Cancer type	Amino acid variation	
		CDK12	*RAD51C*
TCGA-ZF-A9R7-01	Bladder Urothelial Carcinoma	P707S	R249C
P-8178	Colorectal Adenocarcinoma	R983Q	C176Y
TCGA-W3-AA1V-06	Cutaneous Melanoma	P1005L	R249C
P-0004688-T01-IM5	Upper Tract Urothelial Carcinoma	R981C	E89K
TCGA-AP-A059-01	Uterine Endometrioid Carcinoma	P653H	A279D
TCGA-A5-A0G2-01	Uterine Serous Carcinoma	E928K	R260Q

individualized treatment with niraparib at a daily dosage of 200 mg. One week later, a blood test revealed thrombocytopenia, so the dosage was reduced to 100 mg per day.

After taking 100 mg niraparib per day, the patient exhibited a substantial alleviation of headaches without observable adverse effects. The lesions remained stable, and her overall health improved, including notable weight gain. Over the ensuing 2 years, routine check-ups conducted every 3 months revealed no signs of metastasis and normal blood test findings. In March 2023, liver imaging indicated the presence of metastasis, prompting liver radiofrequency ablation. Subsequent Onco PanScan™ testing in March failed to detect *RAD51C* and *CDK12* mutations, suggesting the potential development of drug resistance. However, niraparib treatment was not discontinued (Figure 1). In August of the same year, she experienced head and neck pain due to atlantoaxial vertebral metastasis. She underwent percutaneous vertebroplasty, which caused occlusion of pulmonary vasculature, leading to a deterioration in her condition with an ECOG score of 4. She passed away in October.

Discussion

The current standard treatment for metastatic ccRCC encompass anti-angiogenic agents, mTOR inhibitors, and immunotherapeutic drugs (Yang et al., 2023). After the occurrence of distant metastasis for the patient, we initially employed pazopanib and a combination of axitinib and tislelizumab for treatment. Unfortunately, the efficacy of these approaches proved to be limited, accompanied by significant side effects. Consequently, we found it necessary to explore novel treatment strategies.

In contemporary contexts, PARPi have brought about a substantial transformation in the therapeutic landscape concerning platinum-sensitive ovarian and breast cancers (Marchetti et al., 2012; Robson et al., 2017). As early as 2014, the FDA approved the utilization of PARPi for treating breast cancer in individuals with *BRCA1/2* germline mutations (Kim et al., 2015). Historically, the effectiveness of PARPi in urological cancers was believed to be constrained due to the infrequent occurrence of *BRCA* germline mutation (Pletcher et al., 2021). Hence, there is a scarcity of research on the utilization of PARPi for ccRCC. Despite this, existing studies suggest PARPi potential effectiveness for ccRCC, especially in cases where HRD are present, as demonstrated by experiments conducted on cell lines (Pletcher et al., 2021). At the same time, recent studies propose that the effectiveness of PARPi is not solely dependent on *BRCA* deficiency but may also be affected by mutations in other genes within HRR pathway (Boussios et al., 2020). In a clinical trial of prostate cancer focusing on alterations in the HRR genes, including *BRCA1*, *BRCA2*, *PALB2*, *ATM*, *ATR*, *CHEK2*, *FANCA*, *RAD51C*, *NBN*, *MLH1*, *MRE11A*, and *CDK12*, the group treated with talazoparib showed a significant improvement in progression-free survival compared to the placebo group (Fizazi et al., 2023). Soon afterwards, the FDA granted further approval for the application of talazoparib in the treatment of prostate cancer patients exhibiting mutations in HRR pathway genes, encompassing *CDK12* and *RAD51C* (Akbıyık and Ürün, 2023). Our analysis identified ccRCC patients with co-mutations in the *CDK12* and *RAD51C* genes (Figure 2A), supported by multiple reads for these mutations (Figure 2B, C). Harmfulness analysis of these mutations was conducted, and various algorithm confirmed that there are deleterious variations (Figure 2D). We propose that mutations in *CDK12* and *RAD51C* may impair the functionality of the HRR pathway, causing HRD in the patient and rendering them sensitive to PARPi. After niraparib administration, multiple lesions stabilized and the status of her remains favorable (Figure 1).

CDK12 selectively regulates the expression of DDR pathway genes by regulating transcription elongation, consequently causing HRD. Earlier research believed the heightened susceptibility of DDR genes to *CDK12* loss, potentially attributable to their extended sequences and decreased ratios of U1 snRNP binding to intronic polyadenylation sites (Krajewska et al., 2019). Regarding *RAD51C*, as established previously, *RAD51C* deficiency leads to impaired RAD51-focus formation, and cell lines with diminished *RAD51C* expression demonstrate increased susceptibility to PARPi (Min et al., 2013). Hence, we speculate that the manifestation of HRD in patients with dual mutations in *CDK12* and *RAD51C* is attributed to alterations in both transcription elongation and RAD51-focus formation. We identified 6 patients of co-mutations in the *CDK12* and *RAD51C* genes across various cancer types among 67,083 cancer patients in the cBioPortal database (Table 1). We anticipate that future clinical trials of this co-mutations will be conducted to benefit a broader patient population. Our study contributes by presenting a ccRCC patient with HRD benefiting from the use of PARPi, adding to the growing body of evidence supporting the versatility of PARPi across various cancer types.

To date, there are also reported instances of employing PARPi in the management of renal cancer patients exhibiting defects in the HRR pathway. A particularly noteworthy instance is illustrated in the case study conducted by Olson et al. (Olson et al., 2016), where a patient diagnosed with pRCC and possessing an *ATM* mutation exhibited positive responses to PARPi. Additionally, Lian et al. reported the first case of a ccRCC patient benefiting from PARPi with a *BAP1* frame shift mutation (Lian et al., 2022). Similar to the case reported in this article, the patient with a *BAP1* frame shift mutation also developed lung and brain metastases. After starting niraparib treatment, the patient showed a partial response in the lungs within 2 months. The intracranial lesion also shrank due to radiotherapy, and the headache was completely relieved. This patient developed new lesions in the lungs and brain 5 months after treatment. In contrast, the patient reported in this article, who had dual *CDK12* and *RAD51C* co-mutations, did not develop new metastases during approximately 15 months of treatment. Furthermore, the case of co-mutations in the HRR pathway genes *ATR* and *BRCA2* has been reported in patients with ccRCC. However, the patient with HRD has not received PARPi therapy (Yang et al., 2021). This study presents, for the first time, the therapeutic effects of PARPi in ccRCC with mutations in genes associated with the mutation of *RAD51C* and *CDK12*. Particularly noteworthy are cases harboring mutations in *RAD51C* and *CDK12* genes, where the effectiveness of PARPi treatment has already gained FDA approval in prostate cancer.

In summary, for ccRCC patients with gene mutation in the HRR pathway, particularly in *CDK12* and *RAD51C*, PARPi demonstrate favorable therapeutic efficacy. In China, a notable number of ccRCC patients exhibit gene mutations in the HRR pathway (Chen et al., 2022), offering novel insights into drug treatment possibilities for individuals with ccRCC.

Conclusion

In summary, patients with ccRCC harboring HRR pathway gene mutation may potentially benefit from niraparib. This will present more options for ccRCC patients with limited response to conventional treatments.

Data availability statement

The original contributions presented in the study are included in the article; further inquiries can be directed to the corresponding authors.

Ethics statement

Ethical approval was not required for the studies involving humans because this is a case report. Written informed consent was obtained from the individual(s) for the publication of any potentially identifiable images or data included in this article. The studies were conducted in accordance with the local legislation and institutional requirements. The participants provided their written informed consent to participate in this study. The manuscript presents research on animals that do not require ethical approval for their study.

Author contributions

XY: Data curation, Writing–review and editing. CY: Software, Writing–original draft. DC: Writing–review and editing. YL: Writing–review and editing, Data curation.

Funding

The author(s) declare that financial support was received for the research, authorship, and/or publication of this article. This work was supported financially by Heilongjiang Science Foundation (LC2018039).

Acknowledgments

The authors acknowledge the patient for his participation.

Conflict of interest

CY and DC were employed by Genetron Health (Beijing) Co., Ltd.

The remaining authors declare that the research was conducted in the absence of any commercial or financial relationships that could be construed as a potential conflict of interest.

Publisher's note

All claims expressed in this article are solely those of the authors and do not necessarily represent those of their affiliated organizations, or those of the publisher, the editors and the reviewers. Any product that may be evaluated in this article, or claim that may be made by its manufacturer, is not guaranteed or endorsed by the publisher.

References

Akbıyık, I., and Ürün, Y. (2023). Determining magnitude of benefit from poly (ADP-ribose) polymerase inhibitors in prostate cancer. *Future Oncol.* 19, 2585–2591. doi:10.2217/fon-2023-0550

Boussios, S., Karihtala, P., Moschetta, M., Abson, C., Karathanasi, A., Zakynthinakis-Kyriakou, N., et al. (2020). Veliparib in ovarian cancer: a new synthetically lethal therapeutic approach. *Investig. new drugs* 38, 181–193. doi:10.1007/s10637-019-00867-4

Chen, P., Zhang, Y., Bi, X., Niu, Y., Shayiti, F., Yuan, S., et al. (2022). Abstract 5690: the landscape of homologous recombination repair gene mutations and prognosis in Chinese patients with clear cell renal cell carcinoma. *Cancer Res.* 82, 5690. doi:10.1158/1538-7445.am2022-5690

Eiriz, I., Batista, M. V., Freitas, A. R., Martins, T., Machado, C., Braga, S., et al. (2023). PARP inhibitors in HRD BRCAness breast cancer patients. *J. Cancer* 4, 17–28. doi:10.46439/cancerbiology.4.049

Fizazi, K., Azad, A. A., Matsubara, N., Carles, J., Fay, A. P., De Giorgi, U., et al. (2023). First-line talazoparib with enzalutamide in HRR-deficient metastatic castration-resistant prostate cancer: the phase 3 TALAPRO-2 trial. *Nat. Med.* 30, 257–264. doi:10.1038/s41591-023-02704-x

Hsieh, J. J., Purdue, M. P., Signoretti, S., Swanton, C., Albiges, L., Schmidinger, M., et al. (2017). Renal cell carcinoma. *Nat. Rev. Dis. Prim.* 3, 17009–17019. doi:10.1038/nrdp.2017.9

Jonasch, E. (2019). NCCN guidelines updates: management of metastatic kidney cancer. *J. Natl. Compr. Cancer Netw.* 17, 587–589. doi:10.6004/jnccn.2019.5008

Kim, G., Ison, G., McKee, A. E., Zhang, H., Tang, S., Gwise, T., et al. (2015). FDA approval summary: olaparib monotherapy in patients with deleterious germline BRCA-mutated advanced ovarian cancer treated with three or more lines of chemotherapy. *Clin. cancer Res.* 21, 4257–4261. doi:10.1158/1078-0432.CCR-15-0887

Krajewska, M., Dries, R., Grassetti, A. V., Dust, S., Gao, Y., Huang, H., et al. (2019). CDK12 loss in cancer cells affects DNA damage response genes through premature cleavage and polyadenylation. *Nat. Commun.* 10, 1757. doi:10.1038/s41467-019-09703-y

Lai, Y., Li, Z., Lu, Z., Zheng, H., Chen, C., Liu, C., et al. (2022). Roles of DNA damage repair and precise targeted therapy in renal cancer. *Oncol. Rep.* 48, 1–12. doi:10.3892/or.2022.8428

Li, Q. K., Pavlovich, C. P., Zhang, H., Kinsinger, C. R., and Chan, D. W. (2019). Challenges and opportunities in the proteomic characterization of clear cell renal cell carcinoma (ccRCC): a critical step towards the personalized care of renal cancers. *Seminars cancer Biol.* 55, 8–15. doi:10.1016/j.semcancer.2018.06.004

Lian, B.-J., Zhang, K., Fang, X.-D., Li, F., Dai, Z., Chen, W.-Y., et al. (2022). Clinical benefit of Niraparib to TKI/mTORi-resistance metastatic ccRCC with BAP1-frame shift mutation: case report and literature review. *Front. Oncol.* 12, 927250. doi:10.3389/fonc.2022.927250

Marchetti, C., Imperiale, L., Gasparri, M. L., Palaia, I., Pignata, S., Boni, T., et al. (2012). Olaparib, PARP1 inhibitor in ovarian cancer. *Expert Opin. investigational drugs* 21, 1575–1584. doi:10.1517/13543784.2012.707189

Min, A., Im, S.-A., Yoon, Y.-K., Song, S.-H., Nam, H.-J., Hur, H.-S., et al. (2013). RAD51C-deficient cancer cells are highly sensitive to the PARP inhibitor olaparib. *Mol. cancer Ther.* 12, 865–877. doi:10.1158/1535-7163.MCT-12-0950

Olson, D., Bhalla, S., Yang, X., Martone, B., and Kuzel, T. M. (2016). Novel use of targeted therapy via PARP-inhibition in a rare form of papillary renal cell carcinoma: a case report and literature review. *Clin. Genitourin. Cancer* 14, e445–e448. doi:10.1016/j.clgc.2016.03.012

Pletcher, J. P., Bhattacharjee, S., Doan, J. P., Wynn, R., Sindhwani, P., Nadiminty, N., et al. (2021). The emerging role of poly (ADP-Ribose) polymerase inhibitors as effective therapeutic agents in renal cell carcinoma. *Front. Oncol.* 11, 681441. doi:10.3389/fonc.2021.681441

Posadas, E. M., Limvorasak, S., Sharma, S., and Figlin, R. A. (2013). Targeting angiogenesis in renal cell carcinoma. *Expert Opin. Pharmacother.* 14, 2221–2236. doi:10.1517/14656566.2013.832202

Robson, M., Im, S.-A., Senkus, E., Xu, B., Domchek, S. M., Masuda, N., et al. (2017). Olaparib for metastatic breast cancer in patients with a germline BRCA mutation. *N. Engl. J. Med.* 377, 523–533. doi:10.1056/NEJMoa1706450

Siegel, R. L., Miller, K. D., and Jemal, A. (2018). Cancer statistics, 2018. *CA a cancer J. Clin.* 68, 7–30. doi:10.3322/caac.21442

Yang, J., Wang, J., Liang, Y., Wang, J., Hsu, J., Liu, G., et al. (2021). ATR and BRCA2 simultaneous mutation in a ccRCC with sarcomatoid differentiation and extensive metastases: a case report. *Urology* 154, 45–49. doi:10.1016/j.urology.2021.04.025

Yang, J., Wang, K., and Yang, Z. (2023). Treatment strategies for clear cell renal cell carcinoma: past, present and future. *Front. Oncol.* 13, 1133832. doi:10.3389/fonc.2023.1133832

frontiers | Frontiers in Pharmacology

TYPE Opinion
PUBLISHED 27 June 2024
DOI 10.3389/fphar.2024.1428755

Check for updates

OPEN ACCESS

EDITED BY
Wagdy Mohamed Eldehna,
Kafrelsheikh University, Egypt

REVIEWED BY
Haytham O. Tawfik,
Tanta University, Egypt

*CORRESPONDENCE
Tedi Rustandi,
tedirustandi26@gmail.com

RECEIVED 07 May 2024
ACCEPTED 31 May 2024
PUBLISHED 27 June 2024

CITATION
Rustandi T, Yumassik AM, Ilahi FS, Alfian R, Prihandiwati E, Susanto Y, Susilo YH, Ulfah M and Faizatun F (2024), Repurposing therapy of ibrexafungerp vulvovaginal candidiasis drugs as cancer therapeutics.
Front. Pharmacol. 15:1428755.
doi: 10.3389/fphar.2024.1428755

COPYRIGHT
© 2024 Rustandi, Yumassik, Ilahi, Alfian, Prihandiwati, Susanto, Susilo, Ulfah and Faizatun. This is an open-access article distributed under the terms of the Creative Commons Attribution License (CC BY). The use, distribution or reproduction in other forums is permitted, provided the original author(s) and the copyright owner(s) are credited and that the original publication in this journal is cited, in accordance with accepted academic practice. No use, distribution or reproduction is permitted which does not comply with these terms.

Repurposing therapy of ibrexafungerp vulvovaginal candidiasis drugs as cancer therapeutics

Tedi Rustandi [1]*, Abdul Mahmud Yumassik[1], Fitrah Shafran Ilahi[1], Riza Alfian [1], Erna Prihandiwati[1], Yugo Susanto[1], Yudi Hardi Susilo[1], Maria Ulfah[1] and Faizatun Faizatun[2]

[1]Pharmacy, Sekolah Tinggi Ilmu Kesehatan ISFI Banjarmasin, Banjarmasin, Indonesia, [2]Department of Pharmaceutical Technology, Faculty of Pharmacy, Pancasila University, Jakarta, Indonesia

KEYWORDS

antifungal, anticancer, computational screening, glucan synthase inhibitor, ROS, triterpenoid, UBE2M, autophagy

1 Introduction

The prevalence of cancer in 2022, according to World Health Organization (WHO) data, is 20 million new cases and 9.7 deaths. The comparison of death rates based on gender is that 1 in 9 men and 2 in 12 women die from cancer (WHO, 2024). New cancer cases in the United States (US) in 2024 will be 2,001,140, with 611,720 resulting in death (Siegel et al., 2024).

Cancer is one of the leading causes of death worldwide, with the rate of adoption of new drugs likely to be slower in clinical practice than expected. New drug development takes a long time, with an average of 13 years at a cost of ~USD 2–3 billion (Zhang et al., 2020). This condition has global health and financial burdens (Roth et al., 2018). Discovery and development of new drugs to overcome this need to be done.

The drug repurposing method is a promising approach that will accelerate the research and development cycle. This approach is more effective in terms of cost and time than drug research and development using the *de novo* drug discovery approach (Tran and Prasad, 2020). Ibrexafungerp, approved by the FDA in 2021 as an antifungal derived from natural-product-based small compounds, has excellent potential to be developed using repurposing techniques to become a drug with other functions (Xu et al., 2022). The success of repurposing techniques in the development of anticancer drugs that have been approved by the FDA, such as a combination of aspirin, the antibiotic doxycycline, mifepristone, and the amino acid lysine, is used to prevent cancer metastasis (Wan et al., 2015).

The method used in this opinion article is a literature review. The literature review process uses Pubmed, Scopus, and Springer databases with criteria for articles published from 2015–2024. The article search method uses the query "repurposing therapy" AND/OR "ibrexafungerp" AND/OR "vulvovaginal candidiasis" AND/OR "cancer" AND/OR "computational screening" AND/OR "glucan synthase inhibitor" AND/OR "triterpenoid" AND/OR "ROS" AND/OR "siRNA" AND/OR "cancer mechanism" AND/OR "Tools" AND/OR "Computational" AND/OR "Artificial Intelligence" AND/OR "In Silico" AND/OR "Deep Learning" AND/OR "Machine Learning" AND/OR "bioinformatics."

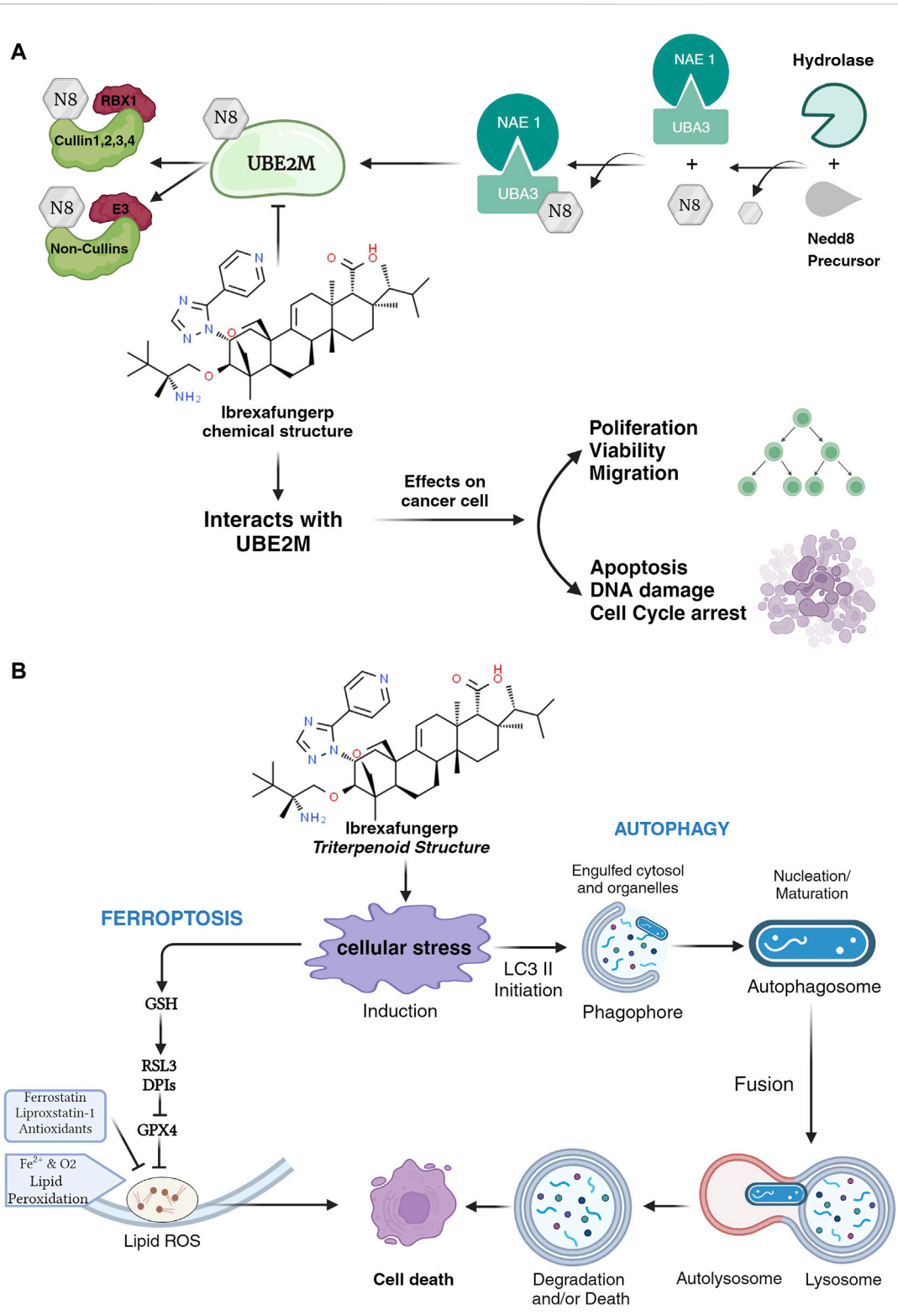

FIGURE 1
(A) Mechanism of Ibrexafungerp in inhibiting the neddylation process and **(B)** Mechanism of Ibrexafungerp as a ROS modulator.

2 Mechanism ibrexafungerp for anticancer

Ibrexafungerp has antifungal activity by inhibiting (1,3)-β-D-glucan synthase (Apgar et al., 2021). This mechanism gives Ibrexafungerp a good toxicity profile in host cells. The pharmacokinetic profile of Ibrexafungerp is well-classified, with the ability to penetrate tissues and organs, such as the liver, lungs, and skin. This pharmacokinetic profile is influenced by the structure of Ibrexafungerp, which has a core phenanthropyran

TABLE 1 Computational tools in cancer research.

Tools	Function	Web link	Reference
The cancer proteome Atlas V3.0 (TCPA V3.0)	Supports research to visualize and analyze Reverse phase protein arrays (RPPA) data	http://tcpaportal.org	Chen et al. (2019)
DemixTallmaterial	Supports research to estimate the proportion of specific cell types (tumor, stromal and immune cells) simultaneously	https://github.com/wwylab/DeMixTallmaterials	Wang et al. (2018)
The Cancer Genom Atlas (TCGA)	Supports research as a Platform that has a catalog of analysis data in large groups to study cancer genetics	https://www.genome.gov/Funded-Programs-Projects/Cancer-Genome-Atlas	Tomczak et al. (2015)
Tumor MAP	Supports research for visualization and interactive analysis in exploring patterns between tumor cells arranged relative to each other based on their molecules	https://tumormap.ucsc.edu/	Gabriel et al. (2020)
SurvNet	Using one of the artificial intelligence (AI) methods, namely, Deep Neural Network (DNN), which is used to analyze lung cancer survival	https://bioinformatics.mdanderson.org/SurvNet/	Wang et al. (2021)
METABRIC, HapMap, Lincs, KEGG, DrugBank	Identification of drug repurposing results of the best analysis for each breast cancer subtype	Not Available (NA)	Firoozbakht et al. (2022)
shinyDeepDR	The study of personalization of cancer treatment through analysis of drug response to differences in genomic attributes	https://shiny.crc.pitt.edu/shinydeepdr/	Wang et al. (2024)
iODA	Tools used for heterogeneous multi-omics data analysis	http://www.sysbio.org.cn/iODA	Yu et al. (2020a)
MLSP	Bioinformatic analysis tools in breast cancer research to predict molecular subtypes and prognosis	https://sujiezhulab.shinyapps.io/BRCA/	Zhu et al. (2022)
DEBay	A tool that can be used in cancer research related to gene expression through quantitative PCR data deconvolution	https://sourceforge.net/projects/debay	Devaraj and Bose (2020)
The HPV Induced Cancer Resource (THInCR)	Tools used to explore the impact of HPV on cellular gene expression (mRNA and microRNA), changes in gene methylation, and their relationship to patient survival and features of the immune landscape	https://thincr.ca/	Salnikov et al. (2022)
DAX-Net	The model that utilizes Convolutional Neural Network (CNN) and Transformer network for multiclass cancer classification	https://github.com/QuIIL/DAX-Net	Bui et al. (2024)
ExplORRNet	Tool for research related to miRNA expression profiles	https://mirna.cs.ut.ee	Lawarde et al. (2024)

carboxylic acid ring system at position 15 and 2-amino-2,3,3-trimethyl-butyl ether at position 14, both of which are derivatives of the naturally occurring hemiacetal triterpene glycoside enfumafungin. The pharmacokinetic profile in animals shows that Ibrexafungerp has a 30%–50% bioavailability when administered orally and has poor penetration into the central nervous system. *In vitro* studies show hydroxylation metabolism by the CYP3A4 isoenzyme with primary excretion via bile. The steady-state volume of distribution (Vss) profile in humans averages 600 L with high binding to protein, mainly albumin (Apgar et al., 2021; Angulo et al., 2022).

The potential of Ibrexafungerp as a cancer therapeutics is based on the use of antifungals, which have been used as anticancer agents. Antifungals with anticancer activity include itraconazole, rapamycin, griseofulvin, clotrimazole, ciclopirox, and nannocystin A (Li et al., 2022; Mohi-ud-din et al., 2023). The mechanisms of antifungal drugs that act as anticancers include the function of increasing autophagy, reducing angiogenesis, increasing tumor regression, and reducing metastasis (Mohi-ud-din et al., 2023).

Ibrexafungerp has a mechanism as a non-competitive glucan synthase inhibitor and the exact mechanism as echinocandins as an antifungal (Jallow and Govender, 2021; Shi et al., 2023; Kumar et al., 2024). Ibrexafungerp's activity includes a broad-spectrum anti-candida fungicide against species resistant to azole drugs. Capable *Candida* species associated with ibrexafungerp activity include auris, dubliniensis, glabrata, guilliermondii, keyfr, krusei, lusitaniae, parapsilosis, and tropicalis (Phillips et al., 2023). Activity as a broad-spectrum antifungal, such as *Candida* species, indicates that ibrexafungerp may have anticancer activity. The anticancer activity of broad-spectrum antifungals such as the triazole group, namely, itraconazole, is related to the mechanism of molecular smoothened (SMO) D477G mutations, sterol carrier protein 2 (SCP2), voltage-dependent anion channel 1 (VDAC1), and Niemann-Pick Type C 1 (NPC1) (Weng et al., 2023).

The mechanism of ibrexafungerp has the same action as micafungin, which is one of the echinocandin classes of antifungal agents. The mechanisms of action of Ibrexafungerp and micafungin as antifungals may have mechanisms similar to anticancer. The predicted mechanism of ibrexafungerp is to inhibit the neddylation process by stabilizing ubiquitin-conjugating enzyme 2 M (UBE2M). This enzyme is essential in molecular mechanisms such as DNA damage, apoptosis, and cell proliferation (Mamun et al., 2023a). The prediction of the Ibrexafungerp mechanism can be seen in Figure 1A (Mamun et al., 2023b; Mamun et al., 2023a; Yu et al., 2020b; Zheng et al., 2021; Zhou et al., 2023).

Prediction of the mechanism of ibrexafungerp as a UBE2M inhibitor can inhibit the neddylation pathway which can reduce tumor-promoting factors and increase levels of tumor suppressors thereby improving the occurrence of tumors and prognosis (Zheng et al., 2021). Anticancers that target UBE2M in the neddylation

process play a role in posttranslational modification mechanisms and target protein activity. The neddylation process begins with NEDD8 which is activated by E1 NEDD8-activating enzyme (NAE-consists of NAE1 and UBA3). This activation process results in the formation of the thioester-linked E1-NEDD8 complex which is then transferred to the NEDD8-conjugating enzyme (E2)/UBE2M (Yu et al., 2020b; Zheng et al., 2021). Ibrexafungerp inhibits the NEDD8 mechanism in UBE2M so that it cannot proceed to the next stage, namely, transferring NEDD8 from charged E2 to lysine residues in its target (Zhou et al., 2023).

Ibrexafungerp has a structure that belongs to the triterpenoid class (Angulo et al., 2022; Kumar et al., 2024). The triterpenoid group has the potential to be a cancer chemotherapy agent with a mechanism as a reactive oxygen species (ROS) modulator that can regulate cell survival and function. The impact of ROS on cancer cells is the mechanism of autophagy and ferroptosis (Endale et al., 2023; Jiang et al., 2021; Lee et al., 2023; Ling et al., 2022; Zeng et al., 2023). Autophagy works by causing cellular lipid accumulation and, ultimately, cell death. Another mechanism is inducing ferroptosis, which can cause increased chemosensitivity to chemotherapy drugs that are used to treat cancer cells. The mechanism of ibrexafungerp as a ROS modulator can be seen in Figure 1B (Ling et al., 2022).

3 Computational approaches ibrexafungerp

The development of ibrexafungerp as a cancer therapeutic can be done through 2 methods: experimental screening and computational (virtual) screening (Oliveira et al., 2023; Prada Gori et al., 2023; Weth et al., 2024). Experimental screening involves *in vivo* and *in vitro* research with drug-based phenotypic screens and target-based high throughput assays. Computational (virtual) screening methods include signature matching (-omics data), artificial intelligence (machine learning and deep learning), GWAS disease/target associations, and chemical similarity and molecular docking (Weth et al., 2024). A virtual screening server that can be used in computational approaches in the development of drug repurposing research, namely, DrugRep. The use of DrugRep in drug repurposing research uses receptor-based and ligand-based screening systems (Gan et al., 2023). Several tools can be used to develop anticancer from Ibrexafungerp, some of which can be seen in Table 1.

4 Conclusion

Ibrexafungerp is predicted to have two anticancer mechanisms. The anticancer mechanism is obtained by inhibiting the neddylation stage by stabilizing UBE2M, and Ibrexafungerp acts as a ROS modulator, which acts through cell death mechanisms with autophagy and ferroptosis.

Author contributions

TR: Writing–original draft, Writing–review and editing, Conceptualization, Data curation, Formal Analysis, Funding acquisition, Investigation, Methodology, Project administration, Resources, Software, Supervision, Validation, Visualization. AY: Writing–review and editing, Conceptualization, Visualization. FI: Writing–review and editing, Data curation, Methodology, Software. RA: Formal Analysis, Validation, Writing–review and editing. EP: Writing–review and editing. YgS: Supervision, Writing–review and editing. YdS: Writing–review and editing, Formal Analysis. MU: Formal Analysis, Writing–review and editing. Faizatun: Writing–review and editing, Supervision.

Funding

The author(s) declare that no financial support was received for the research, authorship, and/or publication of this article.

Acknowledgments

The figure was made using BioRender (https://app.biorender.com).

Conflict of interest

The authors declare that the research was conducted in the absence of any commercial or financial relationships that could be construed as a potential conflict of interest.

Publisher's note

All claims expressed in this article are solely those of the authors and do not necessarily represent those of their affiliated organizations, or those of the publisher, the editors and the reviewers. Any product that may be evaluated in this article, or claim that may be made by its manufacturer, is not guaranteed or endorsed by the publisher.

References

Angulo, D. A., Alexander, B., Rautemaa-Richardson, R., Alastruey-Izquierdo, A., Hoenigl, M., Ibrahim, A. S., et al. (2022). Ibrexafungerp, a novel triterpenoid antifungal in development for the treatment of mold infections. *J. Fungi* 8 (11), 1121. doi:10.3390/jof8111121

Apgar, J. M., Wilkening, R. R., Parker, D. L., Meng, D., Wildonger, K. J., Sperbeck, D., et al. (2021). Ibrexafungerp: an orally active β-1,3-glucan synthesis inhibitor. *Bioorg. Med. Chem. Lett.* 32, 127661. doi:10.1016/j.bmcl.2020.127661

Bui, D. C., Song, B., Kim, K., and Kwak, J. T. (2024). DAX-Net: a dual-branch dual-task adaptive cross-weight feature fusion network for robust multi-class cancer classification in pathology images. *Comput. Methods Programs Biomed.* 248, 108112. doi:10.1016/j.cmpb.2024.108112

Chen, M. J. M., Li, J., Wang, Y., Akbani, R., Lu, Y., Mills, G. B., et al. (2019). TCPA v3.0: an integrative platform to explore the pan-cancer analysis of functional proteomic data. *Mol. Cell. Proteomics* 18 (8), S15–S25. doi:10.1074/mcp.RA118.001260

Devaraj, V., and Bose, B. (2020). DEBay: a computational tool for deconvolution of quantitative PCR data for estimation of cell type-specific gene expression in a mixed population. *Heliyon* 6 (7), e04489. doi:10.1016/j.heliyon.2020.e04489

Endale, H. T., Tesfaye, W., and Mengstie, T. A. (2023). ROS induced lipid peroxidation and their role in ferroptosis. *Front. Cell Dev. Biol.* 11, 1226044. doi:10.3389/fcell.2023.1226044

Firoozbakht, F., Rezaeian, I., Rueda, L., and Ngom, A. (2022). Computationally repurposing drugs for breast cancer subtypes using a network-based approach. *BMC Bioinforma.* 23 (1), 143. doi:10.1186/s12859-022-04662-6

Gabriel, A. A. G., Mathian, E., Mangiante, L., Voegele, C., Cahais, V., Ghantous, A., et al. (2020). A molecular map of lung neuroendocrine neoplasms. *GigaScience* 9 (11), giaa112. doi:10.1093/gigascience/giaa112

Gan, J. H., Liu, J. X., Liu, Y., Chen, S. W., Dai, W. T., Xiao, Z. X., et al. (2023). DrugRep: an automatic virtual screening server for drug repurposing. *Acta Pharmacol. Sin.* 44 (4), 888–896. doi:10.1038/s41401-022-00996-2

Jallow, S., and Govender, N. P. (2021). Ibrexafungerp: a first-in-class oral triterpenoid glucan synthase inhibitor. *J. Fungi* 7 (3), 163. doi:10.3390/jof7030163

Jiang, M., Hu, R., Yu, R., Tang, Y., and Li, J. (2021). A narrative review of mechanisms of ferroptosis in cancer: new challenges and opportunities. *Ann. Transl. Med.* 9 (20), 1599. doi:10.21037/atm-21-4863

Kumar, V., Huang, J., Dong, Y., and Hao, G. F. (2024). Targeting Fks1 proteins for novel antifungal drug discovery. *Trends Pharmacol. Sci.* 45 (4), 366–384. doi:10.1016/j.tips.2024.02.007

Lawarde, A., Sharif Rahmani, E., Nath, A., Lavogina, D., Jaal, J., Salumets, A., et al. (2024). ExplORRNet: an interactive web tool to explore stage-wise miRNA expression profiles and their interactions with mRNA and lncRNA in human breast and gynecological cancers. *Non-Coding RNA Res.* 9 (1), 125–140. doi:10.1016/j.ncrna.2023.10.006

Lee, S., Hwang, N., Seok, B. G., Lee, S., Lee, S. J., and Chung, S. W. (2023). Autophagy mediates an amplification loop during ferroptosis. *Cell Death Dis.* 14 (7), 464. doi:10.1038/s41419-023-05978-8

Li, C. L., Fang, Z. X., Wu, Z., Hou, Y. Y., Wu, H. T., and Liu, J. (2022). Repurposed itraconazole for use in the treatment of malignancies as a promising therapeutic strategy. *Biomed. Pharmacother.* 154, 113616. doi:10.1016/j.biopha.2022.113616

Ling, T., Boyd, L., and Rivas, F. (2022). Triterpenoids as reactive oxygen species modulators of cell fate. *Chem. Res. Toxicol.* 35 (4), 569–584. doi:10.1021/acs.chemrestox.1c00428

Mamun, M., Liu, Y., Geng, Y. P., Zheng, Y. C., Gao, Y., Sun, J. G., et al. (2023). Discovery of neddylation E2s inhibitors with therapeutic activity. *Oncogenesis* 12 (1), 45. doi:10.1038/s41389-023-00490-2

Mamun, M. A. A., Liu, S., Zhao, L., Zhao, L., Li, Z.-R., Shen, D., et al. (2023). Micafungin: a promising inhibitor of UBE2M in cancer cell growth suppression. *Eur. J. Med. Chem.* 260, 115732. doi:10.1016/j.ejmech.2023.115732

Mohi-ud-din, R., Chawla, A., Sharma, P., Mir, P. A., Potoo, F. H., Reiner, Ž., et al. (2023). Repurposing approved non-oncology drugs for cancer therapy: a comprehensive review of mechanisms, efficacy, and clinical prospects. *Eur. J. Med. Res.* 28 (1), 345. doi:10.1186/s40001-023-01275-4

Oliveira, T., Silva, M., Maia, E., Silva, A., and Taranto, A. (2023). Virtual screening algorithms in drug discovery: a review focused on machine and deep learning methods. *Drugs Drug Candidates* 2 (2), 311–334. doi:10.3390/ddc2020017

Phillips, N. A., Rocktashel, M., and Merjanian, L. (2023). Ibrexafungerp for the treatment of vulvovaginal Candidiasis: design, development and place in therapy. *Drug Des. Dev. Ther.* 17, 363–367. doi:10.2147/DDDT.S339349

Prada Gori, D. N., Ruatta, S., Fló, M., Alberca, L. N., Bellera, C. L., Park, S., et al. (2023). Drug repurposing screening validated by experimental assays identifies two clinical drugs targeting SARS-CoV-2 main protease. *Front. Drug Discov.* 2. doi:10.3389/fddsv.2022.1082065

Roth, G. A., Abate, D., Abate, K. H., Abay, S. M., Abbafati, C., Abbasi, N., et al. (2018). Global, regional, and national age-sex-specific mortality for 282 causes of death in 195 countries and territories, 1980–2017: a systematic analysis for the Global Burden of Disease Study 2017. *Lancet* 392 (10159), 1736–1788. doi:10.1016/S0140-6736(18)32203-7

Salnikov, M., Gameiro, S. F., Zeng, P. Y. F., Barrett, J. W., Nichols, A. C., and Mymryk, J. S. (2022). The HPV Induced Cancer Resource (THInCR): a suite of tools for investigating HPV-Dependent human carcinogenesis. *MSphere* 7 (4), e0031722. doi:10.1128/msphere.00317-22

Shi, Z., Zhang, J., Tian, L., Xin, L., Liang, C., Ren, X., et al. (2023). A comprehensive overview of the antibiotics approved in the last two decades: retrospects and prospects. *Molecules* 28 (4), 1762. doi:10.3390/molecules28041762

Siegel, R. L., Giaquinto, A. N., and Jemal, A. (2024). Cancer statistics, 2024. *CA A Cancer J. Clin.* 74 (1), 12–49. doi:10.3322/caac.21820

Tomczak, K., Czerwińska, P., and Wiznerowicz, M. (2015). The Cancer Genome Atlas (TCGA): an immeasurable source of knowledge. *Wspolczesna Onkol.* 1A, A68–A77. doi:10.5114/wo.2014.47136

Tran, A. A., and Prasad, V. (2020). Drug repurposing for cancer treatments: a well-intentioned, but misguided strategy. *Lancet Oncol.* 21 (9), 1134–1136. doi:10.1016/S1470-2045(20)30424-1

Wan, L., Dong, H., Xu, H., Ma, J., Zhu, Y., Lu, Y., et al. (2015). Aspirin, lysine, mifepristone and doxycycline combined can effectively and safely prevent and treat cancer metastasis: prevent seeds from gemmating on soil. *Oncotarget* 6 (34), 35157–35172. doi:10.18632/oncotarget.6038

Wang, J., Chen, N., Guo, J., Xu, X., Liu, L., and Yi, Z. (2021). SurvNet: a novel deep neural network for lung cancer survival analysis with missing values. *Front. Oncol.* 10, 588990. doi:10.3389/fonc.2020.588990

Wang, L. J., Ning, M., Nayak, T., Kasper, M. J., Monga, S. P., Huang, Y., et al. (2024). shinyDeepDR: a user-friendly R Shiny app for predicting anti-cancer drug response using deep learning. *Patterns* 5 (2), 100894. doi:10.1016/j.patter.2023.100894

Wang, Z., Cao, S., Morris, J. S., Ahn, J., Liu, R., Tyekucheva, S., et al. (2018). Transcriptome deconvolution of heterogeneous tumor samples with immune infiltration. *IScience* 9, 451–460. doi:10.1016/j.isci.2018.10.028

Weng, N., Zhang, Z., Tan, Y., Zhang, X., Wei, X., and Zhu, Q. (2023). Repurposing antifungal drugs for cancer therapy. *J. Adv. Res.* 48, 259–273. doi:10.1016/j.jare.2022.08.018

Weth, F. R., Hoggarth, G. B., Weth, A. F., Paterson, E., White, M. P. J., Tan, S. T., et al. (2024). Unlocking hidden potential: advancements, approaches, and obstacles in repurposing drugs for cancer therapy. *Br. J. Cancer* 130 (5), 703–715. doi:10.1038/s41416-023-02502-9

WHO (2024) *Global cancer burden growing, amidst mounting need for services*. Lyon, France, Geneva, Switzerland: World Health Organization. Available at: https://www.who.int/news/item/01-02-2024-global-cancer-burden-growing–amidst-mounting-need-for-services.

Xu, Z., Eichler, B., Klausner, E. A., Duffy-Matzner, J., and Zheng, W. (2022). Lead/Drug discovery from natural resources. *Molecules* 27 (23), 8280. doi:10.3390/molecules27238280

Yu, C., Qi, X., Lin, Y., Li, Y., and Shen, B. (2020). iODA: an integrated tool for analysis of cancer pathway consistency from heterogeneous multi-omics data. *J. Biomed. Inf.* 112, 103605. doi:10.1016/j.jbi.2020.103605

Yu, Q., Jiang, Y., and Sun, Y. (2020). Anticancer drug discovery by targeting cullin neddylation. *Acta Pharm. Sin. B* 10 (5), 746–765. doi:10.1016/j.apsb.2019.09.005

Zeng, X. Y., Qiu, X. Z., Liang, S. M., Huang, J. A., Liu, S. Q., and Wu, J. N. (2023). Interaction mechanisms between autophagy and ferroptosis: potential role in colorectal cancer. *World J. Gastrointest. Oncol.* 15 (7), 1135–1148. doi:10.4251/wjgo.v15.i7.1135

Zhang, Z., Zhou, L., Xie, N., Nice, E. C., Zhang, T., Cui, Y., et al. (2020). Overcoming cancer therapeutic bottleneck by drug repurposing. *Signal Transduct. Target. Ther.* 5 (1), 113. doi:10.1038/s41392-020-00213-8

Zheng, Y. C., Guo, Y. J., Wang, B., Wang, C., Mamun, M. A. A., Gao, Y., et al. (2021). Targeting neddylation E2s: a novel therapeutic strategy in cancer. *J. Hematol. Oncol.* 14 (1), 57. doi:10.1186/s13045-021-01070-w

Zhou, L., Lin, X., Zhu, J., Zhang, L., Chen, S., Yang, H., et al. (2023). NEDD8-conjugating enzyme E2s: critical targets for cancer therapy. *Cell Death Discov.* 9 (1), 23. doi:10.1038/s41420-023-01337-w

Zhu, J., Kong, W., Huang, L., Wang, S., Bi, S., Wang, Y., et al. (2022). MLSP: a bioinformatics tool for predicting molecular subtypes and prognosis in patients with breast cancer. *Comput. Struct. Biotechnol. J.* 20, 6412–6426. doi:10.1016/j.csbj.2022.11.017

frontiers | Frontiers in Pharmacology

TYPE Original Research
PUBLISHED 28 June 2024
DOI 10.3389/fphar.2024.1396761

Check for updates

OPEN ACCESS

EDITED BY
Wagdy Mohamed Eldehna,
Kafrelsheikh University, Egypt

REVIEWED BY
Ahmed Amin,
Kafrelsheikh University, Egypt
João Pereira,
New University of Lisbon, Portugal

*CORRESPONDENCE
Zhiwei Zheng,
zhiweizheng@126.com

†These authors have contributed equally to this work and share first authorship

RECEIVED 11 April 2024
ACCEPTED 10 June 2024
PUBLISHED 28 June 2024

CITATION
Cai H, Fang L and Zheng Z (2024), Sugemalimab combined with chemotherapy for the treatment of advanced esophageal squamous cell carcinoma: a cost-effectiveness analysis. *Front. Pharmacol.* 15:1396761. doi: 10.3389/fphar.2024.1396761

COPYRIGHT
© 2024 Cai, Fang and Zheng. This is an open-access article distributed under the terms of the Creative Commons Attribution License (CC BY). The use, distribution or reproduction in other forums is permitted, provided the original author(s) and the copyright owner(s) are credited and that the original publication in this journal is cited, in accordance with accepted academic practice. No use, distribution or reproduction is permitted which does not comply with these terms.

Sugemalimab combined with chemotherapy for the treatment of advanced esophageal squamous cell carcinoma: a cost-effectiveness analysis

Hongfu Cai[1†], Ling Fang[2†] and Zhiwei Zheng[2*]

[1]Department of Pharmacy, Fujian Medical University Union Hospital, Fuzhou, China, [2]Department of Pharmacy, Cancer Hospital of Shantou University Medical College, Shantou, China

Background: This study aims to systematically analyze the cost-effectiveness of the combination therapy comprising sugemalimab and chemotherapy in the management of advanced ESCC from the Chinese healthcare system perspective.

Methods: An advanced ESCC patient simulation partitioned survival approach model was developed to mimic the disease progression of patients undergoing treatment with sugemalimab in combination with chemotherapy *versus* chemotherapy alone. To ensure accuracy and precision, clinical data, treatment costs, and utility values were collected from comprehensive clinical trials and reliable economic databases. The cost-effectiveness analysis was conducted by assessing the incremental cost-effectiveness ratio in relation to the established willingness-to-pay threshold. One-way and probabilistic sensitivity analyses were performed to assess the robustness of the model.

Results: The cumulative expenditure for the group of patients administered with sugemalimab amounted to US$ 41734.87, whereas the placebo group was associated with a total cost of US$ 22926.25. By evaluating the ICER, which quantifies the additional cost incurred per QALY gained, a value of US$ 61066.96 per QALY was determined. It is imperative to note that this ICER value surpasses the predetermined threshold for WTP in China, set at US$ 39,855.79 per QALY. Sensitivity analyses demonstrated that the results were sensitive to the cost of sugemalimab, progression-free survival, and utility values. These fluctuations did not result in a reversal of the study findings.

Conclusion: The combination of sugemalimab with chemotherapy for the treatment of ESCC in China is currently not considered a cost-effective therapeutic approach. However, it is suggested that additional reductions in price may facilitate the potential for achieving cost-effectiveness.

KEYWORDS

esophageal squamous cell carcinoma, sugemalimab, chemotherapy, cost-effectiveness, partitioned survival approach model

1 Introduction

Esophageal cancer is recognized as one of the most prevalent forms of cancer worldwide, ranking seventh in terms of incidence and sixth in terms of mortality (Jiang et al., 2023). Disturbingly, China bears the greatest burden of this disease, accounting for approximately 50% of all global esophageal cancer cases and deaths each year (Li L. et al., 2022). Esophageal squamous cell carcinoma (ESCC) is an extremely aggressive and deadly malignancy, predominantly found in Eastern Asia, primarily in China (Morgan et al., 2022). It poses a significant health burden in the region, warranting immediate attention. The prognosis for advanced ESCC is exceedingly grim, with a 5-year survival rate of less than 20% (Zhu et al., 2023). Consequently, urgent action is required to devise effective and precise therapeutic approaches to combat this devastating disease. The treatment of advanced ESCC is challenging due to late-stage diagnosis, tumor invasion into adjacent tissues, and distant metastasis. Current therapeutic approaches, including surgery, chemotherapy, and radiation therapy, have limited efficacy, and the development of resistance to these treatments is a common occurrence (Yajima et al., 2021). Therefore, there is a critical need to explore new treatment options that can improve the survival and quality of life for patients with advanced ESCC.

The emergence of immunotherapy has revolutionized the field of cancer treatment (Thuss-Patience and Stein, 2022; Wu et al., 2023). In particular, immune checkpoint inhibitors (ICIs), such as programmed cell death protein 1 (PD-1) and its ligand PD-L1, have demonstrated significant promise in the treatment of various cancers, including ESCC. Several recent clinical trials have provided compelling evidence of the efficacy of immune checkpoint inhibitors in the treatment of advanced ESCC. One notable ICIs that has demonstrated promising results in the treatment of advanced ESCC is pembrolizumab, as shown in the KEYNOTE-590 trial (Sun et al., 2021). This randomized, phase 3 trial investigated the efficacy of pembrolizumab in combination with chemotherapy compared to chemotherapy alone as the first-line treatment for patients with advanced ESCC. The results revealed a significant improvement in overall survival, progression-free survival, and objective response rate in the pembrolizumab group, highlighting its potential as a valuable treatment option for these patients. Similarly, nivolumab, another immune checkpoint inhibitor targeting PD-1, has demonstrated encouraging outcomes in advanced ESCC. The CheckMate 648 trial investigated the efficacy of nivolumab plus chemotherapy as first-line treatment for patients with unresectable advanced or metastatic ESCC (Doki et al., 2022). The trial revealed a significant improvement in overall survival and response rates compared to chemotherapy alone, further supporting the use of immune checkpoint inhibitors in the management of advanced ESCC. Recently, the use of sugemalimab, a novel anti-PD-L1 antibody, has shown great promise as a therapeutic option for patients with advanced ESCC. The GEMSTONE-304 trial evaluated the efficacy and safety of sugemalimab as first-line treatment in patients with advanced ESCC(Li et al., 2024). The results of the GEMSTONE-304 trial demonstrated significant improvements in overall survival (OS), progression-free survival (PFS), and response rates in patients receiving sugemalimab compared to those receiving chemotherapy alone. The median OS was substantially prolonged in the sugemalimab group, indicating a consistent and remarkable survival benefit. Moreover, the sugemalimab combination therapy exhibited a higher objective response rate and disease control rate compared to chemotherapy alone, further highlighting its efficacy in combating ESCC.

However, despite the promising initial results, there is a dearth of comprehensive evaluation regarding the cost-effectiveness of sugemalimab in combination with chemotherapy when compared to chemotherapy alone. Cost-effectiveness analyses are essential tools in healthcare decision-making processes, as they provide a comprehensive evaluation of treatments by considering not only their clinical effectiveness but also their cost implications (Rodriguez and Caughey, 2013). Healthcare decision-making is often confronted with limited resources, and cost-effectiveness analyses assist in prioritizing interventions based on the potential returns on investment. By comparing the costs and outcomes of different treatment options, decision-makers can identify interventions that provide the greatest health gains at a reasonable cost (Turner et al., 2021). This helps promote efficient resource allocation and ensures equitable access to healthcare services. Thus, the lack of cost-effectiveness has hindered our understanding of the economic implications of utilizing sugemalimab therapy for advanced ESCC. In this comprehensive study, our objective is to evaluate the incremental cost-effectiveness ratio (ICER) of combining sugemalimab with chemotherapy, as compared to the use of chemotherapy alone. This analysis will offer critical insights into the financial implications associated with achieving an additional unit of health benefit through the adoption of sugemalimab in combination with chemotherapy. The outcomes of this study will serve as a valuable resource for decision-makers, who are tasked with allocating limited resources efficiently. The results will aid in determining the optimal allocation of healthcare funds while considering both the financial sustainability and clinical effectiveness of treatment options.

2 Methods

2.1 Study design and data sources

We have developed a novel partitioned survival model (PSM) to comprehensively assess the intricate relationship between cost aspects and clinical benefits in patients with advanced ESCC. The PSM categorizes patients into three distinct and mutually exclusive states: progression-free disease, progressive disease, and death (Figure 1). By incorporating a wide range of significant direct healthcare expenditures, including medication costs, management of adverse events, follow-up therapeutic interventions, and optimal supportive care, our model provides a comprehensive framework for evaluating the economic implications of ESCC treatment.

Survival data from the GEMSTONE-304 clinical trial was collected using GetData Graph Digitizer (version 2.25) software. This software reconstructs the raw data from survival curve prior curves to simulate transfer probabilities.

To align with the designated observation time of the GEMSTONE-304 clinical trial, we have selected a simulation

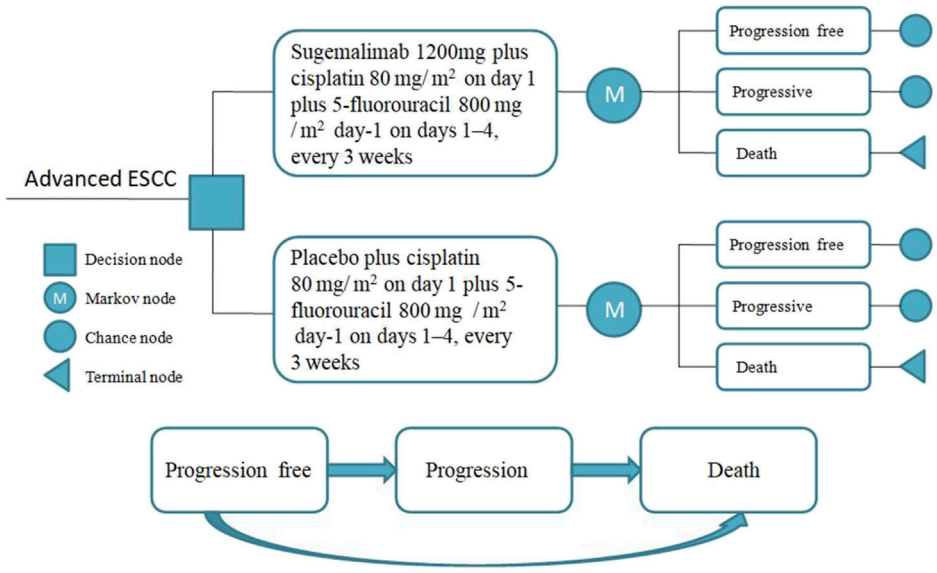

FIGURE 1
Study design model.

period of 21 days per cycle. Because the overall 5-year survival rate for ESCC ranges was 20%, we set the time horizon of our model to 10 years. Furthermore, our PSM analysis provides additional support for this 10-year timeframe by demonstrating that nearly all patients in the model would reach the terminal state within this duration.

According to the latest China Guidelines for Pharmacoeconomic Evaluations in 2020, we have established a threshold for willingness-to-pay (WTP) at $39855.785 per quality-adjusted life year (QALY), which was determined as three times the national gross domestic product (GDP) *per capita* in 2023 (National Bureau of Statistics of China, 2023; Liu et al., 2020). The incorporation of this WTP threshold enables us to compare the incremental cost per QALY gained and assess the economic viability of the intervention. The construction of the PSM framework was executed using TreeAge Pro 2011 software.

3 Population and intervention

The model assumes that the study population is consistent with participants in the GEMSTONE-304 trial. Between 19 December 2019, and 23 December 2021, a total of 785 patients were screened for eligibility across 69 study centers in China. Out of these patients, 540 individuals who met the criteria were randomly assigned to two groups in a 2:1 ratio. Specifically, 358 patients were allocated to receive sugemalimab in conjunction with chemotherapy, while 182 patients were assigned to receive a placebo alongside chemotherapy.All enrolled patients were of Asian ethnicity and had a median age of 62.5 years (range, 40–75 years) and 63.0 years (range, 43–75 years) in the sugemalimab and placebo-chemotherapy groups, respectively. The majority of patients had an Eastern Cooperative Oncology Group (ECOG) performance status score of 1 (79.1% in the sugemalimab group *versus* 78.6% in the placebo-chemotherapy group). The proportion of male patients was similar between the two groups, with 87.7% in the sugemalimab group and 86.8% in the placebo-chemotherapy group. The majority of patients in both treatment groups had stage IV tumors (90.2% in the sugemalimab group *versus* 90.7% in the placebo-chemotherapy group), and a similar proportion of patients had metastasis (79.6% in the sugemalimab group *versus* 79.1% in the placebo-chemotherapy group). The distribution of patients based on PD-L1 expression levels was balanced in both treatment groups, with 57.0% and 57.1% of patients having PD-L1 expression levels below 10% and 43.0% and 42.9% having PD-L1 expression levels of 10 or higher in the sugemalimab and placebo-chemotherapy groups, respectively (Li et al., 2024).

The GEMSTONE-304 trial and our PSM assumes that the study population included a total of 540 eligible patients who were randomly assigned in a 2:1 ratio to receive either sugemalimab along with chemotherapy (n = 358) or placebo along with chemotherapy (n = 182). Participants were randomly allocated to receive either sugemalimab (1,200 mg) every 3 weeks or a placebo for a maximum of 24 months. Additionally, they will receive chemotherapy every 3 weeks, comprising cisplatin (80 mg/m^2, day 1) and 5-fluorouracil (800 mg/m^2, day 1–4), for a total of six treatment cycles.

The administration of subsequent anticancer therapy was observed in 145 individuals (40.5%) within the sugemalimab-chemotherapy cohort, whereas 88 participants (48.4%) received comparable treatment in the placebo chemotherapy group. In light of the cost-effectiveness analysis that needs to be conducted, we have employed the assumption of utilizing a second-line treatment of docetaxel in combination with a platinum-based chemotherapy regimen for both treatment groups. However, due to the considerable uncertainty surrounding the optimal selection of third-line therapy, our study assumes the utilization of the best supportive treatment regimen in the event of disease re-progression.

TABLE 1 Log-logistic survival model parameters.

Variable	Sugemalimab plus chemotherapy cohort	Placebo plus chemotherapy cohort
Log-logistic OS shape (γ)	1.707	1.975
Log-logistic OS scale (λ)	0.00937	0.00773
Log-logistic PFS shape (γ)	2.129	2.501
Log-logistic PFS scale (λ)	0.0173	0.0166

Abbreviations:OS: overall survival; PFS: Progression-Free Survival.

4 Clinical data collection procedures

In this study, we extracted and reconstructed the survival curve data from the GEMSTONE-304 clinical trial using the data extraction tool GetData Graph Digitizer (http://www.getdata-graph-digitizer.com, version 2.25) software.Our primary aim was to extract and simulate the survival curves, encompassing both overall survival and disease-free survival, by identifying the most suitable statistical distributions. In the determination of the optimal distribution, a combination of two principles was employed: firstly, the akaike information criterion (AIC) and the Bayesian Information Criterion (BIC) were utilized as the minimum statistical criteria, and secondly, an intuitive visual inspection was conducted to ensure that the simulated curves adhered to the established clinical observation standards (Hoyle and Henley, 2011). The AIC and BIC values associated with the simulated survival curves can be located in Supplementary Table S1. Furthermore, Supplementary Figure S1 provides a graphical depiction of the reconstructed distribution curves for each respective group.

To enhance the efficacy of our model, we implemented a simulation approach to generate survival times based on a log-logistic distribution. This innovative technique allowed us to extend the applicability of our model beyond the duration of the clinical trial follow-up. By providing a robust estimation of the survival function S(t), we aimed to offer a more comprehensive understanding of the underlying dynamics of the studied population. The survival function, denoted as S(t), plays a crucial role in survival analysis as it quantifies the probability that an individual survives beyond a given time point, t. In our study, we employed the log-logistic distribution to model the survival function,$S(t) = 1/(1+\lambda t^{\gamma})$. This parametric distribution holds immense significance in survival analysis due to its flexibility in capturing various shapes of survival curves.To effectively implement the log-logistic distribution and estimate the parameters, we utilized R software. The estimated values of the parameters, shape (γ) and scale (λ) are presented in Table 1.

5 Cost sources and utility parameters

This study is conducted from the Chinese healthcare system perspective. From this perspective, it can provide decision-making for healthcare and promote rational pricing of medicines. We consider costs related to medication, treatment of serious adverse events caused by medications, follow-up treatment, best supportive care, and expenses related to follow-up. The annual exchange rate from Chinese Renminbi (RMB) to US dollars (US$) for 2023 was705 units of RMB per 100 US$(National Data, 2023).To ensure accurate data on drug costs, we gathered national median drug prices from the China Data Platform (https://data.yaozh.com/) (YaoZH, 2024). Conversely, other costs were derived from pertinent literature that has been previously published.

In order to evaluate the quality of life associated with health status, utility values ranging from 0 to 1 were utilized within this study. Unfortunately, explicit utility value data from the GEMSTONE-304 clinical trial were unattainable. Consequently, we procured utility values from previously published literature. It is important to highlight and emphasize that these cost and utility values obtained from the literature are factored into our sensitivity analysis, which aims to determine the robustness of the results yielded by our model by assessing their impact on the conclusions drawn from our findings. Additionally, our model also accounts for the negative utility associated with adverse drug events. Detailed information regarding cost and utility values can be found in Table 2.

6 Sensitivity analysis

This study utilized sensitivity analyses to enhance the robustness of the model. Firstly, a one-way sensitivity analysis was conducted to assess the impact of varying input parameters on the ICER. Each input parameter was adjusted individually by ±25% to evaluate its influence on the ICER. Additionally, the discount rate was varied from 0% to 8%. The results of this sensitivity analysis were visually represented using a tornado diagram, an effective tool for illustrating the relative importance of each parameter in influencing the ICER.

In order to thoroughly evaluate and quantify the uncertainty associated with estimating the ICER, a comprehensive and rigorous probabilistic sensitivity analysis was carried out. This analysis entailed the execution of 1000 Monte Carlo simulations, allowing for a thorough exploration and investigation of a wide spectrum of probabilistic scenarios. The main objective of the probabilistic sensitivity analysis was to incorporate random sampling of input parameters from specified probability distributions. This approach ensured a robust and comprehensive assessment of the potential variability in the ICER estimates, taking into account the intrinsic uncertainty associated with each parameter. By sampling from specified probability distributions, the analysis allowed for the consideration of parameter values that were not only deterministic, but also probabilistic in nature. This feature enabled a more realistic and accurate representation of the inherent uncertainty in the estimation of the ICER, considering

TABLE 2 The parameters input of the model.

Parameters	Input value	Range		Distribution	Source
		Minimum	Maximum		
TEAE rate of sugemalimab group (%)					
Platelet count decreased	2.50	-	-	Beta	Li et al. (2024)
Vomiting	2.00			Beta	Li et al. (2024)
Nausea	0.80	-	-	Beta	Li et al. (2024)
TEAE rate of placebo group (%)					
Platelet count decreased	2.20	-	-	Beta	Li et al. (2024)
Vomiting	2.10	-	-	Beta	Li et al. (2024)
Nausea	2.20	-	-	Beta	Li et al. (2024)
Medication costs (US$)					
Sugemalimab (600 mg)	1839.85	1379.89	2299.81	Gamma	YaoZH (2024)
Fluorouracil (500 mg)	29.12	21.84	36.40	Gamma	YaoZH (2024)
Cisplatin (10 mg)	1.39	1.04	1.74	Gamma	YaoZH (2024)
Cost of TEAE per cycle (US$)					
Platelet count decreased	1523.82	1142.87	1904.78	Gamma	Liu et al. (2023a)
Vomiting	71.00	53.25	88.75	Gamma	Li et al. (2022b)
Nausea	101.15	75.86	126.44	Gamma	Yang et al. (2021)
Subsequent therapy per cycle (US$)	639.75	479.81	799.69	Gamma	Zheng et al. (2024)
Best supportive care (US$)	182.23	136.67	227.79	Gamma	Liu et al. (2023b)
Follow-up cost per cycle (US$)	73.72	55.29	92.15	Gamma	Liu et al. (2023a)
Utility					
Progression-free disease	0.74	0.56	0.93	Beta	Al-Batran et al. (2016)
Progressive disease	0.58	0.44	0.73	Beta	Al-Batran et al. (2016)
Platelet count decreased	0.20	0.15	0.25	Beta	Zheng et al. (2023a)
Vomiting	0.13	0.10	0.16	Beta	Zheng et al. (2023a)
Nausea	0.13	0.10	0.16	Beta	Zheng et al. (2023b)
Body surface area (m^2)	1.72	1.29	2.15	Beta	Zheng et al. (2023b)
Discount rate	5%	0	8%	Beta	Liu et al. (2020)

Abbreviations: TEAE:Treatment-emergent adverse event.

the various sources of variability and randomness that influence the input parameters. The results of this probabilistic sensitivity analysis are effectively communicated through meticulously crafted scatter plots.

7 Results

7.1 Cost-effectiveness outcomes

The total cost for the group receiving sugemalimab amounted to US$41734.87, whereas the placebo group incurred a total cost of US$22926.25. The administration of the sugemalimab regimen resulted in a statistically significant increase of 0.31 QALYs compared to the placebo group. However, this additional benefit came at an incremental cost of US$18808.62. Consequently, the calculated ICER was US$61066.96 per QALY gained, which exceeds the WTP threshold of US$39855.79 per QALY in China. Thus, the use of the sugemalimab regimen may not be deemed cost-effective within the Chinese healthcare system. Table 3 provides a comprehensive summary of the findings obtained in this analysis.

However, we discovered that reducing the price of sugemalimab by 50% to only $919.92 per 600 mg resulted in an ICER of US$39,547.54 per QALY gained. It is noteworthy that this ICER value closely aligns with the WTP threshold of US$39,855.79 per QALY.

TABLE 3 The results of cost-effectiveness.

Group Result	Sugemalimab group	Placebo group
Cost (US$)	41734.87	22926.25
QALYs	1.54	1.23
Incremental cost (US$)	18808.62	NA
Incremental QALY	0.31	NA
ICER (US$/QALY)	61066.96	NA

ICER, Incremental cost–effectiveness ratio; QALY, Quality-adjusted life year; NA, not applicable.

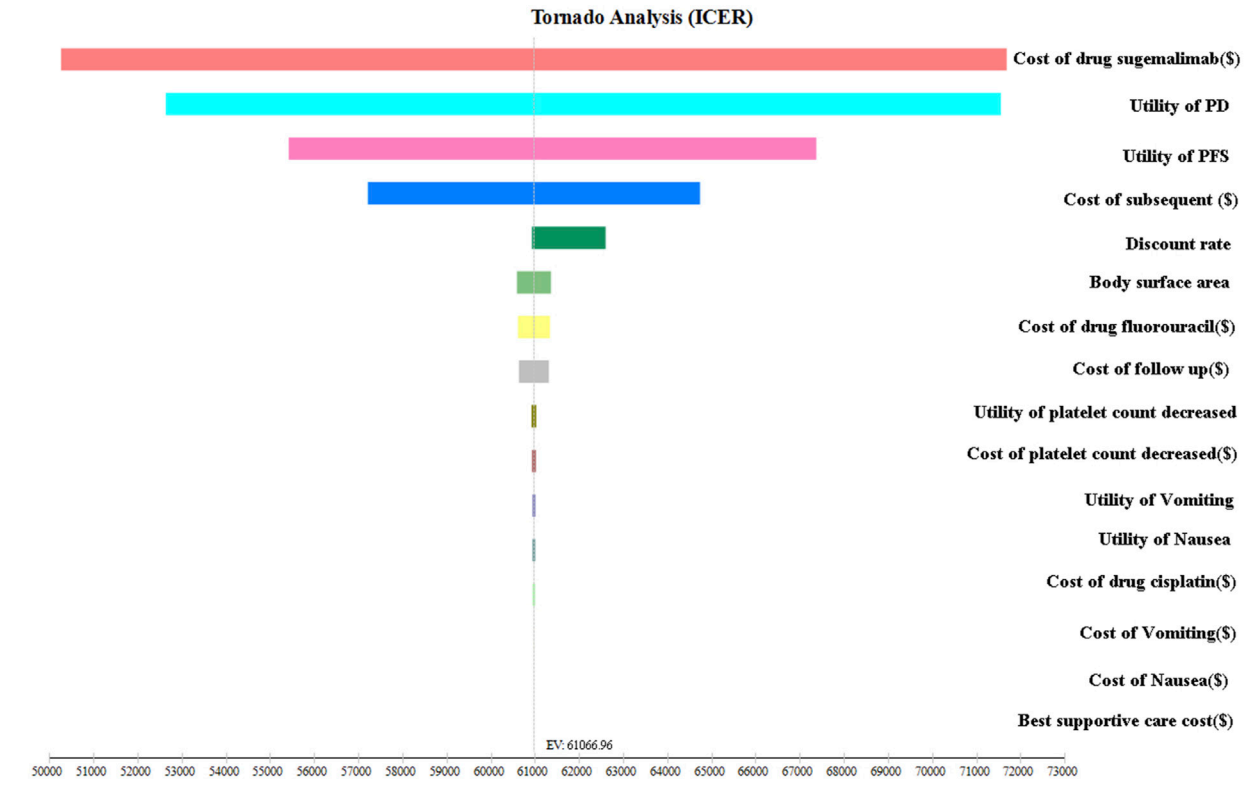

FIGURE 2
The outcomes of sensitivity analysis.

8 Sensitivity analysis outcomes

The tornado diagram presented in Figure 2 depicts the outcomes of one-way sensitivity analysis. The parameter that exerted the greatest impact on the ICER across all populations was the price of sugemalimab. However, it is worth noting that this impact fluctuated within a range of ±25%, which still considerably exceeded the WTP threshold. These fluctuations did not result in a reversal of the study findings. Additionally, other parameters such as PFS utility, PD utility, and Subsequent therapy costs also influenced the ICER, albeit their impact gradually diminished. It is of significance to emphasize that even variations of these parameters within a range of ±25% did not yield significant alterations in the analysis results. Consequently, the consistent finding that the ICER value consistently surpasses three times the GDP strengthens the stability of our findings.

In Figure 3, the ICER plane is visually partitioned into quadrants, enabling a clear depiction of the distribution of the 1000 bootstrap replicates of the ICER. The resulting graph provides valuable insights into the cost-effectiveness of various interventions. Based on the findings derived from the analysis, interventions falling within the North-East quadrant of the cost-effectiveness plane, specifically below the linear ICER line, are inferred to be perceived as cost-effective. The strategic placement of the North-East quadrant on the cost-effectiveness plane signifies interventions that demonstrate superior cost-effectiveness in comparison to other alternatives. This positioning suggests that the interventions in this quadrant

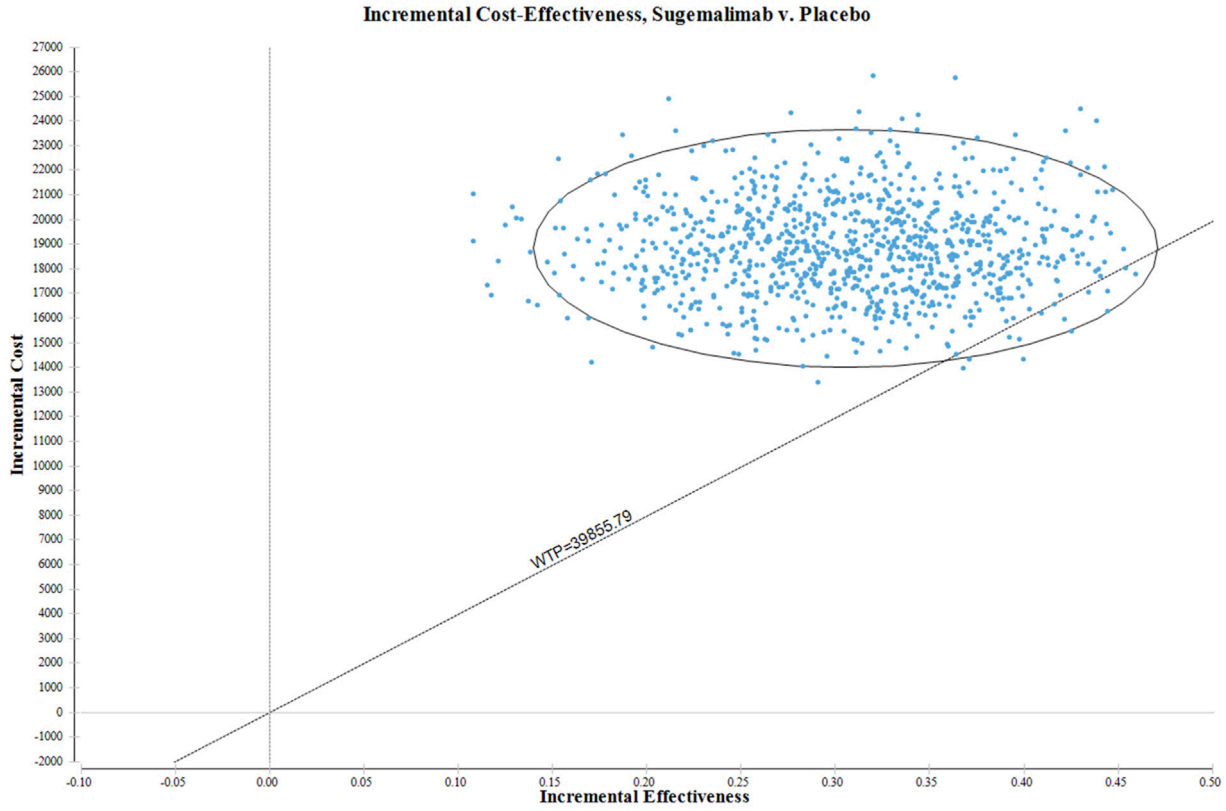

FIGURE 3
The outcomes of the ICER plane scatter plots.

possess a more favorable ICER ratio, indicating lower costs or superior effectiveness relative to interventions in other quadrants. Significantly, when considering the WTP threshold of US$39855.79 per QALY, there is a mere 1.2% probability of deeming the sugemalimab regimen as a more cost-effective option compared to the placebo group.

9 Discussion

In recent years, there have been significant advancements in the field of cancer treatment in China, particularly with the development of innovative PD-1 inhibitors. These inhibitors have shown promising results in terms of providing improved survival benefits and clinical tolerability for patients suffering from various types of cancer (Zhang et al., 2022a). One of the key factors contributing to this positive trend is the implementation of centralized price negotiation mechanisms, which aim to enhance the accessibility and affordability of these treatments for patients (Zhang et al., 2022b). The National Medical Products Administration in China has played a crucial role in strengthening regulatory capacity to ensure the safety and efficacy of these innovative anti-cancer medicines. They have also introduced priority procedures to expedite the development, review, and approval of such drugs. These measures have not only accelerated the availability of these treatments but have also facilitated timely access for patients in need.

To address the concern of rapidly increasing healthcare costs, value-based pricing and national medical insurance negotiations have been pivotal in determining the coverage and reimbursement of innovative drugs by the national medical insurance program (Si et al., 2020). This approach ensures that the cost of these medications aligns with the value they provide in terms of patient outcomes and overall healthcare system sustainability. Through these negotiations, drug prices have been reduced by half, thereby significantly easing the financial burden on patients while ensuring the long-term viability of the medical insurance program (Tang et al., 2020). The Chinese government's concerted efforts in fostering innovation, streamlining regulatory processes, and implementing cost-containment measures have paved the way for the development and accessibility of groundbreaking cancer therapies. These advancements not only offer new hope for cancer patients in China but also contribute to the advancement of global cancer treatment strategies.

Following our research, the utilization of sugemalimab as a therapeutic intervention for advanced ESCC yielded results in terms of an ICER of US $61,066.96 per QALY gained. It is noteworthy that this ICER exceeds the WTP threshold of US$39,855.79 per QALY, thereby indicating that sugemalimab does not meet the criteria for being considered a cost-effective treatment option for this specific condition in China.

Sensitivity analysis holds a critical position in both scientific inquiry and decision-making processes, playing a crucial role in examining the impact of changes in input variables on the outcomes of studies and

models. Through thorough investigation of the sensitivity of various parameters, researchers can develop a deeper understanding of the interdependent relationships and responsiveness of their findings to individual factors. Notably, a consistent observation emerged that the price of sugemalimab exhibited the most profound influence on the ICER. However, even when modifying the parameters within a range of ±25%, the resulting ICER consistently exceeded the threshold deemed acceptable for WTP. This compelling discovery presents robust evidence to substantiate the claim that the current pricing methodology for sugemalimab is comparably costly and lacks cost-effectiveness in its application to the treatment of advanced ESCC. The PSA result showed that when considering the WTP threshold of US$39855.79 per QALY, there is a mere 1.2% probability of deeming the sugemalimab regimen as a more cost-effective option compared to the placebo group. However, if we take into account a threshold increase to US$63,769.25 per QALY, the sugemalimab regimen is found to be 58.10% more cost-effective than the placebo group.

Currently, there is some research aimed at conducting economic evaluations of immunotherapies for patients with advanced ESCC. The economic evaluation of these treatments is of great importance, as it helps to assess their cost-effectiveness and inform decision-making regarding their inclusion in healthcare systems. For example, a study by Xu et al. used a cost-effectiveness analysis to compare the expenses and benefits of toripalimab *versus* standard chemotherapy for ESCC. The findings of this study indicated that toripalimab plus chemotherapy was likely to be the cost-effective first-line option for patients with advanced ESCC compared with chemotherapy alone (Kang et al., 2024). Another study by Liu et al. focused on evaluating the cost-effectiveness of various second-line immunotherapies for the treatment of ESCC patients. The immunotherapies considered were camrelizumab, nivolumab, pembrolizumab, sintilimab, and tislelizumab. Their results demonstrated that sintilimab might be the optimal treatment alternative for second-line therapy of advanced ESCC in China, followed by tislelizumab and camrelizumab (Liu et al., 2024).

Our study distinguishes itself from previous publications in several significant ways. Firstly, our research utilizes data from a unique clinical trial, the GEMSTONE-304 trial, which sets it apart from previous studies that may have relied on different trial data sources. This inclusion of specific data enhances the credibility and reliability of our findings. Moreover, our analysis incorporates a comprehensive range of factors, such as treatment effects, adverse events, and costs. This multidimensional approach underscores the robustness and thoroughness of our investigation. Additionally, it is noteworthy that no previous publication conducting a cost-effectiveness analysis has specifically utilized data from the GEMSTONE-304 clinical trial. This is an important aspect to highlight as it emphasizes the novelty and originality of our study, as well as its potential to contribute to existing literature in a unique and meaningful way.

We strongly advise against utilizing cost-effectiveness analyses, especially the result of our study, as the sole basis for imposing restrictions on the use of sugemalimab. Instead, we propose employing these analyses to inform policy decisions and enhance access to sugemalimab through improvements in the health insurance system (Fang et al., 2021). We contend that cost-effectiveness analyses can serve as a reliable methodological approach to objectively guide recommendations aimed at reducing the prices of costly drugs. The prevailing exorbitant costs associated with anticancer medications pose an additional financial burden on individuals and the healthcare system as a whole. Recognizing this issue, China has implemented measures such as the centralized national procurement of medicines to alleviate financial strains. Notably, successful negotiations between the government and manufacturers in 2016 resulted in a significant price reduction of gefitinib by over 50%.Drug pricing and national reimbursement negotiation led to a marked decrease in prices and a sharp increase in the utilization of negotiated anticancer medicines (Mingge et al., 2023). The Chinese government is currently engaged in proactive efforts to enhance the availability of novel oncology medications. The accelerated pace of reimbursement decision-making for domestically-produced drugs is perhaps attributed to their competitive pricing advantages as well as the regulator's endeavors to foster innovation within the domestic pharmaceutical sector (Liu et al., 2022).

Our research aimed to assess the affordability and value of sugemalimab by conducting a comprehensive cost-effectiveness analysis using the ICER. We discovered that reducing the price of sugemalimab by 50% to only $919.92 per 600 mg resulted in an ICER of US$39,547.54 per QALY gained. It is noteworthy that this ICER value closely aligns with the WTP threshold of US$39,855.79 per QALY. These findings underscore the considerable cost-effectiveness of sugemalimab at the lower price. In essence, our results indicate that aligning the ICER of sugemalimab with established WTP thresholds presents an opportunity to expand access to cost-effective treatment for a larger patient population. By strategically reducing the price of sugemalimab, we can enhance the accessibility of this innovative therapy to a broader range of individuals, ultimately maximizing its cost-effectiveness.

This study has the following limitations. Firstly, by relying solely on the GEMSTONE-304 study, there is an increased level of uncertainty in the estimated parameters. The degree of rigor in the conducted trial will inherently impact the reliability of the results obtained. Moreover, as new survival data becomes available, our findings may be subject to potential influences. In light of this, it is imperative to consistently monitor and update these findings.Secondly, it is imperative to acknowledge that in real-world scenarios, the effectiveness of different interventions might be enhanced when used in combination with other treatments, a factor that our model fails to incorporate. Furthermore, our investigation rests on certain assumptions regarding the cost of subsequent treatment options after disease progression. However, in practice, the choice of subsequent treatment regimen will vary based on the specific circumstances of each patient. Encouragingly, our one-way sensitivity analyses demonstrated that even when modifying the estimated range of subsequent treatment regimens, the ICER values consistently exceeded the WTP thresholds, thereby further supporting our conclusions. Lastly, it is important to note that our analysis did not encompass grade 1 or 2 adverse events. We presumed that these events would have a minimal impact on clinical outcomes, and subsequent sensitivity analyses corroborated that adverse drug events do not significantly influence our findings.

10 Conclusion

Currently, the utilization of sugemalimab in combination with chemotherapy as a therapeutic approach for the treatment of ESCC

in China is not considered cost-effective. However, it is suggested that if the price of sugemalimab is further reduced by 50% to only $919.92 per 600 mg, it may achieving cost-effectiveness in China from the current WTP threshold.

Data availability statement

The original contributions presented in the study are included in the article/Supplementary Material, further inquiries can be directed to the corresponding author.

Author contributions

HC: Project administration, Supervision, Validation, Writing–review and editing. LF: Data curation, Investigation, Software, Writing–review and editing. ZZ: Methodology, Writing–original draft, Writing–review and editing.

Funding

The author(s) declare that financial support was received for the research, authorship, and/or publication of this article. This work was supported by the Guangdong Medical Research Foundation (A2024797).

Conflict of interest

The authors declare that the research was conducted in the absence of any commercial or financial relationships that could be construed as a potential conflict of interest.

Publisher's note

All claims expressed in this article are solely those of the authors and do not necessarily represent those of their affiliated organizations, or those of the publisher, the editors and the reviewers. Any product that may be evaluated in this article, or claim that may be made by its manufacturer, is not guaranteed or endorsed by the publisher.

Supplementary material

The Supplementary Material for this article can be found online at: https://www.frontiersin.org/articles/10.3389/fphar.2024.1396761/full#supplementary-material

References

Al-Batran, S. E., Van Cutsem, E., Oh, S. C., Bodoky, G., Shimada, Y., Hironaka, S., et al. (2016). Quality-of-life and performance status results from the phase III RAINBOW study of ramucirumab plus paclitaxel versus placebo plus paclitaxel in patients with previously treated gastric or gastroesophageal junction adenocarcinoma. *Ann. Oncol.* 27, 673–679. doi:10.1093/annonc/mdv625

Doki, Y., Ajani, J. A., Kato, K., Xu, J., Wyrwicz, L., Motoyama, S., et al. (2022). Nivolumab combination therapy in advanced esophageal squamous-cell carcinoma. *N. Engl. J. Med.* 386 (5), 449–462. doi:10.1056/NEJMoa2111380

Fang, W., Xu, X., Zhu, Y., Dai, H., Shang, L., and Li, X. (2021). Impact of the national health insurance coverage policy on the utilisation and accessibility of innovative anti-cancer medicines in China: an interrupted time-series study. *Front. Public Health* 9, 714127. doi:10.3389/fpubh.2021.714127

Hoyle, M. W., and Henley, W. (2011). Improved curve fits to summary survival data: application to economic evaluation of health technologies. *BMC Med. Res. Methodol.* 11, 139. doi:10.1186/1471-2288-11-139

Jiang, Y., Lin, Y., Wen, Y., Fu, W., Wang, R., He, J., et al. (2023). Global trends in the burden of esophageal cancer, 1990-2019: results from the Global Burden of Disease Study 2019. *J. Thorac. Dis.* 15 (2), 348–364. doi:10.21037/jtd-22-856

Kang, S., Wang, X., Pan, Z., and Liu, H. (2024). Cost-effectiveness analysis of toripalimab plus chemotherapy for patients with advanced esophageal squamous cell carcinoma in China. *Expert Rev. Pharmacoecon Outcomes Res.* 24 (2), 285–292. doi:10.1080/14737167.2023.2270159

Li, J., Chen, Z., Bai, Y., Liu, B., Li, Q., Zhang, J., et al. (2024). First-line sugemalimab with chemotherapy for advanced esophageal squamous cell carcinoma: a randomized phase 3 study. *Nat. Med.* 30, 740–748. doi:10.1038/s41591-024-02797-y

Li, L., Liu, X., Huang, J., Liu, Y., Huang, L., and Feng, Y. (2022a). Cost-effectiveness of camrelizumab versus chemotherapy for the treatment of advanced or metastatic esophageal squamous cell carcinoma. *J. Gastrointest. Oncol.* 13 (1), 40–48. doi:10.21037/jgo-21-870

Li, Y., Xu, J., Gu, Y., Sun, X., Dong, H., and Chen, C. (2022b). The disease and economic burdens of esophageal cancer in China from 2013 to 2030: dynamic cohort modeling study. *JMIR Public Health Surveill.* 8 (3), e33191. doi:10.2196/33191

Liu, G., Hu, S., Wu, J., Wu, J., Yang, L., Li, H., et al. (2020). *The China Guidelines for phaumacoeconomiç evaluation*. 2020 English Edition. Beijing,China: China Market Press.

Liu, G. G., Wu, J., He, X., and Jiang, Y. (2022). Policy updates on access to and affordability of innovative medicines in China. *Value Health Reg. issues.* 30, 59–66. doi:10.1016/j.vhri.2021.12.003

Liu, S., Dou, L., and Li, S. (2023a). Cost-effectiveness analysis of PD-1 inhibitors combined with chemotherapy as first-line therapy for advanced esophageal squamous-cell carcinoma in China. *Front. Pharmacol.* 14, 1055727. doi:10.3389/fphar.2023.1055727

Liu, S., Dou, L., and Li, S. (2024). Immune checkpoint inhibitors versus chemotherapy as second-line therapy for advanced oesophageal squamous cell carcinoma: a systematic review and economic evaluation. *Ther. Adv. Gastroenterol.* 17, 17562848241233134. doi:10.1177/17562848241233134

Liu, S., Jiang, N., Dou, L., and Li, S. (2023b). Cost-effectiveness analysis of serplulimab plus chemotherapy in the first-line treatment for PD-L1-positive esophageal squamous cell carcinoma in China. *Front. Immunol.* 14, 1172242. doi:10.3389/fimmu.2023.1172242

Mingge, X., Jingyu, W., Qi, L., Zhe, Z., and Qing, R. (2023). Promoting access to innovative anticancer medicines: a review of drug price and national reimbursement negotiation in China. *Inquiry* 60, 469580231170729. doi:10.1177/00469580231170729

Morgan, E., Soerjomataram, I., Rumgay, H., Coleman, H. G., Thrift, A. P., Vignat, J., et al. (2022). The global landscape of esophageal squamous cell carcinoma and esophageal adenocarcinoma incidence and mortality in 2020 and projections to 2040: new estimates from GLOBOCAN 2020. *Gastroenterology* 163 (3), 649–658.e2. doi:10.1053/j.gastro.2022.05.054

National Bureau of Statistics of China (2023). *National Bureau of statistics of China*. Available at: https://data.stats.gov.cn/english/(Accessed March 28, 2024).

National Data (2023). *National Bureau of Statistics of China*. Available at: https://data.stats.gov.cn/english/easyquery.htm?cn=C01 (Accessed March 28, 2024).

Rodriguez, M. I., and Caughey, A. B. (2013). Cost-effectiveness analyses and their role in improving healthcare strategies. *Curr. Opin. Obstet. Gynecol.* 25 (6), 487–493. doi:10.1097/GCO.0000000000000020

Si, L., Xu, L., Chen, M., and Jan, S. (2020). Using strategic price negotiations to contain costs and expand access to medicines in China. *BMJ Glob. Health* 5 (1), e002256. doi:10.1136/bmjgh-2019-002256

Sun, J. M., Shen, L., Shah, M. A., Enzinger, P., Adenis, A., Doi, T., et al. (2021). Pembrolizumab plus chemotherapy versus chemotherapy alone for first-line treatment of advanced oesophageal cancer (KEYNOTE-590): a randomised, placebo-controlled, phase 3 study. *Lancet* 398 (10302), 759–771. doi:10.1016/S0140-6736(21)01234-4

Tang, M., Song, P., and He, J. (2020). Progress on drug pricing negotiations in China. *Biosci. Trends* 13 (6), 464–468. doi:10.5582/bst.2019.01339

Thuss-Patience, P., and Stein, A. (2022). Immunotherapy in squamous cell cancer of the esophagus. *Curr. Oncol.* 29 (4), 2461–2471. doi:10.3390/curroncol29040200

Turner, H. C., Archer, R. A., Downey, L. E., Isaranuwatchai, W., Chalkidou, K., Jit, M., et al. (2021). An introduction to the main types of economic evaluations used for informing priority setting and resource allocation in healthcare: key features, uses, and limitations. *Front. Public Health* 9, 722927. doi:10.3389/fpubh.2021.722927

Wu, Y. X., Zhou, X. Y., Wang, J. Q., Chen, G. M., Chen, J. X., Wang, R. C., et al. (2023). Application of immune checkpoint inhibitors in immunotherapy for gastric cancer. *Immunotherapy* 15 (2), 101–115. doi:10.2217/imt-2022-0080

Yajima, S., Suzuki, T., Nanami, T., Oshima, Y., Kikuchi, Y., Funahashi, K., et al. (2021). Randomized phase II study to comparing docetaxel/nedaplatin versus docetaxel for 5-fluorouracil/cisplatin resistant esophageal squamous cell carcinoma. *Ann. Thorac. Cardiovasc Surg.* 27 (4), 219–224. doi:10.5761/atcs.oa.20-00294

Yang, F., Fu, Y., Kumar, A., Chen, M., Si, L., and Rojanasarot, S. (2021). Cost-effectiveness analysis of camrelizumab in the second-line treatment for advanced or metastatic esophageal squamous cell carcinoma in China. *Ann. Transl. Med.* 9 (15), 1226. doi:10.21037/atm-21-1803

YaoZH (2024). *Drug Pice*. Available at: https://data.yaozh.com/(Accessed March 28, 2024).

Zhang, Y., Naci, H., Wagner, A. K., Xu, Z., Yang, Y., Zhu, J., et al. (2022a). Overall survival benefits of cancer drugs approved in China from 2005 to 2020. *JAMA Netw. Open* 5 (8), e2225973. doi:10.1001/jamanetworkopen.2022.25973

Zhang, Y., Wei, Y., Li, H., Chen, Y., Guo, Y., Han, S., et al. (2022b). Prices and clinical benefit of national price-negotiated anticancer medicines in China. *Pharmacoeconomics* 40 (7), 715–724. doi:10.1007/s40273-022-01161-7

Zheng, Z., Chen, H., Cai, H., and Zhu, H. (2024). First-line tislelizumab for advanced or metastatic esophageal squamous cell carcinoma:A cost-effectiveness analysis. *Expert Rev. Pharmacoecon Outcomes Res.* 24 (3), 397–404. doi:10.1080/14737167.2023.2290609

Zheng, Z., Fang, L., Cai, H., and Zhu, H. (2023a). Cost-effectiveness analysis of serplulimab as first-line treatment for advanced esophageal squamous cell carcinoma. *Immunotherapy* 15 (13), 1045–1055. doi:10.2217/imt-2023-0059

Zheng, Z., Fang, L., Cai, H., and Zhu, H. (2023b). Economic evaluation of toripalimab plus chemotherapy compared with chemotherapy as first-line treatment for advanced esophageal squamous cell carcinoma in China. *Expert Rev. Pharmacoecon Outcomes Res.* 23 (6), 683–690. doi:10.1080/14737167.2023.2206570

Zheng, Z., Lin, J., Zhu, H., and Cai, H. (2022). Cost-effectiveness analysis of pembrolizumab plus chemotherapy vs. Chemotherapy alone as first-line treatment in patients with esophageal squamous cell carcinoma and PD-L1 CPS of 10 or more. *Front. Public Health* 10, 893387. doi:10.3389/fpubh.2022.893387

Zhu, H., Ma, X., Ye, T., Wang, H., Wang, Z., Liu, Q., et al. (2023). Esophageal cancer in China: practice and research in the new era. *Int. J. Cancer* 152 (9), 1741–1751. doi:10.1002/ijc.34301

frontiers | Frontiers in Pharmacology

TYPE Original Research
PUBLISHED 28 June 2024
DOI 10.3389/fphar.2024.1424175

Check for updates

OPEN ACCESS

EDITED BY
Wagdy Mohamed Eldehna,
Kafrelsheikh University, Egypt

REVIEWED BY
Ahmed A. Al-Karmalawy,
Ahram Canadian University, Egypt
Hatem A. Abdel-Aziz,
National Research Center, Egypt

*CORRESPONDENCE
Anas Shamsi,
anas.shamsi18@gmail.com

RECEIVED 27 April 2024
ACCEPTED 05 June 2024
PUBLISHED 28 June 2024

CITATION
Shamsi A, Khan MS, Yadav DK and Shahwan M (2024), Structure-based screening of FDA-approved drugs identifies potential histone deacetylase 3 repurposed inhibitor: molecular docking and molecular dynamic simulation approaches.
Front. Pharmacol. 15:1424175.
doi: 10.3389/fphar.2024.1424175

COPYRIGHT
© 2024 Shamsi, Khan, Yadav and Shahwan. This is an open-access article distributed under the terms of the Creative Commons Attribution License (CC BY). The use, distribution or reproduction in other forums is permitted, provided the original author(s) and the copyright owner(s) are credited and that the original publication in this journal is cited, in accordance with accepted academic practice. No use, distribution or reproduction is permitted which does not comply with these terms.

Structure-based screening of FDA-approved drugs identifies potential histone deacetylase 3 repurposed inhibitor: molecular docking and molecular dynamic simulation approaches

Anas Shamsi [1]*, Mohd Shahnawaz Khan [2], Dharmendra Kumar Yadav [3] and Moyad Shahwan [1,4]

[1]Center for Medical and Bio-Allied Health Sciences Research, Ajman University, Ajman, United Arab Emirates, [2]Department of Biochemistry, College of Science, King Saud University, Riyadh, Saudi Arabia, [3]Department of Pharmacy, College of Pharmacy, Gachon Institute of Pharmaceutical Science, Gachon University, Incheon, Republic of Korea, [4]Department of Clinical Sciences, College of Pharmacy and Health Sciences, Ajman University, Ajman, United Arab Emirates

Histone deacetylase 3 (HDAC3) is a member of the histone deacetylase family that has emerged as a crucial target in the quest for novel therapeutic interventions against various complex diseases, including cancer. The repositioning of FDA-approved drugs presents a promising avenue for the rapid discovery of potential HDAC3 inhibitors. In this study, we performed a structure-based virtual screening of FDA-approved drugs obtained from DrugBank. Candidate hits were selected based on their binding affinities and interactions with HDAC3. These promising hits were then subjected to a comprehensive assessment of their biological properties and drug profiles. Our investigation identified two FDA-approved drugs, Imatinib and Carpipramine, characterized by their exceptional affinity and specificity for the binding pocket of HDAC3. These molecules demonstrated a strong preference for HDAC3 binding site and formed interactions with functionally significant residues within the active site pocket. To gain deeper insights into the binding dynamics, structural stability, and interaction mechanisms, we performed molecular dynamics (MD) simulations spanning 300 nanoseconds (ns). The results of MD simulations indicated that Imatinib and Carpipramine stabilized the structure of HDAC3 and induced fewer conformational changes. Taken together, the findings from this study suggest that Imatinib and Carpipramine may offer significant therapeutic potential for treating complex diseases, especially cancer.

KEYWORDS

histone deacetylase 3, FDA approved drugs, imatinib, carpipramine, virtual screening, molecular dynamic (MD) simulations

1 Introduction

Epigenetics has emerged as a critical field in understanding the regulation of gene expression and its role in health and disease (Zhang et al., 2020). One of the primary mechanisms in epigenetics is histone modification, which encompasses acetylation and deacetylation processes (Daskalaki et al., 2018). The addition and removal of acetyl groups on histone proteins are dynamically regulated by histone acetyltransferases (HATs) and histone deacetylases (HDACs), respectively (Lee and Grant, 2019). These modifications have a profound impact on chromatin structure, influencing the accessibility of DNA to transcription factors and RNA polymerase, thereby governing gene expression (Venkatesh and Workman, 2015). Histone deacetylase 3 (HDAC3) is a pivotal regulator of gene expression and chromatin structure that plays a central role in epigenetic modifications (Chen et al., 2015). It is crucially involved in various cellular processes, such as cell cycle control, differentiation, and apoptosis, underscores its significance in health and disease (Sarkar et al., 2020). Dysregulation of HDAC3 activity has been implicated in several complex diseases, making it an attractive target for therapeutic intervention (Sarkar et al., 2020). In recent years, there has been a surge of interest in developing HDAC3 inhibitors as potential therapeutic agents (Amin et al., 2019; Sarkar et al., 2020).

One notable area of application for HDAC3 inhibitors is anticancer therapy (Hu et al., 2019). However, achieving selectivity and specificity for HDAC3 over other HDAC isoforms is a critical challenge (Cheshmazar et al., 2022). The existence of multiple HDAC isoforms with distinct functions necessitates the design of molecules that target HDAC3 without affecting other isoforms, to avoid potential off-target effects. Various FDA-approved drugs, such as Imatinib and Carpipramine have great potential to be explored as repurposed molecules against HDAC3-associated diseases. Imatinib is a tyrosine kinase inhibitor initially developed for chronic myeloid leukemia (CML) and later extended to gastrointestinal stromal tumors (GIST) (Joensuu and Dimitrijevic, 2001; Demetri, 2002). It widely exhibits promising potential beyond its original indications that showcases efficacy in various therapeutic areas (Stegmeier et al., 2010). Carpipramine is a tricyclic antipsychotic primarily used for schizophrenia, and holds promise for repurposing in cancer treatment, although its application in this context remains largely unexplored (Kishi et al., 2014).

In the realm of drug discovery, the repositioning of existing FDA-approved drugs offers an attractive strategy for expediting the development of new therapies (Cha et al., 2018). This approach leverages the extensive knowledge of these molecules, including their safety profiles, pharmacokinetics, and mechanisms of action, to identify novel indications and therapeutic targets (Pushpakom et al., 2019). The advantages of drug repositioning are manifold (Hodos et al., 2016). Firstly, the drug development process is accelerated, as many aspects of preclinical and early clinical testing have already been conducted. Secondly, the safety and tolerability profiles of these drugs have been established, reducing the risk associated with novel molecules. Finally, the cost and resources required for repositioning are often significantly lower than those for *de novo* drug development (Cha et al., 2018). In the context of HDAC3 inhibition, the repositioning of FDA-approved drugs presents a rational and efficient approach. By screening these molecules for their potential to interact with HDAC3 and modulate its activity, we can identify promising candidates for further development as HDAC3 inhibitors. This approach aligns with the broader strategy of precision medicine, as it seeks to target specific molecular pathways associated with diseases while minimizing potential side effects.

The primary objective of this study is to perform structure-based virtual screening of FDA-approved drugs sourced from DrugBank (Wishart et al., 2018), with a focus on identifying molecules that can serve as potential HDAC3 inhibitors. We have employed a multi-step approach, including molecular docking and molecular dynamics (MD) simulations, to select and characterize the candidate molecules. Ultimately, we aim to identify and characterize FDA-approved drugs with the potential to serve as lead candidates for the development of HDAC3 inhibitors. These inhibitors might have the potential to play a pivotal role in the treatment of complex diseases, with a particular focus on cancer. The implications of HDAC3 inhibition extend beyond cancer therapy, encompassing a wide range of complex diseases. Epigenetic modifications have been implicated in neurodegenerative disorders (Kwon et al., 2016), metabolic syndromes (Carson and Lawson, 2018), and autoimmune diseases (Ramming et al., 2014), among others (Duthie, 2011). Overall, this study embarks on a journey to explore the potential of repositioning FDA-approved drugs as HDAC3 inhibitors, addressing the pressing need for novel therapeutic strategies in the battle against complex diseases, with a particular emphasis on cancer. The outcomes of this study may hold transformative implications for the treatment of complex diseases, opening doors to more precise and personalized therapeutic interventions.

2 Materials and methods

2.1 Computational tools and web servers

This study was executed on an HP® Z840, a tower workstation configured for dual-boot functionality with Windows 11 and Ubuntu LTS, boasting 128 GB of RAM, 48 GB of dedicated GPU memory, and a spacious 2 TB SSD. Throughout the study, a reliable power source ensured uninterrupted operation, complemented by high-speed internet connectivity. A variety of bioinformatics software and online resources were employed for data analysis, molecular docking, visualization, and MD simulations. To perform molecular docking, we utilized well-established bioinformatics software, including MGL Tools (Huey et al., 2012), AutoDock Vina (Trott and Olson, 2010), and Discovery Studio (Biovia, 2017). These tools facilitated the reasonable prediction of ligand-receptor interactions. For the visualization and in-depth analysis of molecular structures and interactions, PyMOL (DeLano, 2002)and VMD: Visual Molecular Dynamics (Humphrey et al., 1996) were instrumental. These software tools allowed us to gain insights into the binding modes and structural dynamics of the complexes. Additionally, QtGrace (Turner, 2005) was employed for data visualization and presentation. GROMACS (Van Der Spoel et al., 2005) was employed to conduct all-atom simulations. This software enabled us to explore the conformational changes, stability, and

interaction dynamics of HDAC3 in complexes with the identified molecules over an extended period. Several valuable online resources were consulted throughout the study. The Protein Data Bank served as a crucial source for retrieving the HDAC3 structure. Additionally, DrugBank played a pivotal role in providing essential drug-related information for the evaluation and analysis of the data.

2.2 Retrieval and processing of HDAC3 structure and FDA-approved drugs

The atomic coordinates for the crystal structure of HDAC3 (PDB ID: 4A69) (Watson et al., 2012) were sourced from the Protein Data Bank (Berman et al., 2000). In preparation for virtual screening, we removed all co-crystallized ligands and associated crystal water molecules from the parent structure. These co-crystallized ligands and associated crystal water molecules were removed to ensure that the binding affinity of the screened drugs was not influenced by pre-bound molecules. The resultant HDAC3 structure was refined and prepared for subsequent analysis. To ensure the protein reaches its most stable conformational state, the structure was subjected to energy minimization after ligand removal. To facilitate this process, MGL Tools, a versatile suite of software tools, was employed. Simultaneously, we obtained a diverse library of 3,648 FDA-approved drugs from DrugBank in the PDBQT file format. This library encompassed the three-dimensional representations of these pharmaceutical molecules, which were essential for our structure-based virtual screening analysis. The inclusion of the HDAC3 structure and this comprehensive library of FDA-approved drugs was fundamental to our investigation, enabling precise molecular docking and the subsequent evaluation of potential HDAC3 inhibitors among these molecules.

2.3 Molecular docking

Molecular docking approach was conducted to assess the binding affinity of molecules towards HDAC3. AutoDock Vina within the PyRx platform (Dallakyan and Olson, 2015) was used for the docking screening. This approach allowed us to evaluate the interactions between HDAC3 and the FDA-approved drugs. For the molecular docking procedure, a structurally blind approach was implemented, ensuring that all molecules were assessed without bias. The docking grid dimensions were set to 67, 67, and 73 Å, while the center coordinates for X, Y, and Z were specified as 42.751, 52.009, and 19.418, respectively. A grid spacing of 1 Å and an exhaustiveness parameter of eight were chosen to ensure thorough exploration of the binding conformations and to maximize the accuracy of the binding affinity predictions.

2.4 Selection of hits

The initial selection of potential hits was a meticulous process driven by their binding affinities and interactions with HDAC3. We prioritized molecules that exhibited higher binding affinities for HDAC3. This step allowed us to identify candidates with a strong potential to modulate HDAC3 activity. To comprehensively assess the interactions, all possible conformers of the selected molecules were generated. We performed this step using Discovery Studio, a versatile tool for molecular analysis and visualization. Subsequently, we conducted a detailed interaction analysis of all the docked conformers. This step enabled us to identify selective molecules that interacted effectively with the binding pocket of HDAC3. In the final stage of selection, we exclusively chose molecules that demonstrated interactions with functionally significant binding-site residues of HDAC3. This stringent criterion ensured that the selected hits had the potential to influence the critical regulatory aspects of HDAC3. Through this approach, we pinpointed a subset of molecules that exhibited strong binding affinities and engaged with functionally relevant residues in the HDAC3 binding site. These molecules emerged as the most promising candidates for further investigation and development as potential HDAC3 inhibitors.

2.5 Molecular dynamics simulations

All-atom MD simulations play a crucial role in drug discovery, particularly in understanding the dynamic behavior of proteins and their interactions with ligands (Shukla and Tripathi, 2020). For an in-depth exploration of the protein and protein-ligand complexes, MD simulations were conducted. These simulations spanned a duration of 300 ns and involved both the free-HDAC3 and HDAC3 complexed with the identified molecules, Imatinib and Carpipramine. The simulations were performed at a constant temperature of 300 K with the charmm36-jul2022 force field (Huang and MacKerell, 2013). GROMACS version 5.1.2 served as the primary software tool for this purpose. All systems, including free-HDAC3 and HDAC3 in complex with Imatinib and Carpipramine, were immersed in a cubic box of water with dimensions of 10 Å. The solvation was achieved using the TIP3P model (Mark and Nilsson, 2001) through the *gmx solvate* module. Prior to the simulations, an energy minimization step was executed to remove unfavorable interactions. This involved 1,500 steps of steepest descent energy minimization to optimize the system's stability. A controlled temperature ramp-up was implemented during the equilibration phase, transitioning the system from 0 K to the target temperature of 300 K. This was performed over a 1 ns period, maintaining constant volume and utilizing periodic boundary conditions. Post-simulation, the resulting trajectories were analyzed using various utilities available within GROMACS (Van Der Spoel et al., 2005). These analyses allowed us to gain a comprehensive understanding of the system's behavior and interactions. All graphs and figures, illustrating the outcomes of the MD simulations, were prepared using QtGrace, enhancing the clarity and presentation of the results. A comprehensive and detailed description of the MD simulation procedures and parameters can be found in our recent publications (Mohammad et al., 2020; Shamsi et al., 2021).

3 Result and discussion

3.1 Molecular docking: binding affinity with HDAC3

Molecular docking plays a crucial role in understanding the interactions between drugs and their target proteins at the molecular

TABLE 1 Selected hits and their docking score with HDAC3.

S. No.	Drug	Binding Energy (kcal/mol)	Ligand Efficiency (kcal/mol/non-H atom)	Torsional Energy
1	Picloxydine	−9.5	0.2969	0.6226
2	Aprepitant	−9.0	0.2432	2.4904
3	Conivaptan	−8.9	0.2342	1.2452
4	Eltrombopag	−8.7	0.2636	2.1791
5	Dutasteride	−8.6	0.2324	1.2452
6	Penfluridol	−8.6	0.2389	2.8017
7	Deptropine	−8.5	0.34	0.6226
8	Imatinib	−8.5	0.2297	2.1791
9	Tadalafil	−8.4	0.2897	0.3113
10	Carpipramine	−8.3	0.2515	1.8678
11	RGFP966	−7.5	0.2778	2.1791

level (Singh et al., 2022). Here, we refined the results from an initial pool of 3,648 molecules, strategically narrowing down the selection to the top 10 hits. We have selected the top 10 hits from the pool of 3,648 molecules based on their binding affinity. This results in the identification of compounds with binding affinity within the range of −8.3 kcal/mol to −9.5 kcal/mol (Table 1). Notably, all these selected FDA-approved drugs exhibited a binding affinity surpassing that of the reference HDAC3 inhibitor, RGFP966 (Zhang et al., 2021). RGFP966 is a widely explored compound that acts as a selective inhibitor of HDAC3 (Leus et al., 2016; Zhang et al., 2021; Sun et al., 2022). This finding strongly indicates the potential of these hit molecules as promising candidates for the development of HDAC3 inhibitors. The superior binding affinity displayed by these molecules underscores their efficacy in interacting with HDAC3, suggesting a high likelihood of successful inhibition. This outcome holds significant promise for advancing our understanding of HDAC3 inhibition and provides a foundation for further exploration and development of novel therapeutic interventions.

3.2 Interaction analysis with HDAC3

Protein-ligand interaction analysis is a critical component of drug discovery that provides valuable insights into the molecular mechanisms underlying the efficacy and specificity of potential drug candidates (Du et al., 2016). To gain a comprehensive understanding of the interactions between selected 10 molecules and HDAC3, we conducted a thorough analysis employing Discovery Studio. A total of 90 docked conformers, derived from the output files of these 10 molecules, were generated for analysis. Each conformer was examined for its interactions with HDAC3. During this analysis, we observed that several docked conformations of these molecules exhibited direct and specific interactions within the binding pocket of HDAC3. These interactions were of particular interest, as they indicated the potential of these molecules to modulate the activity of HDAC3. Following the analysis, we have identified two FDA-approved drugs, Imatinib and Carpipramine, which consistently exhibited significant interactions with crucial binding-site residues of HDAC3 (Figure 1). Both molecules were observed to bind in close proximity to the active site residue His135 of the binding site, displaying shared interactions with the reference inhibitor RGFP966 (Figure 1A). Notably, these molecules formed multiple hydrogen bonds with essential residues within the binding pocket (Figure 1B–D). HDACs are metalloenzymes that require metal ions, such as Zn^{2+}, for catalytic activity (Nechay et al., 2016). Their metal-binding sites are crucial for guiding inhibitor design to achieve improved isozyme selectivity over promiscuous metal-chelating agents. Imatinib and Carpipramine bind at the metal-binding site on HDAC3, where the co-crystallized Zn^{2+} is located (Figure 1B, C) (Watson et al., 2012). Importantly, all three molecules demonstrated a commendable complementarity fit while effectively obstructing the binding site. The insights gained from this comprehensive interaction analysis shed light on the potential mechanisms through which Imatinib and Carpipramine may impact the functionality of HDAC3. This reinforces their viability as promising candidates for HDAC3 inhibitors, underlining their potential therapeutic significance.

Further, we conducted an in-depth analysis of the protein-ligand interactions between HDAC3 and the Imatinib and Carpipramine. The examination focused on their interactions with crucial binding-site residues of HDAC3, with particular attention to their comparison with the reference inhibitor RGFP966. Both Imatinib and Carpipramine demonstrated substantial interactions with key binding-site residues of HDAC3, suggesting a potential for therapeutic relevance. Notably, both molecules exhibited shared interactions with the reference inhibitor RGFP966, indicating their ability to engage the target site in a manner similar to the established inhibitor (Figure 2). Moreover, both molecules formed multiple hydrogen bonds and other interactions with essential residues within the binding pocket, highlighting their strong binding affinity. Specifically, Imatinib displayed a noteworthy interaction with Asp92 and Tyr198, forming two hydrogen bonds (Figure 2A). On the other hand, Carpipramine exhibited an even more extensive interaction profile, establishing four hydrogen bonds with Asp92, Asp93, and Phe200 (Figure 2B). When comparing the interactions of Imatinib and Carpipramine with the reference inhibitor RGFP966, it was observed that both molecules shared a common hydrogen bond with Asp92 (Figure 2C). RGFP966 formed three hydrogen bonds with His22, Gly91, and Asp92, emphasizing its crucial role in the binding pocket. The shared interaction with Asp92 between the investigated molecules and the reference inhibitor is particularly significant in the context of drug discovery projects. This suggests that both Imatinib and Carpipramine possess a binding profile that aligns with the established inhibitor, potentially making them promising candidates for further development.

3.3 Molecular dynamics simulations

3.3.1 Structural deviations and compactness

The binding of small molecules within a protein's binding pocket can induce significant conformational changes (Mobley and Dill, 2009). One of the fundamental metrics used to assess

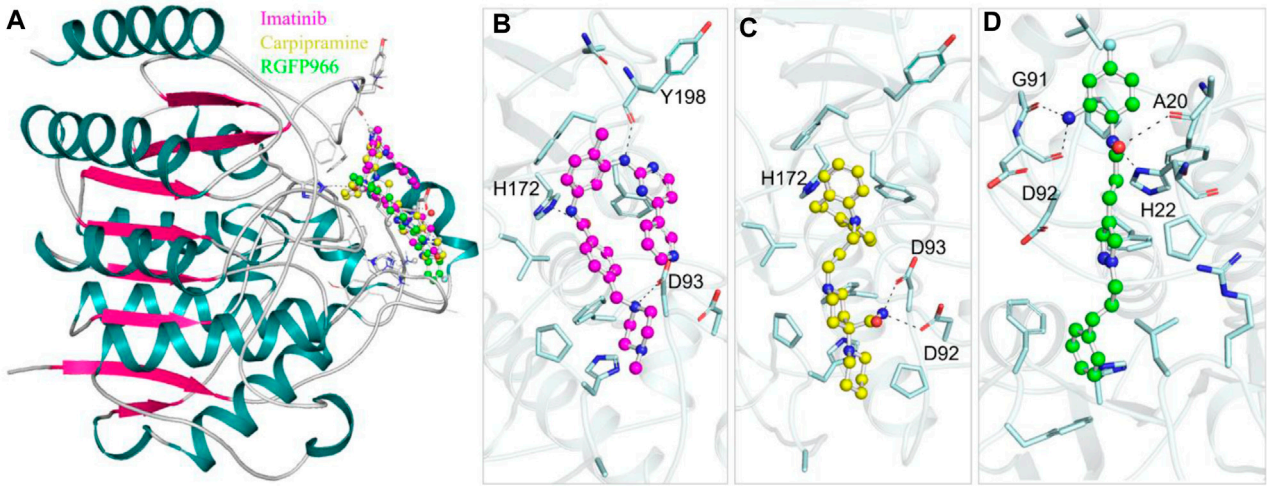

FIGURE 1
Protein-ligand interactions. **(A)** Cartoon representation showing the docked molecules in the binding pocket of HDAC3. **(B)** Imatinib, **(C)** Carpipramine, and **(D)** RGFP966 are shown in magnified view of HDAC3 binding site residues. Residues with polar interactions are labeled in black.

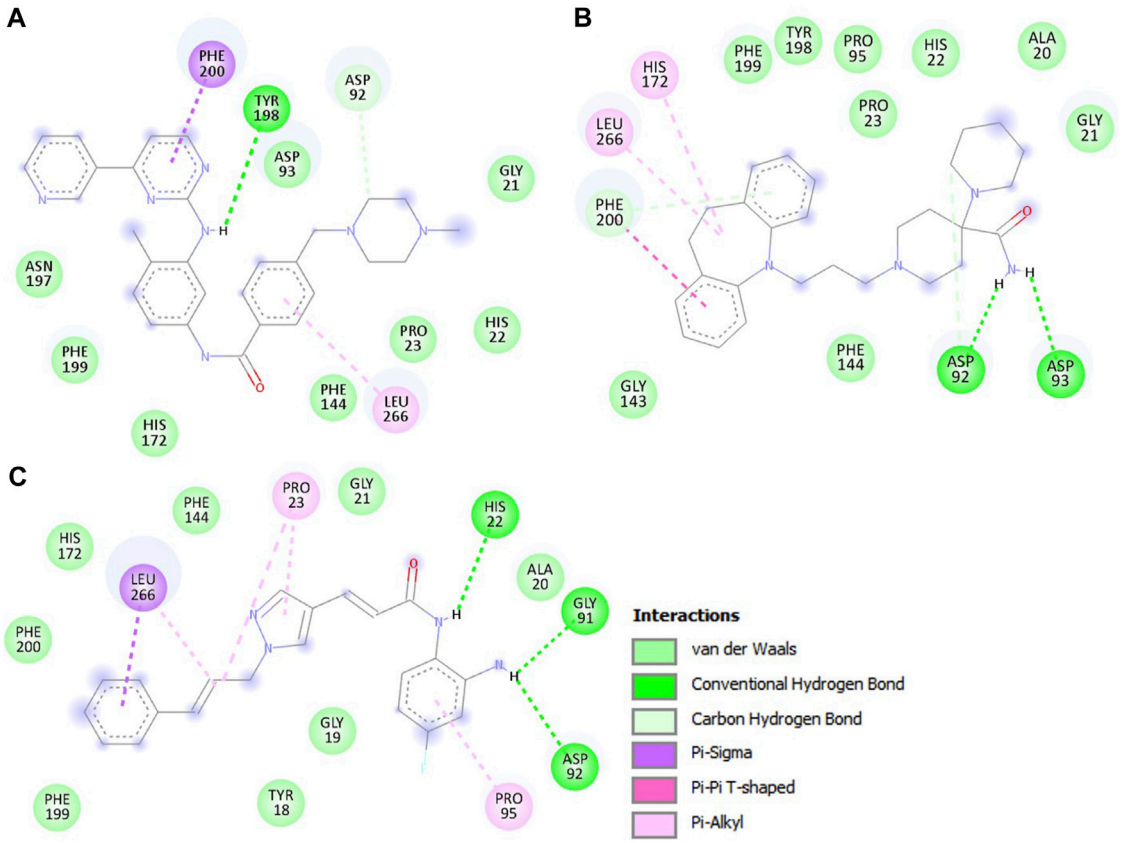

FIGURE 2
The detailed interactions between HDAC3 and the investigated molecules. **(A)** 2D structural representation HDAC3 residues interacting with Imatinib, **(B)** Carpipramine, and, **(C)** RGFP966.

these structural deviations and the overall stability of a protein is the root mean square deviation (RMSD) (Maruyama et al., 2023). In the simulation analysis, we observed average RMSD values for three distinct systems: free HDAC3, HDAC3-Imatinib, and HDAC3-Carpipramine complexes, which were found to be 0.37, 0.32, and 0.30 nm, respectively. A noteworthy observation in the RMSD plot is

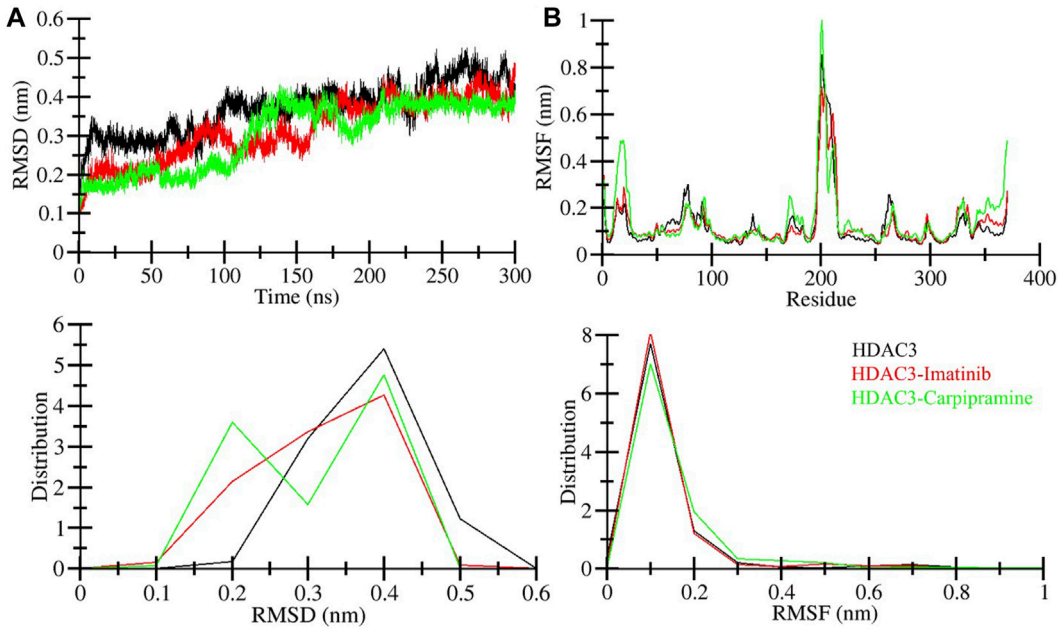

FIGURE 3
Structural dynamics of HDAC3 upon Imatinib and Carpipramine binding: **(A)** RMSD of HDAC3 in complex with Imatinib and Carpipramine. **(B)** Residual fluctuations (RMSF) of HDAC3 and upon Imatinib and Carpipramine binding. Black, red and green represent values obtained for free HDAC3, HDAC3-Imatinib and HDAC3-Carpipramine complexes, respectively.

a higher RMSD for free HDAC3 beyond the 120 ns mark. This deviation can be attributed to the increased flexibility of the loop of the HDAC3 structure. The RMSD plot provided valuable insights, demonstrating that the binding of both Imatinib and Carpipramine significantly stabilized HDAC3, resulting in fewer structural deviations from its native conformation (Figure 3A). Although some minor fluctuations were noted in the RMSD plot upon the binding of Imatinib and Carpipramine, these can be attributed to potential changes in the orientation of the molecules within the HDAC3 binding pocket. However, the binding of Imatinib and Carpipramine displayed consistently lower RMSD values in several regions, indicating equilibration throughout the simulation and the stability of HDAC3 (Figure 3A). This pattern can also be observed in the probability distribution function of the data (Figure 3A, lower panel).

To gain further insights into the local structural flexibility, we examined the root-mean-square fluctuation (RMSF) of individual residues in HDAC3 both in its native form and upon binding with Imatinib and Carpipramine. The RMSF plot revealed residual fluctuations in several regions of the protein structure. However, the binding of Imatinib and Carpipramine led to a noticeable reduction in these residual fluctuations throughout the simulation, particularly in the region spanning from the N-terminal to the C-terminal (Figure 3B). These observations suggest that the binding of Imatinib and Carpipramine stabilizes the overall structure of HDAC3 and minimizes local structural fluctuations, particularly in regions crucial for HDAC3 function. This enhanced structural stability is indicative of the potential therapeutic efficacy of these molecules as HDAC3 binders. To further support this observation, the probability distribution function of the data was examined (Figure 3B, lower panel). Consistent with the RMSF analysis, this distribution function corroborates the trend of reduced structural fluctuations in the presence of Imatinib and Carpipramine, providing additional evidence for the stabilizing effect of these molecules on HDAC3.

The radius of gyration (*Rg*) is a crucial metric directly associated with the tertiary structure volume and overall conformational shape of a protein (Lobanov et al., 2008). It provides valuable insights into the stability of a protein, with a higher *Rg* indicating less tight packing. We calculated the average *Rg* values for three systems: free HDAC3, HDAC3-Imatinib, and HDAC3-Carpipramine complexes. These values were determined to be 2.09, 2.08, and 2.07 nm, respectively. The *Rg* plot revealed no major changes in the packing of HDAC3 in the presence of Imatinib and Carpipramine. While some slight fluctuations were observed after the 40 ns mark in the MD trajectories, the *Rg* plot reached a stable equilibrium throughout the 300 ns simulation (Figure 4A). The consistency in the *Rg* plot indicated minimal structural deviation in HDAC3 upon the binding of Imatinib and Carpipramine. To further support this observation, the probability distribution function of the data was examined (Figure 4A, lower panel). Consistent with the *Rg* plot, the probability distribution function highlighted the reliability of the data, emphasizing the minimal structural deviation in HDAC3 when bound to Imatinib and Carpipramine.

The solvent accessible surface area (SASA) corresponds to the surface area of a protein that interacts with its environment (Marsh and Teichmann, 2011). We calculated the average SASA values for free HDAC3, HDAC3-Imatinib, and HDAC3-Carpipramine complexes throughout the 300 ns MD simulation. The calculated average SASA values were 173.80,

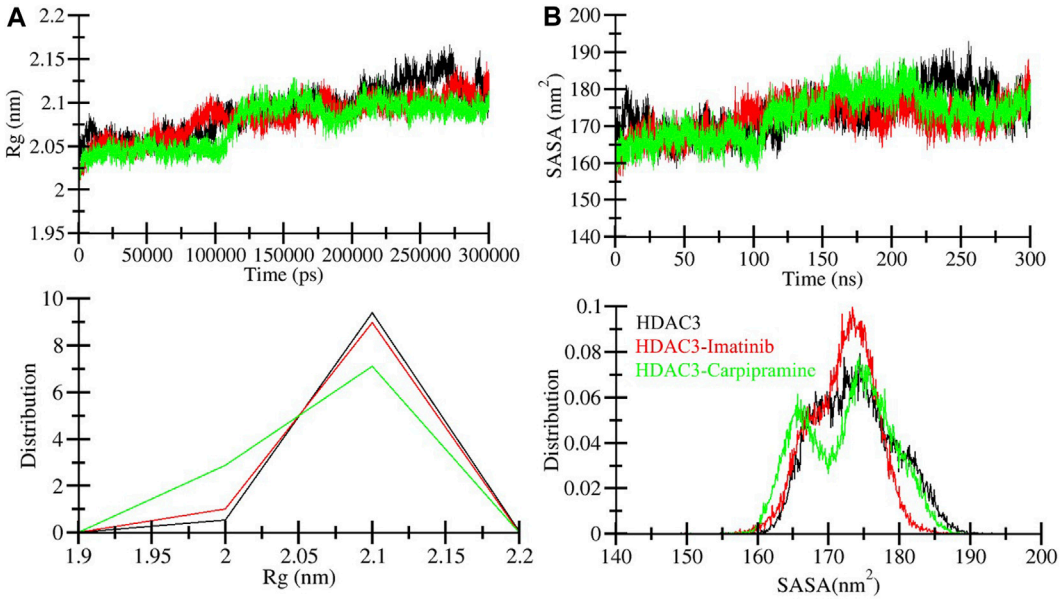

FIGURE 4
Compactness of HDAC3 upon Imatinib and Carpipramine binding: **(A)** Time evolution of radius of gyration (*Rg*). **(B)** SASA plot of HDAC3.

172.06, and 172.68 nm^2 for free HDAC3, HDAC3-Imatinib, and HDAC3-Carpipramine, respectively. Notably, there was a slight increment in SASA values, potentially due to the tighter packing of HDAC3 upon binding with Imatinib and Carpipramine (Figure 4B). This observation suggests that the binding of these molecules influenced the interactions between HDAC3 and its surrounding solvent. The modest change in SASA further supports the notion of enhanced stability and compactness of the HDAC3 structure when in complex with Imatinib and Carpipramine. Overall, the *R*g and SASA analyses reaffirm the structural stability and minimal conformational shifts within HDAC3 upon binding with Imatinib and Carpipramine, further highlighting their potential as HDAC3 inhibitors. To reinforce this observation, we analyzed the probability distribution function of the data (Figure 4B, lower panel). The congruence between the probability distribution function and the SASA plot underscores the trustworthiness of the data, highlighting the negligible structural deviation in HDAC3 when interacting with Imatinib and Carpipramine.

3.3.2 Dynamics of hydrogen bonds

Intramolecular hydrogen bonding plays a pivotal role in maintaining protein stability (Yunta, 2017). The analysis of intramolecular hydrogen bonds can provide valuable insights into the overall stability of protein structures. Additionally, intermolecular hydrogen bond analysis allows us to examine the polar interactions between a protein and a ligand, shedding light on the directionality and specificity of these interactions, a fundamental aspect of molecular recognition (Menéndez et al., 2016). In our pursuit to validate and assess the stability of HDAC3 in complex with Imatinib and Carpipramine, we delved into the dynamics of hydrogen bonds formed within a 0.35 nm distance during the simulation (Figure 5A). During the simulation, we calculated an average of hydrogen bonds within HDAC3 itself, revealing the following values: 255 for free HDAC3, 259 for HDAC3-Imatinib, and 262 for HDAC3-Carpipramine complexes (Figure 5B). These findings illuminate the stability of intramolecular hydrogen bonds within HDAC3 when it is complexed with Imatinib and Carpipramine.

In the context of intermolecular calculations, we focused on the number of hydrogen bonds formed between Imatinib and HDAC3, as well as Carpipramine and HDAC3. Throughout the simulation, an average of 2 hydrogen bonds were consistently observed in both the Imatinib-HDAC3 and Carpipramine-HDAC3 interactions. This analysis provides direct evidence of the specific interactions occurring between the molecules and HDAC3. The dynamics of hydrogen bonds further revealed that Imatinib and Carpipramine bind within the active pocket of HDAC3. During this interaction, they form between 3 and 4 hydrogen bonds with higher fluctuations and between 1 and 2 hydrogen bonds with more minor fluctuations (Figure 6). This observation aligns closely with our molecular docking findings, reinforcing the notion of strong and specific interactions between Imatinib and Carpipramine with HDAC3 (Figure 6A, B). The analysis of hydrogen bonds underscores the structural stability of HDAC3 and emphasizes the robust and specific binding of Imatinib and Carpipramine to the active site of HDAC3, further solidifying their potential as effective HDAC3 binders.

3.3.3 Secondary structure dynamics

To assess changes in the secondary structure of HDAC3 resulting from the binding of Imatinib and Carpipramine during the simulation, we calculated the structural content of HDAC3. This analysis focused on key secondary structure elements such as α-helix, β-sheet, and turn. For each

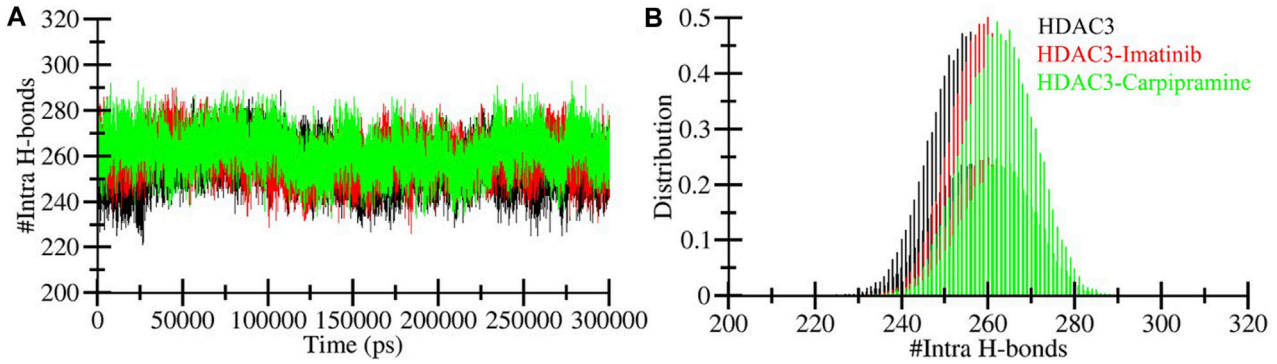

FIGURE 5
Time evolution of hydrogen bonds. **(A)** Intra-HDAC3 hydrogen bonds in HDAC3 and **(B)** their PDF values.

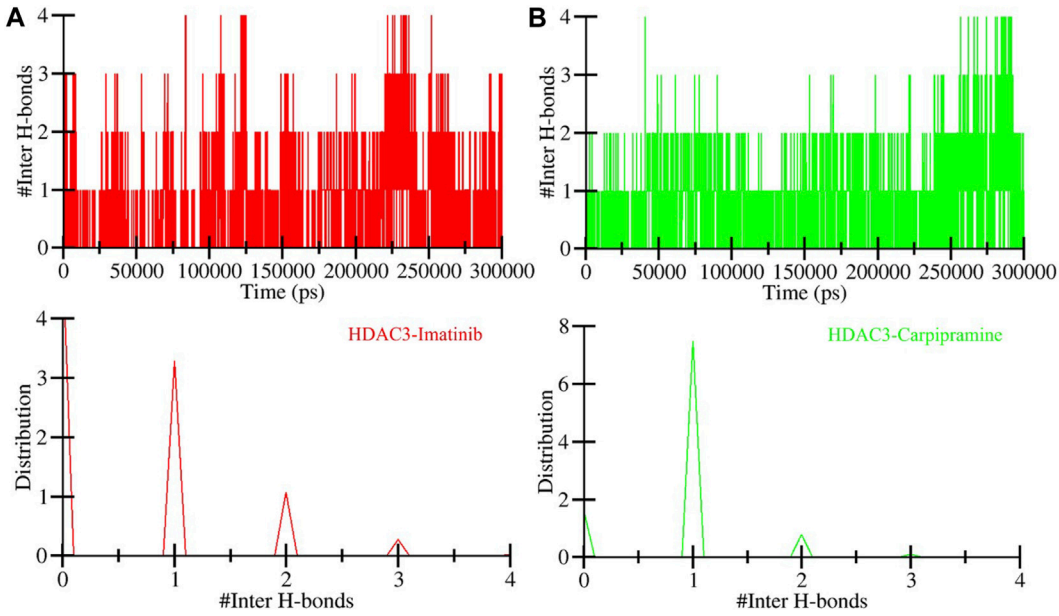

FIGURE 6
Time evolution of hydrogen bonds. **(A)** Intermolecular hydrogen bonds between Imatinib and HDAC3, and **(B)** Intermolecular hydrogen bonds formed between Carpipramine and HDAC3.

time step, we quantified the average number of residues participating in the formation of these secondary structure elements and plotted these values over time. The findings revealed that the secondary structure elements in HDAC3 remained remarkably constant and equilibrated throughout the entire simulation (Figure 7). No significant alterations were observed in the secondary structure content of HDAC3 upon the binding of Imatinib and Carpipramine (Figure 7B, C). This observation underlines the robust stability of the complexes and suggests that the structural integrity of HDAC3 is well-maintained during the interaction with these molecules. The preservation of secondary structure elements and minimal changes in their content further support the hypothesis that Imatinib and Carpipramine form stable complexes with HDAC3, emphasizing their potential as promising HDAC3 inhibitors.

3.4 Principal component analysis

Principal component analysis (PCA) serves as a valuable tool to explore the global motion of a protein, reducing this complexity to a few principal motions characterized by eigenvectors (Muller Stein et al., 2006). Here, we employed PCA to gain insights into the conformational dynamics of free HDAC3, as well as HDAC3 in complex with Imatinib and Carpipramine. The essential subspace of these complexes was analyzed, providing a visualization of the tertiary conformations along the first and second eigenvectors projected by the Cα atom (Figure 8). The analysis revealed that HDAC3 explores a broad range of phase spaces in the presence of Imatinib and Carpipramine, highlighting a cluster of stable states (Figure 8A). Importantly, this observation underscores that the protein maintains its overall conformational stability and that no substantial shifts or switching in the global

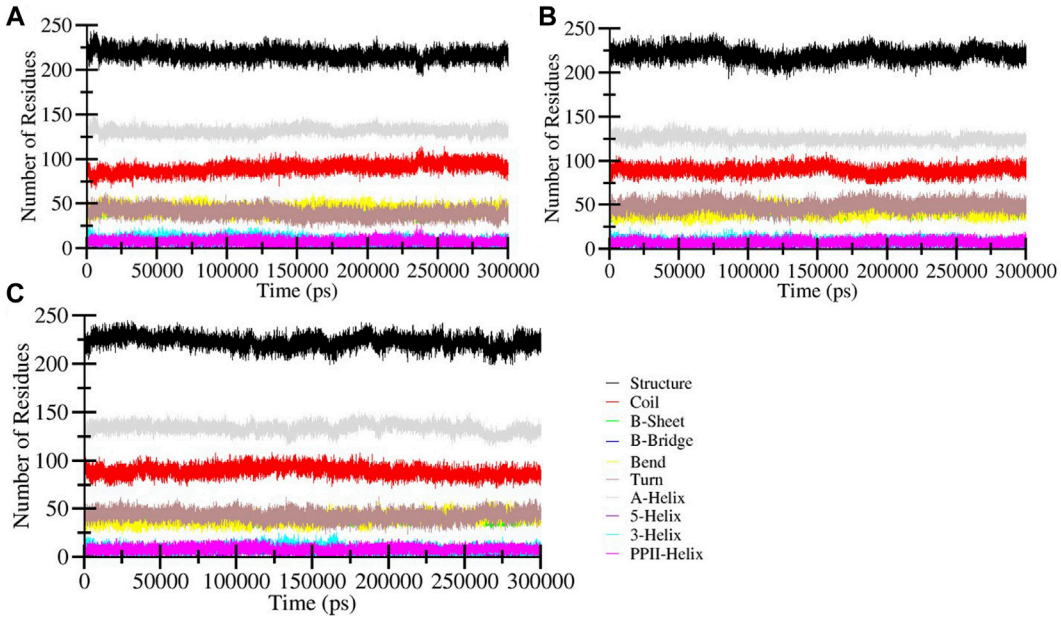

FIGURE 7
Secondary structure content of **(A)** Free HDAC3 and **(B)** HDAC3 upon Imatinib **(C)** Carpipramine binding. *Structure = α-helix + β-sheet + β-bridge + Turn.

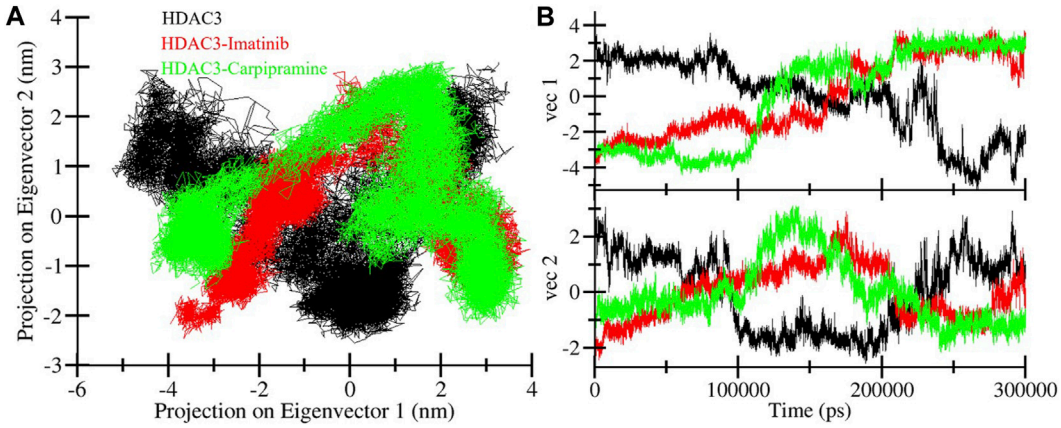

FIGURE 8
Principal component analysis. **(A)** 2D projections of trajectories showed different projections of HDAC3. **(B)** The time-evolution of the projection.

motion of HDAC3 were observed after the binding of Imatinib and Carpipramine (Figure 8B). These findings indicate that the binding of Imatinib and Carpipramine does not induce significant changes in the overall motion of HDAC3. The protein retains its stability while accommodating the presence of these molecules, which aligns with the earlier observations of structural and interaction stability.

3.5 Free energy landscape analysis

To delve deeper into the conformational behavior of the systems, we conducted an analysis of the Gibbs free energy landscapes (FELs) using the first two eigenvectors (Figure 9). The FELs provide critical insights into the energy landscapes of the different systems (Papaleo et al., 2009). As depicted in Figure 9A, the FEL of free HDAC3 revealed multiple stable global minima, primarily confined within 3 basins. However, a striking change in conformational behavior was observed when HDAC3 was in the presence of Imatinib and Carpipramine (Figure 9B, C). The FELs for these complexes displayed a progression to multiple energy minima, signifying the acquisition of numerous stable states by HDAC3. These multiple energy minima suggest a stable and diverse conformational landscape in the presence of Imatinib and Carpipramine, indicative of the impact of these molecules on the conformational folding of HDAC3. The alteration in the FELs emphasizes the considerable influence of Imatinib and Carpipramine on the conformational dynamics of HDAC3, further underlining their potential as modulators of HDAC3 behavior.

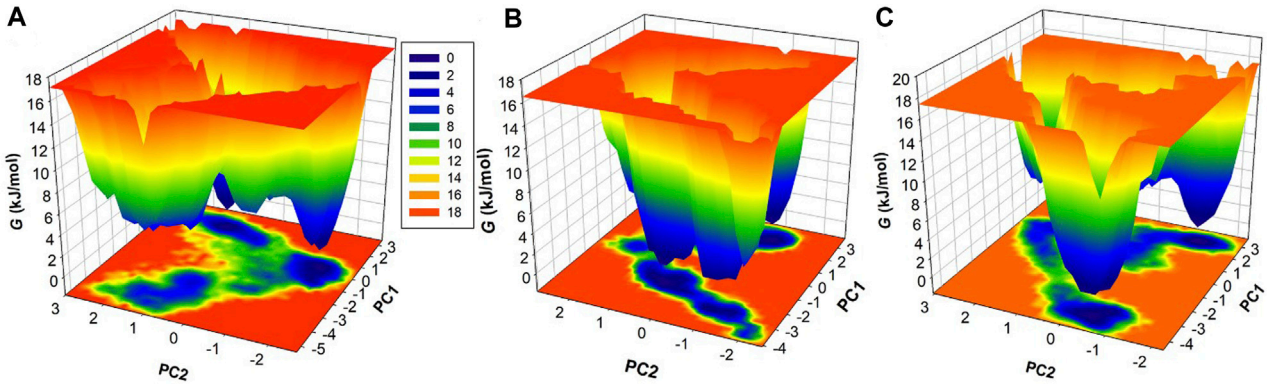

FIGURE 9
The free energy landscapes obtained for **(A)** HDAC3, **(B)** HDAC3-Imatinib, and **(C)** HDAC3-Carpipramine.

4 Conclusion

In this study, we embarked on a comprehensive exploration of the potential for repurposing FDA-approved drugs as inhibitors of HDAC3. We employed a systematic approach that integrated molecular docking, MD simulations, and structural analyses and identified two repurposed drugs, Imatinib and Carpipramine, targeting HDAC3. The analysis of binding affinities through molecular docking pinpointed Imatinib and Carpipramine as potent candidates with remarkable affinities towards HDAC3. Subsequent MD simulations revealed that the binding of these molecules substantially stabilized the HDAC3 structure, leading to fewer structural deviations from its native conformation. The analysis of hydrogen bonding dynamics unveiled strong, specific interactions between Imatinib and Carpipramine with functionally crucial residues of HDAC3. This validates our molecular docking findings and supports the role of these molecules as potential HDAC3 inhibitors. PCA elucidated the global motion of HDAC3, revealing that it maintains stability while accommodating the presence of Imatinib and Carpipramine. The FEL analysis underscored the dynamic conformational behavior of HDAC3 in the presence of these molecules, suggesting a more diverse landscape of stable states. In summary, our study provides compelling evidence for the potential of Imatinib and Carpipramine as effective HDAC3 repurposed inhibitors. These molecules exhibit strong binding affinities and stabilize the structural and dynamic behavior of HDAC3. Their ability to maintain the protein's structural integrity and preserve specific interactions highlights their promise for therapeutic applications against a spectrum of complex diseases, such as cancer. The findings of this research contribute to the growing body of knowledge surrounding drug repurposing and emphasize the potential of FDA-approved drugs as valuable candidates for the development of novel therapeutic agents targeting HDAC3.

Data availability statement

The original contributions presented in the study are included in the article/Supplementary material, further inquiries can be directed to the corresponding author.

Author contributions

AS: Conceptualization, Data curation, Formal Analysis, Funding acquisition, Investigation, Visualization, Writing–original draft. MSK: Data curation, Formal Analysis, Investigation, Validation, Writing–original draft. DKY: Formal Analysis, Investigation, Methodology, Validation, Writing–review and editing. MS: Data curation, Formal Analysis, Funding acquisition, Supervision, Writing–review and editing.

Funding

The author(s) declare that financial support was received for the research, authorship, and/or publication of this article.

Acknowledgments

MSK acknowledges the generous support from the Research Supporting project (RSP 2024R352) by the King Saud University, Riyadh, Kingdom of Saudi Arabia. AS is grateful to Ajman University, UAE for supporting this publication.

Conflict of interest

The authors declare that the research was conducted in the absence of any commercial or financial relationships that could be construed as a potential conflict of interest.

Publisher's note

All claims expressed in this article are solely those of the authors and do not necessarily represent those of their affiliated organizations, or those of the publisher, the editors and the reviewers. Any product that may be evaluated in this article, or claim that may be made by its manufacturer, is not guaranteed or endorsed by the publisher.

References

Amin, S. A., Adhikari, N., Jha, T., and Ghosh, B. (2019). Designing potential HDAC3 inhibitors to improve memory and learning. *J. Biomol. Struct. Dyn.* 37 (8), 2133–2142. doi:10.1080/07391102.2018.1477625

Berman, H. M., Westbrook, J., Feng, Z., Gilliland, G., Bhat, T. N., Weissig, H., et al. (2000). The protein data bank. *Nucleic acids Res.* 28 (1), 235–242. doi:10.1093/nar/28.1.235

Biovia, D. S. (2017) *Discovery studio visualizer*. San Diego, CA, USA: Oregon Graduate Institute of Science and Technology, 936.

Carson, C., and Lawson, H. A. (2018). Epigenetics of metabolic syndrome. *Physiol. genomics* 50 (11), 947–955. doi:10.1152/physiolgenomics.00072.2018

Cha, Y., Erez, T., Reynolds, I. J., Kumar, D., Ross, J., Koytiger, G., et al. (2018). Drug repurposing from the perspective of pharmaceutical companies. *Br. J. Pharmacol.* 175 (2), 168–180. doi:10.1111/bph.13798

Chen, H. P., Zhao, Y. T., and Zhao, T. C. (2015). Histone deacetylases and mechanisms of regulation of gene expression. *Crit. Reviews™ Oncog.* 20 (1-2), 35–47. doi:10.1615/critrevoncog.2015012997

Cheshmazar, N., Hamzeh-Mivehroud, M., Nozad Charoudeh, H., Hemmati, S., Melesina, J., and Dastmalchi, S. (2022). Current trends in development of HDAC-based chemotherapeutics. *Life Sci.* 308, 120946. doi:10.1016/j.lfs.2022.120946

Dallakyan, S., and Olson, A. J. (2015) "Small-molecule library screening by docking with PyRx," in *Chemical biology: methods and protocols*, 243–250.

Daskalaki, M. G., Tsatsanis, C., and Kampranis, S. C. (2018). Histone methylation and acetylation in macrophages as a mechanism for regulation of inflammatory responses. *J. Cell. physiology* 233 (9), 6495–6507. doi:10.1002/jcp.26497

DeLano, W. L. (2002). Pymol: an open-source molecular graphics tool. *CCP4 Newsl. Protein Crystallogr.* 40 (1), 82–92.

Demetri, G. D. (2002). Identification and treatment of chemoresistant inoperable or metastatic GIST: experience with the selective tyrosine kinase inhibitor imatinib mesylate (STI571). *Eur. J. cancer* 38, S52–S59. doi:10.1016/s0959-8049(02)80603-7

Du, X., Li, Y., Xia, Y. L., Ai, S. M., Liang, J., Sang, P., et al. (2016). Insights into protein–ligand interactions: mechanisms, models, and methods. *Int. J. Mol. Sci.* 17 (2), 144. doi:10.3390/ijms17020144

Duthie, S. J. (2011). Epigenetic modifications and human pathologies: cancer and CVD. *Proc. Nutr. Soc.* 70 (1), 47–56. doi:10.1017/S0029665110003952

Hodos, R. A., Kidd, B. A., Shameer, K., Readhead, B. P., and Dudley, J. T. (2016). *In silico* methods for drug repurposing and pharmacology. *Wiley Interdiscip. Rev. Syst. Biol. Med.* 8 (3), 186–210. doi:10.1002/wsbm.1337

Hu, G., He, N., Cai, C., Cai, F., Fan, P., Zheng, Z., et al. (2019). HDAC3 modulates cancer immunity via increasing PD-L1 expression in pancreatic cancer. *Pancreatology* 19 (2), 383–389. doi:10.1016/j.pan.2019.01.011

Huang, J., and MacKerell, A. D., Jr (2013). CHARMM36 all-atom additive protein force field: Validation based on comparison to NMR data. *J. Comput. Chem.* 34 (25), 2135–2145. doi:10.1002/jcc.23354

Huey, R., Morris, G. M., and Forli, S. (2012). Using AutoDock 4 and AutoDock vina with AutoDockTools: a tutorial. *Scripps Res. Inst. Mol. Graph. Laboratory* 10550 (92037), 1000.

Humphrey, W., Dalke, A., and Schulten, K. (1996). VMD: visual molecular dynamics. *J. Mol. Graph.* 14 (1), 33–38. doi:10.1016/0263-7855(96)00018-5

Joensuu, H., and Dimitrijevic, S. (2001). *Tyrosine kinase inhibitor imatinib (STIS71) as an anticancer agent for solid tumours*. Helsinki, Finland: Taylor and Francis, 451–455.

Kishi, T., Matsunaga, S., Matsuda, Y., and Iwata, N. (2014). Iminodibenzyl class antipsychotics for schizophrenia: a systematic review and meta-analysis of carpipramine, clocapramine, and mosapramine. *Neuropsychiatric Dis. Treat.* 10, 2339–2351. doi:10.2147/NDT.S73464

Kwon, M. J., Kim, S., Han, M. H., and Lee, S. B. (2016). Epigenetic changes in neurodegenerative diseases. *Mol. Cells* 39 (11), 783–789. doi:10.14348/molcells.2016.0233

Lee, C. Y., and Grant, P. A. (2019). "Role of histone acetylation and acetyltransferases in gene regulation," in *Toxicoepigenetics* (Elsevier), 3–30.

Leus, N. G., van der Wouden, P. E., van den Bosch, T., Hooghiemstra, W. T. R., Ourailidou, M. E., Kistemaker, L. E. M., et al. (2016). HDAC 3-selective inhibitor RGFP966 demonstrates anti-inflammatory properties in RAW 264.7 macrophages and mouse precision-cut lung slices by attenuating NF-κB p65 transcriptional activity. *Biochem. Pharmacol.* 108, 58–74. doi:10.1016/j.bcp.2016.03.010

Lobanov, M. Y., Bogatyreva, N., and Galzitskaya, O. (2008). Radius of gyration as an indicator of protein structure compactness. *Mol. Biol.* 42, 623–628. doi:10.1134/s0026893308040195

Mark, P., and Nilsson, L. (2001). Structure and dynamics of the TIP3P, SPC, and SPC/E water models at 298 K. *J. Phys. Chem. A* 105 (43), 9954–9960. doi:10.1021/jp003020w

Marsh, J. A., and Teichmann, S. A. (2011). Relative solvent accessible surface area predicts protein conformational changes upon binding. *Structure* 19 (6), 859–867. doi:10.1016/j.str.2011.03.010

Maruyama, Y., Igarashi, R., Ushiku, Y., and Mitsutake, A. (2023). Analysis of protein folding simulation with moving root mean square deviation. *J. Chem. Inf. Model.* 63 (5), 1529–1541. doi:10.1021/acs.jcim.2c01444

Menéndez, C. A., Accordino, S. R., Gerbino, D. C., and Appignanesi, G. A. (2016). Hydrogen bond dynamic propensity studies for protein binding and drug design. *PLoS One* 11 (10), e0165767. doi:10.1371/journal.pone.0165767

Mobley, D. L., and Dill, K. A. (2009). Binding of small-molecule ligands to proteins: "what you see" is not always "what you get". *Structure* 17 (4), 489–498. doi:10.1016/j.str.2009.02.010

Mohammad, T., Siddiqui, S., Shamsi, A., Alajmi, M. F., Hussain, A., Islam, A., et al. (2020). Virtual screening approach to identify high-affinity inhibitors of serum and glucocorticoid-regulated kinase 1 among bioactive natural products: combined molecular docking and simulation studies. *Molecules* 25 (4), 823. doi:10.3390/molecules25040823

Muller Stein, S. A. M., Loccisano, A. E., Firestine, S. M., and Evanseck, J. D. (2006). Principal components analysis: a review of its application on molecular dynamics data. *Annu. Rep. Comput. Chem.* 2, 233–261. doi:10.1016/S1574-1400(06)02013-5

Nechay, M. R., Gallup, N. M., Morgenstern, A., Smith, Q. A., Eberhart, M. E., and Alexandrova, A. N. (2016). Histone deacetylase 8: characterization of physiological divalent metal catalysis. *J. Phys. Chem. B* 120 (26), 5884–5895. doi:10.1021/acs.jpcb.6b00997

Papaleo, E., Mereghetti, P., Fantucci, P., Grandori, R., and De Gioia, L. (2009). Free-energy landscape, principal component analysis, and structural clustering to identify representative conformations from molecular dynamics simulations: the myoglobin case. *J. Mol. Graph. Model.* 27 (8), 889–899. doi:10.1016/j.jmgm.2009.01.006

Pushpakom, S., Iorio, F., Eyers, P. A., Escott, K. J., Hopper, S., Wells, A., et al. (2019). Drug repurposing: progress, challenges and recommendations. *Nat. Rev. Drug Discov.* 18 (1), 41–58. doi:10.1038/nrd.2018.168

Ramming, A., Distler, J. H. W., Schett, G., Gay, S., and Jüngel, A. (2014). Epigenetic modifications in autoimmune diseases. *Z. für Rheumatol.* 73, 636–638. doi:10.1007/s00393-014-1388-x

Sarkar, R., Banerjee, S., Amin, S. A., Adhikari, N., and Jha, T. (2020). Histone deacetylase 3 (HDAC3) inhibitors as anticancer agents: a review. *Eur. J. Med. Chem.* 192, 112171. doi:10.1016/j.ejmech.2020.112171

Shamsi, A., Shahwan, M., Khan, M. S., Husain, F. M., Alhumaydhi, F. A., Aljohani, A. S. M., et al. (2021). Elucidating the interaction of human ferritin with quercetin and naringenin: implication of natural products in neurodegenerative diseases: molecular docking and dynamics simulation insight. *ACS omega* 6 (11), 7922–7930. doi:10.1021/acsomega.1c00527

Shukla, R., and Tripathi, T. (2020). Molecular dynamics simulation of protein and protein–ligand complexes. *Computer-aided drug Des.*, 133–161. doi:10.1007/978-981-15-6815-2_7

Singh, S., Baker, Q. B., and Singh, D. B. (2022). "Molecular docking and molecular dynamics simulation," in *Bioinformatics* (Elsevier), 291–304.

Stegmeier, F., Warmuth, M., Sellers, W. R., and Dorsch, M. (2010). Targeted cancer therapies in the twenty-first century: lessons from imatinib. *Clin. Pharmacol. Ther.* 87 (5), 543–552. doi:10.1038/clpt.2009.297

Sun, W., Zhang, N., Liu, B., Yang, J., Loers, G., Siebert, H. C., et al. (2022). HDAC3 inhibitor RGFP966 ameliorated neuroinflammation in the cuprizone-induced demyelinating mouse model and LPS-stimulated BV2 cells by downregulating the P2X7R/STAT3/NF-κB65/NLRP3 activation. *ACS Chem. Neurosci.* 13 (17), 2579–2598. doi:10.1021/acschemneuro.1c00826

Trott, O., and Olson, A. J. (2010). AutoDock Vina: improving the speed and accuracy of docking with a new scoring function, efficient optimization, and multithreading. *J. Comput. Chem.* 31 (2), 455–461. doi:10.1002/jcc.21334

Turner, P. (2005). *XMGRACE, version 5.1. 19. Center for coastal and land-margin research*, Beaverton: Oregon Graduate Institute of Science and Technology, 2.

Van Der Spoel, D., Lindahl, E., Hess, B., Groenhof, G., Mark, A. E., and Berendsen, H. J. C. (2005). GROMACS: fast, flexible, and free. *J. Comput. Chem.* 26 (16), 1701–1718. doi:10.1002/jcc.20291

Venkatesh, S., and Workman, J. L. (2015). Histone exchange, chromatin structure and the regulation of transcription. *Nat. Rev. Mol. Cell Biol.* 16 (3), 178–189. doi:10.1038/nrm3941

Watson, P. J., Fairall, L., Santos, G. M., and Schwabe, J. W. R. (2012). Structure of HDAC3 bound to co-repressor and inositol tetraphosphate. *Nature* 481 (7381), 335–340. doi:10.1038/nature10728

Wishart, D. S., Feunang, Y. D., Guo, A. C., Lo, E. J., Marcu, A., Grant, J. R., et al. (2018). DrugBank 5.0: a major update to the DrugBank database for 2018. *Nucleic acids Res.* 46 (D1), D1074–D1082. doi:10.1093/nar/gkx1037

Yunta, M. J. (2017). It is important to compute intramolecular hydrogen bonding in drug design. *Am. J. Model. Optim.* 5 (1), 24–57. doi:10.12691/ajmo-5-1-3

Zhang, L., Lu, Q., and Chang, C. (2020). Epigenetics in health and disease. *Epigenetics allergy Autoimmun.* 1253, 3–55. doi:10.1007/978-981-15-3449-2_1

Zhang, W., Sun, X., Ba, G., Tang, R., and Lin, H. (2021). RGFP966, a selective HDAC3 inhibitor, ameliorates allergic and inflammatory responses in an OVA-induced allergic rhinitis mouse model. *Int. Immunopharmacol.* 93, 107400. doi:10.1016/j.intimp.2021.107400

frontiers | Frontiers in Pharmacology

TYPE Review
PUBLISHED 18 July 2024
DOI 10.3389/fphar.2024.1434088

Check for updates

OPEN ACCESS

EDITED BY
Wagdy Mohamed Eldehna,
Kafrelsheikh University, Egypt

REVIEWED BY
Alessandra Fiore,
University of Verona, Italy
Hongbao Fang,
Nanjing Normal University, China

*CORRESPONDENCE
Rui Xia,
xra@ntu.edu.cn
Xiaohua Zheng,
xiaohuaz@ntu.edu.cn
Weiqi Wang,
wwq1990@ntu.edu.cn

†These authors have contributed equally to this work

RECEIVED 17 May 2024
ACCEPTED 01 July 2024
PUBLISHED 18 July 2024

CITATION
Wu J, Shi Y, Zhou M, Chen M, Ji S, Liu X, Zhou M, Xia R, Zheng X and Wang W (2024), Nutrient vitamins enabled metabolic regulation of ferroptosis via reactive oxygen species biology. *Front. Pharmacol.* 15:1434088. doi: 10.3389/fphar.2024.1434088

COPYRIGHT
© 2024 Wu, Shi, Zhou, Chen, Ji, Liu, Zhou, Xia, Zheng and Wang. This is an open-access article distributed under the terms of the Creative Commons Attribution License (CC BY). The use, distribution or reproduction in other forums is permitted, provided the original author(s) and the copyright owner(s) are credited and that the original publication in this journal is cited, in accordance with accepted academic practice. No use, distribution or reproduction is permitted which does not comply with these terms.

Nutrient vitamins enabled metabolic regulation of ferroptosis via reactive oxygen species biology

Junjie Wu[1†], Yanting Shi[1†], Man Zhou[1†], Min Chen[1], Shuying Ji[1], Xingxing Liu[1], Mengjiao Zhou[1], Rui Xia[2]*, Xiaohua Zheng[1]* and Weiqi Wang[1]*

[1]School of Pharmacy, Nantong University, Nantong, Jiangsu, China, [2]School of Public Health, Nantong University, Nantong, Jiangsu, China

Vitamins are dietary components necessary for cellular metabolic balance, especially redox homeostasis; deficient or excessive supply may give rise to symptoms of psychiatric disorders. Exploring the nutritional and metabolic pathways of vitamins could contribute to uncovering the underlying pathogenesis of ferroptosis-associated diseases. This mini-review aims to provide insights into vitamins closely linked to the regulation of ferroptosis from the perspective of cellular reactive oxygen species biology. The mainstream reprogramming mechanisms of ferroptosis are overviewed, focusing on unique biological processes of iron metabolism, lipid metabolism, and amino acid metabolism. Moreover, recent breakthroughs in therapeutic interventions targeting ferroptosis via fully utilizing vitamin-based pharmacological tools were overviewed, covering vitamins (B, C, E, and K). Finally, mechanism insight related to vitamin-associated nutrient signaling was provided, highlighting the pharmacological benefits of metabolically reprogramming ferroptosis-associated diseases.

KEYWORDS

ferroptosis, vitamins, nutrient signaling, metabolic regulation, reactive oxygen species

Introduction

Cell death can occur accidentally or controllably to maintain biological homeostasis by the removal of unnecessary cells and cell debris. In particular, regulated cell death controlled by interconnected signaling pathways is linked with tumorigenesis, apparently different from accidental cell death (Tang et al., 2019; Tong et al., 2022). Since its discovery in 1973, clinical oncology investigation has been devoted to promoting the development of therapeutics that are efficient in apoptosis induction (Kerr et al., 1972; Peng et al., 2022). In-depth studies of this lethal subroutine revealed the general characteristics of cancers that are resistant to apoptosis, and induction of other regulated routes involving necroptosis (Gong et al., 2019), autophagy (White, 2015), and pyroptosis (Yu et al., 2021), and so on. Over the past decades, regulated cell death pathways have been extensively studied in the field of cancer treatment, especially for newly emerging reactive oxygen species (ROS) nanomedicine that is amenable to the therapeutic intervention of ferroptosis execution. ROS-producing nanoparticles function by infiltrating cancerous tissues and exploiting the altered redox balance prevalent in these cells. Once activated, they intensify

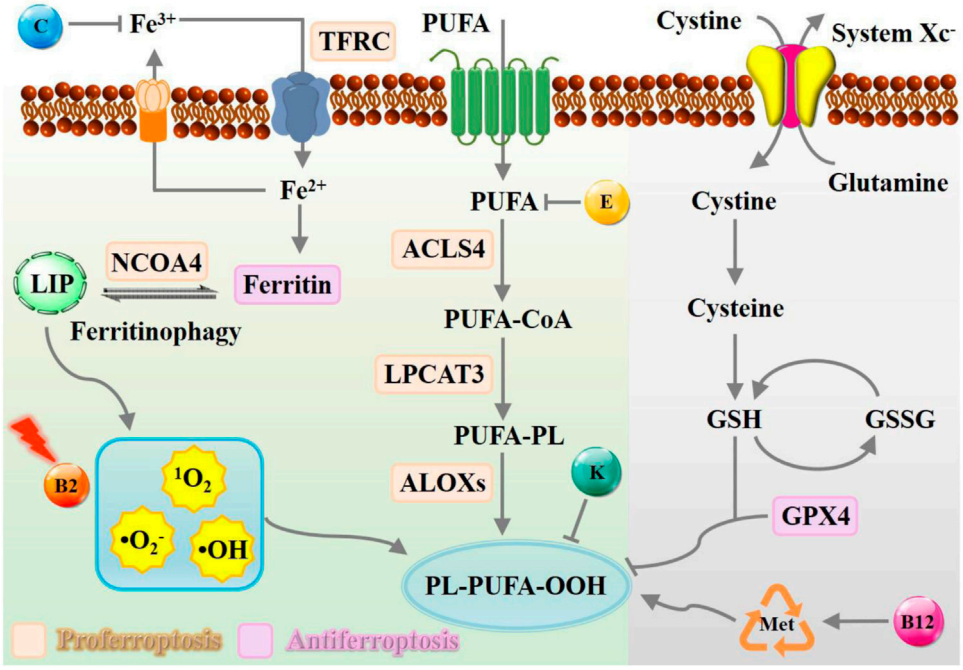

FIGURE 1
Schematic representation of metabolic processes of ferroptosis modulated by nutrient vitamins. The modulation of the ferroptosis process can be facilitated by the presence of vitamin B, C, E, and K, which exert a multifaceted influence towards iron deposition, ROS accumulation, and radical-trapping. Abbreviation: TFRC, transferrin receptor; NCOA4, nuclear receptor coactivator 4; LIP, labile iron pool; PUFA, polyunsaturated fatty acid; ACSL4, acyl-CoA synthetase long-chain family member 4; LPCAT3, lysophosphatidylcholine acyltransferase 3; LOX, lipoxygenase.

intracellular oxidative stress beyond the threshold cancer cells can manage, leading to uncontrolled lipid oxidation and membrane damage-hallmark of ferroptosis.

Up to 2012, ferroptosis featured phospholipid peroxidation driven by an iron-dependent manner, displaying significant differences at morphological, biochemically, and genetic levels (Dixon et al., 2012; Tang et al., 2020). Morphologically, unrepaired cellular damage spreads in a wave-like pattern, characterized by cytoplasmic and organelle ruptures, chromatin condensation, and a rise in autophagosomes (Riegman et al., 2020). Conceptually, ferroptosis was advanced to describe the result of iron accumulation and lipid peroxides (LPO) from the perspective of biochemistry (Liang et al., 2022). At present, GSH depletion and GPX4 inhibition play a crucial role in the initiation of ferroptosis, and other free radical-trapping targets involved ferroptosis suppressor protein 1 (FSP1) and GTP cyclohydrolase 1 (GCH1) (Jiang et al., 2021). To date, the underlying molecular mechanisms related to ferroptotic cell death have been extensively studied for therapeutic purposes.

Intriguingly, recent preclinical evidence suggests that certain malignancies are prone to chemoresistance and metastasis but are exquisitely vulnerable to ferroptosis (Liang et al., 2019; Mou et al., 2019; Lei et al., 2022). Consequently, modulating ferroptosis via metabolic interventions has garnered significant attention (Wu et al., 2020; Koppula et al., 2021). In this mini-review, we first summarized the key metabolic reprogramming of ferroptotic cell death, covering unique biological processes and pathophysiological characteristics in terms of iron metabolism, lipid metabolism, and amino acid metabolism. Further, we delve into the nutritional vitamins harnessed to govern ferroptosis, emphasizing their potential in tumor suppression and immune surveillance, underscoring the therapeutic promise of metabolic reprogramming in ferroptosis-linked diseases. Finally, we also outlined the current understanding of induction/inhibition mechanisms and conceptualized promising strategies that contribute to ROS biology for collaborative ferroptosis regulation.

Nutrient vitamins assosiated ferroptosis regulation

The downstream regulatory network of ferroptotic cell death is driven by the disequilibrium of redox hemostasis, owing to the inactivation of reducing enzymes or lipid oxidation products. As depicted in Figure 1, canonical nutrient vitamins actively participate in metabolic reprogramming mechanisms governing ferroptosis were outlined, including iron metabolism (Rizzollo et al., 2021), lipid metabolism (Snaebjornsson et al., 2020), and amino acid metabolism (Sies, 2021). Overall, vitamin B2 has been proven to be efficient in promoting ROS production assisted by laser or ultrasound irradiation, while B12 functions via methionine cycle to promote ferroptosis execution. In contrast, vitamin C may interfere in iron homeostasis, vitamin E act as endogenous antioxidants participate in neutralizing excessive free radicals to prevent oxidative damage of PUFA. Natural vitamin K is commonly recognized for its role as a potent inhibitor of ferroptosis, whereas synthetic variants can facilitate this process instead.

Iron metabolism

Cancer cells exhibited strong iron dependency to support their rapid proliferation, which is usually accompanied by upregulated transferrin and downregulated ferroportin, thus can be harnessed to therapeutic interventions of ferroptosis-associated diseases (Bao et al., 2020; Bao et al., 2021). Excessive intracellular iron is accompanied by highly oxidative stress that can propagate LPO accumulation (Zhang S. et al., 2022; Zhu et al., 2022). Thus, sensitizing cancer cells to oxidative damage and ferroptosis can be orchestrated by modulating iron uptake, storage, utilization, and export (Hassannia et al., 2019). Generally, cellular transport systems function well to preserve iron homeostasis (Andrews and Schmidt, 2007; Bogdan et al., 2016). In brief, iron can be internalized by circulating glycoprotein transferrin and discharged by ferroportin (Zhang C. et al., 2020). The intracellular labile iron pool (LIP) maintains a delicate balance normally and can be elevated by transferrin-mediated uptake or autophagic degradation (Lin et al., 2020). Inhibition of nuclear receptor coactivator 4 (NCOA4) mediated ferritinophagic flux or abnormal expression of iron metabolism proteins iron-responsive element binding protein 2 can dramatically decrease the vulnerability to ferroptosis (Fang et al., 2021; Zhou H. et al., 2023). Especially, vitamin C may interference iron metabolism by enhancing iron absorption. In the biological system, iron is an essential micronutrient element that can be engaged in hydroxyl radicals (•OH) formation through the Haber-Weiss and Fenton reaction, relying on the cycle between the ferrous (Fe^{2+}) and ferric (Fe^{3+}) states (Wang et al., 2020). Vitamin C helps convert poorly absorbed Fe^{3+} into its more absorbable Fe^{2+}. Additionally, vitamin C acts as an antioxidant, protecting against oxidative stress that are associated with iron metabolism, thereby maintaining iron homeostasis and overall metabolic health.

Lipid metabolism

Lipid peroxidation is one of the canonical processes catalyzed by spontaneous autoxidation or endogenous enzymes that directly contribute to promoting ferroptosis (Yang and Stockwell, 2016; von Krusenstiern et al., 2023). At present, the widely recognized pathway is excessive peroxidation of polyunsaturated fatty acid (PUFA), comprising arachidonic acid and adrenic acid (Bazinet and Layé, 2014; Kagan et al., 2016). PUFAs, especially long-chain ones like ω-3 and ω-6 LCPUFAs, readily oxidize due to their numerous double bonds, rendering them susceptible to free radical assault. Vitamin E, an effective fat-loving antioxidant, acts as a membrane shield, with heightened importance in PUFA-dense areas. It directly neutralizes free radicals, halting their damaging cascade to preserve PUFAs. Teaming up with trace elements like selenium, it enhances the body's antioxidant shield, defending both PUFAs and other cellular elements against oxidative stress. Additionally, vitamin E regulates metabolic interactions with PUFAs, impacting the progression of ferroptosis.

Generally, the peroxidation process of PUFA-containing phospholipids can be divided into three steps. Firstly, acyl-CoA synthetase long-chain family member 4 (ACSL4) converts the PUFA into acylated form (Gan, 2022). Then, lysophosphatidylcholine acyltransferase 3 (LPCAT3) participates in the process of esterifying acyl Co-A derivatives, incorporating PUFAs into phospholipid membranes (Hashidate-Yoshida et al., 2015). Finally, peroxidation occurs to form lipid hydroperoxide under the catalysis of lipoxygenase (LOX) (Stoyanovsky et al., 2019). Excessive oxidation of PUFA-containing phospholipids might disrupt the integrity of biological membranes, eventually decomposing into reactive toxic aldehydes (such as hydroxynonenal or malondialdehydes) facilitating ferroptosis execution (Dyall et al., 2022). Vitamin K1 has also emerged as a potent blocker of ferroptosis, a controlled cellular death mechanism linked to lipid oxidation. Research from Kolbrink et al. (Kolbrink et al., 2022) demonstrated its effectiveness in stopping ferroptosis in cellular models, reversing cell death and suggesting its potential in treating issues arising from oxygen deprivation and restoration cycles, like tissue injury. These discoveries emphasize vitamin K's pivotal role, via unconventional metabolic pathways, in regulating ferroptosis-related diseases and its promise as a target for innovative therapies. Besides, the antioxidant mechanism of nutrient vitamins involves FSP1-triggered reduction, sustaining its radical-trapping properties to interrupt ferroptosis pathways.

Amino acid metabolism

In the biological system, extracellular glutamate and cystine are transported into the cell by amino acid transporter receptors system Xc^-, while inhibiting the function of system Xc^- can decrease the intracellular cysteine and GSH content (Koppula et al., 2021; Xiong et al., 2021). The cysteine required for GSH synthesis is generally obtained by the transsulfuration pathway of sulfur transfer from homocysteine to cysteine (Stockwell et al., 2020; Lee and Roh, 2022). GPX4 can protect cells from ferroptosis by reducing the lethal PUFA-containing phospholipid hydroperoxides (PL-OOH) into phospholipid alcohols (PL-OH) (Yang et al., 2014). Overall, the existing intracellular GSH/Xc^-/GPX4 antioxidant defense system is of great importance in maintaining cellular redox homeostasis.

Moreover, the methionine-synthase cycle has been proven to be relevant to metabolic process of ROS generation, in which vitamin B12 plays a crucial role as a cofactor. It primarily functions to regenerate methionine, an essential amino acid, from homocysteine. The methionine cycle, involving SBP-1/SREBP1 and lipogenesis, is crucial for how early-life B12 levels influence later health outcomes. Research indicates that a lack of vitamin B12 early in life can result in elevated fat levels and toxic lipid accumulation, notably long-chain polyunsaturated fatty acids (LC-PUFAs), during adulthood, which triggers ferroptosis in reproductive cells (Qin et al., 2022). From the perspective of these signaling pathways, amino acid metabolism is crucial for the regulation of intracellular redox balance, especially amino acid-related metabolic processes, which could significantly affect the therapeutic effect of ferroptosis.

Metabolic regulation of ferroptosis with vitamins

Multiple nutrients including exogenous fatty acids and amino acids have been reviewed to regulate redox homeostasis and

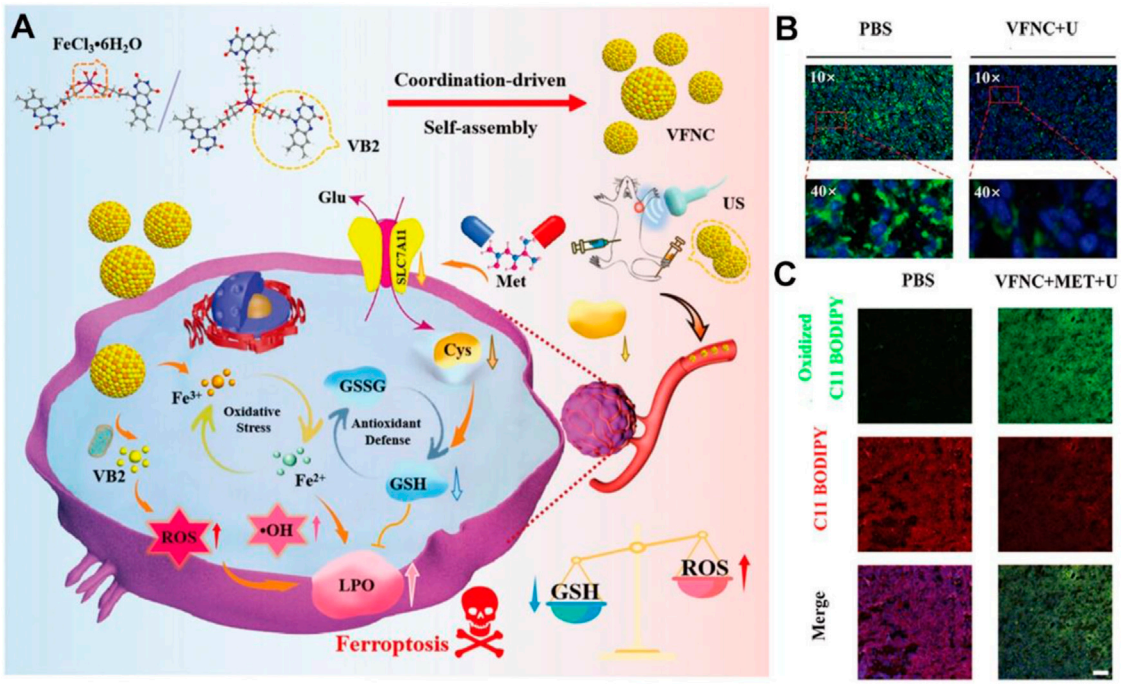

FIGURE 2
Schematic illustration of VFNC-based ferroptosis therapy towards triple-negative breast cancer. **(A)** Schematic of the preparation process and therapeutic mechanism of the VFNC nanoplatform. **(B)** Immunofluorescence staining of GPX4. **(C)** CLSM images of LPO accumulation. Adapted with permission from Zhou M. et al. (2023). Copyright (2023) John Wiley & Sons, Inc.

ferroptosis execution (Koppula et al., 2018; Qi et al., 2021). However, the underlying mechanism of vitamins and ferroptosis and corresponding nutrient signaling related to ferroptosis regulation is still limited. Vitamins are dietary components that have functioned for therapeutic applications over the past decades (Saghiri et al., 2017; Di Tano et al., 2020; Hou et al., 2020). In this section, vitamins B, C, E, and K are essential for regulating cellular homeostasis that directly linked to ferroptotic cell death has been overviewed.

Vitamin B

The vitamin B family generally serves as enzyme cofactors carrying out essential cellular functions, such as energy metabolism, DNA synthesis, and phospholipids metabolism (Lindschinger et al., 2019). B-group vitamins are water-soluble; the metabolic half-life is only a few hours and must be supplemented daily in most cases (Tardy et al., 2020). Existing evidence indicates that insufficient or excessive supply of B vitamins may elicit oxidative stress and modulate the expression of numerous pathogenic genes (Kennedy, 2016; Peterson et al., 2020). As a proof-of-concept, assembled Vitamin B2 nanocrystals have been exploited to favor the massive production of ROS under blue light irradiation taking advantage of optical waveguiding properties (Fei et al., 2019). Inspired by these interesting properties, Zhou et al. subtly reported the strategy by combining Vitamin B2 and trivalent iron in a self-assembly nanostructure (VFNC) for multiple ferroptosis regulation (Figure 2A; Zhou M. et al., 2023). This vitamin B2-ferric nanocomplex exhibited appropriate size and favorable biocompatibility. Activated by ultrasound, VB2 could contribute to producing a significant quantity of lethal $^1O_2$ to inhibit cell proliferation. Simultaneously, the disassembled nanocomplex will release Fe^{3+} ion, which could generate •OH through the Fenton reaction and destroy the System Xc^--GSH-GPX4 antioxidant defense system. The downregulated GPX4 and SLC7A11 protein and more LPO accumulation suggested the effective facilitation of metformin to VFNC-based ferroptosis therapy (Figures 2B,C). The synergistic sonodynamic/ferroptotic therapy and the coactivation effect of metformin could exert a superadditive anti-tumor effect by completely disintegrating the redox homeostasis and antioxidant defense system of triple-negative breast cancer. Overall, this coordination-driven self-assembly system provides a general strategy for nutritional vitamins in clinical applications.

Recently, Qin et al. established the impact of early vitamin B12 insufficiency in ferroptosis induction (Figure 3A; Qin et al., 2022). Vitamin B12 sufficiency has no adverse impact on germ cells; however, early vitamin B12 deficiency leads to ferroptosis in germ cells and causes obesity and infertility. Mechanistically, vitamin B12 deficiency directly affects the methionine cycle-SBP-1/sterol regulatory element-binding protein-1 (SREBP1)-adipogenesis axis, resulting in the accumulation of polyunsaturated fatty acids and heightened peroxidation levels, which was significantly suppressed by the addition of B12 supplementation (Figures 3B,C). Overall, this study highlights the relationship between vitamin B12 deficiency and ferroptosis in early life, providing a potential target for the late-life treatment of the disease in adulthood.

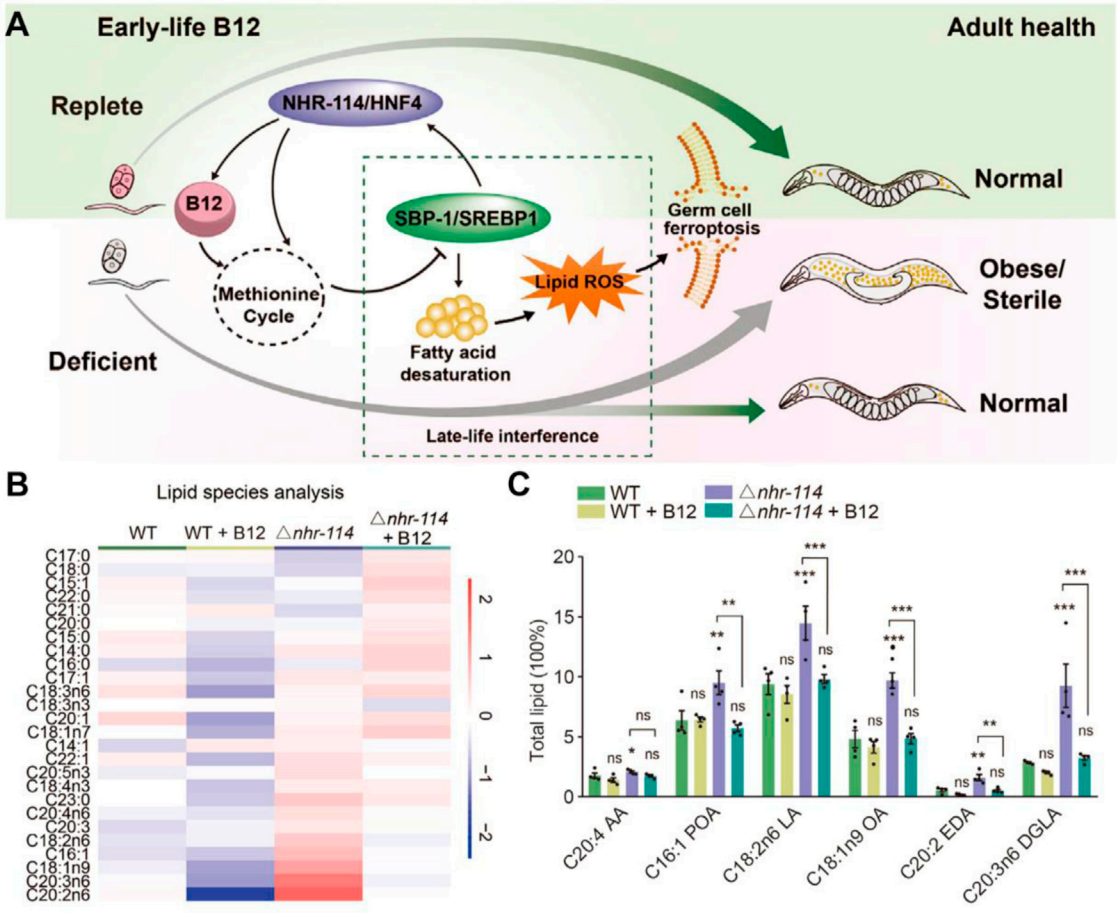

FIGURE 3
(A) Mechanism of action of early-life B12 in programming of adult health. **(B,C)** Heatmap and quantification of lipid species with maternal B12 supplementation. Reproduced with permission (Qin et al., 2022). Copyright 2022, Cell Press.

Vitamin C

In biological systems, vitamin C exists in different redox forms, including ascorbate, ascorbate radical, dehydroascorbic acid (DHA), 2,3-l-diketoglutonate (2,3-DKG), oxalic acid, and so on. Specifically, the ascorbyl radical is generated upon donating electrons to ferric iron, leading to the formation of superoxide anion ($\bullet O_2^-$) and H_2O_2, while ascorbate in pharmacologic concentration can contribute to the suspended formation of •OH (Szarka et al., 2021).

In addition, vitamin C can affect iron metabolism by inhibiting the degradation of ferritin, increasing the synthesis of ferritin, and thus promoting iron absorption (Wang X. et al., 2021). This cellular death pathway shows similar characteristics to erastin-mediated ferroptosis (Liu et al., 2022). Although vitamin C as an anticancer therapeutic is still up for debate, ongoing recent clinical trials are investigating the combination of pharmacological ascorbate with concurrent radiochemotherapy. Various studies have demonstrated the enhanced therapeutic effect of employing vitamin C to treat troublesome non-small cell lung cancer (NSCLC) (Ou et al., 2020). Recently, a nanocatalytic sensitizer strategy with vitamin C involved has been proposed for treating metastatic NSCLC (Figure 4A; Wang et al., 2022). In this nanotherapy platform, the rational encapsulation of vitamin C and ferrous iron within the liposome enabled the reversible redox cycle. The ferrous ions can interact with hydrogen peroxide, yielding highly reactive •OH radicals, inducing lipid peroxidation (LPO) and ultimately triggering ferroptosis. As shown in Figure 4B, cells underwent oxidative stress and formed vacuolated mitochondria after drug administration. In addition, vitamin C is oxidized to produce DHA, which consumes intracellular GSH, resulting in decreased GPX4 expression (Figure 4C). Moreover, this effective nanocatalytic platform can simultaneously solve the problem of resistance to the kinase inhibitor oxitinib in metastasis NSCLC.

It is a widely recognized fact that mitochondria serve as the primary organelles responsible for iron metabolism within cells. Consequently, the development of mitochondria-targeting ferroptosis platforms has demonstrated promising antitumor effects (Gan et al., 2023). Nevertheless, recent studies have revealed that the rational design of lysosome-targeting systems capable of inducing ferroptosis may yield significant outcomes. These findings broaden our understanding of the complex mechanisms involved in ferroptosis and suggest novel therapeutic strategies for targeting this process. For instance, Chen et al. successfully synthesized a lysosome-targeting ferroptosis nanoplatform (Figure 5; Chen et al., 2022). The synthesis process and chemical structures of the components of VC@N3AMcLAVs

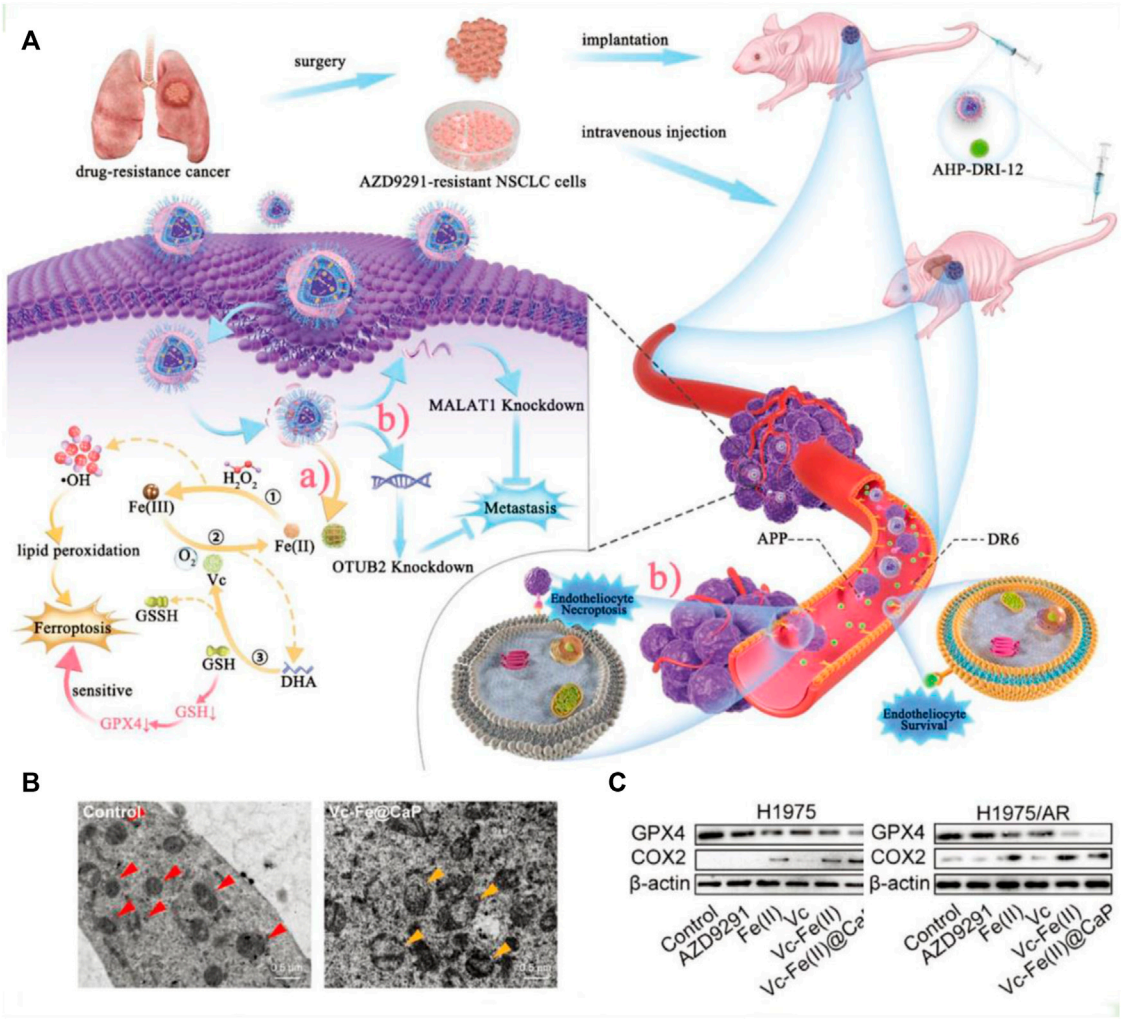

FIGURE 4
(A) Schematic illustration of the tumoricidal effect of combination therapy of VF/S/A@CaP and AHP-DRI-12. **(B)** The cryo-electron microscope images of H1975/AR cells from the control group or Vc−Fe(II)@CaP group. The red triangle serves as a marker for healthy mitochondria, whereas the yellow triangle signifies vacuolated mitochondria that have sustained severe oxidative damage. **(C)** The expression levels of GPX4 and COX2 in both H1975 and H1975/AR cells have been assayed. Reproduced with permission (Wang et al., 2022). Copyright (2022), John Wiley & Sons, Inc.

are thoroughly outlined in Figures 5A,B. Notably, the incorporation of morpholine enabled the nanotherapeutic platform to specifically target lysosomes. Once inside the lysosome, the nanosystem interacts with excess GSH leading to the reduction of lipoic acid and oxidation of vitamin C. Additionally, the oxygen present in the lysosome is converted to hydrogen peroxide. Furthermore, this efficient redox cycle facilitates the conversion of ferric ions to ferrous ions through the degradation of ferritin within the lysosome, further enhancing the antitumor effects of ferroptosis. The produced excess hydrogen peroxide will interact with the ferrous ions to produce highly oxidizing •OH. Due to the depletion of GSH and deficiency of catalase, large numbers of ROS will destroy the redox homeostasis of lysosomes and result in the complete breakdown of the lysosomes membrane, inducing the release of proteolytic enzymes and other substances into the cytosol. This lysosomal membrane permeabilization will cause irreversible damage to tumor cells, resulting in efficient ferroptosis therapy (Figure 5C). The system successfully uses the interaction between the external vitamin C and the intracellular GSH to cause the irreversible death of tumor cells, which provides a new option for effective anticancer therapy. This design offers a promising approach for precision delivery and enhanced antitumor effects through ferroptosis induction in lysosomes.

Recently, vitamin C at pharmaceutical dosage has been demonstrated to be efficient in strengthening the antineoplastic effect by eliciting host immune systems (Ngo et al., 2019). In particular, high-dose vitamin C treatment exhibits great synergy in potentiating the efficacy of immune checkpoint therapy (Magrì et al., 2020). Exploring vitamin C-mediated immunomodulation, Yu et al. proposed hybrid core-shell vesicles (HCSVs) to augment ferroptosis-based therapy by an exogenous circularly polarized magnetic field, as well as responsive magnetic resonance imaging capability (Yu et al., 2020). The HCSVs were constructed by encapsulating ascorbic acid within poly lactic-co-glycolic acid, and the iron oxide nanocubes were embedded into the outer layer. Under the external magnetic field, the vesicle structure is

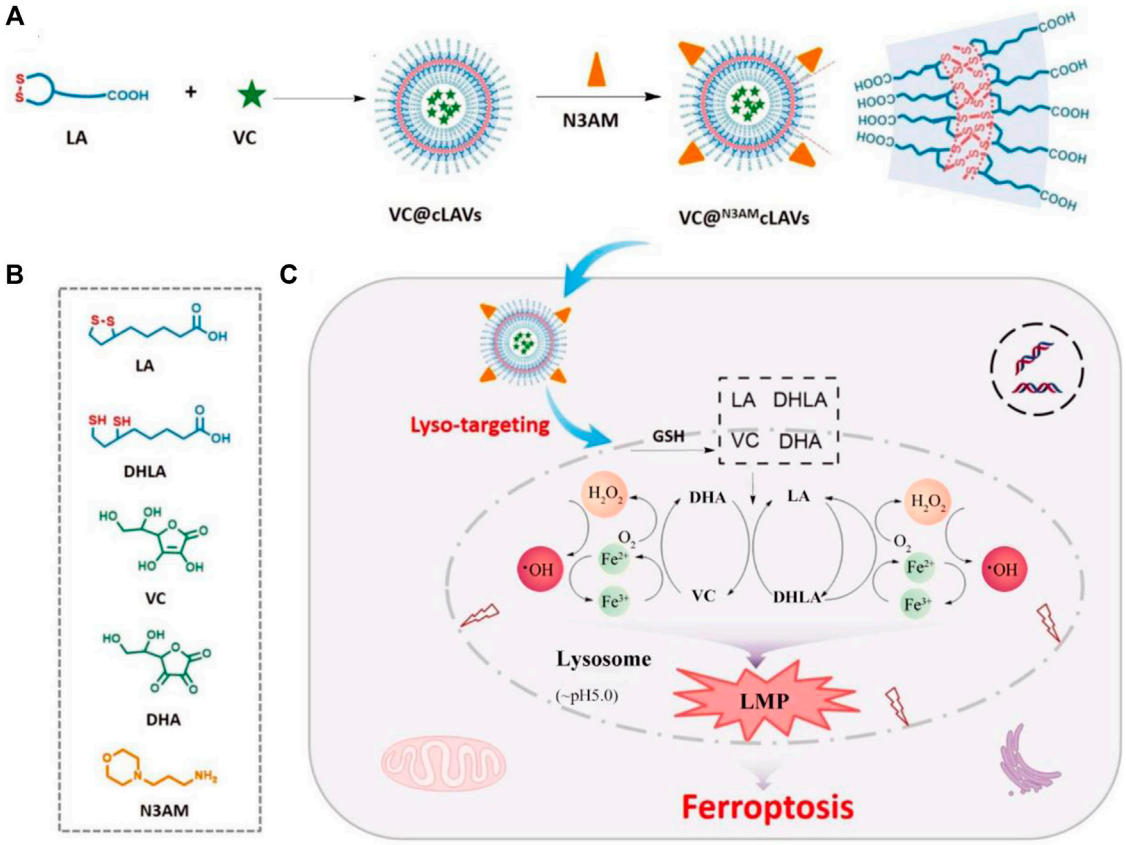

FIGURE 5
The schematic illustration outlines the process of enhancing ROS-mediated lysosomal membrane permeabilization for cancer ferroptosis therapy. **(A)** The design methods of VC@^{N3AM}cLAVs. **(B)** The various molecular structures from the composition of VC@^{N3AM}cLAVs. **(C)** Lysosome-targeting process of VC@^{N3AM}cLAVs and the specific mechanism to promote ROS-mediated lysosomal membrane permeabilization for efficient ferroptosis therapy. Adapted with permission from Chen et al. (2022). Copyright (2023) John Wiley & Sons, Inc.

destroyed along with the release of ascorbic acid to interact with magnetic iron oxide. Ascorbic acid can oxidize ferric ions to produce ferrous ions, which could induce subsequent Fenton chemical reaction processes. Subsequently, the Fenton reaction leads to ferroptosis-mediated cancer inhibition by excessive LPO accumulation. Concurrently, the elevated oxidative stress could induce the activation of dendritic cells and infiltration of cytotoxic T lymphocytes to exert an immunomodulatory effect. During the reduction of magnetic iron oxide by ascorbic acid, the iron-based magnetic resonance imaging signal provides an efficient strategy for visualization of the Fenton reaction.

Vitamin E

As an endogenous radical-trapping antioxidant, vitamin E is a general term for tocopherol substances exhibiting multiple health benefits. Vitamin E comprises different forms of tocopherol and tocotrienol generally functions by the electron-transport coupled enzymatic mechanisms to prevent oxidative damage (Peh et al., 2016; Blaner et al., 2021). For ferroptosis execution, vitamin E actively binds to the PUFA substrate to favor the protective effects against LPO propagation (Hu et al., 2021). Recently, Zhang et al. revealed the anti-ferroptotic defense of nutrient vitamin E for chronic neurological diseases (Zhang X. et al., 2022). Mechanistically, vitamin E exerts neuroprotective effects largely by inhibiting LOX-15, and vitamin E pretreatment can reduce neuronal damage in pentylenetetrazol-induced epileptic rats. In addition, tetrahydrobiopterin (BH4) has been screened out to protect lipids from autoxidation in synergy with vitamin E (Soula et al., 2020). Metabolism-focused screens demonstrated that BH4 biosynthesis is essential for GPX4 inhibition, and can regenerate from its oxidative forms upon dihydrofolate reductase (DHFR), maintaining sustained anti-ferroptotic function. According to the autoxidations of STY-BODIPY, BH4 had similar ferroptosis-inhibitory effects in comparison to α-tocopherol (α-TOH). In the liposomal system, the combination of BH4 and α-TOH yielded superior anti-ferroptosis defenses, partially because of the scavenging of α-TOH-derived radicals.

Vitamin K

Vitamin K is a general term referring to a group of structurally related compounds that possess a common naphthoquinone ring. These compounds encompass both natural and synthetic forms,

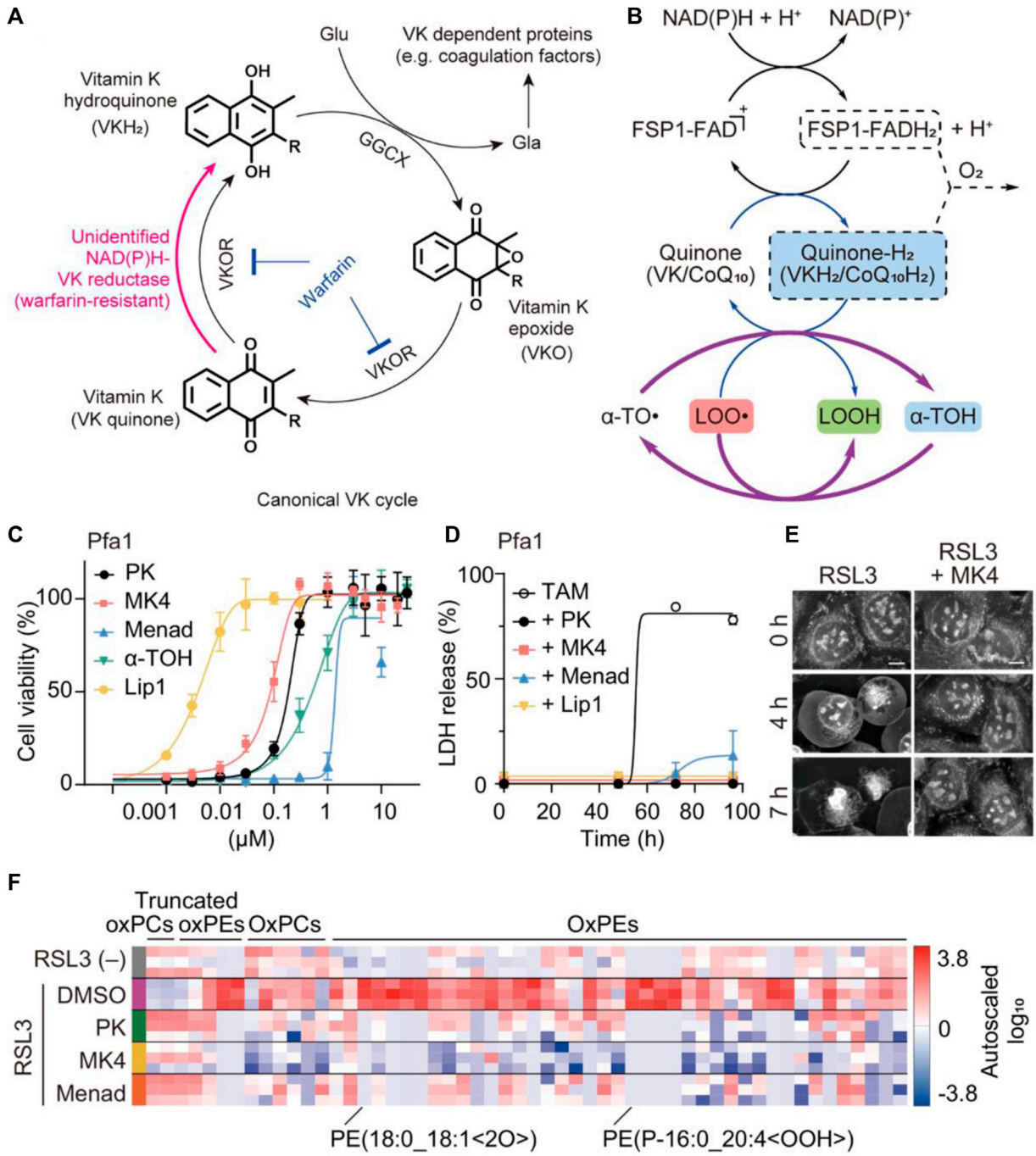

FIGURE 6
The anti-ferroptotic mechanism of non-canonical vitamin K cycle. **(A)** Mechanism of vitamin K supplying VKH2 to GGCX via the alternative vitamin K reduction pathway. **(B)** The possible recycling pathway of α-tocopherol via the CoQ10/VK-hydroquinone transformation process. **(C)** The cell viability and **(D)** lactate dehydrogenase (LDH) release from GPX4-KO mouse embryonic fibroblasts (Pfa1 cells) treated with different conditions (three forms of vitamin K and liproxstatin-1 (Lip1) as a ferroptosis inhibitor). **(E)** The cellular morphology images of RSL3-treated HT-1080 cells were observed irrespective of whether MK4 was present. **(F)** Proportional levels of oxidized phospholipids are visualized through heatmaps during an 8-h exposure to RSL3 in Pfa1 cells (Mishima et al., 2022). Copyright (2021) Springer Nature.

including phylloquinone (known as vitamin K1) found primarily in plants, menaquinones (vitamin K2) found in animal products, and synthetic analogs such as vitamin K3 and menaquinone-4 (MK4) (Welsh et al., 2022). The primary biological role of vitamin K is serving as a cofactor for the γ-carboxylation process, which is crucial in preventing excessive hemorrhaging and osteoporosis. This cofactor function is vital for maintaining bone health and blood coagulation (Wallin and Hutson, 2004; Shearer and Okano, 2018). Recently, vitamin K1 as the predominant dietary form has been investigated as a potential ferroptosis suppressor (Kolbrink et al., 2022). In 2022, Kolbrink et al. proved that vitamin K1 can participate in ferroptosis inhibitory systems, providing

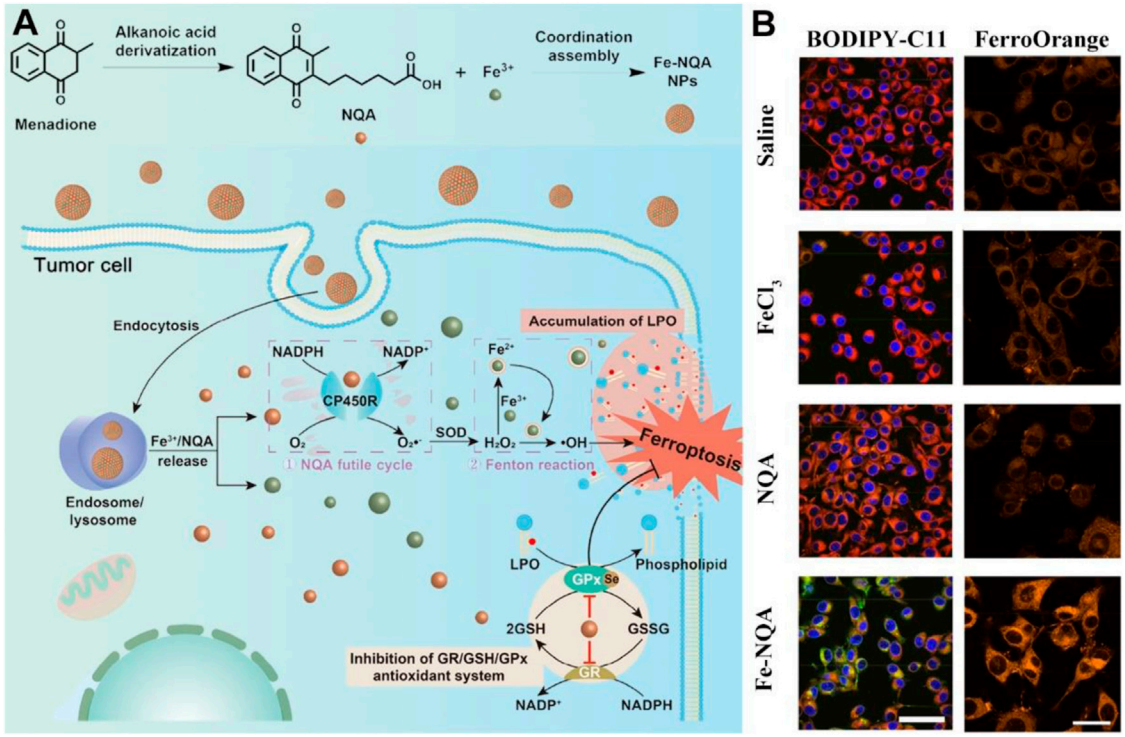

FIGURE 7
The preparation and action mechanism of Fe-NQA for augmenting tumor ferroptotic therapy. **(A)** Schematic illustration of Fe-NQA NPs induced ferroptotic therapy. **(B)** The LSCM images of LPO and Fe^{2+} detected in CT26 cells after incubation of cells with saline, $FeCl_3$, NQA, and Fe-NQA NPs (scale bar: 50 μm). Adapted with permission from Zhang Z. et al. (2020). Copyright (2020) Springer Nature.

pharmacological control of ischemia-reperfusion injury (Kolbrink et al., 2022). In the NIH3T3 cells, the frequency of cell death in the RSL3 group and RSL3 + vitamin K1 group was observed to be 80.8% and 2.2%, respectively. Both vitamin K1 (10 μM) and ferrostatin-1 (1 μM) could remarkably counteract the cytotoxicity by inhibiting RSL3-induced ferroptosis at the cellular level. As evidenced by the phosphatidylserine accessibility, vitamin K1 can also reverse ferroptotic cell death by inhibition of FSP1 and mitochondrially dihydroorotate dehydrogenase (DHODH). For renal ischemia-reperfusion, vitamin K1 had a protective effect on acute kidney injury by inhibiting tubular necrosis and ACSL4 expression. Overall, vitamin K1 demonstrated great therapeutic potential for many diseases associated with ferroptosis by targeting multiple inhibitory pathways. Apart from vitamin K1, variant synthetic menadione has recently been proven to rescue cells from ferroptosis by GPX4 deletion (Mishima et al., 2022). As depicted in Figure 6A, vitamin K elicits ferroptotic inhibitory function that largely depends on FSP1-mediated reduction. In the canonical vitamin K cycle, vitamin K is typically reduced to vitamin K hydroquinone (VKH_2), which is generally recognized as the radical-trapping antioxidant (Figure 6A). However, VKH_2 is easily oxidized to vitamin K epoxide and then converted to vitamin K quinone losing antioxidant activity, this process is also known as warfarin poisoning. Intriguingly, FSP1 was able to form a direct cycle from vitamin K to VKH_2, maintaining lipid radical-trapping activity to attenuate ferroptosis (Figure 6B). In pfa1 cells, MK4 is the most efficacious form of vitamin K derivatives in preventing ferroptosis induced by GPX4 deletion or knockdown (Figure 6C). The significantly reduced release percentage of lactate dehydrogenase further indicated the protective effect of three forms of vitamin K derivative (PK/MK4/Menad) against cell death (Figure 6D). In particular, the presence of MK4 was able to successfully prevent HT-1080 cells from undergoing pathologic changes associated with ferroptosis induced by RSL3 (Figure 6E). Lipid peroxidation is a key process in ferroptosis, where the accumulation of lipid peroxides leads to membrane damage and ultimately cell death. By reducing the level of lipid peroxide, the three forms of vitamin K can mitigate the progression of ferroptosis (Figure 6F). This finding suggests that vitamin K may act as an efficient antioxidant or regulate cellular processes that lead to lipid peroxidation, thereby protecting cells from ferroptosis. Overall, vitamin K metabolism is thought to play a critical role in ferroptosis-associated disease, acting as a natural active ingredient in anti-ferroptotic therapy through the non-classical vitamin K cycle.

Furthermore, the synthetic variant menadione (vitamin K3) is known to be a notable anti-inflammatory drug, which can exacerbate ROS generation to achieve therapeutic effects against bacteria or viruses at appropriate wavelengths (Wang R. et al., 2021). Given that, vitamin K3 and its derivatives have been employed in the field of ROS-based nanomedicine aiming at achieving improved therapeutic index (Yang et al., 2018; Wellington et al., 2020; Chauhan et al., 2023). Utilizing iron ion therapy, nanoscale coordination polymers known as Fe-NQA have been suggested as a potential tumor treatment method, capable of initiating the Fenton reaction while simultaneously suppressing antioxidant activity

(Figure 7; Zhang Z. et al., 2020). The Fe-NQA was prepared by one-step coordination self-assembly of Fe^{3+} and 6-[2-(3-methyl) naphthoquinolyl]hexanoic acid (NQA). The NQA can not only facilitate semiquinone radical formation but also inhibit GPX4 activation by binding cysteine or selenocysteine residues. After internalization, Fe-NQA disassembles in a pH-responsive manner to form a sustained cycle favoring the Fenton reaction by catalyzed cytochrome P450 reductase. Additionally, Fe-NQA sustains GPX4 inactivation, and this cellular death can be reversed by ferroptosis inhibitors. The staining process employed FerroOrange and BODIPY-C11 probes, revealing that the level of lipid peroxide (LPO) in CT26 cells incubated with Fe-NQA nanoparticles was notably elevated compared to the group treated with normal saline (Figure 7B). Taken together, Fe-NQA can synergistically initiate ferroptosis execution, enabling efficient tumor regression, metastasis prevention, and radiotherapy sensitization.

Conclusion and perspectives

Ferroptosis has achieved unprecedented outcomes since coined in 2012, and therapeutic intervention has been demonstrated to be tightly linked to neurodegeneration, viral infection, and cardiovascular disease. Especially for malignant tumors, proferroptotic stimulation has sufficiently indicated significant impacts on the inhibition, development, and metastasis of tumor cells. Existing research has sufficiently indicated ferroptosis inducers or inhibitors, and compartmentalized by regulatory networks involves iron, amino acids, and lipids metabolism. Elucidating these metabolism networks may be critical for therapeutic benefit in various ferroptosis-associated pathophysiological contexts. However, the complicated ferroptosis-based crosstalk between multiple nutrients and metabolic regulation of cellular homeostasis is still limited, especially in the field of vitamin-based essential nutrients.

The administration of nutritional vitamin supplements could potentially serve as an effective approach to modulate sublethal ferroptosis-associated disorders. To date, essential vitamins enabling the regulation of redox homeostasis and LPO generally depend on perturbing ROS hemostasis. However, the current understanding of ROS biology is orchestrated by complex molecular pathways comprising different cell death modalities. Conversely, the interplay between the mechanism of ferroptotic cell death and its associated factors with nutrient signaling remains relatively unexplored.

Furthermore, metabolism regulation of iron availability, cystine deprivation, and ROS biology has yielded insight into the nutrient vitamins in remodeled biological hemostasis. However, interconnected metabolism pathways are highly complex, which is also referred to as metabolic plasticity. The modulation of ferroptosis may involve various endogenous substrates, and vitamins could potentially play a role in other forms of controlled cell death. Nevertheless, the intricate interactions and transitions between ferroptosis and other cell death mechanisms remain elusive.

Finally, the pathophysiological signals of ferroptotic cell death must be unambiguously elucidated stem from the fact that these effectors are directly related to the therapeutic potential of ferroptosis-associated disease. Stratifying ferroptosis sensitivity in patients holds promise for conferring significant health benefits in clinical practice. Current oxidative lipidomics is largely time-consuming, while other reliable molecular imaging methodologies are relatively not enough to favor real-time monitoring of this regulated cell death modality. There is an urgent need for advanced techniques and reagents capable of monitoring treatment processes, in order to rigorously assess the pathological significance of ferroptosis.

Author contributions

JW: Investigation, Writing–original draft, Writing–review and editing. YS: Investigation, Writing–original draft, Writing–review and editing. MaZ: Investigation, Writing–original draft, Writing–review and editing. MC: Formal Analysis, Investigation, Methodology, Writing–original draft. SJ: Formal Analysis, Investigation, Methodology, Writing–original draft. XL: Formal Analysis, Investigation, Methodology, Writing–original draft. MeZ: Formal Analysis, Investigation, Methodology, Writing–original draft. RX: Writing–original draft, Writing–review and editing. XZ: Funding acquisition, Writing–original draft, Writing–review and editing. WW: Writing–original draft, Writing–review and editing.

Funding

The author(s) declare that financial support was received for the research, authorship, and/or publication of this article. This work was supported by the National Natural Science Foundation of China (52103169), Jiangsu Provincial Association for Science and Technology Youth Science and Technology Talent Support Project (TJ-2023-006), the Large Instruments Open Foundation of Nantong University (KFJN2372), Undergraduate Innovation and Entrepreneurship Training Program of Jiangsu Province (202310304155Y), and the College Students' Innovation and Entrepreneurship Training Program of Nantong University (Grant no. 2022239) are gratefully acknowledged.

Conflict of interest

The authors declare that the research was conducted in the absence of any commercial or financial relationships that could be construed as a potential conflict of interest.

Publisher's note

All claims expressed in this article are solely those of the authors and do not necessarily represent those of their affiliated organizations, or those of the publisher, the editors and the reviewers. Any product that may be evaluated in this article, or claim that may be made by its manufacturer, is not guaranteed or endorsed by the publisher.

References

Andrews, N. C., and Schmidt, P. J. (2007). Iron homeostasis. *Annu. Rev. Physiol.* 69, 69–85. doi:10.1146/annurev.physiol.69.031905.164337

Bao, W. D., Pang, P., Zhou, X. T., Hu, F., Xiong, W., Chen, K., et al. (2021). Loss of ferroportin induces memory impairment by promoting ferroptosis in Alzheimer's disease. *Cell Death Differ.* 28, 1548–1562. doi:10.1038/s41418-020-00685-9

Bao, W. D., Zhou, X. T., Zhou, L. T., Wang, F., Yin, X., Lu, Y., et al. (2020). Targeting miR-124/Ferroportin signaling ameliorated neuronal cell death through inhibiting apoptosis and ferroptosis in aged intracerebral hemorrhage murine model. *Aging Cell* 19, e13235. doi:10.1111/acel.13235

Bazinet, R. P., and Layé, S. (2014). Polyunsaturated fatty acids and their metabolites in brain function and disease. *Nat. Rev. Neurosci.* 15, 771–785. doi:10.1038/nrn3820

Blaner, W. S., Shmarakov, I. O., and Traber, M. G. (2021). Vitamin A and vitamin E: will the real antioxidant please stand up? *Annu. Rev. Nutr.* 41, 105–131. doi:10.1146/annurev-nutr-082018-124228

Bogdan, A. R., Miyazawa, M., Hashimoto, K., and Tsuji, Y. (2016). Regulators of iron homeostasis: new players in metabolism, cell death, and disease. *Trends biochem. Sci.* 41, 274–286. doi:10.1016/j.tibs.2015.11.012

Chauhan, A., Anjaly, K., Saini, A., Kumar, R., Kuanr, B. K., and Sharma, D. (2023). Vitamin k3-loaded magnetic nanoparticle-mediated synergistic magnetothermodynamic therapy evokes massive ROS and immune modulation for augmented antitumor potential. *ACS Appl. Mater Interfaces* 15, 27515–27532. doi:10.1021/acsami.3c01702

Chen, Y., Yang, Z., Wang, S., Ma, Q., Li, L., Wu, X., et al. (2022). Boosting ROS-mediated lysosomal membrane permeabilization for cancer ferroptosis therapy. *Adv. Healthc. Mater.* 12, e2202150. doi:10.1002/adhm.202202150

Di Tano, M., Raucci, F., Vernieri, C., Caffa, I., Buono, R., Fanti, M., et al. (2020). Synergistic effect of fasting-mimicking diet and vitamin C against KRAS mutated cancers. *Nat. Commun.* 11, 2332. doi:10.1038/s41467-020-16243-3

Dixon, S. j., Lemberg, K. m., Lamprecht, M. r., Skouta, R., Zaitsev, E. m., Gleason, C. e., et al. (2012). Ferroptosis: an iron-dependent form of nonapoptotic cell death. *Cell* 149, 1060–1072. doi:10.1016/j.cell.2012.03.042

Dyall, S. C., Balas, L., Bazan, N. G., Brenna, J. T., Chiang, N., Da Costa Souza, F., et al. (2022). Polyunsaturated fatty acids and fatty acid-derived lipid mediators: recent advances in the understanding of their biosynthesis, structures, and functions. *Prog. Lipid Res.* 86, 101165. doi:10.1016/j.plipres.2022.101165

Fang, Y., Chen, X., Tan, Q., Zhou, H., Xu, J., and Gu, Q. (2021). Inhibiting ferroptosis through disrupting the NCOA4–FTH1 interaction: a new mechanism of action. *ACS Cent. Sci.* 7, 980–989. doi:10.1021/acscentsci.0c01592

Fei, J., Dai, L., Gao, F., Zhao, J., and Li, J. (2019). Assembled vitamin B2 nanocrystals with optical waveguiding and photosensitizing properties for potential biomedical application. *Angew. Chem. Int. Ed. Engl.* 58, 7254–7258. doi:10.1002/anie.201900124

Gan, B. (2022). ACSL4, PUFA, and ferroptosis: new arsenal in anti-tumor immunity. *Signal Transduct. Target Ther.* 7, 128. doi:10.1038/s41392-022-01004-z

Gan, H., Huang, X., Luo, X., Li, J., Mo, B., Cheng, L., et al. (2023). A mitochondria-targeted ferroptosis inducer activated by glutathione-responsive imaging and depletion for triple negative breast cancer theranostics. *Adv. Healthc. Mater* 12, e2300220. doi:10.1002/adhm.202300220

Gong, Y., Fan, Z., Luo, G., Yang, C., Huang, Q., Fan, K., et al. (2019). The role of necroptosis in cancer biology and therapy. *Mol. Cancer* 18, 100. doi:10.1186/s12943-019-1029-8

Hashidate-Yoshida, T., Harayama, T., Hishikawa, D., Morimoto, R., Hamano, F., Tokuoka, S. M., et al. (2015). Fatty acid remodeling by LPCAT3 enriches arachidonate in phospholipid membranes and regulates triglyceride transport. *Elife* 4, e06328. doi:10.7554/eLife.06328

Hassannia, B., Vandenabeele, P., and Vanden Berghe, T. (2019). Targeting ferroptosis to iron out cancer. *Cancer Cell* 35, 830–849. doi:10.1016/j.ccell.2019.04.002

Hou, X., Zhang, X., Zhao, W., Zeng, C., Deng, B., Mccomb, D. W., et al. (2020). Vitamin lipid nanoparticles enable adoptive macrophage transfer for the treatment of multidrug-resistant bacterial sepsis. *Nat. Nanotechnol.* 15, 41–46. doi:10.1038/s41565-019-0600-1

Hu, Q., Zhang, Y., Lou, H., Ou, Z., Liu, J., Duan, W., et al. (2021). GPX4 and vitamin E cooperatively protect hematopoietic stem and progenitor cells from lipid peroxidation and ferroptosis. *Cell Death Dis.* 12, 706. doi:10.1038/s41419-021-04008-9

Jiang, X., Stockwell, B. R., and Conrad, M. (2021). Ferroptosis: mechanisms, biology and role in disease. *Nat. Rev. Mol. Cell Biol.* 22, 266–282. doi:10.1038/s41580-020-00324-8

Kagan, V. E., Mao, G., Qu, F., Angeli, J. P. F., Doll, S., Croix, C. S., et al. (2016). Oxidized arachidonic and adrenic PEs navigate cells to ferroptosis. *Nat. Chem. Biol.* 13, 81–90. doi:10.1038/nchembio.2238

Kennedy, D. (2016). B vitamins and the brain: mechanisms, dose and efficacy-A review. *Nutrients* 8, 68. doi:10.3390/nu8020068

Kerr, J. F. R., Wyllie, A. H., and Currie, A. R. (1972). Apoptosis: a basic biological phenomenon with wideranging implications in tissue kinetics. *Br. J. Cancer* 26, 239–257. doi:10.1038/bjc.1972.33

Kolbrink, B., Von Samson-Himmelstjerna, F. A., Messtorff, M. L., Riebeling, T., Nische, R., Schmitz, J., et al. (2022). Vitamin K1 inhibits ferroptosis and counteracts a detrimental effect of phenprocoumon in experimental acute kidney injury. *Cell Mol. Life Sci.* 79, 387. doi:10.1007/s00018-022-04416-w

Koppula, P., Zhang, Y., Zhuang, L., and Gan, B. (2018). Amino acid transporter SLC7A11/xCT at the crossroads of regulating redox homeostasis and nutrient dependency of cancer. *Cancer Commun.* 38, 12. doi:10.1186/s40880-018-0288-x

Koppula, P., Zhuang, L., and Gan, B. (2021). Cystine transporter SLC7A11/xCT in cancer: ferroptosis, nutrient dependency, and cancer therapy. *Protein & Cell* 12, 599–620. doi:10.1007/s13238-020-00789-5

Lee, J., and Roh, J.-L. (2022). SLC7A11 as a gateway of metabolic perturbation and ferroptosis vulnerability in cancer. *Antioxidants* 11, 2444. doi:10.3390/antiox11122444

Lei, G., Zhuang, L., and Gan, B. (2022). Targeting ferroptosis as a vulnerability in cancer. *Nat. Rev. Cancer* 22, 381–396. doi:10.1038/s41568-022-00459-0

Liang, C., Zhang, X., Yang, M., and Dong, X. (2019). Recent progress in ferroptosis inducers for cancer therapy. *Adv. Mater* 31, e1904197. doi:10.1002/adma.201904197

Liang, D., Minikes, A. M., and Jiang, X. (2022). Ferroptosis at the intersection of lipid metabolism and cellular signaling. *Mol. Cell* 82, 2215–2227. doi:10.1016/j.molcel.2022.03.022

Lin, L., Wang, S., Deng, H., Yang, W., Rao, L., Tian, R., et al. (2020). Endogenous labile iron pool-mediated free radical generation for cancer chemodynamic therapy. *J. Am. Chem. Soc.* 142, 15320–15330. doi:10.1021/jacs.0c05604

Lindschinger, M., Tatzber, F., Schimetta, W., Schmid, I., Lindschinger, B., Cvirn, G., et al. (2019). A randomized pilot trial to evaluate the bioavailability of natural versus synthetic vitamin B complexes in healthy humans and their effects on homocysteine, oxidative stress, and antioxidant levels. *Oxid. Med. Cell Longev.* 2019, 6082613. doi:10.1155/2019/6082613

Liu, Y., Huang, P., Li, Z., Xu, C., Wang, H., Jia, B., et al. (2022). Vitamin C sensitizes pancreatic cancer cells to erastin-induced ferroptosis by activating the AMPK/Nrf2/HMOX1 pathway. *Oxid. Med. Cell Longev.* 2022, 5361241. doi:10.1155/2022/5361241

Magrì, A., Germano, G., Lorenzato, A., Lamba, S., Chilà, R., Montone, M., et al. (2020). High-dose vitamin C enhances cancer immunotherapy. *Sci. Transl. Med.* 12, eaay8707. doi:10.1126/scitranslmed.aay8707

Mishima, E., Ito, J., Wu, Z., Nakamura, T., Wahida, A., Doll, S., et al. (2022). A non-canonical vitamin K cycle is a potent ferroptosis suppressor. *Nature* 608, 778–783. doi:10.1038/s41586-022-05022-3

Mou, Y., Wang, J., Wu, J., He, D., Zhang, C., Duan, C., et al. (2019). Ferroptosis, a new form of cell death: opportunities and challenges in cancer. *J. Hematol. Oncol.* 12, 34. doi:10.1186/s13045-019-0720-y

Ngo, B., Van Riper, J. M., Cantley, L. C., and Yun, J. (2019). Targeting cancer vulnerabilities with high-dose vitamin C. *Nat. Rev. Cancer* 19, 271–282. doi:10.1038/s41568-019-0135-7

Ou, J., Zhu, X., Chen, P., Du, Y., Lu, Y., Peng, X., et al. (2020). A randomized phase II trial of best supportive care with or without hyperthermia and vitamin C for heavily pretreated, advanced, refractory non-small-cell lung cancer. *J. Adv. Res.* 24, 175–182. doi:10.1016/j.jare.2020.03.004

Peh, H. Y., Tan, W. S., Liao, W., and Wong, W. S. (2016). Vitamin E therapy beyond cancer: tocopherol versus tocotrienol. *Pharmacol. Ther.* 162, 152–169. doi:10.1016/j.pharmthera.2015.12.003

Peng, F., Liao, M., Qin, R., Zhu, S., Peng, C., Fu, L., et al. (2022). Regulated cell death (RCD) in cancer: key pathways and targeted therapies. *Signal Transduct. Target. Ther.* 7, 286. doi:10.1038/s41392-022-01110-y

Peterson, C. T., Rodionov, D. A., Osterman, A. L., and Peterson, S. N. (2020). B vitamins and their role in immune regulation and cancer. *Nutrients* 12, 3380. doi:10.3390/nu12113380

Qi, Y., Zhang, X., Wu, Z., Tian, M., Chen, F., Guan, W., et al. (2021). Ferroptosis regulation by nutrient signalling. *Nutr. Res. Rev.* 35, 282–294. doi:10.1017/S0954422421000226

Qin, S., Wang, Y., Li, L., Liu, J., Xiao, C., Duan, D., et al. (2022). Early-life vitamin B12 orchestrates lipid peroxidation to ensure reproductive success via SBP-1/SREBP1 in *Caenorhabditis elegans*. *Cell Rep.* 40, 111381. doi:10.1016/j.celrep.2022.111381

Riegman, M., Sagie, L., Galed, C., Levin, T., Steinberg, N., Dixon, S. J., et al. (2020). Ferroptosis occurs through an osmotic mechanism and propagates independently of cell rupture. *Nat. Cell Biol.* 22, 1042–1048. doi:10.1038/s41556-020-0565-1

Rizzollo, F., More, S., Vangheluwe, P., and Agostinis, P. (2021). The lysosome as a master regulator of iron metabolism. *Trends Biochem. Sci.* 46, 960–975. doi:10.1016/j.tibs.2021.07.003

Saghiri, M. A., Asatourian, A., Ershadifar, S., Moghadam, M. M., and Sheibani, N. (2017). Vitamins and regulation of angiogenesis: [A, B1, B2, B3, B6, B9, B12, C, D, E, K]. *J. Funct. Foods* 38, 180–196. doi:10.1016/j.jff.2017.09.005

Shearer, M. J., and Okano, T. (2018). Key pathways and regulators of vitamin K function and intermediary metabolism. *Annu. Rev. Nutr.* 38, 127–151. doi:10.1146/annurev-nutr-082117-051741

Sies, H. (2021). Oxidative eustress: on constant alert for redox homeostasis. *Redox Biol.* 41, 101867. doi:10.1016/j.redox.2021.101867

Snaebjornsson, M. T., Janaki-Raman, S., and Schulze, A. (2020). Greasing the wheels of the cancer machine: the role of lipid metabolism in cancer. *Cell Metab.* 31, 62–76. doi:10.1016/j.cmet.2019.11.010

Soula, M., Weber, R. A., Zilka, O., Alwaseem, H., La, K., Yen, F., et al. (2020). Metabolic determinants of cancer cell sensitivity to canonical ferroptosis inducers. *Nat. Chem. Biol.* 16, 1351–1360. doi:10.1038/s41589-020-0613-y

Stockwell, B. R., Jiang, X., and Gu, W. (2020). Emerging mechanisms and disease relevance of ferroptosis. *Trends Cell Biol.* 30, 478–490. doi:10.1016/j.tcb.2020.02.009

Stoyanovsky, D. A., Tyurina, Y. Y., Shrivastava, I., Bahar, I., Tyurin, V. A., Protchenko, O., et al. (2019). Iron catalysis of lipid peroxidation in ferroptosis: regulated enzymatic or random free radical reaction? *Free Radic. Biol. Med.* 133, 153–161. doi:10.1016/j.freeradbiomed.2018.09.008

Szarka, A., Kapuy, O., Lőrincz, T., and Bánhegyi, G. (2021). Vitamin C and cell death. *Antioxid. Redox Signal.* 34, 831–844. doi:10.1089/ars.2019.7897

Tang, D., Chen, X., Kang, R., and Kroemer, G. (2020). Ferroptosis: molecular mechanisms and health implications. *Cell Res.* 31, 107–125. doi:10.1038/s41422-020-00441-1

Tang, D., Kang, R., Berghe, T. V., Vandenabeele, P., and Kroemer, G. (2019). The molecular machinery of regulated cell death. *Cell Res.* 29, 347–364. doi:10.1038/s41422-019-0164-5

Tardy, A. L., Pouteau, E., Marquez, D., Yilmaz, C., and Scholey, A. (2020). Vitamins and minerals for energy, fatigue and cognition: a narrative review of the biochemical and clinical evidence. *Nutrients* 12, 228. doi:10.3390/nu12010228

Tong, X., Tang, R., Xiao, M., Xu, J., Wang, W., Zhang, B., et al. (2022). Targeting cell death pathways for cancer therapy: recent developments in necroptosis, pyroptosis, ferroptosis, and cuproptosis research. *J. Hematol. Oncol.* 15, 174. doi:10.1186/s13045-022-01392-3

Von Krusenstiern, A. N., Robson, R. N., Qian, N., Qiu, B., Hu, F., Reznik, E., et al. (2023). Identification of essential sites of lipid peroxidation in ferroptosis. *Nat. Chem. Biol.* 19, 719–730. doi:10.1038/s41589-022-01249-3

Wallin, R., and Hutson, S. M. (2004). Warfarin and the vitamin K-dependent gamma-carboxylation system. *Trends Mol. Med.* 10, 299–302. doi:10.1016/j.molmed.2004.05.003

Wang, L., Fu, H., Song, L., Wu, Z., Yu, J., Guo, Q., et al. (2022). Overcoming AZD9291 resistance and metastasis of NSCLC via ferroptosis and multitarget interference by nanocatalytic sensitizer plus AHP-DRI-12. *Small* 19, e2204133. doi:10.1002/smll.202204133

Wang, R., Hu, Q., Wang, H., Zhu, G., Wang, M., Zhang, Q., et al. (2021a). Identification of Vitamin K3 and its analogues as covalent inhibitors of SARS-CoV-2 3CL(pro). *Int. J. Biol. Macromol.* 183, 182–192. doi:10.1016/j.ijbiomac.2021.04.129

Wang, W., Jin, Y., Xu, Z., Liu, X., Bajwa, S. Z., Khan, W. S., et al. (2020). Stimuli-activatable nanomedicines for chemodynamic therapy of cancer. *Wiley Interdiscip. Rev. Nanomed Nanobiotechnol* 12, e1614. doi:10.1002/wnan.1614

Wang, X., Xu, S., Zhang, L., Cheng, X., Yu, H., Bao, J., et al. (2021b). Vitamin C induces ferroptosis in anaplastic thyroid cancer cells by ferritinophagy activation. *Biochem. Biophys. Res. Commun.* 551, 46–53. doi:10.1016/j.bbrc.2021.02.126

Wellington, K. W., Hlatshwayo, V., Kolesnikova, N. I., Saha, S. T., Kaur, M., and Motadi, L. R. (2020). Anticancer activities of vitamin K3 analogues. *Invest. New Drugs* 38, 378–391. doi:10.1007/s10637-019-00855-8

Welsh, J., Bak, M. J., and Narvaez, C. J. (2022). New insights into vitamin K biology with relevance to cancer. *Trends Mol. Med.* 28, 864–881. doi:10.1016/j.molmed.2022.07.002

White, E. (2015). The role for autophagy in cancer. *J. Clin. Invest.* 125, 42–46. doi:10.1172/JCI73941

Wu, Y., Zhang, S., Gong, X., Tam, S., Xiao, D., Liu, S., et al. (2020). The epigenetic regulators and metabolic changes in ferroptosis-associated cancer progression. *Mol. Cancer* 19, 39. doi:10.1186/s12943-020-01157-x

Xiong, Y., Xiao, C., Li, Z., and Yang, X. (2021). Engineering nanomedicine for glutathione depletion-augmented cancer therapy. *Chem. Soc. Rev.* 50, 6013–6041. doi:10.1039/D0CS00718H

Yang, G. G., Zhang, H., Zhang, D. Y., Cao, Q., Yang, J., Ji, L. N., et al. (2018). Cancer-specific chemotherapeutic strategy based on the vitamin K3 mediated ROS regenerative feedback and visualized drug release *in vivo*. *Biomaterials* 185, 73–85. doi:10.1016/j.biomaterials.2018.08.065

Yang, W. s., Sriramaratnam, R., Welsch, M. e., Shimada, K., Skouta, R., Viswanathan, V. s., et al. (2014). Regulation of ferroptotic cancer cell death by GPX4. *Cell* 156, 317–331. doi:10.1016/j.cell.2013.12.010

Yang, W. S., and Stockwell, B. R. (2016). Ferroptosis: death by lipid peroxidation. *Trends Cell Biol.* 26, 165–176. doi:10.1016/j.tcb.2015.10.014

Yu, B., Choi, B., Li, W., and Kim, D.-H. (2020). Magnetic field boosted ferroptosis-like cell death and responsive MRI using hybrid vesicles for cancer immunotherapy. *Nat. Commun.* 11, 3637. doi:10.1038/s41467-020-17380-5

Yu, P., Zhang, X., Liu, N., Tang, L., Peng, C., and Chen, X. (2021). Pyroptosis: mechanisms and diseases. *Signal Transduct. Target. Ther.* 6, 128. doi:10.1038/s41392-021-00507-5

Zhang, C., Liu, Z., Zhang, Y., Ma, L., Song, E., and Song, Y. (2020a). Iron free" zinc oxide nanoparticles with ion-leaking properties disrupt intracellular ROS and iron homeostasis to induce ferroptosis. *Cell Death Dis.* 11, 183. doi:10.1038/s41419-020-2384-5

Zhang, S., Xin, W., Anderson, G. J., Li, R., Gao, L., Chen, S., et al. (2022a). Double-edge sword roles of iron in driving energy production versus instigating ferroptosis. *Cell Death Dis.* 13, 40. doi:10.1038/s41419-021-04490-1

Zhang, X., Wu, S., Guo, C., Guo, K., Hu, Z., Peng, J., et al. (2022b). Vitamin E exerts neuroprotective effects in pentylenetetrazole kindling epilepsy via suppression of ferroptosis. *Neurochem. Res.* 47, 739–747. doi:10.1007/s11064-021-03483-y

Zhang, Z., Ding, Y., Li, J., Wang, L., Xin, X., Yan, J., et al. (2020b). Versatile iron-vitamin K3 derivative-based nanoscale coordination polymer augments tumor ferroptotic therapy. *Nano Res.* 14, 2398–2409. doi:10.1007/s12274-020-3241-7

Zhou, H., Chen, J., Fan, M., Cai, H., Dong, Y., Qiu, Y., et al. (2023a). KLF14 regulates the growth of hepatocellular carcinoma cells via its modulation of iron homeostasis through the repression of iron-responsive element-binding protein 2. *J. Exp. Clin. Cancer Res.* 42, 5. doi:10.1186/s13046-022-02562-4

Zhou, M., Yuan, M., Jin, Y., Zhou, Q., Yu, Y., Li, J., et al. (2023b). Vitamin B2-based ferroptosis promoter for sono-enhanced nanocatalytic therapy of triple-negative breast cancer. *Adv. Funct. Mater.* 33. doi:10.1002/adfm.202303899

Zhu, L., You, Y., Zhu, M., Song, Y., Zhang, J., Hu, J., et al. (2022). Ferritin-hijacking nanoparticles spatiotemporally directing endogenous ferroptosis for synergistic anticancer therapy. *Adv. Mater* 34, e2207174. doi:10.1002/adma.202207174

frontiers | Frontiers in Pharmacology

TYPE Case Report
PUBLISHED 13 August 2024
DOI 10.3389/fphar.2024.1431542

Check for updates

OPEN ACCESS

EDITED BY
Francesco Pepe,
University of Naples Federico II, Italy

REVIEWED BY
Jan Trøst Jørgensen,
Dx-Rx Institute, Denmark
Alessandro Rizzo,
National Cancer Institute Foundation (IRCCS), Italy

*CORRESPONDENCE
Xin Wang,
wangxin213@sina.com

†These authors have contributed equally to this work

RECEIVED 12 May 2024
ACCEPTED 29 July 2024
PUBLISHED 13 August 2024

CITATION
Huang P, Wen F and Wang X (2024) Case report: Pyrotinib and tegafur combined with radiotherapy achieved notable response in HER2-amplified rectal cancer with multiple metastases after multiline treatments.
Front. Pharmacol. 15:1431542.
doi: 10.3389/fphar.2024.1431542

COPYRIGHT
© 2024 Huang, Wen and Wang. This is an open-access article distributed under the terms of the Creative Commons Attribution License (CC BY). The use, distribution or reproduction in other forums is permitted, provided the original author(s) and the copyright owner(s) are credited and that the original publication in this journal is cited, in accordance with accepted academic practice. No use, distribution or reproduction is permitted which does not comply with these terms.

Case report: Pyrotinib and tegafur combined with radiotherapy achieved notable response in HER2-amplified rectal cancer with multiple metastases after multiline treatments

Peng Huang[1,2†], Feng Wen[1,3†] and Xin Wang[1,3*]

[1]Division of Abdominal Tumor Multimodality Treatment, Cancer Center, West China Hospital, Sichuan University, Chengdu, Sichuan, China, [2]Department of Medical Oncology, Cancer Center, West China Hospital, Sichuan University, Chengdu, Sichuan, China, [3]Department of Radiation Oncology, Cancer Center, West China Hospital, Sichuan University, Chengdu, Sichuan, China

Metastatic colorectal cancer (mCRC) is characterized by significant phenotypic heterogeneity at the molecular level and presents a poor prognosis. Chemotherapy is commonly employed as the primary treatment option. Nevertheless, the advantages of chemotherapy are constrained, underscoring the critical necessity for novel treatment protocols aimed at enhancing patient outcomes. Human epidermal growth factor receptor 2 (HER2) has been recognized as a promising therapeutic target in mCRC. Pyrotinib, an innovative irreversible dual tyrosine kinase inhibitor targeting HER2, effectively inhibits cancer progression in various types of human cancers. Here, we present a case of a 39-year-old female with metastatic rectal cancer showing amplification of HER2. Despite resistance to multiple therapies, including trastuzumab and pertuzumab, the patient exhibited a remarkable therapeutic response to pyrotinib, tegafur combined with radiotherapy. This case provides evidence for the feasibility and potential efficacy of deploying pyrotinib in the salvage treatment of mCRC patients with HER2 amplification even though resistant to other anti-HER2 drugs.

KEYWORDS

rectal cancer, HER2, pyrotinib, multiline treatments, radiotherapy

1 Introduction

Colorectal cancer (CRC) represents a significant contributor to cancer-related morbidity and mortality worldwide, with rectal cancer cases estimated to be 46,220 in the United States (Shin et al., 2023; Siegel et al., 2024). Approximately 25%–40% of rectal cancer patients are represented with distant metastases at initial diagnosis, which is the primary cause of therapy failure (van Gijn et al., 2011; Fokas et al., 2014). Rectal cancer holds a high potential for metastasizing to the liver, lung, and bone (He et al., 2023). Brain metastases represent the most prevalent type of intracranial tumors in adults, yet they infrequently originate from rectal cancer (Boire et al., 2020).

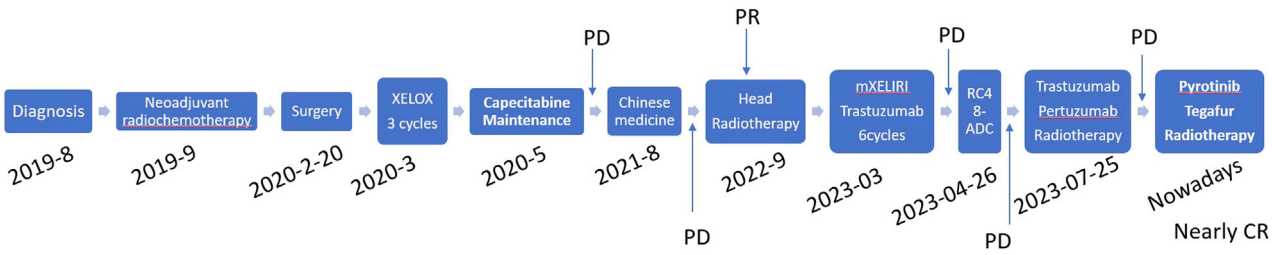

FIGURE 1
Time diagram of the treatment from August 2019 to May 2024 of the patient. PD, progressive disease; CR, complete response.

Multidrug combination regimens such as FOLFOX and FOLFIRI have been recognized as standard therapies for metastatic rectal cancer (Biller and Schrag, 2021). Nevertheless, chemotherapy has significant ceiling effects in the context of long-term toxic events and multi-drug resistance (Kim, 2015). In recent years, advances in comprehending the molecular and genetic complexities of cancer have paved the way for introducing more effective treatment modalities into the later-line treatments for rectal cancer, out of which molecularly targeted therapy has been well-characterized and plays a crucial role in clinical management (Ohishi et al., 2023).

Human epidermal growth factor receptor 2 (HER2), encoded by the oncogene *ERBB2*, belongs to the epidermal growth factor receptor (EGFR) family (Oh and Bang, 2020). Many other solid tumors exhibit high levels of HER2 expression, including gastric cancer, urothelial carcinoma, lung cancer and biliary tract cancer (BTC), and anti-HER2 drugs have exhibited great therapeutic benefits in clinical settings (Lamberti et al., 2020; Mollica et al., 2020; Ricci et al., 2021; Rizzo et al., 2021). For example, in the global basket study SUMMIT, for nine patients with ERBB2-mutated BTC, the overall response rate (ORR) was 22% (Hyman et al., 2018). Additionally, a partial response (PR) was observed in a patient with HER2-amplified gallbladder cancer in a phase I study with the HER2-targeted bispecific antibody ZW2567 (Oh and Bang, 2020). Evidence has revealed that HER2 amplification comprises approximately 2%–11% of metastatic CRC (mCRC) patients with poor prognosis (Greally et al., 2018). The potent antitumor activity of HER2-targeted inhibitors on patients with HER2 amplification has been presented (Greally et al., 2018). Regarding evidence from clinical guidelines, trastuzumab plus pertuzumab has been recommended as the late-line treatment for HER2-amplified metastatic CRC that becomes refractory to chemotherapy (Meric-Bernstam et al., 2019). Pyrotinib is an orally administered, irreversible tyrosine kinase inhibitor (TKI) of the pan-ErbB receptor, which has been authorized for the therapy of HER2-amplified breast cancer in recurrent and neoadjuvant settings (Blair, 2018). Moreover, it exerts a potent antitumor effect in other HER2-amplified solid tumors including lung cancer and gastric cancer (Li et al., 2017; Blair, 2018; Niu et al., 2023). Herein, we report a rare case of rectal cancer harboring HER2 amplification with multiple metastases in the brain, scalp, lung, pancreatic head, and both kidneys, who has been treated with standard chemotherapy and several HER2 inhibitors, finally achieved notable response (nearly complete response) from pyrotinib and tegafur combined with radiotherapy (Figure 1).

2 Case presentation

In August 2019, a 39-year-old female patient was admitted to our hospital presenting with a constellation of intestinal symptoms including changes in stool consistency, bloody stool, and tenesmus. The patient was diagnosed with pulmonary tuberculosis 10 years ago. After undergoing anti-tuberculosis treatment, the condition improved. In addition, the patient has no history of smoking or alcohol consumption and has no family history of malignant or genetic diseases. After being seen by the attending physician, the patient underwent further relevant examinations. Whole-abdominal enhanced CT has revealed a lobulated soft tissue mass of 3.0 cm × 2.2 cm in the rectal wall. Chest CT showed bilateral old pulmonary tuberculosis. Then, the patient underwent a proctoscopy and biopsy. At a distance of 3–6 cm from the anal verge, an ulcerative-type neoplasm is observed, with a congested and ulcerated base, surrounded by mucosal ramparts resembling a dam, involving approximately half of the circumference of the lumen, leading to relative luminal narrowing. The histopathologic examination revealed high-grade intraepithelial neoplasia and mucosal intraepithelial carcinoma formation. The tumor stage was cT3N0M0. Then the patient accepted a neoadjuvant chemo-radiotherapy regimen comprising four treatment cycles of mFOLFOX6 (oxaliplatin, leucovorin, and fluorouracil), one treatment cycle of XELOX, (oxaliplatin and capecitabine) along with external irradiation with a dosage of 50.4Gy/28f. After that, an imaging examination revealed the significant shrinkage of the tumor.

On 20 February 2020, the patient underwent low anterior resection for rectal cancer. Postoperative histological examination confirmed the diagnosis of moderately differentiated adenocarcinoma of the rectum, pT3N0M0, TRG2. Immunohistochemical analyses suggested "*MLH1* (+), *MSH2* (+), *MSH6* (+), *PMS2* (+), Ki–67:50%." After surgery, three cycles of the mFOLFOX6 regimen were given in the adjuvant chemotherapy setting. Then, capecitabine maintenance therapy was followed in December 2020. Subsequent regular follow-ups showed no progression of the disease.

In August 2021, the countercheck of chest CT showed several bilateral pulmonary nodules, while the biggest one was in the upper lobe of the right lung near the mediastinal soft tissue, which was about 1.8 cm × 1.5 cm in size, suggesting tumor metastasis. Palliative chemotherapy with mFOLFOX6 regimen was given for one cycle and the patient spontaneously discontinued the treatment. After that, the patient received treatment with Chinese herbs and was lost

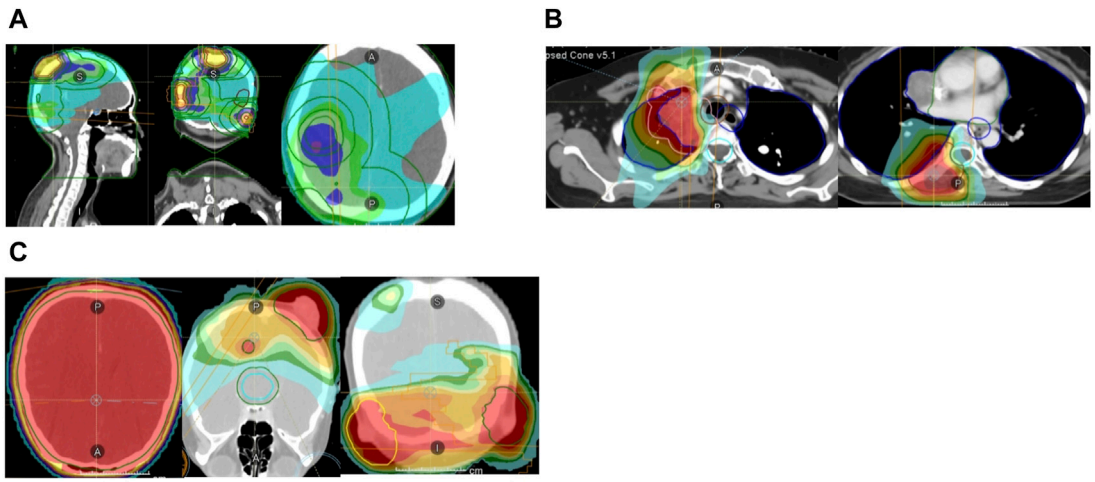

FIGURE 2
(A) Brain and scalp radiotherapy plans (51Gy/17f). **(B)** Mediastinum and vertebral body radiotherapy plans (mediastinum: 56Gy/8f, vertebral body: 40Gy/5f). **(C)** Whole brain radiotherapy (24Gy/8f) and additional dose of all intracranial and scalp lesions (24Gy/8f).

TABLE 1 Gene alterations of the NGS results based on the metastatic scalp specimens.

Genes	Variations	Copy number/abundance
KRAS	Negative	—
NRAS	Negative	—
BRAFV600E	Negative	—
NTRK2	Negative	—
NTRK3	Negative	—
MLH1	Negative	—
MSH2	Negative	—
MSH6	Negative	—
PMS2	Negative	—
RNF43	NM_017763.4 C.953-1GsT amplification	42%
ERBB2	NM_004448.2 amplification	66.8
FGFR1	NM_023110.2 amplification	5.2
MCL1	NM 021960.4 amplification	4.0
CDK6	NM_001145306.1 amplification	3.0
EGFR	NM_005228.3 amplification	3.0
RAD50	NM_005732.3 deficiency	1.4
WRN	NM_000553.4 deficiency	1.4

KRAS, kirsten rat sarcoma viral oncogene homolog; NRAS, neuroblastoma rat sarcoma viral oncogene homolog; BRAF, v-raf murine sarcoma viral oncogene homolog B1; HER2, human epidermal growth factor receptor 2; NTRK1, neurotrophic tyrosine kinase, receptor, type 1; FGFR1, fibroblast growth factor receptor 1; MCL1, myeloid cell leukemia-1; CDK6, cyclin-dependent kinase 6; EGFR, epidermal growth factor receptor; NGS, next-generation sequencing.

to follow-up. From March to June 2022, the patient continued to grow three masses on the scalp which were mistaken for abscesses by herself, and did not receive proper treatment. Then, a constellation of symptoms including intermittent head pain, nausea, vomiting, fatigue, left upper limb and facial twitches were presented. In August 2022, the patient was admitted to our hospital again. Enhanced CT revealed multiple nodules in the parieto-occipital regions and the largest one is about 2.5 cm × 1.5 cm accompanied by significantly

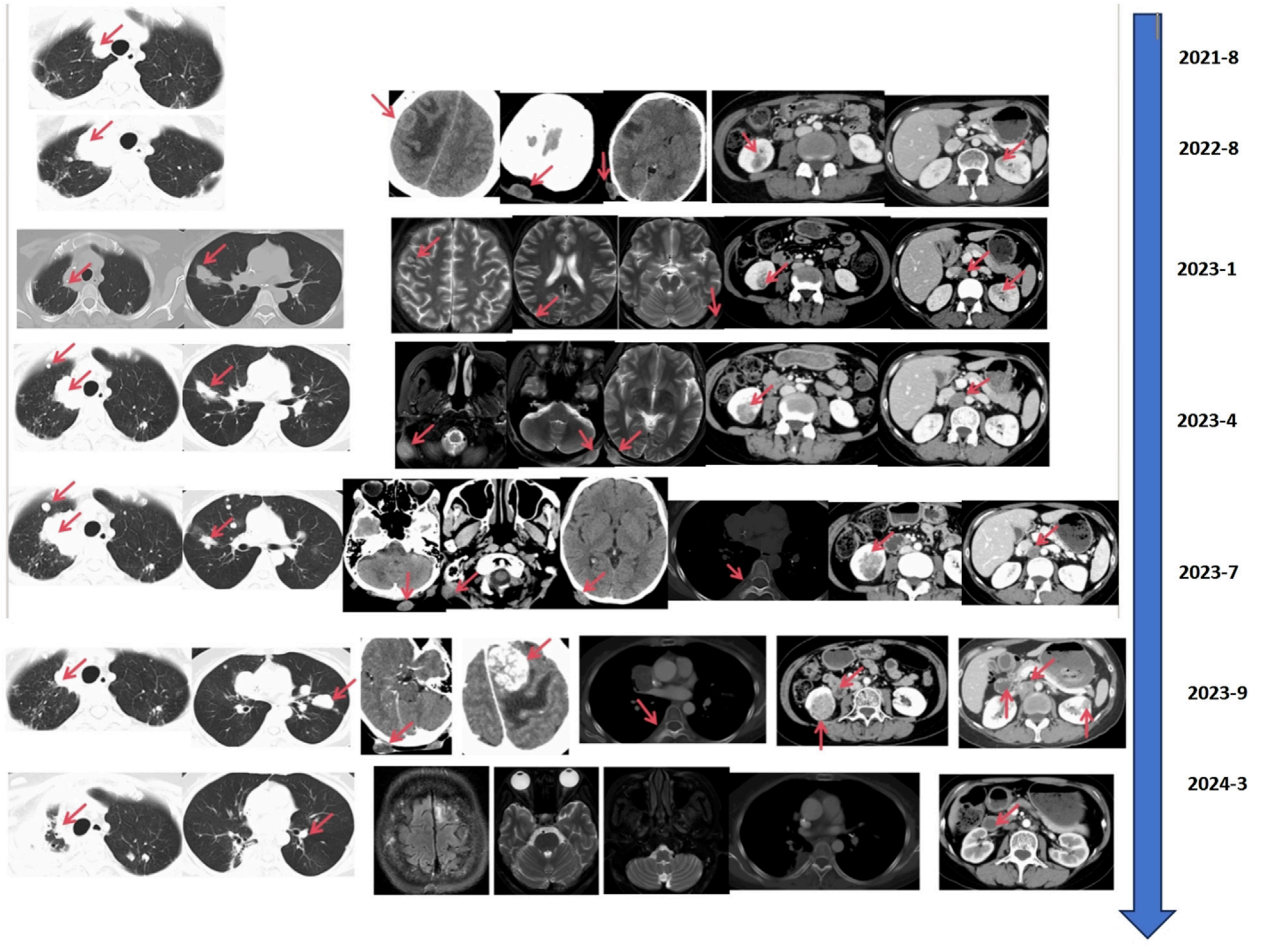

FIGURE 3
Clinical images of the patient.

increased tumor markers (CA199 > 1,000 U/mL, CEA >83.7 U/mL). Moreover, a 2.0 cm × 1.6 cm metastatic node was found in the right frontal cortex. Besides that, metastatic signs were found in both kidneys and the head of the pancreas and the metastatic lesion in the right upper lobe of the lung has increased in size compared to previous CT images. Biopsy of scalp metastases showed that skin metastases tended to originate from rectal cancer. Further immunohistochemistry showed *CK20* (+), *CDX2* (+), *CK7* (−), *CK5/6* (−), *TIF-1* (−), Ki–67: 80% and *HER2* diffuse positive. Capecitabine following the head radiotherapy (51Gy/17f) was performed (Figure 2A). After radiotherapy, the symptoms of headache and limb twitching have significantly improved. The CT re-examination revealed the shrunk tumor mass both in the scalp and brain, which indicated a great therapeutic response to radiotherapy. Then, the next-generation sequencing (NGS) (1,021 genes; Chengdu Huachuang Qide Medical laboratory Co., LTD., Chengdu, China) based on scalp specimens revealed the *HER2* amplification (copy number: 66.8), while *RAS* and *BRAF* were negative. The detailed results are listed in Table 1. Based on the NGS results, the second-line regime: six treatment cycles of mXELIRI (Irinotecan and capecitabin) combined with trastuzumab was initiated on 28 October 2022. The patient tolerated this new regime well, with no apparent side effects. During treatment, the best therapeutic effect is PR. In April 2023, progressive disease was evaluated based on the imaging manifestations of enlarged nodules of the lung, pancreatic head, centrum of the 7th thoracic vertebrae, right kidney and scalp, while paraaortic lymph node metastasis was also presented. The patient volunteered for a Phase II clinical study and was treated with six cycles of RC48-ADC on 26 April 2023. The RC48-ADC represents a new antibody-drug conjugate (ADC) targeting HER2, which specifically transports the cytotoxic compound monomethyl auristatin E (MMAE) to HER2-positive tumor cells (Hong et al., 2023). Previous clinical trials have demonstrated its good tolerability and potential effectiveness in HER2-positive advanced bladder cancer (Sheng et al., 2021; Hong et al., 2023). The disease condition was stable during treatment. Reexaminations from July 2023 indicated the progression of lung and scalp lesions along with hoarseness and back pain. Then the patient was withdrawn from the clinical trial. In August 2023, the patient received trastuzumab + pertuzumab, followed by mediastinal and pyramidal radiotherapy with a dosage of 56Gy/8f, and 40Gy/5f respectively (Figure 2B). However, the enhanced CT examination revealed obvious enlargement of the scalp tumor in September 2023. Then tegafur, pyrotinib combined with head radiotherapy (48Gy/16f) was recommended by the oncologists in October 2023 (Figure 2C).

Notably, follow-up examination revealed significant shrinkage of scalp and brain metastases. Besides, the multiple metastases in the lung, pancreatic head, both kidneys and paraaortic lymph nodes were also dramatically shrunk (Figure 3). Until the submission of the case report, the patient had survived for over 33 months since post-operative recurrence and now continues to receive the combination treatment of pyrotinib and tegafur and a notable response (nearly complete response in brain and scalp metastases) had been achieved. Currently, close follow-up is still underway.

3 Discussion

HER2, encoded by the *ERBB2* gene, will be overexpressed when the *ERBB2* gene is amplified (Oh and Bang, 2020). *HER2* serves as a significant oncogenic driver in mCRC (Chitkara et al., 2023). Regimens involving dual anti-HER2 drugs have shown significant antitumor activity in the relapsed setting (Chitkara et al., 2023). The regime of trastuzumab in conjunction with lapatinib achieved an objective response in 8 (30%) of 27 patients with *HER2* amplification and *KRAS* exon 2 wild-type tumors in the HERACLES-A trail (Sartore-Bianchi et al., 2016). Notably, the median OS and PFS of 46 weeks (95% CI 33–68 weeks) and 21 weeks (95% CI 16–32 weeks) (Sartore-Bianchi et al., 2016). Nevertheless, almost all cases that achieved an objective response in this study developed acquired resistance, mirroring the dilemma observed in the Mypathway study (Sartore-Bianchi et al., 2016; Meric-Bernstam et al., 2019). Mypathway was a multiple-basket phase II study that assessed the antitumor activity of the regime of trastuzumab in combination with pertuzumab in patients with solid tumors (Meric-Bernstam et al., 2019). This study included 69 CRC patients with *KRAS* wild-type and *HER2*-overexpressed tumors, out of which 22 (31.9%) achieved objective responses. However, in the setting of *KRAS*-mutant CRC, the ORR was only 8%, which indicated the limited antitumor activity of trastuzumab plus pertuzumab (Meric-Bernstam et al., 2019). Trastuzumab deruxtecan is an antibody–drug conjugate that has been approved in metastatic, HER2-overexpressed gastric and breast cancer in the United States (Jørgensen, 2023). The DESTINY-CRC01 study was a signal arm, phase II clinical trial that demonstrated the clinical benefits of trastuzumab deruxtecan in 78 patients with RAS wild-type and HER2-expressed mCRC (Siena et al., 2021). Patients with HER2 3+ status received the highest ORR of 57.5% (95% CI 40.9–73.0) (Siena et al., 2021). Interestingly, the ORRs of trastuzumab deruxtecan treatment in patients with or without prior anti-HER2 therapy were 43.8% and 45.9% respectively, which showed the rationality of applying trastuzumab deruxtecan in the later line treatment after prior anti-HER2 treatment (Siena et al., 2021). Moreover, the multicenter DESTINY-CRC02 trial further assessed the antitumor response of trastuzumab deruxtecan in HER2-amplified mCRC patients (NCT04744831) (Zheng-Lin et al., 2023).

Although the anti-HER2 regime exhibits great value in cancer therapy, however, the drug resistance impedes its clinical application. It is acknowledged that *EGFR* and *HER2* activate the *RAS/RAF/ERK* pathway to promote cell division, as well as the phosphatidylinositol 3-kinase (*PI3K*)/*PTEN*/*AKT* pathway to facilitate cell growth and survival (Rusnak et al., 2001). Dysregulation in the downstream pathway leads to resistance to targeted agents. In HER2-overexpressed solid tumors, *PTEN* was identified as a predictive biomarker of trastuzumab resistance (Tekesin et al., 2019; Yokoyama et al., 2021). Belli et al. showed that abnormal changes in *MEK* and *PIK3CA* can give rise to resistance to anti-HER2 agents in mouse models of HER2-amplified CRC (Belli et al., 2019). However, in our case, activating mutations of *PIK3CA* or *MEK* and decreased expression of *PTEN* was not detected in scalp metastasis samples. Notably, the amplification of fibroblast growth factor receptor 1 (*FGFR1*) was observed in the NGS testing. *FGFR* family of receptor tyrosine kinases mediate various cellular processes by dimerizing and activating the downstream signal network, including mitogen-activated protein kinase (*MAPK*) and *PI3K/AKT* (Sami and Karsy, 2013). María et al. revealed that *FGFR1* amplification was associated with a poor response to anti-HER2 treatment (Gaibar et al., 2022). In the cohort comprised breast cancer patients who received trastuzumab and pertuzumab, the pathological complete response rate was lower among those harboring FGFR1 amplification (Gaibar et al., 2022). Moreover, Ariella et al. reported that lapatinib + trastuzumab-resistant tumors exhibited increased *FGFR* phosphorylation, which led to significant stromal alterations in the tumor microenvironment and decreased tumor uptake of drugs (Hanker et al., 2017). These findings indicate that abnormal activation of the *FGFR* pathway is linked to primary or intrinsic resistance to therapeutic blockade of HER2.

Pyrotinib inhibits the autophosphorylation of the HER2, therefore suppressing the *MAPK* and *PI3K/Akt* signaling pathways (Blair, 2018). Several studies have demonstrated that the dual anti-HER2 regime of pyrotinib in combination with trastuzumab has shown significant anti-tumor activity in HER2 amplification, *RAS* wild-type mCRC patients who have become refractory to chemotherapy (Chang et al., 2022; Fu et al., 2023; Zhou et al., 2023). In our case, despite the resistance to trastuzumab + pertuzumab, pyrotinib demonstrated a remarkable clinical response. While trastuzumab and pertuzumab exclusively target HER2, pyrotinib also significantly inhibits *EGFR* signaling (Blair, 2018; Han et al., 2022). Furthermore, pyrotinib has shown high selectivity when assessed against a wide range of diverse kinases, including c-Kit, platelet-derived growth factor receptor β, kinase insert domain receptor, c-Src, and c-Met (Li et al., 2017). Thus, pyrotinib might manifest diverse effects through multiple mechanisms that differ from those of previous anti-HER2 medications, which could partially account for the exceptional response to pyrotinib in our case.

Interestingly, HER2 has been reported to be linked with adaptive radiation resistance, while HER2 inhibition is a promising strategy for overcoming radioresistance (Khan et al., 2024). Pyrotinib treatment reduced the cyclin D1 and cyclin-dependent kinase 4 (CDK4) levels for increasing G0/G1 arrest, resulting in the enhanced anti-proliferation effects of radiotherapy in esophageal cancer cells (Lian et al., 2020). Niu et al. discovered that pyrotinib in combination with radiotherapy achieved more tumor remission in the xenograft model (Niu et al., 2023). Mechanistic investigations have revealed that pyrotinib blocked the activation of the *ERK* signaling pathway mediated by radiation (Niu et al., 2023). Moreover, pyrotinib also promoted DNA damage, induced cell apoptosis, and enhanced senescence, which contributed to increased radiosensitivity (Niu et al., 2023). Brain metastasis frequently leads to mortality in patients with HER2-positive breast cancer. The standard treatment predominantly involves

whole-brain radiotherapy (Kim et al., 2024). Tian et al. assessed the effectiveness of pyrotinib in conjunction with WBRT in patients with HER2-positive brain metastatic breast cancer (Tian et al., 2022). The oral administration of pyrotinib, combined with radiotherapy, significantly enhanced the ORR, and PFS in patients with HER2-positive brain metastases, without increasing adverse events (Tian et al., 2022). Furthermore, pyrotinib improved the radiosensitivity of HER2-positive breast cancer cell lines cultured *in vitro* (Tian et al., 2022). The findings suggest that pyrotinib could be an efficacious agent to increase tumor radiosensitivity and improve clinical prognosis in patients with HER2-positive brain metastatic breast cancer. Moreover, small TKIs such as pyrotinib has been demonstrated to possess enhanced blood-brain barrier permeability and specific anti-intracerebral tumor efficacy (Garcia-Alvarez et al., 2021). Besides, radiotherapy modifies the blood-brain barrier permeability, leading to an increase in the influx of drugs into the brain (Li et al., 2023). And the synergistic effects of pyrotinib combined with radiotherapy contribute to the great therapeutic response in our case.

The limitations of our case stem from the absence of tissue or liquid biopsy findings following the resistance of trastuzumab plus pertuzumab, making it challenging to determine the tumor's genetic status and elucidate the resistance mechanisms. If the patient's condition deteriorates once more, NGS testing based on tissue or blood specimens is required to identify potential therapeutic targets and exploit alternative salvage therapies. Moreover, after the discovery of scalp and brain metastases in the patient, we implemented a treatment strategy combining mXELIRI chemotherapy with the anti-HER2 drug trastuzumab. However, NGS testing revealed EGFR amplification in the patient. If we had concurrently used an anti-EGFR drug at that time, it might have led to a better therapeutic outcome.

4 Conclusion

HER2 is recognized as a promising target for mCRC. In this case report, we presented the case of a patient with treatment-resistant HER2-amplified mCRC who achieved a prolonged response to pyrotinib plus tegafur in combination with radiotherapy following resistance to trastuzumab and pertuzumab. In conclusion, pyrotinib demonstrates activity in the salvage treatment of mCRC patients with HER2 amplification even though resistant to other anti-HER2 drugs. Further studies are needed to validate this finding.

Data availability statement

The original contributions presented in the study are included in the article/supplementary material, further inquiries can be directed to the corresponding author.

Ethics statement

The requirement of ethical approval was waived by West China Hospital of Sichuan University for the studies on humans because Ethical approval was unnecessary for human studies as case reports submission and publication do not mandate ethics approval at our institution. The studies were conducted in accordance with the local legislation and institutional requirements. Written informed consent for participation was not required from the participants or the participants' legal guardians/next of kin in accordance with the national legislation and institutional requirements. The human samples used in this study were acquired from gifted from another research group. Written informed consent was obtained from the individual(s) for the publication of any potentially identifiable images or data included in this article.

Author contributions

PH: Conceptualization, Data curation, Formal Analysis, Investigation, Methodology, Project administration, Software, Writing–original draft. FW: Conceptualization, Formal Analysis, Funding acquisition, Methodology, Project administration, Writing–original draft. XW: Investigation, Methodology, Project administration, Resources, Validation, Visualization, Writing–original draft.

Funding

The author(s) declare that financial support was received for the research, authorship, and/or publication of this article. This research was supported by the Science and Technology Department of Sichuan Province Funding Project (2022NSFSC1564).

Conflict of interest

The authors declare that the research was conducted in the absence of any commercial or financial relationships that could be construed as a potential conflict of interest.

Publisher's note

All claims expressed in this article are solely those of the authors and do not necessarily represent those of their affiliated organizations, or those of the publisher, the editors and the reviewers. Any product that may be evaluated in this article, or claim that may be made by its manufacturer, is not guaranteed or endorsed by the publisher.

References

Belli, V., Matrone, N., Napolitano, S., Migliardi, G., Cottino, F., Bertotti, A., et al. (2019). Combined blockade of MEK and PI3KCA as an effective antitumor strategy in HER2 gene amplified human colorectal cancer models. *J. Exp. Clin. Cancer Res.* 38 (1), 236. doi:10.1186/s13046-019-1230-z

Biller, L. H., and Schrag, D. (2021). Diagnosis and treatment of metastatic colorectal cancer: a review. *Jama* 325 (7), 669–685. doi:10.1001/jama.2021.0106

Blair, H. A. (2018). Pyrotinib: first global approval. *Drugs* 78 (16), 1751–1755. doi:10.1007/s40265-018-0997-0

Boire, A., Brastianos, P. K., Garzia, L., and Valiente, M. (2020). Brain metastasis. *Nat. Rev. Cancer* 20 (1), 4–11. doi:10.1038/s41568-019-0220-y

Chang, J., Xu, M., Wang, C., Huang, D., Zhang, Z., Chen, Z., et al. (2022). Dual HER2 targeted therapy with pyrotinib and trastuzumab in refractory HER2 positive metastatic colorectal cancer: a result from HER2-FUSCC-G study. *Clin. Colorectal Cancer* 21 (4), 347–353. doi:10.1016/j.clcc.2022.07.003

Chitkara, A., Bakhtiar, M., Sahin, I. H., Hsu, D., Zhang, J., Anamika, F., et al. (2023). A meta-analysis to assess the efficacy of HER2-targeted treatment regimens in HER2-positive metastatic colorectal cancer (mCRC). *Curr. Oncol.* 30 (9), 8266–8277. doi:10.3390/curroncol30090600

Fokas, E., Liersch, T., Fietkau, R., Hohenberger, W., Beissbarth, T., Hess, C., et al. (2014). Tumor regression grading after preoperative chemoradiotherapy for locally advanced rectal carcinoma revisited: updated results of the CAO/ARO/AIO-94 trial. *J. Clin. Oncol.* 32 (15), 1554–1562. doi:10.1200/jco.2013.54.3769

Fu, X., Ying, J., Yang, L., Fang, W., Han, W., Hu, H., et al. (2023). Dual targeted therapy with pyrotinib and trastuzumab for HER2-positive advanced colorectal cancer: a phase 2 trial. *Cancer Sci.* 114 (3), 1067–1074. doi:10.1111/cas.15660

Gaibar, M., Novillo, A., Romero-Lorca, A., Malón, D., Antón, B., Moreno, A., et al. (2022). FGFR1 amplification and response to neoadjuvant anti-HER2 treatment in early HER2-positive breast cancer. *Pharmaceutics* 14 (2), 242. doi:10.3390/pharmaceutics14020242

Garcia-Alvarez, A., Papakonstantinou, A., and Oliveira, M. (2021). Brain metastases in HER2-positive breast cancer: current and novel treatment strategies. *Cancers (Basel)* 13 (12), 2927. doi:10.3390/cancers13122927

Greally, M., Kelly, C. M., and Cercek, A. (2018). HER2: an emerging target in colorectal cancer. *Curr. Probl. Cancer* 42 (6), 560–571. doi:10.1016/j.currproblcancer.2018.07.001

Han, X., Zhang, Y., Li, Y., Lin, Z., Pei, X., Feng, Y., et al. (2022). Pyrotinib targeted EGFR-STAT3/CD24 loop-mediated cell viability in TSC. *Cells* 11 (19), 3064. doi:10.3390/cells11193064

Hanker, A. B., Garrett, J. T., Estrada, M. V., Moore, P. D., Ericsson, P. G., Koch, J. P., et al. (2017). HER2-overexpressing breast cancers amplify FGFR signaling upon acquisition of resistance to dual therapeutic blockade of HER2. *Clin. Cancer Res.* 23 (15), 4323–4334. doi:10.1158/1078-0432.Ccr-16-2287

He, K., Wang, Z., Luo, M., Li, B., Ding, N., Li, L., et al. (2023). Metastasis organotropism in colorectal cancer: advancing toward innovative therapies. *J. Transl. Med.* 21 (1), 612. doi:10.1186/s12967-023-04460-5

Hong, X., Chen, X., Wang, H., Xu, Q., Xiao, K., Zhang, Y., et al. (2023). A HER2-targeted antibody-drug conjugate, RC48-ADC, exerted promising antitumor efficacy and safety with intravesical instillation in preclinical models of bladder cancer. *Adv. Sci. (Weinh)* 10 (32), e2302377. doi:10.1002/advs.202302377

Hyman, D. M., Piha-Paul, S. A., Won, H., Rodon, J., Saura, C., Shapiro, G. I., et al. (2018). HER kinase inhibition in patients with HER2-and HER3-mutant cancers. *Nature* 554 (7691), 189–194. doi:10.1038/nature25475

Jørgensen, J. T. (2023). The potential of trastuzumab deruxtecan as a tissue agnostic drug. *Oncology* 101 (12), 836–842. doi:10.1159/000533866

Khan, M. M., Yalamarty, S. S. K., Rajmalani, B. A., Filipczak, N., and Torchilin, V. P. (2024). Recent strategies to overcome breast cancer resistance. *Crit. Rev. Oncol. Hematol.* 197, 104351. doi:10.1016/j.critrevonc.2024.104351

Kim, I. A., Winter, K. A., Sperduto, P. W., De Los Santos, J. F., Peereboom, D. M., Ogunleye, T., et al. (2024). Concurrent lapatinib with brain radiation therapy in patients with HER2+ breast cancer with brain metastases: NRG oncology-KROG/RTOG 1119 phase 2 randomized trial. *Int. J. Radiat. Oncol. Biol. Phys.* 118 (5), 1391–1401. doi:10.1016/j.ijrobp.2023.07.019

Kim, J. H. (2015). Chemotherapy for colorectal cancer in the elderly. *World J. Gastroenterol.* 21 (17), 5158–5166. doi:10.3748/wjg.v21.i17.5158

Lamberti, G., Andrini, E., Sisi, M., Rizzo, A., Parisi, C., Di Federico, A., et al. (2020). Beyond EGFR, ALK and ROS1: current evidence and future perspectives on newly targetable oncogenic drivers in lung adenocarcinoma. *Crit. Rev. Oncol. Hematol.* 156, 103119. doi:10.1016/j.critrevonc.2020.103119

Li, P. J., Lai, S. Z., Jin, T., Ying, H. J., Chen, Y. M., Zhang, P., et al. (2023). Radiotherapy opens the blood-brain barrier and synergizes with anlotinib in treating glioblastoma. *Radiother. Oncol.* 183, 109633. doi:10.1016/j.radonc.2023.109633

Li, X., Yang, C., Wan, H., Zhang, G., Feng, J., Zhang, L., et al. (2017). Discovery and development of pyrotinib: a novel irreversible EGFR/HER2 dual tyrosine kinase inhibitor with favorable safety profiles for the treatment of breast cancer. *Eur. J. Pharm. Sci.* 110, 51–61. doi:10.1016/j.ejps.2017.01.021

Lian, X., Zhu, C., Lin, H., Gao, Z., Li, G., Zhang, N., et al. (2020). Radiosensitization of HER2-positive esophageal cancer cells by pyrotinib. *Biosci. Rep.* 40 (2). doi:10.1042/bsr20194167

Meric-Bernstam, F., Hurwitz, H., Raghav, K. P. S., McWilliams, R. R., Fakih, M., VanderWalde, A., et al. (2019). Pertuzumab plus trastuzumab for HER2-amplified metastatic colorectal cancer (MyPathway): an updated report from a multicentre, open-label, phase 2a, multiple basket study. *Lancet Oncol.* 20 (4), 518–530. doi:10.1016/s1470-2045(18)30904-5

Mollica, V., Maggio, I., Lopez-Beltran, A., Montironi, R., Cimadamore, A., Cheng, L., et al. (2020). Combination therapy in advanced urothelial cancer: the role of PARP, HER-2 and mTOR inhibitors. *Expert Rev. Anticancer Ther.* 20 (9), 755–763. doi:10.1080/14737140.2020.1807334

Niu, Q., Liu, J., Huang, T., Su, B., Zhang, Y., and Yuan, X. (2023). Pan-HER tyrosine kinase inhibitor pyrotinib enhances radiosensitivity via ERK1/2 pathway in HER2-positive gastric cancer. *Oncol. Res. Treat.* 46 (1-2), 11–25. doi:10.1159/000528594

Oh, D. Y., and Bang, Y. J. (2020). HER2-targeted therapies - a role beyond breast cancer. *Nat. Rev. Clin. Oncol.* 17 (1), 33–48. doi:10.1038/s41571-019-0268-3

Ohishi, T., Kaneko, M. K., Yoshida, Y., Takashima, A., Kato, Y., and Kawada, M. (2023). Current targeted therapy for metastatic colorectal cancer. *Int. J. Mol. Sci.* 24 (2), 1702. doi:10.3390/ijms24021702

Ricci, A. D., Rizzo, A., Rojas Llimpe, F. L., Di Fabio, F., De Biase, D., and Rihawi, K. (2021). Novel HER2-directed treatments in advanced gastric carcinoma: AnotHER paradigm shift? *Cancers (Basel)* 13 (7), 1664. doi:10.3390/cancers13071664

Rizzo, A., Ricci, A. D., Bonucci, C., Tober, N., Palloni, A., Frega, G., et al. (2021). Experimental HER2-targeted therapies for biliary tract cancer. *Expert Opin. Investig. Drugs* 30 (4), 389–399. doi:10.1080/13543784.2021.1854724

Rusnak, D. W., Lackey, K., Affleck, K., Wood, E. R., Alligood, K. J., Rhodes, N., et al. (2001). The effects of the novel, reversible epidermal growth factor receptor/ErbB-2 tyrosine kinase inhibitor, GW2016, on the growth of human normal and tumor-derived cell lines *in vitro* and *in vivo*. *Mol. Cancer Ther.* 1 (2), 85–94. doi:10.1158/1535-7163.MCT-11-0697

Sami, A., and Karsy, M. (2013). Targeting the PI3K/AKT/mTOR signaling pathway in glioblastoma: novel therapeutic agents and advances in understanding. *Tumour Biol.* 34 (4), 1991–2002. doi:10.1007/s13277-013-0800-5

Sartore-Bianchi, A., Trusolino, L., Martino, C., Bencardino, K., Lonardi, S., Bergamo, F., et al. (2016). Dual-targeted therapy with trastuzumab and lapatinib in treatment-refractory, KRAS codon 12/13 wild-type, HER2-positive metastatic colorectal cancer (HERACLES): a proof-of-concept, multicentre, open-label, phase 2 trial. *Lancet Oncol.* 17 (6), 738–746. doi:10.1016/s1470-2045(16)00150-9

Sheng, X., Yan, X., Wang, L., Shi, Y., Yao, X., Luo, H., et al. (2021). Open-label, multicenter, phase II study of RC48-ADC, a HER2-targeting antibody-drug conjugate, in patients with locally advanced or metastatic urothelial carcinoma. *Clin. Cancer Res.* 27 (1), 43–51. doi:10.1158/1078-0432.Ccr-20-2488

Shin, A. E., Giancotti, F. G., and Rustgi, A. K. (2023). Metastatic colorectal cancer: mechanisms and emerging therapeutics. *Trends Pharmacol. Sci.* 44 (4), 222–236. doi:10.1016/j.tips.2023.01.003

Siegel, R. L., Giaquinto, A. N., and Jemal, A. (2024). Cancer statistics, 2024. *CA Cancer J. Clin.* 74 (1), 12–49. doi:10.3322/caac.21820

Siena, S., Di Bartolomeo, M., Raghav, K., Masuishi, T., Loupakis, F., Kawakami, H., et al. (2021). Trastuzumab deruxtecan (DS-8201) in patients with HER2-expressing metastatic colorectal cancer (DESTINY-CRC01): a multicentre, open-label, phase 2 trial. *Lancet Oncol.* 22 (6), 779–789. doi:10.1016/s1470-2045(21)00086-3

Tekesin, K., Emin Gunes, M., Bayrak, S., Akar, E., Ozturk, T., Altinay, S., et al. (2019). PTEN loss is a predictive marker for HER2-positive metastatic breast cancer patients treated with trastuzumab-based therapies. *J. Buon* 24 (5), 1920–1926.

Tian, W., Hao, S., Wang, L., Chen, Y., Li, Z., and Luo, D. (2022). Pyrotinib treatment enhances the radiosensitivity in HER2-positive brain metastatic breast cancer patients. *Anticancer Drugs* 33 (1), e622–e627. doi:10.1097/cad.0000000000001199

van Gijn, W., Marijnen, C. A., Nagtegaal, I. D., Kranenbarg, E. M. K., Putter, H., Wiggers, T., et al. (2011). Preoperative radiotherapy combined with total mesorectal excision for resectable rectal cancer: 12-year follow-up of the multicentre, randomised controlled TME trial. *Lancet Oncol.* 12 (6), 575–582. doi:10.1016/s1470-2045(11)70097-3

Yokoyama, D., Hisamori, S., Deguchi, Y., Nishigori, T., Okabe, H., Kanaya, S., et al. (2021). PTEN is a predictive biomarker of trastuzumab resistance and prognostic factor in HER2-overexpressing gastroesophageal adenocarcinoma. *Sci. Rep.* 11 (1), 9013. doi:10.1038/s41598-021-88331-3

Zheng-Lin, B., Graham, R. P., and Bekaii-Saab, TSJCCO (2023). Targeting ERBB2/HER2 genetic alterations: an expanding therapeutic opportunity in gastrointestinal cancers. *Chin. Clin. Oncol.* 12 (5), 55. doi:10.21037/cco-23-72

Zhou, H., Lv, M., Li, W., Wang, Y., Wu, J., Liu, Q., et al. (2023). Efficacy of pyrotinib with/without trastuzumab in treatment-refractory, HER2-positive metastatic colorectal cancer: result from a prospective observational study. *Clin. Colorectal Cancer* 23, 58–66. doi:10.1016/j.clcc.2023.10.008

frontiers | Frontiers in Pharmacology

TYPE Original Research
PUBLISHED 21 August 2024
DOI 10.3389/fphar.2024.1434231

Check for updates

OPEN ACCESS

EDITED BY
Wagdy Mohamed Eldehna,
Kafrelsheikh University, Egypt

REVIEWED BY
Jakrawadee Julamanee,
Prince of Songkla University, Thailand
Melania Rivano,
Azienda Ospedaliero-Universitaria Cagliari, Italy

*CORRESPONDENCE
Yuanming Zhang,
zymdxx@163.com
Li Wu,
405442119@qq.com

RECEIVED 17 May 2024
ACCEPTED 30 July 2024
PUBLISHED 21 August 2024

CITATION
Shi J, Liu X, Jiang Y, Gao M, Yu J, Zhang Y and Wu L (2024) CAR-T therapy pulmonary adverse event profile: a pharmacovigilance study based on FAERS database (2017–2023).
Front. Pharmacol. 15:1434231.
doi: 10.3389/fphar.2024.1434231

COPYRIGHT
© 2024 Shi, Liu, Jiang, Gao, Yu, Zhang and Wu. This is an open-access article distributed under the terms of the Creative Commons Attribution License (CC BY). The use, distribution or reproduction in other forums is permitted, provided the original author(s) and the copyright owner(s) are credited and that the original publication in this journal is cited, in accordance with accepted academic practice. No use, distribution or reproduction is permitted which does not comply with these terms.

CAR-T therapy pulmonary adverse event profile: a pharmacovigilance study based on FAERS database (2017–2023)

Jing Shi[1,2], Xinya Liu[1,3], Yun Jiang[2], Mengjiao Gao[2], Jian Yu[2], Yuanming Zhang[1]* and Li Wu[2]*

[1]Xinjiang Medical University, Urumqi, China, [2]Department of Oncology Cardiology, Xinjiang Medical University Cancer Hospital, Urumqi, China, [3]The Fifth Affiliated Hospital of Xinjiang Medical University, Urumqi, China

Background: Chimeric antigen receptor T-cell (CAR-T) therapy, a rapidly emerging treatment for cancer that has gained momentum since its approval by the FDA in 2017, involves the genetic engineering of patients' T cells to target tumors. Although significant therapeutic benefits have been observed, life-threatening adverse pulmonary events have been reported.

Methods: Using SAS 9.4 with MedDRA 26.1, we retrospectively analyzed data from the Food and Drug Administration's Adverse Event Reporting System (FAERS) database, covering the period from 2017 to 2023. The analysis included the Reporting Odds Ratio Proportional Reporting Ratio Information Component and Empirical Bayes Geometric Mean to assess the association between CAR-T cell therapy and adverse pulmonary events (PAEs).

Results: The FAERS database recorded 9,400 adverse events (AEs) pertaining to CAR-T therapies, of which 940 (10%) were PAEs. Among these CAR-T cell-related AEs, hypoxia was the most frequently reported (344 cases), followed by respiratory failure (127 cases). Notably, different CAR-T cell treatments demonstrated varying degrees of association with PAEs. Specifically, Tisa-cel was associated with severe events including respiratory failure and hypoxia, whereas Axi-cel was strongly correlated with both hypoxia and tachypnea. Additionally, other CAR-T therapies, namely, Brexu-cel, Liso-cel, Ide-cel, and Cilta-cel, have also been linked to distinct PAEs. Notably, the majority of these PAEs occurred within the first 30 days post-treatment. The fatality rates varied among the different CAR-T therapies, with Tisa-cel exhibiting the highest fatality rate (43.6%), followed by Ide-cel (18.8%).

Conclusion: This study comprehensively analyzed the PAEs reported in the FAERS database among recipients of CAR-T cell therapy, revealing conditions such as hypoxia, respiratory failure, pleural effusion, and atelectasis. These CAR-T cell therapy-associated events are clinically significant and merit the attention of clinicians and researchers.

KEYWORDS

chimeric antigen receptor T cells, CAR T cell therapy, FAERS database, real-world study, pharmacovigilance analysis, pulmonary adverse events

1 Introduction

CAR-T cell therapy involves genetically modifying a patient's T cells to recognize specific tumor antigens. These engineered cells are then cultured *ex vivo* and reinfused to launch a targeted attack against the patient's cancer (Abramson et al.). Since the approval of the first chimeric antigen receptor T-cell (CAR-T) therapy, Tisagenlecleucel (tisa-cel), on 30 August 2017, the landscape of chimeric antigen receptor T-cell (CAR-T) products has evolved significantly. As of September 2023, the U.S. Food and Drug Administration (FDA) has granted approval to six CAR-T products. These products and their indications are listed in Table 1 (Munshi et al., 2021; Martin et al., 2023).

Compared with traditional drugs, CAR-T therapy has shown remarkable efficacy in multiple clinical trials for the treatment of hematological malignancies (Maude et al., 2018; Abramson et al., 2020; Jacobson et al., 2022; Wang et al., 2023). Certain experimental data have demonstrated response rates and 1-year survival rates exceeding 60% and 50%, respectively (Schuster et al., 2019). Multiple drug regulatory agencies, including the FDA, have approved over 300 clinical trials of CAR-T cell therapy for both hematological and solid tumors. The use of CAR-T cells is expected to increase rapidly in the coming years, thereby benefiting more patients.

Although CAR-T therapy has shown promising results in numerous clinical trials, potential life-threatening or fatal toxicities cannot be ignored, such as cytokine release syndrome (CRS) and neurotoxicity (Neelapu et al., 2018). Rare adverse events (AEs), such as pulmonary or cardiovascular-related AEs, have also been reported (Alvi et al., 2019; Ganatra et al., 2020; Lefebvre et al., 2020). In a study evaluating the safety of CAR-T cells, 103 patients (8.53%) developed respiratory, thoracic, and mediastinal AEs. The most common type of AE in the respiratory system is hypoxia, which can lead to respiratory failure. Common comorbidities include dyspnea, pleural effusion, pulmonary edema, acute respiratory distress syndrome, and pneumonia (Chen et al., 2022). With multiple new CAR-T treatments approved in recent years, treatment choices may depend on product safety, in addition to efficacy.

Comprehensive studies on the potential toxicities associated with CAR-T therapy are currently lacking. In addition, clinical trials have inherent limitations in the detection of rare drug reactions. Consequently, spontaneous reports of adverse events have emerged as a vital source of information for identifying new safety signals, especially in post-market safety databases, such as FAERS. To effectively sift through these safety signals in a vast volume of reports, researchers have devised data-mining algorithms based on the concept of 'disproportionality.' This analysis detects statistical anomalies by comparing the reporting frequencies of a specific drug with those of all other drugs in a database (Michel et al., 2017). Common metrics used in disproportionality analysis include the Proportional Reporting Ratio (PRR), Reporting Odds Ratio (ROR), Information Component (IC), and Empirical Bayes Geometric Mean (EBGM). Recent publications have advocated the use of this approach (Wang et al., 2021; Yu et al., 2021; Tian et al., 2022; Yang et al., 2022; Chen et al., 2023), arguing that it can offer valuable insights to healthcare decision makers in formulating treatment strategies.

2 Materials and methods

2.1 Data sources

This was an observational, retrospective, pharmacovigilance study that utilized the FAERS database, a global repository of post-market safety reports. With SAS 9.4 and MedDRA 26.1, given the approval of the first CAR-T product in 2017, we decided to initiate our data collection from that year. Additionally, we chose to include data until the third quarter of 2023 as this represents the most recent and comprehensive dataset available to us. We analyzed the data from 2017 to 2023. The study screened reports within the database that contained any of the following trade or generic names of the drugs: "axicabtagene," "ciloleucel," "yescarta," "axi-cel," "KTE-C19," "tisagenlecleucel," "kymriah," "tisa-cel," "CTL019," "brexucabtagene," "autoleucel," "tecartus," "KTE-X19," "lisocabtagene maraleucel," "breyanzi," "JCAR017," "idecabtagene," "vicleucel," "abecma," "bb2121," "ciltacabtagene," "autoleucel," "carvykti" and "JCARH125," This study utilized the FAERS database from Q1 2017 to Q2 2023.

TABLE 1 FDA-Approved car-t cell therapies and indications.

Proper name	Abbreviated name	Indications
Tisagenlecleucel	**Tisa-cel**	• Pediatric and Young Adult B-cell Precursor Acute Lymphoblastic Leukemia (ALL) • Adult Large B-cell Lymphoma • Adult Follicular Lymphoma (FL)
Axicabtagene-ciloleucel	**Axi-cel**	• Adult Patients with Large B-cell Lymphoma • Relapsed or Refractory Large B-cell Lymphoma in Adults • Relapsed or Refractory Follicular Lymphoma (FL) in Adults
Brexucabtagene autoleuce	**Brexu-cel**	• Adult Patients with Relapsed or Refractory Mantle Cell Lymphoma (MCL) • Adult Patients with Relapsed or Refractory B-cell Precursor Acute Lymphoblastic Leukemia (ALL)
Lisocabtagene maraleucel	**Liso-cel**	• Adult Patients with Large B-cell Lymphoma • Chronic Lymphocytic Leukemia or Small Lymphocytic Lymphoma in Adults • Relapsed or Refractory Follicular Lymphoma in Adults • Relapsed or Refractory Mantle Cell Lymphoma in Adults
Ciltacabtagene autoleucel	**Cilta-cel**	• Adult Patients with Relapsed or Refractory Multiple Myeloma
Idecabtagene vicleucel	**Ide-cel**	• Adult Patients with Relapsed or Refractory Multiple Myeloma

TABLE 2 Algorithms used for signal detection.

Algorithms	Equation	Criteria
ROR	$ROR = \frac{(a/c)}{(b/d)} = \frac{ad}{bc}$	lower limit of 95% CI > 1, N ≥ 3
	95%CI = eln (ROR)±1.96 (1/a+1/b+1/c+1/d)0.5	
PRR	$PRR = \frac{a/(a+b)}{c/(c+d)}$	PRR ≥ 2 and χ2≥ 4, N ≥ 3
	$\chi^2 = \frac{(ad-bc)^2 (a+b+c+d)}{(a+b)(a+c)(c+d)(b+d)}$	
IC	$IC = log_2 \frac{a(a+b+c+d)}{(a+b)(a+c)}$	lower limit of 95% CI > 0, N ≥ 3
	95%CI = E (IC) ± 2V(IC)0.5	
EBGM	$EBGM = \frac{a(a+b+c+d)}{(a+c)(a+b)}$	lower limit of 95% CI > 2, N ≥ 3
	$95\%CI = e^{\ln(EBGM) \pm 1.96\sqrt{(\frac{1}{a}+\frac{1}{b}+\frac{1}{c}+\frac{1}{d})}}$	

Equation: a: number of reports containing both the target drug and target adverse drug reaction
b: number of reports containing other adverse drug reaction of the target drug
c: number of reports containing the target adverse drug reaction of other drugs
d: number of reports containing other drugs and other adverse drug reactions
95%CI, 95% confidence interval; ROR, Reporting Odds Ratio; PRR, Proportional Reporting Ratio; IC, Information Component; EBGM, Empirical Bayes Geometric Mean.

2.2 Data deduplication

Spontaneous data collection often results in duplications or withdrawals/deletions from the database. The FDA's official guidelines outline the rules for data deduplication and report deletion. This study strictly adhered to the data cleansing criteria. Initially, duplicate reports were removed using the FDA's method: selecting PRIMARYID, CASEID, and FDA_DT from the DEMO table, and sorted by CASEID, FDA_DT, and PRIMARYID. Among identical CASEIDs, the report with the most recent FDA_DT is retained; if the CASEID and FDA_DT match, a higher PRIMARYID is chosen. Since Q1, 2019, the quarterly data packages have included deletion lists. After deduplication, the reports of CASEIDs on these lists were removed.

2.3 Data extraction

Adverse events (AEs) in the FAERS were coded using preferred terms (PTs) classified by MedDRA, which consists of 27 system organ classes (SOCs). All signal PTs and their corresponding SOCs were included, Specifically, "SOC = Respiratory, Thoracic, and Mediastinal Disorders" is designated as pulmonary adverse events (PAEs) in the context of this study. The clinical characteristics of CAR-T cell-related reports were extracted, including sex, age, reporting region, reporter, and indications. We also calculated the incidence of AEs caused by different CAR-Ts and the proportion of serious outcomes, defined as life-threatening or leading to hospitalization, disability, or death.

2.4 Data deduplication

During the data deduplication process, we first addressed duplicate entries by identifying and selecting the most recent and comprehensive records based on the CASE and FDA_DT fields (i.e., records with the latest FDA_DT or a higher ISR number). Subsequently, we focused on data inconsistencies, validating the values of each field, and deciding whether to retain, correct, or delete abnormalities. Additionally, missing values were appropriately handled by either filling or deleting depending on their significance and impact on the overall dataset. Furthermore, the integrity of the data was ensured by verifying each step of the cleaning process and comparing it with the original data.

2.5 Data mining

Disproportionality analysis was conducted to detect potential signals of AEs caused by CAR-T therapy. This analysis compared the proportion of CAR-T cell therapy AEs reports with the proportion of reports on all other drugs. Algorithms such as the ROR, PRR, IC, and EBGM were used. The equations and corresponding thresholds for the algorithms are listed in Table 2. Only AEs with signals detected by all four algorithms were included in this study.

3 Results

3.1 Descriptive analysis

Between January 2017 and September 2023, 9,400 CAR-T-related AE were recorded, including 940 PAEs (10%), with some patients potentially experiencing multiple occurrences. The retrieval process is illustrated in Figure 1.

With the sequential approval of CAR-T therapy, the incidence of PAEs has increased annually (Figure 2), and males were found to experience these events more frequently (538 cases, 57.23%) than females (350 cases, 37.23%). Most reported patients were between 18 and 65 years of age, with a median age of 59 years. These reports originated primarily in the United States (64.04%), followed by France (3.40%). The number of reports on this topic is increasing annually. More than 80% of the reports were submitted by healthcare professionals, including 41.60% physicians (Table 3).

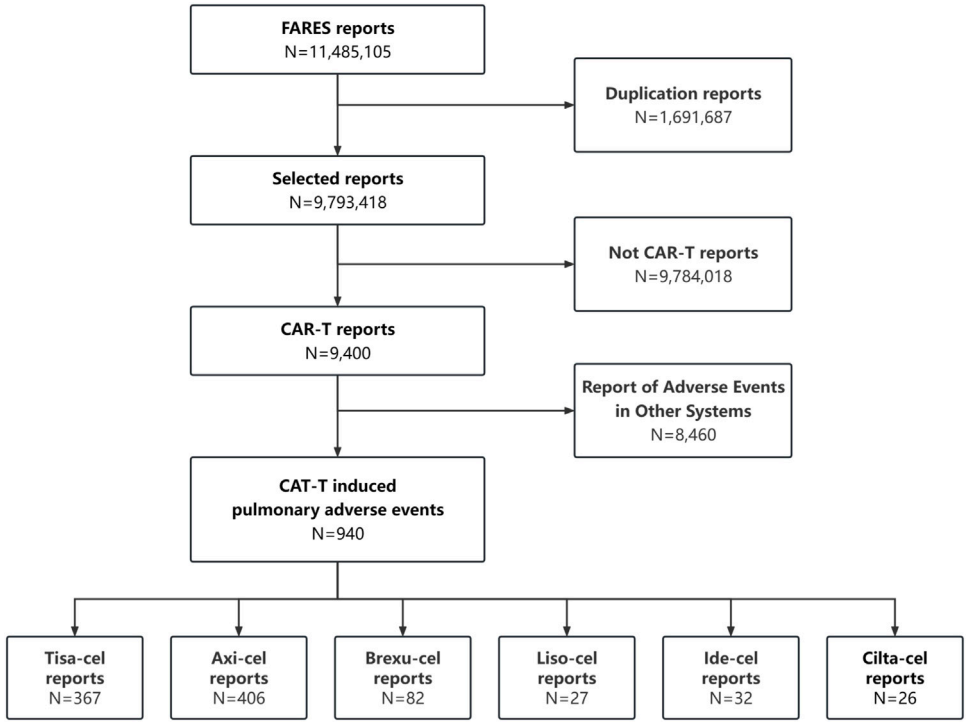

FIGURE 1
The main steps in the processing of the FAERS database.

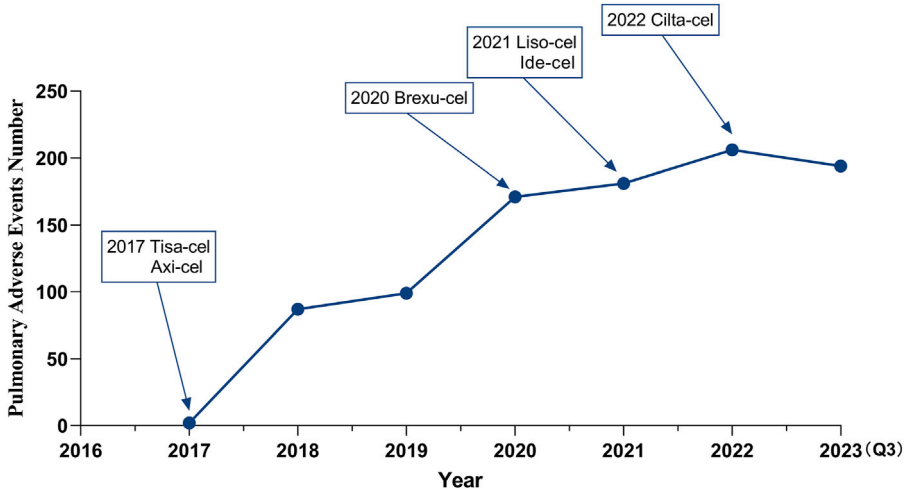

FIGURE 2
The number of CAR-T-related PAEs reported to the FAERS each year.

3.2 Disproportionality analysis

3.2.1 Signal values associated with CAR-T therapies

Figure 2 shows the signal intensity of the CAR-T cell-related PAEs. Hypoxia showed the highest number of reports (n = 344) and the strongest signal in the AE signal calculation method (IC = 4.09, ROR = 17.54), as well as a large number of reports of respiratory failure (n = 127) with strong signals (IC = 1.69, ROR = 3.25).

Other PAEs include Pleural effusion (IC = 1.84, ROR = 3.61), Acute respiratory failure (IC = 1.66, ROR = 3.16), Pulmonary hemorrhage (IC = 1.9, ROR = 3.74), Acute respiratory distress syndrome (ARDS) (IC = 1.54, ROR = 2.93), Organizing pneumonia (IC = 1.85, ROR = 3.62), Respiratory distress (IC = 1.49, ROR = 2.81), Pharyngeal hemorrhage (IC = 2.05, ROR = 4.15), and others. Furthermore, all detected safety signals must be confirmed using all four methods, including the PRR and EMBG. The complete data are shown in Figure 3.

TABLE 3 Main characteristics of the CAR-T reports.

Clinical characteristics	Patients with PAEs (940	Total (9400)
Gender		
Female (%)	350 (37.23)	2853 (30.35)
Male (%)	538 (57.23)	4671 (49.69)
Missing (%)	52 (5.53)	1876 (19.96)
Age		
<18 (%)	132 (14.04)	577 (6.14)
≥18, <65 (%)	383 (40.75)	3278 (34.87)
65≤ (%)	302 (32.13)	2496 (26.56)
Missing (%)	123 (13.09)	3049 (32.44)
Media (IQR)	59 (30,69)	61 (46,69)
Country		
United States(%)	602 (64.04)	6021 (64.05)
France (%)	32 (3.40)	391 (4.16)
Spain (%)	16 (1.70)	295 (3.14)
Germany (%)	26 (2.77)	291 (3.10)
Italy (%)	7 (0.74)	230 (2.45)
Other (%)	257 (27.34)	2172 (23.11)
Reporter type		
Healthcare profession (%)	754 (84.81)	7756 (82.51)
Physician (%)	391 (41.60)	3679 (39.14)
Pharmacist (%)	307 (32.66)	3261 (34.69)
Other health-professional (%)	96 (10.21)	816 (8.68)
Consumer (%)	72 (7.66)	965 (10.27)
Missing (%)	74 (7.87)	679 (7.22)

3.2.2 Analysis of the quantity and distribution of PAEs in CAR-T therapies

As shown in Figure 4A, Hypoxia and Respiratory failure were the most frequently occurring PAEs in all CAR-T therapies, significantly outnumbering the other types. Notably, Pleural effusion is also a prominent issue, especially with Tisa-Cel and Axi-Cel. Although Atelectasis, Acute respiratory failure, and acute respiratory distress syndrome are less common, they still occur. Analysis of the data in Figure 4B revealed 940 adverse respiratory events following six CAR-T cell treatments. Tisa-Cel and Axi-Cel were associated with higher adverse event totals. Specifically, Tisa-Cel had 367 events, including 158 hypoxic and 50 respiratory failure cases. Axi-Cel reported 406 events, with 143 hypoxia and 50 respiratory failure instances. Conversely, Cilta-Cel demonstrated superior respiratory safety with only 26 reported events. Brexu-Cel, Ide-Cel, and Liso-Cel resulted in 82, 32, and 27 events, respectively. Respectively.

3.2.3 Analysis of signal spectra of PAEs following different CAR-T therapies

We further analyzed the signals of specific AEs across the different CAR-T cell therapies. Reports with fewer than 3 cases were excluded to prevent false positives. Using the lower limit of the 95% confidence interval of the information component (IC025) as a metric, we created a heat map for safety signals based on IC025 (Figure 5). Based on the aforementioned results, we determined that an IC025 greater than 0 constituted a safety signal, indicating a stronger correlation between the drug or treatment and a specific AE with increasing values.

When considering different therapies individually, Tisa-cel has been found to be associated with the highest diversity of AEs. Among the 19 PTs detected, 13 demonstrated safety signals, including serious clinical AEs, such as respiratory failure (IC025 = 1.32), acute respiratory failure (IC025 = 1.14), pulmonary hemorrhage (IC025 = 0.63), lung opacity (IC025 = 0.66), and ARDS (IC025 = 0.41). Additionally, Tisa-Cel

PTs	N	ROR(95%CI)	PRR(χ2)	IC(IC025)	EBGM (EBGM05)
Hypoxia	344	17.54(15.75~19.52)	17.38(5196.24)	4.09(3.87)	17.02(15.29)
Tachypnoea	84	10.63(8.57~13.19)	10.61(721.14)	3.39(2.92)	10.48(8.44)
Atelectasis	20	5.09(3.28~7.9)	5.08(65.18)	2.34(1.45)	5.06(3.26)
Pleural effusion	118	3.61(3.01~4.32)	3.6(220.62)	1.84(1.55)	3.59(2.99)
Respiratory failure	127	3.25(2.73~3.87)	3.24(196.5)	1.69(1.41)	3.23(2.72)
Lung consolidation	7	5.14(2.44~10.8)	5.14(23.16)	2.35(0.73)	5.11(2.43)
Acute respiratory failure	38	3.16(2.3~4.35)	3.16(55.96)	1.66(1.12)	3.15(2.29)
Pulmonary haemorrhage	15	3.74(2.25~6.21)	3.74(29.95)	1.9(0.95)	3.73(2.24)
Lung opacity	8	4.4(2.2~8.82)	4.4(20.92)	2.13(0.71)	4.38(2.19)
Organising pneumonia	11	3.62(2~6.55)	3.62(20.79)	1.85(0.73)	3.61(2)
Acute respiratory distress syndrome	28	2.93(2.02~4.24)	2.92(35.34)	1.54(0.92)	2.92(2.01)
Respiratory distress	41	2.81(2.07~3.82)	2.81(47.62)	1.49(0.98)	2.8(2.06)
Pharyngeal haemorrhage	3	4.15(1.33~12.9)	4.15(7.12)	2.05(-0.24)	4.13(1.33)
Pulmonary oedema	42	1.73(1.28~2.34)	1.73(12.81)	0.79(0.32)	1.72(1.27)
Lung infiltration	10	3.03(1.63~5.63)	3.03(13.52)	1.59(0.48)	3.02(1.62)

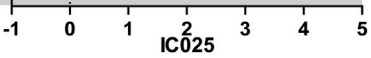

FIGURE 3
The positive signal distribution of CAR-T treatment for PAEs using standardized MedDRA queries. PT, preferred term; ROR, reporting odds ratio; CI, confidence interval; PRR, proportional reporting ratio; χ2, chi-information component; IC, information component; IC025, the lower limit of 95% CI of the IC; EBGM, empirical bayesian geometric mean; EBGM05, the lower limit of 95% CI of EBGM.

demonstrated strong safety signals in hypoxia (IC025 = 4.01) and tachypnea (IC025 = 2.71).

Axi-cel has been found to be associated with nine AEs, with relatively strong associations in hypoxia (IC025 = 3.56) and tachypnea (IC025 = 2.46), and also demonstrating safety signals in pleural effusion (IC025 = 1.66) and respiratory failure (IC025 = 1.02).

Brexu-cel has been found to be associated with five AEs, including respiratory failure (IC025 = 1.22) and pleural effusion (IC025 = 0.83).

Liso-cel showed safety signals for the three AEs, with the strongest association with pleural effusion (IC025 = 1.71).

Ide-Cel was only been found to be associated with hypoxia (IC025 = 1.37) and tachypnea (IC025 = 0.90).

Interestingly, the safety signal spectrum of Cilta-Cel was distinct from those of other CAR-T therapies. It does not exhibit a correlation with the commonly observed AEs of hypoxia and tachypnea, and instead shows a safety signal solely in respiratory failure (IC025 = 1.16) among all AEs.

3.3 Time to onset

Figure 6 illustrates the time difference between the initiation of CAR-T treatment and the occurrence of PAEs, including the overall median and interquartile range (IQR) of the time of onset of these events after each type of CAR-T treatment. No significant differences were observed in the incidence of AEs between the CAR-T therapies. Most adverse reactions occurred within 0–30 days, with Cilta-Cel exhibiting the longest average onset time of 10 days (IQR: 1–18). The median onset time for AEs of other CAR-T therapies was between 1–8 days. After integrating and analyzing the data, we found that the majority of PAEs following CAR-T cell therapy occurred within 30 days of treatment, comprising 89.97% of all reported cases. Furthermore, the median time to onset of these events was 2 days, with an interquartile range (IQR) of 1–7 days.

3.4 Fatality proportion

Figure 7 shows the fatality rates of PAEs following CAR-T cell therapy. According to database statistics, Tisa-cel had the highest number of deaths (160 out of 367 cases, 43.6%) and Axi-cel had the highest incidence of PAEs (406 cases) among all CAR-T therapies, with 141 patients (34.7%) experiencing death. Among the 32 cases of PAEs associated with Ide-cel, only six resulted in death, representing the lowest mortality rate of 18.8%. The mortality rates of the PAEs associated with Brexu-cel and Liso-cel were 28.0% and 33.3%, respectively. Finally, Cilta-cel had 26 cases of PAEs related to it, of which 13 resulted in death, with a mortality rate of 50%. Because of the short time since its market release and the limited overall sample size, the relatively high fatality rate observed may be influenced by "small sample bias." It is necessary to conduct further analyses with a larger sample size in the future to more accurately assess the fatality rate.

4 Discussion

4.1 Overview of PAEs associated with CAR-T therapy

In recent years, CAR-T cell therapy has demonstrated remarkable therapeutic efficacy in the field of antitumor treatment; however, safety concerns have become increasingly prominent. To the best of our knowledge, this is the first comprehensive analysis of PAEs associated with CAR-T therapy.

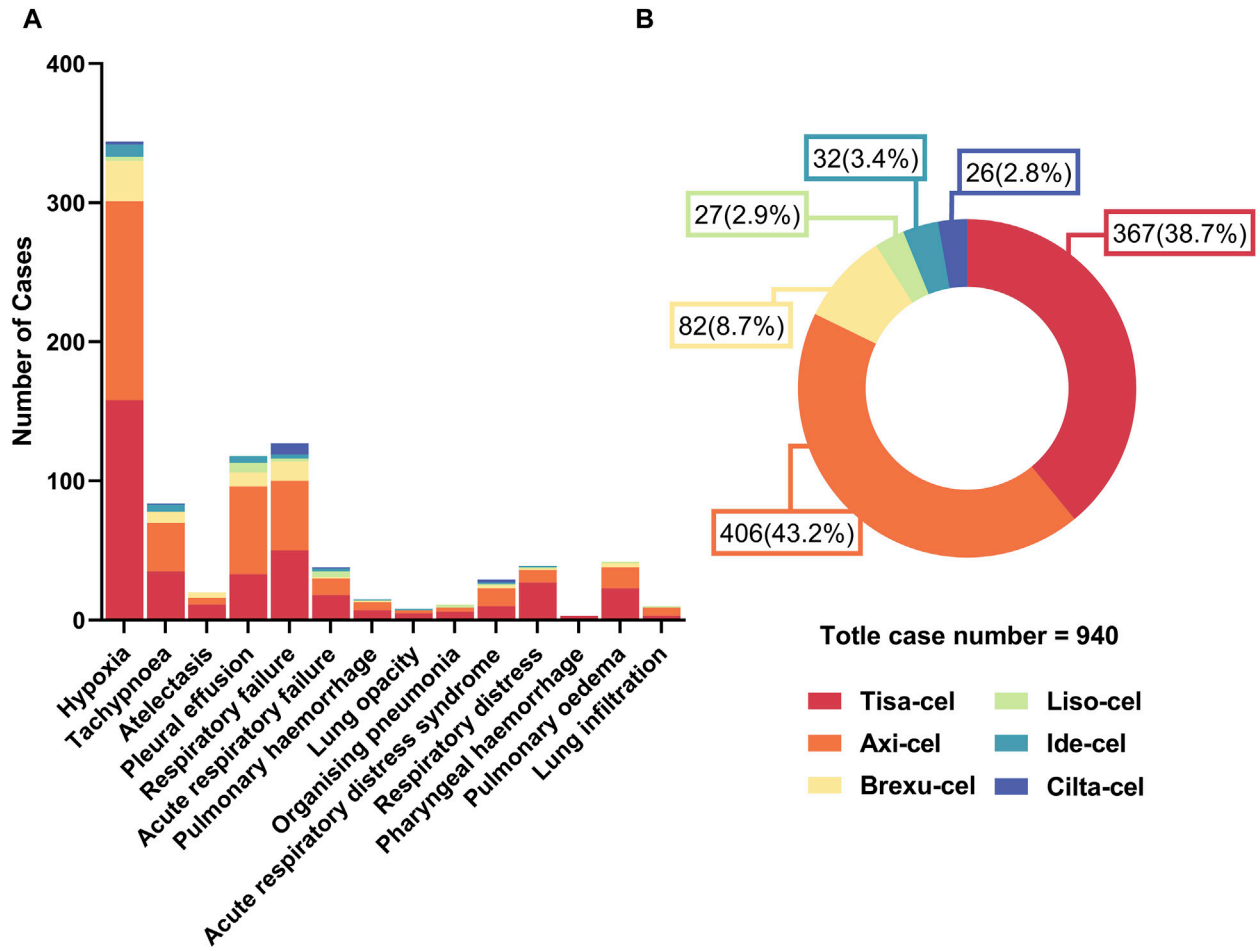

FIGURE 4
Quantitative overview of adverse events in car-t therapies. **(A)** Number of different types of PAEs across car-t therapies. **(B)** Proportional distribution of PAEs among car-t therapies.

From January 2017 to September 2023, 9,400 CAR-T related AE reports were documented, with PAEs accounting for 940 cases (10%), indicating a significant incidence of PAEs associated with CAR-T therapy. With the widespread use of this therapy, the annual incidence of PAEs has increased, posing a major safety concern. Male patients (57.23%) were more prone to these events than female patients (37.23%), suggesting that factors such as physiological and immune system characteristics, drug metabolism, lifestyle habits, and smoking history affect the occurrence of PAEs in CAR-T therapy. The median age of the patients was 59 years, mainly in the age range of 18–65 years old, representing middle-aged individuals. This age group exhibits a gradual decline in physiological functions, including the decreased functionality of the lungs, heart, liver, and kidneys. In addition, they experience hormonal changes that are often accompanied by the emergence of chronic diseases. This physiological decline may affect drug metabolism and the efficacy of CAR-T therapy, leading to variations in the incidence of PAEs among individuals (Kaddu-Mulindwa et al., 2022). Regarding the source of reports, the majority of the reports originate from the United States (64.04%), followed by France (3.40%). Differences in reporting sources are believed to be primarily attributable to disparities in the development of healthcare systems and regulatory frameworks among countries; thus, they cannot be directly linked to geographical differences. More than 80% of the reports were submitted by healthcare professionals, emphasizing their crucial role in monitoring and reporting the safety of CAR-T cell therapy and ensuring the credibility of the reports.

4.2 CAR-T therapy and the causal link to PAEs

In CAR-T cell therapy, CRS is one of the most common adverse reactions, with symptoms ranging from mild infusion reactions and fever to systemic symptoms, such as hypotension (Murthy et al., 2019; Sterner et al., 2019), hypoxia, capillary leak, and organ dysfunction (Srivastava et al., 2019; Castellarin et al., 2020; Labanieh et al., 2022). The consensus criteria set by the American Society for Transplantation and Cellular Therapy (ASTCT) indicate a direct correlation between the severity of CRS and degree of hypoxic symptoms (Lee et al., 2019). The MSKCC team identified objective factors for distinguishing CRS

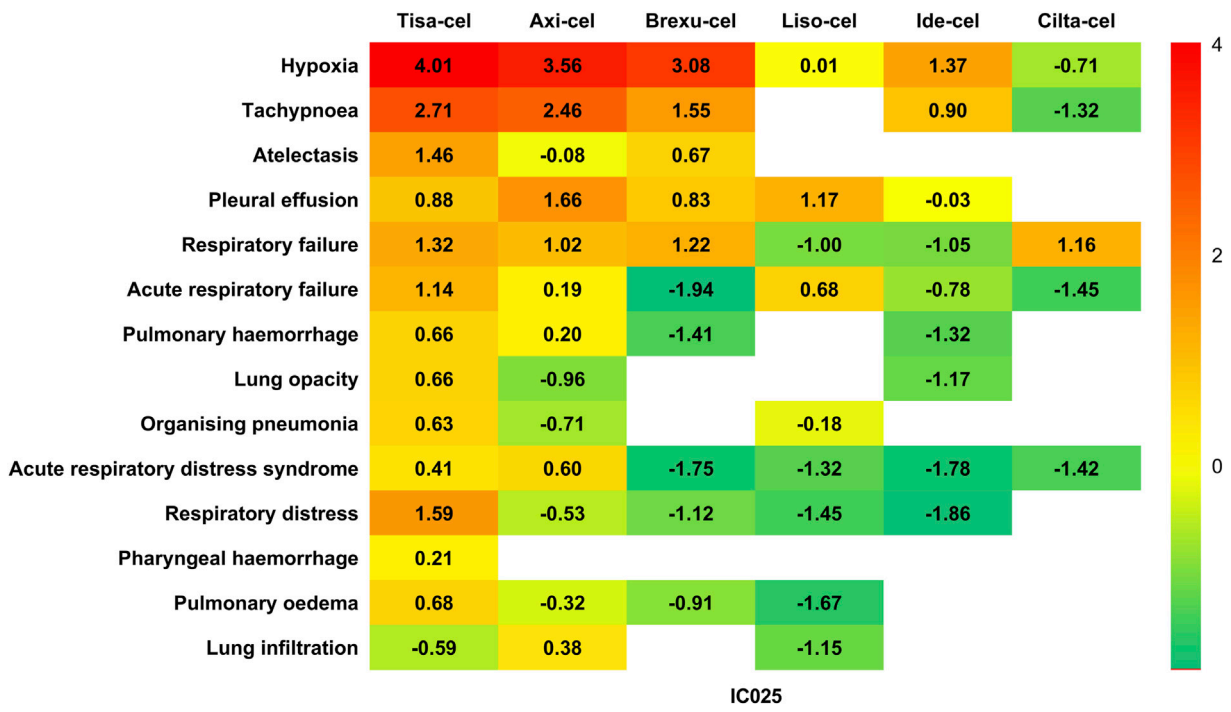

FIGURE 5
Heatmap for safety signals based on the lower limit of the 95% confidence interval of the information component (IC025).

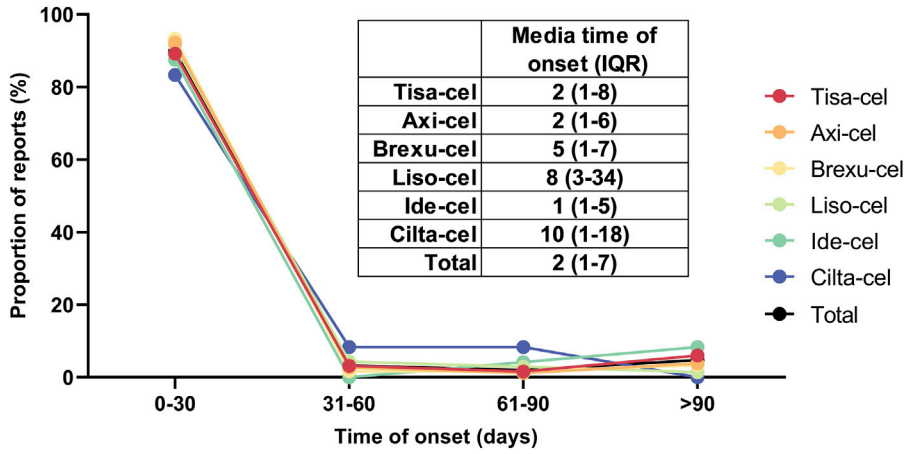

FIGURE 6
Days from CAR-T infusion to adverse event onset.

severity in early clinical trials and established a corresponding grading system. Notably, hypoxia is a pivotal factor, with an FiO2 of 40% marking the boundary between grades 2 and 3, and the need for intubation is defined as grade 4 CRS (Park et al., 2018). Our study showed that hypoxia was the most common pulmonary AE following CAR-T therapy, which is consistent with previous research and clinical practice (Shalabi et al., 2020).

During CAR T-cell therapy, genetically modified cells specifically target and eliminate tumor cells. In this process, cytokines such as IFN-γ and TNF-α are released, activating the body's endogenous immune cells and initiating a series of inflammatory reactions. The lungs, with their unique physiological structure characterized by a thin endothelial cell layer and a dense vascular network, are prime sites for the accumulation and action of these inflammatory mediators. As cytokines accumulate and CAR-T cells proliferate, inflammatory factors infiltrate the lung microvasculature and cause endothelial cell damage. Ultimately, this results in compromised lung function, tissue edema, and a spectrum of subsequent adverse reactions ranging in severity.

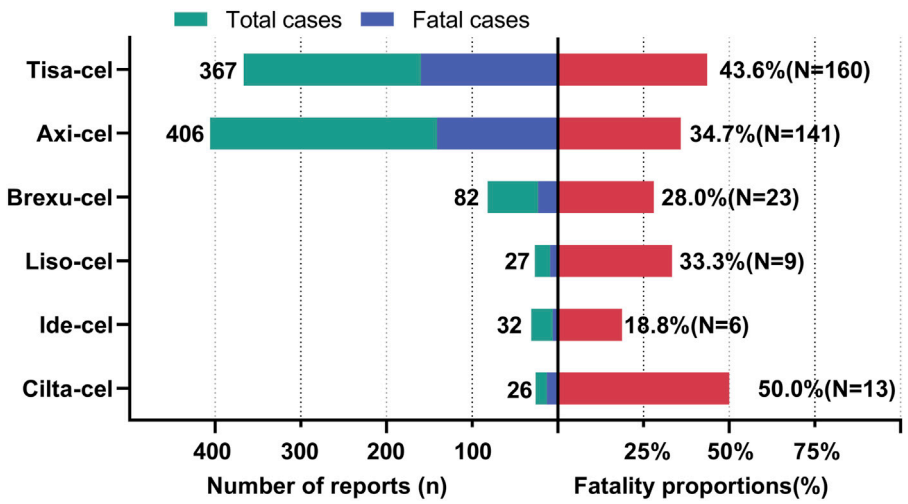

FIGURE 7
Fatalities due to PAEs from various CAR-T therapies.

4.3 Manifestations of CAR-T therapy-associated PAEs

Patients with lung injury commonly experience hypoxia and tachypnea; however, specific AEs are associated with certain CAR-T treatments. Tisa-cel, Axi-cel, and Brexu-cel showed stronger associations with respiratory failure and distress than the other therapies. Although some researchers attribute severe PAEs primarily to CRS, alternative views exist (Lichtenstein et al., 2021; Chohan et al., 2023). In a study of CAR-T cells targeting high-activity mesothelin (MSLN), two patients developed progressive hypoxemia within 48 h of infusion, aligning with CRS clinically and laboratorily. One patient died of respiratory failure, and autopsy revealed acute lung injury, widespread T-cell infiltration, and CAR T-cell accumulation in the lungs. Upregulated MSLN expression in damaged lung cells may lead to dose-limiting toxicity (Haas et al., 2023), suggesting that CAR-T cell therapy may induce targeted tissue damage owing to dynamic antigen expression in normal cells. Vigilant monitoring is crucial for mitigating risks during treatment.

Our study revealed a correlation between CAR-T therapy and AEs diagnosed through imaging examinations, including pleural effusion, atelectasis, lung consolidation, and organizing pneumonia. Compared with AEs based on subjective experiences, such as hypoxia and tachypnea, these events exhibit lower numbers and signal intensities. This discrepancy can be attributed to the diagnostic challenges associated with imaging, which may lead to the underestimation or oversight of mild or ambiguous cases. Physicians also tend to prioritize reporting AEs based on subjective experiences given their accessibility to direct patient perceptions and descriptions. Current studies indicate that specific findings from imaging modalities, such as CT, play a pivotal role in the early detection and prompt intervention of AEs, emphasizing the crucial significance of PET/CT in managing AEs following CAR-T therapy (Smith et al., 2022), The establishment of standardized imaging examination mechanisms is imperative in clinical practice.

4.4 Onset timing and fatality rate of PAEs

We observed variations in the reported mortality rates across the different CAR-T therapies. Tisa-Cel, which has been associated with 159 fatalities, had the highest death toll, raising concerns. The increased number of deaths could potentially be attributed to factors such as target specificity, cell expansion dynamics, duration of persistence, and cytokine storms. Moreover, it is essential to recognize that the extended market duration and extensive patient population of Tisa-Cel could potentially lead to an increased number of reported fatalities. Although axi-cell therapy is associated with the highest number of PAEs, its relatively low mortality rate may suggest some advantages in managing PAEs. However, this does not imply that Axi-Cel is entirely safe for lung function, as a substantial number of AE reports still emphasize the need for further optimization. Despite the limited number of cases, the high mortality rate associated with Cilta-Cel therapy is noteworthy. Given the Cilta-Cel ‘s relatively recent market entry, this could be due to its initial inexperience or other unknown factors, necessitating deeper evaluations and investigations into its safety profile. In addition, we believe that the voluntary nature of reporting in the FAERS database results in certain AEs, particularly moderate and severe AEs, that receive heightened attention and extensive reporting owing to their salience and severity. Conversely, mild events may be overlooked or inadequately reported because of a lack of salience or insufficient attention. This phenomenon of selective reporting contributes to the emergence of information bias, which is a significant factor accounting for the unusually high mortality rates and other adverse outcomes associated with such adverse events in the database.

We obtained some findings regarding the time of occurrence of AEs. Nearly 80% of CAR-T cell-related PAEs occur within 30 days, mainly due to immune responses and cytokine cascades resulting from interactions between CAR-T cells and tumor cells, thereby increasing the risk of Cytokine Release Syndrome (CRS), we firmly

advocate that prompt identification and immediate intervention are essential for managing short-term Adverse Events (AEs), which must be accomplished through rigorous monitoring at the initiation of treatment. However, monitoring discrepancies might affect the initially high incidence, and a decrease in monitoring frequency over time could lead to missed diagnoses of mild or asymptomatic events. We investigated the differences in pulmonary AE onset times among the six CAR-T cell treatments but found no significant variations. This minor similarity suggests a shared level of lung safety, which is potentially linked to common treatment mechanisms, components, and strategies. However, limitations in data collection and analysis, such as an insufficient sample size for detecting subtle distinctions or measurement biases, lead to high consistency and caution against definitive conclusions. Further research is required to validate and enhance our understanding of these observations.

5 Limitations

Data from the FAERS database may be incomplete or missing, thus impeding the comprehensive assessment of the safety of CAR-T therapy. Patient data were mainly obtained from the USA, potentially leading to ethnic and regional disparities. Moreover, most patients in this study had received prior anticancer treatments, which might have influenced the safety evaluations of CAR-T therapy. Disproportionality analysis also has significant limitations in drug safety assessments. This method relies heavily on spontaneously reported data, which lack accurate information on reaction incidence rates, thus impeding the comprehensive assessment of adverse drug reactions. Furthermore, the presence of reporting biases and confounding factors may severely affect the analytical results, thereby diminishing their accuracy. Therefore, a disproportionality analysis can only provide preliminary hypotheses and must be combined with other methodologies to ensure the accuracy and comprehensiveness of the evaluation.

6 Conclusion

This study comprehensively described the PAEs reported in the FAERS database for patients receiving CAR-T cell therapy, including conditions such as hypoxia, respiratory failure, pleural effusion, and atelectasis. These events are associated with a higher incidence and risk in patients undergoing CAR-T cell therapy, can severely impact breathing, and are life-threatening. To minimize these risks, physicians should consider preconditioning drugs, fine-tune CAR-T doses, and alternative treatment plans. Lung issues associated with CAR-T therapy are clinically significant and require attention from both doctors and researchers.

Data availability statement

The original contributions presented in the study are included in the article/Supplementary Material, further inquiries can be directed to the corresponding authors.

Author contributions

JS: Conceptualization, Data curation, Formal Analysis, Methodology, Software, Supervision, Visualization, Writing–original draft, Writing–review and editing. XL: Conceptualization, Data curation, Funding acquisition, Methodology, Supervision, Writing–review and editing. YJ: Conceptualization, Funding acquisition, Investigation, Resources, Writing–review and editing. MG: Formal Analysis, Investigation, Supervision, Writing–review and editing. JY: Conceptualization, Funding acquisition, Supervision, Writing–review and editing. YZ: Formal Analysis, Software, Validation, Visualization, Writing–review and editing. LW: Funding acquisition, Resources, Supervision, Validation, Writing–review and editing.

Funding

The author(s) declare that financial support was received for the research, authorship, and/or publication of this article. This work was funded by Key Natural Science Foundation of Xinjiang Uygur Autonomous Region (Project No. 2022D01D76).

Conflict of interest

The authors declare that the research was conducted in the absence of any commercial or financial relationships that could be construed as a potential conflict of interest.

Publisher's note

All claims expressed in this article are solely those of the authors and do not necessarily represent those of their affiliated organizations, or those of the publisher, the editors and the reviewers. Any product that may be evaluated in this article, or claim that may be made by its manufacturer, is not guaranteed or endorsed by the publisher.

Supplementary material

The Supplementary Material for this article can be found online at: https://www.frontiersin.org/articles/10.3389/fphar.2024.1434231/full#supplementary-material

References

Abramson, J. S., Palomba, M. L., Gordon, L. I., Lunning, M. A., Wang, M., Arnason, J., et al. (2020). Lisocabtagene maraleucel for patients with relapsed or refractory large B-cell lymphomas (Transcend NHL 001): a multicentre seamless design study. *Lancet*. 396, 839–852. doi:10.1016/S0140-6736(20)31366-0

Alvi, R. M., Frigault, M. J., Fradley, M. G., Jain, M. D., Mahmood, S. S., Awadalla, M., et al. (2019). Cardiovascular events among adults treated with chimeric antigen receptor T-cells (CAR-T). *J. Am. Coll. Cardiol.* 74, 3099–3108. doi:10.1016/j.jacc.2019.10.038

Castellarin, M., Sands, C., Da, T., Scholler, J., Graham, K., Buza, E., et al. (2020). A rational mouse model to detect on-target, off-tumor CAR T cell toxicity. *JCI Insight*. 5, e136012. doi:10.1172/jci.insight.136012

Chen, X., Li, P., Tian, B., and Kang, X. (2022). Serious adverse events and coping strategies of CAR-T cells in the treatment of malignant tumors. *Front. Immunol.* 13, 1079181. doi:10.3389/fimmu.2022.1079181

Chen, Y., Fan, Q., Liu, Y., Shi, Y., and Luo, H. (2023). Cardiovascular toxicity induced by SSRIs: analysis of spontaneous reports submitted to FAERS. *Psychiatry Res.* 326, 115300. doi:10.1016/j.psychres.2023.115300

Chohan, K. L., Siegler, E. L., and Kenderian, S. S. (2023). CAR-T cell therapy: the efficacy and toxicity balance. *Curr. Hematol. Malig. Rep.* 18, 9–18. doi:10.1007/s11899-023-00687-7

Ganatra, S., Redd, R., Hayek, S. S., Parikh, R., Azam, T., Yanik, G. A., et al. (2020). Chimeric antigen receptor T-cell therapy-associated cardiomyopathy in patients with refractory or relapsed non-Hodgkin lymphoma. *Circulation*. 142, 1687–1690. doi:10.1161/CIRCULATIONAHA.120.048100

Haas, A. R., Golden, R. J., Litzky, L. A., Engels, B., Zhao, L., Xu, F., et al. (2023). Two cases of severe pulmonary toxicity from highly active mesothelin-directed CAR T cells. *Mol. Ther.* 31, 2309–2325. doi:10.1016/j.ymthe.2023.06.006

Jacobson, C. A., Chavez, J. C., Sehgal, A. R., William, B. M., Munoz, J., Salles, G., et al. (2022). Axicabtagene ciloleucel in relapsed or refractory indolent non-Hodgkin lymphoma (ZUMA-5): a single-arm, multicentre, phase 2 trial. *Lancet Oncol.* 23, 91–103. doi:10.1016/S1470-2045(21)00591-X

Kaddu-Mulindwa, D., Altmann, B., Robrecht, S., Ziepert, M., Regitz, E., Tausch, E., et al. (2022). KIR2DS1-HLA-C status as a predictive marker for benefit from rituximab: a post-hoc analysis of the RICOVER-60 and CLL8 trials. *Lancet Haematol.* 9, e133–e142. doi:10.1016/S2352-3026(21)00369-0

Labanieh, L., Majzner, R. G., Klysz, D., Sotillo, E., Fisher, C. J., Vilches-Moure, J. G., et al. (2022). Enhanced safety and efficacy of protease-regulated CAR-T cell receptors. *Cell.* 185, 1745–1763.e22. doi:10.1016/j.cell.2022.03.041

Lee, D. W., Santomasso, B. D., Locke, F. L., Ghobadi, A., Turtle, C. J., Brudno, J. N., et al. (2019). ASTCT consensus grading for cytokine release syndrome and neurologic toxicity associated with immune effector cells. *Biol. Blood Marrow Transpl.* 25, 625–638. doi:10.1016/j.bbmt.2018.12.758

Lefebvre, B., Kang, Y., Smith, A. M., Frey, N. V., Carver, J. R., and Scherrer-Crosbie, M. (2020). Cardiovascular effects of CAR T cell therapy: a retrospective study. *JACC CardioOncol.* 2, 193–203. doi:10.1016/j.jaccao.2020.04.012

Lichtenstein, D. A., Schischlik, F., Shao, L., Steinberg, S. M., Yates, B., Wang, H. W., et al. (2021). Characterization of HLH-like manifestations as a CRS variant in patients receiving CD22 CAR T cells. *Blood*. 138, 2469–2484. doi:10.1182/blood.2021011898

Martin, T., Usmani, S. Z., Berdeja, J. G., Agha, M., Cohen, A. D., Hari, P., et al. (2023). Ciltacabtagene autoleucel, an anti-B-cell maturation antigen chimeric antigen receptor T-cell therapy, for relapsed/refractory multiple myeloma: CARTITUDE-1 2-year follow-up. *J. Clin. Oncol.* 41, 1265–1274. doi:10.1200/JCO.22.00842

Maude, S. L., Laetsch, T. W., Buechner, J., Rives, S., Boyer, M., Bittencourt, H., et al. (2018). Tisagenlecleucel in children and young adults with B-cell lymphoblastic leukemia. *N. Engl. J. Med.* 378, 439–448. doi:10.1056/NEJMoa1709866

Michel, C., Scosyrev, E., Petrin, M., and Schmouder, R. (2017). Can disproportionality analysis of post-marketing case reports be used for comparison of drug safety profiles? *Clin. Drug Investig.* 37, 415–422. doi:10.1007/s40261-017-0503-6

Munshi, N. C., Anderson, L. D., Jr, Shah, N., Madduri, D., Berdeja, J., Lonial, S., et al. (2021). Idecabtagene vicleucel in relapsed and refractory multiple myeloma. *N. Engl. J. Med.* 384, 705–716. doi:10.1056/NEJMoa2024850

Murthy, H., Iqbal, M., Chavez, J. C., and Kharfan-Dabaja, M. A. (2019). Cytokine release syndrome: current perspectives. *ImmunoTargets Ther.* 8, 43–52. doi:10.2147/ITT.S202015

Neelapu, S. S., Tummala, S., Kebriaei, P., Wierda, W., Gutierrez, C., Locke, F. L., et al. (2018). Chimeric antigen receptor T-cell therapy - assessment and management of toxicities. *Nat. Rev. Clin. Oncol.* 15, 47–62. doi:10.1038/nrclinonc.2017.148

Park, J. H., Rivière, I., Gonen, M., Wang, X., Sénéchal, B., Curran, K. J., et al. (2018). Long-term follow-up of CD19 CAR therapy in acute lymphoblastic leukemia. *N. Engl. J. Med.* 378, 449–459. doi:10.1056/NEJMoa1709919

Schuster, S. J., Bishop, M. R., Tam, C. S., Waller, E. K., Borchmann, P., McGuirk, J. P., et al. (2019). Tisagenlecleucel in adult relapsed or refractory diffuse large B-cell lymphoma. *N. Engl. J. Med.* 380, 45–56. doi:10.1056/NEJMoa1804980

Shalabi, H., Sachdev, V., Kulshreshtha, A., Cohen, J. W., Yates, B., Rosing, D. R., et al. (2020). Impact of cytokine release syndrome on cardiac function following CD19 CAR-T cell therapy in children and young adults with hematological malignancies. *J. Immunother. Cancer*. 8, e001159. doi:10.1136/jitc-2020-001159

Smith, D. A., Kikano, E., Tirumani, S. H., de Lima, M., Caimi, P., and Ramaiya, N. H. (2022). Imaging-based toxicity and response pattern assessment following CAR T-cell therapy. *Radiology*. 302, 438–445. doi:10.1148/radiol.2021210760

Srivastava, S., Salter, A. I., Liggitt, D., Yechan-Gunja, S., Sarvothama, M., Cooper, K., et al. (2019). Logic-gated ROR1 chimeric antigen receptor expression rescues T cell-mediated toxicity to normal tissues and enables selective tumor targeting. *Cancer Cell.* 35, 489–503.e8. doi:10.1016/j.ccell.2019.02.003

Sterner, R. C., and Sterner, R. M. (2021). CAR-T cell therapy: current limitations and potential strategies. *Blood Cancer J.* 11, 69. doi:10.1038/s41408-021-00459-7

Sterner, R. M., Sakemura, R., Cox, M. J., Yang, N., Khadka, R. H., Forsman, C. L., et al. (2019). GM-CSF inhibition reduces cytokine release syndrome and neuroinflammation but enhances CAR-T cell function in xenografts. *Blood*. 133, 697–709. doi:10.1182/blood-2018-10-881722

Tian, X., Chen, L., Gai, D., He, S., Jiang, X., and Zhang, N. (2022). Adverse event profiles of PARP inhibitors: analysis of spontaneous reports submitted to FAERS. *Front. Pharmacol.* 13, 851246. doi:10.3389/fphar.2022.851246

Wang, L., Feng, W., Duan, J., and Liang, J. (2021). Pharmacovigilance bibliometrics: visualizing thematic development in the category of pharmacology and pharmacy in Web of Science. *Front. Pharmacol.* 12, 731757. doi:10.3389/fphar.2021.731757

Wang, Y., Jain, P., Locke, F. L., Maurer, M. J., Frank, M. J., Munoz, J. L., et al. (2023). Brexucabtagene autoleucel for relapsed or refractory mantle cell lymphoma in standard-of-care practice: results from the US lymphoma CAR T Consortium. *J. Clin. Oncol.* 41, 2594–2606. doi:10.1200/JCO.22.01797

Yang, Z., Lv, Y., Yu, M., Mei, M., Xiang, L., Zhao, S., et al. (2022). GLP-1 receptor agonist-associated tumor adverse events: a real-world study from 2004 to 2021 based on FAERS. *Front. Pharmacol.* 13, 925377. doi:10.3389/fphar.2022.925377

Yu, R. J., Krantz, M. S., Phillips, E. J., and Stone, C. A. (2021). Emerging causes of drug-induced anaphylaxis: a review of anaphylaxis-associated reports in the FDA Adverse Event Reporting System (FAERS). *J. Allergy Clin. Immunol. Pract.* 9, 819–829.e2. doi:10.1016/j.jaip.2020.09.021

frontiers | Frontiers in Pharmacology

TYPE Review
PUBLISHED 27 August 2024
DOI 10.3389/fphar.2024.1446486

Check for updates

OPEN ACCESS

EDITED BY
Wagdy Mohamed Eldehna,
Kafrelsheikh University, Egypt

REVIEWED BY
Erdong Zhang,
Guizhou Medical University, China
Haytham O. Tawfik,
Tanta University, Egypt

*CORRESPONDENCE
Shuai Wang,
ws20095072016@163.com
Yihang Dai,
yhdai2018@126.com

†These authors have contributed equally to this work

RECEIVED 09 June 2024
ACCEPTED 16 August 2024
PUBLISHED 27 August 2024

CITATION
Wang S, He H, Qu L, Shen Q and Dai Y (2024) Dual roles of inflammatory programmed cell death in cancer: insights into pyroptosis and necroptosis.
Front. Pharmacol. 15:1446486.
doi: 10.3389/fphar.2024.1446486

COPYRIGHT
© 2024 Wang, He, Qu, Shen and Dai. This is an open-access article distributed under the terms of the Creative Commons Attribution License (CC BY). The use, distribution or reproduction in other forums is permitted, provided the original author(s) and the copyright owner(s) are credited and that the original publication in this journal is cited, in accordance with accepted academic practice. No use, distribution or reproduction is permitted which does not comply with these terms.

Dual roles of inflammatory programmed cell death in cancer: insights into pyroptosis and necroptosis

Shuai Wang[1*†], Huanhuan He[2†], Lailiang Qu[1], Qianhe Shen[1] and Yihang Dai[1*]

[1]Collage of Medicine, Xinyang Normal University, Xinyang, China, [2]State Key Laboratory of Biocontrol, Guangdong Provincial Key Laboratory of Plant Resources and Southern Marine Science and Engineering Guangdong Laboratory (Zhuhai), School of Life Sciences, Sun Yat-sen University, Guangzhou, China

Programmed cell death (PCD) is essential for cellular homeostasis and defense against infections, with inflammatory forms like pyroptosis and necroptosis playing significant roles in cancer. Pyroptosis, mediated by caspases and gasdermin proteins, leads to cell lysis and inflammatory cytokine release. It has been implicated in various diseases, including cancer, where it can either suppress tumor growth or promote tumor progression through chronic inflammation. Necroptosis, involving RIPK1, RIPK3, and MLKL, serves as a backup mechanism when apoptosis is inhibited. In cancer, necroptosis can enhance immune responses or contribute to tumor progression. Both pathways have dual roles in cancer, acting as tumor suppressors or promoting a pro-tumorigenic environment depending on the context. This review explores the molecular mechanisms of pyroptosis and necroptosis, their roles in different cancers, and their potential as therapeutic targets. Understanding the context-dependent effects of these pathways is crucial for developing effective cancer therapies.

KEYWORDS

pyroptosis, necroptosis, cancer, inflammation, anti-cancer drugs

1 Introduction

Programmed cell death (PCD) is a fundamental biological process crucial for maintaining cellular homeostasis, eliminating damaged cells, and defending against infections. PCD can be categorized into inflammatory and non-inflammatory pathways. The inflammatory forms of PCD include pyroptosis and necroptosis, which play significant roles in various pathological conditions, including cancer, infections, and inflammatory diseases. Unlike non-inflammatory forms such as apoptosis, autophagy, and phagoptosis, inflammatory cell death is characterized by the release of pro-inflammatory cytokines and cellular contents that can provoke strong immune responses. Understanding the molecular mechanisms and roles of these inflammatory cell death pathways is essential for developing novel therapeutic strategies.

Pyroptosis was initially observed in macrophages infected with *Shigella* and *Salmonella* (Boise and Collins, 2001), and has since been implicated in a variety of diseases, including cancer. Pyroptosis is a form of programmed cell death distinguished by its reliance on caspases, particularly caspase-1, -4, -5, and -11, leading to the cleavage of gasdermin proteins that form pores in the cell membrane (Shi et al., 2014). This process results in cell lysis and the release of inflammatory cytokines such as IL-1β and IL-18. The discovery of

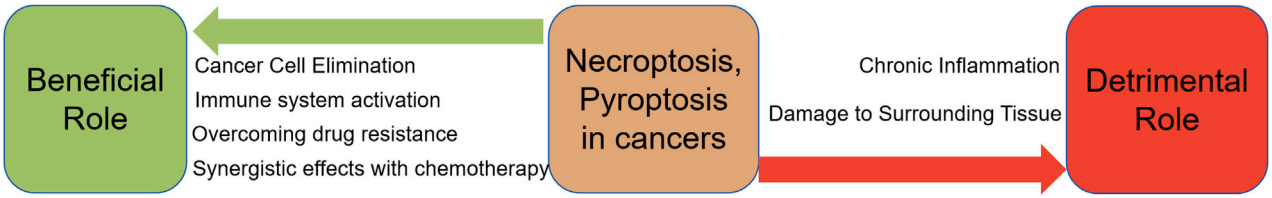

GRAPHICAL ABSTRACT

non-classical pyroptosis pathways involving caspase-3 and caspase-8, as well as the roles of other gasdermin family members like gasdermin E (GSDME) and gasdermin C (GSDMC), has expanded our understanding of this complex cell death mechanism (Wang et al., 2017).

Necroptosis, another form of inflammatory programmed cell death, is mediated by receptor-interacting protein kinases-1/-3 (RIPK1 and RIPK3) and mixed lineage kinase domain-like protein (MLKL). Upon activation by death receptors or pathogen recognition receptors, RIPK1 interacts with RIPK3 to form a necrosome, which subsequently phosphorylates MLKL. The phosphorylated MLKL translocates to the plasma membrane, forming disruptive pores that lead to cell swelling, membrane rupture, and the release of damage-associated molecular patterns (DAMPs). Necroptosis is often a backup mechanism when apoptosis is inhibited, playing a crucial role in immune responses and disease pathogenesis.

Inflammatory programmed cell death, encompassing both pyroptosis and necroptosis, contributes significantly to cancer biology. In the tumor microenvironment, these pathways can either suppress tumor growth by eliminating malignant cells or promote tumor progression through chronic inflammation and immune evasion. For instance, in non-small cell lung cancer (NSCLC), elevated gasdermin D (GSDMD) expression has been linked to increased tumor invasion and metastasis, while the induction of pyroptosis can lead to cancer cell apoptosis. Similarly, in breast cancer, gasdermin B (GSDMB) expression correlates with enhanced cell invasion and poor prognosis. Conversely, activating pyroptosis or necroptosis pathways in colorectal cancer cells has shown potential in overcoming chemoresistance and inhibiting tumor growth.

The dual roles of pyroptosis and necroptosis in cancer underscore the complexity of these pathways. While they can act as tumor suppressors by triggering inflammatory cell death, they can also facilitate a pro-tumorigenic environment through the release of inflammatory mediators. This paradox highlights the importance of precise modulation of these pathways in cancer therapy. Research efforts are increasingly focused on understanding the context-dependent effects of pyroptosis and necroptosis, aiming to harness their therapeutic potential while mitigating adverse inflammatory responses.

2 Mechanisms of pyroptosis

2.1 Inflammasome-mediated canonical pyroptosis pathway

The inflammasome is a multiprotein complex that includes major types such as NLRP1, NLRP3, NLRC4, and AIM2. Upon exposure to exogenous or endogenous microbial infections, stimulatory factors, or damage signals, pattern recognition receptors (PRRs) and DAMPs recognize and bind to their respective ligands, forming the inflammasome complex. This complex subsequently promotes the maturation of pro-caspase-1 into active caspase-1. Caspase-1 then processes various inflammatory cytokines (e.g., IL-1β, IL-6, and IL-18) into their mature forms (Wang et al., 2024). Concurrently, caspase-1 cleaves GSDMD into its active form, GSDMD-N, which translocates to the cell membrane to form pores. The formation of these pores facilitates the rapid release of mature inflammatory cytokines into the extracellular space, triggering an amplified inflammatory response in the surrounding environment, leading to cell swelling, bubbling, and eventual death. This pathway, dependent on inflammasomes, caspase-1, and GSDMD, is known as the classical pyroptosis pathway.

2.2 Non-canonical pyroptosis pathway

Recent studies have demonstrated that some forms of pyroptosis do not rely on the inflammasome. Lipopolysaccharides (LPS) can directly bind to and activate caspase-4, -5, and -11, promoting the cleavage and maturation of GSDMD, thus inducing the non-canonical pyroptosis pathway (Shi et al., 2014). For instance, the *Yersinia* effector protein YopJ inhibits the activity of TGF-β-activated kinase 1 (TAK1), leading to the caspase-8-mediated cleavage of GSDMD (Orning et al., 2018). Additionally, granzyme A (GZMA), secreted by cytotoxic lymphocytes, can induce pyroptosis through the cleavage of GSDMB (Zhou et al., 2020), and neutrophil elastase (ELANE) can induce pyroptosis via GSDMD cleavage (Kambara et al., 2018). These findings suggest that the pathways leading to pyroptosis are complex, with an increasing number of non-inflammasome-mediated pyroptosis mechanisms being discovered.

3 Mechanisms of necroptosis

Necroptosis can be activated by factors such as the tumor necrosis factor receptor (TNFR) superfamily, T-cell receptors, pattern recognition receptors, and oxidative stress (Lalaoui et al., 2015). Taking the classic TNF/TNFR signaling pathway as an example, the binding of TNF to TNFR1 induces the formation of a membrane complex. This complex includes the inhibitor of apoptosis proteins (IAP) family members cIAP1 and cIAP2, which ubiquitinate RIPK1. The ubiquitination of

RIPK1 promotes the activation of nuclear factor kappa-B (NF-κB) and mitogen-activated protein kinase (MAPK) signaling pathways, leading to the transcription of downstream genes, including FLICE-like inhibitory protein (c-FLIP), which inhibits the activity of caspase-8 (Wright et al., 2007; Bertrand et al., 2008). Under normal conditions, RIPK1 and RIPK3 are cleaved and inactivated by caspase-8. However, during necroptosis, the inactivation of caspase-8 prevents the cleavage of RIPK1 and RIPK3. Subsequently, RIPK1 and RIPK3 undergo phosphorylation to form the necrosome, which phosphorylates and oligomerizes MLKL. The oligomerized MLKL complex translocates to the cell membrane to form pores, initiating necroptosis (Cho et al., 2009; Sun et al., 2012; Murphy et al., 2013).

Recent studies have revealed that, beyond the classical RIPK3-MLKL signaling pathway, RIPK3 can also induce necroptosis through phosphoglycerate mutase 5 (PGAM5) and calcium/calmodulin-dependent protein kinase II (CAMK II). PGAM5 has two isoforms, PGAM5L and PGAM5S. Upon activation, RIPK3 phosphorylates PGAM5L, which then binds to PGAM5S on the mitochondrial membrane. The PGAM5L/PGAM5S complex induces mitochondrial fission by dephosphorylating dynamin-related protein 1, leading to necroptosis.

4 Lung cancer

4.1 Necroptosis and lung cancer

Lung cancer encompasses various types with complex etiologies, and recent research into necroptosis has opened new avenues for its treatment. Studies have shown that RIPK3 expression is significantly lower in NSCLC patients, correlating with poor chemotherapy outcomes (Lim et al., 2021). Ectopic expression of RIPK3 markedly increases the sensitivity of lung cancer cells to chemotherapeutic agents such as cisplatin, etoposide, vincristine, and adriamycin (Wang Q. et al., 2020). Traditionally, cisplatin was believed to exert its anticancer effects by inducing apoptosis in lung cancer cells. However, recent findings suggest that cisplatin also mediates its effects through RIPK1-RIPK3-MLKL-dependent necroptosis (Jing et al., 2018). Another study indicates that the compound HS-173 induces necrosis in lung cancer cells by enhancing RIPK3 expression and activating the RIPK3/MLKL signaling pathway (Park et al., 2019). Furthermore, 2-methoxy-6-acetyl-7-methyljuglone (MAM) exerts anticancer effects by targeting RIPK1, causing oxidative stress, and inducing necrosis in A549 and H1299 lung cancer cells (Sun et al., 2019). Additionally, tanshinol A has been shown to mediate necroptosis in lung cancer cells via MLKL, independent of RIPK1 and RIPK3 activation, by directly inducing MLKL phosphorylation and oligomerization (Liu et al., 2020).

4.2 Pyroptosis and lung cancer

Research has demonstrated that GSDMD expression is significantly elevated in NSCLC and is associated with tumor cell invasion and metastasis (Gao et al., 2018), knockout of GSDMD, while not leading to pyroptosis, induces apoptosis when the pyroptotic signaling pathway is activated. Furthermore, the active component of Paris polyphylla, polyphyllin VI, induces pyroptosis in NSCLC cells by activating the NLRP3-Caspase1-GSDMD signaling pathway (Teng et al., 2020). Cucurbitacin B also induces pyroptosis in NSCLC cells by directly binding to Toll-like receptor 4 (TLR4) and activating NLRP3 and GSDMD (Yuan et al., 2021). Moreover, the classical chemotherapeutic agent cisplatin can induce pyroptosis in A549 lung cancer cells by activating Caspase-3, which cleaves GSDME to produce GSDME-N (Zhang CC. et al., 2019). The oncogenic LncRNA-XIST regulates the proliferation, invasion, and migration of NSCLC cells (Sun et al., 2017; Wang X. et al., 2018; Liu A. et al., 2019; Zhang J. et al., 2019). Knockdown of LncRNA-XIST significantly elevates reactive oxygen species levels in A549 cells, inducing pyroptosis in cancer cells (Cui et al., 2019; Liu J. et al., 2019).

Contrary to the aforementioned findings, some studies have reported different outcomes. Wang et al. (2016) demonstrated that LPS combined with ATP enhances the proliferation and migration of A549 cells by activating the NLRP3 inflammasome. Salidroside, on the other hand, reduces LPS-induced inflammasome activation, thereby inhibiting the proliferation and migration of A549 cells (Ma et al., 2021). Liang et al. (2020) found that tumor-derived exosomal TRIM59 promotes lung cancer progression by modulating macrophages to a tumor-promoting phenotype through ABHD5 proteasomal degradation, which in turn activates the NLRP3 inflammasome signaling pathway and promotes IL-1β secretion.

5 Colorectal cancer

5.1 Necroptosis and colorectal cancer

Colorectal cancer (CRC) ranks as the fourth most common cancer worldwide, claiming nearly 700,000 lives annually. Investigating necroptosis and pyroptosis offers promising avenues for discovering new therapeutic strategies for CRC. Studies have demonstrated that bufogenin mediates necroptosis through the upregulation of RIPK3 and phosphorylation of MLKL, effectively inhibiting CRC development and metastasis (Han et al., 2018). Additionally, the small molecule GDC-0326 induces necroptosis in CRC cells by modulating RIPK1 and RIPK3. When combined with 5-fluorouracil (5-FU), GDC-0326 significantly overcomes 5-FU resistance in CRC treatment, enhancing its anticancer efficacy (Zhang et al., 2021). SMYD2, a histone methyltransferase, is implicated in various cancers. Research indicates that SMYD2 expression is significantly elevated in both human and murine colorectal cancer tissues. The absence of SMYD2 sensitizes colon tumor cells to TNF-induced apoptosis and necroptosis. Further studies reveal that SMYD2 targets RIPK1, inhibiting its phosphorylation and thereby preventing necroptosis (Yu et al., 2022).

However, conflicting views exist regarding the role of necroptosis in CRC. Some studies suggest that PGAM5, downstream of RIPK3, is upregulated in CRC, contributing to cancer progression by affecting NADPH production and lipid metabolism (Zhu et al., 2020). Elevated RIPK3 expression is also observed in mouse models of colitis-associated cancer and human

CRC. RIPK3 knockout mice are protected against dextran sulfate sodium (DSS)-induced colitis-associated cancer (Liu ZY. et al., 2019). Since necroptosis is associated with increased inflammation, which is a risk factor for colitis and subsequently CRC, excessive necroptosis may accelerate cancer progression through heightened inflammatory responses.

5.2 Pyroptosis and colorectal cancer

Research indicates that the antitumor drug lobaplatin mediates ROS/JNK/Bax signaling, inducing pyroptosis via caspase-3/-9-dependent GSDME cleavage, thereby exerting its antitumor effects (Yu et al., 2019). Notably, even when GSDME is knocked out, lobaplatin still induces tumor cell death through apoptosis, demonstrating its robust antitumor activity (Yu et al., 2019). Multiple studies have shown that inflammasome-mediated pyroptosis can suppress tumorigenesis. Mice deficient in NLRP1, NLRP3, NLRC4, AIM2, or pyrin inflammasomes exhibit significantly higher tumor incidence (Allen et al., 2010; Hu et al., 2010; Williams et al., 2015; Wilson et al., 2015; Sharma et al., 2018). Additionally, NLRP1 expression is markedly lower in colorectal cancer tissues compared to normal tissues (Chen et al., 2015). The antitumor drug 5-aza-2-deoxycytidine inhibits CRC progression by restoring NLRP1 expression, suggesting that NLRP1 is a potential therapeutic target for CRC (Chen et al., 2015).

The intestinal epithelial barrier is crucial for maintaining gut homeostasis. Its impairment can lead to immune dysregulation and inflammatory responses, accelerating CRC progression. Bauer et al. (2010) found that NLRP3 plays a critical role in DSS-induced colitis. NLRP3 knockout mice exhibit significantly less severe colitis compared to wild-type mice after DSS administration. Moreover, the absence of IL-18 and its receptor protects mice from DSS-induced colitis (Nowarski et al., 2015). Contrarily, other studies report that NLRP1b, NLRP3, and pyrin promote epithelial barrier regeneration and prevent CRC progression in early stages by secreting IL-18 (Allen et al., 2010; Dupaul-Chicoine et al., 2010; Zaki et al., 2010). ASC and caspase-1 knockout mice are also more susceptible to DSS-induced colitis and colitis-associated colorectal cancer (Dupaul-Chicoine et al., 2010; Hirota et al., 2011). These findings suggest that inflammasomes maintain gut homeostasis, reducing inflammation and CRC incidence. The discrepancy in conclusions may arise because inflammasome-mediated IL-18 production aids epithelial barrier regeneration and reduces inflammation in early CRC stages, while excessive cytokine release in advanced stages may accelerate cancer progression. Therefore, pyroptosis plays a significant role in CRC development and treatment, though its mechanisms warrant further investigation.

6 Breast cancer

6.1 Necroptosis and breast cancer

Breast cancer, a malignant tumor originating from the uncontrolled proliferation and malignancy of breast epithelial cells, is the most common malignancy worldwide (Karamanou et al., 2020). The etiology of breast cancer is complex, involving immutable genetic factors and modifiable factors such as obesity and exogenous hormones. Recent research into necroptosis and pyroptosis has provided new insights for breast cancer treatment. Studies have identified Z-DNA binding protein 1 (ZBP1) as a crucial regulator of necroptosis in breast cancer cells. The absence of ZBP1 disrupts necroptosis during tumor development, and glucose deprivation triggers ZBP1-dependent necroptosis (Baik et al., 2021). Additionally, 5-fluorouracil (5-FU) induces necroptosis in breast cancer cells by activating RIPK1 when caspases are inhibited (Zhang et al., 2018). Shikonin inhibits the proliferation of human triple-negative breast cancer cells, with a dose-dependent increase in RIPK1 expression (Yuan et al., 2021). *In vitro* studies have shown that the combination of Goniothalamin and the caspase inhibitor Z-VAD-FMK activates the RIPK1-RIPK3-MLKL pathway, inducing necroptosis in human breast cancer MDA-MB-231 cells (Khaw-On et al., 2019).

6.2 Pyroptosis and breast cancer

Pyroptosis is also closely related to the development and treatment of breast cancer. Various antibiotics can induce pyroptosis in breast cancer cells by upregulating PD-L1 and GSDMC expression and activating Caspase-8 (Hou et al., 2020). Docosahexaenoic acid (DHA) exerts anticancer effects by activating Caspase-1 and GSDMD to induce pyroptosis in breast cancer cells, an effect that can be abolished by Caspase-1 inhibitors (Pizato et al., 2018). Human umbilical cord mesenchymal stem cell-conditioned medium (hUCMSC-CM) can mediate pyroptosis in human breast cancer cells (MCF7) through both NLRP1 and Caspase-4 pathways. When Caspase-4 expression is knocked down, hUCMSC-CM induces pyroptosis via the classical NLRP1 pathway; conversely, knocking down NLRP1 leads to pyroptosis through the non-classical Caspase-4 pathway (Jiao et al., 2020). On the other hand, inflammasomes and the inflammation they mediate are closely associated with breast cancer progression. GSDMB is highly expressed in breast cancer cells and is linked to cancer cell invasion and metastasis (Hergueta-Redondo et al., 2014). The activation of inflammasomes and pyroptosis-derived IL-1β is essential for the proliferation, invasion, and migration of breast cancer cells (Voronov et al., 2003). Tumor growth and metastasis are significantly reduced in NLRP3 knockout mice, with primary and metastatic tumors associated with elevated IL-1β levels. Blocking IL-1β with an IL-1R antagonist inhibits tumor growth and metastasis in breast cancer models (Guo et al., 2016). Obesity increases the risk of breast cancer, and studies by Kolb et al. indicate that the tumor microenvironment in obesity induces tumor-infiltrating myeloid cells via the NLRC4 inflammasome, which activates IL-1β. IL-1β, in turn, drives breast cancer development through adipocyte-mediated expression of vascular endothelial growth factor A (VEGFA) and angiogenesis (Kolb et al., 2016).

7 Liver cancer

7.1 Necroptosis and liver cancer

A research investigates the pivotal role of necroptosis in both human and murine models of non-alcoholic steatohepatitis

(NASH), shedding light on its contribution to hepatocyte death and inflammation (Afonso et al., 2015). Similarly, Gautheron et al. (2014) uncover a positive feedback loop between RIPK3 and JNK in driving hepatocyte death and liver inflammation in NASH. Moreover, Schneider et al. (2017) elucidate the tumor-suppressive function of receptor-interacting protein kinase 1 (RIPK1) in hepatocellular carcinoma (HCC), inhibiting a TNF receptor-associated factor 2 (TRAF2)-dependent pathway to liver cancer. Although another study focuses on the regulatory role of APF long non-coding RNA (lncRNA) in autophagy and myocardial infarction, it underscores the broader relevance of non-coding RNAs in cellular processes (Wang et al., 2015). Collectively, these findings underscore the intricate involvement of necroptosis in liver pathophysiology, highlighting its potential as a therapeutic target for managing liver diseases, including NASH and HCC.

7.2 Pyroptosis and liver cancer

Research has demonstrated that NLRP3 expression is significantly downregulated or even completely lost in HCC, with this deficiency promoting cancer progression (Wei et al., 2014). The same research group later discovered that 17β-estradiol (E2) can inhibit the further development of HCC by upregulating NLRP3 (Wei et al., 2015). This upregulation activates NLRP3-mediated pyroptosis, ultimately leading to cancer cell death and exerting anticancer effects (Wei et al., 2019). On the other hand, some studies suggest that excessive activation of NLRP3 is closely associated with hepatitis, liver fibrosis, and cirrhosis (Wree et al., 2014; Mridha et al., 2017; Xie et al., 2020), all of which increase the risk of liver cancer. Additionally, knocking out interleukin-1 receptor-associated kinase 1 (IRAK1) can inhibit the progression of HCC by blocking the MAPKs/IL-1β pathway through NLRP3 suppression (Chen et al., 2020). Furthermore, anisodamine inhibits HCC cell growth, induces apoptosis, and modulates inflammatory cytokine levels by suppressing NLRP3 activation (Li et al., 2020). Direct targeting of the NLRP3 inflammasome also inhibits HCC proliferation, metastasis, and invasion (Fan et al., 2014). These studies collectively suggest that inflammasomes and pyroptosis play critical roles in the development and treatment of HCC. However, the conclusions are not entirely consistent, and the precise mechanisms of action require further elucidation.

8 Gastric cancer

8.1 Necroptosis and gastric cancer

Necroptosis-related genes (NRGs) have been found to be dysregulated in gastric cancer, suggesting their potential as biomarkers for early diagnosis and prognosis. For instance, studies have identified key NRGs such as CCT6A and FAP, which can effectively predict early Gastric Cancer (GC) and its prognosis. These genes are linked to the response to immunotherapy and immune checkpoint inhibitors, indicating their relevance in personalized cancer treatment strategies. The immunogenic nature of necroptosis could be exploited to enhance anti-cancer immune responses in GC patients (Gong et al., 2019).

A study identified a set of necroptosis-related genes and developed a risk score model to predict prognosis and therapeutic potential in GC patients. This model revealed that patients with higher risk scores had worse clinical outcomes and lower immune cell infiltration, suggesting a correlation between necroptosis and immune response in GC (Wu et al., 2023). Furthermore, necroptosis was found to be triggered by the TNF pathway in myeloid cells, altering the glycolysis pathway and impacting cell functions such as proliferation and migration (Wu et al., 2023).

Additionally, another study highlighted the role of necroptosis-related lncRNAs in distinguishing between "cold" and "hot" tumors in GC. These lncRNAs were associated with different immune infiltration patterns and clinical outcomes, indicating that necroptosis might influence the tumor microenvironment and response to immunotherapy (Zhao et al., 2021).

8.2 Pyroptosis and gastric cancer

Multiple subtypes of the GSDM protein family are closely associated with gastric cancer, though their roles differ. GSDMA, GSDMC, and GSDMD are downregulated in gastric cancer tissues or models and may act as tumor suppressor genes (Saeki et al., 2009). The downregulation of GSDMD activates the STAT3 and PI3K/PKB signaling pathways and accelerates the S/G2 phase transition by regulating cell cycle-related proteins, significantly promoting tumor proliferation both *in vitro* and *in vivo* (Wang WJ. et al., 2018). In contrast, GSDMB may function as an oncogene in gastric cancer. It is either not expressed or expressed at very low levels in normal gastric tissue, moderately expressed in precancerous tissue, and highly expressed in cancerous tissue, indicating its potential involvement in gastric cancer development (Komiyama et al., 2010).

Helicobacter pylori infection is closely related to various gastric diseases, including gastric cancer (Graham, 2014; Hardbower et al., 2014), primarily through the induction of chronic inflammation that leads to chronic gastritis and subsequent gastric cancer. Research by Kim et al. (2013) has shown that dendritic cells infected with *H. pylori* synergistically produce IL-1β via the TLR2/NOD2 and NLRP3 pathways. Subsequently, Semper et al. (2014) confirmed that *H. pylori* activates NLRP3 to mediate IL-1β production. The cytotoxin-associated gene A (CagA), a major virulence factor of *H. pylori*, mediates the invasion and migration of gastric cancer cells through the NLRP3 pathway (Zhang X. et al., 2020).

Moreover, NLRP3 itself is closely associated with gastric cancer. NLRP3 is significantly upregulated in gastric cancer tissues, mediating the secretion of IL-1β, which promotes epithelial cell proliferation and tumor development. *H. pylori* can decrease the expression of miR-22, an NLRP3 inhibitor, thereby enhancing NLRP3 expression (Li et al., 2018). However, there are differing views on the role of NLRP3 in gastric cancer. Diosbulbin-B effectively increases the sensitivity of gastric cancer cells to the chemotherapeutic drug cisplatin by downregulating PD-L1 to activate NLRP3-mediated pyroptosis and inhibit cancer stem cell (CSC) properties, thereby sensitizing cisplatin-resistant gastric cancer cells to cisplatin (Li et al., 2021). LncRNA ADAMTS9-

AS2 acts as a tumor suppressor in gastric cancer cells by activating NLRP3-mediated pyroptosis via miR-223-3p, thereby enhancing cisplatin sensitivity (Ren et al., 2020).

The dual role of NLRP3 in the development and treatment of gastric cancer could be due to its involvement in inflammatory infiltration during early cancer development, where NLRP3-mediated inflammation accelerates cancer progression. Conversely, during gastric cancer treatment, NLRP3-mediated pyroptosis can be exploited to induce cancer cell death, achieving anticancer effects.

9 Leukemia

9.1 Necroptosis and leukemia

Inhibitor of apoptosis proteins (IAPs) impede programmed cell death through various mechanisms and are associated with poor prognosis in acute myeloid leukemia (AML) (Tamm et al., 2000; Lück et al., 2011; Fulda and Vucic, 2012). The second mitochondria-derived activator of caspases (SMAC) can bind to and inactivate IAPs. Consequently, researchers have developed SMAC mimetics to induce necroptosis in apoptosis-resistant AML cells. Studies demonstrate that SMAC mimetics enhance AML cell sensitivity to apoptosis more effectively than birinapant; the combination with the caspase inhibitor IDN-6556, which blocks caspase-8 activity, can potentiate the anti-cancer effects of birinapant by triggering necroptosis (Brumatti et al., 2016) Another SMAC mimetic, BV6, mediates necroptosis by regulating TNF-α and its downstream RIPK1-RIPK3-MLKL signaling pathway. Moreover, BV6 induces necroptosis in apoptosis-resistant patient-derived AML cells (Safferthal et al., 2017). When used in conjunction with standard chemotherapeutic agents such as cytarabine, azacitidine, and decitabine, BV6 promotes necroptosis in resistant AML cells, thereby enhancing their eradication. Several clinical studies on SMAC mimetics for leukemia treatment are underway, offering promising new strategies and potential drug discoveries for combating leukemia.

9.2 Pyroptosis and leukemia

A study (Wang et al., 2017) demonstrated that chemotherapy drugs can induce pyroptosis in leukemia cells by activating caspase-3, which cleaves GSDME, leading to the formation of pores in the cell membrane and subsequent cell death. This process not only eliminates leukemia cells but also enhances the anti-leukemic effects of chemotherapy through the release of pro-inflammatory cytokines.

Another study (Urwanisch et al., 2021) further elucidated the role of the NLRP3 inflammasome in leukemia, showing that it mediates IL-1β release through both GSDMD-dependent and independent mechanisms. This dual pathway highlights the complex regulation of pyroptosis in leukemic cells and its impact on the inflammatory environment within tumors.

Zhang Z. et al. (2020) identified GSDME as a key player in anti-tumor immunity in leukemia. They found that GSDME activation induces pyroptosis in leukemia cells and enhances immune system recognition and attack on these cells. This suggests that targeting GSDME-mediated pyroptosis could be a promising therapeutic strategy to boost immune responses against leukemia.

Fang et al. (2020) detailed the mechanisms by which pyroptosis is activated in leukemia cells, primarily through the caspase-1 and caspase-4/5/11 pathways. The cleavage of GSDMD during pyroptosis results in pore formation in the cell membrane, leading to cell lysis and the release of pro-inflammatory cytokines like IL-1β and IL-18. This process can effectively eliminate leukemia cells and stimulate an anti-tumor immune response. However, they also highlights the potential adverse effects of chronic inflammation associated with pyroptosis, which may contribute to tumor progression and resistance. Therefore, while pyroptosis offers a promising mechanism for anti-leukemic therapy, further research is needed to optimize therapeutic strategies that maximize its benefits and mitigate its inflammatory risks.

10 Other cancers

In addition to the common cancers mentioned above, research indicates that necroptosis and its key targets are involved in the development and progression of various other cancers. For example, reduced expression of RIPK3 has been observed in head and neck squamous cell carcinoma (McCormick et al., 2016), melanoma (Geserick et al., 2015), primary malignant mesothelioma (Tan et al., 2021), and prostate cancer (Wang KJ. et al., 2020). In these cancers, decreased RIPK3 expression is associated with cancer progression, metastasis, and shortened overall survival (Nugues et al., 2014; Geserick et al., 2015; Conev et al., 2019). Similarly, reduced MLKL expression has been noted in ovarian cancer (He et al., 2013), cervical squamous cell carcinoma (Ruan et al., 2015), colon cancer (Li et al., 2017), and in patients with early resected pancreatic adenocarcinoma, correlating with decreased overall survival (Colbert et al., 2013). Furthermore, downregulation of RIPK1 expression in head and neck squamous cell carcinoma has been closely linked to disease progression (McCormick et al., 2016). These findings suggest that necroptosis, akin to apoptosis, serves as a natural barrier against cancer development.

However, in certain cancers, the expression of necroptosis and its key targets is elevated. In pancreatic ductal adenocarcinoma, high levels of RIPK1, RIPK3, and MLKL are observed (Seifert et al., 2016; Wang W. et al., 2018; Ando et al., 2020). Knockout of RIPK3 or inhibition of RIPK1 can prevent the further development of KrasG12D-induced pancreatic ductal adenocarcinoma in mice (Seifert et al., 2016), and gemcitabine chemotherapy further increases the expression of RIPK1 and RIPK3 in cancer tissues. Elevated RIPK1 expression is also associated with poor prognosis in glioblastoma patients (Park et al., 2009), and high levels of phosphorylated MLKL correlate with poor prognosis and reduced overall survival in esophageal cancer patients (Liu et al., 2016). Additionally, studies have shown that RIPK1 expression is significantly elevated in human lung cancer samples and mouse lung tumor models, suggesting its role as a critical target in cancer induction (Wang et al., 2013). Recent research has found that dabrafenib, a drug used for treating melanoma, inhibits MLKL

phosphorylation by disrupting the interaction between RIPK3 and MLKL (Li et al., 2014).

11 Emerging therapeutic strategies and prognostic tools in pyroptosis-driven cancer treatment

Recent advances in cancer research have underscored the significance of pyroptosis-related gene (PRG) signatures as promising prognostic tools and biomarkers across various cancer types. For instance, in breast cancer, 4 PRGs (GPX4, GSDMD, GSDMC, and IL18) were found to predict survival outcomes and the immune landscape of the tumor. This signature was linked to immune cell infiltration and tumor progression, making it a valuable tool for assessing patient prognosis and guiding therapeutic decisions (Gong et al., 2022).

Similarly, in HCC, a study identified a set of 52 differentially expressed PRGs, including key genes like IL-1β, NLRP3, and TP53, which were associated with patient survival and response to treatment. The genetic mutations and expression variations of these PRGs were analyzed, revealing their potential as prognostic markers (Fang et al., 2022). Moreover, the model not only predicted patient survival but also correlated with immune cell infiltration levels in the tumor immune microenvironment (TIME).

Pyroptosis plays a critical role in shaping the TIME. The release of inflammatory cytokines and DAMPs during pyroptosis not only leads to the death of tumor cells but also recruits and activates various immune cells, including macrophages, dendritic cells, and cytotoxic T lymphocytes (Chen Q. et al., 2024; Li and Jiang, 2023; Hu et al., 2024). This inflammatory response can enhance the immunogenicity of the tumor, leading to a more robust anti-tumor immune response. For instance, the activation of the NLRP3 inflammasome in tumor-associated macrophages and the subsequent pyroptosis can shift the immune balance from an immunosuppressive to an immunostimulatory state, potentially improving the efficacy of immunotherapies such as checkpoint inhibitors (Sun et al., 2024).

The ability of pyroptosis to modulate the TIME has significant implications for cancer immunotherapy. By enhancing the infiltration and activation of cytotoxic T lymphocytes and other effector immune cells, pyroptosis can potentially overcome the immunosuppressive barriers often encountered in the tumor microenvironment. Furthermore, the induction of pyroptosis and necroptosis in tumor cells may synergize with existing immunotherapeutic approaches, such as PD-1/PD-L1 blockade, by increasing the visibility of the tumor to the immune system (Liang et al., 2024; Yu et al., 2024). Targeting pyroptosis pathways, therefore, holds promise not only as a direct anti-cancer strategy but also as a means to enhance the effectiveness of immunotherapies.

Nanomaterials have emerged as promising tools in cancer therapy due to their unique physicochemical properties, such as high surface area and tunable surface chemistry, which enable them to interact with biological systems in novel ways. Recent research highlights how these materials, such as mannose-doped metal-organic frameworks, can trigger pyroptosis through pathways like the PERK pathway. For instance, Fe_3O_4@NH_2-MIL-100 nanoparticles doped with mannose have been shown to induce pyroptosis in tumor cells effectively. This effect is achieved by enhancing the activation of GSDMD, leading to cancer cell death (Jin et al., 2023). Another study designed fluorescent nanoprobes composed of AS1411 aptamer and nucleus-targeting peptide on gold nanoparticles to effectively capture and track the nucleolin distribution and expression during pyroptosis triggered by electrical stimulation, which hold great potential for cellular studies of cancer-related diseases (Kong et al., 2024). However, increased biomedical applications of nanomaterials raise considerable attention concerning their toxicological effects. Mesoporous silica nanoparticles (MSN) could trigger liver inflammation and hepatocyte pyroptosis through NLRP3 inflammasome activation, which was caused by MSN-induced ROS generation (Zhang et al., 2018).

The integration of pyroptosis-inducing agents with established cancer therapies, such as chemotherapy and immunotherapy, has shown promising potential in enhancing therapeutic outcomes.

11.1 Combining pyroptosis-inducing agents with chemotherapy

Chemotherapy is a cornerstone of cancer treatment, but resistance to chemotherapeutic agents remains a significant challenge. Recent studies suggest that inducing pyroptosis in conjunction with chemotherapy could overcome this resistance. For example, Diosbulbin-B effectively increases the sensitivity of gastric cancer cells to the chemotherapeutic drug cisplatin by downregulating PD-L1 to activate NLRP3-mediated pyroptosis (Li et al., 2021). This is particularly relevant in chemoresistant cancers, where inducing pyroptosis can overcome resistance mechanisms and improve treatment outcomes.

11.2 Combining pyroptosis-inducing agents with immunotherapy

The integration of pyroptosis-inducing agents with immunotherapy represents another promising avenue. Pyroptosis can lead to the release of damage-associated DAMPs and pro-inflammatory cytokines, which can potentiate anti-tumor immune responses. The use of immune checkpoint inhibitors, such as PD-1/PD-L1 blockers, in combination with pyroptosis-inducing agents, has been proposed to enhance the recruitment and activation of immune cells within the tumor microenvironment (Yu et al., 2024). This combination could potentially turn “cold” tumors, which are immunologically inactive, into “hot” tumors, making them more responsive to immunotherapy (Chen X. et al., 2024).

The combination of pyroptosis-inducing agents with other therapeutic modalities holds great promise for improving cancer treatment outcomes. Future research should focus on optimizing the timing, dosage, and sequence of these combinations to maximize their therapeutic efficacy while minimizing potential adverse effects. Additionally, exploring the molecular mechanisms underlying the synergistic interactions between pyroptosis and other treatments will be crucial for the development of novel therapeutic strategies.

12 Discussion and conclusion

Existing anticancer drugs primarily aim to induce apoptosis in cancer cells; however, cancer cells frequently develop resistance to apoptosis, leading to drug resistance. Consequently, bypassing apoptotic pathways to induce cancer cell death is crucial. Concurrently, an increasing body of research demonstrates that necroptosis and pyroptosis play vital roles in cancer progression, metastasis, prognosis, and immunosurveillance. Inducing necroptosis or pyroptosis through pharmacological means has emerged as a novel therapeutic approach to circumvent apoptosis resistance in cancer treatment. Nevertheless, the precise roles of these processes in cancer development remain contentious.

Studies indicate that RIPK3 is underexpressed in two-thirds of cancer cell lines, suggesting that the inhibition or absence of the necroptosis pathway may facilitate cancer progression (Graham, 2014). Pharmacological restoration or activation of necroptosis has been shown to effectively kill cancer cells. Conversely, some studies reveal that proteins in the necroptosis pathway are overexpressed in certain cancers, and activating necroptosis can lead to cancer cell metastasis and immunosuppression (Dupaul-Chicoine et al., 2010; Kim et al., 2013; Semper et al., 2014). Pyroptosis presents a similar dichotomy: some studies suggest that activation of inflammasomes or pyroptosis pathways promotes tumor microenvironment formation and accelerates cancer progression, while others demonstrate that drugs can induce cancer cell death by activating these pathways to achieve anticancer effects.

The "dual roles" of necroptosis and pyroptosis in cancer are not entirely contradictory. On one hand, necroptosis and pyroptosis can induce a robust immune response by releasing DAMPs and various immunomodulatory cytokines, thereby activating dendritic cells and enhancing antitumor immunity. This can effectively address tumor resistance, especially in cancers resistant to apoptosis, by inducing cancer cell death through programmed cell death pathways. On the other hand, as inflammatory programmed cell death modes, necroptosis and pyroptosis are accompanied by elevated inflammation levels, which significantly promote tumorigenesis and progression. Inflammation may enhance tumor angiogenesis, increase cancer invasiveness, and create an immunosuppressive tumor microenvironment. Early anti-inflammatory treatment in tumors can effectively inhibit tumor progression and malignancy transformation (Coussens and Werb, 2002).

Moreover, although numerous compounds and drugs have been identified that can induce inflammatory programmed cell death and show potential anticancer activity, most studies remain limited to *in vitro* experiments or animal models. The feasibility of these compounds as anticancer drugs requires further evaluation *in vivo* and in clinical trials. Additionally, while drug-induced inflammatory programmed cell death can effectively kill tumor cells, it remains unclear whether this will exacerbate inflammation in adjacent tissues and normal tissues, accelerate the formation of the tumor microenvironment, and promote the transformation of normal tissue into cancerous tissue. Therefore, improving the "target specificity" of such drugs to cancer tissues and reducing their effects on normal tissues is crucial. In summary, inflammatory programmed cell death is closely associated with the development and progression of various cancers. Further research in this area holds promise for the development of novel anticancer drugs.

13 Summary

13.1 Beneficial aspects of necroptosis and pyroptosis in cancer treatment

1. Cancer cell elimination: Both necroptosis and pyroptosis are forms of programmed cell death that lead to the destruction of cancer cells. They can serve as alternative mechanisms to apoptosis, especially in cancer cells that have developed resistance to apoptotic pathways.
2. Immune system activation: The inflammatory response induced by necroptosis and pyroptosis can stimulate the immune system to recognize and attack cancer cells. The release of DAMPs and cytokines during these processes can enhance the anti-tumor immune response.
3. Overcoming drug resistance: Many cancer therapies aim to induce apoptosis in cancer cells. However, some cancer cells develop resistance to apoptosis. Necroptosis and pyroptosis can bypass these resistance mechanisms, providing an effective way to kill apoptosis-resistant cancer cells.
4. Synergistic Effects with Chemotherapy: Compounds that induce necroptosis or pyroptosis can be used in combination with traditional chemotherapeutic agents to enhance their efficacy. This combination can lead to improved outcomes in cancer treatment by targeting cancer cells through multiple pathways.

13.2 Detrimental aspects of necroptosis and pyroptosis in cancer treatment

1. Chronic inflammation: The inflammatory response triggered by necroptosis and pyroptosis, while beneficial in the short term, can lead to chronic inflammation if not properly regulated. Chronic inflammation is a known risk factor for cancer development and progression.
2. Damage to surrounding tissue: The inflammatory nature of necroptosis and pyroptosis can cause collateral damage to surrounding healthy tissues. This non-specific damage can result in adverse side effects and limit the therapeutic window of treatments that induce these forms of cell death.

Author contributions

SW: Writing–original draft. HH: Writing–original draft. LQ: Writing–review and editing. QS: Writing–review and editing. YD: Writing–review and editing.

Funding

The author(s) declare that financial support was received for the research, authorship, and/or publication of this article. This work was supported by the Key Scientific Research Project of Colleges and

Universities in Henan Province (No. 24A330004), the Natural Science Foundation of Henan Province (No. 242300421540).

Conflict of interest

The authors declare that the research was conducted in the absence of any commercial or financial relationships that could be construed as a potential conflict of interest.

Publisher's note

All claims expressed in this article are solely those of the authors and do not necessarily represent those of their affiliated organizations, or those of the publisher, the editors and the reviewers. Any product that may be evaluated in this article, or claim that may be made by its manufacturer, is not guaranteed or endorsed by the publisher.

References

Afonso, M. B., Rodrigues, P. M., Carvalho, T., Caridade, M., Borralho, P., Cortez-Pinto, H., et al. (2015). Necroptosis is a key pathogenic event in human and experimental murine models of non-alcoholic steatohepatitis. *Clin. Sci. (Lond)* 129 (8), 721–739. doi:10.1042/cs20140732

Allen, I. C., Tekippe, E. M., Woodford, R. M., Uronis, J. M., Holl, E. K., Rogers, A. B., et al. (2010). The NLRP3 inflammasome functions as a negative regulator of tumorigenesis during colitis-associated cancer. *J. Exp. Med.* 207 (5), 1045–1056. doi:10.1084/jem.20100050

Ando, Y., Ohuchida, K., Otsubo, Y., Kibe, S., Takesue, S., Abe, T., et al. (2020). Necroptosis in pancreatic cancer promotes cancer cell migration and invasion by release of CXCL5. *PLoS One* 15 (1), e0228015. doi:10.1371/journal.pone.0228015

Baik, J. Y., Liu, Z., Jiao, D., Kwon, H. J., Yan, J., Kadigamuwa, C., et al. (2021). ZBP1 not RIPK1 mediates tumor necroptosis in breast cancer. *Nat. Commun.* 12 (1), 2666. doi:10.1038/s41467-021-23004-3

Bauer, C., Duewell, P., Mayer, C., Lehr, H. A., Fitzgerald, K. A., Dauer, M., et al. (2010). Colitis induced in mice with dextran sulfate sodium (DSS) is mediated by the NLRP3 inflammasome. *Gut* 59 (9), 1192–1199. doi:10.1136/gut.2009.197822

Bertrand, M. J., Milutinovic, S., Dickson, K. M., Ho, W. C., Boudreault, A., Durkin, J., et al. (2008). cIAP1 and cIAP2 facilitate cancer cell survival by functioning as E3 ligases that promote RIP1 ubiquitination. *Mol. Cell* 30 (6), 689–700. doi:10.1016/j.molcel.2008.05.014

Boise, L. H., and Collins, C. M. (2001). Salmonella-induced cell death: apoptosis, necrosis or programmed cell death? *Trends Microbiol.* 9 (2), 64–67. doi:10.1016/s0966-842x(00)01937-5

Brumatti, G., Ma, C., Lalaoui, N., Nguyen, N. Y., Navarro, M., Tanzer, M. C., et al. (2016). The caspase-8 inhibitor emricasan combines with the SMAC mimetic birinapant to induce necroptosis and treat acute myeloid leukemia. *Sci. Transl. Med.* 8 (339), 339ra69. doi:10.1126/scitranslmed.aad3099

Chen, C., Wang, B., Sun, J., Na, H., Chen, Z., Zhu, Z., et al. (2015). DAC can restore expression of NALP1 to suppress tumor growth in colon cancer. *Cell Death Dis.* 6 (1), e1602. doi:10.1038/cddis.2014.532

Chen, Q., Peng, B., Lin, L., Chen, J., Jiang, Z., Luo, Y., et al. (2024a). Chondroitin sulfate-modified hydroxyapatite for caspase-1 activated induced pyroptosis through Ca overload/ER stress/STING/IRF3 pathway in colorectal cancer. *Small* 17, e2403201. doi:10.1002/smll.202403201

Chen, W., Wei, T., Chen, Y., Yang, L., and Wu, X. (2020). Downregulation of IRAK1 prevents the malignant behavior of hepatocellular carcinoma cells by blocking activation of the MAPKs/NLRP3/IL-1β pathway. *Onco Targets Ther.* 13, 12787–12796. doi:10.2147/ott.S260793

Chen, X., Xuan, Y., Chen, Y., Yang, F., Zhu, M., Xu, J., et al. (2024b). Polystyrene nanoplastics induce intestinal and hepatic inflammation through activation of NF-κB/NLRP3 pathways and related gut-liver axis in mice. *Sci. Total Environ.* 935, 173458. doi:10.1016/j.scitotenv.2024.173458

Cho, Y. S., Challa, S., Moquin, D., Genga, R., Ray, T. D., Guildford, M., et al. (2009). Phosphorylation-driven assembly of the RIP1-RIP3 complex regulates programmed necrosis and virus-induced inflammation. *Cell* 137 (6), 1112–1123. doi:10.1016/j.cell.2009.05.037

Colbert, L. E., Fisher, S. B., Hardy, C. W., Hall, W. A., Saka, B., Shelton, J. W., et al. (2013). Pronecrotic mixed lineage kinase domain-like protein expression is a prognostic biomarker in patients with early-stage resected pancreatic adenocarcinoma. *Cancer* 119 (17), 3148–3155. doi:10.1002/cncr.28144

Conev, N. V., Dimitrova, E. G., Bogdanova, M. K., Kashlov, Y. K., Chaushev, B. G., Radanova, M. A., et al. (2019). RIPK3 expression as a potential predictive and prognostic marker in metastatic colon cancer. *Clin. Invest. Med.* 42 (1), E31–e38. doi:10.25011/cim.v42i1.32390

Coussens, L. M., and Werb, Z. (2002). Inflammation and cancer. *Nature* 420 (6917), 860–867. doi:10.1038/nature01322

Cui, J., Zhou, Z., Yang, H., Jiao, F., Li, N., Gao, Y., et al. (2019). MST1 suppresses pancreatic cancer progression via ROS-induced pyroptosis. *Mol. Cancer Res.* 17 (6), 1316–1325. doi:10.1158/1541-7786.Mcr-18-0910

Dupaul-Chicoine, J., Yeretssian, G., Doiron, K., Bergstrom, K. S., Mcintire, C. R., Leblanc, P. M., et al. (2010). Control of intestinal homeostasis, colitis, and colitis-associated colorectal cancer by the inflammatory caspases. *Immunity* 32 (3), 367–378. doi:10.1016/j.immuni.2010.02.012

Fan, S. H., Wang, Y. Y., Lu, J., Zheng, Y. L., Wu, D. M., Li, M. Q., et al. (2014). Luteoloside suppresses proliferation and metastasis of hepatocellular carcinoma cells by inhibition of NLRP3 inflammasome. *PLoS One* 9 (2), e89961. doi:10.1371/journal.pone.0089961

Fang, G., Zhang, Q., Fan, J., Li, H., Ding, Z., Fu, J., et al. (2022). Pyroptosis related genes signature predicts prognosis and immune infiltration of tumor microenvironment in hepatocellular carcinoma. *BMC Cancer* 22 (1), 999. doi:10.1186/s12885-022-10097-2

Fang, Y., Tian, S., Pan, Y., Li, W., Wang, Q., Tang, Y., et al. (2020). Pyroptosis: a new frontier in cancer. *Biomed. Pharmacother.* 121, 109595. doi:10.1016/j.biopha.2019.109595

Fulda, S., and Vucic, D. (2012). Targeting IAP proteins for therapeutic intervention in cancer. *Nat. Rev. Drug Discov.* 11 (2), 109–124. doi:10.1038/nrd3627

Gao, J., Qiu, X., Xi, G., Liu, H., Zhang, F., Lv, T., et al. (2018). Downregulation of GSDMD attenuates tumor proliferation via the intrinsic mitochondrial apoptotic pathway and inhibition of EGFR/Akt signaling and predicts a good prognosis in non-small cell lung cancer. *Oncol. Rep.* 40 (4), 1971–1984. doi:10.3892/or.2018.6634

Gautheron, J., Vucur, M., Reisinger, F., Cardenas, D. V., Roderburg, C., Koppe, C., et al. (2014). A positive feedback loop between RIP3 and JNK controls non-alcoholic steatohepatitis. *EMBO Mol. Med.* 6 (8), 1062–1074. doi:10.15252/emmm.201403856

Geserick, P., Wang, J., Schilling, R., Horn, S., Harris, P. A., Bertin, J., et al. (2015). Absence of RIPK3 predicts necroptosis resistance in malignant melanoma. *Cell Death Dis.* 6 (9), e1884. doi:10.1038/cddis.2015.240

Gong, M., Liu, X., Zhao, X., and Wang, H. (2022). A pyroptosis-related gene signature predicting survival and tumor immune microenvironment in breast cancer and validation. *BMC Cancer* 22 (1), 1005. doi:10.1186/s12885-022-09856-y

Gong, Y., Fan, Z., Luo, G., Yang, C., Huang, Q., Fan, K., et al. (2019). The role of necroptosis in cancer biology and therapy. *Mol. Cancer* 18 (1), 100. doi:10.1186/s12943-019-1029-8

Graham, D. Y. (2014). History of *Helicobacter pylori*, duodenal ulcer, gastric ulcer and gastric cancer. *World J. Gastroenterol.* 20 (18), 5191–5204. doi:10.3748/wjg.v20.i18.5191

Guo, B., Fu, S., Zhang, J., Liu, B., and Li, Z. (2016). Targeting inflammasome/IL-1 pathways for cancer immunotherapy. *Sci. Rep.* 6, 36107. doi:10.1038/srep36107

Han, Q., Ma, Y., Wang, H., Dai, Y., Chen, C., Liu, Y., et al. (2018). Resibufogenin suppresses colorectal cancer growth and metastasis through RIP3-mediated necroptosis. *J. Transl. Med.* 16 (1), 201. doi:10.1186/s12967-018-1580-x

Hardbower, D. M., Peek, R. M., Jr., and Wilson, K. T. (2014). At the Bench: *Helicobacter pylori*, dysregulated host responses, DNA damage, and gastric cancer. *J. Leukoc. Biol.* 96 (2), 201–212. doi:10.1189/jlb.4BT0214-099R

He, L., Peng, K., Liu, Y., Xiong, J., and Zhu, F. F. (2013). Low expression of mixed lineage kinase domain-like protein is associated with poor prognosis in ovarian cancer patients. *Onco Targets Ther.* 6, 1539–1543. doi:10.2147/ott.S52805

Hergueta-Redondo, M., Sarrió, D., Molina-Crespo, Á., Megias, D., Mota, A., Rojo-Sebastian, A., et al. (2014). Gasdermin-B promotes invasion and metastasis in breast cancer cells. *PLoS One* 9 (3), e90099. doi:10.1371/journal.pone.0090099

Hirota, S. A., Ng, J., Lueng, A., Khajah, M., Parhar, K., Li, Y., et al. (2011). NLRP3 inflammasome plays a key role in the regulation of intestinal homeostasis. *Inflamm. Bowel Dis.* 17 (6), 1359–1372. doi:10.1002/ibd.21478

Hou, J., Zhao, R., Xia, W., Chang, C. W., You, Y., Hsu, J. M., et al. (2020). PD-L1-mediated gasdermin C expression switches apoptosis to pyroptosis in cancer cells and facilitates tumour necrosis. *Nat. Cell Biol.* 22 (10), 1264–1275. doi:10.1038/s41556-020-0575-z

Hu, B., Elinav, E., Huber, S., Booth, C. J., Strowig, T., Jin, C., et al. (2010). Inflammation-induced tumorigenesis in the colon is regulated by caspase-1 and NLRC4. *Proc. Natl. Acad. Sci. U. S. A.* 107 (50), 21635–21640. doi:10.1073/pnas.1016814108

Hu, M., Deng, F., Song, X., Zhao, H., and Yan, F. (2024). The crosstalk between immune cells and tumor pyroptosis: advancing cancer immunotherapy strategies. *J. Exp. Clin. Cancer Res.* 43 (1), 190. doi:10.1186/s13046-024-03115-7

Jiao, Y., Wang, L., Lu, L., Liu, J., Li, X., Zhao, H., et al. (2020). The role of caspase-4 and NLRP1 in MCF7 cell pyroptosis induced by hUCMSC-secreted factors. *Stem Cells Int.* 2020, 8867115. doi:10.1155/2020/8867115

Jin, N., Wang, B., Liu, X., Yin, C., Li, X., Wang, Z., et al. (2023). Mannose-doped metal-organic frameworks induce tumor cell pyroptosis via the PERK pathway. *J. Nanobiotechnology* 21 (1), 426. doi:10.1186/s12951-023-02175-9

Jing, L., Song, F., Liu, Z., Li, J., Wu, B., Fu, Z., et al. (2018). MLKL-PITPα signaling-mediated necroptosis contributes to cisplatin-triggered cell death in lung cancer A549 cells. *Cancer Lett.* 414, 136–146. doi:10.1016/j.canlet.2017.10.047

Kambara, H., Liu, F., Zhang, X., Liu, P., Bajrami, B., Teng, Y., et al. (2018). Gasdermin D exerts anti-inflammatory effects by promoting neutrophil death. *Cell Rep.* 22 (11), 2924–2936. doi:10.1016/j.celrep.2018.02.067

Karamanou, K., Franchi, M., Vynios, D., and Brézillon, S. (2020). Epithelial-to-mesenchymal transition and invadopodia markers in breast cancer: lumican a key regulator. *Semin. Cancer Biol.* 62, 125–133. doi:10.1016/j.semcancer.2019.08.003

Khaw-On, P., Pompimon, W., and Banjerdpongchai, R. (2019). Goniothalamin induces necroptosis and anoikis in human invasive breast cancer MDA-MB-231 cells. *Int. J. Mol. Sci.* 20 (16), 3953. doi:10.3390/ijms20163953

Kim, D. J., Park, J. H., Franchi, L., Backert, S., and Núñez, G. (2013). The Cag pathogenicity island and interaction between TLR2/NOD2 and NLRP3 regulate IL-1β production in *Helicobacter pylori* infected dendritic cells. *Eur. J. Immunol.* 43 (10), 2650–2658. doi:10.1002/eji.201243281

Kolb, R., Phan, L., Borcherding, N., Liu, Y., Yuan, F., Janowski, A. M., et al. (2016). Obesity-associated NLRC4 inflammasome activation drives breast cancer progression. *Nat. Commun.* 7, 13007. doi:10.1038/ncomms13007

Komiyama, H., Aoki, A., Tanaka, S., Maekawa, H., Kato, Y., Wada, R., et al. (2010). Alu-derived cis-element regulates tumorigenesis-dependent gastric expression of GASDERMIN B (GSDMB). *Genes Genet. Syst.* 85 (1), 75–83. doi:10.1266/ggs.85.75

Kong, J., Ju, X., Qi, G., Wang, J., Diao, X., Wang, B., et al. (2024). Light-on" fluorescent nanoprobes for monitoring dynamic distribution of cellular nucleolin during pyroptosis. *Anal. Chem.* 96 (2), 926–933. doi:10.1021/acs.analchem.3c05122

Lalaoui, N., Lindqvist, L. M., Sandow, J. J., and Ekert, P. G. (2015). The molecular relationships between apoptosis, autophagy and necroptosis. *Semin. Cell Dev. Biol.* 39, 63–69. doi:10.1016/j.semcdb.2015.02.003

Li, C., Qiu, J., and Xue, Y. (2021). Low-dose Diosbulbin-B (DB) activates tumor-intrinsic PD-L1/NLRP3 signaling pathway mediated pyroptotic cell death to increase cisplatin-sensitivity in gastric cancer (GC). *Cell Biosci.* 11 (1), 38. doi:10.1186/s13578-021-00548-x

Li, J. X., Feng, J. M., Wang, Y., Li, X. H., Chen, X. X., Su, Y., et al. (2014). The B-Raf(V600E) inhibitor dabrafenib selectively inhibits RIP3 and alleviates acetaminophen-induced liver injury. *Cell Death Dis.* 5 (6), e1278. doi:10.1038/cddis.2014.241

Li, P., Liu, Y., and He, Q. (2020). Anisodamine suppressed the growth of hepatocellular carcinoma cells, induced apoptosis and regulated the levels of inflammatory factors by inhibiting NLRP3 inflammasome activation. *Drug Des. Devel Ther.* 14, 1609–1620. doi:10.2147/dddt.S243383

Li, S., Liang, X., Ma, L., Shen, L., Li, T., Zheng, L., et al. (2018). MiR-22 sustains NLRP3 expression and attenuates H. pylori-induced gastric carcinogenesis. *Oncogene* 37 (7), 884–896. doi:10.1038/onc.2017.381

Li, X., Guo, J., Ding, A. P., Qi, W. W., Zhang, P. H., Lv, J., et al. (2017). Association of mixed lineage kinase domain-like protein expression with prognosis in patients with colon cancer. *Technol. Cancer Res. Treat.* 16 (4), 428–434. doi:10.1177/1533034616655909

Li, Y., and Jiang, Q. (2023). Uncoupled pyroptosis and IL-1β secretion downstream of inflammasome signaling. *Front. Immunol.* 14, 1128358. doi:10.3389/fimmu.2023.1128358

Liang, M., Chen, X., Wang, L., Qin, L., Wang, H., Sun, Z., et al. (2020). Cancer-derived exosomal TRIM59 regulates macrophage NLRP3 inflammasome activation to promote lung cancer progression. *J. Exp. Clin. Cancer Res.* 39 (1), 176. doi:10.1186/s13046-020-01688-7

Liang, X., Liu, Q., Zhu, S., Li, Z., Chen, H., and Su, Z. (2024). GSDME has prognostic and immunotherapeutic significance in residual hepatocellular carcinoma after insufficient radiofrequency ablation. *Transl. Oncol.* 39, 101796. doi:10.1016/j.tranon.2023.101796

Lim, J. H., Oh, S., Kim, L., Suh, Y. J., Ha, Y. J., Kim, J. S., et al. (2021). Low-level expression of necroptosis factors indicates a poor prognosis of the squamous cell carcinoma subtype of non-small-cell lung cancer. *Transl. Lung Cancer Res.* 10 (3), 1221–1230. doi:10.21037/tlcr-20-1027

Liu, A., Liu, L., and Lu, H. (2019a). LncRNA XIST facilitates proliferation and epithelial-mesenchymal transition of colorectal cancer cells through targeting miR-486-5p and promoting neuropilin-2. *J. Cell Physiol.* 234 (8), 13747–13761. doi:10.1002/jcp.28054

Liu, J., Yao, L., Zhang, M., Jiang, J., Yang, M., and Wang, Y. (2019b). Downregulation of LncRNA-XIST inhibited development of non-small cell lung cancer by activating miR-335/SOD2/ROS signal pathway mediated pyroptotic cell death. *Aging (Albany NY)* 11 (18), 7830–7846. doi:10.18632/aging.102291

Liu, X., Zhang, Y., Gao, H., Hou, Y., Lu, J. J., Feng, Y., et al. (2020). Induction of an MLKL mediated non-canonical necroptosis through reactive oxygen species by tanshinol A in lung cancer cells. *Biochem. Pharmacol.* 171, 113684. doi:10.1016/j.bcp.2019.113684

Liu, X., Zhou, M., Mei, L., Ruan, J., Hu, Q., Peng, J., et al. (2016). Key roles of necroptotic factors in promoting tumor growth. *Oncotarget* 7 (16), 22219–22233. doi:10.18632/oncotarget.7924

Liu, Z. Y., Zheng, M., Li, Y. M., Fan, X. Y., Wang, J. C., Li, Z. C., et al. (2019c). RIP3 promotes colitis-associated colorectal cancer by controlling tumor cell proliferation and CXCL1-induced immune suppression. *Theranostics* 9 (12), 3659–3673. doi:10.7150/thno.32126

Lück, S. C., Russ, A. C., Botzenhardt, U., Paschka, P., Schlenk, R. F., Döhner, H., et al. (2011). Deregulated apoptosis signaling in core-binding factor leukemia differentiates clinically relevant, molecular marker-independent subgroups. *Leukemia* 25 (11), 1728–1738. doi:10.1038/leu.2011.154

Ma, W., Wang, Z., Zhao, Y., Wang, Q., Zhang, Y., Lei, P., et al. (2021). Salidroside suppresses the proliferation and migration of human lung cancer cells through AMPK-dependent NLRP3 inflammasome regulation. *Oxid. Med. Cell Longev.* 2021, 6614574. doi:10.1155/2021/6614574

Mccormick, K. D., Ghosh, A., Trivedi, S., Wang, L., Coyne, C. B., Ferris, R. L., et al. (2016). Innate immune signaling through differential RIPK1 expression promote tumor progression in head and neck squamous cell carcinoma. *Carcinogenesis* 37 (5), 522–529. doi:10.1093/carcin/bgw032

Mridha, A. R., Wree, A., Robertson, A. B., Yeh, M. M., Johnson, C. D., Van Rooyen, D. M., et al. (2017). NLRP3 inflammasome blockade reduces liver inflammation and fibrosis in experimental NASH in mice. *J. Hepatol.* 66 (5), 1037–1046. doi:10.1016/j.jhep.2017.01.022

Murphy, J. M., Czabotar, P. E., Hildebrand, J. M., Lucet, I. S., Zhang, J. G., Alvarez-Diaz, S., et al. (2013). The pseudokinase MLKL mediates necroptosis via a molecular switch mechanism. *Immunity* 39 (3), 443–453. doi:10.1016/j.immuni.2013.06.018

Nowarski, R., Jackson, R., Gagliani, N., De Zoete, M. R., Palm, N. W., Bailis, W., et al. (2015). Epithelial IL-18 equilibrium controls barrier function in colitis. *Cell* 163 (6), 1444–1456. doi:10.1016/j.cell.2015.10.072

Nugues, A. L., El Bouazzati, H., Hétuin, D., Berthon, C., Loyens, A., Bertrand, E., et al. (2014). RIP3 is downregulated in human myeloid leukemia cells and modulates apoptosis and caspase-mediated p65/RelA cleavage. *Cell Death Dis.* 5 (8), e1384. doi:10.1038/cddis.2014.347

Orning, P., Weng, D., Starheim, K., Ratner, D., Best, Z., Lee, B., et al. (2018). Pathogen blockade of TAK1 triggers caspase-8-dependent cleavage of gasdermin D and cell death. *Science* 362 (6418), 1064–1069. doi:10.1126/science.aau2818

Park, J. H., Jung, K. H., Kim, S. J., Yoon, Y. C., Yan, H. H., Fang, Z., et al. (2019). HS-173 as a novel inducer of RIP3-dependent necroptosis in lung cancer. *Cancer Lett.* 444, 94–104. doi:10.1016/j.canlet.2018.12.006

Park, S., Hatanpaa, K. J., Xie, Y., Mickey, B. E., Madden, C. J., Raisanen, J. M., et al. (2009). The receptor interacting protein 1 inhibits p53 induction through NF-kappaB activation and confers a worse prognosis in glioblastoma. *Cancer Res.* 69 (7), 2809–2816. doi:10.1158/0008-5472.Can-08-4079

Pizato, N., Luzete, B. C., Kiffer, L., Corrêa, L. H., De Oliveira Santos, I., Assumpção, J. a F., et al. (2018). Omega-3 docosahexaenoic acid induces pyroptosis cell death in triple-negative breast cancer cells. *Sci. Rep.* 8 (1), 1952. doi:10.1038/s41598-018-20422-0

Ren, N., Jiang, T., Wang, C., Xie, S., Xing, Y., Piao, D., et al. (2020). LncRNA ADAMTS9-AS2 inhibits gastric cancer (GC) development and sensitizes chemoresistant GC cells to cisplatin by regulating miR-223-3p/NLRP3 axis. *Aging (Albany NY)* 12 (11), 11025–11041. doi:10.18632/aging.103314

Ruan, J., Mei, L., Zhu, Q., Shi, G., and Wang, H. (2015). Mixed lineage kinase domain-like protein is a prognostic biomarker for cervical squamous cell cancer. *Int. J. Clin. Exp. Pathol.* 8 (11), 15035–15038.

Saeki, N., Usui, T., Aoyagi, K., Kim, D. H., Sato, M., Mabuchi, T., et al. (2009). Distinctive expression and function of four GSDM family genes (GSDMA-D) in normal and malignant upper gastrointestinal epithelium. *Genes Chromosom. Cancer* 48 (3), 261–271. doi:10.1002/gcc.20636

Safferthal, C., Rohde, K., and Fulda, S. (2017). Therapeutic targeting of necroptosis by Smac mimetic bypasses apoptosis resistance in acute myeloid leukemia cells. *Oncogene* 36 (11), 1487–1502. doi:10.1038/onc.2016.310

Schneider, A. T., Gautheron, J., Feoktistova, M., Roderburg, C., Loosen, S. H., Roy, S., et al. (2017). RIPK1 suppresses a TRAF2-dependent pathway to liver cancer. *Cancer Cell* 31 (1), 94–109. doi:10.1016/j.ccell.2016.11.009

Seifert, L., Werba, G., Tiwari, S., Giao, Ly N. N., Alothman, S., Alqunaibit, D., et al. (2016). The necrosome promotes pancreatic oncogenesis via CXCL1 and Mincle-induced immune suppression. *Nature* 532 (7598), 245–249. doi:10.1038/nature17403

Semper, R. P., Mejías-Luque, R., Groß, C., Anderl, F., Müller, A., Vieth, M., et al. (2014). Helicobacter pylori-induced IL-1β secretion in innate immune cells is regulated

by the NLRP3 inflammasome and requires the cag pathogenicity island. *J. Immunol.* 193 (7), 3566–3576. doi:10.4049/jimmunol.1400362

Sharma, D., Malik, A., Guy, C. S., Karki, R., Vogel, P., and Kanneganti, T. D. (2018). Pyrin inflammasome regulates tight junction integrity to restrict colitis and tumorigenesis. *Gastroenterology* 154 (4), 948–964. doi:10.1053/j.gastro.2017.11.276

Shi, J., Zhao, Y., Wang, Y., Gao, W., Ding, J., Li, P., et al. (2014). Inflammatory caspases are innate immune receptors for intracellular LPS. *Nature* 514 (7521), 187–192. doi:10.1038/nature13683

Sun, C., Zhan, J., Li, Y., Zhou, C., Huang, S., Zhu, X., et al. (2024). Non-apoptotic regulated cell death mediates reprogramming of the tumour immune microenvironment by macrophages. *J. Cell Mol. Med.* 28 (8), e18348. doi:10.1111/jcmm.18348

Sun, L., Wang, H., Wang, Z., He, S., Chen, S., Liao, D., et al. (2012). Mixed lineage kinase domain-like protein mediates necrosis signaling downstream of RIP3 kinase. *Cell* 148 (1-2), 213–227. doi:10.1016/j.cell.2011.11.031

Sun, W., Yu, J., Gao, H., Wu, X., Wang, S., Hou, Y., et al. (2019). Inhibition of lung cancer by 2-methoxy-6-acetyl-7-methyljuglone through induction of necroptosis by targeting receptor-interacting protein 1. *Antioxid. Redox Signal* 31 (2), 93–108. doi:10.1089/ars.2017.7376

Sun, W., Zu, Y., Fu, X., and Deng, Y. (2017). Knockdown of lncRNA-XIST enhances the chemosensitivity of NSCLC cells via suppression of autophagy. *Oncol. Rep.* 38 (6), 3347–3354. doi:10.3892/or.2017.6056

Tamm, I., Kornblau, S. M., Segall, H., Krajewski, S., Welsh, K., Kitada, S., et al. (2000). Expression and prognostic significance of IAP-family genes in human cancers and myeloid leukemias. *Clin. Cancer Res.* 6 (5), 1796–1803.

Tan, Y., Sementino, E., Cheung, M., Peri, S., Menges, C. W., Kukuyan, A. M., et al. (2021). Somatic epigenetic silencing of RIPK3 inactivates necroptosis and contributes to chemoresistance in malignant mesothelioma. *Clin. Cancer Res.* 27 (4), 1200–1213. doi:10.1158/1078-0432.Ccr-18-3683

Teng, J. F., Mei, Q. B., Zhou, X. G., Tang, Y., Xiong, R., Qiu, W. Q., et al. (2020). Polyphyllin VI induces caspase-1-mediated pyroptosis via the induction of ROS/NF-κB/NLRP3/GSDMD signal Axis in non-small cell lung cancer. *Cancers (Basel)* 12 (1), 193. doi:10.3390/cancers12010193

Urwanisch, L., Luciano, M., and Horejs-Hoeck, J. (2021). The NLRP3 inflammasome and its role in the pathogenicity of leukemia. *Int. J. Mol. Sci.* 22 (3), 1271. doi:10.3390/ijms22031271

Voronov, E., Shouval, D. S., Krelin, Y., Cagnano, E., Benharroch, D., Iwakura, Y., et al. (2003). IL-1 is required for tumor invasiveness and angiogenesis. *Proc. Natl. Acad. Sci. U. S. A.* 100 (5), 2645–2650. doi:10.1073/pnas.0437939100

Wang, K., Liu, C. Y., Zhou, L. Y., Wang, J. X., Wang, M., Zhao, B., et al. (2015). APF lncRNA regulates autophagy and myocardial infarction by targeting miR-188-3p. *Nat. Commun.* 6, 6779. doi:10.1038/ncomms7779

Wang, K. J., Wang, K. Y., Zhang, H. Z., Meng, X. Y., Chen, J. F., Wang, P., et al. (2020a). Up-regulation of RIP3 alleviates prostate cancer progression by activation of RIP3/MLKL signaling pathway and induction of necroptosis. *Front. Oncol.* 10, 1720. doi:10.3389/fonc.2020.01720

Wang, Q., Chen, W., Xu, X., Li, B., He, W., Padilla, M. T., et al. (2013). RIP1 potentiates BPDE-induced transformation in human bronchial epithelial cells through catalase-mediated suppression of excessive reactive oxygen species. *Carcinogenesis* 34 (9), 2119–2128. doi:10.1093/carcin/bgt143

Wang, Q., Wang, P., Zhang, L., Tessema, M., Bai, L., Xu, X., et al. (2020b). Epigenetic regulation of RIP3 suppresses necroptosis and increases resistance to chemotherapy in NonSmall cell lung cancer. *Transl. Oncol.* 13 (2), 372–382. doi:10.1016/j.tranon.2019.11.011

Wang, S., He, H., Chen, Y., Wang, Y., Cui, T., and Ma, N. (2024). TRPV4 modulation participates in paraoxon-induced brain injury via NMDA and NLRP3 regulation. *Brain Inj.* 38, 848–857. doi:10.1080/02699052.2024.2351104

Wang, W., Marinis, J. M., Beal, A. M., Savadkar, S., Wu, Y., Khan, M., et al. (2018a). RIP1 kinase drives macrophage-mediated adaptive immune tolerance in pancreatic cancer. *Cancer Cell* 34 (5), 757–774. doi:10.1016/j.ccell.2018.10.006

Wang, W. J., Chen, D., Jiang, M. Z., Xu, B., Li, X. W., Chu, Y., et al. (2018b). Downregulation of gasdermin D promotes gastric cancer proliferation by regulating cell cycle-related proteins. *J. Dig. Dis.* 19 (2), 74–83. doi:10.1111/1751-2980.12576

Wang, X., Zhang, G., Cheng, Z., Dai, L., Jia, L., Jing, X., et al. (2018c). Knockdown of LncRNA-XIST suppresses proliferation and TGF-β1-induced EMT in NSCLC through the notch-1 pathway by regulation of miR-137. *Genet. Test. Mol. Biomarkers* 22 (6), 333–342. doi:10.1089/gtmb.2018.0026

Wang, Y., Gao, W., Shi, X., Ding, J., Liu, W., He, H., et al. (2017). Chemotherapy drugs induce pyroptosis through caspase-3 cleavage of a gasdermin. *Nature* 547 (7661), 99–103. doi:10.1038/nature22393

Wang, Y., Kong, H., Zeng, X., Liu, W., Wang, Z., Yan, X., et al. (2016). Activation of NLRP3 inflammasome enhances the proliferation and migration of A549 lung cancer cells. *Oncol. Rep.* 35 (4), 2053–2064. doi:10.3892/or.2016.4569

Wei, Q., Guo, P., Mu, K., Zhang, Y., Zhao, W., Huai, W., et al. (2015). Estrogen suppresses hepatocellular carcinoma cells through ERβ-mediated upregulation of the NLRP3 inflammasome. *Lab. Invest.* 95 (7), 804–816. doi:10.1038/labinvest.2015.63

Wei, Q., Mu, K., Li, T., Zhang, Y., Yang, Z., Jia, X., et al. (2014). Deregulation of the NLRP3 inflammasome in hepatic parenchymal cells during liver cancer progression. *Lab. Invest.* 94 (1), 52–62. doi:10.1038/labinvest.2013.126

Wei, Q., Zhu, R., Zhu, J., Zhao, R., and Li, M. (2019). E2-Induced activation of the NLRP3 inflammasome triggers pyroptosis and inhibits autophagy in HCC cells. *Oncol. Res.* 27 (7), 827–834. doi:10.3727/096504018x15462920753012

Williams, T. M., Leeth, R. A., Rothschild, D. E., Coutermarsh-Ott, S. L., Mcdaniel, D. K., Simmons, A. E., et al. (2015). The NLRP1 inflammasome attenuates colitis and colitis-associated tumorigenesis. *J. Immunol.* 194 (7), 3369–3380. doi:10.4049/jimmunol.1402098

Wilson, J. E., Petrucelli, A. S., Chen, L., Koblansky, A. A., Truax, A. D., Oyama, Y., et al. (2015). Inflammasome-independent role of AIM2 in suppressing colon tumorigenesis via DNA-PK and Akt. *Nat. Med.* 21 (8), 906–913. doi:10.1038/nm.3908

Wree, A., Eguchi, A., Mcgeough, M. D., Pena, C. A., Johnson, C. D., Canbay, A., et al. (2014). NLRP3 inflammasome activation results in hepatocyte pyroptosis, liver inflammation, and fibrosis in mice. *Hepatology* 59 (3), 898–910. doi:10.1002/hep.26592

Wright, A., Reiley, W. W., Chang, M., Jin, W., Lee, A. J., Zhang, M., et al. (2007). Regulation of early wave of germ cell apoptosis and spermatogenesis by deubiquitinating enzyme CYLD. *Dev. Cell* 13 (5), 705–716. doi:10.1016/j.devcel.2007.09.007

Wu, N., Liu, F., Huang, Y., Su, X., Zhang, Y., Yu, L., et al. (2023). Necroptosis related genes predict prognosis and therapeutic potential in gastric cancer. *Biomolecules* 13 (1), 101. doi:10.3390/biom13010101

Xie, W. H., Ding, J., Xie, X. X., Yang, X. H., Wu, X. F., Chen, Z. X., et al. (2020). Hepatitis B virus X protein promotes liver cell pyroptosis under oxidative stress through NLRP3 inflammasome activation. *Inflamm. Res.* 69 (7), 683–696. doi:10.1007/s00011-020-01351-z

Yu, J., Li, S., Qi, J., Chen, Z., Wu, Y., Guo, J., et al. (2019). Cleavage of GSDME by caspase-3 determines lobaplatin-induced pyroptosis in colon cancer cells. *Cell Death Dis.* 10 (3), 193. doi:10.1038/s41419-019-1441-4

Yu, L., Huang, K., Liao, Y., Wang, L., Sethi, G., and Ma, Z. (2024). Targeting novel regulated cell death: ferroptosis, pyroptosis and necroptosis in anti-PD-1/PD-L1 cancer immunotherapy. *Cell Prolif.* 57 (8), e13644. doi:10.1111/cpr.13644

Yu, Y. Q., Thonn, V., Patankar, J. V., Thoma, O. M., Waldner, M., Zielinska, M., et al. (2022). SMYD2 targets RIPK1 and restricts TNF-induced apoptosis and necroptosis to support colon tumor growth. *Cell Death Dis.* 13 (1), 52. doi:10.1038/s41419-021-04483-0

Yuan, R., Zhao, W., Wang, Q. Q., He, J., Han, S., Gao, H., et al. (2021). Cucurbitacin B inhibits non-small cell lung cancer *in vivo* and *in vitro* by triggering TLR4/NLRP3/GSDMD-dependent pyroptosis. *Pharmacol. Res.* 170, 105748. doi:10.1016/j.phrs.2021.105748

Zaki, M. H., Vogel, P., Body-Malapel, M., Lamkanfi, M., and Kanneganti, T. D. (2010). IL-18 production downstream of the Nlrp3 inflammasome confers protection against colorectal tumor formation. *J. Immunol.* 185 (8), 4912–4920. doi:10.4049/jimmunol.1002046

Zhang, C. C., Li, C. G., Wang, Y. F., Xu, L. H., He, X. H., Zeng, Q. Z., et al. (2019a). Chemotherapeutic paclitaxel and cisplatin differentially induce pyroptosis in A549 lung cancer cells via caspase-3/GSDME activation. *Apoptosis* 24 (3-4), 312–325. doi:10.1007/s10495-019-01515-1

Zhang, J., Li, W. Y., Yang, Y., Yan, L. Z., Zhang, S. Y., He, J., et al. (2019b). LncRNA XIST facilitates cell growth, migration and invasion via modulating H3 histone methylation of DKK1 in neuroblastoma. *Cell Cycle* 18 (16), 1882–1892. doi:10.1080/15384101.2019.1632134

Zhang, X., Luan, J., Chen, W., Fan, J., Nan, Y., Wang, Y., et al. (2018). Mesoporous silica nanoparticles induced hepatotoxicity via NLRP3 inflammasome activation and caspase-1-dependent pyroptosis. *Nanoscale* 10 (19), 9141–9152. doi:10.1039/c8nr00554k

Zhang, X., Wang, D., Liu, B., Jin, X., Wang, X., Pan, J., et al. (2020a). IMP3 accelerates the progression of prostate cancer through inhibiting PTEN expression in a SMURF1-dependent way. *J. Exp. Clin. Cancer Res.* 39 (1), 190. doi:10.1186/s13046-020-01657-0

Zhang, Z., Ju, F., Chen, F., Wu, H., Chen, J., Zhong, J., et al. (2021). GDC-0326 enhances the effects of 5-fu in colorectal cancer cells by inducing necroptotic death. *Onco Targets Ther.* 14, 2519–2530. doi:10.2147/ott.S302334

Zhang, Z., Zhang, Y., Xia, S., Kong, Q., Li, S., Liu, X., et al. (2020b). Gasdermin E suppresses tumour growth by activating anti-tumour immunity. *Nature* 579 (7799), 415–420. doi:10.1038/s41586-020-2071-9

Zhao, Z., Liu, H., Zhou, X., Fang, D., Ou, X., Ye, J., et al. (2021). Necroptosis-related lncRNAs: predicting prognosis and the distinction between the cold and hot tumors in gastric cancer. *J. Oncol.* 2021, 6718443. doi:10.1155/2021/6718443

Zhou, Z., He, H., Wang, K., Shi, X., Wang, Y., Su, Y., et al. (2020). Granzyme A from cytotoxic lymphocytes cleaves GSDMB to trigger pyroptosis in target cells. *Science* 368 (6494), eaaz7548. doi:10.1126/science.aaz7548

Zhu, Y., Gu, L., Lin, X., Liu, C., Lu, B., Cui, K., et al. (2020). Dynamic regulation of ME1 phosphorylation and acetylation affects lipid metabolism and colorectal tumorigenesis. *Mol. Cell* 77 (1), 138–149. doi:10.1016/j.molcel.2019.10.015

frontiers | Frontiers in Pharmacology

TYPE Case Report
PUBLISHED 26 September 2024
DOI 10.3389/fphar.2024.1447582

Check for updates

OPEN ACCESS

EDITED BY
Mithun Rudrapal,
Technology and Research, India

REVIEWED BY
Samiksha Garse,
DY Patil Deemed to be University, India
Sridhar Vemulapalli,
University of Nebraska Medical Center, United States
André Mauricio De Oliveira,
Federal Center for Technological Education of Minas Gerais, Brazil

*CORRESPONDENCE
Dan Cao,
caodan@scu.edu.cn
Ke Cheng,
183818128@qq.com

†These authors have contributed equally to this work

RECEIVED 11 June 2024
ACCEPTED 10 September 2024
PUBLISHED 26 September 2024

CITATION
Zhang P, Wang X, Li R, Li X, Cheng K and Cao D (2024) A case report: deep and durable response to low-dose lenvatinib and tislelizumab in an elderly patient with advanced intrahepatic cholangiocarcinoma.
Front. Pharmacol. 15:1447582.
doi: 10.3389/fphar.2024.1447582

COPYRIGHT
© 2024 Zhang, Wang, Li, Li, Cheng and Cao. This is an open-access article distributed under the terms of the Creative Commons Attribution License (CC BY). The use, distribution or reproduction in other forums is permitted, provided the original author(s) and the copyright owner(s) are credited and that the original publication in this journal is cited, in accordance with accepted academic practice. No use, distribution or reproduction is permitted which does not comply with these terms.

A case report: deep and durable response to low-dose lenvatinib and tislelizumab in an elderly patient with advanced intrahepatic cholangiocarcinoma

Pei Zhang†, Xin Wang†, Ruizhen Li, Xiaoying Li, Ke Cheng* and Dan Cao*

Division of Abdominal Tumor Multimodality Treatment, Cancer Center, West China Hospital, Sichuan University, Chengdu, Sichuan, China

Background: Older patients with advanced cholangiocarcinoma lack systemic therapy standards. These people have a high risk of chemotherapy, accompanied by adverse reactions and even discontinuation of treatment.

Case presentation: We report a 78-year-old female subject with advanced intrahepatic cholangiocarcinoma presenting with unresectable lesions involving the hepatic veins, along with extensive metastatic lymph nodes. After the geriatric assessment, capecitabine was utilized for only one cycle owing to adverse events (AEs). Next, a combination of low-dose lenvatinib and tislelizumab was administrated as a second-line treatment, which resulted in remarkable early tumor shrinkage. The following individual lenvatinib taper enabled a manageable safety profile and durable deep response. A near-complete response was achieved, with the primary tumor significantly reducing from 5.6 cm × 4.7 cm to nearly complete disappearance, accompanied by complete regression of lymph nodes, and both progression-free survival and overall survival exceeding 24 months.

Conclusion: The case provides valuable insights that could influence future treatment strategies for older patients with advanced cholangiocarcinoma who are unsuitable for chemotherapy. The dose-individualized chemotherapy-free regime of lenvatinib and tislelizumab might be used in similar cases to improve their outcomes.

KEYWORDS

intrahepatic cholangiocarcinoma, lenvatinib, tislelizumab, elderly patient, deep and durable response

Abbreviations: AE, adverse event; AFP, alpha-fetoprotein; CA19-9, carbohydrate antigen 19-9; CR, complete response; DOR, duration of response; ECOG PS, eastern cooperative oncology group performance status; FGFR, fibroblast growth factor receptor; IDH, isocitrate dehydrogenase; KPS, Karnofsky performance status; MDT, multidisciplinary team; MET, mesenchymal–epithelial transition factor; MSI-H, microsatellite instability-high; MSS, microsatellite stability; NGS, next-generation sequencing; ORR, objective response rate; OS, overall survival; PD-1, programmed death-1; PD-L1, programmed death-ligand 1; PFS, progression-free survival; PIVKA-II, protein induced by vitamin K absence or antagonist-II; PR, partial response; QOL, quality of life; SBRT, stereotactic body radiotherapy; TKI, tyrosine kinase inhibitor; TMB-L, tumor mutational burden-low; TPS, tumor proportion score.

Background

Cholangiocarcinoma has a poor prognosis, with a 5-year OS rate of less than 20% (Raggi et al., 2022). The combination of gemcitabine and cisplatin is currently the first-line standard treatment for advanced biliary system tumors (Valle et al., 2010). Adding PD-1/PD-L1 immunotherapy to chemotherapy further benefits patient survival (Oh et al., 2022; Kelley et al., 2023). However, data from patients older than 75 years are relatively scarce. Another study notes that older patients have more chemotherapy side effects, making them more likely to undergo dosage modification or discontinue treatment (Kalsi et al., 2014). Therefore, introducing geriatric assessment and exploring chemotherapy-free options becomes particularly important (Hurria et al., 2011). The combination of PD-1 inhibitors and VEGFR-TKIs represents a promising therapeutic strategy. Tislelizumab, in combination with lenvatinib, has demonstrated notable antitumor activity with a favorable safety profile in hepatocellular carcinoma (Xu et al., 2024). Additionally, emerging small-scale studies suggest potential efficacy in cholangiocarcinoma (Zhang et al., 2021). Against this background, we report an elderly patient diagnosed with advanced cholangiocarcinoma who received individualized dose-reduced combined targeted therapy and immunotherapy, exhibiting both safety and durable deep tumor remission, thereby offering a chemotherapy-free option for elderly patients with cholangiocarcinoma.

Case presentation

A 78-year-old woman presented with upper abdominal pain. Subsequent contrast-enhanced computed tomography (CT) scan in July 2021 revealed a 5.6 cm × 4.7 cm mass in the right hepatic lobe, with extension into the right hepatic vein. Additionally, swollen lymph

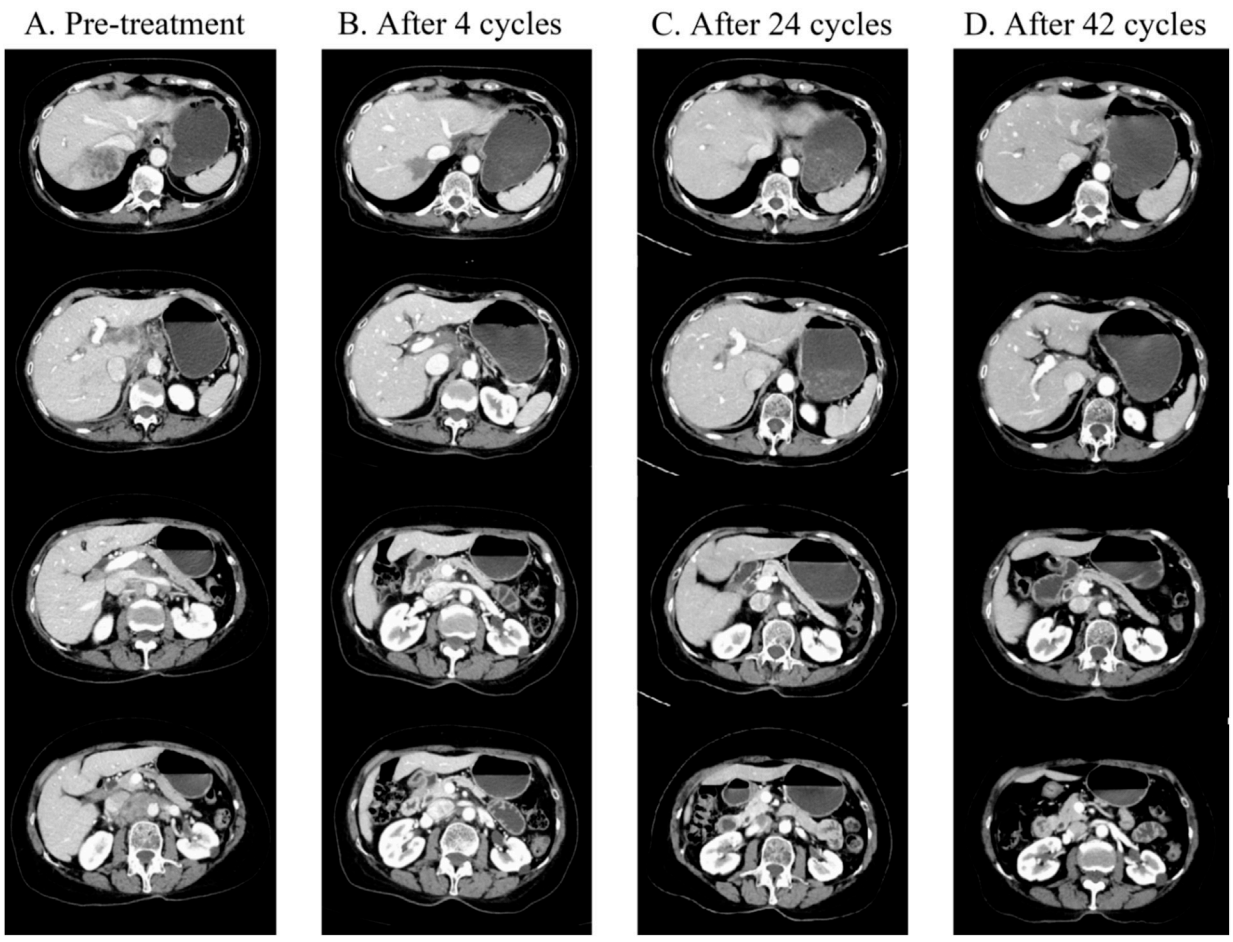

FIGURE 1
(A) Prior to treatment, CT showed a soft tissue mass located in the right lobe of the liver (size 5.6 cm × 4.7 cm), with increased and enlarged lymph nodes in the perigastric, hepatoportal area, hepatogastric ligament, and para-abdominal aorta, which were partially fused, and most of them were metastatic from lymph nodes (2021-07-12). **(B)** CT showed that after four cycles of treatment, compared with the 2021-07-12 CT, the primary tumor in the right lobe of the liver was significantly reduced (size 3.1 cm × 3.0 cm), and the caudate lobe lesion was a new metastasis. The hepatic portal area and hepatogastric ligament, cardiophrenic angle area, and para-abdominal aorta metastasis were significantly reduced compared to the previous area. **(C)** CT on 2022-11-29 showed that after 24 courses of treatment, the primary tumor in the right lobe of the liver almost disappeared, the residual low-density lesions were most likely to be necrotic, and some metastases in the liver almost disappeared. Compared with before, the size of the hepatic portal area and hepatic and gastric ligaments, cardiopulmonary angle area, and para-abdominal aortic lymph nodes continued to shrink. **(D)** CT on 2024-01-05 shows that after 42 courses of treatment, all lesions have almost completely disappeared compared with 2022-11-29 CT.

TABLE 1 Copy number variation detection results.

Gene	Transcription book	Variation type	Functional area	Number of copies
MET	NM_000245.2	Amplification	All exons	7
JUN	NM_002228.3	Amplification	All exons	4.4

TABLE 2 Genome variation detection results.

Gene	Transcription book	Base change	Amino acid change	Functional area	Mutation frequency (%)
TP53	NM_000546.5	c.812A>T	p.E271V	EX8	13.5
EP300	NM_001429.3	c.785G>T	p.G262V	EX3	9.1
HGF	NM_000601.4	c.337G>C	p.G113R	EX3	8.6
SMARCA4	NM_003072.3	c.3555A>T	p.Q1185H	EX26	8.1
CDH23	NM_022124.5	c.7847A>G	p.N2616S	EX55	4.7
TP53	NM_000546.5	c.392A>T	p.N131I	EX5	4.1
ERBB2	NM_004448.2	c.874G>T	p.G292C	EX7	3.9
ABL2	NM_007314.3	c.2222C>T	p.A741V	EX12	3.5

nodes were observed around the stomach, portal area, hepatogastric ligament, and para-aortic region, encircling the superior mesenteric arteries and veins (Figure 1). Poorly differentiated adenocarcinoma was confirmed by biopsy, and immunohistochemistry displayed CK7 (+), PCK (+), GPC3 (weak, +), and Ki-67 (+, ~80%), with other markers being negative, including HER-2 (0). Elevated CA19-9 (42.10 U/mL) and alpha-fetoprotein (AFP) (11.30 ng/mL) were tested, with PIVKA-II under the normal range. The patient had a history of atrial tachycardia and heart failure and underwent radiofrequency ablation without a hepatitis history. Next-generation sequencing (NGS) analysis of the tumor identified MET amplification, low tumor mutational burden (TMB-L), and microsatellite stability (MSS) (Tables 1, 2). Consequently, the patient was diagnosed by the multidisciplinary team (MDT) with unresectable intrahepatic cholangiocarcinoma with multiple abdominal lymph node metastases, classified as clinical stage cT2N1M0 IIIB.

The geriatric assessment score of 5 categorizes the patient as low risk for chemotherapy (Table 3) (Hurria et al., 2011), with favorable performance status (Karnofsky Performance Status (KPS) of 80, Eastern Cooperative Oncology Group (ECOG) PS of 1). Without chemotherapy contraindications, capecitabine (1,500 mg orally twice daily from day 1 to 14) and tislelizumab (200 mg intravenous on day 1, every 3 weeks) were administered as the first-line treatment, with each treatment cycle lasting 3 weeks. However, after only one cycle, the patient discontinued chemotherapy due to grade 2 hand-foot syndrome, fatigue, and diarrhea. The grade 2 hand–foot syndrome, fatigue, and diarrhea observed in this patient are consistent with those reported in other studies involving capecitabine and tislelizumab in similar age groups (van Beek et al., 2018; Zhu et al., 2022).

Subsequently, a reduced-dose lenvatinib (4 mg orally daily) combined with tislelizumab (200 mg intravenous every 3 weeks) was administered as a second-line treatment in August 2021.

After four cycles (October 2021), the hepatic lesion shrank with substantially reduced enhancement, and significant regression of abdominal lymph nodes was observed, achieving a partial response (PR), as illustrated in Figure 1. Concurrently, the patient experienced grade 2 diarrhea. A study indicated that if persistent or intolerable grade 2 or 3 AEs occur during lenvatinib treatment, therapy should be paused until symptoms improve, then resumed at the same or a lower dose (Kim et al., 2022). Therefore, we modified the dose to 4 mg every other day, maintaining efficacy while reducing adverse effects.

Under the following repeated cycles, the lesions continuously decreased in size (Supplementary Figure S1), ensuring good efficacy and satisfactory quality of life (QOL). Consequently, the patient declined further local invasive treatments.

By the 24th treatment cycle (November 2022), over 90% decrease in liver lesion size and complete disappearance of abdominal lymph nodes were observed. Lenvatinib (4 mg every other day) plus tislelizumab (200 mg every 3 weeks) were administered as maintenance therapy. By January 2024, the patient had achieved near-complete response (near-CR), as illustrated in Figure 1, with a duration of response (DOR) close to 26 months and a progression-free survival (PFS) exceeding 28 months. A series of serum tumor markers, including CEA, CA199, and AFP, were monitored throughout the treatment period. All markers remained relatively stable, with no significant fluctuations (Supplementary Figure S2). The patient was still receiving the regimen as of follow-up in June 2024 (Figure 2). Throughout the second-line therapy, the patient experienced grade 2 thrombocytopenia and grade 1 rash, both effectively managed with proper intervention.

Discussion

In recent years, with the introduction of immune checkpoint inhibitors, the treatment prospects for cholangiocarcinoma have significantly improved. The results of the TOPAZ-1 and Keynote

TABLE 3 The results of the geriatric assessment score.

Risk factor	Score
Age >72 years	2
Cancer type GI or GU	0
Chemotherapy dosing, standard dose	2
No. of chemotherapy drugs, polychemotherapy	0
Hemoglobin <11 g/dL (male), 10 < g/dL (female)	0
Creatinine clearance (Jelliffe, ideal weight) < 34 mL/min	0
Hearing, fair or worse	0
No. of falls in last 6 months, one or more	0
IADL: Taking medications, with some help/unable	0
MOS: Walking one block, somewhat limited/limited a lot	0
MOS: Decreased social activity because of physical/emotional health, limited at least sometimes	1

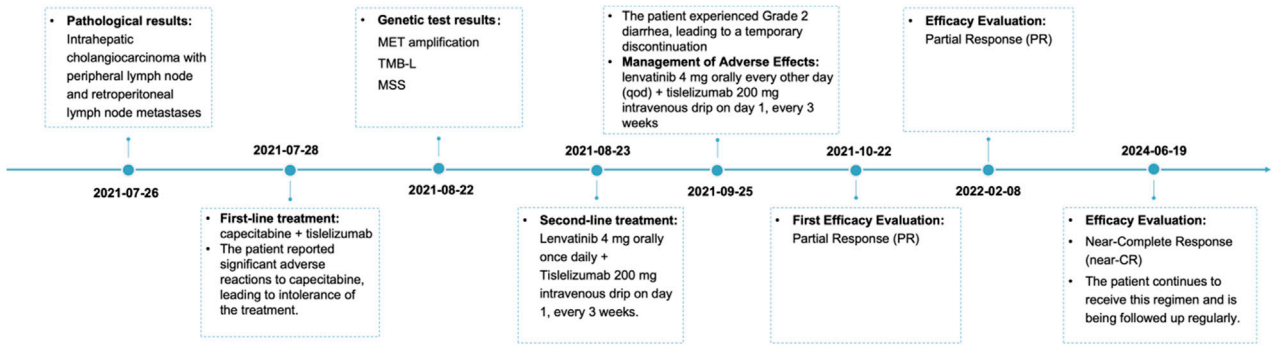

FIGURE 2
Schematic representation of the course of antitumor therapy. First-line treatment consisted of capecitabine (1,500 mg po bid d1-14) plus tislelizumab (200 mg ivgtt d1, q3w), which was not tolerated by the patient. Subsequently, it was changed to lenvatinib (4 mg po qd) plus tislelizumab (200 mg ivgtt d1, q3w). After one cycle, the patient developed second-degree diarrhea, and the dose was reduced to lenvatinib (4 mg po qod) plus tislelizumab (200 mg ivgtt d1, q3w), and the efficacy was PR after three cycles of the reduced treatment; the efficacy is still PR to date. QOL: quality of life; po: per os (oral); bid: bis in die (twice a day); d1-14: day 1–14; ivgtt: intravenous drip; d1: day 1; q3w: every 3 weeks; qd: quaque die (every day); qod: every other day; PR: partial response.

966 studies showed that combining PD-1/PD-L1 inhibitors with gemcitabine and cisplatin significantly improves OS in advanced biliary tract cancer (Oh et al., 2022; Kelley et al., 2023). However, clinical data on elderly cholangiocarcinoma patients remain limited. Elderly patients face unique challenges in terms of immune function and tolerance, leaving us with little knowledge about the effectiveness and safety of treatments in this population (Pawelec, 2019; Zhang et al., 2023). Therefore, research on treatments for elderly cholangiocarcinoma patients urgently needs to be strengthened, and even case reports on elderly patients are of great interest.

Elderly patients with cholangiocarcinoma typically have lower tolerance and high requirements for QOL, making traditional chemotherapy regimens potentially unsuitable. Chemotherapy is not contraindicated for elderly patients, but previous literature emphasizes the importance of geriatric assessment (Hurria et al., 2011). Therefore, we conducted a thorough geriatric assessment for this elderly female patient before chemotherapy, and her score was 5. After excluding chemotherapy contraindications, we chose the single-agent chemotherapy capecitabine combined with immunotherapy as the first-line treatment. However, the patient could not tolerate the toxicity of capecitabine and refused further chemotherapy, so we switched to targeted therapy combined with immunotherapy. In targeted therapy, isocitrate dehydrogenase (IDH) 1 inhibitors and fibroblast growth factor receptor (FGFR) inhibitors have been approved by the Food and Drug Administration for cholangiocarcinoma patients with certain genetic mutations (Lodl et al., 2023). However, most patients cannot choose precision-targeted therapy based on genetic mutations. Many clinical studies of anti-angiogenic targeted drugs combined with PD-1/PD-L1 antibodies are underway (Hack et al., 2020). For patients without driver gene mutations or without microsatellite instability-high (MSI-H) status, anti-angiogenic TKIs enhance synergy with immunotherapy through

mechanisms such as inhibiting angiogenesis and improving T-cell infiltration in the tumor microenvironment (Lee et al., 2020). These treatment options should be tailored based on the patient's specific genetic characteristics and condition.

There are few reports on the application of lenvatinib combined with tislelizumab in cholangiocarcinoma (Ding et al., 2021). However, this combination therapy has shown significant antitumor activity and manageable toxicity in patients with unresectable hepatocellular carcinoma (Xu et al., 2023). A study evaluating lenvatinib combined with toripalimab as a first-line treatment for advanced intrahepatic cholangiocarcinoma demonstrated an objective response rate (ORR) of 32.3%, with good tolerability (Jian et al., 2021). Another study investigating lenvatinib combined with sintilimab as a second-line treatment in chemotherapy-refractory advanced intrahepatic cholangiocarcinoma patients presented an ORR of 93.8% in those with high PD-L1 expression (TPS≥10%) (Ding et al., 2022). Additionally, a study enrolled 40 patients of lenvatinib combined with a PD-1 inhibitor as a second-line therapy and reported a disease control rate of 75.0%, with manageable treatment-related AEs (Xie et al., 2022). Based on these findings, our study further emphasizes the potential value of lenvatinib combined with tislelizumab in elderly patients, particularly those over 75 years old, highlighting the importance of individual dose adjustments in the clinical management of this age group.

Noteworthily, although lenvatinib was administrated at an extreme dose (4 mg every other day), a deep and durable response was observed, with achieved PFS for nearly 3 years, whether the combination treatment as maintenance therapy could be used as a stop-and-go strategy with low dosage lenvatinib or drug withdrawal. Based on evidence from metastatic colorectal cancer, a maintenance strategy provides significant clinical benefits compared to complete drug holidays or continued treatment (Esin and Yalcin, 2016). This patient received combination treatment as maintenance therapy at a low dosage for nearly 3 years without intolerable toxicity. Similarly, researchers have reported that another patient with advanced intrahepatic cholangiocarcinoma showed a dramatic response to first-line therapy and a PD-1 inhibitor combined with capecitabine as maintenance therapy, resulting in ongoing PFS (Wang et al., 2021). Therefore, the optimal strategy for maintenance therapy should still be individualized, even when using chemotherapy-free regimens.

Changes in metabolism and the immune system may alter the pharmacokinetics of lenvatinib in elderly patients, potentially enhancing its efficacy (Wildiers et al., 2003). Additionally, tumors that appear hypervascular on imaging indicate a high dependency on angiogenesis, making them more likely to be sensitive to lenvatinib, which could result in a better therapeutic response (Yamamoto et al., 2014; Huang et al., 2021). Moreover, lenvatinib can modify the tumor microenvironment, facilitating T-cell infiltration and synergizing with PD-1 inhibitors (Lu et al., 2021; Kato et al., 2019). These mechanisms may contribute to the sustained antitumor effects observed even at low doses.

Additionally, locoregional therapies such as liver resection, radiofrequency ablation, microwave ablation, radiotherapy, transarterial chemoembolization, etc., were used in unresectable liver-only or liver-dominant intrahepatic cholangiocarcinoma (Owen et al., 2023). MDT suggested stereotactic body radiotherapy could be used as a suitable locoregional treatment after deep PR was achieved, whereas invasive treatments were refused by the patient.

Among elderly patients with advanced disease, especially highly malignant tumors like cholangiocarcinoma, maintaining independence and QOL were more highly valued than survival or temporary tumor regression. Management of adverse events in patients treated with immunotherapy or targeted therapy was crucial. Fortunately, this elder presented mild treatment-related adverse events, grade 2 diarrhea, and fatigue, and these symptoms were significantly relieved after dose reduction. Individual dosage modification reduces the risk during medication in elderly patients.

Conclusion

Elderly patients lack standardized treatment protocols, making personalized therapy particularly important. The combination of lenvatinib and tislelizumab showed a deep and durable response, as well as prolonged survival in this patient. After experiencing side effects, individualized dose reduction is crucial, and low-dose treatment ensures efficacy without detrimental impact on QOL.

Lenvatinib and tislelizumab were effective and safe. For further validation, cohort studies or randomized controlled trials with large samples are needed. Trials should include patients with other tumors, older patients, and patients intolerant to chemotherapy. Furthermore, long-term follow-up in similar patients is needed to confirm therapy efficacy and monitor late-onset AEs and resistance.

Data availability statement

The original contributions presented in the study are included in the article/Supplementary Material; further inquiries can be directed to the corresponding authors.

Ethics statement

The studies involving humans were approved by the bioethics review board of West China Hospital, Sichuan University. The studies were conducted in accordance with the local legislation and institutional requirements. The participants provided their written informed consent to participate in this study. Written informed consent was obtained from the individual(s) for the publication of any potentially identifiable images or data included in this article.

Author contributions

PZ: writing–original draft and writing–review and editing. XW: writing–original draft and writing–review and editing. RL: writing–original draft. XL: writing–original draft. KC: writing–original draft and writing–review and editing. DC: writing–original draft and writing–review and editing.

Funding

The author(s) declare financial support was received for the research, authorship, and/or publication of this article. This study was sponsored by the 1·3·5 project for disciplines of excellence–Clinical Research Incubation Project, West China Hospital, Sichuan University (ZYJC21016), and the Sichuan Science and Technology Department Key Research and Development Project (2022YFS0336).

Conflict of interest

The authors declare that the research was conducted in the absence of any commercial or financial relationships that could be construed as a potential conflict of interest.

Publisher's note

All claims expressed in this article are solely those of the authors and do not necessarily represent those of their affiliated organizations, or those of the publisher, the editors, and the reviewers. Any product that may be evaluated in this article, or claim that may be made by its manufacturer, is not guaranteed or endorsed by the publisher.

Supplementary material

The Supplementary Material for this article can be found online at: https://www.frontiersin.org/articles/10.3389/fphar.2024.1447582/full#supplementary-material

References

Ding, X., Li, G., Sun, W., Shen, Y., Teng, Y., Xu, Y., et al. (2022). Sintilimab combined with lenvatinib for advanced intrahepatic cholangiocarcinoma in second-line setting—a multi-center observational study. *Front. Oncol.* 12, 907055. doi:10.3389/fonc.2022.907055

Ding, Y., Han, X., Sun, Z., Tang, J., Wu, Y., and Wang, W. (2021). Systemic sequential therapy of CisGem, tislelizumab, and lenvatinib for advanced intrahepatic cholangiocarcinoma conversion therapy. *Front. Oncol.* 11, 691380. doi:10.3389/fonc.2021.691380

Esin, E., and Yalcin, S. (2016). Maintenance strategy in metastatic colorectal cancer: a systematic review. *Cancer Treat. Rev.* 42, 82–90. doi:10.1016/j.ctrv.2015.10.012

Hack, S. P., Zhu, A. X., and Wang, Y. (2020). Augmenting anticancer immunity through combined targeting of angiogenic and PD-1/PD-L1 pathways: challenges and opportunities. *Front. Immunol.* 11, 598877. doi:10.3389/fimmu.2020.598877

Huang, C., Zhu, X.-D., Shen, Y.-H., Wu, D., Ji, Y., Ge, N.-L., et al. (2021). Organ specific responses to first-line lenvatinib plus anti-PD-1 antibodies in patients with unresectable hepatocellular carcinoma: a retrospective analysis. *Biomark. Res.* 9, 19–11. doi:10.1186/s40364-021-00274-z

Hurria, A., Togawa, K., Mohile, S. G., Owusu, C., Klepin, H. D., Gross, C. P., et al. (2011). Predicting chemotherapy toxicity in older adults with cancer: a prospective multicenter study. *J. Clin. Oncol.* 29 (25), 3457–3465. doi:10.1200/JCO.2011.34.7625

Jian, Z., Fan, J., Shi, G.-M., Huang, X.-Y., Wu, D., Liang, F., et al. (2021). Lenvatinib plus toripalimab as first-line treatment for advanced intrahepatic cholangiocarcinoma: a single-arm, phase 2 trial. *J. Clin. Oncol.* 39 (15_Suppl. l), 4099. doi:10.1200/jco.2021.39.15_suppl.4099

Kalsi, T., Babic-Illman, G., Fields, P., Hughes, S., Maisey, N., Ross, P., et al. (2014). The impact of low-grade toxicity in older people with cancer undergoing chemotherapy. *Br. J. cancer* 111 (12), 2224–2228. doi:10.1038/bjc.2014.496

Kato, Y., Tabata, K., Kimura, T., Yachie-Kinoshita, A., Ozawa, Y., Yamada, K., et al. (2019). Lenvatinib plus anti-PD-1 antibody combination treatment activates CD8+ T cells through reduction of tumor-associated macrophage and activation of the interferon pathway. *PloS one* 14 (2), e0212513. doi:10.1371/journal.pone.0212513

Kelley, R. K., Ueno, M., Yoo, C., Finn, R. S., Furuse, J., Ren, Z., et al. (2023). Pembrolizumab in combination with gemcitabine and cisplatin compared with gemcitabine and cisplatin alone for patients with advanced biliary tract cancer (KEYNOTE-966): a randomised, double-blind, placebo-controlled, phase 3 trial. *Lancet* 401 (10391), 1853–1865. doi:10.1016/S0140-6736(23)00727-4

Kim, B. H., Yu, S. J., Kang, W., Cho, S. B., Park, S. Y., Kim, S. U., et al. (2022). Expert consensus on the management of adverse events in patients receiving lenvatinib for hepatocellular carcinoma. *J. Gastroenterology Hepatology* 37 (3), 428–439. doi:10.1111/jgh.15727

Lee, W. S., Yang, H., Chon, H. J., and Kim, C. (2020). Combination of anti-angiogenic therapy and immune checkpoint blockade normalizes vascular-immune crosstalk to potentiate cancer immunity. *Exp. Mol. Med.* 52 (9), 1475–1485. doi:10.1038/s12276-020-00500-y

Lodl, E., Ramnaraign, B., Sahin, I., and Wheeler, S. (2023). Updates in the use of targeted therapies for the treatment of cholangiocarcinoma. *J. Oncol. Pharm. Pract.* 29 (5), 1206–1217. doi:10.1177/10781552231171079

Lu, M., Zhang, X., Gao, X., Sun, S., Wei, X., Hu, X., et al. (2021). Lenvatinib enhances T cell immunity and the efficacy of adoptive chimeric antigen receptor-modified T cells by decreasing myeloid-derived suppressor cells in cancer. *Pharmacol. Res.* 174, 105829. doi:10.1016/j.phrs.2021.105829

Oh, D. Y., Ruth He, A., Qin, S., Chen, L. T., Okusaka, T., Vogel, A., et al. (2022). Durvalumab plus gemcitabine and cisplatin in advanced biliary tract cancer. *NEJM Evid.* 1 (8), EVIDoa2200015. doi:10.1056/EVIDoa2200015

Owen, M., Makary, M. S., and Beal, E. W. (2023). Locoregional therapy for intrahepatic cholangiocarcinoma. *Cancers (Basel)* 15 (8), 2384. doi:10.3390/cancers15082384

Pawelec, G. (2019). Does patient age influence anti-cancer immunity? *Semin. Immunopathol.* 41 (1), 125–131. doi:10.1007/s00281-018-0697-6

Raggi, C., Taddei, M. L., Rae, C., Braconi, C., and Marra, F. (2022). Metabolic reprogramming in cholangiocarcinoma. *J. Hepatol.* 77 (3), 849–864. doi:10.1016/j.jhep.2022.04.038

Valle, J., Wasan, H., Palmer, D. H., Cunningham, D., Anthoney, A., Maraveyas, A., et al. (2010). Cisplatin plus gemcitabine versus gemcitabine for biliary tract cancer. *N. Engl. J. Med.* 362 (14), 1273–1281. doi:10.1056/NEJMoa0908721

van Beek, M. W., Roukens, M., Jacobs, W. C., Timmer-Bonte, J. N., and Kramers, C. (2018). Real-world adverse effects of capecitabine toxicity in an elderly population. *Drugs-real world outcomes* 5, 161–167. doi:10.1007/s40801-018-0138-9

Wang, Z., Zeng, T., Li, Y., Zhang, D., Yuan, Z., Huang, M., et al. (2021). PD-1 inhibitors plus capecitabine as maintenance therapy for advanced intrahepatic cholangiocarcinoma: a case report and review of literature. *Front. Immunol.* 12, 799822. doi:10.3389/fimmu.2021.799822

Wildiers, H., Highley, M. S., de Bruijn, E. A., and van Oosterom, A. T. (2003). Pharmacology of anticancer drugs in the elderly population. *Clin. Pharmacokinet.* 42, 1213–1242. doi:10.2165/00003088-200342140-00003

Xie, L., Huang, J., Wang, L., Ren, W., Tian, H., Hu, A., et al. (2022). Lenvatinib combined with a PD-1 inhibitor as effective therapy for advanced intrahepatic cholangiocarcinoma. *Front. Pharmacol.* 13, 894407. doi:10.3389/fphar.2022.894407

Xu, L., Chen, J., Liu, C., Song, X., Zhang, Y., Zhao, H., et al. (2024). Efficacy and safety of tislelizumab plus lenvatinib as first-line treatment in patients with unresectable hepatocellular carcinoma: a multicenter, single-arm, phase 2 trial. *BMC Med.* 22 (1), 172. doi:10.1186/s12916-024-03356-5

Xu, Y. K., Fu, S. M., Mao, Y., Huang, S. L., Li, D., and Wu, J. B. (2023). Hepatic arterial infusion chemotherapy (HAIC) combined with tislelizumab and lenvatinib for advanced hepatocellular carcinoma (aHCC) with Vp3-4 portal vein tumor thrombosis (PVTT): a single-arm, phase II study. *J. Clin. Oncol.* 41 (16), e16145. doi:10.1200/jco.2023.41.16_suppl.e16145

Yamamoto, Y., Matsui, J., Matsushima, T., Obaishi, H., Miyazaki, K., Nakamura, K., et al. (2014). Lenvatinib, an angiogenesis inhibitor targeting VEGFR/FGFR, shows broad antitumor activity in human tumor xenograft models associated with microvessel density and pericyte coverage. *Vasc. cell.* 6, 18–13. doi:10.1186/2045-824X-6-18

Zhang, J., Zou, Z., Tan, J., Shi, J., Yang, H., Wang, H., et al. (2023). Efficacy and safety analysis of immune checkpoint inhibitors plus angiogenesis inhibitors for the treatment of advanced driver-negative nsclc in elderly patients: a retrospective study. *J. Cancer* 14 (9), 1623–1634. doi:10.7150/jca.83719

Zhang, Q., Liu, X., Wei, S., Zhang, L., Tian, Y., Gao, Z., et al. (2021). Lenvatinib plus PD-1 inhibitors as first-line treatment in patients with unresectable biliary tract cancer: a single-arm, open-label, phase II study. *Front. Oncol.* 11, 751391. doi:10.3389/fonc.2021.751391

Zhu, W., Geng, Q., Peng, H., Jin, Z., Li, D., Pu, X., et al. (2022). Efficacy and safety of low-dose nab-paclitaxel plus tislelizumab in elderly patients with previously treated metastatic non-small cell lung cancer. *Front. Oncol.* 12, 802467. doi:10.3389/fonc.2022.802467

frontiers | Frontiers in Pharmacology

TYPE Case Report
PUBLISHED 01 November 2024
DOI 10.3389/fphar.2024.1433894

Check for updates

OPEN ACCESS

EDITED BY
Hardeep Singh Tuli,
Maharishi Markandeshwar University, India

REVIEWED BY
Luigi De Petris,
Karolinska Institutet (KI), Sweden
Isha Rani,
Maharishi Markandeshwar University, India

*CORRESPONDENCE
Tao Liu,
drliu_ctvs@163.com
Jianji Guo,
guojianji@163.com

RECEIVED 16 May 2024
ACCEPTED 14 October 2024
PUBLISHED 01 November 2024

CITATION
Wang P, Jiang Z, Guo J, Liu T, Liu Z, Wang D and Li H (2024) Case report: Treatment with ensartinib shows good response to SQSTM1-ALK fusion in lung adenocarcinoma.
Front. Pharmacol. 15:1433894.
doi: 10.3389/fphar.2024.1433894

COPYRIGHT
© 2024 Wang, Jiang, Guo, Liu, Liu, Wang and Li. This is an open-access article distributed under the terms of the Creative Commons Attribution License (CC BY). The use, distribution or reproduction in other forums is permitted, provided the original author(s) and the copyright owner(s) are credited and that the original publication in this journal is cited, in accordance with accepted academic practice. No use, distribution or reproduction is permitted which does not comply with these terms.

Case report: Treatment with ensartinib shows good response to SQSTM1-ALK fusion in lung adenocarcinoma

Pandeng Wang[1], Zhuo Jiang[2], Jianji Guo[1]*, Tao Liu[1]*, Zhen Liu[2], Dongdong Wang[3] and Honglin Li[3]

[1]Department of Cardiothoracic Surgery, The First Affifiliated Hospital of Guangxi Medical University, Nanning, Guangxi, China, [2]Shanghai Yinji Technology Co., Ltd., Shanghai, China, [3]Shanghai Zhongyou Inspection & Medical Co., Ltd., Shanghai, China

Lung cancer is a prevalent malignancy, with the rearrangement of the anaplastic lymphoma kinase (ALK) gene being responsible for a minority of cases of non-small cell lung cancer (NSCLC). NSCLC patients harboring ALK fusion proteins demonstrate sensitivity to ALK tyrosine kinase inhibitors (TKIs). In this report, we describe the case of a female patient with metastatic lung adenocarcinoma, identified through NGS to carry a rare inverted SQSTM1-ALK (S5, A20) fusion. The patient received ensartinib as first-line therapy, resulting in a partial response (PR). At the time of publication, the patient's condition remained favorable. We have, for the first time, identified the presence of SQSTM1-ALK fusion in pericardial effusion, with the favorable response to ensartinib validating the oncogenic potential of SQSTM1-ALK fusion. The substantial advancements and extensive utilization of NGS have facilitated the identification of rare fusion variants.

KEYWORDS

SQSTM1-ALK, rearrangement, lung cancer, targeted therapy, ensartinib

Introduction

Lung cancer is a prevalent malignancy, and those with specific molecular genetic alterations in the ALK, BRAF, or EGFR genes have been endorsed by the US Food and Drug Administration (FDA) as first-line targeted therapies. Rearrangement of the anaplastic lymphoma kinase (ALK) gene is observed in 2%–7% of NSCLC patients, and is particularly frequent in younger individuals, non-smokers, and those with adenocarcinoma (Kwak et al., 2010). NSCLC patients harboring ALK fusion proteins demonstrate sensitivity to ALK tyrosine kinase inhibitors (TKIs).

Approximately half of the cases are diagnosed at an advanced, metastatic stage. Advanced lung cancer may result in the occurrence of pericardial effusion. Due to the close relationship between the cardiovascular and pulmonary systems, it is common for patients with advanced lung cancer to exhibit pericardial effusion, bloody pericardial effusion, and metastasis of cancer cells. Typically, only a restricted amount of biopsy

Abbreviations: ALK, Anaplastic lymphoma kinase; CEA, Carcinoembryonic Antigen; IMFT, Inflammatory Myofibroblastic Tumor; TTF1, Thyroid Transcription Factor-1; IMT, Inflammatory Myofibroblastic Tumor; SQSTM1, Sequestosome 1; TPS, Tumor Proportion Score.

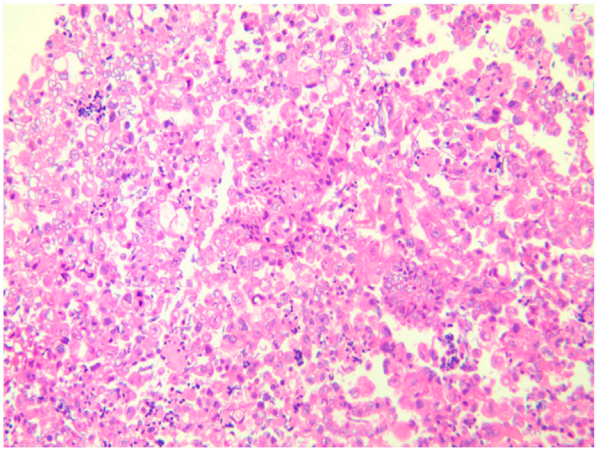

FIGURE 1
Tumor cell content.

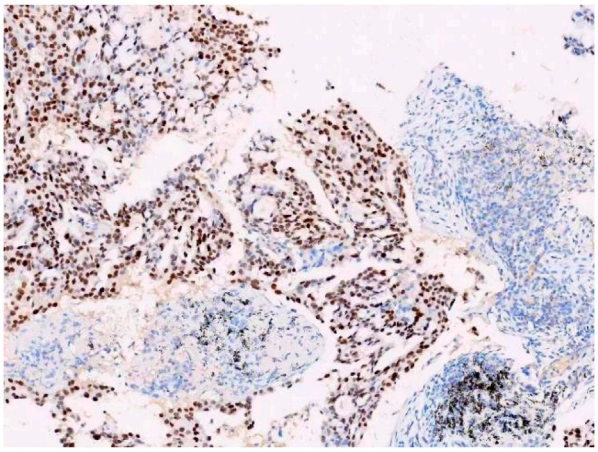

FIGURE 2
TTF1 immunohistochemical results.

material is available for companion diagnosis using NGS panels. In this report, we depict a case study of a patient with metastatic lung adenocarcinoma who declined direct tumor biopsy sampling and instead opted for pericardial effusion extraction for diagnostic purposes. Subsequent testing revealed the presence of SQSTM1-ALK fusion. Subsequent to treatment with ensartinib, the ailment was accurately diagnosed via initial limited samplings, thereby obviating the need for multiple rebiopsies.

Case description

A female patient in her 60s, who is Chinese and of Zhuang nationality, with a junior high school education level, married status, a farmer by occupation and in poor economic condition, presented with chest pain accompanied by dyspnea and was diagnosed with advanced metastatic lung adenocarcinoma upon examination. The patient had no history of smoking and alcohol consumption. Neither her parents

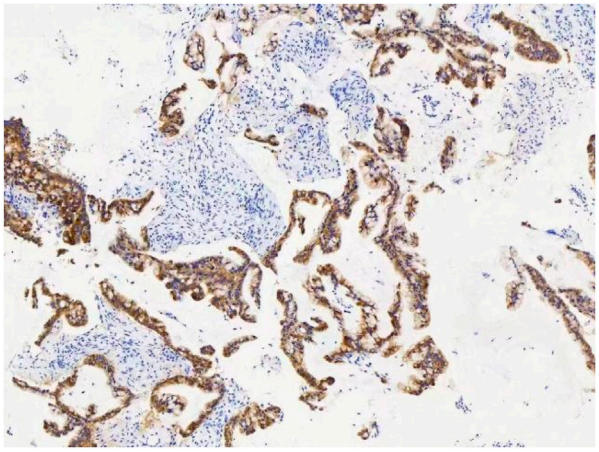

FIGURE 3
ALK immunohistochemical results.

nor her siblings have a history of lung cancer. The clinical stage was T2bN2M1a, with no extrathoracic metastases detected upon radiological follow-up. Due to the patient's decision to decline a lung tumor biopsy, pericardial effusion was obtained for HE staining, which revealed that tumor cells comprised 85% of the sample (Figure 1). TTF1 immunohistochemistry results confirmed that the malignant pericardial effusion originated from metastasis of lung adenocarcinoma (Figure 2). The ALK immunohistochemistry test also showed positive results (Figure 3). Following the confirmation of pericardial effusion as tumor metastasis, DNA of tumor cells was extracted from the effusion for genetic testing.

The presence of SQSTM1-ALK in the pericardial effusion sample was validated through next-generation DNA sequencing (NGS) using a 160-gene panel provided by Shanghai Zhongyou Inspection & Medical Co., Ltd. The genetic testing report (using the GenarsR system from Shanghai Yinji Technology Co., Ltd) revealed the location of the SQSTM1 breakpoint at Exon5 chr5:179255851, and the ALK breakpoint at Exon20 chr2:29447094. A 39-base pair inversion of the ALK gene was observed at the breakpoint location, as illustrated in Figures 4, 5. The patient was also found to harbor an unidentified MSH6 S346C mutation. This fusion has not previously been documented in cases of lung adenocarcinoma, and the Sanger verification results are provided in Figure 6.

Following treatment with ensartinib at 225 mg QD, the patient exhibited a decrease in CEA level from 104.97 ng/mL to 5.25 ng/mL, and a reduction in carbohydrate antigen 125 level from 312.50 μg/mL to 43.84 μg/mL after 1 month. Additionally, the chest CT scan revealed a reduction in tumor size (Figures 7, 8) as well as pericardial effusion (Figures 9, 10). After 6 months of treatment, the tumor size remained the same as after 1 month of treatment (Figure 11). After 6 months of treatment, the condition of pericardial effusion and pleural effusion (Figure 12).

Discussion

In this report, we present the case of a 60-year-old female diagnosed with advanced lung adenocarcinoma harboring the

FIGURE 4
Breakpoint of SQSTM1 gene.

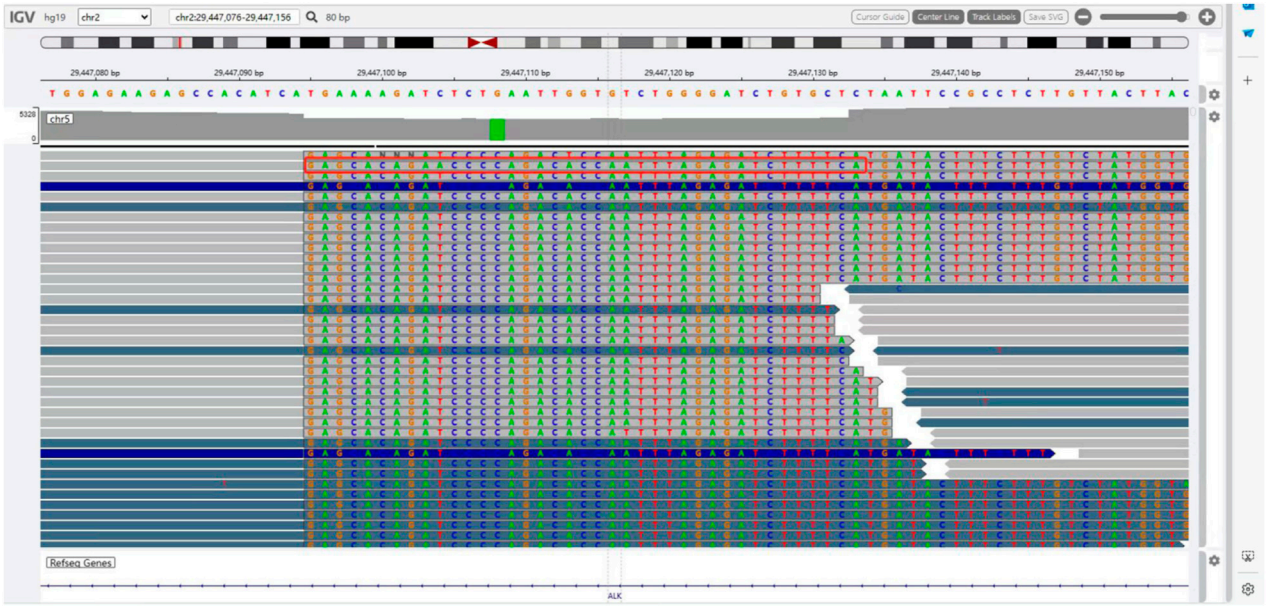

FIGURE 5
Inversion of 39BP base at breakpoint of ALK gene.

rare SQSTM1-ALK fusion, which had metastasized to the pericardium. While several ALK inhibitors have been approved for ALK-rearranged non-small cell lung cancer (NSCLC), this is the first documented case of using Ensartinib to treat a patient with this specific fusion. Our findings show that Ensartinib demonstrated significant efficacy, After 1 month of treatment, the patient achieved partial response (PR), and the effect was sustained for at least 6 months without any observable toxicity. This suggests that Ensartinib may be a promising therapeutic option for lung adenocarcinoma patients with the SQSTM1-ALK fusion, though complete remission (CR) was not achieved during the observation period.

Ensartinib was chosen over other ALK inhibitors such as Crizotinib and Alectinib based on its demonstrated superiority in preclinical and early clinical trials. Ensartinib has shown a broader inhibitory profile, effectively targeting ALK mutations, including

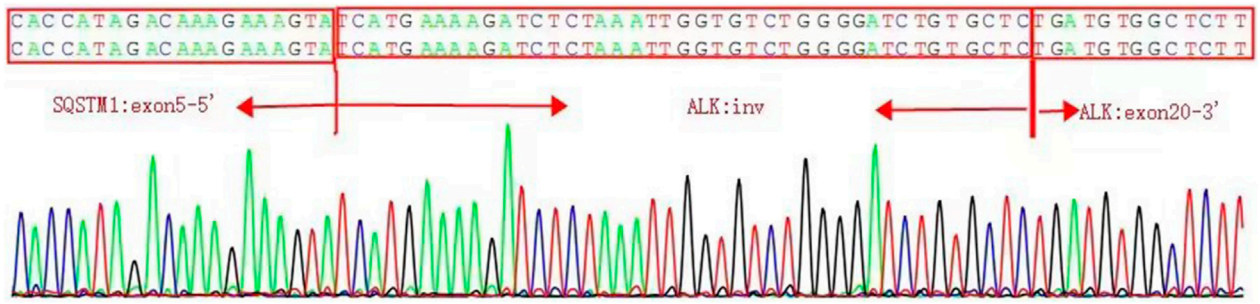

FIGURE 6
SQSTM1-ALK fusion.

FIGURE 7
Tumor condition before treatment.

FIGURE 9
Pericardial effusion condition before treatment.

FIGURE 8
Tumor size after 1 month of treatment.

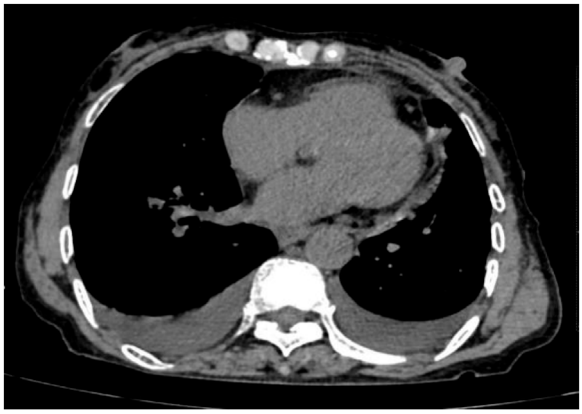

FIGURE 10
Pericardial effusion and pleural effusion after 1 month of treatment.

those resistant to first- and second-generation inhibitors. This makes it a suitable first-line treatment, especially for patients with brain metastases, as Ensartinib crosses the blood-brain barrier more efficiently (Wang et al., 2023). Additionally, the patient's overall health status and multiple metastases influenced the decision to use Ensartinib, as a more comprehensive systemic control was needed. Given the limited data on the effectiveness of

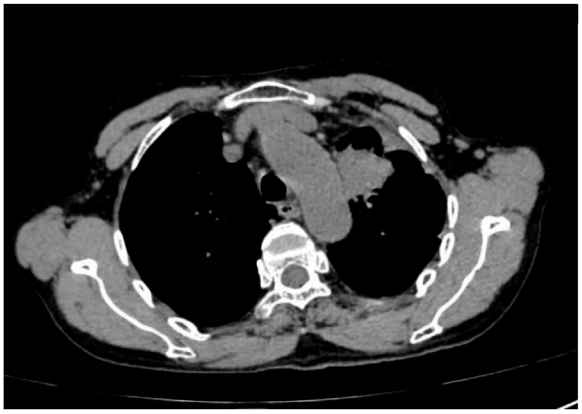

FIGURE 11
Tumor size after 6 months of treatment.

FIGURE 12
Pericardial and pleural effusion after 6 months of treatment.

other ALK inhibitors in patients with SQSTM1-ALK fusion, Ensartinib presented a novel approach for this case.

Although the patient did not experience any drug-related toxicity, Ensartinib's potential side effects should still be considered, especially in comparison to other ALK inhibitors such as Alectinib and Crizotinib. Common side effects of Ensartinib include skin rash, elevated liver enzymes, and fatigue (Zhou et al., 2023). The absence of any significant side effects in this patient is particularly noteworthy, given the advanced stage and the presence of multiple metastases. In contrast, Alectinib and Crizotinib are often associated with gastrointestinal disturbances and muscle pain, with Crizotinib also known to cause higher incidences of vision problems (Zhou et al., 2023). The good tolerability of Ensartinib in this case suggests that it could be an effective treatment for patients unable to endure the side effects of other ALK inhibitors.

The SQSTM1-ALK fusion has been identified in other cancers, such as inflammatory myofibroblastic tumors (IMT), epithelioid fibrous histiocytoma (Dickson et al., 2018), and large B-cell lymphoma (d'Amore et al., 2013). However, the disease course and treatment responses in these cancers differ from those in lung adenocarcinoma. For example, a 46-year-old male with SQSTM1-ALK-positive IMT responded significantly to Alectinib, with a 17-month progression-free survival (Honda et al., 2019). In our patient, the presence of cardiac and brain metastases at diagnosis suggested a more aggressive disease progression. This suggests that the presence of the SQSTM1-ALK fusion in lung adenocarcinoma may lead to rapid progression, emphasizing the need for prompt and aggressive treatment strategies.

The role of STAT3 inhibitors in treating SQSTM1-ALK fusion-positive cancers, as well as the combination of ALK and STAT3 inhibitors, warrants further investigation. In lymphoma cases involving SQSTM1-ALK fusion, STAT3 phosphorylation plays a key role in pathogenesis (d'Amore et al., 2013). Exploring whether this mechanism similarly contributes to lung adenocarcinoma could open new therapeutic avenues, particularly for combined treatment strategies with ALK and STAT3 inhibitors. Moreover, resistance to second-generation ALK inhibitors highlights the need to assess third-generation inhibitors such as Lorlatinib, which has shown efficacy in overcoming resistance mutations (Lin et al., 2024). Clinical trials investigating Lorlatinib in SQSTM1-ALK fusion-positive patients could provide valuable insights into the long-term management of resistant cases.

Conclusion

This study presents the inaugural successful treatment of lung adenocarcinoma patients positive for SQSTM1-ALK with pericardial effusion using ensartinib. The outcomes indicate that ensartinib may be considered as an effective therapeutic option in the presence of SQSTM1-ALK. These findings hold significant implications for clinical practice, emphasizing the necessity of genetic testing and tailored treatment approaches for lung adenocarcinoma.

Data availability statement

The raw data supporting the conclusions of this article will be made available by the authors, without undue reservation.

Ethics statement

The studies involving humans were approved by the First Affifiliated Hospital of Guangxi Medical University, Nanning, Guangxi, China. The studies were conducted in accordance with the local legislation and institutional requirements. The participants provided their written informed consent to participate in this study. Written informed consent was obtained from the individual(s) for the publication of any potentially identifiable images or data included in this article.

Author contributions

PW: Conceptualization, Investigation, Supervision, Writing–original draft, Writing–review and editing. ZJ: Investigation, Writing–original

draft, Writing–review and editing. JG: Data curation, Investigation, Writing–review and editing. TL: Data curation, Resources, Writing–review and editing. ZL: Formal Analysis, Writing–review and editing. DW: Formal Analysis, Writing–review and editing. HL: Visualization, Writing–review and editing.

Funding

The author(s) declare that financial support was received for the research, authorship, and/or publication of this article. This work was supported by the Health Commission of Guangxi Zhuang Autonomous Region self-finances research projects, and Guangxi Medical and Health Appropriate Technology Development and Promotion Application Project, National Clinical Key Specialty Construction Project, the Clinical Key Specialty Construction Project in Guangxi Zhuang Autonomous Region and the Clinical Key Discipline Construction Project in Guangxi Zhuang Autonomous Region.

Conflict of interest

Authors ZJ and ZL were employed by Shanghai Yinji Technology Co., Ltd. Authors DW and HL were employed by Shanghai Zhongyou Inspection & Medical Co., Ltd.

The remaining authors declare that the research was conducted in the absence of any commercial or financial relationships that could be construed as a potential conflict of interest.

Publisher's note

All claims expressed in this article are solely those of the authors and do not necessarily represent those of their affiliated organizations, or those of the publisher, the editors and the reviewers. Any product that may be evaluated in this article, or claim that may be made by its manufacturer, is not guaranteed or endorsed by the publisher.

References

d'Amore, E. S., Visco, C., Menin, A., Famengo, B., Bonvini, P., and Lazzari, E. (2013). STAT3 pathway is activated in ALK-positive large B-cell lymphoma carrying SQSTM1-ALK rearrangement and provides a possible therapeutic target. *Am. J. Surg. pathology* 37 (5), 780–786. doi:10.1097/PAS.0b013e318287791f

Dickson, B. C., Swanson, D., Charames, G. S., Fletcher, C. D., and Hornick, J. L. (2018). Epithelioid fibrous histiocytoma: molecular characterization of ALK fusion partners in 23 cases. *Mod. pathology official J. U. S. Can. Acad. Pathology* 31 (5), 753–762. doi:10.1038/modpathol.2017.191

Honda, K., Kadowaki, S., Kato, K., Hanai, N., Hasegawa, Y., Yatabe, Y., et al. (2019). Durable response to the ALK inhibitor alectinib in inflammatory myofibroblastic tumor of the head and neck with a novel SQSTM1-ALK fusion: a case report. *Investig. new drugs* 37 (4), 791–795. doi:10.1007/s10637-019-00742-2

Kwak, E. L., Bang, Y. J., Camidge, D. R., Shaw, A. T., Solomon, B., Maki, R. G., et al. (2010). Anaplastic lymphoma kinase inhibition in non-small-cell lung cancer. *N. Engl. J. Med.* 363 (18), 1693–1703. doi:10.1056/NEJMoa1006448

Lin, J. J., Horan, J. C., Tangpeerachaikul, A., Swalduz, A., Valdivia, A., Johnson, M. L., et al. (2024). NVL-655 is a selective and brain-penetrant inhibitor of diverse ALK-mutant oncoproteins, including lorlatinib-resistant compound mutations. *Cancer Discov.* 13, OF1–OF20. Published online September. doi:10.1158/2159-8290.CD-24-0231

Wang, W. Q., Xu, T., Zhang, J. J., Wang, Y., Wang, Y., Zhang, W., et al. (2023). A comprehensive clinical evaluation of first-line drugs for ALK-positive advanced non-small cell lung cancer. *J. Thorac. Dis.* 15 (4), 1935–1947. doi:10.21037/jtd-23-380

Zhou, F., Yang, Y., Zhang, L., Cheng, Y., Han, B., Lu, Y., et al. (2023). Expert consensus of management of adverse drug reactions with anaplastic lymphoma kinase tyrosine kinase inhibitors. *ESMO Open* 8 (3), 101560. doi:10.1016/j.esmoop.2023.101560

frontiers | Frontiers in Pharmacology

TYPE Review
PUBLISHED 05 November 2024
DOI 10.3389/fphar.2024.1475998

Check for updates

OPEN ACCESS

EDITED BY
Viviana di Giacomo,
University of Studies G. d'Annunzio Chieti and Pescara, Italy

REVIEWED BY
Gabriela Chiosis,
Memorial Sloan Kettering Cancer Center, United States
Ernest Duah,
Sumitomo Dainippon Pharma Oncology, United States

*CORRESPONDENCE
Sameh Saber,
sampharm81@gmail.co
Mai A. Elhemely,
mai.ali@manchester.ac.uk
Elsayed A. Elmorsy,
a.almarsa@qu.edu.sa
Rabab S. Hamad,
rhamad@kfu.edu.sa
Mustafa Ahmed Abdel-Reheim,
m.ahmed@su.edu.sa

RECEIVED 04 August 2024
ACCEPTED 22 October 2024
PUBLISHED 05 November 2024

CITATION
Saber S, Abdelhady R, Elhemely MA, Elmorsy EA, Hamad RS, Abdel-Reheim MA, El-kott AF, AlShehri MA, Morsy K, AlSheri AS and Youssef ME (2024) PU-H71 (NSC 750424): a molecular masterpiece that targets HSP90 in cancer and beyond.
Front. Pharmacol. 15:1475998.
doi: 10.3389/fphar.2024.1475998

COPYRIGHT
© 2024 Saber, Abdelhady, Elhemely, Elmorsy, Hamad, Abdel-Reheim, El-kott, AlShehri, Morsy, AlSheri and Youssef. This is an open-access article distributed under the terms of the Creative Commons Attribution License (CC BY). The use, distribution or reproduction in other forums is permitted, provided the original author(s) and the copyright owner(s) are credited and that the original publication in this journal is cited, in accordance with accepted academic practice. No use, distribution or reproduction is permitted which does not comply with these terms.

PU-H71 (NSC 750424): a molecular masterpiece that targets HSP90 in cancer and beyond

Sameh Saber[1]*, Rasha Abdelhady[2,3], Mai A. Elhemely[4]*, Elsayed A. Elmorsy[5,6]*, Rabab S. Hamad[7,8]*, Mustafa Ahmed Abdel-Reheim[9,10]*, Attalla F. El-kott[11,12], Mohammed A. AlShehri[11], Kareem Morsy[11,13], Ali S. AlSheri[11] and Mahmoud E. Youssef[1]

[1]Department of Pharmacology, Faculty of Pharmacy, Delta University for Science and Technology, Gamasa, Egypt, [2]Pharmacology and Toxicology Department, Faculty of Pharmacy, Fayoum University, Fayoum, Egypt, [3]Pharmacology and Toxicology Department, Faculty of Pharmacy, Egyptian Chinese University, Cairo, Egypt, [4]School of Medical Sciences, Faculty of Biology, Medicine and Health, The University of Manchester, Manchester, United Kingdom, [5]Department of Pharmacology and Therapeutics, College of Medicine, Qassim University, Buraidah, Saudi Arabia, [6]Department of Clinical Pharmacology, Faculty of Medicine, Mansoura University, Mansoura, Egypt, [7]Biological Sciences Department, College of Science, King Faisal University, Al Ahsa, Saudi Arabia, [8]Central Laboratory, Theodor Bilharz Research Institute, Giza, Egypt, [9]Department of Pharmaceutical Sciences, College of Pharmacy, Shaqra University, Shaqra, Saudi Arabia, [10]Department of Pharmacology and Toxicology, Faculty of Pharmacy, Beni-Suef University, Beni Suef, Egypt, [11]Department of Biology, College of Science, King Khalid University, Abha, Saudi Arabia, [12]Department of Zoology, Faculty of Science, Damanhour University, Damanhour, Egypt, [13]Department of Zoology, Faculty of Science, Cairo University, Cairo, Egypt

Heat shock protein 90 (HSP90) is a pivotal molecular chaperone with multifaceted roles in cellular health and disease. Herein, we explore how HSP90 orchestrates cellular stress responses, particularly through its partnership with heat shock factor 1 (HSF-1). PU-H71, a selective inhibitor of HSP90, demonstrates significant potential in cancer therapy by targeting a wide array of oncogenic pathways. By inducing the degradation of multiple client proteins, PU-H71 disrupts critical signaling pathways such as MAPK, PI3K/Akt, JAK/STAT, EGFR, and mTOR, which are essential for cancer cell survival, proliferation, and metastasis. We examined its impact on combating triple-negative breast cancer and enhancing the effectiveness of carbon-ion beam therapy, offering new avenues for cancer treatment. Furthermore, the dual inhibition of HSP90A and HSP90B1 by PU-H71 proves highly effective in the context of myeloma, providing fresh hope for patients with this challenging malignancy. We delve into its potential to induce apoptosis in B-cell lymphomas that rely on Bcl6 for survival, highlighting its relevance in the realm of hematologic cancers. Shifting our focus to hepatocellular carcinoma, we explore innovative approaches to chemotherapy. Moreover, the current review elucidates the potential capacity of PU-H71 to suppress glial cell activation paving the way for developing novel therapeutic strategies for neuroinflammatory disorders. Additionally, the present report also suggests the promising role of PU-H71 in JAK2-dependent myeloproliferative neoplasms. Eventually, our report sheds more light on the multiple functions of HSP90 protein as well as the potential

therapeutic benefit of its selective inhibitor PU-H71 in the context of an array of diseases, laying the foundations for the development of novel therapeutic approaches that could achieve better treatment outcomes.

KEYWORDS

Hsp90, PU-H71 (NSC 750424), tumorigenesis, apoptosis, oncogenic signals

1 Introduction

Heat shock proteins (HSPs) denote a class of highly conserved proteins playing a pivotal role in safeguarding the cells against several forms of stress. Notably, HSPs are central to a range of cellular functions including protein folding, unfolding, assembly, and disassembly. According to their molecular weight, HSPs are classified into main four subgroups, namely, HSP90, HSP70, HSP60, and the small HSP family (Table 1) (Hu et al., 2022). Conspicuously, HSP90 is a leading chaperone protein indispensable for correcting misfolded proteins. On the other hand, HSP70 functions by binding to partially unfolded protein fragments inhibiting their clumping. Meanwhile, HSP60 plays a fundamental role in the proper folding of proteins within specific cellular compartments (e.g., mitochondria). Lastly, the small HSP family, including HSP27, suppresses the aggregation of misfolded proteins (Navarro-Zaragoza et al., 2021). In times of stress, such as exposure to high temperatures, HSPs play a critical role in cell survival by latching onto and stabilizing damaged or partially unfolded proteins until the stressful conditions subside and normal cellular conditions are restored (Kakkar et al., 2014). This allows the proteins to undergo proper folding with the assistance of HSPs. The initial, inactivated state of the HSP90 chaperone cycle is denoted by the closed conformation. Upon binding of ATP, a structural alteration occurs in HSP90, causing it to transition into the open state. In this open state, HSP90 exhibits increased ATPase activity and becomes receptive to client proteins, which can then engage with it for protein folding (Figure 1) (Youssef et al., 2023). HSPs are classified according to their broad structural classes as described in Table 1.

Inactive Hsp90 (open conformation) forms a dimer at its C terminus, leaving the N termini unassociated, while the Hsp70-captures client proteins and delivers them to Hsp90 with the help of co-chaperones. The co-chaperone Hop binds to both Hsp70 and Hsp90 through its TPR domains, acting as a scaffold to facilitate the transfer of the client protein from Hsp70 to Hsp90 (intermediate complex). Additional co-chaperones, including peptidyl-prolyl cis-trans isomerases (PPIase), associate with Hsp90, leading to the formation of an asymmetric complex. Subsequently, Hsp70 and Hop dissociate, and the co-chaperone p23 replaces them, forming the closed late conformation, where ATP hydrolysis occurs, resulting in the release of the client protein.

Heat shock protein 90 (HSP90) plays a crucial role as a key molecular helper, vital for safeguarding the functional stability and survival of cells when confronted with changing stress factors. Within the purview of HSPs, HSP90 has gained rising attention, fundamentally this could be ascribed to its crucial role in an array of normal physiological cellular processes as well as those correlated with disease progression. Through direct connections, HSP90 was reported to keep proteins associated with cell death in a state that is resistant to programmed cell death (Peng et al., 2022). The wide range of functions exerted by HSP90 is likely attributed to its ability to serve as a helper for numerous client proteins playing indispensable roles in health disorders such as cancer and neurodegenerative diseases (Sumi and Ghosh, 2022).

Targeting and inhibition of HSP90 were achieved by a class of drugs that have been classified as HSP90 inhibitors capable of destabilizing and degrading HSP90 client proteins, with subsequent suppression of multiple oncogenic signaling pathways simultaneously. This multi-target approach suggests that HSP90 inhibitors could be promising therapeutic agents for various neoplasms (Magwenyane et al., 2022). Notably, HSP90 inhibitors, such as geldanamycin derivatives (e.g., 17-AAG and 17-DMAG) and resorcinol-based compounds (e.g., ganetespib), displayed potent anti-cancer activity in preclinical trials and are currently undergoing clinical trials evaluating their safety profiles. The therapeutic benefit of HSP90 inhibitors could potentially exceed anticancer therapy. Markedly, ongoing studies are investigating their potential benefit in neurodegenerative disorders and other health conditions (Luo et al., 2010). HSP90 inhibitors are summarized in Table 2. Table 2 shows the classes of HSP90 inhibitors. The structural diversity of HSP90 inhibitors allows for the development of various drug candidates for cancer and other diseases.

2 Role of HSP90 in tumorigenesis

HSP90 is a crucial molecular chaperone that plays a significant role in cancer biology by facilitating the proper folding, stabilization, and functional regulation of numerous proteins that are essential for tumorigenesis (Birbo et al., 2021). As a prominent member of the heat shock protein family, HSP90 assists in maintaining cellular proteostasis, particularly under the stress conditions often encountered in cancer cells. Its importance in cancer has led to extensive research focusing on HSP90 as a therapeutic target, given its involvement in various oncogenic processes.

HSP90 is known to interact with over 200 client proteins, many of which are involved in critical signaling pathways that control cell growth, survival, and metastasis (Kamal et al., 2004; Xu and Neckers, 2007; Sun et al., 2021). Among these client proteins are receptor tyrosine kinases such as human epidermal growth factor receptor 2 (HER2) and epidermal growth factor (EGFR) (Wang et al., 2016), which are essential for transmitting growth signals from the extracellular environment into the cell interior. HSP90 also interacts with key signaling molecules such as AKT and SRC, which are critical for cell survival and proliferation (Rong and Yang, 2018). HSP90 is also required for the stability and function of transcription factors such as hypoxia inducible factor (HIF-1) and p53, which are responsible for regulating hypoxia responses and controlling the cell cycle, respectively (Albadari et al., 2019; Shirai et al., 2021).

TABLE 1 Classification and characteristics of HSPs.

Classification	Subclassification and characteristics
HSP90	HSP90α is primarily found in the cytoplasm
	HSP90β is found in the mitochondria
HSP70	Constitutive HSP70 (HSC70) is found in the cytoplasm
	Inducible HSP70 (HSP72) is produced in response to cellular stress
HSP60	HSP60 (cytosolic)
	HSP60 (mitochondrial)
HSP40	Constitutive HSP40 is found in the cytoplasm
	Inducible HSP40 is produced in response to cellular stress
Small HSPs	HSP27 is involved in the regulation of the actin cytoskeleton
	HSP20 is involved in protection against cellular damage

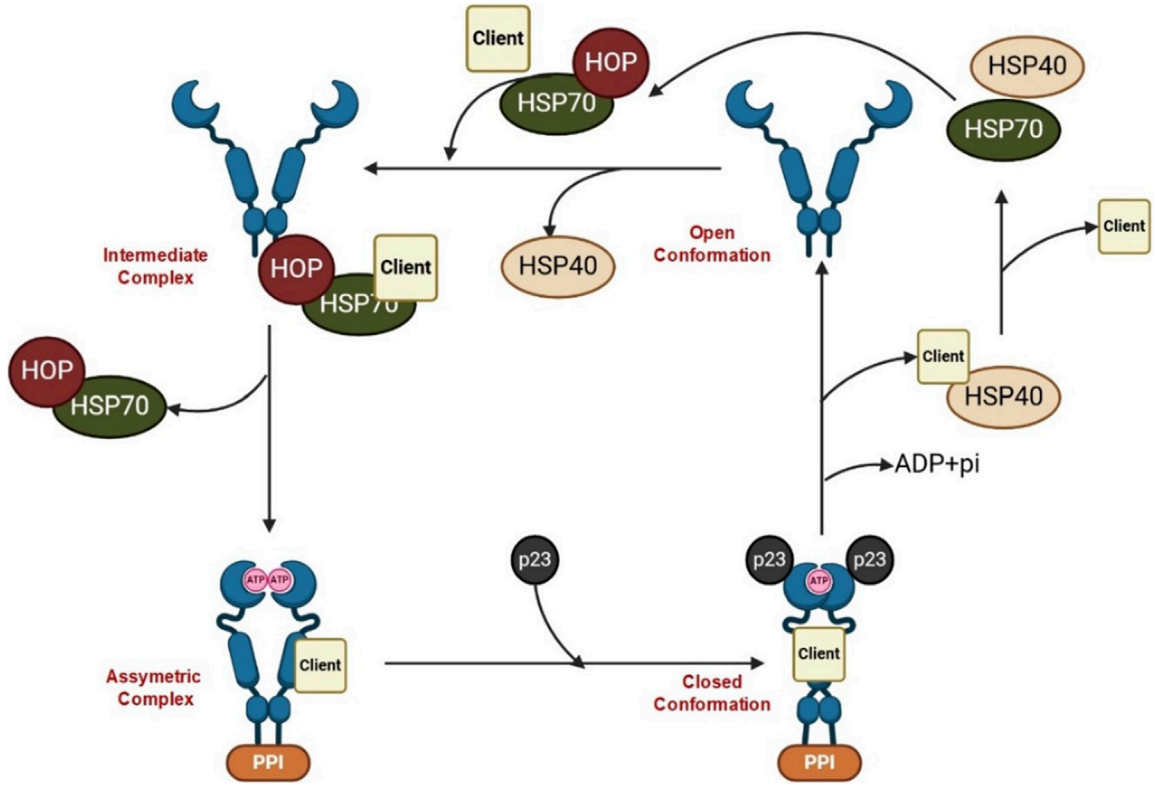

FIGURE 1
HSP90 cycle.

Furthermore, HSP90 stabilizes cell cycle regulators such as CDK4 and CDK6, which are required for cell cycle progression (Sager et al., 2022). In cancer cells, HSP90 protects mutated and overexpressed oncoproteins that would otherwise be degraded. This protective mechanism is especially important because cancer cells frequently experience high levels of cellular stress as a result of rapid proliferation and abnormal protein synthesis. As a result, HSP90 expression levels are typically two to ten times higher in cancer cells than in normal cells (Solárová et al., 2015; Birbo et al., 2021). This overexpression has been linked to a poor prognosis and increased resistance to various therapeutic interventions, highlighting the role of HSP90 in cancer progression.

Hanahan and Weinberg identified several hallmarks of cancer in which HSP90 plays a role. These characteristics include self-sufficiency in growth signals, apoptosis evasion, long-term angiogenesis, and increased tissue invasion and metastasis (Hanahan and Weinberg, 2011). HSP90 allows tumor cells to thrive even in adverse conditions such as nutrient deprivation or

TABLE 2 HSP90 inhibitors.

Inhibitor Name	Mechanism of Action	Reference
Geldanamycin	Binds to the N-terminal ATP-binding pocket, inhibiting its chaperone function	Miyata (2005)
17-AAG (Tanespimycin)	Similar mechanism to Geldanamycin but with improved pharmacokinetics	Modi et al. (2011)
17-DMAG	A more soluble derivative of Geldanamycin that inhibits HSP90	Mellatyar et al. (2018)
IPI-504	Inhibits HSP90 by binding to the N-terminal domain	Akram et al. (2018)
NVP-AUY922	Targets the N-terminal ATP-binding site of HSP90	Ueno et al. (2012)
Ganetespib (STA-9090)	Inhibits the chaperone activity of HSP90 by binding to its N-terminal domain	Youssef et al. (2023)
AT13387	Binds to the N-terminal domain, disrupting client protein interactions	Smyth et al. (2012)
PU-H71	Inhibits HSP90 activity by targeting its ATPase function	Trendowski (2015)
Debio0932 (formerly CUDC-305)	Dual inhibitor of both HSP90 and HDAC	Wu et al. (2023)
Pimitespib (TAS-116)	Inhibits the NF-κB signaling pathway by blocking HSP90 activity	El-Kashef et al. (2022)
CNF-2024	Targets the ATP-binding site of HSP90, disrupting its function	Lopes et al. (2007)
SNX-5422	Targets the N-terminal domain but was abandoned due to ocular toxicity issues	Chen et al. (2021)

therapeutic stress by stabilizing oncogenic proteins involved in these processes (Jaeger and Whitesell, 2019). This ability to support malignant characteristics highlights the potential of targeting HSP90 in cancer therapy as a way to disrupt these critical pathways and induce tumor regression. Understanding the post-translational modifications (PTMs) of HSP90, such as phosphorylation, acetylation, and S-nitrosylation, is critical because they regulate chaperone activity and influence cancer development (Caruso Bavisotto et al., 2020).

3 Post-translational modifications of HSP90

3.1 Phosphorylation: key modulator of HSP90 function

Phosphorylation is one of the most studied HSP90 PTMs, and it has a significant impact on chaperone activity. Several kinases, such as SRC, BRAF, and casein kinase II (CK2), phosphorylate HSP90, affecting its ability to interact with client proteins (Bachman et al., 2018; Firnau and Brieger, 2022; Zhang et al., 2022). For example, SRC phosphorylates HSP90 at Tyr301, which is required for vascular endothelial growth factor receptor 2 (VEGFR2)-mediated angiogenesis, a critical process in tumor growth (Miyata et al., 2013). HSP90 modulates apoptosome formation via phosphorylation of Ser226 and Ser255, highlighting its role in apoptosis regulation (Mollapour and Neckers, 2012). In leukemia, reduced phosphorylation at these sites strengthens the interaction between HSP90 and APAF1, inhibiting cytochrome c-induced apoptosome assembly and contributing to chemoresistance (Ho et al., 2012).

Client kinases such as WEE1 phosphorylate HSP90, resulting in a feedback loop that improves its chaperoning ability for other kinases such as HER2 and CDK1 (Zhang et al., 2024). This interaction demonstrates the complexities of HSP90's regulatory mechanisms in cancer. Interestingly, WEE1-mediated phosphorylation can reduce the efficacy of HSP90 inhibitors such as geldanamycin and 17-AAG, posing a challenge for therapeutic strategies. A better understanding of phosphorylation sites may lead to new approaches for sensitizing cancer cells to HSP90 inhibitors and overcoming resistance (Mollapour et al., 2010; Iwai et al., 2012; Lokeshwar, 2012).

3.2 Acetylation: impact on client protein stability

Acetylation of HSP90 is another important post-translational modification that can affect its chaperone activity. This modification frequently causes destabilization of client proteins, as seen when histone deacetylase (HDAC) inhibitors or HDAC6 silencing increase HSP90 acetylation levels (Liu P. et al., 2021). Acetylation of several lysine residues on HSP90 impairs its ability to bind client proteins and co-chaperones, including p23, resulting in decreased chaperone efficiency (Woodford et al., 2016; Liu et al., 2023). Importantly, the combination of HDAC inhibitors and HSP90 inhibitors has synergistic effects in certain cancers, particularly leukemia, while antagonistic effects are seen in some solid tumors (Krämer et al., 2014; Chen et al., 2020). These findings emphasize the tumor-specific nature of HSP90 acetylation and the complexities of using combination therapies.

3.3 S-nitrosylation: nitric oxide's role in HSP90 inhibition

S-nitrosylation, or the modification of HSP90 by nitric oxide (NO) at Cys597, adds another layer of regulation by inhibiting the chaperone's ATPase activity. This PTM impairs HSP90's ability to stabilize client proteins, especially in endothelial cells where NO-mediated S-nitrosylation inhibits angiogenesis (Siragusa and Fleming, 2016; Rizza and Filomeni, 2020). Interestingly, exogenous NO can inhibit HSP90 in cancer cells, resulting in

telomere shortening and reduced telomerase activity, both of which are required for cancer cell immortality (Trepel et al., 2010; Solárová et al., 2015). This finding lends credence to the theory that manipulating NO levels may have therapeutic potential in HSP90-driven cancers.

3.4 HSP90's role in nuclear and chromatin events

Aside from its cytoplasmic functions, HSP90 influences several nuclear events, including the regulation of steroid hormone receptors, such as androgen and estrogen receptors. These receptors, which move between the cytoplasm and the nucleus, are essential in hormone-driven cancers such as breast and prostate cancer (Baker et al., 2018; Kaziales et al., 2020). HSP90 regulates their localization, stability, and transcriptional activity, influencing cancer progression.

HSP90 also interacts with key transcription factors such as heat shock transcription factor 1 (HSF1), which controls the expression of heat shock proteins in response to stress. Inhibition of HSP90 can prolong HSF1 activity, resulting in enhanced heat shock responses, which could be used in cancer therapy (Kijima et al., 2019; Cyran and Zhitkovich, 2022). Furthermore, HSP90 stabilizes the transcriptional repressor BCL6 in diffuse large B-cell lymphoma, HSP90 stabilizes the transcriptional repressor BCL6 in diffuse large B-cell lymphoma, which promotes tumorigenesis by inhibiting tumor suppressor genes such as TP53 (Xu-Monette et al., 2012). Targeting HSP90 in such situations may deactivate these genes and promote cancer cell apoptosis.

HSP90's involvement in chromatin remodeling expands its role in cancer. The chaperone promotes the activity of chromatin-modifying enzymes, including the histone methyltransferase SMYD3, which is overexpressed in hepatocellular carcinoma and colorectal cancer. HSP90 increases SMYD3 activity, which contributes to the transcription of genes that promote cancer cell proliferation (Abu-Farha et al., 2011; Giakountis et al., 2017). Inhibiting HSP90 in these cancers can reduce SMYD3 activity, providing another therapeutic target.

4 HSP90 and heat shock factor 1 (HSF1)

Under stress, the heat shock response (HSR) is stimulated/triggered, leading to the upregulation of various cytoprotective HSPs. HSPs mediate cellular protective effects by alleviating the drastic consequences of aberrantly folded and distorted proteins, thus lessening their detrimental effects on the cell (Collier and Benesch, 2020). In mammals, cellular response to stress could result in destroying cellular proteins and it is principally regulated by the activation of HSF-1. Significantly, HSF-1 could regulate the expression of heat shock genes (Chang et al., 2021). Of note, HSF-1 activation involves multiple steps that start with oligomerization, then nuclear translocation and accumulation, and finally undergo post-translational modifications (Masser et al., 2020). HSP90 is implicated in controlling the activity of HSF. HSP90 forms a binding interaction with HSF-1, maintaining the monomeric form of the transcription factor under normal, non-stressed conditions. When the cell experiences stressors, such as exposure to elevated temperatures (heat shock), or when the function of HSP90 is disrupted, HSF-1 becomes detached from the HSP90 complex (Chin et al., 2023). This release leads to the activation of HSF-1 and its transformation into a trimeric form, and it then moves into the cell nucleus, where HSF-1 initiates an HSR, marked by the synthesis of HSPS such as HSP70 and HSP40 activator (Schmauder et al., 2022).

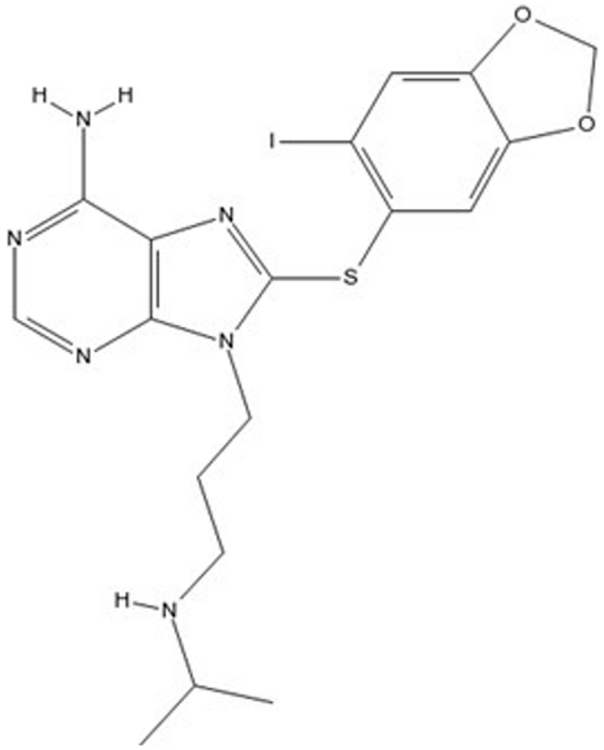

FIGURE 2
Chemical structure of PU-H71 (8-[(6-iodo-1,3-benzodioxol-5-yl)sulfanyl]-9-[3-(propan-2-ylamino)propyl]purin-6-amine).

5 PU-H71

PU-H71 (Figure 2) is a potent small-molecule inhibitor that targets HSP90. HSP90 is frequently overexpressed in various cancers, contributing to the stabilization and activity of numerous proteins involved in tumor growth and survival, making it a critical therapeutic target (Mahajan et al., 2024; Rastogi et al., 2024).

PU-H71 binds with high affinity to the ATP-binding site of HSP90, inhibiting its chaperone activity. This binding disrupts the proper folding of client proteins, leading to their ubiquitination and subsequent proteasomal degradation (Schopf et al., 2017). The loss of these client proteins impairs several oncogenic signaling pathways, thereby inhibiting tumor cell proliferation and inducing apoptosis.

Preclinical studies have demonstrated that PU-H71 exhibits significant antitumor activity across a variety of cancer cell lines

and xenograft models, particularly those dependent on HSP90 client proteins for growth and survival. These studies have highlighted the ability of PU-H71 to induce tumor regression and prolong survival without causing significant toxicity to normal tissues (Ambati et al., 2014; Trendowski, 2015; Martinet et al., 2022).

Clinical evaluations of PU-H71 have also shown promise. Phase I clinical trials have focused on determining the maximum tolerated dose, pharmacokinetics, and preliminary efficacy of PU-H71 in patients with advanced solid tumors and hematological malignancies. Results from these studies indicate that PU-H71 is well-tolerated and demonstrates antitumor activity, with manageable side effects predominantly involving gastrointestinal disturbances and reversible transaminase elevations. PU-H71 has been included in six clinical studies (NCT03166085; NCT03373877; NCT01581541), of which three (NCT03935555; NCT01393509; NCT01269593) are still active or recruiting, indicating that PU-H71 is the most promising purine-based inhibitor of HSP90 (Gerecitano et al., 2015; Speranza et al., 2018; Pemmaraju et al., 2019).

5.1 PU-H71: Discovery

PU-H71 was developed through a rational drug design approach aimed at creating more selective and potent inhibitors of HSP90, compared to previous generations. It is part of a class of compounds synthesized from a purine scaffold, designed to improve both the specificity and solubility of the drug. Earlier compounds like PU3 and PU24FCl, which also targeted HSP90, were optimized through structure-activity relationship studies, refining molecular structures to enhance binding affinity and therapeutic efficacy (Messaoudi et al., 2008). Through this process, PU-H71 emerged as one of the most effective inhibitors, with an IC50 value of approximately 50 nM for HSP90 in epichaperome-containing cells (Ambati et al., 2014).

5.2 Pharmacokinetics of PU-H71

The pharmacokinetics of PU-H71 were thoroughly investigated during clinical trials. One of the key findings was the compound's mean terminal half-life of approximately 8.4 ± 3.6 h, indicating a relatively stable elimination profile across the range of doses tested (Speranza et al., 2018). Biodistribution studies utilizing positron emission tomography imaging revealed that PU-H71 selectively accumulates in tumor tissues that express epichaperomes, with a tumor retention rate observed in about 58% of patients (Dunphy et al., 2020). This tumor-selective accumulation is a promising feature that underscores the drug's potential as a targeted therapy.

In terms of metabolism, *in vitro* studies revealed that PU-H71 undergoes limited biotransformation, with the primary metabolic pathways involving S-oxidation and O-demethylation (Speranza et al., 2018). Metabolites were present in plasma samples but accounted for less than 10% of the parent drug's concentration, suggesting that metabolism has a minimal impact on the overall pharmacologic activity of PU-H71 (Speranza et al., 2018).

5.3 Development of PU-H71

Preclinical studies have demonstrated that PU-H71 exhibits significant antitumor activity across a variety of cancer cell lines and xenograft models, particularly those dependent on HSP90 client proteins for growth and survival. These studies have highlighted the ability of PU-H71 to induce tumor regression and prolong survival without causing significant toxicity to normal tissues (Ambati et al., 2014; Trendowski, 2015; Martinet et al., 2022).

Following successful preclinical testing, the first-in-human clinical trial of PU-H71 was initiated to evaluate its safety, tolerability, and pharmacokinetic profile. This phase I study involved patients with advanced solid tumors who had not responded to standard therapies. The trial followed a dose-escalation design, with doses ranging from 10 to 470 mg/m^2, administered intravenously on days 1 and 8 of a 21-day treatment cycle (De Almeida et al., 2020). The results indicated that PU-H71 was well-tolerated at the tested doses, with no dose-limiting toxicities observed. However, some patients experienced grade 2 and 3 adverse events, which were closely monitored. The positive safety profile allowed for the continuation of the drug's clinical evaluation in subsequent trials. PU-H71 has been included in six clinical studies (NCT03166085; NCT03373877; NCT01581541), of which three (NCT03935555; NCT01393509; NCT01269593) are still active or recruiting, indicating that PU-H71 is the most promising purine-based inhibitor of HSP90 (Gerecitano et al., 2015; Speranza et al., 2018; Pemmaraju et al., 2019).

6 Mechanism of action of PU-H71

PU-H71 demonstrates a high degree of selectivity for the ATP-binding sites of HSP90 that are specifically integrated into tumor epichaperome complexes (Dunphy et al., 2020). This selective binding is of paramount importance, as it significantly reduces the potential for off-target effects on healthy tissues where HSP90 does not exist in this altered form (Speranza et al., 2018; Li and Luo, 2023). The unique conformational landscape of HSP90 in tumors allows PU-H71 to engage with its ATP-binding sites effectively (Trendowski, 2015; Tramentozzi and Finotti, 2019). Upon binding, PU-H71 induces critical conformational changes in the HSP90 structure, which stabilizes client protein-HSP90 complexes. This stabilization is not merely a passive interaction; it actively facilitates the recruitment of these complexes to the proteasome, the cellular machinery responsible for degrading misfolded or unneeded proteins (Caldas-Lopes et al., 2009; Li et al., 2018). Consequently, this process leads to the degradation of oncogenic proteins that are essential for tumor cell survival and proliferation. By disrupting the stability of these proteins, PU-H71 effectively undermines the tumor's ability to maintain its malignant characteristics, thereby presenting a targeted therapeutic strategy against cancer.

The epichaperome represents a highly interconnected network of chaperone proteins that plays a critical role in supporting various cellular processes associated with tumor biology, including proliferation, survival, and invasion (Hadizadeh Esfahani et al., 2018). Within this network, HSP90 acts as a central hub, facilitating the proper folding and function of numerous client proteins that are often dysregulated in cancer. When PU-H71 inhibits HSP90's activity, it disrupts the integrity of this epichaperome network. The destabilization caused by PU-H71

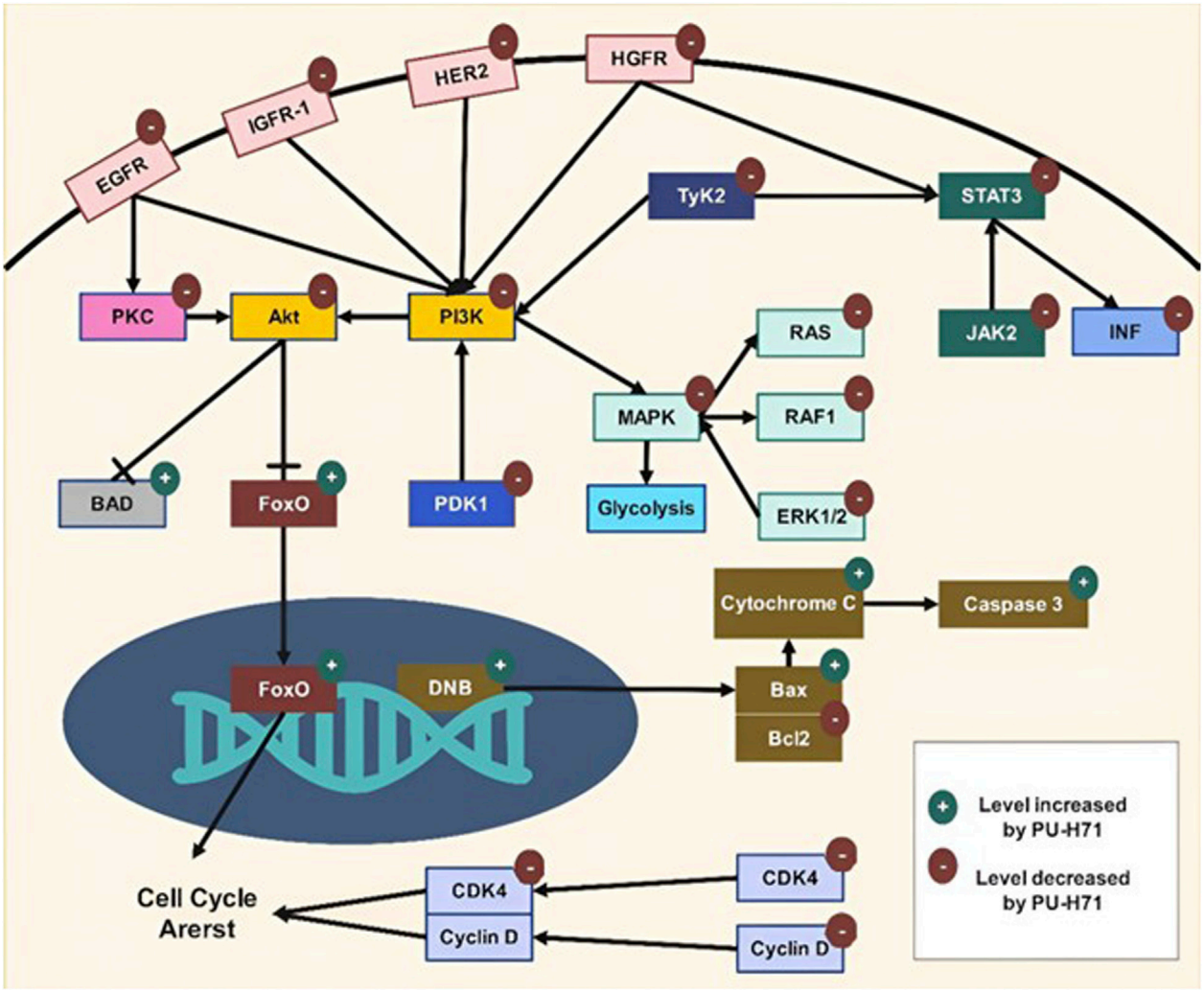

FIGURE 3
Molecular mechanisms of PU-H71.

leads to a significant reduction in the functionality of the epichaperome, impairing its ability to support tumor cell processes. As a result, tumor cells become more susceptible to stressors and less capable of maintaining their survival and proliferative advantages (Speranza et al., 2018; Jhaveri et al., 2020). Ultimately, this disruption contributes to increased tumor cell death, highlighting PU-H71's potential as an effective therapeutic agent in targeting cancer through the modulation of chaperone networks. By interfering with the epichaperomes' formation and function, PU-H71 not only targets individual oncogenic proteins but also undermines the broader chaperone-dependent mechanisms that tumors rely on for their growth and resilience.

7 Molecular mechanisms of PU-H71

Targeting HSP90 by PU-H71 disrupts multiple signaling pathways critical for cancer cell survival, proliferation, and metastasis. The compound exhibits a broad spectrum of anti-cancer activities by inducing the degradation of client proteins involved in key pathways such as Mitogen-Activated Protein Kinase (MAPK), Phosphoinositide 3-Kinase (PI3K)/protein kinase B (Akt), and Janus kinase (JAK)/signal transducers and activators of transcription (STAT) (Figure 3). Additionally, PU-H71 enhances the efficacy of other therapeutic agents and sensitizes cancer cells to treatments like radiation. This multi-faceted approach makes PU-H71 a promising candidate for cancer therapy, addressing the complexity and heterogeneity of tumor biology. Table 3 outlines the various mechanisms through which PU-H71 exerts its anti-cancer effects.

7.1 Epichaperomes

Epichaperomes are novel type of molecular structures formed by the assembly of chaperones and co-chaperones, representing a significant advance in our understanding of cellular stress responses, particularly in cancer and neurodegenerative disorders (Rodina et al., 2016). Unlike traditional chaperones, which help with protein folding and aggregation temporarily, epichaperomes form

TABLE 3 Molecular mechanisms of PU-H71.

Molecular mechanism	Pathways	Effect of PU-H71	Reference
Epichaperomes		PU-H71 binds to Hsp90 within epichaperomes, dismantling them without affecting normal chaperone function The disassembly of epichaperomes restores normal protein-protein interactions, reversing pathological changes in cancer cells	Joshi et al. (2021)
MAPK Signaling	Ras/Raf/MEK/ERK	PU-H71 downregulates Ras, Raf-1, MEK, and ERK, reducing cell proliferation and survival. Disrupts Raf-1 stabilization, inducing degradation of Raf-1 and other oncoproteins. Increases radiosensitivity through p38α MAPK activation	Caldas-Lopes et al. (2009)
	Apoptosis	Inhibits Raf-1, downregulating MAPK pathway, reducing anti-apoptotic factors, enhancing pro-apoptotic factors like Bcl-2 degradation, and leading to increased cell death	Caldas-Lopes et al. (2009)
	Cell Cycle	Induces G2/M phase arrest by downregulating cyclins and CDKs essential for cell cycle progression	Liu et al. (2021a)
Tyrosine kinase 2 (Tyk2)	JAK/STAT, MAPK, PI3K/Akt	Inhibits Tyk2, disrupting cytokine and growth factor signaling, leading to anti-proliferative and pro-apoptotic effects in cancer cells	Caldas-Lopes et al. (2009)
Protein Kinase C (PKC)	PKC Signaling	Induces degradation of PKC by preventing HSP90 chaperoning, reducing PKC-mediated signaling	Yamaki et al. (2011)
ATP	Metabolism	Inhibits Ras/Raf/MAPK pathway, reducing glycolytic ATP production. Decreases PDK1 and Akt activity, reducing oxidative ATP production	Bahar et al. (2023)
DNA double-strand breaks (DSB)	DNA Repair	Sensitizes cancer cells to radiation by inhibiting DSB repair pathways, increasing persistence of γ-H2AX foci, reducing RAD51 foci and DNA-PKcs phosphorylation	Lee et al. (2016), Nickoloff et al. (2017)
Unfolded Protein Response (UPR)	ER Stress	Disrupts HSP90 function, inducing ER stress, activating UPR, leading to apoptosis via ATF4 and CHOP.	Usmani et al. (2010)
Mitochondrial pathway of apoptosis	Apoptosis	Downregulates Bcl-2, upregulates Bax, permeabilizes mitochondrial membrane, releases cytochrome c, activates caspases	Gallerne et al. (2013), Graner et al. (2017)
Endoplasmic reticulum (ER) HSP90	Protein Folding	Could Target gp96 (HSP90B1), destabilizes client proteins, enhancing anti-myeloma drug efficacy	Usmani et al. (2010)
B-cell lymphoma 6 (Bcl6)	Transcription	Inhibits HSP90, destabilizing Bcl6, disrupting its interaction with co-repressors, leading to reduced proliferation and survival of Bcl6-dependent lymphoma cells	Cerchietti et al. (2009)
Hepatocyte growth factor receptor (HGFR)	c-Met Signaling	Inhibits HSP90, leading to c-Met degradation, reducing tumor growth	Breinig et al. (2009)
Protein kinase B (Akt)	PI3K/Akt Signaling	Inhibits HSP90, leading to Akt degradation, reducing phosphorylation at Thr308 and Ser473, disrupting survival and proliferation pathways	Giulino-Roth et al. (2017)
Insulin-like growth factor receptor 1 (IGF1R)	PI3K/Akt, MAPK	Inhibits IGF1R, reducing downstream signaling, promoting apoptosis, and inhibiting cell proliferation	Ambati et al. (2014)
Cyclin Dependent Kinase 4 (CDK4)	Cell Cycle	Downregulates CDK4, cyclin D1, and phosphorylated Rb, inhibiting G1 to S phase transition, causing cell cycle arrest	Knudsen and Witkiewicz (2017)
Interferon (INF)	Inflammatory Response	Reduces IFNγ release, inhibiting activation of inflammatory pathways	Lisi et al. (2013)
Janus kinase 2/signal transducers and activators of transcription 3 (JAK2/STAT3)	JAK/STAT Signaling	Inhibits HSP90, leading to degradation of JAK2 and decreased phosphorylation of STAT3 and STAT5, inhibiting their transcriptional activity	Jego et al. (2019) Niu et al. (2021)
Human Epidermal Growth Factor Receptor 2 (HER2)	Receptor Tyrosine Kinase	Inhibits HSP90, leading to HER2 degradation, reducing activation of downstream signaling pathways like PI3K/Akt and MAPK, promoting apoptosis and reducing cell proliferation	Kale et al. (2020)
Epidermal Growth Factor Receptor (EGFR)	Receptor Tyrosine Kinase	Inhibits HSP90, leading to degradation of EGFR, reducing its activation and downstream signaling pathways like PI3K/Akt and MAPK, inhibiting cell proliferation and survival	Martinelli et al. (2017), Salama et al. (2019), Guerra et al. (2021)

(Continued on following page)

TABLE 3 (*Continued*) Molecular mechanisms of PU-H71.

Molecular mechanism	Pathways	Effect of PU-H71	Reference
Mammalian Target of Rapamycin (mTOR)	PI3K/Akt/mTOR	Inhibits HSP90, leading to degradation of mTOR, disrupting mTORC1 and mTORC2 signaling, reducing cell growth, proliferation, and survival	Giulino-Roth et al. (2017)

stable oligomeric complexes that remain in cells, fundamentally altering cellular proteostasis (Joshi et al., 2018; Yan et al., 2020; Ginsberg et al., 2021). These long-lived structures are critical in modulating protein-protein interactions (PPIs) within cells, especially under chronic stress conditions (Rodina et al., 2023; Chakrabarty et al., 2024). The formation of epichaperomes in diseased tissues provides new insights into disease mechanisms as well as potential therapeutic avenues, making them a promising intervention target.

Epichaperomes are derived from the chaperome, a network of over 300 chaperones and associated factors that regulate protein folding and quality control under normal conditions (Inda et al., 2020). However, epichaperomes differ from conventional chaperones in terms of stability and function. They serve as scaffolding platforms, reorganizing PPIs and altering cellular function in response to chronic stress, particularly in cancer cells (Ginsberg et al., 2023). Their specificity for diseased cells and tissues, as opposed to the widespread presence of traditional chaperones in healthy cells, makes them an appealing therapeutic target. In cancer, epichaperomes promote cell survival by supporting hyperconnected PPI networks, allowing malignant cells to survive in hostile microenvironments and evade therapeutic treatments (Digwal et al., 2022). Tumors with high epichaperomes expression often exhibit heightened vulnerability to specific inhibitors that disrupt these pathological structures.

A key therapeutic discovery is that small molecules, such as PU-H71, can selectively target epichaperomes and dismantle them without interfering with normal chaperone activity (Jhaveri et al., 2020). PU-H71 binds to Hsp90 within the epichaperome and induces conformational changes that cause the epichaperome to disassemble into its constituent chaperones. The disassembly of epichaperomes restores normal interactome structures, reversing pathological PPI changes. This therapeutic strategy has shown particular promise in cancers like Ras-driven pancreatic cancer, which has redundant signaling pathways that contribute to drug resistance (Joshi et al., 2021). In these cases, epichaperomes maintain interactome hyperconnectivity, which occurs when cancer cells rely on highly connected networks of PPIs to survive. Approximately 50%–60% of tumors express epichaperomes, with those displaying the highest levels of epichaperomes expression being characterized by extreme interactome hyperconnectivity and increased vulnerability to therapeutic interventions (Merugu et al., 2020). Furthermore, the breakdown of the epichaperome causes significant changes in cellular signaling pathways involved in survival and proliferation. For instance, decreased phosphorylation of key signaling proteins such as phospho-SYK and phospho-STAT5 has been documented, highlighting the downstream effects of epichaperome disruption on oncogenic signaling cascades (Roboz et al., 2018).

This approach exploits the vulnerability in cancer cells by pharmacologically manipulating epichaperome-mediated protein-protein interaction (PPI) networks. By forcing the interactome to reach maximum hyperconnectivity, cancer cells become more sensitive to existing therapies (Joshi et al., 2021). This strategy reactivates pre-existing protein pathways, preventing cancer cells from utilizing alternative signaling mechanisms to evade treatment. Unlike traditional therapies that target specific genetic mutations or protein aberrations, this method aims to control the entire interactome, thereby shutting down compensatory pathways that contribute to drug resistance (Rodina et al., 2016; Carter et al., 2023). Experiments in pancreatic cancer models, including cell lines, patient biospecimens, and xenografts, show that pharmacologically induced hyperconnectivity significantly improves the efficacy of current treatments (Joshi et al., 2021). By priming cancer cells with PU-H71 to induce a hyperconnected state, the efficacy of previously ineffective therapies was increased. This novel treatment paradigm represents a promising approach to overcoming drug resistance in cancers marked by high epichaperome expression and interactome plasticity (Joshi et al., 2021). PU-H71, by inducing hyperconnectivity, targets entire PPI networks rather than individual molecular nodes, resulting in a more comprehensive and effective therapeutic strategy.

In clinical settings, PU-H71 has shown promising results, especially in cancers with high epichaperome levels. Preclinical and early clinical trials have shown that patients with acute myeloid leukemia, which is characterized by elevated epichaperome expression, respond well to PU-H71 treatment, with some achieving long-term remission (Li and Adams, 2023; Seipel et al., 2023). These findings highlight the potential of PU-H71 as a therapeutic agent in cancers where the epichaperome plays an important role in disease progression.

7.2 Mitogen-activated protein kinase kinase (MAPK) signaling

PU-H71 treatment leads to a potent reduction in the proliferative, anti-apoptotic, and invasive potential of tumors. Among the pathways affected, PU-H71 induces downregulation of components of the Ras/Raf/MAPK pathway, contributing to its anti-proliferative effects (Pastena et al., 2024). In chronic myelogenous leukemia cells, PU-H71 was shown to identify the aberrant signalosome, with a focus on the Raf-MAPK pathway (Moulick et al., 2011). By inhibiting HSP90, PU-H71 destabilizes oncoproteins associated with the MAPK pathway, leading to their downregulation and impairment of downstream signaling (Seipel et al., 2023). PU-H71 has also been found to increase the radiosensitivity of breast cancer cells metastasized to visceral organs. The radiosensitizing effect of PU-H71 in combination with radiation therapy correlates with increased activation of p38α MAPK (García-Flores et al., 2023). Remarkably, recent studies have identified p38α MAPK as a potential tumor

suppressor owing to its capacity to interfere with malignant cell transformation *via* regulating tissue homeostasis. This effect could be ascribed to modulating signals that balance cell proliferation and differentiation or induce apoptosis. As previously noted, PU-H71-mediated inhibition of HSP90 could improve the response of tumor cells to radiotherapy through modulation of p38 MAPK signaling.

Additionally, PU-H71 was reported to target MAPK pathways thus consequently decreasing tumor cell resistance to other anti-cancer treatment regimens enhancing their efficacy. Furthermore, combined administration of PU-H71 and the anti-cancer prodigiosin, displayed remarkable synergistic effects against malignant cells, that could be ascribed to targeting different aberrantly regulated pathways including MAPK (Anwar et al., 2020).

Moreover, PU-H71 was documented to disrupt the stabilization of v-Raf-1 (Raf-1) and other oncogenic proteins, leading to their degradation (Trendowski, 2015). It is noteworthy to highlight that, Raf-1 is a critical component of the MAPK signaling cascade aberrantly activated in cancer cells (Beeram et al., 2005).

Besides, PU-H71 anticancer properties could be due to the reported downregulation of the components of the Ras/Raf/MAPK pathway. The activation of such a pathway is initiated by Ras (a small GTPase) phosphorylation and activation by growth factor receptors. Subsequently, activated Ras interacts with Raf-1, leading to activation of the latter (Terrell and Morrison, 2019; Nolan et al., 2021; Ullah et al., 2022). Herein, the pathway activation could be disrupted by PU-H71 treatment through hampering Ras-Raf-1 interaction, thereby inhibiting Raf-1 activation and consequent downstream signaling through MEK and ERK, which are essential for cell proliferation and survival (Caldas-Lopes et al., 2009; Ambati et al., 2014).

Intriguingly, PU-H71 was reported to induce apoptosis in cancer cells that could be also ascribed to the observed Raf-1 inhibition. Also, MAPK pathway suppression following PU-H71 treatment resulted in a significant downregulation of anti-apoptotic factors that triggered the degradation of pro-survival proteins like B-cell lymphoma-2 (Bcl-2) (Gallerne et al., 2013). The restoration of balance between pro-apoptotic and anti-apoptotic signals leads to increased malignant cell death (Yamaki et al., 2011).

Anti-cancer effects of PU-H71 could result from its capacity to induce G2/M phase arrest interfering with cell cycle progression. This could be linked to the reported downregulation of cyclins and cyclin-dependent kinases (CDKs) that are necessary for cell cycle progression (Liu H. et al., 2021). In addition, Raf-1 inhibition with subsequent suppression of the MAPK pathway could probably contribute to the reported cell cycle arrest (Bahar et al., 2023).

7.3 Tyrosine kinase 2 (Tyk2)

Tyk2 belongs to the Janus kinase (JAK) family of tyrosine kinases, which are closely implicated in cytokine and growth factor signaling pathways playing an essential for cancer progression (Wöss et al., 2019). Tyk2 was reported to be aberrantly activated in different types of neoplasms (e.g., acute myeloid leukemia, and solid tumors including breast cancer) (Wöss et al., 2019). Aberrant activation of Tyk2 was documented to facilitate a range of abnormal characteristics of cancer cells including abnormal cellular growth and proliferation alongside invasion. Fundamentally, abnormal Tyk2 activation results in the activation of downstream signaling cascades, among these the signal transducers and activators of transcription (STAT), MAPK, and Phosphoinositide 3-kinase (PI3K)/Protein Kinase B (Akt) pathways were reported to be the most important. Meanwhile, suppression Tyk2 cascade was shown to interrupt such oncogenic signaling cascades, which could potentially contribute to its anti-tumor effects in preclinical cancer models (Caldas-Lopes et al., 2009; Kucine et al., 2015).

Remarkably, HSP90 is pivotal for Tyk2 stability and function (Akahane et al., 2016; Reynolds and Blagg, 2024), where HSP90 suppression following PU-H71 treatment has been reported to cause Tyk2 and inactivation of Tyk2, in various cancer models. In an earlier investigation on triple-negative breast cancer (TNBC) cells, PU-H71 exposure caused a remarkable downregulation of multiple oncogenic proteins, including components of the Ras/Raf/MAPK pathway. This could lead to further downregulation of Tyk2 (Ravandi et al., 2003; Dimri and Satyanarayana, 2020).

7.4 Protein kinase C (PKC)

HSP90 is important for the stability and function of many protein kinases like PKC (Kawano et al., 2021). PU-H71 binds to HSP90 and prevents it from chaperoning and stabilizing client proteins like PKC (Yamaki et al., 2011). Without the support of HSP90, PKC becomes misfolded and targeted for proteasomal degradation. This leads to a reduction in cellular PKC levels and inhibition of PKC-mediated signaling. The PKC family consists of 10 isozymes that regulate diverse cellular processes (Kawano et al., 2021). By inhibiting HSP90, PU-H71 is expected to affect multiple PKC isoforms simultaneously. However, the relative potency of PU-H71 against each PKC isoform has not been reported.

PU-H71 has been shown to downregulate components of the MAPK signaling pathway, which includes PKC. Specifically, PU-H71 induces the degradation of activated Akt, a key PKC substrate (Yamaki et al., 2011). The documented suppression of PKC signaling has markedly contributed to reported PU-H71 antitumor effects against TNBC. In addition to the reported effects on PKC, PU-H71 also has demonstrated suppression of activated glial cells in experimental autoimmune encephalomyelitis (EAE) and an animal model of multiple sclerosis (Lisi et al., 2013). Additionally, PU-H71's anti-inflammatory properties could be mediated through the inhibition of PKC and other inflammatory signaling pathways.

7.5 Adenosin triphosphate (ATP)

Interestingly, PU-H71-mediated downregulation of Ras/Raf/MAPK pathway components was shown to (Bahar et al., 2023) decrease the rate of glycolytic ATP generation and consequently be implicated in regulating glycolysis and ATP production. Besides, HSP90 was reported be principally involved in regulating the 3-phosphoinositide-dependent protein kinase-1 (PDK1)-Akt signaling pathway (Basso et al., 2002; Xue et al., 2014; Bao et al.,

2021). Markedly, HSP90 inhibition by PU-H71 could trigger PDK1 degradation, subsequently suppressing the Akt pathway that would then lead to a profound decline in both the activity of mitochondrial metabolism and oxidative ATP production (Mookerjee et al., 2017).

Moreover, PU-H71 was reported to promote apoptosis as well as degradation of oncogenic proteins that drive both uncontrolled cell proliferation (Speranza et al., 2018) this effect could be mainly mediated by reducing the demand for ATP by these cellular processes, plus decreasing overall ATP utilization.

7.6 DNA double-strand breaks (DSB)

Particularly, PU-H71 has a significant capability of sensitizing malignant cells to heavy ion radiation that could be owing to the observed inhibition of DSB repair pathways (Lee et al., 2016) as well as increasing the persistence of γ-H2AX foci that represent markers of unrepaired DSBs, in irradiated tumor cells (Lee et al., 2016). This finding suggests PU-H71-induced impairment of radiation-induced DSB repair mechanisms. Also, the displayed sensitization of malignant cells to radiation was attributed to the decreased formation of RAD51 foci as well as diminished phosphorylation of DNA-PKcs in irradiated tumor cells. Reportedly, both RAD51 and DNA-PKcs are DNA repair proteins central to homologous recombination and non-homologous end-joining DSB repair pathways, respectively. Moreover, RAD51 was reported to be upregulated in several neoplasms and it was responsible for chemoresistance, poor cancer prognosis, as well a higher incidence of metastasis (Nickoloff et al., 2017). Significantly, PU-H71 was shown to improve the efficacy of radiotherapy *via* suppressing radiation-induced DSB repair in irradiated tumor cells (Lee et al., 2016) eventually leading to increased cell death.

PU-H71-induced restraining of DSB repair could potentially be implicated in the observed sensitization of various cancer cell lines to heavy ion radiation, including, human lung cancer cells (Lee et al., 2016). As previously reported, PU-H71 promoted the cytotoxic properties of heavy ion radiation as reflected by both reduced clonogenic survival and increased cell death. Interestingly, the reported radio-sensitizing actions of PU-H71 were explicit to tumor cells and did not affect the survival of normal human fibroblasts (Li et al., 2016). Such precise sensitization, recommends PU-H71 as a novel therapeutic agent for enhancing the efficacy of heavy ion radiotherapy.

7.7 Unfolded protein response (UPR)

PU-H71 displayed complex and multiple effects on the UPR including several mechanisms eventually promoting malignant cell apoptosis. Firstly, it was noted that PU-H71 could generate Endoplasmic reticulum (ER) stress probably by suppressing HSP90 normal function. The documented inhibition of HSP90 function accelerates the compilation of both unfolded or misfolded proteins in the ER, triggering the UPR (Gallerne et al., 2013). Of note, UPR represents a cellular response to ER stress that objectively restores protein homeostasis through upregulating certain chaperones including Glucose-regulated protein 78 (GRP78), GRP94, and calreticulin. Outstandingly, PU-H71 triggers the UPR through the induction of the splicing of X-box binding protein 1 (XBP1) mRNA, defined as a key marker of UPR activation (Gallerne et al., 2013).

The main aims of UPR include restoration of protein homeostasis or induction of apoptosis if the stress persists. Apoptosis induction is potentially through activating the downstream transcription factors such as transcription factor 4 (ATF4) and C/EBP homologous protein (CHOP) promoting the expression of pro-apoptotic genes (Rah et al., 2016; Hu et al., 2019).

7.8 Mitochondrial pathway of apoptosis

One of the major actions of PU-H71 is the activation of the mitochondrial pathway of apoptosis *via* upregulation of pro-apoptotic proteins (e.g., Bcl-2-Associated X Protein (Bax)) alongside downregulation of anti-apoptotic proteins (Bcl-2) followed by enhanced permeabilization of the mitochondrial membrane with subsequent release of cytochrome c and caspases activation (Gallerne et al., 2013; Graner et al., 2017).

Mechanistically, the capacity of PU-H71 to trigger apoptosis was underlined by activating this mitochondrial pathway in multiple cancer cell lines such as melanoma, cervix, colon, liver, and lung cancer cells (Rastogi et al., 2024). Interestingly, previous findings displayed that PU-H71-induced apoptosis could potentially attenuate malignant cell resistance attributed to overexpression of the anti-apoptotic protein Bcl-2 (Gallerne et al., 2013). Previous findings also highlighted the remarkable contribution of the pro-apoptotic protein Bax to PU-H71-induced apoptosis where Bax-deficient cells were shown to resist PU-H71-elicited apoptosis (Kubra et al., 2020). Conversely, such resistance was partially overcome by combined administration of PU-H71 treatment with other anticancer therapies (e.g., cisplatin or melphalan) (Gallerne et al., 2013). In addition to apoptosis induction, PU-H71 was shown to cause cell cycle arrest at the G2-M phase that could be mediated through cyclin D1 downregulation (Ambati et al., 2014).

7.9 Endoplasmic reticulum (ER) HSP90

Over the past decade, gp96 or HSP90B1 also referred to as grp94, the ER HSP90 family member, has attracted distinct attention. This attention was due to gp96's remarkable role in chaperoning antigenic peptides, enabling their presentation in the antigen-cross-presentation pathway (Marzec et al., 2012; Duan et al., 2021). Outstandingly, immunizations utilizing pure tumor-derived gp96-peptide complexes have displayed promising preclinical and clinical results in the treatment of multiple myeloma (Randazzo et al., 2012). *In-vitro* investigations demonstrated that bortezomib (disturbing protein anti-myeloma drug), rendered gp96 knockdown cells more susceptible. In addition, gp96 knockdown cells demonstrated a remarkable sensitivity to thalidomide alongside increased cell death induced by genotoxic drugs like melphalan and doxorubicin. These outcomes suggest that gp96 could potentially be involved in diminishing the efficacy of anti-myeloma therapies, meanwhile, gp96 knockdown augmented myeloma cells' response to those agents (Usmani et al., 2010).

Nevertheless, gp96 knockdown negatively affected the anti-myeloma activity of PU-H71 suggesting that the acute cytotoxic effect of HSP90 inhibitors is mediated through modulating both cytosolic HSP90 in addition to gp96 in the ER. PU-H71 displayed *in vitro* anti-myeloma efficacy as well. These findings highlight that HSP90 inhibitors, including PU-H71, target both cytosolic HSP90 and the ER-resident HSP gp96 to exert their anti-myeloma effects.

7.10 B-cell lymphoma 6 (Bcl6)

BCL6 is identified as a master transcription factor regulating T follicular helper cell proliferation, which is central to germinal center development and B cell proliferation. Remarkably, mutations in BCL6 could result in the development of B cell lymphomas that could be owing to unchecked B cell growth, therefor such mutations could be used as diagnostic markers for B cell lymphomas and other cancers (Mintz and Cyster, 2020).

Interestingly, HSP90 plays a pivotal role in the stability as well as the function of the transcription factor BCL6 (Hoter et al., 2018) Herein, PU-H71 binding to the N-terminal ATP/ADP pocket of HSP90 leads to a prominent inhibition of its ATPase activity plus a profound disruption of HSP90 chaperone function with consequent BCL6 destabilization and degradation (Sidera and Patsavoudi, 2014), reducing its activity. This effect was reflected by the reported decline in luciferase activity of BCL6 target promoters in cell lines following exposure to PU-H71.

The downregulation of BCL6 by PU-H71 is thought to be mediated through multiple mechanisms including, reduced stability and increased degradation of the BCL6 protein (Sidera and Patsavoudi, 2014); disruption of the interaction between BCL6 and its transcriptional co-repressors, such as Silencing Mediator of Retinoid and Thyroid hormone receptors (SMRT), Nuclear receptor corepressor (N-CoR), and BCL6 corepressor (BCoR) (Briones, 2010; Kuai et al., 2018; McLachlan et al., 2022); Interference with the autoregulatory loop that maintains high BCL6 expression in lymphoma cells (Yang and Green, 2019); and derepression of BCL6 target genes involved in cell cycle control, DNA repair, metabolism, and immune regulation. This results in the suppression of the proliferation and survival of BCL6-dependent lymphoma cells, making PU-H71 a promising therapeutic agent for BCL6-driven lymphomas.

7.11 Hepatocyte growth factor receptor (HGFR)

The hepatocyte growth factor receptor (HGFR), also known as c-Met, is a receptor tyrosine kinase that is primarily expressed on epithelial cells. Its only known high-affinity ligand is hepatocyte growth factor (HGF) (Fu et al., 2021). The binding of HGF to c-Met activates the receptor, leading to tyrosine phosphorylation and activation of downstream signaling pathways such as MAPK, STAT, and PI3K/Akt (Zhang et al., 2018). Deregulated c-Met signaling, due to factors like receptor overexpression, ligand overexpression, or activating mutations, is implicated in the development, progression, and metastasis of many human cancers. Therefore, c-Met represents an attractive target for anti-cancer therapies, and various agents targeting the HGF/c-Met pathway are under development, including small molecule inhibitors, antibodies, and decoy receptors (Matsumoto et al., 2017).

PU-H71 was found to potently increase the degradation of c-Met as a client protein to HSP90. Treatment with PU-H71 resulted in reduced c-Met protein levels and decreased phosphorylation/activation of c-Met in various cancer cell lines. The inhibition of c-Met by PU-H71 was associated with reduced tumor growth in preclinical cancer models, without causing significant toxicity (Speranza et al., 2018). The mechanism by which PU-H71 inhibits c-Met is through its ability to bind and inhibit the HSP90 chaperone. By disrupting the HSP90-c-Met interaction, PU-H71 leads to the destabilization and degradation of the c-Met receptor, thereby suppressing its oncogenic signaling (Giulino-Roth et al., 2017). This indirect targeting of c-Met via HSP90 inhibition represents a promising therapeutic approach for cancers driven by deregulated c-Met activity.

7.12 Protein kinase B (Akt)

HSP90 was found to have an important role in the PDK1-Akt signaling pathway through binding to PDK1. Meanwhile, proteasome-dependent degradation of PDK1 was demonstrated following HSP90 inhibition by PU-H71 (Yamaki et al., 2011). Akt is a client protein of HSP90 and requires HSP90 for its stability and activation. PU-H71 binds to the N-terminal ATP/ADP pocket of HSP90, inhibiting its ATPase activity. This leads to the destabilization and degradation of Akt by the proteasome (Giulino-Roth et al., 2017). Akt activation requires phosphorylation at two regulatory sites: Thr308 in the activation segment by PDK1 and Ser473 in the hydrophobic motif by mTORC2 (Baffi et al., 2021). The binding of PU-H71 to HSP90 inhibits the phosphorylation of Akt at these sites, preventing its activation (Giulino-Roth et al., 2017). The degradation of PDK1 by PU-H71 also reduces the phosphorylation of Akt at Thr308.

Active, phosphorylated Akt regulates a panel of proteins that control proliferation, growth, survival, and metabolism (Hoxhaj and Manning, 2020). Inhibition of Akt by PU-H71 disrupts these downstream pathways. For example, Akt phosphorylates and inactivates the Bcl-2-associated death promoter (proapoptotic protein Bad) (Trendowski, 2015; Seipel et al., 2023). Degradation of Akt by PU-H71 leads to dephosphorylation of Bad, allowing it to induce apoptosis. Additionally, Akt phosphorylates the forkhead box O (FoxO) transcription factors, inducing their nuclear exclusion and inhibition (Orea-Soufi et al., 2022). This effect was restrained by PU-H71 suppressing Akt activity, leading to nuclear localization of FoxO with subsequent upregulation of genes involved in cell cycle arrest and apoptosis.

7.13 Insulin-like growth factor receptor 1 (IGF1R)

Insulin-like growth factor receptor 1 (IGF1R), represents a receptor tyrosine kinase crucial for mediating the effects of

insulin-like growth factor 1 (IGF-1) (Ambati et al., 2014). Upon binding to IGF1R, IGF-1 activates the receptor's intrinsic kinase activity, leading to autophosphorylation and activation of downstream signaling cascades essential for promoting cell growth, proliferation, and survival, including PI3K/Akt and Ras/Raf/MEK/ERK (Tahimic et al., 2013).

Significantly, PU-H71 was reported to specifically target IGF1R inhibiting its phosphorylation and then consequently suppressing downstream signaling pathways that eventually led to decreased proliferation and apoptosis induction in malignant cells. Earlier investigations reported that PU-H71 could effectively decrease the viability of various cancer cell lines overexpressing IGF1R (Breinig et al., 2011; Terwisscha Van Scheltinga et al., 2014; Trendowski, 2015). Remarkably, suppression of IGF1R signaling following PU-H71 treatment led to a marked inhibition of other signaling trajectories pivotal for malignant cell survival leading to increased efficacy of chemotherapeutic agents potentially through induction of apoptosis (Bulatowicz and Wood, 2022).

Significantly, the PI3K/Akt pathway is a principal signaling cascade activated by IGF1R. Following IGF1R activation, PI3K is recruited and then activated, which in turn activates Akt. Of note, Akt promotes cell proliferation and survival through stimulating protein synthesis and inhibition of apoptotic pathways. PU-H71's inhibition of IGF1R was reported to decrease Akt activation, thereby inducing apoptosis and inhibiting malignant cell proliferation (Gao et al., 2019).

Similar to the PI3K/Akt pathway, the Ras/Raf/MEK/ERK pathway was shown to be inhibited after IGF1R signaling suppression by PU-H71 leading to reduced cell proliferation and induction of apoptosis (Caldas-Lopes et al., 2009).

7.14 Cyclin-dependent kinase 4 (CDK4)

Cyclin Dependent Kinase 4 (CDK4) is defined as a serine/threonine kinase that plays a pivotal role in cell cycle progression. Initially, it complexes with cyclin D and phosphorylates the retinoblastoma protein (Rb) inducing the release of E2F transcription factors that in turn activate the expression of the genes required for the G1 to S phase transition (Pandey et al., 2019). Conversely, PU-H71 was reported to suppress CDK4, this effect could be mediated through either promoting degradation of HSP90 client proteins, including CDK4 (Serwetnyk and Blagg, 2021) or downregulating CDK4 (Knudsen and Witkiewicz, 2017).

A previous *in-vitro* study on breast cancer cells displayed that, PU-H71 attenuated CDK4 and induced G1 phase cell cycle arrest. Notably, PU-H71 exposure induced a profound suppression of the CDK4/cyclin D/Rb pathway through reducing protein expression of CDK4 and cyclin D1 with a subsequent decline in Rb phosphorylation (Pimienta et al., 2011). Additionally, PU-H71 demonstrated a prominent effect on other HSP90 client proteins central to abnormal cell proliferation, survival, and drug resistance, including epidermal growth factor receptor (EGFR), mammalian target of rapamycin (mTOR) and human epidermal growth factor receptor 2 (HER2) (Trendowski, 2015).

7.15 Interferon (INF)

The binding of PU-H71 to HSP90 will lead to the disruption of interferon (IFN) signaling. PU-H71 treatment reduces the release of IFNγ from activated T cells (Lisi et al., 2013). IFNγ is a key cytokine that mediates inflammatory and anti-viral responses. PU-H71 inhibits the activation of astrocytes by lipopolysaccharide and IFNγ, as measured by reduced nitric oxide synthase 2 (NOS2) expression and nitrite production where Activated astrocytes secrete inflammatory mediators like nitric oxide (Lisi et al., 2013).

The exact molecular mechanisms by which PU-H71 modulates interferon signaling are not fully elucidated. However, it likely involves the destabilization of key signaling proteins in the IFN pathway, such as JAK and STATs (Koppikar et al., 2012; Mbofung et al., 2017; Kuykendall et al., 2020). Degradation of these proteins by the proteasome upon HSP90 inhibition would impair IFN-induced gene transcription and the inflammatory response.

7.16 Janus kinase 2/signal transducers and activators of transcription 3 (JAK2/STAT3)

PU-H71 has shown promising antineoplastic effects in preclinical models of malignancies driven by aberrant JAK/STAT signaling (Kucine et al., 2015). PU-H71 can directly bind to oncogenic JAK2 mutants, such as JAK2V617F, which are common driver mutations in myeloproliferative neoplasms (MPNs) (Jego et al., 2019). This binding leads to the proteasomal degradation of mutant JAK2, abrogating its constitutive activation.

By binding to HSP90, PU-H71 disrupts the chaperone complex that maintains JAK2 in an active conformation. This results in a dose-dependent inhibition of JAK2 kinase activity and reduced phosphorylation of its downstream substrates (Rampal et al., 2014).

JAK2-mediated STAT3/STAT5 phosphorylation is a rate-limiting step in the activation of such oncogenic signaling cascade (Halim et al., 2020). Yet, STAT3/STAT5 phosphorylation was mitigated following PU-H71 exposure, which consequently prevented their dimerization, nuclear translocation, and transcriptional activity (Niu et al., 2021).

7.17 Human epidermal growth factor receptor 2 (HER2)

HER2 is a receptor tyrosine kinase that plays a crucial role in regulating the rate of cellular proliferation as well as cell survival. HER2 upregulation was reported to induce a remarkable increase in the rate of cell proliferation alongside apoptosis inhibition, contributing to the pathogenesis as well as the development of an array of malignancies, chiefly breast cancer (Hsu and Hung, 2016). Of note, approximately 20%–30% of diagnosed breast cancer cases demonstrated HER2 overexpression. Herein, HER2-positive tumors significantly demonstrated more aggressive behavior and poor prognosis compared to HER2-negative tumors (Cheng, 2024). Moreover, HER2 overexpression was documented in other malignancies (e.g., gastroesophageal adenocarcinomas, ovarian cancers, and endometrial cancers) (Iqbal and Iqbal, 2014).

HER2 activation involves its dimerization with other members of the ErbB family of receptors followed by provocation of downstream signaling axes, particularly, the PI3K/Akt and MAPK pathways (Elster et al., 2015) promoting cell proliferation, survival, and metastasis, highlighting HER2 as a significant druggable molecular target in our fight against cancer.

Conspicuously, HSP90 inhibition following PU-H71 treatment was shown to disrupt the chaperone's interaction with HER2 stimulating its degradation and then reducing its levels in cancer cells (Li and Luo, 2023). Furthermore, PU-H71-mediated downregulation of HER2 expression was stated. Additionally, PU-H71 exposure displayed a significant impact on key oncogenic cascades indispensable for cancer cell survival and proliferation namely, ERK1/2 and Akt (Kale et al., 2020). The observed inhibition of these signaling cascades consequent to PU-H71 treatment could potentially induce significant cytotoxic effects in different molecular types of breast cancer, among which triple-negative breast cancer (TNBC) is the most important owing to the reported resistance to conventional therapies. This multimodal approach suggested that PU-H71 could be a promising candidate for the treatment of HER2-positive and other aggressive cancer types.

7.18 Epidermal growth factor receptor (EGFR)

EGFR is a key receptor tyrosine kinase, that belongs to the ErbB family that plays a pivotal role in regulating cellular proliferation as well as survival. EGFR is mostly overexpressed in a range of neoplasms (e.g., lung, brain and neck cancers) (Roskoski, 2014). Therefore, EGFR represents a potential druggable target for the development of novel targeted cancer therapies.

EGFR activation results in subsequent activation of other downstream cascades including PI3K/Akt pathway, Ras/Raf/MEK/ERK pathway, and Phospholipase C γ1 (PLCγ1)/PKC pathway (Martinelli et al., 2017; Salama et al., 2019; Guerra et al., 2021). Therefore, HSP90 inhibition by PU-H71 resulted in EGFR destabilization as well as degradation suppressing the activation of downstream cascades. This was shown to increase the sensitivity of cancer cells to conventional anti-cancer agents, especially, malignant cells harboring mutant forms of EGFR, which are often dependent on HSP90 for their stability (Lee et al., 2016).

7.19 Mammalian target of rapamycin (mTOR)

As previously stated, mTOR represents a key serine/threonine protein kinase central to regulating cell metabolism, growth, and survival in response to various environmental cues such as growth factors, nutrients, energy levels, and stress signals (Wu and Storey, 2021). In addition, The mTOR pathway was defined as a chief oncogenic pathway that contributed significantly to the pathogenesis of an array of malignancies as it was aberrantly hyperactivated by mutational activation of its upstream regulators (Popova and Jücker, 2021).

Notably, mTOR forms two distinct complexes, mTOR complex 1 (mTORC1) and mTOR complex 2 (mTORC2) both are key regulators of principal cellular processes. Significantly, mTORC1 is the primary regulator of protein synthesis, lipogenesis, and autophagy, while mTORC2 plays a remarkable role in regulating cell survival and cytoskeleton organization (Szwed et al., 2021). In cancer cells, constitutive activation of the mTOR pathway promotes several hallmarks of cancer, including increased protein synthesis, lipid metabolism, and inhibition of autophagy, which are vital for rapid cell growth and proliferation. Dysregulation of mTOR signaling has been implicated in various types of cancer, including lung, breast, liver, renal, pancreatic, and prostate cancers. PU-H71 was found to disrupt the mTOR pathway, leading to decreased protein synthesis and enhanced apoptosis in cancer cells (Giulino-Roth et al., 2017). This mechanism contributes to the therapeutic efficacy of PU-H71 in targeting mTOR-driven cancers.

PU-H71 exerts its effects through a range of molecular mechanisms targeting various pathways. It downregulates Ras, Raf-1, and ERK in MAPK signaling, reducing cell proliferation, enhancing radiosensitivity, and inducing G2/M phase arrest by disrupting cyclins and CDKs. PU-H71 inhibits Tyk2, impacting JAK/STAT, MAPK, and PI3K/Akt pathways to induce anti-proliferative and pro-apoptotic effects. It also induces PKC degradation by preventing HSP90 chaperoning. By inhibiting ATP production, PU-H71 disrupts glycolytic and oxidative metabolism. It activates mitochondrial apoptosis pathways, downregulating Bcl-2 and upregulating Bax, and targets ER HSP90 to destabilize client proteins. The drug affects HGFR by disrupting its stability and function, thereby reducing tumor growth. PU-H71 also inhibits Akt and IGF1R, affecting survival pathways and promoting apoptosis. It reduces inflammatory responses by decreasing IFNγ release and inhibits JAK2/STAT3 signaling. Finally, it targets HER2 and EGFR, reducing their activation and downstream signaling, thus inhibiting cell proliferation and promoting apoptosis.

8 Impact of PU-H71 on cancer

8.1 Impact on triple-negative breast cancer

Triple-negative breast cancer (TNBC) accounts for about 12% of all breast tumors and is more prevalent in premenopausal women of African and African-American heritage (Howard and Olopade, 2021). TNBCs are defined by their low degree of differentiation, and a significant majority of them are classified within the primary subtype of breast cancers based on gene manifestation analysis (Cserni et al., 2021; Fusco et al., 2022). In breast cancer, there is the existence of the molecular chaperone protein identified as HSP90. HSP90 plays a critical role in maintaining a substantial reservoir of active and properly folded oncoproteins. It has a distinct affinity for its activated form, serving as a safeguarding "biochemical buffer" that shields cancer-promoting oncogenes (Kunachowicz et al., 2024). TNBCs are distinguished by the absence of estrogen, progesterone, and HER2 receptor expression. Because there are no specific targets and targeted therapies available, as well as the diverse molecular makeup of TNBCs, the current treatment guidelines primarily rely on conventional chemotherapy. While this approach proves effective for certain patients, it leads to early

relapse in a substantial portion of instances and does not offer a cure for individuals with metastatic TNBC (Medina et al., 2020; Vagia et al., 2020). The HSP90 inhibitor PU-H71 has demonstrated remarkable efficacy against these tumors. This agent has been shown to produce forcible and enduring anti-tumor impacts in TNBC xenografts, counting instances of full reaction and tumor reversion, free from inducing harm to the host (Anwar et al., 2020). Importantly, TNBC tumors have displayed continued responsiveness to PU-H71 retreatment for multiple cycles, extending over more than 5 months, with no signs of resistance or toxicity. Both in laboratory experiments (*in vitro*) and in living organisms (*in vivo*). PU-H71 has proven highly effective in consistently reducing and deactivating these proteins. It has been identified several mechanisms contributing to its anti-proliferative effects, including the suppression of factors in the Ras/Raf/MAPK pathway and the triggering of apoptosis by breaking down activated Akt and Bcl-xL. Additionally, PU-H71 inhibits various signaling pathways such as NF-κB, Akt, ERK2, Tyk2, and PKC, which collectively decrease the influential domination of TNBC (Caldas-Lopes et al., 2009; Ozgur and Tutar, 2014; He and Hu, 2018; Scott, 2018).

PU-H71's cytotoxicity was evaluated in TNBC cell lines MDA-MB-468, MDA-MB-231, and HCC-1806 employing a test that measures ATP degrees (Caldas-Lopes et al., 2009). It had been noted that PU-H71 effectively prevented the expansion of these cells at concentrations known to bind to HSP90, indicating a correlation between its anti-tumor activity and its interaction with HSP90 (Chiosis et al., 2008). In an experiment conducted over a 48-h incubation period using an intensification of PU-H71 that was 5- to 10-fold more than its IC50 for expansion prevention (1 M), PU-H71 exhibited notable cytotoxicity (Anwar et al., 2020). Using PU-H71 as a data collection method offers preclinical evidence that achieving a comprehensive response is possible across molecularly diverse TNBC tumors using a single agent, an HSP90 inhibitor. The data collected with PU-H71 suggests that the variability in the effectiveness of other HSP90 inhibitors in TNBC tumors is not primarily due to a decrease in the number of HSP90-present tumors. Instead, it suggests that differences in their effectiveness may be attributed to factors unrelated to the target (HSP90), which remain undisturbed. In contrast to approaches that exclusively target specific proteins or signaling pathways within TNBC cells, PU-H71's exceptional efficacy can be linked to its capacity to suppress HSP90, whether in laboratory settings (*in vitro*) or within living organisms (*in vivo*). HSP90 is a protein that forms complexes with numerous proteins pivotal for the cancerous characteristics of TNBC. PU-H71 induces concurrent instability and decrease of several crucial TNBC oncoproteins, a lot of which contribute to processes such as cell proliferation, anti-apoptotic capabilities, and metastasis.

8.2 Impact as cancer cell sensitizer for carbon-ion beam therapy

Carbon-ion radiotherapy (CIRT) has shown its efficacy in treating a range of tumor types, including lung cancer, prostate cancer, and bone/soft tissue cancer (Kamada et al., 2015). However, there is ongoing potential for further progress in the field of CIRT, especially in terms of effectively managing radioresistant tumors while minimizing adverse effects on healthy tissues. Radiosensitizers play a crucial role in enhancing radiotherapy by making tumor cells more responsive to radiation, enabling the achievement of similar therapeutic effects with lower radiation doses (Xie et al., 2019). While there is a wealth of research on radiosensitizers for X-ray-based therapies, there has been relatively limited investigation into radiosensitizers specifically designed for use with carbon-ion beams (Yanagi et al., 2009).

The prospect of targeting HSP90 for cancer treatment holds significant potential owing to its elevated expression in cancer cells in contrast to normal cells, and cancer cells exhibit a greater dependence on HSP90 for their survival (Jhaveri et al., 2012). Numerous inhibitors of HSP90 have been formulated and have demonstrated promising treatment efficacy; however, their therapeutic potential has been constrained due to associated toxicity. In several preclinical investigations, PU-H71 has demonstrated therapeutic efficacy in various preclinical models and is presently undergoing clinical trials. While CIRT has been effective in controlling tumors, there remains an opportunity for enhancement, particularly in terms of achieving tumor-specific radiosensitization (Li et al., 2016; Sokol and Durante, 2023).

There are currently two phase I clinical trials in progress, involving patients with solid tumors or lymphoma, So there is growing interest in PU-H71 as a promising novel drug (Li et al., 2016). PU-H71, regarded as one of the strong potential HSP90 inhibitors, is a resultant of PU-3 that has been created to possess both dispersibility and targeted binding affinity to the ATP-binding sites of HSP90 (Li et al., 2016). HSP90 operates through a sophisticated cycle regulation by ATP combination and dissociation. PU-H71 inhibits the function of HSP90 by preventing ATP from binding to it (Jhaveri et al., 2012). Inhibiting HSP90 represents an appealing approach to combined therapy, as there have been numerous reports indicating that HSP90 inhibitors can induce significant and lethal damage to tumor cells when used in binding with X-ray radiation therapy (Segawa et al., 2014). There have been only a limited number of studies examining the enhancing sensitivity of HSP90 inhibitors on high-LET C-ions, and the results of these studies remain a topic of debate and discussion (Musha et al., 2012). While PU-H71 when examined in isolation, there were no signs of toxicity to LM8 cells, it was demonstrated that after 24 h of incubation, PU-H71 significantly heightened the sensitivity of LM8 cells to both X-ray and C-ion exposure (Li et al., 2016). Due to the potent cell-killing capabilities of C-ions, making tumors more responsive to high-LET radiation, including C-ion therapy, through combination with other treatments, such as anti-cancer medications, can be particularly challenging (Li et al., 2016). Achieving successful combination therapy can indeed be complex. The potency of the standard treatment in a combination therapy approach should ideally surpass the effectiveness of each therapy component. Additionally, the side effects of the combined treatment must be less severe than the cumulative side effects regarding every specific therapy (Schirrmacher, 2019). Consequently, optimized doses for combinatorial treatment often should be administered at lower levels than the individual treatment doses to strike a balance between maximizing therapeutic benefit and minimizing adverse effects (Reece et al., 2007). PU-H71 has demonstrated the ability to

sensitize LM8 cells at a dosage that doesn't disrupt cellular homeostasis. This suggests that PU-H71 holds noteworthy radiosensitizing qualities for CIRT (Li et al., 2015).

The potentially lethal impact of radiation on cells is primarily attributed to the induction of DNA double-strand breaks (DSBs) (Mladenov et al., 2013), HSP90 client proteins are prevalent in numerous DSB-associated proteins. Consequently, the focus was on exploring protein expression in the context of DSB repair and paying special attention to RAD51 and Ku70 levels (Pennisi et al., 2015; Khurana et al., 2016). These proteins play crucial roles in the primary cellular repair pathways, namely, homologous recombination and non-homologous end joining. Treatment with PU-H71 alone caused a reduction in RAD51 expression in LM8 cells (Ren et al., 2014). This suggests that PU-H71's ability to enhance the sensitivity of C-ion therapy may also involve the non-homologous end-joining DSB repair pathway. Nevertheless, further investigation is necessary to fully elucidate the exact mechanism responsible for PU-H71's radiosensitizing effect.

8.3 Impact on myeloma

In preclinical research, several HSP90 inhibitors have demonstrated effectiveness against myeloma, and at least three of these drugs have proceeded to Phase I/II clinical trials for the treatment of relapsed/refractory myeloma (Cavenagh et al., 2017). Preclinical studies utilizing PU-H71 in the treatment of diffuse large B-cell lymphoma and triple-negative breast cancer have indicated significant efficacy while causing minimal hematological or non-hematopoietic toxicity (Usmani et al., 2010). It is worth noting that the effectiveness of PU-H71 in treating multiple myeloma has not been thoroughly studied. However, in both IL-6 independent cell lines and IL-6 reliant cell line INA-6, PU-H71 has demonstrated comparable anti-myeloma efficacy (Usmani et al., 2010). Moreover, PU-H71 has exhibited *in vitro* synergy with other commonly used anti-myeloma medications. Additionally, PU-H71 has been shown to activate the UPR and induce apoptosis through the caspase-dependent pathway (Usmani et al., 2010). Over the past decade, there has been considerable research into the ER HSP90 family member known as gp96, or HSP90B1, also referred to as grp94. This research has been driven by gp96's role in chaperoning antigenic peptides, enabling their presentation in the antigen-cross-presentation pathway (Marzec et al., 2012; Duan et al., 2021). Immunizations utilizing pure tumor-derived gp96-peptide complexes have demonstrated promising preclinical and clinical outcomes in the treatment of multiple myeloma (Qian et al., 2009). To assess the *in vitro* effectiveness of anti-myeloma drugs when gp96 was absent, researchers established a stable gp96 knockdown human myeloma cell line. The results aligned with expectations: bortezomib, known for disturbing protein balance, rendered gp96 knockdown cells more susceptible (Hua et al., 2013). Additionally, gp96 knockdown cells displayed heightened vulnerability to thalidomide, whose mechanism of action remains unidentified, as well as increased cell death induced by genotoxic drugs like melphalan and doxorubicin (Bagratuni et al., 2010; Hua et al., 2013). These findings imply that gp96 may play a role in reducing the efficacy of these anti-myeloma medications, and its absence amplified the sensitivity of myeloma cells to these agents (Usmani et al., 2010). However, the absence of gp96 had a significant negative impact on the anti-myeloma activity of PU-H71. This information indicates that HSP90 inhibitors affect not only cytosolic HSP90 but also gp96 in the ER, contributing to their acute cytotoxic effects (Hua et al., 2013). The novel purine-based HSP90 inhibitor, PU-H71, displayed *in vitro* anti-myeloma efficacy as well. These findings highlight that HSP90 inhibitors, including PU-H71, target both cytosolic HSP90 and the ER-resident HSP gp96 to exert their anti-myeloma effects. It is imperative to initiate a phase I clinical trial to assess the therapeutic efficacy of PU-H71 in individuals with refractory myeloma.

8.4 Effect on B-Cell lymphomas

The function of HSP90 and the impact of HSP90 inhibitors in the most popular kind of lymphoid malignancies, such as diffuse large B-cell lymphomas (DLBCL) that come from germinal center B-cells, remain largely unexplored and not well understood (Klein and Dalla-Favera, 2008). Bcl6, which is the most common oncogenic protein in DLBCL, has been identified as a client protein of HSP90 based on observations of how DLBCL cells respond to HSP90 inhibitors (Cerchietti et al., 2009; Calvo-Vidal et al., 2021). The interaction between HSP90 and Bcl6 influences the biology of normal germinal center B-cells as well as the pathophysiology of DLBCL to varying degrees (Ci et al., 2008). The functional and physical connection between HSP90 and Bcl6 may, in part, illustrate that treatment by directly controlling both Bcl6 mRNA and protein (Cerchietti et al., 2010). It is suggested that both mechanisms contribute to maintaining stable Bcl6 levels, although it is challenging to determine the precise extent to which HSP90 influences Bcl6 mRNA stability versus Bcl6 protein stability.

To establish germinal centers, where B-cells undergo affinity maturation, normal B-cells must undergo an upregulation process. HSP90 may play a role in supporting B-cell development by assisting in the accumulation of Bcl6 within germinal center B-cells, especially considering its localization in the nuclei of healthy Centro blasts (Hatzi and Melnick, 2014). These findings suggest that BCL6, which is part of a larger gene family subject to post-transcriptional regulation, could indeed function as a gene responsive to stress conditions (Cerchietti et al., 2009; Fernando et al., 2019; Liu et al., 2022). The fact that Bcl6 is a key target of HSP90 inhibitors in DLBCL aligns with the idea that it is essential for the survival of a subgroup of DLBCLs. This concept gains support from studies involving PU-H71, which showed that a version of Bcl6 resistant to degradation was enough to protect DLBCL cells (Culjkovic-Kraljacic et al., 2016). Studies like these emphasize the importance of discovering drugs that can enhance the effectiveness of conventional anti-lymphoma therapies while reducing their toxicity. It is noteworthy that HSP90 inhibitors have the propensity to accumulate preferentially within lymphomas for an extended period compared to normal tissues. In this regard, PU-H71 stands out as an exceptionally effective and fine-tolerated anti-lymphoma drug *in vivo*. Furthermore, finding that PU-H71 can play a role in the depression of Bcl6 target genes, that cause DNA damage checkpoints, raises the possibility that such medications could increase the cytotoxic activity of chemotherapy drugs. This effect was observed in various lymphoid cell lines, including DLBCLs (Zhao and Houry, 2005; Shinozaki et al., 2006).

8.5 Impact on human hepatocellular carcinoma

There has been a suggestion that HSP90 might be involved in the progression of hepatocellular carcinoma (HCC), potentially contributing to the hepatocarcinogenesis process (Mohammed et al., 2023a). Several factors that promote hepatocarcinogenesis, such as hepatocyte growth factor receptor, protein kinase B, IGF1R, cyclin-dependent kinase 4, and v-raf-1 murine leukemia viral oncogene homolog 1 exhibit abnormal expression and increased activity when influenced by HSP90. In general, HSP90 regulates the stability and activity of proteins represented as "client proteins," (Saber et al., 2020; El-Kashef et al., 2022; Hasan Khudhair et al., 2022; Shaaban et al., 2022; Mohammed et al., 2023a; Mohammed et al., 2023b) and this is how it impacts protein homeostasis. Its activity is driven by adenosine triphosphate and involves dynamic interactions with co-chaperones (Workman et al., 2007; Pearl et al., 2008). The development of HCC is believed to be influenced by the upregulation of HSP90 in conjunction with increased CDK4 activity (Pascale et al., 2005). HCC typically leads to liver damage (Abdel-Ghany et al., 2015; Saber et al., 2018; Abdelhamid et al., 2022). Considering that geldanamycin analogs, which are HSP90 inhibitors, often cause dose-limiting hepatotoxicity, using HSP90 inhibition with these drugs may not be a suitable treatment option for this type of cancer (Pearl et al., 2008). Novel HSP90 inhibitors that do not contain the benzoquinone component found in geldanamycin, which is believed to contribute to hepatotoxicity, may offer potential prospects for HSP90 inhibition in the therapy of HCC in the future (Pearl et al., 2008). HCC is a major global health concern, with over 500,000 new cases diagnosed annually. It ranks as the sixth most common cancer worldwide (Abd El-Fattah et al., 2022; Nasr et al., 2023; Saber et al., 2023). Its incidence is on the rise globally (Nasr et al., 2023), and notably, it is the fastest-growing reason for cancer-related deaths among men in the United States (Bruix et al., 2004; El–Serag and Rudolph, 2007). Hepatitis B virus (HBV) and hepatitis C virus (HCV) infections are the primary factors contributing to the development of HCC. However, almost any condition that results in cirrhosis, with alcoholism being a prominent example, can potentially lead to the development of hepatocarcinogenesis (Farazi and DePinho, 2006; Abdelhamid et al., 2021).

The prognosis for HCC remains unfavorable because it is often diagnosed at an advanced stage, and tumor recurrence is relatively common (Bruix et al., 2004). Worrisome increases in HCV infection rates are raising concerns about the possibility of an impending HCC pandemic. This underscores the critical and immediate need for effective treatments to address this growing public health issue (El–Serag and Rudolph, 2007). Inhibiting HSP90 simultaneously reduced various factors that promote hepatocarcinogenesis, suppressed the growth of HCC tumors, and induced apoptosis (Nouri-Vaskeh et al., 2020). The use of non-quinone compounds as HSP90 inhibitors appears to be a promising treatment strategy for HCC. In animal studies, the non-quinone HSP90 inhibitor, PU-H71, specifically accumulated in tumors, effectively inhibited the growth of HCC tumors, and was well-tolerated, suggesting a low risk of severe liver toxicity (Breinig et al., 2009). In in vivo experiments, the non-quinone HSP90 inhibitor PU-H71 demonstrated no adverse effects on liver function, and no toxicity was observed (Speranza et al., 2018). This finding underscores the growing evidence that non-quinone HSP90 inhibitors are well-tolerated in living organisms (Rodina et al., 2007; Chandarlapaty et al., 2008; Eccles et al., 2008). The quick removal of PU-H71 from the liver, combined with its effective retention in tumors, improves the advantageous therapeutic characteristics of non-quinone HSP90 inhibitors for treating HCC. Additionally, the fact that PU-H71 treatment did not substantially affect ERK, AKT, or CDK4 in mouse livers further supports this conclusion (Breinig et al., 2009). These findings build upon prior research involving a different non-quinone HSP90 inhibitor, emphasizing the potential advantages of such inhibitors for HCC therapy (Chandarlapaty et al., 2008).

8.6 Impact on glial cells

Geldanamycin (GA) and radicicol are natural compounds known for their ability to inhibit the N-terminal ATPase activity of HSP90. HSP90 primarily acts as a chaperone to oversee a set of proteins known as "client proteins" during the final stages of their maturation and folding, especially as they near their native, functional configuration. HSP90 is heavily involved in various signal transduction processes (Barginear et al., 2008). When compounds like radicicol inhibit the ATPase activity of HSP90, client proteins detach from the chaperone (Roe et al., 1999). Among these client proteins, transcription factors like HSF-1 can become activated, while others may either lose their function or be marked for degradation by the proteasome. The removal of HSF-1 from HSP90 facilitates its movement into the nucleus, where it initiates the heat shock response (HSR). The use of HSP90 inhibitor drugs to stimulate the HSR pharmacologically can efficiently inhibit the pro-inflammatory activation of glial cells and enhance clinical outcomes in conditions such as experimental autoimmune encephalomyelitis (EAE) (Lisi et al., 2013; Seasons et al., 2024). The anti-inflammatory impacts of the HSR appear to be conveyed through a decrease in the activation of the NF-κB transcription factor (Schroeder et al., 2024). Ansamycins, including GA, are indeed potent HSP90 inhibitors. Nevertheless, their practical use in clinical settings is restricted due to notable toxicity concerns and stability challenges (Chiosis et al., 2004). PU-H71 is recognized as a potent HSP90 inhibitor, and datasets related to PU-H71 display a strong correlation in terms of HSP90 inhibition. This suggests that these drugs share a similar molecular method of action. The HSP90 inhibitor PU-H71 has demonstrated beneficial effects in the context of neuroinflammatory diseases (Kim et al., 2009).

PU-H71 was found to inhibit the activation of astrocytes when stimulated by the bacterial endotoxin lipopolysaccharide (LPS). However, it did not have an inhibitory effect on the activation of inflammatory cytokines. Similarly, PU-H71, like 17-AAG (another HSP90 inhibitor), had relatively mild anti-inflammatory influences on microglial initiation. Conversely to ansamycins (like GA), PU-H71 had a restricted impact on the progress of EAE disease. Its effects included a reduction in peripheral T-cell triggering and IFN release (Lisi et al., 2013). These data suggest that PU-H71 shares some anti-inflammatory roles with ansamycins. However, they also indicate significant disparities in their action mechanisms between ansamycins and PU-H71 regarding the initiation of glial cells, which

may explain the lower performance of PU-H71 in EAE. Both 17-AAG and PU-H71 target blocking the ATPase activity of HSP-90 by binding to its N-terminal ATP/ADP pocket. Notably, the chemical structure of PU-H71 is entirely dissimilar from that of 17-AAG. PU-H71 has a simple formulation and lacks the benzoquinone moiety found in 17-AAG (Trendowski, 2015).

The primary difference between PU-H71 and 17-AAG lies in the absence of a benzoquinone group, potentially leading to distinct pharmacological effects. Interestingly, the presence or absence of DT-diaphorase appears to play a significant role in determining the varied response to HSP90 inhibition between the two compounds, possibly serving as a resistance mechanism (Kelland et al., 1999). Additionally, the silencing of the NAD (P) H dehydrogenase quinone 1 (NQO1) gene due to hypermethylation limits the effectiveness of 17-AAG in Hep3B cells, but this limitation does not apply to PU-H71 (Tada et al., 2005; Broekgaarden et al., 2015). Consequently, the anti-tumor response to novel HSP90 inhibitors is greatly enhanced by the NQO1 status (Hadley and Hendricks, 2014). The restricted *in vivo* effectiveness of PU-H71 may be attributed to differences in its selectivity for particular cells and its ability to penetrate the blood-brain barrier (BBB). It is important to highlight that, under normal circumstances, PU-H71 has a very restricted capacity to penetrate the CNS (Lisi et al., 2013). The comparatively modest inhibitory impact of the drug noticed *in vitro*, coupled with the activation of glial cells using a combination of cytokines, may aid in understanding the drug's restricted effects in MOG-induced EAE following treatment. Cytokines such as TNF, IFN, and IL-1, which are closely linked to neuroinflammatory processes, may play a substantial role in this particular context (Sosa and Forsthuber, 2011). Therefore, the use of a combination of these cytokines represents a more pertinent physiopathological stimulus compared to bacterial endotoxin when trying to replicate the conditions that glial cells encounter in neurodegenerative disorders such as multiple sclerosis (MS) within a living organism. In live animal experiments, drugs that exhibit substantial anti-inflammatory effects in laboratory settings and reduce the activity of NOS2 triggered by inflammatory stimuli like TII have been shown to alleviate the clinical symptoms of EAE, which serves as a model for MS (Lubina-Dąbrowska et al., 2017). LPS functions by binding to the Toll-like receptor 4 (TLR4) receptor, while cytokines interact with and activate various receptors through separate intracellular signaling pathways (Ciesielska et al., 2021; Youssef et al., 2021a; Youssef et al., 2021b; Afroz et al., 2022). The anti-inflammatory action of PU-H71 in glial cells appears to involve the inhibition of NF-κB activation, as suggested by *in vitro* studies using stably transfected C6 glioma cells. This mechanism may explain the observed effects in reducing nitrite levels in response to both LPS (LI) and a combination of cytokines (TII). PU-H71, when used at concentrations of 30 nM for LI-stimulated C6 cells and 50 nM for TII-stimulated C6 cells, was found to decrease NFκB promoter activity while simultaneously reducing the production of nitric oxide (NO) (Lisi et al., 2013).

8.7 Impact on myeloproliferative neoplasms

Myeloproliferative neoplasms (MPNs) are set of clonal hematological malignancies that encompass conditions such as polycythemia vera (PV), chronic myeloid leukemia (CML), primary myelofibrosis (PMF) and essential thrombocythemia (ET). These disorders involve the overproduction of certain blood cells in the bone marrow (Luque Paz et al., 2023; Dunn et al., 2024; Guo et al., 2024). Although it has been over three decades since the clonal origin of these conditions stemming from stem cells was established, the genetic basis of BCR-ABL-negative MPNs stayed enigmatic until multiple studies revealed a somatic activating mutation in the JAK2 kinase (JAK2V617F). This mutation is present in the overwhelming majority of PV patients and is observed in nearly 50% of patients with ET and PMF (James et al., 2005; Zhao et al., 2005). Follow-up investigations have uncovered somatic mutations in JAK2 exon 12 in instances of PV where the JAK2V617F mutation is absent. Furthermore, mutations in the thrombopoietin receptor, specifically MPLW515 L/K/A and MPLS505N, have been detected in a subset of patients with ET and PMF who do not possess the JAK2V617F mutation (Mario, 2007; Pietra et al., 2008). *In vitro*, the presence of JAK2/MPL mutations allows hematopoietic cells to proliferate even without the need for cytokines. This leads to increased activation of signaling pathways downstream of JAK2, including the STAT3/5, MAP kinase, and PI3K signaling pathways (Anand et al., 2011; Staerk and Constantinescu, 2012; Rao et al., 2019). Additionally, it is important to highlight that JAK2 or MPL mutations lead to a remarkably consistent pattern of myeloproliferation *in vivo*. This consistency is particularly notable in the context of conditions such as polycythemia (linked with JAK2V617F or JAK2 exon 12 mutations) and thrombocytosis/myelofibrosis (associated with JAK2V617F and MPLW515L mutations) (Wernig et al., 2006), This implies that the persistent activation of the JAK-STAT signaling pathway plays a crucial role in the progression of PV, ET, and PMF. PU-H71 demonstrates enhanced pharmacokinetic and pharmacodynamic characteristics, including its robust and sustained absorption by tumors. As a result, it leads to more efficient and enduring degradation of HSP90 client proteins (Jhaveri et al., 2020). Increasing PU-H71's *in vivo* effectiveness doesn't appear to raise toxicity concerns. Extended treatment at effective doses has not shown significant hematopoietic or non-hematopoietic toxicities (Usmani et al., 2010; Levine et al., 2012).

Scientists used PU-H71 to assess HSP90 inhibition in JAK2-dependent cancers. PU-H71 demonstrated substantial anti-cancer effects in MPN cell lines, mouse models of MPN, and samples from MPN patients. PU-H71 treatment repressed cell proliferation in cells with JAK2/MPL mutations at doses related to JAK2 reduction and the suppression of downstream signaling pathways (Campbell and Green, 2006). Furthermore, giving PU-H71 to mice with JAK2V617F or MPLW515L mutations normalized blood parameters, reduced extramedullary hematopoiesis in both models, and decreased morbidity and mortality in the MPLW515L model, compared to mice receiving a control vehicle. Importantly, this therapeutic effect was achieved without causing hematopoietic or non-hematopoietic toxicities (Marubayashi et al., 2010). Additionally, PU-H71 treatment has been shown to inhibit abnormal erythrocytosis and megakaryopoiesis in the JAK2V617F and MPLW515L rodent models, while it does not impact normal erythrocytosis and megakaryopoiesis (Koppikar et al., 2010). These findings suggest that HSP90 inhibitor therapy with PU-H71 has a

unique impact on the proliferation and signaling of the malignant clone. The specific effect of PU-H71 on JAK2/MPL mutant cells *in vivo* does not seem to be solely due to the mutant or activated JAK2's increased reliance on the HSP90 chaperone complex (Marubayashi et al., 2010; Mullally, 2017).

Unlike previous experiments with a JAK2 inhibitor, PU-H71 treatment reduces the burden of mutant alleles in the MPLW515L murine MPN model. This strongly supports the idea of conducting clinical trials with PU-H71 for treating JAK2V617F/MPLW515L mutant MPN. In preclinical studies of PU-H71 and other HSP90 inhibitors, flow cytometric assays measuring JAK2 protein expression, phospho-STAT5 levels, and HSP70 induction could be utilized as pharmacodynamic assessments (Koppikar et al., 2010). PU-H71 and other HSP90 inhibitors affect numerous client proteins, likely contributing to their impact on myeloproliferation both *in vitro* and *in vivo*. However, evidence suggests that JAK2 is the primary target for HSP90 inhibitors in JAK2/MPL-mediated myeloproliferation (Weigert et al., 2012; Chakraborty et al., 2016; Hobbs et al., 2018). PU-H71 consistently resulted in JAK2 degradation and pathway inhibition *in vitro* and *in vivo* at comparable doses. Additionally, PU-H71 and two different JAK2 kinase inhibitors had a complementary, not synergistic, effect, implying a mutual mechanism of action in this situation (George et al., 2004). PU-H71 can serve as a valuable tool for identifying tumors depending on HSP90 chaperone proteins. This data could be integrated into genomic and proteomic databases to reveal new molecular targets across various human cancer types. The effectiveness of HSP90 inhibition by PU-H71 extends to a range of genetically diverse human cancers, highlighting the importance of conducting targeted drug trials with HSP90 inhibitors for treating MPNs and other malignancies (Gao et al., 2007; Hedvat et al., 2009).

9 The therapeutic potential of PU-H71 in non-tumor disorders

The reasoning behind the connection between protein aggregation and neurodegenerative conditions has been that blocking HSP90 leads to the activation of HSF-1, resulting in the production of HSP70, HSP40, and other chaperones, which in turn facilitate the disaggregation and breakdown of proteins. However, recent findings indicate that HSP90 has an added involvement in neurodegenerative processes. Specifically, HSP90 is involved in upholding the operational integrity of neuronal proteins that have an abnormal tendency, thereby permitting and sustaining the buildup of detrimental protein clumps (Waza et al., 2006).

Parkinson's disease (PD), the most common neurodegenerative movement disorder, is marked by a complex interplay of pathological events (Westerlund et al., 2010). A substantial number of these events have been more recently associated with HSP90. Wang et al. have pointed out that Leucine-rich repeat kinase 2 (LRRK2), an enzyme whose altered forms already are found in both familial and sporadic cases of Parkinson's disease, interacts with HSP90 *in vivo* to form a complex (Wang et al., 2008). The purine-based HSP90 inhibitor PU-H71 disrupted the interaction between HSP90 and LRRK2, resulting in the degradation of LRRK2 via the proteasome system. PU-H71 also decreased the neurotoxic effects induced by mutant LRRK2 and reversed the impairment in axon growth associated with the LRRK2 G2019S mutation in neurons (Wang et al., 2008). PARK6, a subtype of familial Parkinson's disease inherited in an autosomal recessive fashion, is linked to a mutation that occurs in PTEN-induced kinase 1 (PINK1). PINK1 is a gene that codes for a potential mitochondrial serine/threonine kinase (Westerlund et al., 2010). The autosomal recessive inheritance pattern associated with this type of Parkinson's disease indicates a strong connection between the disease's development and the loss of PINK1 function. HSP90 always attaches to PINK1 to enhance its equilibrium. In cells exposed to the HSP90 inhibitor GM, the levels of PINK1 were significantly diminished through the ubiquitin-proteasome pathway (Moriwaki et al., 2008).

10 Conclusion

In this comprehensive review, we have explored the pivotal role of HSP90 as a key molecular player in maintaining cellular health and its intricate involvement in various disease contexts. We discussed how HSP90, in partnership with HSF-1, orchestrates stress responses, shedding light on its role in regulating the HSR. The therapeutic potential of PU-H71, a novel purine-based HSP90 inhibitor, has been a central focus of our investigation. We have elucidated its promise in addressing neurodegenerative disorders and its significant impact on triple-negative breast cancer, offering new avenues for cancer treatment. PU-H71's ability to sensitize cancer cells for carbon-ion beam therapy suggests a novel approach to improving the efficacy of radiation therapy. Furthermore, the dual inhibition of HSP90 A and HSP90B1 by PU-H71 emerges as a potential breakthrough in myeloma treatment. Its capacity to induce apoptosis in B-cell lymphomas dependent on Bcl6 for survival underscores its relevance in hematologic cancers. Our exploration extends to HCC, where innovative chemotherapy approaches and PU-H71's potential to inhibit the activation of glial cells hold promise for patients with hepatic and neuroinflammatory disorders. Finally, we emphasize PU-H71's encouraging role in JAK2-dependent myeloproliferative neoplasms, highlighting its potential as a therapeutic avenue in hematology. Collectively, this review underscores the versatility of HSP90 and the immense therapeutic potential of PU-H71 in diverse disease scenarios, opening new doors to innovative treatments and improved patient outcomes in the realm of health and disease.

11 Authors' perspectives and future considerations

From the author's perspective, the multifaceted roles of HSP90 and the promising therapeutic potential of PU-H71 underscore the need for continued research and development in this field. Shedding more light on the underlying mechanisms of HSP90 and its inhibitors highlights them both as promising candidates for the development of novel targeted cancer therapies. Markedly, special attention should focus on optimizing precise drug delivery strategies to enhance the efficacy as well as selectivity of such novel therapeutic agents and to explore any potential combination therapies for maximum efficacy.

In addition, pondering the molecular pathways underlying PU-H71 actions is indispensable for tailoring novel therapeutic approaches to fulfilling specific patient needs. Further investigations on the long-term safety profiles of HSP90 inhibitors in addition to their potential for resistance mechanisms should be conducted to ensure their clinical success. The integration of pioneering technologies (e.g., precision medicine approaches and advanced imaging techniques) could potentially establish a platform for developing personalized as well as HSP90-targeted therapies.

Author contributions

SS: Conceptualization, Data curation, Formal Analysis, Investigation, Methodology, Project administration, Resources, Software, Supervision, Validation, Visualization, Writing–original draft, Writing–review and editing. RA: Conceptualization, Data curation, Formal Analysis, Investigation, Methodology, Project administration, Resources, Software, Supervision, Validation, Visualization, Writing–original draft, Writing–review and editing. ME: Conceptualization, Data curation, Formal Analysis, Funding acquisition, Investigation, Methodology, Project administration, Resources, Software, Supervision, Validation, Visualization, Writing–original draft, Writing–review and editing. EE: Conceptualization, Data curation, Formal Analysis, Funding acquisition, Investigation, Methodology, Project administration, Resources, Software, Supervision, Validation, Visualization, Writing–original draft, Writing–review and editing. RH: Conceptualization, Data curation, Formal Analysis, Funding acquisition, Investigation, Methodology, Project administration, Resources, Software, Supervision, Validation, Visualization, Writing–original draft, Writing–review and editing. MA-R: Conceptualization, Data curation, Formal Analysis, Funding acquisition, Investigation, Methodology, Project administration, Resources, Software, Supervision, Validation, Visualization, Writing–original draft, Writing–review and editing. AE-K: Conceptualization, Data curation, Formal Analysis, Funding acquisition, Investigation, Methodology, Project administration, Resources, Software, Supervision, Validation, Visualization, Writing–original draft, Writing–review and editing. MA: Conceptualization, Data curation, Formal Analysis, Investigation, Methodology, Project administration, Resources, Software, Supervision, Validation, Visualization, Writing–original draft, Writing–review and editing. KM: Conceptualization, Data curation, Formal Analysis, Investigation, Methodology, Project administration, Resources, Software, Supervision, Validation, Visualization, Writing–original draft, Writing–review and editing. AA: Conceptualization, Data curation, Formal Analysis, Investigation, Methodology, Project administration, Resources, Software, Supervision, Validation, Visualization, Writing–original draft, Writing–review and editing. MY: Conceptualization, Data curation, Formal Analysis, Investigation, Methodology, Project administration, Resources, Software, Supervision, Validation, Visualization, Writing–original draft, Writing–review and editing.

Funding

The author(s) declare that financial support was received for the research, authorship, and/or publication of this article. The authors extend their appreciation to the Deanship of Research and Graduate Studies at King Khalid University for funding this work under grant number RGP2/233/45. This work was supported by the Deanship of Scientific Research, Vice Presidency for Graduate Studies and Scientific Research, King Faisal University, Saudi Arabia (Grant No. KFU242193). The authors would like to thank the Deanship of Scientific Research at Shaqra University for supporting this work. The researchers would like to thank the Deanship of Graduate Studies and Scientific Research at Qassim University for financial support (QU-APC-2024-9/1).

Conflict of interest

The authors declare that the research was conducted in the absence of any commercial or financial relationships that could be construed as a potential conflict of interest.

Publisher's note

All claims expressed in this article are solely those of the authors and do not necessarily represent those of their affiliated organizations, or those of the publisher, the editors and the reviewers. Any product that may be evaluated in this article, or claim that may be made by its manufacturer, is not guaranteed or endorsed by the publisher.

References

Abd El-Fattah, E. E., Saber, S., Youssef, M. E., Eissa, H., El-Ahwany, E., Amin, N. A., et al. (2022). AKT-AMPKα-mTOR-dependent HIF-1α activation is a new therapeutic target for cancer treatment: a novel approach to repositioning the antidiabetic drug sitagliptin for the management of hepatocellular carcinoma. *Front. Pharmacol.* 12. doi:10.3389/fphar.2021.720173

Abdel-Ghany, R., Rabia, I., El-Ahwany, E., Saber, S., Gamal, R., Nagy, F., et al. (2015). Blockade of Pge2, Pgd2 receptors confers protection against prepatent schistosomiasis mansoni in mice. *J. Egypt Soc. Parasitol.* 45, 511–520. doi:10.12816/0017911

Abdelhamid, A. M., Saber, S., Youssef, M. E., Gaafar, A. G. A., Eissa, H., Abd-Eldayem, M. A., et al. (2022). Empagliflozin adjunct with metformin for the inhibition of hepatocellular carcinoma progression: emerging approach for new application. *Biomed. and Pharmacother.* 145, 112455. doi:10.1016/j.biopha.2021.112455

Abdelhamid, A. M., Youssef, M. E., Abd El-Fattah, E. E., Gobba, N. A., Gaafar, A. G. A., Girgis, S., et al. (2021). Blunting p38 MAPKα and ERK1/2 activities by empagliflozin enhances the antifibrotic effect of metformin and augments its AMPK-induced NF-κB inactivation in mice intoxicated with carbon tetrachloride. *Life Sci.* 286, 120070. doi:10.1016/j.lfs.2021.120070

Abu-Farha, M., Lanouette, S., Elisma, F., Tremblay, V., Butson, J., Figeys, D., et al. (2011). Proteomic analyses of the SMYD family interactomes identify HSP90 as a novel target for SMYD2. *J. Mol. Cell Biol.* 3, 301–308. doi:10.1093/jmcb/mjr025

Afroz, R., Tanvir, E. M., Tania, M., Fu, J., Kamal, M. A., and Khan, M. A. (2022). LPS/TLR4 pathways in breast cancer: insights into cell signalling. *Curr. Med. Chem.* 29, 2274–2289. doi:10.2174/0929867328666210811145043

Akahane, K., Sanda, T., Mansour, M. R., Radimerski, T., Deangelo, D. J., Weinstock, D. M., et al. (2016). HSP90 inhibition leads to degradation of the TYK2 kinase and

apoptotic cell death in T-cell acute lymphoblastic leukemia. *Leukemia* 30, 219–228. doi:10.1038/leu.2015.222

Akram, A., Khalil, S., Halim, S. A., Younas, H., Iqbal, S., and Mehar, S. (2018). Therapeutic uses of HSP90 inhibitors in non-small cell lung carcinoma (NSCLC). *Curr. Drug Metab.* 19, 335–341. doi:10.2174/1389200219666180307122441

Albadari, N., Deng, S., and Li, W. (2019). The transcriptional factors HIF-1 and HIF-2 and their novel inhibitors in cancer therapy. *Expert Opin. Drug Discov.* 14, 667–682. doi:10.1080/17460441.2019.1613370

Ambati, S. R., Lopes, E. C., Kosugi, K., Mony, U., Zehir, A., Shah, S. K., et al. (2014). Pre-clinical efficacy of PU-H71, a novel HSP90 inhibitor, alone and in combination with bortezomib in Ewing sarcoma. *Mol. Oncol.* 8, 323–336. doi:10.1016/j.molonc.2013.12.005

Anand, S., Stedham, F., Beer, P., Gudgin, E., Ortmann, C. A., Bench, A., et al. (2011). Effects of the JAK2 mutation on the hematopoietic stem and progenitor compartment in human myeloproliferative neoplasms. *Blood* 118, 177–181. doi:10.1182/blood-2010-12-327593

Anwar, M. M., Shalaby, M., Embaby, A. M., Saeed, H., Agwa, M. M., and Hussein, A. (2020). Prodigiosin/PU-H71 as a novel potential combined therapy for triple negative breast cancer (TNBC): preclinical insights. *Sci. Rep.* 10, 14706. doi:10.1038/s41598-020-71157-w

Bachman, A. B., Keramisanou, D., Xu, W., Beebe, K., Moses, M. A., Vasantha Kumar, M. V., et al. (2018). Phosphorylation induced cochaperone unfolding promotes kinase recruitment and client class-specific Hsp90 phosphorylation. *Nat. Commun.* 9, 265. doi:10.1038/s41467-017-02711-w

Baffi, T. R., Lordén, G., Wozniak, J. M., Feichtner, A., Yeung, W., Kornev, A. P., et al. (2021). mTORC2 controls the activity of PKC and Akt by phosphorylating a conserved TOR interaction motif. *Sci. Signal.* 14, eabe4509. doi:10.1126/scisignal.abe4509

Bagratuni, T., Wu, P., Gonzalez De Castro, D., Davenport, E. L., Dickens, N. J., Walker, B. A., et al. (2010). XBP1s levels are implicated in the biology and outcome of myeloma mediating different clinical outcomes to thalidomide-based treatments. *Blood* 116, 250–253. doi:10.1182/blood-2010-01-263236

Bahar, M. E., Kim, H. J., and Kim, D. R. (2023). Targeting the RAS/RAF/MAPK pathway for cancer therapy: from mechanism to clinical studies. *Signal Transduct. Target. Ther.* 8, 455. doi:10.1038/s41392-023-01705-z

Baker, J. D., Ozsan, I., Rodriguez Ospina, S., Gulick, D., and Blair, L. J. (2018). Hsp90 heterocomplexes regulate steroid hormone receptors: from stress response to psychiatric disease. *Int. J. Mol. Sci.* 20, 79. doi:10.3390/ijms20010079

Bao, F., Hao, P., An, S., Yang, Y., Liu, Y., Hao, Q., et al. (2021). Akt scaffold proteins: the key to controlling specificity of Akt signaling. *Am. J. Physiology-Cell Physiology* 321, C429–C442. doi:10.1152/ajpcell.00146.2020

Barginear, M., Van Poznak, C., Rosen, N., Modi, S., Hudis, C., and Budman, D. (2008). The heat shock protein 90 chaperone complex: an evolving therapeutic target. *Curr. cancer drug targets* 8, 522–532. doi:10.2174/156800908785699379

Basso, A. D., Solit, D. B., Chiosis, G., Giri, B., Tsichlis, P., and Rosen, N. (2002). Akt forms an intracellular complex with heat shock protein 90 (Hsp90) and Cdc37 and is destabilized by inhibitors of Hsp90 function. *J. Biol. Chem.* 277, 39858–39866. doi:10.1074/jbc.M206322200

Beeram, M., Patnaik, A., and Rowinsky, E. K. (2005). Raf: a strategic target for therapeutic development against cancer. *J. Clin. Oncol.* 23, 6771–6790. doi:10.1200/JCO.2005.08.036

Birbo, B., Madu, E. E., Madu, C. O., Jain, A., and Lu, Y. (2021). Role of HSP90 in cancer. *Int. J. Mol. Sci.* 22, 10317. doi:10.3390/ijms221910317

Breinig, M., Caldas-Lopes, E., Goeppert, B., Malz, M., Rieker, R., Bergmann, F., et al. (2009). Targeting heat shock protein 90 with non-quinone inhibitors: a novel chemotherapeutic approach in human hepatocellular carcinoma. *Hepatology* 50, 102–112. doi:10.1002/hep.22912

Breinig, M., Mayer, P., Harjung, A., Goeppert, B., Malz, M., Penzel, R., et al. (2011). Heat shock protein 90-sheltered overexpression of insulin-like growth factor 1 receptor contributes to malignancy of thymic epithelial tumors. *Clin. Cancer Res.* 17, 2237–2249. doi:10.1158/1078-0432.CCR-10-1689

Briones, J. (2010). Targeted therapy of BCL6-dependent diffuse large B-cell lymphomas by heat-shock protein 90 inhibition. *Expert Rev. Hematol.* 3, 157–159. doi:10.1586/ehm.10.11

Broekgaarden, M., Weijer, R., Van Gulik, T. M., Hamblin, M. R., and Heger, M. (2015). Tumor cell survival pathways activated by photodynamic therapy: a molecular basis for pharmacological inhibition strategies. *Cancer Metastasis Rev.* 34, 643–690. doi:10.1007/s10555-015-9588-7

Bruix, J., Boix, L., Sala, M., and Llovet, J. M. (2004). Focus on hepatocellular carcinoma. *Cancer Cell* 5, 215–219. doi:10.1016/s1535-6108(04)00058-3

Bulatowicz, J. J., and Wood, T. L. (2022). Activation versus inhibition of IGF1R: a dual role in breast tumorigenesis. *Front. Endocrinol. (Lausanne)* 13, 911079. doi:10.3389/fendo.2022.911079

Caldas-Lopes, E., Cerchietti, L., Ahn, J. H., Clement, C. C., Robles, A. I., Rodina, A., et al. (2009). Hsp90 inhibitor PU-H71, a multimodal inhibitor of malignancy, induces complete responses in triple-negative breast cancer models. *Proc. Natl. Acad. Sci.* 106, 8368–8373. doi:10.1073/pnas.0903392106

Calvo-Vidal, M. N., Zamponi, N., Krumsiek, J., Stockslager, M. A., Revuelta, M. V., Phillip, J. M., et al. (2021). Oncogenic HSP90 facilitates metabolic alterations in aggressive B-cell lymphomas. *Cancer Res.* 81, 5202–5216. doi:10.1158/0008-5472.CAN-21-2734

Campbell, P. J., and Green, A. R. (2006). The myeloproliferative disorders. *N. Engl. J. Med.* 355, 2452–2466. doi:10.1056/NEJMra063728

Carter, B. Z., Mak, P. Y., Muftuoglu, M., Tao, W., Ke, B., Pei, J., et al. (2023). Epichaperome inhibition targets TP53-mutant AML and AML stem/progenitor cells. *Blood* 142, 1056–1070. doi:10.1182/blood.2022019047

Caruso Bavisotto, C., Alberti, G., Vitale, A. M., Paladino, L., Campanella, C., Rappa, F., et al. (2020). Hsp60 post-translational modifications: functional and pathological consequences. *Front. Mol. Biosci.* 7, 95. doi:10.3389/fmolb.2020.00095

Cavenagh, J., Oakervee, H., Baetiong-Caguioa, P., Davies, F., Gharibo, M., Rabin, N., et al. (2017). A phase I/II study of KW-2478, an Hsp90 inhibitor, in combination with bortezomib in patients with relapsed/refractory multiple myeloma. *Br. J. Cancer* 117, 1295–1302. doi:10.1038/bjc.2017.302

Cerchietti, L. C., Hatzi, K., Caldas-Lopes, E., Yang, S. N., Figueroa, M. E., Morin, R. D., et al. (2010). BCL6 repression of EP300 in human diffuse large B cell lymphoma cells provides a basis for rational combinatorial therapy. *J. Clin. Investigation* 120, 4569–4582. doi:10.1172/JCI42869

Cerchietti, L. C., Lopes, E. C., Yang, S. N., Hatzi, K., Bunting, K. L., Tsikitas, L. A., et al. (2009). A purine scaffold Hsp90 inhibitor destabilizes BCL-6 and has specific antitumor activity in BCL-6–dependent B cell lymphomas. *Nat. Med.* 15, 1369–1376. doi:10.1038/nm.2059

Chakrabarty, S., Wang, S., Roychowdhury, T., Ginsberg, S. D., and Chiosis, G. (2024). Introducing dysfunctional Protein-Protein Interactome (dfPPI) – a platform for systems-level protein-protein interaction (PPI) dysfunction investigation in disease. *Curr. Opin. Struct. Biol.* 88, 102886. doi:10.1016/j.sbi.2024.102886

Chakraborty, S. N., Leng, X., Perazzona, B., Sun, X., Lin, Y. H., and Arlinghaus, R. B. (2016). Combination of JAK2 and HSP90 inhibitors: an effective therapeutic option in drug-resistant chronic myelogenous leukemia. *Genes Cancer* 7, 201–208. doi:10.18632/genesandcancer.111

Chandarlapaty, S., Sawai, A., Ye, Q., Scott, A., Silinski, M., Huang, K., et al. (2008). SNX2112, a synthetic heat shock protein 90 inhibitor, has potent antitumor activity against HER kinase–dependent cancers. *Clin. Cancer Res.* 14, 240–248. doi:10.1158/1078-0432.CCR-07-1667

Chang, Y.-W., Wang, Y.-C., Zhang, X.-X., Iqbal, J., Lu, M.-X., and Du, Y.-Z. (2021). Transcriptional regulation of small heat shock protein genes by heat shock factor 1 (HSF1) in Liriomyza trifolii under heat stress. *Cell Stress Chaperones* 26, 835–843. doi:10.1007/s12192-021-01224-2

Chen, I.-C., Sethy, B., and Liou, J.-P. (2020). Recent update of HDAC inhibitors in lymphoma. *Front. Cell Dev. Biol.* 8, 576391. doi:10.3389/fcell.2020.576391

Chen, T. L., Harrington, B., Truxall, J., Wasmuth, R., Prouty, A., Sloan, S., et al. (2021). Preclinical evaluation of the Hsp90 inhibitor SNX-5422 in ibrutinib resistant CLL. *J. Hematol. Oncol.* 14, 36. doi:10.1186/s13045-021-01039-9

Cheng, X. (2024). A comprehensive review of HER2 in cancer biology and therapeutics. *Genes* 15, 903. doi:10.3390/genes15070903

Chin, Y., Gumilar, K. E., Li, X. G., Tjokroprawiro, B. A., Lu, C. H., Lu, J., et al. (2023). Targeting HSF1 for cancer treatment: mechanisms and inhibitor development. *Theranostics* 13, 2281–2300. doi:10.7150/thno.82431

Chiosis, G., Kang, Y., and Sun, W. (2008). Discovery and development of purine-scaffold Hsp90 inhibitors. *Expert Opin. drug Discov.* 3, 99–114. doi:10.1517/17460441.3.1.99

Chiosis, G., Vilenchik, M., Kim, J., and Solit, D. (2004). Hsp90: the vulnerable chaperone. *Drug Discov. today* 9, 881–888. doi:10.1016/S1359-6446(04)03245-3

Ci, W., Polo, J. M., and Melnick, A. (2008). B-cell lymphoma 6 and the molecular pathogenesis of diffuse large B-cell lymphoma. *Curr. Opin. Hematol.* 15, 381–390. doi:10.1097/MOH.0b013e328302c7df

Ciesielska, A., Matyjek, M., and Kwiatkowska, K. (2021). TLR4 and CD14 trafficking and its influence on LPS-induced pro-inflammatory signaling. *Cell. Mol. Life Sci.* 78, 1233–1261. doi:10.1007/s00018-020-03656-y

Collier, M. P., and Benesch, J. L. P. (2020). Small heat-shock proteins and their role in mechanical stress. *Cell Stress Chaperones* 25, 601–613. doi:10.1007/s12192-020-01095-z

Cserni, G., Quinn, C. M., Foschini, M. P., Bianchi, S., Callagy, G., Chmielik, E., et al. (2021). Triple-negative breast cancer histological subtypes with a favourable prognosis. *Cancers* 13, 5694. doi:10.3390/cancers13225694

Culjkovic-Kraljacic, B., Fernando, T. M., Marullo, R., Calvo-Vidal, N., Verma, A., Yang, S., et al. (2016). Combinatorial targeting of nuclear export and translation of RNA inhibits aggressive B-cell lymphomas. *Blood* 127, 858–868. doi:10.1182/blood-2015-05-645069

Cyran, A. M., and Zhitkovich, A. (2022). Heat shock proteins and HSF1 in cancer. *Front. Oncol.* 12, 860320. doi:10.3389/fonc.2022.860320

De Almeida, S., Regimbeau, M., Jego, G., Garrido, C., Girodon, F., and Hermetet, F. (2020). Heat shock proteins and PD-1/PD-L1 as potential therapeutic targets in myeloproliferative neoplasms. *Cancers* 12, 2592. doi:10.3390/cancers12092592

Digwal, C. S., Sharma, S., Santhaseela, A. R., Ginsberg, S. D., and Chiosis, G. (2022). "Epichaperomes as a gateway to understanding, diagnosing, and treating disease through rebalancing protein–protein interaction networks," in *Protein homeostasis in drug discovery.*, 1–26.

Dimri, M., and Satyanarayana, A. (2020). Molecular signaling pathways and therapeutic targets in hepatocellular carcinoma. *Cancers* 12, 491. doi:10.3390/cancers12020491

Duan, X., Iwanowycz, S., Ngoi, S., Hill, M., Zhao, Q., and Liu, B. (2021). Molecular chaperone GRP94/GP96 in cancers: oncogenesis and therapeutic target. *Front. Oncol.* 11, 629846. doi:10.3389/fonc.2021.629846

Dunn, W. G., Mcloughlin, M. A., and Vassiliou, G. S. (2024). Clonal hematopoiesis and hematological malignancy. *J. Clin. Investigation* 134, e180065. doi:10.1172/JCI180065

Dunphy, M. P. S., Pressl, C., Pillarsetty, N., Grkovski, M., Modi, S., Jhaveri, K., et al. (2020). First-in-Human trial of epichaperome-targeted PET in patients with cancer. *Clin. Cancer Res.* 26, 5178–5187. doi:10.1158/1078-0432.CCR-19-3704

Eccles, S. A., Massey, A., Raynaud, F. I., Sharp, S. Y., Box, G., Valenti, M., et al. (2008). NVP-AUY922: a novel heat shock protein 90 inhibitor active against xenograft tumor growth, angiogenesis, and metastasis. *Cancer Res.* 68, 2850–2860. doi:10.1158/0008-5472.CAN-07-5256

El-Kashef, D. H., Youssef, M. E., Nasr, M., Alrouji, M., Alhajlah, S., Alomeir, O., et al. (2022). Pimitespib, an HSP90 inhibitor, augments nifuroxazide-induced disruption in the IL-6/STAT3/HIF-1α autocrine loop in rats with bleomycin-challenged lungs: evolutionary perspective in managing pulmonary fibrosis. *Biomed. and Pharmacother.* 153, 113487. doi:10.1016/j.biopha.2022.113487

El–Serag, H. B., and Rudolph, K. L. (2007). Hepatocellular carcinoma: epidemiology and molecular carcinogenesis. *Gastroenterology* 132, 2557–2576. doi:10.1053/j.gastro.2007.04.061

Elster, N., Collins, D. M., Toomey, S., Crown, J., Eustace, A. J., and Hennessy, B. T. (2015). HER2-family signalling mechanisms, clinical implications and targeting in breast cancer. *Breast Cancer Res. Treat.* 149, 5–15. doi:10.1007/s10549-014-3250-x

Farazi, P. A., and Depinho, R. A. (2006). Hepatocellular carcinoma pathogenesis: from genes to environment. *Nat. Rev. Cancer* 6, 674–687. doi:10.1038/nrc1934

Fernando, T. M., Marullo, R., Pera Gresely, B., Phillip, J. M., Yang, S. N., Lundell-Smith, G., et al. (2019). BCL6 evolved to enable stress tolerance in vertebrates and is broadly required by cancer cells to adapt to stress. *Cancer Discov.* 9, 662–679. doi:10.1158/2159-8290.CD-17-1444

Firnau, M.-B., and Brieger, A. (2022). CK2 and the hallmarks of cancer. *Biomedicines* 10, 1987. doi:10.3390/biomedicines10081987

Fu, J., Su, X., Li, Z., Deng, L., Liu, X., Feng, X., et al. (2021). HGF/c-MET pathway in cancer: from molecular characterization to clinical evidence. *Oncogene* 40, 4625–4651. doi:10.1038/s41388-021-01863-w

Fusco, N., Sajjadi, E., Venetis, K., Ivanova, M., Andaloro, S., Guerini-Rocco, E., et al. (2022). Low-risk triple-negative breast cancers: clinico-pathological and molecular features. *Crit. Rev. Oncology/Hematology* 172, 103643. doi:10.1016/j.critrevonc.2022.103643

Gallerne, C., Prola, A., and Lemaire, C. (2013). Hsp90 inhibition by PU-H71 induces apoptosis through endoplasmic reticulum stress and mitochondrial pathway in cancer cells and overcomes the resistance conferred by Bcl-2. *Biochimica Biophysica Acta (BBA) - Mol. Cell Res.* 1833, 1356–1366. doi:10.1016/j.bbamcr.2013.02.014

Gao, C., Peng, Y. N., Wang, H. Z., Fang, S. L., Zhang, M., Zhao, Q., et al. (2019). Inhibition of heat shock protein 90 as a novel platform for the treatment of cancer. *Curr. Pharm. Des.* 25, 849–855. doi:10.2174/1381612825666190503145944

Gao, S. P., Mark, K. G., Leslie, K., Pao, W., Motoi, N., Gerald, W. L., et al. (2007). Mutations in the EGFR kinase domain mediate STAT3 activation via IL-6 production in human lung adenocarcinomas. *J. Clin. investigation* 117, 3846–3856. doi:10.1172/JCI31871

García-Flores, N., Jiménez-Suárez, J., Garnés-García, C., Fernández-Aroca, D. M., Sabater, S., Andrés, I., et al. (2023). P38 MAPK and radiotherapy: foes or friends? *Cancers (Basel)* 15, 861. doi:10.3390/cancers15030861

George, P., Bali, P., Cohen, P., Tao, J., Guo, F., Sigua, C., et al. (2004). Cotreatment with 17-allylamino-demethoxygeldanamycin and FLT-3 kinase inhibitor PKC412 is highly effective against human acute myelogenous leukemia cells with mutant FLT-3. *Cancer Res.* 64, 3645–3652. doi:10.1158/0008-5472.CAN-04-0006

Gerecitano, J. F., Modi, S., Rampal, R., Drilon, A. E., Fury, M. G., Gounder, M. M., et al. (2015). Phase I trial of the HSP-90 inhibitor PU-H71. *J. Clin. Oncol.* 33, 2537. doi:10.1200/jco.2015.33.15_suppl.2537

Giakountis, A., Moulos, P., Sarris, M. E., Hatzis, P., and Talianidis, I. (2017). Smyd3-associated regulatory pathways in cancer. *Seminars Cancer Biol.* 42, 70–80. doi:10.1016/j.semcancer.2016.08.008

Ginsberg, S. D., Joshi, S., Sharma, S., Guzman, G., Wang, T., Arancio, O., et al. (2021). The penalty of stress - epichaperomes negatively reshaping the brain in neurodegenerative disorders. *J. Neurochem.* 159, 958–979. doi:10.1111/jnc.15525

Ginsberg, S. D., Sharma, S., Norton, L., and Chiosis, G. (2023). Targeting stressor-induced dysfunctions in protein–protein interaction networks via epichaperomes. *Trends Pharmacol. Sci.* 44, 20–33. doi:10.1016/j.tips.2022.10.006

Giulino-Roth, L., Van Besien, H. J., Dalton, T., Totonchy, J. E., Rodina, A., Taldone, T., et al. (2017). Inhibition of Hsp90 suppresses PI3K/AKT/mTOR signaling and has antitumor activity in burkitt lymphoma. *Mol. Cancer Ther.* 16, 1779–1790. doi:10.1158/1535-7163.MCT-16-0848

Graner, A. N., Hellwinkel, J. E., Lencioni, A. M., Madsen, H. J., Harland, T. A., Marchando, P., et al. (2017). HSP90 inhibitors in the context of heat shock and the unfolded protein response: effects on a primary canine pulmonary adenocarcinoma cell line. *Int. J. Hyperth.* 33, 303–317. doi:10.1080/02656736.2016.1256503

Guerra, F., Quintana, S., Giustina, S., Mendeluk, G., Jufe, L., Avagnina, M. A., et al. (2021). Investigation of EGFR/pi3k/Akt signaling pathway in seminomas. *Biotech. and Histochem.* 96, 125–137. doi:10.1080/10520295.2020.1776393

Guo, J., Walter, K., Quiros, P. M., Gu, M., Baxter, E. J., Danesh, J., et al. (2024). Inherited polygenic effects on common hematological traits influence clonal selection on JAK2V617F and the development of myeloproliferative neoplasms. *Nat. Genet.* 56, 273–280. doi:10.1038/s41588-023-01638-x

Hadizadeh Esfahani, A., Sverchkova, A., Saez-Rodriguez, J., Schuppert, A. A., and Brehme, M. (2018). A systematic atlas of chaperome deregulation topologies across the human cancer landscape. *PLOS Comput. Biol.* 14, e1005890. doi:10.1371/journal.pcbi.1005890

Hadley, K. E., and Hendricks, D. T. (2014). Use of NQO1 status as a selective biomarker for oesophageal squamous cell carcinomas with greater sensitivity to 17-AAG. *BMC Cancer* 14, 334. doi:10.1186/1471-2407-14-334

Halim, C. E., Deng, S., Ong, M. S., and Yap, C. T. (2020). Involvement of STAT5 in oncogenesis. *Biomedicines* 8, 316. doi:10.3390/biomedicines8090316

Hanahan, D., and Weinberg, R. a. (2011). Hallmarks of cancer: the next generation. *Cell* 144, 646–674. doi:10.1016/j.cell.2011.02.013

Hasan Khudhair, D., Al-Gareeb, A. I., Al-Kuraishy, H. M., El-Kadem, A. H., Elekhnawy, E., Negm, W. A., et al. (2022). Combination of vitamin C and curcumin safeguards against methotrexate-induced acute liver injury in mice by synergistic antioxidant effects. *Front. Med.* 9, 866343. doi:10.3389/fmed.2022.866343

Hatzi, K., and Melnick, A. (2014). Breaking bad in the germinal center: how deregulation of BCL6 contributes to lymphomagenesis. *Trends Mol. Med.* 20, 343–352. doi:10.1016/j.molmed.2014.03.001

He, W., and Hu, H. (2018). BIIB021, an Hsp90 inhibitor: a promising therapeutic strategy for blood malignancies (Review). *Oncol. Rep.* 40, 3–15. doi:10.3892/or.2018.6422

Hedvat, M., Huszar, D., Herrmann, A., Gozgit, J. M., Schroeder, A., Sheehy, A., et al. (2009). The JAK2 inhibitor AZD1480 potently blocks Stat3 signaling and oncogenesis in solid tumors. *Cancer Cell* 16, 487–497. doi:10.1016/j.ccr.2009.10.015

Ho, N., Li, A., Li, S., and Zhang, H. (2012). Heat shock protein 90 and role of its chemical inhibitors in treatment of hematologic malignancies. *Pharmaceuticals* 5, 779–801. doi:10.3390/ph5080779

Hobbs, G. S., Hanasoge Somasundara, A. V., Kleppe, M., Litvin, R., Arcila, M., Ahn, J., et al. (2018). Hsp90 inhibition disrupts JAK-STAT signaling and leads to reductions in splenomegaly in patients with myeloproliferative neoplasms. *Haematologica* 103, e5–e9. doi:10.3324/haematol.2017.177600

Hoter, A., El-Sabban, M. E., and Naim, H. Y. (2018). The HSP90 family: structure, regulation, function, and implications in health and disease. *Int. J. Mol. Sci.* 19, 2560. doi:10.3390/ijms19092560

Howard, F. M., and Olopade, O. I. (2021). Epidemiology of triple-negative breast cancer: a review. *Cancer J.* 27, 8–16. doi:10.1097/PPO.0000000000000500

Hoxhaj, G., and Manning, B. D. (2020). The PI3K–AKT network at the interface of oncogenic signalling and cancer metabolism. *Nat. Rev. Cancer* 20, 74–88. doi:10.1038/s41568-019-0216-7

Hsu, J. L., and Hung, M.-C. (2016). The role of HER2, EGFR, and other receptor tyrosine kinases in breast cancer. *Cancer Metastasis Rev.* 35, 575–588. doi:10.1007/s10555-016-9649-6

Hu, C., Yang, J., Qi, Z., Wu, H., Wang, B., Zou, F., et al. (2020). Heat shock proteins: biological functions, pathological roles, and therapeutic opportunities. *MedComm* 3, e161. doi:10.1002/mco2.161

Hu, H., Tian, M., Ding, C., and Yu, S. (2019). The C/EBP homologous protein (CHOP) transcription factor functions in endoplasmic reticulum stress-induced apoptosis and microbial infection. *Front. Immunol.* 9, 3083. doi:10.3389/fimmu.2018.03083

Hua, Y., White-Gilbertson, S., Kellner, J., Rachidi, S., Usmani, S. Z., Chiosis, G., et al. (2013). Molecular chaperone gp96 is a novel therapeutic target of multiple myeloma. *Clin. Cancer Res.* 19, 6242–6251. doi:10.1158/1078-0432.CCR-13-2083

Inda, M. C., Joshi, S., Wang, T., Bolaender, A., Gandu, S., Koren Iii, J., et al. (2020). The epichaperome is a mediator of toxic hippocampal stress and leads to protein connectivity-based dysfunction. *Nat. Commun.* 11, 319. doi:10.1038/s41467-019-14082-5

Iqbal, N., and Iqbal, N. (2014). Human epidermal growth factor receptor 2 (HER2) in cancers: overexpression and therapeutic implications. *Mol. Biol. Int.* 2014, 852748. doi:10.1155/2014/852748

Iwai, A., Bourboulia, D., Mollapour, M., Jensen-Taubman, S., Lee, S., Donnelly, A. C., et al. (2012). Combined inhibition of Wee1 and Hsp90 activates intrinsic apoptosis in cancer cells. *Cell Cycle* 11, 3649–3655. doi:10.4161/cc.21926

Jaeger, A. M., and Whitesell, L. (2019). HSP90: enabler of cancer adaptation. *Annu. Rev. Cancer Biol.* 3, 275–297. doi:10.1146/annurev-cancerbio-030518-055533

James, C., Ugo, V., Le Couédic, J.-P., Staerk, J., Delhommeau, F., Lacout, C., et al. (2005). A unique clonal JAK2 mutation leading to constitutive signalling causes polycythaemia vera. *nature* 434, 1144–1148. doi:10.1038/nature03546

Jego, G., Hermetet, F., Girodon, F., and Garrido, C. (2019). Chaperoning STAT3/5 by heat shock proteins: interest of their targeting in cancer therapy. *Cancers (Basel)* 12, 21. doi:10.3390/cancers12010021

Jhaveri, K., Taldone, T., Modi, S., and Chiosis, G. (2012). Advances in the clinical development of heat shock protein 90 (Hsp90) inhibitors in cancers. *Biochimica Biophysica Acta (BBA)-Molecular Cell Res.* 1823, 742–755. doi:10.1016/j.bbamcr.2011.10.008

Jhaveri, K. L., Anjos, C. H. D., Taldone, T., Wang, R., Comen, E., Fornier, M., et al. (2020). "Measuring tumor epichaperome expression using [^{124}I] PU-H71 positron emission tomography as a biomarker of response for PU-H71 plus nab-paclitaxel," in *HER2-Negative metastatic breast cancer* (Alexandria, Virginia, United States: JCO Precision Oncology), 1414–1424.

Joshi, S., Gomes, E. D., Wang, T., Corben, A., Taldone, T., Gandu, S., et al. (2021). Pharmacologically controlling protein-protein interactions through epichaperomes for therapeutic vulnerability in cancer. *Commun. Biol.* 4, 1333. doi:10.1038/s42003-021-02842-3

Joshi, S., Wang, T., Araujo, T. L. S., Sharma, S., Brodsky, J. L., and Chiosis, G. (2018). Adapting to stress - chaperome networks in cancer. *Nat. Rev. Cancer* 18, 562–575. doi:10.1038/s41568-018-0020-9

Kakkar, V., Meister-Broekema, M., Minoia, M., Carra, S., and Kampinga, H. H. (2014). Barcoding heat shock proteins to human diseases: looking beyond the heat shock response. *Dis. Models and Mech.* 7, 421–434. doi:10.1242/dmm.014563

Kale, Ş., Korcum, A. F., Dündar, E., and Erin, N. (2020). HSP90 inhibitor PU-H71 increases radiosensitivity of breast cancer cells metastasized to visceral organs and alters the levels of inflammatory mediators. *Naunyn-Schmiedeberg's Archives Pharmacol.* 393, 253–262. doi:10.1007/s00210-019-01725-z

Kamada, T., Tsujii, H., Blakely, E. A., Debus, J., De Neve, W., Durante, M., et al. (2015). Carbon ion radiotherapy in Japan: an assessment of 20 years of clinical experience. *Lancet Oncol.* 16, e93–e100. doi:10.1016/S1470-2045(14)70412-7

Kamal, A., Boehm, M. F., and Burrows, F. J. (2004). Therapeutic and diagnostic implications of Hsp90 activation. *Trends Mol. Med.* 10, 283–290. doi:10.1016/j.molmed.2004.04.006

Kawano, T., Inokuchi, J., Eto, M., Murata, M., and Kang, J. H. (2021). Activators and inhibitors of protein kinase C (PKC): their applications in clinical trials. *Pharmaceutics* 13, 1748. doi:10.3390/pharmaceutics13111748

Kaziales, A., Barkovits, K., Marcus, K., and Richter, K. (2020). Glucocorticoid receptor complexes form cooperatively with the Hsp90 co-chaperones Pp5 and FKBPs. *Sci. Rep.* 10, 10733. doi:10.1038/s41598-020-67645-8

Kelland, L. R., Sharp, S. Y., Rogers, P. M., Myers, T. G., and Workman, P. (1999). DT-diaphorase expression and tumor cell sensitivity to 17-Allylamino,17-demethoxygeldanamycin, an inhibitor of heat shock protein 90. *JNCI J. Natl. Cancer Inst.* 91, 1940–1949. doi:10.1093/jnci/91.22.1940

Khurana, N., Laskar, S., Bhattacharyya, M. K., and Bhattacharyya, S. (2016). Hsp90 induces increased genomic instability toward DNA-damaging agents by tuning down RAD53 transcription. *Mol. Biol. Cell* 27, 2463–2478. doi:10.1091/mbc.E15-12-0867

Kijima, T., Prince, T., Neckers, L., Koga, F., and Fujii, Y. (2019). Heat shock factor 1 (HSF1)-targeted anticancer therapeutics: overview of current preclinical progress. *Expert Opin. Ther. Targets* 23, 369–377. doi:10.1080/14728222.2019.1602119

Kim, Y., Alarcon, S., Lee, S., Lee, M.-J., Giaccone, G., Neckers, L., et al. (2009). Update on Hsp90 inhibitors in clinical trial. *Curr. Top. Med. Chem.* 9, 1479–1492. doi:10.2174/156802609789895728

Klein, U., and Dalla-Favera, R. (2008). Germinal centres: role in B-cell physiology and malignancy. *Nat. Rev. Immunol.* 8, 22–33. doi:10.1038/nri2217

Knudsen, E. S., and Witkiewicz, A. K. (2017). The strange case of CDK4/6 inhibitors: mechanisms, resistance, and combination strategies. *Trends Cancer* 3, 39–55. doi:10.1016/j.trecan.2016.11.006

Koppikar, P., Abdel-Wahab, O., Hedvat, C., Marubayashi, S., Patel, J., Goel, A., et al. (2010). Efficacy of the JAK2 inhibitor INCB16562 in a murine model of MPLW515L-induced thrombocytosis and myelofibrosis. *Blood, J. Am. Soc. Hematol.* 115, 2919–2927. doi:10.1182/blood-2009-04-218842

Koppikar, P., Bhagwat, N., Kilpivaara, O., Manshouri, T., Adli, M., Hricik, T., et al. (2012). Heterodimeric JAK–STAT activation as a mechanism of persistence to JAK2 inhibitor therapy. *Nature* 489, 155–159. doi:10.1038/nature11303

Krämer, O. H., Mahboobi, S., and Sellmer, A. (2014). Drugging the HDAC6–HSP90 interplay in malignant cells. *Trends Pharmacol. Sci.* 35, 501–509. doi:10.1016/j.tips.2014.08.001

Kuai, Y., Gong, X., Ding, L., Li, F., Lei, L., Gong, Y., et al. (2018). Wilms' tumor 1-associating protein plays an aggressive role in diffuse large B-cell lymphoma and forms a complex with BCL6 via Hsp90. *Cell Commun. Signal.* 16, 50. doi:10.1186/s12964-018-0258-6

Kubra, K.-T., Uddin, M. A., Akhter, M. S., and Barabutis, N. (2020). Hsp90 inhibitors induce the unfolded protein response in bovine and mice lung cells. *Cell. Signal.* 67, 109500. doi:10.1016/j.cellsig.2019.109500

Kucine, N., Marubayashi, S., Bhagwat, N., Papalexi, E., Koppikar, P., Sanchez Martin, M., et al. (2015). Tumor-specific HSP90 inhibition as a therapeutic approach in JAK-mutant acute lymphoblastic leukemias. *Blood* 126, 2479–2483. doi:10.1182/blood-2015-03-635821

Kunachowicz, D., Król-Kulikowska, M., Raczycka, W., Sleziak, J., Błażejewska, M., and Kulbacka, J. (2024). Heat shock proteins, a double-edged sword: significance in cancer progression, chemotherapy resistance and novel therapeutic perspectives. *Cancers* 16, 1500. doi:10.3390/cancers16081500

Kuykendall, A. T., Horvat, N. P., Pandey, G., Komrokji, R., and Reuther, G. W. (2020). Finding a jill for JAK: assessing past, present, and future JAK inhibitor combination approaches in myelofibrosis. *Cancers* 12, 2278. doi:10.3390/cancers12082278

Lee, Y., Li, H. K., Masaoka, A., Sunada, S., Hirakawa, H., Fujimori, A., et al. (2016). The purine scaffold Hsp90 inhibitor PU-H71 sensitizes cancer cells to heavy ion radiation by inhibiting DNA repair by homologous recombination and non-homologous end joining. *Radiother. Oncol.* 121, 162–168. doi:10.1016/j.radonc.2016.08.029

Levine, R. L., Koppikar, P., Marubayashi, S., Bhagwat, N., Taldone, T., Park, C. Y., et al. (2012). Combination therapy using JAK2 and HSP90 inhibitors increased efficacy in myelofibrosis *in vivo*. *Blood* 120, 805. doi:10.1182/blood.v120.21.805.805

Li, H. K., Matsumoto, Y., Furusawa, Y., and Kamada, T. (2016). PU-H71, a novel Hsp90 inhibitor, as a potential cancer-specific sensitizer to carbon-ion beam therapy. *J. Radiat. Res.* 57, 572–575. doi:10.1093/jrr/rrw054

Li, H. K., Morokoshi, Y., Daino, K., Furukawa, T., Kamada, T., Saga, T., et al. (2015). Transcriptomic signatures of auger electron radioimmunotherapy using nuclear targeting 111In-Trastuzumab for potential combination therapies. *Cancer Biotherapy Radiopharm.* 30, 349–358. doi:10.1089/cbr.2015.1882

Li, S., and Adams, P. D. (2023). Targeting the epichaperome to combat AML. *Blood* 142, 1031–1032. doi:10.1182/blood.2023021386

Li, T., Jiang, H.-L., Tong, Y.-G., and Lu, J.-J. (2018). Targeting the Hsp90-Cdc37-client protein interaction to disrupt Hsp90 chaperone machinery. *J. Hematol. and Oncol.* 11, 59. doi:10.1186/s13045-018-0602-8

Li, Z.-N., and Luo, Y. (2023). HSP90 inhibitors and cancer: prospects for use in targeted therapies (Review). *Oncol. Rep.* 49, 6. doi:10.3892/or.2022.8443

Lisi, L., Mcguire, S., Sharp, A., Chiosis, G., Navarra, P., Feinstein, D. L., et al. (2013). The novel HSP90 inhibitor, PU-H71, suppresses glial cell activation but weakly affects clinical signs of EAE. *J. Neuroimmunol.* 255, 1–7. doi:10.1016/j.jneuroim.2012.10.008

Liu, H., Lu, Z., Shi, X., Liu, L., Zhang, P., Golemis, E. A., et al. (2021a). HSP90 inhibition downregulates DNA replication and repair genes via E2F1 repression. *J. Biol. Chem.* 297, 100996. doi:10.1016/j.jbc.2021.100996

Liu, P., Xiao, J., Wang, Y., Song, X., Huang, L., Ren, Z., et al. (2021b). Posttranslational modification and beyond: interplay between histone deacetylase 6 and heat-shock protein 90. *Mol. Med.* 27, 110. doi:10.1186/s10020-021-00375-3

Liu, Y., Feng, J., Yuan, K., Wu, Z., Hu, L., Lu, Y., et al. (2022). The oncoprotein BCL6 enables solid tumor cells to evade genotoxic stress. *eLife* 11, e69255. doi:10.7554/eLife.69255

Liu, Y., Wang, X., Wang, J., Jin, Q., Cai, W., Pan, C., et al. (2023). *Class* II*b histone deacetylase participates in postoperative cognitive dysfunction in elderly mice via HSP90/GR signaling pathway*.

Lokeshwar, V. B. (2012). Wee1-Hsp90 inhibitor combination treatment. *Cell Cycle* 11, 3722. doi:10.4161/cc.22119

Lopes, E., Joungnam, K., Rondina, A., Moulick, K., and Chiosis, G. (2007). Targeting basal-like breast cancer via purine-scaffold Hsp90 inhibitors. *Cancer Res.* 67, 3964.

Lubina-Dąbrowska, N., Stepień, A., Sulkowski, G., Dąbrowska-Bouta, B., Langfort, J., and Chalimoniuk, M. (2017). Effects of IFN-β1a and IFN-β1b treatment on the expression of cytokines, inducible NOS (NOS type II), and myelin proteins in animal model of multiple sclerosis. *Archivum Immunol. Ther. Exp.* 65, 325–338. doi:10.1007/s00005-017-0458-6

Luo, W., Sun, W., Taldone, T., Rodina, A., and Chiosis, G. (2010). Heat shock protein 90 in neurodegenerative diseases. *Mol. Neurodegener.* 5, 24. doi:10.1186/1750-1326-5-24

Luque Paz, D., Kralovics, R., and Skoda, R. C. (2023). Genetic basis and molecular profiling in myeloproliferative neoplasms. *Blood* 141, 1909–1921. doi:10.1182/blood.2022017578

Magwenyane, A. M., Ugbaja, S. C., Amoako, D. G., Somboro, A. M., Khan, R. B., and Kumalo, H. M. (2022). Heat shock protein 90 (HSP90) inhibitors as anticancer medicines: a review on the computer-aided drug discovery approaches over the past five years. *Comput. Math. Methods Med.* 2022, 2147763. doi:10.1155/2022/2147763

Mahajan, S., Grkovski, M., Staton, K. D., Ravassa, S., Domfe, K., Strauss, H. W., et al. (2024). Epichaperome-targeted myocardial imaging by 124I-PU-H71 PET. *Clin. Transl. Imaging*. doi:10.1007/s40336-024-00658-9

Mario, C. (2007). Somatic mutations of JAK2 exon 12 as a molecular basis of erythrocytosis. *Haematologica* 92, 1585–1589. doi:10.3324/haematol.11506

Martinelli, E., Morgillo, F., Troiani, T., and Ciardiello, F. (2017). Cancer resistance to therapies against the EGFR-RAS-RAF pathway: the role of MEK. *Cancer Treat. Rev.* 53, 61–69. doi:10.1016/j.ctrv.2016.12.001

Martinet, J., Sugita, M., Alhomoud, M., Abad, C., Chiosis, G., Roboz, G. J., et al. (2022). Impact of epichaperome inhibitor PU-H71 on anti-tumor T cell responses and its implications for immune and cellular therapy. *Blood* 140, 1171–1172. doi:10.1182/blood-2022-163563

Marubayashi, S., Koppikar, P., Taldone, T., Abdel-Wahab, O., West, N., Bhagwat, N., et al. (2010). HSP90 is a therapeutic target in JAK2-dependent myeloproliferative neoplasms in mice and humans. *J. Clin. Investigation* 120, 3578–3593. doi:10.1172/JCI42442

Marzec, M., Eletto, D., and Argon, Y. (2012). GRP94: an HSP90-like protein specialized for protein folding and quality control in the endoplasmic reticulum. *Biochimica Biophysica Acta (BBA) - Mol. Cell Res.* 1823, 774–787. doi:10.1016/j.bbamcr.2011.10.013

Masser, A. E., Ciccarelli, M., and Andréasson, C. (2020). Hsf1 on a leash – controlling the heat shock response by chaperone titration. *Exp. Cell Res.* 396, 112246. doi:10.1016/j.yexcr.2020.112246

Matsumoto, K., Umitsu, M., De Silva, D. M., Roy, A., and Bottaro, D. P. (2017). Hepatocyte growth factor/MET in cancer progression and biomarker discovery. *Cancer Sci.* 108, 296–307. doi:10.1111/cas.13156

Mbofung, R. M., Mckenzie, J. A., Malu, S., Zhang, M., Peng, W., Liu, C., et al. (2017). HSP90 inhibition enhances cancer immunotherapy by upregulating interferon response genes. *Nat. Commun.* 8, 451. doi:10.1038/s41467-017-00449-z

Mclachlan, T., Matthews, W. C., Jackson, E. R., Staudt, D. E., Douglas, A. M., Findlay, I. J., et al. (2022). B-Cell lymphoma 6 (BCL6): from master regulator of humoral immunity to oncogenic driver in pediatric cancers. *Mol. Cancer Res.* 20, 1711–1723. doi:10.1158/1541-7786.MCR-22-0567

Medina, M. A., Oza, G., Sharma, A., Arriaga, L. G., Hernández Hernández, J. M., Rotello, V. M., et al. (2020). Triple-negative breast cancer: a review of conventional and advanced therapeutic strategies. *Int. J. Environ. Res. Public Health* 17, 2078. doi:10.3390/ijerph17062078

Mellatyar, H., Talaei, S., Pilehvar-Soltanahmadi, Y., Barzegar, A., Akbarzadeh, A., Shahabi, A., et al. (2018). Targeted cancer therapy through 17-DMAG as an Hsp90 inhibitor: overview and current state of the art. *Biomed. Pharmacother.* 102, 608–617. doi:10.1016/j.biopha.2018.03.102

Merugu, S., Sharma, S., Kaner, J., Digwal, C., Sugita, M., Joshi, S., et al. (2020). "Chapter Thirteen - chemical probes and methods for single-cell detection and quantification of epichaperomes in hematologic malignancies," in *Methods in enzymology*. Editor D. M. Chenoweth (Academic Press), 289–311.

Messaoudi, S., Peyrat, J. F., Brion, J. D., and Alami, M. (2008). Recent advances in Hsp90 inhibitors as antitumor agents. *Anti-Cancer Agents Med. Chem.* 8, 761–782. doi:10.2174/187152008785914824

Mintz, M. A., and Cyster, J. G. (2020). T follicular helper cells in germinal center B cell selection and lymphomagenesis. *Immunol. Rev.* 296, 48–61. doi:10.1111/imr.12860

Miyata, Y. (2005). Hsp90 inhibitor geldanamycin and its derivatives as novel cancer chemotherapeutic agents. *Curr. Pharm. Des.* 11, 1131–1138. doi:10.2174/1381612053507585

Miyata, Y., Nakamoto, H., and Neckers, L. (2013). The therapeutic target Hsp90 and cancer hallmarks. *Curr. Pharm. Des.* 19, 347–365. doi:10.2174/138161213804143725

Mladenov, E., Magin, S., Soni, A., and Iliakis, G. (2013). DNA double-strand break repair as determinant of cellular radiosensitivity to killing and target in radiation therapy. *Front. Oncol.* 3, 113. doi:10.3389/fonc.2013.00113

Modi, S., Stopeck, A., Linden, H., Solit, D., Chandarlapaty, S., Rosen, N., et al. (2011). HSP90 inhibition is effective in breast cancer: a phase II trial of tanespimycin (17-AAG) plus trastuzumab in patients with HER2-positive metastatic breast cancer progressing on trastuzumab. *Clin. Cancer Res.* 17, 5132–5139. doi:10.1158/1078-0432.CCR-11-0072

Mohammed, O. A., Abdel-Reheim, M. A., Alamri, M. M. S., Alfaifi, J., Adam, M. I. E., Saleh, L. A., et al. (2023a). STA9090 as a potential therapeutic agent for liver fibrosis by modulating the HSP90/tβrii/proteasome interplay: novel insights from *in vitro* and *in vivo* investigations. *Pharmaceuticals* 16, 1080. doi:10.3390/ph16081080

Mohammed, O. A., Abdel-Reheim, M. A., Saleh, L. A., Alamri, M. M. S., Alfaifi, J., Adam, M. I. E., et al. (2023b). Alvespimycin exhibits potential anti-TGF-β signaling in the setting of a proteasome activator in rats with bleomycin-induced pulmonary fibrosis: a promising novel approach. *Pharmaceuticals* 16, 1123. doi:10.3390/ph16081123

Mollapour, M., and Neckers, L. (2012). Post-translational modifications of Hsp90 and their contributions to chaperone regulation. *Biochimica Biophysica Acta (BBA) - Mol. Cell Res.* 1823, 648–655. doi:10.1016/j.bbamcr.2011.07.018

Mollapour, M., Tsutsumi, S., and Neckers, L. (2010). Hsp90 phosphorylation, Wee1 and the cell cycle. *Cell Cycle* 9, 2310–2316. doi:10.4161/cc.9.12.12054

Mookerjee, S. A., Gerencser, A. A., Nicholls, D. G., and Brand, M. D. (2017). Quantifying intracellular rates of glycolytic and oxidative ATP production and consumption using extracellular flux measurements. *J. Biol. Chem.* 292, 7189–7207. doi:10.1074/jbc.M116.774471

Moriwaki, Y., Kim, Y.-J., Ido, Y., Misawa, H., Kawashima, K., Endo, S., et al. (2008). L347P PINK1 mutant that fails to bind to Hsp90/Cdc37 chaperones is rapidly degraded in a proteasome-dependent manner. *Neurosci. Res.* 61, 43–48. doi:10.1016/j.neures.2008.01.006

Moulick, K., Ahn, J., Zong, H., Rodina, A., Cerchietti, L., Dagama, E., et al. (2011). Abstract 1263: affinity-based proteomics reveal cancer-specific networks coordinated by Hsp90. *Nat. Chem. Biol.* 7, 818–826. doi:10.1038/nchembio.670

Mullally, A. (2017). MPN: next questions: potential new targets for MPN beside JAK2. *Myeloma Leukemia* 17, S99–S101. doi:10.1016/j.clml.2017.08.048

Musha, A., Yoshida, Y., Takahashi, T., Ando, K., Funayama, T., Kobayashi, Y., et al. (2012). Synergistic effect of heat shock protein 90 inhibitor, 17-allylamino-17-demethoxygeldanamycin and X-rays, but not carbon-ion beams, on lethality in human oral squamous cell carcinoma cells. *J. Radiat. Res.* 53, 545–550. doi:10.1093/jrr/rrs012

Nasr, M., Kira, A. Y., Saber, S., Essa, E. A., and El-Gizawy, S. A. (2023). Telmisartan-loaded lactosylated chitosan nanoparticles as a liver specific delivery system: synthesis, optimization and targeting efficiency. *AAPS PharmSciTech* 24, 144. doi:10.1208/s12249-023-02605-9

Navarro-Zaragoza, J., Cuenca-Bermejo, L., Almela, P., Laorden, M.-L., and Herrero, M.-T. (2021). Could small heat shock protein HSP27 Be a first-line target for preventing protein aggregation in Parkinson's disease? *Int. J. Mol. Sci.* 22, 3038. doi:10.3390/ijms22063038

Nickoloff, J. A., Boss, M.-K., Allen, C. P., and Larue, S. M. (2017). Translational research in radiation-induced DNA damage signaling and repair. *Transl. Cancer Res.* 6, S875–S891. doi:10.21037/tcr.2017.06.02

Niu, M., Song, S., Su, Z., Wei, L., Li, L., Pu, W., et al. (2021). Inhibition of heat shock protein (HSP) 90 reverses signal transducer and activator of transcription (STAT) 3-mediated muscle wasting in cancer cachexia mice. *Br. J. Pharmacol.* 178, 4485–4500. doi:10.1111/bph.15625

Nolan, A. A., Aboud, N. K., Kolch, W., and Matallanas, D. (2021). Hidden targets in RAF signalling pathways to block oncogenic RAS signalling. *Genes* 12, 553. doi:10.3390/genes12040553

Nouri-Vaskeh, M., Alizadeh, L., Hajiasgharzadeh, K., Mokhtarzadeh, A., Halimi, M., and Baradaran, B. (2020). The role of HSP90 molecular chaperones in hepatocellular carcinoma. *J. Cell. Physiology* 235, 9110–9120. doi:10.1002/jcp.29776

Orea-Soufi, A., Paik, J., Bragança, J., Donlon, T. A., Willcox, B. J., and Link, W. (2022). FOXO transcription factors as therapeutic targets in human diseases. *Trends Pharmacol. Sci.* 43, 1070–1084. doi:10.1016/j.tips.2022.09.010

Ozgur, A., and Tutar, Y. (2014). Heat shock protein 90 inhibitors in Oncology. *Curr. Proteomics* 11, 2–16. doi:10.2174/15701646116666140415224635

Pandey, K., An, H. J., Kim, S. K., Lee, S. A., Kim, S., Lim, S. M., et al. (2019). Molecular mechanisms of resistance to CDK4/6 inhibitors in breast cancer: a review. *Int. J. Cancer* 145, 1179–1188. doi:10.1002/ijc.32020

Pascale, R. M., Simile, M. M., Calvisi, D. F., Frau, M., Muroni, M. R., Seddaiu, M. A., et al. (2005). Role of HSP90, CDC37, and CRM1 as modulators of P16INK4A activity in rat liver carcinogenesis and human liver cancer. *Hepatology* 42, 1310–1319. doi:10.1002/hep.20962

Pastena, P., Perera, H., Martinino, A., Kartsonis, W., and Giovinazzo, F. (2024). Unraveling biomarker signatures in triple-negative breast cancer: a systematic review for targeted approaches. *Int. J. Mol. Sci.* 25, 2559. doi:10.3390/ijms25052559

Pearl, L. H., Prodromou, C., and Workman, P. (2008). The Hsp90 molecular chaperone: an open and shut case for treatment. *Biochem. J.* 410, 439–453. doi:10.1042/BJ20071640

Pemmaraju, N., Gundabolu, K., Pettit, K., Talpaz, M., Podoltsev, N. A., Schiller, G. J., et al. (2019). Phase 1b study of the epichaperome inhibitor PU-H71 administered orally with ruxolitinib continuation for the treatment of patients with myelofibrosis. *Blood* 134, 4178. doi:10.1182/blood-2019-130310

Peng, C., Zhao, F., Li, H., Li, L., Yang, Y., and Liu, F. (2022). HSP90 mediates the connection of multiple programmed cell death in diseases. *Cell Death and Dis.* 13, 929. doi:10.1038/s41419-022-05373-9

Pennisi, R., Ascenzi, P., and Di Masi, A. (2015). Hsp90: a new player in DNA repair? *Biomolecules* 5, 2589–2618. doi:10.3390/biom5042589

Pietra, D., Li, S., Brisci, A., Passamonti, F., Rumi, E., Theocharides, A., et al. (2008). Somatic mutations of JAK2 exon 12 in patients with JAK2 (V617F)-negative myeloproliferative disorders. *Blood* 111, 1686–1689. doi:10.1182/blood-2007-07-101576

Pimienta, G., Herbert, K. M., and Regan, L. (2011). A compound that inhibits the HOP–Hsp90 complex formation and has unique killing effects in breast cancer cell lines. *Mol. Pharm.* 8, 2252–2261. doi:10.1021/mp200346y

Popova, N. V., and Jücker, M. (2021). The role of mTOR signaling as a therapeutic target in cancer. *Int. J. Mol. Sci.* 22, 1743. doi:10.3390/ijms22041743

Qian, J., Hong, S., Wang, S., Zhang, L., Sun, L., Wang, M., et al. (2009). Myeloma cell line–derived, pooled heat shock proteins as a universal vaccine for immunotherapy of multiple myeloma. *Blood, J. Am. Soc. Hematol.* 114, 3880–3889. doi:10.1182/blood-2009-06-227355

Rah, B., Nayak, D., Rasool, R., Chakraborty, S., Katoch, A., Amin, H., et al. (2016). Reprogramming of molecular switching events in UPR driven ER stress: scope for development of anticancer therapeutics. *Curr. Mol. Med.* 16, 690–701. doi:10.2174/1566524016666160829152658

Rampal, R., Ahn, J., Abdel-Wahab, O., Nahas, M., Wang, K., Lipson, D., et al. (2014). Genomic and functional analysis of leukemic transformation of myeloproliferative neoplasms. *Proc. Natl. Acad. Sci. U. S. A.* 111, E5401–E5410. doi:10.1073/pnas.1407792111

Randazzo, M., Terness, P., Opelz, G., and Kleist, C. (2012). Active-specific immunotherapy of human cancers with the heat shock protein Gp96—revisited. *Int. J. Cancer* 130, 2219–2231. doi:10.1002/ijc.27332

Rao, T. N., Hansen, N., Hilfiker, J., Rai, S., Majewska, J.-M., Leković, D., et al. (2019). JAK2-mutant hematopoietic cells display metabolic alterations that can be targeted to treat myeloproliferative neoplasms. *Blood* 134, 1832–1846. doi:10.1182/blood.2019000162

Rastogi, S., Joshi, A., Sato, N., Lee, S., Lee, M.-J., Trepel, J. B., et al. (2024). An update on the status of HSP90 inhibitors in cancer clinical trials. *Cell Stress Chaperones* 29, 519–539. doi:10.1016/j.cstres.2024.05.005

Ravandi, F., Talpaz, M., and Estrov, Z. (2003). Modulation of cellular signaling pathways: prospects for targeted therapy in hematological malignancies. *Clin. Cancer Res.* 9, 535–550.

Reece, C., Kumar, R., Nienow, D., and Nehra, A. (2007). Extending the rationale of combination therapy to unresponsive erectile dysfunction. *Rev. Urology* 9, 197–206.

Ren, J., Chu, Y., Ma, H., Zhang, Y., Zhang, X., Zhao, D., et al. (2014). Epigenetic interventions increase the radiation sensitivity of cancer cells. *Curr. Pharm. Des.* 20, 1857–1865. doi:10.2174/13816128113199990529

Reynolds, T. S., and Blagg, B. S. J. (2024). Extracellular heat shock protein 90 alpha (eHsp90α)'s role in cancer progression and the development of therapeutic strategies. *Eur. J. Med. Chem.* 277, 116736. doi:10.1016/j.ejmech.2024.116736

Rizza, S., and Filomeni, G. (2020). Exploiting S-nitrosylation for cancer therapy: facts and perspectives. *Biochem. J.* 477, 3649–3672. doi:10.1042/BCJ20200064

Roboz, G. J., Sugita, M., Mosquera, J. M., Wilkes, D. C., Nataraj, S., Jimenez-Flores, R. A., et al. (2018). Targeting the epichaperome as an effective precision medicine approach in a novel PML-SYK fusion acute myeloid leukemia. *Blood* 132, 1435. doi:10.1182/blood-2018-99-118764

Rodina, A., Vilenchik, M., Moulick, K., Aguirre, J., Kim, J., Chiang, A., et al. (2007). Selective compounds define Hsp90 as a major inhibitor of apoptosis in small-cell lung cancer. *Nat. Chem. Biol.* 3, 498–507. doi:10.1038/nchembio.2007.10

Rodina, A., Wang, T., Yan, P., Gomes, E. D., Dunphy, M. P. S., Pillarsetty, N., et al. (2016). The epichaperome is an integrated chaperome network that facilitates tumour survival. *Nature* 538, 397–401. doi:10.1038/nature19807

Rodina, A., Xu, C., Digwal, C. S., Joshi, S., Patel, Y., Santhaseela, A. R., et al. (2023). Systems-level analyses of protein-protein interaction network dysfunctions via epichaperomics identify cancer-specific mechanisms of stress adaptation. *Nat. Commun.* 14, 3742. doi:10.1038/s41467-023-39241-7

Roe, S. M., Prodromou, C., O'brien, R., Ladbury, J. E., Piper, P. W., and Pearl, L. H. (1999). Structural basis for inhibition of the Hsp90 molecular chaperone by the antitumor antibiotics radicicol and geldanamycin. *J. Med. Chem.* 42, 260–266. doi:10.1021/jm980403y

Rong, B., and Yang, S. (2018). Molecular mechanism and targeted therapy of Hsp90 involved in lung cancer: new discoveries and developments (Review). *Int. J. Oncol.* 52, 321–336. doi:10.3892/ijo.2017.4214

Roskoski, R. (2014). The ErbB/HER family of protein-tyrosine kinases and cancer. *Pharmacol. Res.* 79, 34–74. doi:10.1016/j.phrs.2013.11.002

Saber, S., Abd El-Kader, E. M., Sharaf, H., El-Shamy, R., El-Saeed, B., Mostafa, A., et al. (2020). Celastrol augments sensitivity of NLRP3 to CP-456773 by modulating HSP-90 and inducing autophagy in dextran sodium sulphate-induced colitis in rats. *Toxicol. Appl. Pharmacol.* 400, 115075. doi:10.1016/j.taap.2020.115075

Saber, S., Hasan, A. M., Mohammed, O. A., Saleh, L. A., Hashish, A. A., Alamri, M. M. S., et al. (2023). Ganetespib (STA-9090) augments sorafenib efficacy via necroptosis induction in hepatocellular carcinoma: implications from preclinical data for a novel therapeutic approach. *Biomed. and Pharmacother.* 164, 114918. doi:10.1016/j.biopha.2023.114918

Saber, S., Mahmoud, A., Helal, N., El-Ahwany, E., and Abdelghany, R. (2018). Liver protective effects of renin-angiotensin system inhibition have No survival benefits in hepatocellular carcinoma induced by repetitive administration of diethylnitrosamine in mice. *Open Access Maced. J. Med. Sci.* 6, 955–960. doi:10.3889/oamjms.2018.167

Sager, R. A., Backe, S. J., Ahanin, E., Smith, G., Nsouli, I., Woodford, M. R., et al. (2022). Therapeutic potential of CDK4/6 inhibitors in renal cell carcinoma. *Nat. Rev. Urol.* 19, 305–320. doi:10.1038/s41585-022-00571-8

Salama, M. F., Liu, M., Clarke, C. J., Espaillat, M. P., Haley, J. D., Jin, T., et al. (2019). PKCα is required for Akt-mTORC1 activation in non-small cell lung carcinoma (NSCLC) with EGFR mutation. *Oncogene* 38, 7311–7328. doi:10.1038/s41388-019-0950-z

Schirrmacher, V. (2019). From chemotherapy to biological therapy: a review of novel concepts to reduce the side effects of systemic cancer treatment (Review). *Int. J. Oncol.* 54, 407–419. doi:10.3892/ijo.2018.4661

Schmauder, L., Sima, S., Hadj, A. B., Cesar, R., and Richter, K. (2022). Binding of the HSF-1 DNA-binding domain to multimeric *C. elegans* consensus HSEs is guided by cooperative interactions. *Sci. Rep.* 12, 8984. doi:10.1038/s41598-022-12736-x

Schopf, F. H., Biebl, M. M., and Buchner, J. (2017). The HSP90 chaperone machinery. *Nat. Rev. Mol. Cell Biol.* 18, 345–360. doi:10.1038/nrm.2017.20

Schroeder, H. T., De Lemos Muller, C. H., Heck, T. G., Krause, M., and Homem De Bittencourt, P. I. (2024). Heat shock response during the resolution of inflammation and its progressive suppression in chronic-degenerative inflammatory diseases. *Cell Stress Chaperones* 29, 116–142. doi:10.1016/j.cstres.2024.01.002

Scott, L. M. (2018). "Inhibitors of the JAK/STAT pathway, with a focus on ruxolitinib and similar agents," in *Resistance of targeted therapies excluding antibodies for lymphomas*. Editor A. J. M. Ferreri (Cham: Springer International Publishing), 107–134.

Seasons, G. M., Pellow, C., Kuipers, H. F., and Pike, G. B. (2024). Ultrasound and neuroinflammation: immune modulation via the heat shock response. *Theranostics* 14, 3150–3177. doi:10.7150/thno.96270

Segawa, T., Fujii, Y., Tanaka, A., Bando, S.-I., Okayasu, R., Ohnishi, K., et al. (2014). Radiosensitization of human lung cancer cells by the novel purine-scaffold Hsp90 inhibitor, PU-H71. *Int. J. Mol. Med.* 33, 559–564. doi:10.3892/ijmm.2013.1594

Seipel, K., Kohler, S., Bacher, U., and Pabst, T. (2023). HSP90 inhibitor PU-H71 in combination with BH3-mimetics in the treatment of acute myeloid leukemia. *Curr. Issues Mol. Biol.* 45, 7011–7026. doi:10.3390/cimb45090443

Serwetnyk, M. A., and Blagg, B. S. J. (2021). The disruption of protein–protein interactions with co-chaperones and client substrates as a strategy towards Hsp90 inhibition. *Acta Pharm. Sin. B* 11, 1446–1468. doi:10.1016/j.apsb.2020.11.015

Shaaban, A. A., Abdelhamid, A. M., Shaker, M. E., Cavalu, S., Maghiar, A. M., Alsayegh, A. A., et al. (2022). Combining the HSP90 inhibitor TAS-116 with metformin effectively degrades the NLRP3 and attenuates inflammasome activation in rats: a new management paradigm for ulcerative colitis. *Biomed. and Pharmacother.* 153, 113247. doi:10.1016/j.biopha.2022.113247

Shinozaki, F., Minami, M., Chiba, T., Suzuki, M., Yoshimatsu, K., Ichikawa, Y., et al. (2006). Depletion of hsp90beta induces multiple defects in B cell receptor signaling. *J. Biol. Chem.* 281, 16361–16369. doi:10.1074/jbc.M600891200

Shirai, Y., Chow, C. C. T., Kambe, G., Suwa, T., Kobayashi, M., Takahashi, I., et al. (2021). An overview of the recent development of anticancer agents targeting the HIF-1 transcription factor. *Cancers* 13, 2813. doi:10.3390/cancers13112813

Sidera, K., and Patsavoudi, E. (2014). HSP90 inhibitors: current development and potential in cancer therapy. *Recent Pat. Anti-Cancer Drug Discov.* 9, 1–20. doi:10.2174/15748928113089990031

Siragusa, M., and Fleming, I. (2016). The eNOS signalosome and its link to endothelial dysfunction. *Pflügers Archiv - Eur. J. Physiology* 468, 1125–1137. doi:10.1007/s00424-016-1839-0

Smyth, T., Van Looy, T., Curry, J. E., Rodriguez-Lopez, A. M., Wozniak, A., Zhu, M., et al. (2012). The HSP90 inhibitor, AT13387, is effective against imatinib-sensitive and -resistant gastrointestinal stromal tumor models. *Mol. Cancer Ther.* 11, 1799–1808. doi:10.1158/1535-7163.MCT-11-1046

Sokol, O., and Durante, M. (2023). Carbon ions for hypoxic tumors: are we making the most of them? *Cancers* 15, 4494. doi:10.3390/cancers15184494

Solárová, Z., Mojžiš, J., and Solár, P. (2015). Hsp90 inhibitor as a sensitizer of cancer cells to different therapies (Review). *Int. J. Oncol.* 46, 907–926. doi:10.3892/ijo.2014.2791

Sosa, R. A., and Forsthuber, T. G. (2011). The critical role of antigen-presentation-induced cytokine crosstalk in the central nervous system in multiple sclerosis and experimental autoimmune encephalomyelitis. *J. Interferon and Cytokine Res.* 31, 753–768. doi:10.1089/jir.2011.0052

Speranza, G., Anderson, L., Chen, A. P., Do, K., Eugeni, M., Weil, M., et al. (2018). First-in-human study of the epichaperome inhibitor PU-H71: clinical results and metabolic profile. *Investig. New Drugs* 36, 230–239. doi:10.1007/s10637-017-0495-3

Staerk, J., and Constantinescu, S. N. (2012). The JAK-STAT pathway and hematopoietic stem cells from the JAK2 V617F perspective. *Jakstat* 1, 184–190. doi:10.4161/jkst.22071

Sumi, M. P., and Ghosh, A. (2022). Hsp90 in human diseases: molecular mechanisms to therapeutic approaches. *Cells* 11, 976. doi:10.3390/cells11060976

Sun, P., Wang, Y., Gao, T., Li, K., Zheng, D., Liu, A., et al. (2021). Hsp90 modulates human sperm capacitation via the Erk1/2 and p38 MAPK signaling pathways. *Reproductive Biol. Endocrinol.* 19, 39. doi:10.1186/s12958-021-00723-2

Szwed, A., Kim, E., and Jacinto, E. (2021). Regulation and metabolic functions of mTORC1 and mTORC2. *Physiol. Rev.* 101, 1371–1426. doi:10.1152/physrev.00026.2020

Tada, M., Yokosuka, O., Fukai, K., Chiba, T., Imazeki, F., Tokuhisa, T., et al. (2005). Hypermethylation of NAD(P)H: quinone oxidoreductase 1 (NQO1) gene in human hepatocellular carcinoma. *J. Hepatol.* 42, 511–519. doi:10.1016/j.jhep.2004.11.024

Tahimic, C. G. T., Wang, Y., and Bikle, D. D. (2013). Anabolic effects of IGF-1 signaling on the skeleton. *Front. Endocrinol.* 4, 6. doi:10.3389/fendo.2013.00006

Terrell, E. M., and Morrison, D. K. (2019). Ras-mediated activation of the raf family kinases. *Cold Spring Harb. Perspect. Med.* 9, a033746. doi:10.1101/cshperspect.a033746

Terwisscha Van Scheltinga, A. G. T., Berghuis, P., Nienhuis, H. H., Timmer-Bosscha, H., Pot, L., Gaykema, S. B. M., et al. (2014). Visualising dual downregulation of insulin-

like growth factor receptor-1 and vascular endothelial growth factor-A by heat shock protein 90 inhibition effect in triple negative breast cancer. *Eur. J. Cancer* 50, 2508–2516. doi:10.1016/j.ejca.2014.06.008

Tramentozzi, E., and Finotti, P. (2019). Effects of purine-scaffold inhibitors on HUVECs: involvement of the purinergic pathway and interference with ATP. Implications for preventing the adverse effects of extracellular Grp94. *Biochem. Biophysics Rep.* 19, 100661. doi:10.1016/j.bbrep.2019.100661

Trendowski, M. (2015). PU-H71: an improvement on nature's solutions to oncogenic Hsp90 addiction. *Pharmacol. Res.* 99, 202–216. doi:10.1016/j.phrs.2015.06.007

Trepel, J., Mollapour, M., Giaccone, G., and Neckers, L. (2010). Targeting the dynamic HSP90 complex in cancer. *Nat. Rev. Cancer* 10, 537–549. doi:10.1038/nrc2887

Ueno, T., Tsukuda, K., Toyooka, S., Ando, M., Takaoka, M., Soh, J., et al. (2012). Strong anti-tumor effect of NVP-AUY922, a novel Hsp90 inhibitor, on non-small cell lung cancer. *Lung Cancer* 76, 26–31. doi:10.1016/j.lungcan.2011.09.011

Ullah, R., Yin, Q., Snell, A. H., and Wan, L. (2022). RAF-MEK-ERK pathway in cancer evolution and treatment. *Seminars Cancer Biol.* 85, 123–154. doi:10.1016/j.semcancer.2021.05.010

Usmani, S. Z., Bona, R. D., Chiosis, G., and Li, Z. (2010). The anti-myeloma activity of a novel purine scaffold HSP90 inhibitor PU-H71 is via inhibition of both HSP90A and HSP90B1. *J. Hematol. and Oncol.* 3, 40. doi:10.1186/1756-8722-3-40

Vagia, E., Mahalingam, D., and Cristofanilli, M. (2020). The landscape of targeted therapies in TNBC. *Cancers* 12, 916. doi:10.3390/cancers12040916

Wang, L., Xie, C., Greggio, E., Parisiadou, L., Shim, H., Sun, L., et al. (2008). The chaperone activity of heat shock protein 90 is critical for maintaining the stability of leucine-rich repeat kinase 2. *J. Neurosci.* 28, 3384–3391. doi:10.1523/JNEUROSCI.0185-08.2008

Wang, M., Shen, A., Zhang, C., Song, Z., Ai, J., Liu, H., et al. (2016). Development of heat shock protein (Hsp90) inhibitors to combat resistance to tyrosine kinase inhibitors through hsp90–kinase interactions. *J. Med. Chem.* 59, 5563–5586. doi:10.1021/acs.jmedchem.5b01106

Waza, M., Adachi, H., Katsuno, M., Minamiyama, M., Tanaka, F., Doyu, M., et al. (2006). Modulation of Hsp90 function in neurodegenerative disorders: a molecular-targeted therapy against disease-causing protein. *J. Mol. Med.* 84, 635–646. doi:10.1007/s00109-006-0066-0

Weigert, O., Lane, A. A., Bird, L., Kopp, N., Chapuy, B., Van Bodegom, D., et al. (2012). Genetic resistance to JAK2 enzymatic inhibitors is overcome by HSP90 inhibition. *J. Exp. Med.* 209, 259–273. doi:10.1084/jem.20111694

Wernig, G., Mercher, T., Okabe, R., Levine, R. L., Lee, B. H., and Gilliland, D. G. (2006). Expression of Jak2V617F causes a polycythemia vera–like disease with associated myelofibrosis in a murine bone marrow transplant model. *Blood* 107, 4274–4281. doi:10.1182/blood-2005-12-4824

Westerlund, M., Hoffer, B., and Olson, L. (2010). Parkinson's disease: exit toxins, enter genetics. *Prog. Neurobiol.* 90, 146–156. doi:10.1016/j.pneurobio.2009.11.001

Woodford, M. R., Dunn, D., Miller, J. B., Jamal, S., Neckers, L., and Mollapour, M. (2016). "Chapter two - impact of posttranslational modifications on the anticancer activity of Hsp90 inhibitors," in *Advances in cancer research*. Editors J. Isaacs, and L. Whitesell (Academic Press), 31–50.

Workman, P., Burrows, F., Neckers, L., and Rosen, N. (2007). Drugging the cancer chaperone HSP90: combinatorial therapeutic exploitation of oncogene addiction and tumor stress. *Ann. N. Y. Acad. Sci.* 1113, 202–216. doi:10.1196/annals.1391.012

Wöss, K., Simonović, N., Strobl, B., Macho-Maschler, S., and Müller, M. (2019). TYK2: an upstream kinase of STATs in cancer. *Cancers* 11, 1728. doi:10.3390/cancers11111728

Wu, C.-W., and Storey, K. B. (2021). mTOR signaling in metabolic stress adaptation. *Biomolecules* 11, 681. doi:10.3390/biom11050681

Wu, J., Wang, D., Nie, J., Zhang, D., Sun, L., Kan, S., et al. (2023). Design and synthesis of an Hsp90 and HDAC dual inhibitor as antitumor agent. *Lett. Drug Des. and Discov.* 20, 619–627. doi:10.2174/1570180819666220530145951

Xie, J., Gong, L., Zhu, S., Yong, Y., Gu, Z., and Zhao, Y. (2019). Emerging strategies of nanomaterial-mediated tumor radiosensitization. *Adv. Mater.* 31, 1802244. doi:10.1002/adma.201802244

Xu, W., and Neckers, L. (2007). Targeting the molecular chaperone heat shock protein 90 provides a multifaceted effect on diverse cell signaling pathways of cancer cells. *Clin. Cancer Res.* 13, 1625–1629. doi:10.1158/1078-0432.CCR-06-2966

Xue, N., Jin, J., Liu, D., Yan, R., Zhang, S., Yu, X., et al. (2014). Antiproliferative effect of HSP90 inhibitor Y306zh against pancreatic cancer is mediated by interruption of AKT and MAPK signaling pathways. *Curr. Cancer Drug Targets* 14, 671–683. doi:10.2174/1568009614666140908101523

Xu-Monette, Z. Y., Medeiros, L. J., Li, Y., Orlowski, R. Z., Andreeff, M., Bueso-Ramos, C. E., et al. (2012). Dysfunction of the TP53 tumor suppressor gene in lymphoid malignancies. *Blood* 119, 3668–3683. doi:10.1182/blood-2011-11-366062

Yamaki, H., Nakajima, M., Shimotohno, K. W., and Tanaka, N. (2011). Molecular basis for the actions of Hsp90 inhibitors and cancer therapy. *J. Antibiotics* 64, 635–644. doi:10.1038/ja.2011.60

Yan, P., Patel, H. J., Sharma, S., Corben, A., Wang, T., Panchal, P., et al. (2020). Molecular stressors engender protein connectivity dysfunction through aberrant N-glycosylation of a chaperone. *Cell Rep.* 31, 107840. doi:10.1016/j.celrep.2020.107840

Yanagi, T., Mizoe, J.-E., Hasegawa, A., Takagi, R., Bessho, H., Onda, T., et al. (2009). Mucosal malignant melanoma of the head and neck treated by carbon ion radiotherapy. *Int. J. Radiat. Oncology* Biology* Phys.* 74, 15–20. doi:10.1016/j.ijrobp.2008.07.056

Yang, H., and Green, M. R. (2019). Epigenetic programing of B-cell lymphoma by BCL6 and its genetic deregulation. *Front. Cell Dev. Biol.* 7, 272. doi:10.3389/fcell.2019.00272

Youssef, M. E., Cavalu, S., Hasan, A. M., Yahya, G., Abd-Eldayem, M. A., and Saber, S. (2023). Role of ganetespib, an HSP90 inhibitor, in cancer therapy: from molecular mechanisms to clinical practice. *Int. J. Mol. Sci.* 24, 5014. doi:10.3390/ijms24055014

Youssef, M. E., El-Mas, M. M., Abdelrazek, H. M., and El-Azab, M. F. (2021a). α7-nAChRs-mediated therapeutic angiogenesis accounts for the advantageous effect of low nicotine doses against myocardial infarction in rats. *Eur. J. Pharmacol.* 898, 173996. doi:10.1016/j.ejphar.2021.173996

Youssef, M. E., Moustafa, Y., and Abdelrazek, H. (2021b). Molecular mechanisms of α7-nAchR-mediated anti-inflammatory effects. *Indian J. Physiology Pharmacol.* 64, 158–173. doi:10.25259/ijpp_129_2020

Zhang, W., Li, Q., and Yin, R. (2024). Targeting WEE1 kinase in gynecological malignancies. *Drug Des. Devel Ther.* 18, 2449–2460. doi:10.2147/DDDT.S462056

Zhang, X., Li, S., Li, Z., Cheng, L., Liu, Z., and Wang, C. (2022). The therapeutic potential of targeting hsp90-cdc37 interactions in several diseases. *Curr. Drug Targets* 23, 1023–1038. doi:10.2174/1389450123666220408101544

Zhang, Y., Xia, M., Jin, K., Wang, S., Wei, H., Fan, C., et al. (2018). Function of the c-Met receptor tyrosine kinase in carcinogenesis and associated therapeutic opportunities. *Mol. Cancer* 17, 45. doi:10.1186/s12943-018-0796-y

Zhao, R., and Houry, W. A. (2005). Hsp90: a chaperone for protein folding and gene regulation. *Biochem. Cell Biol.* 83, 703–710. doi:10.1139/o05-158

Zhao, R., Xing, S., Li, Z., Fu, X., Li, Q., Krantz, S. B., et al. (2005). Identification of an acquired JAK2 mutation in polycythemia vera. *J. Biol. Chem.* 280, 22788–22792. doi:10.1074/jbc.C500138200

Glossary

17-AAG	17-Allylamino-17-demethoxygeldanamycin
17-DMAG	17-Dimethylaminoethylamino-17-demethoxygeldanamycin
Akt	Protein Kinase B
ATF4	Activating Transcription Factor 4
ATP	Adenosine Triphosphate
ATPase	Adenosine Triphosphatase
Bax	Bcl-2-Associated X Protein
Bcl-xL	B-Cell Lymphoma-extra Large
Bcl6	B-Cell Lymphoma 6
Bcl-2	B-Cell Lymphoma 2
BCoR	BCL6 Corepressor
C-ions	Carbon Ions
CIRT	Carbon-Ion Radiotherapy
CDK	Cyclin-Dependent Kinase
CHOP	C/EBP Homologous Protein
CK2	casein kinase II
DNA-PKcs	DNA-Dependent Protein Kinase Catalytic Subunit
DSB	DNA Double-Strand Break
DLBCL	Diffuse Large B-Cell Lymphoma
ER	Endoplasmic Reticulum
ERK	Extracellular Signal-Regulated Kinase
FoxO	Forkhead Box O
GRP78	Glucose-Regulated Protein 78
gp96	Glucose-Regulated Protein 94
HDAC	histone deacetylase
HSP27	Heat Shock Protein 27
HSP40	Heat Shock Protein 40
HSP60	Heat Shock Protein 60
HSP70	Heat Shock Protein 70
HSP72	Inducible Heat Shock Protein 70
HSP90	Heat Shock Protein 90
HSP90α	Heat Shock Protein 90 Alpha
HSP90β	Heat Shock Protein 90 Beta
HSP90B1	Heat Shock Protein 90 Beta Family Member 1
HSC70	Constitutive Heat Shock Protein 70
HSF-1	Heat Shock transcription Factor 1
HSR	Heat Shock Response
IC50	Half Maximal Inhibitory Concentration
IL-6	Interleukin 6
INF	Interferon
IGF1R	Insulin-Like Growth Factor 1 Receptor
JAK	Janus Kinase
LET	Linear Energy Transfer
MAPK	Mitogen-Activated Protein Kinase
mTORC	Mammalian Target of Rapamycin Complex
NF-κB	Nuclear Factor kappa-light-chain-enhancer of activated B cells
NOS2	Nitric Oxide Synthase 2
PKC	Protein Kinase C
PDK1	3-Phosphoinositide-Dependent Protein Kinase-1
PI3K	Phosphoinositide 3-Kinase
PTMs	post-translational modifications
RAD51	RAD51 Recombinase
Raf	v-Raf-1 Murine Leukemia Viral Oncogene Homolog 1
Ras	Rat Sarcoma (a family of related proteins)
SMRT	Silencing Mediator for Retinoid and Thyroid Receptors
STAT	Signal Transducers and Activators of Transcription
TNBC	Triple-Negative Breast Cancer
Tyk2	Tyrosine Kinase 2
UPR	Unfolded Protein Response
VEGFR2	vascular endothelial growth factor receptor 2
XBP1	X-Box Binding Protein 1

frontiers | Frontiers in Oncology

TYPE Original Research
PUBLISHED 12 November 2024
DOI 10.3389/fonc.2024.1446945

Check for updates

OPEN ACCESS

EDITED BY
Vita Golubovskaya,
ProMab Biotechnologies, United States

REVIEWED BY
Alessandro Ottaiano,
IRCCS Istituto Nazionale per lo Studio e la Cura dei Tumori "Fondazione Giovanni Pascale", Italy
Maha Houssen,
Damanhour University, Egypt

*CORRESPONDENCE
Pilar Sotoca Rubio
pilarsotocarubio@gmail.com

RECEIVED 10 June 2024
ACCEPTED 15 October 2024
PUBLISHED 12 November 2024

CITATION
Sotoca Rubio P, Barrill Corpa AM, Alia Navarro V, Pérez de Aguado Rodríguez P, Moreno Doval J, Calvo Pérez JC, Guerrero Serrano P, García Merino C, García de Quevedo Suero C, Fernández-Fradejas J, Serrano Domingo JJ, Martínez Delfrade Í, Morón García BI, Ferreiro Monteagudo MR and de Frutos González B (2024) Efficacy and safety of regorafenib for the treatment of metastatic colorectal cancer in routine clinical practice: results from a Spanish hospital. *Front. Oncol.* 14:1446945. doi: 10.3389/fonc.2024.1446945

COPYRIGHT
© 2024 Sotoca Rubio, Barrill Corpa, Alia Navarro, Pérez de Aguado Rodríguez, Moreno Doval, Calvo Pérez, Guerrero Serrano, García Merino, García de Quevedo Suero, Fernández-Fradejas, Serrano Domingo, Martínez Delfrade, Morón García, Ferreiro Monteagudo and de Frutos González. This is an open-access article distributed under the terms of the Creative Commons Attribution License (CC BY). The use, distribution or reproduction in other forums is permitted, provided the original author(s) and the copyright owner(s) are credited and that the original publication in this journal is cited, in accordance with accepted academic practice. No use, distribution or reproduction is permitted which does not comply with these terms.

Efficacy and safety of regorafenib for the treatment of metastatic colorectal cancer in routine clinical practice: results from a Spanish hospital

Pilar Sotoca Rubio[1*], Ana María Barrill Corpa[1], Víctor Alia Navarro[1], Patricia Pérez de Aguado Rodríguez[1], Jaime Moreno Doval[1], Juan Carlos Calvo Pérez[1], Patricia Guerrero Serrano[1], Carlos García Merino[1], Coral García de Quevedo Suero[1], Jorge Fernández-Fradejas[2], Juan José Serrano Domingo[1], Íñigo Martínez Delfrade[1], Blanca Isabel Morón García[1], María Reyes Ferreiro Monteagudo[1] and Belén de Frutos González[1]

[1]Medical Oncology Department, Ramon y Cajal University Hospital, Madrid, Spain, [2]Pharmacy Department, Ramon y Cajal University Hospital, Madrid, Spain

Introduction: Regorafenib is indicated as treatment in third-line and beyond in patients with metastatic colorectal cancer.

Methods : This is a retrospective study of a cohort of patients with mCRC treated with regorafenib in Hospital Universitario Ramón y Cajal, in Madrid, Spain.

Results: With the aim to assess the efficacy and safety of regorafenib, 91 patients treated between 2013 and 2023 were included. Only 1.1% of patients achieved disease control. Median progression free survival was 2.40 months and median overall survival was 4.76 months. The most frequent adverse events were fatigue and hand-foot skin reaction (59.34% and 28.57%, respectively).

Discussion: Our results confirm the safety of regorafenib as treatment of mCRC in real clinical practice. Although our population is less pretreated than in the CORRECT trial, our disease control rate was inferior. This difference may be due to a worse baseline status and a high percentage of hepatic disease showed in our patients.

KEYWORDS

metastatic colorectal cancer, regorafenib, real-life, routine clinical practice, real world data

1 Introduction

Colorectal cancer (CRC) is the fourth most frequent tumor after breast, prostate, and lung cancers and the third cause of death worldwide. It is estimated that a total of 1,926,425 cases were diagnosed in 2022, with 904,019 deaths. In Europe, 538,584 were diagnosed (1). Approximately 15%–30% of cases are diagnosed as metastatic disease. From those patients diagnosed in localized stages, 20%–50% will have a metastatic relapse. Liver, lungs, and peritoneum are the most frequent areas of metastasis (2).

Several cytotoxic drugs are used in metastatic scenario, with fluoropyrimidines being the most used, in monotherapy or in combination with oxaliplatin and/or irinotecan. These drugs can be combined with monoclonal antibodies, depending on KRAS status. If KRAS is mutated, a drug targeting vascular endothelial growth factor (VEGF) such as bevacizumab can be used, while if it is in a wild-type status, monoclonal antibodies targeting epidermal growth factor receptor (EGFR) like cetuximab or panitumumab can be also used (2). After progression to treatments described above and in patients who maintain good performance status, other options should be offered. Regorafenib or trifluridine/tipiracil are available drugs in this scenario. Trifluridine/tipiracil in monotherapy or in combination with bevacizumab has shown effectiveness and safety in RECOURSE and SUNLIGHT (3, 4).

Regorafenib is a novel oral multikinase inhibitor that blocks VEGF receptor (VEGFR) or EGFR just as additional angiogenic kinases (VEGFR 1/3, platelet-derived growth factor receptor or band fibroblast growth factor receptor 1). Additionally, it blocks regulatory cascades such as RAS-RAF-MEK-ERK and PI3K-PTEN-AKT-mTOR pathways. In summary, regorafenib inhibits tumoral angiogenesis, tumor microenvironment, and cellular signaling (5). The phase 1b clinical trial (BAY 73-4506) showed a tolerable toxicity profile at dose of 160 mg daily for 3 weeks of each 4 weeks and a preliminary evidence of antitumor activity in metastatic CRC (6).

The CORRECT trial was a randomized multicentric phase 3 trial where 760 patients with metastatic CRC were randomized 2:1 to regorafenib or placebo after failure to standard therapies. The primary endpoint was overall survival (OS). Secondary endpoints included progression-free survival (PFS), objective response rate (ORR), disease control rate (DCR), and safety (7). The study met its primary endpoint of OS at the second planned interim analysis, although crossover from the placebo group was allowed after progression. The benefit was modest, with a median OS of 6.4 months in regorafenib group versus 5 months in the placebo group [hazard ratio (HR) 0.77, p=0.0052] (7).

PFS and DCR were also improved with regorafenib. Stable disease was the best response in 41% of patients, and none of the patients reached complete response. In the regorafenib group, 76% of patients had to reduce the dose due to adverse events. The most frequent adverse events of any grade were fatigue and hand–foot skin reaction (especially at first or second cycle). Grade 3 or 4 toxicities appeared in 54% patients in the regorafenib group, mostly hand–foot skin reaction, diarrhea, fatigue, and hypertension (7).

Li et al. were supported in CONCUR, another phase 3 clinical trial with regorafineb in Asiatic population, a similar benefit in OS (8.8 months in regorafenib group vs. 6.3 months in placebo group, HR=0.55, p=0.00016) and a consistent toxicity profile (8).

Based in those clinical trials, regorafenib is nowadays an option for metastatic CRC patients in third line or beyond. Some real-world data (RWD) studies have been published afterwards. Metges et al. confirmed a real-world evidence of efficacy and safety in a prospective and observational study in the 242 French patients who participated in CORRELATE trial. Median OS and PFS were 6.8 months and 2.8 months, respectively (9).

The aim of our study is to evaluate the efficacy and safety of regorafenib in the real-life setting in a tertiary hospital in Spain (Hospital Universitario Ramón y Cajal, Madrid).

2 Materials and methods

We conducted a single-center observational, retrospective study of a cohort of 91 patients with metastatic CRC treated with regorafenib in routine clinical practice in third line or beyond between 1 December 2013 and 15 June 2023.

Patients included in the study met the following inclusion criteria: (1) 18 years of age or older; (2) ECOG 0–2; (3) diagnosis of metastatic CRC previously treated with a fluoropyrimidine (alone or in combination with oxaliplatin and/or irinotecan) with or without cetuximab, panitumumab, bevacizumab, or aflibercept; (4) treatment with regorafenib in third line or beyond; and (5) regorafenib as exclusive oncology treatment.

The data of patients were obtained from medical records from the real clinical practice. None of the patients were followed up in a prospective way. Patients were evaluated every 2–3 months with CT scan of the thorax, abdomen, and pelvis according to local guidelines. All re-evaluations were done at our hospital. The main variables assessed were OS, PFS, and ORR according to RECIST 1.1 criteria; adverse events according to NCI-CTCAE (National Cancer Institute Common Terminology Criteria for Adverse Events) versions 4.0 and 5.0; number and dose of cycles of regorafenib and previous; and subsequent treatments received.

The primary objective was to evaluate the effectiveness of regorafenib in patients with metastatic CRC in real clinical practice in terms of PFS. Other objectives were as follows: (1) assess the effectiveness of regorafenib in terms of OS and ORR and (2) know the safety profile in real clinical practice.

Data were analyzed with Stata v16.1. Descriptive statistics were reported as frequencies and percentages for categorical variables and as median and range for continuous variables. Median OS (mOS) and median PFS (mPFS) were estimated using the Kaplan–Meier method and compared by log rank. Cox regression model was used to evaluate the HR and the 95% confidence interval (CI) in univariate analysis.

3 Results

A total of 91 patients with metastatic CRC treated with regorafenib in third or beyond line were included. Median age

was 65 years (35–85) and 58.24% of the patients (59) were men. Of the patients, 59.34% had metastasis in three or more locations, with 86.81% of them in the liver and 30.77% in the peritoneum. Colorectal cancer had left location in 68.14% of patients. The primary tumor site was the rectum in 24.18% of patients. KRAS/NRAS was mutated in 61.54% of patients. BRAF mutations and MMR deficiency were not found in any patient.

Most patients had ECOG 1 (65.93%), followed by ECOG 0 (20.88%). Only 12.09% of patients had ECOG 2. Regorafenib was administered in third line in 21.98% of patients, and 50.55% of patients had been treated with three or more lines of treatment before regorafenib. In those patients treated in third line, 100% received FOLFOX and FOLFIRI regimens, with 17 (85%) receiving bevacizumab in first and second line and three patients receiving anti-EGFR in first line and bevacizumab in second line.

Regarding trifluridine/tipiracile, 62.64% of patients were treated with this drug before regorafenib and 12.09% of patients received it after regorafenib. A total of 28 patients received other treatments after regorafenib, most of them with 5-fluoruracil.

The most frequent response was progression of the disease, found in 74 patients (81.31%), while 16 patients were not evaluated and only one had disease control.

The characteristics are summarized in Table 1.

Median follow-up was 6.13 months (range, 0.20–35.0 months). The mPFS was 2.40 months (95% CI, 2.04–2.66 months) (Figure 1A), and the mOS was 4.76 months (95% CI, 3.78–6.28 months) (Figure 2A). Median duration of treatment was 2.52 months (range, 0.20–10.9 months). According to ECOG, patients with ECOG 0, 1, and 2 or more had an mPFS of 2.73, 2.40, and 1.84 months, respectively. There was a significant difference between ECOG 0 and 1 with an HR of 0.54 (95% CI, 0.30–0.97, p=0.041) (Figure 1B). The mOS in these patients was 6.83 months, 4.67 months, and 2.30 months, respectively. ECOG 2 had a worse OS than ECOG 0 (HR 0.31, 95% CI, 0.14–0.68, p=0.004) and ECOG 1 (HR 0.45, 95% CI, 0.23–0.90, p=0.024), with no differences between ECOG 0 and 1 (Figure 2B).

Those patients with liver metastasis had worse mPFS, with 2.23 months vs. 2.50 months, not statistically significant (HR 0.49, 95% CI, 0.23–1.05, p=0.066) (Figure 1C), and worse mOS, with 4.60 months vs. 9.26 months (HR 0.42, 95% CI, 0.20–0.88, p=0.021) (Figure 2C). Patients with peritoneal involvement had similar mPFS (2.37 months vs. 2.40 months; HR 1.03, 95% CI, 0.63–1.67, p=0.909) and similar mOS (4.34 vs. 4.90 months; HR 1.30, 95% CI, 0.80–2.12, p=0.291).

There was no difference between patients with two or less and three or more metastatic sites in terms of mPFS: 2.23 months and 2.40 months (Figure 1D). In terms of mOS, there was a difference, with 5.68 months vs. 4.21 months (HR 0.57, 95% CI, 0.35–0.93, p=0.024) (Figure 2D). There was no difference in terms of PFS between patients with tumor in the rectum and other locations (mPFS 2.2 months vs. 2.40 months; HR 1.67, 95% CI, 0.99–2.82, p=0.055), neither in OS (mOS 3.78 months vs. 4.90 months; HR, 1.39; 95% CI, 0.83–2.32; p=0.208).

According to treatment line, those patients treated with two prior regimens had better mPFS than those treated with three (2.66 months vs. 2.23 months; HR 0.53, 95% CI, 0.29–0.96, p=0.036).

TABLE 1 Cohort's characteristics.

Characteristic	Value
Median age, years (range)	65 (35–85)
Sex, no. (%)	
Male	53 (58.24%)
Female	38 (41.76%)
ECOG, no. (%)	
0	19 (20.88%)
1	60 (65.93%)
2	11 (12.09%)
Unknown	1 (1.1%)
Primary location, no. (%)	
Ascendent	27 (29.67%)
Transversum	2 (2.2%)
Sigma	40 (43.96%)
Rectum	22 (24.18%)
KRAS, no. (%)	
Wild type	35 (38.46%)
Mutated	56 (61.54%)
Metastatic affection, no. (%)	
≤2 sites	37 (40.66%)
≥3 sites	54 (59.34%)
Metastatic site, no. (%)	
Liver	79 (86.81%)
Peritoneum	28 (30.77%)
Prior regimens, no. (%)	
2	20 (21.98%)
3	46 (50.55%)
≥4	25 (27.47%)
Best response, no. (%)*	
Stable disease	1 (1.1%)
Progression	74 (81.32%)
Not evaluated	16 (17.58%)
Trifluridine/Tipiracil, no. (%)	
Before regorafenib	57 (62.64%)
After regorafenib	11 (12.09%)
Not received at any time	23 (25.27%)
Subsequent treatment, no. (%)	40 (43.96%)

*According to RECIST 1.1 criteria.

Patients treated with four or more prior regimens had an mPFS of 2.37 months without differences comparing the other groups (Figure 1E). In terms of OS, we have observed a better mOS in

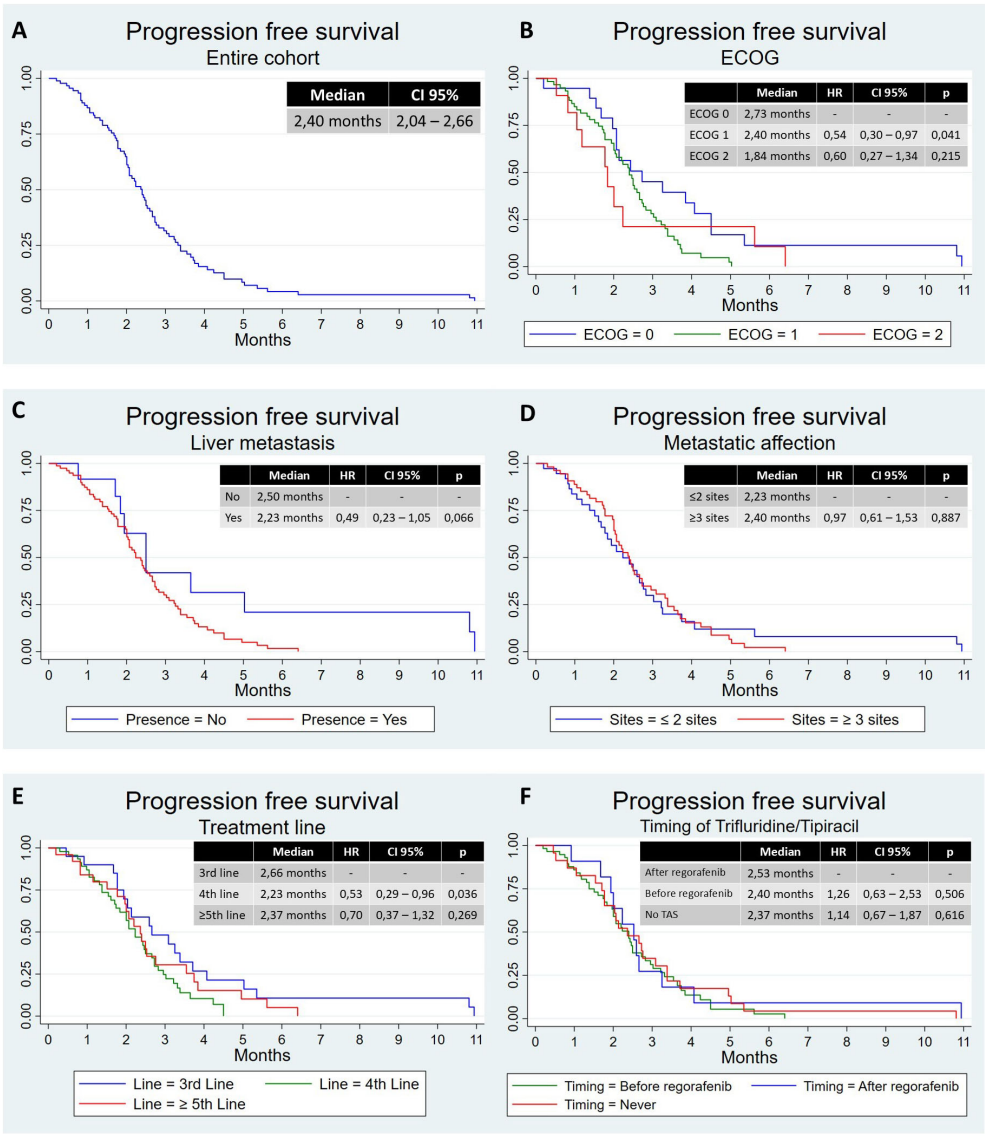

FIGURE 1
Progression-free survival in different populations. **(A)** Progression-free survival in the entire cohort, **(B)** progression-free survival according to ECOG, **(C)** progression-free survival according to liver metastasis, **(D)** progression-free survival according to metastatic affection, **(E)** progression-free survival according to treatment line, and **(F)** progression-free survival according to timing of trifluridine/tipiracil. CI, confidence interval; HR, hazard ratio; TAS, trifluridine/tipiracil.

patients treated with two prior regimens than those treated with four or more (4.93 months vs. 4.21 months; HR 0.45, 95% CI, 0.23–0.88, p=0.020). Patients treated with three or more prior regimens had an mOS of 4.67 months without differences comparing the other groups (Figure 2E).

Finally, and considering the sequence with trifluridine/tipiracil, there was no difference in mPFS, with 2.40 months for those treated first with trifluridine/tipiracil, 2.53 months for those treated first with regorafenib, and 2.37 for those not treated with trifluridine/tipiracil (Figure 1F). However, those patients treated first with regorafenib had better mOS (7.16 months) than those treated first with trifluridine/tipiracil (4.67 months; HR 0.44, 95% CI, 0.20–0.95, p=0.036) and those not treated with trifluridine/tipiracil (3.81 months; HR 0.31, 95% CI, 0.13–0.71, p=0.006) (Figure 2F).

A total of 40 patients (43.96%) started regorafenib at 160 mg/day and 46 (50.55%) with 120 mg/day (one level dose reduction). A total of 26 patients (28.57%) required a dose reduction, without impact in mOS. Regarding safety, 62 patients (68.13%) presented toxicity grades 1 and 2, and 14 patients (15.38%) presented toxicity grades 3 and 4. The safety profile is summarized in Table 2.

4 Discussion

Our study has assessed the efficacy and safety of regorafenib in third line and beyond in the treatment of patients with metastatic CRC in real clinical practice. The main clinical outcomes included a DCR of 1.1%, an mPFS of 2.40 months and an mOS of 4.76 months.

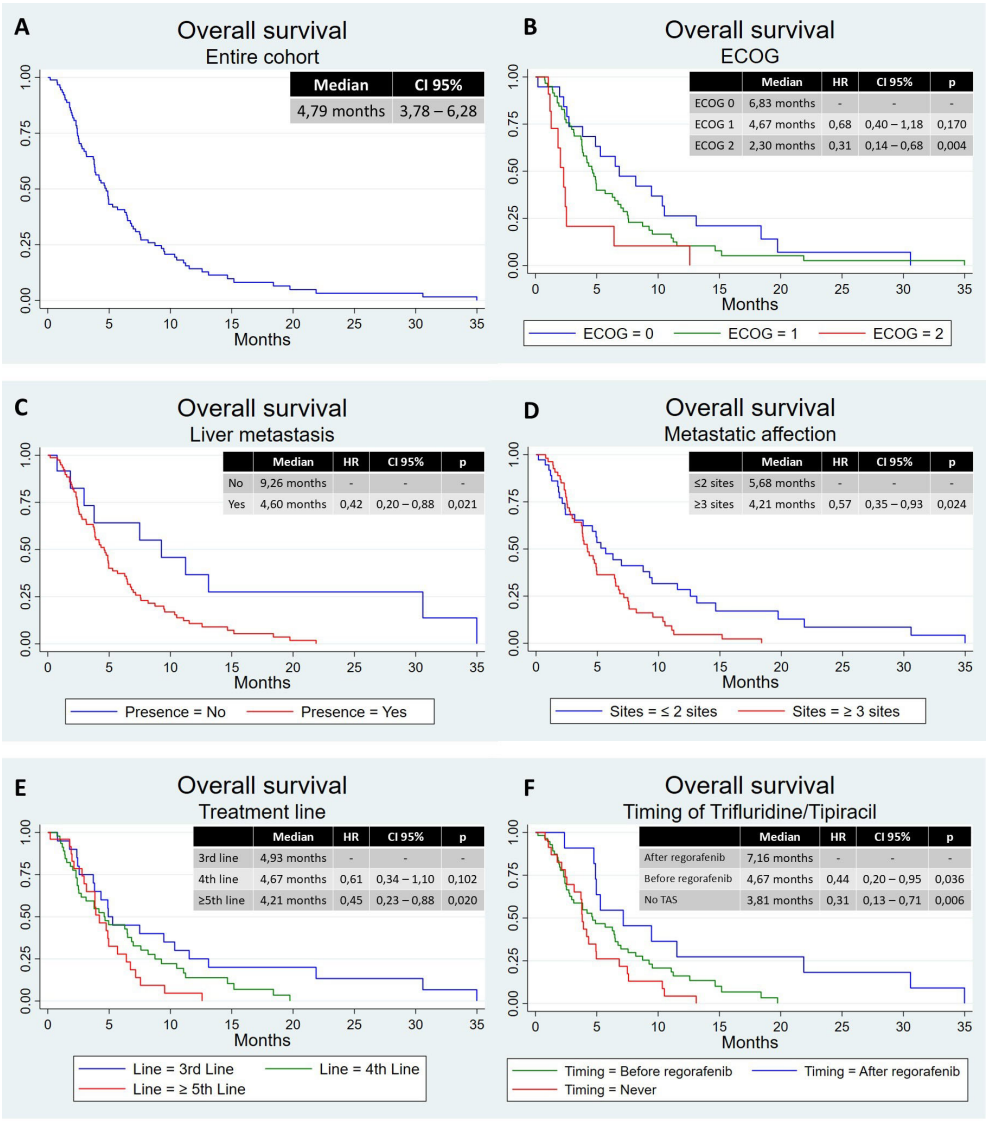

FIGURE 2
Overall survival in different populations. **(A)** Overall survival in the entire cohort, **(B)** overall survival according to ECOG, **(C)** overall survival according to liver metastasis, **(D)** overall survival according to metastatic affection, **(E)** overall survival according to treatment line, and **(F)** overall survival according to timing of trifluridine/tipiracil. CI, confidence interval; HR, hazard ratio; TAS, trifluridine/tipiracil.

Hand–foot skin reaction was the most frequent adverse event. ECOG 2, liver metastasis, and having three or more metastatic sites showed worse OS, as expected. In a similar way, patients treated in third line have also a better OS than those treated in fifth or greater line. Conversely, the presence of peritoneal disease does not negatively impact survival. Since colon and rectal cancer are actually diseases with biological, clinical, and molecular characteristics (10), we have assessed the impact that this could have in our study. However, no differences in survival had been observed between patients with colon and rectal cancer. This observation is in line with what was observed by the authors of CORRELATE study in relation to the sidedness of the primary tumor (11), reinforcing the idea that prognostic differences are lost in latter lines.

Our results are slightly lower to those observed in the randomized phase III CORRECT clinical trial in terms of OS, with a difference in mOS of 4.76 months vs. 6.4 months. This can also be observed in comparison to the CORRELATE study (7.7 months). This difference may be due to the fact that our population has a worse baseline status. In the CORRECT trial and in the CORRELATE study, 52% and 41% of patients were ECOG 0, respectively, while in our database, it was 20.88%; 12.09% of the patients in our database were ECOG 2, while in CORRELATE, it was 6% and was an exclusion criterion from the CORRECT trial. In our population, 86.81% had liver metastasis, which is recognized as a poor prognostic factor. These data were missing from the CORRECT trial, while it was 72% in the CORRELATE study.

In the CORRECT trial, 27% of patients have received one to two prior regimens, 25% have received three prior regimens, and 49% have received four or more prior regimens. In our database, this corresponds to 21.98%, 50.55%, and 27.47%, which shows that our

10.3389/fonc.2024.1446945

TABLE 2 Safety profile.

Characteristic	Value
Starting dose, no. (%)	
160 mg	40 (43.96%)
120 mg	46 (50.55%)
80 mg	5 (5.49%)
Dose reductions, no. (%)	26 (28.57%)
Toxicity, no. (%)*	
No toxicity	15 (16.48%)
Grade 1–2	62 (68.13%)
Grade 3–4	14 (15.38%)
Fatigue	
Grade 1–2	53 (58.24%)
Grade 3–4	1 (1.10%)
Hand–foot skin reaction	
Grade 1–2	24 (26.37%)
Grade 3–4	2 (2.20%)
Diarrhea	
Grade 1–2	6 (6.59%)
Grade 3–4	1 (1.10%)
Hypertension	
Grade 1–2	6 (6.59%)
Grade 3–4	3 (3.30%)

mg, milligrams.
*According to National Cancer Institute Common Terminology Criteria for Adverse Events (NCI-CTCAE) versions 4.0 and 5.0.

population is less pretreated than in the CORRECT trial. This may explain that in our study, the mPFS is slightly superior: 2.4 months vs. 1.9 months. In the CORRELATE study, patients treated in the third, fourth, or fifth line and beyond were 30%, 30%, and 39%, respectively, with an mPFS of 2.9 months. The DCR has been clearly inferior in our study, with 1.1% (with only one patient with stable disease) versus 41% in the CORRECT trial and 26% in the CORRELATE study. Different times of revaluation between clinical practice and clinical trial could explain this fact. Patients are usually evaluated every 3–4 months in real clinical practice, while in the CORRECT trial, they were evaluated every 8 weeks. These data were not shown in the CORRELATE study. The median duration of treatment was similar in our study and in CORRELATE (2.5 months), both superior to that in CORRECT (1.7 months). This difference could be also explained because of the different times of revaluation.

Several studies have evaluated the role of the sequence between regorafenib and trifluridine/tipiracil, with better result in OS with the sequence trifluridine/tipiracil followed by regorafenib (12, 13). In contrast, in our study, we have observed contrary results. We suggest that it may be due to the fact that treatment selection is made according to the patient's characteristics. In general,

TABLE 3 Results comparison.

Outcome	CORRECT^	CORRELATE	Actual series^^
Median age, years (range)	61 (64–67)	65 (24–93)	65 (35–85)
Male, %	62%	61%	58%
ECOG			
0	52%	41%	21%
1	48%	46%	66%
≥2	NA*	6%	12%
KRAS			
Wild type	41%	37%	38%
Mutated	54%	56%	62%
Unknown	5%	7%	0%
Liver metastasis	NS	72%	87%
Peritoneum metastasis	NS	13%	31%
Prior regimens			
1–2	27%	30%	22%
3	25%	30%	51%
≥4	49%	39%	27%
Response evaluation			
Partial response	1%	4%	0%
Stable disease	40%	22%	1%
Progression	59%**	47%	81%
Not evaluated		27%	18%
mTD	1.7 months	2.5 months	2.52 months
mPFS	1.9 months	2.9 months	2.40 months
mOS	6.4 months	7.7 months	4.76 months
Safety			
Dose reduction	38%	40%	29%
Inferior starting dose	NA	43%	56%
Toxicity			
Grade 1–2	39%	45%	68%
Grade 3–4	54%	35%	15%
Fatigue	47%	41%	59%
Hand–foot skin reaction	47%	26%	29%
Diarrhea	34%	19%	8%

NA, not applicable; NS, not specified; mTD, median treatment duration; mPFS, median progression-free survival; mOS, median overall survival.
^These data are from the cohort treated with regorafenib, not the entire population.
^^Data may not be the same as those reflected in this study because percentages have been rounded in this table.
*ECOG 2 was an exclusion criterion.
**Separate data not provided.

trifluridine/tipiracil is better tolerated than regorafenib, so those patients with a better performance status could be selected to start regorafenib, given that subsequent clinical deterioration may not allow its use. However, since only 11 patients received the sequence of regorafenib followed by trifluridine/tipiracil, no firm conclusions can be drawn. Furthermore, this question would currently be outdated following the data from the SUNLIGHT study, which showed that the addition of bevacizumab to trifluridine/tipiracil is superior to trifluridine/tipiracil as monotherapy (4).

The safety profile observed in our study had some differences with that in the CORRECT trial and with those reported in other retrospective studies of RWD (11). In the CORRECT trial, 38% of the patients in the regorafenib group needed a dose reduction, similar to the CORRELATE study, where 40% required a dose reduction (11). In contrast, in our study, dose reduction was lesser (28.57%), maybe because 54.94% of patients started at a lower dose. Regarding the CORRELATE study, 43% of patients started at a lower dose, mainly due to their fragility (11).

Hand–foot skin reaction and fatigue were the most frequent adverse events shown in the CORRECT trial, in the CORRELATE study, and in our study, with some differences. In the CORRECT trial, 47% of patients had any grade of fatigue and 47% had any grade of hand–foot skin reaction; in the CORRELATE study, 41% and 26%, respectively (11); and in our study, 59.34% and 28.57%, respectively. We have summarized the differences between the studies in Table 3.

It must be taken into account that this is a retrospective study, with the usual limitations of these types of studies. The information collected is limited to that obtained from the patients' medical records, so it is subject to possible bias and lack of information. In addition, the absence of centralized revaluation could influence the reliability of data in PFS. This is why it is not possible to draw more robust conclusions.

4.1 Conclusion

Our results confirmed the efficacy and safety of regorafenib as treatment of metastatic CRC in real clinical practice. There are several differences between the results of clinical trials and studies based on routine clinical practice, such as previous lines administered and rates of control disease. Fatigue and hand–foot skin reaction were the most adverse event associated with regorafenib.

Prospective studies are needed to evaluate which sequence of treatments may be most beneficial for patients with advanced colorectal cancer in later lines.

Data availability statement

The raw data supporting the conclusions of this article will be made available by the authors, without undue reservation.

Ethics statement

Ethical approval was not required for the study involving humans in accordance with the local legislation and institutional requirements. Written informed consent to participate in this study was not required from the participants or the participants' legal guardians/next of kin in accordance with the national legislation and the institutional requirements.

Author contributions

PSR: Visualization, Writing – original draft, Writing – review & editing. AMBC: Writing – original draft, Writing – review & editing. VAN: Writing – original draft, Writing – review & editing. PPdAR: Data curation, Writing – review & editing. JMD: Data curation, Writing – review & editing. JCCP: Data curation, Writing – review & editing. PGS: Data curation, Writing – review & editing. CGM: Data curation, Writing – review & editing. CGdQS: Data curation, Writing – review & editing. JF: Resources, Writing – review & editing. JJSD: Formal analysis, Resources, Visualization, Writing – review & editing. IMD: Project administration, Writing – review & editing. BIMG: Project administration, Writing – review & editing. MRFM: Conceptualization, Project administration, Supervision, Writing – review & editing. BdFG: Project administration, Supervision, Writing – review & editing.

Funding

The author(s) declare that no financial support was received for the research, authorship, and/or publication of this article.

Acknowledgments

The authors are grateful to the patients and their families.

Conflict of interest

The authors declare that the research was conducted in the absence of any commercial or financial relationships that could be construed as a potential conflict of interest.

Publisher's note

All claims expressed in this article are solely those of the authors and do not necessarily represent those of their affiliated organizations, or those of the publisher, the editors and the reviewers. Any product that may be evaluated in this article, or claim that may be made by its manufacturer, is not guaranteed or endorsed by the publisher.

References

1. World Health Organization. *International agency for research on cancer. Global cancer observatory. Cancer today. Absolute numbers, incidence/mortality, both sexes, in 2022 [Internet]*. (2022). Available at: https://gco.iarc.fr/today/en/dataviz/pie?mode=cancer&key=total&cancers=41&group_cancers=1&multiple_cancers=1&group_populations=1&types=0 (Accesed March 1, 2024).

2. Cervantes AM, Adam R, Rosello S, Arnold D, Normanno N, Taïeb J, et al. Metastatic colorectal cancer: ESMO Clinical Practice Guideline for diagnosis, treatment and follow-up. *Ann Oncol*. (2023) 34:10–32. doi: 10.1016/j.annonc.2022.10.003

3. Mayer RJ, Van Cutsem E, Falcone A, Yoshino T, Garcia-Carbonero R, Mizunuma N, et al. Randomized trial of TAS-102 for refractory metastatic colorectal cancer. *N Engl J Med*. (2015) 372:1909–19. doi: 10.1056/NEJMoa1414325

4. Prager GW, Taieb J, Fakih M, Ciardiello F, Cutsem EV, Elez E, et al. Trifluridine-tipiracil and bevacizumab in refractory metastatic colorectal cancer. *N Engl J Med*. (2023) 388:1657–67. doi: 10.1056/NEJMoa2214963

5. Wilhelm SM, Dumas J, Adnane L, Lynch M, Carter CA, Schütz G, et al. Regorafenib (BAY 73-4506): a new oral multikinase inhibitor of angiogenic, stromal and oncogenic receptor tyrosine kinases with potent preclinical antitumor activity. *Int J Cancer*. (2011) 129:245–55. doi: 10.1002/ijc.v129.1

6. Strumberg D, Scheulen ME, Schultheis B, Richly H, Frost A, Büchert M, et al. Regorafenib (BAY 73-4506) in advanced colorectal cancer: a phase I study. *Br J Cancer*. (2012) 106:1722–27. doi: 10.1038/bjc.2012.153

7. Grothey A, Van Cutsem E, Sobrero A, Siena S, Falcone A, Ychou M, et al. Regorafenib monotherapy for previously treated metastatic colorectal cancer (CORRECT): an international, multicentre, randomised, placebo-controlled, phase 3 trial. *Lancet*. (2013) 381:303–12. doi: 10.1016/S0140-6736(12)61900-X

8. Li J, Qin S, Xu R, Yau TC, Ma B, Pan H, et al. Regorafenib plus best supportive care versus placebo plus best supportive care in Asian patients with previously treated metastatic colorectal cancer (CONCUR): a randomised, double-blind, placebo-controlled, phase 3 trial. *Lancet Oncol*. (2015) 16:619–29. doi: 10.1016/S1470-2045(15)70156-7

9. Metges JP, Genet D, Tougeron D, Ligeza C, Ducreux M, Borg C, et al. Real-world safety and effectiveness of Regorafenib in metastatic colorectal cancer: the French CORRELATE cohort. *Future Oncol*. (2021) 17:3343–53. doi: 10.2217/fon-2021-0266

10. Tamas K, Walenkamp AME, de Vries EGE, van Vugt MATM, Beets-Tan RG, van Etten B, et al. Rectal and colon cancer: Not just a different anatomic site. *Cancer Treat Rev*. (2015) 41:671–9. doi: 10.1016/j.ctrv.2015.06.007

11. Ducreux M, Petersen LN, Öhler L, Bergamo F, Metges JP, de Groot JW, et al. Safety and effectiveness of Regorafenib in patients with metastatic colorectal cancer in routine clinical practice in the prospective, observational CORRELATE study. *Eur J Cancer*. (2019) 123:146–54. doi: 10.1016/j.ejca.2019.09.015

12. Ottaiano A, Santorsola M, Perri F, Granata V, Cascella M, Sabbatino F, et al. Survival and toxicites of metastatic colorectal cancer patients treated with regorafenib before or vice versa: a mono-institutional real-practice study. *J Clin Med*. (2023) 12:596. doi: 10.3390/jcm12020596

13. Nakashima M, Takeuchi M, Kowakami K. Effectiveness and safety of regorafenib vs. trifluridine/tipiracil in unresectable colorectal cancer: a retrospective cohort study. *Clin Colorectal Cancer*. (2020) 19(4):e208–25. doi: 10.1016/j.clcc.2020.05.003

frontiers | Frontiers in Pharmacology

TYPE Original Research
PUBLISHED 03 January 2025
DOI 10.3389/fphar.2024.1511627

Check for updates

OPEN ACCESS

EDITED BY
Wagdy Mohamed Eldehna,
Kafrelsheikh University, Egypt

REVIEWED BY
Ruo Wang,
Shanghai Jiao Tong University, China
Somia Gul,
Jinnah University for Women, Pakistan

*CORRESPONDENCE
Isaac Karimi,
isaac_Karimi2000@yahoo.com,
karimiisaac@razi.ac.ir
Helgi B. Schiöth,
helgi.schioth@uu.se

†These authors have contributed equally to this work

RECEIVED 15 October 2024
ACCEPTED 09 December 2024
PUBLISHED 03 January 2025

CITATION
Muslim WT, Mohammad LJ, Naji MM, Karimi I, Al-Sabti MD, Jabir M, Najm MAA and Schiöth HB (2025) Synthesis, characterization, and computational evaluation of some synthesized xanthone derivatives: focus on kinase target network and biomedical properties.
Front. Pharmacol. 15:1511627.
doi: 10.3389/fphar.2024.1511627

COPYRIGHT
© 2025 Muslim, Mohammad, Naji, Karimi, Al-Sabti, Jabir, Najm and Schiöth. This is an open-access article distributed under the terms of the Creative Commons Attribution License (CC BY). The use, distribution or reproduction in other forums is permitted, provided the original author(s) and the copyright owner(s) are credited and that the original publication in this journal is cited, in accordance with accepted academic practice. No use, distribution or reproduction is permitted which does not comply with these terms.

Synthesis, characterization, and computational evaluation of some synthesized xanthone derivatives: focus on kinase target network and biomedical properties

Wisam Taher Muslim[1], Layth Jasim Mohammad[2†], Munaf M. Naji[3], Isaac Karimi[4*†], Matheel D. Al-Sabti[5], Majid Jabir[6], Mazin A. A. Najm[7] and Helgi B. Schiöth[8*†]

[1]Department of Pharmaceutical Chemistry, College of Pharmacy, Kufa University, Najaf City, Iraq, [2]Department of Microbiology, College of Medicine, Babylon University, Hilla City, Iraq, [3]Clinical Laboratory Sciences, College of Pharmacy, Kufa University, Najaf City, Iraq, [4]Research Group of Bioengineering and Biotechnology, Laboratory for Computational Physiology, Department of Biology, Faculty of Science, Razi University, Kermanshah, Iran, [5]Department of Science, College of Science, Uruk University, Baghdad, Iraq, [6]Department of Applied Science, University of Technology, Baghdad, Iraq, [7]Department of Pharmacy, Mazaya University Collage, Nasiriyah, Iraq, [8]Department of Surgical Sciences, Functional Pharmacology and Neuroscience, Uppsala University, Uppsala, Sweden

Background: Xanthones are dubbed as putative lead-like molecules for cancer drug design and discovery. This study was aimed at the synthesis, characterization, and *in silico* target fishing of novel xanthone derivatives.

Methods: The products of reactions of xanthydrol with urea, thiourea, and thiosemicarbazide reacted with α-haloketones to prepare the thiazolone compounds. Xanthydrol reacted sequentially with ethyl chloroacetate, hydrazine, carbon disulfide, and α-haloketones to prepare the dithiolane. The xanthydrol reacted with propargyl bromide and it submitted to click reaction with azide to prepare triazole ring.

Results: Finally, four novel xanthones derivatives including (*E*)-2-(2-(9*H*-xanthen-9-yl)hydrazono)-1,3-dithiolan-4-one (L3), 2-(2-(9*H*-xanthen-9-yl)hydrazinyl)thiazol-5(4*H*)-one (L5), 2-(9*H*-xanthen-9-ylamino)thiazol-5(4H)-one (L7), and 4-((9*H*-xanthen-9-yloxy)methyl)-1-(4-nitrophenyl)-1*H*-1,2,3-triazole (L9) were synthesized and characterized using thin layer chromatography, Fourier-transform infrared spectroscopy, and nuclear magnetic resonance (^{1}H and ^{13}C). ADMET, Pfizer filter, adverse drug reaction, toxicity, antitarget interaction profiles, target fishing, kinase target screening, molecular docking validation, and protein and gene network analysis were computed for derivatives. Ligands obeyed Pfizer filter for drug-likeness, while all ligands were categorized as toxic chemicals. Major targets of all ligands were predicted to be kinases including Haspin, WEE2, and PIM3. Mitogen-activated protein kinase 1 was the *hub gene* of target kinase network of all derivatives. All the ligands were predicted to show hepatotoxic potentials, while L7 presented cardiac toxicity.

Conclusion: Acute leukemic T-cells were one of the top predicted tumor cell lines for these ligands. The possible antileukemic effects of synthesized xanthone derivatives are potentially very interesting and warrant further studies.

KEYWORDS

xanthone, total synthesis, ADMET, molecular docking, network analysis, target fishing

Highlights

- Xanthone derivatives possess numerous significant properties with biomedical applications.
- Four xanthone derivatives were synthesized from xanthydrol using dithiolan and thiazol.
- All stable xanthone derivatives were characterized using TLC and FTRI, and they were stable.
- Ligands did not express any violations to the Lipinski (Pfizer) filter for drug-likeness.
- Major targets of xanthone derivatives were subsets of the kinase family.
- Among synthesized derivatives, L9 expressed promiscuous potential in target binding.

1 Introduction

Xanthydrol ($C_{13}H_{10}O_2$; total molecular weight of 198.221 g/mol; Supplementary Figure 1) belongs to heterocyclic compounds known as xanthones or 9H-xanthen-9-ones, characterized by a tricyclic framework containing two benzene rings fused to a central pyrone ring. This heterocyclic system is widely in nature and is found in various natural products and bioactive compounds (Goldberg and Wragg, 1957; Badiali et al., 2023). Xanthydrol-based assays offer a sensitive and reliable method for measuring urea concentrations, providing valuable information for diagnosing and monitoring conditions such as kidney disease and dehydration (Supplementary Scheme 1) (Abrahamson, 1956). Xanthine and its derivatives have anticancer, anti-inflammatory, and antioxidative effects (Huang et al., 2021; Ramakrishnan et al., 2021; Kapri et al., 2022; Veríssimo et al., 2022). Moreover, recent studies have focused on innovative chemical synthesis approaches involving xanthydrol derivatives to develop novel compounds with potential anticancer properties. These studies aimed to harness the inherent reactivity and structural characteristics of xanthydrol for the targeted synthesis of compounds that could exhibit enhanced efficacy against cancer (Jiang et al., 2018). Synthesis and biopharmaceutical evaluation of xanthone derivatives were pursued by some researchers because these chemicals exert good anti-cancer activity by targeting topoisomerase II (TOP2) (Song et al., 2022). Besides their therapeutic potential, xanthydrol derivatives have been employed as fluorescent probes for cancer imaging, enabling researchers to visualize and study specific cellular processes associated with cancer. The development of these probes allows for precise and real-time monitoring of cancer-related biomolecules, contributing to the understanding of tumor progression, and facilitating early detection (Liu et al., 2018; Tian et al., 2024). In summary, further investigations are warranted to determine the targets and probable promiscuity potential of these derivatives.

Xanthones have emerged as a promising source for drug development especially in oncology (Kurniawan et al., 2021). Xanthones are a class of three-ring phenolic acids with a wide range of bioactivities, including antimicrobial, antiviral, anticancer, antioxidative, antidiabetic, and anti-inflammatory effects (Choodej et al., 2022). For instance, gambogic acid, a prenyl xanthone known in *Garcinia hanburyi*, Clusiaceae, exhibited noteworthy induction of apoptosis, inhibition of cell proliferation and tumor angiogenesis, and antioxidative and anti-inflammatory activities (Wang et al., 2009; Chen and Chen, 2012). In this line, xanthones exerted antitumor effects mediating through autophagy, apoptosis, cell cycle arrest, and tuning signaling pathways such as PI3K/Akt and MAPK (Gunter et al., 2023). More interestingly, in a second-phase clinical trial conducted in China, *algambog acid*, a derivative of xanthones, was investigated for its anti-tumor properties (Zhou and Wang, 2007). Furthermore, *gambogic acid*, a xanthone found in mangosteen, is dubbed as a dietary supplement for immune promotion, anti-inflammation, and induction of cell-mediated immunity (Gutierrez-Orozco and Failla, 2013; Rizaldy et al., 2021). In this continuum, a comprehensive survey has summarized the structure-activity relationships (SARs) of xanthones, providing valuable insights for further drug research, expansion, and development (Miladiyah et al., 2018). For instance, triazoles as pharmacophores are five-membered heterocyclic rings containing three nitrogen atoms with two main types of 1,2,3-triazoles and 1,2,4-triazoles (Supplementary Figure 2) (Matin et al., 2022; Raman et al., 2024). Both triazoles have tautomerized as reported previously (Supplementary Scheme 2) (Pylypenko et al., 2023). Numerous 1,2,3-triazoles have been synthesized through 1,3-dipolar cycloaddition reactions of acetylenes with azides. Typically, more electron-withdrawing substituents on the acetylene facilitates the cycloaddition reactions. Conversely, electron-withdrawing substituents on azides exert the opposite effect. Bulky substituents on azides may hinder the reaction rate but often result in an improved selectivity (Supplementary Scheme 3) (Dai et al., 2022; Drelinkiewicz and Whitby, 2022). Therefore, xanthones and their derivatives are promising anticancer compounds and they can be submitted to the computational pipeline of drug discovery and design.

Dithiolane (C3H6S2) is a diverse organic cyclic compound comprised a pentagon ring containing two sulfur atoms, giving rise to different structural isomers, including 1,2-dithiolane and 1,3-dithiolane (Supplementary Figure 3). Derivatives of this compound are collectively referred to as dithiolanes (Taguchi et al., 1987). Dithiolane compounds, exemplified by dithiolane and its derivatives, have emerged as intriguing subjects in cancer research due to their potential therapeutic effects (Nikitjuka et al., 2023). Dithiolan compounds have emerged as intriguing candidates in cancer research, offering potential therapeutic avenues for combating various malignancies. These compounds

were derived from a cyclic structure saturated with chemicals and they have diverse pharmacological properties in the cancer progression (Cao et al., 2023). In addition, their antioxidative activity may help counteract oxidative stress, a factor linked to cancer development (Theodosis-Nobelos et al., 2021). Also, dithiolanes have shown antiproliferative effects by influencing cell cycle progression and inducing apoptosis, providing potential avenues for inhibiting cancer cell growth (Ismail et al., 2023). Mechanistically, dithiolanes may interfere with crucial mechanisms involved in cancer progression through modulation of PI3K/AKT/mTOR and MAPK pathways (Felber et al., 2023). Furthermore, certain dithiolane compounds have been explored for their ability to enhance cancer cell sensitivity to chemotherapy, potentially improving treatment outcomes (Nikitjuka et al., 2023). Dithiolane was initially prepared by reacting carbon disulfide with methylene-active compounds in the presence of sodium ethoxide, followed by adding 1,2-dichloroalkanes to the reaction mixture (Supplementary Scheme 4) (Greene and Wuts, 1999). In conclusion, dithiolanes are pharmacophores used for anticancer drug design.

Thiazole (C3H3NS), also known as 1,3-thiazole, is a heterocyclic compound containing sulfur and nitrogen atoms, existing as a pale-yellow liquid with a pyridine-like odor (Supplementary Figure 4). Its structural simplicity contradicts its importance, as the thiazole ring serves as a component in the various biologically active molecules including vitamin thiamine (B1) (Kashyap et al., 2012). Although studies focusing on the direct roles of thiazole in oncotherapy are scarce, its derivatives showed promise in combating cancer through multiple mechanisms, including antiproliferative effects, induction of apoptosis, and inhibition of angiogenesis (Elmaati and El-Taweel, 2002; Mohareb et al., 2013). Thiazoles illustrate extensive applications in various fields due to their diverse properties. It is widely utilized in decomposing agricultural chemicals and pharmaceuticals, acting as a precursor for non-peptide protease inhibitors of human immunodeficiency viruses and anti-schistosomal agents (Cascioferro et al., 2020; Ibrahim and Rizk, 2020). Moreover, thiazole plays a crucial role in the production of tinctures in pharmaceuticals, and thiazole derivatives have demonstrated anticancer activities through various portals (El-Taweel and Elmaati, 2002; Shawali et al., 2002; Abdelrazek et al., 2010). Therefore, development of novel synthesized xanthone derivatives using thiazoles may have large potential for applications in both industry and medicine.

Here, we initially reported some synthetic and physicochemical features of xanthones derivatives and finally, we used a package of *in silico* tools to predict toxic and pharmacological properties and targets of xanthones derivatives for future applications in oncotherapy.

2 Experimental section

2.1 Chemistry

All reagents used in the synthesis and characteristics were purchased from Sigma-Aldrich Co. and Merck Co. (United States) and used without additional purification. Melting points were determined with a Thomas–Hoover capillary apparatus (Thomas Scientific, United States). Perkin Elmer Model 1,420 spectrometer was used to acquire infrared spectra (Thermo Fisher Scientific, United States). ^{1}H-NMR spectra with tetramethylsilane (TMS) as an internal standard were acquired with Bruker FT-500 MHz instrument (Brucker Biosciences, United States). Chloroform-D was used as a solvent. Coupling constant (J) values were estimated in hertz (Hz) and spin multiples were given as s (singlet), d (doublet), t (triplet), q (quartet), and m (multiplet). The mass spectral measurements were performed on a 6410 Agilent liquid chromatography/mass spectrometry (LCMS) triple quadrupole mass spectrometer (LCMS; AGILENT Technologies, United States) with an electrospray ionization (ESI) interface. Microanalyses, determined for C and H, were within ±0.4% of theoretical values. Analytical thin layer chromatography (TLC; CAMAG, Switzerland) was performed on silica gel plates using a mixture of ethanol in different proportions, coloring agents, benzene, and methanol to obtain different polarity and the best retention factor readout.

2.2 Synthesis

Many heterocyclic compounds were prepared (*vide infra*). In brief, xanthydrol reacted firstly with urea, thiourea, and thiosemicarbazide; then, the products reacted with α-haloketones to prepare the thiazolone compounds. Secondly, xanthydrol reacted firstly with hydrazine; then, it reacted with carbon disulfide. The resulting products then reacted with α-haloketones to prepare dithiolane. Thirdly, xanthydrol reacted with carbon disulfide and then reacted with α-haloketones. Fourthly, xanthydrol reacted sequentially with ethyl chloroacetate, hydrazine, carbon disulfide, and α-haloketones to prepare the dithiolane. Fifthly, xanthydrol reacted with propargyl bromide and it submitted to click reaction with azide to prepare a triazole ring.

2.2.1 Synthesis of (9H-xanthen-9-yl)hydrazine (L1)

A mixture of xanthydrol (0.01 M, 2.00 g) and hydrazine (0.01 M, 0.504 g) was dissolved in ethanol (25 mL) with a few drops of glacial acetic acid and stirred in a water bath at 67°C for 5–6 h. The progress of the reaction was monitored by TLC. At room temperature (RT), ethanol was evaporated, and the compound was then purified by recrystallization to obtain a whitish powder (Supplementary Scheme 5) (De Perre and McCord, 2011).

2.2.2 Synthesis of potassium 2- 9H-xanthen-9-yl) hydrazinecarbodithioate (L2)

A mixture of compound (L1; 0.005 M, 1.00 g) and CS2 (0.006 M, 0.358 g) was dissolved in ethanol (25 mL), stirred in a water bath at 67°C for 9–10 h, and drops of alcoholic KOH were added slowly. The progress of the reaction was monitored by TLC. At RT, ethanol was evaporated and the compound was then purified by recrystallization to obtain a yellowish powder (Supplementary Scheme 6) (Vasiliev and Polackov, 2000).

2.2.3 Synthesis of (E)-2-(2-(9H-xanthen-9-yl) hydrazono)-1,3-dithiolan-4-one (L3)

A mixture of compound (L2; 0.003 M, 1.00 g) and ethyl 2-chloroacetate (0.003 M, 0.375 g) was dissolved in ethanol (25 mL) using a few drops of tri-ethylamine and stirred in a water bath at

67°C for 6–7 h. The progress of the reaction was monitored by TLC. Ethanol was evaporated at RT, and the compound was then purified by recrystallization to obtain a nutty powder (Supplementary Scheme 7) (Lipin et al., 2019).

2.2.4 Synthesis of 2-(9H-xanthe-9-yl) hydrazinecarbothioamide (L4)

A mixture of xanthydrol (0.01 M, 2.00 g) and thiosemicarbazide (0.005 M, 0.518 g) was dissolved in ethanol (25 mL) using a few drops of glacial acetic acid and stirred in a water bath at 67°C for 5–6 h. The progress of the reaction was trailed by TLC. Ethanol was evaporated at RT to achieve yellow crystals (Supplementary Scheme 8) (De Perre and McCord, 2011).

2.2.5 2-(2-(9H-xanthen-9-yl)hydrazinyl)-1,3-thiazol-5(4H)-one (L5)

A mixture of compound (L4) (0.002 M, 1.00 g) and ethyl 2-chloroacetate (0.003 M, 0.451 g) was dissolved in ethanol (25 mL). The stirring in a water bath at 67°C for 7–8 h. The progress of the reaction was monitored by TLC. Ethanol was evaporated at RT, and the compound was then purified by recrystallization to obtain dark brown crystals (Supplementary Scheme 9) (Zheng and Huang, 2023).

2.2.6 Synthesis of 1-(9H-xanthen-9-yl)thiourea (L6)

A mixture of xanthydrol (0.01 M, 2.00 g) and thiourea (0.005 M, 0.384 g) was dissolved in ethanol (25 mL) with a few drops of glacial acetic acid and stirred in a water bath at 67°C for 6–7 h. The progress of the reaction was monitored by TLC. Ethanol was evaporated at RT, and the compound was then purified by recrystallization to obtain brown powder (Supplementary Scheme 10) (De Perre and McCord, 2011).

2.2.7 Synthesis of 2-(9H-xanthen-9-ylamino) thiazol-5(4H)-one (L7)

A mixture of compound (L6) (0.003 M, 1.00 g) and ethyl 2-chloroacetate (0.003 M, 0.478 g) was dissolved in ethanol (25 mL) and stirred in a water bath at 67°C for 8–9 h. The progress of the reaction was monitored by TLC. Ethanol was evaporated at RT, and the compound was then purified by recrystallization to obtain nutty crystals (Supplementary Scheme 11) (Resende et al., 2020).

2.2.8 Synthesis of 9-(prop-2-ynyloxy)-9H-xanthene (L8)

A mixture of xanthydrol (0.015 M, 3.00 g) and propargyl bromide (0.01 M, 1.200 g) was dissolved in DMF (dimethylformamide; 25 mL) and stirred, then 0.50 g potassium carbonate (K2CO3) was added slowly in a water bath at 75°C for 25–26 h. The progress of the reaction was monitored by using TLC, and it followed by adding 30 mL of distilled water, and two organic and aqueous phases were separated. Finally, the organic phase was evaporated and the compound was purified by recrystallization to reach a dark nutty powder (Supplementary Scheme 12) (Ramakrishnan et al., 2021).

2.2.9 Synthesis of 4-((9H-xanthen-9-yloxy) methyl)-1-(4-nitrophenyl)-1H-1,2,3-triazole (L9)

A mixture of compound (L8) (0.004 M, 1.00) and 1-azido-4-nitrobenzene (0.004 M, 0.731 g) was dissolved in DMF (25 mL) and stirred. Then, 5 mL of the resulting mixture was strongly added to the suspension of sodium ascorbate (0.4 g) and CuSO4.5H2O (0.3 g) in DMF (4 mL) in a water bath at 75°C for 45–50 h. The progress of the reaction was monitored by TLC. The reaction mixture was poured into distilled water (30 mL) and the product recrystallized from ethanol to reach a dark brown powder (Supplementary Scheme 13) (Ghasemi et al., 2019).

2.3 Computational methods (*in silico*)

2.3.1 Cheminformatics

The structures of the synthesized ligands were drawn using ChemSketch freeware, and their canonical SMILES formats were submitted to SwissADME (http://www.swissadme.ch/) to compute standard features of drug-likeness. In essence, the calculation of physicochemical properties, medicinal chemistry, and ADMET (absorption, distribution, metabolism, excretion, and toxicity) features using various filters provide information for the estimation of lead- and drug-likeness of hits (Lagorce et al., 2017). For instance, Lipinski's rule of five (RO5) or Pfizer filter screens lead-likeness of hits based on the criteria including, molecular weight ≤500, MLOGP ≤4.15, the number of (N + O) ≤ 10, and the number of (NH + OH) ≤ 5 (Lipinski et al., 2012; Kralj et al., 2023).

2.3.1.1 Adverse drug reaction (ADR) assay

ADVERPred server was launched at PASS (Prediction of Activity Spectra for Substances) technology (https://www.way2drug.com/PASSonline) for *in silico* prediction of ADRS such as myocardial infarction, arrhythmia, cardiac failure, myocardial infarction, hepatotoxicity, and nephrotoxicity. Prediction is based on the training sets encompassing manually curated information from drug labels. Practically, SMILES formats of synthesized ligands were submitted to the ADVERPred server containing training data sets for similarity research to estimate ADR (Ivanov et al., 2018). In addition, the Toxtree version 3.1.0.1851 software platform (http://toxtree.sourceforge.net/) was hired to forecast the toxicity class of synthesized ligands.

2.3.1.2 Prediction of antitarget interaction profiles

GUSAR software builds quantitative structure–activity relationship (QSAR) models using training sets characterized as structural data files (SDF; Way2Drug.com, 2011–2016). The QSAR models for the sets of 32 endpoints (50% inhibitory concentration—IC_{50}, inhibition constant—K_i, and activation constant—K_{act}) comprise the data about 4,000 chemical compounds interacting with 18 antitarget proteins (13 receptors, 2 enzymes, and 3 transporters). The biological profiles for antitargets of our new chemical entities (NCEs) were screened *in silico* using the machine learning-based software PASS 2020 (*vide supra*). The biological profile is categorized as a list of activities along with the probabilities of being active Pa and inactive Pi and with two conditions Pa > Pi and Pa ≥0.5.

2.3.1.3 Target fishing

The SwissTargetPrediction web server predicts probable protein targets based on the structural similarity of NCEs to already known

active library compounds. The SMILES strings of NCEs served as input for the computing of all standard features of drug-likeness (Daina et al., 2019). All targets of each ligand were presented in Excel files, and selected common targets of all ligands were submitted for validation using *in silico* molecular docking (*vide infra*).

2.3.1.4 Kinase target screening

Protein kinases are ubiquitous regulators of cell physiology, and their pathological activity switches cells from normal to abnormal state and disease phenotype. Accordingly, kinases are therapeutic targets, and more than ten kinase inhibitors have been entered into clinical practice in the last 4 years. Selectivity would be a core concept in the discovery of novel kinase inhibitors. Thus, to find safe and potent NCEs, their interactions with kinases would be initial steps in drug development. In essence, KinScreen (https://www.way2drug.com/KinScreen/) was aimed to optimize this process. The key features of KinScreen include the prediction of kinase targets with PASS software, untangling molecular mechanism of action of NCEs, the visualization of results on the kinome tree, and the search for analogous compounds across the ChEMBL database to find experimental data on them that were ignored in this study.

2.3.1.5 Molecular docking validation

The structures of synthesized ligands were converted into.pdb format using Open Babel (O'Boyle et al., 2011). The X-ray crystal structure of targets was retrieved from Protein Data Bank (PDB; http://www.RCSB.org), edited, optimized, and trimmed using Molegro Virtual Docker machine (Thomsen and Christensen, 2006) and Chimera 1.8.1 (http://www.rbvi.ucsf.edu/chimera). The *in silico* molecular docking was performed using PyRx software version 0.8 and the results were represented as binding affinity (BA; kcal/mol) values (Dallakyan and Olson, 2015).

2.3.2 Bioinformatics

The UniProt accession identification of target kinases was converted to gene symbols for humans using the SynGO gene set analysis tool (Koopmans et al., 2019), and pooled together, and submitted to GeneMANIA to construct target kinase network. GeneMANIA is a handy web interface for acquiring gene ontology, scrutinizing gene lists, and highlighting genes for functional assays (Warde-Farley et al., 2010). After choosing *Homo sapiens* from the list of optional organisms, the genes of interest in the previous step were entered into the search bar and the results were collated and high-scored genes were culled for further discussion. Moreover, the protein-protein network was also constructed in STRING *ver*. 12 launched at https://string-db.org, and submitted to Cytoscape *ver*. 3.10.2 for network analysis using a novel Cytoscape plugin *cytoHubba* and visualization (Shannon et al., 2003).

3 Results and discussion

3.1 Chemical synthesis and validation

The physicochemical properties of synthesized ligands have been shown in (Supplementary Table 1).

3.1.1 Characterization of)9H-xanthen-yl) hydrazine (L1)

The compound (L1) was synthesized by the reaction of xanthydrol with hydrazine hydrate. This compound was identified by FTIR spectroscopy by appearing (N-H, N-H2) stretching vibration at 3,200 and 3,500 cm^{-1} in compound (L1) and also the disappearance of the (O-H) bond at 3,345 cm^{-1} in xanthydrol (Supplementary Figure 1).

3.1.2 Synthesis of potassium 2-)9H-xanthen-yl) hydrazinecarbodithoate (L2)

The compound (L2) was synthesized by the reaction of compound (L1) with carbon disulfide. This compound was identified by FTIR spectroscopy by the disappearance of the (N-H2) bond at 3,200–3,400 cm^{-1} in the compound and appearing of (C=S) stretching vibration at 1,270 cm^{-1} for compound (L2) (Supplementary Figure 2).

3.1.3 Characterization of (E)-2-(2-(9H-xanthen-9-yl)hydrazono)-1,3-dithiolan-4-one (L3)

Compound (L3) was synthesized by the reaction of L2 with ethyl 2-chloroacetate. This compound was identified by FTIR spectroscopy by appearing (C=O) stretching vibration at 1,738 cm^{-1} and (N=C) at 1,671 cm^{-1} compound (L3) and also the disappearing the (C=S) bond at 1,207 cm^{-1} in compound (L2) (Figure 1).

3.1.4 Characterization of 2-(9H-xanthe-9-yl) hydrazinecarbothioamide (L4)

The compound (L4) was synthesized by the reaction of xanthydrol with hydrazinecarbothioamide. These compounds were identified by FTIR spectroscopy by appearing (N-H, NH2) stretching vibration at 3,200 and 3,500 cm^{-1} for compounds (L4), respectively, and also the disappearing the (O-H) bond at 3,200–3,400 cm^{-1} in xanthydrol and appearance of (C=S) stretching vibration at 1,200 cm^{-1} for compound (L4) (Supplementary Figure 3). The mechanism of the reaction was shown (Supplementary Scheme 1).

3.1.5 Characterization of 2-(2-(9H-xanthen-9-yl) hydrazinyl)thiazol-5(4H) one (L5)

The compound (L5) was synthesized by the reaction of (L4) with ethyl 2-chloroacetate. This compound was identified by FTIR spectroscopy by appearing (C=O) stretching vibration at 1,731 cm^{-1} and disappearing of the (N-H2) bond at 3,200–3,400 cm^{-1} in compound (L4) and disappearing the (C=S) stretching vibration at 1,200 cm^{-1} for compound (L4), and appearing of (C=N) stretching vibration at 1,617 cm^{-1} for compound (L5) (Figure 2). ^{13}C-NMR appearing (55) (C-N) 9H-xanthene (62) (=N-C)thiazol (130–140) Aromatic (166) (C=N) thiazol (176) (C=O)thiazol (155) (=C-O)9H-xanthene (Figure 3). The compound (L5) was also determined by the appearance of ^{1}H-NMR from (NH) amine (1H) is about (2.1) while (2H) (=N-CH2) thiazol is at (3) and (CH-NH)9H-xanthene (1H) is at (5.3) while aromatic is at (7–8) (Figure 4). The reaction mechanism is depicted below (Scheme 1). The L5 (C16H13N3O2S; Figure 4) has been composed of C (59.49%–61.72%), H (4.21%–5.23%), N (13.50%–15.12%), and S (10.30%–10.71%).

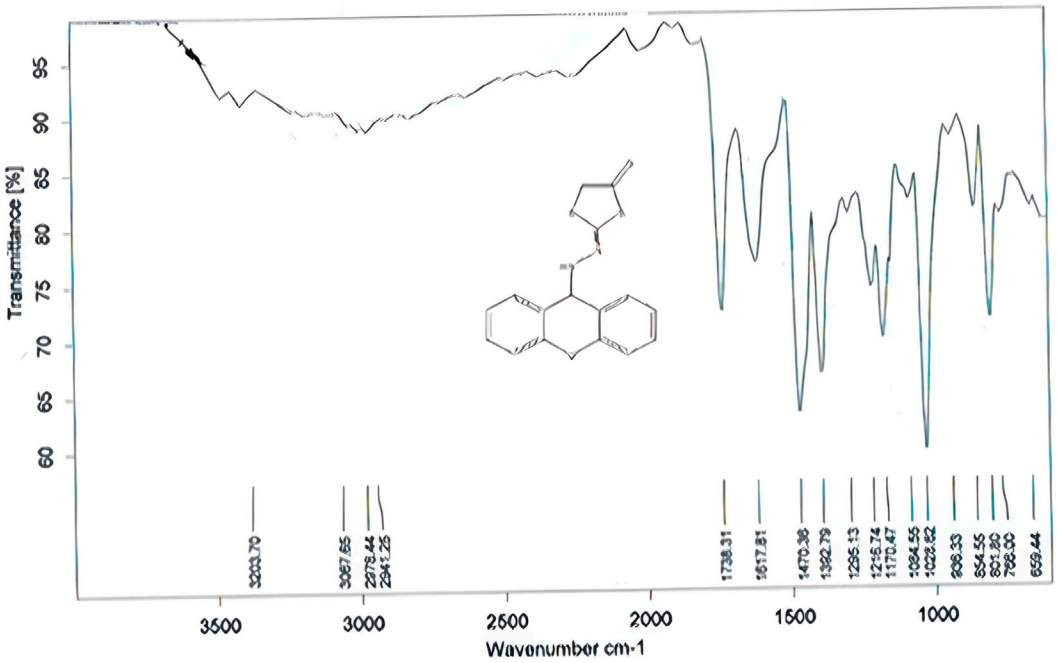

FIGURE 1
FTIR spectrum of compound (L3).

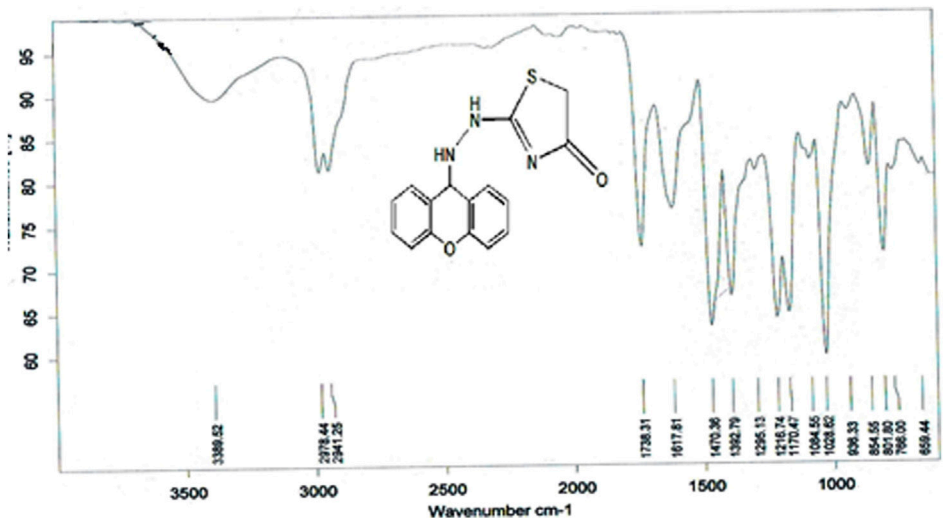

FIGURE 2
FTIR spectrum of compound (L5).

3.1.6 Characterization of 1-(9H-xanthen-9-yl) thiourea (L6)

The compound (L6) was synthesized by the reaction of xanthydrol with thiourea, and identified by FTIR spectroscopy by appearing (N-H, NH2) stretching vibration at 3,200 and 3,500 cm^{-1} for compound (L6) respectively, and also the disappearing the (O-H) bond at 3,200–3,400 cm^{-1} in xanthydrol, and appearing (C=S) stretching vibration at 1,209 cm^{-1} for compound (L6) (Supplementary Figure 4).

3.1.7 Characterization of 2-(9H-xanthen-9-ylamino)thiazol-5(4H)-one (L7)

Compound (L7) was synthesized by the reaction of (L6) with ethyl 2-chloroacetate. This compound was identified by FTIR spectroscopy by appearing (C=O) stretching vibration at 1,739 cm^{-1} in compound (L7) and also the disappearing the (N-H2) bond at 3,200–3,400 cm^{-1} in compound (L6), and appearing of (C=N) stretching vibration at 1,648 cm^{-1} for compound (L7) (Figure 5).

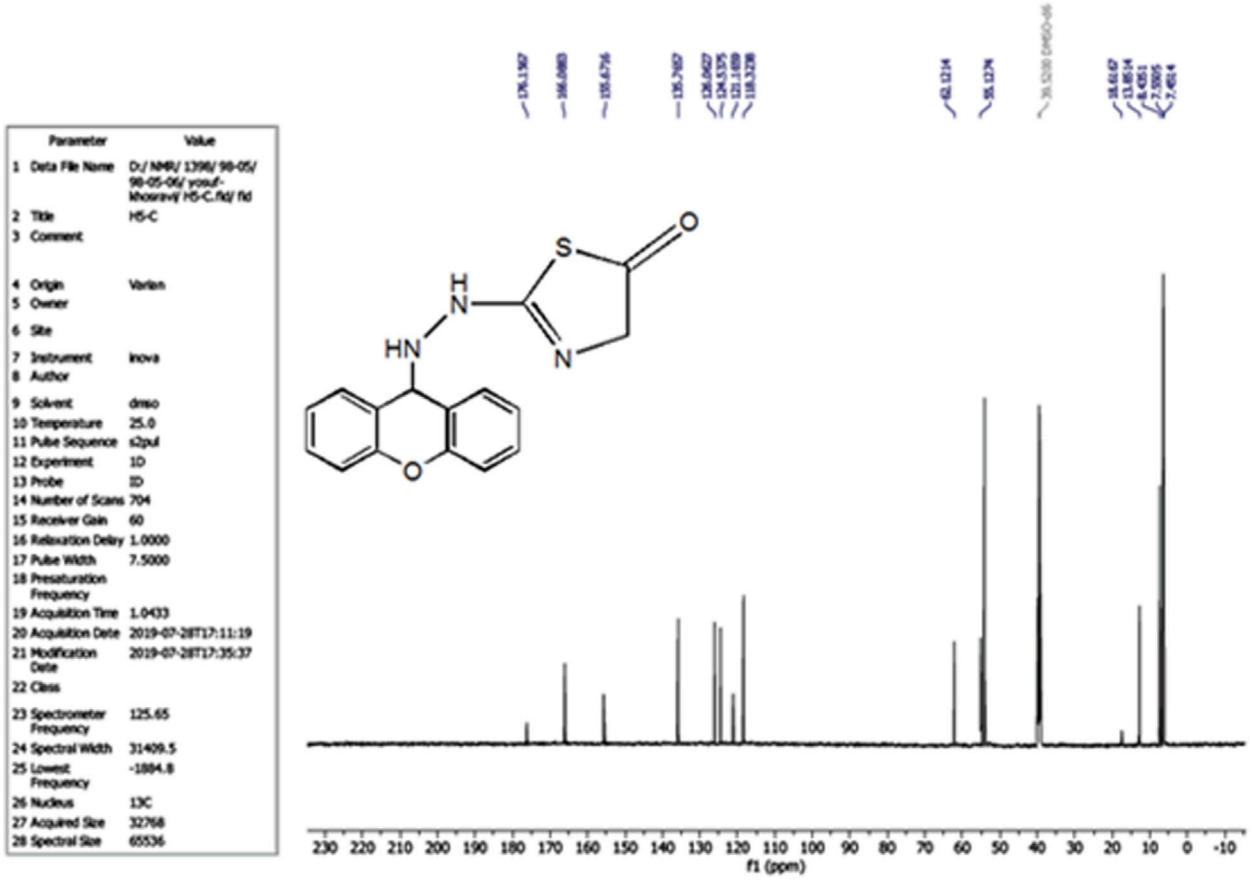

FIGURE 3
^{13}C-NMR Spectrum of compound (L5).

3.1.8 Characterization of 9-(prop-2-ynyloxy)-9H-xanthene (L8)

The compound (L8) was synthesized by the reaction of xanthydrol with propargyl bromide. This compound was identified by FTIR spectroscopy by appearing (HC≡——H) stretching vibration at 2,123 cm^{-1} for compounds (L8) and also the disappearing the (O-H) bond at 3,200–3,400 cm^{-1} in xanthydrol and appearing (C-H) vibration for compound (L8) (Supplementary Figure 5).

3.1.9 Characterization of 4-((9H-xanthen-9-yloxy) methyl)-1-(4-nitrophenyl)-1H-1,2,3-triazole (L9)

The compound (L9) was synthesized by the reaction of (L8) with 1-azido-4-nitrobenzene. This compound was identified by FTIR spectroscopy by appearing (NH) stretching vibration at 3,362 and 3,474 cm^{-1} for compound (L9), and also the disappearing the (HC≡——H) bond at 2,123 cm^{-1} in compound (L8) and disappearance of (C-H) vibration for compound (L8; Figure 6).

3.2 ADMET scan

Ligands obeyed the Lipinski (Pfizer) filter for drug-likeness without positive alerts for considering pan-assay interference compounds (PAINS; Supplementary Figure 7; Supplementary Table 1). PAINS react promiscuously to various targets because they possess disruptive functional groups that have been traced by SwissADME (Baell and Holloway, 2010; Daina et al., 2017). In this line, MWs of ligands were less than 500 g/mol and they can be absorbed from the gastrointestinal tract. MLOGP of L9 (3.2) was increased in comparison to other ligands (Table 1), while other ligands had identical MLOGP of 1.9 which reflects lesser lipophilicity of all ligands. The bioavailability scores of all ligands were the same. Among all ligands, L7 showed blood-brain barrier (BBB) permeation. The topical polar surface areas (TPSAs) of all ligands were less than 140 $Å^2$ which obeys the RO5. The number of rotatable bonds, single bonds that can freely rotate around their axis, was higher in L9 as compared to those of other ligands. The number of rotatable bonds in a molecule affects its efficacy, pharmacokinetic properties, conformational flexibility, interaction with target proteins, and ADMET properties. Based on the higher number of rotatable bonds in L9, this ligand may be too flexible to bind tightly to its target. The flexibility of L9 was higher than those of other ligands which showed similar flexibility. In this regard, the number of rotatable bonds should not surpass nine rotatable bonds. The role of flexibility as a filter for ADMET properties besides TPSA, and hydrogen bond count are the key determinants of bioavailability (Veber et al., 2002). The number of rotatable bonds in the Csp^3 configuration dictates the flexibility of a molecule (Caron et al., 2020). Although this configuration was decreased in L9 as compared

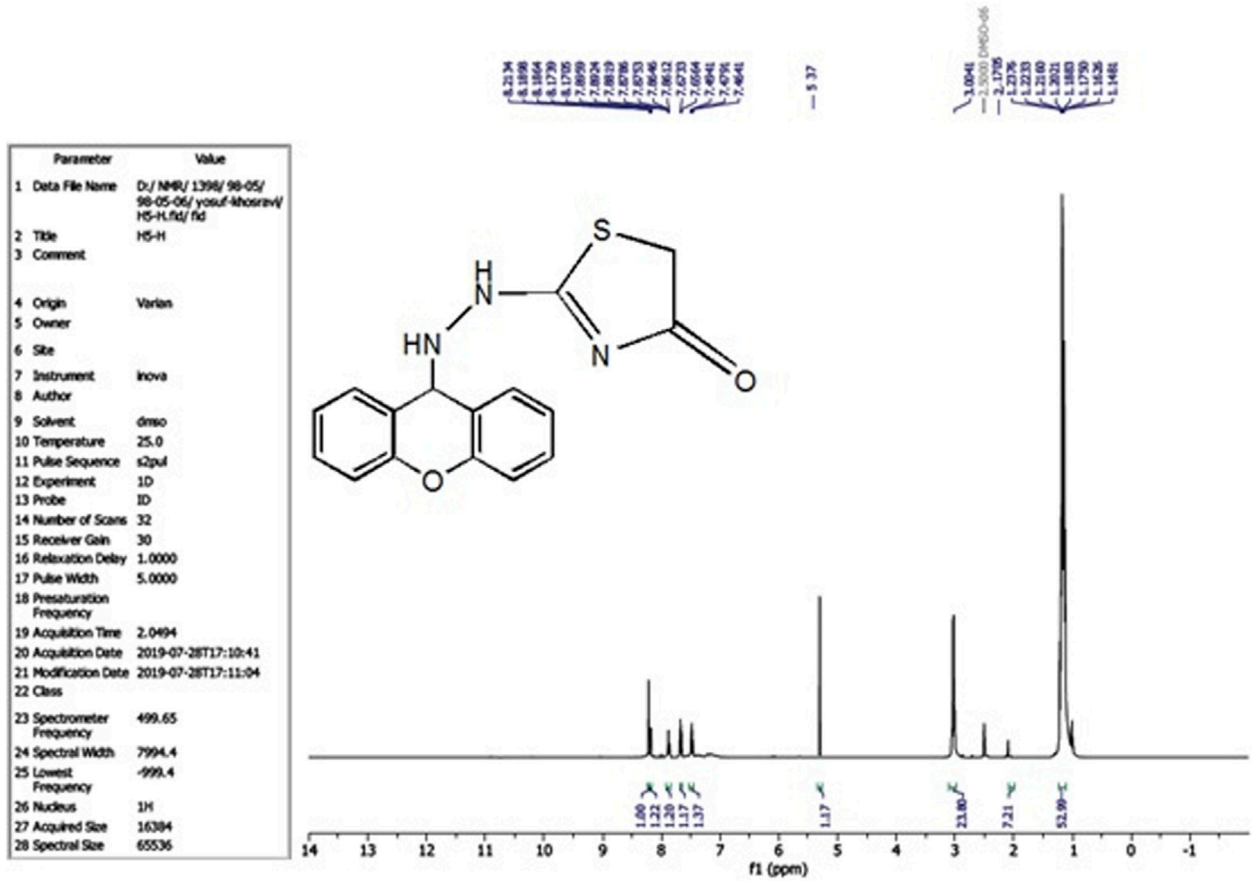

FIGURE 4
^{1}H-NMR Spectrum of compound (L5).

to those of other ligands, it was more flexible. Among proper physicochemical properties of ligands for oral bioavailability (Figure 7), only saturation (fraction Csp^3) was lesser than the cutoff value of 0.22. All ligands had fraction Csp3 values of 0.12 except L9 which had 0.09 (Supplementary Material S4). In this study, all synthesized ligands possessed a SP^3 hybridization fraction lesser than 0.25. The percentage of SP^3 fraction in a molecule is a main descriptor for the prediction of the three-dimensionality and intricacy of molecular structures. Computationally, the SP^3 fraction is used to evaluate the "drug-likeness" or "lead-likeness" of NCEs, and molecules with a higher SP^3 fraction often display better pharmacological profiles. These molecules are expected to adopt diverse spatial conformations, allowing more specific interactions with the intricate shapes of biological targets. In summary, synthesized ligands were accepted as lead-like compounds and they should be submitted to QSAR screening for their biological activities to optimize their pharmaceutical applications.

All ligands had high human intestinal absorption (HIA), while L7 just displayed BBB permeation (Supplementary Material S4). L5 and L9 were substrates of P-glycoprotein (P-gp) as a subset of ATP-binding cassette (ABC) transporters that can efflux drugs of cells to shorten the duration of their pharmacological effects (Amezian and Van Leeuwen, 2024). Moreover, all synthesized ligands except L9 were cytochrome P450 (CYP450) inhibitors. CYP450 enzymes facilitate the phase I of xenobiotics metabolism to make them more soluble for excretion (Esteves et al., 2021). All NCEs should be computationally tested for categorizing as inhibitors or substrates of CYP450 enzymes to forecast their drug-drug interactions and ADRs (Daina et al., 2017). In this continuum, L3, L5, and L7 contain heterocyclic rings with complex substituents, while L9 contains functional groups associated with enhanced toxicity. All ligands were categorized as Class III of toxicity according to the Cramer decision tree (Cramer et al., 1976). In this line, the triazole ring is known as one of the main pharmacophores of the nitrogen-containing heterocycles (Guo et al., 2021), and it can enhance the toxicological activities of other molecules. Therefore, the synthesized ligands should be checked through a battery of bioassays for consideration as lead-like, drug, or poison.

3.3 Target fishing and validation

Target fishing is a bottleneck in the laborious and expensive pipeline of experimental pharmacology for dissecting the interaction of a bioactive compound with its druggable target proteins. In this continuum, *in silico* target fishing employs machine learning algorithms and chemi- and bio-informatic tools for the prediction of the targets of NCEs. Here, we used the

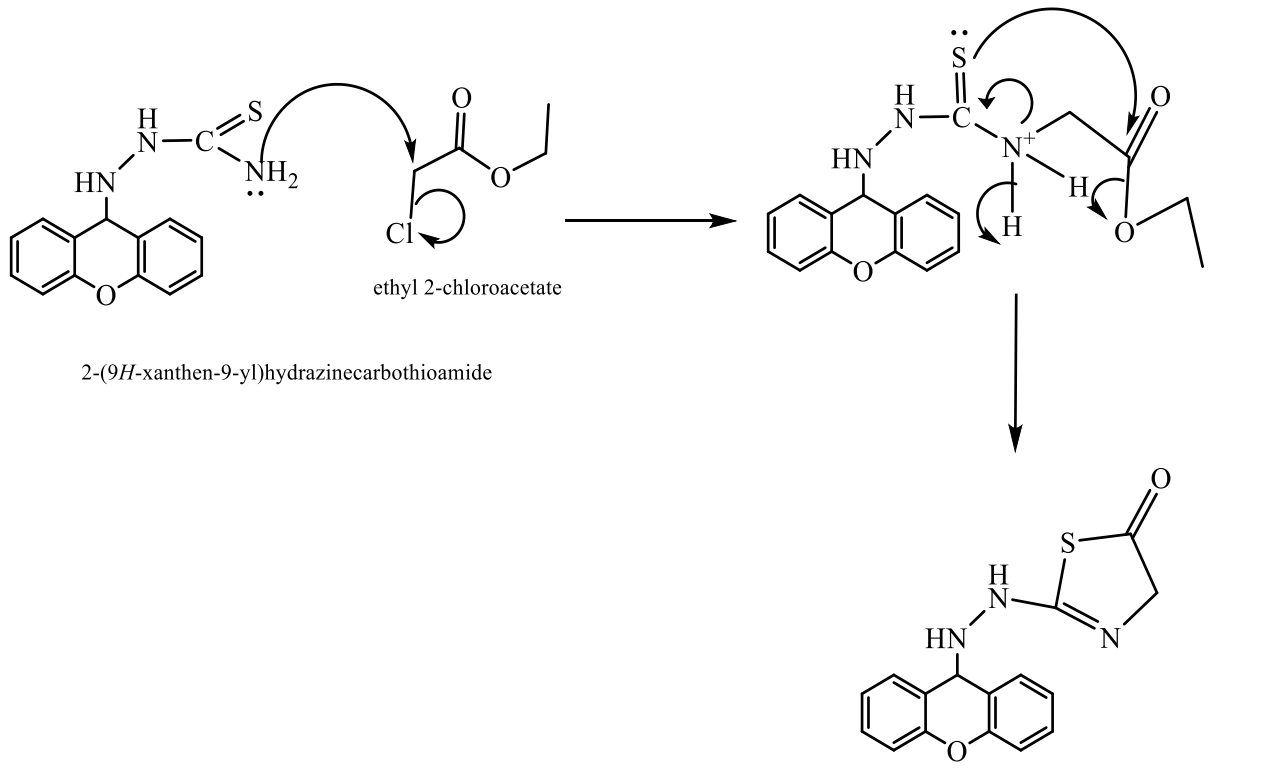

SCHEME 1
Mechanism of synthesis of compound (L5).

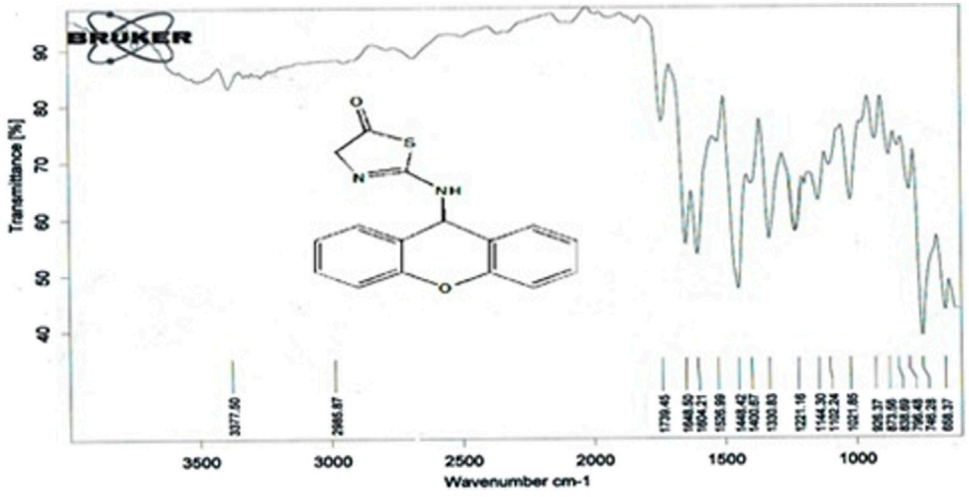

FIGURE 5
FTIR spectrum of compound (L7).

SwissTargetPrediction to predict chemical-protein interactions (Supplementary Material S5). Four common targets of all ligands were extracted from target sets of each ligand and submitted to *in silico* molecular docking validation (Supplementary Material S6). Four common targets were three kinases including vascular endothelial growth factor receptor 2 (CHEMBL279; PDB ID: 1YWN), tyrosine-protein kinase (CHEMBL2148; PDB ID: 3LXL), and epidermal growth factor receptor (erbB1; CHEMBL203; PDB ID: 5UG9), and sodium channel protein type IX alpha subunit (CHEMBL4296; PDB ID: 5EKO) which belongs to the family of

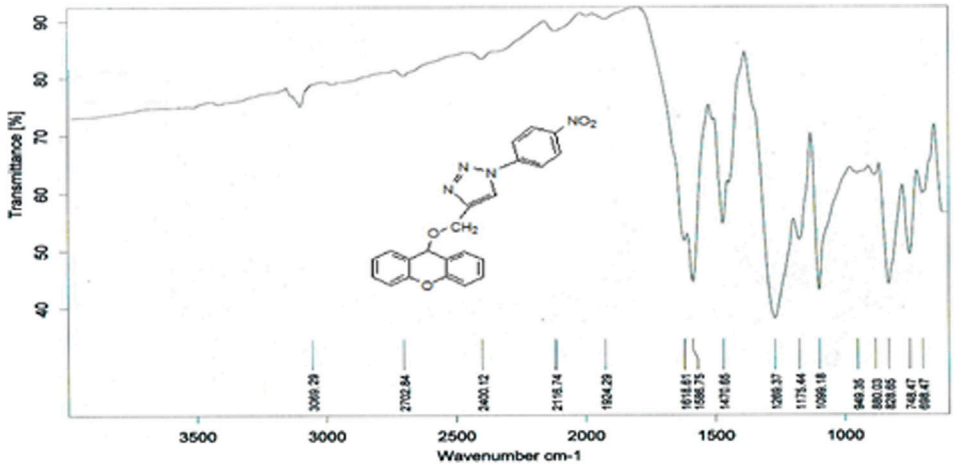

FIGURE 6
FTIR spectrum of compound (L9).

TABLE 1 Pharmacological and toxicological features of synthesized xanthone derivatives.

Ligand	MW g/mol	MLOGP	Hdon	Hacc	BS	BBB	TPSA Å^2	RBN	Lipinski #violations	PAINS #alert
L3	328	1.99	1	3	0.55	NO	101.29	2	0	0
L5	311	1.97	2	4	0.55	No	88.02	3	0	0
L7	296	1.99	1	3	0.55	Yes	75.99	2	0	0
L9	401	3.26	1	6	0.55	No	89.48	5	0	0

Note: MW, molecular weight (kDa); MLOGP, Moriguchi Log $P_{o/w}$; Hdon, the number of H-bond donors; Hacc, the number of H-bond acceptors; BS, oral bioavailability score; Caco-2, permeability; BBB, blood-brain barrier; TPSA, topographical polar surface area; RBN, the number of rotatable bonds: HL, half-life; PAINS, Pan-assay interference compounds. 2-[2-(9H-xanthen-9-yl)hydrazinyl]-1,3-dithiolan-4-one (L3; SMILE: O=C1CS\C(S1)=N/NC1C2=CC=CC=C2OC2=C1C=CC=C2), 2-[2-(9H-xanthen-9-yl)hydrazinyl]-1,3-thiazol-5(4H)-one (L5 SMILE: O=C1CN=C(NNC2C3=CC=CC=C3OC3=C2C=CC=C3)S1), 2-(9H-xanthen-9-ylamino)-1,3-thiazol-5(4H)-one (L7 SMILE: O=C1CN=C(NC2C3=CC=CC=C3OC3=C2C=CC=C3)S1), and lower right; hydroxy(oxo)(4-{4-[(9H-xanthen-9-yloxy)methyl]-1H-1,2,3-triazol-1-yl}phenyl)ammonium (L9 SMILE: ON(=O)C1=CC=C(C=C1)N1C=C(COC2C3=CC=CC=C3OC3=CC=CC=C23)N=N1).

voltage-gated ion channels. In this context, L3 predominantly docked with family erbB1, however it interacted reliably with other kinases like MAP kinase ERK1 and protein kinase C mu (Table 2). In this continuum, L5 docked firmly with erbB1 and tyrosine-protein kinase, and it interacted with MAP kinase ERK1. L7 docked with tyrosine-protein kinase more reliably than other ligands, and it was the weakest binder in this study. Interestingly, L9 showed the strongest BAs with all common targets, while it docked tyrosine-protein kinase with the highest BA of −11.1 kcal/mol (Supplementary Material S6). In summary, these synthesized ligands docked reliably with tyrosine-protein kinase and erbB1 (Supplementary Material S6).

3.4 Kinase target fishing

Except for L9, the major target family of synthesized ligands was the kinase family as predicted by SwissTarget (Figure 8). Moreover, KinScreen launched at https://www.way2drug.com/KinScreen/ predicted the interaction of pharmacological substances with human kinome (see Supplementary Material S7). In essence, the main top 5 list targets and therapeutic classes of ligands have been presented (Supplementary Table 1). In this continuum, various serine/threonine-protein kinases were common kinase targets for synthesized ligands. Protein kinase C mu, MAP kinase ERK1, dual specificity protein kinase CLK3, and casein kinase I gamma 2 were highly accurate predicted targets for L3, L5, L7, and L9, respectively (Supplementary Table 1). Consistent with the results of KinScreen, SwissTarget also showed that the common targets for four synthesized ligands were three kinases and one target belongs to the voltage-gated ion channel (VIC) superfamily (Figure 8).

3.5 Kinase target network

All target kinases were harvested from KinScreen and submitted to GeneMANIA and STRING servers (*vide supra*). In this regard, three genes showed the highest weights in the kinase target network of synthesized ligands in the output of GeneMANIA (see Supplementary Table 1). In this line, haploid germ cell-specific nuclear protein kinase (Haspin) showed the maximum weight in the network constructed using the GeneMANIA server. This gene encodes a serine/threonine kinase that is known as a promising target against cancer (Liu et al., 2023). WEE2 is a kinase that is expressed in an array of cancers (https://www.proteinatlas.org/ENSG00000214102-WEE2/pathology). The PIM3 belongs to the

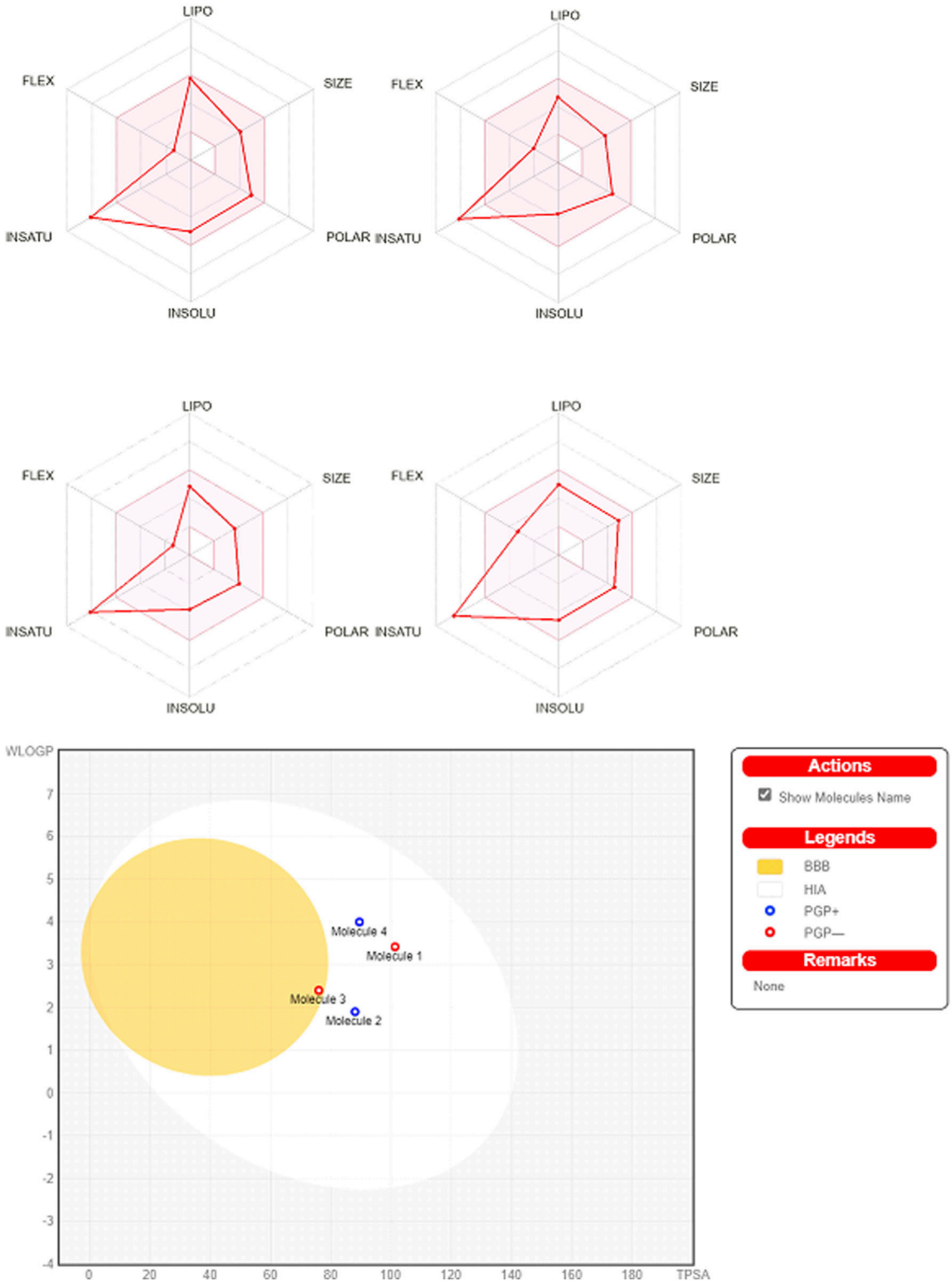

FIGURE 7
Bioavailability radars and BOILED-Egg scan. The pink area symbolizes the optimal range for physicochemical properties (size: MW (molecular weight; 150–500 g/mol, lipophilicity: XLOGP3 −0.7-+5.0, polarity: TPSA (topological polar surface area; 20–130Å^2, solubility: log S ≤ 6, saturation: fraction of carbons in the Csp^3 hybridization ≥0.25, and flexibility: ≤9 rotatable bonds. Note: upper left; 2-[2-(9H-xanthen-9-yl)hydrazinyl]-1,3-dithiolan-4-one (L3); upper right; 2-[2-(9H-xanthen-9-yl)hydrazinyl]-1,3-thiazol-5(4H)-one (L5); lower left; 2-(9H-xanthen-9-ylamino)-1,3-thiazol-5(4H)-one (L7), and lower right; hydroxy (oxo)(4-{4-[(9H-xanthen-9-yloxy)methyl]-1H-1,2,3-triazol-1-yl}phenyl)ammonium (L9). Human intestinal absorption (HIA), blood-brain barrier (BBB) penetration, lipophilicity (WLOGP), and polarity (TPSA) have been computed. The mutually exclusive white and region (yolk) region depict the highest probability of being absorbed by gut and being permeated to the brain, respectively.

TABLE 2 *In silico* molecular docking [binding affinity (lower bound, upper bound)] of xanthone derivatives with top-list predicted targets.

Ligand	Top-list target (PDB)					
	1YWN	3LXL	5EK0	5UG9	3W8Q	4U7Z
L3	−7.8 (7.926; 4.45)	−8.8 (4.122; 1.989)	−8.1 (5.771; 3.003)	−9.0 (3.675; 0.069)	−8.7 (3.675; 0.116	−8.5 (3.676; 0.122)
L5	−8.2 (3.675; 0.074)	−9.1 (3.676; 0.093)	−7.0 (37.57; 34.943)	−9.0 (3.675; 0.062)	−9.5 (3.676; 0.1)	−8.9 (3.676; 0.104
L7	−7.9 (3.761; 0.008)	−8.5 (3.762; 0.065)	−6.9 (3.761; 0.027)	−8.3 (3.762; 0.049)	−8.5 (3.762; 0.017)	−8.3 (3.762; 0.016)
L9	−10.1 (3.261; 0.17)	−11.1 (3.259; 0.115)	−9.3 (2.786; 2.234)	−10.2 (3.265; 0.221)	−10.3 (3.92; 2.373)	−10.2 (3.258; 0.055)

Note: 2-[2-(9H-xanthen-9-yl)hydrazinyl]-1,3-dithiolan-4-one (L3), 2-[2-(9H-xanthen-9-yl)hydrazinyl]-1,3-thiazol-5(4H)-one (L5), 2-(9H-xanthen-9-ylamino)-1,3-thiazol-5(4H)-one (L7), and hydroxy (oxo)(4-{4-[(9H-xanthen-9-yloxy)methyl]-1H-1,2,3-triazol-1-yl}phenyl)ammonium (L9).

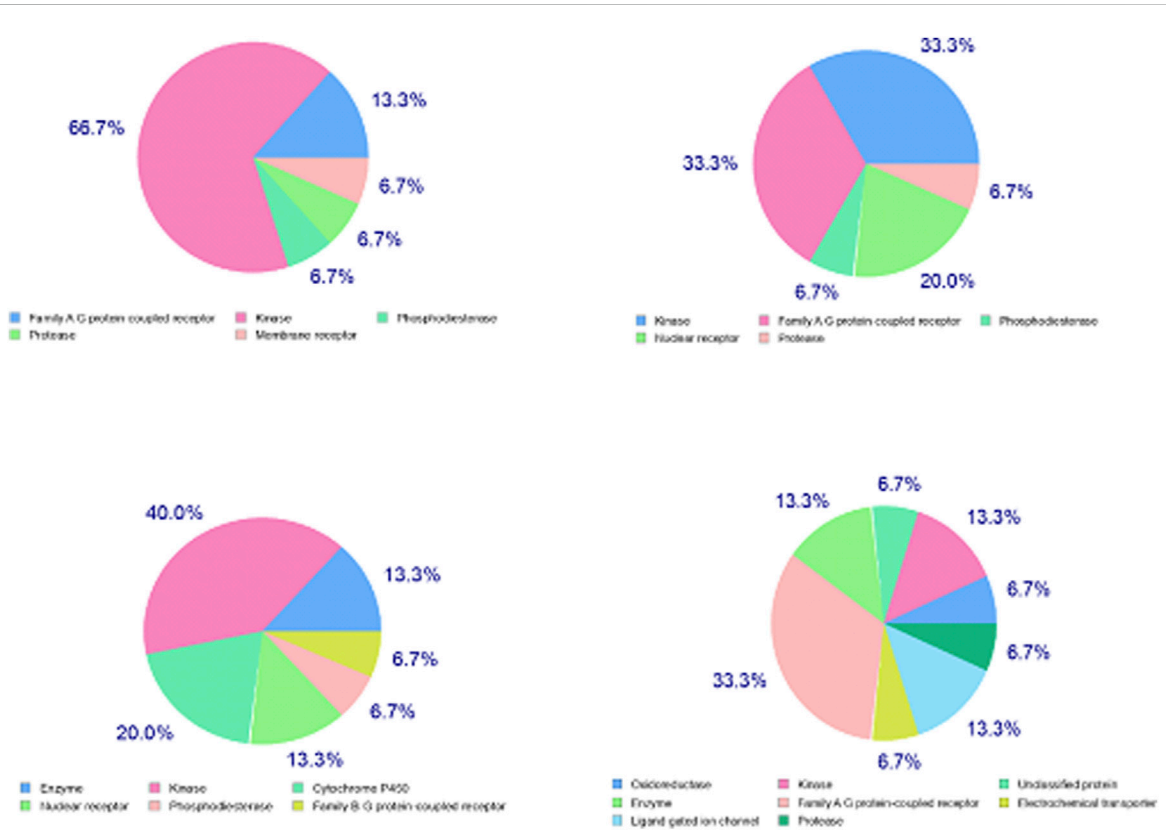

FIGURE 8
Distribution of targets in various classes for xanthones derivatives. Note: upper left; 2-[2-(9H-xanthen-9-yl)hydrazinyl]-1,3-dithiolan-4-one (L3); upper right; 2-[2-(9H-xanthen-9-yl)hydrazinyl]-1,3-thiazol-5(4H)-one (L5); lower left; 2-(9H-xanthen-9-ylamino)-1,3-thiazol-5(4H)-one (L7), and lower right; hydroxy (oxo)(4-{4-[(9H-xanthen-9-yloxy)methyl]-1H-1,2,3-triazol-1-yl}phenyl)ammonium (L9).

Ser/Thr protein kinase family, and PIM subfamily is overexpressed in epithelial and hematological tumors and associated with MYC coexpression. It plays roles in signal transduction, cell proliferation and survival, and tumorigenesis like human hepatoblastoma cells (Marayati et al., 2022).

The results of kinase network analysis were shown (Supplementary Material S9), and the degree sorted circle layout of the network was presented in Figure 9. Statistics of the network were summarized as follows: number of nodes: 222; number of edges: 1,344; average number of neighbors: 13,039; network diameter: 6; network radius: 3; characteristic path length: 2,601; clustering coefficient: 0.404; network density: 0.064; network heterogeneity: 0.893; network centralization: 0.231; connected components: 16; analysis time (sec): 0.152. In this line, the top-listed nodes with the highest degree (n) were MAPK1 (n = 60), FYN (n = 53), MAPK14 (n = 52), ERBB2 (n = 51), ABL1 (n = 47), ATM (n = 47), MAPK3 (n = 46), and GSK3B (n = 44) (see Supplementary Material S9). CytoHubba App was employed to search the hub node of the kinase target network (see Supplementary Material S10). Then, the top ten nodes ranked by degree were presented in Figure 10. Mitogen-activated protein kinase 1 (MAPK1) was the main *hub gene* among all target kinases for synthesized ligands which were submitted to molecular docking for further validation (Supplementary Table 2). We intentionally used two PDB IDs of

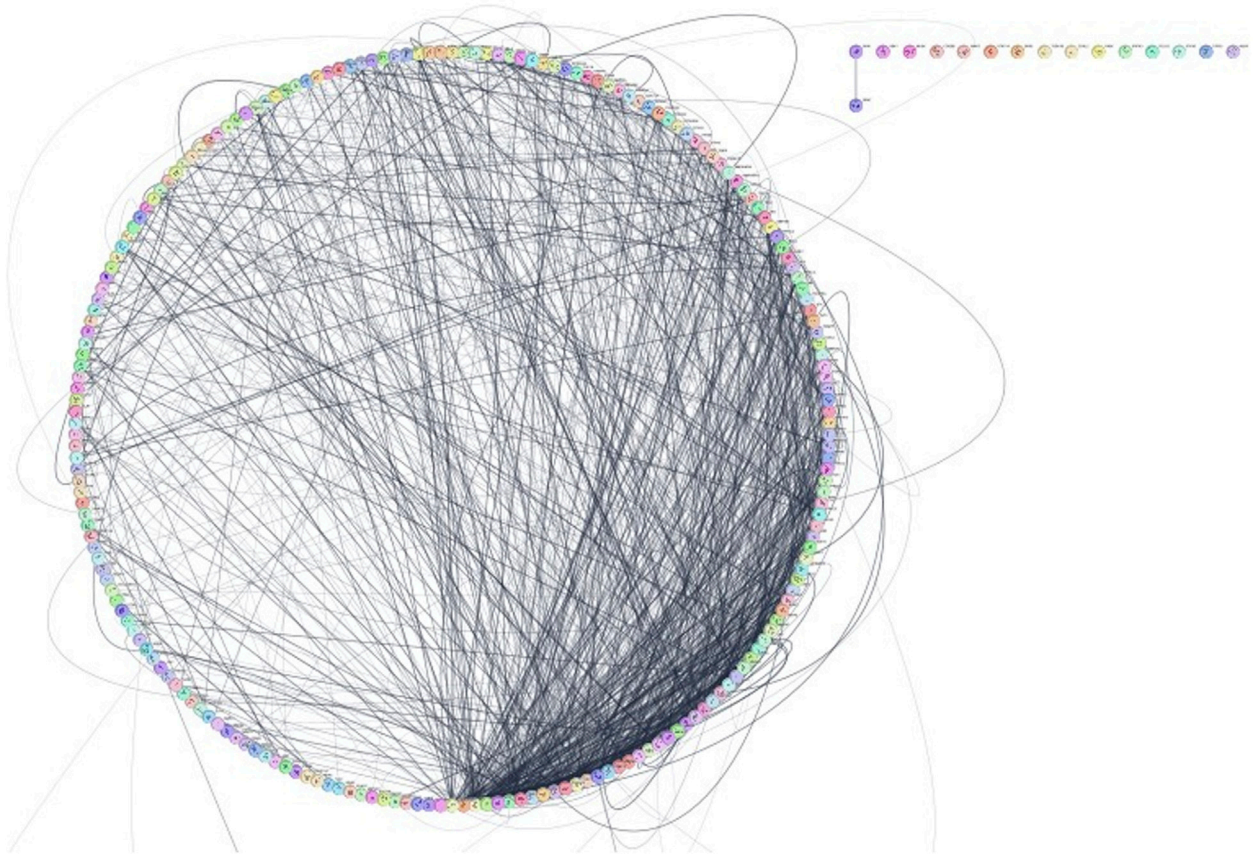

FIGURE 9
Visualization of the constructed network in Cytoscape results page.

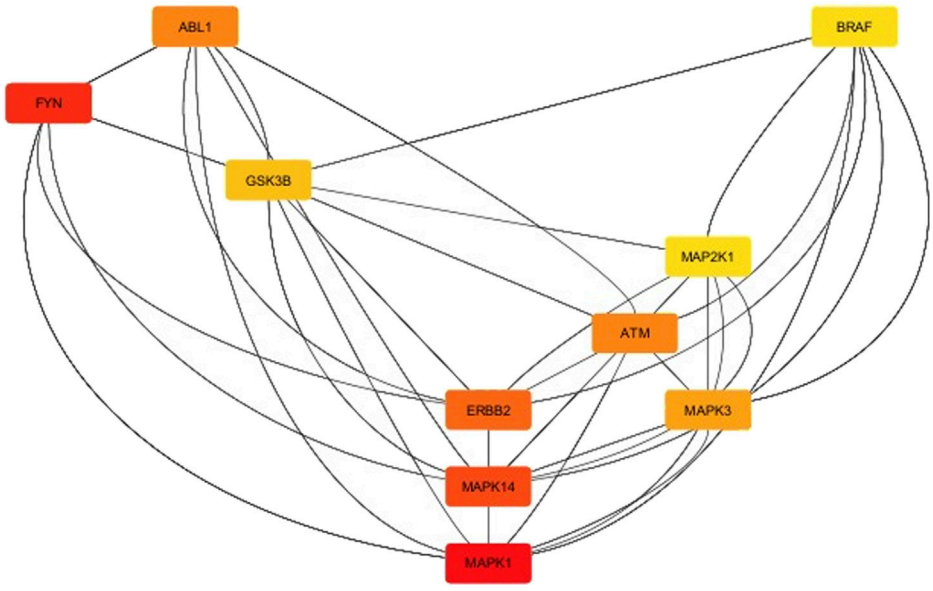

FIGURE 10
Top ten nodes ranked by degree using the CytoHubba app installed in Cytoscape.

MAPK1 to check the accuracy of BAs of synthesized ligands with a hub target that was determined through PPI network analysis. In essence, similar binding modes of synthesized ligands with MAPK1 PDBs were seen. In this case, L9 presented the best BA with MAPK1 (Table 2). MAPK1 is a serine/threonine kinase in the MAP kinase signal transduction pathway that is involved in the pathogenesis of many diseases and various types of cancers (Kim and Choi, 2010).

3.6 Antitarget and ADRs screening

Computation of the interaction of NCEs with *antitargets* is a crucial step to disclosing ADRs in the pipeline of drug discovery and development and clinical practice. In this regard, previous experimental data that are presented as K_i, K_{act}, and IC_{50} values can be categorized and used as models to create (quantitative) structure and activity relationship [(Q)SAR] (Lagunin et al., 2018). In this study, we used GUSAR software launched at http://www.pharmaexpert.ru/GUSAR/antitargets.html, finds antitargets of hit of interest among about 4,000 chemicals interacting with 18 antitarget proteins (13 receptors, 2 enzymes and 3 transporters; see Supplementary Material S8). Based on GUSAR, rational accuracy ($Q^2_{model} > 0.6$ and $R^2_{test} > 0.6$) has been considered for computational prediction of antitargets of NCEs (Zakharov et al., 2012). All ligands showed altering activity of carbonic anhydrase II (see Supplementary Table 2) that may be the cause of aplastic anemia, anxiety, bone marrow suppression, chronic fatigue syndrome, alopecia, anaphylaxis, depression, and renal tubular acidosis (Rang et al., 1999). The interaction of synthesized ligands with 5-hydroxytryptamine 2C receptors as antagonists were also significant. In this case, the ADRs of antagonists to 5-hydroxytryptamine receptors are sickness, emesis, diarrhea, insomnia, and anxiety (Hoyer, 2020).

The specific potential of interacting with antitargets was also observed among our synthesized ligands. In this regard, trustful interaction of L3 was found with the 5-hydroxytryptamine 2A receptor and d3 dopamine receptor. Similarly, L5 also interacted with alpha1b adrenergic receptors. Adrenergic receptor antagonists may cause reflex tachycardia, orthostatic hypotension, nasal congestion, insomnia, and palpitation (Rang et al., 1999). L7 also interacted 5-hydroxytryptamine 2C receptor, while L9 interacted overtly with the kappa-type opioid receptor (see Supplementary Table 2). Antagonism to opioid receptors may cause emesis, sickness, respiratory depression, and sedation (Brunton et al., 2023). All synthesized ligands showed hepatotoxic potentials, while L7 presented cardiac toxicity (see Supplementary Table 3). Therefore, these ligands may possess some ADRs that must be considered in future experimental bioassays.

3.7 Antitumor potential

The cytotoxicity of NCEs against tumor cell lines is in the initial stages of development, repositioning, and drug research. However, the interaction of NCEs with normal cell lines gives impressive cues regarding their toxic potential. In this line, all synthesized ligands showed a low probability of activity against common normal cell lines that were used for snap-screening of cytotoxicity (see Supplementary Table 4). All ligands except L9, showed interaction with prostate epithelial cells. Embryonic lung fibroblast was also a target of all ligands except L7. In this context, L7 was less toxic for the normal cell line among ligands, and L3 showed a broad spectrum of toxicities against the normal cell lines.

Acute leukemic T-cells display one of the top predicted tumor cell lines for L5 (see Supplementary Table 5). All ligands except L9 showed weak interaction with glioblastoma and oligodendroglioma, and L9 showed a different pattern of tissue tumor targeting among ligands (see Supplementary Table 5). Allanxanthone C and macluraxanthone, two phyto-xanthones, exhibited proapoptotic and antiproliferative activities in leukemic cells from chronic lymphocytic leukemia and leukemia B cell lines (Loisel et al., 2010). Future investigations are welcomed to dissect the mechanism of possible antileukemic effects of synthesized xanthone derivatives that proposed in this study.

4 Conclusion

In conclusion, the total synthesis of nine novel xanthone derivatives was accomplished in a multi-step linear sequence and characterized. Finally, four compounds (L3, L5, L7, and L9) were selected for the computational assessment based on the Pfizer filter. Kinase network analysis showed that the top-listed nodes were MAPK1, FYN, MAPK14, ERBB2, ABL1, ATM, MAPK3, and GSK3B. MAPK1 was the main *hub gene* involved in the pathogenesis of many diseases and cancers. Interestingly, future investigations are needed to dissect the mechanism of possible antileukemic effects of synthesized xanthone derivatives that proposed in this study.

Data availability statement

The datasets presented in this study can be found in online repositories. The names of the repository/repositories and accession number(s) can be found in the article/Supplementary Material.

Author contributions

WM: Conceptualization, Data curation, Formal Analysis, Methodology, Validation, Project administration, Visualization, Funding acquisition, Investigation, Resources, Supervision, Writing–original draft. LM: Data curation, Formal Analysis, Investigation, Methodology, Software, Writing–original draft. MuN: Formal Analysis, Funding acquisition, Investigation, Methodology, Writing–original draft. IK: Formal Analysis, Methodology, Conceptualization, Data curation, Project administration, Software, Validation, Visualization, Writing–review and editing. MA-S: Formal Analysis, Investigation, Methodology, Writing–original draft. MJ: Formal Analysis, Investigation, Methodology, Writing–original draft, Data curation. MaN: Formal Analysis, Investigation,

Methodology, Writing–original draft. HS: Conceptualization, Funding acquisition, Project administration, Resources, Supervision, Validation, Visualization, Writing–review and editing.

The author(s) declared that they were an editorial board member of Frontiers, at the time of submission. This had no impact on the peer review process and the final decision.

Funding

The author(s) declare that financial support was received for the research, authorship, and/or publication of this article. Kufa University paid the fee of synthesis and Uppsala University paid the publication fee.

Acknowledgments

All thanks, gratitude and appreciation to the Babylon, Najaf and Razi Universities and to everyone who helped us complete this study.

Conflict of interest

The authors declare that the research was conducted in the absence of any commercial or financial relationships that could be construed as a potential conflict of interest.

Generative AI statement

The author(s) declare that no Generative AI was used in the creation of this manuscript.

Publisher's note

All claims expressed in this article are solely those of the authors and do not necessarily represent those of their affiliated organizations, or those of the publisher, the editors and the reviewers. Any product that may be evaluated in this article, or claim that may be made by its manufacturer, is not guaranteed or endorsed by the publisher.

Supplementary material

The Supplementary Material for this article can be found online at: https://www.frontiersin.org/articles/10.3389/fphar.2024.1511627/full#supplementary-material

References

Abdelrazek, F. M., Sharaf, M. F., Metz, P., and Jaeger, A. (2010). The reaction of 2-dimethylaminomethylene-3-oxo-N-phenylbutyramide with active methylene nitriles. *J. Heterocycl. Chem.* 47, 528–533. doi:10.1002/jhet.356

Abrahamson, E. (1956). A convenient apparatus for the xanthydrol method of determining blood urea. *Am. J. Clin. Pathol.* 26, 103–106. doi:10.1093/ajcp/26.1_ts.103

Amezian, D. N. R., and Van Leeuwen, T. (2024). The role of ATP-binding cassette transporters in arthropod pesticide toxicity and resistance. *Curr. Opin. Insect. Sci.* 63, 101200. doi:10.1016/j.cois.2024.101200

Badiali, C., Petruccelli, V., Brasili, E., and Pasqua, G. (2023). Xanthones: biosynthesis and trafficking in plants, fungi and lichens. *Plants* 12, 694. doi:10.3390/plants12040694

Baell, J. B., and Holloway, G. A. (2010). New substructure filters for removal of pan assay interference compounds (PAINS) from screening libraries and for their exclusion in bioassays. *J. Med. Chem.* 53, 2719–2740. doi:10.1021/jm901137j

Brunton, L. L., Knollmann, B. C., and Hilal-Dandan, R. (2023). Goodman and Gilman's the pharmacological basis of therapeutics. *Surg. Neurol. Int.* 14, 1549. doi:10.25259/SNI_184_2023

Cao, R., Du, F., Liu, Z., Cai, P., Qi, M., Xiao, W., et al. (2023). The synthesis and bioactivities of ROCK2 inhibitors with 1, 2-Dithiolan-3-Yl motif. *RSC Med. Chem.* 28, 3576–3596. doi:10.1039/D4MD00438H

Caron, G. D. V., Solaro, S., and Ermondi, G. (2020). Flexibility in early drug discovery: focus on the beyond-Rule-of-5 chemical space. *Drug. Discov. Today* 25, 621–662. doi:10.1016/j.drudis.2020.01.012

Cascioferro, S., Parrino, B., Carbone, D., Schillaci, D., Giovannetti, E., Cirrincione, G., et al. (2020). Thiazoles, their benzofused systems, and thiazolidinone derivatives: versatile and promising tools to combat antibiotic resistance. *J. Med. Chem.* 63, 7923–7956. doi:10.1021/acs.jmedchem.9b01245

Chen, X. W. A. W., and Chen, W. (2012). Gambogic acid is a novel anti-cancer agent that inhibits cell proliferation, angiogenesis and metastasis. *Anticancer Agents Med. Chem.* 12, 994–1000. doi:10.2174/187152012802650066

Choodej, S., Koopklang, K., Raksat, A., Chuaypen, N., and Pudhom, K. (2022). Bioactive xanthones, benzophenones and biphenyls from mangosteen root with potential anti-migration against hepatocellular carcinoma cells. *Sci. Rep.* 12, 8605. doi:10.1038/s41598-022-12507-8

Cramer, G., Ford, R., and Hall, R. (1976). Estimation of toxic hazard—a decision tree approach. *Food Cosmet. Toxicol.* 16, 255–276. doi:10.1016/S0015-6264(76)80522-6

Dai, J., Tian, S., Yang, X., and Liu, Z. (2022). Synthesis methods of 1, 2, 3-/1, 2, 4-triazoles: a review. *Front. Chem.* 10, 891484. doi:10.3389/fchem.2022.891484

Daina, A., Michielin, O., and Zoete, V. (2017). Swissadme: a free web tool to evaluate pharmacokinetics, drug-likeness and medicinal chemistry friendliness of small molecules. *Sci. Rep.* 7, 42717. doi:10.1038/srep42717

Daina, A., Michielin, O., and Zoete, V. (2019). Swisstargetprediction: updated data and new features for efficient prediction of protein targets of small molecules. *Nucleic Acids Res.* 47, W357-W364–W364. doi:10.1093/nar/gkz382

Dallakyan, S., and Olson, A. J. (2015). Small-molecule library screening by docking with pyrx. *Methods Mol. Biol.* 1263, 243–250. doi:10.1007/978-1-4939-2269-7_19

De Perre, C., and Mccord, B. (2011). Trace analysis of urea nitrate by liquid chromatography–UV/fluorescence. *Forensic Sci. inte.* 211, 76–82. doi:10.1016/j.forsciint.2011.04.021

Drelinkiewicz, D., and Whitby, R. J. (2022). A practical flow synthesis of 1, 2, 3-triazoles. *RSC Adv.* 12 (45), 28910–28915. doi:10.1039/d2ra04727f

Elmaati, T. M. A., and El-Taweel, F. M. (2002). Studies with alkylheterocycles: novel synthesis of functionally substituted isoquinoline and pyridopyridines derivatives. *J. Chin. Chem. Soc.* 49, 1045–1050. doi:10.1002/jccs.200200150

El-Taweel, F., and Elmaati, T. A. (2002). Cyclization reactions of 5-aminopyrazoles with β-ketoesters, enamines and β-keto anilides: new synthetic routes to pyrazolo[1,5-a]Pyrimidine derivatives. *J. Chin. Chem. Soc.* 49, 1051–1055. doi:10.1002/jccs.200200151

Esteves, F., R, J., and Kranendonk, M. (2021). The central role of cytochrome p450 in xenobiotic metabolism-a brief review on a fascinating enzyme family. *J. Xenobiot.* 3, 94–114. doi:10.3390/jox11030007

Felber, J. G., Kitowski, A., Zeisel, L., Maier, M. S., Heise, C., Thorn-Seshold, J., et al. (2023). Cyclic dichalcogenides extend the reach of bioreductive prodrugs to harness thiol/disulfide oxidoreductases: applications to seco-duocarmycins targeting the thioredoxin system. *ACS Cent. Sci.* 9, 763–776. doi:10.1021/acscentsci.2c01465

Ghasemi, Z., Mirzaie, A., Arabzadeh, R., Fathi, Z., and Abolghassemi Fakhree, A. (2019). Synthesis and optical properties of novel 1, 2, 3-triazole derivatives possessing highly substituted imidazoles. *J. Chem.l Res.* 43, 262–267. doi:10.1177/1747519819861004

Goldberg, A., and Wragg, A. (1957). 972. Spasmolytics derived from xanthen. *J. Chem. Soc.*, 4823–4829. doi:10.1039/JR9570004823

Greene, T. W., and Wuts, P. G. (1999). Protective groups in organic synthesis. 494–653. doi:10.1002/0471220574

Gunter, N. V., Teh, S. S., Jantan, I., Cespedes-Acuña, C. L., and Mah, S. H. (2023). The mechanisms of action of prenylated xanthones against breast, colon, and lung cancers,

and their potential application against drug resistance. *Phytochem. Rev.* 22, 467–503. doi:10.1007/s11101-022-09846-9

Guo, H. Y., Chen, Z.-A., Shen, Q. K., and Quan, Z. S. (2021). Application of triazoles in the structural modification of natural products. *J. Enzyme Inhib. Med. Chem.* 36, 1115–1144. doi:10.1080/14756366.2021.1890066

Gutierrez-Orozco, F., and Failla, M. L. (2013). Biological activities and bioavailability of mangosteen xanthones: a critical review of the current evidence. *Nutrients* 5, 3163–3183. doi:10.3390/nu5083163

Hoyer, D. (2020). Targeting the 5-HT system: potential side effects. *Neuropharmacology* 179, 108233. doi:10.1016/j.neuropharm.2020.108233

Huang, Q., Wang, Y., Wu, H., Yuan, M., Zheng, C., and Xu, H. (2021). Xanthone glucosides: isolation, bioactivity and synthesis. *Molecules* 26, 5575. doi:10.3390/molecules26185575

Ibrahim, S. A., and Rizk, H. F. (2020). "Synthesis and biological evaluation of thiazole derivatives," in *Azoles-synthesis, properties, applications and perspectives 2020 jun 29* (London, UK: IntechOpen).

Ismail, M. A., Abusaif, M. S., El-Gaby, M. S., Ammar, Y. A., and Ragab, A. (2023). A new class of anti-proliferative activity and apoptotic inducer with molecular docking studies for a novel of 1, 3-dithiolo [4, 5-B] quinoxaline derivatives hybrid with a sulfonamide moiety. *RSC Adv.* 13, 12589–12608. doi:10.1039/D3RA01635H

Ivanov, S. M., Lagunin, A. A., Rudik, A. V., Filimonov, D. A., and Poroikov, V. V. (2018). Adverpred–web service for prediction of adverse effects of drugs. *J. Chem. Inf. Model.* 58, 8–11. doi:10.1021/acs.jcim.7b00568

Jiang, C. H., Sun, T. L., Xiang, D.-X., Wei, S. S., and Li, W. Q. (2018). Anticancer activity and mechanism of xanthohumol: a prenylated flavonoid from hops (*Humulus Lupulus* L.). *Front. Pharmacol.* 9, 530. doi:10.3389/fphar.2018.00530

Kapri, A., Gupta, N., and Nain, S. (2022). Recent advances in the synthesis of xanthines: a short review. *Scientifica* 1, 8239931. doi:10.1155/2022/8239931

Kashyap, S. J., Garg, V. K., Sharma, P. K., Kumar, N., Dudhe, R., and Gupta, J. K. (2012). Thiazoles: having diverse biological activities. *Med. Chem. Res.* 21, 2123–2132. doi:10.1007/s00044-011-9685-2

Kim, E. K., and Choi, E. J. (2010). Pathological roles of MAPK signaling pathways in human diseases. *Biochim. Biophys. Acta* 1802, 396–405. doi:10.1016/j.bbadis.2009.12.009

Koopmans, F., Van Nierop, P., Andres-Alonso, M., Byrnes, A., Cijsouw, T., Coba, M. P., et al. (2019). Syngo: an evidence-based, expert-curated knowledge base for the synapse. *Neuron* 103, 217–234. doi:10.1016/j.neuron.2019.05.002

Kralj, S., Jukič, M., and Bren, U. (2023). Molecular filters in medicinal chemistry. *Encyclopedia* 3, 501–511. doi:10.3390/encyclopedia3020035

Kurniawan, Y. S., Priyangga, K. T. A., Jumina, Pranowo, H. D., Sholikhah, E. N., Zulkarnain, A. K., et al. (2021). An update on the anticancer activity of xanthone derivatives: a review. *Pharmaceuticals* 14, 1144. doi:10.3390/ph14111144

Lagorce, D., Douguet, D., Miteva, M. A., and Villoutreix, B. O. (2017). Computational analysis of calculated physicochemical and ADMET properties of protein-protein interaction inhibitors. *Sci. Rep.* 7, 46277. doi:10.1038/srep46277

Lagunin, A. A., Romanova, M. A., Zadorozhny, A. D., Kurilenko, N. S., Shilov, B. V., Pogodin, P. V., et al. (2018). Comparison of quantitative and qualitative (Q) SAR models created for the prediction of Ki and IC50 Values of antitarget inhibitors. *Front. Pharmacol.* 9, 1136. doi:10.3389/fphar.2018.01136

Lipin, K., Ershov, O., Belikov, M. Y., and Fedossev, S. (2019). One-pot synthesis of 2-ylidene-1, 3-dithiolanes. *Russ. J. Org. Chem.* 55, 276–278. doi:10.1134/S1070428019020246

Lipinski, C. A., Lombardo, F., Dominy, B. W., and Feeney, P. J. (2012). Experimental and computational approaches to estimate solubility and permeability in drug discovery and development settings. *Adv. Drug Deliv. Rev.* 23, 3–26. doi:10.1016/s0169-409x(00)00129-0

Liu, H. W., Chen, L., Xu, C., Li, Z., Zhang, H., Zhang, X. B., et al. (2018). Recent progresses in small-molecule enzymatic fluorescent probes for cancer imaging. *Chem. Soc. Rev.* 47, 7140–7180. doi:10.1039/c7cs00862g

Liu, Y., Yang, H., Fang, Y., Xing, Y., Pang, X., Li, Y., et al. (2023). Function and inhibition of haspin kinase: targeting multiple cancer therapies by antimitosis. *Pharm. Pharmacol.* 75, 445–465. doi:10.1093/jpp/rgac080

Loisel, S., Le Ster, K., Meyer, M., Berthou, C., Youinou, P., Kolb, J. P., et al. (2010). Therapeutic activity of two xanthones in a xenograft murine model of human chronic lymphocytic leukemia. *Hematol. Oncol.* 3, 49–53. doi:10.1186/1756-8722-3-49

Marayati, R., Stafman, L. L., Williams, A. P., Bownes, L. V., Quinn, C. H., Markert, H. R., et al. (2022). CRISPR/Cas9-mediated knockout of PIM3 suppresses tumorigenesis and cancer cell stemness in human hepatoblastoma cells. *Cancer Gene Ther.* 29, 558–572. doi:10.1038/s41417-021-00334-4

Matin, M. M., Matin, P., Rahman, M. R., Ben Hadda, T., Almalki, F. A., Mahmud, S., et al. (2022). Triazoles and their derivatives: chemistry, synthesis, and therapeutic applications. *Front. Mol. Biosci.* 9, 864286. doi:10.3389/fmolb.2022.864286

Miladiyah, I., Jumina, J., Haryana, S. M., and Mustofa, M. (2018). Biological Activity, quantitative structure–activity relationship analysis, and molecular docking of xanthone derivatives as anticancer drugs. *Drug Des. devel. Ther.* 12, 149–158. doi:10.2147/DDDT.S149973

Mohareb, R. M., Abbas, N. S., and Ibrahim, R. A. (2013). New Approaches for the synthesis of thiophene derivatives with anti-tumor activities. *Acta Chim. Slov.* 60, 583–594. doi:10.21608/ejchem.2012.1173

Nikitjuka, A., Krims-Davis, K., Kaņepe-Lapsa, I., Ozola, M., and Žalubovskis, R. (2023)). 2-dithiolane-4-carboxylic acid and its derivatives serve as a specific thioredoxin reductase 1 inhibitor? *Molecules* 28, 6647. doi:10.3390/molecules28186647

O'Boyle, N. M., Banck, M., James, C. A., Morley, C., Vandermeersch, T., and Hutchison, G. R. (2011). Open Babel: an open chemical toolbox. *J. Cheminform.* 3, 1–14. doi:10.1186/1758-2946-3-33

Pylypenko, O. O., Okovytyy, S. I., Sviatenko, L. K., Voronkov, E. O., Shabelnyk, K. P., and Kovalenko, S. I. (2023). Tautomeric behavior of 1, 2, 4-triazole derivatives: combined spectroscopic and theoretical study. *Struct. Chem.* 34, 181–192. doi:10.1007/s11224-022-02057-0

Ramakrishnan, S., Paramewaran, S., and Nasir, N. M. (2021). Synthetic approaches to biologically active xanthones: an update. *Chem. Pap.* 75, 455–470. doi:10.1007/s11696-020-01320-0

Raman, A. P. S., Aslam, M., Awasthi, A., Ansari, A., Jain, P., Lal, K., et al. (2024). An updated review on 1, 2, 3-/1, 2, 4-triazoles: synthesis and diverse range of biological potential. *Mol. Diver.*, 1–66. doi:10.1007/s11030-024-10858-0

Rang, H., Dale, M., Ritter, J., and Moore, P. (1999). *Pharmacology*. 4th edition. London: Churchill Livingstone.

Resende, D. I., Durães, F., Maia, M., Sousa, E., and Pinto, M. M. (2020). Recent advances in the synthesis of xanthones and azaxanthones. *Org. Chem. Front.* 7, 3027–3066. doi:10.1039/D0QO00659A

Rizaldy, D., Hartati, R., Nadhifa, T., and Fidrianny, I. (2021). Chemical compounds and pharmacological activities of mangosteen (*Garcinia Mangostana* L.)—updated review. *Biointerface Res. Appl. Chem.* 12, 2503–2516. doi:10.33263/BRIAC122.25032516

Shannon, P., Markiel, A., Ozier, O., Baliga, N. S., Wang, J. T., Ramage, D., et al. (2003). Cytoscape: a software environment for integrated models of biomolecular interaction networks. *Genome Res.* 13, 2498–2504. doi:10.1101/gr.1239303

Shawali, A. S., Abdelkader, M. H., and Eltalbawy, F. M. (2002). Synthesis and tautomeric structure of novel 3, 7-Bis (arylazo)-2, 6-diphenyl-1H-imidazo-[1, 2-B] pyrazoles in ground and excited states. *Tetrahedron* 58, 2875–2880. doi:10.1016/S0040-4020(02)00157-6

Song, Y., Zhu, X., Yang, K., Feng, S., Zhang, Y., Dong, J., et al. (2022). Synthesis and biological evaluation of xanthone derivatives as anti-cancer agents targeting topoisomerase II and DNA. *Med. Chem. Res.* 31, 720–734. doi:10.21203/rs.3.rs-857564/v1

Taguchi, Y., Yanagiya, K., Shibuya, I., and Suhara, Y. (1987). The synthesis of 1, 3-dithiolane-2-thione derivatives. *Bull. Chem. Soc. Jap.* 60, 727–730. doi:10.1246/bcsj.60.727

Theodosis-Nobelos, P., Papagiouvannis, G., Tziona, P., and Rekka, E. A. (2021). Lipoic acid. kinetics and pluripotent biological properties and derivatives. *Mol. Biol. Rep.* 48, 6539–6550. doi:10.1007/s11033-021-06643-z

Thomsen, R., and Christensen, M. H. (2006). Moldock: a new technique for high-accuracy molecular docking. *J. Med. Chem.* 49, 3315–3321. doi:10.1021/jm051197e

Tian, M., Wu, R., Xiang, C., Niu, G., and Guan, W. (2024). Recent advances in fluorescent probes for cancer biomarker detection. *Molecules* 29, 1168. doi:10.3390/molecules29051168

Vasiliev, A., and Polackov, A. (2000). Synthesis of potassium (1, 1-dioxothiolan-3-yl)-dithiocarbamate. *Molecules* 5, 1014–1017. doi:10.3390/50801014

Veber, D. F., Johnson, S. R., Cheng, H.-Y., Smith, B. R., Ward, K. W., and Kopple, K. D. (2002). Molecular properties that influence the oral bioavailability of drug candidates. *J. Med. Chem.* 45, 2615–2623. doi:10.1021/jm020017n

Veríssimo, A. C., Pinto, D. C., and Silva, A. M. (2022). Marine-derived xanthone from 2010 to 2021: isolation, bioactivities and total synthesis. *Mar. Drugs* 20, 347. doi:10.3390/md20060347

Wang, J., Liu, W., Zhao, Q., Qi, Q., Lu, N., Yang, Y., et al. (2009). Synergistic effect of 5-fluorouracil with gambogic acid on BGC-823 human gastric carcinoma. *Toxicology* 256, 135–140. doi:10.1016/j.tox.2008.11.014

Warde-Farley, D., Donaldson, S. L., Comes, O., Zuberi, K., Badrawi, R., Chao, P., et al. (2010). The genemania prediction server: biological network integration for gene prioritization and predicting gene function. *Nucleic Acids Res.* 8, W214–W220. doi:10.1093/nar/gkq537

Zakharov, A. V., Lagunin, A. A., Filimonov, D. A., and Poroikov, V. V. (2012). Quantitative Prediction of antitarget interaction profiles for chemical compounds. *Chem. Res. Toxicol.* 25, 2378–2385. doi:10.1021/tx300247r

Zheng, S., and Huang, D. (2023). Design, Synthesis and fungicidal activities evaluation of N-(thiazol-4-ylmethyl) benzenesulfonamide derivatives. *Chem. Pap.* 77, 1059–1066. doi:10.1007/s11696-022-02540-2

Zhou, Z., and Wang, J. (2007). Phase i human tolerability trial of gambogic acid. *Chin. J. New Drugs.* 16, 79.

frontiers | Frontiers in Oncology

TYPE Systematic Review
PUBLISHED 08 January 2025
DOI 10.3389/fonc.2024.1487376

Check for updates

OPEN ACCESS

EDITED BY
Wagdy Mohamed Eldehna,
Kafrelsheikh University, Egypt

REVIEWED BY
Giuseppe Vizzielli,
University of Udine, Italy
Longjie Xia,
People's Hospital of Guangxi Zhuang Autonomous Region, China

*CORRESPONDENCE
Maria Lúcia Hirata Katayama
maria.katayama@fm.usp.br

†These authors have contributed equally to this work and share last authorship

RECEIVED 28 August 2024
ACCEPTED 06 December 2024
PUBLISHED 08 January 2025

CITATION
Simonsen M, Mendoza López RV, Maistro S, Ikeoka LT, Pereira GFdL, Lugão AB, Sadalla JC, Katayama MLH and Folgueira MAAK (2025) Peritoneal chemotherapy delivery systems for ovarian cancer treatment: systematic review of animal models.
Front. Oncol. 14:1487376.
doi: 10.3389/fonc.2024.1487376

COPYRIGHT
© 2025 Simonsen, Mendoza López, Maistro, Ikeoka, Pereira, Lugão, Sadalla, Katayama and Folgueira. This is an open-access article distributed under the terms of the Creative Commons Attribution License (CC BY). The use, distribution or reproduction in other forums is permitted, provided the original author(s) and the copyright owner(s) are credited and that the original publication in this journal is cited, in accordance with accepted academic practice. No use, distribution or reproduction is permitted which does not comply with these terms.

Peritoneal chemotherapy delivery systems for ovarian cancer treatment: systematic review of animal models

Marcelo Simonsen[1,2], Rossana Verónica Mendoza López[3], Simone Maistro[3], Lucas Takeshi Ikeoka[4], Glaucia Fernanda de Lima Pereira[5], Ademar Benévolo Lugão[6], José Carlos Sadalla[7], Maria Lúcia Hirata Katayama[3*†] and Maria Aparecida Azevedo Koike Folgueira[3†]

[1]Departamento de Radiologia e Oncologia, Instituto do Cancer do Estado de Sao Paulo, Hospital das Clinicas, Faculdade de Medicina, Universidade de Sao Paulo (HCFMUSP), Sao Paulo, SP, Brazil, [2]Gynecology and Obstetrics Department, Instituto de Assistência Médica ao Servidor Público Estadual (IAMSPE), São Paulo, SP, Brazil, [3]Departamento de Radiologia e Oncologia, Comprehensive Center for Precision Oncology (C2PO), Centro de Investigação Translacional em Oncologia (CTO), Instituto do Cancer do Estado de Sao Paulo, Hospital das Clinicas, Faculdade de Medicina, Universidade de Sao Paulo (HCFMUSP), Sao Paulo, SP, Brazil, [4]Faculdade de Medicina, Undergraduate program, Universidade de Sao Paulo (FMUSP), Sao Paulo, SP, Brazil, [5]Instituto do Cancer do Estado de Sao Paulo, Hospital das Clinicas, Faculdade de Medicina, Universidade de Sao Paulo (HCFMUSP), Sao Paulo, SP, Brazil, [6]Nuclear and Energy Research Institute, IPEN-Comissão Nacional de Energia Nuclear (CNEN)/SP—University of São Paulo, São Paulo, SP, Brazil, [7]Departamento de Ginecologia e Obstetrícia, Instituto do Câncer do Estado de Sao Paulo do Hospital das Clínicas da Faculdade de Medicina da Universidade de São Paulo, Sao Paulo, SP, Brazil

Introduction: Intraperitoneal chemotherapy for ovarian cancer treatment has controversial benefits as most methodologies are associated with significant morbidity. We carried out a systematic review to compare tumor response, measured by tumor weight and volume, between intraperitoneal chemotherapy delivered via drug delivery systems (DDSs) and free intraperitoneal chemotherapy in animal models of ovarian cancer. The secondary aim was to assess the toxicity of DDS-delivered chemotherapy, based on changes in animal body weight.

Methods: Based on PRISMA and SYRCLE guidelines, we identified 38 studies for review, of which 20, were used in the meta-analysis. We evaluated outcome, through tumor volume and tumor weight and, toxicity, through animal weight. Analysis was based on drugs employed and treatment duration.

Results: Most studies were performed on mice. Ovarian cancer cell lines most commonly used to induce xenografts were SKOV3 (19 studies) and A2780 (6 studies). Intraperitoneal device, also known as drug delivery systems (DDS), consisted in nanoparticles, hydrogels, lipid polymer and others. The most commonly used drugs were paclitaxel and cisplatin. Most studies used as the control treatment the same chemotherapy applied free intraperitoneally and tumor response/animal weight were evaluated weekly. There was a small benefit in overall tumor reduction in animals treated with intraperitoneal chemotherapy applied through the slow release device compared with animals treated with intraperitoneal free chemotherapy, as evaluated through tumor weight - results in standardized mean difference. (-1.06; 95% CI: -1.34, -0.78) and tumor volume (-3.72; 95% CI: -4.47, -2.97),

a benefit that was seen in most weekly evaluations and for most chemotherapy drugs, such as carboplatin (tumor weight: -5.60; 95% CI: -7.83, -3.37), paclitaxel (tumor weight: -1.18; 95% CI: -1.52, -0.83), and cisplatin (tumor volume: -2.85; 95% CI: -3.66, -2.04) carboplatin (tumor volume: -12.71; 95% CI: -17.35, -8.07); cisplatin (tumor volume: -7.76; 95% CI: -9.88, -5.65); paclitaxel (tumor volume: -2.85; 95% CI: -3.66, -2.04). Regarding animal weight, there was no weight reduction in animals treated with intraperitoneal chemotherapy applied through the slow-release device compared with animals treated with intraperitoneal free chemotherapy. However, significant heterogeneity was observed in some comparisons.

Conclusion: slow-release devices are overall safe and effective in animal models of ovarian cancer. It was not possible to evaluate which one is the most promising device to treat ovarian cancer, because many different types were used to apply chemotherapy intraperitoneally.

Systematic Review Registration: https://www.crd.york.ac.uk/prospero/, identifier CRD42021224573.

KEYWORDS

ovarian cancer, drug delivery systems, animal model, intraperitoneal chemotherapy, meta-analysis

1 Introduction

Ovarian cancer is the most lethal gynecologic cancer, with the majority of cases being diagnosed when the patient already presents with ascites and peritoneal dissemination of the tumor, restricting the 5-year survival to 30% (1). This situation impairs complete cytoreduction, and limits the chemotherapy response (2–4). The majority of patients have relapsed disease (1, 5, 6).

The most common chemotherapy protocol for high grade advanced stage serous ovarian cancer is based on six cycles of systemic carboplatin and paclitaxel (1, 5). Toxicity is related to unfavorable drug distribution and results in frequent peripheral neuropathy, anemia, neutropenia due to bone marrow suppression, alopecia and gastrointestinal symptoms.

Peritoneal administration of chemotherapy has been implemented over the last few decades to increase drug concentration in neoplastic spots with acceptable systemic toxicity due to lower absorption (3, 7), but sequential outpatient administration did not improve survival in the most expressive clinical trial (8). The single application during cytoreduction of hyperthermic intraperitoneal chemotherapy (HIPEC) was effective in three clinical trials.

The rational of HIPEC is to directly or indirectly affect the residual neoplastic cells after cytoreduction. In this case, the desperitonized region, which is more prone to the adhesion of neoplastic cells, is protected by direct contact with the chemotherapy agent (9). The technique presents promising results even in patients with platinum resistance (10, 11). Studies show better survival compared with standard treatment, when performed during interval cytoreduction surgery with cisplatin (12) and in the context of secondary cytoreduction with cisplatin (13) or cisplatin associated with paclitaxel (10).

The main disadvantage of HIPEC is the higher surgical morbidity and mortality. The most frequent complications are bleeding, surgical wound infection, sepsis, abscess, fistulas, renal failure, pleural effusion and hematological toxicity associated with chemotherapy (7).

Although some series present good results regarding the morbidity of the procedure (10), others report morbidity rates that exceed 50% of patients (14), encouraging studies in murine models for less toxic formulations.

The PIPAC (pressurized intraperitoneal aerosol chemotherapy) resembles the principles of HIPEC with an innovative technology for delivering drugs into the peritoneal cavity, that involves aerosolized chemotherapy delivered under pressure. Unfortunately, it is mainly offered to palliative patients, as there are still no randomized clinical trials evaluating PIPAC as first therapeutic option (15).

Chemotherapy slow-release devices, also known as drug delivery systems (DDSs), are designed to converge the advantage of *in loco* peritoneal treatment with lower toxicity. The classification of DDSs is based on its main mechanism of action and the types most currently used are liposomes, micelles and nanoparticles (16). Its efficacy in disease control has been demonstrated in several animal models but (17, 18) its application in humans is limited to a few studies on slow-release systems containing paclitaxel (19, 20). Several DDS formulations have been tested *in vitro* and in murine models, and most studies have been conducted in mice with ovarian tumor xenografts (17). The efficacy of various DDS formulations reinforces this therapeutic option and supports the creation of a device to be tested in animals with a larger peritoneal cavity.

The primary aim of this study was to compare the tumor response, assessed by tumor weight and volume, between intraperitoneal chemotherapy delivered via drug delivery systems (DDSs) and free intraperitoneal chemotherapy in animal models of ovarian cancer. The secondary aim was to evaluate the toxicity of intraperitoneal chemotherapy delivered through DDSs, compared to free intraperitoneal chemotherapy, based on changes in animal body weight.

2 Methods

The research protocol was inserted into the PROSPERO (Prospective Register of Systematic Reviews) platform with the register code CRD42021224573, following the PRISMA (Preferred Reporting Items for Systematic Review and Meta-Analysis) checklist recommendations (21). We performed a literature search using descriptors according to PICO methodology, as described in Supplementary Table 1: (Ovarian OR carcinomatosis) AND (Polymers OR Drug Delivery Systems OR Absorbable Implants OR Phospholipids OR Delayed-Action Preparations OR Infusion Pumps, Implantable OR Chitosan OR Polyvinyl Alcohol OR sustained release OR slow release OR controlled release OR membrane OR hydrogel OR Polyethylene Glycol Acid OR Implant System OR Injectable Biomaterial OR Continuous Release OR continuous intraperitoneal delivery OR continuous chemotherapy OR continuous docetaxel OR continuous cisplatin OR continuous paclitaxel OR continuous carboplatin OR micellar OR micelle) AND (Intraperitoneal OR peritoneal) AND (Toxicity OR survival OR treatment OR tumor burden). The search strategy focused on DDSs capable of slow-release chemotherapy in ovarian cancer animal models.

The literature search was performed on PubMed, MEDLINE, Embase, Cochrane Central Register of Clinical Trials and Web of Science, without any date restrictions on 2th October 2023. All results were inserted into the Rayyan App, a multitask program created to enable better management and selection of papers (22). Repeated studies on different platforms were excluded, and papers were selected by six researchers working in blinded pairs. After interrupting the blind approach, discordant papers between the authors were reviewed by a third author for final judgment on inclusion.

The selection criteria included studies with peritoneal application of the device in which one or more of the following chemotherapy drugs were used: cisplatin, docetaxel, paclitaxel and carboplatin. The device type was restricted to gels, membranes, microdevices or micelles.

Study inclusion required at least one of the following outcomes: side effects (animal weight as a sign of toxicity), tumor response (assessed by tumor weight, volume or bioluminescence), or animal survival. Experimental group had be compared at least with one control group (no treatment, empty device or free chemotherapy) and minimal sample size and animal species were not an exclusion criteria. Only studies published in English were included. Studies on human beings were excluded. Data compilation for meta-analysis was prepared when at least three studies with the same outcome, unit of measure and standard deviation were present.

Authors of abstracts and posters were contacted digitally (email/LinkedIn platforms) and kindly asked to send additional data that would facilitate the inclusion of the research in the review.

The selected studies had their data extracted and inserted into a standardized Excel table by all researchers. The corresponding pair reviewed all data entries; text, tables or graphs had their numbers copied. When the results were presented only graphically, the *WebPlotDigitizer* program was used to identify the results more accurately. Data extracted from the papers consisted of authors, year of publication, number of animals in each group (experimental and control), cell lines, intervention, and outcomes.

Meta-analysis was performed using STATA MP version 14 software. When the variation in mouse weight was recorded as a percentage, we considered the initial weight to be 20g to include the data in the analysis.

We conducted a meta-analysis using a fixed-effect model. The outcome measures were assessed based on continuous variables. The effect of the treatment interventions and controls was evaluated by calculating mean differences and their corresponding 95% confidence intervals. The overall treatment effect was further assessed using the standardized mean difference (SMD). A p-value of < 0.05 was considered statistically significant. The degree of heterogeneity across studies was evaluated using the I^2 statistic, with the following interpretation: 0–25% indicating low heterogeneity, 26–50% moderate heterogeneity, 51–75% substantial heterogeneity, and >75% high heterogeneity (23).

2.1 Studies quality

The SYRCLE (Systematic Review Centre for Laboratory animal Experimentation) risk of Bias Tool was used to quantify the quality of the studies (24); this is an adaptation of the Cochrane Instrument developed specifically for animal studies. Selection, performance, detection, attrition and reporting biases were evaluated by the same researchers who selected the articles, in pairs.

3 Results

The search was carried out on October 2, 2023 and 399 studies were found in PubMed, 417 in Embase, 226 in Web of Science, 443 in the Virtual Health Library, 195 in Scopus and 23 in Cochrane, totaling 1,703 articles. It should be noted that the terms were searched in the title, abstract or entire text; only in Scopus was the search for terms restricted to the title and abstract, as the high number of articles in the text would make the selection of articles unfeasible.

A total of 597 articles were excluded, resulting in an evaluation of 1,106 articles. Of these, 104 papers were selected based on the relevance of the title or summary for the final evaluation of the full text (Figure 1). It was not possible to get in contact with the authors of the six posters initially included.

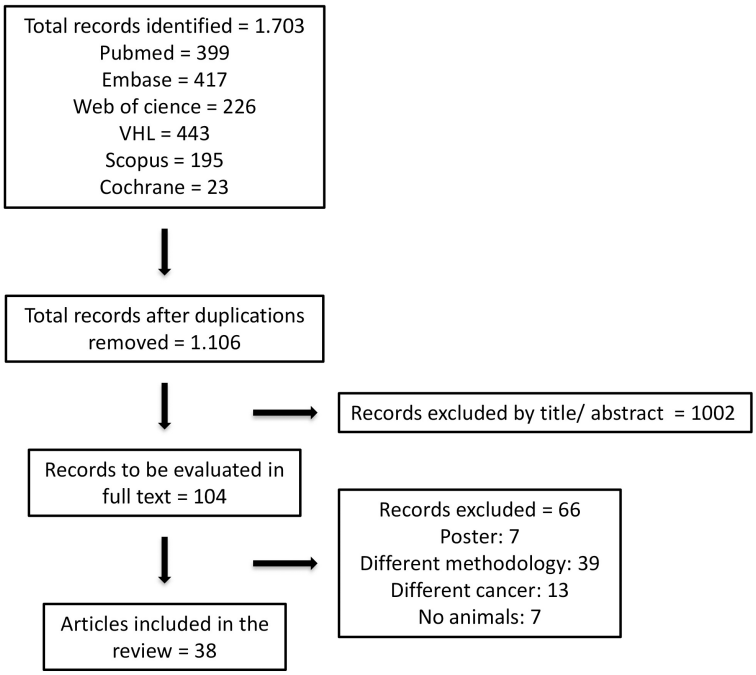

FIGURE 1
Flowchart of selected studies.

3.1 Systematic review

A total of 38 articles fulfilled the inclusion criteria and were selected for a systematic review. The analysis was performed according to treatment duration and chemotherapy drugs used. A total of 11 studies published from databank inception up to 2010 were selected, from 2011 to 2015, 14 studies, from 2016 to 2023, 10 studies, and from 2021 to 2023, 3 studies.

Eighteen studies were excluded from the meta-analysis. The main reason for this was that the outcomes did not include the predefined parameters. The reasons for excluding these studies and their outcomes are summarized in Table 1.

TABLE 1 Main features of the studies selected for the systematic review and reason for exclusion.

Author	Year	Chemo	Physical Presentation	*N* Control *vs.* Experimental	Evaluated Outcomes	Exclusion Reason
Amoozgar et al. (53)	2014	paclitaxel	nanoparticles	16 *vs.* 8	survival	missing standard deviation
Bajaj et al. (28)	2012	paclitaxel	hydrogel	27 *vs.* 19	tumor weight	*
Bortot et al. (54)	2020	cisplatin	nanoparticles	12 *vs.* 7	bioluminescence and animal weight	*
Cho H and Kwon GS et al. (55)	2014	paclitaxel	micels and gel	10 *vs.* 10	bioluminescence and survival	missing standard deviation
Cho H and Lai et al. (56)	2013	paclitaxel	Micels	8 *vs.* 16	animal weight	*
Cho, S. and Sun et al. (45)	2015	cisplatin	nanoparticles	30 *vs.* 20	bioluminescence and tumor weight	*
Clercq et al. (27)	2019	paclitaxel	nanoparticles	22 *vs.* 44	animal weight	time treatment missing
De Souza R and Zahedi P et al. (33)	2010	docetaxel	hydrogel	12 *vs.* 36	bioluminescence	outcomes missing

(Continued)

TABLE 1 Continued

Author	Year	Chemo	Physical Presentation	*N* Control *vs.* Experimental	Evaluated Outcomes	Exclusion Reason
Desale SS et al. (35)	2015	cisplatin and paclitaxel	nanoparticles	32 *vs.* 16	bioluminescence	outcomes missing
Gilmore D et al. (57)	2013	paclitaxel	nanoparticles	13 *vs.* 11	animal and tumor weight	*
Hagiwara et al. (58)	1993	cisplatin	microspheres	240 *vs.* 20	survival	outcomes missing
Chunbai He et al. (59)	2016	cisplatin	siRNA polymer	18 *vs.* 24	animal weight, tumor volume and survival	*
Ho et al. (60)	2007	paclitaxel	nanoparticles	6 *vs.* 3	–	outcomes missing
Kumagai et al. (25)	1996	cisplatin	microspheres	5 *vs.* 40	survival	outcomes missing
Lee, S.E. and Bairstow et al. (61)	2014	paclitaxel	nanoparticles	30 *vs.* 10	survival	outcomes missing
Li SD and Howell et al. (62)	2010	cisplatin	microparticles	14 *vs.* 6	survival	missing standard deviation
Lu H and Li B et al. (63)	2007	paclitaxel	nanoparticles	45 *vs.* 15	tumoral weight	*
Lu Z and Tsai M et al. (31)	2008	paclitaxel	microparticles	43 *vs.* 26	survival	outcomes missing
Padmakumar S et al. (64)	2019	paclitaxel	nanotextile	10 *vs.* 10	animal weight	*
Poon, C. et al. (43)	2016	carboplatin	nanoparticles	20 *vs.* 10	tumor weight and volume	*
Sun et al. (65)	2016	paclitaxel	nanocristals	27 *vs.* 18	bioluminescence and survival	missing standard deviation
Tong et al. (66)	2014	paclitaxel	liposome with nanoparticles	30 *vs.* 20	survival	missing standard deviation
Vassileva et al. (38)	2008	paclitaxel	device not specified	24 *vs.* 12	tumor weight	*
Wang et al. (47)	2020	cisplatin	polymer stent	12 *vs.* 6	tumor and animal weight	*
Xiao et al. (29)	2009	paclitaxel	nanoparticles	15 *vs.* 10	bioluminescence, tumor weight, animal weight and survival	*
Xie et al. (67)	2019	paclitaxel	microspheres	19 *vs.* 23	bioluminescence and Survival	missing standard deviation
Xiong et al. (68)	2012	paclitaxel	nanoparticles	6		no DDs with Slow release
Xu et al. (44)	2016	paclitaxel	hydrogel	24 *vs.* 8	tumor and animal weight	*
Yang et al. (69)	2017	gencitabin and paclitaxel	polymer	20 *vs.* 15	tumor and animal weight	*
Yang et al. (34)	2014	paclitaxel	microsphere	15 *vs.* 27	bioluminescence and PCI	missing standard deviation
Ye et al. (37)	2015	cisplatin	microdevice	40 *vs.* 26	bioluminescence, tumor and animal weight	*
Ye et al. (70)	2013	paclitaxel	liposome	27 *vs.* 21	tumor weight	missing standard deviation

(Continued)

TABLE 1 Continued

Author	Year	Chemo	Physical Presentation	*N* Control *vs.* Experimental	Evaluated Outcomes	Exclusion Reason
Zahedi et al. (36)	2010	docetaxel and cepharanthine	hydrogel	12 *vs.* 6	tumor weight	*
Zahedi et al. (26)	2012	docetaxel	hydrogel	36 *vs.* 24	tumor volume	*
Zahedi et al. (32)	2009	docetaxel	hydrogel	4 x 8	tumor volume	missing standard deviation
Zhang et al. (71)	2022	docetaxel	micels	24 x 18	tumor and animal weight	*
Yamaguchi et al. (46)	2022	cisplatin	hydrogel	18 x 12	tumor volume and animal weight	*
Zhao et al. (72)	2022	cisplatin	nanotubes	15 x 5	animal weight	*

*Included in the meta-analysis.

Almost all studies were performed on mice, except for one performed on rats (25), and the experimental number varied from 3 (26) to 44 (27) animals, aged between 4 (28) and 12 (29) weeks. The unique study in porcine model was excluded in the initial phase due to lack information about DDS (30). The slow-release chemotherapy device was applied from 1 (27) to 28 (31) days after the induction of tumor formation. The most commonly used cell lines to induce xenografts were the ovarian cancer lineages SKOV3, in 19 studies and A2780, in six studies.

The models of slow-release chemotherapy devices used in each study are listed in Table 1. The device formulation showed significant variations among the studies. The most commonly used presentations consisted of nanoparticles (12 studies) and hydrogels (seven studies). The only standardized material used in more than one study (a total of three articles) was a lipid-polymer containing docetaxel (polygel), which showed good performance and low toxicity (26, 32, 33). The most commonly used chemotherapy drugs were paclitaxel (22 studies) and cisplatin (11 studies).

Most studies used only one chemotherapy drug but, Yang et al. (34), Desale et al. (35) and Zahedi et al. (36) used a combination of chemotherapy drugs. In addition Bajaj et al. (28) tested only one drug, paclitaxel, dissolved in Cremophor or DMSO, and assessed the outcomes separately.

Mouse survival was the most studied outcome, assessed in 19 studies. However, we did not evaluate this parameter because most studies presented the Kaplan Meier curve without confidence intervals. Tumor response was assessed based on tumor weight (17 studies). Xenograft bioluminescence was observed in 12 studies, and tumor volume in 5 studies. Mouse weights were quantified in 14 studies. In total, 18 studies compared outcomes of DDS vs intraperitoneal PBS, 10 of DDSs vs empty device (no chemotherapy), and 18 of DDS vs intraperitoneal free chemotherapy. We present results of comparisons between DDS versus intraperitoneal free in the text, and the other two DDS comparisons (with intraperitoneal PBS or DDS without chemotherapy) in Supplementary Material.

Most studies used as the control treatment the same chemotherapy, administered intraperitoneally in bolus, using various regimens, such as 1 dose every 3 days for 5 doses or 2 doses separated by 1 week interval, and others. The studies also compared DDS with the absence of treatment (with phosphate-buffered saline (PBS) infusion or application of a slow-release device without any drug).

The risks of bias are shown in Figure 2. Most studies have clearly described the methods used to equalize different groups under the same care. The random/alternating cage distribution in the vivarium or the blinding of caregivers was not reported in any

FIGURE 2
Risk of bias represented by the percentage of studies included.

study, negatively affecting the performance of the selection, performance and detection domains. The presentation of all data proposed initially in the methodology section, in the results section and the presentation of different parameters to quantify the tumor response (such as tumor weight and bioluminescence) guaranteed satisfactory results in attrition and selection bias.

3.2 Meta-analysis

Data selection for the meta-analysis was based on the outcomes of tumor volume, tumor weight, mouse weight and mouse survival in 6, 11, 16 and 19 studies, respectively. The large variation in the data units among the studies evaluating tumor growth by bioluminescence precluded their inclusion in the meta-analysis, even though it was described in 12 studies. Survival was not evaluated because most studies provided Kaplan Meier curve without Confidence intervals, which precluded meta-analysis.

In the meta-analysis, we evaluated the outcomes of each study considering weeks after the application of the slow-release device. We compared the results of the device with those of three control groups: I, peritoneal or intravenous application of the same free chemotherapy (without conjugated formulation and without release device), II, no treatment or PBS, and III, application of the slow-release device without chemotherapy, The first, presented in the text (II and III presented in Supplementary Material).

For the analysis of tumor weight and volume, animals were euthanized at different time intervals, and separate groups were analyzed at each time point. This approach allowed us to stratify the tumor response and carry out the meta-analysis, as they were independent groups. When analyzing the weight of the animals, the same animals were weighed at multiple time points throughout the

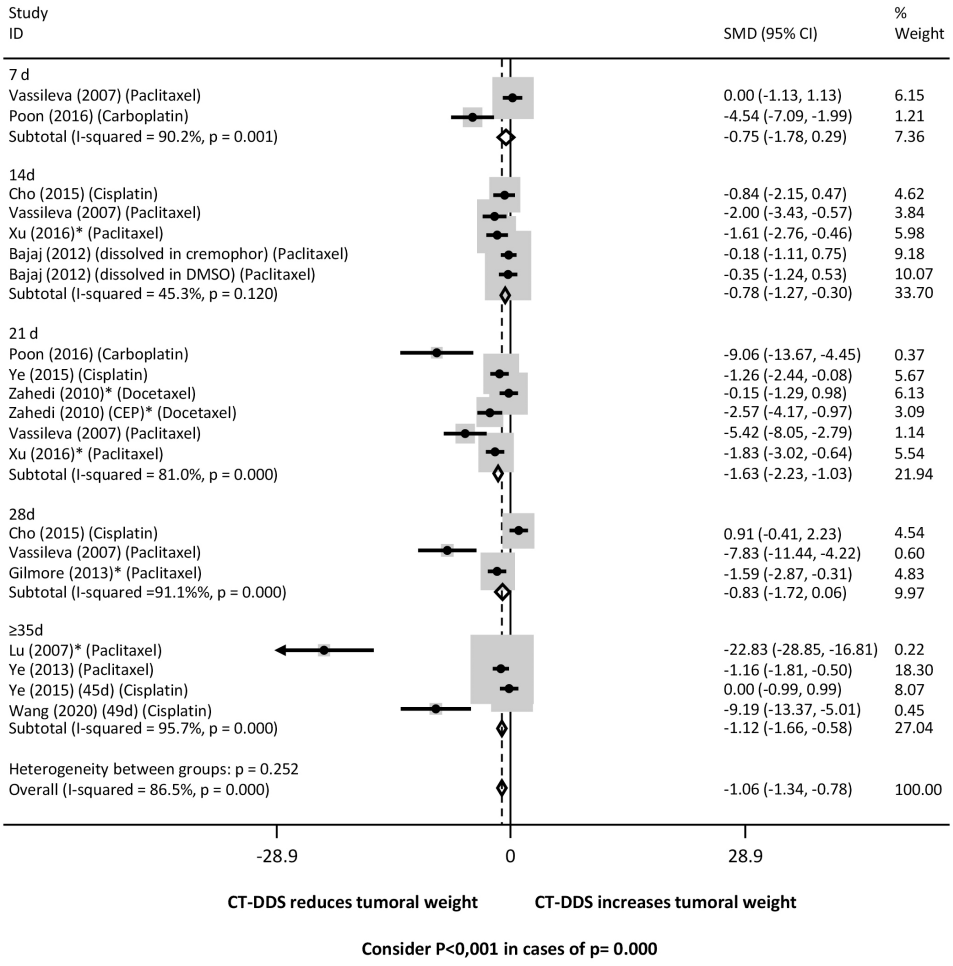

FIGURE 3
Tumor weight at different time points following intraperitoneal chemotherapy administered via drug delivery systems (DDS) compared to free intraperitoneal chemotherapy. Forrest plot presenting the pooled effect estimates from the meta-analysis with 95% confidence intervals (CIs) for each study. The size of each square represents the weight of each study in the meta-analysis, with larger squares corresponding to studies with greater weight. The horizontal lines through each square represent the confidence intervals for each study's effect estimate. The diamond at the bottom of the plot represents the overall pooled effect estimate and its confidence interval. Heterogeneity across studies was assessed using the I^2 statistic, with values of 0-25%, 26-50%, 51-75%, and >75% indicating low, moderate, substantial, and high heterogeneity, respectively. A fixed-effect model was used for the analysis, assuming that all studies estimate the same underlying effect. * Studies that only evaluated xenografts other than SKOV3.

study. The outcomes could only be evaluated independently at each time interval because the animals were grouped by different treatment periods, resulting in the same group being assessed more than once.

3.3 Meta-analysis – study outcomes

Tumor response was evaluated based on the tumor weight and tumor volume. Regarding the period of treatment (duration), tumor weight was lower in the group treated with DDS for: a) 14, 21 and 35 days and overall (grouping all time intervals) when compared with intraperitoneal free chemotherapy (Figure 3) and PBS (Supplementary Figure 1); b) 14, 21, and 35 days and overall, when compared with the empty device (Supplementary Figure 2). However, there was significant heterogeneity, varying from moderate to high, between groups.

Considering the chemotherapy drugs released by DDS, there was a significant regression in tumor weight in mice treated with DDS containing: a) carboplatin, docetaxel and paclitaxel and overall when compared with mice treated with intraperitoneal free chemotherapy (Figure 4); b) carboplatin, cisplatin, docetaxel, and paclitaxel compared with mice treated with PBS (Supplementary Figure 3); and c) docetaxel, paclitaxel and overall compared with mice treated with the empty device (Supplementary Figure 4). There was significant heterogeneity between all the three groups.

Tumor response was also evaluated based on the tumor volume. Regression of tumor volume was significantly greater in mice treated with DDS for all time periods (7 - ≥35 days) than in mice from all control groups, treated with intraperitoneal free chemotherapy (Figure 5), or PBS (Supplementary Figure 5), or the empty device (Supplementary Figure 6). There was significant heterogeneity between groups for all comparisons.

Regarding chemotherapy drugs, there was a reduction in tumor volume for mice treated with DDS containing: a) carboplatin, cisplatin and paclitaxel, and overall, compared with mice treated with intraperitoneal free chemotherapy (Figure 6); b) all drugs tested, i.e., carboplatin, cisplatin, docetaxel, paclitaxel, and overall, compared with mice treated with PBS (Supplementary Figure 7); c) cisplatin and overall, compared with mice treated with the empty device (Supplementary Figure 8). Significant heterogeneity between

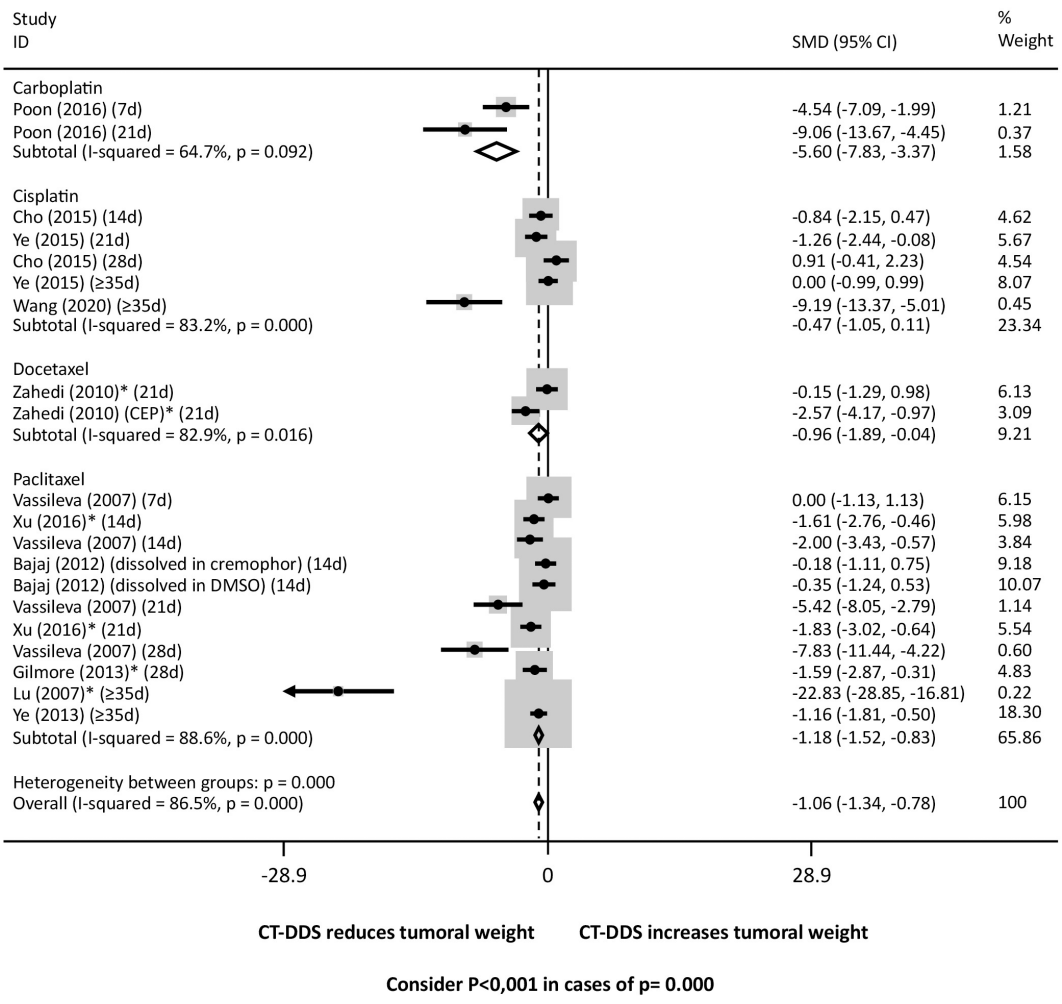

FIGURE 4
Tumor weight following intraperitoneal administration of various chemotherapy drugs via drug delivery systems (DDS) compared to free intraperitoneal chemotherapy. Consider P<0,001 in cases of p= 0.000. * Studies that only evaluated xenografts other than SKOV3.

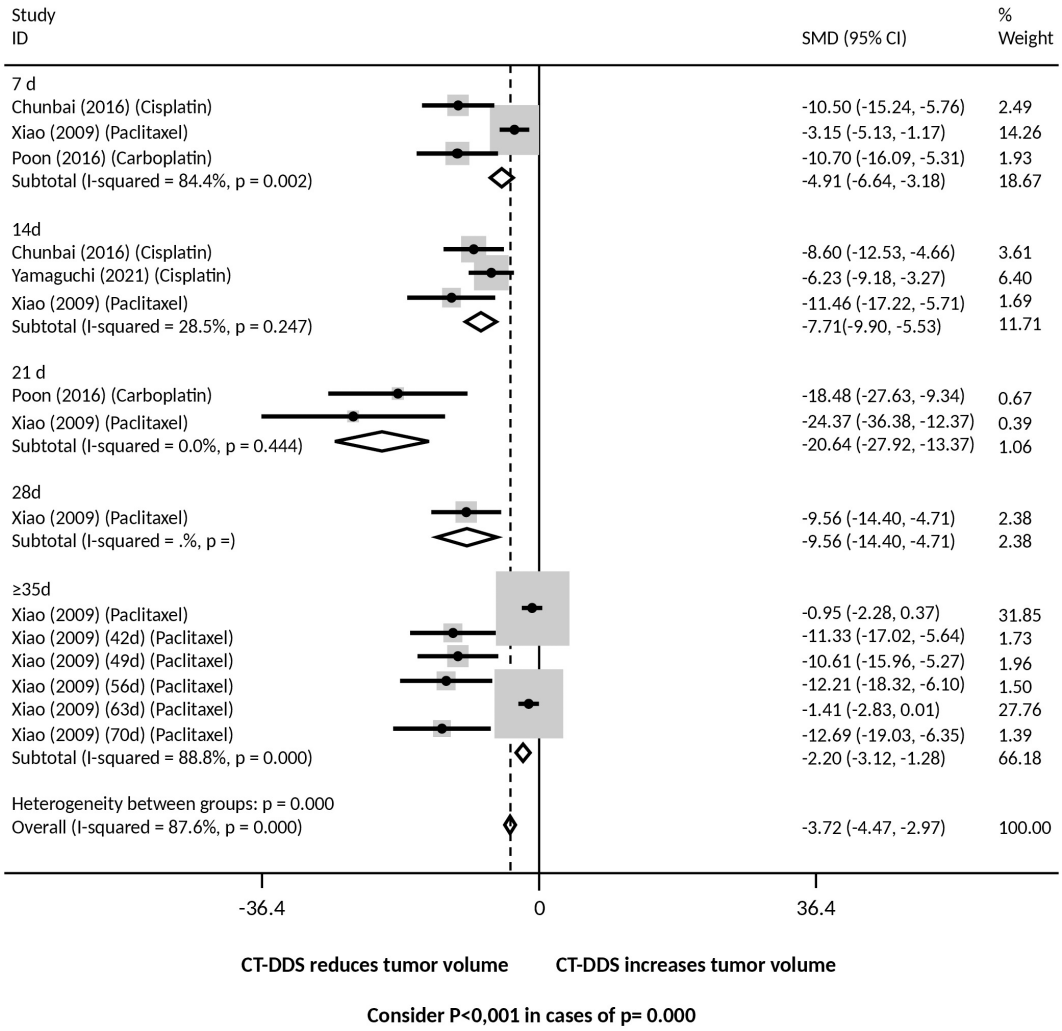

FIGURE 5
Tumor volume at different time points following intraperitoneal chemotherapy administered via drug delivery systems (DDS) compared to free intraperitoneal chemotherapy. Consider P<0,001 in cases of p= 0.000.

groups was observed in comparisons of the DDS with PBS and intraperitoneal free chemotherapy.

We next evaluated animal body weight within treatments, because it was the most common evaluation of toxicity among studies. Indirect signs such as inactivity or change in eye color were not commonly described.

Although 4/13 studies used percentage variation to evaluate weight gain or loss, these studies reported an initial mice weight of approximately 20g, which allowed us to estimate a numerical value and build the meta-analysis. Animals treated with DDS were heavier after 7, 28, and ≥35 days of treatment and overall, when compared to the group that received intraperitoneal free chemotherapy (Figure 7) for the same time period. There was no weight difference in mice treated with DDS in most time periods (7, 14, 21, 28 days), but mice treated for ≥35 days and overall were heavier when compared to mice that received PBS (Supplementary Figure 9). In addition, mice treated with DDS were less heavy at 4, 21 days and overall, but not at 7, 28 and ≥35 days, compared to animals treated with the empty device (Supplementary Figure 10). The studies that evaluated mice weight variation along the periods of treatment showed 64.5% of heterogeneity among them.

Regarding the drugs used, mice treated with docetaxel, paclitaxel and overall were heavier, but not mice treated with cisplatin, when compared with mice treated with intraperitoneal free chemotherapy (Figure 8). There was no significant weight difference in mice treated with DDS containing docetaxel, and paclitaxel, but there was a reduced weight in mice treated with cisplatin and overall, when compared with the group treated with PBS (Supplementary Figure 11), with no heterogeneity between groups. Besides that, mice treated with DDS containing paclitaxel and overall were less heavy, but not those treated with DDS with cisplatin, than mice treated with the device devoid of chemotherapy (Supplementary Figure 12). There was heterogeneity between groups for comparisons of DDS with intraperitoneal free chemotherapy or the free device.

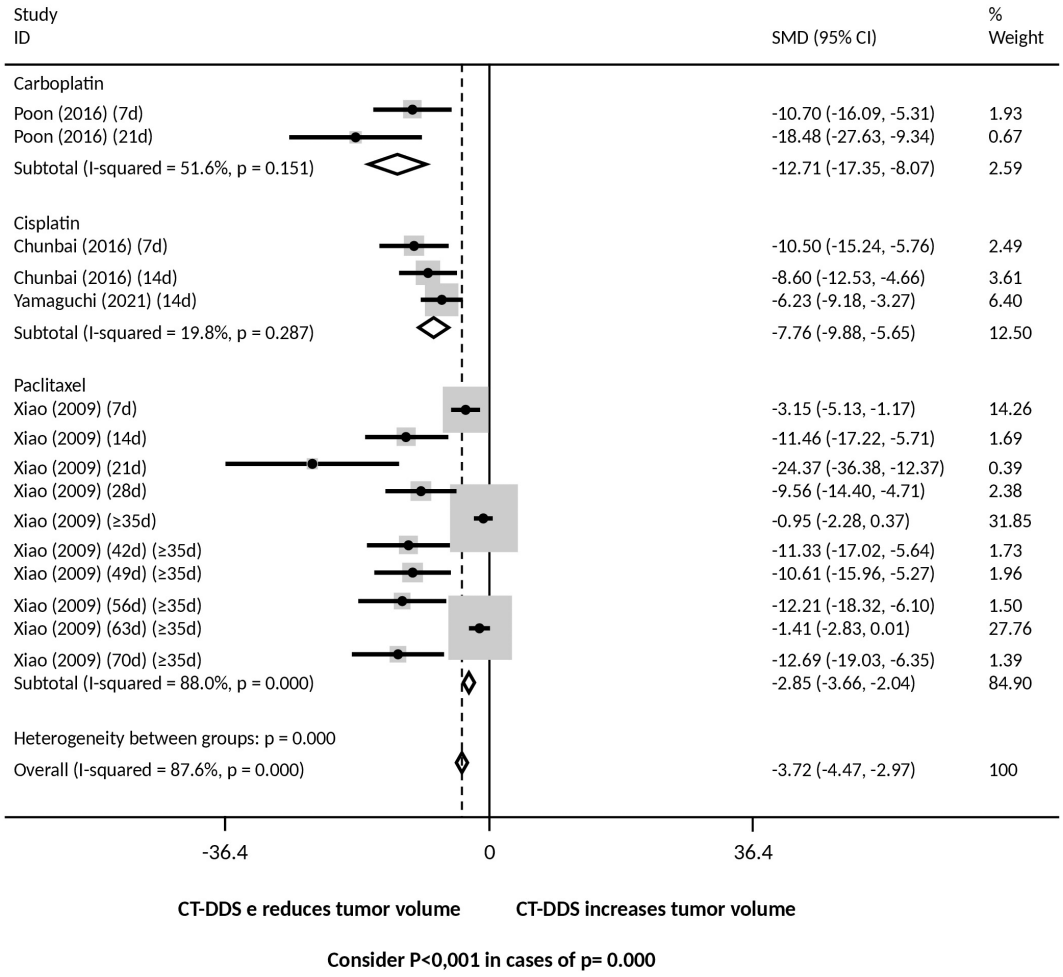

FIGURE 6
Tumor volume following intraperitoneal administration of various chemotherapy drugs via drug delivery systems (DDS) compared to free intraperitoneal chemotherapy. Consider P<0,001 in cases of p= 0.000.

4 Discussion

We evaluated tumor response and treatment toxicity in studies that compared intraperitoneal devices of chemotherapy release with free chemotherapy intraperitoneal administration in animal models of ovarian cancer xenografts. In the meta-analysis we observed a small benefit in overall tumor reduction in animals treated with intraperitoneal chemotherapy applied through the slow release device compared with animals treated with intraperitoneal free chemotherapy. In addition, there was no important toxicity that negatively impacted animal weight in rodents treated with DDSs, compared with rodents treated with free chemotherapy.

Continuous, low-dose release of chemotherapy is called metronomic (37) and its efficacy is based mainly on compromising integrity of endothelial cells, reducing angiogenesis (33, 38). A long release time of the chemotherapy agent also allows the drug to achieve favorable distribution to different organs. and not just on the peritoneal surface (26, 38), and may have beneficial effects against inadequate distribution of intraperitoneal chemotherapy, that is a recurrent problem, possibly compromising peritoneal chemotherapy efficacy (39).

A previous meta-analysis, published in 2015, compared animal studies of drug delivery systems for ovarian cancer treatment (17). In this review, the outcomes were grouped into only one treatment time interval, which allowed a greater number of studies to be included in the same analysis. The selected studies included peritoneal and intravenous release formulations (17). In the present study, 15 new studies were available for inclusion, eight of which using cisplatin and seven using paclitaxel. In 2022, a publication of an equivalent systematic review on murine models of gastrointestinal cancer involving 35 studies showed an important clinical improvement in tumor reduction in animals that received the prototype, consisting of DDSs containing cytostatics for the treatment of gastro-intestinal peritoneal metastasis, compared to those that received free chemotherapy in the abdominal cavity (18). Mice survival was one important outcome in both studies (17, 18). In agreement some studies included in this meta-analysis showed an increased survival without important variation in animal weight. In most studies, animal survival was described in Kaplan-Meier curves, which made a meta-analysis not possible due to the absence of confidence intervals.

One of the major concerns with intraperitoneal delivery devices is erratic chemotherapy release that could eventually increase the

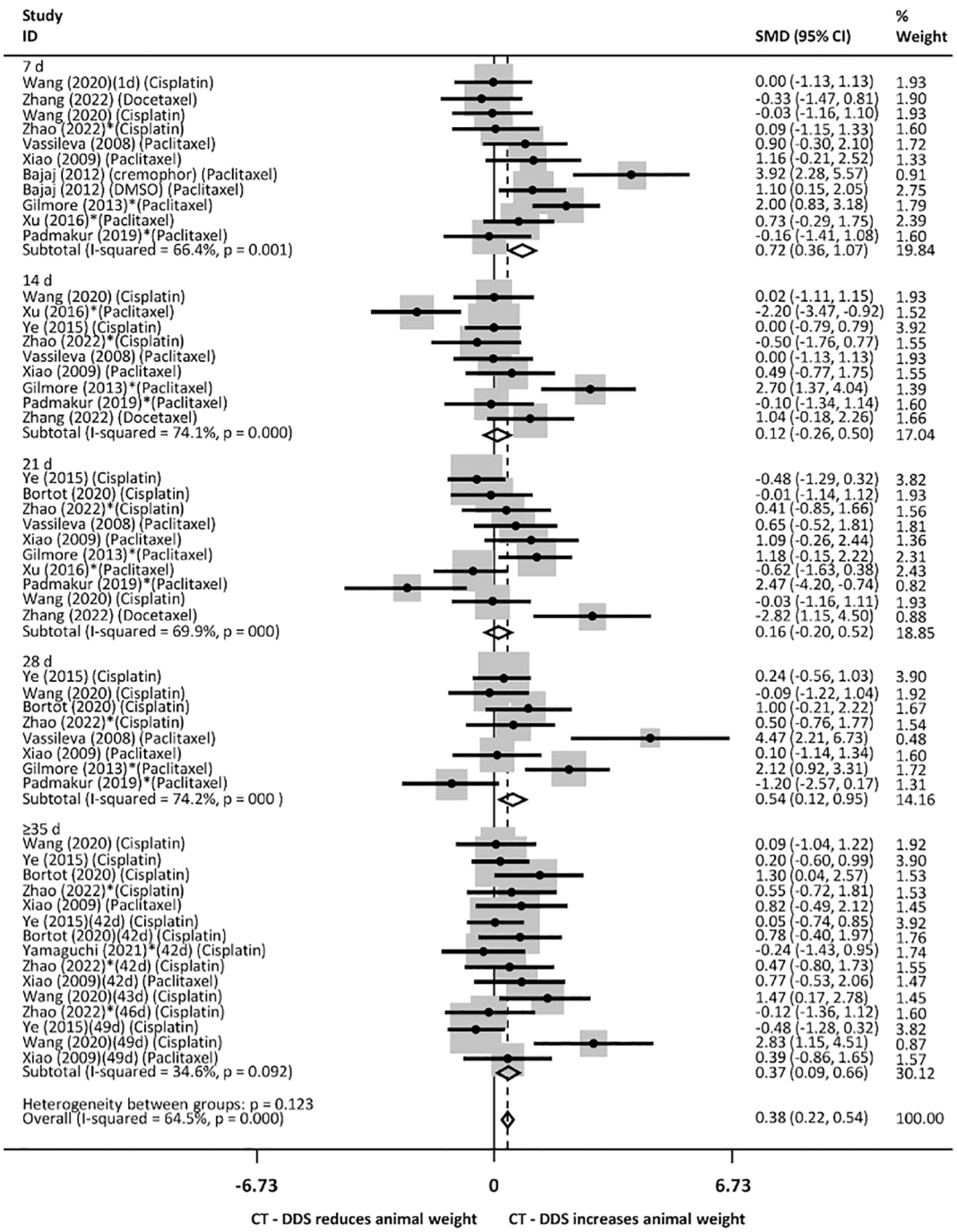

FIGURE 7
Animal weight at various time points following intraperitoneal administration of chemotherapy drugs via drug delivery systems (DDS), compared to free intraperitoneal chemotherapy. Consider P<0,001 in cases of p= 0.000. * Studies that only evaluated xenografts other than SKOV3.

toxicity of the treatment or interrupt the supply of medication prematurely. By separating the outcomes of each study into weekly intervals, we were able to unravel the benefit of DDSs in terms of the time after implantation. The maintained benefit over various time intervals of follow-up supports the advantage of the devices in favor of continued drug release, compared to free chemotherapy administered in bolus.

The present data show that slow drug release devices did not exhibit a deleterious impact on animal body weight compared with intraperitoneal free chemotherapy administration. Besides that, overall analysis of mice treated with DDS revealed they were less heavy than those treated without chemotherapy, i.e., PBS or the device devoid of the drug. Measurement of mouse weight as an outcome of treatment efficacy is controversial (40). Even though a decrease in body weight of > 20% is an important sign of toxicity and is prone to animal euthanasia, weight gain may be associated with tumor weight growth and not necessarily with adequate nutrition. In addition, weight stability is interpreted as an adequate indicator of

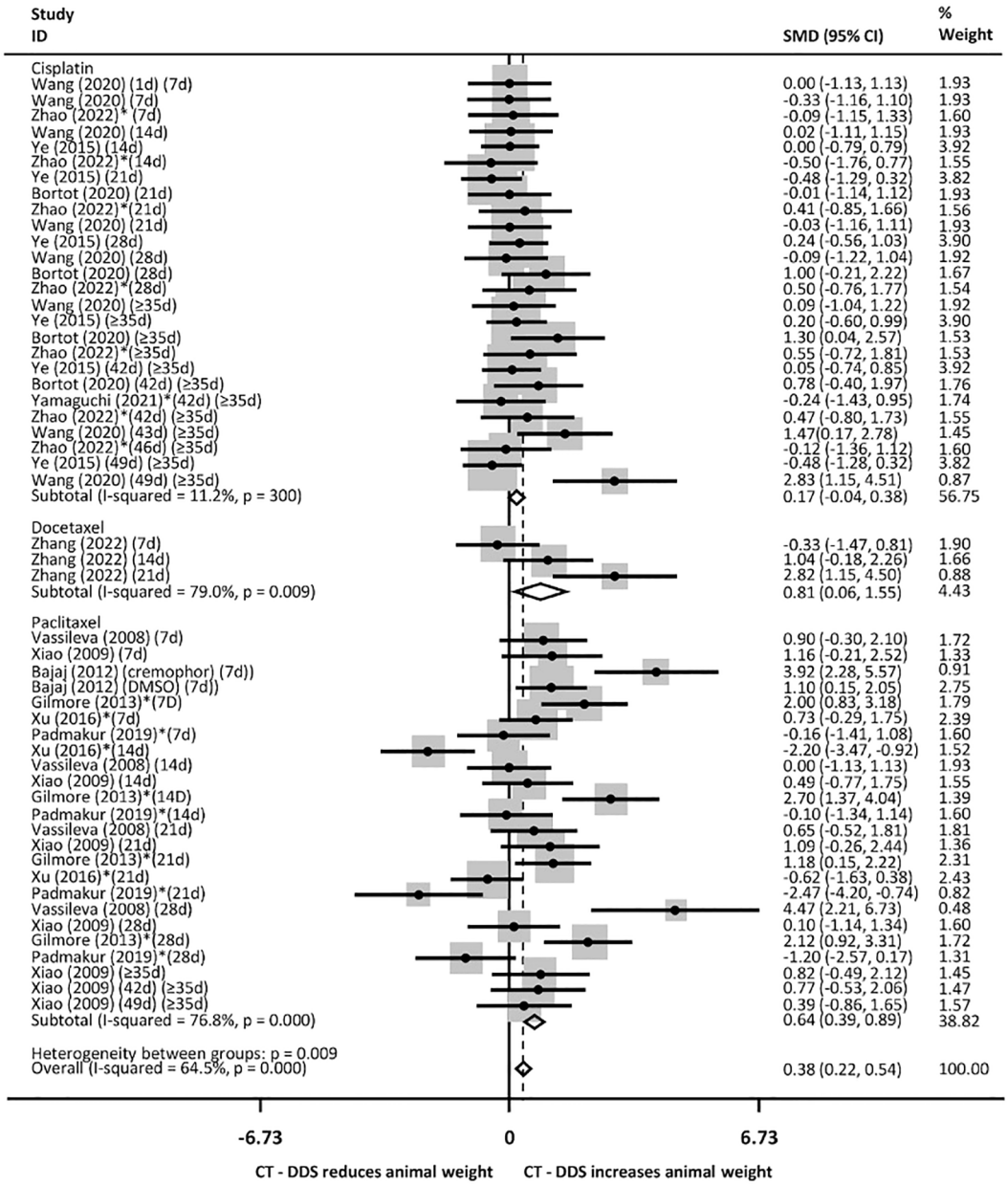

FIGURE 8
Animal weight following intraperitoneal administration of various chemotherapy drugs via drug delivery systems (DDS) compared to free intraperitoneal chemotherapy (over different time periods, from 7 days to more than 35 days). Consider P<0,001 in cases of p= 0.000. * Studies that only evaluated xenografts other than SKOV3.

favorable toxicity (37). No study in the present review described euthanasia associated with mouse weight reduction and weight stability is considered a favorable finding for treatment (37, 41).

An important finding described in most studies is tumor regression, evaluated by tumor weight, tumor volume or tumor bioluminescence. A meta-analysis of the tumor bioluminescence could not be performed because there was a significant variation in the way the studies expressed measurement units. The weight and volume of the residual tumor are direct and objective methods, however, in rodents, it is more reproducible in rats, because mice normally develop very small tumor implants, that are difficult to quantify (40).

Most studies evaluated less than ten mice in each group and, consequently, only a few reached statistical significance individually. In total, 11 studies compared the regression of tumor weight in the experimental groups, in comparison with PBS, and in nine of them the evaluation was undertaken after 21 days of treatment. Indeed, most devices are designed to slowly release medication over two weeks. Studies that evaluated continuous treatment after 21 days also report maintenance of good results after this period compared with free chemotherapy (36, 37, 42–44) and the device without medication (36, 44).

It is important to note that various types of devices that release chemotherapy drugs in different manners were evaluated in the

studies, as is expected in investigational experiments (17, 18). The association of chemotherapy drugs with other agents that would assist in the intracellular transport of the substance is quite common and generally brings benefits in tumor regression. It is noteworthy that the most recent studies looked for presentations with nanoparticles and micelles because of their potential for greater penetration into neoplastic tissue (17).

The most commonly used chemotherapy drugs in the present review were paclitaxel and cisplatin, which are commonly used in clinical practice. There is great interest in the development of cisplatin slow release devices, because in a recent clinical trial, there was efficacy when was applied to the peritoneal cavity in the HIPEC procedure for interval ovarian cytoreduction (12).

In the present analysis, treatment of ovarian cancer xenografts with cisplatin intraperitoneal delivery devices elicited dubious benefits, i.e., enhanced or absent additional growth inhibition, as evaluated through tumor volume or tumor weight, respectively, compared with intraperitoneal free chemotherapy. A trend toward tumor reduction might be due to the optimization of cisplatin uptake by tumor cells through formulations with nanoparticles (45–47). In a previous systematic review, cisplatin intraperitoneal device also showed inconsistent results with no additional benefit compared to free drug administration regarding tumor inhibition, but with improved survival (17). The use of nanotechnology can assist in targeted release of hydrophobic agents, stabilization of transport molecules and reduction of systemic toxicity of antineoplastic agents (48).

In the present review, the performance of intraperitoneal paclitaxel release device was superior to that of intraperitoneal free chemotherapy. Paclitaxel has been used in most studies, mainly through nanoparticles. The contrast between the limited use of nanoparticles in chemotherapy formulations in clinical practice (49) and their high performance in *in vitro* studies (50) may have driven further research using murine models.

Few studies evaluated the performance of carboplatin delivered through intraperitoneal devices, but they showed favorable results in reducing both tumor weight and volume of ovarian cancer xenografts. Carboplatin has adequate intraperitoneal pharmacokinetics and has been used in HIPEC clinical studies in humans with good tolerability (51). In addition, carboplatin was used in the largest clinical trial for outpatient peritoneal chemotherapy (8), although it did not result in a survival gain, compared to conventional intravenous application in advanced ovarian cancer.

Docetaxel has a high cytotoxic potential *in vitro*, but it is not superior to most chemotherapy drugs in human studies (52) and its use is generally limited to relapsed cases of ovarian cancer. Three animal studies using a standardized formulation of docetaxel showed favorable results, but unfortunately, did not evaluate the same outcomes.

We used the SYRCLES instrument to identify biases. Animal studies do not usually detail some methodological steps, such as the random selection of animals and blinding of evaluators, which may compromise some aspects of the instrument, as previously reported (18).

This systematic review has some limitations. In most studies, animal survival was mainly shown in Kaplan-Meier curves, that precluded a meta-analysis due to the absence of confidence intervals. In addition, Xenografts bioluminescence could not be evaluated due to a lack of analysis standardization. We have then used tumor response as a surrogate of treatment benefit. However, tumor weight and volume are rather difficult to evaluate and lack precision in mice (40). In addition, a limited number of animals evaluated in each study and the large methodological variability led to marked heterogeneity regarding tumor weight and volume. The same scenario has been described in a previous study by Raave et al. (17). Furthermore, although most studies compared DDS to release chemotherapy intraperitoneally with the same chemotherapy administered intraperitoneally in bolus, the dose and regimen of administration varied and pharmacokinetic evaluations were performed in some, but not all of them. These differential chemotherapy doses and regimens may have also influenced heterogeneity between groups.

The major contribution of this meta-analysis is a comprehensive analysis of tumor response through the evaluation of tumor volume and tumor weight, considering the drugs employed and treatment duration, comparing the intraperitoneal drug delivery systems (DDSs) containing chemotherapy with intraperitoneal administration of free chemotherapy. In addition, treatment toxicity, through animal weight was evaluated considering the drugs used and time of treatment.

4 Conclusion

The present review further supports the notion that slow-release intraperitoneal chemotherapy devices are effective and safe in animal models of ovarian cancer.

Data availability statement

The original contributions presented in the study are included in the article/Supplementary Material. Further inquiries can be directed to the corresponding author.

Author contributions

MS: Conceptualization, Data curation, Formal analysis, Funding acquisition, Investigation, Methodology, Project administration, Resources, Software, Validation, Visualization, Writing – original draft, Writing – review & editing. RM: Conceptualization, Data curation, Formal analysis, Methodology, Writing – review & editing. SM: Data curation, Formal analysis, Writing – original draft, Visualization. LI: Writing – original draft, Data curation, Formal analysis. GP: Data curation, Writing – original draft, Conceptualization. AL: Conceptualization, Writing – original draft, Supervision. JS: Writing – original draft, Data curation, Formal analysis. MK: Conceptualization, Data curation, Formal analysis, Investigation, Project administration, Visualization, Writing – original draft, Writing – review & editing. MF: Conceptualization,

Methodology, Project administration, Supervision, Validation, Visualization, Writing – original draft, Writing – review & editing.

Funding

The author(s) declare financial support was received for the research, authorship, and/or publication of this article. This work was carried out within the scope of the Universidade de Sao Paulo – Faculdade de Medicina postgraduate program. This work was supported by FAPESP grant 2020/11698-2; GP received a scholarship from CAPES (Fundação Coordenação de Aperfeiçoamento de Pessoal de Nível Superior). MF received research support from Conselho Nacional de Desenvolvimento Científico e Tecnológico, Brazil (CNPq-308052/2022-6).

Acknowledgments

The authors are very grateful to Maria Cristina Piñeiro Grandal, for editing the figures.

Conflict of interest

The authors declare that the research was conducted in the absence of any commercial or financial relationships that could be construed as a potential conflict of interest.

Publisher's note

All claims expressed in this article are solely those of the authors and do not necessarily represent those of their affiliated organizations, or those of the publisher, the editors and the reviewers. Any product that may be evaluated in this article, or claim that may be made by its manufacturer, is not guaranteed or endorsed by the publisher.

Supplementary material

The Supplementary Material for this article can be found online at: https://www.frontiersin.org/articles/10.3389/fonc.2024.1487376/full#supplementary-material

References

1. Lheureux S, Gourley C, Vergote I, Oza AM. Epithelial ovarian cancer. *Lancet*. (2019) 393:1240–53. doi: 10.1016/S0140-6736(18)32552-2

2. Yeung TL, Leung CS, Yip KP, Au Yeung CL, Wong ST, Mok SC. Cellular and molecular processes in ovarian cancer metastasis. A Review in the Theme: Cell and Molecular Processes in Cancer Metastasis. *Am J Physiol Cell Physiol*. (2015) 309:C444–56. doi: 10.1152/ajpcell.00188.2015

3. Cascales-Campos P, Gil J, Feliciangeli E, Parrilla P. HIPEC in ovarian cancer: treatment of a new era or is it the end of the pipeline? *Gynecol Oncol*. (2015) 139:363–8. doi: 10.1016/j.ygyno.2015.06.012

4. Halkia E, Spiliotis J, Sugarbaker P. Diagnosis and management of peritoneal metastases from ovarian cancer. *Gastroenterol Res Pract*. (2012) 2012:541842. doi: 10.1155/2012/541842

5. Webber K, Friedlander M. Chemotherapy for epithelial ovarian, fallopian tube and primary peritoneal cancer. *Best Pract Res Clin Obstet Gynaecol*. (2017) 41:126–38. doi: 10.1016/j.bpobgyn.2016.11.004

6. Zahedi P, Yoganathan R, Piquette-Miller M, Allen C. Recent advances in drug delivery strategies for treatment of ovarian cancer. *Expert Opin Drug Delivery*. (2012) 9:567–83. doi: 10.1517/17425247.2012.665366

7. Spiliotis J, Halkia E, de Bree E. Treatment of peritoneal surface Malignancies with hyperthermic intraperitoneal chemotherapy-current perspectives. *Curr Oncol*. (2016) 23:e266–75. doi: 10.3747/co.23.2831

8. Walker JL, Brady MF, Wenzel L, Fleming GF, Huang HQ, DiSilvestro PA, et al. Randomized trial of intravenous versus intraperitoneal chemotherapy plus bevacizumab in advanced ovarian carcinoma: an NRG oncology/gynecologic oncology group study. *J Clin Oncol*. (2019) 37:1380-90. doi: 10.1200/JCO.18.01568

9. Konigsrainer I, Zieker D, Beckert S, von Weyhern C, Lob S, Falch C, et al. Local peritonectomy highly attracts free floating intraperitoneal colorectal tumour cells in a rat model. *Cell Physiol Biochem*. (2009) 23:371–8. doi: 10.1159/000218183

10. Spiliotis J, Halkia E, Lianos E, Kalantzi N, Grivas A, Efstathiou E, et al. Cytoreductive surgery and HIPEC in recurrent epithelial ovarian cancer: a prospective randomized phase III study. *Ann Surg Oncol*. (2015) 22:1570–5. doi: 10.1245/s10434-014-4157-9

11. Elias D, Goere D, Dumont F, Honore C, Dartigues P, Stoclin A, et al. Role of hyperthermic intraoperative peritoneal chemotherapy in the management of peritoneal metastases. *Eur J Cancer*. (2014) 50:332–40. doi: 10.1016/j.ejca.2013.09.024

12. van Driel WJ, Koole SN, Sikorska K, Schagen van Leeuwen JH, Schreuder HWR, Hermans RHM, et al. Hyperthermic intraperitoneal chemotherapy in ovarian cancer. *N Engl J Med*. (2018) 378:230–40. doi: 10.1056/NEJMoa1708618

13. Classe J-M, Meeus P, Leblanc E, Wernert R, Quenet François, Marchal Frédéric, et al. Hyperthermic intraperitoneal chemotherapy in platinum-sensitive relapsed epithelial ovarian cancer: the chipor randomised phase III trial. *Journal of Clinical Oncology - ASCO MeetingAbstract from the 2023 ASCO Annual Meeting* (2023) 33:A29. doi: 10.1136/ijgc-2023-ESGO.43

14. Chua TC, Robertson G, Liauw W, Farrell R, Yan TD, Morris DL. Intraoperative hyperthermic intraperitoneal chemotherapy after cytoreductive surgery in ovarian cancer peritoneal carcinomatosis: systematic review of current results. *J Cancer Res Clin Oncol*. (2009) 135:1637–45. doi: 10.1007/s00432-009-0667-4

15. Taliento C, Restaino S, Scutiero G, Arcieri M, Bernardi G, Martinello R, et al. Pressurized intraperitoneal aerosol chemotherapy (PIPAC) with cisplatin and doxorubicin in patients with ovarian cancer: A systematic review. *Eur J Surg Oncol*. (2023) 49:107250. doi: 10.1016/j.ejso.2023.107250

16. Adepu S, Ramakrishna S. Controlled drug delivery systems: current status and future directions. *Molecules*. (2021) 26:5905. doi: 10.3390/molecules26195905

17. Raavé R, de Vries RB, Massuger LF, van Kuppevelt TH, Daamen WF. Drug delivery systems for ovarian cancer treatment: a systematic review and meta-analysis of animal studies. *PeerJ*. (2015) 3:e1489. doi: 10.7717/peerj.1489

18. Wintjens AGWE, Simkens GA, Fransen PKH, Serafras N, Lenaerts K, Franssen GHLM, et al. Intraperitoneal drug delivery systems releasing cytostatic agents to target gastro-intestinal peritoneal metastases in laboratory animals: a systematic review. *Clin Exp Metastasis*. (2022) 39:541–79. doi: 10.1007/s10585-022-10173-8

19. Armstrong DK, Fleming GF, Markman M, Bailey HH. A phase I trial of intraperitoneal sustained-release paclitaxel microspheres (Paclimer) in recurrent ovarian cancer: a Gynecologic Oncology Group study. *Gynecol Oncol*. (2006) 103:391–6. doi: 10.1016/j.ygyno.2006.02.029

20. Cristea MC, Frankel P, Synold T, Rivkin S, Lim D, Chung V, et al. A phase I trial of intraperitoneal nab-paclitaxel in the treatment of advanced Malignancies primarily confined to the peritoneal cavity. *Cancer Chemother Pharmacol*. (2019) 83:589–98. doi: 10.1007/s00280-019-03767-9

21. Page MJ, McKenzie JE, Bossuyt PM, Boutron I, Hoffmann TC, Mulrow CD, et al. The PRISMA 2020 statement: an updated guideline for reporting systematic reviews. *Rev Esp Cardiol (Engl Ed)*. (2021) 74:790–9. doi: 10.1016/j.recesp.2021.06.016

22. Ouzzani M, Hammady H, Fedorowicz Z, Elmagarmid A. Rayyan-a web and mobile app for systematic reviews. *Syst Rev*. (2016) 5:210. doi: 10.1186/s13643-016-0384-4

23. Zlowodzki M, Poolman RW, Kerkhoffs GM, Tornetta P 3rd, Bhandari M, Group ObotIE-BOSW. How to interpret a meta-analysis and judge its value as a guide for clinical practice. *Acta Orthopaedica*. (2009) 78:598–609. doi: 10.1080/17453670710014284

24. Hooijmans CR, Rovers MM, de Vries RB, Leenaars M, Ritskes-Hoitinga M, Langendam MW. SYRCLE's risk of bias tool for animal studies. *BMC Med Res Methodol*. (2014) 14:43. doi: 10.1186/1471-2288-14-43

25. Kumagai S, Sugiyama T, Nishida T, Ushijima K, Yakushiji M. Improvement of intraperitoneal chemotherapy for rat ovarian cancer using cisplatin-containing microspheres. *Jpn J Cancer Res*. (1996) 87:412–7. doi: 10.1111/j.1349-7006.1996.tb00238.x

26. Zahedi P, Stewart J, De Souza R, Piquette-Miller M, Allen C. An injectable depot system for sustained intraperitoneal chemotherapy of ovarian cancer results in favorable drug distribution at the whole body, peritoneal and intratumoral levels. *J Control Release*. (2012) 158:379–85. doi: 10.1016/j.jconrel.2011.11.025

27. De Clercq K, Xie F, De Wever O, Descamps B, Hoorens A, Vermeulen A, et al. Preclinical evaluation of local prolonged release of paclitaxel from gelatin microspheres for the prevention of recurrence of peritoneal carcinomatosis in advanced ovarian cancer. *Sci Rep*. (2019) 9:14881. doi: 10.1038/s41598-019-51419-y

28. Bajaj G, Kim MR, Mohammed SI, Yeo Y. Hyaluronic acid-based hydrogel for regional delivery of paclitaxel to intraperitoneal tumors. *J Control Release*. (2012) 158:386–92. doi: 10.1016/j.jconrel.2011.12.001

29. Xiao K, Luo J, Fowler WL, Li Y, Lee JS, Xing L, et al. A self-assembling nanoparticle for paclitaxel delivery in ovarian cancer. *Biomaterials*. (2009) 30:6006–16. doi: 10.1016/j.biomaterials.2009.07.015

30. Tan HL, Kim G, Charles CJ, Li RR, Jang CJ, Shabbir A, et al. Safety, pharmacokinetics and tissue penetration of PIPAC paclitaxel in a swine model. *Eur J Surg Oncol*. (2021) 47:1124–31. doi: 10.1016/j.ejso.2020.06.031

31. Lu Z, Tsai M, Lu D, Wang J, Wientjes MG, Au JL. Tumor-penetrating microparticles for intraperitoneal therapy of ovarian cancer. *J Pharmacol Exp Ther*. (2008) 327:673–82. doi: 10.1124/jpet.108.140095

32. Zahedi P, De Souza R, Piquette-Miller M, Allen C. Chitosan-phospholipid blend for sustained and localized delivery of docetaxel to the peritoneal cavity. *Int J Pharm*. (2009) 377:76–84. doi: 10.1016/j.ijpharm.2009.05.003

33. De Souza R, Zahedi P, Moriyama EH, Allen CJ, Wilson BC, Piquette-Miller M. Continuous docetaxel chemotherapy improves therapeutic efficacy in murine models of ovarian cancer. *Mol Cancer Ther*. (2010) 9:1820–30. doi: 10.1158/1535-7163.MCT-10-0249

34. Yang M, Yu T, Wood J, Wang YY, Tang BC, Zeng Q, et al. Intraperitoneal delivery of paclitaxel by poly(ether-anhydride) microspheres effectively suppresses tumor growth in a murine metastatic ovarian cancer model. *Drug Delivery Transl Res*. (2014) 4:203–9. doi: 10.1007/s13346-013-0190-7

35. Desale SS, Soni KS, Romanova S, Cohen SM, Bronich TK. Targeted delivery of platinum-taxane combination therapy in ovarian cancer. *J Control Release*. (2015) 220:651–9. doi: 10.1016/j.jconrel.2015.09.007

36. Zahedi P, De Souza R, Huynh L, Piquette-Miller M, Allen C. Combination drug delivery strategy for the treatment of multidrug resistant ovarian cancer. *Mol Pharm*. (2011) 8:260–9. doi: 10.1021/mp100323z

37. Ye H, Tanenbaum LM, Na YJ, Mantzavinou A, Fulci G, Del Carmen MG, et al. Sustained, low-dose intraperitoneal cisplatin improves treatment outcome in ovarian cancer mouse models. *J Control Release*. (2015) 220:358–67. doi: 10.1016/j.jconrel.2015.11.001

38. Vassileva V, Moriyama EH, De Souza R, Grant J, Allen CJ, Wilson BC, et al. Efficacy assessment of sustained intraperitoneal paclitaxel therapy in a murine model of ovarian cancer using bioluminescent imaging. *Br J Cancer*. (2008) 99:2037–43. doi: 10.1038/sj.bjc.6604803

39. Dawson SJ, Hicks RJ, Johnston V, Allen D, Jobling T, Quinn M, et al. Intraperitoneal distribution imaging in ovarian cancer patients. *Intern Med J*. (2011) 41:167–71. doi: 10.1111/j.1445-5994.2009.02112.x

40. Paster EV, Villines KA, Hickman DL. Endpoints for mouse abdominal tumor models: refinement of current criteria. *Comp Med*. (2009) 59:234–41.

41. Padmakumar S, Parayath NN, Nair SV, Menon D, Amiji MM. Enhanced anti-tumor efficacy and safety with metronomic intraperitoneal chemotherapy for metastatic ovarian cancer using biodegradable nanotextile implants. *J Control Release*. (2019) 305:29–40. doi: 10.1016/j.jconrel.2019.05.022

42. Vassileva V, Grant J, De Souza R, Allen C, Piquette-Miller M. Novel biocompatible intraperitoneal drug delivery system increases tolerability and therapeutic efficacy of paclitaxel in a human ovarian cancer xenograft model. *Cancer Chemother Pharmacol*. (2007) 60:907–14. doi: 10.1007/s00280-007-0449-0

43. Poon C, Duan X, Chan C, Han W, Lin W. Nanoscale coordination polymers codeliver carboplatin and gemcitabine for highly effective treatment of platinum-resistant ovarian cancer. *Mol Pharm*. (2016) 13:3665–75. doi: 10.1021/acs.molpharmaceut.6b00466

44. Xu S, Fan H, Yin L, Zhang J, Dong A, Deng L, et al. Thermosensitive hydrogel system assembled by PTX-loaded copolymer nanoparticles for sustained intraperitoneal chemotherapy of peritoneal carcinomatosis. *Eur J Pharm Biopharm*. (2016) 104:251–9. doi: 10.1016/j.ejpb.2016.05.010

45. Cho EJ, Sun B, Doh K-O, Wilson EM, Torregrosa-Allen S, Elzey BD, et al. Intraperitoneal delivery of platinum with *in-situ* crosslinkable hyaluronic acid gel for local therapy of ovarian cancer. *Biomaterials*. (2015) 37:312–9. doi: 10.1016/j.biomaterials.2014.10.039

46. Yamaguchi K, Hiraike O, Iwaki H, Matsumiya K, Nakamura N, Sone K, et al. Intraperitoneal administration of a cisplatin-loaded nanogel through a hybrid system containing an alginic acid-based nanogel and an *in situ* cross-linkable hydrogel for peritoneal dissemination of ovarian cancer. *Mol Pharm*. (2021) 18:4090–8. doi: 10.1021/acs.molpharmaceut.1c00514

47. Wang Y, Qiao X, Yang X, Yuan M, Xian S, Zhang L, et al. The role of a drug-loaded poly (lactic co-glycolic acid) (PLGA) copolymer stent in the treatment of ovarian cancer. *Cancer Biol Med*. (2020) 17:237–50. doi: 10.20892/j.issn.2095-3941.2019.0169

48. Barani M, Bilal M, Sabir F, Rahdar A, Kyzas GZ. Nanotechnology in ovarian cancer: Diagnosis and treatment. *Life Sci*. (2021) 266:118914. doi: 10.1016/j.lfs.2020.118914

49. NCPGiOv. *Ovarian Cancer Including Fallopian Tube Cancer and Primary Peritoneal Cancer* (2024). Available online at: https://www.nccn.org/. (Accessed August 26, 2024).

50. Zhang J, Ding H, Zhang F, Xu Y, Liang W, Huang L. New trends in diagnosing and treating ovarian cancer using nanotechnology. *Front Bioeng Biotechnol*. (2023) 11:1160985. doi: 10.3389/fbioe.2023.1160985

51. Mikkelsen MS, Blaakaer J, Petersen LK, Schleiss LG, Iversen LH. Pharmacokinetics and toxicity of carboplatin used for hyperthermic intraperitoneal chemotherapy (HIPEC) in treatment of epithelial ovarian cancer. *Pleura Peritoneum*. (2020) 5:20200137. doi: 10.1515/pp-2020-0137

52. Vasey PA, Jayson GC, Gordon A, Gabra H, Coleman R, Atkinson R, et al. Phase III randomized trial of docetaxel-carboplatin versus paclitaxel-carboplatin as first-line chemotherapy for ovarian carcinoma. *J Natl Cancer Inst*. (2004) 96:1682–91. doi: 10.1093/jnci/djh323

53. Amoozgar Z, Wang L, Brandstoetter T, Wallis SS, Wilson EM, Goldberg MS. Dual-layer surface coating of PLGA-based nanoparticles provides slow-release drug delivery to achieve metronomic therapy in a paclitaxel-resistant murine ovarian cancer model. *Biomacromolecules*. (2014) 15:4187–94. doi: 10.1021/bm5011933

54. Bortot B, Mongiat M, Valencic E, Dal Monego S, Licastro D, Crosera M, et al. Nanotechnology-based cisplatin intracellular delivery to enhance chemo-sensitivity of ovarian cancer. *Int J Nanomedicine*. (2020) 15:4793–810. doi: 10.2147/IJN.S247114

55. Cho H, Kwon GS. Thermosensitive poly-(d,l-lactide-co-glycolide)-block-poly (ethylene glycol)-block-poly-(d,l-lactide-co-glycolide) hydrogels for multi-drug delivery. *J Drug Target*. (2014) 22:669–77. doi: 10.3109/1061186X.2014.931406

56. Cho H, Lai TC, Kwon GS. Poly(ethylene glycol)-block-poly(ÃÂμ-caprolactone) micelles for combination drug delivery: evaluation of paclitaxel, cyclopamine and gossypol in intraperitoneal xenograft models of ovarian cancer. *J Control Release*. (2013) 166:1–9. doi: 10.1016/j.jconrel.2012.12.005

57. Gilmore D, Schulz M, Liu R, Zubris KAV, Padera RF, Catalano PJ, et al. Cytoreductive surgery and intraoperative administration of paclitaxel-loaded expansile nanoparticles delay tumor recurrence in ovarian carcinoma. *Ann Surg Oncol*. (2013) 20:1684–93. doi: 10.1245/s10434-012-2696-5

58. Hagiwara A, Takahashi T, Yamaguchi T, Taniguchi H, Iwamoto A, Yoneyama C, et al. Intracavitary microspheres incorporating cisplatinum in the treatment of Malignant effusions–clinical trials. *Gan To Kagaku Ryoho*. (1990) 17:1575–8.

59. He C, Poon C, Chan C, Yamada SD, Lin W. Nanoscale coordination polymers codeliver chemotherapeutics and siRNAs to eradicate tumors of cisplatin-resistant ovarian cancer. *J Am Chem Soc*. (2016) 138:6010–9. doi: 10.1021/jacs.6b02486

60. Ho EA, Soo PL, Allen C, Piquette-Miller M. Impact of intraperitoneal, sustained delivery of paclitaxel on the expression of P-glycoprotein in ovarian tumors. *J Control Release*. (2007) 117:20–7. doi: 10.1016/j.jconrel.2006.10.007

61. Lee SE, Bairstow SF, Werling JO, Chaubal MV, Lin L, Murphy MA, et al. Paclitaxel nanosuspensions for targeted chemotherapy - nanosuspension preparation, characterization, and use. *Pharm Dev Technol*. (2014) 19:438–53. doi: 10.3109/10837450.2013.789911

62. Li S-D, Howell SB. CD44-targeted microparticles for delivery of cisplatin to peritoneal metastases. *Mol Pharm*. (2010) 7:280–90. doi: 10.1021/mp900242f

63. Lu H, Li B, Kang Y, Jiang W, Huang Q, Chen Q, et al. Paclitaxel nanoparticle inhibits growth of ovarian cancer xenografts and enhances lymphatic targeting. *Cancer Chemother Pharmacol*. (2007) 59:175–81. doi: 10.1007/s00280-006-0256-z

64. Padmakumar S, Menon D. Nanofibrous polydioxanone depots for prolonged intraperitoneal paclitaxel delivery. *Curr Drug Delivery*. (2019) 16:654–62. doi: 10.2174/1567201816666190816102949

65. Sun B, Taha MS, Ramsey B, Torregrosa-Allen S, Elzey BD, Yeo Y. Intraperitoneal chemotherapy of ovarian cancer by hydrogel depot of paclitaxel nanocrystals. *J Control Release*. (2016) 235:91–8. doi: 10.1016/j.jconrel.2016.05.056

66. Tong L, Chen W, Wu J, Li H. Folic acid-coupled nano-paclitaxel liposome reverses drug resistance in SKOV3/TAX ovarian cancer cells. *Anticancer Drugs*. (2014) 25:244–54. doi: 10.1097/CAD.0000000000000047

67. Xie F, De Clercq K, Vervaet C, Van Bocxlaer J, Colin P, Vermeulen A. Model-based analysis of treatment effects of paclitaxel microspheres in a microscopic peritoneal carcinomatosis model in mice. *Pharm Res*. (2019) 36:127. doi: 10.1007/s11095-019-2660-1

68. Xiong XY, Guo L, Gong YC, Li ZL, Li YP, Liu ZY, et al. *In vitro* &*in vivo* targeting behaviors of biotinylated Pluronic F127/poly(lactic acid) nanoparticles through biotin-avidin interaction. *Eur J Pharm Sci*. (2012) 46:537–44. doi: 10.1016/j.ejps.2012.04.011

69. Yang J, Zhang R, Pan H, Li Y, Fang Y, Zhang L, et al. Backbone degradable N-(2-hydroxypropyl)methacrylamide copolymer conjugates with gemcitabine and paclitaxel: impact of molecular weight on activity toward human ovarian carcinoma xenografts. *Mol Pharm*. (2017) 14:1384–94. doi: 10.1021/acs.molpharmaceut.6b01005

70. Ye L, He J, Hu Z, Dong Q, Wang H, Fu F, et al. Antitumor effect and toxicity of Lipusu in rat ovarian cancer xenografts. *Food Chem Toxicol*. (2013) 52:200–6. doi: 10.1016/j.fct.2012.11.004

71. Zhang Y, Wang S, Duan X, Xu X, Gao Y, Zhou J, et al. mPEG-PDLLA micelles potentiate docetaxel for intraperitoneal chemotherapy in ovarian cancer peritoneal metastasis. *Front Pharmacol*. (2022) 13:861938. doi: 10.3389/fphar.2022.861938

72. Zhao J, Huang X, Liu P, Qiu M, Li B, Wen Y, et al. Engineering alendronate-composed iron nanochelator for efficient peritoneal carcinomatosis treatment. *Adv Sci (Weinh)*. (2022) 9:e2203031–e. doi: 10.1002/advs.202203031

frontiers | Frontiers in Oncology

TYPE Case Report
PUBLISHED 04 February 2025
DOI 10.3389/fonc.2025.1487334

Check for updates

OPEN ACCESS

EDITED BY
Zhaofeng Liang,
Jiangsu University, China

REVIEWED BY
Elisa Roca,
Casa di cura Pederzoli, Italy
Keitaro Matsumoto,
Nagasaki University, Japan

*CORRESPONDENCE
Qianqian Zhang
zxxych@163.com
Xiaoju Zhang
zhangxiaoju@zzu.edu.cn

RECEIVED 27 August 2024
ACCEPTED 16 January 2025
PUBLISHED 04 February 2025

CITATION
Wang X, Wei N, Yang H, Wang X, Zhang X and Zhang Q (2025) Long term survival of advanced hepatoid adenocarcinoma of lung secondary to idiopathic pulmonary fibrosis: a case report.
Front. Oncol. 15:1487334.
doi: 10.3389/fonc.2025.1487334

COPYRIGHT
© 2025 Wang, Wei, Yang, Wang, Zhang and Zhang. This is an open-access article distributed under the terms of the Creative Commons Attribution License (CC BY). The use, distribution or reproduction in other forums is permitted, provided the original author(s) and the copyright owner(s) are credited and that the original publication in this journal is cited, in accordance with accepted academic practice. No use, distribution or reproduction is permitted which does not comply with these terms.

Long term survival of advanced hepatoid adenocarcinoma of lung secondary to idiopathic pulmonary fibrosis: a case report

Xiaoli Wang[1,2], Nan Wei[1,2], Huizhen Yang[1,2], Xiaoyan Wang[3], Xiaoju Zhang[1,2*] and Qianqian Zhang[1,2*]

[1]Department of Respiratory and Critical Care Medicine, Zhengzhou University People's Hospital, Henan Provincial People's Hospital, Zhengzhou, Henan, China, [2]Henan International Joint Laboratory of Diagnosis and Treatment for Pulmonary Nodules, Zhengzhou University People's Hospital, Henan Provincial People's Hospital, Zhengzhou, Henan, China, [3]Department of Pathology, Zhengzhou University People's Hospital, Henan Provincial People's Hospital, Zhengzhou, Henan, China

Background: Alpha-fetoprotein (AFP)-producing hepatoid adenocarcinoma of lung (HAL) is a rare type of lung cancer, with its characteristics being not yet fully clarified. We recently encountered a case of HAL combined with idiopathic pulmonary fibrosis (IPF), which has never been reported.

Case presentation: A 66-year-old man consulted our hospital with a chief complaint of cough. Chest computed tomography (CT) revealed multiple nodules measuring from 8mm to 20mm in diameter located in bilateral lung, along with an enlarged left hilar lymph node. CT-guided percutaneous lung biopsy confirmed the diagnosis of AFP-producing primary HAL combined with IPF. Systemic treatment according to guidelines for advanced non-small cell lung cancer resulted in a long-term survival.

Conclusions: This case report documents the first occurrence and prognosis of AFP-producing HAL in a patient with IPF. The long-term survival brought by the diagnosis and treatment model in our case may provide significant prognostic value for this rare condition.

KEYWORDS

hepatoid adenocarcinoma, lung cancer, idiopathic pulmonary fibrosis, alpha-fetoprotein, immune checkpoint inhibitor

Background

Hepatoid adenocarcinoma of the lung (HAL) is an extremely rare tumor type, which was first reported as an Alpha-fetoprotein (AFP)-producing lung cancer by Ysunami (1). The pathological features of HAL were fully defined by Ishikura in 1990 (2) and were modified by Haninger in 2014 (3). Since AFP-producing HAL has scarcely been reported,

the clinical features and molecular mechanism of this type of lung cancer are still unclear, with no standard treatment regime being recommended. When concomitant idiopathic pulmonary fibrosis (IPF) was diagnosed, the prognosis of lung cancer maybe much poorer (4–6).

Interestingly, we encountered a case of AFP-producing HAL in a patient with IPF, which benefit from the systematic treatment and achieved a long-term survival for this rare type of lung cancer. To the best of our knowledge, this is the first report of AFP-producing HAL in a patient with IPF.

Case presentation

A 66-year-old man was admitted to our hospital with the chief complaint of cough in March 2018. Chest computed tomography (CT) revealed multiple nodules measuring from 8mm to 20mm in diameter located in bilateral lung, along with an enlarged #11L lymph node (Figures 1A–D). The patient had been diagnosed of IPF four years prior. Of the tumor markers, most were within the normal range, except for a markedly elevated serum AFP level of 6753ng/ml. A CT-guided percutaneous lung biopsy was performed in the largest pulmonary nodule located in the S6 segment of the left lung.

Hematoxylin and eosin staining indicated the poorly differentiated cancer cells resembling hepatocellular carcinoma (Figures 2A, B). Immunohistochemical staining showed that the tumor cells were negative for TTF-1 (Figure 2C), but positive for Hepatocyte (Figure 2D) and CK8/18 (Figure 2E), with moderate positivity for Ki-67 (40%, Figure 2F). Abdominal magnetic resonance imaging (MRI) and CT examination showed no evidence of hepatic or other digestive system tumors. Positron emission tomography/computed tomography (PET-CT) revealed increased standard uptake value (SUV) in the lung nodules (SUV max: 8.1) and in the enlarged #11L lymph node (SUV max: 4.1). No abnormal hypermetabolic lesions were observed in any other organs. Serum biochemical tests did not reveal any evidence of hepatic dysfunction or hepatitis B or C infection. Based on these findings, the patient was diagnosed with AFP-producing primary HAL, clinical stage IV (T4N1M1a). Molecular studies were negative for EGFR, ROS-1, ALK, RET, MET, PIK-3CA, ERBB-2, KRAS, and BRAF mutations.

Subsequently, the patient received six cycles of pemetrexed plus cisplatin chemotherapy, with bevacizumab administered every 21 days concurrently. There was a slight decrease in the AFP serum level (4679 ng/ml), as well as a reduction in the diameter of nodule in left lower lobar. However, due to the side effects, the patient refused further chemotherapy and was instead treated with oral

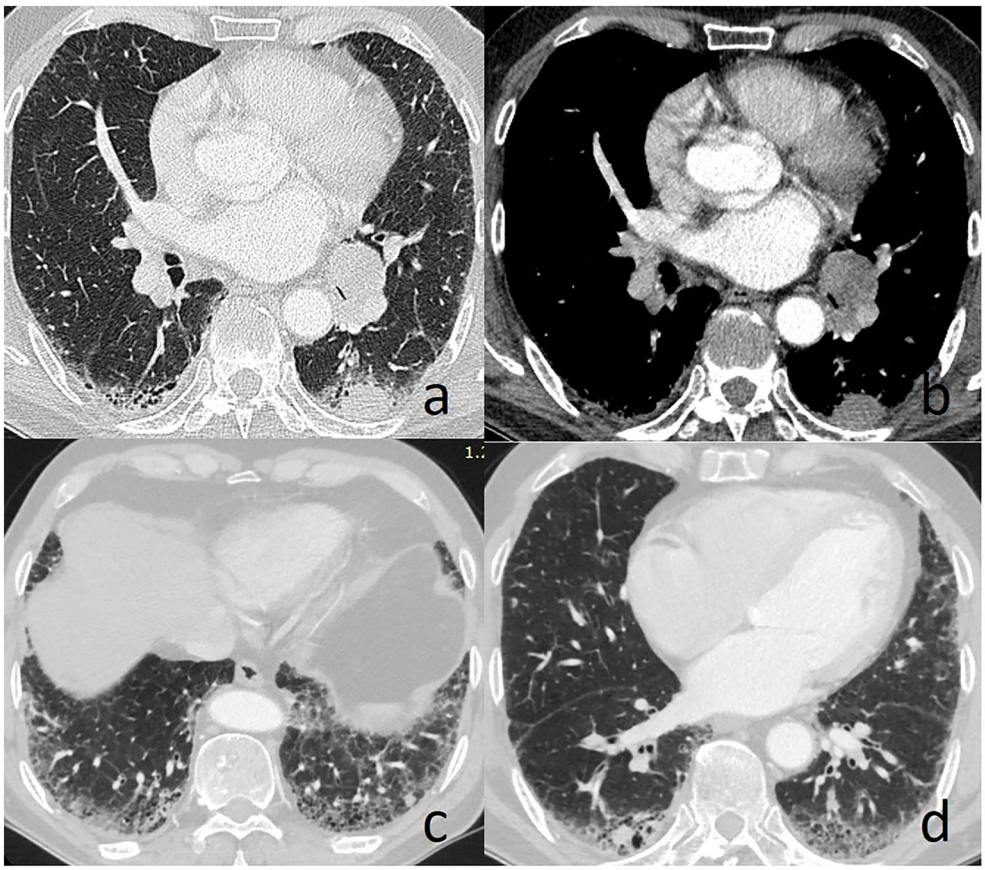

FIGURE 1
Chest computed tomography reveals left lung nodule and enlarged #11L lymph node **(A, B)**, and multiple lung nodules in the area with obvious fibrotic changes **(C, D)**.

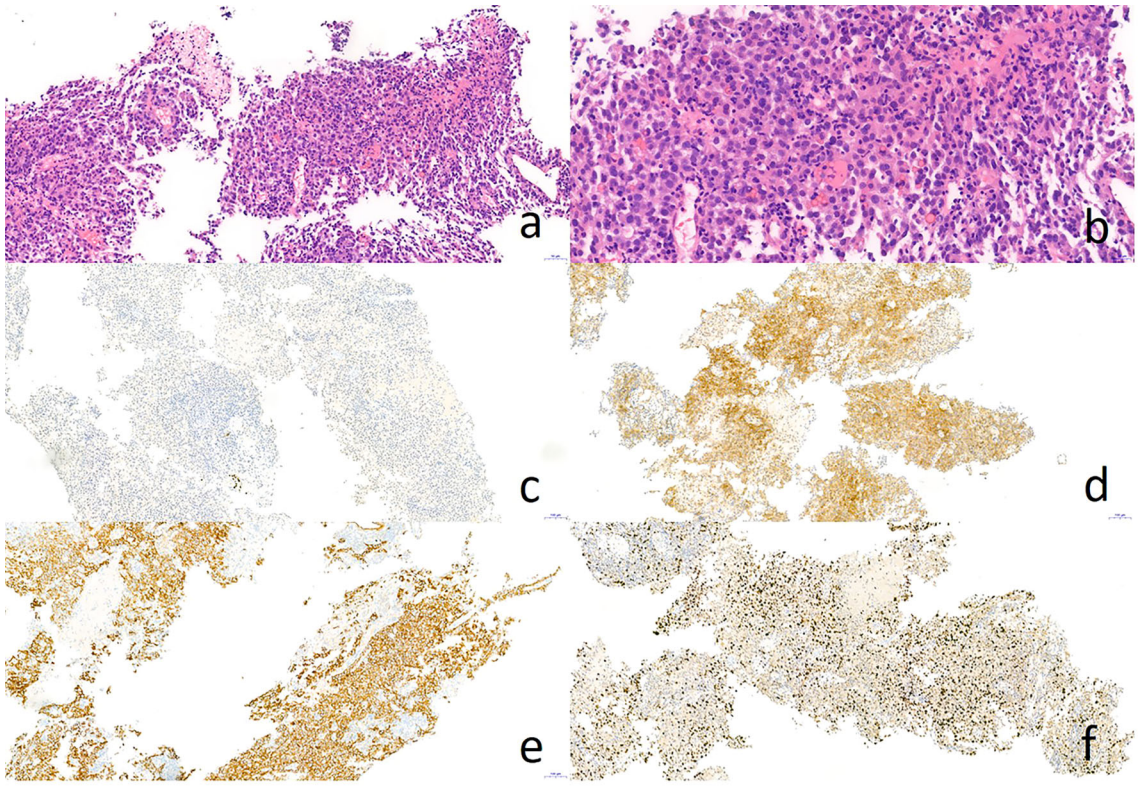

FIGURE 2
Pathology result of CT-guided percutaneous lung biopsy. Hematoxylin-eosin staining showed poorly differentiated adenocarcinoma like hepatocellular carcinoma **(A, B)**. Immunohistochemical staining showed negative for TTF-1 **(C)** and positive for Hepatocyte **(D)** and CK8/18 **(E)**, as well as Ki-67 40% **(F)**.

Nintedanib for both lung cancer and IPF. After five months, an increase in the AFP serum level and enlargement of lung nodule and lymph node were noted. Consequently, the patient continued to receive docetaxel as second-line therapy, resulting in partial regression of the pulmonary lesions. Upon subsequent progression, Anlotinib was administrated for 16 months. Since March 2021, the patient has been treated with pembrolizumab, leading to the partial shrinkage of the pulmonary lesion and lymph node. After 2 years of treatment with pembrolizumab, the primary lesion progressed again and pemetrexed plus anlotinib was given for 2 cycles. Due to side effects, chemotherapy was stopped and anlotinib was taken orally intermittently, and the efficacy was evaluated to be stable. The primary lesion developed again 6 months later, and tracheoscopic tissue biopsy was performed, and the pathological results indicated hepatoid adenocarcinoma. The treatment with sintilimab combined with anlotinib lasted for 2 cycles, and the progress of efficacy was evaluated, followed by bronchial artery embolization. The patient is currently being followed up. The patient survived for 75 months following the diagnosis of AFP-producing IPF-HAL.

No acute exacerbation of IPF or immune-related injuries associated with chemotherapy or immune checkpoint inhibitors occurred throughout the treatment process. Figure 3 illustrate the diagnostic and treatment timeline.

Discussion and conclusions

The incidence of lung cancer in patients with IPF increases with each year following an IPF diagnosis (4–6). Squamous cell carcinoma and adenocarcinoma are the most frequent types of lung cancer in IPF patients, with isolated cases of large cell carcinoma and small cell lung cancer also reported (4). However, to our knowledge, AFP-producing HAL has not been previously reported. Here, we report a case of this rarely type of lung cancer in an IPF patient to raise awareness for clinicians.

Hepatoid adenocarcinoma of the lung is a relatively rare primary malignant tumor of the lung, with an incidence of 0.014/100000 people (7). Clinically, patients with HAL typically presented with nonspecific symptoms. Grossman et al. found that 96% of the tumors occur in men with elevated serum AFP levels and a history of tobacco use. HAL usually presents as a bulky mass in an upper lobe with metastasis and follows an aggressive clinical course (8). HAL closely mimics hepatocellular carcinoma (HCC) and can be misdiagnosed by both pathologists and clinicians, especially when serum AFP level is elevated (9). PET-CT can be used to comprehensively examine patients, aiding in confirm the origin of tumor when the serum AFP levels are elevated (10). Although it is not necessary for the diagnosis of HAL according to recent criteria, serum AFP level is still an important predictive factor in this condition (8, 11).

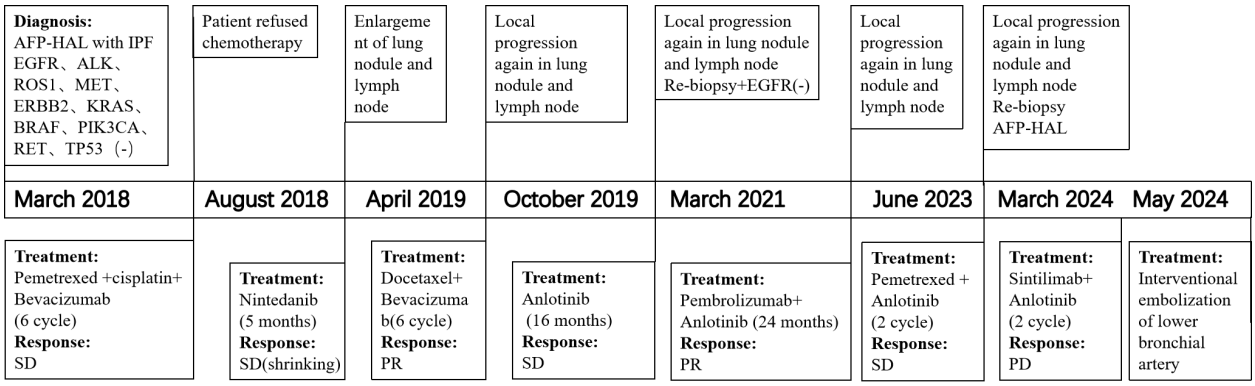

FIGURE 3
Flow chart of diagnosis and treatment process.

HAL is an extremely heterogeneous tumor type, and currently, no standard treatment is available. According to the guidelines for diagnosis and treatment of lung cancer, the common treatments for HAL patients include surgical resection, chemotherapy and radiotherapy. Recently, new treatments such as sorafenib, immunotherapy (Anti-PD-L1, Durvalumab), and radiofrequency ablation have been prescribed for HAL (12–16). However, when HAL is combined with IPF, many risk factors must be considered in treatment decisions. Lung status and postoperative complications should be fully evaluated before lung resection. The early and long-term outcomes of surgery in lung cancer patients with IPF are poor due to the high risk of acute exacerbation (AE) of IPF and lung cancer recurrence (17, 18). Radiation and chemotherapy are also known risk factors for AE-IPF (19, 20). With a deeper understanding of IPF and lung cancer, more treatment modalities are being explored (21–23). In our study, surgery and radiation were not performed; instead, long-term survival of 75 months was achieved through sequential chemotherapy (pemetrexed plus cisplatin, Docetaxel), anti-angiogenesis therapy (Bevacizumab, Anlotinib), antifibrotic therapy (Nintedanib), immunotherapy (Pembrolizumab, Sintilimab) and local treatment (Interventional embolization of lower bronchial artery).

In conclusion, this case report is the first to describe the occurrence of AFP-producing HAL in an IPF patient. The disease courses of both IPF and HAL are variable and somewhat unpredictable, potentially altered by the co-occurrence. Currently, there is no consensus on the treatment of patients with both diseases. The long-terms survival achieved in our case may provide prognostic value for this rare condition. Further understanding of the pathogenic overlap between lung cancer and IPF could guide the development of specific diagnostic modalities and targeted treatments for both conditions in the future.

Data availability statement

The original contributions presented in the study are included in the article/supplementary material, further inquiries can be directed to the corresponding author/s.

Ethics statement

The studies involving humans were approved by Ethics Committee of Henan Provincial People's Hospital. The studies were conducted in accordance with the local legislation and institutional requirements. The participants provided their written informed consent to participate in this study. Written informed consent was obtained from the individual(s) for the publication of any potentially identifiable images or data included in this article.

Author contributions

QQZ: Conceptualization, Formal analysis, Writing – review & editing. XLW: Conceptualization, Writing – original draft. NW: Conceptualization, Writing – review & editing. HZY: Conceptualization, Writing – original draft. XYW: Formal analysis, Writing – original draft. XJZ: Conceptualization, Formal analysis, Writing – review & editing.

Funding

The author(s) declare that no financial support was received for the research, authorship, and/or publication of this article.

Acknowledgments

We are very grateful to the staff of the Department of Pathology of Henan Provincial People's Hospital for their help and their efforts.

Conflict of interest

The authors declare that the research was conducted in the absence of any commercial or financial relationships that could be construed as a potential conflict of interest.

Publisher's note

All claims expressed in this article are solely those of the authors and do not necessarily represent those of their affiliated organizations, or those of the publisher, the editors and the reviewers. Any product that may be evaluated in this article, or claim that may be made by its manufacturer, is not guaranteed or endorsed by the publisher.

References

1. Yasunami R, Hashimoto Z, Ogura T, Hirao F, Yamamura Y. Primary lung cancer producing alpha-fetoprotein: a case report. *Cancer-am Cancer Soc*. (1981) 47:926–9. doi: 10.1002/1097-0142(19810301)47:5<926::AID-CNCR2820470518>3.0.CO;2-O

2. Ishikura H, Kanda M, Ito M, Nosaka K, Mizuno K. Hepatoid adenocarcinoma: a distinctive histological subtype of alpha-fetoprotein-producing lung carcinoma. *Virchows Arch A Pathol Anat Histopathol*. (1990) 417:73–80. doi: 10.1007/BF01600112

3. Haninger DM, Kloecker GH, Bousamra Ii M, Nowacki MR, Slone SP. Hepatoid adenocarcinoma of the lung: report of five cases and review of the literature. *Mod Pathol*. (2014) 27:535–42. doi: 10.1038/modpathol.2013.170

4. Ballester B, Milara J, Cortijo J. Idiopathic pulmonary fibrosis and lung cancer: mechanisms and molecular targets. *Int J Mol Sci*. (2019) 20(3):593. doi: 10.3390/ijms20030593

5. Xiaohong X, Liqiang W, Na L, Xinqing L, Yinyin Q, Ming L, et al. Management and prognosis of interstitial lung disease with lung cancer (ILD-LC): A real-world cohort from three medical centers in China. *Front Mol Biosci*. (2021) 8:660800. doi: 10.3389/fmolb.2021.660800

6. Strock SB, Alder JK, Kass DJ. From bad to worse: when lung cancer complicates idiopathic pulmonary fibrosis. *J Pathol*. (2018) 244:383–5. doi: 10.1002/path.2018.244.issue-4

7. Wang W, Li G. Incidence and prognostic factors of hepatoid adenocarcinoma: a population-based analysis. *Transl Cancer Res*. (2020) 9:5401–10. doi: 10.21037/tcr-20-1126

8. Grossman K, Beasley MB, Braman SS. Hepatoid adenocarcinoma of the lung: Review of a rare form of lung cancer. *Respir Med*. (2016) 119:175–9. doi: 10.1016/j.rmed.2016.09.003

9. Chen Z, Ding C, Zhang T, He Y, Jiang G. Primary hepatoid adenocarcinoma of the lung: A systematic literature review. *Onco Targets Ther*. (2022) 15:609–27. doi: 10.2147/OTT.S364465

10. Wang S, Li M, Chen H, Li J, Zeng Q. FDG PET/CT in hepatoid adenocarcinoma of the lung. *Clin Nucl Med*. (2016) 41:e340–341. doi: 10.1097/RLU.0000000000001231

11. Tonyali O, Gonullu O, Ozturk MA, Kosif A, Civi OG. Hepatoid adenocarcinoma of the lung and the review of the literature. *J Oncol Pharm Pract*. (2020) 26:1505–10. doi: 10.1177/1078155220903360

12. Gavrancic T, Park YH. A novel approach using sorafenib in alpha fetoprotein-producing hepatoid adenocarcinoma of the lung. *J Natl Compr Canc Netw*. (2015) 13:387–91. doi: 10.6004/jnccn.2015.0054

13. Wang C, Xu G, Wu G, Chen Z, Sun Z, Zheng P, et al. Hepatoid adenocarcinoma of the lung metastasizing to the gingiva. *Onco Targets Ther*. (2019) 12:8765–8. doi: 10.2147/OTT.S222974

14. Chen L, Han X, Gao Y, Zhao Q, Wang Y, Jiang Y, et al. Anti-PD-1 therapy achieved disease control after multiline chemotherapy in unresectable KRAS-positive hepatoid lung adenocarcinoma: A case report and literature review. *Onco Targets Ther*. (2020) 13:4359–64. doi: 10.2147/OTT.S248226

15. Basse V, Schick U, Guéguen P, Le Maréchal C, Quintin-Roué I, Descourt R, et al. A mismatch repair-deficient hepatoid adenocarcinoma of the lung responding to anti-PD-L1 durvalumab therapy despite no PD-L1 expression. *J Thorac Oncol*. (2018) 13:e120–2. doi: 10.1016/j.jtho.2018.03.004

16. Li J, Qi H, Xu B, Zhao J, Gao H, Ma X, et al. Genomic profiles of a patient of pulmonary hepatoid adenocarcinoma with high AFP level: A case report. *Front Oncol*. (2019) 9:1360. doi: 10.3389/fonc.2019.01360

17. Tane S, Ando Y, Matsumoto G, Ueda S, Uchino K. Basal segment deep wedge resection for lung cancer with pulmonary fibrosis. *Gen Thorac Cardiovasc Surg*. (2022) 70:413–5. doi: 10.1007/s11748-021-01764-5

18. Sato S, Shimizu Y, Goto T, Kitahara A, Koike T, Ishikawa H, et al. Survival after repeated surgery for lung cancer with idiopathic pulmonary fibrosis: a retrospective study. *BMC Pulm Med*. (2018) 18:134. doi: 10.1186/s12890-018-0703-8

19. Wang H, Yang R, Jin J, Wang Z, Li W. Impact of concomitant idiopathic pulmonary fibrosis on prognosis in lung cancer patients: A meta-analysis. *PLoS One*. (2021) 16:e0259784. doi: 10.1371/journal.pone.0259784

20. Saha A, Dickinson P, Shrimali RK, Salem A, Agarwal S. Is thoracic radiotherapy an absolute contraindication for treatment of lung cancer patients with interstitial lung disease? A systematic review. *Clin Oncol (R Coll Radiol)*. (2022) 34:e493–504. doi: 10.1016/j.clon.2022.01.043

21. Otsubo K, Kishimoto J, Ando M, Kenmotsu H, Minegishi Y, Horinouchi H, et al. Nintedanib plus chemotherapy for nonsmall cell lung cancer with idiopathic pulmonary fibrosis: a randomised phase 3 trial. *Eur Respir J*. (2022) 60(6):2200380. doi: 10.1183/13993003.00380-2022

22. Naoi H, Suzuki Y, Mori K, Aono Y, Kono M, Hasegawa H, et al. Impact of antifibrotic therapy on lung cancer development in idiopathic pulmonary fibrosis. *Thorax*. (2022) 77:727–30. doi: 10.1136/thoraxjnl-2021-218281

23. Tomassetti S, Gurioli C, Ryu JH, Decker PA, Ravaglia C, Tantalocco P, et al. The impact of lung cancer on survival of idiopathic pulmonary fibrosis. *Chest*. (2015) 147:157–64. doi: 10.1378/chest.14-0359

frontiers | Frontiers in Pharmacology

TYPE Original Research
PUBLISHED 21 February 2025
DOI 10.3389/fphar.2025.1448095

Check for updates

OPEN ACCESS

EDITED BY
Viviana di Giacomo,
University of Studies G. d'Annunzio Chieti and Pescara, Italy

REVIEWED BY
Daniele Mengato,
University Hospital of Padua, Italy
Leonardo Stella,
Agostino Gemelli University Polyclinic (IRCCS), Italy

*CORRESPONDENCE
Xingxi Pan,
lypanxx@scut.edu.cn

†These authors have contributed equally to this work

RECEIVED 12 June 2024
ACCEPTED 27 January 2025
PUBLISHED 21 February 2025

CITATION
He W, Tong L, Yuan Y, Yang X, Yang W and Pan X (2025) Adverse drug reactions to atezolizumab in combination with bevacizumab in hepatocellular carcinoma patients: an analysis of the food and drug administration adverse event reporting system database.
Front. Pharmacol. 16:1448095.
doi: 10.3389/fphar.2025.1448095

COPYRIGHT
© 2025 He, Tong, Yuan, Yang, Yang and Pan. This is an open-access article distributed under the terms of the Creative Commons Attribution License (CC BY). The use, distribution or reproduction in other forums is permitted, provided the original author(s) and the copyright owner(s) are credited and that the original publication in this journal is cited, in accordance with accepted academic practice. No use, distribution or reproduction is permitted which does not comply with these terms.

Adverse drug reactions to atezolizumab in combination with bevacizumab in hepatocellular carcinoma patients: an analysis of the food and drug administration adverse event reporting system database

Wanming He†, Lihua Tong†, Yanling Yuan, Xia Yang, Wen Yang and Xingxi Pan*

Department of Oncology, The Sixth Affiliated Hospital, School of Medicine, South China University of Technology, Foshan, China

Purpose: The objective of the study is to systematically identify and evaluate the adverse drug reactions (ADRs) associated with the combination therapy of systematically and bevacizumab in patients with unresectable hepatocellular carcinoma (HCC).

Patients and methods: Data were extracted from the Food and Drug Administration (FDA) Adverse Event Reporting System FDA Adverse Event Reporting System database. Disproportionality analysis was conducted using the reporting odds ratio (ROR), proportional reporting ratio (PRR) and Bayesian confidence propagation neural network (BCPNN) of information components (IC). Time-to-onset (TTO) profiles were analyzed using the Weibull shape parameter (WSP) test, while cumulative incidences were assessed using the Kaplan–Meier method. Valuable preferred term (PT) signals were identified for designated medical event (DME) screening, comparing these signals with system organ class (SOC) analysis.

Results: A total of 2,831 adverse events (AEs) reports were identified in the FAERS database, of which 124 positive AEs were detected across multiple SOCs. The median TTO of AEs was 43 days, with the highest proportion occurring within 0–30 days of TTO (n = 450, 41.17%). The WSP test indicated that patients with abnormal hepatic function and hepatic failure exhibited early failure-type profiles. Ten PT signals consistent with those on the DME list were identified, involving six SOCs.

Conclusion: Our study provides valuable pharmacological insights for early clinical intervention in managing ADRs and offers significant clinical benefits for HCC patients undergoing combination therapy with atezolizumab and bevacizumab.

KEYWORDS

anti-vascular endothelial growth factor, immune checkpoint inhibitor, programmed cell death protein 1, adverse events, hepatocellular carcinoma

Introduction

Hepatocellular carcinoma (HCC) is a prevalent malignancy and the third leading cause of cancer-related mortality worldwide (Balogh et al., 2016; Llovet et al., 2021; Sung et al., 2021). Although patients with early-stage disease can be effectively managed by surgical and locoregional treatments, approximately 70%–80% of patients are diagnosed at an advanced stage (Llovet et al., 2022), necessitating systemic therapies as the primary treatment modality.

Atezolizumab, an immune checkpoint inhibitor (ICI), targets programmed death 1 ligand 1 (PD-L1) to block its interaction with its receptors programmed cell death protein 1 (PD-1) and B7-1, which relieves the suppression of T cells and tumor immune escape (Herbst et al., 2014). Bevacizumab, a monoclonal antibody, inhibits angiogenesis and tumor growth by targeting anti-vascular endothelial growth factor (VEGF) (Boige et al., 2012; Ferrara et al., 2005; Finn et al., 2009; Siegel et al., 2008). The global, open-label, phase three IMbrave150 trial demonstrated that the combination of atezolizumab and bevacizumab significantly improved the median overall survival (OS) and progression-free survival (PFS) compared to sorafenib (Finn et al., 2020), a previously FDA-approved oral multikinase inhibitor for unresectable HCC (Lang, 2008; Llovet et al., 2008). Consequently, this combination therapy has been approved by the FDA over 70 countries as a first-line treatment for unresectable HCC in patients who have not received prior systemic therapy (Finn et al., 2020; Vogel et al., 2021; Yang et al., 2022).

With the increasing utilization of ICIs, immune-related adverse events (irAEs) have emerged as a significant challenge, limiting their clinical application and benefit. irAEs can affect multiple organ systems, including the skin, lungs, liver and endocrine tissues (Kennedy and Salama, 2020). Adverse drug reactions (ADRs) associated with bevacizumab include hypertension, asymptomatic proteinuria, bleeding, gastrointestinal perforation and thromboembolic events (Kazazi-Hyseni et al., 2010; Wichelmann et al., 2021; Ventura et al., 2023; Fukushima et al., 2023). However, the ADR profile of atezolizumab in combination with bevacizumab remains incompletely characterized. Given the complex biological interactions of this combined regimen, the potential for increased toxicity in HCC patients requires further investigation. Additionally, large-scale cohort studies evaluating this combination therapy are limited, which may not fully reflect real-world clinical outcomes.

Therefore, to investigate the ADRs of atezolizumab plus bevacizumab in HCC patients in depth, we conducted an analysis using the United States FDA Adverse Event Reporting System (FAERS) database (Rodriguez et al., 2001; van Puijenbroek et al., 2002), a large real-world database reporting hazardous drug events. Our aim is to guide early clinical intervention for managing ADRs and to provide clinical benefits for HCC patients undergoing this combination therapy.

Materials and methods

Data sources and procedures

The data for this study were obtained from the FAERS database, a spontaneous reporting system that collects information about adverse events (AEs) and medication errors reported to the FDA. It is free and publicly available online at https://open.fda.gov/data/faers/. No institutional ethics approval was required because this study utilized anonymized data from an open-access database.

Data extraction

To extract AE reports, we collected data from the FAERS database covering the period from the second quarter of 2016 to the second quarter of 2023 using the online tool OpenVigil 2.1 (http://openvigil.sourceforge.net/). Only drugs listed as "primary suspects" were included in the analysis because they were most likely related to AEs. AEs were defined as adverse reactions in patients treated with atezolizumab combined with bevacizumab. AE reports are standardized using preferred terms (PTs) from the Standardized MedDRA Queries (SMQ) of the Medical Dictionary for Regulatory Activities (MedDRA Version 26.1), grouped by system organ class (SOC). Designated medical events (DMEs) were selected according to the lists developed by the European Medicines Agency (EMA) (Liu et al., 2023). The multistep process of data extraction and analysis is shown in Figure 1.

Statistical analysis

Three algorithms, reporting odds ratio (ROR), proportional reporting ratio (PRR) and Bayesian confidence propagation neural network (BCPNN) of information components (IC), were used based on disproportionality analysis and Bayesian analysis. The equations and criteria for the three algorithms are described in Supplementary Table S1.

The time-to-onset (TTO) analysis was conducted using the Weibull shape parameter (WSP) test (Abe et al., 2016; Tisdale et al., 1995). The shape of the Weibull distribution was described by two parameters: scale (α) and shape (β). For our study, only the parameter β was used. The shape parameter β of the Weibull distribution indicated that the hazard without a reference population. When parameter β was <1 and its 95% CI was <1, the hazard of ADR occurrence was deemed to have decreased over time (early failure-type profile); when parameter β was equal to or nearly 1 and its 95% CI included value 1, the hazard was regarded as constant occurrence over time (random failure-type profile); and when parameter β was >1 and its 95% CI excluded value 1, the hazard was estimated to increase over time (wear-out failure-type profile) (Kinoshita et al., 2020; Nakamura et al., 2015; Sauzet et al., 2013). Additionally, to further determine whether age and sex had effects on TTO, cumulative incidences were assessed using the Kaplan–Meier method, with differences determined using the log-rank test. A statistically significant threshold was set at a p value of <0.05 for all analyses. All the analyses were performed in R (version 4.2.3; R Foundation, Vienna, Austria).

Results

Baseline characteristics of patients

A total of 12,016,786 AEs were recorded in the FAERS database from the second quarter of 2016 to the second quarter of 2023. After

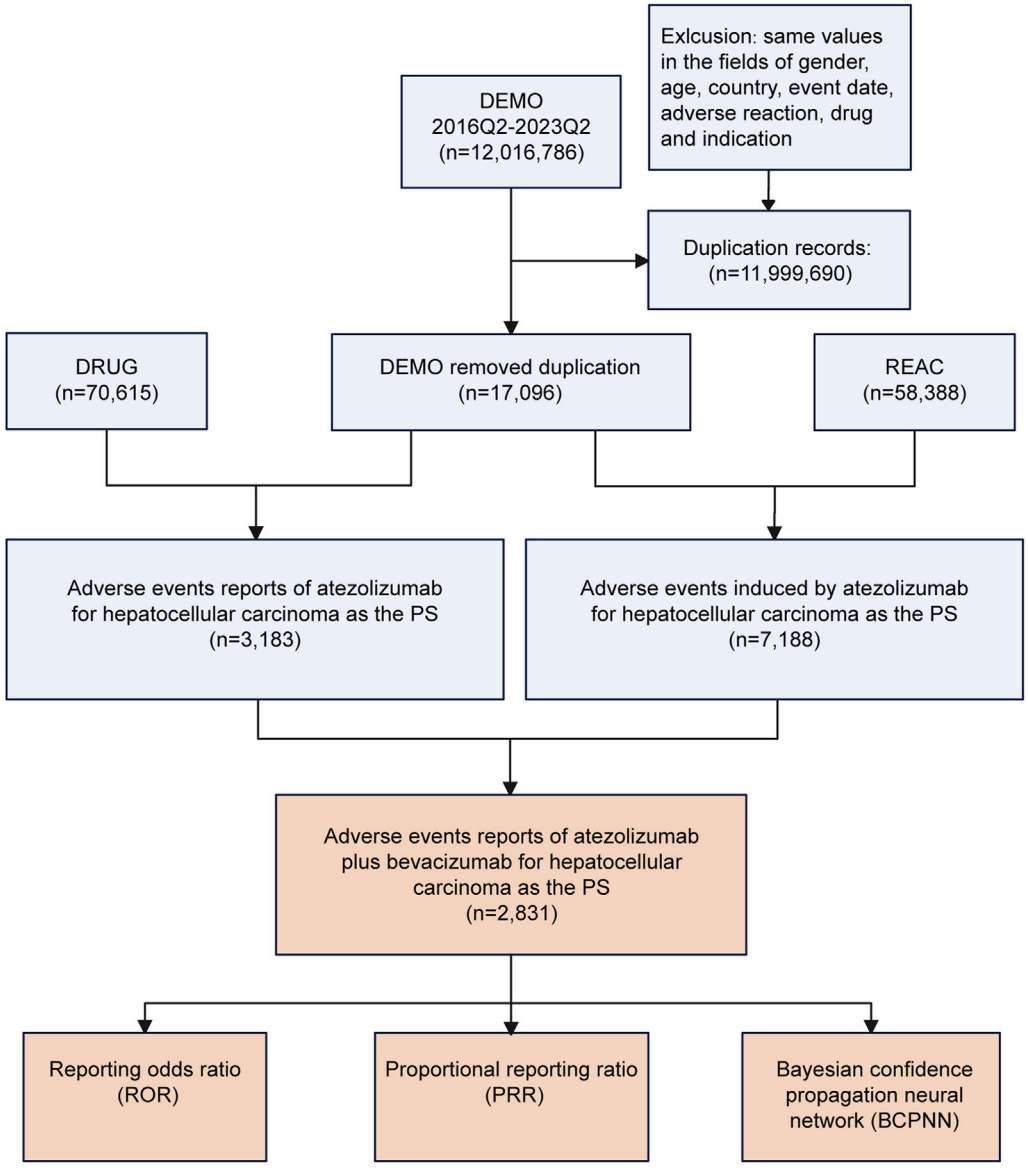

FIGURE 1
Flowchart for screening and data analysis of reports in the FAERS database. DEMO, demographic and administrative information; DRUG, drug information; REAC, preferred terminology for adverse events; PS, primary suspected drug.

removing duplicates, a total of 17096 case reports of the primary suspected (PS) drug were included. Overall, 2,831 reports of atezolizumab and bevacizumab were included in the analysis. The process flowchart is shown in Figure 1.

The baseline characteristics of patients are summarized in Table 1. There was a greater proportion of male patients (72.6%) than female patients (13.8%), and sex information was missing for 13.6% of the patients. The largest proportion of patients were aged 65–85 years. These reports were collected mainly from Japan (63.9%), followed by the United States (3.6%) and China (3.2%). The majority of cases were reported by physicians (83.1%). The number of reports increased annually during the 2021–2023 period (31.5%, 38.9%, and 23.2%, respectively), indicating that combination therapy with atezolizumab and bevacizumab is widely used in the clinic. Hospitalization occurred in 31.4% of all patients, and death occurred in 17.5%.

Disproportionality analysis

A total of 124 positive PTs was identified by three algorithms for disproportionality analysis and Bayesian analysis, namely, PRR, ROR and BCPNN of ICs (Figure 2A). A total of 54 PTs were identified as being related to atezolizumab, while three PTs were related to bevacizumab. Additionally, 27 PTs were found to be related to both drugs (Supplementary Table S2). The signal strength of all reported AEs was shown in Figure 2B.

10.3389/fphar.2025.1448095

TABLE 1 Clinical characteristics of HCC patients treated with atezolizumab in combination with bevacizumab.

Clinical characteristics	N	%
Total	2,831	
Sex		
Male	2054	72.6%
Female	391	13.8%
Missing	386	13.6%
Age		
18–64	466	16.5%
65–85	1042	36.8%
≥86	53	1.9%
Missing	1270	44.9%
Reporting country		
Japan	1809	63.9%
United States	101	3.6%
China	90	3.2%
India	83	2.9%
France	81	2.9%
Other countries	663	23.4%
Unknow	4	0.1%
Reporter type		
Physician	2,353	83.1%
Pharmacist	169	6.0%
Consumer	166	5.9%
Health-professional	143	5.1%
Reporting year		
2018	4	0.1%
2019	49	1.7%
2020	130	4.6%
2021	891	31.5%
2022	1101	38.9%
2023	656	23.2%
Outcome[a]		
Other serious	1569	46.1
Hospitalization	1070	31.4%
Death	595	17.5%
Life-Threatening	96	2.8%
Disability	27	0.8%
Missing	50	1.5%

[a]Multiple responses were possible in each report.

Hypopituitarism, secondary adrenocortical insufficiency, urinary occult blood, haemolytic anaemia and meningitis were the strongest five risk reports. The AEs were grouped according to SOC, and 22 organ systems were involved in atezolizumab- and bevacizumab-induced AEs (Figure 2C), of which ten significant SOCs were identified, including endocrine disorders, immune system disorders, hepatobiliary disorders, cardiac disorders, renal and urinary disorders, infections and infestations, blood and lymphatic system disorders, respiratory, thoracic and mediastinal disorders, vascular disorders and eye disorders. The most common SOC was hepatobiliary disorders (n = 591, 9.10%).

TTO analysis

After excluding patients with missing data, a total of 1093 patients were included, and the median TTO of AEs was 43 days (Table 2). To investigate the factors related to TTO, patients were stratified by age and sex. The median TTO in the 18–64, 65–85 and >85 years age groups were 43.5, 45 and 63, respectively (log-rank test, P = 0.4). Males had a median TTO of 45 days compared to 42 days for females (log-rank test, P = 0.4) (Table 2). However, there was no statistically significant difference in TTO among patients of different ages or sexes, indicating that age and sex are not factors influencing TTO due to AEs (Figure 3A). The number and proportion of patients stratified by TTO are shown in Figure 3B. The results indicated that the largest proportion (41.17%, n = 450) occurred in the 0–30 days TTO group.

WSP analysis

The WSP test is used for statistical analysis of time-to-onset data and can describe the non-constant rate of incidence of ADRs. Time-to-onset analysis with WSP has been used to evaluate hazard functions for detecting adverse events (Abe et al., 2016; Sauzet et al., 2013; Cornelius et al., 2012). To further assess severe AEs, WSP analysis of the top five PTs in terms of death outcomes is summarized in Table 3. The medians and quartile ranges (IQRs) for the onset day of disease progression, abnormal hepatic function, hepatic failure, interstitial lung disease and ascites were 42 (IQR: 20.5–92), 21 (7–66.25), 23 (10–70.5), 64.50 (26–117.25) and 50.50 (21–109) days, respectively. According to the WSP test for abnormal hepatic function and hepatic failure, the shape parameter β and the upper limit of the 95% CI were <1, suggesting an early failure-type profile, which indicated that the incidence of abnormal hepatic function and hepatic failure decreased over time. In the WSP test for disease progression, disease progression interstitial lung disease and ascites, the shape parameter β was nearly 1, and the 95% CI included the value 1, suggesting a random failure-type profile. This suggests the risks of disease progression, interstitial lung disease and ascites are almost constant.

DME list screening

The DME is a list published by the EMA to identify suspected ADRs that deserve special attention (Liu et al., 2023). The valuable positive signals extracted for DME screening and the SOCs corresponding to PT signals consistent with those on the DME list are shown in Figure 4. There are ten signals consistent with the PT signals on the DME list involved in six SOCs. The two most common DMEs were pancreatitis (n = 19, ROR: 18.22) and erythema multiforme (n = 19, ROR: 3.09), which are gastrointestinal disorders and skin and subcutaneous tissue disorders, respectively. The strongest PT signal was hemolytic anemia (ROR: 47.76). The most frequent corresponding SOCs were blood and lymphatic system disorders, including febrile neutropenia (n = 16), immune thrombocytopenia (n = 8) and hemolytic anemia (n = 6).

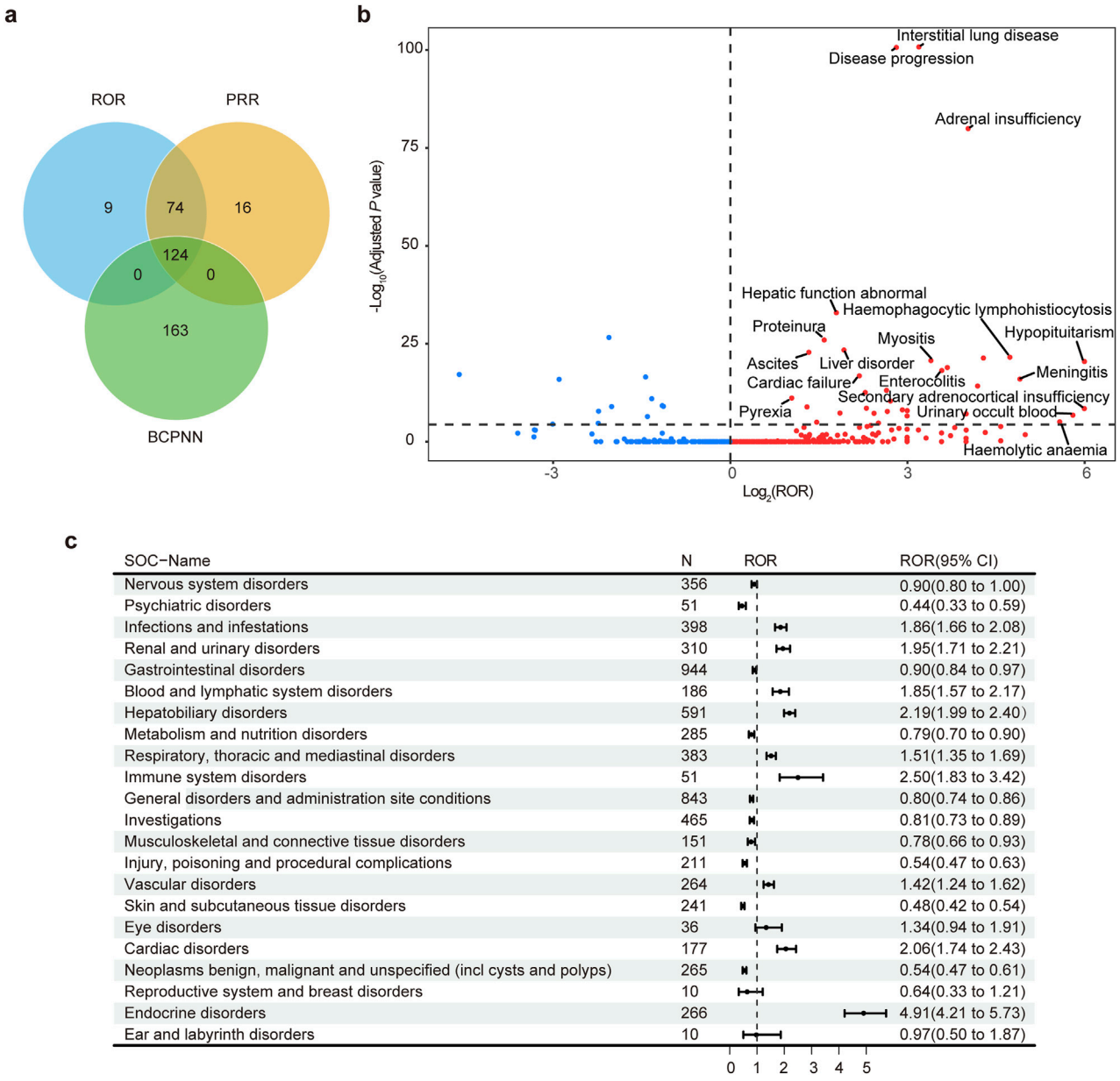

FIGURE 2
Adverse events (AEs) and system organ classes (SOCs) of atezolizumab in combination with bevacizumab. **(A)** Venn diagram showing the three algorithms used for disproportionality analysis. **(B)** The volcano plot shows the 1114 AEs. *P* values were adjusted with Bonferroni test. Adjusted *P* value = 4.89×10^{-5}. **(C)** The forest plot shows the SOCs of AEs. ROR, reporting odds ratio; PRR, proportional reporting ratio; BCPNN, Bayesian confidence propagation neural network.

TABLE 2 Time-to-onset analysis of patients stratified by age and sex.

		Age			Sex	
		18–64	65–85	>85	Male	Female
N	1093	274	570	27	879	156
Min TTO	1	1	1	1	1	1
Max TTO	1521	1307	1521	398	1521	1284
Median TTO	43	43.5	45	63	45	42
Logrank_test	-	$P = 0.4$			$P = 0.4$	

TTO, time to onset; N, number of patients with available TTO.

Discussion

To the best of our knowledge, this study represents the first analysis of ADRs associated with the combination of atezolizumab and bevacizumab in HCC patients from the FAERS database. Our findings indicate that the predominant AEs identified in the FAERS database include ascites, pyrexia, interstitial lung disease, abnormal hepatic function, adrenal insufficiency, and others, categorized under various SOCs. Patients with abnormal hepatic function and hepatic failure exhibited early failure-type profiles, which indicated that their incidence decreased over time. Ten PT signals were identified across six SOCs on the DME list.

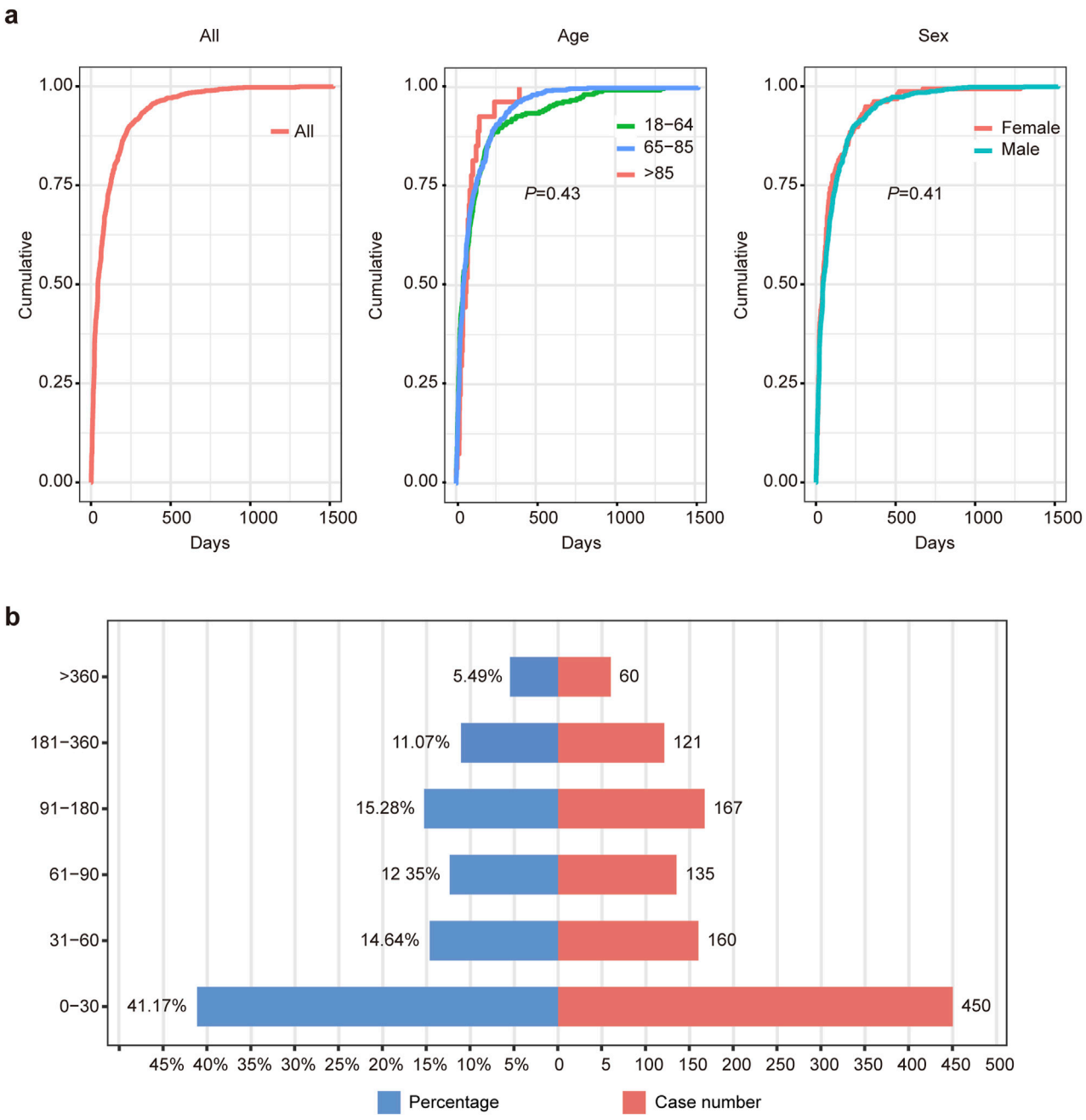

FIGURE 3
Time-to-onset (TTO) analysis of patients treated with atezolizumab plus bevacizumab. **(A)** Cumulative incidence of patients stratified by age and sex. **(B)** Number and proportion of patients stratified by time to onset.

This research help to enhance the early detection and prevention of ADRs related to atezolizumab-bevacizumab combination therapy, thereby contributing to patient safety.

Most of the PTs identified in our study align with findings from previous studies and drug labels for atezolizumab and bevacizumab (Finn et al., 2020; Fukushima et al., 2023), such as interstitial lung disease, liver disorder, abnormal hepatic function, proteinuria, ascites, and hepatic failure. In the IMbrave150 trial, 22 adverse events occurred with an incidence of more than 10% among patients receiving atezolizumab and bevacizumab (Finn et al., 2020). In contrast, no PTs with an incidence exceeding 10% were identified in our study. This discrepancy is likely due to the nature of FAERS as a spontaneous reporting database, which may introduce quantitative biases stemming from diverse reporting practices. Notably, it is challenging to definitively classify disease progression as an ADR. This phenomenon may partly be attributed to hyperprogression (HP) or hyperprogressive disease (HPD). A subset of cancer patients treated with ICIs appears to experience more aggressive tumor progression, characterized by accelerated tumor proliferation and growth, leading to a shorter OS, which is regarded as HPD (Leake, 2023; Chan, 2021; Wong et al., 2019; Díaz López et al., 2024). The incidence of HPD in HCC

10.3389/fphar.2025.1448095

TABLE 3 WSP analysis of the five PTs with the most deaths.

PT	Case (n)	TTO (days)		Weibull distribution				Failure type
				Shape parameter		Scale parameter		
		Median (IQR)	Min–max	α	95% CI	β	95% CI	
Disease progression	175	42 (20.50–92.00)	1–420	70.06	45.48–94.64	0.83	0.65–1.00	Random Failure
Hepatic function abnormal	57	21 (7.00–66.25)	1–370	46.14	31.55–60.73	0.80	0.65–0.94	Early failure
Hepatic failure	29	23 (10.00–70.5)	2–410	61.82	23.03–100.62	0.69	0.48–0.90	Early failure
Interstitial lung disease	25	64.50 (26.00–117.25)	1–607	94.34	67.81–120.87	0.95	0.77–1.13	Random Failure
Ascites	24	50.50 (21.00–109.00)	1–718	86.94	64.41–109.47	0.87	0.73–1.01	Random Failure

PT, preferred term; TTO, time to onset; n, number of patients with available TTO; IQR, interquartile range; CI: confidence interval.

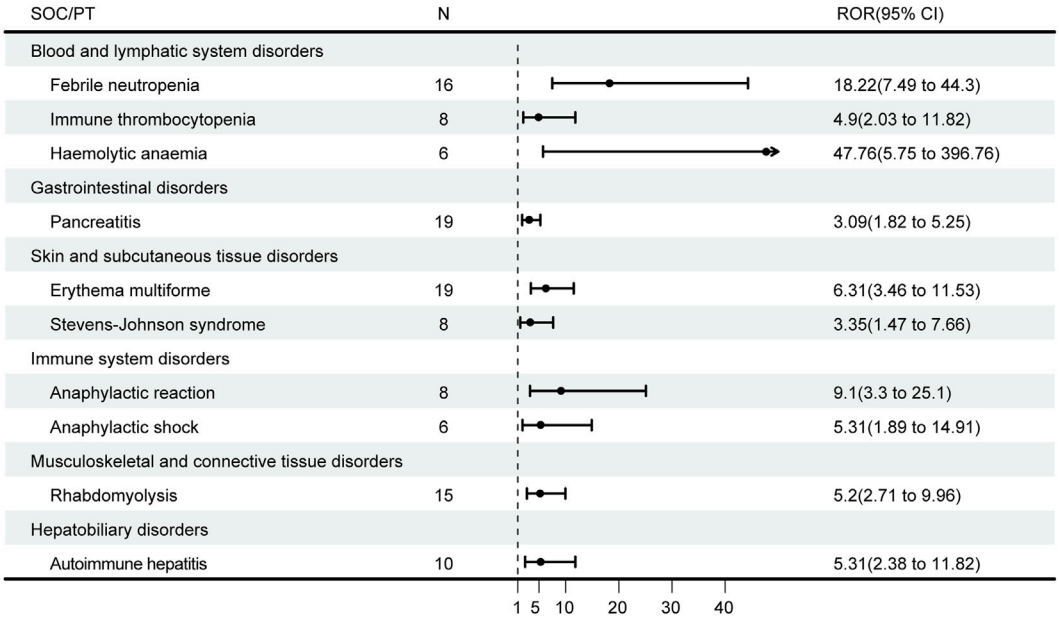

FIGURE 4
Detection of atezolizumab in combination with bevacizumab designated medical event (DME) signals. The forest plot showed that the DME signals and the SOCs corresponding to PT signals were consistent with those on the DME list. SOC, system organ class; PT, preferred term; ROR, reporting odds ratio; CI: confidence interval.

patients is approximately 14% (Kim et al., 2021). To differentiate HPD from natural disease progression, key predictors of HPD have been identified, including higher tumor burden, elevated lactate dehydrogenase (LDH), increased neutrophil-to-lymphocyte ratio (NLR) and lower albumin levels in blood (Chan, 2021). However, predictive factors for HPD in HCC remain poorly defined, and early detection of HPD remains challenging until radiological progression or clinical deterioration occurs.

The median TTO of AEs was 43 days, with 41.17% of patients experiencing related AEs within 30 days. These findings showed that nearly half of the AEs occurred early in the treatment course, particularly those involving abnormal hepatic function and hepatic failure. Moreover, the WSP test showed that abnormal hepatic function and hepatic failure had early failure-type profiles, which suggested that the incidence of AEs decreased over time Therefore, it is imperative for healthcare providers to conduct a thorough pre-treatment evaluation of liver function in patients diagnosed with HCC. Such an assessment facilitates the identification of patients at higher risk for hepatic complications, thereby enabling the development of more personalized and cautious treatment strategies. Additionally, close monitoring of patients during early combination therapy is essential. This approach allows healthcare professionals to promptly detect and manage any emerging hepatic-related AEs, thereby mitigating the overall risk and potential severity of such events.

There are some limitations to be considered. First, because the FAERS is a spontaneous reporting system, some quantitative bias may exist due to incomplete reports or underreported cases. For example, more severe ADRs, such as life-threatening conditions or those requiring hospitalization, are generally reported more frequently than mild or moderate ones. Consequently, the FAERS database may disproportionately represent severe ADRs, while

underreporting milder reactions, potentially leading to a skewed perception of the overall safety profile of a drug. Second, detailed clinical information such as OS and PFS data, therapy time and dose adjustments are missing. Third, the majority of reports originate from Asian populations, with 63.9% specifically from Japan, while there is limited data from European and African populations. Finally, the ROR merely indicates the correlation intensity of the risk of reported AEs without establishing a causal relationship between drugs and AEs. However, additional cohort studies and long-term data are essential to verify these findings. Despite the aforementioned intrinsic limitations, our study provides valuable insights into the safety profile of the combination of atezolizumab and bevacizumab, serving as a reference for future research.

Conclusion

Overall, our study is the first to analyze the AEs associated with the combination of atezolizumab and bevacizumab in HCC patients from the FAERS database. We observed that these AEs affected multiple organ systems. Notably, patients with abnormal hepatic function and hepatic failure exhibited early failure-type profiles. Additionally, nearly half of the AEs occurred within 1 month. Our findings provide valuable pharmacological insights for clinical practice and have significant implications for early clinical intervention in managing AEs related to atezolizumab and bevacizumab combination therapy.

Data availability statement

The original contributions presented in the study are included in the article/Supplementary Material, further inquiries can be directed to the corresponding author.

Author contributions

WH: Methodology, Project administration, Validation, Visualization, Writing–original draft. LT: Methodology, Project administration, Validation, Writing–original draft. YY: Methodology, Project administration, Writing–review and editing. XY: Formal Analysis, Methodology, Writing–review and editing. WY: Data curation, Supervision, Validation, Writing–review and editing. XP: Conceptualization, Funding acquisition, Project administration, Resources, Software, Supervision, Writing–review and editing.

Funding

The author(s) declare that financial support was received for the research, authorship, and/or publication of this article. This work was funded by Beijing Xisike Clinical Oncology Research Foundation (Y-2019AZQN-0401) and Foshan Fourteen Five Key Specialty Construction Project (2022).

Conflict of interest

The authors declare that the research was conducted in the absence of any commercial or financial relationships that could be construed as a potential conflict of interest.

Publisher's note

All claims expressed in this article are solely those of the authors and do not necessarily represent those of their affiliated organizations, or those of the publisher, the editors and the reviewers. Any product that may be evaluated in this article, or claim that may be made by its manufacturer, is not guaranteed or endorsed by the publisher.

Supplementary material

The Supplementary Material for this article can be found online at: https://www.frontiersin.org/articles/10.3389/fphar.2025.1448095/full#supplementary-material

References

Abe, J., Umetsu, R., Mataki, K., Kato, Y., Ueda, N., Nakayama, Y., et al. (2016). Analysis of Stevens-Johnson syndrome and toxic epidermal necrolysis using the Japanese Adverse Drug Event Report database. *J. Pharm. health care Sci.* 2, 14. doi:10.1186/s40780-016-0048-5

Balogh, J., Victor, D., 3rd, Asham, E. H., Burroughs, S. G., Boktour, M., Saharia, A., et al. (2016). Hepatocellular carcinoma: a review. *J. Hepatocell. carcinoma* 3, 41–53. doi:10.2147/JHC.S61146

Boige, V., Malka, D., Bourredjem, A., Dromain, C., Baey, C., Jacques, N., et al. (2012). Efficacy, safety, and biomarkers of single-agent bevacizumab therapy in patients with advanced hepatocellular carcinoma. *Oncol.* 17 (8), 1063–1072. doi:10.1634/theoncologist.2011-0465

Chan, S. L. (2021). Hyperprogression in hepatocellular carcinoma: illusion or reality? *J. hepatology* 74 (2), 269–271. doi:10.1016/j.jhep.2020.09.025

Cornelius, V. R., Sauzet, O., and Evans, S. J. (2012). A signal detection method to detect adverse drug reactions using a parametric time-to-event model in simulated cohort data. *Drug Saf.* 35 (7), 599–610. doi:10.2165/11599740-000000000-00000

Díaz López, S., Jimeno Maté, C., Fernández Parra, E. M., and Sánchez Vegas, A. (2024). Pseudoprogression in a patient with hepatocellular carcinoma treated with immunotherapy plus bevacizumab. *Rev. espanola enfermedades Dig.* doi:10.17235/reed.2024.10942/2024

Ferrara, N., Hillan, K. J., and Novotny, W. (2005). Bevacizumab (Avastin), a humanized anti-VEGF monoclonal antibody for cancer therapy. *Biochem. biophysical Res. Commun.* 333 (2), 328–335. doi:10.1016/j.bbrc.2005.05.132

Finn, R. S., Bentley, G., Britten, C. D., Amado, R., and Busuttil, R. W. (2009). Targeting vascular endothelial growth factor with the monoclonal antibody bevacizumab inhibits human hepatocellular carcinoma cells growing in an orthotopic mouse model. *Liver Int. official J. Int. Assoc. Study Liver* 29 (2), 284–290. doi:10.1111/j.1478-3231.2008.01762.x

Finn, R. S., Qin, S., Ikeda, M., Galle, P. R., Ducreux, M., Kim, T. Y., et al. (2020). Atezolizumab plus bevacizumab in unresectable hepatocellular carcinoma. *N. Engl. J. Med.* 382 (20), 1894–1905. doi:10.1056/NEJMoa1915745

Fukushima, T., Morimoto, M., Kobayashi, S., Ueno, M., Uojima, H., Hidaka, H., et al. (2023). Association between immune-related adverse events and survival in patients with hepatocellular carcinoma treated with atezolizumab plus bevacizumab. *Oncol.* 28 (7), e526–e533. doi:10.1093/oncolo/oyad090

Herbst, R. S., Soria, J. C., Kowanetz, M., Fine, G. D., Hamid, O., Gordon, M. S., et al. (2014). Predictive correlates of response to the anti-PD-L1 antibody MPDL3280A in cancer patients. *Nature* 515 (7528), 563–567. doi:10.1038/nature14011

Kazazi-Hyseni, F., Beijnen, J. H., and Schellens, J. H. (2010). Bevacizumab. *Oncol.* 15 (8), 819–825. doi:10.1634/theoncologist.2009-0317

Kennedy, L. B., and Salama, A. K. S. (2020). A review of cancer immunotherapy toxicity. *CA a cancer J. Clin.* 70 (2), 86–104. doi:10.3322/caac.21596

Kim, C. G., Kim, C., Yoon, S. E., Kim, K. H., Choi, S. J., Kang, B., et al. (2021). Hyperprogressive disease during PD-1 blockade in patients with advanced hepatocellular carcinoma. *J. hepatology* 74 (2), 350–359. doi:10.1016/j.jhep.2020.08.010

Kinoshita, S., Hosomi, K., Yokoyama, S., and Takada, M. (2020). Time-to-onset analysis of amiodarone-associated thyroid dysfunction. *J. Clin. Pharm. Ther.* 45 (1), 65–71. doi:10.1111/jcpt.13024

Lang, L. (2008). FDA approves sorafenib for patients with inoperable liver cancer. *Gastroenterology* 134 (2), 379. doi:10.1053/j.gastro.2007.12.037

Leake, I. (2023). Hyperprogression during immunotherapy. *Nat. cancer* 4 (12), 1640. doi:10.1038/s43018-023-00666-0

Liu, P., He, M., Xu, X., He, Y., Yao, W., and Liu, B. (2023). Real-world safety of Lacosamide: a pharmacovigilance study based on spontaneous reports in the FDA adverse event reporting system. *Seizure* 110, 203–211. doi:10.1016/j.seizure.2023.07.003

Llovet, J. M., Castet, F., Heikenwalder, M., Maini, M. K., Mazzaferro, V., Pinato, D. J., et al. (2022). Immunotherapies for hepatocellular carcinoma. *Nat. Rev. Clin. Oncol.* 19 (3), 151–172. doi:10.1038/s41571-021-00573-2

Llovet, J. M., Kelley, R. K., Villanueva, A., Singal, A. G., Pikarsky, E., Roayaie, S., et al. (2021). Hepatocellular carcinoma. *Nat. Rev. Dis. Prim.* 7 (1), 6. doi:10.1038/s41572-020-00240-3

Llovet, J. M., Ricci, S., Mazzaferro, V., Hilgard, P., Gane, E., Blanc, J. F., et al. (2008). Sorafenib in advanced hepatocellular carcinoma. *N. Engl. J. Med.* 359 (4), 378–390. doi:10.1056/NEJMoa0708857

Nakamura, M., Umetsu, R., Abe, J., Matsui, T., Ueda, N., Kato, Y., et al. (2015). Analysis of the time-to-onset of osteonecrosis of jaw with bisphosphonate treatment using the data from a spontaneous reporting system of adverse drug events. *J. Pharm. health care Sci.* 1, 34. doi:10.1186/s40780-015-0035-2

Rodriguez, E. M., Staffa, J. A., and Graham, D. J. (2001). The role of databases in drug postmarketing surveillance. *Pharmacoepidemiol. drug Saf.* 10 (5), 407–410. doi:10.1002/pds.615

Sauzet, O., Carvajal, A., Escudero, A., Molokhia, M., and Cornelius, V. R. (2013). Illustration of the weibull shape parameter signal detection tool using electronic healthcare record data. *Drug Saf.* 36 (10), 995–1006. doi:10.1007/s40264-013-0061-7

Siegel, A. B., Cohen, E. I., Ocean, A., Lehrer, D., Goldenberg, A., Knox, J. J., et al. (2008). Phase II trial evaluating the clinical and biologic effects of bevacizumab in unresectable hepatocellular carcinoma. *J. Clin. Oncol. official J. Am. Soc. Clin. Oncol.* 26 (18), 2992–2998. doi:10.1200/JCO.2007.15.9947

Sung, H., Ferlay, J., Siegel, R. L., Laversanne, M., Soerjomataram, I., Jemal, A., et al. (2021). Global cancer statistics 2020: GLOBOCAN estimates of incidence and mortality worldwide for 36 cancers in 185 countries. *CA a cancer J. Clin.* 71 (3), 209–249. doi:10.3322/caac.21660

Tisdale, J. E., Follin, S. L., Ordelova, A., and Webb, C. R. (1995). Risk factors for the development of specific noncardiovascular adverse effects associated with amiodarone. *J. Clin. Pharmacol.* 35 (4), 351–356. doi:10.1002/j.1552-4604.1995.tb04072.x

van Puijenbroek, E. P., Bate, A., Leufkens, H. G., Lindquist, M., Orre, R., and Egberts, A. C. (2002). A comparison of measures of disproportionality for signal detection in spontaneous reporting systems for adverse drug reactions. *Pharmacoepidemiol. drug Saf.* 11 (1), 3–10. doi:10.1002/pds.668

Ventura, I., Sanchiz, L., Legidos-García, M. E., Murillo-Llorente, M. T., and Pérez-Bermejo, M. (2023). Atezolizumab and bevacizumab combination therapy in the treatment of advanced hepatocellular cancer. *Cancers* 16 (1), 197. doi:10.3390/cancers16010197

Vogel, A., Martinelli, E., and ESMO Guidelines Committee. Electronic address: clinicalguidelines@esmo.org, and ESMO Guidelines Committee (2021). Updated treatment recommendations for hepatocellular carcinoma (HCC) from the ESMO Clinical Practice Guidelines. *Ann. Oncol. official J. Eur. Soc. Med. Oncol.* 32 (6), 801–805. doi:10.1016/j.annonc.2021.02.014

Wichelmann, T. A., Abdulmujeeb, S., and Ehrenpreis, E. D. (2021). Bevacizumab and gastrointestinal perforations: a review from the FDA adverse event reporting system (FAERS) database. *Alimentary Pharmacol. and Ther.* 54 (10), 1290–1297. doi:10.1111/apt.16601

Wong, D. J., Lee, J., Choo, S. P., Thng, C. H., and Hennedige, T. (2019). Hyperprogressive disease in hepatocellular carcinoma with immune checkpoint inhibitor use: a case series. *Immunotherapy* 11 (3), 167–175. doi:10.2217/imt-2018-0126

Yang, Y., Sun, J., Wu, M., Lau, W. Y., Zheng, S., Wang, X. H., et al. (2022). Chinese expert consensus on immunotherapy for hepatocellular carcinoma (2021 edition). *Liver cancer* 11 (6), 511–526. doi:10.1159/000526038

frontiers | Frontiers in Pharmacology

TYPE Original Research
PUBLISHED 27 February 2025
DOI 10.3389/fphar.2025.1510319

Check for updates

OPEN ACCESS

EDITED BY
Viviana di Giacomo,
University of Studies G. d'Annunzio Chieti and Pescara, Italy

REVIEWED BY
Sirajudheen Anwar,
University of Hail, Saudi Arabia
Yuwei Wang,
Shaanxi University of Chinese Medicine, China

*CORRESPONDENCE
Xiaotian Yang,
15695110492@163.com
Yanming Zhang,
zhangyanming2005@126.com

†These authors have contributed equally to this work

RECEIVED 12 October 2024
ACCEPTED 03 February 2025
PUBLISHED 27 February 2025

CITATION
Hong Y, Wang Y, Hao Z, Zhang X, Si Y, Lin G, Zhang S, Niu M-M, Yang X and Zhang Y (2025) Discovery of highly potent and novel LSD1 inhibitors for the treatment of acute myeloid leukemia: structure-based virtual screening, molecular dynamics simulation, and biological evaluation.
Front. Pharmacol. 16:1510319.
doi: 10.3389/fphar.2025.1510319

COPYRIGHT
© 2025 Hong, Wang, Hao, Zhang, Si, Lin, Zhang, Niu, Yang and Zhang. This is an open-access article distributed under the terms of the Creative Commons Attribution License (CC BY). The use, distribution or reproduction in other forums is permitted, provided the original author(s) and the copyright owner(s) are credited and that the original publication in this journal is cited, in accordance with accepted academic practice. No use, distribution or reproduction is permitted which does not comply with these terms.

Discovery of highly potent and novel LSD1 inhibitors for the treatment of acute myeloid leukemia: structure-based virtual screening, molecular dynamics simulation, and biological evaluation

Ye Hong[1,2†], Yuting Wang[3†], Ziyi Hao[1†], Xingxia Zhang[1], Yejun Si[1], Guoqiang Lin[1], Shurong Zhang[1], Miao-Miao Niu[3], Xiaotian Yang[1*] and Yanming Zhang[1*]

[1]Department of Hematology, The Affiliated Huai'an Hospital of Xuzhou Medical University, Huai'an, Jiangsu, China, [2]Department of Hematology, Binhai Couty People's Hospital, Yancheng, Jiangsu, China, [3]Department of Pharmaceutical Analysis, China Pharmaceutical University, Nanjing, Jiangsu, China

Acute myeloid leukemia (AML) is a highly aggressive hematological malignancy with a significant unmet clinical need for new therapeutic agents. Lysine-specific demethylase 1 (LSD1), a key regulator of leukemia stem cell self-renewal, has emerged as a promising epigenetic target for AML treatment. Herein, we employed an innovative multi-step integrated screening protocol, encompassing pharmacophore modeling, docking screening, molecular dynamics simulation, and biological evaluation, to identify novel LSD1 inhibitors. This comprehensive approach led to the discovery of six potent LSD1 inhibitors (we named these inhibitors LTMs 1–6), with LTM-1 exhibiting the most pronounced inhibitory effects on LSD1 (IC_{50} = 2.11 ± 0.14 nM) and the highest selectivity for LSD1 over LSD2 (>2370-fold). Notably, LTM-1 demonstrated outstanding antitumor activity both *in vitro* and *in vivo*. *In vitro*, LTM-1 showed potent anti-proliferative effects against LSD1-addicted MV-4-11 leukemia cells (IC_{50} = 0.16 ± 0.01 μM). *In vivo*, LTM-1 treatment significantly reduced tumor growth in MV-4-11 xenografted mice. Moreover, LTM-1 did not induce significant changes in liver and kidney function indices, suggesting a favorable safety profile. These results indicate that LTM-1 is a highly promising preclinical candidate for AML treatment, offering a new strategy for the development of more effective and selective LSD1 inhibitors.

KEYWORDS

acute myeloid leukemia, LSD1 inhibitors, structure-based virtual screening, molecular dynamics simulation, biological evaluation

1 Introduction

Acute myeloid leukemia (AML) accounts for about 80% of all adult acute leukemia patients and is the most common type of acute leukemia in adults (Dong et al., 2020). AML is a heterogeneous hematological malignancy characterized by abnormal clonal expansion of hematopoietic progenitor cells with differentiation defects (Miles et al.,

2020; Rubnitz et al., 2010; Prada-Arismendy et al., 2017). With a mortality rate of up to 60%, AML is one of the deadliest leukemias (Jani et al., 2023). In the past 30 years, despite significant progress in traditional cytotoxic chemotherapy, targeted therapy, and immunotherapy for AML, the number of newly diagnosed leukemia patients worldwide has increased by 46% annually due to aging and the widespread use of chemotherapy leading to secondary leukemia (Wei et al., 2023; Martínez-Cuadrón et al., 2022). Furthermore, the 5-year overall survival rate of patients with AML is less than 50% (Shallis et al., 2019; Tang et al., 2024). With the rapid development of molecular cancer biology, more precise and personalized targeted therapy strategies have shown great potential (Newell and Cook, 2021). However, considerable challenges persist in overcoming treatment resistance and improving the efficacy of AML therapies. There is an urgent and unmet clinical need for the development of novel therapeutic agents that can significantly enhance the prognosis and survival of AML patients.

As the first discovered histone demethylase in 2004, LSD1 is a member of the flavin adenine dinucleotide (FAD)-dependent amine oxidase demethylase family, and another isoform LSD2 was subsequently discovered in 2009 (Shi et al., 2004; Ciccone et al., 2009). LSD1 catalyzes the demethylation of histone 3 lysine 4 methyl 1/2 (H3K4me1/2) and histone 3 lysine 9 methyl 1/2 (H3K9me1/2) (Metzger et al., 2005). Additionally, LSD1 has been found to catalyze the demethylation of some non-histone lysines, including p53, STAT3, E2F transcription factor 1, and DNA methyltransferase 1 (DNMT1), thereby regulating their downstream cellular functions (Xie et al., 2011; Huang et al., 2007; Wang et al., 2008). However, abnormal overexpression of LSD1 has been found in various hematological diseases, including AML, acute lymphocytic leukemia (ALL), myeloproliferative tumors, and chronic myelomonocytic leukemia. Particularly in AML, LSD1 is overexpressed in approximately 60% of cases (Niebel et al., 2014). Moreover, Harri et al. have elucidated that LSD1 is a critical regulator for the self-renewal of leukemia stem cells using the human MLL-AF9 leukemia model (Harris et al., 2012). Furthermore, previous studies have shown that the compound effectively inhibiting LSD1 exhibits synergistic activity with anti-leukemic drugs (Binda et al., 2010). In addition, LSD1 inhibition can enhance the sensitivity of AML cells to all-trans retinoic acid (ATRA) treatment, which was first used to treat AML by inducing cell differentiation (Lokken and Zeleznik-Le, 2012; Schenk et al., 2012). These findings collectively underscore the promise of LSD1 as a highly promising epigenetic target for the treatment of AML (Zhang et al., 2021), providing a compelling biological basis for our investigation.

Given the central role of LSD1 in AML pathogenesis and its association with poor prognosis, targeting LSD1 presents a unique opportunity to develop a new class of therapeutics that could potentially overcome the limitations of current treatments. By inhibiting LSD1, we may be able to disrupt the self-renewal capacity of leukemia stem cells, a key factor in disease relapse, and also modulate the expression of critical genes involved in leukemia progression. This could lead to more effective and durable responses in patients, improving both survival rates and quality of life. Therefore, the motivation for our study stems from the need to develop more effective and selective LSD1 inhibitors. Tranylcypromine (TCP) has been identified as an irreversible and non-selective LSD1 inhibitor by forming a covalent TCP-FAD adduct (Figure 1) (Lee et al., 2006; Fioravanti et al., 2020). Based on the importance of the TCP scaffold in inhibiting LSD1 activity and the clinical demand for developing more effective and selective LSD1 inhibitors, various TCP derivatives have been synthesized (Ganesan et al., 2017; Schulz-Fincke et al., 2018; Koda et al., 2022). Currently, irreversible LSD1 inhibitors based on the TCP scaffold, including TCP, GSK2879552, and ORY-1001 are undergoing clinical trials for AML (Zheng et al., 2016; Huang et al., 2017; Somervaille et al., 2016). In addition, reversible LSD1 inhibitors such as CC-90011 and SP-2577 have also been evaluated in clinical trials (Kanouni et al., 2020; Kurmasheva et al., 2021). However, Sacilotto et al. conducted a comprehensive evaluation of the *in vitro* inhibitory potential of LSD1 inhibitors at clinical stages and found that SP-2577 had minimal effects on AML markers and did not exhibit satisfactory targeting of LSD1, thereby raising doubts about the efficacy of reversible LSD1 inhibitors in the treatment of AML (Sacilotto et al., 2021; Baby et al., 2023). In summary, there is still an urgent need for the development of highly selective LSD1 inhibitors inhibitors that can potently inhibit cancer cell proliferation without side effects for AML treatment.

The novelty of our approach lies in the application of a multi-step integrated screening protocol to identify novel LSD1 inhibitors. At present, structure-based virtual screening is widely utilized for identifying lead compounds and optimizing drug candidates, attributed to its high efficiency and cost-effectiveness (Aziz et al., 2022; Ballante et al., 2021). Pharmacophore-based screening, utilizing key pharmacophore elements, rapidly screens large databases to identify potential active molecules (Lanka et al., 2023). Molecular docking-based screening analysis evaluates the binding modes and affinities of target proteins with ligands for identification of candidate drugs (Raval and Ganatra, 2022). In prior studies conducted by our group, we successfully employed an integrated screening strategy combining pharmacophore modeling and molecular docking to discover effective inhibitors, including dual KRASG12D single targeted inhibitors and tubulin/NRP1 dual targeted inhibitors (Wang et al., 2022; Zheng et al., 2023). In this study, a multi-step integrated screening protocol encompassing pharmacophore modeling, docking screening, molecular dynamics simulation, and biological evaluation led to the identification of six novel LSD1 inhibitors for the treatment of myeloid leukemia (we named these inhibitors LTMs 1–6). Notably, LTM-1 and LTM-3 exhibited strong *in vitro* enzymatic inhibitory activity. In particular, LTM-1demonstrated outstanding antitumor activity both *in vitro* and *in vivo*. Overall, these results indicate that LTM-1 may be a promising preclinical candidate for further investigation.

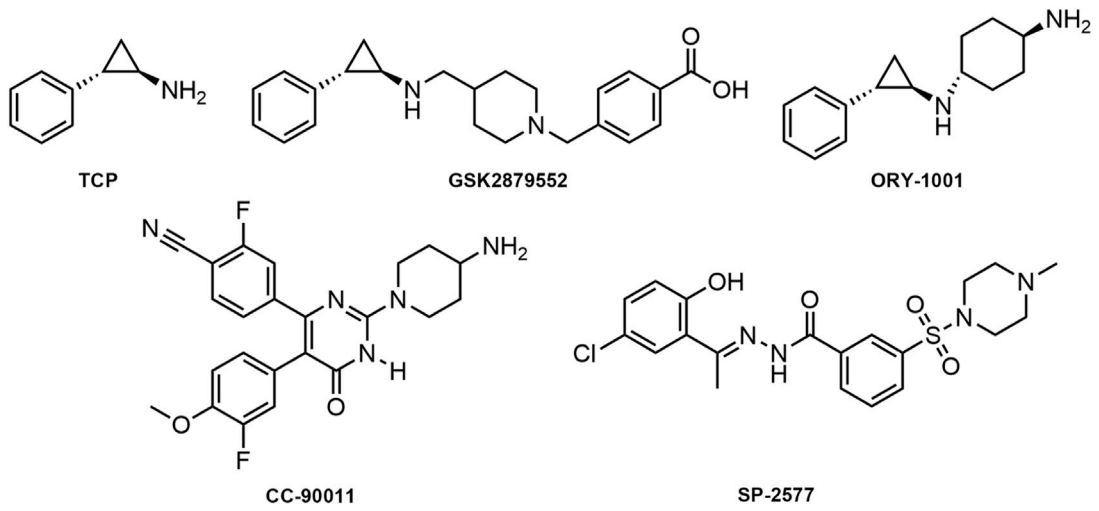

FIGURE 1
Structures of published LSD1 inhibitors.

2 Materials and methods

2.1 General

The compounds LTMs 1–6, identified in our study, and the positive control GSK2879552 were purchased from WuXi AppTec (Shanghai, China). These were utilized in both *in vitro* and *in vivo* assays. Iscove's Modified Dulbecco's Medium (IMDM), Roswell Park Memorial Institute (RPMI)-1640 medium, fetal bovine serum (FBS) and penicillin/streptomycin were purchased from Gibco (Grand Island, New Nork, United States). Recombinant human LSD1 (172–852 aa) and full-length LSD2 were obtained from Sino Biological Inc. and ActiveMotif.

2.2 Cell lines and culture conditions

The myeloid leukemia cell lines MV-4-11, MOLT-4, MOLM-16, HL-60, and the human B lymphocyte cell line RPMI-226 were purchased from the American Type Culture Collection (ATCC, Manassas, VA, United States). The myeloid leukemia cell line HAL-01 was obtained from the Deutsche Sammlung von Mikroorganismen und Zellkulturen GmbH (DSMZ, Braunschweig, Germany). All cells were cultured in IMDM or RPMI -1640 medium supplemented with 10% FBS, 100 U/mL penicillin, and 100 μg/mL streptomycin. The cells were maintained in a humidified incubator with an atmosphere of 5% CO_2 at 37°C.

2.3 Establishment of a structure-based pharmacophore model for LSD1

The X-ray crystal structure of LSD1 complexed with the inhibitor CC-90011 (PDB ID: 6W4K) was obtained from the Protein Data Bank (PDB) and loaded into the molecular operating environment (MOE, Chemical Computing Group Inc, Montreal, Quebec, Canada). 6W4K was selected due to its high-resolution structure and relevance in previous studies related to LSD1 inhibitors (Kanouni et al., 2020). Within MOE, the QuickPrep tool was employed to execute a series of preparatory steps essential for refining the crystal structure. These steps included the elimination of unbound water molecules, the addition of polar hydrogen atoms, the computation of partial charges, and energy minimization. Subsequently, the Ligand Interaction tool in MOE was engaged to dissect the key key interactions between the LSD1 protein and its bound ligand. Finally, leveraging the detailed understanding of the LSD1 crystal structure, pharmacophore features were meticulously constructed using Pharmacophore Query Editor. These features encapsulate the critical interaction points necessary for the binding of inhibitors to LSD1, including hydrogen-bond donors (Don), hydrophobic features (Hyd), and aromatic centers (Aro).

2.4 Virtual screening

As described in the previously reported methods, virtual screening was performed using the MOE software (Liang et al., 2023). Initially, a database of 121,000 two-dimensional compounds assembled through combinatorial chemistry was converted into three-dimensional structures using an energy minimization algorithm. Subsequently, the prepared LSD1 pharmacophore features were used as a template for preliminary pharmacophore-based screening. Finally, the docking score of −8.53 kcal/mol, obtained from the LSD1 inhibitor GSK2879552, which is in the clinical trial phase, was used as a reference value for docking-based screening. The MOE docking scoring function was employed to evaluate the binding free energy of the ligand with the target protein. Compounds with scores lower than the set reasonable reference value were selected to obtain potential LSD1-targeting candidate inhibitors.

2.5 Molecular dynamics simulation

The crystal structure of LSD1 (PDB ID: 6W4K) was retrieved from the PDB. The crystal complex structures of the ligand LTM-1 with the protein LSD1 were constructed in the MOE and used as the initial coordinates for MD simulations. The ligand LTM-1 and the protein LSD1 were individually subjected to MD simulations using GROMACS (version 2021.5). LSD1 was topologically modeled under periodic boundary conditions, employing the AMBER99SB-ILDN force field for accurate representation. The Acpype Server (www.bio2byte.be) was engaged to generate the topology file of LSD1, which was then integrated with the ligand file to create a comprehensive complex system. Subsequently, the ligand file was added to the protein file to form a complex system. This complex system was immersed in a 1.0 nm cubic simulation box, employing the SPC water model to ensure solvation and equilibrium. To ensure system neutrality, Na^+ and Cl^- were introduced. The solvated system underwent energy minimization, applying the steepest descent algorithm for 50,000 steps. A 100 ps NVT simulation was then performed on the system using the V-rescale thermostat to maintain the system temperature at 300 K. This was followed by a 100 ps NPT simulation, where the Parrinello-Rahman barostat was used to maintain a pressure of 1 bar. Finally, a 500 ns molecular dynamics simulation is conducted for each system, with trajectory data recorded at intervals of 0.1 ns. Data processing is performed using GraphPad Prism 10 software (GraphPad Software Inc., San Diego, CA), and stability is analyzed in conjunction with the root mean square deviation (RMSD), root mean square fluctuation (RMSF), binding-induced conformational changes and protein's radius of gyration (Rg).

2.6 Binding free energy calculation using MM/PBSA method

The Molecular Mechanics/Generalized Born Surface Area (MM/GBSA) method was exploited through the GMX - PBSA tool for calculating the free binding energy of the LSD1 - LTM - 1 complex (Al-Khafaji and Tok, 2020). This computational tool included the PCM and SGB models for solvation energy calculations, along with consideration of van der Waals and electrostatic interaction energies to evaluate the overall energy within the complex. Finally, from the calculation results, we obtained the total binding Gibbs free energy (ΔGtotal). ΔGtotal comprises Van der Waals, Electrostatic, Polar solvation, Non - polar solvation, Net gas phase, and Net solvation. Van der Waals is the contribution of attractive or repulsive forces between molecules or within a single molecule. Electrostatic is the contribution of electrostatic interactions between charged particles within molecules. Polar solvation is the polar contribution to solvation free energy. Non - polar solvation is the non - polar contribution to solvation free energy. Net gas phase is the sum of internal energies of the isolated molecules in vacuum. Net solvation is the energy change when molecules interact with a solvent environment.

2.7 Enzyme inhibition assay

The inhibitory effects of the tested compounds on LSD1 and LSD2 enzymes were methodically assessed using the Lance Ultra LSD1 Histone H3-Lysine 4 Demethylase Assay Kit from PerkinElmer, adhering to previously published methodologies (Li et al., 2022). In brief, the reaction was initiated by adding 4 μL of enzyme solution, with concentrations specified at 2 nM for LSD1 or 172 nM for LSD2, 4 μL of substrate solution [2.5 μM Bio-H3K4me2 (124 amino acids)], and 2 μL of tested compound to a Tris buffer (50 mM Tris-HCl, 50 mM NaCl, 0.01% Tween 20, 1 mM DTT, 10 μM FAD, 10% glycerol, pH 9.0) at room temperature and incubated for 1 h. Following the incubation, 5 μL of a detection mixture, comprising an Eu-labeled H3K4me0 antibody and ULight Streptavidin, was added to the reaction. The fluorescence intensity was then measured employing TR-FRET mode with excitation and emission wavelengths set at 320 nm and 665 nm, respectively, utilizing the Envision (PerkinElmer) system. Each experiment was performed in triplicate.

2.8 Kinase selectivity assays

The kinase selectivity analysis of LTM-1 was performed utilizing the SelectScreen Kinase Profiling Service offered by Thermo Fisher Scientific. In a dose-response assay featuring a ten-point dilution series from 0.25 μM to 128 μM, the inhibitory effects of LTM-1 on substrate phosphorylation reactions catalyzed by a panel of kinases were assessed. Consequently, the half-maximal inhibitory concentrations (IC_{50} values) for each kinase were determined.

2.9 Cell proliferation assay

The *in vitro* anti-proliferative activity of the compounds was determined using the CellTiter 96® AQueous NonRadioactive Cell Proliferation Assay Kit (Promega, Madison, United States) as previously described (Ji et al., 2017). In brief, 5–10 × 10^3 cells and 180 μL of medium were first seeded into each well of a 96-well plate. Subsequently, the cells were exposed to either 0.2% Dimethyl sulfoxide (DMSO, Aladdin Reagent, Shanghai, China) or a serial dilution of the compounds, prepared from a 10 mM stock solution in DMSO, with the final concentration of DMSO being 0.2% for 72 h. 20 μL of MTS reagent was added to each well, and the culture was incubated in the dark at 37°C for 4 h. Finally, the optical density (OD) was then recorded at 490 nm and 690 nm using a microplate reader from Molecular Devices. The proliferation inhibition rate was calculated according to the following formula: inhibition ratio = (OD of DMSO treated wells - OD of compound treated wells)/(OD of DMSO treated wells - OD of blank wells) × 100%. The IC_{50} values of the compounds inhibiting cell proliferation were calculated using GraphPad Prism 10 (GraphPad Software Inc., San Diego, CA).

2.10 *In vivo* experiments

Given the potent inhibitory effect of LTM-1 on MV-4-11 cell proliferation *in vitro*, a previously reported xenograft animal model was established to measure the anti-tumor growth and development effects of LTM-1 (Zhou et al., 2022). The animal experimental design of this study was reviewed and confirmed by the Ethics Committee of China Pharmaceutical University. The experimental procedures

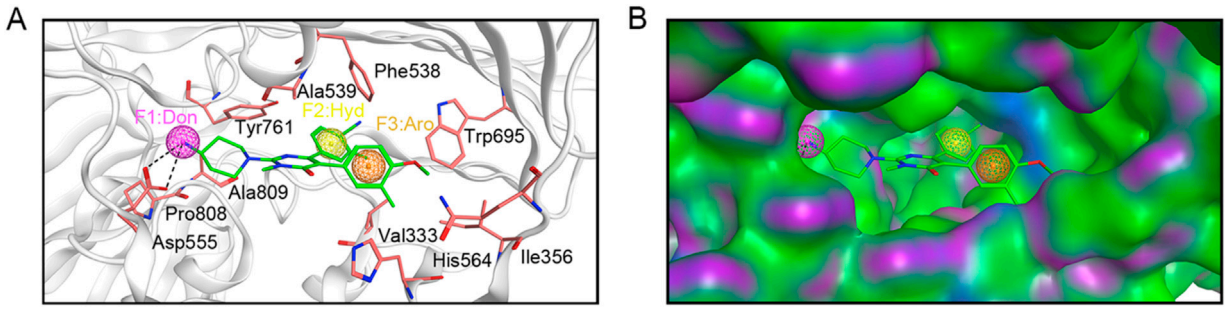

FIGURE 2
Pharmacophore model based on LSD1. **(A)** Details of pharmacophore model features. Hydrogen-bond donor (F1) is represented by magenta sphere, hydrophobic feature (F2) is depicted by yellow sphere, and aromatic center (F3) is illustrated by brown sphere. Each critical amino acid is represented by a pink stick model and annotated with a three-letter amino acid code. Hydrogen bonds are depicted with black dashed lines. **(B)** Spatial constraints of the pharmacophore model within the LSD1 active site.

complied with the ARRIVE guidelines (https://arriveguidelines.org/). Female BALB/c nude mice aged 4–6 weeks were purchased from Changzhou Cave Animal Co., Ltd. (Changzhou, China). Mice were housed in a specific pathogen-free (SPF) environment, where the temperature was precisely regulated to 25°C ± 2°C, the relative humidity was kept at 50% ± 5%, and a strict 12-h light-dark cycle was maintained. A 200 μL suspension of MV-4-11 cells (1×10^6 cells) was injected subcutaneously into the mice. When the tumor volume was observed to reach 80–100 mm^3, the mice were randomly divided into two groups: the vehicle group and the LTM-1 treatment group (10 mg/kg). The mice were administered drugs via intraperitoneal injection daily, with a total treatment period of 15 days. Mouse weight and tumor volume were measured every 3 days. The tumor volume was calculated using the formula $(c \times c \times d)/2$ (where c represents the smallest diameter, and d represents the largest diameter). When the animals could no longer access food and/or the average tumor diameter exceeded 15 mm, the mice were anesthetized with 2.5% isoflurane and euthanized by cervical dislocation to minimize suffering. In addition, the liver and kidney index levels were measured using an automatic biochemical analyzer to evaluate the toxic effects of LTM-1 on mice.

2.11 Statistical analysis

The entire statistical analysis was performed with GraphPad Prism 10. The t-tests were employed to evaluate whether there was a significant difference between the two sets of data. P values less than 0.05 were considered as significant. The data are presented as the mean ± standard deviation (SD), n = 3.

3 Results

3.1 Establishment of pharmacophore model

Based on the crystal structure of LSD1 (PDB ID: 6W4K), a pharmacophore model was constructed using MOE to provide clues for identifying novel LSD1 inhibitors. Firstly, the LSD1 protein was preprocessed by removing water molecules, adding polar hydrogens, and calculating partial charges. Subsequently, the binding details of the LSD1 protein and its ligand were analyzed using the ligand interaction tool of MOE to yield key information for constructing the pharmacophore model. As depicted in Figure 2A, the ligand formed two hydrogen bonds with Asp555. Moreover, the ligand engaged in hydrophobic interactions with key amino acid residues Val333, Ile356, Phe538, Ala539, Tyr761, and Ala809 of LSD1. Based on the structure-activity relationship analysis of the LSD1 protein-ligand complex, three representative pharmacophore features were constructed using the pharmacophore query editor: a hydrogen-bond donor feature (F1) corresponding to the Asp555 residue; a hydrophobic interaction feature (F2) corresponding to the Phe538, Ala539, and Tyr761 residues; and an aromatic feature (F3) corresponding to the Trp695 residue. Additionally, the spatial constraints of the pharmacophore model within the LSD1 active site demonstrated that the established pharmacophore features were properly embedded into the depressions of the LSD1 binding pocket (Figure 2B). The constructed pharmacophore model offered critical chemical features for the subsequent virtual screening of novel LSD1 inhibitors.

3.2 Virtual screening

As illustrated in Figure 3, this study employed a comprehensive screening strategy that integrated pharmacophore-based screening, molecular docking-based screening, molecular dynamics (MD) simulation, and biological evaluation to identify novel and potent LSD1 inhibitors. Initially, an energy optimization algorithm was applied to convert 121,000 compounds from a combinatorial chemistry-derived database from two-dimensional (2D) to three-dimensional (3D) structures. Subsequently, the LSD1 pharmacophore model was utilized as a probe for pharmacophore-based docking. The 207 compounds obtained through preliminary screening were docked to the LSD1 binding site for further docking-based screening and the binding free energy of each compound was calculated. The lower the binding free energy, the stronger the binding affinity between the compound and the target protein. Based on the docking score of the positive control GSK2879552 (−8.53 kcal/mol), which served as the

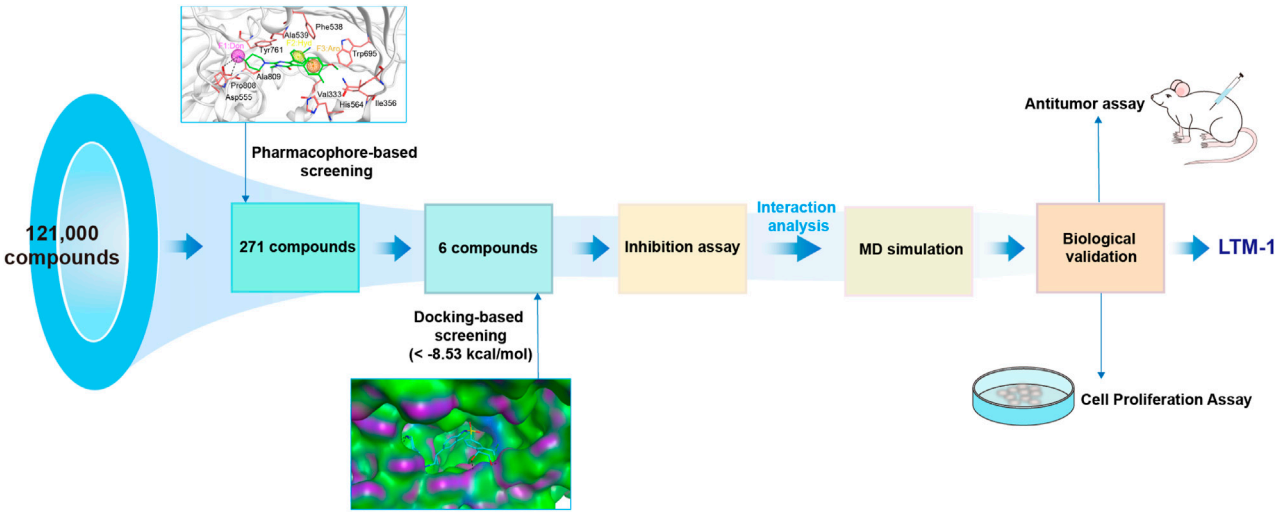

FIGURE 3
A flowchart of the identification of LSD1 inhibitors via an integrated strategy of *in silico* screening and biological evaluation.

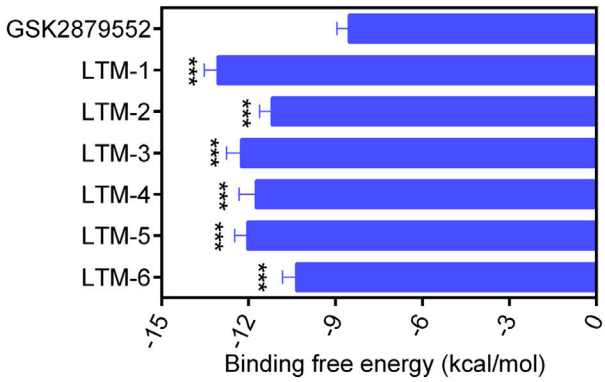

FIGURE 4
The docking scores of LTMs 1–6 and GSK2879552. [a]Binding free energy between the compounds and the targets (lower binding free energies show stronger binding affinities). The data are presented as the mean ± SD, n = 3. ***p < 0.001, as compared to GSK2879552.

threshold, the top six compounds (LTMs 1–6) were ultimately identified (Figure 4). The structures of these compounds are displayed in Figure 5, and according to SciFinder and Reaxys databases, LTMs 1–6 have not yet been reported internationally. Subsequently, these hit compounds were prepared for subsequent *in vitro* enzyme inhibition assays.

3.3 *In vitro* LSD1 inhibitory activity

The enzyme inhibitory activity of the six candidate inhibitors obtained was further determined. The LSD1 inhibitor GSK2879552, which has entered the clinical trial stage, was used as a positive control. As shown in Table 1, LTMs 1–6 exhibited nanomolar inhibition of LSD1 (IC_{50} = 2.11–16.54 nM), and LTMs 1–6 had stronger enzyme inhibition of LSD1 than GSK2879552 (IC_{50} = 24.53 ± 2.26 nM). Particularly, the enzyme inhibitory activities of LTM-1 (IC_{50} = 2.11 ± 0.14 nM) and LTM-3 (IC_{50} = 4.57 ± 0.32 nM) were the most prominent. Moreover, the enzyme inhibitory capacities of LTMs 1–6 against LSD2 were evaluated to determine the selectivity of their inhibition. The selectivity of LTMs 1–6 for LSD1 over LSD2 was superior to that of GSK2879552, with LTM-1 (>2370-fold) and LTM-3 (668-fold) showing the most significant selectivity. In addition, the excellent enzyme inhibitory activity and selectivity of LTM-1 and LTM-3 are consistent with the lowest docking scores of LTM-1and LTM-3 with LSD1 mentioned above. Additionally, the compound with the most potent inhibitory activity and selectivity against LSD1, LTM-1, underwent comprehensive kinase panel analysis to assess its broad-spectrum inhibition potential against 60 different kinases. The data presented in Supplementary Table S1 demonstrate that the IC50 values of LTM-1 against each of the 60 evaluated kinases were all greater than 10 μM. Overall, these results indicate the significant selectivity of LTM-1 for LSD1, reducing the risk of off-target effects and associated toxicity.

3.4 Interaction analysis

Given that LTM-1 and LTM-3 were identified as having the most favorable docking scores for binding to LSD1 and exhibited the highest potency in *in vitro* enzyme inhibition assays among the six candidates evaluated. Consequently, we conducted an analysis to elucidate the potential binding modes of LTM-1 and LTM-3 with LSD1. As illustrated in Figures 6A, C, LTM-1 and LTM-3 engaged in hydrogen bonding with the critical amino acid residues Asp555, Pro808, and His564 of LSD1. Additionally, they both formed hydrophobic interactions with Val333, Phe538, Ala539, Tyr761, and Trp695 of LSD1. It is noteworthy that LTM-1 established an additional hydrogen bond with Gln358, potentially contributing to its superior binding affinity and inhibitory efficacy. Additionally, the surface topography of the LSD1's active site, as depicted in Figures

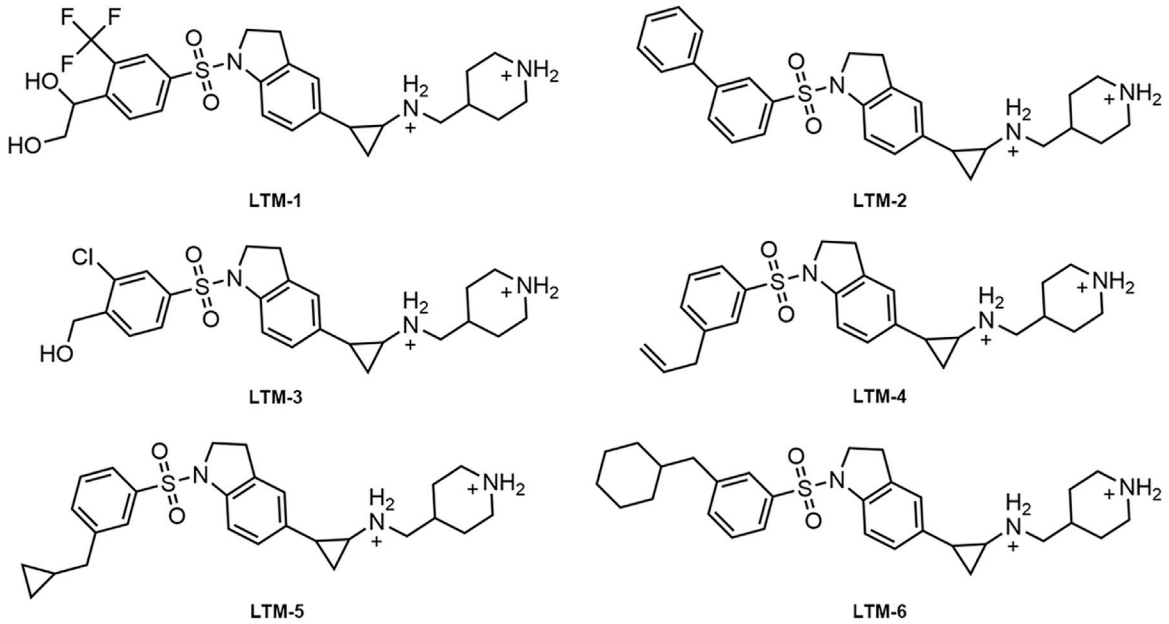

FIGURE 5
The chemical structures of LTMs 1–6.

TABLE 1 The inhibitory activities of LTMs 1–6 against LSD1 and LSD2.

Compounds	LSD1 (IC_{50}, nM)	LSD2 (IC_{50}, nM)	LSD2/LSD1 selectivity (folds)
LTM-1	2.11 ± 0.14	>5,000	>2,370
LTM-2	10.23 ± 2.71	2,196.02 ± 146.25	215
LTM-3	4.57 ± 0.32	3,054.75 ± 177.86	668
LTM-4	8.92 ± 0.57	861.49 ± 26.73	97
LTM-5	7.31 ± 0.46	673.67 ± 21.48	92
LTM-6	16.54 ± 2.39	>5,000	>302
GSK2879552	24.53 ± 2.26	103.56 ± 5.75	4

Data represent mean values ± SD, n = 3.

6B, D, revealed a pronounced geometric congruence with the molecular contours of LTM-1 and LTM-3, indicative of an optimal shape complementarity within the binding pocket.

3.5 MD simulation

To determine the binding affinity and persistence of LTM-1 with LSD1, comprehensive molecular dynamics (MD) simulations were conducted over a 500 ns timescale using GROMACS software (version 2021.5). Trajectory analyses indicated that for the LSD1-LTM-1 complex, the root mean square deviation (RMSD) displayed a moderate initial rise, subsequently stabilizing within the range of 0.14 nm–0.20 nm after approximately 7 ns (Figure 7A). This observation suggests that LTM-1 exhibits stable binding with LSD1. Additionally, Figure 7B presents the root mean square fluctuation (RMSF) of LSD1 residues over the 500 ns simulation period. The RMSF values for key residues, including Val333, Phe538, Ala539, Asp555, His564, Trp695, Tyr761, and Pro808, were all below 0.15 nm, which play a crucial role in binding, exhibit minimal fluctuation and maintain stable binding. Furthermore, the radius of gyration (Rg) values for the LSD1-LTM-1 complex exhibited fluctuations of less than 0.1 nm, suggesting that the protein maintained its structural compactness throughout the simulation (Figure 7C). Based on the obtained structural analysis and RMSD values, the conformational stability of the LSD1-LTM1 complex was also analyzed. As shown in Figure 7D, compared with the initial pose in the LSD1-LTM-1 complex, the superposition of the initial pose and the binding-induced pose did not show any conformational changes, and the RMSD value of the LSD1-LTM-1 complex before and after dynamic simulation was less than 0.5 Å, indicating that the LSD1-LTM-1 complex is in a stable conformation. Collectively, these

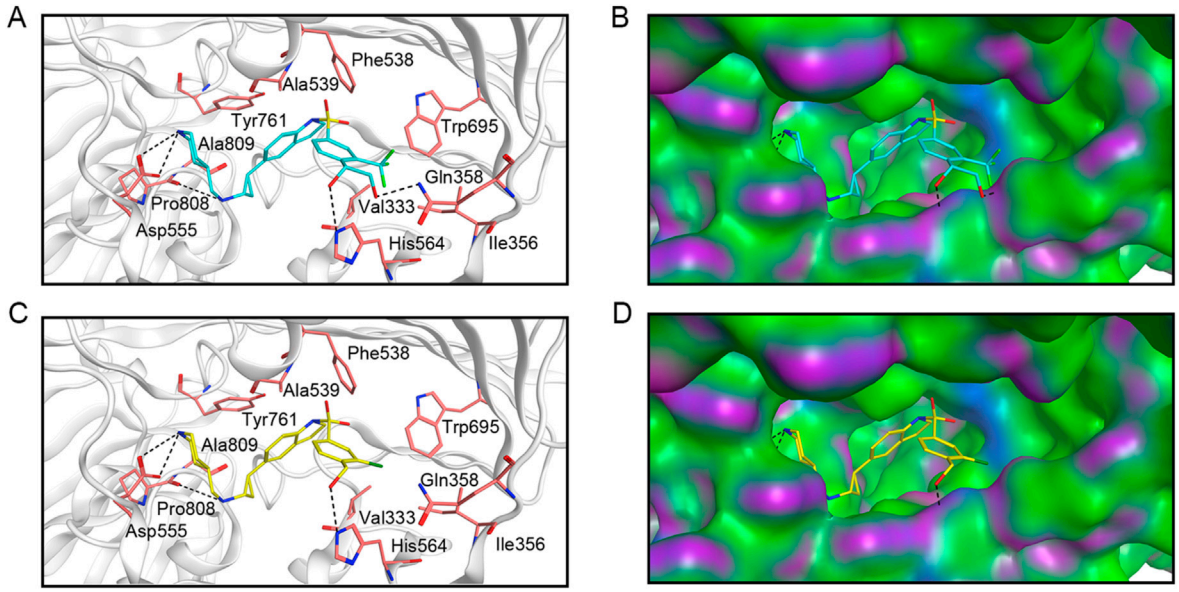

FIGURE 6
The predicted docking poses and binding surface of LTM-1 and LTM-3 in the active site of LSD1, respectively. **(A)** and **(B)** represent LTM-1; **(C, D)** represent LTM-3. The structure of LTM-1 is represented by cyan sticks. The structure of LTM-3 is depicted by yellow sticks. Key amino acids in the active site are represented by pink sticks and annotated with three-letter amino acid codes. The surface of the LSD1 protein is rendered with hydrogen bond regions (purple), hydrophobic regions (green), and moderately polar regions (blue).

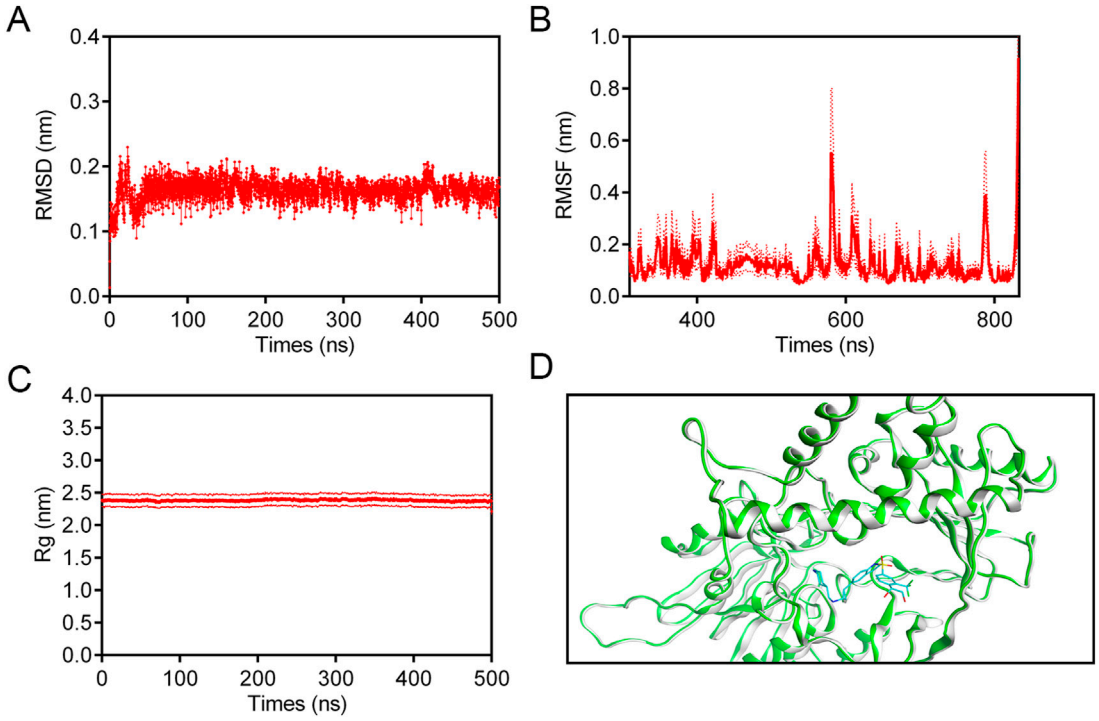

FIGURE 7
MD simulation of LSD1 in complex with LTM-1. **(A)** RMSD of LSD1-LTM-1 complex. **(B)** RMSF of LSD1 residues in LSD1-LTM-1 complex. **(C)** Rg of LSD1 in the complex of LSD1-LTM-1. **(D)** The conformational changes induced upon binding of the LTM-1 (represented in cyan) to the LSD1 protein (represented in green and gray). The data are presented as the mean ± SD, n = 3. Error bars representing the standard deviation are indicated by red dashed lines.

TABLE 2 MM/GBSA energy components of the LSD-1-LTM-1 complex expressed in kcal/mol.

Energy component	LSD-1-LTM-1
$\triangle G_{total}$	−8,995.02 ± 210.65
Van der Waals	−3,327.19 ± 25.94
Electrostatic	−29188.78 ± 146.72
Polar solvation	−4,621.30 ± 126.66
Non-polar solvation	156.05 ± 2.35
Net gas phase	−4,529.77 ± 168.30
Net solvation	−4,465.26 ± 126.69

TABLE 3 Antiproliferative activities of LTMs 1–6 against human MV-4-11 and RPMI-8226 cells by MTS assay.

Compounds	IC_{50} (μM)	
	MV-4-11	RPMI-8226
LTM-1	0.16 ± 0.01	>100
LTM-2	0.74 ± 0.06	>100
LTM-3	0.32 ± 0.04	>100
LTM-4	0.63 ± 0.05	>100
LTM-5	0.51 ± 0.03	>100
LTM-6	0.98 ± 0.07	>100
GSK2879552	1.17 ± 0.28	21.26 ± 2.69

findings substantiate the stable binding of LTM-1 to the LSD1 active site throughout the entire simulation timeframe.

3.6 Binding free energy calculation using MM/PBSA method

In this study, the MM/GBSA method was employed to evaluate the strength and stability of interactions between the LSD-1 protein and the LTM-1, performing free energy calculations. Detailed energy components are provided in Table 2. The results showed that the LSD-1-LTM-1 complex had a ΔG_{total} energy of −8,995.02 ± 210.65 kcal/mol, and the electrostatic energy of the LSD-1-LTM-1 complex was −29,188.78 ± 146.72 kcal/mol. The lower the electrostatic energy of the LSD-1-LTM-1 complex, the stronger its binding stability. Further analysis revealed that the electrostatic energy plays a crucial role in providing maximum stability during the binding process, as its contribution to the total binding free energy is significantly greater than the other components. This confirms its importance in the affinity of LTM-1 with the target protein LSD-1.

3.7 *In vitro* cancer cell assays

To further evaluate the *in vitro* anti-proliferative effects of LTMs 1–6, we conducted an experiment utilizing the MTS assay to assess the cytotoxicity of these compounds against LSD1-addicted MV-4-11 leukemia cells and LSD1-non-sensitive RPMI-8226 cells. The results, as presented in Table 3, indicated that LTMs 1–6 demonstrated significant anti-proliferative activity against the LSD1-addicted MV-4-11 cells compared to GSK2879552 (IC_{50} = 1.17 ± 0.28 μM), with LTM-1 showing particularly potent effects (IC_{50} = 0.16 ± 0.01 μM). It was noteworthy that the impact of LTMs 1–6 on the LSD1-non-sensitive RPMI-8226 cells was markedly weaker (IC_{50} > 100 μM). Taken together, the potent inhibition of LSD1 by LTM-1 shows its potential as a therapeutic candidate for AML. Additionally, we assessed the antiproliferative activity of LTM-1 against other AML cell lines, including MOLT-4, MOLM-16, HAL-01, and HL-60, to confirm its broader applicability. As shown in Supplementary Table S2, LTM-1 demonstrated significant antiproliferative effects across these AML cell lines (IC_{50} = 0.19–0.39 μM). These findings indicate that LTM-1 not only exerts potent antiproliferative activity against the MV-4-11 cell line but also shows a broad spectrum of anticancer activity against other AML cell lines.

3.8 Antitumor activity of LTM-1 *in vivo*

Considering the outstanding inhibitory effect of LTM-1 on LSD1 protein and MV-4-11 cell proliferation, the MV-4-11 xenograft model was used to further evaluate the *in vivo* anti-tumor activity of LTM-1. Tumor-bearing mice were randomly treated with the vehicle group and 10 mg/kg of LTM-1. As depicted in Figure 8A; Supplementary Figure S1, the tumor growth in mice was significantly reduced upon treatment with LTM-1, compared to the control group. Furthermore, throughout the experimental process, the nude mice in two groups were slowly gaining weight, with no significant differences (Figure 8B), suggesting that treatment with LTM-1 did not induce severe systemic side effects.

We conducted an additional assessment of the potential toxicity of LTM-1. The levels of alanine aminotransferase (ALT), aspartate aminotransferase (AST), blood urea nitrogen (BUN), and creatinine (CRE) in mouse serum were measured to evaluate the functional status of the liver and kidneys, respectively. As illustrated in Supplementary Figure S2, compared to the vehicle control group, there were no significant changes in the levels of ALT, AST, BUN and CRE among mice treated with various doses of LTM-1. This indicates that LTM-1 does not exert notable toxic effects on the liver or kidneys in mice. In summary, while effectively suppressing tumor growth, LTM-1 demonstrates no apparent toxic impact on major organs such as the liver and kidneys in mice. These findings suggest that LTM-1 possesses a favorable safety profile and potential clinical application value.

4 Discussion

Acute myeloid leukemia (AML) is a formidable heterogeneous malignant hematologic neoplasm. An increasing body of research has confirmed that lysine-specific demethylase 1 (LSD1) is a key regulatory factor in the self-renewal of leukemic stem cells. Although

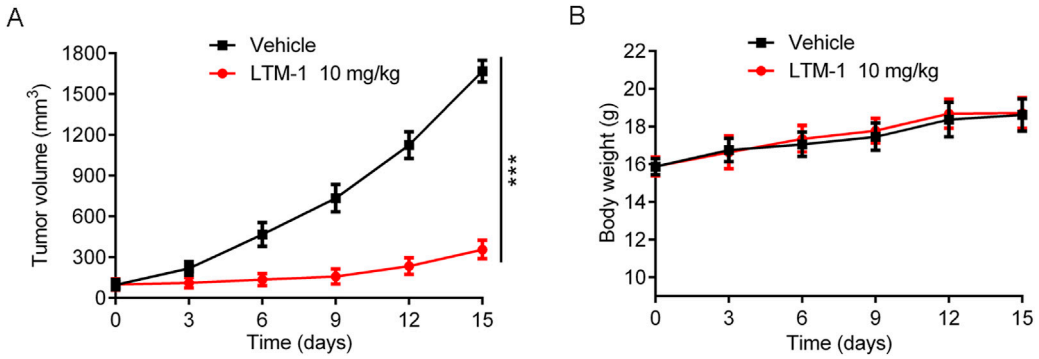

FIGURE 8
Evaluation of *in vivo* anti-tumor activity of LTM-1. **(A)** Changes in tumor volume. **(B)** Body weight of mice. Results are expressed as means ± SD (n = 3). ***p < 0.001, as compared to the vehicle group.

several LSD1 inhibitors have been reported, they have exhibited unsatisfactory targeting specificity and concerning side effects. Consequently, there is an urgent clinical demand for the development of highly selective and potent LSD1 inhibitors. In this study, an integrated strategy combining pharmacophore modeling, docking screening, MD simulation, and biological validation was employed to identify six LSD1 inhibitor (LTMs 1–6). The results of *in vitro* enzymatic inhibition assays revealed that all six compounds demonstrated potent nanomolar-level inhibitory activity against LSD1. Moreover, the weak inhibitory capacity of LTMs 1–6 against LSD2 underscored their excellent target selectivity. Particularly, LTM-1 and LTM-3 exhibited the most pronounced inhibitory effects on LSD1 and the highest selectivity for LSD1 over LSD2. Then, subsequent interaction analyses indicated that both LTM-1 and LTM-3 formed hydrogen bond interactions with key residues within the LSD1 active site, including Asp555, Pro808, and His564, and also engaged in hydrophobic interactions with Val333, Phe538, Ala539, Tyr761, and Trp695. Additionally, LTM-1 maintained a stable binding state with LSD1 throughout the entire 500 ns MD simulation process. Furthermore, the results of the cell proliferation activity assessment demonstrated that LTMs 1–6 possess strong cytotoxicity against the LSD1-addicted MV-4-11 cells, while having negligible effects on the LSD1-insensitive RPMI-8226 cells, with LTM-1 exhibiting the most potent ability to inhibit cancer cell proliferation. Notably, in the MV-4-11 xenograft model, LTM-1 displayed excellent *in vivo* antitumor activity without significant toxic side effect. In comparison to other LSD1 inhibitors in clinical trials, such as SP-2577 and GSK2879552, LTM-1 has shown superior enzyme inhibition and selectivity against LSD1 (Liu et al., 2023). This comprehensive comparison underscores the potential of LTM-1 as a promising lead compound for preclinical research of AML and reinforces the significance of our research in the context of ongoing clinical trials. While LTM-1 shows promising results in inhibiting AML progression, we acknowledge the need for further structural optimization to improve its pharmacokinetics and minimize toxicity. Therefore, we propose a detailed plan for future structural modifications, which involves substituting the trifluoromethyl group in LTM-1 with other halogens like chlorine, bromine, or iodine. This modification aims to alter the compound's lipophilicity, potentially enhancing its pharmacokinetic properties and reducing toxicity, thereby providing valuable insights for designing more effective and safer LSD1 inhibitors. Additionally, the virtual screening methodologies utilized in this study, comprising pharmacophore modeling, docking screening, and molecular dynamics (MD) simulations, are conducive to the expeditious identification of novel therapeutics. This methodological framework can be adapted to recognize potential inhibitors from other natural databases and FDA marketed drug databases, so that discovering other novel and efficient natural active small molecules and marketed drugs targeting LSD1. Consequently, it constitutes a potent instrument in the nascent stages of drug discovery, facilitating the identification of target compounds and hastening the lead optimization process.

5 Conclusion

In summary, we have designed and identified a series of new potent LSD1 inhibitors (LTMs 1–6). In particular, LTM-1 exhibited the most prominent nanomolar enzyme inhibition ability and strongest inhibition selectivity against LSD1. Our *in vitro* and *in vivo* assays have shown that LTM-1 significantly inhibits the progression of AML without notable toxic side effects, positioning it as a highly promising lead compound for preclinical AML research. While these findings are promising, we recognize the necessity for further experimental validation to substantiate the safety and efficacy of LTM-1 before advancing to preclinical development. As we continue to optimize the structure of LTM-1 in our laboratory, we are also looking ahead to further enhance its potency and selectivity through additional structural modifications. We plan to conduct extensive pharmacokinetic studies to fully characterize LTM-1, ensuring its safety and efficacy. Moreover, we are committed to moving our preclinical findings towards clinical applications and will explore the potential of LTM-1 and its analogs as dual-target inhibitors to improve therapeutic outcomes. We believe that the integration of computational modeling and experimental validation, as demonstrated in this study, will streamline the drug discovery

process and significantly contribute to the development of new treatments for AML. The structure-based virtual screening, molecular dynamics simulation, and biological evaluation methods outlined here offer a novel strategy for designing and optimizing more effective and selective LSD1 inhibitors, setting the stage for future research directions that will build upon our current findings.

Data availability statement

The original contributions presented in the study are included in the article/Supplementary Material, further inquiries can be directed to the corresponding authors.

Ethics statement

The animal study was approved by the Ethics Committee of China Pharmaceutical University. The study was conducted in accordance with the local legislation and institutional requirements.

Author contributions

YH: Writing–review and editing, Investigation, Methodology, Validation, Software. YW: Investigation, Supervision, Validation, Writing–original draft, Writing–review and editing. ZH: Conceptualization, Investigation, Methodology, Visualization, Writing–original draft. XZ: Data curation, Methodology, Writing–review and editing. YS: Data curation, Investigation, Validation, Writing–review and editing. GL: Investigation, Supervision, Validation, Writing–review and editing. SZ: Project administration, Resources, Software, Writing–review and editing. M-MN: Formal Analysis, Supervision, Visualization, Writing–review and editing. XY: Conceptualization, Investigation, Methodology, Writing–original draft. YZ: Data curation, Funding acquisition, Investigation, Methodology, Validation, Writing–review and editing.

Funding

The author(s) declare that financial support was received for the research, authorship, and/or publication of this article. This work was financially supported by Jiangsu Commission of Health scientific research project (Geriatrics) (LKM2023045), Campus Collaborative Innovation Research Project of Jiangsu Medical Vocational College (202491004), Huai'an Health Commission Research General Project (HAWJ2024017), and the research project of Huai'an Science and Technology Bureau (HAB2023).

Conflict of interest

The authors declare that the research was conducted in the absence of any commercial or financial relationships that could be construed as a potential conflict of interest.

Generative AI statement

The author(s) declare that no Generative AI was used in the creation of this manuscript.

Publisher's note

All claims expressed in this article are solely those of the authors and do not necessarily represent those of their affiliated organizations, or those of the publisher, the editors and the reviewers. Any product that may be evaluated in this article, or claim that may be made by its manufacturer, is not guaranteed or endorsed by the publisher.

Supplementary material

The Supplementary Material for this article can be found online at: https://www.frontiersin.org/articles/10.3389/fphar.2025.1510319/full#supplementary-material

References

Al-Khafaji, K., and Tok, T. T. (2020). Molecular dynamics simulation, free energy landscape and binding free energy computations in exploration the anti-invasive activity of amygdalin against metastasis. *Comput. Meth Prog. Bio* 195, 105660. doi:10.1016/j.cmpb.2020.105660

Aziz, M., Ejaz, S. A., Zargar, S., Akhtar, N., Aborode, A. T., Wani, T. A., et al. (2022). Deep learning and structure-based virtual screening for drug discovery against NEK7: a novel target for the treatment of cancer. *Molecules* 27, 4098. doi:10.3390/molecules27134098

Baby, S., Shinde, S. D., Kulkarni, N., and Sahu, B. (2023). Lysine-specific demethylase 1 (LSD1) inhibitors: peptides as an emerging class of therapeutics. *ACS Chem. Biol.* 18, 2144–2155. doi:10.1021/acschembio.3c00386

Ballante, F., Kooistra, A. J., Kampen, S., de Graaf, C., Carlsson, J., and Schulte, G. (2021). Structure-based virtual screening for ligands of G protein–coupled receptors: what can molecular docking do for you? *Pharmacol. Rev.* 73, 527–565. doi:10.1124/pharmrev.120.000246

Binda, C., Valente, S., Romanenghi, M., Pilotto, S., Cirilli, R., Karytinos, A., et al. (2010). Biochemical, structural, and biological evaluation of tranylcypromine derivatives as inhibitors of histone demethylases LSD1 and LSD2. *J. Am. Chem. Soc.* 132, 6827–6833. doi:10.1021/ja101557k

Ciccone, D. N., Su, H., Hevi, S., Gay, F., Lei, H., Bajko, J., et al. (2009). KDM1B is a histone H3K4 demethylase required to establish maternal genomic imprints. *Nature* 461, 415–418. doi:10.1038/nature08315

Dong, Y., Shi, O., Zeng, Q., Lu, X., Wang, W., Li, Y., et al. (2020). Leukemia incidence trends at the global, regional, and national level between 1990 and 2017. *Exp. Hematol. and Oncol.* 9, 14. doi:10.1186/s40164-020-00170-6

Fioravanti, R., Romanelli, A., Mautone, N., Di Bello, E., Rovere, A., Corinti, D., et al. (2020). Tranylcypromine-based LSD1 inhibitors: structure-activity relationships, antiproliferative effects in leukemia, and gene target modulation. *ChemMedChem* 15, 643–658. doi:10.1002/cmdc.201900730

Ganesan, A., Zhou, C., Wu, F., Lu, L., Wei, L., Pai, E., et al. (2017). Structure activity relationship and modeling studies of inhibitors of lysine specific demethylase 1. *Plos One* 12, e0170301. doi:10.1371/journal.pone.0170301

Harris, W. J., Huang, X., Lynch, J. T., Spencer, G. J., Hitchin, J. R., Li, Y., et al. (2012). The histone demethylase KDM1A sustains the oncogenic potential of MLL-AF9 leukemia stem cells. *Cancer Cell* 21, 473–487. doi:10.1016/j.ccr.2012.03.014

Huang, J., Sengupta, R., Espejo, A. B., Lee, M. G., Dorsey, J. A., Richter, M., et al. (2007). p53 is regulated by the lysine demethylase LSD1. *Nature* 449, 105–108. doi:10.1038/nature06092

Huang, M., Chen, C., Geng, J., Han, D., Wang, T., Xie, T., et al. (2017). Targeting KDM1A attenuates Wnt/β-catenin signaling pathway to eliminate sorafenib-resistant stem-like cells in hepatocellular carcinoma. *Cancer Lett.* 398, 12–21. doi:10.1016/j.canlet.2017.03.038

Jani, C. T., Ahmed, A., Singh, H., Mouchati, C., Al Omari, O., Bhatt, P. S., et al. (2023). Burden of AML, 1990-2019: estimates from the global burden of disease study. *JCO Glob. Oncol.* 9, e2300229. doi:10.1200/GO.23.00229

Ji, Y.-Y., Lin, S.-D., Wang, Y.-J., Su, M.-B., Zhang, W., Gunosewoyo, H., et al. (2017). Tying up tranylcypromine: novel selective histone lysine specific demethylase 1 (LSD1) inhibitors. *Eur. J. Med. Chem.* 141, 101–112. doi:10.1016/j.ejmech.2017.09.073

Kanouni, T., Severin, C., Cho, R. W., Yuen, N. Y. Y., Xu, J., Shi, L., et al. (2020). Discovery of CC-90011: a potent and selective reversible inhibitor of lysine specific demethylase 1 (LSD1). *J. Med. Chem.* 63, 14522–14529. doi:10.1021/acs.jmedchem.0c00978

Koda, Y., Sato, S., Yamamoto, H., Niwa, H., Watanabe, H., Watanabe, C., et al. (2022). Design and synthesis of tranylcypromine-derived LSD1 inhibitors with improved hERG and microsomal stability profiles. *ACS Med. Chem. Lett.* 13, 848–854. doi:10.1021/acsmedchemlett.2c00120

Kurmasheva, R. T., Erickson, S. W., Han, R., Teicher, B. A., Smith, M. A., Roth, M., et al. (2021). *In vivo* evaluation of the lysine-specific demethylase (KDM1A/LSD1) inhibitor SP-2577 (Seclidemstat) against pediatric sarcoma preclinical models: a report from the Pediatric Preclinical Testing Consortium (PPTC). *Pediatr. Blood and Cancer* 68, 68. doi:10.1002/pbc.29304

Lanka, G., Begum, D., Banerjee, S., Adhikari, N., P, Y., and Ghosh, B. (2023). Pharmacophore-based virtual screening, 3D QSAR, Docking, ADMET, and MD simulation studies: an *in silico* perspective for the identification of new potential HDAC3 inhibitors. *Comput. Biol. Med.* 166, 107481. doi:10.1016/j.compbiomed.2023.107481

Lee, M. G., Wynder, C., Schmidt, D. M., McCafferty, D. G., and Shiekhattar, R. (2006). Histone H3 lysine 4 demethylation is a target of nonselective antidepressive medications. *Chem. and Biol.* 13, 563–567. doi:10.1016/j.chembiol.2006.05.004

Li, C., Su, M., Zhu, W., Kan, W., Ge, T., Xu, G., et al. (2022). Structure–activity relationship study of indolin-5-yl-cyclopropanamine derivatives as selective lysine specific demethylase 1 (LSD1) inhibitors. *J. Med. Chem.* 65, 4335–4349. doi:10.1021/acs.jmedchem.1c02156

Liang, S., Geng, Y., Niu, M.-M., Zhang, Y., He, W., Li, J., et al. (2023). Discovery and biological evaluation of novel CARM1/HDAC2 dual-targeting inhibitors with anti-prostate cancer agents. *J. Enzyme Inhibition Med. Chem.* 38, 2241118. doi:10.1080/14756366.2023.2241118

Liu, H. M., Zhou, Y., Chen, H. X., Wu, J. W., Ji, S. K., Shen, L., et al. (2023). LSD1 in drug discovery: from biological function to clinical application. *Med. Res. Rev.* 44, 833–866. doi:10.1002/med.22000

Lokken, A. A., and Zeleznik-Le, N. J. (2012). Breaking the LSD1/kdm1a addiction: therapeutic targeting of the epigenetic modifier in AML. *Cancer Cell* 21, 451–453. doi:10.1016/j.ccr.2012.03.027

Martínez-Cuadrón, D., Megías-Vericat, J. E., Serrano, J., Martínez-Sánchez, P., Rodríguez-Arbolí, E., Gil, C., et al. (2022). Treatment patterns and outcomes of 2310 patients with secondary acute myeloid leukemia: a PETHEMA registry study. *Blood Adv.* 6, 1278–1295. doi:10.1182/bloodadvances.2021005335

Metzger, E., Wissmann, M., Yin, N., Müller, J. M., Schneider, R., Peters, A. H. F. M., et al. (2005). LSD1 demethylates repressive histone marks to promote androgen-receptor-dependent transcription. *Nature* 437, 436–439. doi:10.1038/nature04020

Miles, L. A., Bowman, R. L., Merlinsky, T. R., Csete, I. S., Ooi, A. T., Durruthy-Durruthy, R., et al. (2020). Single-cell mutation analysis of clonal evolution in myeloid malignancies. *Nature* 587, 477–482. doi:10.1038/s41586-020-2864-x

Newell, L. F., and Cook, R. J. (2021). Advances in acute myeloid leukemia. *Bmj* 375, n2026. doi:10.1136/bmj.n2026

Niebel, D., Kirfel, J., Janzen, V., Höller, T., Majores, M., and Gütgemann, I. (2014). Lysine-specific demethylase 1 (LSD1) in hematopoietic and lymphoid neoplasms. *Blood* 124, 151–152. doi:10.1182/blood-2014-04-569525

Prada-Arismendy, J., Arroyave, J. C., and Röthlisberger, S. (2017). Molecular biomarkers in acute myeloid leukemia. *Blood Rev.* 31, 63–76. doi:10.1016/j.blre.2016.08.005

Raval, K., and Ganatra, T. (2022). Basics, types and applications of molecular docking: a review. *IP Int. J. Compr. Adv. Pharmacol.* 7, 12–16. doi:10.18231/j.ijcaap.2022.003

Rubnitz, J. E., Gibson, B., and Smith, F. O. (2010). Acute myeloid leukemia. *Hematology/Oncology Clin. N. Am.* 24, 35–63. doi:10.1016/j.hoc.2009.11.008

Sacilotto, N., Dessanti, P., Lufino, M. M. P., Ortega, A., Rodríguez-Gimeno, A., Salas, J., et al. (2021). Comprehensive *in vitro* characterization of the LSD1 small molecule inhibitor class in oncology. *ACS Pharmacol. and Transl. Sci.* 4, 1818–1834. doi:10.1021/acsptsci.1c00223

Schenk, T., Chen, W. C., Göllner, S., Howell, L., Jin, L., Hebestreit, K., et al. (2012). Inhibition of the LSD1 (KDM1A) demethylase reactivates the all-trans-retinoic acid differentiation pathway in acute myeloid leukemia. *Nat. Med.* 18, 605–611. doi:10.1038/nm.2661

Schulz-Fincke, J., Hau, M., Barth, J., Robaa, D., Willmann, D., Kürner, A., et al. (2018). Structure-activity studies on N -Substituted tranylcypromine derivatives lead to selective inhibitors of lysine specific demethylase 1 (LSD1) and potent inducers of leukemic cell differentiation. *Eur. J. Med. Chem.* 144, 52–67. doi:10.1016/j.ejmech.2017.12.001

Shallis, R. M., Wang, R., Davidoff, A., Ma, X., and Zeidan, A. M. (2019). Epidemiology of acute myeloid leukemia: recent progress and enduring challenges. *Blood Rev.* 36, 70–87. doi:10.1016/j.blre.2019.04.005

Shi, Y., Lan, F., Matson, C., Mulligan, P., Whetstine, J. R., Cole, P. A., et al. (2004). Histone demethylation mediated by the nuclear amine oxidase homolog LSD1. *Cell* 119, 941–953. doi:10.1016/j.cell.2004.12.012

Somervaille, T., Salamero, O., Montesinos, P., Willekens, C., Perez Simon, J. A., Pigneux, A., et al. (2016). Safety, phamacokinetics (PK), pharmacodynamics (PD) and preliminary activity in acute leukemia of ory-1001, a first-in-class inhibitor of lysine-specific histone demethylase 1A (LSD1/KDM1A): initial results from a first-in-human phase 1 study. *Blood* 128, 4060. doi:10.1182/blood.v128.22.4060.4060

Tang, Y., Zheng, Y., Hu, X., Zhao, H., and Cui, S. (2024). Discovery of potent and selective PI3Kδ inhibitors for the treatment of acute myeloid leukemia. *J. Med. Chem.* 67, 6638–6657. doi:10.1021/acs.jmedchem.4c00094

Wang, J., Hevi, S., Kurash, J. K., Lei, H., Gay, F., Bajko, J., et al. (2008). The lysine demethylase LSD1 (KDM1) is required for maintenance of global DNA methylation. *Nat. Genet.* 41, 125–129. doi:10.1038/ng.268

Wang, Y., Zhang, H., Li, J., Niu, M.-M., Zhou, Y., and Qu, Y. (2022). Discovery of potent and noncovalent KRASG12D inhibitors: structure-based virtual screening and biological evaluation. *Front. Pharmacol.* 13, 1094887. doi:10.3389/fphar.2022.1094887

Wei, Q., Yao, K., Yang, J., Zhou, Q., Liu, P., Chen, J., et al. (2023). Structure-based drug design of novel triaminotriazine derivatives as orally bioavailable IDH2R140Q inhibitors with high selectivity and reduced hERG inhibitory activity for the treatment of acute myeloid leukemia. *J. Med. Chem.* 66, 12894–12910. doi:10.1021/acs.jmedchem.3c00835

Xie, Q., Bai, Y., Wu, J., Sun, Y., Wang, Y., Zhang, Y., et al. (2011). Methylation-mediated regulation of E2F1 in DNA damage-induced cell death. *J. Recept. Signal Transduct.* 31, 139–146. doi:10.3109/10799893.2011.552914

Zhang, S., Liu, M., Yao, Y., Yu, B., and Liu, H. (2021). Targeting LSD1 for acute myeloid leukemia (AML) treatment. *Pharmacol. Res.*, 164. doi:10.1016/j.phrs.2020.105335

Zheng, L., Zou, Y., Xie, T., Wu, X., Tan, Y., Mei, S., et al. (2023). Discovery of a dual tubulin and neuropilin-1 (NRP1) inhibitor with potent *in vivo* anti-tumor activity via pharmacophore-based docking screening, structure optimization, and biological evaluation. *J. Med. Chem.* 66, 16187–16200. doi:10.1021/acs.jmedchem.3c01572

Zheng, Y.-C., Yu, B., Chen, Z.-S., Liu, Y., and Liu, H.-M. (2016). TCPs: privileged scaffolds for identifying potent LSD1 inhibitors for cancer therapy. *Epigenomics* 8, 651–666. doi:10.2217/epi-2015-0002

Zhou, Y., Zou, Y., Yang, M., Mei, S., Liu, X., Han, H., et al. (2022). Highly potent, selective, biostable, and cell-permeable cyclic d-peptide for dual-targeting therapy of lung cancer. *J. Am. Chem. Soc.* 144, 7117–7128. doi:10.1021/jacs.1c12075

Frontiers in Pharmacology

Explores the interactions between chemicals and living beings

The most cited journal in its field, which advances access to pharmacological discoveries to prevent and treat human disease.

Discover the latest Research Topics

See more →

Frontiers

Avenue du Tribunal-Fédéral 34
1005 Lausanne, Switzerland
frontiersin.org

Contact us

+41 (0)21 510 17 00
frontiersin.org/about/contact